Pernate extraction from molybdenum oxide samples and synthesis of rhenium oxide nanoparticles and investigation of its application to remove methylene blue

Mohadeseh Haddadi*[a], Daryoush Afzali [b], Hadis Mirhoseni[c]

Corresponding Author E-mail: mohadeseh76hadadi@gmail.com

[a] Department of Nanotechnology, Graduate University of Advanced Technology, Kerman.

[b] Department of Environment, Institute of Science and High Technology and Environmental Sciences, Graduate University of Advanced Technology, Kerman.

[c] Department of Chemistry, Shahid Bahonar University, Kerman.

Abstract: There are many molybdenum compounds with copper minerals. In addition to molybdenum compounds, rhenium compounds are also found, which due to the increasing use of rhenium, it is necessary to separate these compounds and make nanoparticles and investigate their application. Here, rhenium oxide nanoparticles were synthesized by chemical precipitation method from molybdenum oxide dust. The average size of synthesized nanoparticles was 40.9 nm. Rhenium oxides are used in industry for many applications. Among the applications of rhenium oxide nanoparticles is their use as a catalyst in removing environmental pollutants such as organic dyes. Here, the effect of these nanoparticles on the removal of methylene blue, which is included in the category of aromatic compounds of environmental pollutants, was investigated. The effect of effective variables on removal was investigated. The results of the influence of different parameters such as pH, temperature, catalyst amount and intensity of ultrasonic waves on the methylene blue removal process were investigated. The parameters were optimized. In optimal conditions (5 mg of rhenium oxides nanoparticles, power intensity of 250, pH=10), they were able to remove more than 90% of methylene blue in 10 ml of aqueous solution with a concentration of 5 µg/ml.

Keywords: Rhenium oxide nanopartcles; Methylene blue removal; Sonocatalyst

Introduction

Rhenium, element number 75 of the periodic table, is one of the rarest elements in nature, it is difficult to extract rhenium directly [1].The researchers isolated the first gram of rhenium from 660 kg of molybdenite MoS2, which contained 2.4 ppm of rhenium [2].Except for the two cases of ore claimed in Kazakhstan and Australia, practically no ore or specific deposit has been discovered for rhenium [3]. Except for the two cases of ore claimed in Kazakhstan and Australia, practically no ore or other dedicated deposits have been discovered for rhenium [4]. Chile has the largest amount of rhenium reserves.

Today, most of the world's rhenium is mainly supplied from these sources

1) Molybdenite concentrate
2) Copper concentrate
3) Byproduct of lead, zinc, cadmium factories
4) Metal waste containing rhenium
5) Wastes of chemical industry catalysts [5].

One of the reasons for the increasing importance of rhenium is its unique properties (chemical, physical and mechanical properties) that have made rhenium suitable for various applications. As this metal is considered as one of the most expensive and strategic elements after gold and platinum.

Physical and chemical properties of rhenium:

Physical properties: Rhenium, an element of group 7 of the periodic table, has the same physical properties as group 6 "molybdenum and tungsten", and on the other hand, it shows the characteristics of the platinum group. The color of molten rhenium is white and when it is powdered in solid form, it is silver gray [6]. Rhenium is a very hard and wear-resistant element.

Chemical properties: rhenium has many oxidation states from -1 to +7. And it is called the only element with eight capacity. Rhenium is similar to group 7 elements in terms of chemical properties. Rhenium starts to oxidize at a temperature higher than 300 degrees [7].

Rhenium does not react with strong acids such as hydrofluoric acid and sulfuric acid; but it dissolves in nitric acid. Rhenium reacts with silicon, boron, and phosphorus at high temperature [8].

The most important rhenium oxide compounds are: Re2O7, ReO2, ReO3 [9]. Rhenium oxides have been investigated as catalytic materials in the oxidation reactions of sulfur dioxide to sulfur trioxide, sulfite to sulfate, and nitrite to nitrate [10]. So far, various synthesis methods have been reported for the synthesis of rhenium oxide nanoparticles

Introduction of methylene blue

22nd Iranian Chemistry Congress (ICC22)
Iranian Research Organization for Science and Technology (IROST)
13-15 May 2024

03231-97589

Methylene blue is one of the aromatic chemical dyes. The chemical formula of this compound is C16H18N3SCl and it has a molar mass of 319.85 g/mol and it is blue in color when dissolved in water [11].

Experimental Section
Some of the molybdenum oxide dust sample was removed and then heated by adding (distilled water, sulfonic acid, hydrogen peroxide) on the heater stirrer at a temperature of 90°. Then the solution containing the sediment was filtered. The obtained solution was heated again by adding amounts of (distilled water, sulfonic acid, hydrogen peroxide) as in the previous step and then filtered. After straining and adding some amounts of lime and making the solution alkaline, the solution was heated and then after straining the obtained solution was placed in a paraffin bath. In the next step, rhenium oxide precipitate was obtained by adding iron and acid. The sediment was smoothed, in order to remove the impurities, the sediment was washed with hydrochloric acid, and then the prepared sediment was placed inside the oven at a temperature of 70 degrees.

Results and Discussion
Among the applications of rhenium oxide nanoparticles is their use as a catalyst in removing or destroying environmental pollutants such as organic dyes. Here, rhenium oxide nanoparticles were synthesized by chemical precipitation method with an average size of 40.9 nm, and the effect of these nanoparticles on the removal of methylene blue, which is included in the category of aromatic compounds of environmental pollutants, was investigated. The effect of effective variables on removal was investigated.

The results of the effect of different parameters such as pH, temperature, catalyst amount and intensity of ultrasonic waves on the methylene blue removal process were investigated. Using these data, the optimal conditions for this process were predicted. In optimal conditions (5 mg of rhenium oxides nanoparticles, power intensity of 250, pH=10), they were able to remove more than 90% of methylene blue in 10 ml of aqueous solution with a concentration of 5 μg/ml.

Conclusions
In this work, we report the successful synthesis of rhenium oxide nanoparticles from molybdenum oxide dust. Rhenium oxide nanoparticles were synthesized by chemical deposition method. Prepared rhenium oxide nanoparticles were used as a sonocatalyst to remove methylene blue. By optimizing various parameters, the synthesized nanoparticle is able to remove a high percentage of methylene blue.

References
[1] Lebedev K. B. (1962) "The Chemistry of Rhenium", Butterworths, London.

[2] Habashi F. (2010) "Rhenium: Chemistry, Metallurgy and History", TECSUP, Invest. Apl.

[3] Šajn, R., Ristović, I., & Čeplak, B. (2022). Mining and Metallurgical Waste as Potential Secondary Sources of Metals A Case Study for the West Balkan Region. Minerals, 12(5), 547.

[4] Abisheva, Z. S., Zagorodnyaya, A. N., & Bekturganov, N. S. (2011). Review of technologies for rhenium recovery from mineral raw materials in Kazakhstan. *Hydrometallurgy*, *109*(1-2), 1-8.

[5] Hariat, M. H. and Hasani, M., "Rhenium recovery from sarcheshmeh molybdenite concentrate",The First Iranian Conference on Metallurgy of Non-Ferrous Metals, Sarcheshmeh, (1997).

[6] A. Millensifer, T., Sinclair, D., Jonasson, I., & Lipmann, A. (2014). Rhenium. Critical metals handbook, 340-360

[7] Nadler H. G. (2012) "Rhenium and Rhenium Compounds", Ullmann's encyclopedia of industrial chemistry, 527-537

[8] Kinas, S., Jermakowicz-Bartkowiak, D., Pohl, P., Dzimitrowicz, A., & Cyganowski, P. (2023).

[9] G. W. Leddicotte , "The Radiochemistry of Rhenium", National Academy of Science, April 1981.

[10] Rukini, A., Rhamdhani, M. A., Brooks, G. A., & Van den Bulck, A. (2022). Metals production and metal oxides reduction using hydrogen: a review. Journal of Sustainable Metallurgy, 8(1), 1-24.

[11] Kannan, N., & Sundaram, M. M. Kinetics and mechanism of removal of methylene blue by adsorption on various carbonsa comparative study.Dyes and pigments, 2001, 51, 25-40

The influence of Bi2Ce2O7 metal oxides for the photocatalytic degradation of tetracycline in water

Zohreh Zafari*, Ali Reza mahjoub*

Corresponding Author E-mail: Zohre.zafari22@gmail.com

Abstract: The Bi2Ce2O7 photocatalysts were prepared by precipitated method. the photocatalysts were characterized by XRD and SEM. the photocatalytic activities were appraised by degradation of tetracycline. The result showed that, the metal oxides photocatalysts were successfully prepared and sample UV spectrum indicated relevant effect on photodegradation of tetracycline at the right time.

Keywords: Bi2Ce2O7, tetracycline, photocatalyst

Introduction

Tetracycline pollution is a growing global threat to aquatic and terrestrial biodiversity due to its unprecedented use in aquaculture, livestock, and human disease prevention. [1]. Tetracycline residues have frequently been detected in multi-environmental media, and it could induce antibiotic resistance genes (ARGs) in microorganisms [2]. Photodegradation of water contaminants by semiconductors is a safe and non-costly methods[3] . In the recent past decade, bismuth metal oxides have established consideration because of their electronic band structure characterises appropriate narrow band-gap for visible light photocatalytic activity [4]. The recombination rate of electron–hole pairs in bismuth relatively high, so leading to a poor efficiency of photocatalytic reaction, therefore Researchers suggested that ions of rare earth metal have the ability to speed up the absorption of photogenerated electron–hole pairs during the photocatalytic reaction due to presence of special f electron orbital [5]. Bi2Ce2O7 which is considered as a promising optical material with a band gap of 2.3 eV has been investigated for solar photocatalytic activity materials. The low band gap systems allow easily to fine tune the band gap, also this system contains less toxic elements like Bi and Ce would make them eco-friendly host material [6]. this substance can be useful in water pollutant destruction that investigated in this article.

Experimental Section

BCO was synthesized by solution combustion. (NH4)2Ce(NO3)2·6H2O and Bi(NO3)3·6H2O were taken in stoichiometric amounts and dissolved in double distilled water to make a clear solution. Bi(NO3)3·6H2O was dissolved in nitric acid to make a clear solution before adding (NH4)2Ce- (NO3)2·6H2O. A stoichiometric amount of fuel was added to the clear solution and the resulting mixture was kept in a preheated furnace maintained at 500 °C.

Results and Discussion

The XRD analysis

The phase analysis of the powdered materials (Bi2Ce2O7) was characterized by X-ray diffraction analysis. The calcined sample's XRD pattern exclusively shows diffraction peaks corresponding to the fluorite structure, indicating the successful insertion of Bi3+ ions in the ceria lattice(fig.1).
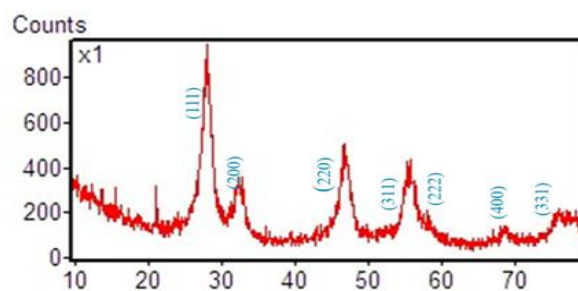

Fig.1: Bi2Ce2O7 XRD pattern

Photocatalytic degradation of tetracycline

UV-Vis analysis

The phothocatalytic performance was measured by the degradation of tetracyclin under visible light. Figure 2 shows the decrease in the adsorption peaks of tetracycline. The figure 2 shows the degradation of antibiotics over the Bi2Ce2O7 photocatalysts.

For evaluation the removal yield into prepared sample, the blank experiment was also investigated for 30 min. the data in the figure 2 and table1 show different photocatalytic degradation rates after 90 min.
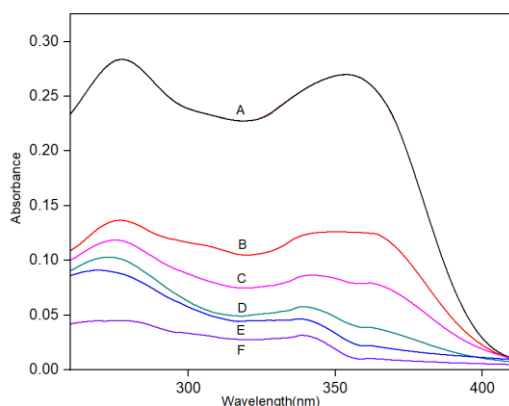
Fig.2: A.Sample (tetracycline) / B.Dark (30min) / C. 15 min/ D. 30 min/ E. 45 min/ F. 60 min

Table1: Photodegradation of tetracycline by prepared photocatalysts in 90 min

Time	Degradation Percent
Dark (30 min)	48
15 min	68
30 min	82
45 min	91
60 min	96

Conclusions

In summary, we report a simple precipitated route for the fabrication of pure Bi2Ce2O7 semiconductor. The as prepared Bi2Ce2O7 indicate the better photocatalytic decomposition for degrading tetracycline.

The XRD analysis showed that prepared photocatalysts are present in fluorite phase. By examining the tauc equation, determined the band gap in district of 2.3 ev which due to cerium element in combination.

The enhancements in the photocatalytic activity is attributed to the reduction rate of electron-hole recombination leading to higher charge separation .the photodegradation that report in paper showed the higher degradation in short time.

References

[1] Ahmad, F., Zhu, D., & Sun, J. (2021). Environmental fate of tetracycline antibiotics: degradation pathway mechanisms, challenges, and perspectives. *Environmental Sciences Europe*, *33*(1), 64.

[2] Zyoud, A. H., Zubi, A., Zyoud, S. H., Hilal, M. H., Zyoud, S., Qamhieh, N., ... & Hilal, H. S. (2019). Kaolin-supported ZnO nanoparticle catalysts in self-sensitized tetracycline photodegradation: zero-point charge and pH effects. *Applied Clay Science*, *182*, 105294.

[3] Chawla, H., Chandra, A., Ingole, P. P., & Garg, S. (2021). Recent advancements in enhancement of photocatalytic activity using bismuth-based metal oxides Bi2MO6 (M= W, Mo, Cr) for environmental remediation and clean energy production. *Journal of Industrial and Engineering Chemistry*, *95*, 1-15.

[4] Raza, W., Bahnemann, D., & Muneer, M. (2018). A green approach for degradation of organic pollutants using rare earth metal doped bismuth oxide. *Catalysis Today*, *300*, 89-98.

[5] Saha, D., Madras, G., & Row, T. N. G. (2012). Synthesis and structure of Bi 2 Ce 2 O 7: a new compound exhibiting high solar photocatalytic activity. *Dalton Transactions*, *41*(32), 9598-9600.

[6] Saha, D., Madras, G., & Row, T. N. G. (2012). Synthesis and structure of Bi 2 Ce 2 O 7: a new compound exhibiting high solar photocatalytic activity. *Dalton Transactions*, *41*(32), 9598-9600

22nd Iranian Chemistry Congress (ICC22)
Iranian Research Organization for Science and Technology (IROST)
13-15 May 2024

03231-97589

IROST

Construction of Electrochemical Sensor Based on ZnO-PANI Nanocomposite Modified Carbon Paste Electrode for the Determination of Methotrexate

Mohammad Shahsavani, Javad Tashkhourian[*]
Corresponding Author E-mail: tashkhourian@shirazu.ac.ir
Chemistry Department, Shiraz University, Shiraz 71454, Iran.

Abstract: Analyzing the levels of anticancer medications in biological samples and body fluids reveals important details on the course and effects of chemotherapy. In this study, an electrochemical sensor based on zinc oxide-polyaniline (ZnO-PANI) modified carbon paste electrode was developed for the voltammetric determination of methotrexate (MTX). Studying the electrochemical characteristics of modified electrode using cyclic voltammetry (CV) and square wave voltammetry (SWV) techniques revealed the modified electrode can exhibit excellent catalytic activity, wide dynamic linear range, low detection limit, good sensitivity, and high accuracy. Under optimized conditions, using the developed electrochemical sensor, a linear response range of 0.005–100.0 μM with a limit of detection of 1.8 nM was achieved for MTX. Finally, the ZnO-PANI/CPE sensor was successfully applied toward the determination of MTX in the biological matrix.

Keywords: Electrochemical sensor; Methotrexate; Polyaniline; Zinc oxide; Square wave voltammetry

Introduction

Methotrexate (MTX) (2,4-diamine-N10-methylpteroyl-glutamic acid), is a member of the antimetabolite and antineoplastic medication classes. It slows down the immune system to prevent it from attacking your body's cells and shows significant antitumor activity in childhood acute leukemia and head and neck cancer, psoriasis, rheumatoid arthritis, and other neoplastic diseases[1]. On the other hand, MTX leads to certain severe side effects, such as hepatic failure, bone marrow suppression, and hypoalbuminuria. Because of the high dose levels and long duration of treatments of chemotherapy, it becomes very important to develop a simple, rapid, and cost-effective method for timely on-site analysis of physiological samples for the quantitative analysis of active MTX concentration[2]. Among the analytical techniques, due to their advantages such as high sensitivity, good stability, ease of on-site applications, and appropriate accuracy, electrochemical methods have received great attention for determining pharmaceutical chemical components and drugs in real clinical samples. Herein, we investigated the fabrication and development of an electrochemical sensor for the determination of MTX in biological samples using zinc oxide and polyaniline-modified carbon paste electrode (ZnO/PANI/CPE). The electrochemical behavior of the analyte and the electrochemical characterization of the ZnO/PANI/CPE were investigated by cyclic voltammetry and square wave voltammetry. It was shown by the results that ZnO-PANI nanocomposite has excellent catalytic activity, wide dynamic linear range, low detection limit, good sensitivity, and high accuracy.

Experimental Section

The bare carbon paste electrode (BCPE) was prepared by hand-mixing graphite powder with nujol oil at a ratio of 70:30 (w/w). A certain amount of ZnO/PANI was exerted to create the modified electrode with different percentages. The resulting mixture and nujol oil were blended by hand mixing until a uniform paste was obtained. The resulting paste was inserted at the bottom of a plastic tube (internal diameter 1.0 mm) and an electrical connection was implemented by a stainless steel wire fitted into the tube. A fresh electrode surface was obtained by squeezing out a small portion of the paste and polishing it with filter paper until a smooth surface was obtained.

Results and Discussion

The prepared nanocomposite is characterized through scanning electron microscopy (SEM), Fourier transform infrared spectroscopy (FT-IR), X-ray photoelectron spectroscopy (XPS), and X-ray diffraction (XRD). The morphology of the synthesized ZnO-PANI was investigated and the SEM images are shown in Fig.1. Fig. 1a depicts the surface morphology of PANI. It is evident that the PANI sample, as produced, displays a well-defined morphology that is fiber-like. These nanofibers seem to be interconnected with each other and have merged in a web-like structure with empty spaces. For ZnO-PANI (Fig. 1b), the distribution pattern between ZnO-NPs and the PANI revealed that the PANI nanofibers were surrounded by ZnO-NPs. It can be considered that the ionic interaction between PANI and the ZnO-NPs has led to the successful formation of ZnO/PANI
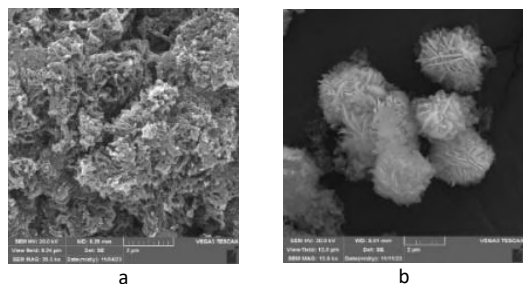
Fig.1: SEM images of (a) PANI, and (b) ZnO-PANI

In order to investigate the performance of the modified electrode, the cyclic voltammograms of the bare CPE and ZnO-PANI/CPE in a solution containing methotrexate with a concentration of 1.0 mM were measured. The obtained results show an irreversible oxidation peak at 0.97 V. The significant increase in the current on the modified electrode compared to the unmodified electrode shows that this modifier improves the electron transfer process of methotrexate on the electrode.
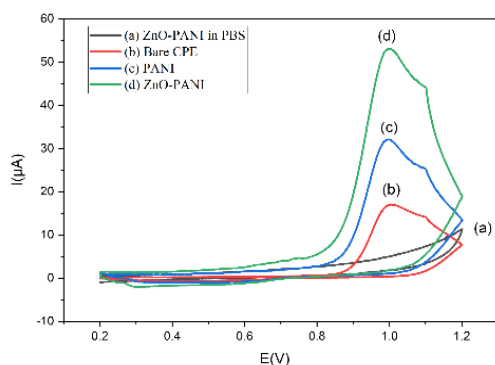

Fig.2: CV recorded at (a) ZnO-PANI in the absence of MTX (1.0mM) in PBS (0.1M, pH=2.0), (b) Bare CPE, (c) PANI/CPE, and (d) ZnO-PANI/CPE in presence of MTX (0.5mM) in PBS (0.1 M, pH=2.0). Scan rate 50 mV/s.

In this study, square wave voltammetry (SWV) was used as an effective electrochemical method to detect the oxidation reaction of MTX, which was performed under optimal conditions. The SWV curves (Fig. 3a) clearly exhibited that the peak current of MTX increased as the concentration increased from 0.005 µM to 100.0 µM. Afterward, two linear relationships could be observed by drawing the calibration curves in Fig. 3b,c. The corresponding linear regression equations were I (µA) = 3.1303 C (µM) + 1.4556(R^2 = 0.997) in the range of 0.005 µM to 1.0 µM and I (µA) = 0.5601 C (µM) + 9.4303(R^2 = 0.995) in the range of 1.0 µM to 100.0 µM. After that, the limit of detection (LOD) of the prepared sensor was estimated to be 1.8 nM. Finally, the ZnO-PANI/CPE was successfully applied toward the determination of MTX in the real samples. The results indicated a very good

accuracy in terms of recoveries for the determination of MTX in urine and plasma samples.
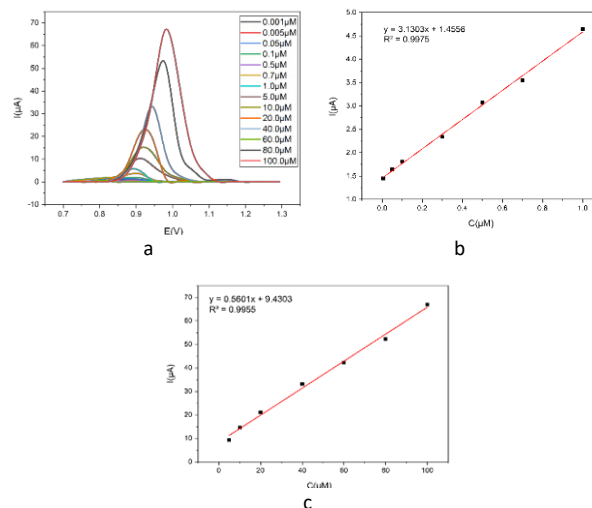

Fig.3: (a) SWV curves of the ZnO-PANI/CPE in different concentrations of MTX: 0.005, 0.05, 0.1, 0.5, 0.7, 1.0, 5.0, 10.0, 20.0, 40.0, 60.0, 80.0, and 100.0 µM. (b, c) Calibration curves of MTX under the optimized conditions.

Conclusions

The results of the present study showed the successful construction of ZnO-PANI nanocomposite for the voltammetric detection of methotrexate. The modified electrode showed high electrocatalytic activity and acceptable analytical performance for the methotrexate detection. Under optimized conditions, the linear response for the determination of methotrexate was obtained in the concentration range from 0.005 to 100.0 µM and the detection limit was found to be 1.8 nM. Moreover, the modified electrode was successfully applied for the determination of MTX content in real samples (urine and plasma samples) with excellent recoveries.

References

[1] Wang, Y., Li, S., Gao, Y., Du, B., Vafaei, S., Li, M., ... & Chen, Y. (2023). Synthesis of poly (L-cysteine)/g-C3N4 modified glassy carbon electrodes for electrochemical detection of methotrexate as a medicine for the treatment of breast cancer in pharmaceutical fluid samples. *Chemosphere*, *331*,138769.

[2] Göksel, Y., Zor, K., Rindzevicius, T., Thorhauge Als-Nielsen, B. E., Schmiegelow, K., & Boisen, A. (2021). Quantification of methotrexate in human serum using surface-enhanced Raman scattering Toward therapeutic drug monitoring. *ACS sensors*, *6*(7), 2664-2673.

Spectroscopic study of [(C$_2$H$_5$)(C$_6$H$_5$)(S)-(−)CHNH$_3$][(C$_6$H$_5$)(NC$_5$H$_4$NH)P(O)(O)]

Farnaz Eslami,[a] Mehrdad Pourayoubi*[b], Fahimeh Sabbaghi,[c] Sahar Baniyaghoob[a]

Corresponding Author E-mail: pourayoubi@um.ac.ir

[a] Department of Chemistry, Science and Research Branch, Islamic Azad University, Tehran, Iran.

[b] Department of Chemistry, Faculty of Science, Ferdowsi University of Mashhad, Mashhad, Iran.

[c] Department of Chemistry, Zanjan Branch, Islamic Azad University, Zanjan, Iran.

Abstract: A two-step reaction of (C$_6$H$_5$)P(O)Cl$_2$ with NC$_5$H$_4$NH$_2$ and NH$_2$-(S)-(−)CH(C$_2$H$_5$)(C$_6$H$_5$) in the presence of an HCl scavenger (N(C$_2$H$_5$)$_3$) yielded [(C$_2$H$_5$)(C$_6$H$_5$)(S)-(−)CHNH$_3$][(C$_6$H$_5$)(NC$_5$H$_4$NH)P(O)(O)]. In the ^{13}C{^{1}H}-NMR spectrum, some phosphorus-carbon couplings were observed ($^nJ_{CP}$, n = 1, 2 and 3 for the phenyl group directly attached to phosphorus and $^2J_{CP}$ for amino-pyridinyl fragment). The main topics related to ^{31}P{^{1}H}-NMR, ^{1}H-NMR, ^{13}C{^{1}H}-NMR and IR were addressed.

Keywords: NMR; phosphorus-carbon coupling constant; IR.

Introduction

Phosphonamidates are well-known in the field of medicinal chemistry, to form some pro-drugs, and anti-bacterial, anti-infective and anti-viral materials [1–5]. Besides, some phosphonamide compounds were prepared as flame retardants [6]. In the salts including the [O—P=O]$^−$ moiety, the strengths of hydrogen bonds, which assisted from the existing negative charge, were discussed. In order to spectroscopy/structural study, it is possible to use various segments for binding to phosphorus and/or as counter-cation to design the targeted structures [7].

Here, we report on the synthesis and spectroscopic characterization of a new cation-anion compound, [(C$_2$H$_5$)(C$_6$H$_5$)(S)-(−)CHNH$_3$][(C$_6$H$_5$)(NC$_5$H$_4$NH)P(O)(O)] (Scheme 1).

Experimental Section

The title compound was prepared in two steps, as follows: (step 1) to a solution of (C$_6$H$_5$)P(O)Cl$_2$ in chloroform, a solution of (NC$_5$H$_4$NH$_2$) and triethylamine (1:1:1 mole ratio) in the same solvent was added at 273 K. After 5 h of stirring, the solution which includes (NC$_5$H$_4$NH)(C$_6$H$_5$)ClP(O)/[N(C$_2$H$_5$)$_3$HCl] was used for the next step. (Step 2), to the solution noted, a solution of NH$_2$-(S)-(−)CH(C$_2$H$_5$)(C$_6$H$_5$) and triethylamine (1:1:1 mole ratio) in chloroform was added at 273 K. After 5 h of stirring, the solvent was removed in a vacuum and the obtained solid was washed with distilled water to remove (C$_2$H$_5$)$_3$NHCl salt (and partially hydrolysis of compound). Colorless crystals were obtained from a CHCl$_3$ solution after slow evaporation of solvent at room temperature.

Analytical data: IR (KBr, v, cm^{-1}): 3337, 3198, 3059, 2964, 2924, 2875, 2665, 2105, 1963, 1899, 1510, 1485, 1446, 1386, 1301, 1186, 1134, 917, 764, 699, 522, 460. ^{1}H-NMR (400.22 MHz, DMSO-d$_6$): δ = 8.64 (broad/exchanged, NH), 8.00 (d, J = 4.0 Hz, 1H), 7.71 (m, 2H), 7.50 – 7.25 (m, 10H), 6.93 (s, 1H, NH), 6.60 (m, 1H), 4.01 (dd, J = 9.2, 5.6 Hz, 1H), 1.98 (m, 1H), 1.79 (m, 1H), 0.71 (t, J = 7.4 Hz, 3H). ^{13}C{^{1}H}-NMR (100.64 MHz, DMSO-d$_6$): δ = 157.24 (d, J = 5.0 Hz), 147.84 (s), 141.22 (d, J = 160.8 Hz), 138.83 (s), 137.34 (s), 131.23 (d, J = 9.0 Hz), 129.24 (s), 129.00 (s), 128.66 (s), 127.99 (s), 127.82 (d, J = 12.7 Hz), 114.37 (s), 110.55 (s), 56.30 (s), 28.06 (s), 10.53 (s). ^{31}P{^{1}H}-NMR (162.01 MHz, DMSO-d$_6$): δ = −0.84 (s).
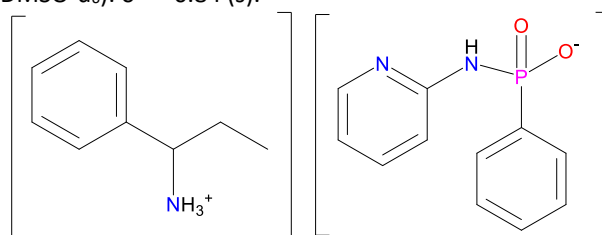
Scheme 1: Chemical structure of [(C$_2$H$_5$)(C$_6$H$_5$)(S)-(−)CHNH$_3$][(C$_6$H$_5$)(NC$_5$H$_4$NH)P(O)(O)]

Results and discussion

The ^{31}P{^{1}H}-NMR spectrum shows a singlet phosphorus signal at −0.84 ppm in DMSO-d$_6$. The N—H protons (^{1}H-NMR spectrum) of the chiral ammonium component and amino-pyridinyl moiety appear at 8.64 and 6.93 ppm as broad peaks.

In the ^{13}C{^{1}H}-NMR spectrum, the phenyl ring directly bonded to phosphorus appear three well-resolved doublets: the doublet centered at 141.22 ppm ($^1J_{CP}$= 160.8 Hz) is related to the carbon atom attached to phosphorus, and the two doublets at 131.23 ppm (J = 9.0 Hz) and

22nd Iranian Chemistry Congress (ICC22)
Iranian Research Organization for Science and Technology (IROST)
13-15 May 2024

03231-97589

IROST

127.82 ppm (J = 12.7 Hz) associate to the *ortho*- and *meta*-carbon atoms of phenyl. The pyridinyl fragment also shows a doublet at 157.24 ppm ($^2J_{CP}$= 5.0 Hz), which is assigned to the carbon atom with a two-bond separation from phosphorus (*ipso*-carbon atom) (Figure 1). None of the carbon signal of chiral ammonium cation show coupling with phosphorus.

The broad overlapped band within 3337 to 2665 cm^{-1} (in the IR spectrum) is an evidence to the presence of strong hydrogen bonding between $[(C_2H_5)(C_6H_5)(S)-(-)CHNH_3]^+$ cation and $[(C_6H_5)(NC_5H_4NH)P(O)(O)]^-$ anion in the prepared salt.
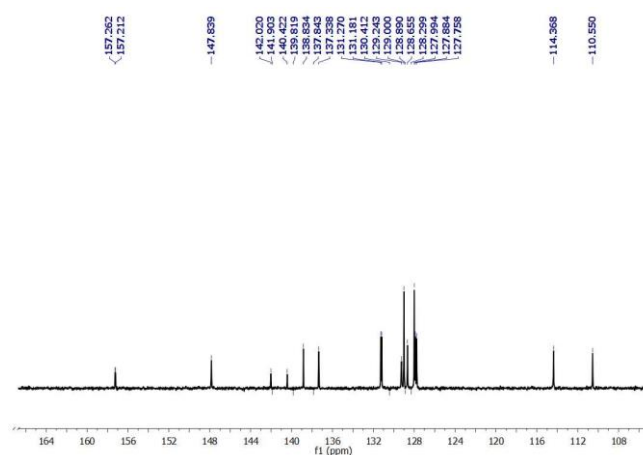
Fig. 1: $^{13}C\{^1H\}$-NMR of $[(C_2H_5)(C_6H_5)(S)-(-)CHNH_3][(C_6H_5)(NC_5H_4NH)P(O)(O)]$ within 108 to 160 ppm (aromatic region)

Conclusion

Spectroscopic features of $[(C_2H_5)(C_6H_5)(S)-(-)CHNH_3][(C_6H_5)(NC_5H_4NH)P(O)(O)]$ salt were studied. In the $^{13}C\{^1H\}$-NMR spectrum, the phenyl group directly attached to phosphorus shows three well-resolved doublets (^1J, ^2J and ^3J), and the pyridinyl moiety shows a doublet for the carbon atom with a two-bond separation from phosphorus. In the ^1H-NMR spectrum, the N—H protons of chiral ammonium cation and amino-pyridinyl fragment appear as broad peaks.

References

[1] Voráčová, M., Matej, Z., Yli-Kauhaluoma, J., & Kiuru, P. (2023). Harvesting phosphorus-containing moieties for their antibacterial effects. Bioorganic & Medicinal Chemistry, 96, 117512. https://doi.org/10.1016/j.bmc.2023.117512.

[2] Zhang, Q., Peng, Y., Hou, J., Chen, Y., Liu, B., Zhang, P., Yu, W., & Chang, J. (2022). An O-benzyl phosphonamidate prodrug of tenofovir for the treatment of hepatitis B virus infection. Journal of Medicinal Chemistry, 65(13), 9493-9505. https://doi.org/10.1021/acs.jmedchem.2c00869.

[3] Qureshi, A., Ouattara, L. A., El-Sayed, N. S.,Verma, A., Doncel, G. F., Choudhary, M. I., Siddiqui, H., & Parang, K. (2022). Synthesis and evaluation of anti-HIV activity of mono- and di-substituted phosphonamidate conjugates of tenofovir. Molecules, 27(14), 4447. https://doi.org/10.3390/molecules27144447.

[4] Oulding, L. V., Kiss, E., Vrancken, R., Goris, N., Luo, M., Groaz, E., Herdewijn, P., & Dixon, L. (2022). O-2-Alkylated cytosine acyclic nucleoside phosphonamidate prodrugs display pan-genotype antiviral activity against African swine fever virus. mSphere, 7(6), e00378-22. https://doi.org/10.1128/msphere.00378-22.

[5] Alissa, S. A., Alghulikah, H. A., Alothman, Z. A., Osman, S. M., Del Prete, S., Capasso, C., Nocentini, A., & Supuran, C. T. (2020). Phosphonamidates are the first phosphorus-based zinc binding motif to show inhibition of β-class carbonic anhydrases from bacteria, fungi, and protozoa. Journal of Enzyme Inhibition and Medicinal Chemistry, 35(1), 59-64. https://doi.org/10.1080/14756366.2019.1681987.

[6] Hu, J., Jin, Zu., Zhong, H., Zhan, H., Zhou, Y., & Li, Z. (2012). A new phosphonamidate as flame retardant additive in electrolytes for lithium ion batteries. Journal of Power Sources, 197, 297-300. https://doi.org/10.1016/j.jpowsour.2011.09.012.

[7] Eslami, F., Pourayoubi, M., Sabbaghi, F., Dušek, M., Baniyaghoob, S., & Skořepová, E. (2022). Database Survey of Single-and-Half Phosphorus–Oxygen Bonds in Salts with the C_2PO_2 Segment: Crystal Structure of $[NH_2C_5H_4NH][(C_6H_5)_2P(O)(O)]\cdot 2H_2O$. Crystallography Reports, 67(2), 218-223. https://doi.org/10.1134/S1063774522020043.

Quantitative analysis of Citrullus colocynthis fruit and seed extracts by GC-MS coupled with Multivariate curve resolution method

Baghgoli Tayebeh, Mousavi Mehdi*, Amiri Fatemeh

Corresponding Author E-mail: mmousavi@mail.uk.ac.ir

Department of Chemistry, Faculty of Sciences, Shahid Bahonar University of Kerman, P.O. Box 76175-133, Kerman, Iran.

Abstract: In traditional medicine Citrullus colocynthis is known as a medicinal plant which is effective in treatment of diabetes. Citrullus colocynthis seed and fruit constituents were extracted using n-pentane solvent and were analyzed by GC/MS technique. Due to the complexity of the obtained chromatograms, MCR method were applied for more accurate and precise analysis of the chromatograms.
Keywords: Citrullus colocynthis; GC-MS; solvent extraction; Multivariate curve resolution

Introduction

Plants are used generally as resources for food and medicines by humans. Citrullus colocynthis is mostly found in Africa, Asia and many regions of Iran. In traditional medicine a broad range of pharmacological activities such as antidiabetic, hypolipidemic, antineoplastic, antioxidant, anti-inflammatory, profibrinolytic, analgesic, antiallergic, antimicrobial, pesticidal and immunostimulant are attributed to Citrullus colocynthis. Among them, its anti-diabetic activity is prominent [1,2].

Gas chromatography/mass spectrometry (GC/MS) is a very powerful separation technique for multi component mixtures of analytes. But, for real sample analysis some problems may arises due to baseline drift, low S/N ratio and co-elution. To reduce the effect of these problems, multivariate curve resolution techniques have been applied in chromatographic studies [3.4].

The aim of this study is qualitative and quantitative analysis of the fruit and seeds exteracts of citrullus colocynthis. Thus, a combination of GC-MS and MCR techniques were used for analysis of the samples.

Experimental Section

The plant Citrullus colocynthis was collected from Rudbar town located at south of Jiroft city in Kerman province. The fruit of Citrullus colocynthis were dried under shade at room temperature for 3 days. Then, 70 and 27 g of the fruit and seeds of Citrullus colocynthis were ground separately and in order to extract their constituents, 100 ml of n-pentan was added to each samples. The mixtures were stirred for 30 minute every day during the 7 dayes of extractions. After that, they were centrifused and filterd. The exterated samples were analyzed by injecting 0.1μL of the sample to GC_MS followed by analysing the chromatograms by MCR method.

Results and Discussion

The total ion chromatograms (TIC) of the Citrullus colocynthis samples are shown in Fig. 1. Basically, the direct method of analysis based on similarity index and retention index comparison are applied for identification and assignment of constituting compounds. Unfortunately, for some of the chromatographic peaks at different scans numbers, various compounds may be attributed to the single peak. Therefore, MCR method was used for more precise analysis of the chromatograms. The results of an analysis on a peak cluster with the MCR method are shown in Fig. 2. and Table .1. The number of components assigned to the fruit and the seed extracts of Citrullus colocynthis by direct and MCR methods are 53 and 42, respectively.
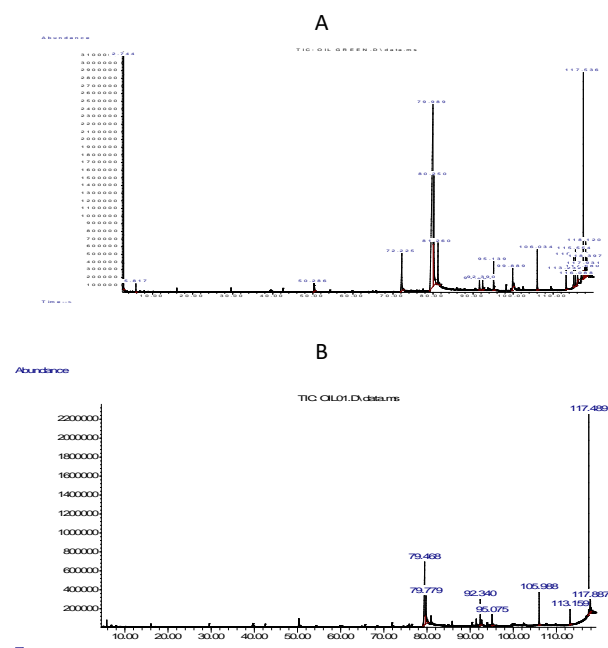

Fig.1: total ion chromatogram of A) fruit B) seed extract of citrullus colocynthis
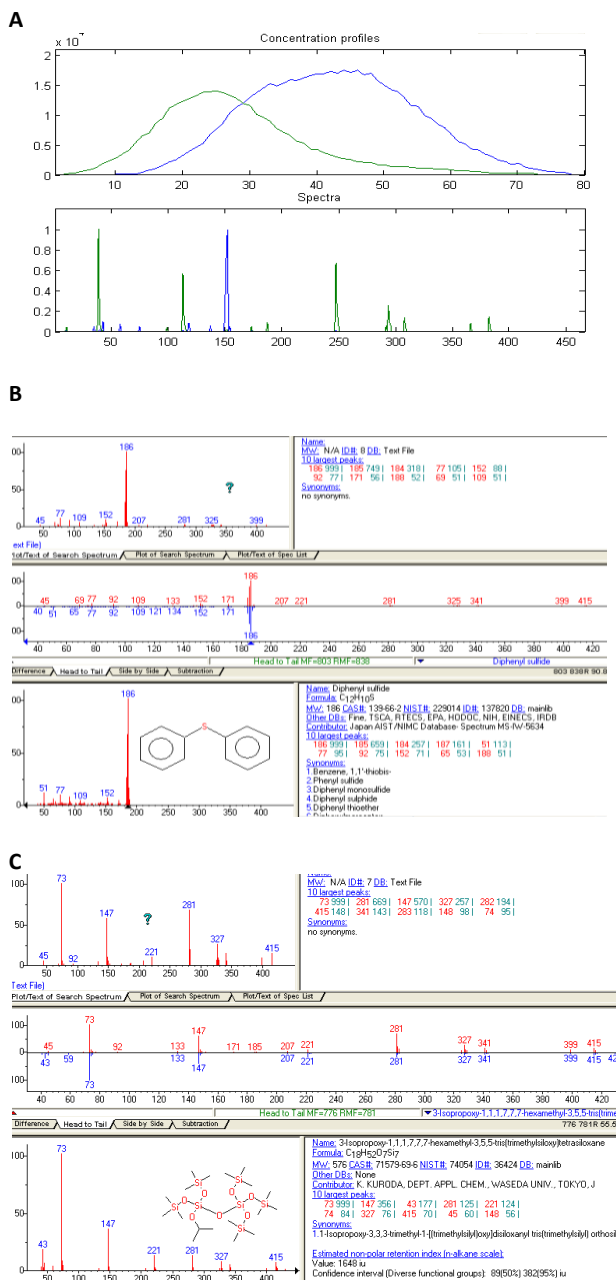
22nd Iranian Chemistry Congress (ICC22)
Iranian Research Organization for Science and Technology (IROST)
13-15 May 2024

03231-97589

IROST

A

B

C

Fig.2: MCR analysis of a peak cluster A) MCR_ALS output profiles B) first compound C) second compound

Table1: Comparison of direct and MCR results method for a peak cluster

Method	Direct analysis	MCR analysis
Number of compounds	1	2
Name of compound	Diphenyl sulfide	Diphenyl sulfide
		3-Isopropoxy-1,1,1,7,7,7-hexamethyl
Rmatch	78	90.7
		81.9

Conclusions

More information with higher precision and accuracy can be obtained from raw experimental data by coupling GC-MS and chemometric resolution methods such as MCR-ALS. In the present work, the number of componentes that were accuratley identified and assigend to the chromatographic peaks using the MCR methods is more predominant that those identified by the Direct method.

References

[1] Benariba, N., Djaziri, R., Bellakhdar, W., Belkacem, N., Kadiata, M., Malaisse, W., Sener, A. (2013). Phytochemical screening and free radical scavenging activity of *Citrullus colocynthis* seeds extracts. Asian Pacific Journal of Tropical Biomedicine, 3, 35-40. https://doi.org/10.1016/S2221-1691(13)60020-9.

[2] Kalantari Meybodi, M. S. (2020). A review on pharmacological activities of citrullus colocynthis (L.) Schrad. Asian Journal of Research and Reports in Endocrinology, 3(1), 25-34.

[3] Jalali-Heravi, M., Parastar, H. (2011). Recent trends in application of multivariate curve resolution approaches for improving gas chromatography-mass spectrometry analysis of essential oils. Talanta, 85, 835-849. https://doi.org/10.1016/j.talanta.2011.05.045.

[4] Nikpour, H., Mousavi, M., Asadollahzadeh, H. (2018). Qualitative and quantitative analysis of Teucrium polium essential oil components by GC-MS coupled with MCR and PARAFAC methods. Phytochemical Analysis, 29, 590-600. https://doi.org/10.1002/pca.2772.

Synthesis and study of E/Z isomerization in 3-(2-(2,4-dimethylphenyl) hydrazono)-6-fluoroquinolin-(1*H*, 3*H*)-2, 4-dione

Enayatollah Moradi Rufchahi, Fatemeh Ashuri Mirsadeghi*

Corresponding Author E-mail: fatemeh.ashouri.mirsadeghi@gmail.com

Department of Chemistry, Faculty of Science, Islamic Azad University, Lahijan branch, P.O. Box: 1616, Lahijan, Iran.

Abstract: 6-Fluoro-4-hydroxyquinolin-2(1H)-one was synthesized and reacted with diazotized 2, 4-dimethyl aniline in basic medium and a deep yellow solid was obtained product was confirmed using FT-IR, NMR and mass analyses and DFT calculations showed, the hydrazone form is more stable than the azo structure. pH were also studied.

Keywords: azo-hydrazone; DFT; E/Z isomerization

Introduction

compounds bearing azo chromophore (-N=N-) adjacent to hydroxyl group (OH) tend to rearrange to give corresponding hydrazone structure (-NH-N=) which may be frequently the more preferred tautomer. there is an equilibrium between two tautomers.[1-2] azo and hydrazone tautomers interconvert and sometimes not. This structural transformation often causes distinct alteration in the chemical and applied properties. [3-4] Two factors affect the position of azo-hydrazone tautomeric equilibrium: structural factors including type and position of the substituents on the aromatic rings, media factors like temperature, pH and solvent. [5]

Experimental Section

6-Fluoro-4-hydroxyquinolin-2(1*H*)-one was synthesized and reacted with diazotized 2, 4-dimethyl aniline in basic medium and a deep yellow solid crystalline compound was obtained (Scheme 1). The FT-IR spectra for the synthesized compounds were obtained using a VERTEX 70 Bruker FT-IR Spectrophotometer with pressed KBr discs. NMR spectroscopy was conducted using a Bruker FT-NMR apparatus operating at 400 MHz, with DMSO-d_6 as solvent. Mass spectra were recorded using a 5973 Network Mass Selective Detector Agilent Technologies (HP) spectrometer, operating at 70eV. The ground states of the proposed azo and hydrazone structures were optimized using DFT/B3LYP level theory, with 6-311++G (d, p) for all atoms. Analytic frequency calculations were carried out to confirm that the optimized structures are in minimum energy.

Results and Discussion

As it is evident from the table 1, hydrazone-E, which has the lowest optimal total energy, is the most preferred structure in the gas phase system. While in chloroform and dimethyl sulfoxide systems, it can be seen that hydrazone-Z is the most stable one. However, it is worth mentioning that the energy differences between the E and Z isomers are very small in three selected systems and this conclusion is in accordance with ^{1}H NMR results and can be the reason why both E and Z isomers co-exist in solution. As shown in Fig 1, the geometric optimization of compound 2 indicated that hydrazone tautomer, having configuration Z, is a more stable one and has a lower relative energy (ΔE_{DMSO}=1.86 kcal/mol) than hydrazone-E tautomer, which has a lower energy (ΔE_{DMSO}=7.54 kcal/mol) than azo tautomer.
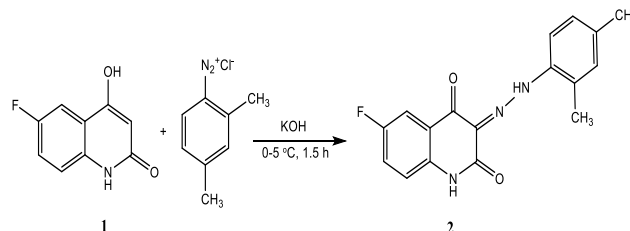
Scheme1. Synthetic route to 3-(2-(2,4-dimethylphenyl) hydrazono)-6-fluoroquinolin-(1*H*, 3*H*)-2, 4-dione (**2**).

Table1: Total energies, relative energies and dipole moments of three proposed tautomers of compound **2** in three selected systems (gas phase, CHCl$_3$ and DMSO).

structure	E (kcal/mol)	RE (kcal/mol)	μ(debye)
Azo-enol(gas)[a]	-672112.056	17.10	0.78
Hydrazone-Z(gas)[a]	-672118.656	10.50	4.68
Hydrazone-E(gas)[a]	**-672119.209**	9.94	1.25
Azo-enol(CHCl₃)	-672118.690	10.46	1.30
Hydrazone-Z(CHCl₃)	**-672125.993**	3.16	6.13
Hydrazone-E(CHCl₃)	-672124.311	4.85	1.42
Azo-enol(DMSO)	-672121.617	7.54	1.66
Hydrazone-Z(DMSO)	**-672129.157**	0.00	6.88
Hydrazone-E(DMSO)	-672127.299	1.86	1.48

22nd Iranian Chemistry Congress (ICC22)
Iranian Research Organization for Science and Technology (IROST)
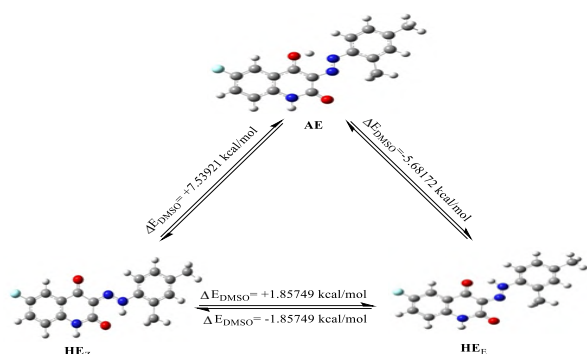**13-15 May 2024**

03231-97589

Fig.1: Relative energies required for interconversion of proposed tautomers of compound **2**.

The UV-visible absorption spectra of compound 2 were studied in solvents with different polarity conditions: DMSO (polar aprotic), C_2H_5OH (polar protic), $CHCl_3$ (less polar aprotic), cyclohexane (nonpolar), and ethanol.
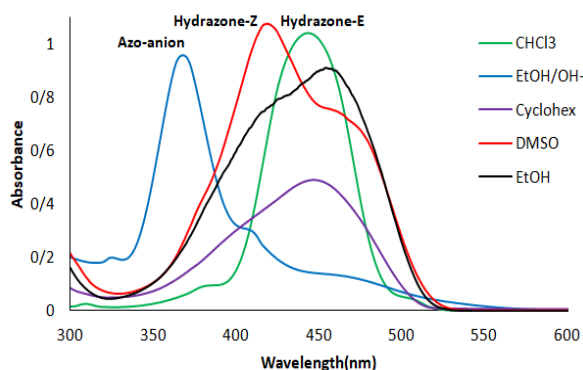

Fig.2: Absorption spectra of compound **2** in solvents with different polarity.

As can be seen in Fig2, dye 2 displayed two absorption bands at 419 nm and 466 nm (in DMSO), 423 and 454 nm (in EtOH), 385 and 444 nm (in chloroform), 405 and 446 (in cyclohexane), and three absorption bands at 522, 550 and 600 (in ethanol containing hydroxide ion). These absorption bands can be attributed to n-π∗ and/or π-π∗ electronic transitions of the hydrazone-E and hydrazone-Z tautomeric forms. According to Fig. 4, depending on the polarity of the solvents, the electronic absorption spectra can be divided into two characteristic bands: broad bands at 388-419 nm attributed to the hydrazone-Z form and broad bands at 444-466 nm assigned to the hydrazone-E-form. The results are in accordance with the HOMO-LUMO energy gap as schematically shown in Fig 3, in which the electronic energy required for the transition in hydrazone-Z is higher than hydrazone-E in both solvent systems (chloroform and dimethyl sulfoxide). This can be due to the more extended π-conjugated system present in the Z configuration.

Conclusions

the optimized geometries of all the selected dyed predicted the increased stability of the E isomers over the Z isomers. the product adopts exclusively hydrazone structure which exists as an equilibrated E and Z geometrical isomeric mixture in solution state. Based on the results of DFT quantum calculations, the hydrazone form of the compound (2) is more stable than the proposed azo structure and the hydrazone-Z form has the lowest total energy. Figure 3 shows the calculated energy values of HOMO (E_{HOMO}), LUMO (E_{LUMO}), and the energy gap (ΔE) of the synthesized azo derivative 2 in its azo and hydrazone tautomeric forms in three selected environments: gas phase, chloroform, and dimethyl sulfoxide. As can be extracted from the figure, the hydrazone structures of the dye have a higher HOMO-LUMO energy gap than those of the corresponding azo ones. Accordingly, in accordance with ^{1}H NMR results, hydrazone structures are more stable than azo forms.
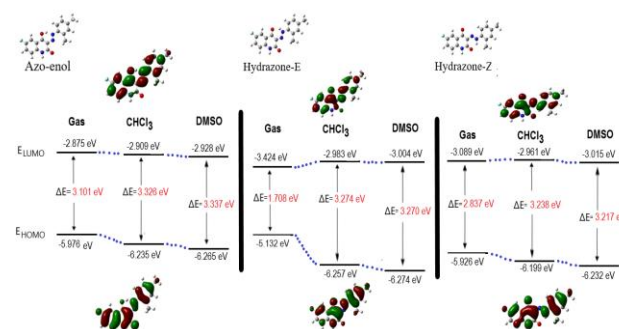

Fig.3: The frontier molecular orbitals and HOMO-LUMO energy gap of the **proposed** azo-enol and hydrazone-E and hydrazone-Z tautomers of (**2**) in the gas phase, $CHCl_3$ and DMSO.

References

[1] V. Deneva, A. Lyčka, S. Hristova, A. Crochet, K.M. Fromm, L. Antonov, Tautomerism in azo dyes: Border cases of azo and hydrazo tautomers as possible NMR reference compounds. Dyes and Pigments 165 (2019) 157–163, doi: 10.1016/j.dyepig.2019.02.015.

[2] H. Y Lee, X. Song, H. Park, M-H. Baik, D. Lee, Torsionally Responsive C3-Symmetric Azo Dyes: Azo–Hydrazone Tautomerism, Conformational Switching, and Application for Chemical Sensing. Journal of American Chemical Society 132(2010) 12133–12144, https://doi.org/10.1021/ja105121z.

[3] H. Zollinger, Color Chemistry: Synthesis, Properties and application of organic dyes and pigments. third ed. VCH, Weinheim, 1987.

[4] D. Waring, G. Hallas, The chemistry and application of dyes. Plenum, New York, 1990.

[5] W. Herbst, K. Hunger, Industrial organic pigments, WILEY-VCH Verlag GmbH & Co. KGaA, Weinheim, 3rd Ed., 2004.

Development of Curcumin-Loaded PCL-PEG Nanofibers as a Sustainable Drug Delivery System for Cancer Treatment

Danial Fatahnaei, Abolfazl Barzgar*, Mehdi Haghi, Nazli Bahari, Abbas Nobakht, Amir Hossein Behrouzi

Corresponding Author E-mail: barzegar@tabrizu.ac.ir

Department of biology, Faculty of natural sciences, University of Tabriz.

Abstract: Curcumin-loaded PCL-PEG nanofibers were fabricated using electrospinning as a promising strategy for cancer treatment. Scanning Electron Microscopy (SEM) confirmed the nanofiber morphology, while UV-vis spectroscopy monitored curcumin release kinetics. This study evaluates the potential of these nanofibers for sustained delivery and efficacy against cancer cells.

Keywords: Electrospun nanofibers; Anticancer; Colon cancer.

Introduction

Cancer, marked by uncontrollable cell growth and proliferation, represents a complex and multifaceted ailment, posing one of the foremost challenges in contemporary medicine and biology [1]. In the quest for targeted therapies, integrating anticancer and anti-inflammatory agents like curcumin into nanofibers presents an innovative strategy [2, 3]. The significant hydrophobic nature of curcumin greatly hampers its bioavailability and clinical efficacy, given its insolubility in water but solubility in organic solvents [4]. Loaded nanofibers serve as carriers for this compound, offering a platform for accurate and controlled delivery to treated cells.

Experimental Section

PCL and PEG polymers were dissolved in a 1:1 (v/v) solvent mixture of acetic acid and formic acid at room temperature (25 ± 2 °C). This solvent system helps dissolve both the hydrophobic PCL and hydrophilic PEG, creating a homogenous solution suitable for electrospinning. Curcumin was then added to the polymer solution and stirred thoroughly. Even dispersion of curcumin throughout the solution is crucial for uniform loading within the nanofibers. The prepared solution was loaded into a syringe connected to a high-voltage electrospinning machine (20 KV). The grounded collector was positioned at a distance of 16 cm from the tip of the needle. The collector rotation speed was set to 120 to 150 rpm. The injection rate was maintained at 0.8 ml/h relative to the solvent volume and collector speed.

Characterization of nanofibers:

Surface morphology:
The morphology of the electrospun medicated fibers was investigated by scanning electron microscope (SEM, MIRA3 TSCAN SEM microscope). The surfaces were coated with a thin layer of gold .

In vitro curcumin release assay
To evaluate the release kinetics of curcumin from the nanofiber mats, a disc-shaped sample (5 ± 0.5 mg, 10 mm x 10 mm) was cut from the mat and placed in a vial containing 1.5 mL of phosphate-buffered saline (PBS, pH 7.4) supplemented with 30% (w/w) ethanol. Ethanol was included due to curcumin's low solubility in pure water [5]. The vial was incubated at 25 °C with periodic replacement of the entire incubation medium (1.5 mL) with fresh PBS/ethanol solution at predetermined time points. The amount of curcumin released in the collected medium was quantified, and the cumulative release profile as a function of time was established.

Results and Discussion

Field emission scanning electron microscopy (FE-SEM) was employed to investigate the morphology of the electrospun nanofibers. Figure 1 presents images of both PCL-PEG nanofibers and PCL-PEG nanofibers loaded with 5% (w/w) curcumin.

As observed in Figure 1, the PCL-PEG nanofibers exhibit a smooth and bead-free structure, indicating a successful electrospinning process. Compared to the controls, the morphology of the curcumin-loaded nanofibers (Figure 1) shows slight changes. While they maintain a fibrous structure, a broader diameter distribution is evident. This observation suggests that curcumin incorporation might influence the solution properties and jet formation during electrospinning, potentially leading to variations in fiber diameter.
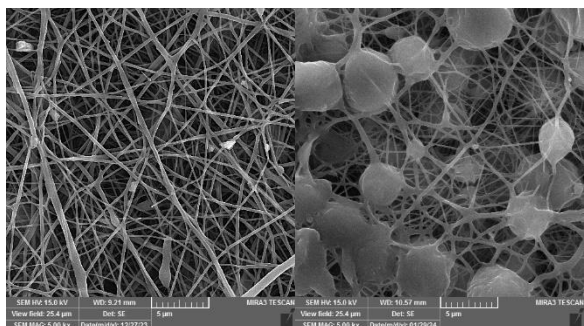
22nd Iranian Chemistry Congress (ICC22)
Iranian Research Organization for Science and Technology (IROST)
13-15 May 2024

03231-97589

Fig.1: SEM images of PCL-PEG nanofibers (left panel) and those containing 5 wt.% of curcumin (right panel).

UV-Vis absorption spectra of curcumin solutions:

The absorption spectra of curcumin solutions in acetic acid was syudies at various concentrations. As observed, curcumin exhibits a characteristic absorbance at λ_{max} = 425 nm. The intensity of this peak increases linearly with increasing curcumin concentration, demonstrating a concentration-dependent response.

In vitro curcumin release profile :

The in vitro release profile of curcumin from the PCL-PEG nanofiber mats, as depicted in Figure 3, demonstrates a sustained release pattern. An initial burst release of curcumin is observed within the first 8 hours, followed by a slower and more controlled release phase (Figure 4). This biphasic release behavior suggests the potential for an initial therapeutic dose followed by a sustained delivery of curcumin over a prolonged period.
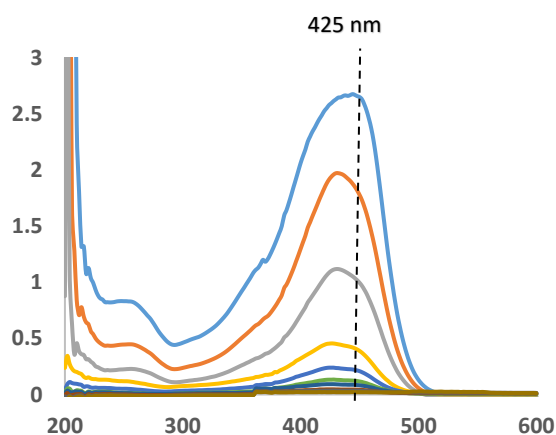

Fig.2: The absorption spectra of curcumin solutions in acetic acid at various concentrations: 0.78, 1.56, 3.12, 6.25, and 12.5 μg/mL.
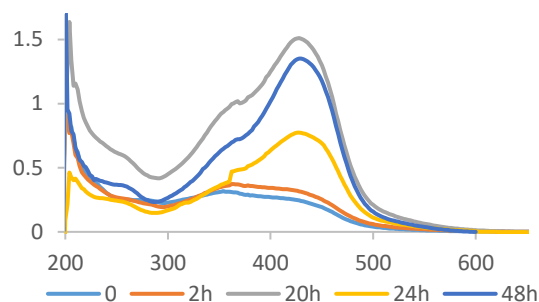
.

Fig.3: Absorption spectra of PCL-PEG-curcumin nanofibers in PBS-Ethanol (30%) solution in different times from 0 to 48 hours.
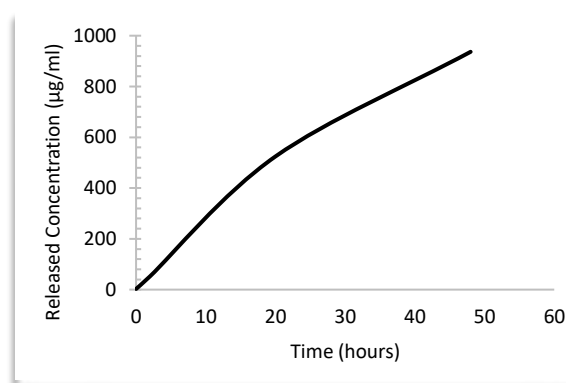

Fig. 4. Release profiles of curcumin from the curcumin loaded in PCL-PEG electrospun nanofibers.

Conclusions

This study successfully fabricated novel nanofibrous scaffolds loaded with curcumin, a promising anti-cancer and anti-inflammatory agent. The in vitro release profile demonstrated a sustained release pattern with an initial burst followed by a slower release phase. While the impact of curcumin on the nanofiber's mechanical properties requires further investigation, this sustained release profile suggests potential benefits for prolonged therapeutic delivery.

References

[1] Cunningham, D., et al., *Colorectal cancer.* Lancet, 2010. **375**(9719): p. 1030-47.

[2] Peng, Y., et al., *Anti-Inflammatory Effects of Curcumin in the Inflammatory Diseases: Status, Limitations and Countermeasures.* Drug Des Devel Ther, 2021. **15**: p. 4503-4525.

[3] Pereira, D.G., et al., *Antagonistic anticancer effect of paclitaxel and digoxin combination.* J Cell Biochem, 2019. **120**(8): p. 13107-13114.

[4] Guo, G., et al., *Preparation of curcumin loaded poly(ε-caprolactone)-poly(ethylene glycol)-poly(ε-caprolactone) nanofibers and their in vitro antitumor activity against Glioma 9L cells.* Nanoscale, 2011. **3**(9): p. 3825-32.

[5] Shababdoust, A., et al., *Controlled curcumin release from nanofibers based on amphiphilic-block segmented polyurethanes.* Int J Pharm, 2020. **575**: p. 118947.

Development of an efficient and simple method for the synthesis of dimethyl fumarate API at room temperature via one-pot, one-step reaction

Iman Rezaei[a]*, Iliya nazeriyeh[b], Raoofeh Sattari Nobarzad[c], forouzan shahri[a], Issa Mousazadeh Moghaddampour[d]

Corresponding Author E-mail: rezaee.imaan@gmail.com

[a]Department of Chemistry, Faculty of Sciences, University of Guilan, P.O. Box 41335-1914, Rasht, Iran.
[b]Department of Medical Sciences, Faculty of Medicinal Chemistry, Islamic Azad University of Medical Sciences, P.O. Box 19395/1495, Tehran, Iran.
[c]Department of Chemistry, Faculty of Science, University of Maragheh, P.O. Box 55181-83111, Maragheh, Iran.
[d]Department of Industrial Chemistry, Faculty of Rajaie, Lahijan Branch, Technical and Vocational University (TVU), Guilan, Iran.

Abstract: Dimethyl fumarate (DMF) is a drug and prodrug with various medicinal uses and is used in the treatment of Multiple sclerosis (MS). One of the common methods for the synthesis of DMF is through esterification reactions. It involves the reaction between fumaric acid and methanol in the presence of a catalyst. Esterification process requires precise control of temperature, reaction time and reactant ratio to achieve high efficiency. In current report, we have developed a process for the synthesis of dimethyl fumarate from the reaction between fumaric acid and methanol using HCl 20% and Zinc chloride as catalysts at room temperature. This method is able to synthesize dimethyl fumarate active pharmaceutical ingredient (API) at room temperature in short reaction time and excellent yield.

Keywords: Dimethyl fumarate, API, Synthesis, Drug

Introduction

Dimethyl fumarate (DMF) is a pharmaceutical compound that has gained significant attention in recent years due to its potential therapeutic applications. It is primarily used in the treatment of multiple sclerosis, a chronic autoimmune disease affecting the central nervous system. DMF has shown promising results in reducing disease activity and slowing down the progression of multiple sclerosis [1]. In recent years, research has shown that Dimethyl fumarate (DMF) also possesses immunomodulatory and anti-inflammatory properties, making it a promising candidate for the treatment of multiple sclerosis (MS). MS is a chronic autoimmune disease that affects the central nervous system, leading to inflammation and damage to the protective covering of nerve fibers. Aside from MS, DMF has also shown potential in other inflammatory conditions such as psoriasis and inflammatory bowel disease. In psoriasis, DMF has been found to improve symptoms by reducing inflammation and inhibiting the abnormal growth of skin cells. Inflammatory bowel disease encompasses conditions like Crohn's disease and ulcerative colitis, where DMF may help alleviate symptoms by modulating the immune response. The active pharmaceutical ingredient (API) is a crucial component of any medicine [2, 3]. These methods focus on utilizing renewable feedstocks, employing environmentally friendly solvents, and reducing energy consumption during the synthesis process. In this work, we have presented a novel, effective and inexpensive method at room temperature in order to synthesis of Dimethyl Fumarate (DMF) by the reaction between fumaric acid and methanol using HCl 20% and Zinc chloride as catalysts at room temperature. Among the obvious advantages of this method, high reaction yield, short reaction time, easily purification of products without the need for chromatographic separation can be mentioned.
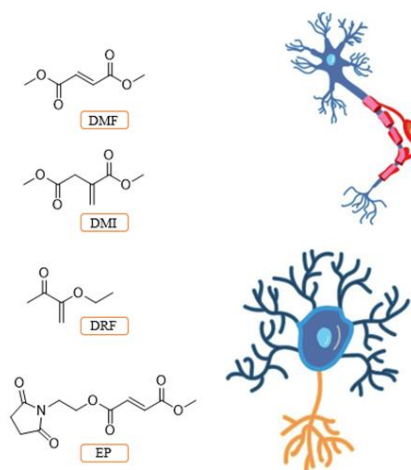
Fig.1. Structures of dimethyl fumarate derivatives

Experimental Section

In this work, all of chemicals were purchased from Merck and Fluka. Melting points were obtained on a Büchi B-545 apparatus in open capillary tubes. FT-IR spectra were considered on a α-Bruker spectrometer. ^{1}H NMR spectra were determined on a 300 MHz Bruker DRX-300 in DMSO-d6 as solvent and TMS as internal standard. ^{13}C NMR

22nd Iranian Chemistry Congress (ICC22)
Iranian Research Organization for Science and Technology (IROST)
13-15 May 2024

03231-97589

IROST

spectra were done on a 75 MHz Bruker DRX-75 in DMSO-d_6 as solvent. Mass spectrum were checked using AB SCIEX 3200 QTRAP. Water contents of API was determined by Kar Fisher coulometric Metrohm.

preparation of Dimethyl Fumarate:
Dimethyl fumarate was synthesized from the reaction between fumaric acid (1 mmol) and methanol (5 ml) using HCl 20% (1 ml) and Zinc Chloride (10% mmol) as catalysts at room temperature. At the end of the reaction, the obtained product was purified using recrystallization with methanol and product dimethyl fumarate was produced with 98% yield. The sample of product analysed by FT-IR, ^{1}H NMR, ^{13}C NMR, Mass Spectrum, Melting point and water content was determined using Karl Fisher coulometric.

Physical and Spectroscopic data of the Dimethyl Fumarate API synthesized:

Dimethyl Fumarate API synthesized: Yield 98%, White Solid; M. p. 101-103 °C, M. p. FT-IR (KBr), v, cm^{-1}: 2957 (C-H), 1721 (C=O), 1657, 1589 (C=C), 1381 (C-H, sp^3). ^{1}H NMR (300 MHz, DMSO-d^6), δ, ppm: 3.76 (s, 6H, CH3-O), 6.80 (s, 2H), ^{13}C NMR spectrum (75 MHz, DMSO-d_6), δ, ppm: 165.3 (C=O), 133.5 (C=C), 52.8 (CH3-O), MS, m/z (%): 144.1. Water Content by Karl Fisher: 638.59 ppm (0.06) %.

Results and Discussion
Isomerization of DMF involves the conversion of its geometric isomer, trans-DMF, to its cis-isomer, cis-DMF. This process is of interest because the cis-isomer exhibits different chemical and physical properties compared to the trans-isomer. Several factors influence the isomerization process. Temperature plays a crucial role as higher temperatures promote faster conversion rates. However, excessively high temperatures can lead to side reactions or decomposition of DMF. Therefore, an optimal temperature range needs to be determined for efficient isomerization. performing the reaction at room temperature prevents the production of impurities.

The effect of the temperature, time and the amount of catalyst used on the progress of the reaction was investigated in the different conditions, the results of which are given in **Table 1**.

Table 1. Synthesis of DMF API in the different conditions.

entry	Catalyst	Temperature (°C)	Time (min)	Yield (%)[a,b]
1	HCl 20% /ZnCl$_2$	r. t.	20	98
2	HCl 20% /ZnCl$_2$	55	20	98
3	HCl 22% /ZnCl$_2$	55	20	98
4	SOCl$_2$	r. t.	60	95
5	HCl 20% / AlCl$_3$	55	90	88
6	MeI / K$_2$CO$_3$	r. t.	20	95

[a]isolated yield. [b]Reaction conditions: Fumaric Acid 1(1 mmol), Methanol (5 mL)

It is evident from the results that using HCl 20% / ZnCl2 in Methanol at room temperature leads to dimethyl fumarate API in 20 min and 98 % yield (Table 1, Entry 1). This method is able to synthesize dimethyl fumarate API at room temperature in short reaction time and excellent yield with high purity as a green method (**Scheme 1**).

Scheme 1. Two novel methods for the synthesis of dimethyl fumarate at room temperature.

The current method is compared with other methods reported in scientific references. This study showed that the method reported in this research provides dimethyl fumarate with high purity at room temperature with high yield and short time reaction as a green method.

Conclusions
In this research, we have presented a novel, effective and inexpensive method at room temperature in order to synthesis of Dimethyl Fumarate (DMF). Among the obvious advantages of this method, high reaction yield, short reaction time, easily purification of products without the need for chromatographic separation can be mentioned.
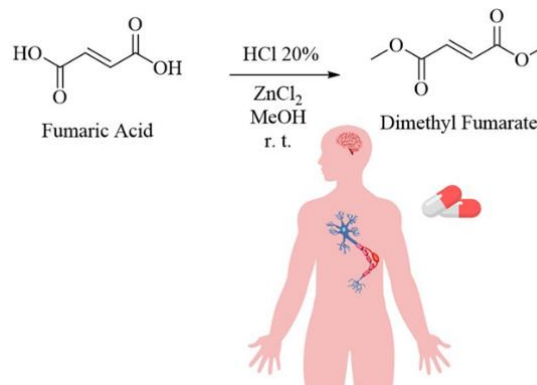
References
[1] Lima M. T., Finelli F. G., de Oliveira A. V., Kartnaller V., Cajaiba J. F., Leão R. A. and de Souza R. O. (**2020**) RSC advances, 10 (5), 2490-2494.

[2] Love B. E., and Bennett L. J. (**2017**) J. Chem. Educ., 94 (10) 1543-1546.

[3] Pullagurla M. P., Rangisetty J. B., Nandakumar M. V., Radha N. (**2015**), US Patent 126,526.

Synthesis of Hydrogels by Deep Eutectic Solvents to Increase Absorption Power

Abdolreza Abri[*], Mohammad Gharajedaghi

Corresponding Author E-mail: Ar.abri@yahoo.com

Chemistry Department, Faculty of Basic Sciences, Azarbaijan Shahid Madani university, Tabriz, Iran.

Abstract: Hydrogels have garnered significant interest in various fields ranging from biomedicine to environmental engineering due to their unique properties and versatile applications. In this study, we present a novel approach for synthesizing hydrogels utilizing Deep Eutectic Solvents (DES). DES offers several advantages over traditional solvents, including low toxicity, biodegradability, and tunable properties, making them promising candidates for sustainable hydrogel synthesis. Our methodology involves the facile preparation of hydrogels through the sol-gel transition of DES-based precursor solutions. The resulting hydrogels exhibit excellent mechanical strength, high water absorption capacity, and biocompatibility, making them suitable for drug delivery, tissue engineering, and environmental remediation applications. We elucidate the influence of DES composition and processing parameters on the physicochemical properties of the hydrogels, providing insights into the design and optimization of DES-based hydrogel systems. Overall, this study demonstrates the feasibility and potential of Deep Eutectic Solvents as green and effective alternatives for synthesizing hydrogels with tailored properties, paving the way for sustainable advancements in various technological domains.

Keywords: DES (Deep Eutectic Solvent); Hydrogel; Halide salts; Hydrogen bond donors

Introduction

For the past several decades, a major part of the industrial community particularly those dealing with chemical, pharmaceutical, petrochemical, construction, reservoir engineering, beverages, dyes, adhesives and allied industries have been completely dependent on the usage of industrial solvents [1,2]. (Fig1) The applications of these solvents are not limited to these industries but also include extraction, drug delivery and several other applications. Millions of gallons of these solvents are consumed globally in these industries for various product formulations and synthesis [3] (Fig2). The solvent usage by such industries is about 80–90% of total mass and they also account for 80–85% waste it produces. Very large human population is exposed to these solvents directly or indirectly through various means. The downside of these is that a vast majority of them are Volatile Organic Compounds (VOCs) with a high degree of toxicity and volatility, and whose usage leads to very serious and irreparable environmental hazards. A vast majority of VOCs are carcinogenic and mutagenic [4] and prolonged exposure to solvents and VOCs can cause reproductive hazards, respiratory problems, skin and eye irritation. The untreated disposal of these solvents can severely harm the environment through water bodies, air pollution, soil pollution, etc. [5]. The environmental concerns emanating due to the vast consumption of these highly toxic and environmentally hazardous chemicals have generated a deep concern for moving towards greener and more sustainable solvents which would be aligned with the 12 Green principles of environmental chemistry. Chemical and pharmaceutical industries have been restricted from the usage of toxic and environmentally susceptible solvents but still needs essential properties like polarity and solubility of particular solvents in production. These solvents are carefully replaced or chosen according to Solvent Selection Guide that has been set up by pharmaceutical companies [6]. The scientific and research community at large is on a continuous quest for developing and employing greener and benign alternatives which include water gas-expanded liquids, liquid polymers, supercritical fluids, liquids derived from biomass, ionic liquids (ILs) and deep eutectic solvents (DESs) In this article, we want to achieve specific hydrogels
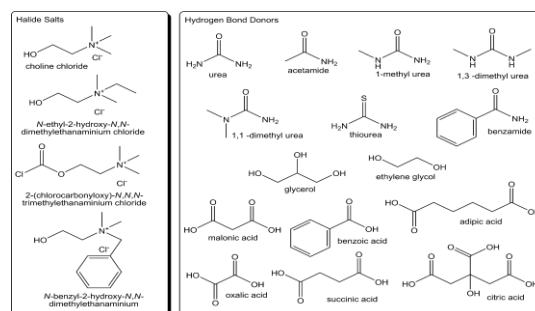
Fig1: Structures of some halide salts and hydrogel bond donors used in the formation of deep eutectic solvents.

1. Hydrogel

Hydrogel is a self-supporting, water-swellable three-dimensional viscoelastic network, which allows molecular diffusion and cell adhesion. Hydrogel is composed of a cross-linked polymer matrix, which can absorb a large amount of water in water but does not dissolve. Different hydrogels have different chemical and structural

22nd Iranian Chemistry Congress (ICC22)
Iranian Research Organization for Science and Technology (IROST)
13-15 May 2024

03231-97589

IROST

response parts, which can respond to external stimuli such as temperature, pH, ion concentration, light and magnetic field. As a response to external stimuli, hydrogel has great potential in tissue engineering, wearable electronic devices, bionic materials and pharmaceuticals through the change of its volume and structure [۵-۶].

Experimental Section

First, we synthesize the deep solvent used, and then we synthesize the desired hydrogel from chitosan compounds and some vinyl compounds.

We use different percentages of hydrogels using deep eutectic solvents as the optimal composition when the gel is formed. (Table 1, Fig2)

Table 1: Comparison of Hydrogel Properties Synthesized with Different Deep Eutectic Solvents (DES)

ES Type	Crosslinking Agent	Mechanical Strength	Swelling Ratio	Biocompatibility
Choline Chloride: Urea	Glutaraldehyde	High	Moderate	Excellent
Choline Chloride: Glycerol	Ethylene Glycol Diglycidyl Ether	Moderate	High	Good
Choline Chloride: Ethylene Glycol	Poly(ethylene glycol) diacrylate	Very High	Low	Excellent

Fig 2: Prepared hydrogel by Deep Eutectic Solvent

Results and Discussion

A successful reaction was synthesized with combinations of deep eutectic solvents and the desired hydrogel, which was then used to remove cationic and anionic dyes and release the drug, and the corresponding curves were drawn.

The use of DES increased the speed of hydrogel formation and the rate of water absorption and swelling, as well as high thermal stability and easy biodegradability.
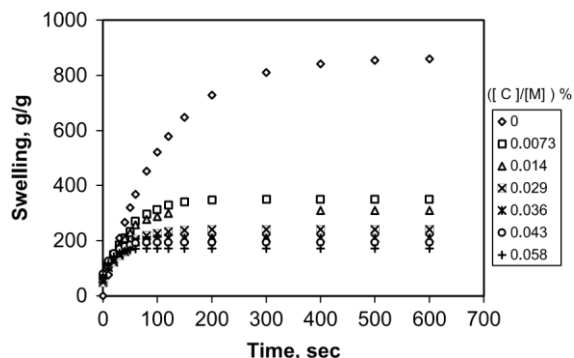

Fig3: Increase the absorption power of the hydrogel

Conclusions

We got the best results by hydrogen donors and hydrogen receivers, which swell a lot due to water absorption(swelling). Then it was used in different parts.

References

[1] N. Winterton, The green solvent: a critical perspective, Clean Technologies and Environmental Policy 2021 23:9. 23 (2021) 2499–2522 doi: 10.1007/ S10098-021-02188-8.

[2] G. Wypych, M. Matsumoto, S. Isken, J.A.M. de Bont, K. Botzenhart, T. Hahn, F. Schweinsberg, T. Yamane, K.D. Hasenclever, P.J. Wakelyn, P.J. Wan, G. Volland, M. Bauer, C. Barthélémy, M. Serageldin, D. Reeves, SOLVENTS USE IN VARIOUS INDUSTRIES, Handbook of Solvents, Volume 2: Use, Health, and Environment. (2019) 901–1124 doi: 10.1016/B978-1-927885-41-3.50003-6.

[3] What are Industrial Solvents and Where are They Typically Used? - Maratek Environmental, (n.d.). https://www.maratekenvironmental.com/whatareindustrial-solvents-and-where-are-they-typicallyused/.

[4] A.J. Li, V.K. Pal, K. Kannan, A review of environmental occurrence, toxicity, biotransformation and biomonitoring of volatile organic compounds, Environ. Chem. Ecotoxicol. 3 (2021) 91–116, https://doi.org/10.1016/J. ENCECO.2021.01.001.

[5] S. Mehra, M. Singh, P. Chadha, Adverse impact of textile dyes on the aquatic environment as well as on human beings, Toxicol Int. 28 (2021) 165–176, https://doi.org/10.18311/ti/2021/v28i2/26798

[6] F.P. Byrne, S. Jin, G. Paggiola, T.H.M. Petchey, J.H. Clark, T.J. Farmer, A.J. Hunt, C. Robert McElroy, J. Sherwood, Tools and techniques for solvent selection: green solvent selection guides, Sustainable Chemical Processes 2016 4:1. 4 (2016) 1–24 doi: 10.1186/S40508-016-0051-Z.

Zeolitic imidazolate framework-8 (ZIF-8) as an adsorbent for vortex assisted dispersive solid phase microextraction of Co(II) ions from environmental samples prior to flame atomic absorption spectrometry

Narges Vaezi, Naser Dalali*

Corresponding Author E-mail: naser.dalali@znu.ac.ir

Department of chemistry, Faculty of science, University of zanjan, Zanjan, 45371- 38791, Iran.

Abstract: In the present work, zeolitic imidazolate framework-8 (ZIF-8) was synthesized and characterized. It was utilized as an adsorbent for the precise and sensitive determination of Co(II) ions with a novel and rapid vortex-assisted dispersive solid phase microextraction from soli, vegetable juice, and water samples before their determination by flame atomic absorption spectrometry.

Keywords: Zeolitic imidazolate framework-8 (ZIF-8), Vortex-assisted dispersive solid phase microextraction, Flame atomic absorption spectrometry

Introduction

During the last decades, pollution possibilities with a wide range of pollutants including heavy metals, pesticides, and so on were increased [1]. From these pollutants, most heavy metal cations may be harmful to human health even at low concentrations because of their non-biodegradable nature and their mobility within the environmental components including soil, air, and water [2]. Cobalt is a vital element for humans at trace levels to sustain biological processes. However, if consumed in excess amounts, it can even cause various damages [3]. Hence, the accurate determinations of trace heavy metal ions in various environmental samples are an important part of the studies in analytical chemistry. Flame atomic absorption spectrometry (FAAS) is one of the best widely used instruments for the measurement of heavy metal ions at trace levels because of its simplicity and lower cost than other instruments. So, an initial preconcentration procedure could be an important issue before the determination of trace metal ions by FAAS [4]. The development of several simplified and miniaturized sample preparation methods for component investigation and speciation has been done to solve these issues. Among these, Dispersive solid phase microextraction (DSPME) was presented by Tsai et al. as a miniaturized SPE procedure. The DSPME has several advantages over the conventional SPE, such as a decreased use of solvent, less adsorbent usage, a shorter extraction time, and a high extraction efficiency. Besides, it is simple, economical, and easy to perform and a wide range of adsorbents can be employed In DSPME, the adsorption materials play an awfully important role in enhancing the analytical performance in ways like sensitivity, precision, and selectivity. Thus, the selection of novel adsorbents has become the attention of interest to researchers [5]. In the past few years, metal-organic frameworks (MOFs) have been developed as beneficial materials. Recently MOFs have attracted considerable research interest within the field of adsorption and separation because of their ultrahigh porosity, great surface areas, and tunable pore size. Zeolitic imidazolate frameworks (ZIFs) which are supported by the bridge of imidazole with metal nodes (such as zinc and cobalt), could be a subgroup of metal-organic frameworks. Accordingly, ZIFs combine the benefits of both MOFs and natural zeolite. Zeolitic imidazolate framework-8 (ZIF-8), a member of a subclass of ZIFs, has been selected as a decent candidate recently. Moreover, ZIF-8 has already demonstrated attractive characteristics large accessible surface area, high porosity, and good chemical stability which make it a possibly ideal adsorbent for heavy metal pollutants [6]. The goal of this study was to see the efficiency of the synthesized zeolitic imidazolate framework-8 (ZIF-8) in VADSPME to preconcentrate Co(II) ions from the soil, vegetable juice, and water samples.

Experimental Section

The DSPME-ZIF-8 method was carried out as follows: ZIF-8 adsorbent (10 mg) was added to 10 mL of a solution containing 0.5 mgL^{-1} of Co (II) ions in a 12 mL falcon tube. Thereupon, the pH value of the solutions was adjusted to 7(The pH adjustment was done by adding 0.1 molL^{-1} of hydrochloric acid, and 0.1 molL^{-1} of sodium hydroxide solution to prepare the desired pH solution). Afterward, the mixtures were vortexed for 30 seconds and then filtered using Whatman filter paper grade 42, and the solutions were completely discarded. The adsorbent was eluted with 4 mL of 0.01 molL^{-1} HCl solution for recovery of Co(II) ions. Finally, the adsorbent was separated from the solutions by filtering, and Co (II) ions in the eluent were determined using FAAS.

22nd Iranian Chemistry Congress (ICC22)
Iranian Research Organization for Science and Technology (IROST)
13-15 May 2024

03231-97589

Results and Discussion

ZIF-8 was synthesized and then the phase structure of the ZIF-8 was determined using an X-ray diffractometer. The spectral and analysis data confirmed the successful synthesis of the ZIF-8 which is in agreement with the XRD pattern simulated from the SOD-type single crystal data reported in the papers. The bonding nature and purity of the as-synthesized ZIF-8 structure are studied by the FT-IR. The FT-IR studies are in agreement with the XRD patterns of the ZIF-8 which both confirm the presence of a SOD zeolite type structure ZIF-8. The FESEM images demonstrated that the ZIF-8 crystals were in nanometer sizes. Furthermore, BET surface area analysis was done to determine pore textural properties of the produced sample, including the specific BET surface area, Langmuir surface area, pore volume, and pore size distribution, N_2 adsorption and desorption isotherms. N_2 adsorption and desorption isotherms illustrated the type I IUPAC classification of adsorption isotherms indicating a characteristic of adsorbent is microporous. Influential parameters of the extraction procedure were optimized by altering one parameter while keeping the other parameters constant. The optimal experimental conditions were as follows: the amount of ZIF-8: 10 mg; pH of sample solution: 7; adsorption and elution time: 30 seconds; elution solvent: HCl; concentration of eluent: 0.01 $molL^{-1}$ and volume of eluent: 4mL. Under the optimal conditions of the method, the limit of detection, preconcentration factor and precision as RSD% were found to be 0.6 μgL^{-1}, 62.5 and 0.98%, respectively. The adsorption capacity of the adsorbent for Co(II) ions was found to be 48.93 mg g^{-1}. All of the extraction experiments were performed in the absence of salt. By adding salt, the ionic strength of the solution is increased. The presence of dissolved salt can increase the density of the aqueous solution, which, in turn, may cause a change in the physical properties of the Nernst diffusion film and reduce the speed of diffusion of the target analytes into the sorbent. On the other hand, the electrostatic interaction of metal cations with salt anions causes a reduction in the number of metal cations and as a result, diminishes the extraction efficiency. The method was applied to determine Co(II) ions in water samples (well water, and tap water) and vegetable juice (tomato, potato, and carrot). The recoveries for metal ions were from 90 to 107%, showed that the DSPME-ZIF-8 method is precise, and have high applicability for samples with different matrices.

Conclusions

The presented vortex-assisted dispersive solid phase microextraction was successfully used for the preconcentration of Co(II) ions from soil, vegetable juice, and water samples. Determination was done by flame atomic absorption spectrometer. The VA-DSPME allows the rapid extraction of Co(II)ions using a low amount of adsorbent. The other advantages of this method are its simplicity, ease of operation, good accuracy , short extraction time, low cost, and good preconcentration factor.

References

[1] Briffa, J., Sinagra, E., & Blundell, R. (2020).

[2] Heavy metal pollution in the environment and their toxicological effects on humans. Heliyon, 6(9). https://doi.org/10.1016/j.heliyon.2020.e04691.

[3] Mishra, S., Bharagava, R. N., More, N., Yadav, A., Zainith, S., Mani, S., & Chowdhary, P. (2019). Heavy metal contamination: an alarming threat to environment and human health. Environmental biotechnology: For sustainable future, 103-125.

[4] https://doi.org/10.1007/978-981-10-7284-0_5.

[5] Kosiorek, M., & Wyszkowski, M. (2019). Effect of cobalt on the environment and living organisms-a review. Applied Ecology & Environmental Research, 17(5). http://10.15666/aeer/1705_1141911449.

[6] Saçmacı, Ş., & Kartal, Ş. (2010). Determination of some trace metal ions in various samples by FAAS after separation/preconcentration by copper (II)-BPHA coprecipitation method. Microchimica Acta, 170, 75-82. https://doi.org/10.1007/s00604-010-0391-4.

[7] Ghorbani, M., Aghamohammadhassan, M., Chamsaz, M., Akhlaghi, H., & Pedramrad, T. (2019). Dispersive solid phase microextraction. TrAC Trends in Analytical Chemistry, 118, 793-809. https://doi.org/10.1016/j.trac.2019.07.012.

[8] Mo, Z., Tai, D., Zhang, H., & Shahab, A. (2022). A comprehensive review on the adsorption of heavy metals by zeolite imidazole framework (ZIF-8) based nanocomposite in water. Chemical Engineering Journal, 443, 136320. https://doi.org/10.1016/j.cej.2022.136320.

Preparation of IL@ZIF-8 composite as a new adsorbent for preconcentration of Cd(II) ions from environmental samples with vortex assisted dispersive solid phase microextraction

Narges Vaezi, Naser Dalali*

Corresponding Author E-mail: naser.dalali@znu.ac.ir

Department of chemistry, Faculty of science, University of zanjan, Zanjan, 45371- 38791, Iran.

Abstract: Ionic liquid (IL) was incorporated in a zeolitic imidazolate framework 8 (ZIF-8) under mild conditions. The IL was synthesized from 1-methylimidazole and 1-bromobutane inside the pore structure of the ZIF-8 via the ship-in-bottle (SIB) technique. IL@ZIF-8 employed as a novel adsorbent for the preconcentration of Cd(II) ions in various sample matrices.

Keywords: Ionic liquid, ZIF-8, IL@ZIF-8, ship-in-bottle (SIB)

Introduction

The presence of heavy metal ions in water reservoirs in natural settings is a result of various industrial operations and their associated discharge [1]. Hazardous substances are able to enter the human and animal body through food and water contamination, which subsequently accumulates within their respective systems [2]. Cadmium is a nonessential element that can pose a significant health risk even at low levels in water. Even at low concentrations, Cd(II) ions can cause harm to the kidneys, liver, and lungs, as documented [3]. The determination of heavy metal ions has been done using various instruments. FAAS is a widely used technique because it has great selectivity, low operating and maintenance costs, speed, and simplicity. The presence of many pollutants and low analyte concentrations makes direct determination of metal ions in complex matrices like food samples challenging. Solid phase extraction (SPE) is a preferred technique because of its advantages such as simple operation, lower cost, higher enrichment factor, and the ability to combine with other detection techniques. However, this procedure suffers from certain shortcomings, including solvent loss, large secondary wastes, and a long procedure [4]. To solve the problems mentioned above, a number of simplified and miniaturized sample pretreatment techniques have developed for analysis of elements and their speciation. Among them, dispersive solid phase micro extraction (DSPME) as a new sample preparation technique has received an increasing attention. Compared with traditional SPE, DSPME can offer many benefits of reduced solvent consumption, less adsorbent usage, short extraction time, and high extraction efficiency [5]. In DSPME, an adsorbent material plays a crucial role to improve the analytical performance of a method. Thus, the development of new adsorbents has become a focus of interests to researchers. zeolitic imidazolate framework-8 (ZIF-8) is a crucial branch of MOFs that has a topology similar to a regular zeolitic sodalite and has advantages such as easy synthesis, superior thermal stability, commercial access, and the ability to develop under mild conditions. In truth, it is highly appreciated for its micro porosity, uniform-structured cavities, and high surface area [6]. Herein, we report a new adsorbent comprising of two components ionic liquid (IL) and ZIF-8 for the adsorption of metal ions that combine for the first time the advantages of the IL and ZIF-8. IL refers to a liquid composed entirely by ions. It is usually composed by organic cations and inorganic anions. [6]. Leaching is the main cause of the lack of stability or longevity in liquid phase operations for the IL supporting porous solids. A few attempts have been made to make stable IL-based porous materials, such as the ship-in-bottle (SIB). Based on this adsorbent, the method of VADSPME/FAAS was developed for the determination of Cd(II) ions within the soil, vegetable juice, and water samples.

Experimental Section

The DSPME-(IL-ZIF-8) method was carried out as follows: IL@ZIF-8 adsorbent (10 mg) was added to 10 mL of a solution containing 0.5 mgL^{-1} of metal ions in a 12 mL falcon tube. Thereupon, the pH value of the solutions was adjusted to 7(The pH adjustment was done by addition 0.1 molL^{-1} of hydrochloric acid, and 0.1 molL^{-1} of sodium hydroxide solution to prepare the desired pH solution). Afterward, the mixture was vortexed for 30 seconds and then filtered using what man filter paper grade 42, and the solutions were completely discarded. The adsorbent was eluted with 3 mL of 0.07 molL^{-1} HCl solution for recovery of Cd(II) ions. Finally, the adsorbent was separated from the solutions by filtering and the metal ions in the eluent were determined using FAAS.

Results and Discussion

IL@ZIF-8 was synthesized and then the phase structure was determined using an X-ray diffractometer. the XRD patterns of IL@ZIF-8 demonstrated a close resemblance

to ZIF-8 with no noticeable changes in the crystal structure after the IL introduction, except for low intense peaks, which may suggest the presence of a guest component (IL) supported by the ZIF-8. The surface functional groups of IL@ZIF-8 were identified through FT-IR analysis. FTIR spectrum of IL@ZIF-8 is very similar to the spectrum of ZIF-8, the increase in the height of the spectral band and the slight displacement can be attributed to the placement of the ionic liquid on the ZIF-8 adsorbent. The surface morphologies and structural characteristics of IL@ZIF-8 were explored using FESEM that indicated uniform particles of pristine ZIF-8 with a size of about 0.25um in comparison to IL@ZIF-8 particle size is 1.5um. It seems that the size of IL@ZIF-8 is bigger than pristine ZIF-8. This is maybe because of ionic liquid particles formed on the surface of ZIF-8. Furthermore, BET surface area analysis was done in order to determine the pore textural properties of the produced sample, including the specific BET surface area, Langmuir surface area, pore volume, and pore size distribution, N_2 adsorption and desorption isotherms. N_2 adsorption and desorption isotherms illustrated the type I IUPAC classification of adsorption isotherms, indicating that is a microporous adsorbent. Influential parameters of the extraction procedure were optimized by altering one parameter while keeping the other parameters constant. The optimal experimental conditions were as follows: the amount of ZIF-8: 10 mg; pH of sample solution: 7; adsorption and elution time: 1 min; elution solvent: HCl; Concentration of eluent: 0.07 molL^{-1}; and volume of eluent: 3mL. Under the optimal conditions of the method, the limit of detection, preconcentration factor and precision as RSD% were found to be 0.33 μgL^{-1}, 25 and 0.75%, respectively. The adsorption capacity of the adsorbent for Cd(II) ions was found to be 70.60 mg g^{-1}. All of the extraction experiments were performed in the absence of salt. By adding salt, the ionic strength of the solution is increased. The presence of dissolved salt in water can increase the density of the aqueous solution, which, in turn, may cause a change in the physical properties of the Nernst diffusion film and reduce the speed of diffusion of the target analytes into the sorbent. On the other hand, the electrostatic interaction of metal cations with salt anions causes a reduction in the number of metal cations and as a result diminishes the extraction efficiency. The method was applied to determine Cd(II) in water samples (well water, and tap water) and vegetable juice (tomato, potato, and carrot). The recoveries for metal ions was from 90 to 107%, showing that the DSPME-IL@ZIF-8 method is precise and have high applicability for samples with different matrices.

Conclusions

The presented vortex-assisted dispersive solid phase microextraction was successfully used for the preconcentration of Cd(II) ions from soil, vegetable juice, and water samples. Determination was done by a flame atomic absorption spectrometer. The VA-DSPME allows the rapid extraction of Cd(II) ions using a low amount of adsorbent. Moreover, since, the method presented in the paper is resistant to the presence of most interfering ions. it can be applied in routine analysis of real environmental samples. The other advantages of this method are its simplicity, ease of operation, good accuracy, short extraction time, low cost, low detection limit, and good preconcentration factor.

References

[1] Qing, X., Yutong, Z., & Shenggao, L. (2015). Assessment of heavy metal pollution and human health risk in urban soils of steel industrial city (Anshan), Liaoning, Northeast China. Ecotoxicology and environmental safety, 120, 377-385. https://doi.org/10.1016/j.ecoenv.2015.06.019.

[2] Cui, L., Wu, J., & Ju, H. (2015). Electrochemical sensing of heavy metal ions with inorganic, organic and bio-materials. Biosensors and Bioelectronics, 63, 276-286. https://doi.org/10.1016/j.bios.2014.07.052.

[3] Satarug, S., Garrett, S. H., Sens, M. A., & Sens, D. A. (2010). Cadmium, environmental exposure, and health outcomes. Environmental health perspectives, 118(2), 182-190. https://doi.org/10.1289/ehp.0901234.

[4] Shariati, S., Parto, N., Bozorgzadeh, E., Zanjanchi, P., & Rahnama, S. (2020). Magnetic solid phase preconcentration of cadmium in water samples using sulfonic acid functionalized Kit-6 magnetite mesoporous nanocomposites followed by flame atomic absorption spectrometry. Journal of the Iranian Chemical Society, 17, 3375-3382. https://doi.org/10.1007/s13738-020-01995-y.

[5] Biata, N. R., Dimpe, K. M., Ramontja, J., Mketo, N., & Nomngongo, P. N. (2018). Determination of thallium in water samples using inductively coupled plasma optical emission spectrometry (ICP-OES) after ultrasonic assisted-dispersive solid phase microextraction. Microchemical Journal, 137, 214-222.

[6] Khan, N. A., Bhadra, B. N., & Jhung, S. H. (2018). Heteropoly acid-loaded ionic liquid@ metal-organic frameworks: Effective and reusable adsorbents for the desulfurization of a liquid model fuel. Chemical Engineering Journal, 334, 2215-2221. https://doi.org/10.1016/j.cej.2017.11.159

22nd Iranian Chemistry Congress (ICC22)
Iranian Research Organization for Science and Technology (IROST)
13-15 May 2024

03231-97589

IROST

Hollow fiber solid phase microextraction (HF-SPME) with ZIF-8@GO reinforced sol-gel for preconcentration of paraquat prior to determination by UV -Vis spectrophotometry

Narges Vaezi, Naser Dalali*

Corresponding Author E-mail: naser.dalali@znu.ac.ir

Department of chemistry, Faculty of science, University of zanjan, Zanjan, 45371- 38791, Iran.

Abstract: Hollow fiber solid phase microextraction (HF-SPME) with ZIF-8@GO reinforced sol-gel was utilized in combination with UV -Vis spectrophotometry at 257 nm for the preconcentration and determination of paraquat in soil samples. Silica-based ZIF-8@GO was arranged using sol-gel technology by the reaction of tetraethyl orthosilicate (TEOS) with an acid catalyst (HCl).

Keywords: ZIF-8@GO ; HF-SPME; UV -Vis spectrophotometry ; sol-gel technology

Introduction

Paraquat (1,1-dimethyl-4,4-bipyridinium chloride, PQ) is a chemical herbicide marketed worldwide as a fast acting and non-selective herbicide. PQ is classified as a moderate but lethal poison [1]. The mechanism of PQ toxicity is related to the accumulation of reactive oxygen species (ROS) and toxic free radicals in various tissues, particularly the lungs. Recent studies have shown that PQ is associated with Parkinson's disease [2]. Various methods have been used to analyze PQ in natural samples including gas chromatography (GC), gas chromatography-mass spectrometry (GC-MS), high-performance liquid chromatography (HPLC), as well as liquid chromatography-mass spectrometry (LC-MS), capillary electrophoresis (CE) and derivatization spectroscopy [3]. Some of these are extensive or time-consuming sampling methods. UV-Vis spectrophotometry has been utilized for its simplicity, speed, adaptability, accuracy, and low cost [4]. Due to matrix interferences and low concentration of paraquat, analysis of real samples is difficult. It is essential to create strategies for the determination of paraquat with high affectability, selectivity, and precision. Within the choice of methods for preconcentration, extraordinary consideration should be paid to decreasing or replacing harmful solvents with friendly solvents and decreasing sample preparation steps [5]. In recent years, a new mode of SPME, namely, hollow fiber solid-phase microextraction has emerged and attracted increasing attention. In this mode, a commercial polypropylene hollow fiber is used as supporter for adsorbents instead of a quartz fiber or a stainless steel conventionally used in SPME. The superiority of hollow fiber as supporter is attributed to its interior properties, such as many micropores extending to its surface and interior, extremely high mechanic strength and corrosion resistance. More importantly, hollow fiber itself has an excellent sample clean-up function because the micropores in the wall possess a certain size and the large molecules and particles cannot permeate through these pores, which is applicable to various complicated matrix samples. Besides, owing to the low cost, hollow fiber is disposable after each use thus avoiding cross-contamination and carry-over problems [6]. In the present work, we have introduced a novel, basic, delicate, and specific SPME technique that uses hollow fiber-supported sol–gel combined with ZIF-8@GO named HF-SPME for the determination of paraquat in soil samples with UV-Vis spectrophotometry. A silica-based, ZIF-8@GO was prepared by sol–gel technology via the reaction of tetraethyl orthosilicate (TEOS) with an acidic catalyst (HCl). This sol was then injected into a polypropylene hollow fiber segment, and the gel formation process was implemented in situ. This disposable device was operated in direct immersion sampling mode during sample analysis. The impact of different parameters such as pH, extraction time, stirring rate, and sample volume were completely explored, and the best conditions were chosen.

Experimental Section

The hollow fibers were manually cut into 2 cm pieces and washed with acetone to remove impurities, and left to dry. Finally, 6 µL of the sol solution was gradually injected into the lumen of hollow fiber using a micro syringe. The fibers were left to dry in ambient conditions. Both open ends of the fibers were closed to prevent leakage. The prepared fibers were placed in a glass vial (15.2 cm³) and exposed to 10 mL of an aqueous solution of the analyte (optimized pH value). The content was stirred at 700 rpm magnetically for 30 min. During the appropriate extraction time, the analyte diffuses from the solution into the sorbent through the porous hollow fiber. After extraction, the hollow fiber was removed and immersed in 0.5 mL of methanol as a desorption solvent in a closed vial, and the analyte was desorbed from the adsorbent.

22nd Iranian Chemistry Congress (ICC22)
Iranian Research Organization for Science and Technology (IROST)
13-15 May 2024

03231-97589

The extracted analyte was measured by UV-Vis spectrophotometry.

Results and Discussion :

ZIF-8@GO was synthesized and characterized through X-ray diffraction (XRD), Field Emission Scanning Electron Microscopy (FESEM), Fourier transform infrared spectroscopy (FT-IR) and BET surface area analysis. critical microextraction parameters including donor phase pH, donor phase volume, stirring rate, extraction time, and desorption conditions such as type of desorption solvent, volume of desorption solvent and desorption time were examined and optimized. The optimal experimental conditions were as follows: the amount of ZIF-8@GO: 5mg; pH of donor phase : 5; adsorption and desorption time, 30 min; Stirring rate: 700 rpm; donor phase volume:10mL; desorption solvent: methanol, Volume of desorption solvent: 0.5mL. Under the optimal conditions of the method, the limit of detection, preconcentration factor and precision as RSD% were found to be 0.15 μgL^{-1}, 631.07 and 0.48%, respectively. The proposed HF-SPME procedure showed good linear behavior in the concentration range of 0.5–2000 μgL^{-1} and showed an acceptable coefficient of determination of 0.9992. The method was used to determine the paraquat in several soil samples. The accuracy and precision of the method were investigated by extracting and analyzing spiked samples with different levels of selected analyte. The results confirmed that the method was capable of extracting and determining the selected analytes in real samples.

Conclusions

A modern type of hollow fiber containing ZIF-8@GO has been made and illustrated the viable application of HF-SPME combined with UV-Vis spectrophotometry for the preconcentration and determination of paraquat. ZIF-8 was synthesized and accommodated on the surface of (GO) nanosheets. ZIF-8@GO was fabricated through the sol-gel method and injected into the lumen of the hollow fiber. The prepared composite was successfully utilized in the process of preconcentration of paraquat residue in soil samples. The above composite moreover had the advantage of the strong interaction between analyte and adsorbent. Polypropylene walls have channels in which the analytes molecules (within the feed solution) and the adsorbent (ZIF-8@GO reinforced sol-gel inside the fiber) are in contact with each other. Meanwhile, the pores can cause a kind of dimensional selectivity to the analyte molecules. Adaptability, simplicity, disposable nature of the device that eliminates the possibility of sample carryover, more convenient handling than the other traditional SPME fibers, and high preconcentration factors are among the advantages of this method. Under the optimized conditions, the proposed method provided low LOD, good LDR and acceptable precision.

References

[1] Rashidipour, M., Maleki, A., Kordi, S., Birjandi, M., Pajouhi, N., Mohammadi, E., ... & Davari, B. (2019).Pectin/chitosan/tripolyphosphate nanoparticles: Efficient carriers for reducing soil sorption, cytotoxicity, and mutagenicity of paraquat and enhancing its herbicide activity. Journal of agricultural and food chemistry, 67(20), 5736-5745. https://doi.org/10.1021/acs.jafc.9b01106

[2] Fortenberry, G. Z., Beckman, J., Schwartz, A., Prado, J. B., Graham, L. S., Higgins, S., ... & Calvert, G. M. (2016). Magnitude and characteristics of acute paraquat-and diquat-related illnesses in the US: 1998–2013. Environmental research, 146, 191-199. https://doi.org/10.1016/j.envres.2016.01.003

[3] Rajaram, R., & Neelakantan, L. (2023). Recent advances in estimation of paraquat using various analytical techniques: A review. Results in Chemistry, 5, 100703. https://doi.org/10.1016/j.rechem.2022.100703

[4] Alian, E., Semnani, A., Firooz, A., Shirani, M., & Azmoon, B. (2018). Application of response surface methodology and genetic algorithm for optimization and determination of iron in food samples by dispersive liquid–liquid microextraction coupled UV–visible spectrophotometry. Arabian Journal for Science and Engineering, 43, 229-240. https://doi.org/10.1007/s13369-017-2856-9.

[5] Ghavidel, F., Shahtaheri, S. J., Torabbeigi, M., & Froushani, A. R. (2016). Optimization of solid phase microextraction procedure for determination of paraquat using reduction process. Journal of Analytical Chemistry, 71, 648-652. https://doi.org/10.1134/S106193481607008X.

[6] Ebrahimi, M., Es'haghi, Z., Samadi, F., Bamoharram, F. F., & Hosseini, M. S. (2012). Rational design of heteropolyacid-based nanosorbent for hollow fiber solid phase microextraction of organophosphorus residues in hair samples. Journal of Chromatography A, 1225, 37-44. https://doi.org/10.1016/j.chroma.2011.12.077

From Waste to Wealth: Synthesis of Silica Nanoparticles from Almond Peel Agricultural Waste

Akbar Jabbarzadeh, Ahmad Poursattar Marjani*, Fatemeh Zanbili

Corresponding Author E-mail: a.poursattar@urmia.ac.ir; a.poursattar@gmail.com

Department of Organic Chemistry, Faculty of Chemistry, Urmia University, Urmia, Iran.

Abstract: In this study, silica nanoparticles (SiO_2 NPs) were synthesized from almond peel, and their properties were characterized by FTIR and FESEM analyses. By exploring this approach, this study contributes to developing novel and eco-friendly strategies to utilize agricultural wastes and convert them into valuable and useful nanoparticles.

Keywords: Silica Nanoparticles.; Agricultural Waste; Nanoparticle Synthesis

Introduction

Environmental concerns and the need to minimize waste have contributed to a steady increase in global demand for sustainable and environmentally friendly materials [1]. Agricultural waste management has become a pressing concern due to agricultural waste accumulation's significant ecological and economic challenges [2]. To address this challenge, agricultural waste can be used as a feedstock for nanomaterial synthesis [3]. As a byproduct of the almond processing industry, almond peel has gained considerable attention due to its potential for synthesizing silica nanoparticles (SiO_2 NPs) [4]. There are approximately 32% of the earth's total weight made up of silica (Si), the second most abundant element. Consequently, soil-rooted plants always contain Si in their tissues [5]. Si is a naturally occurring compound in almond peel that can be extracted and converted into valuable SiO_2 NPs.

Various applications of SiO_2 NPs have been reported in various fields, including biomedicine, catalysis, materials science, and environmental remediation. Using almond peel to synthesize SiO_2 NPs is a sustainable method of disposing of agricultural waste. Furthermore, it offers the opportunity to produce value-added products from readily available and inexpensive raw materials [6]. An almond peel that would otherwise be thrown away is repurposed into a valuable product, providing a sustainable solution to agricultural waste management. In contrast to traditional methods of producing SiO_2 NPs, synthesizing SiO_2 NPs from agricultural waste is cost-effective and environmentally friendly. It is possible to utilize the resulting SiO_2 NPs in various applications. Consequently, this contributes to developing a circular economy [7].

Experimental Section

First, the almond peel (prepared locally) was washed with distilled water (DI) to remove soluble dust or other contaminants. Then, it was dried in an oven at 70 °C for 48 h. 10 grams of almond peel were placed in the laboratory furnace at 700 °C for 5 h and converted to ash powder. 6 grams of ash powder were treated with 90 mL of 1 M NaOH solution (purchased from Sigma Aldrich) to form sodium silicate. The obtained solution was transformed into silicic acid (H_3SiO_4) by titration with 1 M HCl solution (purchased from Sigma Aldrich) under constant stirring to reach pH 4. HCl was added to the obtained Na_2SiO_3 solution, which caused the precipitate formation and condensation of the silanol group (Si–OH). To remove the NaCl residue, the precipitate was rinsed with hot DI water and centrifuged thrice for 10 minutes at 3000 rpm. The residue was dried at 50 °C for 24 h to produce SiO_2 NPs powder.

Results and Discussion

Fourier transform infrared spectroscopy (FTIR) was performed to identify functional groups and chemical bonds in SiO_2 NPs and almond peel powder.

The peak observed in the spectrum of almond peel powder and its ash (Fig. **1**) in the range of 3500 cm^{-1} to 1330 cm^{-1} is related to the stretching vibration of OH-cellulose and hemicellulose within their structure. Furthermore, the peak observed from 2935 to 2900 cm^{-1} is related to the –CH stretching vibration. The observed peak in the 1735 to 1640 cm^{-1} range is attributed to the C=O stretching vibration of lignin and hemicellulose. It is related to lignin's benzene ring in the range of 1605 to 1580 cm^{-1}. Also, the peak observed from 1430 to 1320 cm^{-1} is attributed to CH-bending vibration. Also, the 1045 to 1025 cm^{-1} peak is related to the C–O stretching vibration of cellulose, hemicellulose, and lignin.

In the FTIR spectrum of SiO_2 NPs (Fig. **1**), the peak seen at 3429 cm^{-1} is related to the stretching vibration of the –OH bond. While the peak observed at 1631 cm^{-1} is associated with the bending vibration of H_2O from the silanol group (Si–OH). Also, the peaks observed at 1096 and 798 cm^{-1} are due to the asymmetric vibration of Si–O–Si and the symmetric stretching vibration of the Si–O–Si bond. The

22nd Iranian Chemistry Congress (ICC22)
Iranian Research Organization for Science and Technology (IROST)
03231-97589
13-15 May 2024

IROST

Si–O–Si bond bending vibrational peak is 470 cm^{-1}. Also, the apparent difference observed between the three FTIR spectra obtained from almond peel powder, almond peel ash, and SiO$_2$ NPs confirms the correctness of the synthesis of these NPs.
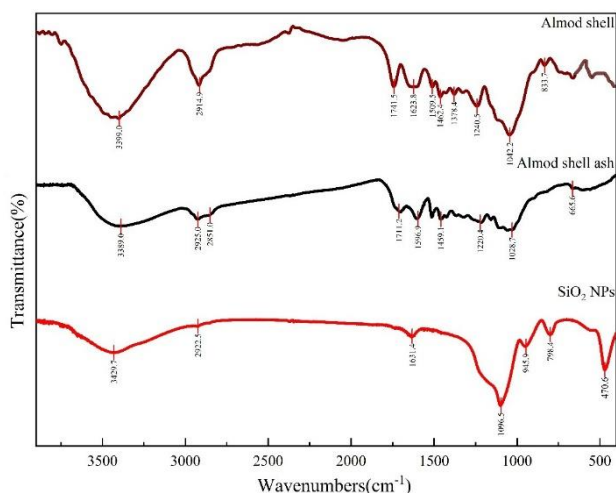

Fig. 1: FTIR spectrum of the almond peel powder, its ash attained in 700 ^{0}C, and synthesized SiO$_2$ NPs.

The surface morphology of SiO$_2$ NPs synthesized from almond peel ash was investigated by a field emission scanning electron microscope (FESEM). As shown in Fig. **2**, FESEM images at a magnification of 100 nm demonstrate that SiO$_2$ NPs were successfully synthesized in an almost dispersed, spherical shape and uniform size distribution. The particle size of SiO$_2$ NPs was distributed within a range of 40–70 m.
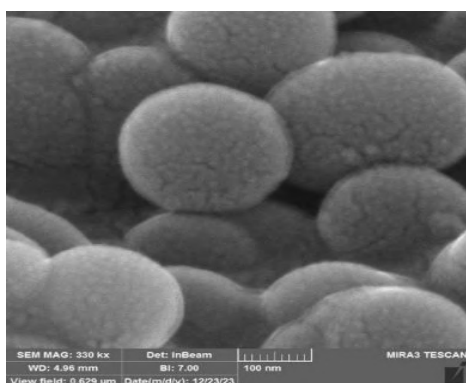

Fig. 2: FESEM images of synthesized SiO$_2$ NPs

Conclusions

This study employed a simple, low-cost, environmentally friendly, and low-energy method to produce SiO$_2$ NPs from almond peel ash. In this method, the alkaline extraction of sodium silicate from almond peel ash and precipitation through sodium silicate solution acidification. The produced SiO$_2$ NPs were spherical with average 40–70 nm sizes. The synthesized SiO$_2$ NPs could

be used in chromatography packing columns, cosmetics, pharmaceuticals, paints, coatings, etc.

References

[1] Zamani, A., Marjani, A. & Mousavi, Z. (2019). Agricultural waste biomass-assisted nanostructures: Synthesis and application. *Green Processing and Synthesis*, *8*(1), 421–429. https://doi.org/10.1515/gps-2019-0010

[2] Lin, C. S. K., Pfaltzgraff, L. A., Herrero-Davila, L., Mubofu, E. B., Abderrahim, S., Clark, J. H., Luque, R. (2013). Food waste as a valuable resource for the production of chemicals, materials, and fuels. Current situation and global perspective. *Energy & Environmental Science,* *6*(2), 426–464. https://doi.org/10.1039/C2EE23440H

[3] Li, X., Liu, Y., Hao, J., & Wang, W. (2018). Study of Almond Shell Characteristics. *Materials, 11*(9). https://doi.org/10.3390/ma11091782

[4] Huang, Y., Li, P., Zhao, R., Zhao, L., Liu, J., Peng, S., Zhang, Z. (2022). Silica nanoparticles: Biomedical applications and toxicity. *Biomedicine & Pharmacotherapy,* *151*, 113053. https://doi.org/10.1016/j.biopha.2022.113053

[5] Rovani, S., Santos, J. J., Corio, P., & Fungaro, D. A. (2018). Highly Pure Silica Nanoparticles with High Adsorption Capacity Obtained from Sugarcane Waste Ash. *ACS Omega, 3*(3), 2618–2627. https://doi.org/10.1021/acsomega.8b00092

[6] Shafiei, N., Nasrollahzadeh, M., & Iravani, S. (2021). Green Synthesis of Silica and Silicon Nanoparticles and Their Biomedical and Catalytic Applications. *Comments on Inorganic Chemistry, 41*, 317 - 372. https://doi.org/10.1080/02603594.2021.1904912

[7] Liu, N., Huo, K., McDowell, M., Zhao, J., & Cui, Y. (2013). Rice husks as a sustainable source of nanostructured silicon for high performance Li-ion battery anodes. *Scientific reports, 3*, 1919. https://doi.org/10.1038/srep01919

22nd Iranian Chemistry Congress (ICC22)
Iranian Research Organization for Science and Technology (IROST)
13-15 May 2024

03231-97589

ISC
Islamic World Science Citation Center

IROST

In Situ Generation of 1,1-(Dithiolate) Anions as Key Intermediates in the Synthesis of Sulfur-Containing Hybrid Compounds

Farough Nasiri, Leila Sabahi Aghabagher, Saiedeh Akhavane, Jaber Salehzadeh, and Maedeh Rabiei

Corresponding Author E-mail nasiri@uma.ac.ir

University of Mohaghegh Ardabili, Faculty of Science, Department of Applied Chemistry.

Abstract: In this study, we present an efficient one-pot synthesis approach for creating hybrid compounds that combine pyrazolones and sulfur-containing heterocycles. These hybrids result from reactions involving *in situ* generated 1,1-dithiolate anions, which form when pyrazolones react with carbon disulfide, and diverse difunctional electrophiles. Additionally, our examination explores the structural attributes of these newly synthesized compounds.
Keywords: Hybrid compounds; Proaromaticity; Pyrazolones; One-pot reactions.

Introduction

The utilization of reactive intermediates in the synthesis of organic compounds is regarded as one of the fundamental approaches in organic chemistry. 1,1-Dithiolate anions serve as convenient synthetic intermediates for creating a diverse range of sulfur-containing heterocyclic compounds. These anions form through the reaction of different active methylene compounds, such as 1,3-dicarbonyl compounds or pyrazolones, with carbon disulfide in the presence of a suitable base. Subsequently, these intermediates react with various difunctional electrophiles, resulting in the production of sulfur-containing organic compounds.

A comprehensive survey of the literature reveals that the biological activities of bioactive compounds are often enhanced when two or more biologically active units are combined within a single molecule. Consequently, pyrazolone hybrids that incorporate diverse heterocycles have demonstrated varied chemotherapeutic effects and have been employed as antimicrobial, antifungal, and antiviral agents. Furthermore, sulfur-containing heterocycles, which serve as biologically active components, are found in numerous natural compounds and pharmaceutical drugs. Given the potential of pyrazolones and sulfur-containing heterocycles, we are intrigued by the synthesis of hybrid molecules that combine both pyrazolones and various sulfur-containing heterocycles.

Experimental Section

A mixture of pyrazolones (1 mmol) and triethylamine (2 mmol, 200 mol%) in a convenient solvent or under solvent-free conditions was stirred at room temperature. Next, carbon disulfide (1.2 mmol) was added, and the mixture was stirred for 30 to 60 minutes until the pyrazolone spot disappeared in thin-layer chromatography (TLC). Subsequently, difunctional electrophiles such as propargyl bromide (1 mmol) were added, and the reaction progress was monitored using TLC. Upon completion of the reaction, the product was separated using standard laboratory methods.

Results and Discussion

The synthesis of pyrazolone derivatives, carbon disulfide, and various difunctional electrophiles involved a two-step process (see Fig. 1). In the initial step, a base was introduced to a mixture of pyrazolone and carbon disulfide (CS_2). The reaction's progress was tracked using thin-layer chromatography (TLC) to observe the disappearance of the pyrazolone spot. Once pyrazolone spot vanished, difunctional electrophiles were added to the mixture, and the reaction progress was again monitored using TLC (Step 2). After the reaction was complete, the final products were separated using standard laboratory techniques [2-4].
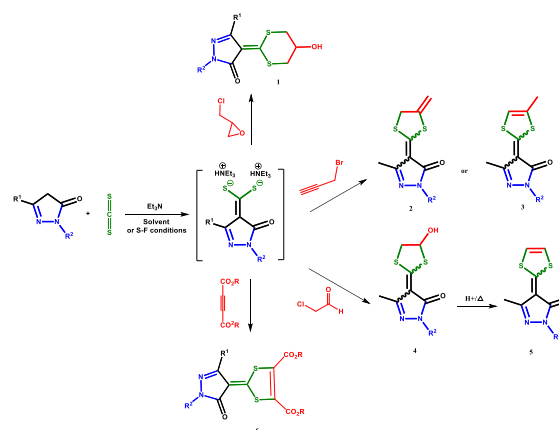

Fig.1: Two-step reactions involving pyrazolones, carbon disulfide, and various difunctional electrophiles.

The methylene protons of the 1,3-dithiane moiety in compound **1** (where R^1 = Ph and R^2 = H) exhibit diastereotopic behaviour due to the molecular constitution and symmetry considerations. Analyzing the splitting pattern of these hydrogens in conjunction with

22nd Iranian Chemistry Congress (ICC22)
Iranian Research Organization for Science and Technology (IROST)
13-15 May 2024

03231-97589

IROST

the methine hydrogen (H^x), as seen in compound **1** (refer to Fig. 2), allows us to discern the position of the hydroxy group (whether it is axial or equatorial). In Fig. 2, each methylene hydrogen (designated as H^a, H^b, H$^{a'}$, H$^{b'}$) manifests as a doublet of doublets at the following chemical shifts:

- 2.67 ppm (with $^2J_{HH}$ = 13.5 Hz and $^3J_{HH}$ = 5.0 Hz)

- 2.81 ppm (with $^2J_{HH}$ = 13.5 Hz and $^3J_{HH}$ = 6.3 Hz)

- 3.13 ppm (with $^2J_{HH}$ = 13.9 Hz and $^3J_{HH}$ = 6.3 Hz)

- 3.22 ppm (with $^2J_{HH}$ = 13.9 Hz and $^3J_{HH}$ = 5.0 Hz)

The absence of a significant coupling constant ($^3J_{HH}$ > 10 Hz) for vicinal hydrogens indicates that, in the preferred conformation of compound **1** (as depicted in Fig. 2), the OH functional group occupies the axial position. This preference for the axial position of the hydroxy group in compound **1** may arise from hydrogen bond interactions between the hydroxy group and the sulfur atoms of the 1,3-dithian ring.
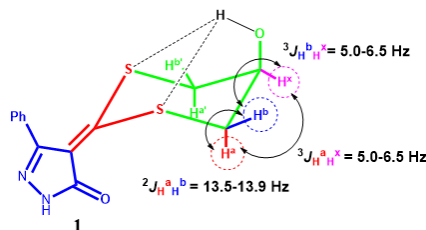

Fig.2: Coupling constants of the methylene hydrogens in the 1,3-dithian moiety where observed in the ^1H NMR spectrum of compound **1** (250.1 MHz, DMSO-$d6$)

In compound **3**, the C=C exocyclic bond connects the two pyrazolone and 1,3-dithiol moieties. ^1H NMR serves as a valuable tool for assessing the aromatic property of a compound. The expected chemical shift for CH protons in the ^1H NMR spectrum of the localized 1,4-dithiafulvene structure, similar to compound **3**, is approximately 6.38 ppm. In the ^1H NMR spectrum of the isomeric mixture (E and Z) of **3**, the olefinic proton appears at around 7.07-7.30 ppm in DMSO. Conversely, in CDCl$_3$, the ^1H NMR spectrum of **3** shows that the olefinic proton appears at 6.64 and 6.69 ppm. When the spectrum of **3** is taken in DMSO-$d6$, the vinylic hydrogen emerges at 7.35 and 7.41 ppm. These results indicate that the 1,4-dithiafulvene moieties in **3** exhibit aromatic properties when dissolved in DMSO. Additionally, several resonance forms can be considered for **3** (as shown in Fig. 3). Among these forms, resonance form **3-I** appears more stable than **3-II** and **3-III** due to the aromaticity arising from the linkage between the pyrazole and 1,3-dithiol moieties.
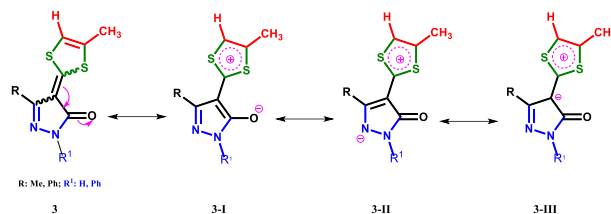

Fig.3: Some resonance structures of compound **3**

Resonance forms of compounds, as exemplified in this study, are sensitive to changes in solvent polarity. To explore this phenomenon, we optimized the geometries of compound 3 in both CDCl$_3$ and DMSO using the *B3LYP/6-311G level*. Comparing bond lengths in these solvents, we observe that the zwitterionic form 3-I becomes more prominent in the ground state of the molecule when dissolved in a more polar solvent. This observation aligns with the proton chemical shifts of the dithiole ring hydrogen atom in compound **3**, which experience deshielding due to increased polarity. Overall, the chemical shift of the dithiole ring proton indicates the aromatic nature of the dithiol ring moiety.

Conclusions

In conclusion, we have developed a straightforward procedure for synthesizing novel pyrazolone-sulfur-containing heterocycles through a one-pot reaction involving 2-pyrazoline-5-ones, carbon disulfide, and various difunctional electrophiles.

References

[1] Yavari, I., Saffarian, H., & Naeimabadi, M. (2017). A one-pot synthesis of novel cyclic ketene dithioacetals from Nef-isocyanide-Perkow adduct. *Journal of Sulfur Chemistry*, *38*(6), 679-685.

[2] Sabahi-Agabager, L., Akhavan, S., & Nasiri, F. (2022). A facile one-pot, solvent-free synthesis of new pyrazolone-1, 3-dithiolan hybrids through the reaction between 2-pyrazoline-5-ones, CS2, and α-chloroacetaldehyde. *Journal of Sulfur Chemistry*, *43*(4), 391-401.

[3] Rabiei, M., & Nasiri, F. (2024). Facile one-pot synthesis of hydroxylated 1, 3-dithiane-pyrazolone hybrids. *Research on Chemical Intermediates*, 1-12.

[4] Salehzadeh, J., & Nasiri, F. (2023). A versatile solvent-free synthesis of novel pyrazolone-1, 3-dithiolan and pyrazolone-1, 3-dithiole hybrids. *Research on Chemical Intermediates*, *49*(10), 4621-4637.

22nd Iranian Chemistry Congress (ICC22)
Iranian Research Organization for Science and Technology (IROST)
13-15 May 2024

03231-97589

IROST

A microfluidic paper-based Analytical device for simultaneous measurement of total phenol and flavonoid contents and antioxidant power of plant extracts

Raziyeh Shahali, Zahra Shojaeefard, Bahram Hemmateenejad *

Corresponding Author E-mail: hemmatb@shirazu.ac.ir

Chemistry Department, Shiraz University, Shiraz, Iran.

Abstract: In this research, a new paper based microfluidic device (µPAD) is introduced that is able to measure the antioxidant power and total content of phenol and flavonoids in plant samples with colorimetric method. This µPAD is made by creating an appropriate design on a Whatman paper substrate. For widely used tests including (2,2'-azino-bis(3-ethylbenzothiazoline-6-sulfonic acid, Total phenol content, Total flavonoid content and ferric reducing antioxidant power) analysis was performed by measuring the colour changes caused by the interaction of the indicators with the real sample. The applicability of the proposed method was investigated by determining those properties of four different plant samples (green tea, black tea, Lavandula and Matricaria) and comparison with the standard samples**.**

Keywords: Antioxidant Power; µPAD; Colorimetric

Introduction

Antioxidants are compounds that, if present in food or the human body, even in very low concentrations, control the oxidative processes [1]. Many studies show that antioxidants play an essential role in maintaining human health and preventing diseases due to their ability to reduce free radicals. Measuring the antioxidant activity of foods and biological samples is necessary to ensure the quality of foods and more importantly to study the effectiveness of food antioxidants in the prevention and treatment of related diseases [2].

Phenols and flavonoids are among the important compounds found in plant that show antioxidant properties. The amount of these compounds in different plants varies depending on where the plant is grown, how ripe it is, and how it is transported and prepared [3].

Various physical and chemical methods are used to measure the antioxidant power and the total content of phenol and flavonoids. Among these methods, high-performance liquid chromatography (HPLC) have found wider applications [4,5]. Nevertheless, these methods usually are time consuming and require expensive instruments. To solve the problems of the above methods, two antioxidant power assays including ABTS and FRAP test and total flavonoid and phenolic content assay by using $AlCl_3$ and Folin Ciocaltue reagent (FC) were employed on a paper base with a unique design.

Experimental Section

In this research, we introduce a simple, rapid, portable and inexpensive paper-based device that requires a very small amount of analyte. The intended device was designed by using the AutoCAD software (Figure 1). After that by using the printer, a waterproof barrier was created around the desired design.

Fig.1: Image of designed micropad

The central circular zone with a diameter of (7mm) is embedded for real sample injection (Sample Zone). The middle circles with a diameter of (5mm) are places for the addition of the standard solutions with different concentrations (Pretreatment Zone) and the end circles, which are the same size as the middle circles, are used for addition of indicators (Detection Zone).

In order to measure the biological properties by using the introduced µPAD, 0.5 µl of the desired indicator solutions were injected in the detection zones, then 0.5 µl of standard solutions with different concentrations were injected in the pretreatment areas, and the sensor images were recorded by using a scanner.

In the measurement step, a 40 µl portion of the aqueous extract of the plant sample was injected in the sample zone. Due to the capillarity of the paper, the sample extract passes through the channels and reacts with the indicators and standard solutions. Then, the sensor images and the color change of the indicators in the detection zones were recorded.

22nd Iranian Chemistry Congress (ICC22)
Iranian Research Organization for Science and Technology (IROST)
13-15 May 2024

03231-97589

Results and Discussion

With the help of the Imagej software, the color differences of the detection zones in the presence and absence of the analyte were obtained. the calibration curve of different concentrations of standard solutions considering total phenol and flavonoids content, and the antioxidant power obtained were used to calculate the plant sample properties, the results of which are summarized in Table1.

Table1: The measured values of biological properties using the introduced device

sample	TPC	TFC	FRAP	ABTS
Green tea	52.70	41.74	20.83	12.16
Black tea	35.29	29.21	10.39	8.80
Lavanda	20.22	15.39	4.91	6.50
Matricaria	28.34	20.63	5.73	7.12

Conclusions

The proposed device can measure the biological properties of different extracts with a single injection of the sample solution with a small volume. Also, the color change resulting from the interaction of the analyte with the indicators is stable for a long time on the paper substrate. Moreover, the proposed paper-based sensor is cheap, easy and portable. Also, the results of this method showed a good correlation with spectroscopic methods.

References

[1] Rodrigo, R., & Rodrigo, R. (2009). Oxidative stress and antioxidants: their role in human disease (Vol. 358). New York: Nova Biomedical Books.

[2] Antolovich, M., Prenzler, P. D., Patsalides, E., McDonald, S., & Robards, K. (2002). Methods for testing antioxidant activity. Analyst, 127(1), 183-198.

[3] Carocho, M., & Ferreira, I. C. (2013). A review on antioxidants, prooxidants and related controversy: Natural and synthetic compounds, screening and analysis methodologies and future perspectives. *Food and chemical toxicology*, *51*, 15-25.

[4] Burnaz, N. A., Küçük, M., & Akar, Z. (2017). An on-line HPLC system for detection of antioxidant compounds in some plant extracts by comparing three different methods. Journal of Chromatography B, 1052, 66-72.

[5] Vijayalakshmi, M., & Ruckmani, K. (2016). Ferric reducing antioxidant power assay in plant extract. ||| Bangladesh Journal of Pharmacology|||, 11(3), 570-572.

22nd Iranian Chemistry Congress (ICC22)
Iranian Research Organization for Science and Technology (IROST)
13-15 May 2024

03231-97589

ISC

IROST

Design of 0D Particle-1D Nanobelt Plasmonic Ag₂CrO₄/AgVO₃ Nanophotocatalyst for Deletion of Toxic Organic Dyes from Polluted Water

Ehsan Mohammadi Avansar, Mohammad Haghighi*, Maryam Shabani[a], Fatemeh Chapari, Hamed Moradi

Corresponding Author E-mail: haghighi@sut.ac.ir

Chemical Engineering Faculty, Reactor and Catalysis Research Center (RCRC), Sahand University of Technology P.O. Box 51335-1996, Sahand New Town, Tabriz, Iran.

Abstract: In this study, a visible-light-active nanophotocatalyst was synthesized via precipitation method, enhancing the degradation of toxic dyes in simulated wastewater. XRD and FESEM characterized the photocatalyst, affirming phase formation and showcasing morphology. Tested under simulated solar light, it achieved 97.2% degradation efficiency for crystal violet, respectively, in 120 minutes.

Keywords: Ag₂CrO₄/Ag-AgVO₃ nanophotocatalyst; Toxic Organic Dyes; Water Treatment

Introduction

The increasing presence of diverse organic pollutants in global water sources due to industrial expansion poses a significant threat to human health. Particularly, the widespread utilization of organic dyes like crystal violet (CV) and acid orange 7 (AO7) across industries necessitates urgent solutions to ensure sustainable human development[1]. In recent times, diverse methods have been employed to remove organic pollutants, such as adsorption, biodegradation, chemical oxidation, electrochemical conversion/combustion, and membrane separation. Among these, advanced oxidation processes (AOPs) are recognized as efficient techniques for treating organic wastewater[2]. Photocatalyst is a novel AOP method that's increasingly recognized as a viable remedy for global water pollution[3]. Over the last few decades, a wide range of semiconductor photocatalysts have been developed, primarily categorized into ultraviolet light-driven (ULD) and visible-light-driven (VLD) varieties[4]. One notable instance is Ag₂CrO₄, an emerging photocatalyst responsive to visible light. It exhibits a narrow bandgap of 1.75 eV, enabling functionality within the visible spectrum up to 570 nm[5]. This study investigates the photocatalytic efficiency of Ag₂CrO₄ as a visible-light-driven (VLD) nanophotocatalyst and AgVO₃ as an ultraviolet light-driven (ULD) nanophotocatalyst, prepared via precipitation methods. Their performance in degrading Crystal Violet and AO7 under simulated solar light is assessed. These materials have garnered considerable attention from researchers in recent times.

Experimental Section

To synthesize 1g of Ag₂CrO₄, 0.9g of AgVO₃ was used. The AgVO₃ was synthesized using a hydrothermal method, maintaining a temperature of 180°C for a duration of 24 hours. The synthesis involved dispersing the AgVO₃ in 50mL of deionized water and stirring the solution for 30 minutes to form solution A. Subsequently, 0.11g of AgNO₃ was dispersed in 50mL of deionized water and stirred for 30 minutes to create solution B. Meanwhile, 0.06g of K₂CrO₄ was dispersed in 50mL of deionized water to form solution C. Solution A was then combined with solution B along with 20mL of deionized water to produce solution D. Solution C was added dropwise to solution D, and the resulting mixture was aged for 2 hours. Finally, the obtained powder was washed, filtered, and dried overnight at 60°C in a vacuum oven.

Results and Discussion

A. XRD Analysis:

The XRD patterns of Ag₂CrO₄/AgVO₃ nanophotocatalyst are shown in Figure1. All the peaks of synthesized nanophotocatalyst are consistent with those of pure Ag₂CrO₄ and AgVO₃. This indicates successful synthesis, accurate phase formation, and no impurities in the sample.
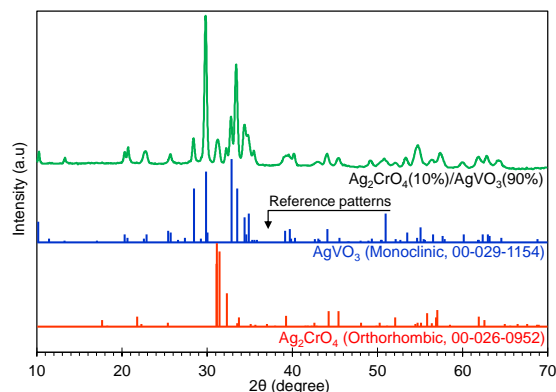

Fig.1: XRD analysis of 0D particle-1D nanobelt plasmonic Ag₂CrO₄/AgVO₃ nanophotocatalyst

22nd Iranian Chemistry Congress (ICC22)
Iranian Research Organization for Science and
Technology (IROST)
13-15 May 2024

03231-97589

IROST

B. FESEM Analysis:

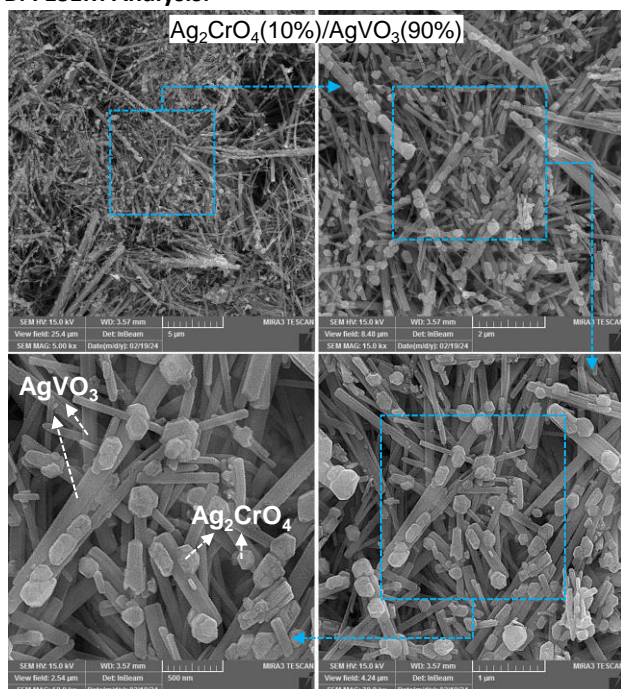**Fig.2:** FESEM analysis of 0D particle-1D nanobelt plasmonic $Ag_2CrO_4/AgVO_3$ nanophotocatalyst

Field emission scanning electron microscopy (FESEM) images of synthesized photocatalysts are shown in Figure 2. Observations indicate that $AgVO_3$ particles exhibit a broad rod-like morphology, with Ag_2CrO_4 nanoparticles arranged on their surface, thereby forming a nanocomposite structure.

C. Evaluation of Photocatalytic Performance

The degradation trials of CV, serving as refractory model pollutants, were conducted in a 600 mL beaker acting as a photocatalytic reactor at room temperature. A 400W Halogen lamp, specifically a HALOLINE ECO SST 400 W by OSRAM in Germany, was employed as the simulated solar light source. This setup aimed to evaluate and gauge the photocatalytic efficacy of the prepared macro-structured rod-like Ag_2CrO_4 nanophotocatalyst**.** Figure 4 illustrates that with a catalyst dosage of 1g/L and an initial concentration of 10mg/L CV, the adsorption rate reaches 50.04% within 60 minutes, while the degradation rate rises to 97.2% after 120 minutes of simulated solar light exposure. These results demonstrate the remarkable performance of the Ag_2CrO_4 nanophotocatalyst. Moreover, the photographs of removal CV in Fig. 4 during process time are represented. The nanophotocatalyst's efficacy stems from defect formation, enhancing light absorption and reducing recombination rates, while macropores aid in pollutant adsorption.
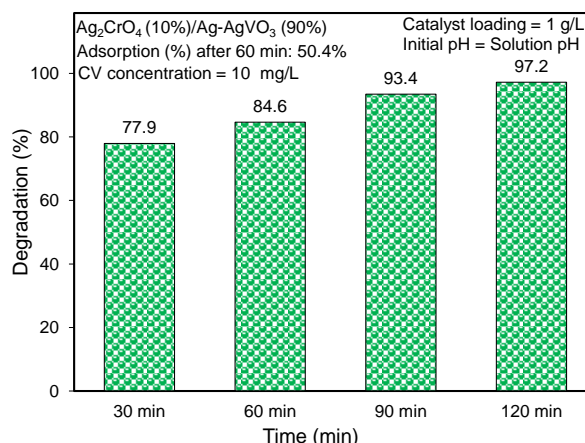

Fig.3 Photocatalytic performance of 0D particle-1D nanobelt plasmonic $Ag_2CrO_4/AgVO_3$ nanophotocatalyst in crystal violet removal.

Conclusions

Nanostructured Ag_2CrO_4 was prepared via a precipitation method and exhibited significant efficacy in the photodegradation of organic dye pollutants like CV. This enhanced performance is likely due to its suitable bandgap and enhanced performance across the solar spectrum, resulting from efficient light absorption, which could lead to an augmentation in excitons (electron-hole pairs). Furthermore, the plasmonic effect of Ag particles might aid in diminishing recombination occurrences.

References

[1] Sivakumar, V., et al., *AgVO3 nanorods: Synthesis, characterization and visible light photocatalytic activity.* Solid State Sciences, 2015. **39**: p. 34-39.

[2] Zhang, P., et al., *A novel Z-scheme BiOI/BiOCl nanofibers photocatalyst prepared by one-pot solvothermal with efficient visible-light-driven photocatalytic activity.* Materials Chemistry and Physics, 2021. **272**: p. 125031.

[3] Ma, R., et al., *A critical review on visible-light-response CeO2-based photocatalysts with enhanced photooxidation of organic pollutants.* Catalysis Today, 2018. **335**.

[4] Li, S., et al., *Synthesis of flower-like Ag2O/BiOCOOH p-n heterojunction with enhanced visible light photocatalytic activity.* Applied Surface Science, 2017. **397**.

[5] Azami, M., M. Haghighi, and S. Allahyari, *Sono-precipitation of Ag2CrO4-C composite enhanced by carbon-based materials (AC, GO, CNT and C3N4) and its activity in photocatalytic degradation of acid orange 7 in water.* Ultrasonics Sonochemistry, 2018. **40**: p. 505-516.

22ⁿᵈ Iranian Chemistry Congress (ICC22)
Iranian Research Organization for Science and Technology (IROST)
13-15 May 2024

03231-97589

IROST

Removal of Zn²⁺ from Aqueous Solution Using Peat Mass from Oshnavieh

Nosrat Heidari, Elnaz Zaher*

Corresponding Author E-mail: st_e.zaher@urmia.ac.ir

Urmia University.

Abstract: In this research, the effect of Zn²⁺ ion concentration on its removal from aqueous solutions was investigated, and the results showed the highest removal percentage at the lowest concentration (5ppm). From the study of relevant isotherms (Langmuir, Freundlich), it has been better with the results of experiments, which indicates chemical absorption.

Keywords: Removal of Zn²⁺; Peat Mass; Surface absorption

Introduction

Heavy metal pollution in water has become a common global problem. Metal pollutants in the environment mainly come from anthropogenic industrial and agricultural activities, and they can enter the water system in different ways, such as atmospheric sedimentation, waste water irrigation, and slag leaching [1]. Zinc is one of the most common and widely distributed heavy metals in the environment, and as an essential element for many organisms, it is beneficial to organisms when the content does not exceed the standard. However, due to industrial activities such as smelting, electroplating, mining, plastic manufacturing, and metallurgy, a large amount of wastewater carrying Zn²⁺ is discharged into the environment; moreover, Zn²⁺ is not easy to degrade in the environment, resulting in the content of zinc in water bodies increasing [2]. Therefore, it is of essential significance to reduce the concentration of Zn²⁺ in industrial wastewater by technical means before it is discharged into the environment, so as to reduce its impact on the environment [3]. Therefore, the purpose of this study is to improve the ability Peat Mass from Oshnavieh to remove Zn²⁺ from aqueous solution. On this basis, we obtained their adsorption characteristics of Zn²⁺ in aqueous solution. The research results will help to understand the removal effect and conditions of this new material so as to provide a theoretical basis for their industrial promotion to remove Zn²⁺ from wastewater.

Experimental Section

Materials and devices used in this research:
Zinc chloride ($ZnCL_2$), sodium hydroxide (to regulate basic pH), Oshnavieh peat soil, atomic absorption device(Varian 240FS), pH meter(Metroohm827Ph lab)
The zinc adsorption capacity in the adsorption experiments was evaluated by Formula (1).

$$A_{Zn2+} = (C_e - C_0) V/M \tag{1}$$

Where A_{Zn2+} is the zinc adsorption capacity, C_e is the solution concentration after adsorption (mg/L), C_0 is the solution concentration before adsorption (mg/L), V is the

volume of the solution (L), and M is the mass of the adsorption material (g).
Langmuir isotherm model calculations are obtained from linear formula 2:

$$\frac{1}{q_e} = \frac{1}{Q^0} + \frac{1}{b \cdot Q^0} \cdot \frac{1}{C_e} \tag{2}$$

Where q_e is equilibrium concentration of adsorbed species on solid phase adsorbent (mg/g), Q^0 the maximum adsorbed amount on the adsorbent (mg/g), b Langmuir constant and C_e is the solution concentration after adsorption (mg/L).
Freundlich isotherm model calculations are obtained from linear formula 3:

$$\log q_e = \log K_f + \frac{1}{n} \log C_e \tag{3}$$

Where K_f is Freundlich isotherm constant and $1/n$ Experimental constant related to absorption intensity.

Results and Discussion

Solutions containing Zn²⁺ with concentrations of 5, 20, 50, 100,200, and 300 mg/L were prepared, and the pH value was adjusted to 6 with pH regulating solution. A total of 0.1 g of biomass ash and modified material was accurately weighed, and 25 mL amounts of the Zn²⁺ solutions with different concentrations listed above were and placed in a constant temperature shaker for 1 h (25 °C). Then the Solutions were filtered with 11 μm micron microporous filter membrane and taken out and placed in the centrifuge for 4 min (3000 rpm). The Zn²⁺ concentration was measured with atomic absorption spectrometry. The concentration of the prepared samples in terms of the removal percentage is given in Table 1:

Table.1: The effect of the initial concentration of Zn²⁺ on the removal percentage

C_0(ppm)	R%
5	73.956
20	65.9704
50	37.2074
100	40.7393
200	38.1325
300	36.9328

22ⁿᵈ Iranian Chemistry Congress (ICC22)
Iranian Research Organization for Science and
Technology (IROST)
13-15 May 2024

03231-97589

IROST

With an increase in the initial concentration of zinc ions (Zn^{2+}), the pollutant removal percentage decreases. At low concentrations of Zn^{2+} ion, due to the large number of absorbent active sites compared to Zn^{2+} ion, the removal percentage increases, but with increasing concentration and with a constant the ratio of the absorbent value of the solution decreases due to the limitation of the absorption sites due to the saturation of the sites.
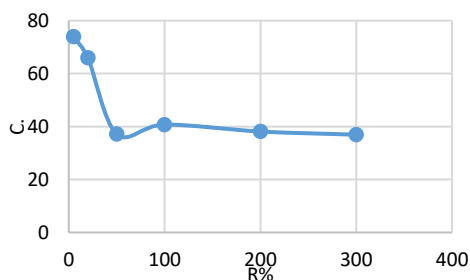
Fig.1: The effect of the initial concentration of Zn^{2+} on the removal percentage

Two linear Langmuir– Freundlich isotherm models were used to describe the adsorption mechanism between Zn^{2+} and peat soil. The behaviours of these two isotherms are interpreted in figures 2 and 3, respectively, and the corresponding results are shown.
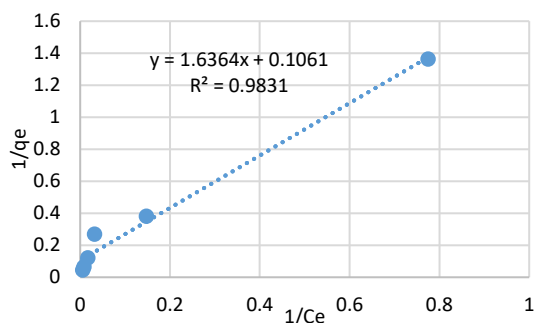

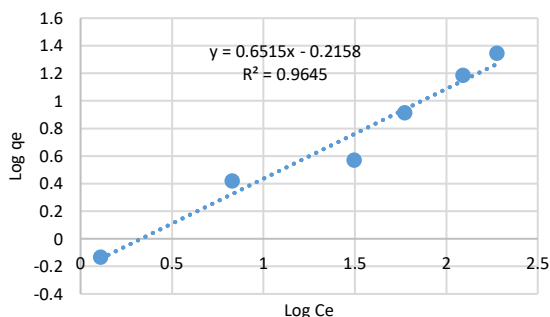**Fig.2:** Linear diagram of Langmuir isotherm for Zn^{2+} adsorption on Oshnavieh peat soil

Fig.3: Linear diagram of Freundlich isotherm for Zn^{2+} adsorption on Oshnavieh peat soil

Table2: Constants of isotherm models for Zn^{2+} adsorption by Oshnavieh peat soil

absorbent	Langmuir isotherm			Freundlich isotherm		
	R^2	Q_{max} (mg.g^{-1})	b (L.g^{-1})	R^2	n	K (L.g^{-1})
Oshnavieh Peat soil	0.98	9.4250	0.0648	0.96	1.53	0.81

Figure 2 is related to the Langmuir isotherm, with the correlation coefficient R^2 = 0.9831. Using the slope and width from the origin obtained from the equation of the corresponding line, the values of the parameters related to this isotherm were calculated. The calculated parameters show that this model has a high accuracy correlation coefficient. In addition, the maximum absorption capacity obtained from this isotherm is 9.4250 mg/g.

Figure 3 corresponds to the Freundlich isotherm with the correlation coefficient R^2 = 0.9645. The value of n obtained from this model is equal to n=1.53. Considering that the Langmuir isotherm has a higher accuracy correlation coefficient than the Freundlich isotherm, this isotherm model is desirable and more suitable than the Freundlich model, and the Zn2+ absorption process in peat soil follows this model.

Conclusions

In this study, the removal of Zn^{2+} ions from aqueous solutions on Oshnavieh peat soil was investigated. The optimum concentration in this experiment was 5 ppm. Langmuir and Freundlich isotherm models were used to mathematically describe Zn^{2+} adsorption on peat soil, and isotherm constants were deduced from these models. The Langmuir isotherm model was chosen as the best model to describe the adsorption process.

References

[1] Kapoor, D.; Singh, M.P. Heavy metal contamination in water and its possible sources. Heavy Met. Environ. 2021, 3, 179–189.

[2] Tonh, M.S.; Garnier, J.; Ara, J.O.D.; Cunha, B.C.A.; Machado, W.; Dantas, E.; Ara, R.; Kutter, V.T.; Bonnet, M.P.; Swyler, P. Behavior of metallurgical zinc contamination in coastal environments: A survey of Zn from electroplating wastes and partitioning in sediments. Sci. Total Environ. 2020, 743, 140610–140619.

[3] Saranya, K.; Palanisami, T.; Mallavarapu, M. Potential of Melaleuca diosmifolia leaf as a low-cost adsorbent for hexavalent chromium removal from contaminated water bodies. Process Saf. Environ. Prot. 2016, 100, 173–182.

Theoretical study of conductivity and electronic properties of poly(-4H-cyclopentadithiophene) using HOMO and LUMO orbitals

Maryam Manafi Moghadam[a*], Reza Banaei[a], Ali Ramazani[a,b]

Corresponding Author E-mail: m73.manafimoghadam@gmail.com.

[a] The Organic Chemistry Research Laboratory (OCRL), Department of Chemistry, Faculty of Science, University of Zanjan, Zanjan 45371-38791, Iran.
[b] The Convergent Sciences & Technologies Laboratory (CSTL), Research Institute of Modern Biological Techniques (RIMBT), University of Zanjan, Zanjan 45371-38791, Iran.

Abstract: One of the fundamental challenges in the field of conducting polymers is to design low band gap intrinsically conducting polymers so that there is no need to dope them. Some of the important applications of electrically conducting polymers are also discussed to highlighting the great potential of these materials.
Keywords: poly(-4H-cyclopentadithiophene); Band-gap; Electronic structure

Introduction

Polymers have always been considered as insulators of electricity. No one would have believed 30 y ago that polymers could conduct as good as metals. But now such feats have been achieved and that through simple modification of ordinary organic conjugated polymers. Called electrically conducting polymers or synthetic metals, these materials combine the electrical properties of metals with the advantages of polymers such as, lighter weight, greater workability, resistance to corrosion and chemical attack and the lower cost and have infiltrated our day-to-day life with a wide range of products, extending from most common consumer goods to highly specialized applications in space, aeronautics, electronics, and non-linear optics. It is, therefore, no wonder that these polymers are called the Materials of the twentyfirst century [1].

The first major breakthrough in the field of electrically conducting polymers took place around 1978 when it was demonstrated by Shirakawa et al.1,2 that polyacetylene (PA), an intrinsically insulating organic conjugated polymer, exhibits dramatic increase in electrical conductivity3 on treatment with oxidizing (electron-accepting) or reducing (electron-donating) agents. These oxidation and reduction reactions, which induce high conductivity in PA are termed as p-doping and n-doping, respectively [2, 3].

Theoretical Section

In the case of polymers, an unlimited group of molecular orbitals are formed. The width of the band of molecular orbitals depends on the degree of orbital overlap. As the number of orbitals increases, the width of this band increases; That is, high overlap leads to the formation of wide bands and low overlap leads to the formation of narrow bands. The electronic properties of a polymer compound are closely related to its band structure. The band whose electrons have the highest amount of energy is the valence or valence band, and the first empty band above the valence band is called the conduction band [4]. In this article, The B3LYP3 density functional method, 6-311G(d,p) basis set and Gaussian 2009 software (version D.01) were used to optimize the geometric structure of the studied compounds. Also, molecular orbital diagrams were calculated to check the electronic properties and conductivity of the desired compounds.

Results and Discussion

According to the energy levels of homo and lomo orbitals, it was calculated for trimer as -4.16 and -1.62 eV, respectively. In the case of pentamer, these values were predicted as -5.11 eV and -3.40 eV, respectively (Figure 1). These results show that the homo-pentamer orbital is more stable than the homo-trimer orbital, and its lomo is more unstable. Also, other differences in energy and alignment of other molecular orbitals of trimer and pentamer were observed. According to Figure 1, in the trimer structure, the electron density is symmetrically distributed over the entire molecule. In contrast, in the pentamer structure, the electron density is asymmetrically concentrated on one half of the molecule. The energy gap was calculated from the difference in the energy levels of the homo and lomo orbitals, 2.54 eV for the trimer and 1.71 eV for the pentamer. On the other hand, the closer the energy levels of filled and empty levels are to each other, the more easily the excitation and transfer of electrons is done in them and the conductivity increases [5, 6]. These results clearly show that the structure of the mentioned polymer is in the semi-conductor range from the point of view of the energy gap. Also, from the comparison of the energy gap of the two structures of trimer and pentamer -4H-cyclopenta dithiophen, it is clear that the increase in the degree of polymerization leads to a decrease in the energy gap. As a result, the conductivity of this polymer increases.
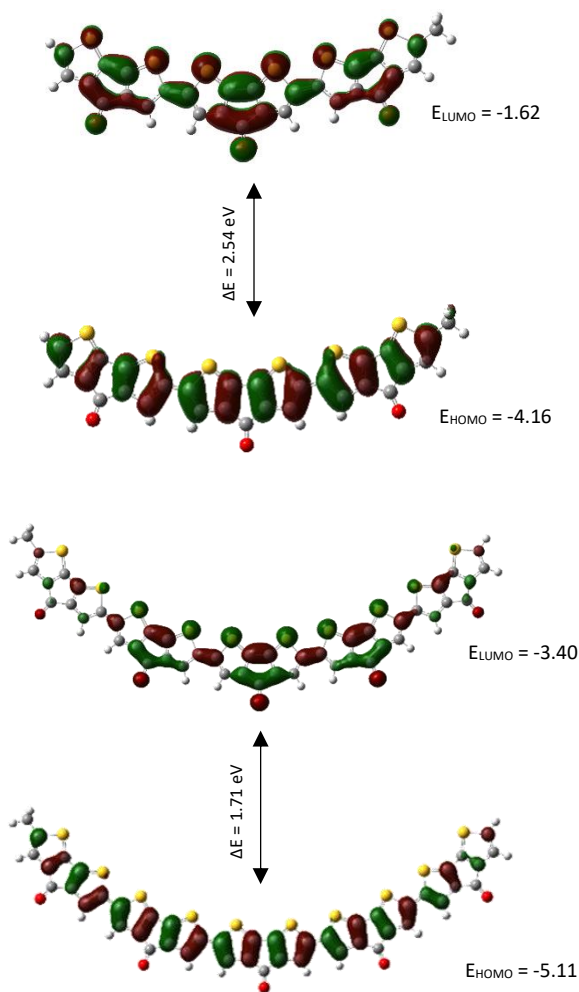
22nd Iranian Chemistry Congress (ICC22)
Iranian Research Organization for Science and
Technology (IROST)
13-15 May 2024

03231-97589

IROST

$E_{LUMO} = -1.62$

$\Delta E = 2.54$ eV

$E_{HOMO} = -4.16$

$E_{LUMO} = -3.40$

$\Delta E = 1.71$ eV

$E_{HOMO} = -5.11$

Fig.1: HOMO orbital and LUMO orbital of the trimer and pentamer -4H-cyclopenta dithiophen calculated by B3LYP/6-311G(d,p) level of theory.

The electronic properties and charge distribution have been visualized using an Electrostatic Potential (ESP) map, as shown in Figure 2. The ESP maps for trimer and pentamer -4H-cyclopenta dithiophen were derived using the B3LYP/6-311G(d,p) level of theoretical calculation. Blue colors on maps indicate the regions with the highest positive electrostatic potential, green colors indicate the regions with the most zero electrostatic potential, and red colors indicate the regions with the most negative electrostatic potential for the trimer and pentamer -4H-cyclopenta dithiophen. Moreover, the blue and cyan regions is related to the positive electrostatic potential that indicates the repulsion of a proton by the nucleus. On the other hand, the red and yellow regions is related to the negative electrostatic potential that indicates the absorption of a proton by the total electron density in the molecule and is mainly on the oxygen atoms [6].
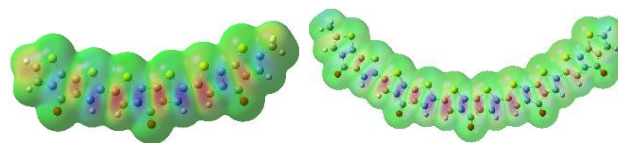

Fig.2: The ESP map for trimer and pentamer -4H-cyclopenta dithiophen via B3LYP/6-311G(d,p) level of theory.

Conclusions

In this paper, density functional theory (DFT) and molecular orbital diagrams were used to investigate the electronic properties and conductivity of poly (-4H-cyclopenta dithiophen). These results showed that the studied polymer is semi-conductive, and its conductivity increases with the increase in the length of the polymer chain.

References

[1] Stejskal, J. (2015). Polymers of phenylenediamines. Progress in Polymer Science, 41, 1-31.

[2] Sestrem, R. H., Ferreira, D. C., Landers, R., Temperini, M. L. A., & do Nascimento, G. M. (2009). Structure of chemically prepared poly-(para-phenylenediamine) investigated by spectroscopic techniques. Polymer, 50(25), 6043-6048.

[3] Le, T.-H., Kim, Y., & Yoon, H. (2017). Electrical and electrochemical properties of conducting polymers. Polymers, 9(4), 150.

[4] Bakhshi, A. K., & Bhalla, G. (2004). Electrically conducting polymers: Materials of the twentyfirst century.

[5] Manafi Moghadam, M., & Zamani, M. (2021). Performance of NO_2-rich multifunctionalized C60 derivatives as new high-energy-density nanomaterials. International Journal of Quantum Chemistry, 121(5), e26504.

[6] Moghadam, M. M., & Zamani, M. (2021). Electronic structure and spectroscopy of C60 nitroaryl radical adducts. Computational and Theoretical Chemistry, 1198, 113185.

22nd Iranian Chemistry Congress (ICC22)
Iranian Research Organization for Science and Technology (IROST)
13-15 May 2024

03231-97589

Electrochemical Characterization of Nanocomposite Metal-Organic Framework

Fatemeh Shahrab, Azadeh Tadjarodi*

Corresponding Author E-mail: tajarodi@iust.ac.ir

Research Laboratory of Inorganic Materials Synthesis, Department of Chemistry, Iran University of Science and Technology (IUST), 16846-13114, Tehran, Iran.

Abstract: A nanocomposite of bismuth ferrite nanoparticles and Cu(BDC) was synthesized using a solid-state microwave-assisted combustion method, enhancing their properties. Analytical methods, including FT-IR, XRD, SEM and VSM, confirmed synthesis. Electrochemical properties of $BiFeO_3$/Cu(BDC) were explored, emphasizing cyclic voltammetry. Using various electrolytes and scan rates, the nanocomposite exhibited stability and promising electrocatalytic activity, making it a highly potential electrocatalyst for supercapacitor applications and advanced energy storage systems.

Keywords: Metal-Organic Framework; Bismuth Ferrite Nanoparticles; Electrochemical, Cyclic voltammetry.

Introduction

Bismuth ferrite ($BiFeO_3$), known for its perovskite structure consisting of bismuth (Bi), iron (Fe), and oxygen (O), is a significant material in materials science due to its distinctive multiferroic traits[1-3]. Its crystalline structure induces ferroelectricity through ion displacement, alongside antiferromagnetic ordering at room temperature, leading to extensive research into its electronic and magnetic properties[4,5]. Ferroelectric characteristics suggest applications in non-volatile memories and sensors, while antiferromagnetism is pertinent to magnetic storage and spintronics. In electrochemistry, it is explored as an electrode material for supercapacitors and lithium-ion batteries. Integrating bismuth ferrite with metal-organic frameworks (MOFs) yields nanocomposites, enhancing electrochemical properties such as conductivity and charge transfer kinetics. This strategy offers adjustability in electrochemical behavior, tailoring properties for specific applications. Recent studies emphasize the capability of bismuth ferrite nanocomposites to address challenges in electrode stability and efficiency, making them crucial in advancing electrochemical systems[5-9].

Experimental Section

The synthesis of $BiFeO_3$ nanoparticles involved mixing $Bi(NO_3)_3 \cdot 5H_2O$, $Fe(NO_3)_3 \cdot 9H_2O$, glycine, and ammonium nitrate in a crucible, then transferring it with CuO powder to expedite the reaction via microwave irradiation. Copper oxide enhanced kinetics by absorbing microwave radiation. The resulting residue was washed and dried. For composite synthesis, $BiFeO_3$ nanoparticles dispersed in DMF were mixed with Cu(BDC) MOF solution and irradiated with microwaves. Cu(BDC) solution was made by dissolving $Cu(NO_3)_2 \cdot 5H_2O$ and terephthalic acid in DMF, mixing, filtering, and washing.

Results and Discussion

IR: The FT-IR spectra of synthesized $BiFeO_3$ shows peaks at 440 and 560 cm^{-1}, indicating FeO_6 groups. Peaks at 1699 and 1400 cm^{-1} correspond to carboxylate groups. These groups bridge Cu nodes, confirming successful composite formation via microwave method (Fig. 1).
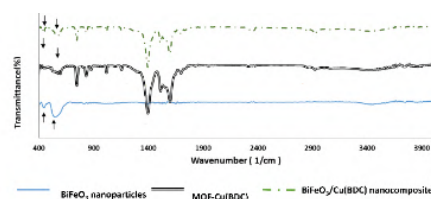

Fig.1: FT-IR spectra

XRD: The XRD pattern of $BiFeO_3$ aligns closely with ASTM card No. 01-086-1518, with notable peaks indicating various crystallographic planes. A peak at $2\theta = 27.82°$ suggests Bi_2O_3 impurities. Cu(BDC) XRD pattern shows no impurities, affirming phase purity, while composite patterns confirm successful formation (Fig. 2)..
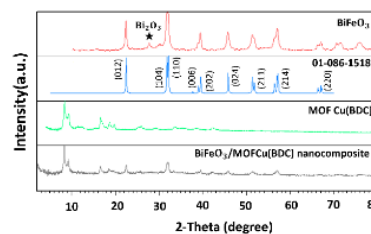

Fig.2: The X-ray Diffraction (XRD) patterns

SEM: SEM images in Fig. 3 show porous bismuth ferrite structure due to nanoparticle agglomeration during gas emissions. Cu(BDC) framework reveals uniform cubic particles synthesized via microwave method. Incorporating bismuth ferrite alters Cu(BDC) structure to cubic form.
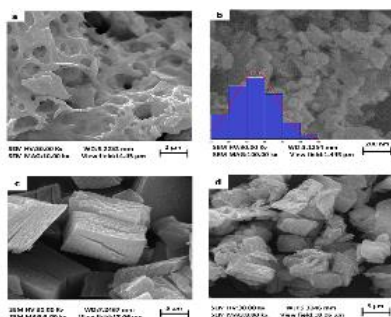
22nd Iranian Chemistry Congress (ICC22)
Iranian Research Organization for Science and Technology (IROST)
13-15 May 2024

03231-97589

IROST

Fig.3: SEM images. a,b) BiFeO$_3$ nanoparticles, c) Cu(BDC) framework synthesized by microwave method, d) Nanocomposite.

VSM: Magnetic properties of BiFeO$_3$ nanoparticles and resulting composites were assessed via VSM. BiFeO$_3$ exhibited a narrow, sharp hysteresis loop in Fig. 4a, indicating soft magnetic characteristics. Fig. 4b confirmed BiFeO$_3$ NPs and Cu(BDC) presence in composites with magnetic properties.
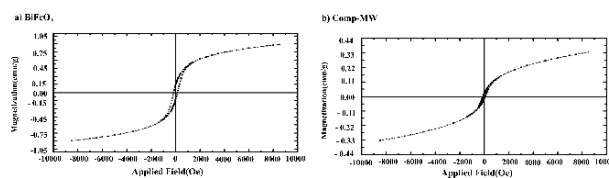
Fig.4: Vibrating Sample Magnetometer, a) BiFeO$_3$ nanoparticles, b) Nanocomposite.

Electrochemical measurement:

The electrochemical response of synthesized materials was analyzed using cyclic voltammetry (CV) with platinum and silver/silver chloride electrodes. Electrolytes included KOH, H$_2$SO$_4$, and LiClO$_4$. Lithium perchlorate exhibited the highest current density due to its strong oxidizing properties. Optimal scan rate was 0.1 mV s^{-1}. Nanocomposites showed enhanced current density attributed to particle size. Anodic and cathodic peaks corresponded to Bi oxidation and reduction processes. Utilizing nanocomposites induced a positive potential shift, indicating nuanced electrochemical behavior. The microwave-synthesized nanocomposite demonstrated enhanced current density due to its particle size facilitating ion transfer (Fig. 5).

Conclusions

Bismuth ferrite stands out in materials science for its unique ferroelectric and antiferromagnetic properties. Explored for applications in non-volatile memories and sensors, its electrochemical process makes it a promising electrode material. Investigating the voltammetric cycle provides crucial insights into its redox behavior. Integration with metal frameworks enhances properties, with nanocomposites addressing challenges in electrode
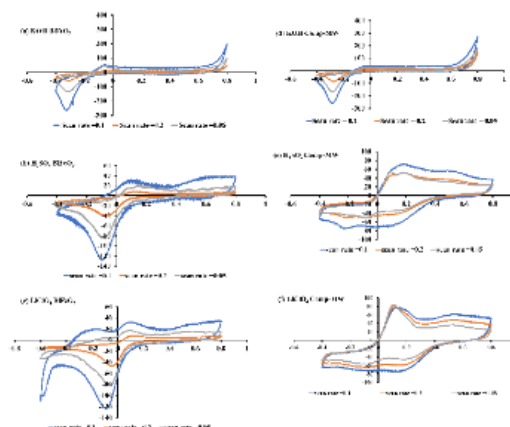

Fig.5: CV curves of bismuth ferrite nanoparticles, nanocomposite synthesized by microwave method in the different electrolytes: (a,d) KOH, (b,e) H$_2$SO$_4$, (c,f) LiClO$_4$.

stability. Bismuth ferrite's versatility positions it as a focal point in advancing electrochemical technologies, promising applications in energy storage and catalysis.

References

[1] Kharbanda, S., Dhanda, N., Sun, A. C. A., Thakur, A., & Thakur, P. (2023). Multiferroic perovskite bismuth ferrite nanostructures: A review on synthesis and applications. Journal of Magnetism and Magnetic Materials, 170569. https://doi.org/10.1016/j.jmmm.2023.170569.

[2] Aishwarya, K., Jeniffer, I. H., Maruthasalamoorthy, S., Nirmala, R., Punithavelan, N., & Navamathavan, R. (2022). State of the Art of the Multifunctional Bismuth Ferrite: Synthesis Method and Applications. *ECS Journal of Solid State Science and Technology*, 11(4), 043010. https://doi.org/10.1149/2162-8777/ac627a.

[3] GadelHak, Y., Hafez, S. H., Mohamed, H. F., Abdel-Hady, E. E., & Mahmoud, R. (2023). Nanomaterials-modified disposable electrodes and portable electrochemical systems for heavy metals detection in wastewater streams: A review. Microchemical Journal, 109043. https://doi.org/10.1016/j.microc.2023.109043

[4] Deka, B., & Cho, K. H. (2021). BiFeO3-Based relaxor ferroelectrics for energy storage: progress and prospects. Materials, 14(23), 7188. https://doi.org/10.3390/ma14237188.

[5] Deng, X., Wu, Y., Gao, Z., & Zhou, G. (2023). Advance in modulation engineering of ferroelectrics and multiferroics with non-chemical agents and factors: a review. Journal of Materials Chemistry A. https://doi.org/10.1039/D3TA04405J.

[6] Chen, X., Sun, D., He, Z., Kang, S., Miao, Y., & Li, Y. (2023). Ferrite bismuth-based nanomaterials: from ferroelectric and piezoelectric properties to nanomedicine applications. *Colloids and Surfaces B: Biointerfaces*, 113642. https://doi.org/10.1016/j.colsurfb.2023.113642.

[7] Wang, N., Luo, X., Han, L., Zhang, Z., Zhang, R., Olin, H., & Yang, Y. (2020). Structure, performance, and application of BiFeO$_3$ nanomaterials. Nano-micro letters, 12, 1-23. https://doi.org/10.1007/s40820-020-00420-6.

[8] Zhao, X., Menzel, S., Polian, I., Schmidt, H., & Du, N. (2023). Review on resistive switching devices based on multiferroic BiFeO$_3$. *Nanomaterials*, 13(8), 1325. https://doi.org/10.3390/nano13081325.

[9] Dai, W., Li, Y., Jia, C., Kang, C., Li, M., & Zhang, W. (2020). High-performance ferroelectric non-volatile memory based on La-doped BiFeO$_3$ thin films. *RSC Advances*, 10(31), 18039-18043. https://doi.org/10.1039/D0RA02780D.

Synthesis and spectroscopic study of (X)(C₆H₅CH₂NH)₂P(O) (X = C₆H₅ and CCl₃C(O)NH)

Fatemeh Gholiniarad, Mehrdad Pourayoubi*

Corresponding Author E-mail: pourayoubi@um.ac.ir

Department of Chemistry, Faculty of Science, Ferdowsi University of Mashhad, Mashhad, Iran.

Abstract: The $(C_6H_5)(C_6H_5CH_2NH)_2P(O)$ (**I**) phosphonicamide and $(CCl_3C(O)NH)(C_6H_5CH_2NH)_2P(O)$ (**II**) phosphoric triamide were synthesized and studied by spectroscopic methods. All carbon atoms belonging to the phenyl group attached to phosphorus (in **I**), and the *ipso*-carbon atom of benzyl moiety in both compounds appear doublets due to the coupling with phosphorus nucleus ($^nJ_{PC}$, n = 1 to 4 and $^3J_{PC}$, respectively).

**Keywords:** Phosphonicamide; Phosphoric triamide; NMR; Phosphorus-carbon coupling constant.

Introduction

Biochemical properties of phosphoramides [1] and fire retardant properties of phosphonamides [2] have been studied in literature.

The $CP(O)(NR^1R^2)_2$ fragment defines phosphonicamide compounds, and phosphoramides are introduced with the $X_2P(O)NR^1R^2$ formula (X = nitrogen from amine/amide groups (phosphoric triamide), halogen, and/or oxygen attached to hydrogen or hydrocarbon groups and R^1/R^2 are H or hydrocarbon fragment). In this research, the synthesis and spectroscopic characterization of two new compounds, $(C_6H_5)(C_6H_5CH_2NH)_2P(O)$ (**I**) phosphonicamide (Scheme 1) and $(CCl_3C(O)NH)(C_6H_5CH_2NH)_2P(O)$ (**II**) phosphoric triamide (Scheme 2) are investigated. Some topics related to the phosphorus chemical shifts and phosphorus-carbon coupling constants were addressed.
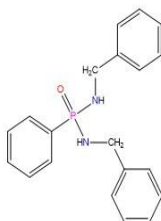
Scheme 1: Chemical structure of **I**
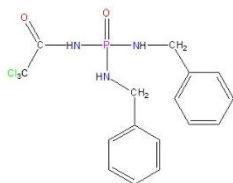
Scheme 2: Chemical structure of **II**

Experimental Section

Synthesis and Identification

$(C_6H_5)(C_6H_5CH_2NH)_2P(O)$ (**I**)

To a solution of dichlorophenylphosphine oxide in CHCl₃, a solution of benzylamine (1 to 4 mole ratio) in the same solvent was added at 0°C (ice bath) and stirred (4 hours). Then, the solvent was removed and the solid obtained was washed with distilled water. The product was dried in air and recrystallized from chloroform and normal hexane.

$^{31}P\{^1H\}$ (121.76 MHz, DMSO-d₆): δ = 19.80 (s). ^1H NMR (300.81 MHz, DMSO-d₆): δ = 4.00 (m, 4H, CH₂), 5.10 (m, 2H, NH), 7.07–7.54 (m, 13H), 7.83 (m, 2H). $^{13}C\{^1H\}$ NMR (75.65 MHz, DMSO-d₆): δ = 44.04, 126.86, 127.70, 128.43, 128.43 (d, J = 13.1 Hz), 131.18 (d, J =2.2 Hz), 131.88 (d, J = 8.0 Hz), 135.38 (d, J = 148.5 Hz), 141.86 (d, J = 6.3 Hz). IR (KBr, cm^{-1}): 3214, 3157, 3066, 2887, 2638, 1962, 1641, 1599, 1455, 1300, 1251, 1176, 1120, 1023, 949, 909, 876, 814, 739, 695.

$(CCl_3C(O)NH)(C_6H_5CH_2NH)_2P(O)$ (**II**)

The $(CCl_3C(O)NH)Cl_2P(O)$ reagent was obtained from a reaction between 2,2,2-trichloroacetamide and PCl₅ in CCl₄ under reflux condition (2 hours) and then the treatment of HCOOH in ice bath temperature (2 hours) (molar ratio: 1:1:1).

The $(CCl_3C(O)NH)Cl_2P(O)$ reagent was reacted with benzylamine (1 to 4 mole ratio) in CHCl₃ at 0°C (ice bath) for 4 hours. Then, the solvent was removed and the solid obtained was washed with distilled water. The product was dried in air and recrystallized from chloroform and normal hexane.

$^{31}P\{^1H\}$ (121.76 MHz, DMSO-d₆): δ = 7.75 (s). ^1H NMR (300.81 MHz, DMSO-d₆): δ = 4.05 (m, 4H, CH₂), 5.51 (m, 2H, NH), 7.27–7.57 (m, 10H), 9.52 (s, 1H, NH). $^{13}C\{^1H\}$ NMR (75.65 MHz, DMSO-d₆): δ = 43.54, 93.62 (d, J = 10.2 Hz), 128.41, 129.55, 131.66, 140.33 (d, J = 5.2 Hz), 162.06. IR

22nd Iranian Chemistry Congress (ICC22)
Iranian Research Organization for Science and Technology (IROST)
13-15 May 2024

03231-97589

(KBr, cm^{-1}): 3328, 3233, 2930, 2866, 1714, 1655, 1556, 1491, 1440, 1214, 1176, 1088, 1014, 884, 826, 677.

Results and Discussion

NMR spectroscopy

The phosphorus signals (in ^{31}P{^{1}H} NMR spectra) of compounds **I** and **II** appear at 19.80 and 7.75 ppm, respectively. The more value of chemical shift of **I** is related to the anisotropic effect of phenyl ring directly attached to phosphorus.

In the ^{1}H NMR spectra, the CH$_2$ and NH protons of C$_6$H$_5$CH$_2$NH moieties are revealed as multiplets at 4.00 and 5.10 ppm for **I** and at 4.05 and 5.51 ppm for **II**. The NH proton of the C(O)NHP(O) moiety of compound **II** appears as broad signal at 9.52 ppm.

In the ^{13}C{^{1}H} NMR spectrum of **I**, all carbon atoms of the phenyl group directly attached to phosphorus show coupling with phosphorus (^{1}J, ^{2}J, ^{3}J and ^{4}J). The doublet signal at 131.18 ppm (^{4}J =2.2 Hz) is assigned to the *para*-carbon atom of the noted phenyl ring with four bonds separation from phosphorus. The doublet centered at 135.38 ppm (^{1}J = 148.5 Hz) is related to carbon atom directly attached to phosphorus. The doublets at 128.43 ppm (J = 13.1 Hz) and 131.88 ppm (J = 8.0 Hz) are assigned to the *ortho-* and *meta*-carbon atoms. There is also one singlet at 128.43 ppm which is situated in the center of doublet at 128.43 ppm. The *ipso*-carbon atom of benzyl moiety shows a doublet at 141.86 ppm (^{3}J = 6.3 Hz) (Fig. 1 and Fig. 2).

In the ^{13}C{^{1}H} NMR spectrum of **II**, the doublets at 93.62 ppm (J = 10.2 Hz) and 140.33 ppm (J = 5.2 Hz) associate to the carbon atoms of CCl$_3$ and phenyl moieties, both with three bonds separation from phosphorus (Fig. 3).

Fig. 2: ^{13}C{^{1}H}-NMR spectrum of **I** (aromatic region)

Fig. 3: ^{13}C{^{1}H}-NMR spectrum of **II**

Conclusion

The (C$_6$H$_5$)(C$_6$H$_5$CH$_2$NH)$_2$P(O) phosphonicamide (**I**) and (CCl$_3$C(O)NH)(C$_6$H$_5$CH$_2$NH)$_2$P(O) phosphoric triamide (**II**) were synthesized and studied by IR, ^{1}H-NMR, ^{31}P{^{1}H}-NMR and ^{13}C{^{1}H}-NMR. The phenyl group attached to phosphorus atom in **I** shows the doublet signals for all carbon atoms (^{n}J$_{CP}$, n = 1, 2, 3 and 4 coupling constants), and the ^{1}J and ^{4}J values are 148.5 and 2.2 Hz, respectively. The *ipso*-carbon atoms of benzyl moieties in two compounds are also revealed as doublets ^{3}J$_{CP}$ = 6.3 Hz in **I** > ^{3}J$_{CP}$ = 5.2 Hz in **II**. The CCl$_3$ moiety in **II** appears a doublet (^{3}J$_{CP}$ = 10.2 Hz). The phosphorus signal in **I** is revealed in a higher value of chemical shift (^{31}P{^{1}H} NMR) with respect to the phosphorus signal in **II**, due to the anisotropic effect of phenyl ring directly attached to phosphorus in **I**.

References

[1] Corbridge, D. E. C. Phosphorus, an Outline of its Chemistry, Biochemistry and Technology; 5th ed. Elsevier Science: New York, 1995.

[2] Li, Z., Liu, C., Cao, W. & Yao, Q. (2018). *J. Appl. Polym. Sci*. 135, 47411.

Fig. 1: ^{13}C{^{1}H}-NMR spectrum of **I**

Synthesis and Evaluation of Lap Shear Strength of Polyurethane Hot Melt Adhesive

Javad Barzouei[a], Gholam Hossein zohuri[a*], Mohammad Nourmohammadi[b]

Corresponding Author E-mail: Zohuri@um.ac.ir

[a] Department of Chemistry, Faculty of Science, ferdowsi University of Mashhad, Mashhad, Iran.

[b] Department of Research and Development Center, Ayegh Khodro Toos (AKT) Co. of Part Lastic Group, P.O. Box 91851-77209, Mashhad, Iran.

Abstract: Polyurethane hot melt adhesives (HMPUA) are extensively utilized for their notable benefits. A lap shear test was used to check the strength of the synthesized adhesive. The highest lap shear strength of the HMPUA adhesive reached up to 4.17 MPa after 10 days of curing.

Keywords: polyurethane; hot-melt adhesive; lap shear strength.

Introduction

Polyurethane (PU) is a type of polymer that features carbamate bonds (NH-COO) in its main chain, which can be obtained through a stepwise addition process involving isocyanates and polyols [1]. Preparation of urethane occurs from the reaction between the polyol hydroxyl group with isocyanate group using a suitable catalyst (figure 1). Sometimes, to minimize the free -NCO groups in the formed polyurethane, the NCO/OH index is set to its lowest value, or other hydroxyl groups are also used. HMPUA without any free isocyanate groups can be completely cured at room temperature, which leads to a long shelf life in an open environment, which is more suitable for practical use [2,3]. The polymer widely used in various industries, polyurethane has a long service life, high resistance to impact loading, and low wear loss. Some common uses of polyurethanes include packaging, coatings, automobiles, furniture, construction, and adhesives [4]. Polyurethane has gained increasing attention in recent years due to environmental concerns. Traditional solvent-based polyurethane adhesives are being gradually replaced by environmentally friendly alternatives, as they release toxic volatile organic compounds (VOCs) during usage. As a result, eco-friendly adhesives are becoming a key area of development in the adhesive industries. HMPUA are particularly favored for their solvent-free simple sizing, easy storage, and transportation properties [5].

Experimental Section

A 250 mL round-bottom flask with four necks, a mechanical stirrer, and a thermometer were used to make the HMPUA. Polypropylene Glycol (M_n= 1000 g/mol, 70 w%), 1,4-butanediol (3.10 w%), and glycerin (2.00 w%) were mixed and dried under reduced pressure (120 °C for 2-3 h). The temperature was cooled down to 60-70 °C, and the reaction was carried out with addition of toluene diisocyanate (24.50 w%) with a constant NCO/OH ratio of 1.05 along with 0.5 w% dimorpholinodiethyl ether (DMDEE) catalyst was added to the flask and stirred (2-3 hours at a temperature of 70-80 °C). The mixture was poured into a teflon mold and the formed film reacted at 50 °C for 18-24 h in an oven.
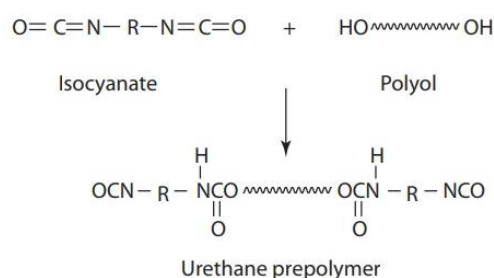
Fig. 1: Reaction of polyol hydroxyl group with isocyanate [2].

Results and Discussion

structure of the curred sample of the polyurethane was monitored using ATR-FTIR spectroscopy (Figure 2). The appearance of a sharp peak around 1728 cm^{-1} region related to the carbonyl group of the disappearance of the NCO group peak in the around 2270 cm^{-1} region and the appearance of a weak N-H peak in the around 3290 cm^{-1} region indicate the formation of polyurethane hot melt adhesive.

The adhesion properties were studied using lap shear strength test on the substrate/HMPUA/substrate joint. The HMPUA film was cut into rectangle shapes (25 mm × 12.5 mm) and then placed between two identical substrates (100 mm × 25 mm × 2 mm) with an overlap area (25 mm × 12.5 mm). A plate of stainless steel was used as a typical adhesion substrate, and the substrates with adhesive film were held together by paper clips. The

22ⁿᵈ Iranian Chemistry Congress (ICC22)
Iranian Research Organization for Science and Technology (IROST)
13-15 May 2024

03231-97589

HMPUA samples were melted at 130 °C and evenly coated on one piece to form a film with a size of (25 mm × 10 mm × 0.1 mm). The bonded substrates were kept at a room temperature of (23±2 °C) and a relative humidity of 45%-50% RH at different times to cure. According to Figure 3, which examines the curing of adhesive in different periods of time, it is clear that the complete curing of adhesive is done after 10 days. The final strength of bonding value reaches to 4.17 MPa.
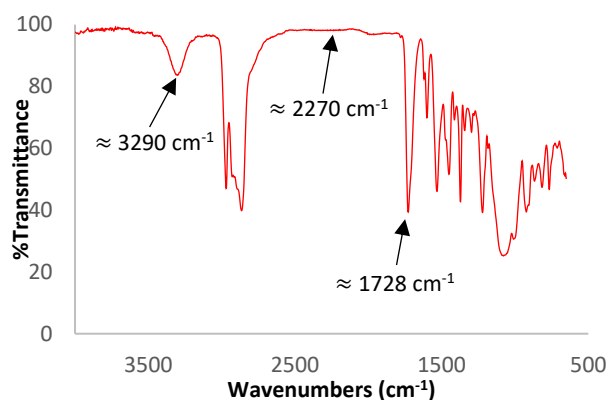
Fig. 2: ATR-FTIR analysis of the HMPUA.
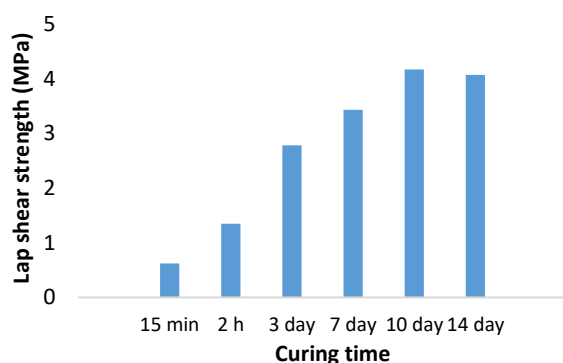
Fig. 3: Lap shear strength of HMPUA to a plate of stainless steel under different curing times at room temperature.

Conclusions

A polyurethane hot melt adhesive was prepared and analysed using ATR-FTIR technical, we see the formation of urethane groups and the structure of the synthesized adhesive. The synthesized adhesive is completely cured after 10 days and its lap shear strength is 4.17 MPa.

Acknowledgements

References

[1] Szycher, M. (2012). Structure–property relations in polyurethanes. Szycher's Handbook of Polyurethanes, 2nd ed.; CRC Press: Boca Raton, FL, USA, 37-86.

[2] A. Pizzi and K. L. Mittal (2017). Polyurethane Adhesives. Handbook of Adhesive Technology, 3nd ed.; CRC Press: Boca Raton, FL, 321-344.

[3] Mohammed, M. M., ALJarrah, M. M., & Lateef, A. A. A. (2008). Effect of NCO/OH on the Mechanical properties of Polyurethane Elastomers. *Al-Nahrain Journal for Engineering Sciences*, *11*(3), 485-493.

[4] Du, L., Liu, Z., Ye, Z., Hao, X., Ou, R., Liu, T., & Wang, Q. (2023). Dynamic cross-linked polyurethane hot-melt adhesive with high biomass content and high adhesive strength simultaneously. *European Polymer Journal*, *182*, 111732.

[5] Ren, X., Fan, C., Tu, J., Deng, B., Xia, S., Wu, Y., & Shou, Y. (2023). Study on Preparation and Performance of Polyurethane Hot Melt Adhesive Films. *Advances in Engineering Technology Research*, *5*(1), 407-407.

Effect of Silica Nanoparticles on Tensile Strength and Hardness in Polyurethane Hot Melt Adhesive

Javad Barzouei[a], Gholam Hossein zohuri[a*], Mohammad Nourmohammadi[b]

Corresponding Author E-mail: Zohuri@um.ac.ir

[a]Department of Chemistry, Faculty of Science, ferdowsi University of Mashhad, Mashhad, Iran.

[b]Department of Research and Development Center, Ayegh Khodro Toos (AKT) Co. of Part Lastic Group, P.O. Box 91851-77209, Mashhad, Iran.

Abstract: A hot melt adhesive of polyurethane (HMPUA) was synthesized and investigate some of its mechanical properties nano silica was used as the additive. With the addition of the nano silica (0.4 w%), the mechanical properties such as; tensile strength, elongation at break and hardness were improved (2.02 MPa, 343%, and 50 respectively).

Keywords: Polyurethane hot-melt adhesive, Hardness Shore A, Elongation at Break, Tensile Strength.

Introduction

In recent years, there has been increasing interest in reactive polyurethane hot melt adhesive (HMPUR) due to its superior performance compared to traditional adhesives. HMPUR offers benefits such as temperature resistance, high initial adhesion strength, high tensile strength, easy processing, and environmental friendly. HMPUR adhesives are highly viscous or solid prepolymers with a low melting point that can yield rigid or elastic bonds and can bond to a wide variety of substrates. Additionally, HMPUR adhesives can be designed and developed with widely varying properties for specific applications [1]. Adhesives play a crucial role in various industries and everyday life. Hot-melt adhesives (HMAs) are particularly promising as environmentally friendly adhesives due to their solvent-free nature, which helps avoid the emission of volatile organic compounds (VOCs). The adhesive is widely used in electronics assembly, automotive, aerospace, wood processing, and the footwear industry [2]. Sometimes to increase some adhesive properties including; additives such as fillers, softeners, etc. are used to increase brittleness, tensile strength, increase hardness and flexibility, etc [3]. Silica nanoparticle is one of the most common fillers for polyurethane adhesives. Adding a very small amount of nanoparticle silica improves wear resistance, tensile properties, and hardness, but adding large amounts of it causes lower mechanical properties [4].

Experimental Section

To prepare polyurethane hot melt adhesine, polypropylene glycol (Mn=1000 g/mol, 65-75 w%), 1,4-butanediol (3-5 w%), and glycerin (0.5-2 w%) are poured into a 250 ml reactor a round bottom, were mixed and dried under reduced pressure (110-120 °C for 2-3 h). The isocyante calculated for the index [NCO]/[OH]=1.02 (toluene diisocyanate 20-30 w%) along with the dimorpholinodiethyl ether (0.1-0.5 w%) was added to the reactor and reacted for 3-4 hours at a temperature of 50-60 °C under a nitrogen atmosphere until all the calculated isocyanates were consumed, which were measured by Karl Fischer device is carried out and continues. After completing the steps to form the film, the final solution was transferred into a teflon mold and it in an oven (40-50 °C for 12-18 h). To prepare polyurethane hot melt adhesive containing silica nanoparticles, a certain amount of silica nanoparticles (0 w%, 0.2 w%, 0.4 w%, and 0.6 w%) was added to the mixture of polyols and stirred for 12 h with a mechanical stirrer. The compound was sonicated (3 times and each time for 5 minutes) to homogenize ten it was stirred (30-40 minutes).

Results and Discussion

Hardness is resistance to penetration, abrasion, and resistance to cutting and scratching. The synthesized HMPUA was a low-hardness material. hardness in the sample HMPUA-0 was 43. The thickness of the tested samples was 4-6 mm. Silica nanoparticle filler was used to increase the hardness. As can be seen (Table 1), the addition of nanoparticles up to a certain value (0.4 w%) causes an increase in hardness, further addition however decreases the hardness of the sample.

Table 1: The hardness of the HMPUA containing nano silica (0, 0.2, 0.4, and 0.6 w%).

	HMPUA-0	HMPUA-0.2	HMPUA-0.4	HMPUA-0.6
Shore A (mm)	43	47	50	45

22nd Iranian Chemistry Congress (ICC22)
Iranian Research Organization for Science and Technology (IROST)
13-15 May 2024

03231-97589

IROST

Figures 1 and 2 show the tensile test results of HMPUA films with nano silica (0, 0.2, 0.4, 0.6 w%) films, the tensile strength and elongation at break show a very good mechanical behaviour by increasing the amount of silica nanoparticles to some extent. Tensile strength for HMPUA containing nano silica 0, 0.2, 0.4, and 0.6 w% are 1.46, 1.67, 2.02, and 1.38, MPa respectively (Figure 1). Elongation at break was for samples 0, 0.2, 0.4, and 0.6 w% are equal to 253%, 283%, 343%, and 225%, respectively (Figure 2). Therefore, similar to the tensile strength results, the addition of the nanoparticles 0.4 w% can be the optimum value according to the mechanical obtained properties.
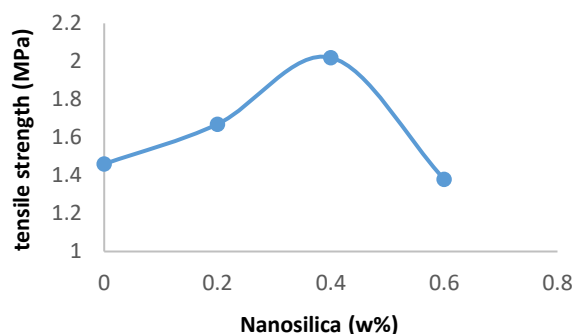
Fig. 1: change in tensile strength of HMPUA with nano silica (0, 0.2, 0.4, 0.6 w%).
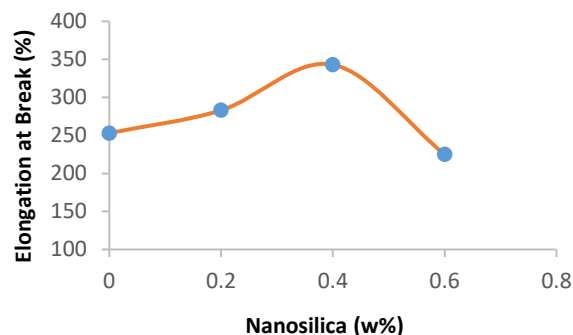
Fig. 2: change in elongation at break of HMPUA with nano silica (0, 0.2, 0.4, 0.6 w%).

Conclusion
There is an optimum concentration of nano silica for the adhesive to obtain maximum tensile strength, elongation at break, and hardness. For this study, the concentration was 0.4 w% which case tensile strength, elongation at break, and hardness (2.02 MPa, 343%, and 50 respectively).

Acknowledgements

References
[1] Lu, Z., Xue, W., Zeng, Z., & Zhou, Z. (2021). Synthesis and properties of reactive polyurethane hot melt adhesive based on a novel phosphorus-nitrogen-containing polyol. *Journal of Adhesion Science and Technology*, *35*(9), pp. 941-954.

[2] Wang, S., Liu, Z., Zhang, L., Guo, Y., Song, J., Lou, J., ... & You, Z. (2019). Strong, detachable, and self-healing dynamic crosslinked hot melt polyurethane adhesive. *Materials Chemistry Frontiers*, *3*(9), pp. 1833-1839.

[3] Rudawska, A. (Ed.). (2016). *Adhesives: Applications and Properties*. BoD–Books on Demand.

[4] Sepulcre-Guilabert, J., T.P. Ferrándiz-Gómez, and J.M. Martín-Martínez. (2001). Properties of polyurethane adhesives containing natural calcium carbonate+ fumed silica mixtures. Journal of adhesion science and technology, 15(2): pp. 187-203.

22nd Iranian Chemistry Congress (ICC22)
Iranian Research Organization for Science and Technology (IROST)
13-15 May 2024

03231-97589

IROST

Copper nitrate as a powerful and eco-friendly natural catalyst for mediator-free aerobic oxidation of 1,4-dihydropyridines under mild conditions

Hamzeh Veisi, Amin Rostami[*]

Corresponding Author E-mail: a_rostami372@yahoo.com

University of Kurdistan, Department of Chemistry, Faculty of Science, Sanandaj, Iran.

Abstract: For the first time, copper (II) nitrate trihydrate was used as an efficient, eco-friendly, operational ease, inexpensive, and commercially available catalyst for the biomimetic aerobic oxidative synthesis of Hantzsch pyridines from their corresponding 1,4-dihydropyridines. The products were obtained in acetonitrile as a solvent. these techniques can be utilized in pharmaceuticals and other delicate synthesis processes.

Keywords: Pyridines; Copper (II) nitrate; Aerobic oxidative.

Introduction

copper nitrate is a common cupric salt that appears as a blue crystalline solid [1]. Due to its exclusive physical characteristics, eco-friendly nature, and variable reactivity, copper nitrate has developed as a useful reagent for organic synthesis and attracted the interest of organic chemists [2].

Pyridines, among the most crucial heterocycles, are commonly found in flavors and fragrances, natural products, additives, pharmaceuticals, agrochemicals, polymers, and dyes. They are utilized as reagents and building blocks in organic synthesis and as ligands in coordination chemistry [3]. A widely used method for the preparation of pyridines involves the oxidation of corresponding 1,4-dihydropyridines [4].

The aerobic oxidative synthesis of these valuable compounds has been developed in the presence of organocatalysts or transition metal catalysts [5]. Previous methods include problems such as low catalytic efficiency, high reaction temperatures, the use of toxic organic solvents and transition metals as catalysts, tedious catalyst preparation, and more importantly the use of expensive and toxic mediators. Green chemistry promotes the use of O_2 or air as an environmentally friendly oxidant and minimizes the production of hazardous waste [6]. It emphasizes reducing the production of hazardous materials, benefiting the environment, and enhancing chemical process efficiency and safety. It would be beneficial if molecular oxygen or air could be used as a terminal oxidant in Cu-mediated reactions [7]. In this study, we introduce a straightforward and effective method for producing Hantzsch pyridines through aerobic oxidation. This procedure includes aerobic oxidation with a copper (II) nitrate trihydrate catalyst, using O_2 or air as an oxidant and acetonitrile solution as a solvent without any mediator involved.

Experimental Section

General procedure for the aerobic oxidative synthesis of pyridine derivatives

A 25 mL round-bottomed flask equipped with a magnetic stirrer bar was charged with 1,4-dihydropyridine (1 mmol), $Cu(NO_3)_2 \cdot 3H_2O$ (24.1 mg, 0.1 mmol) and acetonitrile (5 mL). The resulting mixture was then stirred under O_2 (balloon) at room temperature until the completion of the reaction (monitored by TLC, n-hexane/ethyl acetate = 8/2).

Results and Discussion

The 1,4-dihydropyridines were produced using the procedure that was reported previously [53]. The effect of the amount of copper (II) nitrate and solvent, and temperature on the oxidation reaction of 1,4-dihydropyridine to pyridine was investigated. Then with the optimized conditions candidates in hand, the substrate scope of the reaction was investigated. The results showed that the reaction in the presence of electron-donating groups is faster and has a higher product efficiency (Scheme 1).
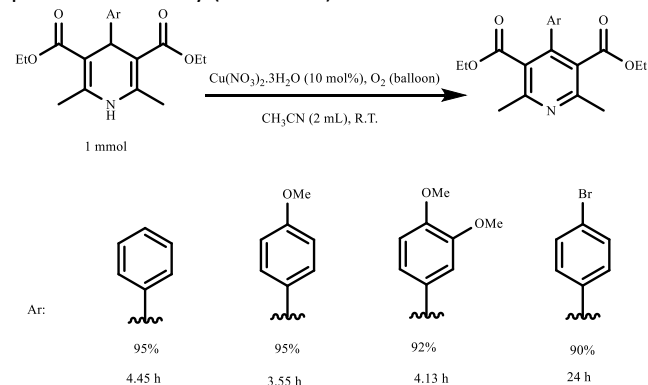
Scheme 1: aerobic oxidative of 1,4-dihydropyridines

22nd Iranian Chemistry Congress (ICC22)
Iranian Research Organization for Science and Technology (IROST)
13-15 May 2024

03231-97589

Conclusions

In summary, this catalyst can be used to oxidize of nitrogen-containing heterocycles such as 1,4-dihydropyridines without any mediators under mild conditions. These green procedures represent various attractive characteristics, such as the use of Cu $(NO_3)_2 \cdot 3H_2O$ as the robust catalyst, and O_2 or air as the greenest, inexpensive, and most abundant oxidant. In addition, the present methods are superior to other currently available ones because they are free from any toxic halide, or mediators and conform to several of the guiding principles of green chemistry.

References

[1] Guo, X. X., Gu, D. W., Wu, Z., & Zhang, W. (2015). Copper-catalyzed C–H functionalization reactions: efficient synthesis of heterocycles. Chemical reviews, 115(3), 1622-1651.

[2] Gao, M., Ye, R., Shen, W., & Xu, B. (2018). Copper nitrate: a privileged reagent for organic synthesis. Organic & Biomolecular Chemistry, 16(15), 2602-2618.

[3] Shariati, M., Imanzadeh, G., Rostami, A., Ghoreishy, N., & Kheirjou, S. (2019). Application of laccase/DDQ as a new bioinspired catalyst system for the aerobic oxidation of tetrahydroquinazolines and Hantzsch 1, 4-dihydropyridines. Comptes Rendus Chimie, 22(4), 337-346.

[4] Stout, D. M., & Meyers, A. I. (1982). Recent advances in the chemistry of dihydropyridines. Chemical reviews, 82(2), 223-243.

[5] Gonzalez-de-Castro, A., & Xiao, J. (2015). Green and efficient: Iron-catalyzed selective oxidation of olefins to carbonyls with O_2. Journal of the American Chemical Society, 137(25), 8206-8218.

[6] Lesnikov, V. K., Golovanov, I. S., Nelyubina, Y. V., Aksenova, S. A., & Sukhorukov, A. Y. (2023). Crown-hydroxylamines are pH-dependent chelating N, O-ligands with a potential for aerobic oxidation catalysis. Nature Communications, 14(1), 7673.

[7] Yu, Y., Zhai, D., Zhou, Z., Jiang, S., Qian, H., & Ma, S. (2023). Copper-catalyzed aerobic oxidation of primary alcohols to carboxylic acids. Chemical Communications, 59(35), 5281-5284.

Copper nitrate as a catalyst for mediator-free aerobic oxidation of 2,3-dihydroquinazolinones mild conditions

Hamzeh Veisi, Amin Rostami[*], Kamal Amani

Corresponding Author E-mail: a_rostami372@yahoo.com

University of Kurdistan, Department of Chemistry, Faculty of Science, Sanandaj, Iran.

Abstract: Copper (II) nitrate trihydrate was used as an efficient, inexpensive, and commercially available catalyst for the biomimetic aerobic oxidative of 2,3-dihydroquinazolinones. These methods are more eco-friendly, efficient, simple, and practical than currently available ones because the method conforms to several of the guiding principles of green chemistry.

Keywords: Aerobic oxidative; Copper (II) nitrate; dihydroquinazolinones.

Introduction

Copper salts are commonly used in organic synthesis as catalysts, mediators, and oxidants. It is known for its low toxicity, inexpensiveness, commercial availability, and operational ease [1,2]. Moreover, the influence of the solvent is another crucial aspect to consider. For instance, the dissolvability of copper nitrate in acetonitrile is significantly better than that in most organic solvents [3].

Heterocycles containing nitrogen are the most prevalent and essential structures found universally in a range of synthetic drugs, pharmaceuticals, bioactive natural compounds, and agrochemical [4]. Among these heterocycles, quinazolin-4(3H)-ones stand out as significant nitrogen-containing heterocycles. They show a wide range of biological and medicinal properties, including anticancer, antibacterial, antidiabetic, antimicrobial, anticonvulsant, antifungal, and antiallergy [5].

Due to the significance of quinazolinones, a great number of stoichiometric or great excess quantities of oxidants, as well as heterogeneous and homogeneous catalysts, have been documented in scientific literature for the preparation quinazolinones. It emphasizes reducing the production of hazardous materials, benefiting the environment, and enhancing chemical process efficiency and safety. It would be beneficial if molecular oxygen or air could be used as a terminal oxidant in Cu-mediated reactions [6,7]. In this work, we present a simple and efficient method for the aerobic oxidative synthesis of 2-substituted quinazolines. This process involves aerobic oxidation in the presence of a Copper (II) nitrate trihydrate catalyst, utilizing O_2 or air as an oxidant and an acetonitrile solution as a solvent in the absence of any mediator.

Experimental Section

General procedure for the aerobic oxidative synthesis of pyridine derivatives

A round-bottomed flask (25 mL) with a magnetic stir bar was charged with 2,3-dihydroquinazolin-4(1H)-one (1 mmol), $Cu(NO_3)_2 \cdot 3H_2O$ (0.25 mmol) and acetonitrile (5 mL). Then, the resulting mixture was then stirred under O_2 (balloon) at 50 °C.

Results and Discussion

To optimize the aerobic oxidation of 2-phenyl-2,3-dihydroquinazolin-4(1H)-one to 2-phenyl quinazolin-4(3H)-one, the effects of the amounts of copper (II) nitrate trihydrate, solvents, and temperature were examined. The result shows that the reaction did not proceed after 24 hours in the absence of the catalyst. During the experiment, 2,3-dihydroquinazolin-4(1H)-one was completely converted to the desired product when 25 mol% of copper (II) nitrate trihydrate was used as a catalyst in CH_3CN solvent at 50 ℃. The scope of the reaction was extended to different 2,3-dihydroquinazolinones under optimized conditions. The results presented in demonstrate that aromatic aldehydes containing electron-donating groups and electron-withdrawing groups were efficiently converted to their respective products with yields ranging from good to excellent (Scheme 1).
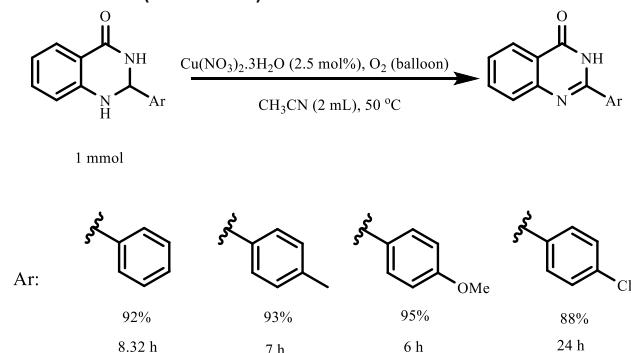
Scheme 1: aerobic oxidative synthesis of quinazoline-4(3H)-ones

22nd Iranian Chemistry Congress (ICC22)
Iranian Research Organization for Science and Technology (IROST)
13-15 May 2024

03231-97589

Conclusions

In conclusion, we have developed the first copper nitrate-catalyzed aerobic oxidation of 2,3-dihydroquinazolinones without any mediators under mild conditions. Copper nitrate catalyst is inexpensive, has low toxicity, operational ease, and commercial availability.

References

[1] Qi, R., Chen, Q., Liu, L., Ma, Z., Pan, D., Wang, H., ... & Xu, Z. (2023). Copper-catalyzed asymmetric C (sp3)-H cyanoalkylation of glycine derivatives and peptides. Nature Communications, 14(1), 3295.

[2] McCann, S. D., & Stahl, S. S. (2015). Copper-catalyzed aerobic oxidations of organic molecules: pathways for two-electron oxidation with a four-electron oxidant and a one-electron redox-active catalyst. Accounts of Chemical Research, 48(6), 1756-1766.

[3] Gao, M., Ye, R., Shen, W., & Xu, B. (2018). Copper nitrate: a privileged reagent for organic synthesis. Organic & Biomolecular Chemistry, 16(15), 2602-2618.

[4] Qi, S. S., Dong, J. Y., Sun, X. P., Zhai, J. J., Sun, Y. B., Wang, Y. F., ... & Xu, D. Q. (2024). Diastereo-and Enantioselective Synthesis of Eight-Membered N-Heterocycles from Benzofuran-Derived Azadienes and Ynones. The Journal of Organic Chemistry, 89(2), 975-985.

[5] Cao, S. L., Feng, Y. P., Jiang, Y. Y., Liu, S. Y., Ding, G. Y., & Li, R. T. (2005). Synthesis and in vitro antitumor activity of 4 (3H)-quinazolinone derivatives with dithiocarbamate side chains. Bioorganic & medicinal chemistry letters, 15(7), 1915-1917.

[6] Zheng, Y., Shen, Q., Li, Z., Jing, X., & Duan, C. (2022). Two copper-containing polyoxometalate-based metal–organic complexes as heterogeneous catalysts for the C–H bond oxidation of benzylic compounds and olefin epoxidation. Inorganic Chemistry, 61(29), 11156-11164.

[7] Ghorashi, N., Shokri, Z., Moradi, R., Abdelrasoul, A., & Rostami, A. (2020). Aerobic oxidative synthesis of quinazolinones and benzothiazoles in the presence of laccase/DDQ as a bioinspired cooperative catalytic system under mild conditions. RSC advances, 10(24), 14254-14261.

22nd Iranian Chemistry Congress (ICC22)
Iranian Research Organization for Science and Technology (IROST)
13-15 May 2024

03231-97589

ISC

IROST

Phosphoramidate synthesis via Atherton-Todd reaction in the presence of Dimethyl sulfoxide as a mild oxidant

Zahra Abdi, Fatemeh Darvish[*]

Corresponding Author E-mail: Darvish@kntu.ac.ir

Department of chemistry, Faculty of science, K. N. Toosi University of Technology, Tehran, Iran.

Abstract: A simple and efficient protocol has been developed for the synthesis of phosphoramidate via Atherton-Todd reaction in the presence of dimethyl sulfoxide (DMSO) and sodium iodide. This protocol is metal free, easy to conduct and can be scaled-up. Various phosphoramidates are readily obtained in moderate to excellent yields.

Keywords: Dimethyl sulfoxide (DMSO); Phosphoramidate; Atherton-Todd reaction

Introduction

The creation of P-N bonds is a significant area of research due to their wide range of applications in organic synthesis. Among various organophosphorus compounds, phosphoramidates stand out for their efficiency in producing biologically active molecules, medical treatments, and industrial products. An example is Sofosbuvir, an antiviral medication used for chronic hepatitis C treatment [1].

The conventional approach to forming P(O)N bonds primarily involves combining amines as nucleophiles with H-phosphonates. The Atherton-Todd reaction, a common method, initiates the process by halogenating P(O)H compounds with hazardous agents like CCl_4 to produce a phosphoryl chloride intermediate. Subsequent nucleophilic attack on the phosphoryl chloride yields the desired product. However, these traditional methods often yield low results, have limited amine compatibility, and rely on toxic halogen sources. This research aims to develop a more efficient alternative [2].

Herein, we report a simple and efficient oxidative cross-coupling reaction between amines and P(O)H compounds using DMSO as a mild, cheap, and readily accessible oxidant, providing various phosphoramidates in moderate to excellent yields under metal-free conditions [3].

Experimental Section

Diethyl phosphite (110.5mg, 0.8mmol), Amine (1equiv. 0.8mmol) and Sodium Iodide (1equiv. 114mg) with Dimethyl sulfoxide (DMSO) as an oxidant and solvent (0.5cc) were stirred at room temperature for 24 hours. under Argon Gas condition. After the completion of the reaction (monitored by TLC), the solvent was removed with added water (15cc) and extracted with CH_2Cl_2 (3x5cc). The combined organic layer was dried over $MgSO_4$ and the solvent was evaporated under vacuum the final product was purified on a silica gel column using hexane/EtOAc (3:1) to get the pure product.

Results and Discussion

We initiated our study by selecting diethyl phosphite and Morpholine as the model reaction for the monitoring reaction elements. First, the model reaction was carried out in the presence of Dimethyl sulfoxide(DMSO) as an oxidant and solvent at room temperature for 24 hours and the result demonstrated that, unfortunately, the desired product was not detected. In the next step, we used NaI as catalyst and the best result was obtained with equivalent amount of sodium iodide. Also, temperature screening studies revealed that there was not difference in the desired product's yield between carrying out the reaction at room temperature and conducting it in the wide range of temperatures. Therefore, we opted for conducting the reaction at room temperature, as it is more energy-efficient.

With optimized conditions in hand, we investigated the scope of this transformation by using diethyl phosphite and various primary and secondary amines that all of them produced the desired phosphoramidates in good to excellent yields (Scheme 1).
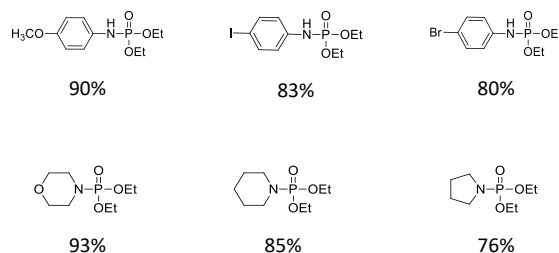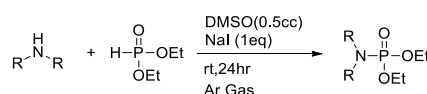
Scheme 1. Scope of all reaction: Phosphorylation of Amines

On the basis of the results from experiments and literature reports, this plausible reaction path has been proposed [4](Scheme 2). In this path; initially, Dimethyl

22nd Iranian Chemistry Congress (ICC22)
Iranian Research Organization for Science and
Technology (IROST)
13-15 May 2024

03231-97589

IROST

solfoxide(DMSO) react with NaI to generate iodine radical (I•). Addition of iodine radical to diethyl phosphite produces phosphoryl iodide. This further undergoes nucleophilic substitution reaction to afford the corresponding cross coupled product.

a) $DMSO + 2NaI \longrightarrow DMS + I_2 + Na_2O$

b) $2HI + DMSO \longrightarrow DMS + I_2 + H_2O$
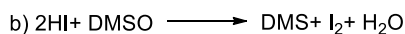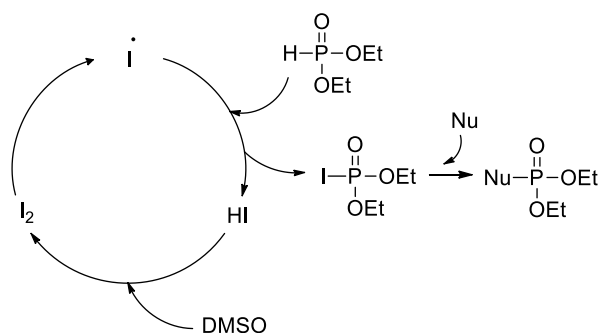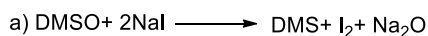
Scheme 2. Plausible mechanism

Conclusions

In conclusion, we have developed a simple and direct oxidative N-P(O) coupling method for an efficient preparation of phosphoramidates starting with available amines and P(O)H compounds using common and cheap DMSO as the mild oxidant. These transformations occur without any transition metal and desired product can be obtained in good to excellent yields. Further studies on the mechanism and the synthetic applications are ongoing in our laboratory.

References

[1] Zhu, Y. Y., Niu, Y., Niu, Y. N., & Yang, S. D. (2021). Recent advances in the synthesis and applications of phosphoramides. *Organic & Biomolecular Chemistry*, *19*(47), 10296-10313.
[2] Itumoh, E. J., Data, S., & Leitao, E. M. (2020). Opening up the toolbox: synthesis and mechanisms of phosphoramidates. *Molecules*, *25*(16), 3684.
[3] Cai, S. Q., Zhang, K. F., & Cai, X. H. (2022). Recent Advances in Dimethyl Sulfoxide (DMSO) Used as a Multipurpose Reactant. *Current Organic Chemistry*, *26*(2), 91-121.
[4] Fu, Y., Duan, F., & Du, Z. (2021). Visible Light Driven Oxidative Coupling of Amines and P (O)– H/P– OR Compounds under Photocatalyst-Free Conditions. *Asian Journal of Organic Chemistry*, *10*(5), 1071-1075.

22nd Iranian Chemistry Congress (ICC22)
Iranian Research Organization for Science and Technology (IROST)
13-15 May 2024

03231-97589

Synthesis of gold nanodendrites on hollow carbon spheres as an electrochemical sensor for the determination of morphine in biological samples

Hamideh Imanzadeh[a], Alireza Khataee[*a], Leila Hazraty[b], Mandana Amiri[b]

[a] Research Laboratory of Advanced Water and Wastewater Treatment Processes, Department of Applied Chemistry, Faculty of Chemistry, University of Tabriz, 51666-16471 Tabriz, Iran.

[b] Department of Chemistry, University of Mohaghegh Ardabili, 56199-13131 Ardabil, Iran.

Abstract: In this study, first broken hollow carbon spheres (BHCS) was synthesized using the well-known Stober templating method. Then, Au nanodendrites (Au NDs) were loaded on the BHCS modified glassy carbon electrode by one-step electrodeposition to obtain Au NDs/BHCS/GC electrode as a selective and sensitive electrochemical sensor for detecting morphine at low concentration. The proposed electrochemical sensor exhibited a highly selective assay for monitoring of MOR with a wide dynamic linear range 0.01–300 μM, accompanied by a low detection limit of 8.3 nM. In addition, the proposed electrochemical sensor had satisfactory interference rejection and good stability.

Keywords: Nanosensor; Morphine; Au nanodendrites; Broken hollow carbon spheres

Introduction

Morphine (MPH) is a narcotic drug that can relieve severe and chronic pain, particularly chronic cancer pain [1]. Nevertheless, this drug can cause many potential side effects such as slow heart rate, slow breathing, weakness, CNS disturbance, itching, choking and low blood pressure. Even excessive consumption of this drug leads to death due to respiratory depression. [2]. In addition, the user of morphine becomes addicted to this drug after three days. Considering that morphine is considered as an illegal drug, therefore, it needs careful monitoring in many biological samples, which is very important in the clinical and forensic fields [3].

Experimental Section

Five mg of MoS_2-FeS_2 was dispersed in 1.0 mL of ethanol containing 0.1 % of Nafion with ultrasonic agitation for an hour to achieve a well dispersed suspension. Then, 3 μL of the prepared suspension was placed on the surface of a glassy carbon electrode (3 mm diameter). The prepared modified electrode, GCE/MoS_2-FeS_2, was dried in air and ready for use. Then the electrocatalytic performances of the prepared MoS_2-FeS_2 towards HER, IOR, and FOR were evaluated using linear sweep voltammetry (LSV).

Results and Discussion

The as-synthesized nanocomposite was structurally characterized by Fouriertransform infrared spectroscopy (FT-IR), X-ray photoelectron spectroscopy (XRD), field emission scanning electron microscopy (FE-SEM) andenergy dispersive spectroscopy (EDS), The obtained results confirmed the successful synthesis of Au NDs/BHCS nanocomposite.
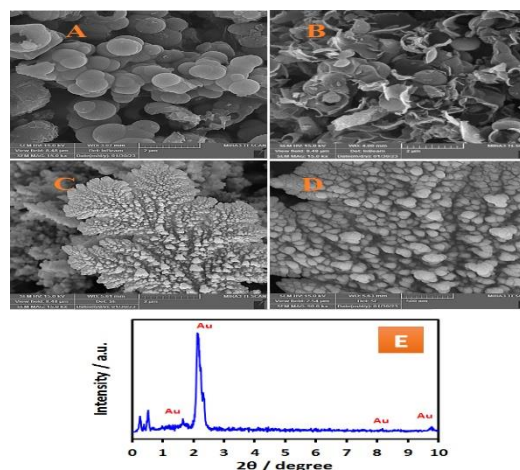
Fig.1: FE-SEM images of (A) SiO2@C, (B) BHCS and (C-D) Au NDs/BHCS/GCE; (E) EDX pattern of the Au dendrites.

To improve the analytical response of the nanosensor, some parameters have been studied, the pH of the electrolyte solution, the effect of the scan rate, the effect of accumulation potential and time. The following experimental conditions were found to give the best results: PBS solution (100 mM, pH = 7.0); a linear relationship between the peak current and the of the of scan rates; accumulation potential: -0.7 V; accumulation time: 30 s.

In order to examine the current response of Au NDs/BHCS/GCE at different morphine concentrations, a calibration study was performed. Figure 3. demonstrated obtained DPV current responses in different concentrations of morphine in 100 mM PBS solution, pH = 7.0 on the Au NDs/BHCS/GCE. As illustrated in Figure 3. A, the obtained DPV current signal increases as the MPH

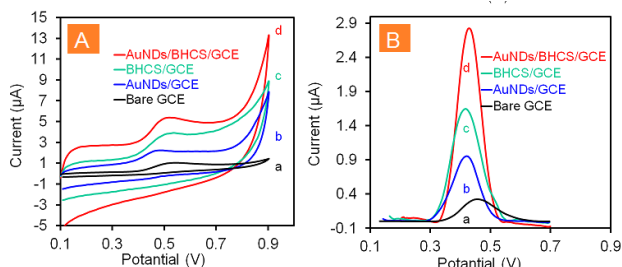concentration increases from 0.01 to 300 µM with adetection limit of 0.0083 µM under optimal experimental conditions.

Fig 2: (A) Cyclic voltammograms and (B) Differential pulse voltammograms of 200 µM MPH at Bare GCE, Au NDs/GCE, BHCS/GCE and Au NDs/BHCS/GCE in PB solution (100 mM, pH = 7.0).
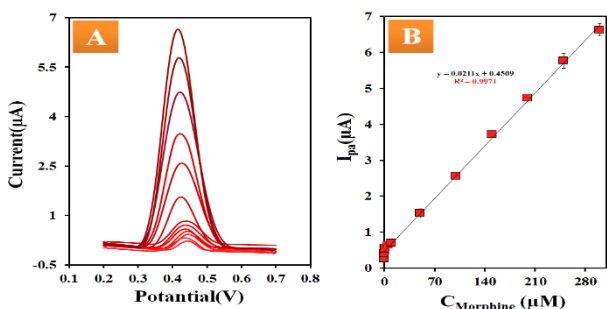

Fig 3: (A) The obtained Adsorptive stripping differential pulse voltammograms at the of Au NDs/BHCS/GCE for MPH (in 100 mM PB solution, pH = 7.0) at various concentrations and (B) the calibration curve for sensing of MPH in the range of 0.01-300 µM.

The proposed procedure was very efficient for MPH determination from human serum and saliva samples with high recoveries.

Table 1: Determination of MPH in biological fluids using Au NDs/BHCS/GCE nanosensor.

Sample	Added ($\times 10^{-6}$ M)	Found ($\times 10^{-6}$ M)	RSD (%, n = 3)	Recovery (%)
Serum	10	9.71	0.97	97.17
	40	40.01	3.06	100.02
	80	82.58	2.24	103.22
Saliva	10	9.82	2.93	98.27
	40	40.14	0.833	100.35
	80	79.87	0.742	99.83

Conclusions

In summary, an effective nanosensor with a new method was constructed for nanolevel detection of an abuse drug MPH using Au NDs/BHCS modified GCE. Au nanodendrites were synthesized using the simple electrodeposition

route onto BHCS/GCE. The as-prepared Au NDs/BHCS nanocomposite was studied by several characterization techniques. Under optimized conditions, the designed Au NDs/BHCS/GCE sensor exhibited a wide dynamic range (0.01-300 µM). The proposed method illustrated excellent sensitivity and selectivity, satisfactory stability, and repeatability. Additionally, the application of the designed nanosensor to detect MPH in actual samples was successfully investigated, particularly saliva samples, as the non-invasive specime. The high electrochemical performance of Au NDs/BHCS is because of the high surface area, electron transfer ability and good conductivity of broken hollow carbon spheres and the electrocatalytic activity of Au NDs. Since the synthesized Au NDs/BHCS nanocomposite in this research was prepared by green and fast methods, it can be efficient in other electrochemical sensors.

References

[1] Ho, J. F. V., Yaakup, H., Low, G. S. H., Wong, S. L., Tho, L. M., & Tan, S. B. (2020). Morphine use for cancer pain: A strong analgesic used only at the end of life? A qualitative study on attitudes and perceptions of morphine in patients with advanced cancer and their caregivers. Palliative medicine, 34(5), 619-629.

[2] Kish, S. S., Ehzari, H., Shekarbeygi, Z., Shahlaei, M., Moradi, S., & Jalalvand, A. R. (2023). Fabrication of a novel electrochemical biosensor based on easy and efficient modifications of a glassy carbon electrode for sensitive and selective determination of morphine. Sensing and Bio-Sensing Research, 40, 100555.

[3] Noonan, O., Zhang, H., Song, H., Xu, C., Huang, X., & Yu, C. (2016). In situ Stöber templating: facile synthesis of hollow mesoporous carbon spheres from silica–polymer composites for ultra-high level in-cavity adsorption. Journal of Materials Chemistry A, 4(23), 9063-9071.

22nd Iranian Chemistry Congress (ICC22)
Iranian Research Organization for Science and Technology (IROST)
13-15 May 2024

03231-97589

Synthesis, characterization and application of nanonet composite of Co_3O_4/g-C_3N_4 to photocatalytic degradation of sertraline at visible irradiation

Mehdi Hosseini

Corresponding Author E-mail: Hosseini.mih@gmail.com

Biosensor and Energy Research Center, Faculty of Basic Sciences, Ayatollah Boroujerdi University, Boroujerd, Iran.

Abstract: Radiation catalysis proves potent and eco-friendly in water treatment. Sertraline degradation in water using Co_3O_4/g-C_3N_4 was studied. Synthesized nanocatalyst was characterized via XRD, SEM, TEM, BET, and Zeta-potential analyses. Over 60 min, 97% sertraline degraded at RT. Rate constant was 0.0536 min^{-1} (First order kinetics). BET analysis revealed porous nanonet structures, enhancing photocatalytic performance. Co_3O_4/g-C_3N_4 (97%) outperformed pristine Co_3O_4 (68%) and g-C_3N_4 (60%).

Keywords: Water treatment; Sertraline degradation; Nanonet porous of Co_3O_4/g-C_3N_4; Photodegradation.

Introduction

Antidepressants, led by sertraline, are vital in treating mental disorders like anxiety and depression [1]. Their increased global usage, notably during the COVID-19 pandemic, has raised concerns about their presence in wastewater, contributing to environmental pollution. Various methods, including advanced oxidation processes (AOPs) like photocatalysis, offer effective solutions for removing these pollutants. Co_3O_4/g-C_3N_4, known for its visible light absorption and redox activity, stands out as a promising photocatalyst [2]. Coupling it with other semiconductors enhances its efficiency, particularly in visible light photocatalysis. This study aims to explore its effectiveness in degrading pollutants, especially sertraline, from water samples, contributing to sustainable solutions for environmental remediation. Co_3O_4/g-C_3N_4 capability, along with its ability to form heterojunctions, signifies its potential in addressing water pollution challenges [3]. Research into its application further underscores the importance of advancing environmentally friendly technologies for water treatment and remediation.

Experimental Section

Sertraline degradation experiments were conducted under ultraviolet irradiation in a glassy semi-reactor equipped with a fluorescent lamp (300 W, Xe, wavelength> 350 nm). Each experiment dispersed 10 mg of photocatalyst (Co_3O_4, g-C_3N_4, or Co_3O_4/g-C_3N_4 nanocomposite) in 100 mL of 100 mg L^{-1} sertraline solution, then sonicated for 2 minutes. The solution was stirred in dark conditions for 30 minutes, followed by exposure to visible light for 0 to 60 minutes for sertraline degradation. Samples were centrifuged, and sertraline concentration was measured using a UV-vis spectrophotometer at 507 nm to calculate degradation percent using following equation (1).

$$\text{Degradation of sertraline (\%)} = ((C_0 - C_f)/C_0) \times 100 \quad (1\text{-}1)$$

Results and Discussion

Figure 1 displays XRD patterns, comparing material crystalline phases. Analysis revealed the crystalline structure of pristine Co_3O_4 and Co_3O_4/g-C_3N_4 nanocomposite. Peaks align with standard card number 42-146 for Co_3O_4. Differences include peaks related to g-C_3N_4 and absence of impurities in the nanocomposite, confirming its well-formed phase.

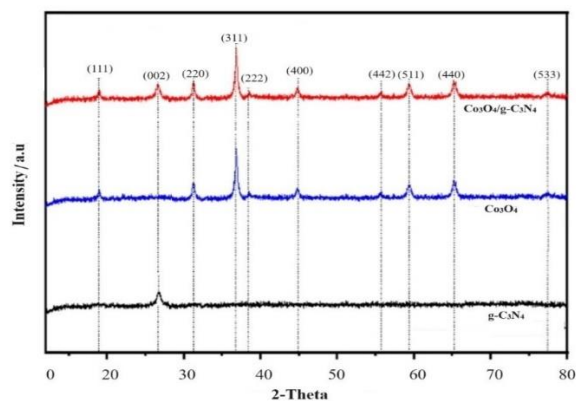**Fig.1:** XRD patterns for pristine g-C_3N_4, pristine Co_3O_4 and nanocomposite of Co_3O_4/g-C_3N_4 nanocomposite.

SEM and TEM images in **Figure 2 (a-f)** show material morphology, with pristine g-C_3N_4 displaying a sheet-like structure (a,b) and pure Co_3O_4 showing agglomerated particles (c,d). The Co_3O_4/g-C_3N_4 nanocomposite exhibits a sponge-like porous interconnected structure (e,f). The Co_3O_4/g-C_3N_4 nanocomposite SEM images also obviously demonstrate the foam-rubber like porous configuration.

22nd Iranian Chemistry Congress (ICC22)
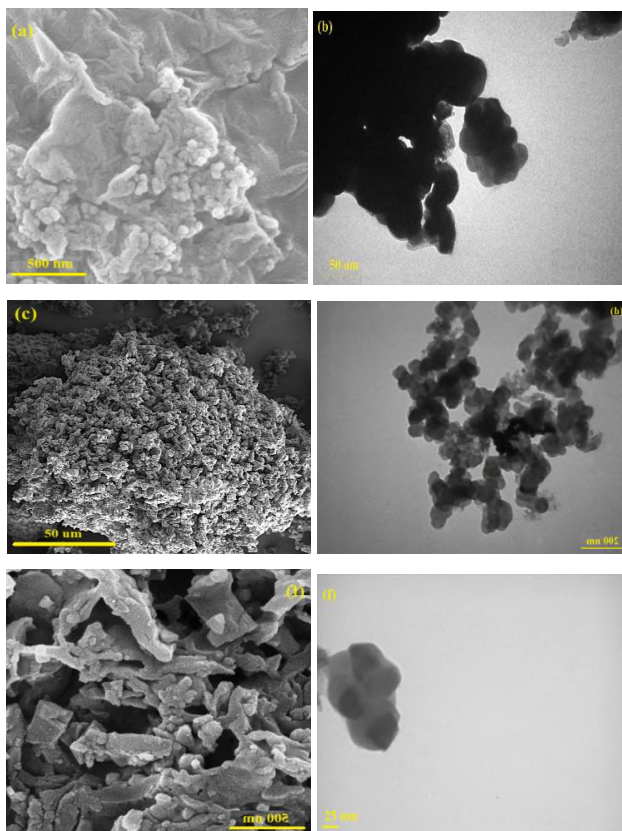Iranian Research Organization for Science and
Technology (IROST)
13-15 May 2024

03231-97589

Fig.2: SEM and TEM of (a,b): Pristine g-C_3N_4, (c,d): Pristine Co_3O_4 and (e,f): nanocomposite of Co_3O_4/g-C_3N_4.

Particularly, the TEM image in shows two layers of materials containing cobalt oxide as the core and g-C_3N_4 as the shell.

Figure 3 assesses the water degradation of sertraline under various conditions. Combining photocatalyst and Vis achieved 93% degradation after 60 min, indicating Vis light's significant contribution to sertraline degradation.

COD, measures necessary oxygen for organic material oxidation. Monitoring sertraline mineralization involves COD reduction. Vis/photocatalyst processes showed effective mineralization, reaching 8% COD reduction in 60 min (**Figure 4**).

The obtained experimental employing the linear regression coefficient (R^2) method, a chemical kinetic model for sertraline photodegradation was established, and the corresponding results can be found in **Table 1**.

Table 1: Regression coefficients and rate constant of various kinetic models for the sertraline degradation.

Kinetic Model	(R^2) Value	Rate Constant (k_f)
0-order	0.953	0.0002
1-order	0.988	0.0536
2-order	0.975	22.815
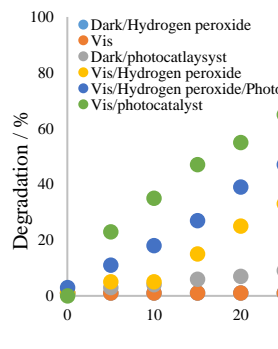
Fig.3: Sertraline degradation at different conditions/process.
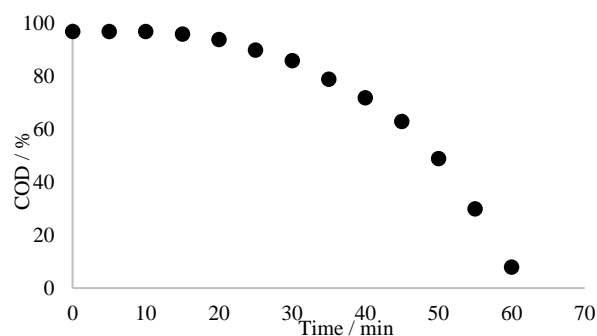
Fig.4: COD changes as functions of time during photocatalytic sertraline degradation.

Conclusions

A cost-effective and reusable Co_3O_4/g-C_3N_4 nanocomposite was synthesized and employed as an efficient photocatalyst for sertraline degradation in water. Characterization techniques confirmed its development and superior performance, achieving 97% degradation. The nanocomposite's enhanced efficiency, attributed to synergistic effects and increased surface-active sites, positions it as an ideal photocatalyst.

References

[1] Huijbregts, K.M., Hoogendoorn, A., Slottje, P., van Balkom, A.J.L.M. & Batelaan, N.M. (2017). Long-term and short-term antidepressant use in general practice: Data from a large cohort in the netherlands. Psychotherapy and Psychosomatics, 86(6), 362-369. https://doi.org/10.1159/000480456.

[2] Pliego, G., Xekoukoulotakis, N., Venieri, D. & Zazo, J.A. (2014). Complete degradation of the persistent anti-depressant sertraline in aqueous solution by solar photo-Fenton oxidation. Journal of Chemical Technology and Biotechnology, 89(6), 814-818. https://doi.org/10.1002/jctb.4314.

[3] Yang, L., Liu, J., Yang, L., Zhang, M., Zhu, H., Wang, F., Yin, J. (2020). Co3O4 imbedded g-C3N4 heterojunction photocatalysts for visible-light-driven hydrogen evolution. Renewable Energy 145, 691-698. https://doi.org/10.1016/j.renene.2019.06.072.

22nd Iranian Chemistry Congress (ICC22)
Iranian Research Organization for Science and Technology (IROST)
13-15 May 2024

03231-97589

IROST

Solvent-based microextraction (SBME) of mercury(II) in water samples using an ecofriendly agent: Synthesis and application of a task-specific imidazolium-based ionic liquid as green extractant

Mehdi Hosseini

Corresponding Author E-mail: Hosseini.mih@gmail.com

Biosensor and Energy Research Center, Faculty of Basic Sciences, Ayatollah Boroujerdi University, Boroujerd, Iran.

Abstract: Here, a solvent-based method to the microextraction of Hg(II) ions relies on the utilization of a synthesized/characterized imidazolium-based ionic liquid ($[C_1C_6Sim][Cl]$) as a task-specific ionic liquid is described. Based on the obtained results, the limit of detection (LOD) and limit of quantification (LOQ) were determined to be 0.015 ng ml^{-1} and 0.078 ng ml^{-1}, respectively. The precision as relative standard deviation (RSD%) for seven replicates are found to be 1.7%. Furthermore, linear dynamic range (LDR) 0.1–80 ng ml^{-1} was achieved. The validity of the method was confirmed through its successful utilization to the determination of Hg(II) ions in various real water and wastewater samples.

Keywords: Functionalized ionic liquid; Task-specific ionic liquid imidazolium-based; characterization; Hg(II) determination; solvent-based microextraction.

Introduction

All mercury species are toxic and mercury is one of the most toxic elements impacting on human, animals and ecosystem health. Mercury is a naturally occurring element that is found in every source such as air, water and soil which exposure to mercury, even small amounts may cause serious health problems [1]. Numerous famous and sensitive methods are available for the pre-concentration and subsequent determination of trace concentration of various species at ppb or sub-ppb levels. ISFME/SBME is classified as another mode dispersive liquid–liquid microextraction (DLLME) with few differences in principals. Nonetheless, DLLME offers some goodness, like a high concentration factor, very low solvent consumption, rapidity, simplicity, and cost-effectiveness [2]. Task-specific ionic liquids (TSILs) or functionalized ionic liquids (FILs) represent a sub-family of ionic liquids characterized by their high specificity towards various target analytes. The applications of TSILs in the treatment of water, wastewater, soil, food, and biological samples are extensively reviewed. In the extraction of inorganic analytes, TSILs can be employed as complexing agents to eliminate any additional components, reduce process costs, and simplify the procedure [3].

Experimental Section

Firstly, a 10 ml solution containing 50 ng mL^{-1} of mercury (II), 0.20% (w/v) of TSIL/FIL, 20% (w/v) NaNO$_3$, in a buffer with pH of 6.0 was poured into a 15 mL conical centrifuge tube. The mixture was shaken for less than a minute to generate a hydrophilic Hg-TSIL/FIL complex (Hg-$[C_1C_6Sim][Cl]$) in the aqueous phase. Then, 0.20% (w/v)

NaBF$_4$ as counter ion was incorporated into the tube, resulting in a cloudy solution and the formation of the hydrophobic chelate of mercury (Hg-$[C_1C_6Sim][BF_4]$). The tube was then centrifuged for 2 minutes at 3000 rpm. Finally, approximately 20 µL of the hydrophobic Hg-TSIL complex settled at the conical bottom of the centrifuge tube. To ease its transfer by reducing viscosity, to this phase, about 20 µL of pure ethanol was added. The analytical procedure schematic for extraction of Hg(II) ions using SBME procedure is shown in Figure 1.
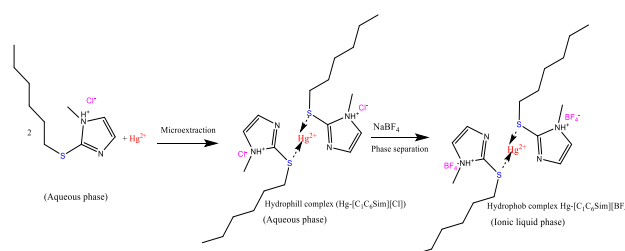

Fig.1. The schematically procedure route for solvent-based extraction of Hg(II) using TSIL/FIL.

Results and Discussion

To optimization of mixroextraction procedure, various factors including the sample solution pH, TSIL/FIL amount, salt effect, amount of anion-exchange, centrifugation conditions were assessed.

The effect of pH on the preconcentration of 50 ng mL^{-1} mercury (II) ions was investigated in the range of 1.0-9.0. The obtained results are shown in Figure 2. Results showed that the ability of the solvent-based microextraction method to extraction of Hg(II) ions goes up to pH of 6.0 and then decreasing at higher pH value.

22nd Iranian Chemistry Congress (ICC22)
Iranian Research Organization for Science and
Technology (IROST)
13-15 May 2024

03231-97589

IROST

Probably, at pH greater than 6.0, the concentration of free Hg(II) ions decreases due to the hydroxide formation and leading to a decrease in extraction efficiency. Furthermore, at acidic pH (pH<4), thiol groups -S in TSIL/FIL become protonated and deactivated.
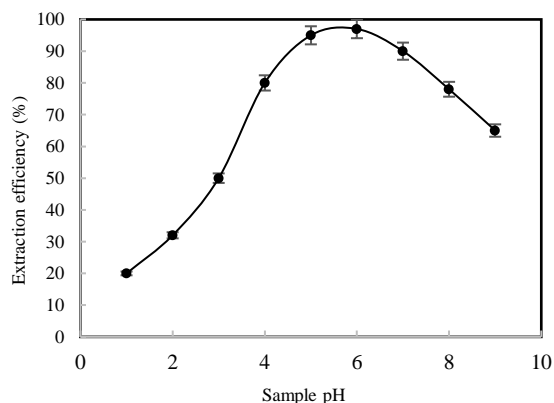

Fig. 2: The effect of sample solution pH on the solvent-based microexraction efficiency of Hg(II).

The results from Figure 3 indicate that up to 0.2% (w/v) TSIL amounts, the extraction efficiency for Hg(II) was increased. The maximum extraction efficiency for Hg(II) was 95% in the 0.2% w/v of TSIL/FIL. At higher amount of 0.2%, the extraction efficiency was constant and does not change. It is worth noting that at high concentration of TSIL/FIL (>0.8 % w/v) the extraction efficiency slightly decreases.
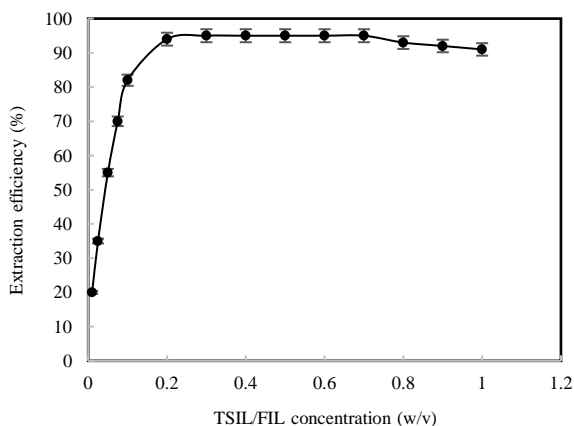
Fig. 3: The effect of TSIL/FIL concentration on the solvent-based microexraction efficiency of Hg(II).

The tetrafluoroborate anion (BF_4^-) replaces the chloride anion (Cl^{-1}) in TSIL/FIL structure, rendering the hydrophobic complex [C_1C_6Sim][BF_4] and, as a results, separation of phases was complete and efficient.
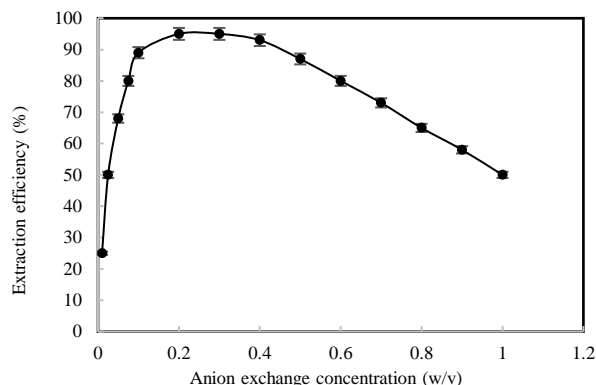
Fig. 4: The effect of anion exchange reagent ($NaBF_4$) concentration on the solvent-based microexraction efficiency of Hg(II).

It is noteworthy that the chloride anion serves as a satisfactory leaving group. Therefore, the impact of BF_4^- amount in the range of 0.01–1.0% (w/v) was investigated. According to the results from Figure 4, up to a sodium hexafluorophosphate concentration of 0.2% (w/v) the extraction efficiency significantly increased.

Conclusions

The synthesized TSIL/FIL, functioning as a green solvent, was utilized for the extraction/preconcentration of mercury. Leveraging the advantages of TSIL/FIL, the developed solvent-based method is environmentally friendly, eliminates the need for disperser solvents, and demonstrates sensitivity, selectivity, speed, and exceptional sample preconcentration capabilities. Consequently, the method determination of mercury ions content in various real water and wastewater samples, successfully. Results show that the recovery range of mercury ions from real water samples analyzed was between 98.0 to 101.2%.

References

[1] Miao, J., Wang, X., Fan, Y., Li, J., Zhang, L., Hu, G., He, C. & Jin, C. (2018). Journal of Food and Drug Analyses, 26, 670-677. https://doi.org/10.1016/j.jfda.2017.08.004.

[2] Hosseini, M., Naderi, A. & Fazli, Z. (2020). Application of a task-specific functionalized ionic liquid to simultaneous preconcentration of Cd and Pb as toxic pollutant in real water and saline samples by in-situ solvent formation microextraction technique. Iranian Journal of Analytical Chemistry, 7(2), 1-11. https://doi.org/10.30473/ijac.2020.52928.1170.

[3] Hosseini, M., Khoshfetrat S.M., Panahimehr, M. & Rezaei, A. (2024). ISFME extraction of As species from some real water samples using an imidazolium-based task-specific ionic liquid (TSIL): Synthesis and characterization. Separation Science and Technology, In press.https://doi.org/10.1080/01496395.2024.2328678.

22nd Iranian Chemistry Congress (ICC22)
Iranian Research Organization for Science and Technology (IROST)
13-15 May 2024

03231-97589

IROST

Simultaneous Determination of 13 Preservatives in Cosmetics by High-Performance Liquid Chromatography

Hadi Behrooj, Afshin Rahimi, Mohammad Dehsarayi

Corresponding Author E-mail: Behrooj.hadi@gmail.com

Samet Tech Azma laboratory, Rasht, Iran.

Abstract: A high-performance liquid chromatographic (HPLC) procedure is presented for the separation, identification and quantification of 13 preservatives that are listed in the current EEC Council Directive on cosmetic products or have been permitted in the past. The method consists of an extraction of acidified cosmetics with methanol, and separation of the extracts by HPLC.

Keywords: HPLC, preservative, separation.

Introduction

Cosmetics are a common component of our daily lives, often containing preservatives, which are added to prevent microbial growth. These preservatives are also widely found in foods, pharmaceuticals and other products of common use. The most frequently used preservatives in cosmetics are the alkyl esters of P-hydroxybenzoic acid (parabens), due to their strong stability, lack of volatility and low irritability (1). In addition to parabens, benzoic acid (BA), benzyl alcohol(BenA), salicylic acid (SA), sorbicacid (SO), dehydroacetic acid (DHA) and phenoxyethanol (PE) are also added to many cosmetics. The determination of preservatives in cosmetic and food industry products is important, not only when considering the quality control of these preparations,but also because of the numerous reports of allergic reactions that they can cause. Therefore, the relevant regulations limiting the contents of the individual ingredients in cosmetics and pharmaceuticals are introduced to increase the safety of their application. To analyze the preservatives in cosmetics, a number of chromatographic methods have been developed using highperformance liquid chromatography (HPLC) (2–4). However, few methods that are capable of simultaneously analyzing 13 preservatives. In this study, we successfully established an HPLC method for the simultaneous determinationof 13 preservatives: methylparaben (MP), ethylparaben (EP), propylparaben (PP), isopropylparaben(IPP),benzyl paraben(BZP),butylparaben(BP), isobutylparabrn(IBP), BA, SA, SO, DA, BenA, and PE .

Experimental Section

Instrumentation and chromatographic conditions:

HPLC was performed using a Agilent 1260 HPLC system equipped with an auto sampler, a vacuum degasser and a variable-wavelength detector. AHimacCR5L centrifuge (HITACHI, Ibaraki, Japan) and an 8510J-MT ultrasonicator device (BRANSON, Danbury, CT, USA) were also used to prepare the samples. An L-column ODS (5 µm particle size column, 250_ 4.6 mm was used to separate the components of the preservatives. The mobile phase was 5 mmol/L ammonium acetate solution (pH 4.2 adjusted by acetic acid) and acetonitrile. The column temperature was set at 35 C, the flow rate was 1ml/min.

Reagents

The chemicals MP, EP, PP, BP, SO, PE, IPP DA, SA, BenA, BZP, BA and IBP were purchased from Sigma-Aldrich (St. Louis, MO, USA). Amonium acetate, acetic acid, methanol and acetonitrile were purchased from Merck (Darmstadt, Germany). Water purified by a Millipore Elixsystem (Milford, MA, USA) was used for the mobile phase. Cosmetic products for the analyses were face tonics, creams, lotions, shower gels, and face masks. These products came from different manufacturers.

Results and Discussion

Preparation of Cosmetics

Clear liquid formulations were analyzed directly or, if necessary, after the appropriate dilution with distilled water. Solid samples and liquid formulations with a high density and viscosity required ultrasonic extraction with methanol prior to analysis. Approximately 0.5 g of the samples (toothpaste, cream, gel, etc.) were weighed and 10 mLof acidified methanol was added, after which the samples were sonicated in an ultrasonic bath for 15 minutes, and later transferredquantitatively into a 10.0 mL volumetric flask filled to the mark with methanol and mixed. Then the solutions were filtered through a nylon filter with a pore size of 0.45 μ m and the resulting filtrates were analyzed by the HPLC method (where necessary, samples were diluted with methanol or water).

22ⁿᵈ Iranian Chemistry Congress (ICC22)
Iranian Research Organization for Science and
Technology (IROST)
13-15 May 2024

03231-97589

IROST

Detection wavelength

To simultaneously examine all the 13 preservatives in cosmetics by HPLC, the detection wavelength was selected under the appropriate conditions (i.e., when only a single wavelength was used, all preservatives could be analyzed). Each preservative possesses a unique maximum absorption wavelength: parabens at 254 nm, BA at 230 nm, SA at 205 nm, SO at 256 nm, DA at 310 nm, BenA and PE at 220 nm. In consideration of these maximum absorption wavelengths, a wavelength programme was selected to maximize sensitivty of each analyte. The overlayed chromatogram of different concentration was shown in Fig. 1.
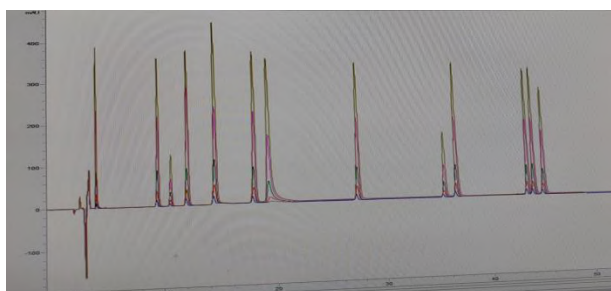
Fig.1: Overlaid chromatograms of 13 preservatives in order of retention time:SA, BA, BenA, SO,PE, MP, DA, EP, IPP, PP, IBP,BP, BZP.

Linearity and limit of quantification

We prepared solutions at 6 different concentrations of standard mixture solutions diluted with methanol in the range 5–100 mg/mL, and constructed a calibration curve by plotting peak area against concentration. All of pereservative show good correlation coefficient between peak area and concentration. The calibration curve of butyl paraben is presented in Fig. 2.

Recovery and precision

For experiments on recovery and precision (n = 6), samples from three types of cosmetics (a cosmetic lotion, a milky lotion and a cosmetic cream) containing none of the 13 preservatives were used. The samples were then spiked with preservatives at a concentration of 100, 500, 1000 and 4000 mg/L. The results in represent high-quality data with percent recoveries of 90–108% and relative standard deviations (RSDs) of ,5.3%. There were no frustrating peaks in any of the samples.

$$y = 47.682x - 2.9005$$
$$R^2 = 0.9956$$
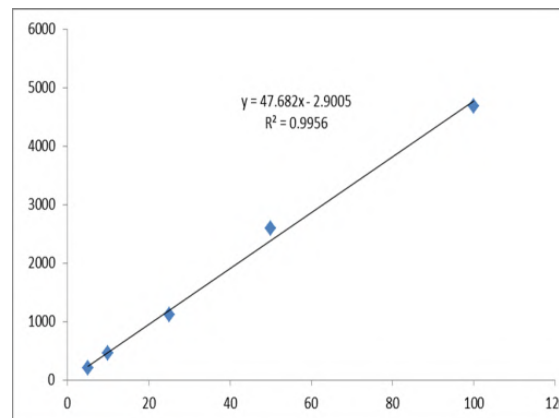
Fig.2: Calibration curve of butyl paraben.

Conclusions

Our paper presents the new chromatography method and sample preparation procedures (for cosmetics with different matrix composition and physical form, for the simultaneous isolation and determination of 13 preservatives. Excellent resolution and good separation were achieved, and system suitability experiments showed the robustness and high precision for this kind of application.The high precision of the retention times and peak areas ensures reliable results when quantitation is needed for quality control. The variable wavelength detector can be used with programmed wavelength to adjust to the maximum absorbance for all the compounds.

References

[1]. Ikarashi, Y., Uchino, T., Nishimura, T.; Analysis of preservatives used in cosmetic products: Bulletin of National Institute of Health Science, (2010); 128: 85–90.

[2] 2. Harvey, P.W.,Journal of Applied Toxicology, (2003); 23: 285–288.

[3]. Byford, J.R., Shaw, L.E., Drew, M.G.B., Pope, G.S., Sauer, M.J., Darbre,P.D.; The Journal of Steriod Biochemistry and Molecular Biology, (2002); 80: 49–60.

[4]. Darbre, P.D., Aljarrah, A., Miller, W.R., Coldham, N.G., Sauer, M.J., Pope, G.S.; Journal of Applied Toxicology, (2004); 24: 5–13.

Simultaneous Determination of 12 artificial colors in food samples by High-Performance Liquid Chromatography

Afshin Rahimi, Hadi Behrooj, Mohammad Dehsarayi

Corresponding Author E-mail: Behrooj.hadi@gmail.com

Samet Tech Azma laboratory, Rasht, Iran.

Abstract: A high-performance liquid chromatographic (HPLC) procedure is presented for the separation, identification and quantification of 12 artificial colors in food samples. The method consists of a liquid extraction of artificial colors with extraction solvent, separation and quantification of the extracts by HPLC.

Keywords: HPLC, artificial color, separation.

Introduction

In food technology, food colorants, of several types, are chemical substances that are added to food matrices, to enhance or sustain the sensory characteristics of the food product, which may be affected or lost during processing or storage, and in order to retain the desired color appearance [1-3]. These are classified based on several criteria: firstly, based on their origin in nature, nature-identical or, if synthetic, whether they are organic or inorganic. Another classification could be based on their solubility (e.g., soluble or insoluble) or covering ability (e.g., transparent or opaque), though an overlap may exist among one or more of these classifications. The most common and widely used classification is based on the distinction between soluble and insoluble color additives (colorants or pigments), which can be further categorized as natural or synthetic [4] The need to determine synthetic colorants in food matrices originating from their known toxicity, renders the analytical task even more challenging as food matrices are ordinarily very complex. Various analytical techniques are used to determine synthetic food colorants in food samples, including spectrophotometry, thin layer chromatography, capillary electrophoresis, high performance liquid chromatography and mass spectrometry (MS). Among all LC methods available for food colors, very few of them offer simultaneous quantitation and resolution of several permitted food colors and nonpermitted dyes in a variety of food commodities. Therefore, an optimized method was developed and validated to analyze various foodstuffs where authorized food colors as well as some nonpermitted colors, are resolved and quantitated. In this paper, we present the development, optimization, and validation of a quantitative method of analysis for the determination of 12 synthtetic colors in foodstuffs.

Experimental Section

Instrumentation and chromatographic conditions:

HPLC was performed using a Agilent 1260 HPLC systemequipped with an auto sampler, a vacuum degasser and a variable-wavelength detector. A HimacCR5L centrifuge (HITACHI, Ibaraki, Japan) and an 8510J-MT ultrasonicator device (BRANSON, Danbury, CT, USA) were also used to prepare the samples. An L-column ODS (5 µm particle size column, 250_ 4.6 mm was used to separate the components of the dyes. The mobile phase was 20 mmol/L phosphate solution (pH 7.0 adjusted by phosphoric acid) and acetonitrile in a gradient elution. The column temperature was set at 35 ˚C, the flow rate was 1ml/min.

Reagents

Tartrazine, amaranth, sunset yellow FCF, allura red , fast green FCF, brilliant blue FCF, erythrosine, ponceau 4R, quinoline yellow, carmoisine, indigo carmine and acid red33 were purchased from Sigma-Aldrich (St. Louis, MO, USA). Potasium dihydrogen phosphate, phosphoric acid, methanol and acetonitrile were purchased from Merck (Darmstadt, Germany). Water purified by a Millipore Elixsystem (Milford, MA, USA) was used for the mobile phase. Cosmetic products for the analyses were face tonics, creams, lotions, shower gels, and face masks. These products came from different manufacturers.

Results and Discussion
Extraction Procedure

Starch-Containing Commodities

A 10 g portion of each food commodity was weighed in duplicate and transferred to 125 mL Erlenmeyers. To each replicate, 5 mL of the α-amylase solution and 30 mL of the 100 mM ammonium acetate solution were added. Samples were sonicateded for 15 min. Then, 5 mL of methanol and 25 mL of 100 mM ammonium acetate solution were added. Extracts were quantitatively transferred into 100 mL volumetric flasks, then filling to mark with 100 mM ammonium acetate solution. Volumetric flasks were shaken, and about 12 mL was

22nd Iranian Chemistry Congress (ICC22)
Iranian Research Organization for Science and Technology (IROST)
13-15 May 2024

03231-97589

ISC

IROST

transferred into polypropylene centrifuge tubes. Extracts were centrifuged for 5 min at 14 000 rpm at room temperature. The supernatant was transferred to LC vial, and 25 µL was injected onto the LC system.

Other Commodities

Food colors were extracted using the same procedure as described previously without the enzymatic treatment step. The initial addition of the extraction solution was performed with 35 mL of 100 mM ammonium acetate solution.

.Detection wavelength

To simultaneously examine all the 12 dyes in food samples by HPLC, the detection wavelength was selected under the appropriate conditions (i.e., when only a single wavelength was used, all colors could be analyzed). Each color possesses a unique maximum absorption wavelength.In consideration of these maximum absorption wavelengths, a wavelength programme was selected to maximize sensitivty of each analyte. The overlayed chromatogram of different concentration was shown in Fig. 1.
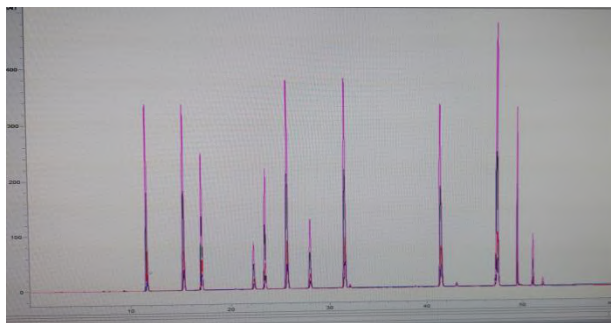
Fig.1: Overlaid chromatograms of 12 preservatives in order of retention time:tartarazin, amaranth, indigotin, ponceau 4R, quinoline yellow, sunset yellow, acid red33, allura red, carmoisine, brilliant blue, erythrosine and fast green.

Linearity and limit of quantification

We prepared solutions at 6 different concentrations of standard mixture solutions diluted with water in the range 2.5-50 mg/mL, and constructed a calibration curve by plotting peak area against concentration. All of colors show good correlation coefficient between peak area and concentration. The calibration curve of erythrosine is presented in Fig. 2.

Recovery and precision

Food commodities were spiked with standard solutions at three concentration levels.. Triplicate fortified samples were prepared for the low and high levels, respectively, at 25 and 200 mg/Kg, while six replicates were analyzed for the mid-level at 100 mg/Kg. The recovery (R) was calculated by the method described in Appendix D of AOAC guidelines as $R_{marginal} = [(C_f - C_u)/C_a] \times 100$, where

C_f is the concentration found in the spiked sample, C_u is the concentration in the unfortified sample, whereas C_a is the added concentration in the spiked sample. Typically, C_a is calculated by injecting standard preparations with the same concentrations as in spiked samples. The repeatability precision (S_r, RSD_r) was expressed as the mean RSD and was calculated from repeated determinations across the food commodities tested. RSD was calculated with color additive recoveries from replicate sample preparations (n = 6) at one single concentration level (100 mg/Kg). On the other hand, intermediate precision was calculated with recoveries of color additives from replicate sample preparations on a different day. The overall precision was below 10%.
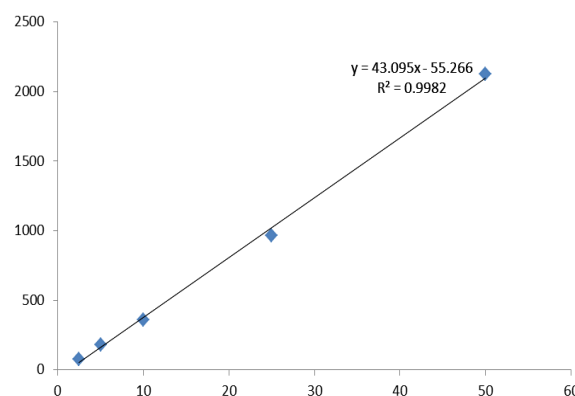

Fig.2: Calibration curve of erythrosine.

Conclusions

The validation results demonstrated the purpose, sensitivity, and fitness for purpose of the method to simultaneously quantitate color additives in food matrices. In terms of color additives extraction, the use of ammonium acetate as the ion-pairing agent offers similar performance as other cationic ion-pairing agents at a fraction of the price.. The LC UV–vis analytical method described herein is a successful approach to separate and quantitate color additives in food commodities.

References

[1]. Marmion, D. M. Handbook of U.S. Colorants for Foods, Drugs, and Cosmetics, 1st ed.; Wiley-Interscience Publication, John Wiley & Sons, 1979.

[2]. Health Canada. C.R.C. Ch. 870, Food And Drugs Regulation; Part B.16.001, Division 16 Food Additives, Table III , April 16, 2014.

[3]. Šrámek, J. Paper chromatography of dyes: IV. Paper chromatography of water-soluble dyes. J. Chromatogr. A 1964, 15, 57– 64, DOI: 10.1016/s0021-9673(01)82739-4.

Sorbitol-Nitrate Microwave-Combustion Synthesis of CuO(15%)-CuFe₂O₄(85%) Nanophotocatalyst with Substantial Removal of Pharmaceutical

Hamed Moradi[a,b], Gholamreza Foroutan[*a], Mohammad Haghighi[†b], Maryam Shabani[b], Ehsan Mohammadi[b]

Corresponding Author E-mail: [*]foroutan@sut.ac.ir, [†] haghighi@sut.ac.ir

[a] Basic Sciences Faculty, Physics-Plasma, Sahand University of Technology, Sahand New Town, Tabriz, Iran.

[b] Chemical Engineering Faculty, Reactor and Catalysis Research Center (RCRC), Sahand University of Technology, Sahand New Town, Tabriz, Iran.

Abstract: Efficient CuFe₂O₄-CuO nanoparticles were synthesized via microwave-assisted combustion to degrade TCH antibiotic under solar spectrum. Characterized by XRD and FESEM, the magnetic material displayed macroporous structure and ferromagnetic properties. CuFe₂O₄-CuO removed 50 mg/L TCH by 60.8% after 150 min.

Keywords: Sorbitol-Nitrate Microwave-Combustion Synthesis; CuO(15%)-CuFe₂O₄(85%) Nanophotocatalyst; Pharmaceutical Removal

Introduction

Water pollution by tetracycline antibiotics is a significant environmental concern due to their widespread use in human and veterinary medicine. Tetracyclines can enter water bodies through various pathways, including runoff from agricultural activities, discharge from pharmaceutical manufacturing plants, and improper disposal of unused medications. Once in water, tetracycline antibiotics can persist for long periods and pose a threat to aquatic ecosystems and human health[1]. Advanced Oxidation Processes (AOPs) are innovative water treatment methods that utilize hydroxyl radicals to break down pollutants in water[2]. These processes are effective for treating various contaminants such as pharmaceuticals and industrial chemicals, ensuring cleaner water sources. CuFe₂O₄ has gained attention as a versatile compound due to its stability, cost-effectiveness, high photochemical stability, and efficient separation compared to other catalysts for degrading pollutants[3]. Its magnetic photocatalytic properties allow easy separation from suspension. However, the bulk CuFe₂O₄ semiconductor's performance is inadequate, leading to efforts to enhance its efficiency. By adjusting the components of CuFe₂O₄ and CuO photocatalysts, a CuFe₂O₄-CuO composite was developed[4].Its photocatalytic performance was assessed in solutions containing TCH and CIP under simulated sunlight.

Experimental Section

Cu(NO₃)₂·3H₂O (Merck) and Fe(NO₃)₃·9H₂O (Merck) were dissolved in 15 ml of water. Sorbitol was then added to the solution, which was stirred continuously at room temperature. After 60 minutes, the turbid solution was transferred to a microwave and irradiated at 1000 W for 10 minutes. The resulting powder was further ground using a mortar and pestle, followed by calcination at 800°C for 10 hours in a muffle furnace.

Results and Discussion

A. XRD Analysis:

The XRD pattern of the magnetic CuFe₂O₄-CuO nanophotocatalyst is illustrated in Figure 1. The characteristic peaks align closely with tetragonal CuFe₂O₄ (Reference code: 96-901-1013) and monoclinic CuO (Reference code: 96-900-8962). The nanocomposite comprises 85% CuFe₂O₄ and 15% CuO, as indicated.
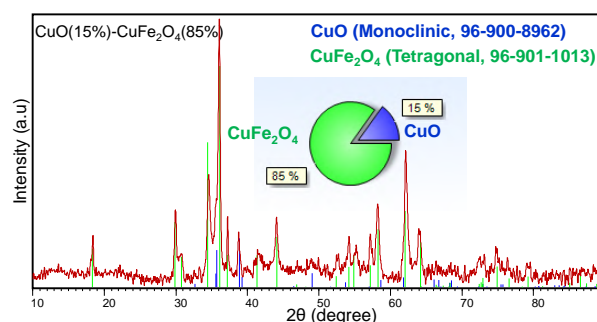

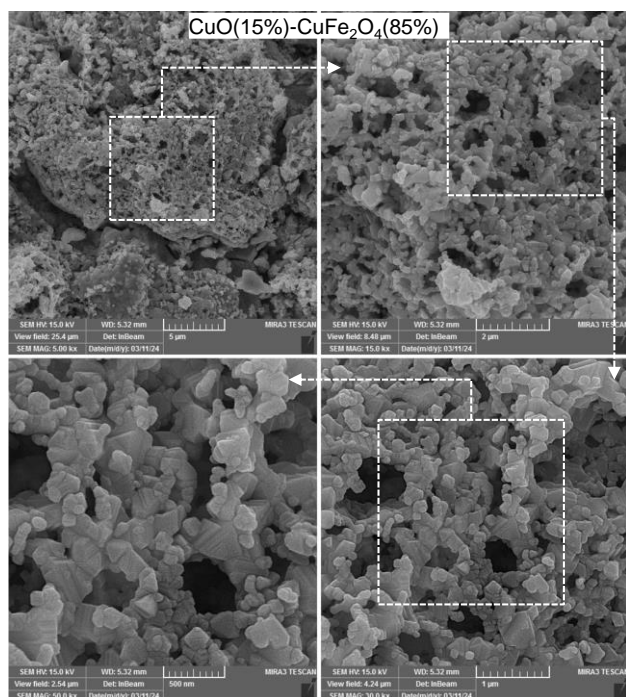**Fig.1:** XRD analysis of CuO(15%)-CuFe₂O₄(85%) Nanophotocatalyst

22nd Iranian Chemistry Congress (ICC22)
Iranian Research Organization for Science and Technology (IROST)
13-15 May 2024

03231-97589

IROST

Fig.2: FESEM analysis of CuO(15%)-CuFe$_2$O$_4$(85%) Nanophotocatalyst

Fig.3 Photocatalytic performance of CuO(15%)-CuFe$_2$O$_4$(85%) Nanophotocatalyst in Pharmaceutical Removal.

A. FESEM Analysis:

The nanostructured magnetic CuFe$_2$O$_4$-CuO nanophotocatalyst's morphology is depicted in Figure 2. The images reveal a honeycomb-like structure with combustion pores. The application of microwave energy facilitates the even distribution of pores and the creation of nanoparticles. Consequently, this honeycomb nanostructure, enhancing diffusion, enhances photocatalytic activity.

C. Photocatalytic Performance for Removal of Pharmaceutical

To assess the photocatalytic activity of the magnetic CuFe$_2$O$_4$-CuO nanophotocatalyst, tetracycline-HCl (TCH) was used as the model contaminant. The degradation levels during the removal of 50 mg/L TCH using the magnetic CuFe$_2$O$_4$-CuO nanophotocatalyst are presented in Figure 3. As depicted in Figure 3, after 150 minutes of irradiation, approximately 60.8% degradation was achieved. These results can be attributed to the unique morphology of this sample, which enables the absorption of high-energy light and reduces light scattering. Additionally, the presence of large pores facilitates the diffusion of reactant molecules. Furthermore, the nanocomposite structure aids in the separation of charge carriers, contributing to enhanced photocatalytic activity.

Conclusions

A honeycomb-like magnetic CuFe$_2$O$_4$-CuO nanophotocatalyst was synthesized using a simple microwave-assisted reaction method. The photocatalytic efficiency of this catalyst was studied in the degradation of TCH solutions. The successful removal of TCH with this nanophotocatalyst can be attributed to its efficient light absorption, enhanced diffusion, increased availability of active sites, and reduced electron-hole pair recombination rate.

References

[1]   Wang L, Tang M, Jiang H, Dai J, Cheng R, Luo B, et al. Sustainable, efficient, and synergistic photocatalytic degradation toward organic dyes and formaldehyde gas via Cu2O NPs@wood. Journal of Environmental Management. 2024;351:119676.

[2]   Mahbub P, Duke M. Scalability of advanced oxidation processes (AOPs) in industrial applications: A review. Journal of Environmental Management. 2023;345:118861.

[3]   Cai H, Ma Z, Zhao T. Fabrication of magnetic CuFe2O4@PBC composite and efficient removal of metronidazole by the photo-Fenton process in a wide pH range. Journal of Environmental Management. 2021;300:113677.

[4]   Reddy NR, Kumar AS, Reddy PM, Kakarla RR, Joo SW, Aminabhavi TM. Novel rhombus Co3O4-nanocapsule CuO heterohybrids for efficient photocatalytic water splitting and electrochemical energy storage applications. Journal of Environmental Management. 2023;325:116650.

Synthesis of polyethylene glycol hydrogel and investigation of its application

Adeleh Behi, Goldasthe Zarei*, Faezeh Khalilian, Jamshid Najafpour, Farrokh Roya Nikmaram

Corresponding Author E-mail: goldasthe@yahoo.com, g.zarei@aiusr.ac.ir

Department of Chemistry, Yadegar-e-Imam Khomeini (RAH) Shahre Rey Branch, Islamic Azad University, Tehran, Iran.

Abstract: The synthesis of polyethylene glycol hydrogels was investigated, and the synthesis conditions were optimized. Subsequently, the utilization of these hydrogels for the removal of heavy metals from wastewater, along with factors such as contact time, removal efficiency for individual metal ions, and reusability, will be examined.

Keywords: removal of heavy metals; hydrogels.

Introduction

Hydrogels are three-dimensional and flexible polymer networks with the ability to absorb water due to the large number of groups they possess, resulting in a swollen state. As an adsorbent, hydrogels have shown remarkable advantages over other adsorbents, such as lower production costs, low operational costs, easy preparation, and simple separation after the adsorption process. They also possess the ability to recover and be reused over the long term. Hydrogels can be utilized in natural waters for contaminant removal without the need for pre- and post-treatments (e.g., pH adjustments). They can be employed at all scales, ranging from single-household to large industrial-scale applications, in an efficient manner. Research results indicate that by controlling synthetic parameters such as reactor type, reaction temperature, reaction time, and the type and amount of raw materials, improved hydrogenated tubes with desirable properties can be prepared. Hydrogels should be designed to possess the ability to remove contaminants over a wide range of pH levels[1-3].

Experimental Section

In this method, free radical polymerization is carried out using an optimized synthesis method. Initially, PEG is added to distilled water and mixed until completely dissolved to obtain a transparent solution. Then, Ammonium Persulfate (ASP) is dissolved in distilled water. Subsequently, the Ammonium Persulfate solution is gradually added to the polymer solution. In the next step, acrylic acid (AA) is gradually added to the transparent polymer solution, and of EGDMA is slowly added to the solution as a crosslinker. This reaction is carried out under a nitrogen gas atmosphere to remove oxygen from the reaction environment.

Results and Discussion

In this research, the synthesis of polyethylene glycol-based hydrogels with functional groups will be investigated, and the synthesis conditions will be optimized. Subsequently, the use of these hydrogels for the removal of heavy metals from wastewater will be explored, focusing on factors such as contact time, removal efficiency for individual metal ions, and reusability.

Conclusions

The hydrogel was synthesized, and FTIR was employed for its identification, while TEM, SDL, SEM, and XRD were utilized to examine its structure. To assess the removal of heavy metals, atomic absorption spectroscopy and UV analysis were performed.

References

[1] Shadman, S. M.; Daneshi, M.; Shafiei, F.; Azimimehr, M.; Khorasgani, M. R.; Sadeghian, M.; Motaghi, H.; Mehrgardi, M. A. Aptamer-based electrochemical biosensors. In Electrochemical Biosensors; Elsevier, 2019, pp 213–251.

[2] Lakherwal, D. (2014). Adsorption of heavy metals: a review. Int. J. Environ. Res. Dev., 4, 41–48.

[3] Zhang, M.; Yin, Q.; Ji, X.; Wang, F.; Gao, X.; Zhao, M. (2020). High and fast adsorption of Cd (ii) and Pb (ii) ions from aqueous solutions by a waste biomass based hydrogel. Sci. Rep., 10, 3285.

Removal of sarafloxacin from aqueous solution through Ni/Al-layered double hydroxide@ZIF-8

Sahar Abaskhani Davanlo, Abdolraouf Samadi-Maybodi[*]

Corresponding Author E-mail: samadi@umz.ac.ir

Analytical division, Faculty of Chemistry, University of Mazandaran, Babolsar, Iran.

Abstract: Ni/Al-LDH@ZIF-8 nanocomposite was synthesized and used to remove the antibiotic sarafloxacin (SRF) in the aqueous solution. The results showed that 97% of SRF was removed under optimized conditions (initial concentration of SRF = 40 mg·L^{-1}, pH = 6.3, adsorbent dose = 49 mg, and contact time = 44 min).

Keywords: Sarafloxacin; Layered double hydroxide; absorbent.

Introduction

In recent years, there has been excessive use of drugs, such as antibiotics, to combat COVID-19 and other viruses. Unfortunately, this has led to the release of significant amounts of drugs and their metabolites as toxic pollutants in aquatic systems [1,2]. In this research, Ni/Al-LDH@ZIF-8 nanocomposite was synthesized from layered double hydroxides and metal-organic frameworks and used to remove the antibiotic sarafloxacin (SRF) in the aqueous solution. The aim of this work was to synthesize an efficient absorbent with some properties such as high surface area, adjustable porosity and low-density structure.

Experimental Section

Various methods, such as Fourier transform infrared spectroscopy, X-ray diffraction, field emission scanning electron microscopy, and energy-dispersive X-ray spectroscopy, were applied to caracterize the nanocomposite. The central composite design was performed to evaluate statistics and the response level method to optimize the factors affecting the absorption process.

Results and Discussion

The results showed that under optimized conditions (initial concentration of SRF = 40 mg·L^{-1}, pH = 6.3, adsorbent dose of Ni/Al-LDH@ZIF-8 = 49 mg, and contact time = 44 min). Results showed that 97% of SRF was removed. According to the model of isotherms parameters, different adsorption models were examined and results indicated that adsorption process is more consistent with the Freundlich model, with an absorption capacity of 79.7 mg·g^{-1}. Mechanisms of adsorption include hydrophobic effects of the absorbent composite, π-π interactions, penetration of pollutants into the composite's layers and pores, and the possibility of forming hydrogen bonding (Fig. 1).
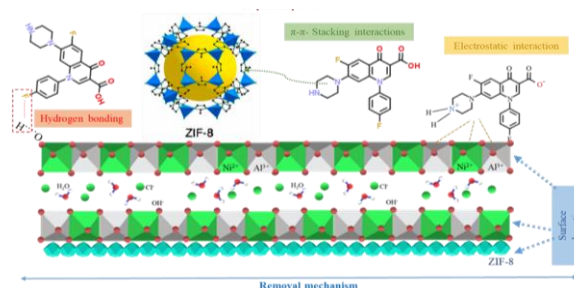

Fig.1: Schematic diagram showing different interactions between Ni-Al/LDH@ZIF-8 and SRF.

Conclusions

Results of this experiment revealed that the Ni/Al-LDH@ZIF-8 nanocomposite is a good adorbent for removal of sarafloxacin. Under optimized condtions up to 97% of sarafloxacin was removed. Numerous mechanisms have been suggested to explain how nanocomposites absorb pollutants. These mechanisms include hydrophobic effects of the absorbent composite, π-π interactions, penetration of pollutants into the composite's layers and pores, and the possibility of forming hydrogen bonding.

References

[1] Tamtam, F., Mercier, F., Le Bot, B., Eurin, J., Dinh, Q. T., Clément, M., & Chevreuil, M. (2008). Occurrence and fate of antibiotics in the Seine River in various hydrological conditions. *Science of the total environment*, *393*(1), 84-95.

[2] A. Samadi-Maybodi, A. Rahmati (2019). Synthesis and characterization of dual metal zeolitic imidazolate frameworks and their application for removal of cefixime. *Journal of coordination chemistry*, 72 (18), 3171–3182.

Application of CdS–ZnS quantum dots as sensitive fluorescence probe for detection of copper ion

Seyfollah Ghasemi, Abdolraouf Samadi-Maybodi*

Corresponding Author E-mail: samadi@umz.ac.ir

Analytical division, Faculty of Chemistry, University of Mazandaran, Babolsar, Iran.

Abstract: The capped CdS-ZnS quantum dots were synthesized with various thiol capping agents of glycolic acid (TGA), mercaptosuccinic acid (MSA) and L-cysteine (LCY) and used as fluorescence probe for determination of Cu (II) ions. The limit of detection for CdS – ZnS@ QDs capped with TGA, MSA and LCY was obtained 1.15×10^{-7}, of 1.32×10^{-7} and of 2.19×10^{-7} mol L^{-1} respectively with linear dynamic range of 3.13×10^{-6} mol L^{-1} to 1.41×10^{-4} mol L^{-1}.

Keywords: CdS-ZnS quantum dots; thiol capping agents; Cu (II) ions.

Introduction

Most QDs are composed of elements of groups II-IV , III-V and II-VI of the periodic table of chemical elements. In comparison with organic dyes, QDs have some advantages such as tunable fluorescence emission, high resistance to photobleaching and broad excitation bands[1] These properties of QDs cause to use them as a fluorescence probe for chemistry and biochemistry applications. The electronic and optical properties of QDs resulting from high surface-to-volume ratio as well as quantum confinements [2].In this work, CdS-ZnS QDs were capped with thioglycolic acid , mercaptosuccinic acid and L-cysteine.

Experimental section

The synthesized nanocomposites were used for determination of copper ion. Surface modification of CdS-ZnS-QDs with compounds of thiols not only prevents the aggregation of QDs, but also makes them available for interaction with target materials and can be used for specific applications. The method of two -level 3-factor full-factorial experiment design was used to achieve the best optical fluorescence emission.

The synthetic method for the preparation of capped CdS-ZnS QDs from thiol compounds was carried out with some modifications from previous reports. To synthesize of capped CdS-ZnS QDs following procedure was performed. The capping agents of L-cysteine (LCY), mercaptosuccinic acid (MSA) and thioglycholic acid (TGA) were used in this study.

Various methods, such as Fourier transform infrared spectroscopy, X-ray diffraction, field emission scanning electron microscopy, and energy-dispersive X-ray spectroscopy, were applied to caracterize the synthesized quantum dots. Response level method to optimize the factors affecting the absorption process.

Results and Discussion

At the first, CdS-ZnS@TGA QDs was examined as fluorescence probe for trace analysis of Cu^{2+}. Figure 9a presents the fluorescence spectra of the CdS-ZnS@TGA in the presence of different concentrations of Cu^{2+} (0.2–9 ppm). All spectra were recorded at excitation wavelength (λ_{ex}) of 235 nm under the same circumstances. As can be clearly observed the band intensity of the fluorescence is decreased by increasing the concentration of the Cu^{2+}. This phenomenon indicates that the Cu^{2+} played the role of the quencher. It can be said that the Cu^{2+} ion interact with CdS-ZnS@TGA and form a complex that has no efficient fluorescence property that is mean the process of deactivation is nonradiative (Fig. 1).
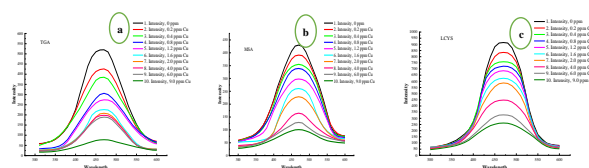

Fig.1: Fluorescence spectra: (a) CdS-ZnS@TGA, (b) CdS-ZnS@MSA and (c) CdS-ZnS@LCY in the presence of different concentrations of Cu^{2+} (0.2-0.9ppm).

Conclusions

Water-soluble CdS-ZnS quantumdots capped with mercaptosuccinic acid (MSA), thioglycolic acid (TGA) and L-cysteine (LCY) were prepared and used as a fluorescent probe to measure Cu^{2+} ions. Fluorescence quenching was used as the basis method for measurement of the Cu^{2+} ions concentration, Stern–Volmer equation was applied for construction of calibration curve. A good correlation between the analytical signal (F$_0$/F) and concentration of Cu^{2+} was found with R^2 =0.99.

References

[1] H. Abdelsalam, Q. Fang Zhang 2022 Properties and applications of quantum dots derived from two-dimensional materials Advances in physics: x. 7 (1), 2048966

[2] S. Fallah, R. Baharfar, A. Samadi-Maybodi 2023 Simple and green approach for photoluminescent carbon dots prepared from faba bean seeds as a luminescent probe for determination of Hg$^+$ ions and cell imaging Luminescence 38 (11), 1929-1937

Exploring the Quantum Mechanics of Iptacopan Drug: A Comprehensive Analysis of Structural, Vibrational, and Electronic Characteristics

Hossein Shirani[a,b,*] and Reza Golmohammadi[b]

Corresponding author. E-mail: hossein_shirani@iust.ac.ir
[a]Department of Chemistry, Iran University of Science and Technology, P.O. Box 16846-13114, Tehran, Iran.
[b]Department of Microbiology, Faculty of Biological Sciences and Technology, University of Science and Culture, Tehran, Iran.

Abstract: This study employs quantum mechanical calculations using the B3LYP/6-311+G computational approach to assess the structural and electronic attributes of Iptacopan as a treatment for Paroxysmal Nocturnal Hemoglobinuria (PNH). By delving into the molecular structure, vibrational frequencies, and electronic energy, we analyze the connections distances, connections angles, torsion angles, and the energy disparity between the Highest Occupied Molecular Orbital (HOMO) and the Lowest Unoccupied Molecular Orbital (LUMO).

Keywords: B3LYP; Iptacopan; Paroxysmal Nocturnal Hemoglobinuria (PNH); HOMO-LUMO

Introduction

The loss of two GPI-anchored surface proteins, CD55 and CD59, from red blood cells causes unregulated complement activation and hemolysis in classical PNH disease. In PNH patients, PIGA-mutant, GPI hematopoietic cells clonally expand to make up a large portion of patients' blood production, yet mechanisms leading to clonal expansion of GPI cells remain enigmatic Historical models of PNH in mice and the more recent PNH model in rhesus macaques showed that GPI (-) cells reconstitute near-normal hematopoiesis but have no intrinsic growth advantage and do not clonally expand over time. Recent advancements in disease models and immunologic technologies, together with the growing understanding of autoimmune marrow failure, offer new opportunities to evaluate the mechanisms of clonal expansion in PNH. Here, we critically review published data on PNH cell biology and clonal expansion and highlight limitations and opportunities to further our understanding of the emergence of PNH clones. Iptacopan is a factor B inhibitor used to treat paroxysmal nocturnal hemoglobinuria. Iptacopan is a small-molecule factor B inhibitor previously investigated as a potential treatment for the rare blood disease paroxysmal nocturnal hemoglobinuria (PNH). In this context, a breakthrough emerged with the FDA's sanctioning of Daybue oral solution, marking it as the new treatment specifically for PNH. This novel drug represents a beacon of hope for those affected by PNH, signifying a monumental step forward in the realm of targeted therapies.

Methods

Firstly, we found the structure of Iptacopan on the Drug Bank website and designed it in the GaussView graphic program followed by quantum mechanical calculations at the B3LYP/6–311+G theoretical level using Gaussian09 software.

After the calculations were done in the Gauss view program, we were able to extract the bond length and the angle between the atom and the IR spectrum, etc.

Results and Discussion

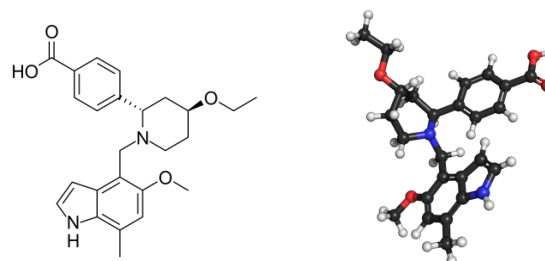Ipatacopan, as shown in Fig.1, has the chemical formula $C_{25}H_{30}N_2O_4$

Fig.1: 3D on the right and 2D on the left side are the structures obtained from B3LYP/6-311+G** calculations.

The distance between two atoms in a molecule, measured in angstroms, determines the strength of a particular bond. In general, a shorter bond indicates a higher electronegativity of the cation, resulting in increased strength and electron density. Thermodynamic data for the configuration of Iptacopan using the B3LYP/6–311+G computational approach reveals the following values: Hartree Fock energy=-866635.677843546 kcal/mol, Specific heat capacity (CV)=112.524 cal/mol-kelvin, Zero-point energy=866313.04759311 kcal/mol.

**Table 1.** B3LYP/6-311+G* optimized values of bond lengths (Å) for Iptacopan.

bond lengths	bond lengths	bond lengths
C23.C26	C17.C23	C24.C18
1.40256	1.39274	1.41165
C28.N6	O2.C31	C21.C24
1.39199	1.44764	1.39598

22nd Iranian Chemistry Congress (ICC22)
Iranian Research Organization for Science and
Technology (IROST)
13-15 May 2024

03231-97589

IROST

Table 2. B3LYP/6-311+G* optimized values of bond angles (°) for Iptacopan

bond angles	bond angles	bond angles
C12.C14.C16	Copy (Font: Calibri 8)	C8.C9.O1
121.8		106.2
N5.C7.C8	C14.C18.C24	C20.N6.C28
110.4	122.3	109

Table 3. B3LYP/6 -311+G* optimized values of bond dihedral for Iptacopan.

bond dihedral	bond dihedral	bond dihedral
C12.C14.C15.C25	C11.C10.C9.O1	C15.C20.C21.C24
1.4	64.1	0.2
C12.C14.C15.C20	C8.C9.O1.C19	C24.C18.C14.O2
-177.9	164.2	0.3
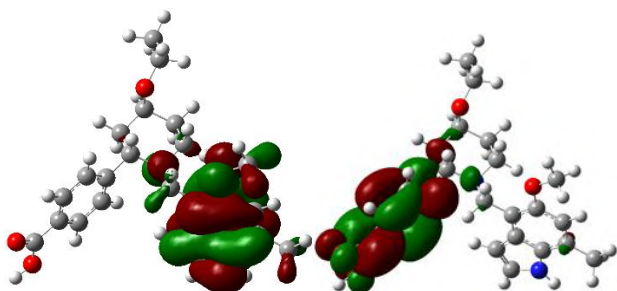
Fig. 2. HOMO-LUMO for Iptacopan is generally the lowest energy electronic excitation that is possible in a molecule.

IR Spectrum

The infrared spectrum, renowned for its increased sensitivity in detecting molecular chemical and structural characteristics, has a wide range of uses in the fields of chemistry, physics, biochemistry, and pharmaceuticals.
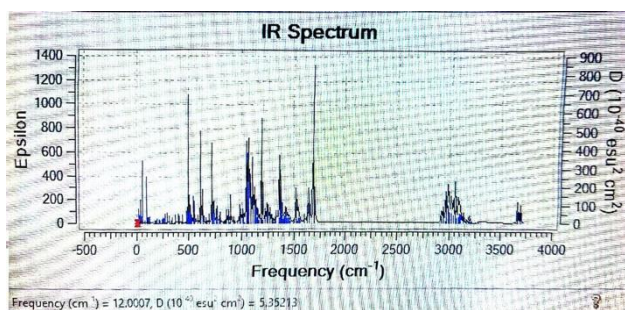
Fig. 3. Vibrational-Frequency IR Spectrum of the Trofinetide Molecule calculated at the B3LYP/6–311+G Level of theory.

Conclusions

The primary objective of this research is to explore the complex world of quantum computing to analyze the distinct characteristics of the Iptacopan medication. By conducting a thorough investigation, our goal is to uncover the molecular and electronic attributes of this healing substance. Studies have indicated that Iptacopan has the potential to be a successful remedy and to demonstrate its capability in treating Rett PNH. The configuration of the Iptacopan compound was simulated using Gaussian and View Gauss software, followed by the optimization of the structure using B3LYP/6-311+G*. Additionally, the atomic charges, IR spectrum, frequency and intensity, as well as various energies of the molecule were extracted and assessed.

References

[1] Panse J. (2023). Paroxysmal nocturnal emoglobinuria: Where we stand. *American Journal of Hematology*, *98 Suppl 4*, S20–S32.https://doi.org/10.1002/ajh.26832
[2] Colden, M. A., Kumar, S., Munkhbileg, B., & Babushok, D. V. (2022). Insights Into the Emergence of Paroxysmal Nocturnal Hemoglobinuria. *Frontiers in immunology*, *12*, 830172. https://doi.org/10.3389/fimmu.2021.830172
[3] Kulasekararaj, A. G., & Lazana, I. (2023). Paroxysmal nocturnal hemoglobinuria: Where are we going? *American journal of hematology*, *98 Suppl 4*, S33–S43. https://doi.org/10.1002/ajh.26882

Appendix:
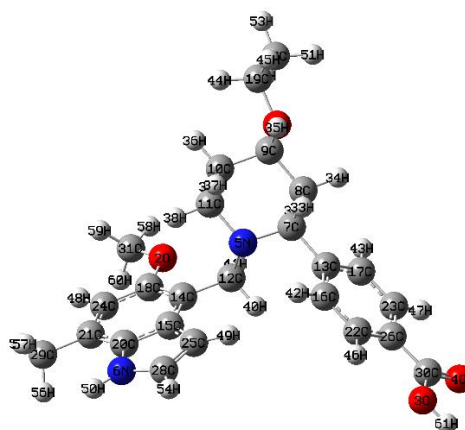
Scheme 1. The numbering scheme of the Trofinetide studied in this work.

22nd Iranian Chemistry Congress (ICC22)
Iranian Research Organization for Science and Technology (IROST)
13-15 May 2024

03231-97589

IROST

Preparation and application of a Deep Eutectic Solvent based on Choline chloride as a capable and new catalyst for the synthesis of heterocyclic compounds.

Zahra Jahaniyan, Davood Habibi*****,Arezo Monem, Elnaz Chegeni

Corresponding Author E-mail: davood.habibi@gmail.com

Department of Organic Chemistry, Faculty of Chemistry, Bu-Ali Sina University, Hamedan, Iran.

Abstract: A novel Deep Eutectic Solvent was prepared by a mixture of Choline chloride (ChCl) and acid used as a novel catalyst for the green synthesis of chromeno[4,3-*d*]pyrimidine.

Keywords: Deep Eutectic Solvent; synthesis; Choline chloride

Introduction

Deep eutectic solvents (DES) were first reported by the Abbott research group. These compounds are a mixture of hydrogen bond acceptor groups (HBA) such as ammonium or phosphonium-based salts and hydrogen bond donor compounds (HBD) such as alcohols, amines, and acids, which are synthesized under mild conditions [1]. Choline chloride-based DESs are generally accessible, easy to handle, relatively cheap, nontoxic, and moisture-stable, which fulfill several green chemistry principles. The real advantage of choline chloride-based DES came in the phase separation and could be easily isolated by decantation [2]. N-heterocyclic compounds are a class of organic compounds that contain at least one nitrogen atom in the heterocyclic ring and often exhibit unique properties and reactivity due to the presence of the nitrogen atom [3]**.** DESs have many prospective applications, and ongoing researches overlap each other in many areas for example Metallurgy and Electrodeposition, Power Systems, and Battery Technologies [4-5].

Experimental Section

General procedure for preparation of DES catalyst:
A mixture of ChCl and acid was prepared in a molar ratio of 2:1, heated at 70 °C, and stirred until a homogeneous and transparent liquid was obtained. After cooling and without any purification s, the DES catalyst was stored for further reactions.

General procedure for the synthesis of chromeno[4,3-*d*]pyrimidine:
The DES catalyst (1 mmol), was added to a mixture of 4-Hydroxycoumarin (1 mmol), urea (1 mmol), and aldehyde (1 mmol) under solvent-free conditions for an appropriate time. After completion of the reaction (TLC) , the mixture was diluted with water (10 mL) and ethyl acetate (10 mL) and shaken vigorously. The products are soluble in ethyl acetate (organic layer) and insoluble in water or ethanol, while the DES catalyst is soluble in water or ethanol and insoluble in ethyl acetate. The organic layer was separated by decanting, ethyl acetate was removed, and the solid was washed with H_2O/ethanol, dried, and characterized with different techniques. Water was removed from the aqueous layer, and the DES catalyst was kept for further reactions.

Results and Discussion

The prepared DES was characterized by FT -IR, NMR, TGA/DTA, densitometer, and eutectic points.
The ^{1}H NMR spectrum of DES **Fig 1** shows the ^{1}H NMR spectrum (^{1}H NMR (250 MHz, DMSO) δ 7.20 (s, 1H), 6.96 (s, 1H), 6.73 (s, 1H), 6.00 (s, 2H), 3.79 (s, 4H), 3.44 (d, *J* = 6.7 Hz, 4H), 3.15 (s, 36H). The results show that the intensity of the peak of the acidic group has reduced due to the hydrogen bonding and also the peak of the ChCl hydrogens has shifted. These observations indicate hydrogen bonding interactions between acid and ChCl, confirming the structure of the newly formed DES.
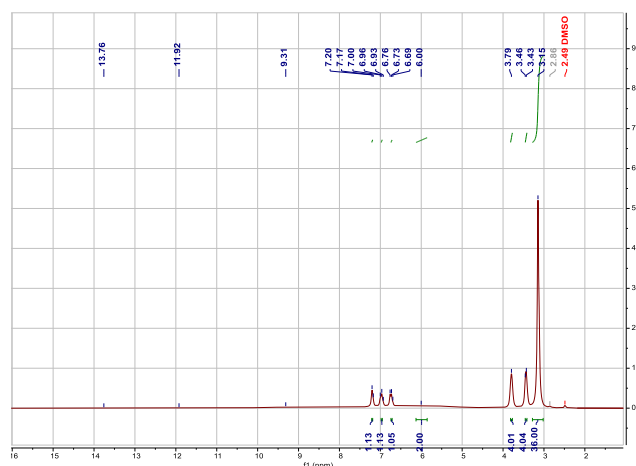

Fig. 1 . The ^{1}H NMR of DES

Based on the results obtained from the optimization of the reaction conditions(synthesis of model reaction: 4-Hydroxycoumarin, urea, and benzaldehyde), the derivatives were synthesized at 70°C and one millimol of catalyst and solvent-free conditions (Table 1).
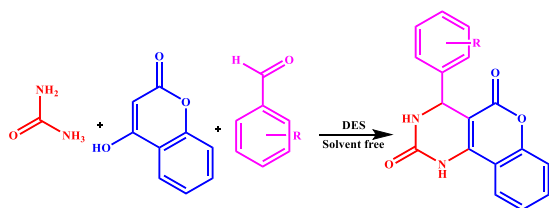
22nd Iranian Chemistry Congress (ICC22)
Iranian Research Organization for Science and Technology (IROST)
13-15 May 2024

03231-97589

IROST

Table1: Synthesis of chromeno[4,3-*d*]pyrimidine by DES

Entry	Aldehyde	Time (min)	M.P. (˚C)
1	Benzaldehyde	30	160-165
2	3-NO2-benzaldehyde	20	180-185
3	4-Cl-benzaldehyde	25	200-203

Conclusions

Based on the principles of green chemistry, solvents used in chemical industries should have some criteria such as low toxicity and safety with less negative impacts on the environment. In addition, green chemistry strongly recommends the use of catalytic reagents, in particular the ones with high selectivity. Green chemistry also emphasizes the renewability of feedstock and raw materials used in chemical industries. DES efficiently functions not only as an unobtrusive, cheap, and environmentally friendly solvent but also as a recyclable and reusable organocatalyst to promote organic transformations. The most outstanding advantages of the novel choline-based DES catalyst are reasonable yields of the desired products, short reaction times, low costs of starting materials for catalyst preparation, and mild reaction media.

References

[1] Abbott, A. P., Capper, G., Davies, D. L., Munro, H. L., Rasheed, R. K. & Tambyrajah, V. Preparation of novel, moisture-stable, Lewis-acidic ionic liquids containing quaternary ammonium salts with functional side chains electronic supplementary information (ESI) available: plot of conductivity vs. temperature for the ionic liquid formed from zinc chloride and choline chloride (2:1). Chem. Commun. 2010–2011 (2001). https://doi.org/10.1039/B106357J

[2] Z. Duan, Y. Gu, Y. Deng
Green and moisture-stable Lewis acidic ionic liquids (choline chloride . x$ZnCl_2$) catalyzed protection of carbonyls at room temperature under solvent-free conditions.Catal.Commun. 7 (2006) 651-656. https://doi.org/10.1016/j.catcom.2006.02.008

[3] Rezayati, S., Kalantari, F., Ramazani, A., Sajjadifar, S.,

Aghahosseini, H., & Rezaei, A. (2021). Magnetic silica-coated picolylamine copper complex [fe3o4@sio2@gp/picolylamine-cu (ii)]-catalyzed biginelli annulation reaction. Inorganic chemistry, 61(2), 992-1010.https://doi.org/10.1021/acs.inorgchem.1c03042.

[4] Abbott, A. P.; Boothby, D.; Capper, G.; Davies, D. L.; Rasheed, R. K. Deep Eutectic Solvents Formed Between Choline Chloride and Carboxylic Acids: Versatile Alternatives to Ionic Liquids. J. Am. Chem. Soc. 2004, 126, 9142–9147. https://doi.org/10.1021/ja048266j

[5] Di Marino, D.; Shalaby, M.; Kriescher, S.; Wessling, M. Corrosion of Metal Electrodes in Deep Eutectic Solvents. Electrochem. Commun. 2018, 90, 101–105. https://doi.org/10.1016/j.elecom.2018.04.011

22nd Iranian Chemistry Congress (ICC22)
Iranian Research Organization for Science and Technology (IROST)
13-15 May 2024

03231-97589

Polymeric Prodrugs of Mefenamic Acid Based on Glycidyl Methacrylate: Synthesis, Characterization and *In-vitro* Evaluation

Mirzaagha Babazadeh

Corresponding Author E-mail: babazadeh@iaut.ac.ir

Department of Chemistry, Tabriz Branch, Islamic Azad University, Tabriz, Iran.

Abstract: This work describes the synthesis, characterization and *in-vitro* evaluation of mefenamic acid polymeric prodrugs based on glycidyl methacrylate. Hydrolysis of polymeric prodrugs in different buffer solutions showed that the release rate of mefenamic acid from polymeric prodrugs strongly depends on the hydrophilicity of polymer and pH conditions of hydrolysis medium.

Keywords: Mefenamic acid; Esterification; Polymeric prodrugs

Introduction

A prodrug is a form of a drug that remains inactive during its delivery to the site of action and is activated by the specific conditions in the targeted site. Polymeric prodrug as a conjugation of a drug with a polymer has many advantages compared to other drug-delivery systems, such as increased drug solubility, prolonged drug release, decreased drug toxicity, and decreased drug side effects [1-4]. Mefenamic acid is a non-steroidal anti-inflammatory drug and widely used as therapeutic agents that have anti-inflammatory, analgesic, and antipyretic activities [5]. This research focus on design, characterization and *in- vitro* hydrolysis of novel polymeric prodrugs of mefenamic acid based on glycidyl methacrylate (GMA) copolymers.

Experimental Section

Copolymerization of GMA with acrylic-type monomers

A mixture of GMA (10 mmol), α,ά-azobisisobutyronitrile (AIBN) as an initiator (0.4 mmol) and 30 mmol of acrylamide (AAm) or methyl methacrylate (MMA) were separately dissolved in dried DMF, and shaken in a water bath at 70±2°C for 20 h. The viscous solutions were then poured into excess cooled methanol as non-solvent. The white solid precipitates of poly(GMA-*co*-AAm) and poly(GMA-*co*-MMA) were separately collected, washed with non-solvent dried under vacuum.

Attaching of mefenamic acid to the copolymers

In a two-necked flask, 2.4 g (10 mmol) of mefenamic acid was dissolved in dried DMF and cooled until 0-5°C. A solution of 2.0 g (10 mmol) of dicyclohexylcarbodiimide (DCC) dissolved in dried DMF was added dropwise into flask solution and stirred at 0-5°C for 10 min. Then, 1 g of poly(GMA-*co*-AAm) or poly(GMA-*co*-MMA) was dissolved in dried DMF and added dropwise to the flask mixture. The reaction was slowly returned to room temperature, stirred vigorously about 12 h and filtered for remove of white dicyclohexylurea. The remaining solution was then added dropwise into excess cooled methanol. The precipitated polymer-drug conjugates were collected by filtration, washed several times and dried under vacuum.

Method of hydrolysis

Each of dried polymer-drug conjugates (20 mg) was poured into 5 ml of aqueous buffered solution (pH 1, 7.4 and 8.5) at 37°C and the mixture was conducted into a cellophane membrane dialysis bag. The quantity of released drug was analyzed by means of an UV spectrophotometer and determined from the calibration curve obtained previously under the same conditions.

Results and Discussion

GMA was respectively copolymerized with AAm and MMA in dried DMF solutions at 70±2°C, using AIBN as a free radical initiator (Fig.1).
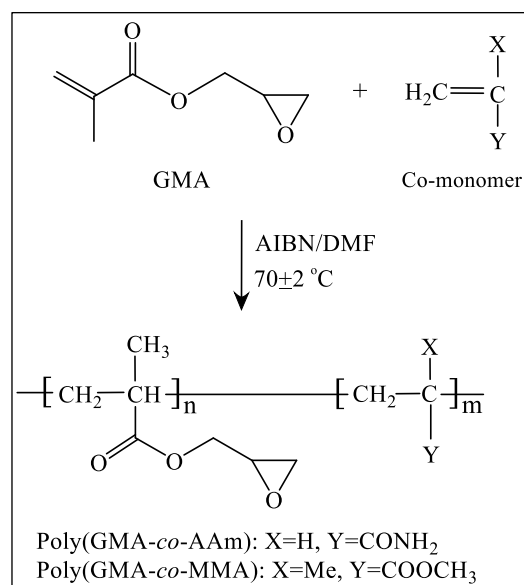

Fig.1: Copolymerization of GMA with AAM and MMA.

22nd Iranian Chemistry Congress (ICC22)
Iranian Research Organization for Science and Technology (IROST)
13-15 May 2024

03231-97589

IROST

Table 1 shows the preparation conditions of copolymers.

Table 1. The preparation conditions of the copolymers

sample	$[M_1]$ (mmol/L)	$[M_2]$ (mmol/L)	yield (%)
poly(GMA-*co*-AAm)	GMA (10)	AAm (30)	65
poly(GMA-*co*-MMA)	GMA (10)	MMA (30)	63

Mefenamic acid was then easily attached to the synthesized copolymers by transesterification procedure in the presence of DCC as a water absorbent. The epoxide group of GMA during a ring opening reaction reacted with carboxyl group of mefenamic acid and gave a new hydroxyl group and ester bond (Fig.2). After completing of reaction, the white precipitate isolated and each solution poured in proper non-solvent. The copolymers containing mefenamic acid were filtered, and dried in high yields.

Poly(GMA-*co*-AAm): X=H, Y=CONH₂
Poly(GMA-*co*-MMA): X=Me, Y=COOCH₃
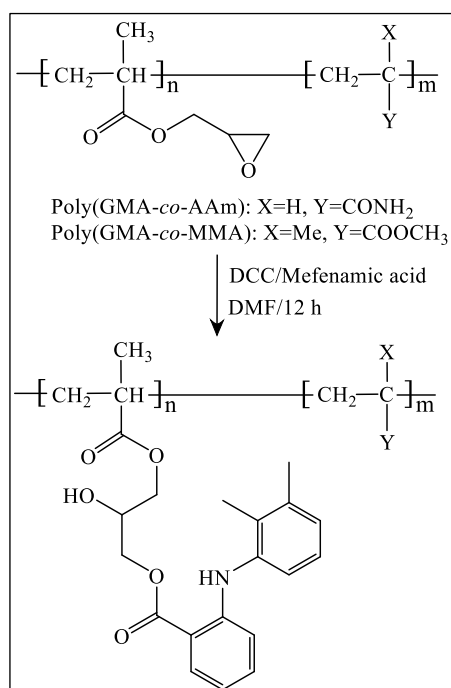
Fig.2: Attaching of mefenamic acid to polymeric prodrugs.

The FT-IR, and NMR spectra data confirmed the structure of the synthesized copolymers and polymeric prodrugs.

The in vitro hydrolysis behaviour of polymeric prodrugs was studied in physiological conditions. The results showed that the release rate of mefenamic acid at alkaline medium was higher than the release rate of drug in acidic condition. It seems that polymeric prodrugs have a low degree of swelling in the acidic medium and the drug is protected against hydrolysis. In alkali pH, the polymers have reached a degree of swelling that makes the labile bonds accessible to hydrolysis. Also, hydrophilicity or hydrophobicity of side groups in

prodrugs can affect the overall rate of hydrolysis. Poly(GMA-*co*-AAm) as a hydrophilic copolymer was hydrolyzed rather than poly(GMA-*co*-MMA) as a hydrophobic copolymer. The percent of drug released from polymeric carriers at pH 8.5 is shown in Fig.3.
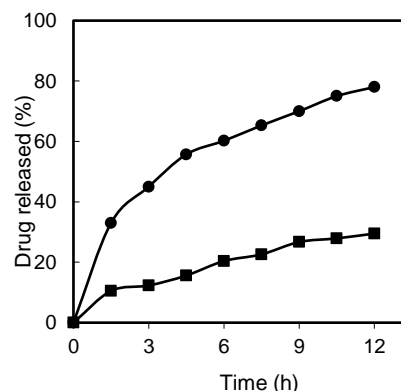
Fig.3: Percent of mefenamic acid released from polymeric carriers as a function of time at pH 8.5 in 37°C. ● poly(GMA-*co*-AAm); ■ poly(GMA-*co*-MMA)

Conclusions

The studied polymers containing mefenamic acid showed that they have potential useful as drug carriers for production of pH-sensitive polymeric prodrugs and can be used to prolong the transit time. The use of these polymers as a drug delivery system is expected after *in vivo* studies.

References

[1] Babazadeh, M. (2014). Formulation and in-vitro evaluation of vinyl ester type polymeric prodrugs of naproxen as drug delivery systems. Indian Journal of Novel Drug Delivery, 6(1), 43-50.

[2] Mousavi, S.M.J., Babazadeh, M., Nemati, M., & Es'haghi, M. (2024). Fabrication of graphene oxide nanocomposite based on poly(3-hydroxybutyrate)-chitosan as a useful drug carrier. Journal of Applied Chemical Research, 18(1), 45-59.

[3] Amiyaghoubi, S.N. & Babazadeh, M. (2015). Novel polymeric prodrugs of valproic acid as an anti-epilepsy drugs: synthesis, characterization and in-vitro evaluation. Tropical Journal of Pharmaceutical Research, 14(7), 1183-1189. https://dx.doi.org/10.4314/tjpr.v14i7.9.

[4] Babazadeh, M. (2007). Synthesis, characterization and in-vitro drug-release properties of 2-hydroxyethyl metha-crylate copolymers. Journal of Applied Polymer Science, 104, 2403-2409. https://doi.org/10.1002/app.25913.

[5] Javanbakht, M. & Babazadeh, M. (2024). Synthesis, characterization and in-vitro evaluation of novel polymeric prodrugs of mefenamic acid. Chemical Review & Letters, 7(1), 45-52. 10.22034/CRL.2024.429780.1268.

Non-invasive salivary detection of progesterone by the ultrasensitive and selective electrochemical aptasensor consisting of the nitrogen-doped hollow carbon nanospheres

Mahsa Ghanbarzadeh [a], Ali Ghaffarinejad [*a,b], Faezeh Shahdost-Fard [*c]

Corresponding Author's E-mail: ghaffarinejad@iust.ac.ir and F.Shahdost@cfu.ac.ir

[a] Research Laboratory of Real Samples Analysis, Faculty of Chemistry, Iran University of Science and Technology (IUST), Tehran 1684613114, Iran.
[b] Electroanalytical Chemistry Research Center, Iran University of Science and Technology (IUST), Tehran, 1684613114, Iran.
[c] Department of Chemistry Education, Farhangian University, P.O. Box 14665-889, Tehran, Iran.

Abstract: This study reports the development of an efficient aptasensor for the non-invasive detection of P4 based on N-HCSs to not only increase the electrode surface area but also high-dense load Apt on the surface. Aptasensor measured P4 from 10 fM to 5.6 µM with a low LOD of 3.33 fM.
Keywords: Progesterone; N-doped hollow carbon spheres; Electrochemical aptasensor; Non-invasive detection.

Introduction

Progesterone (P4) is a natural steroid hormone in humans and other vertebrates that plays many pivotal roles in bioactivity [1]. It is widely prescribed for the prevention of endometrial cancer, the treatment of gender dysphoria and contraceptives in women. Furthermore, this endocrine-disrupting chemical is abused for growth-promoting and animal fattening for economic benefits in the livestock industry. The imbalance of P4 levels increases the breast and cervical cancer risk in women. Importantly, this multifunctional hormone has received great global concern due to its harmful high amounts in drinking water, food products and other environmental samples for wildlife survival and human health [2]. Several P4 sensors based on spectrophotometry, chromatography and electrochemical methods have been reported. Although some of them present accurate results, most have practical limitations. The expensive immunoassay sensors have been criticized concerning cross-reactivity, chromatography methods require professional operation with time-consuming and laborious protocols and the radioimmunoassay methods have received environmental protection alarms. So, developing an ultraselective sensor for the non-invasive assay of P4 in complex samples is still in demand [3].

Experimental Section

An amino-Apt sequence specific to P4 was used for the aptasnsor fabrication [3]. N-HCSs were synthesized by a low-cost hydrothermal process based on the famous Stöber templating method [3]. some urine and saliva samples collected from a healthy girl were diluted by 0.1 M PB (pH 7.4). 10 µL of each human sample as the real sample was separately dropped on the aptasensor surface to analyze P4.

Results and Discussion

The step-by-step process of P4 aptasensor fabrication is graphically shown in Fig. 1A.

As shown in Fig. 1B, a pair of well-defined redox peaks related to unmodified GCE indicates a reversible electrochemical process (curve a). By attachment of N-HCSs on the GCE surface, the peak current of the N-HCSs/GCE is increased compared to the unmodified GCE (curve b), presenting the efficient role of this modifier in the active surface area increasing and the electron transformation facilitating. The voltammogram of Apt/GA/N-HCSs/GCE in the next step illustrates a dramatic decrease in the current signal intensities and an increase of ΔE value to 120 mV (curve c). This electron transfer ability decrease may be ascribed to the attachment of Apt on GA/N-HCSs/GCE via GA linker through the covalent bond forming that leads to a repulsive force between the negative charges of the Apt sequence and the anion probe species. Finally, with incubation of the P4 onto the aptasensor surface (BSA/Apt/GA/N-HCSs/GCE) the peak current was decreased and ΔE value was increased to 190 mV.

These findings are in good agreement with the preceding results from the EIS Nyquist curves in Fig. 1C and both confirm the successful construction of the proposed aptasensor. Different P4 concentrations were incubated onto the aptasensor surface and DPV signals were gradually decreased by P4 increasing under two linear relationships for low concentrations (1 fM to 4.2 pM) and high concentrations (1nM to 5.6 µM) with a LOD of 3.33 fM.
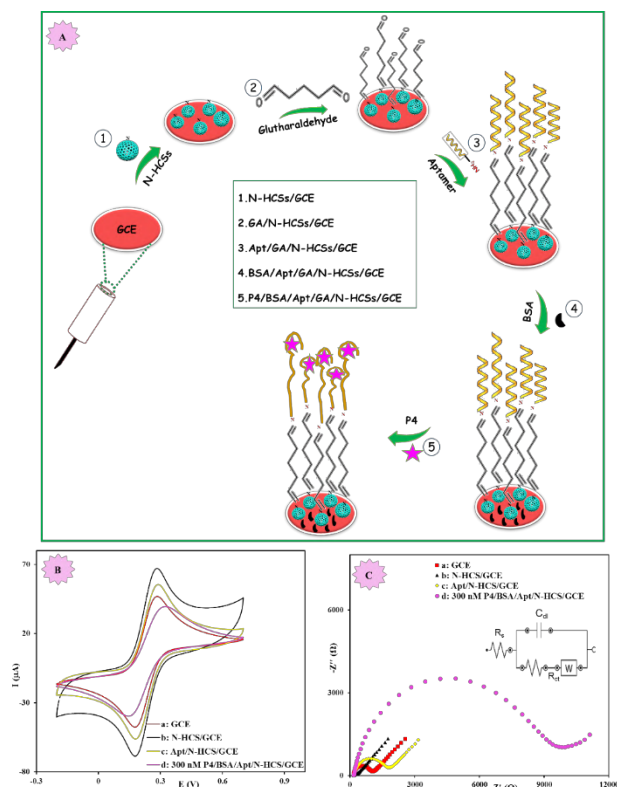
22nd Iranian Chemistry Congress (ICC22)
Iranian Research Organization for Science and Technology (IROST)
13-15 May 2024

03231-97589

IROST

Fig.1: (A) Schematic of the P4 aptasensor preparation process, (B) CVs and (C) EIS plots of each step of the GCE modification process recorded in 0.1 M PB (pH 7.4) containing 5.0 mM $[Fe(CN_6)]^{3-/4-}$ and 0.1 M KCl as the redox probe (inset (C): the equivalent circuit).

Conclusions

In this research, P4 was detected by the proposed aptasensor based on the non-invasive and point-of-care recognition system to overcome some challenges faced by other methods. The proposed aptasensor capability in P4 sensing in human biofluids was successfully verified. These remarkable achievements can mainly be rooted in (1) the superior synthesized N-HCSs nanostructure as an efficient platform for high electrical conductivity and high potential in creating large active surface area as well as embedding high dens-building sites for loading Apt and (2) utilizing Apt receptor with high affinity toward P4. Importantly, the N-HCSs employed in this study was synthesized from cost-effective primary substrate with a simple, fast and green method which is a benefecial parameter in sensor/aptasensor designing.

References

[1] Motomura, K., Miller, D., Galaz, J., Liu, T. N., Romero, R., & Gomez-Lopez, N. (2023). The effects of progesterone on immune cellular function at the maternal-fetal interface and in maternal circulation. *The Journal of steroid biochemistry and molecular biology*, *229*, 106254.

https://doi.org/10.1016/j.jsbmb.2023.106254.

[2] Qaid, M. M., & Abdoun, K. A. (2022). Safety and concerns of hormonal application in farm animal production: A review. *Journal of Applied Animal Research*, *50*(1), 426-439.

https://doi.org/10.1080/09712119.2022.2089149.

[3] Ghanbarzadeh, M., Ghaffarinejad, A., & Shahdost-Fard, F. (2024). A nitrogen-doped hollow carbon nanospheres-based aptasensor for non-invasive salivary detection of progesterone. *Talanta*, *273*, 125927.

https://doi.org/10.1016/j.talanta.2024.125927.

Green nanocomposite consisting of nitrogen and sulfur co-doped carbon dots derived from eggshell and silver nanocube as a low-cost platform for ultraselective aptasensing of metronidazole

Maryam Ghiasi [a], Mahsa Ghanbarzadeh [a], Ali Ghaffarinejad [*a,b], Faezeh Shahdost-Fard [*c]

Corresponding Author's E-mail : ghaffarinejad@iust.ac.ir and F.Shahdost@cfu.ac.ir

[a] Research Laboratory of Real Samples Analysis, Faculty of Chemistry, Iran University of Science and Technology (IUST), Tehran 1684613114, Iran.
[b] Electroanalytical Chemistry Research Center, Iran University of Science and Technology (IUST), Tehran, 1684613114, Iran.
[c] Department of Chemistry Education, Farhangian University, P.O. Box 14665-889, Tehran, Iran.

Abstract: This study introduces the applicability of the green nanocomposite consisting of nitrogen and sulfur co-doped carbon dots derived from eggshell waste and silver nanocubes for a low-cost aptasensor fabrication to measure the banned metronidazole drug under a wide linear dynamic range (1 fM-901.4 nM) with an ultralow LOD of 333.3 aM.
Keywords: Metronidazole; Eggshell; Electrochemical aptasensor; Silver nanocubes; Carbon dots.

Introduction

The Metronidazole (MTZ) antibiotic overdose (more than 140 mM) with serious side effects [1] on the one hand and its abuse in the feed of some animals and the subsequent pollution in agricultural products and aquatic environments in the creation of the drug-resistant microorganisms, on the other hands [2], endanger human health and the environment.

By emphasizing the reducing costs and smart use of waste-based nanomaterials according to the evaluated green chemistry criteria, this study reports a novel method for sensitive detection of MTZ residues in human samples based on a green nanocomposite. Nitrogen and sulfur co-doped carbon dots (N-S-CDs) synthesized from eggshell membrane (ESM) waste embeds a sub-layer and silver nanocubes (AgNCs) acts as a linker to load high amounts of aptamer (Apt) biocaptures on the modified glassy carbon electrode (GCE) surface.

Experimental Section

An amino-Apt specific to MTZ was used [3]. ESM waste was easily utilized to greenly produce N-S-CDs under the simple synthesis route. Some urine and saliva samples were collected from a healthy girl and diluted by 0.1 M PB (pH 7.4). Finally, 10 µL of each spiked MTZ sample was separately dropped on the aptasensor surface to analyze MTZ. The molecular dynamic (MD) simulation was used to visually predict how the Apt binds to MTZ

Results and Discussion

The step-by-step process of MTZ aptasensor preparation is graphically shown in Fig. 1A.

As shown in Fig. 1B, the N-S-CDs/GCE surface (curve b) illustrates a less anodic current ($I_{p,a}$) and cathodic current ($I_{p,c}$) value with a more ΔE value (140 mV) compared to the bare GCE surface (curve a). Further decrease of the current values by the increase of ΔE value to 210 mV for voltammogram of the AgNCs/N-S-CDs/GCE surface (curve c) compared to the previous layers proves the attachment of AgNCs on the N-S-CDs/GCE surface. The fixation of Apt on the AgNCs/N-S-CDs/GCE surface via linking between NH_2 group on the 5'-terminal of the Apt sequence and AgNCs is confirmed by a decrease in the current values and increase in ΔE value to 280 mV (cure d). This behavior can arise from the bonding of Apt sequence on the AgNCs layer owing to the spatial hindrance increasing and more repulsion between the negative charge of the Apt sequence's phosphate groups and the anion redox couple. By incubation of 1 pM of MTZ on the BSA/Apt/AgNCs/N-S-CDs/GCE surface as the prepared aptasensor (cure e), ΔE value is increased to 310 mV. These findings are in good agreement with the preceding results from the EIS Nyquist in Fig.1C and both certify the successful generation of the aptasensor for MTZ detection.The resulting aptasensor measured MTZ in a wide linear range from 1 fM to 901.4 nM with a LOD of 333.3 aM with high selectivity regarding some possible interferences. Additionally, the greenness of the applied strategy was well evaluated by the two criteria including the complimentary green analytical procedure index (ComplexGAPI) and the analytical greenness approach (AGREE).
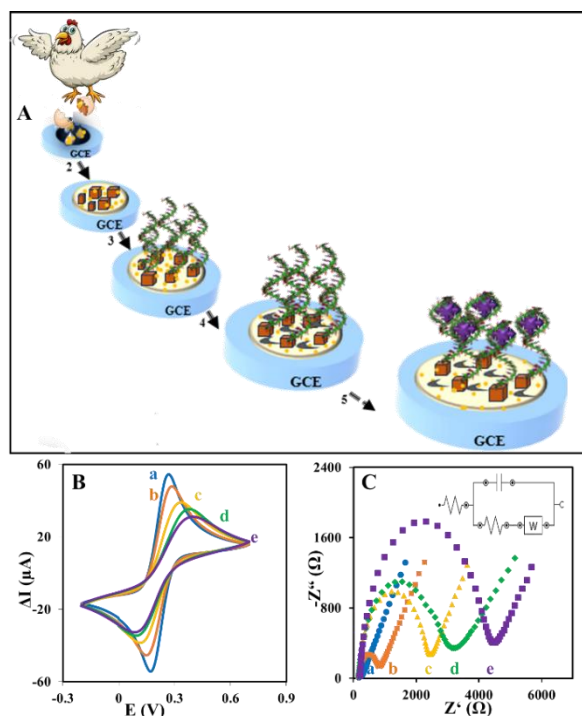
22nd Iranian Chemistry Congress (ICC22)
Iranian Research Organization for Science and Technology (IROST)
13-15 May 2024

03231-97589

Fig.1: (A) Schematic of the MTZ aptasensor preparation process, (B) CVs and (C) Nyquist curves (at 230 mV with an equivalent circuit) of the different modified electrodes at each stage of the modification process. Electrolyte: 0.1 M of PB (pH= 7.4) containing 5 mM $K_3Fe(CN)_6$/$K_4Fe(CN)_6$ and 0.1 M KCl as the redox probe.

Conclusions

Smart and easy synthesis of the green nanostructures not only preciously recycles the massive amount of discarded materials but also paves the way to the utilizing of the unusable waste-based nanomaterials in different applications according to the sustainable chemistry principles. The aptasensor efficiency for MTZ measurement in the human saliva, urine and tap water samples may promise the reliability of the proposed methodology for routine MTZ tests, especially saliva monitoring as the non-invasive analysis.

References

[1] Boechat, N., Carvalho, A. S., Salomão, K., de Castro, S. L., Araujo-Lima, C. F., Mello, F. V., ... & Haufe, G. (2015). Studies of genotoxity and mutagenicity of nitroimidazoles: demystifying this critical relationship with the nitro group. *Memórias do Instituto Oswaldo Cruz*, *110*, 492-499.

https://doi.org/10.1590/0074-02760140248.

[2] Du, M., Chen, Q., & Xu, X. (2022). A novel and label-free electrochemical aptasensor based on exonuclease III and G-quadruplex DNAzyme for sensitive and selective detection of metronidazole. *Microchemical Journal*, *179*, 107577.

https://doi.org/10.1016/j.microc.2022.107577.

[3] Wei, H., Cai, R., Yue, H., Tian, Y., & Zhou, N. (2020). Screening and application of a truncated aptamer for high-sensitive fluorescent detection of metronidazole. *Analytica Chimica Acta*, *1128*, 203-210.

https://doi.org/10.1016/j.aca.2020.07.003.

CuMn₂O₄/CuMnO nanocomposites: Co-precipitation synthesis and investigation of their applications for removing EBT

A. Sobhani, F. Aliabadi, E. Rohani

Corresponding Author E-mail: sobhani@kub.ac.ir

Department of Chemistry, Kosar University of Bojnord, Bojnord, P. O. Box. 94104455, Republic of Iran.

Abstract: CuMn₂O₄/CuMnO nanocomposites were prepared via the co-precipitation method and used to remove EBT from aqueous solution. The photocatalytic property of the products for EBT degradation was investigated.

Keywords: Co-precipitation; Copper manganese oxide; CuMnO

Introduction

Elimination of dye pollution from the solvent phase by adsorption is a necessary aspect of research. Using the degradation process of dyes by a photocatalyst is an effective method for polluted and toxic water treatment. CuMn₂O₄ is a mixed metal oxide. It can incorporate into the spinel structure. Many methods have been used to the synthesis of CuMn₂O₄ [1, 2]. Also, there are some researchers have made to synthesize composites of CuMn₂O₄. Among these techniques, the co-precipitation method is the simplest and sophisticated in the sense that there is no need of high pressure and high temperature, cost-effective, the crystalline size and structure of the particles can be easily tailored by varying the pH of the medium and large amount of sample can be prepared at a time. This work reports the synthesis of CuMn₂O₄/CuMnO nanocomposites (CMO NCs) and copper manganese oxide nanostructures. Also, the photocatalytic behaviors of the as-prepared nanocomposites and nanostructures are studied. The investigations show that CMO NCs have high photocatalytic efficiency for EBT degradation.

Experimental Section

CMO NCs were synthesized via co-precipitation method. Two aqueous solutions of metal nitrate salts were prepared and mixed. Then, NH₃ was added. After stirring for 60 min the product was centrifuged and washed. In order to remove impurities, the product was calcined in furnace at 400 ˚C for 2h.

Results and Discussion

Fig. 1 shows XRD patterns of the products prepared via co-precipitation method. The product prepared in the absence of capping agent (sample 1) was CuMnO along with a small amount of CuMn₂O₄. Fig.1b shows XRD pattern of the product prepared in the presence of the sucrose (sample 2). This sample is pure CuMnO with lower crystallinity than the CuMnO synthesized in the absence of the capping agent.

The SEM images in Fig. 2 show the size and morphology of samples 1 and 2 in the different magnifications. The nanoparticles with diameters of about 15 nm form without the capping agent. Fig. 2a-c shows that these nanoparticles are as agglomerated. Fig. 2d-f shows formation of the agglomerated nanoparticles, bulk structures and aggregated microstructures in the presence of sucrose. SEM images show sucrose is not a suitable capping agent for manganite synthesis.

FT-IR spectrum of sample 1 has been shown in Fig. 3. The frequency at 594.79 cm⁻¹ belongs to the Mn–O stretching vibration. The bonds below 1000 cm⁻¹ are related to the M–O stretching vibrations [3]. The bands centered at 1417.77, 1200.77, and 1049.02 cm⁻¹ belong to the organic residues in sample 1 (C–OH groups) [4]. The peak at 1558.28 cm⁻¹ corresponds to the water-bending vibrational modes. The broad bond at 3364.02 cm⁻¹ (in the range 2800–3700 cm⁻¹) is related to the stretching vibrations of absorption water on the surface of the nanostructures.

In this work, the photocatalytic studies investigated for degradation of dye pollutions under visible light irradiation. Two dyes, MV and EBT, were used, and their photocatalytic degradation was studied (Fig. 4). The effects of the dye concentration and catalyst dose were studied on the photocatalytic activity of sample 1 (Fig. 5). It is clear from Fig. 5a that the degradation percentage decreases with the increase in EBT concentration. Fig. 5b shows the effect of photocatalyst dose on the degradation of a solution of EBT with 10ppm concentration. It is clear that degradation percentage of EBT increases with increase in catalyst dose up to an optimum amount. The more increase in catalyst dose results a decrease in the degradation percentage.
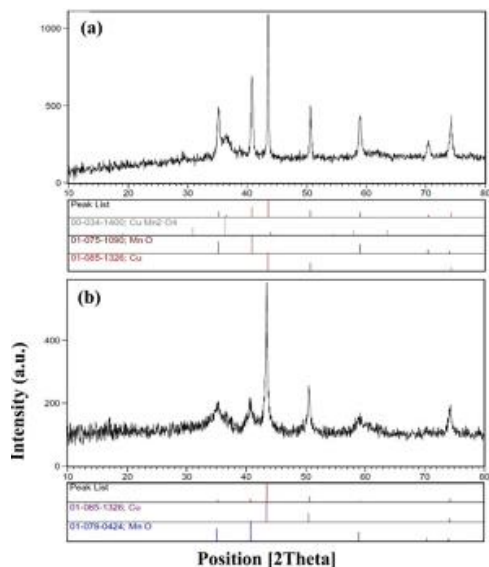
22nd Iranian Chemistry Congress (ICC22)
Iranian Research Organization for Science and
Technology (IROST)
13-15 May 2024

03231-97589

IROST

Fig.1: XRD patterns of samples prepared from
$Cu(NO_3)_2.3H_2O$ and $Mn(NO_3)_2.4H_2O$ via co-precipitation
method: (a) in the absence of the capping agent (sample 1)
and (b) in the presence of sucrose (sample 2).

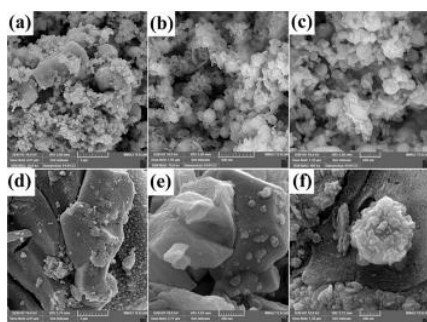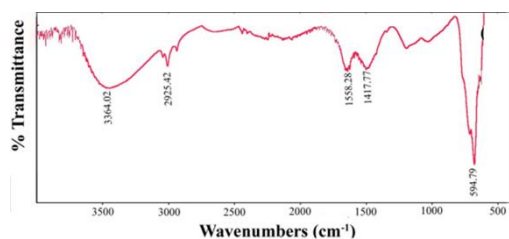**Fig.2:** SEM images of: (a, b, c) sample 1 , (d, e, f) sample 2.
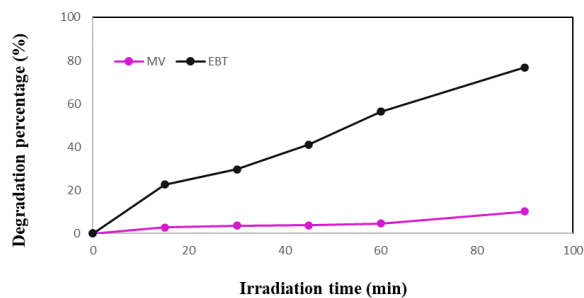

Fig.3: FT-IR spectra of sample 1.

Fig.4: Photocatalytic activity of sample 1 for degradation of the
different dyes, under visible light irradiation.
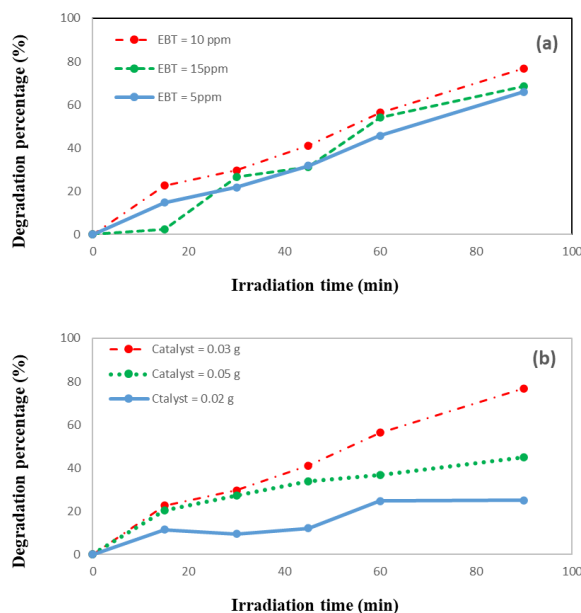
Fig.5: Investigation of the effects of the: (a) dye concentration,
and (b) photocatalyst dose in photocatalytic activity of sample
1 for degradation of EBT.

Conclusions

The CMO NCs were successfully prepared via the co-
precipitation and used as photocatalysts for EBT removal.
The experiments were repeated in the presence of
sucrose. The effects of the dye type, photocatalyst dose
and dye concentration were investigated and the
optimum conditions were reported.

References

[1] B. Saravanakumar, S. Muthu Lakshmi, G. Ravi, V.
Ganesh, A. Sakunthala, R. Yuvakkumar, J. Alloys Compd.
723 (2017) 115–122.

[2] A. Sobhani, Int. J. Hydrogen Energy 47 (2022) 20138–
20152.

[3] L.J. Wang, Q. Zhou, Y. Liang, H. Shi, G. Zhang, B. Wang,
W. Zhang, B. Lei, W.Z. Wang, Appl. Surf. Sci. 271 (2013)
136–140.

[4] P. Ma, Q. Geng, X. Gao, S. Yang, G. Liu, Ceram. Int. 42
(2016) 11966–11973.

Mn/Cu/O/chitosan nanocomposites: hydrothermal synthesis and its application for removal of MB

A.Sobhani*, F. Aliabadi, E. Rohani

Corresponding Author E-mail: sobhani@kub.ac.ir

Department of Chemistry, Kosar University of Bojnord, Bojnord, P. O. Box. 94104455, Republic of Iran.

Abstract: Mn/Mn_2O_3 nano/microstructures were synthesized by hydrothermal method in the presence of onion (Allium cepa L.). Then Mn/Cu/O/chitosan nanocomposites were synthesized using chitosan, CuO powder, and Mn/Mn_2O_3. The nanocomposites were used as photocatalyst for organic dye degradation.

Keywords: Adsorption; Chitosan; Metal oxide

Introduction

Hydrothermal is a method for the crystal growth and synthesis of the nanostructures in an autoclave, under high pressure, and in hot water [1]. It has the advantages of green, easy operation and low cost. In this work, we use chitosan for the green synthesis of Mn/Cu/O/chitosan nanocomposites. The as-prepared nanocomposites help us to remove MB from the aqueous solution. MB is a cationic dye and biologically dangerous, and control of its content is necessary [2]. The novelty of this work lies in the introduction of a new nanocomposite for photocatalysis in visible light. Chitosan is a biocompatible, biodegradable, nontoxic, and low-cost biomaterial, and can be significantly used in the synthesis of the nanocomposites. It is a family of molecules with differences in their size, composition, and monomer distribution. It has garnered much interest due to its technological and biological performance, properties, and applications.

Dye pollution elimination from the solvent phase is a necessary aspect of research. Some methods to remove organic pollutions from the aqueous system have been studied, including microbial degradation, coagulation, adsorption, chemical oxidation, and photocatalysis [3, 4]. Among these methods, photocatalysis is the most efficient and consistent method because it is simple, fast, and doesn't generate toxic materials [5].

The efficiency of the photocatalytic process is an effect resulted of photocatalysis. It depends on the yield of the created holes and electrons. We can evaluate this efficiency by comparing the initial dye concentration and concentration after the photocatalytic reactions. One of the factors reducing the efficiency of the photocatalytic activity is the recombination of the hole-electron pair [6]. Decreasing the recombination rate and ensuring separation between electrons and holes can increase this efficiency [6].

Experimental Section

2.1. Synthesis of Mn/Mn_2O_3 nanostructures

An aqueous solution of $Mn(NO_3)_2.4H_2O$ was prepared. Then Allium cepa L. was added drop-wise into the solution under stirring. After stirring for 15 min, the final solution was transferred into an autoclave and maintained at 180 ˚C for 12 h. Then the products were calcined under vacuum at 400 ˚C for 2 h.

2.2. Synthesis of Mn/Cu/O/chitosan nanocomposites

In this work, we use chitosan for the green synthesis of Mn/Cu/O/chitosan nanocomposites. Chitosan was dissolved in distilled water and acetic acid. Then CuO powder was dispersed in distilled water and added to the chitosan solution. In the next step, Mn/Mn_2O_3 nanostructures, prepared in the before step, were added. The mixture was stirred for 24 hours. The nanocomposites were washed and dried.

Results and Discussion

XRD patterns of manganese oxide, chitosan and Mn/Cu/O/chitosan nanocomposites are shown in Fig. 1. The product obtained via hydrothermal reaction of Mn salt is amorphous. XRD pattern of this sample after its calcination under vacuum at 400 ˚C has been shown in Fig. 1b, it is a mixture of Mn and Mn_2O_3. Fig. 1c shows XRD pattern of pure chitosan with a sharp peak at 2Theta~20. Also, the XRD pattern of Mn/Cu/O/chitosan nanocomposite has been shown in Fig.1d. By comparing XRD patterns of this figure with Fig. 1c, it can be found that the peaks of the chitosan are weak in the XRD pattern of the nanocomposites. Other diffraction peaks in Fig. 1d related to Cu and Mn oxides. Also the intensity of these peaks is lower than those in Fig. 1b. The XRD patterns of the nano/microstructures (Fig. 1b) and nanocomposites (Fig. 1d) synthesized in this work are broad and low intensity, which suggest a low crystallinity and an amorphous nature of the products and or the formation of the products with small particle sizes. The weak peaks in Fig. 1d reflect great disarray in chain alignment of chitosan with the production of new peaks that identify the presence of Cu and Mn oxides. These patterns reveal the successful inclusion of Cu and Mn oxides in nanocomposite membranes. Moreover, the presence of these metal oxides impede the order of polymer chains by both steric effect and intermolecular hydrogen bonds. So, the introduction of Cu and Mn oxides in chitosan decrease the crystallinity of composite membranes and increase the flexibility of polymer chain [7].

Fig. 2 shows SEM images of the nanocomposite prepared with chitosan. The figure shows the formation of the agglomerated spheres with diameters ranging from 1.5 μm to 7 μm. A closer look at this figure also shows the formation of the agglomerated nanoparticles on the spheres. The particle size distribution of the nanoparticles and microspheres is not uniform.

22nd Iranian Chemistry Congress (ICC22)
Iranian Research Organization for Science and Technology (IROST)
13-15 May 2024

03231-97589

IROST

In continuation, the effects of the photocatalyst and dye concentrations for degradation of MB under visible light irradiation were investigated (Fig. 3). Fig. 3a shows the effect of the photocatalyst concentration on the degradation percentage of MB. The figure shows the rate of degradation of the photocatalyst is proportional to its concentration. Fig. 3b shows the evolution of the degradation of MB with irradiation time for three solutions with different concentrations, including 5, 10, and 15 ppm. This figure reveals with increasing dye concentration, the photocatalytic degradation is decreased.
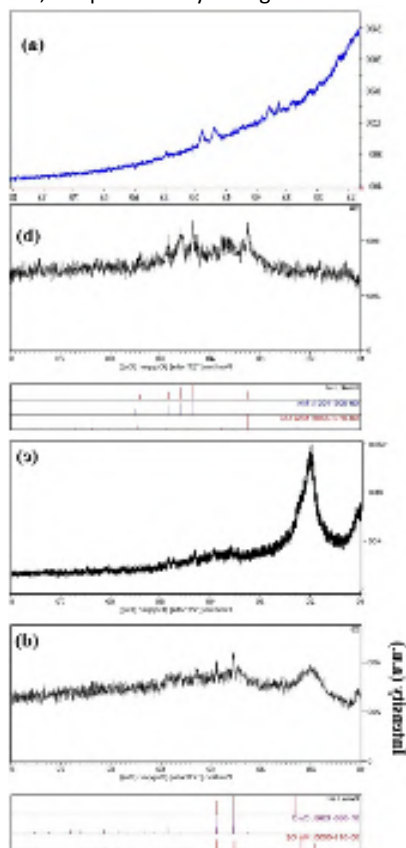
Fig.1: XRD patterns of: a) the product prepared via hydrothermal method , b) product after calcination at 400 ^{O}C , c) chitosan , d) CuO/Mno2/chitosan nanocomposite.
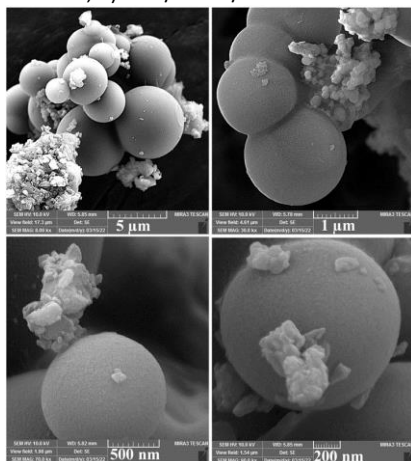
Fig.2: SEM images of the nanocomposite prepared with chitosan.
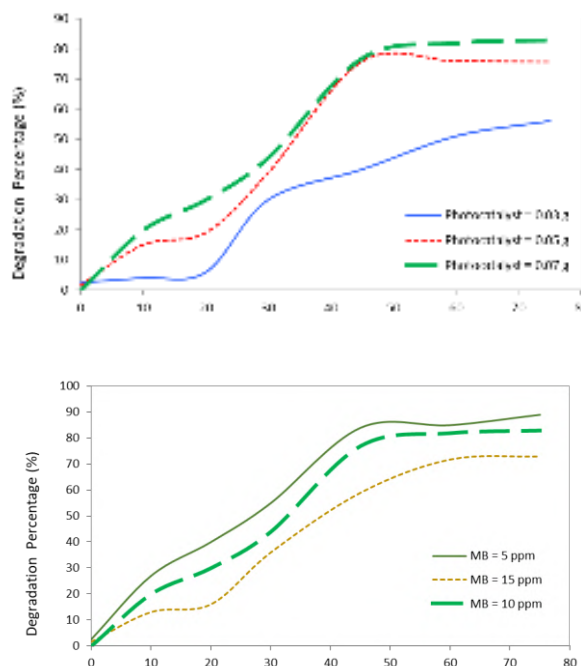
Fig.3: Effects of: (a) photocatalyst and (b) dye concentrations for degradation of MB under visible light irradiation.

Conclusions

In conclusion, Mn/Mn$_2$O$_3$ nano/microstructures were synthesized in the presence of Allium cepa L. via hydrothermal method. Then Mn/Cu/O/chitosan nanocomposites were synthesized using chitosan, CuO powder, and Mn/Mn$_2$O$_3$ prepared in the first step. The as-prepared nanocomposites were used as photocatalysts for MB degradation.

References

[1] Liu, H., Wang, S., Li, Z., Zhuo, R., Zhao, J. Duan, Y., Liu, L., & Yang, J. (2024). Experimental study on the preparation of monodisperse nano-silver by hydrothermal synthesis. Materials Chemistry and Physics, 314, 128902.

[2] Wollner, A., Lange, F., Schemelz, H., Knozinger, H. (1993) Characterization of mixed copper-manganese oxides supported on titania catalysts for selective oxidation of ammonia, Appl Catal A: Gen, 1993; 94: 181.

[3] Lu, M., Wang, Y., Yu, J., Li, D., Zhao, Q., Chi, R. (2023) Recycling waste with waste: Adsorption of anionic dyes in wastewater with surfactant-modified phosphogypsum. Environ. Res. 237, 116963.

[4] Glaubitz, F., Vogel, A.R., Kolberg, Y., Tümpling, W., Kahlert, H. (2023). Detailed insights in adsorption process of heavy metals on tire wear particles, Environ. Res. 335, 122293.

[5] Ehsan, M.F., Barai, H.R., Islam, M.M., Susan, M.A.B.H., Joo, S.W., Miran, M.S. (2023) ZnO nanocomposites supported by acid-activated kaolinite as photocatalysts for the enhanced photodegradation of an organic dye, Mater. Today Commun. 36, 106563.

[6] Lima, Lucas V.C., Rodriguez, M., Freitas, V.A.A., Souza, T.E., Machado, A.E.H.,Patrocínioc, A.O.T., Fabris, José D., Oliveira, Luiz C.A., and Pereiraa, Márcio C. (2015) Synergism between n-type WO3and p-type FeOOH semiconductors:High interfacial contacts and enhanced photocatalysis. Appl. Catal. B, 165, 579–588.

[7] Dong, Z.F., Du, Y.M., Fan, L.H., Wen, Y., Liu, H., Wang, X.H.J. (2004) Funct Polym. 17, 61.

22nd Iranian Chemistry Congress (ICC22)
Iranian Research Organization for Science and Technology (IROST)
13-15 May 2024

03231-97589

IROST

Photoassisted Degradation of salicylic acid on the Dye Modified TiO₂ Particles

Simin Janitabar Darzi [a], Hajieh Bastami[b*]

Corresponding Author E-mail: Hbastami@tvu.ac.ir; Hajiehbastami@gmail.com

[a] Nuclear Science & Technology Research Institute, Nuclear Fuel cycle Research School, Tehran, Iran, P.O. Box: 14395-836.

[b]Assistant Professor, Department of Materials and Metallurgical Engineering, Technical and Vocational University (TVU), Tehran, Iran.

Abstract: Photoassisted decomposition of salicylic acid solution are achieved on the surface of TiO₂ semiconductor modified with Asceptichrome by using visible light. After 4h of irradiation with two 26W Osram lamps, over 60% degradation of sample is achieved. A working mechanism involving excitation of surface bound dye, followed by charge injection into the TiO₂ conduction band is proposed.
Keywords: Dye sensitization; visible light; TiO₂; salicylic acid; degradation; Asceptichrome.

Introduction

In recent years advance oxidation processes (AOPs) involving hydrogen peroxide, ozone and/or fenton reagents, with or without a source of uv light have been reported to be useful for the photooxidation of organic pollutants in wastewaters [1].

In the present investigations, we explore the possibility of photodegradation of salicylic acid as a model of organic pollutants using TiO₂ semiconductor particles modified with Asceptichrome (Fig. 1). The depletion of salicylic acid was estimated spectrophotometrically.
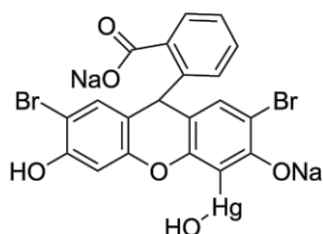

Fig. 1. The molecular structure of the Asceptichrome molecule.

Experimental and Procedures

TiO₂ particles were supplied by Degussa (P25, surface area -50 m2 g-1', mean diameter approximately 30 nm), which is a mixture of anatase and rutile TiO₂. salicylic acid and other materials such as Asceptichrome and ethanol were obtained from Merck. Solutions were prepared by dissolving appropriate amount of the salicylic acid in deionized and doubly distilled water.

Photoreactor and light source

For this process, reaction was performed in a batch photoreactor of 100 ml in volume. The radiation source consists of two Vis lamps (26W, manufactured by Osram, Germany) in vertical arrays, which were placed in around of the glass photoreactor. The distance between the lamps and the glass reactor containing reaction mixture was fixed at 2 cm and setup was cooled with a fan. Air was bubbled through reaction by an aquarium pump.

Preparation of the Asceptihrome -sensitized TiO₂ particles. Before preparing the modified photocatalyst, the TiO₂ powers were sintered at 500°C for 1h to eliminate water adsorbed on the semiconductor surface. A 0.5 mmol/dm³ ethanolic solution of Asceptichrome was prepared [2]. Then 1 g of sintered TiO₂ powers was added to 50 ml of this solution and then refluxed at 80°C for 1h to fix the dye on the surface of semiconductor particles. After dye adsorption, the color of the TiO₂ nano particles changed to red. Study of the morphological and structural properties of the prepared catalyst was done by scanning electron microscopy (SEM).

Photocatalytic degradation of salicylic acid

In photocatalytic experiment, aqueous suspension (50 ml) of salicylic acid (10 ppm) containing 0.025 g of surface modified hotocatalyst designated as TiO₂-D was taken in a glass photoreactor. The aquarium pump bubbles air through the reaction and mixture was magnetically stirred during irradiation. The progress of photocatalytic degradation was monitored by measuring the absorbance of the solution sample with UV-Vis spectrophotometer (Shimadzu UV 2100). Absorption peaks corresponding to salicylic acid appeared at 224.5and 295 nanometer. By this method conversion percent of salicylic acid can be obtained in different intervals. After each interval the reaction mixture were filtered and subjected to UV-Vis spectrophotometer.

Results and discussion

The morphology of modified TiO₂ particles was observed by SEM, which shows the typical shapes of the small crystallites, as seen in Fig.2.
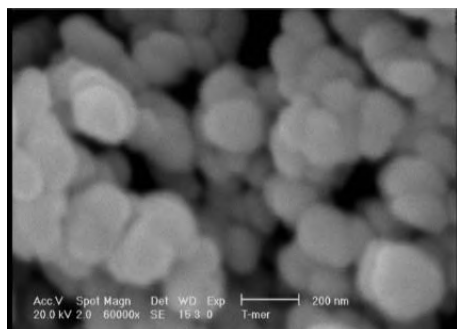
22nd **Iranian Chemistry Congress (ICC22)**
Iranian Research Organization for Science and
Technology (IROST)
13-15 May 2024

03231-97589

ISC

IROST

Fig. 2. SEM photographs of modified TiO_2 nano particles

IR absorption spectra of Asceptichrome in diffuse reflectance mode are shown in Fig. 3. The absorption peak at 1540cm~1 for Asceptichrome is attributed to O-C-O asymmetric stretching band of carboxyl group (spectrum a). The peaks 1300-1400cm^{-1} are due to O-C-O symmetric stretching band. The absorption of O-C-O asymmetric stretching is observed at 1560cm^{-1} for Asceptichrome adsorbed on TiO_2, as shown in Fig. 3 (spectrum b). O-C-O stretching band around near 1700cm^{-1} attributed to the ester bonding is not observed. This indicates that Asceptichrome molecules are adsorbed on TiO_2 substrate with carboxylate COO$^-$ linkage. All absorption peaks of Asceptichrome adsorbed on TiO_2 are shifted about 20cm^{-1} to large wave numbers compared to the peaks of free dye, as shown in Fig. 3. This shift is due to the interaction between dye molecule and TiO_2[3] . It has been reported that Ru complexes such as Ru(dcbpy)$_2$(NCS)$_2$ are adsorbed on the TiO_2 surface with esterlike bonding [4-6].
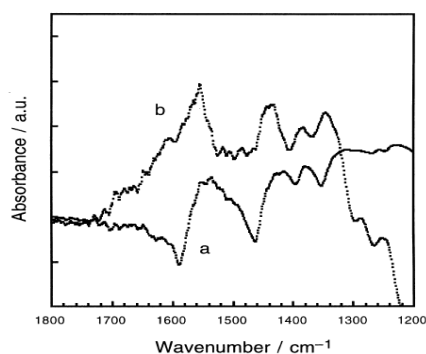
Fig. 3. IR absorption spectra of Asceptichrome: (a) free Asceptichrome and (b) Asceptichrome adsorbed on TiO_2

The absorption spectra of this aqueous salicylic acid solution (initial concentration:10 ppm) recorded following irradiation with visible light at various times are shown in Fig. 4. The absorption peaks corresponding to the salicylic acid diminished under photocatalytic process, indicating the degradation of salicylic acid. It can be seen from Fig.4 that degradation accompanied by a red shift in salicylic acid UV-Vis spectrum This can be explained by a change in the energy levels of HOMO and LUMO of sample, due to producing of carboxilated intermediates.
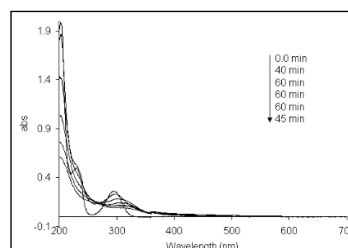

Fig. 4. Spectral changes that occurs during photocatalysis of aerated aqueous solution of salicylic acid(10 ppm)

The temporal changes in normalized absorption of salicylic acid are illustrated in Fig. 5. it shows that in this photocatalytic system, by using visible light, after 4 h of irradiation with two 26 W Osram lamps, over 60% degradation of sample is achieved.
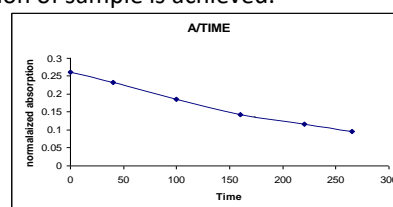

Fig. 5. normalized absorption of salicylic acid versus time of photocatalytic conversion

Conclusion

The results of the present work clearly demonstrate that the surface adsorbed Asceptichrome dye can sensitize TiO_2 semiconductor particulate

system for degradation of pollutants studied using visible light. No ppreciable leaching of dyes was noticed spectrophotometrically after 4 h of photolytic reaction. The results of the present studies explore the possibility of using dye fixed TiO_2 semiconductor in visible light driven photodetoxification of contaminated water. Studies pertinent to this matter are in progress.

Refrences

[1] chen, G., lei, L., Yue, P. L., (**1999). Wet Oxidation of** High-Concentration Reactive Dyes. Industrial and Engineering Chemistry Research, 38(5), 1837–1843. https://doi.org/10.1021/ie980617d.

[2] Chatterjee, D.,Mahata, A., (2001). Adsorption and photocatalysis of colour removal from waste water using flyash and sunlight. Catalysis Communications, 2(3-4), 113-117, https://doi.org/10.1016/S1566-7367(01)00017-6.

[3].Smestad, G., Bignozzi., C., Argazzi., R., (1994).Testing of dye sensitized TiO_2 solar cells I: Experimental photocurrent output and conversion efficiencies, Solar Energy Materials and Solar Cells, 32 (3), 259-272. https://doi.org/10.1016/0927-0248(94)90263-1.

[4] Rohatgi, K.K., Singhal, G.S., (1966). Nature of Bonding in Dye Aggregates, Journal of Physical Chemistry, 70 (6), 1695. https://doi.org/10.1021/j100878a002.

[5] Murakoshi, K., Kano, G., Wada, Y., Yanagida, S., Miyazaki,H., Matsumoto, M., Murasawa, S.,(1995). Importance of binding states between photosensitizing molecules and the TiO_2 surface for efficiency in a dye-sensitized solar cell, Journal of Electroanalytical Chemistry, 396 (1-2), 27-34. https://doi.org/10.1016/0022-0728(95)04185-Q.

[6] Argazzi, R., Bignozzi, C.A., Heimer,T. A. Castellano, F.N., Meyer, G., Enhanced Spectral Sensitivity from Ruthenium(II) Polypyridyl Based Photovoltaic Devices.Inorganic Chemisrty, 33 (25),5741. https://doi.org/10.1021/ic00103a022.

[7] Kalyanasundaram, K., GraKtzel, M.,(1998). Applications of functionalized transition metal complexes in photonic and optoelectronic devices, Coordination Chemistry Reviews, 177(1), 347-414. https://doi.org/10.1016/S0010-8545(98)00189-1.

[8] Hagfeldt, A., GraK tzel, M.,(1995). Light-Induced Redox Reactions in Nanocrystalline Systems,Chemical Reviews, 95 (1), 49-68. https://doi.org/10.1021/cr00033a003.

22nd Iranian Chemistry Congress (ICC22)
Iranian Research Organization for Science and Technology (IROST)
13-15 May 2024

03231-97589

IROST

Microwave-Combustion-Sonoprecipitation Hybrid Synthesis of MgO/CaMn₂O₄-Ca₂Mn₃O₈ Nanocatalyst for Biodiesel Production via Transesterification Process: Influence of Carbonaceous Hard Templating

Mehdi Eisa Khajehlou, Mohammad Haghighi*, Mehdi Mohammadpour, Reza Shokrani

Corresponding Author E-mail: haghighi@sut.ac.ir

Chemical Engineering Faculty, Reactor and Catalysis Research Center (RCRC), Sahand University of Technology P.O.Box 51335-1996, Sahand New Town, Tabriz, Iran.

Abstract: The study is focused on MgO/CaMn₂O₄-Ca₂Mn₃O₈ synthesis with/without carbon templates and its influence on the biodiesel production. Employing FESEM and XRD, it discloses that the carbon template has improved pore structures, leading to the higher biodiesel conversion rate because of better diffusion of the reactants and the active site accessibility.

Keywords: MgO/CaMn₂O₄-Ca₂Mn₃O₈ Nanocatalyst; Microwave-Combustion-Sonoprecipitation Hybrid Method; Biodiesel Production

Introduction

Biodiesel, derived from vegetable oils, is a renewable and environmentally friendly alternative fuel. Perovskite $Ca_2Mn_3O_8$ and spinel $CaMn_2O_4$ have been examined in several research as support catalysts in the transesterification reaction. Also, MgO, as an active phase, has garnered the interest of several researchers due to its advantageous features, including its inexpensive precursor cost, alkalinity, and insoluble nature in methanol. Designing a catalyst with specific morphology, strong mechanical and thermal properties, and good interaction with the active phase is crucial for the transesterification reaction. Cost-effective carbon templates with appropriate particle sizes that may be readily eliminated during calcination can be employed to enhance the pore size and porosity of catalysts. Also, Sono-precipitation improves active phase control and catalyst-active phase interaction [1,2,3]. In this study, we first synthesized $CaMn_2O_4$-$Ca_2Mn_3O_8$ with and without activated carbon as template to shape the pore sizes of $CaMn_2O_4$-$Ca_2Mn_3O_8$ and then, through the utilization of ultrasonic irradiation to facilitate the impregnation technique, the active phase of MgO was introduced onto the $CaMn_2O_4$-$Ca_2Mn_3O_8$ catalyst. The prepared catalysts were characterized using XRD and FESEM.

Experimental Section

To synthesis of MgO/CaMn₂O₄-Ca₂Mn₃O₈ two solutions were prepared with Ca and Mn, and a carbon template was added to one of them. The mixtures were stirred for 45 min, heated to 80°C to evaporate excess water and form viscous gel, and then underwent a combustion process in a microwave at 900 W. Finally obtained powders calcined at 600 °C for 15 hr. To incorporate 5 wt% MgO onto the support catalysts, magnesium nitrate was dissolved in deionized water with the pre-synthesized catalysts. After stirring for 30 min, the mixture underwent 30 minutes of sonication at 250 W. The resulting powders were washed, filtered, dried in an oven at 110 °C for 24 hr, and calcined at 550 °C for 4 hr, yielding the MgO/MCM(UC0) and MgO/MCMO(UC5) nanocatalysts. Performance of synthesized nanocatalysts was investigated under identical conditions (90 °C, methanol/oil 1:2, catalyst/feed 3, 150 min). Finally, the pure biodiesel was analyzed by gas chromatography, using a FID, SUPRAWAX-280 column, and hydrogen carrier gas.

Results and Discussion

A. XRD Analysis:

X-ray diffraction (XRD) analysis results are shown in Fig.1. The presence of cubic MgO was confirmed by the characteristic peaks observed at 43, 62.4, 74.9, and 78.7°, which correspond to the JCPDS reference pattern (01-071-2364). Additionally, peaks at 17.1, 20.9, 28.0, 30.6, 37.3, 47.9, 55.7, and 65.0° were identified, aligning with the JCPDS reference pattern (01-073-2290) for the monoclinic phase of $Ca_2Mn_3O_8$. MgO/MCMO(UC5) sample exhibited further peaks at 18.3, 31.1, 33.0, 35.1, 39.2, 40.5, and 43.8°, indicative of the orthorhombic phase of the $CaMn_2O_4$ spinel crystal structure. The absence of any extraneous peaks in the XRD patterns confirms the purity of the precursors and the successful synthesis of the desired material without the introduction of impurities.
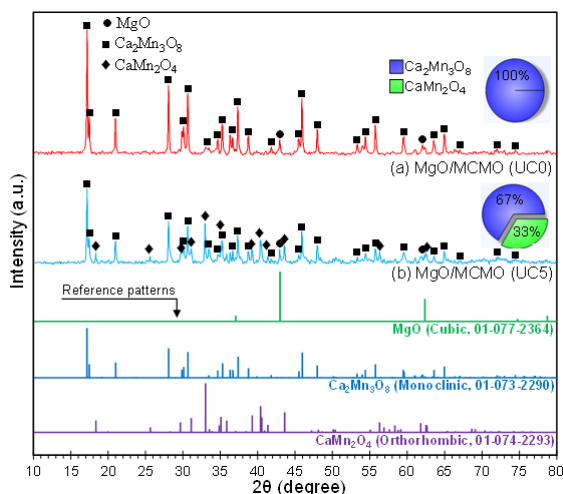
22nd Iranian Chemistry Congress (ICC22)
Iranian Research Organization for Science and Technology (IROST)
13-15 May 2024

03231-97589

IROST

Fig.1: XRD analysis of MgO/CaMn$_2$O$_4$-Ca$_2$Mn$_3$O$_8$ Nanocatalyst

B. FESEM Analysis:

FESEM analysis (Fig.2) employed to investigate the surface morphology of MgO/CaMn$_2$O$_4$-Ca$_2$Mn$_3$O$_8$ catalysts. Both catalysts exhibited a spherical nanoparticle morphology. Notably, the sample prepared without a carbon template (Fig.2(a)) displayed a low-porosity structure with minimal pore development. Conversely, the incorporation of a carbon template during the synthesis (Fig.2(b)) resulted in the formation of meso and macropores alongside the inherent combustion pores, generated by the removal of carbon template during calcination process. This observation suggests that the carbon template effectively promotes the development of a well-defined porous structure with significantly larger pore diameters.
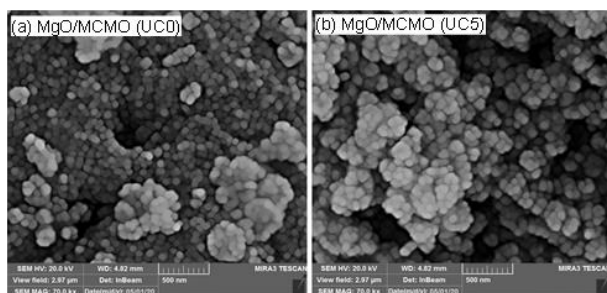
Fig.2: FESEM analysis of MgO/CaMn$_2$O$_4$-Ca$_2$Mn$_3$O$_8$ Nanocatalyst

C. Catalytic Performance Study toward Transesterification Process

Fig.3 displays shows performance of MgO/MCMO(UC0) and MgO/MCMO(UC5) nanocatalysts. Conversion rate of MgO/MCMO(UC5) was 77.7%, which is considerably greater than the 52% conversion rate of MgO/MCMO(UC0). The variation in performance can be ascribed to the utilization of a carbon template during the synthesis of MgO/MCMO(UC5). According to the findings of the FESEM analysis, the carbon template

caused the formation of mesopores, which provide a suitable structure for the large molecules in the feedstock. Undoubtedly, the presence of larger pores in MgO/MCMO(UC5) promotes the diffusion of large oil molecules, enabling them to readily reach the active sites of the manufactured nanocatalyst. This leads to a substantial enhancement in the efficacy of this catalyst.
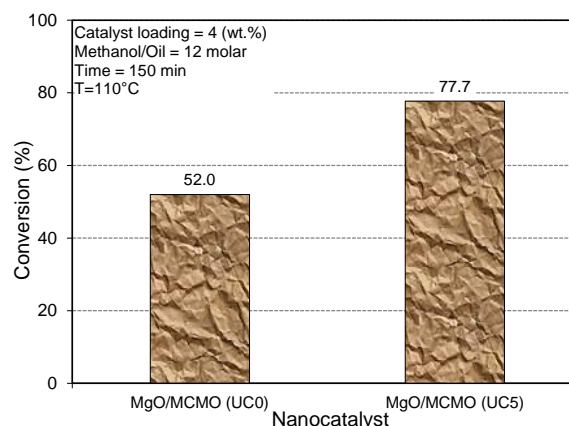

Fig.3 Catalytic performance of MgO/CaMn$_2$O$_4$-Ca$_2$Mn$_3$O$_8$ Nanocatalyst for Biodiesel Production via Transesterification Process.

Conclusions

This study investigates the use of carbon templates in designing efficient biodiesel production catalysts. MgO/CaMn$_2$O$_4$-Ca$_2$Mn$_3$O$_8$ nanocatalysts were synthesized using microwave combustion, with successful synthesis and a well-developed pore structure. MgO/MCMO (UC5) showed higher biodiesel conversion (77.7%) due to its mesopore structure which facilitates reactant diffusion and improves active site accessibility.

References

[1] Mohammadpour, M., Haghighi, M., & Shokrani, R. (2020). Influence of heating approach (microwave vs. muffle furnace) and fuel in auto-combustion design of nanostructured Ca$_2$Mn$_3$O$_8$ as support for efficient and reusable catalyst used in green fuel production. Ceramics International, 46(8), 12180-12191.

[2] Kwong, T. L., & Yung, K. F. (2015). Heterogeneous alkaline earth metal–transition metal bimetallic catalysts for synthesis of biodiesel from low grade unrefined feedstock. RSC advances, 5(102), 83748-83756.

[3] Sutapa, I. W., Taba, P., Shiomori, K., Taipabu, M. I., & Kamari, A. (2024). Impregnation process and kinetics studies of MgO nanocatalyst/montmorilonite-K10 for biodiesel production from Cerbera odollam oil in modified-microwave reactor. Kuwait Journal of Science, 100209.

22nd Iranian Chemistry Congress (ICC22)
Iranian Research Organization for Science and Technology (IROST)
13-15 May 2024

03231-97589

IROST

Polyphenol content and antioxidant activity of different *Stachys byzantine* extracts

Saeed Mollaei*, Fatemeh Jodari*

Corresponding Author E-mail: s.mollaei@azaruniv.ac.ir

Phytochemical Laboratory, Department of Chemistry, Faculty of Sciences, Azarbaijan Shahid Madani University, Tabriz, Iran.

Abstract: *Stachys byzantine* belongs to Lamiaceae family, and has numerous biological activities. In this study, different extracts of *Stachys byzantine* (n-hexane, ethyl acetate, and methanole) were obttained, and then their total phenol and flanavoid contents were investigated. Also, their antioxidant activities were studied. The results indicated that the highest phenol content was related to the methanol extract. Also, this extract had the highest flavonoid content. The analysis of antioxidant activity revealed that the ethyl acetate extract could inhibit high percentage of DPPH radicals. So, the highest antioxidant activity of *Stachys byzantine* belonged to ethyl acetate extract.

Keywords: Antioxidant; DPPH; Flavonoid; Phenol

Introduction

Stachys byzantine, Lamiaceae family, is native to Turkey, Armenia and Iran, and known as lamb's ears. This plant is generally applied to treat rheumatic disorders, digestive problems such as cramp, dysentery, and abdominal pains, epilepsy and neuropathy, and also it is used as a diuretic and sedative agent in folk medicine. This plant also has many biological properties such as cytotoxic, antioxidant, immunomodulatory, anti-inflammatory, and antibacterial effects [1].

Phenolic compounds such as flavonoids are the secondary metabolites distributed in plants. They are derived from pentose phosphate, shikimate, and phenylpropanoid pathways in plants. They can act as nutrient uptake, protein synthesis, enzyme activity, photosynthesis, structural components, and allelopathy. Phenols led to antibacterial effects especially against Gram positive bacteria. The structure of phenolic compounds is related to their radical-scavenging and metal-chelating activity. [2, 3].

Up to our knowledge, the polyphenol content and antioxidant activity of different Stachys byzantine extracts was not studied. So, the present work aimed to analysis total phenol and flavonoid contents as well as antioxidant activity of different Stachys byzantine extracts.

Experimental Section

Plant materials

Stachys byzantine was gathered from its wild habitat in June 2022 in the Northen regions of Mazandaran province, Iran.

Extraction process

For obtaining n-hexane extract, 2 gram of Powdered *Stachys byzantine* was added to 20 mL of n-hexane, and stirred for 2 hours at room temperature. After centrifugation, the n-hexane extract was dried at 60°C.

Then, 20 mL of ethyl acetate was added to the waste, and stirred (2 hours, room temperature), and finally the ethyl acetate extract was dried. For obtaining methanol extract, 20 mL of methanol was added to the waste which remained from previous step, and then stirred (2 hours, room temperature), and finally the methanol extract was dried.

Total phenolic and flavonoid contents assay

To measure the Total Phenolic Content, the Folin-Ciocalteu method was applied. Also, The Total Flavonoid Content in the extracts was obtained by $AlCl_3$ colorimetric method.

Antioxidant activity

The antioxidant activity was studied by measuring the amount of free radicals DPPH. Briefly, 100 μL of the extract was added to DPPH solution (100 μL, 0.1 mM), and mixed for 30 minutes at 25°C. Then, the absorbance of the samples was read at 517 nm. The inhibition percentage of DPPH free radicals was determined.

Results and Discussion

Polyphenols are compounds which are found inside the plant cells and can have numerous biological properties. Some of these properties include anti-cancer, anti-diabetes, anti-inflammatory, antimicrobial, antioxidants, etc [5]. In this study, different extracts of *Stachys byzantine* (n-hexane, ethyl acetate, and methanole) were obttained, and then their total phenol and flanavoid contents were investigated. Figure 1 indicates the total phenol content of different extracts obtained from *Stachys byzantine*. As shown, the highest total phenol content belonged to methanol extract (248 mgGAL/g extract), followed by ethy acetat extract (134 mgGAL/g extract).
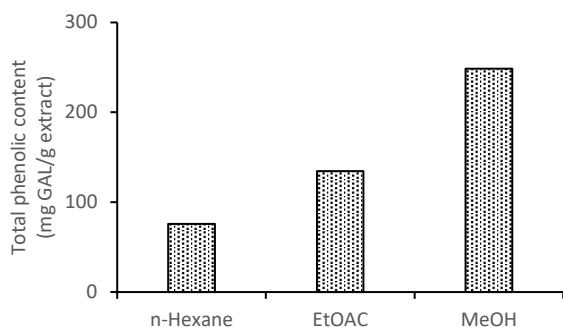
22nd Iranian Chemistry Congress (ICC22)
Iranian Research Organization for Science and Technology (IROST)
13-15 May 2024

03231-97589

Fig. 1: Total phenol content of different extracts obtained from *Stachys byzantine*

Figure 2 indicates the total flavonoid content of different extracts. The results indicated that the highest total flavonoid content belonged to methanol extract (43 mgQE/g extract), followed by n-hexane extract (30 mgQE/g extract).
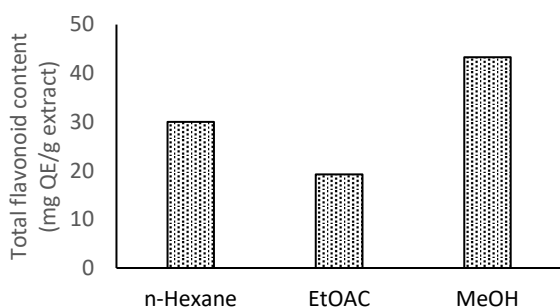

Fig. 2: Total flavonoid content of different extracts obtained from *Stachys byzantine*

Free radicals are compounds with single electrons that irreversibly react with biological molecules. They damage and cause many diseases such as cancer, cataracts, cardiovascular diseases, etc. Non-enzymatic factors such as phenols inhibit many reactive oxygen species and free radicals. These compounds are valuable secondary metabolites that are abundant in some plants and have many biological benefits [6]. In this study, the antioxidant activities of the extracts were assayed by DPPH methods, and the results were shown at Figure 3. The results revealed that the ethyl acetate extract could inhibit high percentage of DPPH radicals, and the n-hexane extract was at second level. So, the highest antioxidant activity of *Stachys byzantine* belonged to ethyl acetate extract.
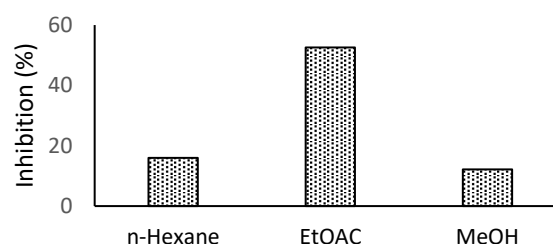

Fig. 3: Antioxidant activity of different extracts obtained from *Stachys byzantine*

Conclusions

The results of this study indicated that the highest total phenol and flavonoid contents was related to the methanol extract. Also, the ethyl acetate extract could inhibit high percentage of DPPH radicals. So, the highest antioxidant activity of Stachys byzantine belonged to ethyl acetate extract.

References

[1] Stegăruș, D. I., Lengyel, E., Apostolescu, G. F., Botoran, O. R., & Tanase, C. (2021). Phytochemical analysis and biological activity of three Stachys species (Lamiaceae) from Romania. Plants, 10(12), 2710.

[2] Lin, D., Xiao, M., Zhao, J., Li, Z., Xing, B., Li, X., ... & Chen, S. (2016). An overview of plant phenolic compounds and their importance in human nutrition and management of type 2 diabetes. Molecules, 21(10), 1374.

[3] Al Mamari, H. H. (2021). Phenolic compounds: Classification, chemistry, and updated techniques of analysis and synthesis. Phenolic Compounds: Chemistry, Synthesis, Diversity, Non-Conventional Industrial, Pharmaceutical and Therapeutic Applications, 73-94.

[4] Hazrati, S., Mollaei, S., Rabbi Angourani, H., Hosseini, S. J., Sedaghat, M., & Nicola, S. (2020). How do essential oil composition and phenolic acid profile of Heracleum persicum fluctuate at different phenological stages?. Food Science & Nutrition, 8(11), 6192-6206.

[5] Sauceda, A. E. Q., Sáyago-Ayerdi, S. G., Ayala-Zavala, J. F., Wall-Medrano, A., de la Rosa*, L. A., González-Aguilar*, G. A., & Álvarez-Parrilla, E. (2017). Biological actions of phenolic compounds. Fruit and Vegetable Phytochemicals: Chemistry and Human Health, 2nd Edition, 125-138.

[6] Mollaei, S., & Ebadi, M. (2022). A review of phenolic antioxidants isolated from endophytic fungi. Journal of Plant Process and Function, (1), 99-117.

22nd Iranian Chemistry Congress (ICC22)
Iranian Research Organization for Science and Technology (IROST)
13-15 May 2024

03231-97589

Isostructurality in Pseudo-Polymorphic Cadmium Coordination Polymers

Bahare Ebrahimi, Behrouz Notash*

Corresponding Author E-mail: b_notash@sbu.ac.ir

Department of Inorganic Chemistry, Shahid Beheshti University, 1983969411, Tehran, Iran.

Abstract: Two isostructural pseudo-polymorphic coordination polymers $[Cd(L)(MeOH)_2(ClO_4)_2]_n$ (**1**) and $[Cd(L)(MeCN)_2(ClO_4)_2]_n$(**2**), have been successfully prepared with layering method by using the electron-deficient tetrazine ligand (L) and cadmium perchlorate. The structure analysis shows that compounds **1** and **2** crystallizes in the triclinic system and have the same 1D linear chain structural motifs. Our results indicate the important role of solvent in the formation of two pseudo-polymorphic compounds **1** and **2**.

Keywords: Coordination polymer; Solvent effect; Pseudo-polymorph; Isostructuturality.

Introduction

During recent years, research in the field of coordination polymers has focused on discovering new and smart materials with a variety of compositions and architectures [1,2]. In fact, coordination polymers are the most prominent branches of inorganic and materials chemistry that have attracted the attention of chemists because of their brilliant potential in magnetism, catalysis, sensing, gas adsorption and separation, and drug delivery. Various factors such as anion, temperature, ratio of metal and ligand, and especially the diverse nature of metal ion and ligand structure have a significant impact on the targeted design of coordination polymers and ultimately lead to the formation of coordination polymers with different structures and dimensions [3]. In addition, the solvent plays an essential role as another influential factor in designing of coordination polymers [3]. According to previous reports, the solvent can directly participate in the crystal structure and / or indirectly affect the formation of the final structural framework [4,5].

Experimental Section

Synthesis of $[Cd(L)(CH_3OH)_2(ClO_4)_2]_n$ (1). A solution of L in chloroform was placed in a test tube. Then a solution of $Cd(ClO_4)_2.6H_2O$ in methanol was gently layered on top of the buffer layer. The test tube was sealed and allowed to diffuse solutions (Fig 1). Mp > 260 °C. Yield: 63%. IR (ATR, cm^{-1}): 3484(m), 1606(m), 1446(w), 1390(s), 1201(m), 1117(s), 1044(m), 1029(m), 993(m), 945(w), 924(m), 822(m), 750(w), 693(s).

Synthesis of $[Cd(L)(CH_3CN)_2(ClO_4)_2]_n$ (2). A solution of L in chloroform was placed in a test tube. Then a solution of $Cd(ClO_4)_2.6H_2O$ in acetonitrile was gently layered on top of the buffer layer. The test tube was sealed and allowed to diffuse solutions (Fig 1). Mp > 260 °C. Yield: 87%. IR (ATR, cm^{-1}): 2304(w), 2273(m), 1608(m), 1446(w), 1398(s), 1362(w), 1200(m), 1116(s), 1024(s), 967(w), 920(s), 819(m), 753(w), 692(s).

Results and Discussion

According to the single-crystal X-ray diffraction analysis, both compounds **1** and **2** crystallized in the triclinic crystal system and $P\bar{1}$ space group. Part of crystallographic data for these two compounds are listed in Table 1. In compound **1**, the six-coordinated cadmium atom adopts a slightly distorted octahedral geometry that is surrounded by two pyridyl nitrogen atoms of two tetrazine ligands and four oxygen atoms belonging to two perchlorate anions and two methanol molecules. In compound **2**, the cadmium center is bound to two pyridyl nitrogen atoms of two tetrazine ligands and two oxygen atoms belonging to two perchlorate anions and two nitrogen atoms of two acetonitrile molecules which defines a slightly distorted octahedral geometry. The crystal packing of both compounds represents ABC patterns of 1D linear chains (Fig 2).
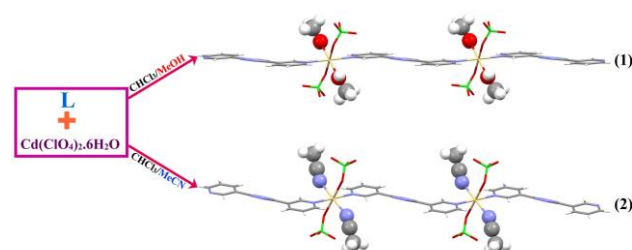

Fig 1. Representation of the Reaction Conditions for the Synthesis of Coordination Polymers **1** and **2**.

As shown in Fig 3, the d_{norm} map and the 2D fingerprint plots were used to gain further insights about various intermolecular interactions in the crystal structures of compounds **1** and **2**. The most

22nd Iranian Chemistry Congress (ICC22)
Iranian Research Organization for Science and
Technology (IROST)
13-15 May 2024

03231-97589

IROST

significant contribution was observed with two sharp symmetric spikes related to O⋯H/H⋯O interactions [34.8% (**1**) and 33.6% (**2**)]. The relative contribution of different intermolecular interactions of compounds **1** and **2** indicated in Fig 4.

Table 1. Crystallographic Data for Compounds **1** and **2**.

	1	**2**
a / Å	7.7210(15)	6.9882(14)
b / Å	7.7969(16)	8.1710(16)
c / Å	9.4083(19)	10.384(2)
α / °	81.87(3)	88.56(3)
β / °	79.69(3)	75.56(3)
γ / °	72.82(3)	81.62(3)

(a)

(b)
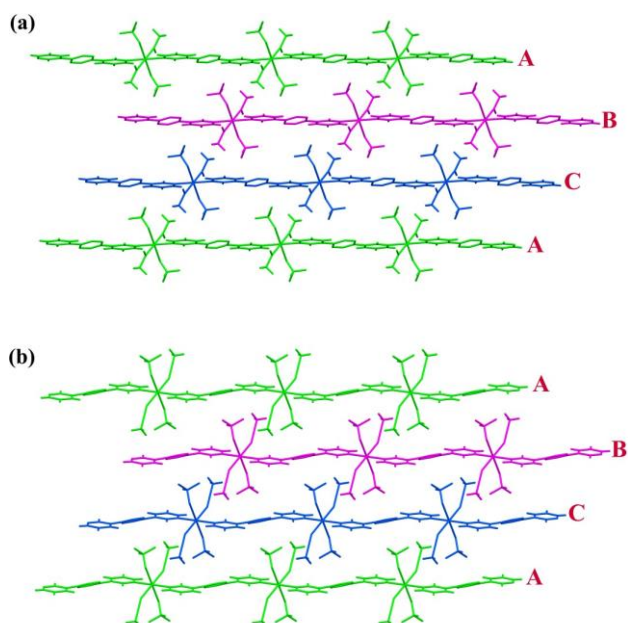
Fig 2. (a) and (b) view of the ABC arrangement of 1D linear chains in **1** and **2**, respectively.

Conclusion

In the present study, two new cadmium coordination polymers [Cd(L)(MeOH)$_2$(ClO$_4$)$_2$]$_n$ (**1**) and [Cd(L)(MeCN)$_2$(ClO$_4$)$_2$]$_n$ (**2**) were prepared and characterized. Their structural motif similarity is related to the coordination nature of the solvent molecule. The results confirmed the effective role of solvent in the formation of these two pseudo-polymorphs.
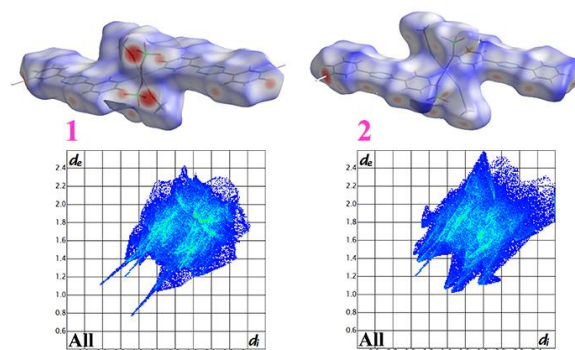

Fig 3. Hirshfeld surfaces mapped with d_{norm} and fingerprint plot for compounds **1** and **2**.
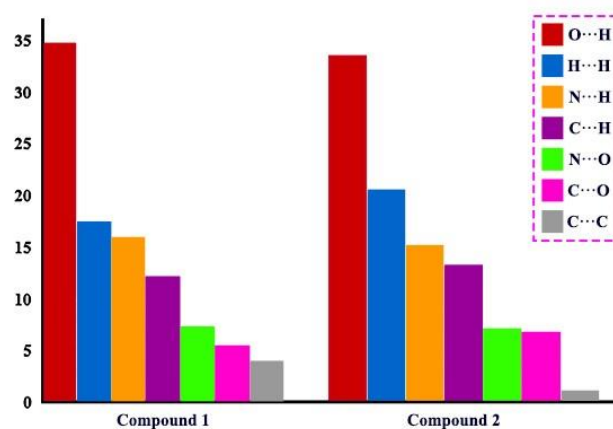

Fig 4. The relative contribution of intermolecular interaction to Hirshfeld surface area in compounds **1** and **2**.

References

[1] Ortiz, O. L., & Ramírez, L. D. (2012). Coordination polymers and metal organic frameworks: properties, types, and applications.

[2] Batten, S. R., Neville, S. M., & Turner, D. R. (2008). *Coordination polymers: design, analysis and application*. Royal Society of Chemistry.

[3] Banerjee, D., Finkelstein, J., Smirnov, A., Forster, P. M., Borkowski, L. A., Teat, S. J., & Parise, J. B. (2011). Synthesis and structural characterization of magnesium based coordination networks in different solvents. *Cryst. Growth Des.*, *11*(6), 2572-2579.

[4] Chen, S. C., Zhang, Z. H., Huang, K. L., Chen, Q., He, M. Y., Cui, A. J., ... & Du, M. (2008). Solvent-controlled assembly of manganese (II) tetrachloroterephthalates with 1D chain, 2D layer, and 3D coordination architectures. *Cryst. Growth Des.*, *8*(9), 3437-3445.

[5] Li, L., Wang, S., Chen, T., Sun, Z., Luo, J., & Hong, M. (2012). Solvent-dependent formation of Cd (II) coordination polymers based on a C 2-symmetric tricarboxylate linker. *Cryst. Growth Des.*, *12*(8), 4109-4115.

22nd Iranian Chemistry Congress (ICC22)
Iranian Research Organization for Science and Technology (IROST)
13-15 May 2024

03231-97589

ISC

IROST

Microencapsulation of lime (*Citrus aurantifolia*) essential oil by spray drying Technique

Azita Shafiei[a, b], Javad Safaei-Ghomi[a]*, Reihaneh Masoomi[a,b]

Corresponding Author E-mail: safaei@kashanu.ac.ir

[a]Department of Organic Chemistry, Faculty of Chemistry, University of Kashan, Kashan, Iran.
[b]Barij Medicinal Plants Research Center, Kashan, Iran.

Abstract: This study aimed to investigate the effect of maltodextrin, gum Arabic and gelatin at different ratios to microencapsulation of lime by spray dryer. The optimal formulation was evaluated in terms of physicochemical characteristics, morphology, and GC analysis. The results showed that process with 96.4% encapsulation efficiency was done successfully.

Keywords: Encapsulation; *Citrus aurantifolia*; Spray dryer; Essential oil

Introduction

The essential oil of lime (*Citrus aurantifolia*) used to relieve common cold, flu, decreased appetite and other diseases. Also, it has been used for its good organoleptic properties as a food additive. However, due to having volatile compounds sensitive towards light, oxygen, heat which limits their application [1].

Microencapsulation process involves the formation of a protective thin film layer typically composed by one or several hydrocolloid. One of the most important challenges in this process is choosing the right wall mateial. Combination of encapsulating agents is one of the process variables that can influence the protection of the core including active substances [2].

This research was done with the aim of choosing the best composition wall for lime essential oil encapsulation and evaluating its characteristics.

Experimental Section
Preparation of feed sample for spray dryer

The following five formulation were prepared in purifued water: F1 (maltodextrin), F2 and F3 (maltodextrin, gum Arabic with different ratio); F4 (maltodextrin, gum Arabic, gelatin); F5 (maltodextrin, gelatin). After 24 h, lime essential oil was added to the hydrocolloid suspension dropwise in a ratio of 1:4 (EO/wall material) while the mixture was uniformed for 5 min using homogenizer at 10,000 rpm.

Preparation of suspension for spray drying

Suspension prepared in the previous step, was fed into a spray-dryer (Dorsa, Iran). Fluid nozzle of apparatus has 1.2 mm diameter. The feedflow rate by a peristaltic pump was 0.3 L/h and the compressed airflow rate was 7 L/min. Prepared powders were stored in opaque containers for further experiments.

Characterization of lime essential oil microcapsules

The physicochemical properties of the powder like moisture content (MC), oil retention (OR), encapsulation efficiency (EE), hygroscopicity (HR), Gas chromatography analyses (GC), Infrared spectroscopy (IR) and morphology were determined to a standard procedure.

Results and Discussion
Encapsulation efficiency (EE %)

As Table 1 shows, the encapsulation efficiency (EE %) for all treatments is high and over 78.8%. This results indicates that the encapsulation process was carried successfully.

Table1: Characterization of lime microcapsules produced with different treatments

Treatments	EE%	HR w/w%	OR w/w%	MC w/w%
F1	78.8±0.4	16.8±0.3	58.1±0.5	5.4±0.2
F2	87.3±0.3	17.4±0.1	71.8±0.6	4.8±0.3
F3	96.4±0.1	18.2±0.2	79.3±0.6	3.5±0.2
F4	93.2±0.3	22.5±0.1	67.5±0.4	2.2±0.1
F5	90.3±0.2	21.3±0.2	68.7±0.5	3.8±0.3

The highest amount of encapsulation is related to the F3. Also, Suitable solid material with high viscosity increases the oil retention because it reduces the time of crust formation. Carbohydrate chains in maltodextrin and protein in gum arabic, as a good film-forming factor, trap and encapsulate essential oil components.

Hygroscopisty of microparticles were different for every treatment. So that the highest amount of water absorption is related to formula 4 (22.5%). This effect could be attributed to the hygroscopicity intrinsic of composition maltodextrin, gelatin and gum Arabic.

22nd Iranian Chemistry Congress (ICC22)
Iranian Research Organization for Science and Technology (IROST)
13-15 May 2024

03231-97589

Gas chromatography analyses

To evaluate successful encapsulation, the pure Lime EO and EOs obtained from microparticles were analyzed using GC/FID. The analysis results shows that components were preserved after encapsulation. The amount of limonene, beta-pinene, gamma-terpinene, sabinene were 65.4, 13.1, 9.3, 1.8, respectively, in the capsulated essential oil, which does not show a significant difference with the unencapsulated essential oil.
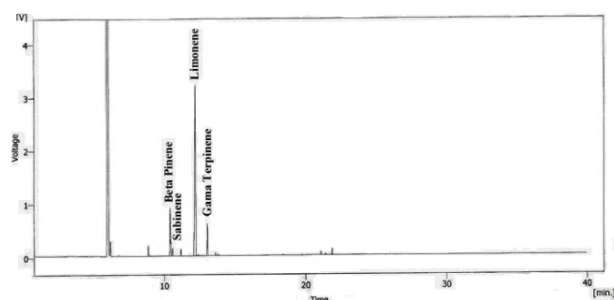
Fig.1: GC profile of lime essential oil extracted from microcapsule

Fourier Transform Infrared Spectroscopy

The Mid-IR spectrum of pure lime essential oil shows the characteristic peak at 810 cm^{-1} and 890 cm^{-1} (bending vibration of = C-H), 1107 cm^{-1} (C-O-C stretching), 1431
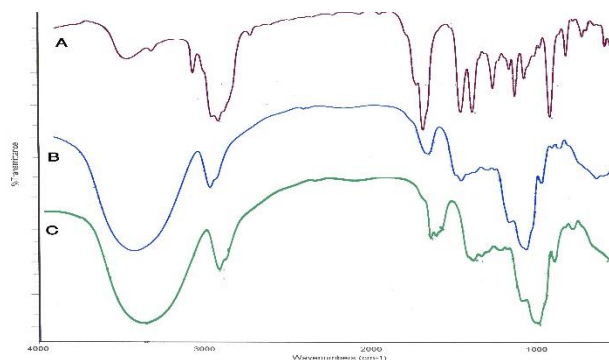

Fig.2: FTIR spectra of lime orange essential oil (A); lime EO matrix(B); microcapsule (C)
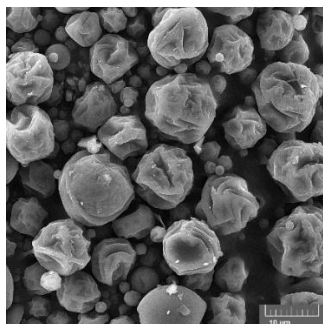

Fig.3: SEM of lime essential oil microparticles

cm^{-1} (CH2 bending), 1686 cm^{-1} (C-O stretching), and 2930 cm^{-1} (C-H stretching). The FT-IR spectrum of optimum treatment was very similar to that of the matrix. This phenomenon is related to the successful microencapsulation of lime essential oil in maltodextrin and gum Arabic mixture.

Powder morphology

Examining the morphology of the optimal formula shows that the microcapsules are formed correctly. Although there are dents and wrinkles in them, but no fracture and crack is observed in the microcapsules.

Conclusions

The results demonstrated that lime microspheres can be prepared by emulsification using maltodextrin and gum arabic as wall materials followed by spray drying, resulting in high yields. The FT-IR spectra and SEM analysis confirmed the formation of microcapsules. Also, no changes were observed in the composition of essential oils after encapsulation. The results of this study showed that lime microcapsule Due to increased stability can be used for pharmaceutical and other applications e.g. flavoring of food.

References

[1] Campelo-Felix, P. H., Souza, H. J. n. B., Figueiredo, J. d. & Borges, S. V. (2017). Prebiotic carbohydrates: Effect on reconstitution, storage, release, and antioxidant properties of lime essential oil microparticles. Journal of agricultural and food chemistry, 65(2), 445-453. https://doi.org/10.1021/acs.jafc.6b04643

[2] De Araújo, J. S. F., de Souza, E. L. & Oliveira, J. R., (2020). Microencapsulation of sweet orange essential oil (Citrus aurantium var. dulcis) by liophylization using maltodextrin and maltodextrin/gelatin mixtures: Preparation, characterization, antimicrobial and antioxidant activities. International journal of biological macromolecules, 143, 991-999.

https://doi.org/10.1016/j.ijbiomac.2019.09.160

Electrochemical detection of glucose in human blood serum using modified glassy carbon electrode

Mohammad Javad Khatami, Mohammad Mazloum-Ardakani*, Hamideh Mohammadian-Sarcheshmeh, Rasoul Vafazadeh

Corresponding Author E-mail: mazloum@yazd.ac.ir

Department of Chemistry, Faculty of Science, Yazd University, Yazd, Iran.

Abstract: Due to the importance of glucose detection, in recent years there has been a lot of researches on electrochemical glucose sensors. In this research, a non-enzymatic electrochemical glucose sensor was designed, which has a good detection limit of 0.015 mM and a linear dynamic range of 0.1-1.1 mM that was used to measure glucose in human blood serum.

Keywords: Glucose; modifier; non-enzymatic

Introduction

Glucose is a crucial component of biological processes and a key metabolite for living organisms, particularly in the diagnosis of diabetes, a global health challenge that contributes to mortality and disability worldwide. Detecting glucose is vital for human health, so it is essential to advance rapid, sensitive, selective, and dependable methods for glucose monitoring in clinical settings, food production, and biotechnology [1,2]. Enzymatic sensors face various enzyme-related challenges like enzyme denaturation, poor stability, ineffective enzyme immobilization on electrodes, and intricate enzyme purification procedures. Enzyme-free glucose sensors offer a hopeful solution by eliminating enzyme-related issues. Nevertheless, current non-enzymatic glucose sensors need significant enhancements in sensitivity and selectivity before they can be utilized for commercial applications [3,4]. Non-enzymatic sensors can be developed using a range of materials, including nanomaterials, complexes, and polymeric materials and etc. They are firmly attached to the electrode surface and facilitate the oxidation of glucose, thereby enhancing the responses and LOD value [5]. Nickel stands out as one of the best options among metals for a cost-effective, sensitive and selective non-enzymatic electrode. A modified GCE with a nickel complex was used to create a non-enzymatic electrochemical glucose sensor in this study. The nickel complex acts as a modifier to improve the electrochemical function of the sensor in detecting glucose. Various techniques, including cyclic voltammetry (CV) and differential pulse voltammetry (DPV), were employed to evaluate the performance of the electrochemical sensor.

Experimental Section

All materials such as Sodium hydroxide (NaOH) and glucose were purchased from Merck company without further purification. Synthesis of the complex as a modifier was prepared according to the method mentioned in the following reference [6].

Results and Discussion

The characterization investigation of the sensor was done using FE-SEM and FT-IR which is a confirmation of the used complex (Fig.1a,b). According to Fig.1c, the glassy carbon electrode modified with a complex of nickel was investigated in the presence of different concentrations of glucose using cyclic voltammetry technique in the 0.1 M NaOH solution, and with the increasing in glucose concentration, we see an increase in the oxidation peak current. As the glucose concentration increases, the cathodic peak current of glucose decreases due to NiOOH consumption during glucose electrooxidation. Moreover, higher glucose concentration shift the anodic peak current towards a more positive potential, which indicates a decline in the electron transfer kinetics [7].

The modified glassy carbon electrode with nickel complex was used to measure glucose in real samples, specifically human blood serum samples from a medical laboratory. To assess its efficiency, DPV and standard addition methods were employed. According to the obtained results (Fig.1d and Fig.1e) with the calibration curve and using extrapolation, the glucose concentration was calculated. Based on the data presented in in Table 1, it can be concluded that the sensor performs accurately in measuring glucose. It should be mentioned that for the measurement of glucose in human blood serum, to eliminate the matrix effect, the standard addition method is used. In this method, human blood serum was diluted and the concentrations reported in the Table 1 have been converted into millimolar unit.
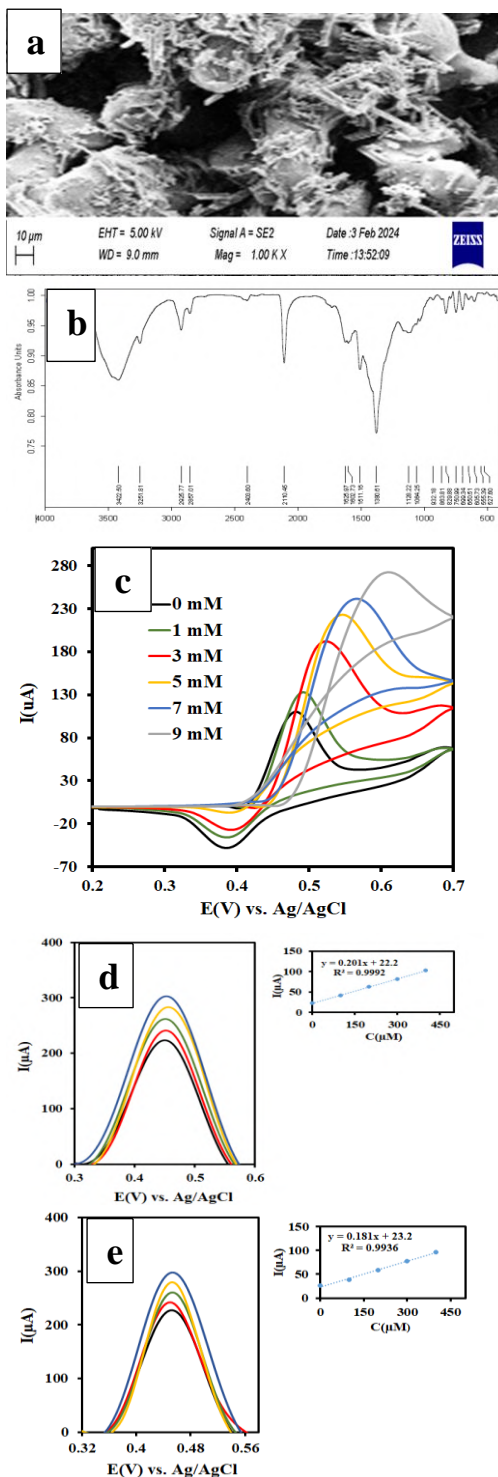
22nd Iranian Chemistry Congress (ICC22)
Iranian Research Organization for Science and Technology (IROST)
13-15 May 2024

03231-97589

Fig.1: a) FE-SEM of comlex, b) FT-IR of complex, c) CV voltammograms of modified GCE in 0.1 M NaOH solution containing different concentrations of glucose at scan rate of 0.05 V/s and potential window of 0.2-0.7 V, d,e) DPV voltammograms of standard addition method for measuring glucose in human blood serum (d: diabetic sample, e: normal sample)

Table1: Measuring glucose in human blood serum

Sample	Initial concentration	Founded concentration	RSD(%) N=4
Diabetic	11.27	11.04 ± 0.25	2.26
Normal	5.05	5.12 ± 0.16	3.12

Conclusions

A glassy carbon electrode was modified with a nickel complex to create an electrochemical sensor for detecting glucose in this study. The modifier showed excellent stability on the electrode surface and effectively covered it. Presence of nickel in modifier structure faciliates the oxidation of glucose on the electrode surface, particularly in alkaline environment. The sensor successfully measured glucose in human blood serum, yielding results that closely matched those from medical laboratory tests.

References

[1] Mazloum-Ardakani, M., Amin-Sadrabadi, E., & Khoshroo, A. (2016). Enhanced activity for non-enzymatic glucose oxidation on nickel nanostructure supported on PEDOT: PSS. *Journal of Electroanalytical Chemistry*, *775*, 116-120.

[2] Khan, R., Ahmad, R., Rai, P., Jang, L. W., Yun, J. H., Yu, Y. T., ... & Lee, I. H. (2014). Glucose-assisted synthesis of Cu2O shuriken-like nanostructures and their application as nonenzymatic glucose biosensors. *Sensors and Actuators B: Chemical*, *203*, 471-476.

[3] Haghparas, Z., Kordrostami, Z., Sorouri, M., Rajabzadeh, M., & Khalifeh, R. (2021). Highly sensitive non-enzymatic electrochemical glucose sensor based on dumbbell-shaped double-shelled hollow nanoporous CuO/ZnO microstructures. *Scientific Reports*, *11*(1), 344.

[4] Wei, M., Qiao, Y., Zhao, H., Liang, J., Li, T., Luo, Y., ... & Sun, X. (2020). Electrochemical non-enzymatic glucose sensors: Recent progress and perspectives. *Chemical communications*, *56*(93), 14553-14569.

[5] González, D. M., Hernández, L. A., Oyarce, J., Alfaro, A., Novoa, N., Cisterna, J., ... & Manzur, C. (2021). A new and efficient high-performance electrochemical glucose sensor based on a metallopolymer derived from a cobaltate (III) Schiff base complex. *Synthetic Metals*, *271*, 116633.

[6] Vafazadeh, R., Aghayani, S., & Willis, A. C. (2021). Synthesis, structure characterization and Hirshfeld surface analysis of Ni (II) complexes with a flexidentate ligand: a dinuclear complex with O– H– O bond. *Journal of Molecular Structure*, *1246*, 131192.

[7] Alghazzawi, W., Danish, E., Alnahdi, H., & Salam, M. A. (2020). Rapid microwave-assisted hydrothermal green synthesis of rGO/NiO nanocomposite for glucose detection in diabetes. *Synthetic Metals*, *267*, 116401.

22nd Iranian Chemistry Congress (ICC22)
Iranian Research Organization for Science and Technology (IROST)
13-15 May 2024

03231-97589

IROST

Paclitaxel-Loaded Nanofibers: A Promising Approach for Improved Cancer Treatment

Nazli Bahari, Abolfazl Barzgar*, Mehdi Haghi, Danial Fatahnaei, Somayyeh Ebrahimzadeh

Corresponding Author E-mail: barzegar@tabrizu.ac.ir

Department of biology, Faculty of natural sciences, University of Tabriz.

Abstract: Nanotechnology has adopted a new approach for the treatment of diseases, such as cancer, because of the beneficial properties of nanofibers and nanoparticles. Electrospinning produced paclitaxel-loaded PCL-PEG nanofibers for cancer treatment. We evaluate their physical behavior and potential for controlled release against cancer cells, aiming to improve therapeutic efficacy.

Keywords: Paclitaxel; Electrospun Nanofiber; SEM; Anticancer

Introduction

Cancer, characterized by uncontrolled cell division, remains a significant challenge despite conventional therapies like chemotherapy. These therapies often suffer from limitations such as rapid drug clearance and non-targeted effects. Polymer-based nanofibers offer a promising alternative for overcoming these limitations [1]. Electrospinning, a well-established technique, offers a simple and efficient method for producing drug-loaded nanofibers with desirable characteristics. Synthetic polymers (e.g., polyethylene, polyamide) or natural polymers (e.g., chitosan) can be used as building blocks, and the choice of polymer influences the final nanofiber properties. Nanofibers, with their unique properties, have revolutionized drug delivery, targeted therapy, and regenerative medicine. These properties include high porosity, and Large surface area that provides, a platform for cell growth or drug loading capacity and sustained release.

Experimental Section

Poly(ε-caprolactone) (PCL) and Poly(ethylene glycol) (PEG) were purchased from Sigma-Aldrich. Paclitaxel (anticancer drug) was obtained from the pharmacy of Tabriz University of Medical Sciences. All other chemicals were analytical grade reagents from Merck.

Methods:

PCL and PEG polymers were dissolved in a 1:1 (v/v) mixture of acetic acid and formic acid at room temperature (25 °C) under magnetic stirring. Paclitaxel was then added to the polymer solution and stirred vigorously until thoroughly dispersed. Ensuring homogenous distribution of paclitaxel throughout the solution is crucial for uniform drug loading within the nanofibers.

Electrospinning: The prepared solution was loaded into a syringe connected to a high-voltage electrospinning machine. The following electrospinning parameters were used:

High voltage: (Specify voltage used - typical range is 22 kV).

Flow rate: 0.8 ml/h
Collector distance: 15 cm from the needle tip
Collector rotation speed: 120-150 rpm (Collector rotation helps create a more uniform nanofiber mat).

Under these parameters, the solution was electrospun immediately [2]. All experiments were conducted at room temperature (25 °C).

Characterization of nanofibers

The morphology (size, shape, and surface features) of the electrospun nanofibers was analyzed using Field Emission Scanning Electron Microscopy (FE-SEM) [3].

UV-Vis assay:
Paclitaxel exhibits characteristic absorption peaks in the ultraviolet-visible (UV-Vis) spectrum. Understanding these peaks is crucial for quantifying the amount of paclitaxel released from the nanofibers in the in vitro release assay.

Release assay: The release kinetics of paclitaxel from the electrospun nanofibers were evaluated using an in vitro release assay. A disc-shaped sample (10 mm x 10 mm, weighing approximately 5 mg) containing the loaded paclitaxel was placed in a vial containing 3 mL of phosphate-buffered saline (PBS, pH 7.4) at 37 °C [4]. To simulate physiological conditions, the release medium was maintained under constant shaking within an incubator. At predetermined time intervals, half of the incubation medium (1.5 mL) was collected and replaced with an equal volume of fresh PBS. The collected medium was then analyzed using UV-Vis spectroscopy to quantify the amount of paclitaxel released.

Results and Discussion

FE-SEM offers high-resolution [5] images, allowing for detailed examination of the fiber diameter, smoothness, and presence of any beads or defects as depicted in Figure 1. As observed in Figure 1, the neat PCL-PEG nanofibers exhibit a smooth, bead-free, and fibrous structure, indicating an optimal electrospinning process.

Paclitaxel-Loaded Nanofibers: Compared to the unloaded controls, the paclitaxel-loaded nanofibers (Figure 1) show a slight increase in fiber diameter and a broader diameter

22nd Iranian Chemistry Congress (ICC22)
Iranian Research Organization for Science and Technology (IROST)
13-15 May 2024

03231-97589

IROST

distribution. This suggests that paclitaxel incorporation may influence the physical properties of PCL-PEG during electrospinning.
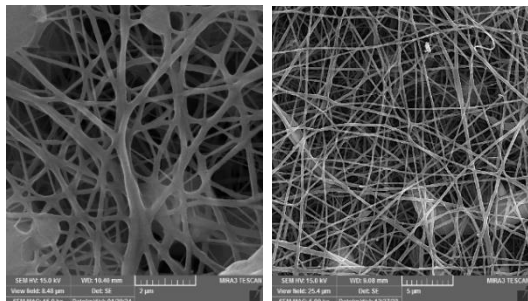

Fig. 1: PCL-PEG electrospun nanofiber (right) and PCL-PEG loaded 5 wt.% Paclitaxel (left) electrospun nanofibers.

UV-Vis absorption spectra of Paclitaxel:
As expected, a prominent peak is observed at approximately λ_{max} = 232 nm for all paclitaxel concentrations (Figure 2.). This peak will be used for subsequent quantification of paclitaxel released from the nanofibers in the in vitro release assay.

In vitro drug release results:

As shown in Figure 3, the wavelength 232 nm was used to quantify the amount of paclitaxel released from the nanofibers in the in vitro release assay. As mentioned, the UV absorption of the pure paclitaxel in different concentrations of the drug was taken by a spectrophotometer and it was observed that paclitaxel has a significant absorption at the wavelength of 232 nm [6]. An initial burst release of paclitaxel is observed within the first 8 hours. This initial release might be attributed to paclitaxel loosely associated with the nanofiber surface or within larger pores. Following the initial burst, a slower and more controlled release phase is observed.
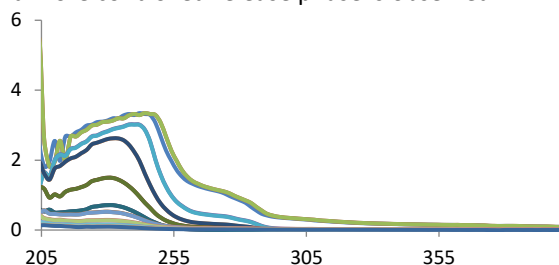

Fig. 2. UV-Vis absorption spectra of paclitaxel solutions. The graph displays the UV-Vis absorption spectra of paclitaxel solutions at various concentrations.

This sustained release suggests the potential for prolonged drug delivery, which could be beneficial for cancer therapy (Figure 4). This Figure could depict the cumulative release percentage of paclitaxel over time,

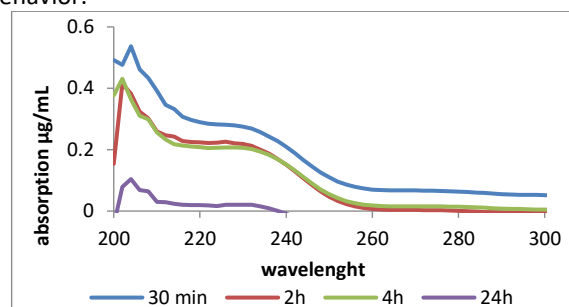providing a more quantitative view of the release behavior.

Fig. 3. In Vitro Release Profile of Paclitaxel. This figure shows the release profile of paclitaxel from PCL-PEG nanofibers over time. The nanofibers were incubated in 3 mL of phosphate-buffered saline (PBS) at 37 °C. Measurements were taken at four different time points to quantify the amount of paclitaxel released.
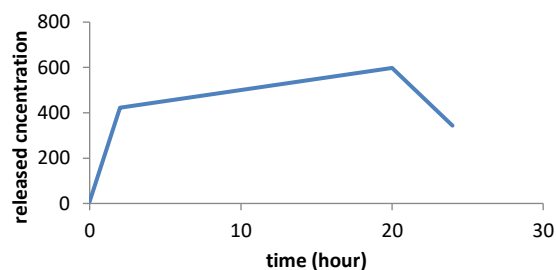

Fig.4: Cumulative release of paclitaxel over 24 hours. This figure depicts the cumulative release of paclitaxel from the PCL-PEG nanofibers over a 24-hour period. As observed, the release profile exhibits a decreasing trend, suggesting the continuous release of paclitaxel from the nanofibers.

Conclusions
This study successfully fabricated paclitaxel-loaded nanofibers using electrospinning for sustained drug release. The in vitro release profile demonstrated a biphasic pattern, with an initial burst followed by a slower and more controlled release phase. This suggests the potential for both a rapid initial therapeutic effect and prolonged drug delivery, which could be beneficial for cancer treatment.

References
[1] Agrawal, G., et al., *Electrospun Nanofiber-Based Drug Carrier to Manage Inflammation.* Adv Wound Care (New Rochelle), 2023. **12**(9): p. 529-543.
[2] Yang, S., S. Zhao, and S. Chen, *Recent advances in electrospinning nanofiber materials for aqueous zinc ion batteries.* Chem Sci, 2023. **14**(46): p. 13346-13366.
[3] de Souza, W., L. Campanati, and M. Attias, *Strategies and results of field emission scanning electron microscopy (FE-SEM) in the study of parasitic protozoa.* Micron, 2008. **39**(2): p. 77-87.
[4] Wen, M., et al., *Accumulation, Directional Delivery and Release of Nanoparticles along a Nanofiber.* Molecules, 2022. **27**(10).
[5] 5. Verschatse, O., et al., *Microscale and Macroscale Deformation Behavior of Electrospun Polymeric Nanofiber Membranes Using In Situ SEM during Mechanical Testing.* Polymers (Basel), 2023. **15**(7).
[6] 6. Zupančič, Š., et al., *Impact of PCL nanofiber mat structural properties on hydrophilic drug release and antibacterial activity on periodontal pathogens.* Eur J Pharm Sci, 2018. **122**: p. 347-358.

Quantum Mechanical Simulation of Bevacizumab Drug Interaction with C60 Fullerene

Hossein Shirani[a,b,*], Bahar Abolghasem[b]

Corresponding Author E-mail: hossein_shirani@iust.ac.ir

[a] Department of Chemistry, Iran University of Science and Technology, P.O. Box 16846-13114, Tehran, Iran

[b] Department of Biotechnology, Faculty of Biological Sciences and Technology, University of Science and Culture, Tehran, Iran.

Abstract: In this study, quantum mechanical calculations were utilized to analyze the adsorption of the anticancer drug Bevacizumab on C60 Fullerene as a nanocarrier in a simulated drug delivery system. Using the B3LYP/6-311+G computational method, we extensively examined the molecular structure, bond lengths, bond angles, dipole moments, and HOMO-LUMO energy gap of Bevacizumab.

Keywords: Cancer; Bevacizumab; HOMO-LUMO Gap; DFT; B3LYP/6-311+G; Fullerene

Introduction

Bevacizumab, a type of monoclonal antibody that targets vascular endothelial growth factor (VEGF), plays a vital role in modern cancer treatment. By stopping VEGF activity, Bevacizumab interferes with the formation of blood vessels within tumors, which ultimately hinders tumor growth and spread. This is why Bevacizumab is effective in fighting various types of cancers such as colorectal, lung, breast, and renal carcinomas. The U.S. Food and Drug Administration (FDA) has approved Bevacizumab for treating metastatic colorectal cancer, advanced nonsquamous non-small cell lung cancer, metastatic renal cell carcinoma, recurrent glioblastoma, advanced cervical cancer, and platinum-resistant ovarian cancer. Despite these approvals, there are still challenges in optimizing Bevacizumab's delivery and fully understanding its molecular intricacies. Moreover, while Bevacizumab has shown positive results in certain cancer cases, its effectiveness can vary depending on factors such as the type of tumor, genetic mutations, and overall health of individuals. The main goal of this study is to carefully analyze Bevacizumab's molecular actions to improve our understanding of how it works in treating cancer. This insight has the potential to revolutionize cancer treatment strategies in the future [1,2].

Methods

At the outset, Bevacizumab's molecular structure was crafted through the utilization of GaussView software, then proceeded with quantum mechanical estimations at the B3LYP/6-311+G theoretical method via Gaussian09 software.

Results and Discussion

Molecular computations were conducted on the drug Bevacizumab utilizing the GaussView software at the B3LYP/6-311+G theoretical level, and the resulting structural parameters were documented. The molecular structure of concern was originally crafted in the GaussView software (Fig. 1).
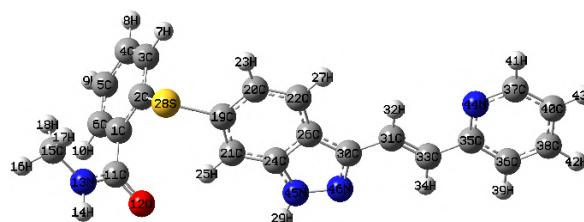

Fig. 1. The optimized structure of Bevacizumab at the B3LYP/6–311+G level of theory.

Reported are the thermodynamic properties of the Bevacizumab structure calculated using the B3LYP/6–311+G computational method. The total energy is found to be 91.788 kcal/mol, the zero-point energy is 967115.250605 kcal/mol, and the Gibbs free energy is determined to be 0.299548 kcal/mol. Tables 1 to 3 showcase the structural parameters of Bevacizumab. Moreover, Tables 4 and 5 display the Calculated Dipole Moments (Debye) Values and HOMO-LUMO Energy for the Bevacizumab Molecule, obtained using the B3LYP/6-311+G** Computational method, respectively.

Table 1. Calculated Bond Length Values for Bevacizumab Molecule using the B3LYP/6-311+G Computational Method.

C19-C21	C1-C2	C30-N46	C11-O12	C37-C40	C3-C4
1.38748	1.40239	1.34793	1.25904	1.39856	1.39647

Table 2. Calculated Bond Angles Values for Bevacizumab Molecule using B3LYP/6-311+G Computational.

C19-C21-C24	C30-C31-C33	C35-C36-C38	N44-C37-C40	C24-N45-N46	C1-C2-C3
116.2	125.5	119.7	123.3	112.3	120.3

22nd Iranian Chemistry Congress (ICC22)
Iranian Research Organization for Science and Technology (IROST)
13-15 May 2024

03231-97589

IROST

Table 3. Calculated Dihedral Angle Values for Bevacizumab Molecule using B3LYP/6-311+G Computational.

C24-C26-C30-N46	C31-C33-C35-C36	C1-C2-C3-C4	C24-N45-N46-C30	C2-S28-C19-C21	C30-C31-C33-C35
-0.1	-179.7	-0.5	0.3	-59.1	179.1

Table 4. Calculated Dipole Moments Values for Bevacizumab Molecule using B3LYP/6-311+G Computational.

μ_x	μ_y	μ_z	μ_{tot}
-3.4467	-1.3144	0.6288	3.7420

Table 5. Calculated HOMO-LUMO Energy Gap Values for Bevacizumab Molecule using B3LYP/6-311+G Computational.

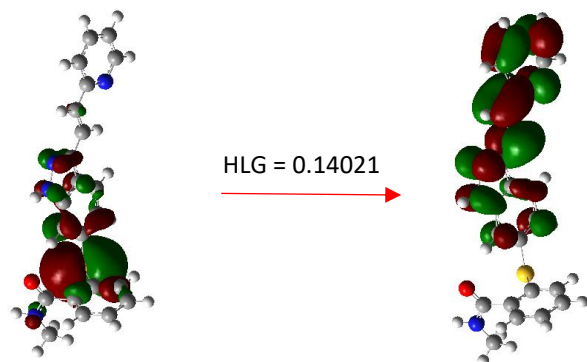| E_{HOMO} (eV)	HLG (eV)	E_{LUMO} (eV)
-0.20880	0.14021	-0.06859

HLG = 0.14021

Fig. 2. The molecular orbital shapes of the HOMO and LUMO of the Bevacizumab molecule at the B3LYP/6–311+G level.

IR Spectrum Vibrational Frequencies

The infrared (IR) spectrum, renowned for its exceptional ability to identify molecular characteristics and structures, is widely utilized across various fields including chemistry, physics, biochemistry, and pharmaceuticals. Within the displayed spectrum, the primary peak at 1633.6548 indicates the frequency of oscillations per second, located on the left side of the graph. Meanwhile, the value 683.632 on the right side represents the dielectric constant. Noteworthy is the presence of three distinct peaks within this IR spectrum.
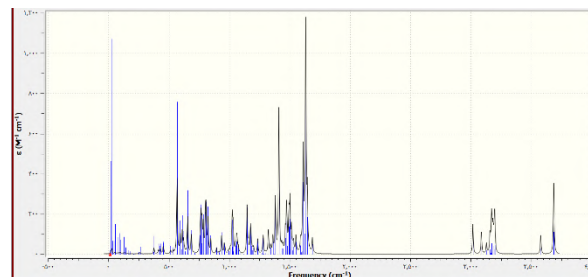

Fig 3. Vibrational Frequency in IR Spectrum for Bevacizumab Molecule at B3LYP/6–311+G Level. without encountering negative frequencies.

Exploring Bevacizumab Delivery Utilizing C60 Fullerene Nanocarriers: This research focuses on the use of C60 fullerene nanocarrier for transporting Bevacizumab, a crucial monoclonal antibody used in cancer treatment. This study provides valuable information on the ability of nanocarriers to boost therapeutic techniques in cancer treatment, presenting exciting opportunities for advancing oncology treatments.
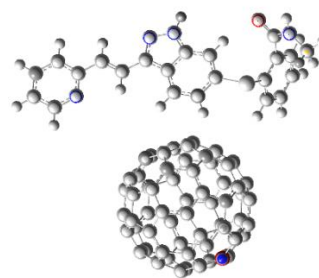

Fig. 4. The optimized structure of Bevacizumab and C60 at the B3LYP/6–311+G level.

Conclusions

In our study, we thoroughly examined the chemical characteristics of Bevacizumab and discovered its promising potential in transforming cancer treatment. Additionally, our research on using C60 fullerene nanocarriers to deliver Bevacizumab highlights exciting opportunities for improving therapeutic approaches in oncology. These results represent a major advancement in the realm of drug development, providing valuable information on how to enhance treatment options for cancer patients and leading the path to further progress in oncology care.

References

[1] Li, M. Y., & Kroetz, D. L. (2018b). Bevacizumab-induced hypertension: Clinical presentation and molecular understanding. Pharmacology & Therapeutics, 182,152–160.
[2] Ferrara, N., & Adamis, A. P. (2016). Ten years of anti-vascular endothelial growth factor therapy. Nature Reviews Drug Discovery, 15(6), 385–403.

22nd Iranian Chemistry Congress (ICC22)
Iranian Research Organization for Science and Technology (IROST)
13-15 May 2024

03231-97589

Quantum Calculations Investigation of the Ibandronate Drug

Hossein Shirani[a,b,*], Bahar Abolghasem[b]

Corresponding Author E-mail: hossein_shirani@iust.ac.ir
[a] Department of Chemistry, Iran University of Science and Technology, P.O. Box 16846-13114, Tehran, Iran.
[b] Department of Biotechnology, Faculty of Biological Sciences and Technology, University of Science and Culture, Tehran, Iran.

Abstract: The present study delves into the molecular characteristics of Ibandronate, investigating its molecular orbitals, dipole moments, atomic charges and structural parameters using the B3LYP/6-31+G theory. Through a detailed analysis, we explore the complex molecular features and pharmacological properties that underlie Ibandronate's potential efficacy as a treatment option.
Keywords: Ibandronate; HOMO-LUMO Gap; DFT; B3LYP/6-31+G

Introduction

Bisphosphonates stand as the cornerstone in managing hypercalcemia of malignancy and metastatic bone disease (MBD), alongside postmenopausal osteoporosis (PMO). Among them, Ibandronate emerges as a potent nitrogen-containing bisphosphonate, boasting proven efficacy in these arenas. Its robust therapeutic outcomes extend to PMO, corticosteroid-induced osteoporosis (CIO), and Paget's disease of the bone, promising enhanced clinical benefits with reduced dosing frequencies. Ibandronate's superior potency allows for less frequent administration, paving the way for innovative dosing regimens with sustained efficacy. Approved for postmenopausal osteoporosis treatment in numerous countries, Ibandronate's heightened efficacy permits extended dosing intervals, marking a paradigm shift in osteoporosis management. With Osteogenesis imperfecta (OI) - characterized by bone fragility and deformities - presenting significant physical disabilities, exploring Ibandronate's potential in mitigating its pathophysiological manifestations holds promise for novel therapeutic strategies [1-3].

Methods

In the initial stage, the molecular structure of Ibandronate was designed using GaussView software, followed by quantum mechanical calculations at the B3LYP/6–31+G theoretical level using Gaussian09 software.

Results and Discussion

Molecular calculations of the drug Ibandronate were performed using the GaussView software at the B3LYP/6–31+G theoretical level, and the structural parameters wer reported.Using the GaussView software, the molecular structure of interest was initially designed in this software (Fig.1).
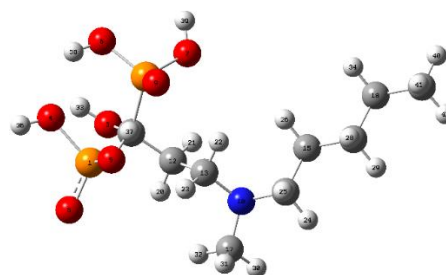

Fig. 1. The optimized structure of Ibandronate at the B3LYP/6–31+G level.

Table 1. Calculated Bond Length Values for Ibandronate Molecule using B3LYP/6-31+G Computational Method.

N10-C14	C12-C13	C11-P2	P1-O5	C16-C18	O5-H37
1.47759	1.54138	1.92731	1.70143	1.54002	1.01077

Table 2. Calculated Bond Angles Values for Ibandronate Molecule using B3LYP/6-31+G Computational.

O7-P2-O9	O4-P1-O8	C11-C12-C13	C14-N10-C17	C16-C18-C19	H34-C18-H35
116.9	113.5	116.8	113.8	113.1	106.2

Table 3. Calculated Dihedral Angle Values for Ibandronate Molecule using B3LYP/6-31+G Computational.

P2-C11-C12-C13	C15-C14-N10-C17	O4-P1-O8-O5	H38-O6-P2-O9	H40-H41-H42-C19	C14-C15-C16-C18
56.7	154.2	-120.4	-59.4	-37.7	179.9

Table 4. Calculated Dipole Moments Values for Ibandronate Molecule using B3LYP/6-31+G Computational.

μx	μy	μz	μtot
-4.0522	-1.1323	-0.2295	4.2137

Table 5. Calculated Mulliken Charge Values for Ibandronate Molecule using B3LYP/6-31+G Computational Method.

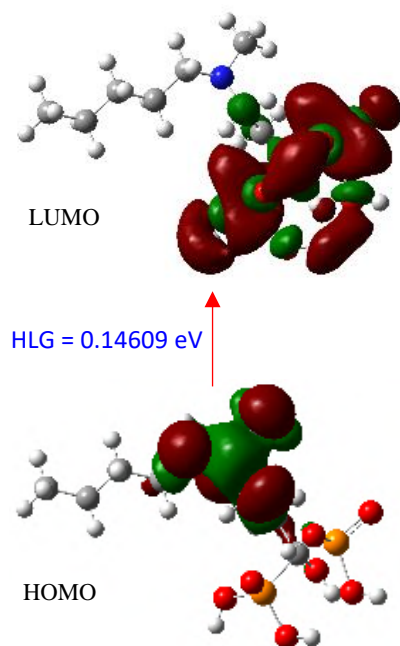| P1	P2	N10	C11	C12	C13
1.29	1.34	-0.44	-0.37	-0.24	-0.15

LUMO

HLG = 0.14609 eV

HOMO

Fig. 2. The molecular orbital shapes of the HOMO and LUMO of the Ibandronate molecule at the B3LYP/6–31+G level.

Table 6. Calculated HOMO-LUMO Energy Gap Values for Ibandronate Molecule using B3LYP/6-31+G Computational.

E_{HOMO}	HLG	E_{LUMO}
-0.20472	0.14609	-0.05863

Conclusions

Our comprehensive investigation into Ibandronate's chemical properties has elucidated its potential as a ground breaking development in the treatment of bone resorption diseases. Moreover, our exploration of C60 fullerene nanocarriers as a delivery system for Ibandronate presents exciting possibilities for enhanced therapeutic efficacy and improved patient outcomes. These findings represent a significant contribution to the field of bone health therapeutics, offering valuable insights for optimizing treatment strategies and paving the way for advancements in bone disease management through the utilization of novel nanocarrier technologies.

References

[1] Barrett, J., Worth, E., Bauss, F., & Epstein, S. (2004). Ibandronate: a clinical pharmacological and pharmacokinetic update. *The Journal of Clinical Pharmacology*, *44*(9), 951-965.

[2] Ralston SH, Thiébaud D, HerrmannZ, Steinhauer EU, ThurlimannB, Walls J, et al: Dose-response study of ibandronate in the treatment of cancer-associated hypercalcaemia. Br J Cancer 1997;75:295-300

[3] Cranney, A., Wells, G.A., Yetisir, E. *et al.* Ibandronate for the prevention of nonvertebral fractures: a pooled analysis of individual patient data. *Osteoporos Int* **20**, 291–297 (2009). https://doi.org/10.1007/s00198-008-0653-8

Quantum-mechanical DFT Investigation of the Budesonide Drug

Hossein Shirani[a,b,*], Bahar Abolghasem[b]

Corresponding Author E-mail: hossein_shirani@iust.ac.ir
[a] Department of Chemistry, Iran University of Science and Technology, P.O. Box 16846-13114, Tehran, Iran.
[b] Department of Biotechnology, Faculty of Biological Sciences and Technology, University of Science and Culture, Tehran, Iran.

Abstract: This study explores Budesonide's adsorption in simulated drug delivery systems via quantum mechanical calculations using the B3LYP/6-311+G computational method. Budesonide is crucial in treating COPD exacerbated by prevalent air pollution in Iran. Investigating its molecular interactions offers insights into enhancing therapeutic efficacy for COPD patients affected by environmental pollutants.
Keywords: Budesonide; Drug Delivery; HLG Gap; DFT; B3LYP/6-311+G

Introduction

Budesonide holds a significant position in respiratory medicine, offering a versatile approach to managing various pulmonary conditions. Its efficacy in asthma management, particularly in pediatric populations and recurrent wheezing, highlights its importance in diverse patient demographics. Furthermore, budesonide's role extends to chronic obstructive pulmonary disease (COPD), where its potent anti-inflammatory properties show promise in alleviating the inflammatory burden associated with the condition plus It has greater topical anti-inflammatory activity than many other glucocorticoids, but does not reduce cortisol levels. Against the backdrop of escalating COPD prevalence and the detrimental effects of air pollution, understanding budesonide's therapeutic potential becomes crucial, especially in regions like Iran. With Iran witnessing a concerning rise in COPD-related burden over the past two decades, budesonide emerges as a key player in addressing the evolving respiratory health landscape. As research continues to unfold its mechanisms of action and clinical applications, budesonide remains a cornerstone in the quest for improved respiratory health outcomes [1-4].

Methods

Initially, the molecular configuration of Budesonide was conceived through the utilization of GaussView software. Subsequently, quantum mechanical computations were performed at the B3LYP/6–311+G theoretical framework utilizing Gaussian09 software.

Results and Discussion

Molecular calculations of the drug Budesonide were performed using the GaussView software at the B3LYP/6–311+G theoretical level, and the structural parameters were reported. Using the GaussView software, the molecular structure of interest was initially designed in this software (see Fig. 1).
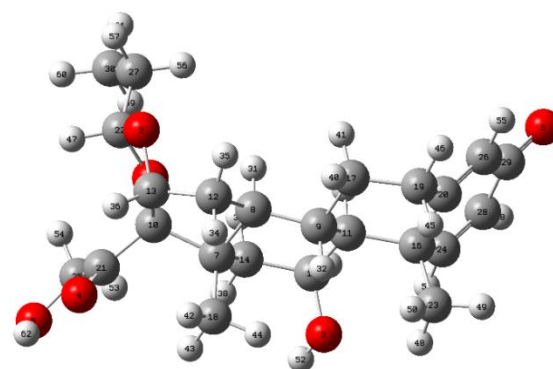

Fig. 1. The optimized structure of Budesonide at the B3LYP/6–311+G level.

Table 1. Calculated Bond Length Values for the Budesonide Molecule using the B3LYP/6-311+G Computational Method.

C10-O1	C21-C25	O3-C15	C20-C26	C7-C10	C25-O5
1.43067	1.52016	1.43621	1.34413	1.57885	1.40372

Table 2. Calculated Bond Angles Values for Budesonide Molecule using B3LYP/6-311+G Computational.

C20-C16-C24	C7-C10-C13	O1-C22-O2	H52-O3-C15	C7-C8-C12	C22-C27-C30
112.1	104.8	105.1	108.9	103.9	113.2

Table 3. Calculated Dihedral Angle Values for Budesonide Molecule using B3LYP/6-311+G Computational.

C19-C20-C26-C29	O1-C22-O2-C13	O4-C21-C25-H53	C7-C8-C9-C11	H40-C17-C9-H32	C20-C26-C29-C28
-177.3	-34.3	-127.1	58.5	-53.6	-0.7

Table 4. Calculated Dipole Moments Values for Budesonide Molecule Using B3LYP/6-311+G Computational.

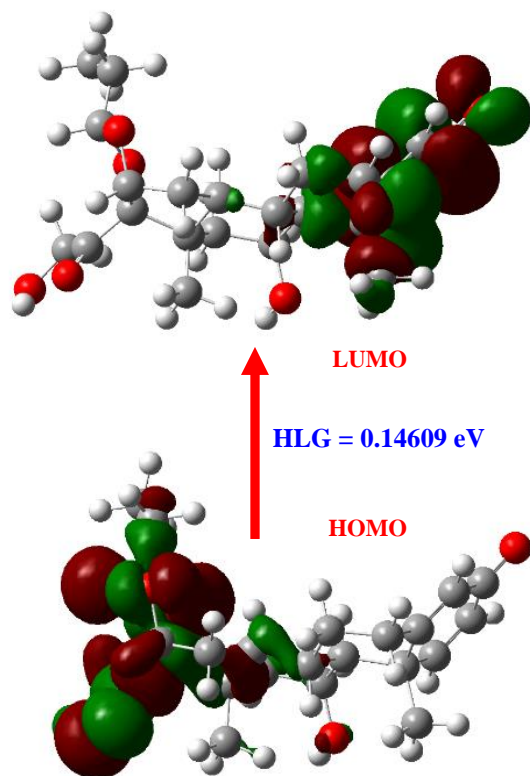| μ_x	μ_y	μ_z	μ_{tot}
-1.6350	-1.1176	0.1011	1.9831

LUMO

HLG = 0.14609 eV

HOMO

Fig. 2. The molecular orbital shapes of the HOMO and LUMO of the Budesonide molecule at the B3LYP/6–311+G level.

Table 5. Calculated Mulliken Charge Values for Budesonide Molecule using B3LYP/6-311+G Computational Method.

O2	C10	C12	C20	C30	H60
0.07	0.34	-0.73	0.52	-0.93	0.24

Table 6. Calculated HOMO-LUMO Energy Gap Values for Budesonide Molecule using B3LYP/6-311+G Computational.

EHOMO	HLG	ELUMO
-0.24796	0.18007	-0.06789

Conclusions

In our conversation regarding Budesonide, we are highlighting its crucial role in managing COPD exacerbated by environmental factors such as air pollution, which is a significant issue in areas like Iran. By utilizing quantum mechanical calculations, we have explored how Budesonide interacts in simulated drug delivery systems,

providing insights into possible methods for improving its therapeutic effectiveness. As we navigate the complexities of COPD treatment, Budesonide stands out as a vital tool in reducing the burden of this disease, offering promise for better outcomes for individuals worldwide. The structure of the Budesonide compound was simulated using Gaussian and View Gauss software, followed by structure optimization with B3LYP/6-311+G. The HOMO LUMO energy gap, crucial for understanding electronic and optical properties, was determined to be -0.14609 eV. The bond length and angle were also calculated to examine their impact on the molecule, along with analyzing the atomic charges within the compound.

References

[1] Spencer, C.M., McTavish, D. Budesonide. *Drugs* **50**, 854–872 (1995).

[2] 2.P.J. Barnes, S.D. Shapiro, R.A. Pauwels

[3] European Respiratory Journal 2003 22: 672-688; **DOI:** 10.1183/09031936.03.00040703

[4] Ko, F. W., & Hui, D. S. (2012). Air pollution and chronic obstructive pulmonary disease. *Respirology*, *17*(3), 395-401

[5] Hashemi, S. Y., Momenabadi, V., Faramarzi, A., & Kiani, A. (2020). Trends in burden of chronic obstructive pulmonary disease in Iran, 1995–2015: findings from the global burden of disease study. *Archives of Public Health*, *78*, 1-7

Quantum-mechanical DFT Calculation of the Memantine Drug

Hossein Shirani[a,b,*], Bahar Abolghasem[b]

Corresponding Author E -mail: hossein_shirani@iust.ac.ir
[a] Department of Chemistry, Iran University of Science and Technology, P.O. Box 16846-13114, Tehran, Iran.
[b] Department of Biotechnology, Faculty of Biological Sciences and Technology, University of Science and Culture, Tehran, Iran.

Abstract: Memantine is a ground-breaking innovation in managing Alzheimer's disease, as it targets NMDA receptors to combat cognitive decline. This research investigates the optimized structural features, atomic charges, dipole moments, electronic energies, and HOMO-LUMO gaps of Memantine through the DFT/B3LYP method with a 6-31+G basis set.
Keywords: Memantine; HOMO-LUMO Gap; DFT; B3LYP/6-31+G

Introduction

Memantine, a versatile drug employed in various neurological disorders, notably Alzheimer's disease, showcases a distinctive mode of action by antagonizing N-methyl-D-aspartate (NMDA) receptors. While NMDA receptor blockers like ketamine often evoke adverse effects, memantine's therapeutic efficacy stems from shared inhibitory pathways with ketamine, alongside unique actions. These differences, encompassing channel gating and receptor binding, significantly influence clinical outcomes, as modulation of NMDA receptor activity intricately regulates neuronal circuit excitability.

Functioning as a moderate-affinity, uncompetitive antagonist, memantine swiftly regulates calcium influx via NMDA receptors, offering a promising treatment avenue for moderate to severe Alzheimer's dementia. Its distinct pharmacokinetic profile and neuroprotective attributes make it a key contender in combating pathological NMDA receptor activation, preserving cognitive function in vivo. However, despite advancements in treating mild-to-moderate Alzheimer's disease, challenges persist in addressing its progressive stages, underscoring the urgent need for innovative therapeutic strategies.

Moreover, amidst the growing burden of neurological ailments, including Alzheimer's disease and migraine, memantine and its counterparts like ketamine emerge as potential anti-migraine agents. Given the gender-prevalent nature of migraines and the promising efficacy of glutamate receptor-targeting drugs, investigating memantine's role in migraine therapy warrants exploration. Hence, this article aims to delve into the therapeutic potential of memantine and ketamine as NMDA receptor antagonists, shedding light on their applications beyond Alzheimer's disease treatment [1-3]·

Methods

In the initial stage, the molecular structure of Memantine was designed using GaussView software, followed by quantum mechanical calculations at the B3LYP/6–31+G theoretical level using Gaussian09 software.

Results and Discussion

Molecular calculations of the drug Memantine were performed using the GaussView software at the B3LYP/6–31+G theoretical level, and the structural parameters were reported. Using the GaussView software, the molecular structure of interest was initially designed in this software (Fig. 1).
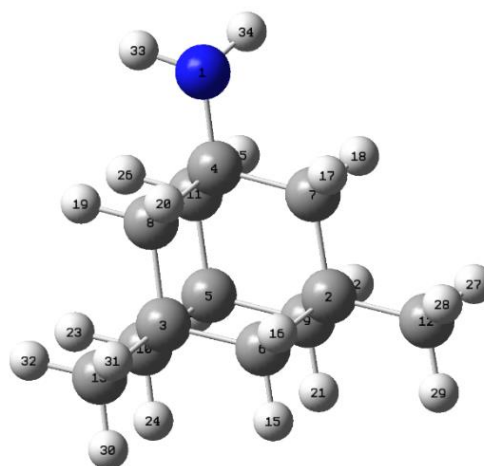

Fig. 1. The optimized structure of Memantine calculated at the B3LYP/6–31+G level.

Table 1. Calculated Bond Length Values for Memantine Molecule using B3LYP/6-31+G Computational Method.

N1-C4	C3-C6	C2-C9	C12-H28	C5-C10	C10-H24
1.47042	1.55284	1.55341	1.09742	1.54682	1.09959

Table 2. Calculated Bond Angles Values for Memantine Molecule using B3LYP/6-31+G Computational.

N1-C4-C8	C2-C5-C3	H31-C13-H30	C9-C2-C7	H15-C6-C3	H20-C8-H19
108.7	60.6	107.9	108.6	109.5	107.2

22nd Iranian Chemistry Congress (ICC22)
Iranian Research Organization for Science and
Technology (IROST)
13-15 May 2024

03231-97589

IROST

Table 3. Calculated Dihedral Angle Values for Memantine Molecule using B3LYP/6-31+G Computational.

H34-N1-C4-C8	C4-C8-C3-C13	C12-C2-C6-C3	C9-C5-C10-H23	H17-C7-C2-C12	C10-C3-C6-C18
174.5	179.7	179.6	-179.0	-58.7	-179.4

Table 4. Calculated Dipole Moments Values for Memantine Molecule using B3LYP/6-31+G Computational.

μx	μy	μz	μtot
-0.0122	-0.0031	1.4856	1.4856

Table 5. Calculated Mulliken Charge Values for Memantine Molecule using B3LYP/6-31+G Computational Method.

N1	C2	C10	C12	H20	H30
-0.69	0.03	-0.23	-0.39	0.13	0.12

LUMO

HLG = 0.27825 eV
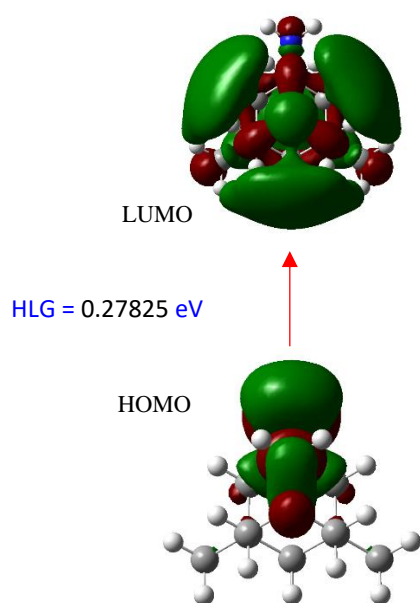
HOMO

Fig. 2. The molecular orbital shapes of the HOMO and LUMO of the Memantine molecule at the B3LYP/6–31+G level.

Table 6. Calculated HOMO-LUMO Energy Gap Values for Memantine Molecule Using B3LYP/6-31+G Computational.

EHOMO	HLG	ELUMO
-0.21297	0.27825	0.06528

Conclusions

In summary, memantine shines brightly as a beacon of hope in the field of neurological treatment. Its distinct way of working, focusing on NMDA receptors, has transformed the way Alzheimer's disease is managed. Not only that, but its potential uses in treating migraines suggest a wider range of neurological disorders it could help with. With ongoing research revealing more about how it works and its therapeutic possibilities, memantine remains at the forefront of cutting-edge treatments, promising better outcomes and improved quality of life for patients worldwide. We delve into the optimized structural characteristics, atomic charges, dipole moments, electronic energies, and HOMO-LUMO gaps of Memantine using the DFT/B3LYP method with a 6-311+G** basis set.

References

[1] Robinson, D.M., Keating, G.M. Memantine. *Drugs* **66**, 1515–1534 (2006).

[2] Reisberg, (2003). Memantine in moderate-to-severe Alzheimer's disease. *New England Journal of Medicine*, *348*(14), 1333-1341.

[3] Podkowa, K. (2023). The NMDA receptor antagonists memantine and ketamine as anti-migraine agents. *Naunyn-Schmiedeberg's Archives of Pharmacology*, *396*(7), 1371-1398.

22nd Iranian Chemistry Congress (ICC22)
Iranian Research Organization for Science and Technology (IROST)
13-15 May 2024

03231-97589

ISC

IROST

Biological and thermodynamic Studies of Schiff base Vanadium Complexes

Sheida Esmaielzadeh

Corresponding Author E-mail: esmaielzadehsheida@yahoo.com

Department of Chemistry, Darab branch, Islamic Azad University, Darab, Iran.

Department of Applied Researches, Chemical, Petroleum & Polymer Engineering Research Center, Shiraz branch, Islamic Azad University, Shiraz, Iran.

Abstract: The formation constants and free energies of some novel Schiff base vanadium (IV) complexes were measured spectrophotometrically, at constant ionic strength at 25˚C in DMF solvent. The complexes were tested against bacterial species. The results revealed that the vanadium complexes are more potent against the microbes than the parent ligand.

Keywords: Schiff base vanadium (IV) complexes; Formation constants; Antibacterial activity.

Introduction

Interest in vanadium coordination chemistry over the past decade has been increasing because of its biological importance and its catalytic abilities. Oxovanadium (IV) metal complexes with Schiff bases derived from primary amine and carbonyl precursors drew the interest of many workers based on their ability to insert oxygen to organic substance, in several biological processes, such as glycogen metabolism and insulin mimicking in vitro and in vivo has passed phase I and II clinical tests, demonstrating the usability of coordinating compounds of vanadium for the treatment of diabetes mellitus in humans [1,2]. The vanadium complexes increased the performance of known reactions such as the catalytic oxidative halogenation of organic compounds, epoxidation, oxidation of alcohols to aldehydes and ketones [3,4] has stimulated the study of coordination chemistry of vanadium with multidentate ligands. Schiff base ligands containing oxygen and nitrogen donors have been of interest for many years, because of the versatility of their steric and electronic properties, which can be modified by choosing appropriate amine and ring substitutes

Experimental Section

The formation constants measurements were carried out by spectrophotometric titration at constant ionic strength 0/1 M ($NaClO_4$) at 25 °C (±0/1°C). UV-Vis spectra were recorded in the range 250-700 nm about 5 minutes after each addition. The in vitro antibacterial activities were performed the synthesized compounds against some bacteria. Antibacterial activity of the Schiff base ligand and their complexes were screened against E.Coli and S.Aureus following the published methods using disc diffusion technique [5].

Results and Discussion

The formation constants, K_f, were calculated using SQUAD computer program, designed to calculate the best values for the formation by employing a non-linear, least-squares approach. Also, the free energy change, $\Delta G°$, of the complexes were determined by $\Delta G° = -RT \ln K_f$. The electronic effect of the para substituented Schiff base ligand plays important role in stability and reactivity of their complexes. The formation constants for VO[(cd3-, 4-, 5-OMesalpd complexes has the following trend: cd5OMesalpd > cd3OMesalpd > cd4OMesalpd
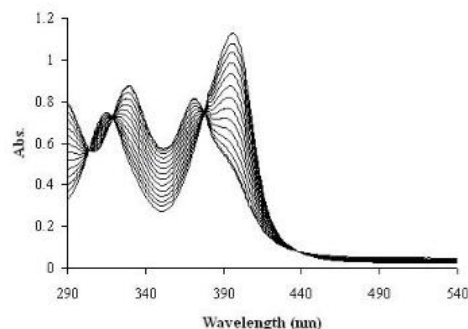

Fig.1: The variation of the electronic spectra of [H_2 cd5OMesalpd] with VO(IV) acetylacetonate at 25°C in DMF.

The results concerning in vitro antibacterial investigation of the Schiff base ligands and their VO (IV) complexes (Table 1) show a remarkable inhibitor activity against pathogenic bacterial species of Gram positive and Gram negative bacteria.

Table1: Antibacterial screening results

Compounds	E. coli	S. aureus
H_2 cd3-OMesalpd	22	21
H_2 cd4-OMesalpd	20	20

22nd Iranian Chemistry Congress (ICC22)
Iranian Research Organization for Science and Technology (IROST)
13-15 May 2024

03231-97589

Compounds	E. coli	S. aureus
H_2 cd5-OMesalpd	17	20
[VO(cd3-OMesalpd)]	29	26
[VO(cd4-OMesalpd)]	26	23
[VO(cd5-OMesalpd)]	28	23
tetracycline	32	34

Conclusions

The use of UV-Vis spectroscopy enabled us to determine the formation constant and the free energy data formation for the unsymmetrical Schiff base ligands (H_2 cd3-,4-,5-OMesalpd) as donor and VO(IV) ion as acceptor. The following conclusion have been done: On the bases of the effects of electronic and steric properties of methoxy group on the formation constant of unsymmetrical Schiff base complexes follows the sequence: [VO(cd5-OMesalpd)] > [VO(cd3-OMesalpd)] > [VO(cd4-OMesalpd)]. All the schiff base ligands and their VO(VI) complexes were tested for their antibacterial activity in vitro against the Gram positive bacteria (S.aureus) and Gram negative bacteria (E.coli) indicate that the metal complexes are more biologically active than the ligands.

References

[1] Hashmi, K., Gupta, S., Siddique, A., Khan, T., & Joshi, S. (2023). Medicinal applications of vanadium complexes with Schiff bases. Journal of Trace Elements in Medicine and Biology, 127245. https://doi.org/10.1016/j.jtemb.2023.127245

[2] Hasan, M. A., Rahman, H., Haque, M. M., & Islam, M. N. (2024). Oxovanadium (IV) Complexes of α-Amino Acid Schiff Bases and Polypyridyl Ligands: Synthesis, Characterization and Antimicrobial Activity. Asian Journal of Chemical Sciences, 14(2), 7-20. https://doi.org/10.9734/ajocs/2024/v14i2290

[3] Bendia, S., Benabid, W., Bourzami, R., & Ouari, K. (2023). Spectroscopic characterization of a mononuclear oxovanadium (IV) Schiff base complex. Oxidation catalysis applications and antibacterial activities. Journal of Molecular Structure, 1281, 135131. https://doi.org/10.1016/j.molstruc.2023.135131.

[4] Romanowski, G., Budka, J., & Inkielewicz-Stepniak, I. (2024). Oxidovanadium (V) complexes with chiral tetradentate Schiff bases: Synthesis, spectroscopic characterization, catalytic and biological activity. Journal of Molecular Structure, 137929. https://doi.org/10.1016/j.molstruc.2024.137929

[5] Keshtkar, N., Zamanpour, A., & Esmaielzadeh, S. (2022). Bioactive Ni (II), Cu (II) and Zn (II) complexes with an N3 functionalized Schiff base ligand: Synthesis, structural elucidation, thermodynamic and DFT calculation studies. Inorganica Chimica Acta, 541, 121083. https://doi.org/10.1016/j.ica.2022.121083

A Quantum Mechanical Investigation on Vortioxetine Drug

Hossein Shirani[a,b,*], Hamid Kianpour[b]

Corresponding Author E-mail: hossein_shirani@iust.ac.ir
[a] Department of Chemistry, Iran University of Science and Technology, P.O. Box 16846-13114, Tehran, Iran.
[b] Department of Microbiology, Faculty of Biological Sciences and Technology, University of Science and Culture, Tehran, Iran.

Abstract: In our study, we investigate the potential of Vortioxetine for treating major depressive disorder through an electronic structural analysis. Using Density Functional Theory (DFT) at the B3LYP/6-311+G level, we analyze the molecular structure to uncover its chemical properties. By examining structural parameters, molecular orbital energies, and the HOMO-LUMO energy gap, we highlight the drug-like qualities of Vortioxetine, enhancing our knowledge and aiding in the search for new medications
Keywords: Vortioxetine; DFT; HOMO-LUMO Gap; B3LYP/6-311+G

Introduction

Major depressive disorder (MDD), also known as clinical depression, is a mental health condition characterized by persistent feelings of sadness, loss of interest in activities, fatigue, and a sense of worthlessness [1]. It affects approximately 3.44% of the global population, making it a common psychiatric disorder with significant impacts on quality of life, increased risk of suicide, and societal burden. Treatment for MDD typically involves a combination of medication and therapy [2]. Selective serotonin reuptake inhibitors (SSRIs) are often prescribed as a first-line treatment due to their relatively low side effect profile. However, for many patients, a combination of medication and therapy does not guarantee long-term relief, with up to 40% experiencing a relapse within a year of achieving remission [3].

Vortioxetine, a novel antidepressant, offers a different approach to treating depression by targeting multiple pathways involved in the disorder. Clinical trials have shown that vortioxetine effectively improves symptoms of depression, response rates, and cognitive function compared to a placebo. Additionally, vortioxetine has demonstrated benefits for a wider range of patients, including those with comorbid anxiety disorders, heart disease, diabetes, and older adults [4]. In conclusion, vortioxetine's unique mechanism of action and broad efficacy make it a promising treatment option for individuals with major depressive disorder who have not responded well to traditional medications or therapies [5].

Methods

At the outset, the molecular composition of Vortioxetine was meticulously crafted with the aid of GaussView software, before delving into intricate quantum mechanical computations at the B3LYP/6–311+G theoretical level employing Gaussian09 software.

Results and Discussion

Computational modeling of the medication Vortioxetine was conducted through the utilization of GaussView software at the B3LYP/6–311+G theoretical method, with the subsequent presentation of structural data. The molecular structure of interest was created in GaussView software (Fig.1) to facilitate the analysis.
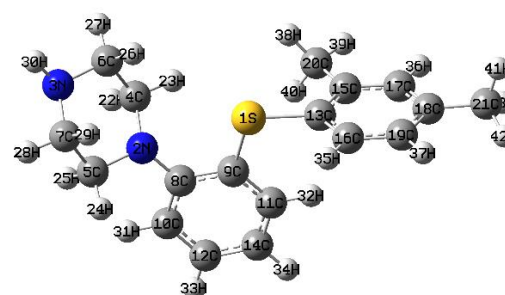

Fig. 1. The calculated optimized structure of Vortioxetine at the B3LYP/6–311+G level.

The thermodynamic properties for the molecular structure of Vortioxetine have been determined at the B3LYP/6–311+G computational level. The calculated heat of formation value is found to be -757295.5065 kcal/mol. Tables 1 to 3 showcase the structural parameters of Vortioxetine. Moreover, Tables 4 and 5 display the calculated dipole moments (Debye) Values and HOMO-LUMO energy for the Vortioxetine molecule, obtained using the B3LYP/6-311+G** computational method, respectively.

Table 1. Calculated Bond Length Values for Vortioxetine Molecule using B3LYP/6-311+G Computational Method.

N3-C7	N2-C8	S1-C9	S1-C13	C15-C20	C13-C16
1.47118	1.42748	1.86312	1.85620	1.50998	1.39738

22nd Iranian Chemistry Congress (ICC22)
Iranian Research Organization for Science and
Technology (IROST)
13-15 May 2024

03231-97589

IROST

Table 2. Calculated Bond Angles Values for Vortioxetine Molecule using B3LYP/6-311+G Computational.

C6-N3-C7	C5-N2-C8	C11-C9-S1	C9-S1-C13	S1-C13-C15	C18-C19-C16
113.2	117.9	122.5	102.2	121.6	120.4

Table 3. Calculated Dihedral Angle Values for Vortioxetine Molecule using B3LYP/6-311+G Computational.

C4-C6-N3-C7	C5-N2-C8-C10	C12-C14-C11-C9	C9-S1-C13-C16	S1-C13-C16-C19	C20-C15-C17-C18
58.1	33	-0.2	-101.2	-176.6	179.6

Table 4. Calculated Dipole Moments Values for Vortioxetine Molecule using B3LYP/6-311+G Computational.

μ_x	μ_y	μ_z	μ_{tot}
1.2300	-0.1145	0.2344	1.2573

Table 5. Calculated HOMO-LUMO Energy Gap Values for Vortioxetine Molecule using B3LYP/6-311+G Computational.

E_{HOMO}	HLG	E_{LUMO}
-0.20112	0.17636	-0.02476

HOMO

HLG = 0. 17636 eV
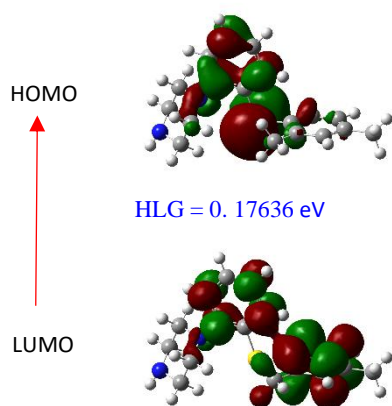
LUMO

Fig. 2. The molecular orbital shapes of the HOMO and LUMO of the Vortioxetine molecule at the B3LYP/6–311+G level.

Conclusions

Our research delved into the chemical characteristics of Vortioxetine through advanced quantum mechanical calculations, shedding light on its potential for treating major depressive disorder. Utilizing Gaussian and Gauss View software, we initially modeled the structure of Vortioxetine, followed by optimization using the B3LYP/6-311+G method. Through these calculations, we determined both three-dimensional dipole moments and the total electric dipole vector, which amounted to 1.26 Debye. The crucial HOMO-LUMO energy gap, which influences electronic, optical, and redox properties, was found to be -0.18 eV. Furthermore, we investigated thermodynamic values, the impact of bond lengths on molecular behavior, and various structural parameters using the B3LYP/6-311+G method. We also analyzed atomic charges, bond angles, and lengths, as well as drug-nanoparticle interactions for targeted drug delivery applications. Ultimately, the optimization of the drug molecule resulted in the most favorable outcome. In this study, we delve into the quantum mechanical aspects of Vortioxetine, a fascinating compound. By conducting thorough electronic and structural investigations, we aim to gain a deeper understanding of its properties.

References

[1] Uher R, Payne JL, Pavlova B, Perlis RH. Major depressive disorder in DSM-5: implications for clinical practice and research of changes from DSM-IV. Depress Anxiety.(2014)31:459–71.
https://doi.org/10.1002%2Fda.22217
[2] Institute for Health Metrics and Evaluation. GBD 2019 Cause and Risk Summary: Depressive Disorders 2022. Seattle, WA: IHME; (2020).
[3] Daly EJ, Trivedi MH, Wisniewski SR, Nierenberg AA, Gaynes BN, Warden D, et al.. Health-related quality of life in depression: a STAR*D report. Ann Clin Psychiatry. (2010) 22:43–55.
[4] Qaseem A, Barry MJ, Kansagara D. Nonpharmacologic versus pharmacologic treatment of adult patients with major depressive disorder: a clinical practice guideline from the American College of Physicians. Ann Intern Med. (2016)164:350–9. https://doi.org/10.7326%2FM15-2570
[5] Rouillon F, Gorwood P. The use of lithium to augment antidepressant medication. J Clin Psychiatry. (1998) 59:32–9.

22nd Iranian Chemistry Congress (ICC22)
Iranian Research Organization for Science and Technology (IROST)
13-15 May 2024

03231-97589

IROST

Preparation of Copper(Ⅱ) Complex Stabilized on Magnetic Iron Nanoparticles as a New and Recyclable Catalyst in One-Pot Preparation of Aminonaphthoquinone Compounds

Sara Shafaati[a], Javad Safaei-Ghomi [*a], Zahra Elyasi[b]

Corresponding Author E-mail : safaei@kashanu.ac.ir

[a] Department of Organic Chemistry, Faculty of Chemistry, University of Kashan, Kashan, 51167, Iran.
[b] Department of Chemistry, Qom Branch, Islamic Azad University, Qom, Iran.

Abstract: Regarding the signifcance of medicinal and pharmacological sciences, we explored one-pot multicomponent reaction of aromatic aldehydes, aryl amines and, 2-hydroxynaphthoquinone in the presence of [Fe_3O_4/EDA]Co(II) as a novel, stable and strong catalyst. The remarkable features of this approach are good to excellent yields (90–99%), short reaction times, low catalyst loading, reusability and stability of the catalyst. The prepared [Fe_3O_4/EDA]Co(II)was identifed via XRD, EDS, and FT-IR techniques.

Keywords: Multicomponent Reaction; New Catalyst; Aminonaphthoquinone

Introduction

Magnetic nanoparticles, which are composed of a magnetic core chemistry such as Fe_3O_4 or γ-Fe_2O_3, are typically defined by their size range of 1 nm to 100 nm in at least one dimension [1]. In recent years, there has been significant interest in magnetic micro/nanocomposites due to their unique physical properties that offer potential applications across various fields, including but not limited to magnetic separation, chemical sensors, data storage, catalysis, biomedicine/biotechnology, environmental remediation, and solar cells [2]. The practical and potential usefulness of these nanoparticles is largely attributed to their small size and high surface area to volume ratio [3]. Naphthoquinone compounds have garnered significant attention due to their various biological features such as fluorescence behavior, molluscicidal, antitumor, antifungal, and antibacterial activities. Incorporating nitrogen atom-containing functional groups, such as amino group or nitrogen atom, into the naphthoquinone structure has been shown to improve its anticancer, molluscicidal, and antibacterial activities [4-5]. In this research, for the first time, a copper(II) complex immobilized on magnetic iron nanoparticles was prepared and characterized using various spectroscopic techniques including FTIR, EDX, and XRD analysis. Another goal of this research work is the utilization of the synthesized structure as a new catalyst in organic reactions. However, it is noteworthy that the use of green and environmentally friendly reactions with minimal environmental impact and achieving a suitable and recyclable catalyst are the main objectives of this research.

Experimental Section

1.1. Preparation of Fe_3O_4 nanostructures functionalized with amine groups

To begin, anhydrous sodium acetate, $FeCl_3\cdot6H_2O$, and ethylenediamine were added to a three-necked flask containing glycol while being vigorously mechanically stirred. As the temperature reached 180°C, the color of the reaction system changed from yellow to red and eventually to deep black. After being stirred for 7 hours at 180°C, the amine-functionalized magnetite Fe_3O_4 was separated from the solution using a magnet and washed with distilled water and alcohol multiple times. The resulting magnetite was then dried at 50°C in an oven.

2.2. Synthesis of [Fe_3O_4/EDA]Co(II)

In the last stage, the Fe_3O_4 nanostructures material containing 0.01% weight of $CoCl_2$ was mixed with 0.1 g and reacted in absolute ethanol at room temperature for a period of 24 hours. The resulting catalyst was then carefully washed with ethanol and deionized water before being dried at room temperature for 24 hours to obtain the [Fe_3O_4/EDA]Co(II) catalyst.

2.3. General procedure for the synthesis of aminonaphthoquinone derivatives

Aromatic aldehyde (1.0 mmol), lawsone (1.0 mmol), aryl amine (1.0 mmol), and catalyst (1.0 mg) was completely mixed in a round bottom flask at room temperature under continuous stirring. The progress of the reaction was followed by thin layer chromatography (TLC). After cooling the reaction, the precipitate was separated and crystallized using hot ethanol.

22nd Iranian Chemistry Congress (ICC22)
Iranian Research Organization for Science and
Technology (IROST)
13-15 May 2024

03231-97589

IROST

Results and Discussion

The FT-IR spectra of Fe_3O_4 nanostructures functionalized with amine are presented in Figure 1. The Fe-O vibration absorption peak was observed at 588 cm^{-1}, indicating the presence of Fe_3O_4. The bands at 892 cm^{-1}, 1563 cm^{-1}, and 1366 were attributed to ethylenediamine as they were absent in the unfunctionalized Fe_3O_4. Therefore, it can be concluded that the amine-functionalization of Fe_3O_4 nanostructures was successful.
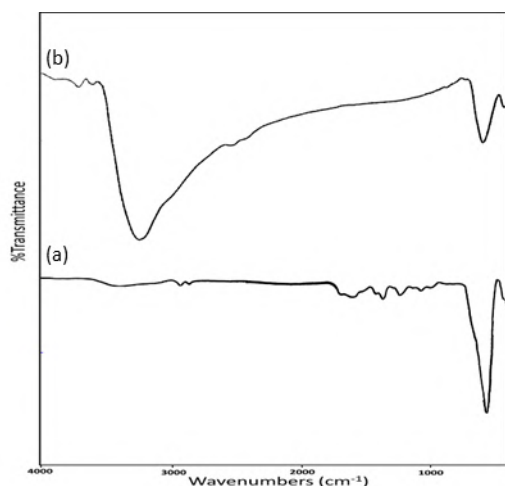
Fig.1: FT-IR spectra of the Fe_3O_4(a) and amine-functionalization of Fe_3O_4 nanostructures (b) .

Elt	Line	w%
C	Ka	1.12
N	Ka	0.36
O	Ka	7.62
Fe	Ka	90.41
Co	Ka	0.49
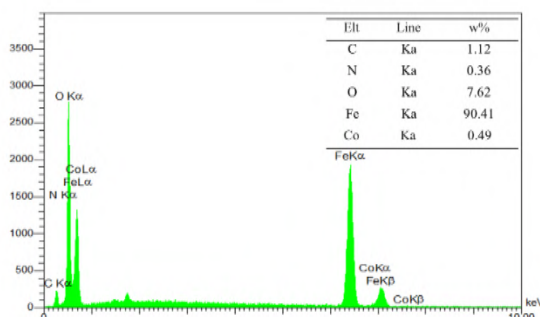
Fig.2: EDX analysis of the catalyst [Fe_3O_4/EDA]Co(II).

Fig. 2. shows the EDX analysis of the suggested catalyst, with all lines attributed to C, N, Fe,O and Co elements in the catalyst [Fe_3O_4/EDA]Co(II). The XRD analysis was used to determine the phase structure and purity of the Fe_3O_4 spheres that were prepared. Figure 3 shows a typical XRD pattern of the as-prepared Fe_3O_4 nanostructures. All the diffraction peaks were identified as pure Fe_3O_4, which matches the literature value. No impurity phase diffraction peaks were observed, indicating that the sample was pure.
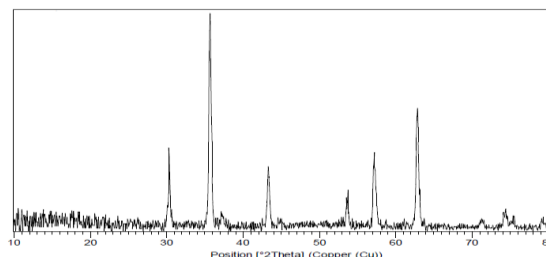
Fig. 3: XRD patterns of amine-modified Fe_3O_4 nanostructures.

Conclusions

To summarize, we have created a highly efficient and durable catalyst called [Fe_3O_4/EDA]Co(II) for the one-step production of aminonaphthoquinone derivatives. This was achieved by combining aromatic aldehydes, aryl amines, and 2-hydroxynaphthoquinone under optimized conditions. The heterogeneous catalyst was characterized using various spectroscopy techniques such XRD, EDS, and FT-IR analysis. This process offers numerous benefits, including high yields of aminonaphthoquinones, short reaction times, an environmentally friendly process, and low catalyst loading. As a result, this method provides an effective and eco-friendly approach to synthesizing aminonaphthoquinones under mild reaction conditions.

References

[1] Liu, Sh., Yu, B., Wang, s., Shen, y., & Cong, H. (2020). Preparation, surface functionalization and application of Fe_3O_4 magnetic nanoparticles. Advances in Colloid and Interface Science, 281, 102165. https://doi.org/10.1016/j.cis.2020.102165.

[2] Heng, T., Ze, W., Wen-sheng, T., Jian-guo, Q., & Xiao-Hong, T. (2018). Synthesis of magnetic Fe_3O_4 micro/nanospheres in organic solvent. Applied Biomaterials & Functional Materials, 16(1S), 26-31. https://doi.org/10.1177/228080001775332.

[3] Wierucka, M., & Biziuk M. (2014). Application of magnetic nano-particles for magnetic solid-phase extraction in preparing biological, environmental and food samples, TrAC Trends in Analytical Chemistry, 59(2), 50–58. https://doi.org/10.1016/j.trac.2014.04.007.

[4] Tandon,V.K., Yadav, D.B., Singh, R.V., Vaish, M., Chaturvedi, A.K., & Shukla, P.K. (2005). Synthesis and biological evaluation of novel 1,4-naphthoquinone derivatives as antibacterial and antiviral, agentsBioorganic & Medicinal Chemistry Letters, 15(14), 3463-3466. https://doi.org/10.1016/j.bmcl.2005.04.075.

[5] Mahnaz Mirheidari, M., & Safa ei-Ghomi, J., (2021). Design, synthesis, and catalytic performance of modified graphene oxide based on a cobalt complex as a heterogenous catalyst for the preparation of aminonaphthoquinone derivatives, RSC Advances, 11, 17108. http:// doi.org /10.1039/d1ra01790j.

22nd Iranian Chemistry Congress (ICC22)
Iranian Research Organization for Science and Technology (IROST)
13-15 May 2024

03231-97589

IROST

Analysis of phenolic acids in juice and waste of *Berberis integerrima*

Saeed Mollaei*, Solmaz Karimi Kahran

Corresponding Author E-mail: s.mollaei@azaruniv.ac.ir

Phytochemical Laboratory, Department of Chemistry, Faculty of Sciences, Azarbaijan Shahid Madani University, Tabriz, Iran.

Abstract: *Berberis integerrima* belongs to the Berberidaceae family, and has many pharmacological activities such as hepatoprotective, antimicrobial, antihypertensive, antioxidant, and antidiabetic effects. In this study, phenolic acid constituents of the juice and waste of *Berberis* integerrima were studied. The results indicated that the main phenolic acids were rosmarinic acid (1446.1 and 339.5 mg/10g), para-coumaric acid (151.4 and 73.1 mg/10g), and protocatechuic acid (51.3 and 59.4 mg/10g) in the juice and waste, respectively. So, these sample can exhibit high antioxidant properties s because of the high amounts of these compounds.

Keywords: Antioxidant; *Berberis*; Rosmarinic acid; Waste

Introduction

Berberis integerrima, commonly known as barberry, belongs to the Berberidaceae family. It is considered a good source of natural antioxidants, and it has been investigated concerning cardiovascular risk factors due to their richness in berberine and anthocyanins in experimental studies. In traditional medicine, this plant was used to cure diseases such as infectious fevers, typhus and diarrhoea. The studies indicate biological activities including hepatoprotective, antimicrobial, antihypertensive, and antioxidant effects [1].

Phenolic compounds are the secondary metabolites which distributed in the plants. They are derived from pentose phosphate, shikimate, and phenylpropanoid pathways in plants. They can act as nutrient uptake, protein synthesis, enzyme activity, photosynthesis, structural components, and allelopathy. They have many biological activities such as antioxidant, antibacterial, anticancer. The structure of phenolic compounds is related to their radical-scavenging and metal-chelating activity [2, 3].

Up to our knowledge, the phenolic acid content of juice and waste of Berberis integerrima was not studied. So, the present work aimed to analysis the phenolic acids content in juice and waste of Berberis integerrima.

Experimental Section

Plant materials

Berberis integerrima was gathered from its wild habitat in June 2022 in the Northen regions of Gilan province, Iran.

Extraction process

For extraction of the juice from seeds, cold pressing was used. 100 grams of the seeds were pressed with a 6YZ180 automatic hydraulic press (Zhengzhou Bafang Machinery and Equipment Co., Ltd., Zhengzhou, China) at 25°C and 10 MPa for 0.5 h to obtain the juice.

For the extraction of phenolic compounds from waste, 20 mL of ethanol 80% (0.1% acetic acid) was added to 20 grams of waste, and stirred for 20 hours. The sample was centrifuged for 10 minutes at 1000 rpm. Finally, the supernatant solution was dried at 60°C.

HPLC analysis

HPLC was used for the analysis of phenolic acids (free, esterified and bonded). The applied column was C18 (250 mm × 0.46 mm, 5 μm). Moreover, methanol and water (0.1% trifluoroacetic was used as mobile phase, and the flow rate was adjusted at 0.5 mL/min. The injection volume was 100 μL, and UV was applied as detector, which was adjusted at a wavelength of 275 nm. The phenolic acids was quantified using the regression equation derived from standards, and was expressed as mg per gram of dry plant (mg/g DW).

Results and Discussion

Polyphenols are compounds which are found inside the plant cells and can have numerous biological properties. Some of these properties include anti-cancer, anti-diabetes, anti-inflammatory, antimicrobial, antioxidants, etc [4]. In this study, the phenolic acids contents of the juice and waste of *Berberis integerrima* were investigated. Figures 1 and 2 indicate the HPLC chromatograms of Berberis integerrima juice and waste, respectively. Also, Table 1 shows the amount of phenolic acids in the samples.
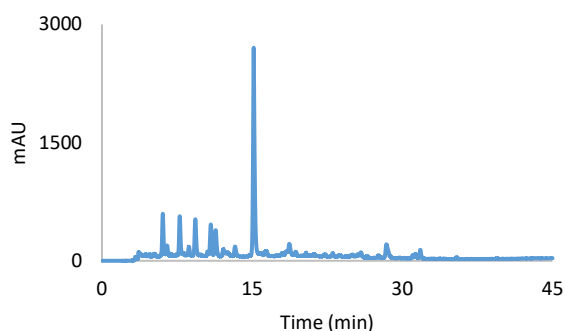
22nd Iranian Chemistry Congress (ICC22)
Iranian Research Organization for Science and Technology (IROST)
13-15 May 2024

03231-97589

IROST

Fig. 1: HPLC chromatogram of phenolic acids obttained from the *Berberis integerrima* juice
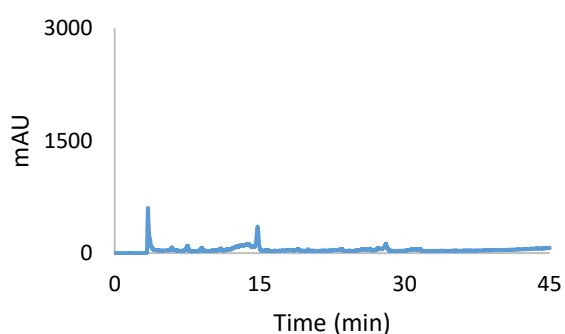

Fig. 2: HPLC chromatogram of phenolic acids obttained from the *Berberis integerrima* waste

As shown, the main phenolic acids in *Berberis integerrima* juice were rosmarinic acid, para-coumaric acid, and protocatechuic acid with the amounts of 1446.1, 151.4, and 51.3 mg/10g, respectively. The analysis of *Berberis integerrima* waste extract indicated that rosmarinic acid (339.5 mg/g DW), para-coumaric acid (73.1 mg/g DW), and protocatechuic acid (59.4 mg/g DW) were the main phenolic acids.

Table 1: The amount of phenolic compounds in juice and waste of *Berberis integerrima* (mg/10g)

Compounds	Juice	Waste
Gallic acid	24.9	59.4
Protocatechuic acid	51.3	9.2
Rosmarinic acid	1446.1	339.5
para-Hydroxybenzoic acid	15.5	1.9
Vanillic acid	10.3	7.0
Caffeic acid	12.2	11.6
para-Coumaric acid	151.4	73.1
Ferulic acid	11.6	2.5
meta-Coumaric acid	10.0	12.0
Salicylic acid	11.3	14.7
Cinnamic acid	2.7	0.7
Sum	1747.3	531.6

As shown rosmarinic acid was main compounds in all samples. This compounds, a caffeic acid ester, has many biological properties including antimicrobial properties, anti-cancer properties, anti-inflammatory properties, antioxidant properties, antidepressant properties, and anti-aging properties. This compound has high antioxidant properties and can be used as food pigments in the food industry to prevent food oxidation, storage, and stability [5, 6]. Therefore, based on the previous studies and our results, it can be concluded that *Berberis integerrima* juice and waste can exhibit high antioxidant properties because of the high level of rosmarinic acid.

Conclusions

The results of this study showed that rosmarinic acid, para-coumaric acid, and protocatechuic acid were the main phenolic acids in the juice and waste of *Berberis integerrima*, and these sample can exhibit high antioxidant properties s because of the high levels of these compounds.

References

[1] Behrad, Z., Sefidkon, F., Ghasemzadeh, H., Rezadoost, H., & Balandary, A. (2023). Determination of phenolic compounds and antioxidant activities of 55 Iranian Berberis genotypes. Journal of Medicinal plants and By-product, 12(2), 181-189.

[2] Lin, D., Xiao, M., Zhao, J., Li, Z., Xing, B., Li, X., ... & Chen, S. (2016). An overview of plant phenolic compounds and their importance in human nutrition and management of type 2 diabetes. Molecules, 21(10), 1374.

[3] Al Mamari, H. H. (2021). Phenolic compounds: Classification, chemistry, and updated techniques of analysis and synthesis. Phenolic Compounds: Chemistry, Synthesis, Diversity, Non-Conventional Industrial, Pharmaceutical and Therapeutic Applications, 73-94.

[4] Sauceda, A. E. Q., Sáyago-Ayerdi, S. G., Ayala-Zavala, J. F., Wall-Medrano, A., de la Rosa*, L. A., González-Aguilar*, G. A., & Álvarez-Parrilla, E. (2017). Biological actions of phenolic compounds. Fruit and Vegetable Phytochemicals: Chemistry and Human Health, 2nd Edition, 125-138.

[5] Noor, S., Mohammad, T., Rub, M. A., Raza, A., Azum, N., Yadav, D. K., ... & Asiri, A. M. (2022). Biomedical features and therapeutic potential of rosmarinic acid. *Archives of Pharmacal Research*, *45*(4), 205-228.

[6] Kernou, O. N., Azzouz, Z., Madani, K., & Rijo, P. (2023). Application of rosmarinic acid with its derivatives in the treatment of microbial pathogens. *Molecules*, *28*(10), 4243.

Conversional carbon dioxide to cyclic carbonates via mn₂o₃ hollow sphere

Marziyeh Alaei Faradonbeh, Reza Khalifeh[*], Nasrin Zarei, Maryam Rajabzadeh

Corresponding Author E-mail: marziye.alaei73@gmail.com

Department of Chemistry, Shiraz University of Technology, Shiraz**,** Iran.

Abstract: In this research, a novel and effective method without the use of solvents was developed to produce cyclic carbonate derivatives through the chemical conversion of CO_2. This process utilized manganese oxide hollow spheres as a highly capable nano-catalyst with excellent efficiency.

Keywords: CO_2 fixation; cyclic carbonates; hollow spheres of Mn_2O_3

Introduction

In recent times, the issue of 'global warming' has escalated significantly as a result of the rising levels of CO_2 in the atmosphere. So,The transformation of carbon dioxide into valuable chemical substances is a key objective in the field of environmental chemistry. To address this issue effectively, the integration of carbon dioxide into epoxide compounds leading to the formation of 5-membered cyclic carbonates emerges as the optimal solution for the aforementioned challenge. Carbonate derivatives are found in natural products and possess different worthwhile applications such as building blocks in organic synthesis, electrolytes in batteries, raw materials for cosmetics, green solvents, polymers, and pharmaceuticals. Many homogeneous catalysts have been effectively created for the cycloaddition of carbon dioxide to epoxides as a result. These catalysts include metal-based homogeneous catalysts, ionic liquids, organocatalysts, transition metal complexes , and alkali metal salts. Surely, homogenous catalysts have verified to give excellent yields of cyclic carbonates, but their homogeneous nature prevents reutilization, and restricts their practical application. In this context, employing diverse catalysts like metal oxides, metal-organic frameworks, and carbon-based materials can effectively overcome these limitations. Among the above catalysts, metal oxides due to their low cost and full availability have gained interest in promoting the cycloaddition of epoxides to CO_2.

Experimental Section

The cycloaddition of CO_2 to epoxides was conducted in a stainless steel high pressure , batch reactor at 70 °C and 1 bar pressure. In a typical reaction, the reactor was charged with 1mol% of catalyst, 10 mmol of epoxide and tetrabutylammonium bromide (TBAB) (10 mol%). Then, CO_2 was introduced into the reactor at the desired pressure. The reactor was sealed and then immersed into an oil bath at the selected temperature and stirred for a predetermined period time. After the reaction was
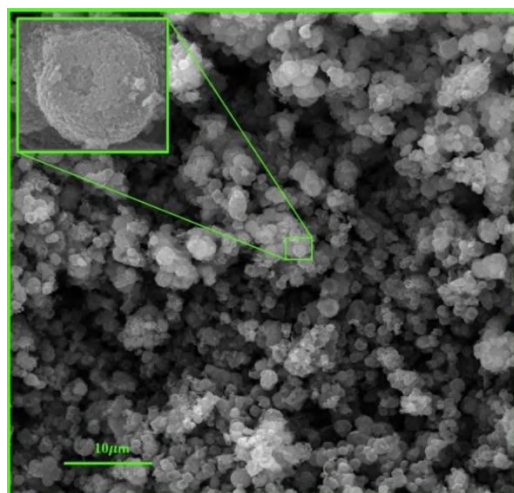
completed, the reactor was cooled to 0 °C in the ice-water bath, and the remaining CO_2 was slowly vented. The reaction mixture was diluted with ethyl acetate, and the catalyst was removed by filtration. The residue was purifed by conducting chromatography on glass plates using silica gel as the stationary phase and ethyl acetate-n hexane (1:8) as the eluent to aford the desired product. All the products were confrmed by the spectroscopic method using 1H and 13 C NMR.

Results and Discussion

In this research, firstly, Mn_2O_3 hollow catalyst spheres was synthesized by hydrothermal method with a hard carbon template. Then, it was identified using Feld emission scanning electron microscopy (FESEM)(Fig.1).

After successful synthesis and characterization of the Mn_2O_3 hollow sphere, its catalytic activity was tested for the synthesis of cyclic carbonates from CO_2 and epoxide under solvent free conditions.

For this purpose, the cycloaddition of styrene oxide with CO_2 was chosen as a model reaction for the best-experimented condition and the infuence of diferent parameters (CO_2 pressure, temperature, amount of the catalyst) was examined. The results are summarized in Table 1.

Finally, for the synthesis of cyclic carbonate derivatives from various epoxides,the reactions were carried out at 70 °C and 1 bar of constant CO_2 pressure, 10 mmol styrene oxide, and 10 mol% TBAB (tetra butyl ammonium bromide). Several compounds were synthesized under these conditions, that some of derivatives synthesized with excellent yields are shown in Figure 2.
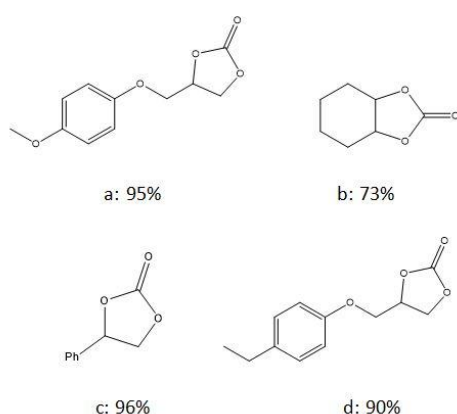
22nd Iranian Chemistry Congress (ICC22)
Iranian Research Organization for Science and Technology (IROST)
13-15 May 2024

03231-97589

Fig.1: FE-SEM of Mn_2O_3

Table1: optimization of reaction

Entry	Amount of catalyst (g)	TABAB (mol%)	T (ºC)	P	Time (h)	Yield (%)
1	0.006	10	70	1	5	94
2	0.015	10	70	1	5	90
3	0.003	10	70	1	5	96
4	0.003	5	70	1	5	94
5	0.003	2.5	70	1	5	92
6	0.003	10	70	5	5	98
7	0.003	10	70	3	5	96

a: 95% b: 73%

c: 96% d: 90%

Fig.2: some of derivatives synthesized

Conclusions

In brief, we have effectively produced hollow spheres of Mn_2O_3 using a simple and uncomplicated hydrothermal technique. The prepared hollow sphere showed excellent performance as a catalyst for solvent-free cycloaddition of CO_2 to epoxides under mild conditions. Different reaction parameters such as reaction temperature, reaction pressure, reaction time, catalyst weight percentage were examined successively. This study shows the possible efciency of the proposed structure as a potential high-performance catalyst for cycloaddition of CO_2 to epoxides.

References

[1] He, M., Sun, Y., & Han, B. (2013). Green carbon science: scientific basis for integrating carbon resource processing, utilization, and recycling. Angewandte Chemie International Edition, 37(52), 9620-9633.

[2] Sakakura, T., Choi, J. C., & Yasuda, H. (2007). Transformation of carbon dioxide. Chemical reviews, 107(6), 2365-2387.

[3] Yang, Z. Z., Zhao, Y., Ji, G., Zhang, H., Yu, B., Gao, X., & Liu, Z. (2014). Fluoro-functionalized polymeric ionic liquids: highly efficient catalysts for CO 2 cycloaddition to cyclic carbonates under mild conditions. Green chemistry, 16(8), 3724-3728.

[4] Yang, L. C., Rong, Z. Q., Wang, Y. N., Tan, Z. Y., Wang, M., & Zhao, Y. (2017). Construction of nine-membered heterocycles through palladium-catalyzed formal [5+ 4] cycloaddition. Angewandte Chemie International Edition, 56(11), 2927-2931.

[5] Chowdhury, A. H., Bhanja, P., Salam, N., Bhaumik, A., & Islam, S. M. (2018). Magnesium oxide as an efficient catalyst for CO2 fixation and N-formylation reactions under ambient conditions. Molecular Catalysis, 450, 46-54.

22nd Iranian Chemistry Congress (ICC22)
Iranian Research Organization for Science and Technology (IROST)
13-15 May 2024

03231-97589

IROST

Theoretical study of Photophysical properties of hole-transporting material quinoxaline-based in perovskite solar cells

Shabnam Jahanbani Korabbaslo[a], Rahim Ghadari[b]*

Corresponding Author E-mail: r-ghadari@tabrizu.ac.ir

[a] Organic Chemistry Laboratory, Faculty of Chemistry, University of Tabriz, Iran.

[b] Department of Organic and Biochemistry, Faculty of Chemistry, University of Tabriz, 5166616471 Tabriz, Iran.

Abstract: The role of the hole transport material (HTM) layer is critical to obtaining high performances for perovskite solar cells (PSCs). The favorable alignment of the FMO's energy level of HTM and $MAPbI_3$ is essential for charge transfer. The results show that HTM (TQ5) exhibit suitable energy levels.

Keywords: hole transport materials; perovskite solar cells; quinoxaline.

Introduction

Perovskite solar cells (PSCs) are a popular candidate for the next generation of solar technology due to their beneficial properties such as intense light absorption, and high charge carrier mobility [1]. The energy levels of frontier molecular orbitals (FMOs) and the distribution of the orbitals in a π-conjugated molecule play vital roles in intermolecular and intramolecular charge transport, light emission/absorption, and charge extraction/injection [2]. So, studying the mechanism of hole transport and expansion of modern HTMs with better hole mobility, a suitable HOMO level relative to perovskite, is urgent.

Experimental Section

Calculations are done using the Gaussian 09 software package with DFT and TD-DFT methods [3].

Results and Discussion

The chemical structure of HTM is given in **Fig 1**.
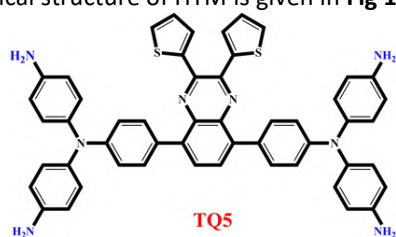
Fig. 1. Chemical structure of the studied HTM.

The E_{HOMO}, E_{LUMO}, and E_{gap} are essential factors for probing the optical, charge transfer, and electronic properties of HTMs [4]. Results **Table 1** show that the HOMO energy level of HTM is higher than the HOMO of $MAPbI_3$. So HTM has an energy level desirable alignment with $MAPbI_3$, as a result, the hole is quickly injected from the absorbent layer into the HTM. Also, the LUMO energy level of HTM must be higher than the conduction band of perovskite to block the electron transport of perovskite to the counter electrode and charge recombination. An ideal E_{gap} of a compound is beneficial for light absorption at long wavelengths; it increases the interaction between the donor-acceptor groups of the combination and also facilitates the transfer of excited electrons [5, 6].

Table 1. Values of FMOs energy levels of HTM, $MAPbI_3$, Au.

HTM	E^*_{HOMO} (eV)	E^*_{LUMO} (eV)	E_{gap}(eV)
TQ_5	-5.02	-2.99	2.03
$MApbI_3$	-5.43	-3.93	1.5
Au	-5.1		

Conclusions

In this study, a new HTM was designed based on quinoxaline. The theoretical investigation was done based on DFT, aiming to investigate the capability of the designed structure as a hole transport material. The FMO's energy level of HTM (TQ5) has a favorable alignment with the FMO's energy level of MAPbI3. Therefore, TQ5 is an HTM suitable.

References

[1] Sun, Z., Liu, Z., Zhang, J., Zhou, C., Chen, Z., Chen, L., ... & Ding, J. (2022). Impact of alkyl chain length on the properties of fluorenyl-based linear hole-transport materials in pin perovskites solar cells. ACS Applied Energy Materials, 5(7), 7988-7996. doi: 10.1021/acsaem.2c00197.

[2] Bronstein, H., Nielsen, C. B., Schroeder, B. C., & McCulloch, I. (2020). The role of chemical design in the performance of organic semiconductors. Nature Reviews Chemistry, 4(2), 66-77. doi: 10.1038/s41570-019-0152-9.

[3] Zhang, Z., Hu, W., Cui, J., He, R., Shen, W., & Li, M. (2017). Theoretical insights into the effect of a conjugated core on the hole transport properties of hole-transporting materials for perovskite solar cells. Physical Chemistry Chemical Physics, 19(36), 24574-24582. doi:10.1039/C7CP04754A.

[4] Deng, J., Hu, W., Shen, W., Li, M., & He, R. (2019). Exploring the electrochemical properties of hole transporting materials from first-principles calculations: an efficient strategy to improve the performance of perovskite solar cells. Physical Chemistry Chemical Physics, 21(3), 1235-1241. doi:10.1039/C8CP06693K.

[5] Saputra, R. M., Yang, C., Zhao, D., Zheng, X., & Li, Y. (2022). Electronic and photovoltaic properties of triphenylamine-based molecules with D-π-AA structures. Computational and Theoretical Chemistry, 1207, 113467. doi:10.1016/j.comptc.2021.113467.

[6] Yang, L., Guo, L., Chen, Q., Sun, H., Yan, H., Zeng, Q., ... & Dai, S. (2012). Substituent effects on zinc phthalocyanine derivatives: A theoretical calculation and screening of sensitizer candidates for dye-sensitized solar cells. Journal of Molecular Graphics and Modelling, 38, 82-89. doi: 10.1016/j.jmgm.2012.08.006.

22nd Iranian Chemistry Congress (ICC22)

Iranian Research Organization for Science and Technology (IROST)

13-15 May 2024

03231-97589

ISC

IROST

Theoretical study of charge transfer properties of hole-transporting material quinoxaline-based in perovskite solar cells

Shabnam Jahanbani Korabbaslo[a], Rahim Ghadari[b]*

Corresponding Author E-mail: r-ghadari@tabrizu.ac.ir

[a] Organic Chemistry Laboratory, Faculty of Chemistry, University of Tabriz, Iran.

[b] Department of Organic and Biochemistry, Faculty of Chemistry, University of Tabriz, 5166616471 Tabriz, Iran.

Abstract: A theoretical study was done to investigate the charge transport properties of quinoxaline derivatives using density functional theory. The electron transfer mechanism from the ground state to the first singlet excited state was investigated by electron and hole analysis. The results show that TQ5 has ideal hole-electron distribution indices.

Keywords: small organic molecules; DFT; hole transport materials.

Introduction

Among various solar photovoltaics, organic-inorganic hybrid perovskite solar cells (PSCs) are promising optoelectronic devices. In recent years, small organic molecules (SOM) as HTMs have been used as HTM due to the flexibility of molecular structure design to adjust electrical and optical properties, practical synthesis and purification, and an abundance of raw materials [1, 2]. The classic small organic HTM is spiro-OMeTAD and can induce instability in the device. The HTM based on quinoxaline has (over 21.03 % efficiency) to the commercial HTM of spiro-OMeTAD with an efficiency (of 20.28%) [3]. In this work, a series of indexes was studied to evaluate the separation of electron-hole. We hope this study can provide a deep insight into the transport properties of HTMs.

Experimental Section

Calculations are done using the Gaussian 09 software package with DFT and TD-DFT methods. The wave function analysis program Multiwfn 3.8 was used to calculate and evaluate the hole-electron distribution, which is the difference between the electron density of the initial singlet excited state and the ground stat [4].

Results and Discussion

The chemical structure of HTM is given in **Fig 1**.
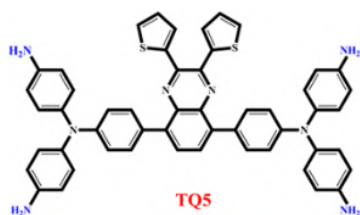
Fig. 1. Chemical structure of the studied HTM.

Results Table 1 shows that TQ5 has a D index with values (1.74 Å) indicating the distance between the hole and the electron centers. The larger the D index, the greater the distance between the main distribution areas of the hole and the electron. The H index reflects the breadth of the average distribution of holes and electrons. The higher value of the H index shows that the holes and electrons of HTM are more widely distributed in space. The t index measures the degree of separation between electron-hole. The t index of the TQ5 has negative values, so the electron and hole are not completely separate. The Sr index determines the overlapping extent between the hole and electron centers. The upper limit of the S_r index is 1.0 [4].

Table 1. Calculation results for the electron-hole distribution index.

HTMs	D(Å)	H(Å)	t(Å)	S_r
TQ5	1.74	4.58	-0.11	0.62

Conclusions

Results show that hole-electron distribution indices are for TQ5 of (D= 1.74 Å, H= 4.58 Å, t= -0.11 Å, S_r= 0.62). Due to the superior hole-electron distribution indices and better hole mobility, it is suggested that TQ5 has desirable properties as HTM in PSCs.

References

[1] Sheibani, E., Yang, L., & Zhang, J. (2020). Recent advances in organic hole transporting materials for perovskite solar cells. Solar RRL, 4(12), 2000461. doi: 10.1002/solr.202000461.

[2] Xu, Y. L., Ding, W. L., & Sun, Z. Z. (2018). How to design more efficient hole-transporting materials for perovskite solar cells? Rational tailoring of the triphenylamine-based electron donor. Nanoscale, 10(43), 20329-20338. doi: 10.1039/C8NR04730H.

[3] Guo, H., Zhang, H., Shen, C., Zhang, D., Liu, S., Wu, Y., & Zhu, W. H. (2021). A coplanar π-extended quinoxaline based hole-transporting material enabling over 21% efficiency for dopant-free perovskite solar cells. Angewandte Chemie International Edition, 60(5), 2674-2679. doi:10.1016/j.solener.2021.04.040.

[4] Lu, T., & Chen, F. (2012). Multiwfn: A multifunctional wavefunction analyzer. Journal of computational chemistry, 33(5), 580-592. doi:10.1002/jcc.22885.

The choline chloride-based DES is a capable and new catalyst for the synthesis of benzo[4,5]thiazolo[3,2-a]chromeno[4,3-d]pyrimidin-6-one

Elnaz Chegeni , Davood Habibi[*], Arezo Monem, Zahra Jahaniyan

Corresponding Author E-mail : davood.habibi@gmail.com

Department of Organic Chemistry, Faculty of Chemistry, Bu-Ali Sina University, Hamedan, Iran.

Abstract: A novel Deep Eutectic Solvent was prepared by a mixture of Choline chloride (ChCl) and acid used as a novel catalyst for the green synthesis of benzo[4,5]thiazolo[3,2-a]chromeno[4,3-d]pyrimidin-6-one.

Keywords: Deep Eutectic Solvent; synthesis; Choline chloride

Introduction

Deep eutectic solvents (DESs) are now widely acknowledged as a new class of ionic liquid (IL) analogs because they share many characteristics and properties with ILs. DESs are systems formed from a eutectic mixture of Lewis or Brønsted acids and bases which can contain a variety of anionic and/or cationic species.

DESes are made of mixture a of hydrogen-bond acceptors (HBA) and hydrogen-bond donors (HBD)[2]. Choline chloride-based DESs are generally accessible, easy to handle, relatively cheap, nontoxic, and moisture-stable, which fulfill several green chemistry principles. The real advantage of choline chloride-based DES came in the phase separation and could be easily isolated by decantation [3].

Multicomponent reactions (MCRs) have been used for almost 150 years and are an important tool in organic synthesis. They offer various benefits such as high atomic economy, fast reaction times, energy efficiency, and environmental compatibility.

MCRs are versatile chemical processes that allow for the synthesis of a wide range of heterocyclic compounds. These reactions involve the combination of three or more reagents to produce a final molecular product that is highly useful in organic synthesis [4].

Experimental Section

General procedure for preparation of DES catalyst:

A mixture of ChCl and acid was prepared in a molar ratio of 2:1, heated at 70 °C, and stirred until a homogeneous and transparent liquid was obtained. After cooling and without any purification s, the DES catalyst was stored for further reactions.

General procedure for the synthesis of benzo[4,5]thiazolo[3,2-a]chromeno[4,3-d]pyrimidin-6-one:

The DES catalyst (1 mmol), was added to a mixture of 4-Hydroxycoumarin (1 mmol), 2-amino-6-methyl benzothiazole (1 mmol), and aldehyde (1 mmol) under solvent-free conditions for an appropriate time. The reaction product was separated and purified from the reaction medium by filter paper, washed with ethanol and The structure of each purified compound was confirmed with a comparison of their melting points, FT-IR, [1] HNMR, ^{13}C NMR, and Mass spectra with authentic samples.

Results and Discussion

In the FT-IR spectrum of DES, the IR spectra of ChCl (a), Acid (b), the fresh DES (c), and the recovered DES catalyst (d) are presented in **Fig 1.**

In spectrum (a), the broad absorption band observed in 3415 cm^{-1} is related to the OH group. The peak at 3000 cm-1 corresponds to the bond, and a relatively sharp absorption band at 1092 cm^{-1} is related to the C-O group. In spectrum (b), the peaks at 3373 and 1683 cm^{-1} are related to the O-H and C=O of the -COOH group, respectively. These two peaks can be seen in the (a), (b), and (c) spectra, which confirm the structure of the DES catalyst.

To confirm the structure of the recovered DES, the corresponding IR spectrum (d) was recorded which shows that there is no significant difference between the original (fresh) and the recovered (used) IR spectra.
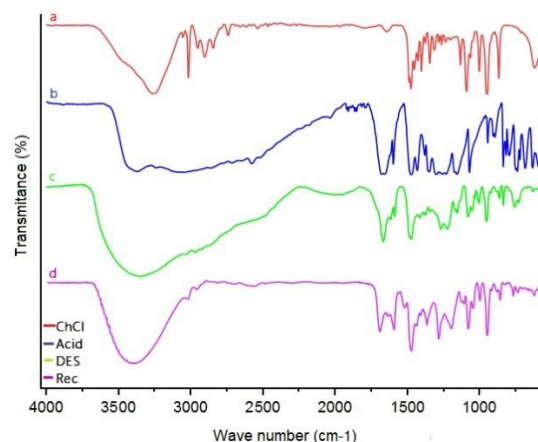

Fig. 1. The FT-IR spectra of (a), (b), (c), and (d).

22nd Iranian Chemistry Congress (ICC22)
Iranian Research Organization for Science and Technology (IROST)
13-15 May 2024

03231-97589

IROST

After optimizing the reaction conditions, 4-hydroxycoumarin, 2-amino-6-methyl benzothiazole, and benzaldehyde derivatives were synthesized solvent-free at 70°C with 1 mmol of catalyst (**Table 1**).
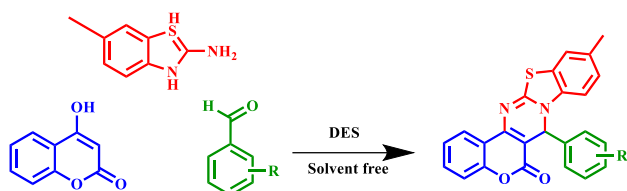

Table1: Synthesis of benzo[4,5]thiazolo[3,2-a]chromeno[4,3-d]pyrimidin-6-one by DES

Entry	Aldehyde	Time (min)	M.P. (°C)
1	Benzaldehyde	30	160-168
2	3-NO2-benzaldehyde	20	245-248
3	4-Cl-benzaldehyde	25	160-163

Conclusions

In keeping with the principles of green chemistry, solvents used in the chemical industry should meet certain criteria, such as being low in toxicity and safe for the environment. Deep eutectic solvents (DES) are effective as both a cost-effective and environmentally friendly solvent, as well as a recyclable and reusable organocatalyst for promoting organic transformations. The innovative choline-based DES catalyst offers several benefits, including reasonable yields of the desired products, short reaction times, low costs for starting materials used in catalyst preparation, and mild reaction media.

References

[1] Smith, Emma L., Andrew P. Abbott, and Karl S. Ryder. "Deep eutectic solvents (DESs) and their applications." Chemical reviews 114, no. 21 (2014): 11060-11082.https://doi.org/10.1021/cr300162p

[2] Maugeri, Zaira, and Pablo Domínguez de María. "Novel choline-chloride-based deep-eutectic-solvents with renewable hydrogen bond donors: levulinic acid and sugar-based polyols." Rsc Advances 2, no. 2 (2012): 421-425 DOI: 10.1039/C1RA00630D.

[3] Z. Duan, Y. Gu, Y. Deng
Green and moisture-stable Lewis acidic ionic liquids (choline chloride . xZnCl2) catalyzed protection of carbonyls at room temperature under solvent-free conditions.Catal.Commun. 7 (2006) 651-656. https://doi.org/10.1016/j.catcom.2006.02.008

[4] Ghasemzadeh, Mohammad Ali, Boshra Mirhosseini-Eshkevari, Mona Tavakoli, and Farzad Zamani. "Metal–organic frameworks: advanced tools for multicomponent reactions." Green Chemistry 22, no. 21 (2020): 7265-7300.https://doi.org/10.1039/D0GC01767A

Improving the photovoltaic performance of CdS/CdSe quantum dot-sensitized solar cells using an Al-ZnS ternary passivation layer

Fatemeh Fattahiyan [a], Hossein Dehghani [*a], Maryam Ostadebrahim [b]

Corresponding Author E-mail: dehghani@kashanu.ac.ir

[a] Department of Inorganic Chemistry, Faculty of Chemistry, University of Kashan, Kashan, Iran.
[b] Department of Analytical Chemistry, Faculty of Chemistry, Alzahra University, Tehran 1993893973, Iran.

Abstract: We have improved the photovoltaic characteristics of the CdS/CdSe quantum dot-sensitized solar cells(QDSSCs)by employing the Al-ZnS ternary passivation layer after the deposition of CdSe QDs, which caused a lower charge recombination at the interfaces of TiO$_2$/CdS/CdSe/polysulfide and thereby a higher collection of photoelectrons in the TiO$_2$ film.

Keywords: Quantum dot sensitized solar cells; Photoanode; Passivation layer; Aluminium ion-doped ZnS; Charge recombination

Introduction

Currently, due to the pressing demand for energy and the fast depletion of fossil fuels, along with the environmental issues associated with their usage, quantum dot-sensitized solar cells (QDSSCs) have emerged as a potential kind of photovoltaic (PV) technology [1-2]. A PV device is a solar cell that turns sunlight into energy by utilizing the photoelectric effect. quantum dot (QD) based solar cells, which are considered third-generation PVs, have gained significant interest due to their advantageous characteristics. These include a high absorption coefficient, the ability to multiple excitons generate (MEG) effects, the capacity to tune the band gap through size or composition control, ease of fabrication, hot electron transfer, low cost, superior light, moisture, and thermal stability compared to lead halide perovskites and dye molecules [3]. Regrettably, despite the remarkable characteristics of the power conversion efficiency (PCE), the actual efficiency achieved in QDSSCs remains small compared to the theoretical PCE of 44%. The low PCE can be attributed to several factors, including inadequate crystallinity, elevated defect density, subpar photoelectric performance of QD sensitizers, increased charge recombination in vices, and significant loss of carrier transport [4-6]. ZnS coating is an excellent method for achieving the suppression of charge recombination by providing effective surface passivation of the photoanode.

Experimental Section

Cadmium acetate dihydrate [Cd(Ac)$_2$.2H$_2$O], cadmium nitrate tetrahydrate [Cd(NO$_3$)$_3$.4H$_2$O], zinc acetate dihydrate [Zn(Ac)$_2$.2H$_2$O], sodium sulfide nonahydrate [Na$_2$S.9H$_2$O], sodium sulfite anhydrous [Na$_2$SO$_3$], sulfur powder [S], selenium powder [Se], aluminum nitrate [Al(NO$_3$)$_3$.9H$_2$O], sodium hydroxide pellet [NaOH], methanol [CH$_3$OH], and ethanol [C$_2$H$_5$OH] were purchased from the Merck company. In this work, titanium dioxide nanoparticles (TiO$_2$ NPs, with an average particle size of ~25 nm) were synthesized by the hydrothermal method and were directly used as metal oxide semiconductor (MOS) material for the preparation of photoanode. Deionized (DI) water was used for washing fluorine-doped tin oxide (FTO) substrates and the preparation of all aqueous solutions. The successive ionic layer adsorption and reaction (SILAR) method was used for the deposition of CdS/CdSe QDs on the TiO$_2$ film, as well as ZnS and Al-doped ZnS doped passivation layers, with a certain molar percentage of 10%, on the surface of CdS/CdSe QDs.

Results and Discussion

In Figure 1 (a) and (b), field-emission scanning electron microscope (FESEM) images (low magnification) show the surface morphology of TiO$_2$ and TiO$_2$/CdS/CdSe/10% Al-ZnS layers on FTO and FTO/TiO$_2$ substrates. In this way, the morphology of the TiO$_2$ transparent layer consists of a uniform and homogeneous distribution of nanoparticles with dimensions of about 20 nm on the FTO substrate. However, after layering CdS/CdSe/10% Al-ZnS CdSe QDs on the transparent semiconductor TiO$_2$ layer based on image (b), a slight increase in the dimensions of the nanoparticles and also the distance between them is observed. To confirm the presence of Al^{3+} in this film, energy-dispersive X-ray spectroscopic analysis (EDX) was used. As seen in Figure 1 (C), this layer is composed of Ti, O, Al, Zn, Cd, S, and Se elements, and the presence of these elements together indicates the TiO$_2$/CdS/CdSe/10% Al-ZnS structure. To identify the crystalline phase of both TiO$_2$ and TiO$_2$/CdS/CdSe/10% Al-ZnS films, X-ray diffraction (XRD) patterns of these films were prepared. As can be seen in Figure 1 (d), the presence of seven identical peaks in both patterns at 2θ values of 4.25°, 4.27°, 38°, 48°, 54°, 55°, and 62° are formed. These peaks are due to the presence of crystal

planes (101), (110), (112), (001), (211), (002) in the anatase phase (JCPDS No. 01-086-1157) and also the rutile phase (JCPDS No. 01 -089-4920) TiO_2 nanoparticles are mentioned in both films. The peaks of CdS, CdSe, and ZnS coincide with the peaks of TiO_2. Hence, the peaks observed at 2θ, 48.1° and 25.3° with (103), (220), and (111) crystal planes are assigned to the hexagonal structure of CdS (JCPDS No. 01-080-0006), the cubic structures of ZnS (JCPDS No. 01-080-0020) and CdSe (JCPDS No. 00-019-0191) are assigned. Also, due to the presence of a small amount of Al_2S_3 in ZnS and high background noise, no indicative peak is observed. In Figure 1 (e), the Nyquist diagrams of the two evaluated TiO_2/CdS/CdSe/ZnS and TiO_2/CdS/CdSe/10% Al-ZnS cells consist of a semi-circle, which is due to the presence of Al^{3+} ions in the ZnS layer, the charge transfer resistance (R_{ct}) at the photoelectrode/electrolyte interface decreases, which indicates a reduction in the electron-hole recombination process and an increase in the efficiency of the solar cell.

Figure 1 (f) shows the current density-voltage (J-V) curves of the CdS/CdSe/ZnS and CdS/CdSe/10% Al-ZnS QDSSCs based on Cu_2S-brass counter electrode under a simulated AM 1.5 G sunlight with an intensity of 100 mW/cm^2. The photovoltaic parameters of these mentioned devices are listed in Table 1.

Table 1. Photovoltaic parameters obtained from the J-V curves of CdS/CdSe/ZnS and CdS/CdSe/10% Al-ZnS QDSSCs under AM 1.5 G, 100 mW/cm^2 sunlight.

QDSSCs	V_{OC} (V)	J_{SC} (mA/cm^2)	FF (%)	PCE (η, %)
CdS/CdSe/ZnS	0.51	11.60	0.53	3.1
CdS/CdSe/10% Al-ZnS	0.54	12.01	0.52	3.4

Conclusions

Basically, in this study, the ZnS was used as the outer passivation layer in the CdS/CdSe QDSSCs. The results of FESEM, EDX, XRD, J-V, and EIS analyses show that the presence of the Al-ZnS ternary layer as the outer passivation layer in the CdS/CdSe QDSSCs significantly increases the performance of these devices by reducing charge recombination at the interfaces of TiO_2/CdS/CdSe/polysulfide and thereby increasing the collection of photoelectrons in the TiO_2 film. Finally, a champion PCE of 3.4% was obtained for the CdS/CdSe/10% Al-ZnS QDSSCs, which represents a ~10% improvement in comparison with bare ZnS (CdS/CdSe/ZnS).

References

[1] Li, L., Cao, Y., Fan, R., Sun, P., Yu, M., Zhang, Y., & Li, L. (2022). Effect of Ga ion doping in the ZnS passivation layer for high-efficiency quantum dot-sensitized solar cells. *Journal of Alloys and Compounds*, *899*, 162910.

[2] Firoozi, N., Dehghani, H., & Afrooz, M. (2015). Cobalt-doped cadmium sulfide nanoparticles as efficient strategy to enhance performance of quantum dot sensitized solar cells. *Journal of Power Sources*, *278*, 98-103.

[3] Ostadebrahim, M., & Dehghani, H. (2020). Improving the photovoltaic performance of CdSe0. 2S0. 8 alloyed quantum dot sensitized solar cells using CdMnSe outer quantum dot. *Solar Energy*, *199*, 901-910.

[4] Ostadebrahim, M., & Dehghani, H. (2021). ZnS/CdSe0. 2S0. 8/ZnSSe heterostructure as a novel and efficient photosensitizer for highly efficient quantum dot sensitized solar cells. *Applied Surface Science*, *545*, 148958.

[5] Hanna, M. C., & Nozik, A. J. (2006). Solar conversion efficiency of photovoltaic and photoelectrolysis cells with carrier multiplication absorbers. *Journal of Applied Physics*, *100*(7).

[6] Kusuma, J., & Balakrishna, R. G. (2018). A review on electrical characterization techniques performed to study the device performance of quantum dot sensitized solar cells. *Solar Energy*, *159*, 682-696.
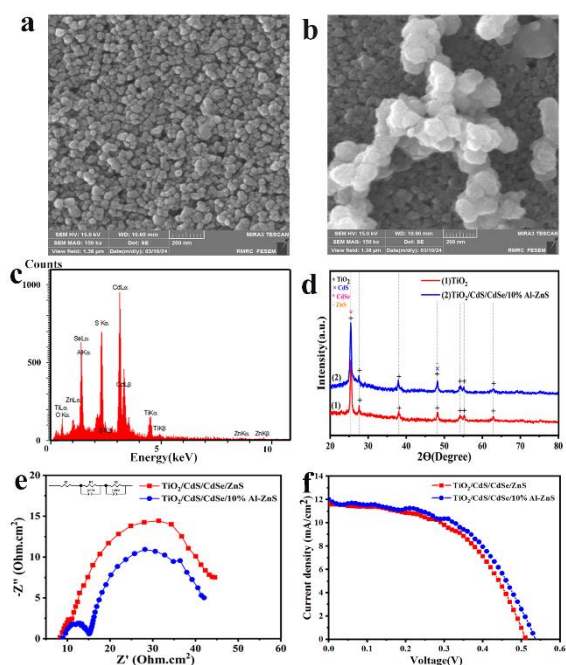
Fig. 1. FESEM images of the bare-TiO_2 (a) and TiO_2/CdS/CdSe/10% Al-ZnS (b) films on the FTO substrate. (c) EDX spectrum of the TiO_2/CdS/CdSe/10% Al-ZnS electrode. (d) P-XRD patterns of the bare-TiO_2 and TiO_2/CdS/CdSe/10% Al-ZnS films. (e) Nyquist curves and (f) J-V curves of the QDSSCs based on CdS/CdSe/ZnS and CdS/CdSe/10% Al-ZnS QDs.

22nd Iranian Chemistry Congress (ICC22)
Iranian Research Organization for Science and Technology (IROST)
13-15 May 2024

03231-97589

IROST

The substituent and solvent effect on the salicylaldehyde-based azine ESIPT fluorophores

Hossein Roohi, Tahereh Pouryahya*

Corresponding Author E-mail: tpouryahya20@gmail.com

Department of Chemistry Faculty of Science, University of Guilan, Rasht, Iran.

Abstract: In this study, the mechanism of the excited state intramolecular proton transfer (ESIPT) process in the donor-acceptor-structured salicylaldehyde-based unsymmetrical azine dyes **L1-L3** was investigated by density functional theory (DFT) and time-dependent density functional theory (TD-DFT) methods based on PBE0 functional and 6-31++g(d,p) basis set. Upon photoexcitation the intramolecular hydrogen bond strength was enhanced at the S_1 state. The influence of electron-donating ($-NH_2$) and electron-withdrawing ($-CN$) groups on the photophysical properties of these molecules was studied in the gas phase and three solvents with different polarities. The appearance of dual fluorescence emission bands in both gas phase and solution of enol and keto forms of these dyes confirmed the occurrence of ESIPT in all the compounds in good agreement with the reported experimental results.
Keywords: ESIPT, azine dye, DFT, TD-DFT

Introduction

Organic luminescent materials that exhibit excited-state intramolecular proton-transfer (ESIPT) reactions have been ceaselessly studied for more than six decades due to their potential applications such as chemosensors, and fluorescent probes [1]. The modification of the dye structure by introducing a functional group induces interesting changes in the excited-state dynamics and photophysical properties of the proton-transfer molecules. Among the most common ESIPT dyes, azine molecules have received significant interest in recent years. Azine-based compounds are Schiff bases synthesized from two identical carbonyl compounds and a hydrazine molecule (symmetrical azines) or two different carbonyl compounds (unsymmetrical azine). Particularly, unsymmetrical azines are important to tune fluorescent properties due to the presence of two dissimilar moieties with unique features, which are connected by a freely rotatable N–N bond. ESIPT-active unsymmetrical azines present potential abilities in biochemical sensing fields and optoelectronic devices [2]. In this study, we have investigated the ESIPT mechanism in the **L1**, **L2** and **L3** azine-based fluorophores (Fig. 1) by using the Density functional theory (DFT) and the Time-Dependent Density functional theory (TD-DFT) approaches at PBE0/6-31++G(d,p) level of theory in the gas phase and solution. In the main molecule **L1** triphenylamine is a well-known π-electron-donating group and salicylaldimine is a common acceptor as well as an ESIPT-active unit. These dyes possess donor-acceptor units with additional substituents on the proton donor part. This article reports how various substituents and solvent polarity affect photophysical properties of **L1** and its derivatives in the ground and excited states.
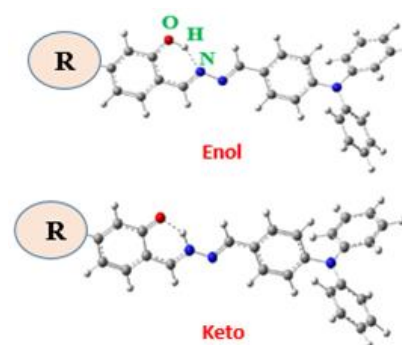

Fig. 1: Molecular structures of **L1** (R= -H), **L2** (R=-NH$_2$) and **L3** (R= -CN) in enol and Keto forms.

Computational details

All the calculations were carried out by DFT and TD–DFT methods based on PBE0 functional [3] and 6-31++G(d,p) basis set using the Gaussian 16 program package. Dimethylsulfoxide (DMSO), methanol (MeOH) and toluene solvents were selected to study the effect of solvent polarity on the absorption and fluorescence properties based on the polarizable continuum model (PCM) [4].

Results and Discussion

The structures of azine derivatives **L1** (R= −H), **L2** (R= −NH$_2$) and **L3** (R= −CN) in enol (E) and keto (K) forms in the ground (S_0) and excited states (S_1) were optimized by DFT and TD-DFT methods, respectively. For a deeper understanding of the proton transfer behaviour, the main bond length and bond angle involved in the hydrogen bonds in the S_0 and S_1 states were calculated and are reported in Table 1. For Enol configurations of **L1** and its derivatives the O−H bond length and δ(O−H−N) bond

22nd Iranian Chemistry Congress (ICC22)
Iranian Research Organization for Science and
Technology (IROST)
13-15 May 2024

03231-97589

IROST

angle all increase whereas the N−H bond lengths decrease after the photoabsorption process. These results indicate that the IHB of **L1-L3** dyes is strengthened in the S_1 state which can promote the occurrence of the proton transfer process.

Table 1: Main bond lengths and angles for azine dyes **L1-L3** in the S_0 and S_1 states

	state	O−H	N−H	δ(O−H−N)
L1	S_0-E	0.994	1.724	147.1
	S_1-E	1.002	1.684	149.3
L2	S_0-E	0.997	1.712	147.8
	S_1-E	1.005	1.673	149.7
L3	S_0-E	0.996	1.715	147.2
	S_1-E	1.001	1.681	149.3

To further understand the photophysical characteristic of **L1-L3**, the absorption and emission wavelengths in enol (E) and keto (K) forms were calculated in three solvents. Based on TD-DFT calculations, the longest-wavelength absorption is fonud for **L3** dye at 476 nm that possesses the −CN electron withdrawing substituent in DMSO solvent. For **L1**, **L2** and **L3** molecules only a small red shift is observed in absorption bands from nonpolar to polar solvents. Based on our calculated result, **L1**, **L2** and **L3** show dual enol and keto emissions in polar and nonpolar solvents. The enol emission of studied compounds display red shift from toluene to MeOH and DMSO solvents. The S_1-E form is transformed into S_1-K through the ESIPT process and then converted to S_0-K form via fluorescence radiation. The results show a slight red shift in keto emission of **L1-L3** with an increase in the polarity of the solvent. The trend of the red shift of the keto tautomer emission in term of peak wavelength is in the order of **L2** ($-NH_2$) < **L1** (−H) < **L3** (−CN) in solvent media. The largest Stokes shift is observed in MeOH solvent and is in the order of 143 nm (**L3**) > 133 (**L1**) > 115 (**L2**). It can be concluded that the Stokes shift for **L3** with electron-withdrawing group is greater than **L1** and **L2** fluorophores. The calculate keto fluorescence emission peaks of **L1-L3** in MeOH are shown in Fig. 2.
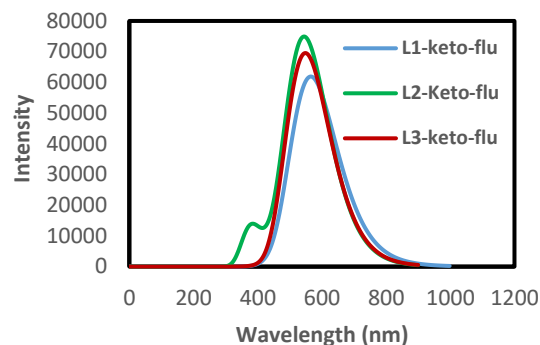
Fig. 2: The calculated emission spectrum of **L1-L3** in MeOH at PBE0/6-31++G(d,p) level.

Conclusions

In this work, the ESIPT process of a series of donor-acceptor triphenylamine–salicylaldehy unsymmetrical azine derivatives was studied based on DFT and TD-DFT methods. The effects of different substituents on the absorption and emission of azine dyes in solvent media was explored. Both S_1-E and S_1-K fluorescence emissions were observed for all studied molecules. The longest emission wavelengths were corresponded to fluorophore with electron-withdrawing group.

References

[1] Sedgwick, A. C., Wu, L., Han, H. H., Bull, S. D., He, X. P., James, T. D. & Yoon, J. (2018). Excited-state intramolecular proton-transfer (ESIPT) based fluorescence sensors and imaging agents. Chemical Society Reviews, 47(23), 8842-8880.

[2]. Kagatikar, S., & Sunil, D. (2019). Aggregation-induced emission of azines: An up-to-date review. Journal of Molecular Liquids, 292, 111371.

[3]. Adamo, C., & Barone, V. (1999). Toward reliable density functional methods without adjustable parameters: The PBE0 model. *The Journal of chemical physics*, *110*(13), 6158-6170.

[4]. Cossi, M., Barone, V., Mennucci, B., & Tomasi, J. (1998). Ab initio study of ionic solutions by a polarizable continuum dielectric model. *Chemical Physics Letters*, *286*(3-4), 253-260.

Palladium-supported periodic mesoporous organosilica based on imidazolium ionic liquid framework (Pd@PMO-IL) as an Efficient Catalyst for Heterogeneous Oxidative Heck Reaction

Masoumeh Hatami [a], Mina Ghahremani [a], Babak Karimi*[a,b]

Corresponding Author E-mail: karimi@iasbs.ac.ir , Masomhatami@iasbs.ac.ir

[a] Department of Chemistry, Institute for Advanced Studies in Basic Sciences (IASBS), Prof. Sobouti Boulevard, Zanjan 45137-66731, Iran.

[b] Research Center for Basic Sciences & Modern Technologies (RBST), Institute for Advanced Studies in Basic Sciences (IASBS), Prof. Sobouti Boulevard, Zanjan 45137-66731, Iran.

Abstract: Palladium-supported periodic mesoporous organosilica with bridged imidazolium ionic liquid framework (Pd@PMO-IL) obtained through the stabilization of catalytic Pd nanoparticles by imidazolium units. The catalyst presented a high activity and selectivity in the heterogeneous oxidative boron heck coupling reactions of various arylboronic acids with different olefins at very low catalyst loading and under mild reaction (base free) conditions. There is no observation of biphenyl- and other- byproducts in all reactions.

Keywords: Oxidative Heck Reaction; periodic mesoporous organosilica; Ionic Liquid; Pd nanoparticles.

Introduction

The C-C bond-forming reactions have played a remarkable role in organic synthesis as well as widely used to synthesize a wide variety of key structural motifs in biologically active products as well as building blocks for many oligomers and polymers. The progress in C-C cross-coupling came from the use of reactive homogeneous and heterogeneous palladium catalysts for the reaction of aryl halides or vinyl halides with organometallic compounds (Suzuki reaction, etc.), or with olefins (Heck reaction), or with alkynes (Sonogashira reaction). Nowadays, Suzuki–Miyaura and Mizoroki–Heck reactions have become among the most robust and efficient synthetic protocols for the formation of C-C bonds and also they have widely applied in the synthesis of many drugs, natural products and starting materials via both intermolecular and intramolecular reactions [1].

Despite eye-catching progress in the synthesis of a wide variety of valuable compounds using palladium catalysts in a homogeneous and heterogeneous manner during the years, beside the high cost in many cases, the use of external aryl-or vinyl- halides which in turn accompanied with the production of copious amounts of hazardous halide salts, limits the vast applications of these reactions. Due to the extensive environmental concerns, much effort has been dedicated to develop the halide-free coupling reactions using both transmetallation and direct C–H activation [2].

In this line, Thanks to their relatively stable, easily available and nontoxic nature, aryl boronic acids have received immense attention in recent years as a highly desirable surrogate for the aryl halides, which display great role in carbon-carbon type couplings with the emergence of the Pd(II)-catalysed oxidative Heck, which in turn provides relatively mild reaction conditions and offers superior catalytic activities in the coupling challenging substrates including highly substituted and cyclic olefins [3]. Considering the extensive use of palladium in these reactions, its high cost and toxicity on the other hand, there is a growing interest in applying heterogeneous and recoverable palladium catalysts, therefore the heterogenization of palladium catalysts is extremely important from both environmental and economic points of view.

In this regard, we have demonstrated that a catalytic Pd nanoparticles supported on periodic mesoporous organosilica with imidazolium ionic liquid framework having 2D-hexagonal structure is an efficient and highly selective catalyst in the oxidative heck coupling of arylboronic acid compounds and different olefins at very low catalyst loading and under mild reaction conditions.

Experimental Section

Periodic mesoporous organosilica containing ionic liquid (PMO-IL) were prepared according our previously reported procedure [4]. In this regard, hydrolysis and co-condensation of 1,3- bis(trimethoxysilylpropyl) imidazolium chloride and tetra methoxysilane in the presence of P123 as structure directing agent under acidic conditions afforded the corresponding PMO-IL. The resulting PMO-IL material was thus employed as a catalyst support for deposition of Pd NPs using Pd(OAc)$_2$ as Pd source for the Pd@PMO-IL preparation

Results and Discussion

Our initial studies were conducted by deposition of Pd NPs using a simple ion exchange protocol between Br⁻ ions in imidazolium rings with Pd species.

Fig. 1 (in which isotherms are shifted along the yaxis for clarity) illustrates the textural properties of Pd@PMO-IL

22nd **Iranian Chemistry Congress (ICC22)**
Iranian Research Organization for Science and Technology (IROST)
13-15 May 2024

03231-97589

ISC

IROST

catalyst. The N_2 adsorption-desorption isotherm is of type IV with hysteresis loops characteristic of mesoporous materials. According to the IUPAC classification, the hysteresis loops of the Pd@PMO-IL can be classified as H1 types which are characteristics of mesoporous materials with narrow pore size distributions.

The decrease of the surface area (from 571 to 432 $m^2 g^{-1}$) and almost slight decrease of pore volume (from 0.98 to 0.84 $cm^3 g^{-1}$) of the PMO-IL support upon deposition of the Pd nanoparticles clearly indicates that the Pd nanoparticles are supported inside the nanospaces of periodic mesoporous organosilica with an imidazolium network, with no pore obstruction.
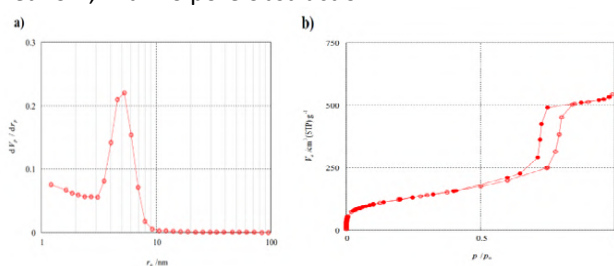
Fig.1: a) BJH pore size distributions and b) Nitrogen adsorption–desorption isotherm for Pd@PMO-IL

The X-ray photoelectron spectrum of the region corresponding to the binding energy of 330-350 eV showed peaks located approximately at 342.3 and 336.6 eV, which can assigned to components of the Pd(II) in fresh Pd@PMO-IL (Fig. 2).
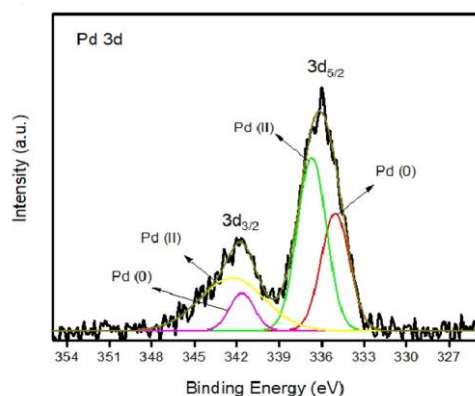
Fig.2: XPS spectra of Pd@PMO-IL

The catalytic activity of obtained material has been tested in the oxidative boron heck coupling reactions of various arylboronic acids and olefins under relatively mild conditions (1 atm O_2, 100 °C), the resulted catalyst (Pd@PMO-IL) exhibited considerably more activity and selectivity than the homogenous catalysts, as well as of a few reported heterogeneous analogies (Table 1).

Table1: Catalytic activity of some Pd-based catalysts reported for the oxidative boron heck coupling reaction

Catalyst	Cat. (mol %)	Time	Conv. (%)	Ref.
Pd@PMO-IL	0.65	6 h	> 90	**This work**
Pd(OAc)$_2$	2	20 h	82	[5]
MCM-41@aPEI-Pd	4	24 h	65	[6]

Conclusions

In conclusion, we demonstrated that Pd@PMO-IL, which simply synthized through the deposition of Pd NPs on periodic mesoporous organosilica with ionic liquid framework material, is an efficient and recyclable hetergenoues catalytic system for oxidative boron Heck coupling reactions. The reactions needed exceptionally small amount of the catalyst to achieve desired products with excellent selectivity. The high stability, simple recoverability, efficient reusability and selectivity for the preparation of the desired products are some of advantages of this heterogeneous nanocatalyst.

References

[1] Beletskaya, I. P., Cheprakov, A. V.; The Heck reaction as a sharpening stone of palladium catalysis, *Chem Rev.* **2000**, 100, 3009.

[2] Lee, A.-L., Enantioselective oxidative boron Heck reactions. *Organic & Biomolecular Chemistry* **2016,** *14* (24), 5357-5366.

[3] Andappan, M. M.; Nilsson, P.; Larhed, M., Arylboronic acids as versatile coupling partners in fast microwave promoted oxidative Heck chemistry. *Molecular diversity* **2003,** *7*, 97-106.

[4] Elhamifar, D.; Karimi, B.; Rastegar, J.; Banakar, M. H., Palladium-Containing Ionic Liquid-Based Ordered Mesoporous Organosilica: An Efficient and Reusable Catalyst for the Heck Reaction. *ChemCatChem* **2013,** *5* (8), 2418-2424.

[5] Ruan, Ji.; Li, Xi.; Saidi, O.; Xiao, Ji.; Oxygen and Base-Free Oxidative Heck Reactions of Arylboronic Acids with Olefins, *Am. Chem. Soc.* **2008**, 130, 2424-2425.

[6] Motevalizadeh, SF.; Alipour, M.; Ramazani, A.; Gholibegloo E. Appl Organometal Chem. **2017**, 32(3):e4123.

Optimization of electrospun polycaprolactone /polyethyleneimine nanofibers using response surface methodology

Fereshteh Amini [a], Hamid Delavari [*a], Shahrokh Ghovvati [b], Reza Poursalehi [a]

Corresponding Author E-mail: hamid.delavari@modares.ac.ir

[a] Department of Materials Engineering, Tarbiat Modares University, P.O. Box 14115-143, Tehran, Iran.

[b] Department of Animal Science, Faculty of Agricultural Sciences, University of Guilan, P.O. Box 41635-1314, Rasht, Iran.

Abstract: The electrospinning of polyethyleneimine/polycaprolactone nanofibers is done by using response surface methodology based on Box-Benken design. The effect of three important factors including PCL/PEI solution concentration, PCL: PEI mass ratio and applied voltage on the nanofibers' diameter were investigated, and the optimal conditions for the fabrication of nanofibers were determined.

Keywords: electrospinning; polyethyleneimine; polycaprolactone; optimization; response surface methodology.

Introduction

Electrospun nanofibers have been widely used in various fields including textiles, cosmetics, environmental remediation, energy, biomedical and healthcare applications [1], due to their excellent properties such as large specific surface area, light weight, three dimensional structure, high porosity, small pores, flexibility, tunable surface functionalities, and higher mechanical properties compared to the bulk materials [2].

Branched polyethyleneimine is a polycationic and water soluble polymer which contains a large number of primary, secondary, and tertiary amino groups [3]. That's why, it has strong adsorption capability toward anionic compounds and has been widely used in a wide range of fields including gene delivery and water treatment [4]. Electrospinning of PEI solutions is difficult due to its strong molecular interaction and high polarity [5]. Therefore, blending PEI with polycaprolactone as biocompatible, biodegradable, robust and easily electrospinnable polymer has been done to improve the electrospinnability of PEI and meanwhile the hydrophilicity of PCL [6].

Although several studies have investigated the effect of electrospinning parameters (including polymer solution, process and ambient factors) on the morphology and diameter of the nanofibers, the traditional methods are expensive and time-consuming; Therefore, the design of experiments (DOE) has been introduced as an effective method to investigate the effect of each factor and optimize them to achieve desired nanofibers [7].

Experimental Section

PCL granules (M_w=80kDa) and branched PEI (M_w=25kDa) were obtained from Sigma-Aldrich. N, N-Dimethyl formamide and chloroform were purchased from Merck company. Polymer blend solutions were prepared using Chloroform: DMF 3:1 v:v as the solvent and mixing for 24 h on the magnetic stirrer in room temperature.

The optimal conditions for the electrospinning of PEI/ PCL nanofibers with the minimum diameter and maximum amount of PEI were determined using response surface methodology based on Box-Benken design (Design Expert 12 software).

After initial screening of numerous tests by using optical microscope, three factors: i.e., concentration of PCL/ PEI solution, PCL: PEI blend ratio and applied voltage have been chosen as the most effective factors. The range of the factors is presented in Table 1. feeding rate and tip to collector distance were set in 0.2 ml/h and 16 cm, respectively. The average diameter of nanofibers was measured by using ImageJ 1.54g for 17 BBD designed experiments.

Table1: Factors used to optimize PEI/PCL electrospun nanofibers

Factor	Symbol	level		
		-1	0	+1
Blend solution concentration (%w/v)	X_1	18	20	22
PCL: PEI mass ratio (w/w)	X_2	3	5	7
Applied voltage(kV)	X_3	15	20	25

Results and Discussion

The results of measuring nanofibers' diameter in SEM images have been evaluated using the ANOVA test to assess significance of the fitted model and independent variables as well as their possible interactions in order to obtain a mathematical model. It is proved that the Quadratic fitted model is significant in 95% confidence level. Values of R^2 and adj. R^2 for the model are 0.98 and 0.95, respectively. All three factors (X_1, X_2 and X_3) have shown P values less than 0.05, which indicates the significant effect of them on the response. Meanwhile, the factors of concentration (X_1) and blend ratio (X_2) of PCL and PEI have the lowest p value and as a result, the most effect on nanofibers' diameter. only the quadratic expressions (X_{12}, X_{22} and X_{32}) had P values less than 0.05.

22nd Iranian Chemistry Congress (ICC22)
Iranian Research Organization for Science and Technology (IROST)
13-15 May 2024

03231-97589

After eliminating the insignificant interaction factors, the obtained model for the diameter of PCL/PEI composite nanofibers is expressed as following relation:

$$y = 2809.92500 - 270.87500A + 40.37500B - 9.02000C + 7.17500A^2 - 3.20000B^2 + 0.328000C^2$$

The terms A, B, and C are the concentration of PCL/ PEI solution, PCL: PEI mass ratio, and applied voltage in the electrospinning process, respectively.

As it is illustrated in Fig.1, increasing the concentration of the blend solution from 18 to 19.3% w/v will decrease nanofibers' diameter and after that will increase it. Increasing PCL: PEI mass ratio, will increase nanofibers' diameter. Therefore, increasing the amount of PEI, in addition to creating a more positive charge in the electrospun mat, will lead to a decrease in the diameter; As a result, an increase in the specific surface area and adsorption of negatively charged species will be achieved. Increasing the voltage from 15 to 18.5 kV will decrease the diameter of electrospun nanofibers and after that will increase the diameter. Fig.2 shows the morphology and diameter distribution of the optimal electrospun nanofibers achieved by desirability function.
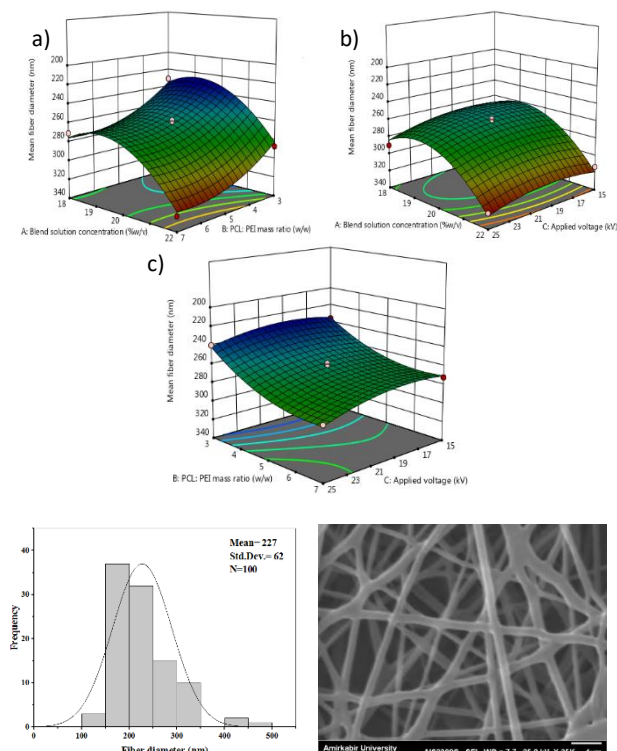
Fig.2: Morphology and diameter distribution of optimized PCL/ PEI nanofibers

Conclusions

This study has presented a statistical model to predict diameter of PCL/ PEI electrospun nanofibers which can be used in adsorption of different anionic compounds in environmental or biomedical applications. Optimum conditions of electrospun nanofibers to get minimum average diameter (227nm) based on the desirability function were considered as: concentration of the blend solution 19.273% w/v, mass ratio of PCL: PEI 3.019 w/w and the applied voltage 17.836 kV.

References

[1] Liu, H., Gough, C. R., Deng, Q., Gu, Z., Wang, F., & Hu, X. (2020). Recent advances in electrospun sustainable composites for biomedical, environmental, energy, and packaging applications. *International Journal of Molecular Sciences*, *21*(11), 4019. https://doi.org/10.3390/ijms21114019.

[2] Barhoum, A., Pal, K., Rahier, H., Uludag, H., Kim, I. S., & Bechelany, M. (2019). Nanofibers as new-generation materials: From spinning and nano-spinning fabrication techniques to emerging applications. *Applied Materials Today*, *17*, 1-35. https://doi.org/10.1016/j.apmt.2019.06.015.

[3] Gong, X., Yang, D., Wang, N., Sun, S., Nie, J., & Ma, G. (2020). Polyethylenimine grafted chitosan nanofiber membrane as adsorbent for selective elimination of anionic dyes. *Fibers and Polymers*, *21*, 2231-2238. https://doi.org/10.1007/s12221-020-1321-7.

[4] Tang, Y., Li, M., Mu, C., Zhou, J., & Shi, B. (2019). Ultrafast and efficient removal of anionic dyes from wastewater by polyethyleneimine-modified silica nanoparticles. *Chemosphere*, *229*, 570-579. https://doi.org/10.1016/j.chemosphere.2019.05.062.

[5] Altinkok, C., Sagdic, G., Daglar, O., Ayra, M. E., Durmaz, Y. Y., Durmaz, H., & Acik, G. (2023). A new strategy for direct solution electrospinning of phosphorylated poly (vinyl chloride)/polyethyleneimine blend in alcohol media. *European Polymer Journal*, *183*, 111750. https://doi.org/10.1016/j.eurpolymj.2022.111750.

[6] Shahrousvand, M., & Ebrahimi, N. G. (2022). Designing nanofibrous poly (ε-caprolactone)/hydroxypropyl cellulose/zinc oxide/Melilotus Officinalis wound dressings using response surface methodology. *International Journal of Pharmaceutics*, *629*, 122338. https://doi.org/10.1016/j.ijpharm.2022.122338.

[7] Hadipour-Goudarzi, E., Hemmatinejad, N., & Shokrgozar, M. A. (2023). Fabrication and DOE optimization of electrospun chitosan/gelatin/PVA nanofibers for skin tissue engineering. *Macromolecular Materials and Engineering*, *308*(5), 2200562. https://doi.org/10.1002/mame.202200562.

Application of box–behnken design for optimizing methyl orange removal from aqueous solutions using electrospun polyethyleneimine/ polycaprolactone membranes

Fereshteh Amini [a], Hamid Delavari H. [*a], Shahrokh Ghovvati [b], Reza Poursalehi [a], Mohammad naimi joubani [c]

Corresponding Author E-mail: hamid.delavari@modares.ac.ir

[a] Department of Materials Engineering, Tarbiat Modares University, Tehran, Iran.

[b] Department of Animal Science, Faculty of Agricultural Sciences, University of Guilan, Rasht, Iran.

[c] Department of Environmental Health Engineering, Guilan University of Medical Sciences, Rasht, Iran.

Abstract: The effect of adsorption factors including solution pH, contact time, dye concentration and adsorbent dosage on methyl orange removal by electrospun polyethyleneimine/ polycaprolactone membranes were investigated using box- behnken design. On the optimized conditions (pH: 3.9, 230 min, dye concentration: 35ppm and adsorbent dosage: 0.6 g/L) dye removal was 98%.

Keywords: methyl orange; adsorption; electrospun membrane; optimization; box–behnken design.

Introduction

Methyl orange (MO) is a widely used water soluble, non-biodegradable anionic azo dye which is highly toxic, carcinogenic, mutagenic and teratogenic due to the presence of stable aromatic rings and azo (N=N) groups on it's molecular structure [1]. Therefore, removal of it from wastewater is necessary to protect aquatic ecosystem and human health. Lots of research has been done on removing dyes from wastewater by different techniques such as membrane filtration, coagulation, flocculation, photocatalysis, adsorption, chemical oxidation, irradiation, ion exchange, reverse osmosis and precipitation. Adsorption is the most effective method due to it's ease of use, high efficiency, low-energy requirment, low cost, availability of various adsorbents, regeneration and recyclability of the adsorbent [2], [3].

Electrospun nanofiberous membranes are one of the favorable materials used in filtration and adsorption. Polyethyleneimine containing nanofibers can effectively remove negatively charged dye molecules in wastewater due to their cationic nature, large specific surface area and high porosity of the nanofibers [4]. In this study, we fabricated PEI/PCL nanofibers by blend electrospinning and then response surface methodology based on box-behnken design was used for optimizing the adsorption conditions of MO dye.

Experimental Section

A mixture of Polycaprolactone/ polyethyleneimine solution with concentarion of 19.5% w/v was prepared by dissolving 3:1 mass ratio of PCL:PEI polymers in 3:1 v:v chloroform: DMF solvents.

For fabricating nanofibers with minimum diameter and bead-free structure containing maximum amount of PEI, electrospinning is developed by optimizing processing parameters. The feeding rate was 0.2 mL/h, applied voltage 18 kV and tip to collector distance 16cm. Fig. 1 depicts SEM morphology and diameter distribution of electrospun PCL/ PEI nanofibers
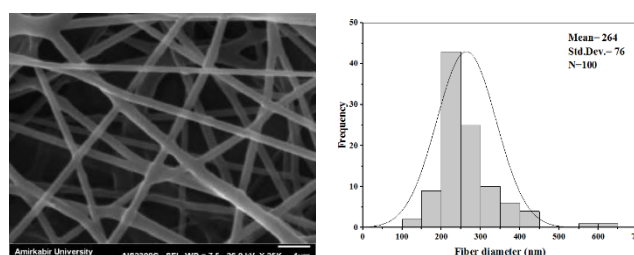
Fig.1: SEM image and corresponding fiber diameter distribution of PCL/ PEI electrospun nanofibrous mat.

27 runs presented by box- behnken design was done to optimize MO adsorption experiments. Solution pH (A), contact time (B), dye concentration (C) and adsorbent dosage (D) were chosen as independent variables. MO removal percent was selected as the response and calculated by the following formula:

$$R\% = \frac{C_0 - C_e}{C_0} \times 100$$

Table1: Independent variables and their levels to optimize MO adsorption by PCL/ PEI electrospun nanofibers

Factor	Symbol	level		
		-1	0	+1
Solution pH	A	3	6	9
Contact time (min)	B	10	65	120
Dye concentration (ppm)	C	20	110	200
Adsorbent dosage (g/L)	D	0.4	2.2	4

Results and Discussion

The ANOVA test obtained from the response surface quadratic model (table 2) represents that the model and varibles including A,B , C , D, AD, BD, CD, A^2, B^2, C^2 and D^2

22nd Iranian Chemistry Congress (ICC22)
Iranian Research Organization for Science and Technology (IROST)
13-15 May 2024

03231-97589

IROST

are significant (p-value<0.05). Values of R^2= 0.98 and adj. R^2= 0.95 show a good agreement between the experimental results and the predicted values from model. Moreover F value of 39.25 implies that the model is significant. There is only a 0.01% chance that it could occur due to noise.

Table 2. ANOVA results for response surface quadratic model of Mo removal

Source	Sum of Squares	df	Mean Square	F-value	p-value	
Model	2631.54	14	187.97	39.25	< 0.0001	significant
A-solution pH	806.55	1	806.55	168.40	< 0.0001	
B-contact time	121.22	1	121.22	25.31	0.0003	
C-dye concentration	84.75	1	84.75	17.69	0.0012	
D-adsorbent dosage	972.18	1	972.18	202.98	< 0.0001	
AB	0.4692	1	0.4692	0.0980	0.7597	
AC	0.8010	1	0.8010	0.1672	0.6898	
AD	237.78	1	237.78	49.65	< 0.0001	
BC	2.31	1	2.31	0.4824	0.5006	
BD	89.97	1	89.97	18.78	0.0010	
CD	28.73	1	28.73	6.00	0.0306	
A^2	59.42	1	59.42	12.41	0.0042	
B^2	45.85	1	45.85	9.57	0.0093	
C^2	25.79	1	25.79	5.39	0.0387	
D^2	103.92	1	103.92	21.70	0.0006	
Residual	57.47	12	4.79			
Lack of Fit	49.64	10	4.96	1.27	0.5195	not significant
Pure Error	7.84	2	3.92			
Cor Total	2689.01	26				

The obtained model for dye removal percentage is expressed as following relation:

$y = 79.5105 - 1.1061A + 0.0665B + 0.0137C + 3.7223D + 1.4278AD - 0.0479BD + 0.0165CD - 0.3709A^2 + 0.001B^2 - 0.0003C^2 - 1.3624D^2$

Effect of independent variables on the removal of MO shows that with increasing initial pH and dye concentration of solution dye removal decrese. Increasing contact time and adsrbent dosage will improve dye removal persentage. Fig. 2 shows 3D surface plots of the model for MO removal. It is clear that with increasing adsorbent dosage and meanwhile decreasing solution pH, Mo dye removal will be enhance. Increasing both adsorbent dosage and contact time will increase percentage of dye removal. Maximum dye removal will be obtained at high adsorbent dosage and low dye concentration.
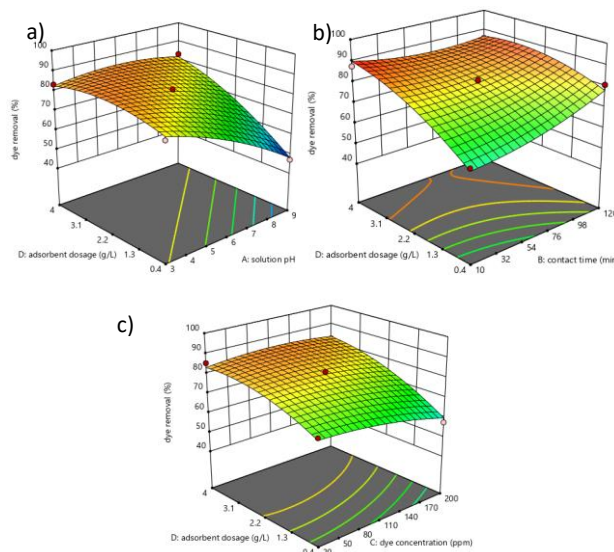
Fig.2: 3D surface plots of dye removal percent a) adsorbent dosage vs solution pH b) adsorbent dosage vs contact time c) adsorbent dosage vs dye concentration.

Conclusions

This study has presented a statistical model for predicting MO removal by using PCL/ PEI electrospun nanofibrous mat. Optimum conditions for Mo removal based on the desirability function were pH: 3.9, 230 min, dye concentration: 35 ppm and adsorbent dosage: 0.6 g/L

References

[1] Tamer, T. M., Abbas, R., Sadik, W. A., Omer, A. M., Abd-Ellatif, M. M., & Mohy-Eldin, M. S. (2024). Development of novel amino-ethyl chitosan hydrogel for the removal of methyl orange azo dye model. *Scientific Reports*, *14*(1), 1284. https://doi.org/10.1038/s41598-024-51538-1.

[2] Abdulhameed, A. S., Jawad, A. H., & Mohammad, A. K. T. (2020). Statistical optimization for dye removal from aqueous solution by cross-linked chitosan composite. *Science Letters (ScL)*, *14*(2), 1-14. https:// doi.org/ 10.24191/sl.v14i2.9537.

[3] Dbik, A., El Messaoudi, N., Bentahar, S., El Khomri, M., Lacherai, A., & Faska, N. (2022). Optimization of methylene blue adsorption on agricultural solid waste using box–behnken design (BBD) combined with response surface methodology (RSM) modeling. *Biointerface Res. Appl. Chem*, *12*(4), 4567-4583. https://doi.org/10.33263/BRIAC124.45674583.

[4] Fang, X., Xiao, S., Shen, M., Guo, R., Wang, S., & Shi, X. (2011). Fabrication and characterization of water-stable electrospun polyethyleneimine/polyvinyl alcohol nanofibers with super dye sorption capability. *New Journal of Chemistry*, *35*(2), 360-368. https://doi.org/10.1039/C0NJ00764A.

A new strategy for the synthesis of macrocycle linkers in metal organic frame works compounds

Moayad Hossaini Sadr*, Ali Pashazadeh*

Corresponding Author E-mail: hosainis@yahoo.com; a.pashazadeh20@gmail.com

Department of Chemistry, Faculty of Science, Azarbaijan Shahid madani University, Tabriz 53714-161, Iran.

Abstract: Now adays, one of the greatest challenges in synthesizing metal-organic frameworks (MOFs) is the lack of a linker and its accompanying metals [1,2]. To overcome this challenge, researchers have used from functional ligands (custom-designed organic ligands) and functionalization of the organic ligands with side groups including $-NH_2$, $-COOH$, and $-CONH$, which lead to MOFs materials possessing wonderful properties [3]. In this research, we designed an azamacrocyclic tetraimidazolat ligand 1,4,7,10-tetraazadodecine N,N',N'',N'''-tetra benzimidazole (TACTBI) through an eco-friendly condensation methods. In the next step, a new microporous MOFs was prepared with triggered self-assembly TACTBI ligand with Ni (II) cations under solvothermal conditions. Various studies (surface analysis and chemical identification methods (viz. SEM, EDX, etc.)) have shown, that the metal bond formed between TACTBI ligand with an imidazolate group and metal junction, which can be act as electron transport channel and significantly increase charge transfer in various reactions. Therefore, for practical application of Ni-MMOFs, the surface of the glassy carbon electrode was covered by Ni-MMOFs as a suitable matrix for determining CN- in different environmental water samples with various electrochemical methods. The measurement based on the behaviour of the anodic peak of Ni-MMOFs due to formation of stable complex between Ni (II)/ Ni (III) in organic framework and CN^-, when the potential is directed in the positive direction. The method was applied satisfactorily for analysis of CN^- in environmental natural water samples. The results show that, the proposed sensor exhibited wide linear range, low LOD value and good selectivity.

Keywords: synthesis; macrocycle; metal organic frame works.

References

[1] Habibi, B., Pashazadeh, A., Pashazadeh, S., & Saghatforoush, L. A. (2022). Electrocatalytic oxidation and determination of hydrazine in alkaline medium through in situ conversion thin film nanostructured modified carbon ceramic electrode. Journal of Electroanalytical Chemistry, 907,116038.https://doi.org/10.1016/j.jelechem.2022.116038.

[2] Habibi, B., Pashazadeh, A., Pashazadeh, S., & Saghatforoush, L. A. (2024). A new method for the preparation of MgAl layered double hydroxide-copper metal–organic frameworks structures: application to electrocatalytic oxidation of formaldehyde. Scientific Reports, 14(1), 1-17. https://doi.org/10.1038/s41598-024-55770-7.

[3] Tavakoli, S., Abbasi, A., Yousefi, M., & Sadr, M. H. (2024). A facile strategy of designing a new crystalline cobalt metal-organic framework as a new efficient and robust heterogeneous catalyst for olefin oxidation reaction. Journal of Molecular Structure, 137706. https://doi.org/10.1016/j.molstruc.2024.137706.

Enhancing crude oil recovery using Gemini imidazolium ionic liquid based-deep eutectic solvent

Shima Yaghoubi, Javad Saien*, Mona Kharazi

Corresponding Author E-mail: saien@basu.ac.ir

Faculty of Chemistry and Petroleum Science, Bu-Ali Sina University, Hamedan 6517838695, Iran.

Abstract: In recent developments, deep eutectic solvents (DESs) with interfacial activity have been emerged as a compelling alternative to conventional surfactants across various applications. In this research, for the first time, the effect of Gemini imidazolium ionic liquid based DESs on various aspects of the enhanced oil recovery (EOR) has been evaluated. The obtained results show the significant effect of this material in increasing crude oil extraction with high reduction in interfacial tension (IFT) up to 99.6%, increasing wettability up to 75.1%, and forming stable crude oil–water emulsion.

Keywords: Deep eutectic solvent; Enhanced oil recovery; Interfacial tension; Emulsification; Contact angle

Introduction

Despite worldwide growing demand for energy, primary and secondary recoveries produce low percentages of potential crude oils from mature reservoirs. Accordingly, injection of surfactants for reducing crude oil–water interfacial tension (IFT), altering rock wettability, and forming emulsion have been attempted in different ways [1]. Recently, new chemicals such as deep eutectic solvents (DESs) have been utilized for reducing residual oil saturation. The foundation of DES formation lies in the establishment of hydrogen bonds between two or more hydrogen bond donor (HBD) and hydrogen bond acceptor (HBA) resulting in a mixture with a lower melting point than its constituents. By lowering the viscosity of intrinsic polar components, and giving high interfacial activity, DESs manifest promising potential for application in enhanced oil recovery (EOR).

This study delves into an experimental exploration of the potential impact of the imidazolium Gemini ionic liquid-based DES ($[C_4im-C_6-imC_4][Br_2]$/urea) on the primary mechanisms behind oil recovery, encompassing IFT reduction, wettability alteration, and emulsification. Additionally, the influence of temperature on IFT is examined. It is worth that to increase stability and interfacial activity, Gemini ionic liquid is used as hydrogen bond donors (HBD) to form a novel structure of DES in mixtures with urea [2]. To the best of our knowledge, this investigation represents new endeavour, marking the first exploration of the application of Gemini ionic liquid-based DES in EOR with respect to different aspects.

Experimental

The crude oil used in this study was sourced from an oil field in south western of Iran. All the employed chemicals were of analytical grade and used without further purification.

The DES composed of $[C_4im-C_6-imC_4][Br_2]$/urea (molar ratio 3:2; DES molecular weight: 319.428 g/mol) was synthesized. The synthesis process of the DES includes mixing the IL powder (dried in an oven) with appropriate amount of urea considering their molecular weight which gives the DES. Subsequently, the mixtures were subjected to heating and agitation for 8 h at 80°C, resulting in the formation of a transparent, homogeneous liquid phase. Upon cooling, the product remained in a liquid state at room temperature. The physical state of the ingredients as well as the formed IL-based DES (IL/urea) are illustrated in Figure 1. IFT and contact angle were measured by means of a pendant drop equipment.

$$IL + Urea \xrightarrow[\text{8h at 80°C}]{\text{mixing}} DES$$
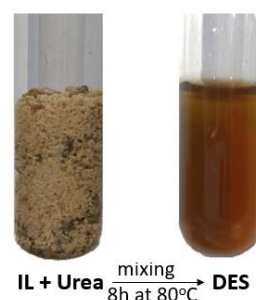
Fig. 1: The physical state of the ingredients as well as the formed IL-based DES (IL/urea).

Results and Discussion

The study delved into exploring the impact of the surface-active DES on various aspects of the EOR including two phase IFT, rock wettability, and crude oil–water emulsification.

Interfacial tension: Figure 2 illustrates the IFT of the mixtures (DES/oil) measured at various temperatures. As is apparent, presence of DES, up to the critical micelle concentration, CMC, causes drastic decrease in IFT from 30.26 to 0.03 mN/m (it is ≈ 99.8%) reduction at a typical temperature of 328.2 K. This high reduction is much

22nd Iranian Chemistry Congress (ICC22)
Iranian Research Organization for Science and
Technology (IROST)
13-15 May 2024

03231-97589

ISC

IROST

important in EOR, as it increases the capillary number in the oil reservoirs. The strong effect in reducing IFT is due to the amphiphilic nature of the DES components, which causes a great tendency to migrate towards the crude oil–water interface.

After reaching CMC, the adsorbed particles completely saturate the interface with no free sites. This condition forces the DES particles to self-assemble spontaneously and form micelles in the bulk phase. It can be seen that after this concentration, the IFT remains almost constant. The results of experiments conducted at different temperatures (from 298.2 to 328.2 K) show that temperature causes additional reduction of IFT in the way that the minimum IFT was determined to be at the extreme low value of 0.09 mN/m (it is ≈ 99.6%) at 298.2 K and decreased to 0.03 mN/m (it is ≈ 99.8%) upon elevating the temperature to 328.2 K. This phenomenon is ascribed to the diminution of cohesive forces as molecular vibrations intensify with rising temperatures, leading to weakening the intermolecular forces at the interface.
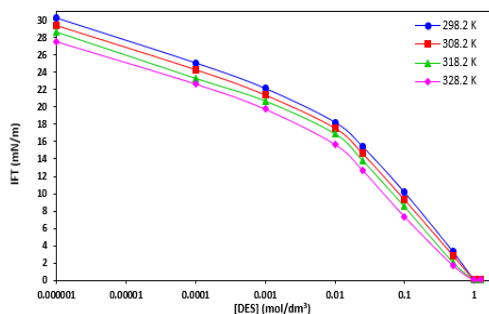
Fig.2: IFT values between heavy oil and different solutions of DES at different temperature.

Wettability alteration: Contact angle measurements provide a qualitative insight into the surface wetting behaviour in the presence of DESs. Figure 3 illustrates the changes of the contact angle with increasing DES concentration at 298.2 K. The contact angle of crude oil-pure water, initially at 137°, is significantly reduced to 34° when using a concentration of 1 mol/dm^3 of DES. This reduction signifies the alteration of the oil-wet surface to water-wet. The imidazolium Gemini ionic liquid-based DESs molecules are accumulation on both the oil drops and the solid surface, contributing to this change.

Fig. 3: Changes of contact angle with the DES concentration.

Emulsification: In the context of crude oil recovery, the transfer of surfactants to low permeable zones and formation of stable oil in water emulsions are crucial. Emulsification facilitate the movement of residual crude oil [3]. It is important to note that a low IFT is essential for the formation of a stable emulsion.

Figure 4 presents images of the pure crude oil/water (without DES) as well as with a 1 mol/dm^3 of the DES. Addition of DES results in the formation of emulsions that remain stable after one day and one week. This also indicates high potential of the DES as an effective agent for EOR through emulsification.
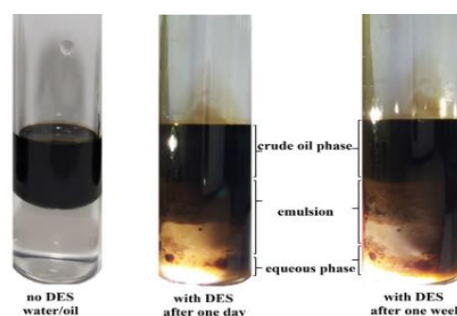
Fig.4: The images of the pure crude oil/water with no DES as well as with 1 mol/dm^3 of the DES after one day and one week.

Conclusions

The outcomes of this study clearly demonstrate that the novel DES presents a promising alternative to conventional surfactants in the realm of enhanced oil recovery. However, its field applications necessitate thorough exploration to identify and address operational challenges effectively.

References

[1] Kianinejad, A., Saidian, M., Mavaddat, M., Ghazanfari, M. H., Kharrat, R. & Rashtchian, D. (2015). https://doi.org/10.1002/cjce.22166.
[2] Zhang, Z., Kang, N., Wang, J., Sui, H., He, L. & Li, X. (2018). https://doi.org/10.1016/j.ces.2018.02.023.
[3] Saien, J., Kharazi, M., Shokri, B., Torabi, M., & Zolfigol, M. (2023). https://doi.org/10.1039/d3ra01783d.

Synthesis and characterization of a novel Gemini imidazolium ionic liquid-based deep eutectic solvents

Shima Yaghoubi, Javad Saien*, Mona Kharazi

Corresponding Author E-mail: saien@basu.ac.ir

Faculty of Chemistry and Petroleum Science, Bu-Ali Sina University, Hamedan 6517838695, Iran.

Abstract

A highly intended branch of green solvents, during recent decades, is the deep eutectic solvents (DES), which have become prevalent in industry. This study was devoted to introduce a DES based on the Gemini imidazolium $[C_4im-C_6-imC_4][Br_2]$ IL and urea. A molar ratio of 3:2 for respectively, the Gemini-IL and urea was determined from the phase diagram with a melting point of only 14 °C, much less than that of forming constituents (156 and 133 °C). The preparation of DES was notably energy-efficient and could be accomplished through simple mixing and heating of the components, bypassing the need for purification. The structure of the novel DES was proposed and underwent validation through FT-IR analysis, revealing consistent structures.

Keywords: Deep Eutectic Solvent; Gemini Ionic Liquid surfactant; Imidazolium, Urea

Introduction

Over the past few years, significant advancements have emerged in the realm of green solvents, which play a crucial role in promoting sustainable development and curbing environmental pollution [1]. Within this category, Deep Eutectic Solvents (DESs) and Ionic Liquids (ILs) have risen the attention and are most commonly utilized. DES represent a developing category of ILs have gained traction in recent years.

The foundation of DES formation lies in the establishment of hydrogen bonds between two or more hydrogen bond donor (HBD) mostly consists of phosphonium or ammonium salts, and hydrogen bond acceptor (HBA) mostly includes alcohols, acids, amines, and amino acids, resulting in a mixture with a lower melting point than its constituents. Initial research on DESs was conducted by Abbott et al. [2], in which the lowest melting point of (23 - 25)°C was observed for eutectic that achieved from mixing choline chloride with $ZnCl_2$. Such DESs have unique properties such as low melting point, resistance to moisture and air, low vapor pressure, and high thermal stability. Beyond their role as solvents, these compounds have found widespread use as precursors or fundamental components in carbon dioxide separation, electrochemical applications, catalysts [3], enhanced oil recovery [4], and extraction [5].

Due to the critical importance of developing DESs as part of the green solvent for industrial and laboratory processes, this study was devoted to present the novel preparation of a DES based on the Gemini imidazolium IL $[C_4im-C_6-imC_4][Br_2]$, and urea. To our knowledge, this investigation represents a pioneering endeavour as the use of DESs based on Gemini ILs has not been explored previously.

Experimental Section

All reagents were purchased from the chemical suppliers Merck or Sigma Aldrich and used without further purification. Thin layer chromatography (TLC) was carried out using silica gel 60 F-254 [Merck, Germany]. FT-IR (KBr) spectra were recorded using an Alpha Perkin Elmer spectrophotometer. Melting points were determined using a Stuart melting point meter.

General procedure for preparation of DES

The synthesis process for DESs is very easy. These solvents are created through a simple mixing of components and heating, alleviating the necessity for purification and separation steps. Different mixtures in molar rations of the Gemini imidazolium IL and urea where prepared and was stirred at high temperature under solvent-free conditions until a homogeneous liquid was achieved. Upon slow cooling at room temperature, the corresponding temperature of transferring from homogenous phase to heterogeneous two phase system was detected at the threshold. The mixture with the lowest temperature was considered as the DES of the mixture.

Results and Discussion

DESs performance is underpinned by the formation of hydrogen bonds. The resulting eutectic point phase diagram (see Fig. 2) unveiled that the most favourable ratio for the formation of the novel DES is 3 moles of the IL to 2 moles of urea (mole fractions of 0.6:0.4). It is interesting to note that while the individual melting points of the IL and urea are 156°C and 133°C, respectively, the novel DES gives a marked reduction in melting point to only 14 °C.
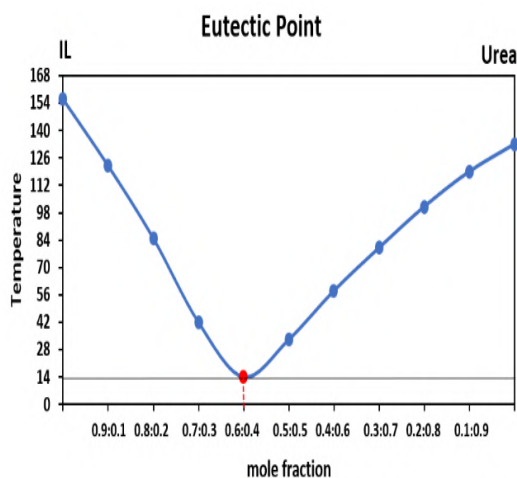
22nd **Iranian Chemistry Congress (ICC22)**
Iranian Research Organization for Science and Technology (IROST)
13-15 May 2024

03231-97589

IROST

Fig.1: The eutectic point phase diagram for the mixtures of the IL and urea.

The structure of the DES synthetizing components as well as the proposed chemical structure of the product with the corresponding hydrogen bonds are presented in Scheme 1.
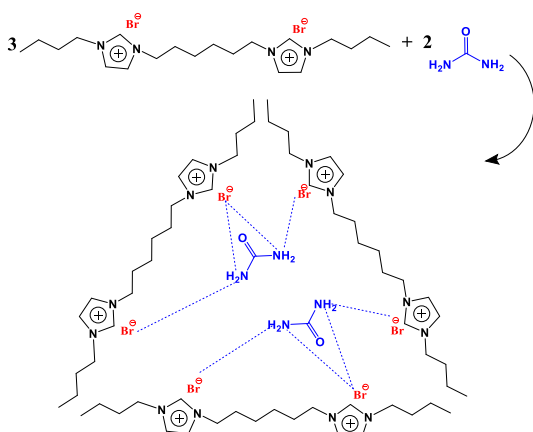
Scheme.1: The DES synthetizing components and the proposed chemical structure.

Characterization of DES

The newly synthetized DES was characterization through the primary methods of Fourier-transform infrared spectroscopy (FT-IR analysis) and the structural composition of the DES was confirmed. Figure 1 illustrates the FT-IR spectra of the Gemini imidazolium IL (a), urea (b), and the resulting DES (c). In spectrum (a), peaks within the range of 2900 - 3100 cm^{-1} are indicative of the aromatic and aliphatic hydrogens. Meanwhile, in spectrum (b), peaks at 1467, 1629, 1673 and 3339 cm^{-1} are corresponding to the C–N, N–H (amide), C=O and N–H(amine) functional groups, respectively. Interestingly, the spectrum for the resulting DES (c) demonstrates the similar peaks to both the Gemini imidazolium IL and urea, thus verifying the structure of the DES. Notably, minor shifts in the peaks associated with the O–H and C=O groups were observed at 3183 and 1697 cm^{-1}, indicating successful synthesis of the DES.
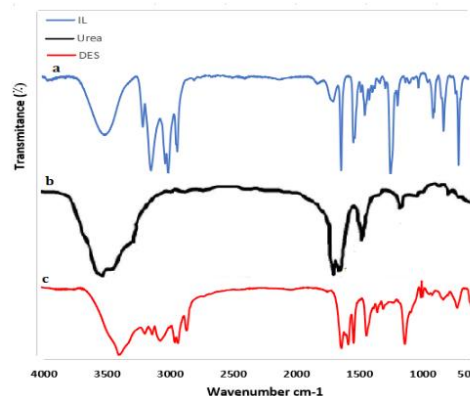
Fig.2: The FT-IR spectra of the Gemini imidazolium IL (a), urea (b), and the resulting DES (c).

Conclusion

In summary, a novel DES of [C_4im-C_6-imC_4][Br_2]/urea (IL:Urea–DES) was produced with the molar ratio of 3:2 of respectively the Gemini-IL and urea as determined from the eutectic point phase diagram. The preparation of DES is notably energy-efficient and can be accomplished through simple mixing and heating of the components, bypassing the need for purification. The structure of the novel DES was proposed and underwent validation through FT-IR analysis, representing the same picks of the used constituent compounds.

References

[1] Hansen, B. B., Spittle, S., Chen, B., Poe, D. (2021). https://doi.org/10.1021/acs.chemrev.0c00385.

[2] Abbott, A. P., Capper, G., Davies, D. L., Munro, H. L., Rasheed, R. K., and Tambyrajah, V. (2001). http://www.rsc.org/suppdata/cc/b1/b106357j.

[3] Goudarzi, H., Habibi, D., Monem, A., (2023). https://doi.org/10.1038/s41598-023-32882-0.

[4] Mohsenzadeh, A., Al-Wahaibi, Y., Jibril, A., AlHajri, R., Shuwa, S., (2015). https://doi.org/10.1016/j.petrol.2015.03.018.

[5] Saien, J., Bahiraei, M., Jafari, F. (2023). https://doi.org/10.1038/s41598-023-44600-x.

22nd Iranian Chemistry Congress (ICC22)
Iranian Research Organization for Science and Technology (IROST)
13-15 May 2024

03231-97589

IROST

Fabrication of Bi-based plasmonic photocatalysts as efficient visible-light-active photocatalysts for pharmaceutical and organic contaminants degradation

Zahra Salmanzadeh-Jamadi*, Aziz Habibi-Yangjeh

Corresponding Author E-mail: z.salmanzadeh@uma.ac.ir

Department of Chemistry, Faculty of Science, University of Mohaghegh Ardabili, Ardabil, Iran.

Abstract: Herein, some novel Bi-based plasmonic photocatalysts, such as $TiO_{2-x}/Bi_6Cr_2O_{15}/Bi$ and $TiO_{2-x}/Ag/AgBiO_3/Bi$ nanocomposites were prepared easily to degrade pharmaceutical and organic pollutants. The decreasing particle size, creating oxygen vacancies, the presence of elemental bismuth nanoparticles with plasmonic characteristics were the main reasons for the promoted photocatalytic activity.

Keywords: Plasmon Bi; Photocatalysis; Photodegradation of antibiotics

Introduction

Recently, the utilization of heterogeneous photocatalysts has been proposed as an effective solution for environmental purification, as one of the solar energy conversion processes, under mild conditions [1-3]. Until today, numerous researches have been carried out to exploit plasmonic-based noble metals containing photocatalysts to improve the photocatalytic activities. Regrettably, noble metals including Pt, Ag, and Au are rare and expensive, which prevents their widespread use in photocatalytic technology. Luckily, semimetal bismuth (Bi) has become a suitable candidate to replace the noble metals due to its abundance and cheap price. So, we are trying to fabricate efficient Bi-based plasmonic photocatalysts for pharmaceutical and organic cintaminants degradation. In these regards, very recently, we synthesized photocatalysts like $TiO_{2-x}/Bi_6Cr_2O_{15}/Bi$ and $TiO_{2-x}/Ag/AgBiO_3/Bi$ nanocomposites and applied them for pharmaceutical and organic contaminanats degradation reactions, and impressive performances were observed.

Experimental Section

-Preparation of materials

The hydrothermal method was used to prepare brown TiO_{2-x} nanoparticles [4]. The precursors of $Bi(NO_3)_3.5H_2O$, $Cr(NO_3)_3 \cdot 9H_2O$, and NaOH were employed for synthesis of $TiO_{2-x}/Bi_6Cr_2O_{15}$ nanocomposite via a sonochemical-calcination route. In addition, a facile precipitation route was used to prepare $TiO_{2-x}/Ag/AgBiO_3$ samples. Finally, by treating the above samples with aqueous solution of $NaBH_4$ (Lobachemie, 99%), the reduction of bismuth elements were taken place [5, 6].

-Photocatalytic experiments

To investigate the photocatalytic performance of the synthesized samples, TC was used as the target pollutant. For photocatalytic experiments, a 50W LED lamp was used as a light source. The amount of 0.1 g of prepared nanocomposite was loaded in the mentioned pollutant solution. To measure TC adsorption on the nanocomposite surface, the resulting mixture was stirred for one hour in a double-walled glass reactor equipped with a thermostat in the dark. After the lamp is turned on, sampling is done at certain time intervals. TC concentration was monitored on a UV-vis spectrophotometer by monitoring the specific wavelength of the supernatant at 370 nm.

Results and Discussion

The phase structure, electronic environment, spectroscopic characteristics, surface area, electrochemical properties, and morphology of the resultant nanocomposites were explored using XRD, XPS, EDX, FTIR, UV-vis DRS, PL, SEM, TEM, HRTEM, and EIS analyses. Figures 1(a, b) shows the FESEM images related to $TiO_{2-x}/Bi_6Cr_2O_{15}/Bi$ and $TiO_{2-x}/Ag/AgBiO_3/Bi$ nanocomposites, respectively. According to the provided images, the morphology of both synthesized photocatalysts is spherical.
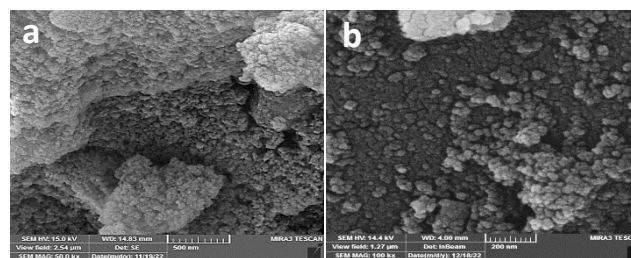

Fig.1 (a, b): FESEM images for $TiO_{2-x}/Bi_6Cr_2O_{15}/Bi$ and $TiO_{2-x}/Ag/AgBiO_3/Bi$ nanocomposites.

In figure 2, the photocatalytic activity of the prepared nanocomposites for the degradation of tetracycline is shown. Based on the results, the degradation rate of $TiO_{2-x}/Bi_6Cr_2O_{15}/Bi$ nanocomposites is about 45.7, 12.8, 19.3, and, 4.26 times higher than TiO_2, TiO_{2-x}, $Bi_6Cr_2O_{15}$, and $TiO_{2-x}/Bi_6Cr_2O_{15}$ samples, respectively. Furthermore,

22nd Iranian Chemistry Congress (ICC22)
Iranian Research Organization for Science and Technology (IROST)
13-15 May 2024

03231-97589

photocatalytic performance of $TiO_{2-x}/Ag/AgBiO_3/Bi$ sample is about 91.9, 25.9, and 20.3 times more than TiO_2, TiO_{2-x}, and $Ag/AgBiO_3/Bi$ samples, respectively.

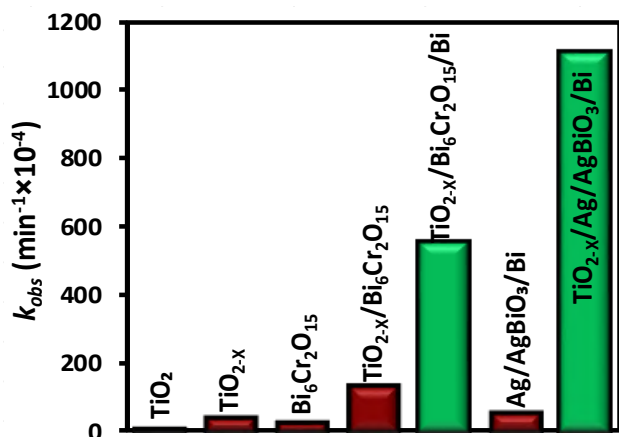As a result, the prepared nanocomposites showed significant activity in the degradation of tetracycline at room temperature, which can be promising for industrial use [5, 6].

Fig. 2: The degradation of TC on prepared photocatalysts.

Conclusions

In conclusion, $TiO_{2-x}/Bi_6Cr_2O_{15}/Bi$ and $TiO_{2-x}/Ag/AgBiO_3/Bi$ heterojunction photocatalysts were synthesized through a facile method. The synthesized samples showed better performance in detoxification of antibiotics and colored pollutants than pure samples. The superior photocatalytic ability of the mentioned photocatalysts was attributed to the rapid charge migration/separation between their constituents through S-scheme heterojunctions and the presence of bismuth nanoparticles with plasmonic resonance properties. The presente work provide new insight into the fabrication of bismuth-based plasmonic photocatalytic materials with the synergistic effect of colored titanium dioxides for water detoxification.

References

[1] Habibi-Yangjeh, A., Pournemati, K., 2024. A review on emerging homojunction photocatalysts with impressive performances for wastewater detoxification. Critical Reviews in Environmental Science and Technology, 54, 290-320.
https://doi.org/10.1080/10643389.2023.2239125.

[2] Hemmati-Eslamlu, P., Habibi-Yangjeh, A., 2023. A review on impressive Z-and S-scheme photocatalysts composed of g-C_3N_4 for detoxification of antibiotics. FlatChem, 43, 100597. https://doi.org/10.1016/j.flatc.2023.100597.

[3] Seifikar, F., Habibi-Yangjeh, A., 2024. Floating photocatalysts as promising materials for environmental detoxification and energy production: A review. Chemosphere (2024): https://doi.org/10.1016/j.chemosphere.2024.141686.

[4] Saadati, A., Habibi-Yangjeh, A., Feizpoor, S., Ramazan Keyikoglu, R., Khataee, A., 2022. Combining brown titanium dioxide with BiOBr and AgBr nanoparticles using a facile one-pot procedure to promote visible-light photocatalytic performance. Journal of Photochemistry and Photobiology A: Chemistry, 431, 114034. https://doi.org/10.1016/j.jphotochem.2022.114034.

[5] Salmanzadeh-Jamadi, Z., Habibi-Yangjeh, A., Khataee, A., Nurbolat, K., 2023. Rational designed novel $TiO_{2-x}/Bi_6Cr_2O_{15}/Bi$ quantum dots: Bi-based plasmonic photocatalysts for boosted detoxifying organic and inorganic wastewaters under visible light. Surfaces and Interfaces, 41, 103199.

https://doi.org/10.1016/j.surfin.2023.103199.

[6] Salmanzadeh-Jamadi, Z., Habibi-Yangjeh, A., Khataee, A., 2024. Decoration of Ag/Bi nanoparticles over brown $TiO_{2-x}/AgBiO_3$ nanocomposites: QDs-sized photocatalysts for impressive mitigation of water pollutants. Colloids and Surfaces A: Physicochemical and Engineering Aspects, 682, 132945.
https://doi.org/10.1016/j.colsurfa.2023.132945.

Electrochemical and supercapacitive study of self-assembled thin film of 2, 2'-bis (ethyl-ferroceneyl) propane on graphite electrode

Zahra Samiei, Sajjad Damiri*, Hamid R. Pouretedal

Corresponding Author E-mail : SajjadDamiri@chmail.ir

Department of Applied Chemistry, Maleke-ashtar University of Technology, Shahin-shahr, Esfahan, Iran.

Abstract: In this paper, the electrochemical and supercapacitive behavior of a thin film and self-assembled layer of the liquid redox of catocene, 2, 2'-bis (ethyl-ferroceneyl) propane, on a basal plane pyroelectric graphite (BPPG) electrode in comparison to a solid ferrocene film, inside aqueous sodium sulfate electrolyte was studied. The modified electrode surfaces were evaluated to assess the redox material film formation and iron content quality using scanning electron microscopy (SEM), laser-induced breakdown spectroscopy (LIBS), and attenuated total reflectance (ATR). The performance of the electrodes and their specific capacitance were assessed and compared using cyclic voltammetry (CV) and galvanostatic charge-discharge (GCD) in a three-electrode system and an asymmetric two-electrode supercapacitor system. Electrochemical studies displayed that the electrode processes are diffusion-controlled, and the liquid catocene exhibits more effective interaction with the BPPG surface in comparison solid ferrocene. The catocene surface coverage (Γ) on graphite is nearly 50-75% higher than ferrocene, leading to improved interaction and charge transfer resistance, observed in electrochemical impedance spectroscopy (EIS) studies. The specific energy density of the catocene-based supercapacitor reaches 56.7 Wh/kg at a power density of 2.9 kW/kg. Moreover, the overall capacitance of the supercapacitor is maintained around 94% efficiency for 3000 charge-discharge cycles.

Keywords: Supercapacitor; Catocene; Ferrocene; Liquid redox; thin film; Electrochemical.

Introduction

Nowadays, with the development of new technologies and environmental concerns, there is an ever-increasing demand for clean, lightweight, high-capacity and cyclically stable electrical energy storage resources such as supercapacitores(SCs). The electrode material is a crucial component of a supercapacitor, and its structure design significantly affects the overall performance of SCs. Thin-film electrodes (TFEs), are a category of intelligent supercapacitor electrodes realized through deposition in the range of a few nanometers to several micrometers. In the development of TFEs or composite electrode active materials for fast charge-discharge supercapacitors, the most common method is the chemical functionalization of redox materials such as ferrocene derivatives on porous conductive electrodes. However, this synthesis process is often expensive, and the surface coverage of the bonded material is relatively low [1]. In surface absorption methods, some solid active materials such as crystalline ferrocene derivatives are usually used, leading to a decrease in electrochemical efficiency. The use of liquid redox materials compared to solids provides a more desirable interaction with carbonaceous electrodes due to their ability to molecularly absorb compared absorbing crystalline particles [2].

In this research, an attempt has been made to compare and analyze the electrochemical behavior and energy storage capacity of two redox materials of solid ferrocene and liquid 2,2'-bis(ethyl-ferrocenyl) propane (catocene), self-assembled on the basal plane pyroelectric graphite (BPPG) electrodes. Catocene is a dark brownish-orange liquid with the chemical formula $C_{27}H_{32}Fe_2$ and an atomic mass of 282.2 g/mol, which is used as an effective catalyst in solid propellants containing ammonium perchlorate [3].

Experimental Section

Working electrodes with coating of thin layer of catocene on BPPG electrode (Cat/BBPG) or ferrocene thin film on BPPG (Fc/BPPG) were prepared by first cleaning the graphite electrode with acetone and keeping it in a vacuum at 45.0 ºC for one hour to remove surface impurities. The electrodes were then cooled to room temperature and weighed. Subsequently, 2.0 Molar concentrations of redox reactants, catocene or ferrocene, were prepared in the DMF solvent. The graphite sheet with a geometric area of 0.2 cm^2 was then immersed in the solution for 5.0 minutes. Afterwards, the solvent-soaked electrode was dried and cooled for 10.0 minutes to stabilize the catocene or ferrocene films on the surface of the graphite electrode.

22nd Iranian Chemistry Congress (ICC22)
Iranian Research Organization for Science and Technology (IROST)
13-15 May 2024

03231-97589

IROST

Results and Discussion

Various techniques including Fourier-transform infrared spectroscopy (FT-IR), attenuated total reflectance (ATR), scanning electron microscopy (SEM), energy-dispersive X-ray spectroscopy (EDS) and laser-induced breakdown spectroscopy (LIBS) were utilized to assess the quality and quantity of catocene and ferrocene films formed on the relatively smooth surface of BPPG electrodes. SEM images and the distribution of Fe element with EDS mapping on the surfaces of Cat/BPPG and Fc/BPPG electrodes were investigated. It was observed that iron atoms from catocene and ferrocene are distributed with relatively low concentration and almost uniform distribution across the entire mapped window. Upon closer evaluation of SEM images, crystalline solid particles of ferrocene with partial iron enrichment are also observed. It is expected that the self-assembled liquid catocene on graphite exhibits a more uniform distribution compared to solid ferrocene.

Cyclic voltammetry (CV) was performed on liquid catocene-coated graphite electrode (Cat/BPPG), ferrocene-coated graphite electrode (Fc/BPPG), and bare graphite electrode (BPPG) in a three-electrode system with a 1.0 M Na2SO4 electrolyte solution. The investigation covered the potential range of -0.5 to 2.0 V at different scan rates from 20.0 to 140 mV/s. CV curves of the samples at various scan rates Showed two main peaks associated with the oxidation-reduction processes on Fc/BPPG and Cat/BPPG electrodes. Similar to the redox processes of ferrocene derivatives.

Figure (1) presents the EIS Nyquisit plots and galvanostatic charge/discharge (GCD) curves of the samples at different current densities within the potential window -0.5 to +1.2 V. It is observed that the discharge time of the samples increases with a decrease in current density. The specific capacitance (F/g) of the electrodes is calculated from their discharge curves at different current densities. By comparing GCD curves of Cat/BPPG and Fc/BPPG samples at different current densities, the specific capacitance and performance of catocene-based film electrodes are 10-15 F/g higher. Due to the favorable performance of the liquid redox material catocene at a positive potential, it was decided to construct an asymmetrical supercapacitor by pairing it with a graphite negative electrode saturated with electrolyte.
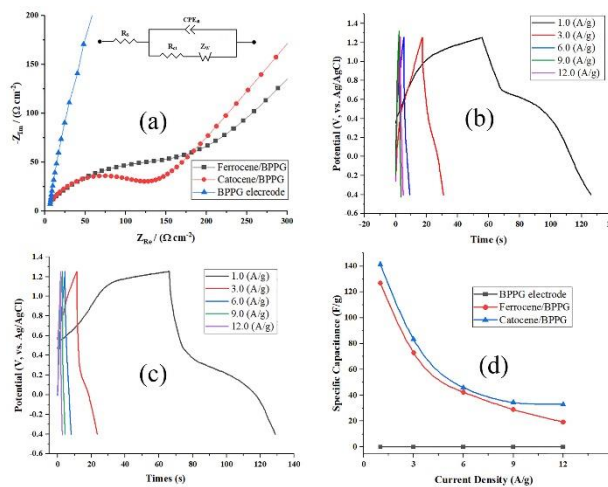
Fig.1: EIS and galvanostatic charge-discharge studies of Cat/BPPG and Fc/BPPG electrodes

Conclusions

This catocene based electrode exhibited a specific capacitance close to 185.0 F/g at a potential scan rate of 20.0 mV/s, compared to 125.0 F/g for ferrocene, and provided lower charge transfer resistance during oxidation. The energy density of the asymmetrical capacitor based on catocene was measured at 56.7 Wh/kg at a power density of 2.9 kW/kg, while the ferrocene-based capacitor showed an energy density of 50.9 Wh/kg at a power density of 2.8 kW/kg, and both capacitors maintained nearly 94% of their overall capacitance in consecutive charge-discharge cycles up to 3000 cycles. References.

References

[1] Oyedotun, K. O., Ighalo, J. O., Amaku, J. F., Olisah, C., Adeola, A. O., Iwuozor, K. O., Akpomie, K. G., Conradie, J., & Adegoke, K. A. (2022). Advances in Supercapacitor Development: Materials, Processes, and Applications. Journal of Electronic Materials, 52(1), 96–129.

[2] Kurapati, N., Pathirathna, P., Ziegler, C. J., & Amemiya, S. (2019). Adsorption and Electron-Transfer Mechanisms of Ferrocene Carboxylates and Sulfonates at Highly Oriented Pyrolytic Graphite. ChemElectroChem, 6(22), 5651–5660.

[3] Sa'at, M., Yarmohammadi, M., Zamani Pedram, M., Shahidzadeh, M., & Amini-Fazl, M. S. (2019). Evaluation of the catocene/graphene oxide nanocomposite catalytic activity on ammonium perchlorate thermal decomposition. International Journal of Chemical Kinetics, 51(5), 337–345.

22nd Iranian Chemistry Congress (ICC22)
Iranian Research Organization for Science and Technology (IROST)
13-15 May 2024

03231-97589

IROST

Synthesis, Characterization and Investigation of Fluorescence Properties Copper (I) Complexes with Nitrogen- Sulfur Donor Pyrazole Besed Ligands

Behzad Soltani, Yeganeh akrami*

Corresponding Author E-mail: yeganeh.kh91@gmail.com

Chemistry Department, Faculty of Basic Science, Azarbaijan Shahid Madani University, Tabriz, Iran.

Abstract: In this study, new copper (I) complexes were prepared with N,S donor pyrazole ligands as the main ligand and triphenylphosphine as adjuvant ligand.these compounds were characterized by different spectral techniques.fluorescence studies of the compounds showed the fluorescence intensity of the complexes is several times higher than of the ligands.

Keywords: N,S donor ligand; Copper complexs ; Fluorescence

Introduction

For decades, coordination chemistry has been the subject of great interest.the coordination complexes of nitrogen and sulfur donor ligands have been widely investigated and they often show new structural features. these compounds play an important role in many applications such as biological,nonlinear optical and luminescent applications[1-2]. luminescent compounds are attracting much current research interest because of their many applications including emitting materials for organic light emitting diodes, light harvesting materials for photocatalysis and fluorescent sensors for organic or inorganic analyses[3-4]. in the present study, we report the synthesis and fluorescence properties of copper (I) complexes with nitrogen-sulfur donor pyrazole besed ligands.

Experimental Section

All of solvents and chemicals were purchased from merck and solvents were dried by standard procedures.
Synthesis of ligands
Na(PhNCSPz)(**1**) and Na(PhNCSPz^{Me2})(**2**) was performe according to a modified literature procedure[4].
synthesis of the complexes
[Cu(PPh$_3$)$_2$ PhNCSPz](**3**)
ligand **1** (1mmol) was added to solution of CuI (I)(1mmol) in acetonitrile and the reaction mixture was stirred for1h at room temperature, in the next step added triphenylphosphine (2mmol) was refluxed and stirred for 2 h. the resultant red precipitate, was filtered,dried in vacuum.m.p:decompose180°C.FTIR(cm^{-1}):3403(broad), 3048(m),1480(s),1432(s),1308(w),1154(m),1091(s),1029 (w),997(m),742(s),505(s). UV-Vis(λ$_{max}$,nm): 230,260,310
[Cu(PPh3)$_2$ PhNCSPz ^{Me2}](**4**)

similar to complex (3),obtained light green precipitate. m.p: decompose190°C,FT-IR(cm^{-1}):3422(broad),3051(m),

1433 (m),1179(w),1156(w),1096(s),1027(w),880(s) 747(s) ,694(s),520(s),502(s).UV-Vis(λ$_{max}$,nm): 220,240,330 suggested structure for complexes showed (Fig1).
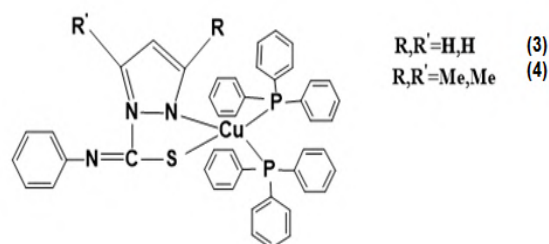
Fig.1: suggested structure for complexes[Cu(PPh$_3$)$_2$ PhNCSPz] (**3**)and[Cu(PPh$_3$)$_2$PhNCSPz^{Me2}](**4**)

Results and Discussion

A novel series of complexes copper (I) with N,S donor pyrazole ligands have been synthesized and characterized by different spectral techniques. all complexes are colored , stable in the solid state,and having high melting points.fluorescence intensity is an important parameter that can be used to measure the concentration of a target in a fluorescence detection method[5].in this work The fluorescence properties of the ligands and its complexes in DMF solvent at a concentration of 0.001 M in room temperature were recorded.Upon excitation at 370 nm, the emission spectrum of ligand 1and 2 shows emission peaks at 430 and 418 nm respectively and the metal complexes 3 and 4 shows peaks in 407 and 402 nm respectively.the fluorescence intensity of this complex is several times higher than of the ligands, also the λ$_{max}$ of this complexes is shifted to lower wavelengths compared to the ligands. The increase in fluorescence intensity is due increase in rigidity due coordination of the ligand to the central metal and complex formation. the comparing the fluorescence

22nd Iranian Chemistry Congress (ICC22)
Iranian Research Organization for Science and Technology (IROST)
13-15 May 2024

03231-97589

intensity of the complex with the ligands is showed(Fig2,3).
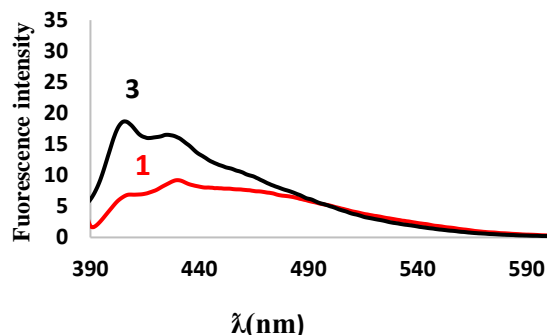

Fig.2: Comparison of fluorescence intensity of complex [Cu(PPh3)$_2$PhNCSPz](**3**) and ligand Na(PhNCSPz)(**1**)
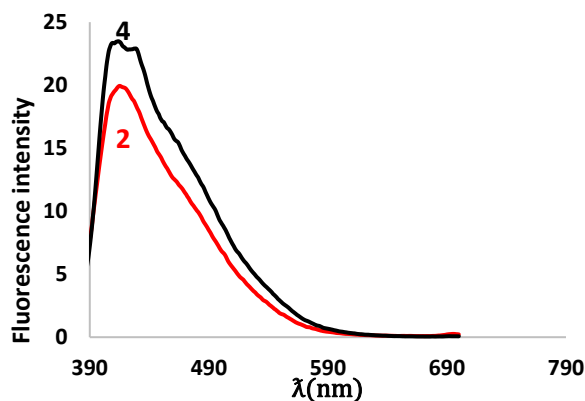

Fig.3: Comparison of fluorescence intensity of complex [Cu(PPh$_3$)$_2$PhNCSPz^{Me2}](**4**)and ligand Na(PhNCSPz^{Me2})(**2**)

Conclusions

A novel series of complexes copper (I) complexes with N,S donor pyrazole ligands have been synthesized. All complexes are colored, stable in the solid state, having high melting points. fluorescence studies showed that fluorescence intensity of this complex is several times higher than the ligands.

References

[1] Soltani, B., Ghorbanpour, M., Ziegler, C. J., Ebadi-Nahari, M., & Mohammad-Rezaei, R. (2020). Nickel (II) and cobalt (II) complexes with bidentate nitrogen-sulfur donor pyrazole derivative ligands: Syntheses, characterization, X-ray structure, electrochemical studies, and antibacterial activity. *Polyhedron*, *180*(114423), 114423. https://doi.org/10.1016/j.poly.2020.114423.

[2] Ali, O. A. M., El-Medani, S. M., Abu Serea, M. R., & Sayed, A. S. S. (2015). Unsymmetrical Schiff base (ON) ligand on complexation with some transition metal ions: synthesis, spectral characterization, antibacterial,

fluorescence and thermal studies. *Spectrochimica Acta. Part A, Molecular and Biomolecular Spectroscopy*, *136 Pt B*, 651–660. https://doi.org/10.1016/j.saa.2014.09.079.

[3] Gulcan, M., Karataş, Y., Işık, S., Öztürk, G., Akbaş, E., & Şahin, E. (2014). Transition metal (II) complexes of a novel symmetrical benzothiazole-based ligand: synthesis, spectral/structural characterization and fluorescence properties. Journal of fluorescence, *24*, 1679-1686. https://doi.org/ 10.1007/s10895-014-1455-3 .

[4] Zhang, Y., Lee, T. S., Favale, J. M., Leary, D. C., Petersen, J. L., Scholes, G. D., ... & Milsmann, C. (2020). Delayed fluorescence from a zirconium (IV) photosensitizer with ligand-to-metal charge-transfer excited states. *Nature chemistry*, *12*(4), 345-352. https:// doi.org/10.1038/s4 1557-020-0430-7

[5] Sadr, M. H., Jalili, A. R., Razmi, H., & Ng, S. W. (2005). A new family of pyrazolyl-based anionic bidentate ligands and crystal structure of bis (N-phenyl-2- pyrazolyl-1-carboximidothioato) copper (II). Journal of organometallic chemistry,*690*(8),2128-2132.https://doi.org/10.1016/j.jorganchem.2005.01.019

[6] Choi, Y. J., & Sawada, K. (2023). Physical sensors: Fluorescence sensors. *Encyclopedia of Sensors and Biosensors*, 1-19. Elsevier.

22nd Iranian Chemistry Congress (ICC22)
Iranian Research Organization for Science and Technology (IROST)
13-15 May 2024

03231-97589

IROST

Investigation of the Antitoxic Effect of a Novel Mn (II) Nano Particle on A549 Cell Line

Niloufar Akbarzadeh- T*, Bahare Karami

Corresponding Author E-mail : n.akbarzadeh@chem.usb.ac.ir

Department of Chemistry, University of Sistan and Baluchestan, P.O. Box 98135-674, Zahedan, Iran.

Abstract: A nanoscale of Mn(II) ion with 2-aminobenzamide (2AB) and glycine was synthesized. These nanoparticles were characterized by SEM images, X-ray diffraction and IR. The cytotoxic activity particle was evaluated on the A549 cell line and the inhibitory effect of these compounds against lung cancer cells showed acceptable results.
Keywords: glycine; SEM images; A549 cell line

Introduction

In the last few decades, the synthesis of nanoscale compounds has increased. This is because by producing metal nanocomplexes, it has created their unique electronic, magnetic, biological, chemical and physical properties. Combinations of transition metal complexes are also necessary to optimize biomedical applications. Recently, many scientists have been working on the synthesis of nano complexes, especially complexes with transition metal ions.

The size and shape of nanomaterials are important factors in the formation of their properties such as optical, electrical, magnetic, catalytic, and antimicrobial. Metal nano complexes and metal oxides have wide applications. Among them are heterogeneous catalysts, electronic and chemical sensing devices, environmental recycling, separations, pharmaceutical fields, inks, disinfectants, thin films, and also anti-microbial activity. The various applications mentioned depend on the morphology and size of the particles. The surface size shape and purity of nanoparticles depend on their production method. Therefore, their synthesis method is fundamental. The main method of producing nanomaterials is the chemical method. In the chemical method for preparing nanomaterials from a raw material in which metal ions are homogeneously distributed. is also used. Then they are prepared by methods such as sol-gel, co-precipitation, thermal degradation, solvent, aqueous, sonochemical, thermal, electrochemical, combustion, and microemulsion, under controlled conditions and metal compounds or microwave and metal nanoparticles. It should be noted that in all the mentioned methods, chemistry plays a significant role, so that by controlling the conditions, including the sensitivity of the process to temperature changes, and the composition of the pH of the environment, materials with desired properties can be produced. The main advantage of these methods is the possibility of achieving chemical homogeneity. Because the chemical processing of materials causes the homogeneity of the chemical composition at the molecular level, and as a result, the final product is homogeneous. Therefore, coordination chemistry is a topic of interest for researchers. The importance of designing new ligands is mainly due to their use as models for protein and metal binding sites in a significant group of metalloproteins in biological systems such as bacteria, and models for magnetic exchange phenomena. , therapeutic reagents in chelation therapy for the treatment of metal poisoning and cyclic antibiotics whose antibiotic activities are preserved by forming a metal complex. Many studies have been conducted in the field of metal-based chemotherapy agents, but to find metal complexes with fewer side effects and similar cytotoxicity, most attention has been directed to new compounds.

Therefore, in this research, we decided to prepare a new Mn(II) ion nanocomplex with the formulas [Mn(2AB)(gly)] and then investigate their antitoxic effect against the A549 cell line.[1-4]

Method

To synthesize the nano complex, manganese (II) salt was dissolved in a suitable solvent with a mixture of ligands, and then the mixture was refluxed for 4 hours at the boiling temperature of the solvent. After this time, the product was collected.

Characterization

In the investigation of the infrared spectrum of the nano complex, the band observed in the 1600 cm-1 region corresponds to C=O, the vibration in the 3400 cm-1 region is related to the amide group, and the vibrations in the 3300 cm-1 region are attributed to the O-H group of the water molecule. Fig. 1.

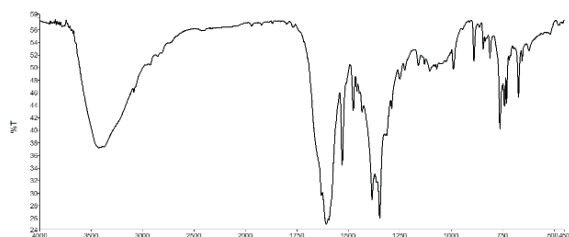**22nd Iranian Chemistry Congress (ICC22)**
Iranian Research Organization for Science and
Technology (IROST)
03231-97589
13-15 May 2024

IROST

Fig. 1. Infrared spectrum of [Mn(2AB)(gly)]   nano complex in KBr environment

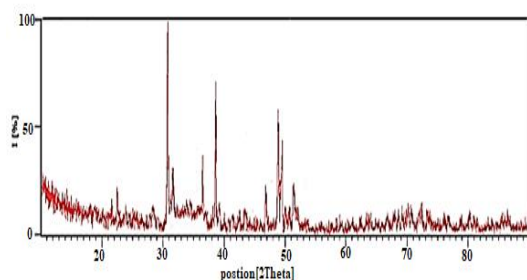Powder Diffraction (XRD) analysis is shown in Fig. 2.

Fig. 2 (XRD) analysis

The SEM image of [Mn(2AB)(gly)] nanocomplex is shown in Figure 3.
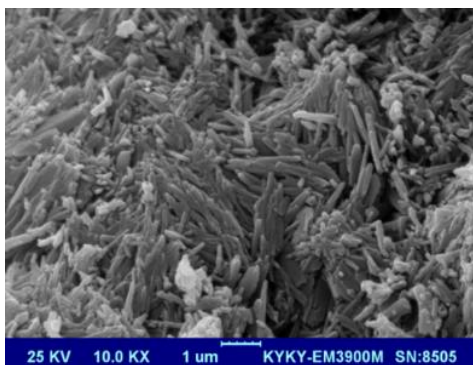As it is clear in the figure, the prepared sample is in the form of nanoparticles and almost with a uniform and stringy morphology.

Fig. 3 SEM image of [Mn(2AB)(gly)] nano complex

Cytotoxicity activity of nanocomplex [Mn(2AB)(gly)] on the A549 cell line was evaluated by reducing MTT. And IC50 values, i.e. the power to inhibit cell activity for each compound, i.e. a concentration of the sample in question that inhibits 50% of cancer cell activity, were calculated and the results were consistent with similar cases. Therefore, the prepared nanocomplex can inhibit the activity of lung cancer cells. Fig.4.
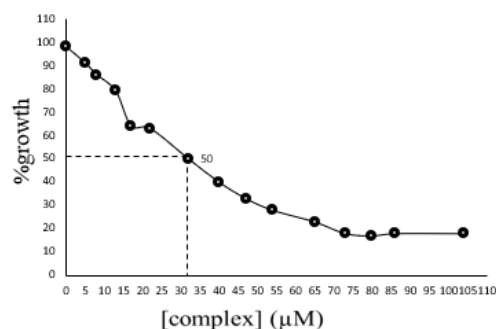
Fig.4. Inhibition of cell growth and proliferation by [Mn(2AB)(gly)] after 24

Conclusions

A Mn(II) ion nanoscale with 2-aminobenzamide (2AB) and glycine was synthesized. These nanoparticles were characterized by SEM images, X-ray diffraction and IR. In the investigation of the infrared spectrum of the nano complex, the band observed in the 1600 cm-1 region corresponds to C=O, the vibration in the 3400 cm-1 region is related to the amide group, and the vibrations in the 3300 cm-1 region are attributed to the O-H group of the water molecule. The cytotoxic activity particle was evaluated on the A549 cell line and the inhibitory effect of these compounds against lung cancer cells showed acceptable results. the prepared sample is in the form of nanoparticles and almost with a uniform and stringy morphology. The crystal size is reported to be 48 nanometers using the Debye-Sherr equation.

References

[1] Saif, M. Journal of Molecular Structure, (2016). Synthesis, characterization, and antioxidant/cytotoxic activity of new chromone Schiff base nano-complexes of Zn(II), Cu(II), Ni(II) and Co(II) 1118, 75-82. dodoi.org/10.1016/j.molstruc.2016.03.060

[2] Zare N. Bioorganic Chemistry, (2018) Synthesis of spherical Fe_2O_3 nanoparticles from the thermal decomposition of iron (III) nano-structure complex: DFT studies and evaluation of the biological activity 80, 334-346. doi.org/10.1016/j.bioorg.2018.07.005

[3] Yousefi M. Soradi Zeid, S. Khorasani Motlagh M. Applied Chemistry, (2017.) Preparation and characterization of orthoferrite neodymium nanoparticles (NdFeO₃) by Co-precipitation route in the presence of oleic acid as a surfactant. 12(43) 93-102. doi. 10.22075/CHEM.2017.236412(43) 93-

[4] Mousavi S., Applied Organometallic Chemistry (2020). Some novel hexa-coordinated cadmium Schiff base complexes: X-ray structure, Hirshfeld surface analysis, antimicrobial and thermal analysis 34(4) 5550. doi.org/10.1002/aoc.5550

22nd Iranian Chemistry Congress (ICC22)
Iranian Research Organization for Science and Technology (IROST)
13-15 May 2024

03231-97589

IROST

DNA-Binding and molecular docking of a copper complex with Schiff base ligand

Niloufar Akbarzadeh- T*, Tahere Kondori

Corresponding Author E-mail: n.akbarzadeh@chem.usb.ac.ir

Department of Chemistry, University of Sistan and Baluchestan, P.O. Box 98135-674, Zahedan, Iran.

Abstract: A Schiff base ligand (a) and its copper complex (b) were synthesized. They were characterized using spectroscopic methods. The study also investigated the interactions between the complex and FS-DNA. According to the thermodynamic parameters data, Vander Waals interactions play an important role in the interaction.

Keywords: Schiff base; thermodynamic parameters; Vander Waals interactions

Introduction

The DNA binding of the transition metal complexes has been studied since these complexes bear potential applications in bioinorganic chemistry. The metal compounds of Schiff bases have potential applications as drugs. The interaction of metal complexes to DNA may cause DNA damage in cancer cells, prevent the division of cancer cells, and finally result in cell death. Changes in the structure of DNA can be easily seen using many experimental methods. Here, we have synthesized the Schiff base ligand (4-nitroaniline-2 Hydroxybenzaldehyde) (a), and its complex [Cu (4-nitroaniline-2-Hydroxybenzaldehyde) (b). Also, we have reported the interaction of (b) with FS-DNA (salmon sperm DNA). The DNA binding properties were investigated through fluorescence, UV-Vis and gel electrophoresis. CD and viscosity data were used to suggest the groove binding mode. [1]

Experimental Section

The Schiff base ligand was prepared according to the literature. The complex (b), was prepared according to the literature. Complex (b) was synthesized by the addition of acetonitrile solution of ligand (a) to a constantly stirring methanol solution of $Cu(CH_3COO)_2 \cdot H_2O$. The resulting solution was refluxed for 6 hours at 40-50 °C. The mixture was maintained at room temperature for slow crystallization (m.p> 300 °C). Elemental analysis calculated for (b) (MW= 628.10): C: 57.37, H: 3.85, N: 13.38, O: 15.28. Found: C: 57.28, H: 3.87, N: 13.35, O: 15,21 FT-IR (KBr, cm^{-1}, w = weak, m = medium, s = strong): 3443m, 1827w, 1703s, 1467w, 1206m, 1198m, 924m, 513s. UV-Vis: (absorption band in 415 nm, assigned to a ligand-metal charge transfer (LMCT) and a band at around 448 nm correspond to d→d transitions). The structure of the molecule of complex (b) is shown in Fig 1.[2]
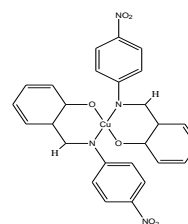

Fig.1. Structure of complex (b

DNA *binding experiments*

To study the interaction of the synthesized complex Cu(II) and fish DNA, the electronic absorption titration assay was carried out. In this test, a constant concentration of the synthesized metal compound was titrated by adding concentrations of DNA. For fluorescence measurements, the spectra were recorded in the presence and absence of FS-DNA solution. In this research, the concentration of **(b)** was preserved constant so long as the amount and concentration of FS-DNA 0-100 mM for the complex. Also, the effects of ionic strength on the synthesized complex with FS-DNA interaction were studied by fluorescence spectroscopy. The gel electrophoresis experiments were performed. The prepared samples were blended with 4 µl of a loading buffer, 5 µl of DNA, and methylene blue and were shaken. The prepared solution was loaded onto an agarose gel, and the electrophoresis was done at 110 V for 25 min. The peaks were recorded using UV irradiation.

Viscosity *measurements*

Anubbelohde viscometer was used in the measurements when **(b)** was absent and present. Viscosity measurement was appraised by comparing the average values of flow times. The data were expressed as $(\eta/\eta_0)^{1/3}$ vs. r, where r is the concentration ratio of the complex **(b)** to the concentration of DNA, η is the DNA viscosity with complex, and η_0 is the viscosity of DNA alone [3].

Molecular docking study

Molecular docking provides an initial model of interactions between ligands and receptors and affords a valuable tool for creating the mode of binding and

22nd Iranian Chemistry Congress (ICC22)
Iranian Research Organization for Science and
Technology (IROST)
13-15 May 2024

03231-97589

IROST

interactions. Docking simulations were performed based on our previous studies [4].

UV-Vis absorption spectroscopy

Fig. 2 exhibits the effect of FS-DNA on the UV-Vis absorption of complex (**b**), suggesting that the interaction of complex (**b**) with FS-DNA has occurred. The maximum absorption was observed at 447 nm, which decreases with an increase in DNA concentration. Upon further increase in FS-DNA concentration, no changes in the absorption spectra were observed, proposing the saturation of the FS-DNA binding site. To prove the mode of interaction, absorption spectra of complex (**b**) at a constant concentration (2.4×10^{-6} M) in the absence and presence of DNA were recorded.

The DNA binding capability of the prepared compound was evaluated through UV-Vis absorption titrations. (Fig. 2).
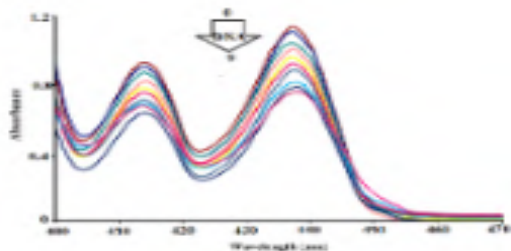
Fig. 2. Absorption spectra of complex (**b**) in the absence (curve 0) and the presence of increasing amounts of FS-DNA (curves 1–9). Arrow indicates the absorbance changing upon the increase of DNA concentration.
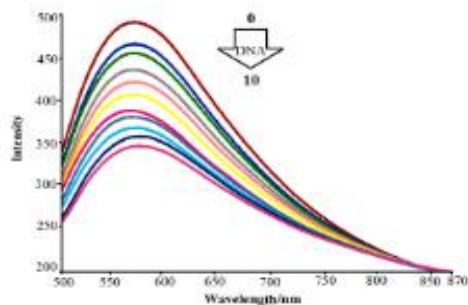
Fig. 3. Fluorescence spectra of complex (**b**) in the absence (curve 0) and presence (curves 1-10) of DNA; [complex] = 1.8×10^{-7}, [DNA] = 1.4×10^{-4}, T = 298 K.
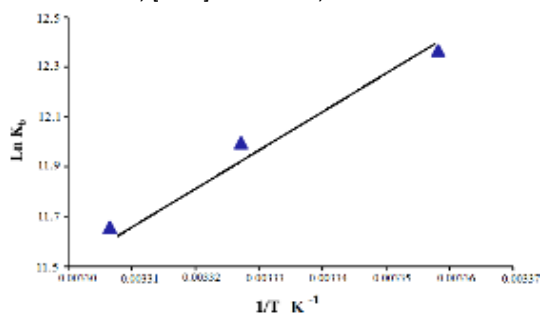
Fig. 4. The van't Hoff plot in the interaction of (b) with FS-DNA at three different temperatures of 293, 298, and 303 K.

Table 1. The thermodynamic parameters in the interaction of (**b**) with FS-DNA at three different temperatures of 293, 298 and 303 K.

T (K)	$\Delta H°$ (kJ/mol)	$\Delta S°$ (J/mol K)	$\Delta G°$ (kJ/mol)
303			-28.56
298	-13.56	-8.13	-29.72
293			-31.04

decrease in the K_b values upon increasing the temperature (Table 1).
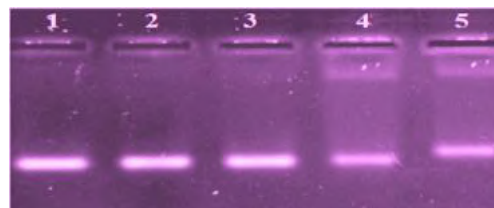
Fig. 5. Gel electrophoresis of cleavage of FS- DNA with different concentrations of the Cu(II) complex. Lane 1: DNA control; Lanes 2-5: (**b**) + DNA.

Viscosity measurement test shows that binding mode should be non-interactive (groove or electrostatic). Hex molecular docking software was applied to predict the interaction mode of the synthesized complex in the DNA binding site.
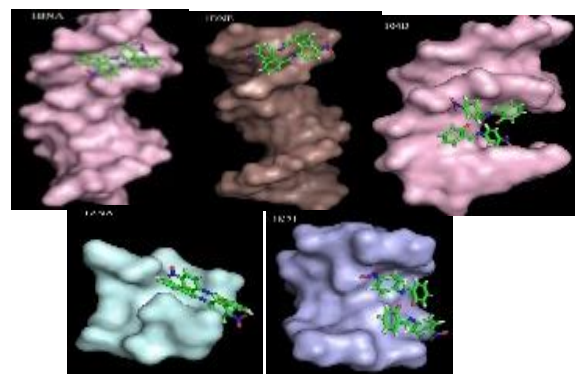

Fig. 6. Docking poses of the synthesized complex in groove binding with different DNA structures.

Conclusions

In this article, Schiff base ligand of (4-nitroaniline-2-Hydroxybenzaldehyde) (**a**) and complex of [Cu(4-nitroaniline-2-Hydroxybenzaldehyde)$_2$] (**b**), were prepared and characterized according to the literature[11]. The interaction between complex (**b**) and FS-DNA in physiological (pH=7.2) solutions was investigated via several spectroscopic methods and agarose gel electrophoresis. UV–Vis investigations indicated that Cu(II) compound has a good interaction with DNA molecules with a suitable value of the binding constant. The results of fluorescence studies showed quenching of Cu(II) complex by DNA via the static mechanism and decrease in K_b values with increasing temperature showing the exothermic interaction.

22nd Iranian Chemistry Congress (ICC22)
Iranian Research Organization for Science and
Technology (IROST)
13-15 May 2024

03231-97589

Negative values of the thermodynamic parameters ΔH^o and ΔS^o calculated from fluorescence data showed that metal complex **(b)** is bounded to DNA grooves using van der Waals forces and hydrogen bonding. The results

References

[1] Singh, B.K., Rajour, H.K., & Prakash, A.(2012). Synthesis, characterization and biological activity of transition metal complexes with Schiff bases derived from 2-nitrobenzaldehyde with glycine and methionine, Spectrochimica Acta Part A: Molecular and Biomolecular Spectroscopy. 94, 143–151. doi:10.1016/j.saa.2012.03.077

[2] Kondori, T. Akbarzadeh- T, N. Fazli, M. Mir, B. Dušek, M. & Eigner, V. (2020). A novel Schiff base ligand and its copper complex: Synthesis, characterization, X-ray crystal structure and biological evaluation, Journal of Molecular Structure. 129395. doi: 10.1016/j.molstruc.2020.129395

[3] Cohen, G. & Eisenberg, H. (1969). Viscosity and sedimentation study of sonicated DNA–proflavine complexes, Biopolymers: Original Research on Biomolecules. 8, 45–55. doi: 10.1002/bip.1969.360080105

[4] Kondori,T. Shahraki, O. Akbarzadeh-T, N. & Aramesh-Boroujeni, Z. (2020).Two Novel Bipyridine-based Cobalt (II) Complexes: Synthesis, Characterization, Molecular Docking, DNA-Binding and Biological Evaluation., Journal of Biomolecular Structure and Dynamics. 1–27. doi: 10.1080/07391102.2020.1713893

22nd Iranian Chemistry Congress (ICC22)
Iranian Research Organization for Science and Technology (IROST)
13-15 May 2024

03231-97589

Phytochemical analysis of the Ethyl Acetate Extract of the Leaves of *Hyoscyamus senecionis*

Peyman Piran Kashani *[a,b], Zeinab Toluei [c], Mahdi Abbas-Mohammadi [d]

Corresponding Author E-mail: peymanpk1995@gmail.com

[a] Essential Oil Research Institute, University of Kashan, Kashan, I.R. Iran.

[b] Department of Phytochemistry, Medicinal Plants and Drugs Research Institute, Shahid Beheshti University, Evin, Tehran, Iran.

[b] Biotechnology Division, Department of Cell and Molecular Biology, Faculty of Chemistry, University of Kashan, Kashan, Iran.

[c] Department of Organic Chemistry, Faculty of Chemistry, University of Kashan, Kashan, Iran.

Abstract: Plants of the *Hyoscyamus* genus, has been traditionally used for stomach cramps, psychosis and severe coughs. Herein, a phytochemical analysis was performed on the ethyl acetate extract of the leaves of *H. senecionis*. Applying the column chromatography and NMR techniques resulted in purification and identification of compounds gastrodin and daucosterol.

Keywords: Hyoscyamus; purification; chromatography

Introduction

Natural products play a vital role in drug discovery due to their diverse chemical structures and biological activities [1]. Hyoscyamus senecionis, a native Iranian herb, is a valuable source of natural products with medicinal properties such as antispasmodic and analgesic effects [2]. Column chromatography, a widely used technique in isolating compounds, enables the separation and purification of complex mixtures effectively [3]. Gastrodin, a compound found in certain plants, shows potential neuroprotective effects, while daucosterol, a phytosterol, exhibits various biological activities including anti-inflammatory properties [4].

Experimental Section

The plant matterial of *H. senecionis* were collected at full flowering stage. Dried leaves of the plant were powdered and successively extracted at room temperature with n-hexane (1 × 2.5 L) and ethyl acetate (3 × 2.5 L) for 3 days each. The extracts were concentrated under reduced pressure. The ethyl acetate extract was subjected to a silica gel CC with a gradient of the n-hexane–EtOAc and then EtOAc–MeOH as eluent to obtain fractions with different polarities. The similar effluents were combined with togethere based on TLC patterns and in continue, further purification was performed using preparative TLC and column chromatography techiques. Purified compounds were structurally identified using extensive spectroscopic methods including 1D (¹H, ¹³C) and 2D NMR (COSY, HSQC, HMBC, NOESY) experiments.

Results and Discussion

Column chromatography of the EA extract led to the isolation and purification of two compounds. They were elucidated as gastrodin and daucosterol (Figure 1)based on their spectral data including 1D and 2D NMR (1H NMR, 13C NMR, COSY, HSQC, and HMBC)
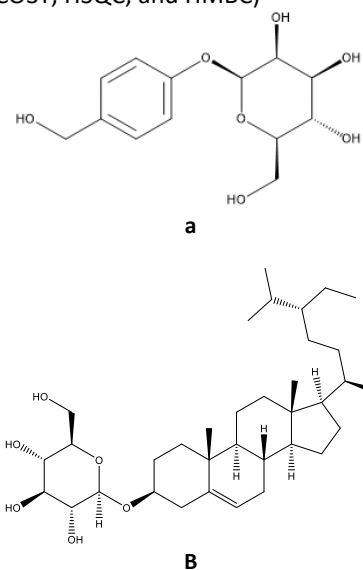

Fig.1: Structure of (a) Gastrodin and (b) Daucosterol

In this study, the importance of Gastrodin and Daucosterol in the Hyoscyamus genus has been identified for the first time. Gastrodin, a natural compound found in certain plants, has been recognized for its potential neuroprotective and anti-inflammatory properties. Its presence in the Hyoscyamus genus sheds light on the potential pharmacological significance of this plant species [5].

Similarly, Daucosterol, another compound identified in the Hyoscyamus genus for the first time, is known for its various biological activities. This steroid compound has been reported to possess antioxidant, anti-inflammatory, and anti-cancer properties [6]. The discovery of

22nd Iranian Chemistry Congress (ICC22)
Iranian Research Organization for Science and
Technology (IROST)
13-15 May 2024

03231-97589

Daucosterol in the Hyoscyamus genus opens up new avenues for exploring the medicinal potential of this plant.

The identification of Gastrodin and Daucosterol in the Hyoscyamus genus marks a significant advancement in our understanding of the chemical composition and pharmacological properties of these plants. Further research is warranted to elucidate the specific roles and mechanisms of action of these compounds in the Hyoscyamus genus, which could potentially lead to the development of novel therapeutic agents with diverse health benefits.

Conclusions

In this research, we explored two natural compounds: gastrodin and daucosterol in the ethyl acetate extract obtained from the leaves of H. senecionis. Given the diverse properties associated with these compounds, it is suggested to investigate the therapeutic potential of this group of natural compounds in future studies.

References

[1] Birchfield, A. S., & McIntosh, C. A. (2020). Metabolic engineering and synthetic biology of plant natural products–A minireview. *Current Plant Biology*, *24*, 100163.

[2] Aboalola, D. M., Weli, A. M., Hossain, M. A., & Al Touby, S. (2020). Toxicological study of various crude extracts of Hyoscyamus gallagheri native to Oman. *Toxicology Reports*, *7*, 680-684.

[3] Kondeti, R. R., Mulpuri, K. S., & Meruga, B. (2014). Advancements in column chromatography: A review. *World Journal of Pharmaceutical Sciences*, 1375-1383.

[4] Jiang, L. H., Yang, N. Y., Yuan, X. L., Zou, Y. J., Zhao, F. M., Chen, J. P., ... & Lu, D. X. (2014). Daucosterol promotes the proliferation of neural stem cells. *The Journal of steroid biochemistry and molecular biology*, *140*, 90-99.

[5] Du, F., Wang, X., Shang, B., Fang, J., Xi, Y., Li, A., & Diao, Y. (2016). Gastrodin ameliorates spinal cord injury via antioxidant and anti-inflammatory effects. Acta Biochimica Polonica, 63(3), 589-593.

[6] El Omari, N., Jaouadi, I., Lahyaoui, M., Benali, T., Taha, D., Bakrim, S., ... & Bouyahya, A. (2022). Natural Sources, Pharmacological Properties, and Health Benefits of Daucosterol: Versatility of Actions. Applied Sciences, 12(12), 5779.

A Bis(NHC)-Pd(II) Complex Supported on Magnetic Mesoporous Silica for Hydroxylation of Aryl Halides With Boric Acid

Somayeh Fekri [*a], Yagoub Mansoori[b]

Corresponding Author E-mail: somayeh.fekri99@gmail.com

[a] Department of Applied Chemistry, Faculty of Science, University of Mohaghegh Ardabili, Ardabil, Iran.

[b] Nanoscience and Nanotechnology Research Group, University of Mohaghegh Ardabili, Ardabil, Iran.

Abstract: Application of a bis(NHC)-Pd(II) catalyst supported on a magnetic mesoporous silica, $Fe_3O_4@SiO_2@SBA$-AP-CC-bis(NHC)-Pd(II), for the hydroxylation of aryl halides with boric acid was investigated. The surface of magnetic SBA-15 was subsequently treated with (3-aminopropyl)triethoxysilane (APTES), cyanuric chloride (CC), imidazole, and 2-bromopyridine. The modified magnetic SBA-15 was then further reacted with trans-[Pd(Cl)$_2$(SMe$_2$)$_2$] complex to give $Fe_3O_4@SiO_2$-SBA-AP-CC-bis(NHC)-Pd(II). The obtained catalyst was fully characterized with conventional methods. The supported complex was sufficiently catalyzed the hydroxylation of aryl halides with boric acid.

Keywords: Magnetic SBA-15, Hydroxylation, Supported complex.

Introduction

In recent years, metal-catalyzed hydroxylation of aryl halides has emerged as an attractive method for the preparation of phenols [1-3]. Herein, we wish to report the application of $Fe_3O_4@SiO_2$-SBA-AP-CC-bis(NHC)-Pd(II) for catalyzing the hydroxylation of aryl halides with boric acid.

Experimental Section

The surface of magnetic SBA-15 was treated with APTES, cyanuric chloride, imidazolide salt, 2-bromopyridine, and trans-[Pd(Cl)$_2$(SMe$_2$)$_2$] complex to give $Fe_3O_4@SiO_2$-SBA-AP-CC-bis(NHC)-Pd(II). The Pd content of the supported Pd(II) catalyst was 2.83 %wt (0.266 mmol/g) as obtained by atomic adsorbtion analysis, **(Fig. 1)**.
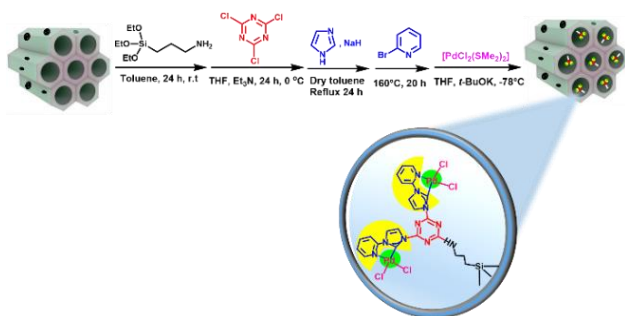
Fig.1: Synthesis of the magnetically supported bis-NHC-Pd(II).

Results and Discussion

Regular channels of SBA-15 and dispersed $Fe_3O_4@SiO_2$ particles around SBA-15 channels can be clearly seen in the SEM image, **(Fig.2a)**.
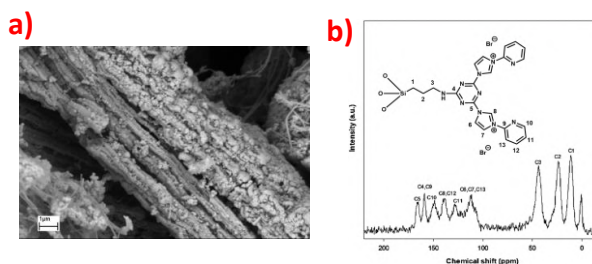
Fig.2: a) SEM image of $Fe_3O_4@SiO_2@SBA$-15, **b)** CP/MAS ^{13}C NMR spectrum of supported ligand

Different carbon atoms in the structure of the $Fe_3O_4@SiO_2$-SBA-AP-CC-bis(PIP) can be distinguished in the CP/MAS ^{13}C NMR spectrum **(Fig.2b)**.

The Pd 3d spectrum for $Fe_3O_4@SBA$-AP-CC-bis(NHC)-Pd(II) shows two unsymmetrical peaks associated with electron transitions of Pd $3d_{5/2}$ and Pd $3d_{3/2}$, respectively (Figure 3). Both peaks are deconvoluted in a major contribution centered at 337.8 eV and 342.9 eV and a minor contribution at 335.6 eV and 340.9 eV, which are associated with Pd(II) and Pd(0), respectively.
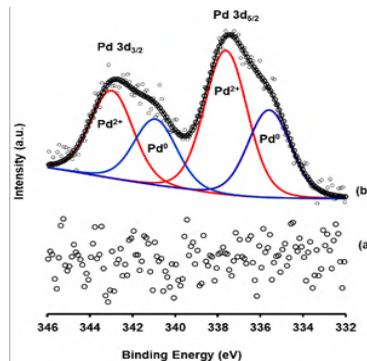

Fig.3: High-resolution XPS spectra of Pd 3d for: a) supported ligand, b) Pd(II) catalyst

In the EDX spectrum, the characteristic signal corresponding to Pd is seen **(Fig.4).**

22nd Iranian Chemistry Congress (ICC22)
Iranian Research Organization for Science and Technology (IROST)
03231-97589
13-15 May 2024

IROST

BET measurement revealed that magnetic SBA-15 and supported Pd(II) catalyst show IV type isotherms with H2 hypothesis loops s is attributed to the formation of an ordered mesoporous cylindrical structure **(Fig.5)**.
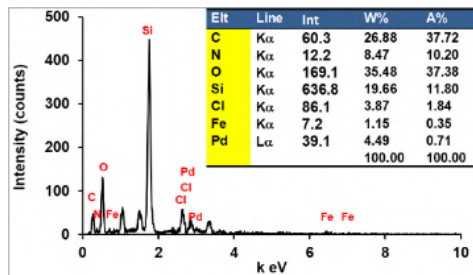

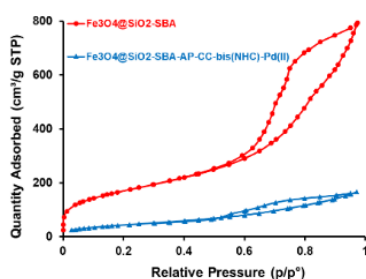**Fig.4:** EDX spectrum of Pd(II) catalyst.

Fig.5: N_2 adsorption-desorption isotherms of the mesoporous materials.

The magnetic catalyst was used to convert *p*-Br-aniline to *p*-aminophenol with boric acid as the model reaction. The reaction was conducted at different reaction conditions such as solvent, base, B(OH)$_3$, temperature, and catalyst dosage, **(Fig. 6)**.
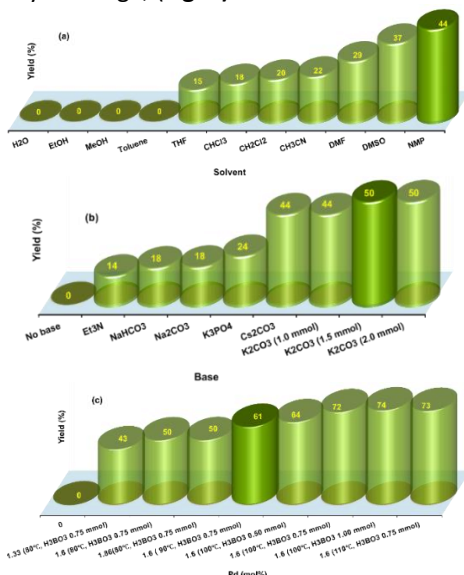
Fig. 6: Optimization of the amination reaction conditions: *p*-Br-aniline (0.50 mmol), B(OH)$_3$ (0.75 mmol), K$_2$CO$_3$ (1.50 mmol), Solvent (1.0 mL), and reaction time 20 h; a) Solvent (Pd(II): 1.6 mol%, 30 mg, reaction temperature: 80℃, K$_2$CO$_3$: 1.00 mmol), b) Base (Pd(II): 1.6 mol%, 30 mg, reaction temperature: 80℃, NMP: 1.0 ml), and c) Temperature, B(OH)$_3$, and the catalyst dosage.

The supported bis-(NHC)-Pd(II) was employed in the hydroxylation of different halo arenes with boric acid under optimal reaction conditions. The reaction proceeded in the presence of boric acid as a hydroxyl source. The results are summerized in **Table 1**. Aryl bromides exhibited enhanced acitvity than aryl chlorides, **(1d, and 1e)**. Haloarenes substituted with an electron-donating group showed high activity compared to haloarenes substituted with an electron-withdrawing group, **(1d, and 1h)**.

Table 1: Hydroxylation of haloarenes.[a, b]

2a
m.p.(℃): Liquid
1a: X = I, 23 h, 56%
1b: X = Br, 24 h, 47%
1c: X = Cl, 24 h, 31%

2b
m.p.(℃): 171-173
1d: X = Br, 20 h, 72%
1e: X = Cl, 20 h, 54%

2c
m.p.(℃): 214-217
1f: X = Br, 21 h, 40%
1g: X = Cl, 22 h, 30%

2d
m.p.(℃):112-114
1h: X = Br, 25 h, 30%

2e
m.p. (℃): 111-115
1i: X = Br, 22 h, 53%

2f
m.p.(℃):105-107
1j: X = Br, 25 h, 40%
1k: X = Cl, 25 h, -

2g
m.p.(℃): 120-122
1l: X = Br, 25 h, 40%
1m: X = Cl, 26 h, 33

2h
m.p.(℃): 82-84
1n: X = Br, 25 h, 40%
1o: X = Cl, 25 h, -

2i
m.p.(℃): 185-188
1p: X = Br, 20 h, 62%
1q: X = Cl, 23 h, 49%

2j
m.p.(℃): 170-172
1r: X = Br, 25 h, 21%

2k
m.p. (℃): Liquid
1s: X = Br, 22 h, 46%

2l
m.p.(℃): 119-121
1t: X = Br, 22 h, 60%

[a] Reaction conditions: Arylhalide 0.5 mmol, K$_2$CO$_3$ 1.5 mmol, B(OH)$_3$ 0.75 mmol, Pd mol% 1.6, and NMP 1.0 ml. [b] Isolated yields.

Conclusions

The synthesis of a supported palladium complex, Fe$_3$O$_4$@SiO$_2$@SBA-AP-CC-bis(NHC)-Pd(II), was presented. The prepared catalyst showed good catalytic activity in the hydroxylation of different chloro-, bromo- and iodoarenes under mild conditions. The prepared catalyst could be retrieved magnetically. The catalyst was thermally stable and could be re-used several times in the catalytic cycle without significant deactivation.

References

[1] Song, Z.-Q.Wang, D.-H., 2020. *Organic Letters*. 22(21): 8470-8474.
[2] Yang, L.Xue, D., 2021. *Synlett*. 32(19): 1891-1896.
[3] Yang, L., Yan, Y., Cao, N., Hao, J., Li, G., Zhang, W., Cao, R., Wang, C., Xiao, J., Xue, D., 2022.. *Organic Letters*. 24(51): 9431-9435.

22nd Iranian Chemistry Congress (ICC22)
Iranian Research Organization for Science and Technology (IROST)
13-15 May 2024

03231-97589

DFT study on the mechanism of the cycloaddition reaction of azaheptafulvene with fulvene

Mina Haghdadi*Hoora Kabirnataj

Corresponding Author E-mail: mhaghdadi2@gmail.com

Department of Chemistry, Babol Branch, Islamic Azad University, Babol, Iran.

Abstract: The cycloaddition reactions of fulvene with azaheptafulvene have been investigated using density functional theory (DFT)-based reactivity indices and activation energy calculations at the M06-2X/cc-pVDZ level of theory. Two modes of [4+6] and [4+2] cycloaddition reactions can occur from the results of Diels-Alder reactions of fulvene with azaheptafulvene. The energy results indicated that the [6+4] cycloaddition reaction is more favorable than [4+2] cycloaddition reaction. The reactions take place via an asynchronous one-step mechanism with a polar character, and an analysis of the conceptual DFT indices explains the polar character of these reactions. which proceeds through a two-stage one-step mechanism.

Keywords: Diels-Alder; DFT method; fulvene and azaheptafulvene; regioselectivity; Reactivity indices.

Introduction

Cycloaddition reactions are among the most important reactions in Organic Chemistry, allowing the construction of any cyclic compound with highly stereo- and regioisomeric outcomes [1,2]. The Diels–Alder or [4+2] cycloaddition reaction between a diene and an ethylene derivative is the most common [3]. When a conjugated triene such as azaheptafulvene 1, which is a imine derivative of cycloheptatriene, used to build larger cyclic compounds, cycloadditions such as [4+2], [4+3], [4+4], [6+2], and even [8+2] become possible. The formation of different constitutional isomeric [m+n] cycloadducts (CAs) is achievable in these higher-order cycloaddition (HOCA) reactions involving three or more double bonds that allow for the construction of medium-size rings [4] with diverse region- and stereoisomeric possibilities. The competition among thermally allowed [4+2], [6+4], and [8+2] cycloaddition reactions has prompted much investigation. Cycloaddition reactions involving more than six π electrons are termed higher-order cycloadditions.[1] The origins of periselectivity of higher-order cycloadditions are poorly understood. The cycloaddition reactions of 8-(p-Chlorophenyl)-8-azaheptafulvene with various fulvenes, which reported by Liu et al., give [4+6] and [4+2] cycloadducts, depending on the substituents present on the fulvene [5]. The highly peri-, regio- and stereoselective cycloaddition of 8-azaheptafulvene to disubstituted fulvenes renders these reactions an interesting platform upon which to investigate origins of periselectivity in higher-order cycloaddition reactions. Here in we have used density functional theory calculations to explore the entire reaction pathway, with a focus on the selectivities of the cycloaddition reactions of Liue experiments. The mechanism and origins of stereoselectivity were explained using the M06-2X density functional theory.
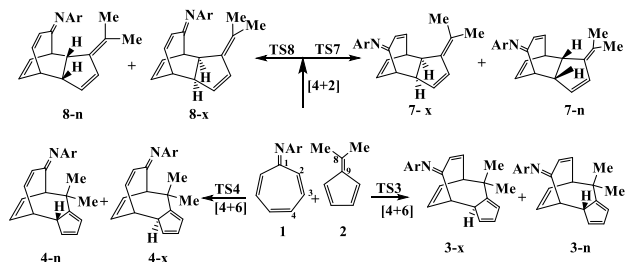
Computational Section

In this study all of geometries were optimized with hybrid metafunctional method, M06-2X, with the cc-pVDZ basis set. All calculations were done using the Gaussian 09 program

Results and Discussion

All competitive stereoisomeric reaction paths considered, and an exhaustive analysis of the potential energy surface (PES) associated with these cycloaddition reactions show their complexity. In the [6+4] cycloadditions, fulvene could behave as the 6π electron addend, and azaheptafulvene act as the 4π electron component (Scheme 1).

Analogously, in the [4+2] cycloadditions, azaheptafulvene and fulvene could serves as the 2π and 4π component, respectively. For each mode of cycloaddition, there are four different originating from different regio- (syn/anti) or stereo- (endo/exo) approaches of the reactants.

The analysis of the relative energies indicates that the most favorable reaction path of the [4+6] cycloaddition reaction is associated with the nucleophilic attack of the C8 carbon of fulvene 2 on the C4 position of azaheptafulvene 2 via TS3-n, by 10.8 kcalmol^{-1}. The formation of the exothermic corresponding adduct of 3-n by −8 kcalmol^{-1}is much lower in energy than its exo isomer, 3-x, in agreement with the generally observed endo selectivity of [4+6] cycloadditions.

22nd Iranian Chemistry Congress (ICC22)
Iranian Research Organization for Science and Technology (IROST)
13-15 May 2024

03231-97589

IROST

Scheme 1: The possible reaction pathways for the cycloaddition reactions of azaheptafulvene with fulvene.

The analysis of the relative energies indicates that the most favorable reaction path of the [4+6] cycloaddition reaction is associated with the nucleophilic attack of the C10 carbon of fulvene 1 on the C1 position of azaheptafulvene 2 via TS3-n, by 10.8 kcalmol^{-1}. The formation of the exothermic corresponding adduct of 3-n by −8 kcalmol^{-1} is much lower in energy than its exo isomer, 3-x, in agreement with the generally observed endo selectivity of [4+6] cycloadditions.

In the [4+2] cycloaddition reaction pathways, while, the cycloadducts are the most stable pathway from the thermodynamically view, TSs have much higher in energy than the reactants. As can be seen from Table 1, the most favorable pathway with the lowest energy barrier can take place through TS8-n by 18.52 Kcalmol^{-1} with the formation of adduct 8-n by ΔGr=−12.81 kcalmol^{-1}. It is the most thermodynamically favorable mode of these cycloadditions. These results suggested that, [6+4] cycloaddition reaction pathways are favorable from a kinetic point of view, while [4+2] cycloaddition reaction pathways are stable from thermodynamic point of view. It seems both cycloadducts of 3-n and 8-n could be generated in the reaction mixture, as in agreement with the experimental results.

Table1: Calculated activation energies (ΔE$^{\#}$/kcalmol^{-1}), reaction energies (ΔE$_r$/kcalmol^{-1}), activation Gibbs free energies (ΔG$^{\#}$/kcalmol^{-1}), reaction Gibbs free energies (ΔG$_r$/kcalmol^{-1}), in the gas phase at the M06-2X/cc-pVDZ level of theory.

Reaction	TSs	ΔE$^{\#}$	ΔG$^{\#}$	ΔE$_r$	ΔG$_r$
1+2→3-x	TS3-x	19.46	34.36	-19.35	-3.6
1+2→3-n	TS3-n	**10.95**	**26.05**	**-24.31**	**-8.28**
1+2→4-n	TS4-n	20.93	36.93	-18.00	-2.22
1+2→4-x	TS4-x	21.93	37.54	-23.69	-7.63
1+2→7-n	TS7-n	18.10	32.06	-26.47	-11.80
1+2→7-x	TS7-x	20.47	34.79	-28.03	-12.07
1+2→8-n	TS8-n	15.52	29.91	-28.21	-12.81
1+2→8-x	TS8-x	16.80	32.27	-27.40	-11.16

Table 2. HOMO energies/au, LUMO energies/au, electronic chemical potential (μ/eV), chemical hardness (η/eV), global electrophilicity (ω/eV) and nucleophilicity (N/eV) for the reactants obtained at the B3LYP/6-31g(d,p) level of theory.

Species	E$_{HOMO}$	E$_{LUMO}$	μ	η	ω	N
1	-0.25477	-0.04700	-4.10	5.65	1.48	2.21
2	-0.26109	-0,02249	-3.85	6.490	1.14	2.04

The global reactivity indices of fulvene, 2, and azaheptafulvene, 1, are analyzed and reported in Table 2. As can be seen from Table 2, the electronic chemical potentials of 1 μ=−4.10 eV is lower than 2, therefore, the charge transfer for these cycloaddition reactions will take place from the studied fulvene, 2 to the azaheptafulvene 1. According to the global electrophilicity, ω, and global nucleophilicity, N, azaheptafulvene 2 is classified as strong electrophiles and moderate nucleophiles based on the electrophilicity and nucleophilicity scales.

Conclusions

The cycloaddition reaction of fulvene 2 with azaheptafulvene 1 has been carried out in order to explain the experimental outcomes, through DFT calculations at the M06-2X/cc-pVDZ level of theory. The regio-, and stereoisomeric reaction pathways have studied. Analysis of the relative energies and thermodynamic parameters indicates that these cycloaddition reactions are completely regio- and stereoselective and take place via a polar process. In the studied reactions of 1 with 2, the most favorable pathway is related to the [6+4] reaction in terms of the kinetic view of point. Analysis of the reactivity indices shows that azaheptafulvene 1 and fulvene 2 present a strong electrophilic and moderate nucleophilic character, respectively, explaining the polar character of these cycloaddition reactions.

References

1. Cookson, R. C.; Drake, B. V.; Hudec, J.; Morrison, A. J. Chem. Soc., Chem. Commun. 1966, 15.
2. Ito, S.; Fujise, Y.; Okuda, T.; Inoue, Y. (1966) Reaction of tropone with cyclopentadiene. Bull. Chem. Soc. Jpn, 39, 1351.
3. Machiguchi, T.; Hasegawa, T.; Otani, H.; Ishii, Y. (1987) Cycloaddition reaction of cycloheptatrienethione with cyclopentadiene. J. Chem. Soc., Chem. Commun., 1375
4. Wang, Z.; Addepalli, Y.; He, Y. (2018) Construction of Polycyclic Indole Derivatives via Multiple Aryne Reactions with Azaheptafulvenes. Org. Lett., 20, 644
5. Liu, C-Y.; Chen, C-C.; Shie, Y-J.; Chung, L-W.; Cheng, T-S.; Shie, M-Y.; Lin, S-Y.; Tsai, Y-L. (2003) Stereoselectivity, periselectivity, and regioselectivity in the cycloadditions of 8-(p-chlorophenyl)-8-azaheptafulvene with cyclopentadiene and fulvenes. Tetrahedron, 59, 6341–6352.

Synthesis of hydrogel composites based on bacterial cellulose membrane modified by PSMA and gelatin for anti-microbial wound healing applications

Fatemeh Mokhtari, Sedigheh Ehsanimehr, Peyman Najafi Moghadam*

Corresponding Author E-mail: p_najafi27@yahoo.com

Department of Organic Chemistry, Faculty of Chemistry, Urmia University, Urmia, Iran.

Abstract: This study focuses on synthesizing hydrogel composites using bacterial cellulose membranes modified with poly (styrene-alt-maleic anhydride) (PSMA) and gelatin for antimicrobial wound healing. Firstly, Poly (styrene-alt-maleic anhydride) (PSMA) copolymer is synthesized, then modified with gelatin, silver nanoparticles, and bacterial cellulose membrane. Vitamin C loading onto the membrane surface and controlled release evaluation are conducted. Structural, and antimicrobial properties, as well as wound healing effects, are analyzed.

Keywords: Hydrogel composite; Bacterial Cellulose membrane; Antibacterial wound healing.

Introduction

In recent years, the synthesis of cellulose-based hydrogels has garnered attention due to their unique properties, biocompatibility, and wound-healing capabilities. Various research endeavors have been undertaken in this regard. Gupta et al. presented silver nanoparticles synthesized using curcumin and hydroxypropyl-β-cyclodextrin complex, then loaded onto bacterial cellulose hydrogels. These hydrogels exhibited a moist environment with high compatibility and resistance against wound-infecting bacteria [1]. Deng et al. introduced hydrogels prepared from cellulose and linseed gum for treating bleeding wounds, demonstrating high thermal stability, swelling capacity, drug absorption, and biocompatibility [2]. In this research work, natural and synthetic polymers and bioactive materials with antibacterial properties are used to improve chronic wounds and diabetic ulcers by synthesizing hydrogel films. First, poly(styrene-alt-maleic anhydride) (PSMA) copolymer is synthesized by radical polymerization method, then, the target hydrogel composites are synthesized through in-situ chemical and physical modification reactions with PSMA, gelatin, silver nanoparticles, and BC membrane. Vitamin C is loaded onto the prepared membrane surface. The controlled loading and release of vitamin C from the synthesized membranes will be evaluated.

Experimental Section

Synthesis of poly (styrene-alt-maleic anhydride) copolymer (PAM)

For the preparation of the copolymer, styrene (0.52 g, 5 mmol) and maleic anhydride (0.5 g, 5 mmol) as the monomers were introduced with a molar ratio of 1:1. Then, 30 mL of anhydrous THF solvent was added to the flask and the contents of the flask were bubbled under inert nitrogen gas to remove the dissolved oxygen. The amount of benzoyl peroxide (0.024 g, 0.1 mmol) was added to the flask as an initiator and the reaction was exposed to inert gas at 65 °C for 24 h. Subsequently, the contents of the flask were cooled and the contents of the flask precipitated into methanol and dried at ambient temperature for 24 h.
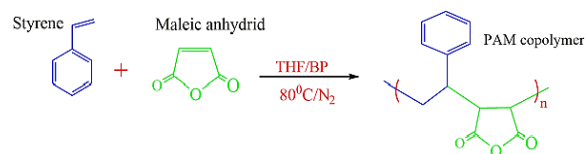

Fig.1. Synthesis of poly (styrene-alt-maleic anhydride)

Preparation of the hydrogel composites based on BC membrane

For the preparation of the hydrogel composites, PSMA, gelatin, and BC membrane were added to the flask containing deionized water (pH 11-10). Then, each piece of the purified BC /gelatin/PSMA membrane was added to an aqueous AgNO$_3$ solution (10, 20, 30 mM) and stirred in the dark at room temperature, then kept under UV radiation at different times. The colorless solution and BC sheet started the gradual color change to dark brown indicating the chemical reduction of silver ions. Then, the obtained composite was rinsed several times with distilled water and dried at room temperature. The composite nanosheet and colloidal AgNPs were stored at 4 °C for further use. Finally, Vitamin C was loaded onto the membrane surface and evaluated for controlled release.

Results and Discussion

Infrared spectroscopy (FT-IR) analysis

The FT-IR spectra analysis confirms the presence of various chemical groups on the nanocomposite structure. In Figure 1, the FT-IR spectra of both pure BC and hydrogel

22nd Iranian Chemistry Congress (ICC22)
Iranian Research Organization for Science and Technology (IROST)
13-15 May 2024

03231-97589

composites are depicted. For pure BC, characteristic bands are observed at 3340, 1158, 1022, and 1107 cm^{-1}, indicating an abundance of –OH groups. A peak at 2976 cm^{-1} corresponds to CH$_2$ stretching vibrations. The bands around 1426 cm^{-1} and 1640 cm^{-1} can be attributed to C–O stretching vibrations of the carboxyl group and –OH deformation, respectively. A peak ranging from 1321 to 1369 cm^{-1} is assigned to O–H in-plane bending. The band at 1022 cm^{-1} represents the C–O–C and C–O–H stretching vibrations of the ring [4]. The FTIR spectrum of the hydrogel composite exhibits all the characteristic peaks of BC, along with a new band at 1545 cm^{-1} for AgNP in the hydrogel composite synthesized under UV radiation due to the hydrogen bonding between BC and AgNPs [5]. Additionally, peaks at 3126 cm^{-1} and 1593 cm^{-1} correspond to the stretching and bending vibrations of the N-H group, while the presence of bands at 1469 cm^{-1} is associated with the C-N bond of the amino group. Moreover, the sharp peak at 1628 cm^{-1} for the amidic carbonyl group is good evidence for the connection of gelatine and PSMA.
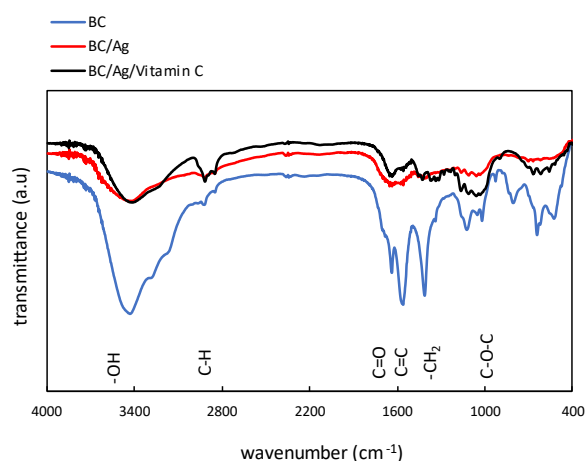
Fig2. FT-IR spectrum of the Pure BC and hydrogel composites

Conclusions

The synthesis of hydrogel composites based on bacterial cellulose membranes modified with poly(styrene-alt-maleic anhydride) (PSMA) and gelatin presents a promising approach for antimicrobial wound healing applications. The incorporation of PSMA, gelatin, and silver nanoparticles onto bacterial cellulose membranes enhances the structural and antimicrobial properties of the hydrogels. Furthermore, the controlled release evaluation of vitamin C loaded onto the membrane surface demonstrates the potential of these hydrogel composites for targeted drug delivery. This study underscores the importance of polymer-based drug delivery systems in improving therapeutic efficacy while minimizing adverse effects, contributing to advancements in wound healing technology.

References

[1] Gupta, A., et al., Synthesis of silver nanoparticles using curcumin-cyclodextrins loaded into bacterial cellulose-based hydrogels for wound dressing applications. Biomacromolecules, 2020. 21(5): p. 1802-1811.

[2] Deng, Y., et al., Preparation and characterization of cellulose/flaxseed gum composite hydrogel and its hemostatic and wound healing functions evaluation. Cellulose, 2020. 27: p. 3971-3988.

[3] Khamrai, M., et al., Curcumin entrapped gelatin/ionically modified bacterial cellulose based self-healable hydrogel film: An eco-friendly sustainable synthesis method of wound healing patch. International journal of biological macromolecules, 2019. 122: p. 940-953.

[4] Dash R, Foston M, Ragauskas AJ (2013) Improving the mechanical and thermal properties of gelatin hydrogels cross-linked by cellulose nanowhiskers. Carbohyd Polym 91(2):638–645.

[5] Wang Y, Gu FQ, Ni LJ, Liang K, Marcus K, Liu S, Yang F, Chen J, Feng Z (2017) Easily fabricated and lightweight PPy/PDA/AgNW composites for excellent electromagnetic interference shielding. Nanoscale 9(46):18318–18325.

Preparation and study of physicochemical properties of Anti bacterial biocomposite films based on Alginate-Carboxymethyl kappa carrageenan

Zahra Abbasi-Ravasjani, Nasser Arsalani*

Corresponding Author E-mail: arsalani@tabrizu.ac.ir

Polymer Research Laboratory, Faculty of Chemistry, University of Tabriz, Tabriz, Iran.

Abstract: Development of wound dressings with exudate management potential is essential to provide appropriate moisture content in wounds. In this study, we aimed to prepare a new bioactive wound dressing based on alginate-carboxymethyl kappa-carrageenan to control wound bed exudate. Our findings revealed that the developed dressing is efficient in exudate absorption.
Keywords: Alginate; Carboxymethyl Kappa-Carrageenan; Exudate; Wound healing

Introduction

The wound healing process is complex and continuous and is influenced by many variables and requires an ideal environment to proceed rapidly. Compared to dry dressings, wet dressings can accelerate the healing process of wounds. In fact, only in a moist environment, fresh skin appears free of inflammation and scarring [1] .An ideal wound dressing should follow the following characteristics: (1) control the moisture around the wound. (2) high gas transmission; (3) removal of excess secretions. and (4) protecting the wound from microorganisms and infections. (5) reducing the amount of necrosis on the wound surface. (6) providing mechanical protection; (7) Easily designed and removed. (8) biocompatible, biodegradable, elastic and non-toxic. 9) reduction of wound pain; and 10) have a reasonable price [2, 3]. Polysaccharide-based hydrogels composed of natural polymers, such as alginate, cellulose, chitosan, hyaluronic acid, etc. were identified to better meet the requirements of wound healing compared with other hydrogels. The backbone of polysaccharide polymer contains a large number of hydroxyl and carboxyl groups, which enables the formed hydrogel higher water content and better swelling performance, resulting in unparalleled moisturizing properties to absorb tissue exudate and negligible adhesion to the wound tissue. However, these hydrogels are inferior to synthetic hydrogels in terms of mechanical properties and stability, and a single polysaccharide hydrogel cannot meet the component requirements for wound healing. Among these polymers, anionic polysaccharides, Alginate and Carboxymethyl K-carrageenan were investigated in this research due to their biodegradability, high similarity to skin tissue, availability and suitable properties for biomedical applications.

Experimental Section

Carboxymethyl kappa-carrageenan was synthesized in two steps as described previously. The film was prepared by solvent casting technique. Briefly, sodium alginate and carboxymethyl k-carrageenan (1:3) were dissolved in distilled water at 60-70°C under magnetic stirring for 1 hour. After complete dissolution, glycerol was added as a plasticizer to increase film flexibility, reduce brittleness, and facilitate their separation from Petri dishes. 0.5% calcium chloride was used as crosslinker. The hydrogels were cast onto transparent glass Petri dishes and then placed in vacuum for 30 min to remove air bubbles at room temperature. Finally, the hydrogels were dried at 30°C for 48 h allowing the forming of thin films.
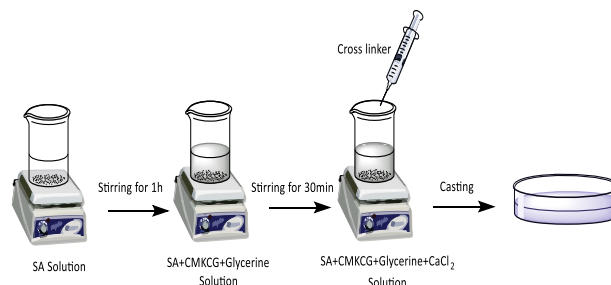
Results and Discussion

The IR spectra (Fig. 1) of carboxymethyl k-carrageenan and k-carrageenan showed the successful synthesis of carboxymethyl k-carrageenan (CMKC). The bands at 1260 cm^{-1}, 850 cm^{-1} were assigned respectively to O=S=O symmetric vibration and C_4–O–S stretching vibration. They stood for total $-SO_4$ and C_4–O–S of B-d-galactose respectively. The band at 930 cm^{-1} proved the existence of C–O–C of 3,6-anhydro-dgalactose. It also displayed an absorbance band at 1159 cm^{-1} due to bridge –O stretch. And band around 1070 cm^{-1}, 2933 cm^{-1},and 3411 cm^{-1} was reported to be related to C–O stretch, C–H stretch and O–H stretch respectively. The intensity of each absorption band standing for quantity of functional group in IR spectrum of CMKC had changed greatly. Compared with IR of KC, the peak intensity at around 1325 cm^{-1} of CMKC increased obviously, which proved the quantity of

22nd Iranian Chemistry Congress (ICC22)
Iranian Research Organization for Science and Technology (IROST)
13-15 May 2024

03231-97589

IROST

C–O stretch on the galactose increased. The typical absorption band around 1760 cm^{-1},1624 cm^{-1} and 1424 cm^{-1}, corresponding to the asymmetric vibration and symmetric vibration of $-COO^-$, indicated the introduction of carboxymethyl groups. As shown in Fig 2. Tensile strength and elongation at break are useful in predicting the film's ability to maintain its integrity when used as wound dressing. the tensile strength of the SA/CMKCG film was 12.31 MPa. The elongation at break percentage of film was 54.94%. Figure 3 shows the water absorption capacity of the film prepared with optimal concentration in PBS environment at different times. The water absorption capacity of the film in the first six hours had the highest value (2344.66%) and then its value was constant.

Conclusions

Using the solvent casting method, we prepared a mixed film of polysaccharides with an optimized concentration. The mixture of desired polymers forms a homogeneous, biodegradable, biocompatible and non-toxic film. The mechanical properties of the film and water absorption capacity are also improved due to mixing. The prepared film can be used as a wound dressing for Exudative ulcer and other wounds.

References

[1] Z. Fan *et al.*, "A novel wound dressing based on Ag/graphene polymer hydrogel: effectively kill bacteria and accelerate wound healing," *Advanced Functional Materials,* vol. 24, no. 25, pp. 3933-3943, 2014.

[2] W. Khan, V. G. S. Challa, R. Langer, and A. J. Domb, "Biodegradable polymers for focal delivery systems," *Focal Controlled Drug Delivery,* pp. 3-32, 2014.

[3] M. Kokabi, M. Sirousazar, and Z. M. Hassan, "PVA–clay nanocomposite hydrogels for wound dressing," *European polymer journal,* vol. 43, no. 3, pp. 773-781, 2007.

Fig.1: FT-IR of K-Carrageenan/Carboxymethyl K-Carrageenan
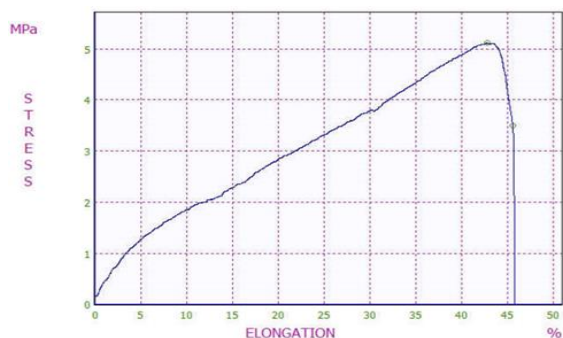
Fig.2: Tensile strength of film
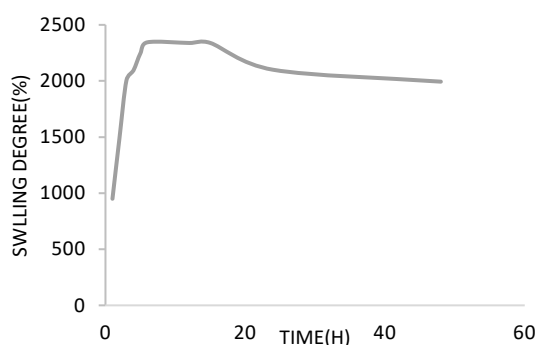
Fig.3: Swelling degree of Film

22nd Iranian Chemistry Congress (ICC22)
Iranian Research Organization for Science and Technology (IROST)
13-15 May 2024

03231-97589

IROST

Electrodeposition of transparent tungsten oxide film as a potential electron-transport layer in optoelectronic devices

M. Mohebbi*, F. Sadegh, V. Mirkhani*, M. Moghadam, S. Tangestaninejad, I. Mohammadpoor-Baltork

Corresponding Author E-mail: chemophile90@gmail.com

Department of Chemistry, Catalysis Division, University of Isfahan, Isfahan 81746-73441, Iran.

Abstract: Electrochemical deposition is one of the available, cheap, and precise techniques to prepare a thin film of tungsten oxide (WO_3) with promising properties as an electron-transport layer (ETL) in optoelectronic devices. In the current study, electrodeposited WO_3 photoelectrode has been successfully synthesized, optimized, and characterized using techniques such as XRD and UV-Vis. The transparent WO_3 layer is aimed to show perfect performance in optoelectronic devices.

Keywords: Tungsten oxide; Electron-transport layer (ETL); Electrodeposition; Optoelectronic device.

Introduction

The development of optoelectronic devices is one of the important research fields of chemistry. In this regard, enhanced device performance could be achieved by designing promising semiconductor nanostructures as transport layers, between different candidates, metal oxide semiconductors are suitable alternative materials for transport layers owing to their high carrier mobility, good chemical stability, suitable energy levels, low cost, and environmental friendliness. Tungsten oxide (WO_3) shows suitable properties such as an appropriate band gap of 2.6-3.1 eV, high electron mobility, and chemical stability [1].

Various methods have been devoted to depositing WO_3 for instance spin coating, sputtering, atomic layer deposition (ALD), etc. Compared to other synthetic techniques, electrochemical deposition is a scalable method that can be manipulated easily by controllable parameters of the technique. Therefore, rigorous research effort is needed to further investigate the effects of different parameters on the deposition of a homogenous and stable film with appropriate optoelectronic properties.

Experimental Section

The electrolyte of electrochemical deposition is a Peroxytungstic acid solution prepared by solving metal W powder in hydrogen peroxide and then diluted to 25mM in isopropanol. In a three-electrode system conductive fluorine-doped tin oxide (FTO) substrate, steel mesh and Ag/AgCl are working, counter, and, reference electrodes respectively. Several parameters of the deposition were optimized and Prepared layers were then calcinated at 450°C for 2 hours [2].

Results and Discussion

The predominant peroxytungstate is $W_2O_{11}^{2-}$ or $[(O)W(O_2)_2(O)(O_2)_2W(O)]^{2-}$, where O_2 denotes a peroxide ligand. Noteworthy W is in its usual 6^+ state. The anion is formed according to the equation below:

$$2W + 10H_2O_2 \rightarrow W_2O_{11}^{2-} + 2H^+ + 9H_2O \qquad (1)$$
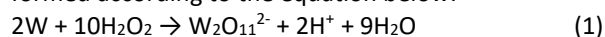
A possible decomposition reaction, generating solid tungsten trioxide is:

$$W_2O_{11}^{2-} + 2H^+ \rightarrow 2WO_3 + 2O_2 + H_2O \qquad (2)$$
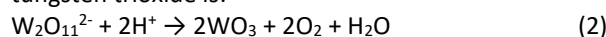
Note that the sequence of Eq.1 and Eq.2 describes the decomposition of H_2O_2 into water and oxygen [3].

Figure 1 shows the X-ray diffraction (XRD) pattern of the electrodeposited WO_3 layer on FTO. Diffraction peaks of (002), (020), and (200) confirm the successful formation of the tungsten trioxide crystals [3].
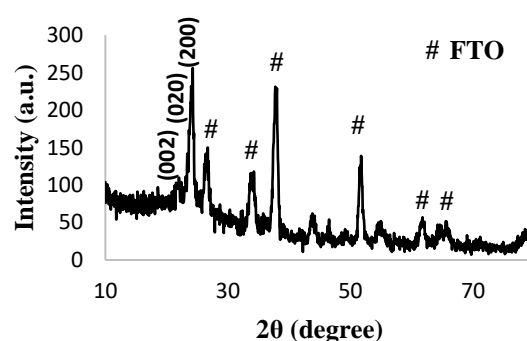

Fig.1: XRD pattern of tungsten oxide on FTO.

22ⁿᵈ Iranian Chemistry Congress (ICC22)
Iranian Research Organization for Science and
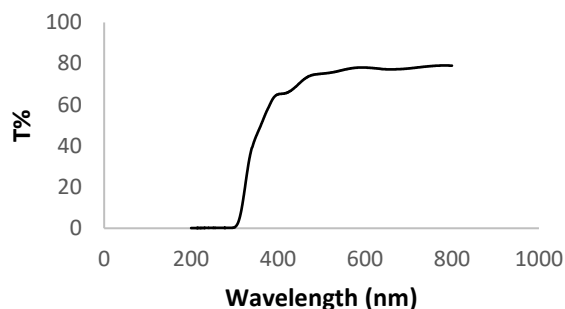Technology (IROST)
13-15 May 2024

03231-97589

IROST

Fig.2: UV-vis transmittance spectra of tungsten oxide.

For optoelectronic devices, it is crucial that the ETL possesses adequate optical properties and the transmittance of the ETL must be maximized to achieve higher light harvesting efficiency. The UV-vis. transmittance of the electrodeposited WO_3 layer was investigated (Fig. 2). The spectrum demonstrates 80% transparency in the visible region with an absorbance edge of about 300 nm.

Conclusions

In this study, we electrodeposited and optimized a transparent tungsten trioxide (WO3) thin film on FTO using the metal powder of tungsten as a precursor. The crystallized layer shows all representative peaks of WO_3 as well as high transparency in the visible range which fulfills the requirements of an efficient ETL in optoelectronic devices.

References

[1] Simchi, H., McCandless, B. E., Meng, T., & Shafarman, W. N. (2014). Structural, optical, and surface properties of WO_3 thin films for solar cells. Journal of alloys and compounds, 617, 609-615.

[2] Baeck, S. H., Jaramillo, T., Stucky, G. D., & McFarland, E. W. (2002). Controlled electrodeposition of nanoparticulate tungsten oxide. Nano letters, 2(8), 831-834.

[3] Yun, G., Balamurugan, M., Kim, H. S., Ahn, K. S., & Kang, S. H. (2016). Role of WO_3 layers electrodeposited on SnO_2 inverse opal skeletons in photoelectrochemical water splitting. The Journal of Physical Chemistry C, 120(11), 5906-5915.

[4] Meulenkamp, E. A. (1997). Mechanism of WO_3 Electrodeposition from Peroxy-Tungstate Solution. Journal of the Electrochemical Society, 144(5), 1664.

22nd Iranian Chemistry Congress (ICC22)
Iranian Research Organization for Science and Technology (IROST)
13-15 May 2024

03231-97589

IROST

One-pot and sequential synthesis of bis-imidazopyridine disulfide derivatives

Sadegh Khashei, Fateme Mahmoudi*, Ayoub Bazgir

Corresponding Author E-mail: sadeghkhashei74@gmail.com

Abstract: An efficient, one-pot method of the reaction of phenacyl bromide and 2-aminopyridine in the presence of sulfur and trimethylsilyl cyanide for the synthesis of bis-imidazopyridine disulfide derivatives is reported.

Keywords: Bisimidazopyridine disulfide; Thiol oxidation; Imidazo[1,2-a]pyridine; Organic sulfur compounds

Introduction

Oxidation of thiols to disulfides is of interest from the point of view of synthetic, biological and oil industries [1-5] for the selective oxidation of thiols by various methods such as iodine/hydrogen iodide, bromine, copper sulfate/potassium permagnate, dihydrogen peroxide , in trifluoroethanol and dimethylsulfoxide-N phenyltriazolinedione, potassium dichromate and enzymatic and electrochemical methods are used for this conversion. Among its drawbacks is the use of stoichiometric values and reagents that produce waste materials. To overcome these drawbacks, catalytic oxidation using oxygen as oxidant has been developed by several groups. One of the efficient oxidation connections of thiols to disulfides using metallophthalocyanines in aqueous environments has been reported [6-8]. However, not only aqueous bases always cause the problem of producing waste materials, but the main drawbacks of these catalysts are poor solubility in common organic solvents and the formation of exodimers in the case of water-soluble tetrasulfone phthalocyanines, which reduces reactivity in aqueous environments. [9] Therefore, metallophthalocyanines were used for the stability and easy recovery of the catalyst on a variety of solid surfaces. However, to increase the efficiency of these catalytic systems, dihydrogen peroxide or potassium hydrogen sulfate was used as an activator of metallophthalocyanines. [10]

Experimental Section

To start the research, the imidazopyridine nucleus was formed from the reaction of phenacyl bromide (1) with 2-aminopyridine (2) in the presence of Dabco catalyst (3).
In the following, the imidazopyridine core was converted to thiocyana imidazopyridine in the presence of trimethylsilicon cyanide (5) and sulfur (6).
Finally, tert-butylamine (8) was added to it, and our disulfide product (9) was obtained with a yield of 71%.
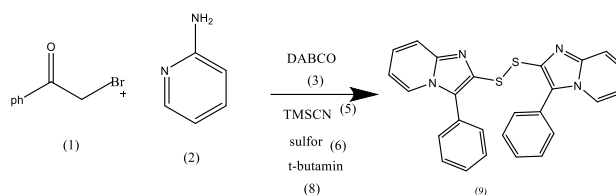
Fig.1

Results and Discussion

From the reaction of phenacyl bromide and 2-aminopyridine in the presence of DABCO, the imidazopyridine core was formed. Next, intermediate 2 was formed with sulfur, which is formed with TMSCN through the radical mechanism of product number 4. By adding base to two radical or nucleophilic methods, We get the final product.
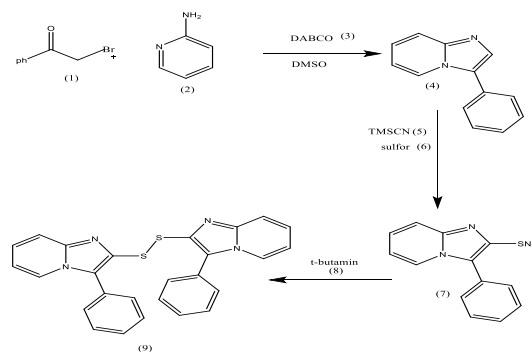

Fig.2

In the synthesis of {1,2-bis(3-phenylimidazo[1,2-a]pyridin-2-yl)disulfane}, different solvents were tested in a single container. The table is as follows.
According to the table, because sulfur has good solubility in dimethyl sulfoxide solvent. According to the reported reference, the reaction is only possible in this solvent in a single container.

Row	solvent	Efficiency	time
1	DMSO	70%	10min
2	EtOH	trace	-
3	EtOAC	trace	-
4	CH_2Cl_2	trace	-
5	$CHCL_3$	trace	-
6	CH_3CN	trace	-

22nd Iranian Chemistry Congress (ICC22)
Iranian Research Organization for Science and Technology (IROST)
13-15 May 2024

03231-97589

Different openings were tried for optimization, and the results are summarized in the table below.

Row	base	Efficiency	time
1	t-butamin	90%	5min
2	Cyclohexylamin	87%	10min
3	MENH$_2$	81%	10min
4	DABCO	50%	8h
5	Dmap	50%	8h
6	pipyridine	50%	0.5h
7	ETNH$_2$	75%	15min
8	ET$_3$N	80%	15min
9	K$_2$CO$_3$	Trace	-
10	DBU	Trace	-

Conclusions

Imidazo[1,2-a]pyridines [11] are a family of aza-heterocycles that have a special place in medicinal chemistry (Figure 1.2). Imidazo[1,2-a]pyridines are biologically important molecules and show a wide range of pharmacological effects including anticancer, antiapoptotic, antianxiety, antipain, anti-inflammatory, anti-viral, anti-tuberculosis. Recently, the antibacterial activity of 3-arylimidazo[1,2-a]pyridines against Staphylococcus aureus has been demonstrated. Considering their wide biological importance, it is not surprising that the chemical community has devoted many efforts towards the synthesis and functionalization of imidazo[1,2-a]pyridine derivatives.

References

[1] Ogawa, A., Nishiyama, Y., Kambe, N., Murai, S., & Sonoda, N. (1987). Selenium, carbon monoxide and water as a new reduction system: Reductive cleavage of disulfides and diselenides to thiols and selenols. Tetrahedron letters, 28(28), 3271-3274.

[2] Antebi, S., & Alper, H. (1985). Cobalt carbonyl catalyzed reactions of disulfides: carbonylation to thioesters and desulfurization to sulfides. Tetrahedron letters, 26(22), 2609-2612.

[3] Bischoff, L., David, C., Martin, L., Meudal, H., Roques, B. P., & Fournié-Zaluski, M. C. (1997). 2, 4-Dinitrophenyl 4-methoxybenzyl disulfide: a new efficient reagent for the electrophilic sulfenylation of β-amino ester enolates. The Journal of Organic Chemistry, 62(14), 4848-4850.

[4] Bodanszky, M. (2012). Principles of peptide synthesis (Vol. 16). Springer Science & Business Media.

[5] Bodanszky, M. (2012). Principles of peptide synthesis (Vol. 16). Springer Science & Business Media.

[6] Jeyakumar, K., & Chand, D. K. (2009). Application of molybdenum (VI) dichloride dioxide (MoO2Cl2) in organic transformations. Journal of chemical sciences, 121(2), 111-123.

[7] Karimi, B., & Zareyee, D. (2004). Trimethylchlorosilane (TMCS) catalyzed efficient reduction of sulfoxides to thioethers using 3-mercaptopropionic acid under mild reaction conditions. Phosphorus, Sulfur, and Silicon, 179(1), 77-81.

[8] Chatti, I., Ghorbel, A., Grange, P., & Colin, J. M. (2002). Oxidation of mercaptans in light oil sweetening by cobalt (II) phthalocyanine–hydrotalcite catalysts. Catalysis today, 75(1-4), 113-117.

[9] Chauhan, S. M. (2003). S, Kumar A, Srinivas KA. Chem. Commun, 2348.

[10] Perathoner, S., & Centi, G. (2005). Wet hydrogen peroxide catalytic oxidation (WHPCO) of organic waste in agro-food and industrial streams. Topics in Catalysis, 33(1), 207-224.

[11] Bagdi, A. K., Santra, S., Monir, K., & Hajra, A. (2015). Synthesis of imidazo [1, 2-a] pyridines: a decade update. Chemical Communications, 51(9), 1555-1575.

Computational Analysis of Pentostatin Drug Using Quantum Mechanics

Hossein Shirani[a,b,*], Amir Hossein Teimouri[b]
Corresponding Author E-mail: hossein_shirani@iust.ac.ir
[a] Department of Chemistry, Iran University of Science and Technology, P.O. Box 16846-13114, Tehran, Iran
[b] Department of Microbiology, Faculty of Biological Sciences and Technology, University of Science and Culture, Tehran, Iran.

Abstract: This research delves into the efficacy of Pentostatin as a potential chemotherapy agent using Density Functional Theory at the B3LYP/6-311+G** level. The study encompasses molecular optimization, analysis of electronic energy, examination of vibrational frequencies, assessment of structural parameters, and provides valuable insights into the behavior of Pentostatin. Furthermore, it explores the interactions of Pentostatin with various substances, particularly nanoparticles within drug delivery systems.
Keywords: Hairy Cell Leukemia (HCL); Pentostatin; Density Functional Theory; B3LYP/6-311+G**; HOMO-LUMO

Introduction

Hairy cell leukemia, a slow-growing cancer first documented in 1958 by Bouroncle and his team, is characterized by low blood cell counts and enlargement of the spleen, making up about 2% of all leukemia cases. It is estimated that there were 61,780 new cases of leukemia in the United States in 2019. Pentostatin, a powerful inhibitor of adenosine deaminase, is a drug used to treat various lymphoproliferative disorders. Its chemical name is (R)-3-(2-deoxy-ß-D-erythropentofuranosyl), with a molecular formula of C11 H16 N4 O4 and a molecular weight of 268.27. Pentostatin, also known as deoxycoformycin, is a medication commonly used in the treatment of certain types of cancer. It works by stopping the growth of cancer cells and reducing the spread of the disease. Pentostatin is often prescribed by doctors to help patients manage their condition and improve their quality of life [1-3].

Methods

In the first step, the molecular configuration of Pentostatin was created using GaussView software, then proceeded with quantum mechanical calculations at the B3LYP/6–311+G theoretical level using Gaussian09 software [4].

Results and Discussion

Molecular computations were conducted to analyze the drug Pentostatin, utilizing the GaussView program at the B3LYP/6–311+G theoretical level, with the resulting structural parameters documented. The molecular structure of interest was first created in GaussView software (See Fig.1) for this investigation.
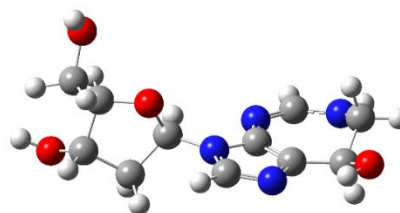
Fig.1: 3D structure obtained from B3LYP/6-311+G** calculations

Table 1 presents the computed thermodynamic properties obtained using the B3LYP/6-311+G** level of theory. The properties include electronic energy, zero point energy, entropy, enthalpy, Gibbs free energy, and heat capacity (CV) in units of kcal/mole. kcal/mol-kelvin

Table 1: the computed thermodynamic properties obtained using the B3LYP/6-311+G** level of theory. The characteristics encompass electronic energy (E_{ele}), zero-point energy (ZPE), enthalpy (H), Gibbs free energy (G) in kcal/mole units, as well as entropy (S) and heat capacity (CV) in kcal/mol-kelvin units.

E_{ele}	ZPE	S	CV	H	G
-595447.6	179.0	0.1	0.7	-948.6	147.8

Tables 2 to 4 showcase the structural parameters of Pentostatin. Moreover, Tables 5 and 6 display the Calculated Dipole Moments (Debye) Values and HOMO-LUMO Energy for the Pentostatin Molecule, obtained using the B3LYP/6-311+G** Computational method, respectively.

22nd Iranian Chemistry Congress (ICC22)
Iranian Research Organization for Science and
Technology (IROST)
13-15 May 2024

03231-97589

Table 2: B3LYP/6-311+G** optimized values of bond lengths (Å) for Pentostatin.

O_2-C_3	C_3-C_5	C_5-N_8	N_8-C1_0
1.42075	1.53836	1.46229	1.36674
$C_{10}-N_{12}$	$C_{14}-N_{15}$	$C_{16}-N_{18}$	$C_{31}-O_{34}$
1.28723	1.37421	1.36642	1.42074

Table 3: B3LYP/6-311+G** optimized values of bond angles (°) for Pentostatin.

$O_1-C_2-C_3$	$C_3-C_5-N_8$	$N_{18}-C_{19}-O_{30}$
107.45878	113.56835	108.93756
$O_{30}-C_{19}-C_{21}$	$N_{18}-C_{19}-O_{30}$	$C_{21}-C_{24}-O_{25}$
104.84975	108.93756	109.40464

Table 4: B3LYP/6 -311+G** optimized values of bond dihedral for Pentostatin.

$O2-C3-C5-N8$	$N_{12}-C_{13}-C_{14}-N_{15}$	$C_3-C_{14}-N_{15}-C_{16}$
174.58129	-177.48564	178.50343
$C_{19}-C_{21}-C_{24}-O_{25}$	$O_{25}-C_{24}-C_{28}-O_{30}$	$C_{24}-C_{28}-C_{31}-O_{34}$
118.23577	-139.15413	-166.18461

Table 5: Calculated Dipole Moments (Debye) Values for Pentostatin Molecule using B3LYP/6-311+G Computational.

μ_x	μ_y	μ_z	μ_{tot}
-2.8280	1.2266	0.1099	3.0846

Table 6: Calculated HOMO-LUMO Energy Gap (ev) Values for Pentostatin Molecule using B3LYP/6-311+G Computational. (See also Fig. 2)

E_{HOMO}	HLG	E_{LUMO}
-0.20456	0.17881	-0.02575
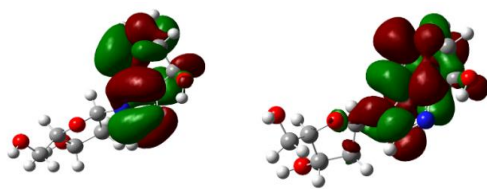
HOMO   LUMO

Fig. 2. Molecular orbital energy spacing, including HOMO–LUMO gap (HLG) for Pentostatin.
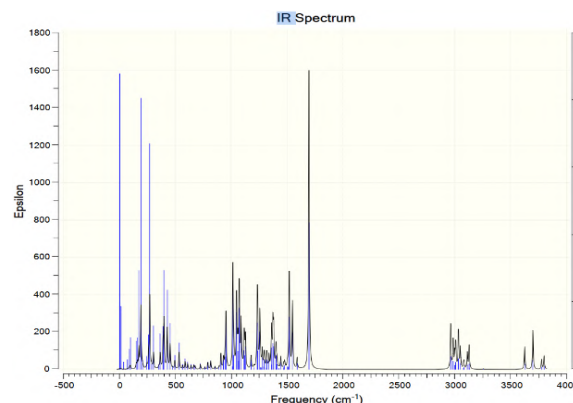
Fig 3. IR spectrum for Pentostatin obtained from B3LYP/6-311+G**calculations.

Conclusions

Pentostatin's structure was initially modeled using Gaussian and Gauss View software, which was then followed by optimization using the B3LYP/6-311+G** method. The determination of three-dimensional dipole moments and a total electric dipole vector (measured at 3.0846 Debye) was successfully achieved. Additionally, the HOMO-LUMO energy gap, which is crucial for understanding electronic, optical, and redox properties, was calculated to be 0.17881 eV. Furthermore, thermodynamic values, the impact of bond lengths on molecular behavior, and various structural parameters were also analyzed using the B3LYP/6-311+G method. The discussion on bond angles, bond lengths, and drug-nanoparticle interactions for targeted drug delivery was thorough and insightful. Finally, the optimization of the drug molecule resulted in the lowest energy level without any negative frequencies encountered during the process.

References

[1] Bouroncle BA, Wiseman BK, Doan CA.. Leukemic Reticuloendotheliosis.1958;13(7):609-630.

[2] Chadha P, Rademaker AW, Mendiratta P,et al. Treatment of hairy cell leukemia with 2-chlorodeoxyadenosine (2-CdA): long-term follow-up of the Northwestern University experience. Blood.2005;106(1):241-246.

[3] Michael R Grever md, Charles A Doan, Eric H Kraut md. Pentostatin in the treatment of hairy-cell leukemia.2003

[4] h Behara, P.K.; Dupuis, M. Electron transfer in extended systems: Characterization by periodic density functional theory including the electronic coupling. Phys. Chem. 2020

Exploration of Pentostatin and C_{60} Fullerene Interaction for Improved Drug Delivery: A Quantum Mechanics Analysis

Hossein Shirani[a,b,*], Amir Hossein Teimouri[b]
Corresponding Author E-mail: hossein_shirani@iust.ac.ir
[a] Department of Chemistry, Iran University of Science and Technology, P.O. Box 16846-13114, Tehran, Iran.
[b] Department of Microbiology, Faculty of Biological Sciences and Technology, University of Science and Culture, Tehran, Iran.

Abstract: This study delves into the interaction between Pentostatin and a C60 fullerene nanocarrier. The design and optimization of the molecules were conducted meticulously using Gaussian09 software, with important characteristics determined through DFT calculations (B3lyp/6-311 level of theory).
Keywords: Pentostatin; C_{60} Fullerene; DFT; B3lyp/6-311; HOMO-LUMO; Drug delivery

Introduction

This piece delves into the utilization of fullerenes as nano-scale carriers for delivering Pentostatin in the treatment of Hairy cell leukemia, a particularly deadly form of cancer that accounts for approximately 2% of all leukemia cases [1]. Despite the effectiveness of Pentostatin, similar to numerous other chemotherapy medications, it is accompanied by notable adverse effects such as a weakened immune system, bleeding, anemia, inflammation of the mouth and throat, fatigue, nausea, and hair loss. To alleviate these side effects and improve the overall effectiveness of the treatment, specialized drug delivery systems utilizing nanocarriers have been devised. The focus of the article centers around investigating the characteristics and potential of delivering Pentostatin using fullerenes [2].

Methods

All calculations were executed utilizing the Gaussian 09 software. Initially, all clusters were sketched out with the GaussView 05 program. The refinement of the fullerene molecule, Pentostatin, and the cluster was accomplished using Density Functional Theory (DFT) [3]. The configurations and various characteristics of the medication and cluster were determined using the B3LYP theory and the G311 basis set. To assess the electronic interaction between fullerene and Pentostatin, the energies of the HOMO and LUMO orbitals for free C_{60} fullerene and the cluster were computed. The energy gap (Eg) for each was calculated individually using the formula [4]:

$$E_g = E_{LUMO} - E_{HOMO}$$

To assess the stability of the nanostructure-drug interactions, the absorption energy of the complex was calculated using the equation [5]:

$$E_{ad} = E_{Complex} - E_{Fullerene} - E_{Pentostatin}$$

Results and Discussion

Central position   Side position
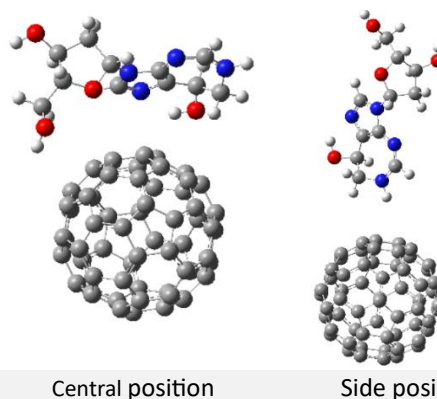
Adsorption Energy: The study revealed that the absorption energies of fullerene and Pentostatin were measured at -1.63 kcal/mol in the side state and -2.3 kcal/mol in the central state. This suggests a decrease of 0.7 kcal/mol, indicating that the bond between fullerene and the drug may be slightly more robust at the central level. This data is summarized in Table 1.

Table 1: Adsorption Energy (E_{ad}) in kcal/mol

Molecules	E_{ele} (Hartree/particle)	E_{ad}
Pentostatin	-948.6481101	-
Fullerene	-2286.1741400	-
Complex (side)	-3234.8248472	-1.63
Complex (central)	-3234.8259252	-2.30

22nd Iranian Chemistry Congress (ICC22)
Iranian Research Organization for Science and Technology (IROST)
13-15 May 2024

03231-97589

IROST

Gap Energy: To gain a deeper insight into the nanoelectric properties of fullerene, the gap energy of this molecule was analyzed in both its pure and complex forms. The gap energy for pure fullerene was found to be 0.102 eV, suggesting that the molecule acts as an insulator. Interestingly, in the complex side state, the gap energy decreased slightly to 0.061 eV, while in the central state, it was measured at 0.078 eV. These values indicate subtle variations in the HOMO-LUMO level difference, as shown in Table 2.

Table 2: Homo Energies (E_{HOMO}), LUMO Energies (E_{LUMO}), HOMO–LUMO Energy Gap (E_g)

Molecules	E_{homo} (ev)	E_{lumo} (ev)	E_g (ev)
fullerene	-0.2199	-0.1185	0.102
Complex (side)	-0.1861	-0.1247	0.061
Complex (central)	-0.1939	-0.1186	0.078

Conclusion

This study delves into the interaction between pentostatin and a C60 fullerene nanocarrier. The design and optimization of the molecules were conducted meticulously using GaussView and Gaussian software, with important characteristics determined through DFT calculations (B3lyp/6-311 level of theory). The research examined the reactivity and electronic response of the fullerene to pentostatin in two distinct positions. Interestingly, minimal interaction was observed in the side position, while a slightly stronger connection was noted in the central position. Surprisingly, the fullerene did not exhibit significant electronic sensitivity to pentostatin in either position. These results suggest that fullerenes have the potential to serve as effective nanocarriers for pentostatin.

References

[1] Chadha P, Rademaker AW, Mendiratta P,et al. Treatment of hairy cell leukemia with 2-chlorodeoxyadenosine (2-CdA): long-term follow-up of the Northwestern University experience. Blood.2005;106(1):241-246.
https://doi.org/10.1182/blood-2005-01-0173

[2] Kumar M, Raza K (2017) C60-fullerenes as drug delivery carriers for anticancer agents: promises and hurdles. Pharm Nanotech- nol 5:169–179. https://doi.org/10.2174/2211738505666617030114 2232

[3] Medvedev, Michael G.; Ivan S. Bushmarinov (2017). "Density functional theory is straying from the path toward the exact functional". Science. 355 (6320): 215–241. DOI: 10.1126/science.aah5975

[4] Elham Alipour & Farzaneh Alimohammady & Alexei Yumashev & Andino Maseleno ,Fullerene C60 containing porphyrin-like metal center as drug delivery system for ibuprofen drug, 2019,springer. https://doi.org/10.1007/s00894-019-4267-1

[5] Ali Ahmadi Peyghan, Nasser L. Hadipour, and Zargham Bagheri, Effects of Al Doping and Double-Antisite Defect on the Adsorption of HCN on a BC2N Nanotube: Density Functional Theory Studies, 2013. https://doi.org/10.1021/jp312503h

Novel, Reusable and Green Magnetically Nano Catalysts of Heteropolyacid; Preparation, Characterization and Application in Pyranopyrazoles Synthesizes

Mahla Firouzi Fariman, Ali Javid[*]

Corresponding Author E-mail: alijavids@yahoo.com

Department of Chemistry, Mashhad Branch, Islamic Azad University, Mashhad, Iran.

Abstract: In this work, silica coated magnetic nanoparticles of modified polyphosphoric acid was synthesized, characterized by different methods, and applied as a catalyst for one-pot synthesis of pyranopyrazoles at room temperature in water as green solvent. The magnetic catalyst can be easily removed and reused without any loss of its high catalytic activity.

Keywords: magnetic nanoparticle; heteropolyacid; pyranopyrazoles

Introduction

Pyranopyrazoles constitute an emerging class of heterocycles, which is extensively explored as an important core for emerging drugs that display numerous biological properties [1]. Therefore, considerable efforts have been expended to explore new simple and direct approaches towards the construction of the pyranopyrazole skeleton.

Heterogeneous catalysts are of higher demand than homogeneous catalysts due to their recyclability [2]. Thus, design of new heterogeneous catalysts that demonstrate activity and selectivity is high importance. Polyoxometalates are a large group of mineral clusters. In recent years, various applications of polyoxometalates have been reported. But one of the most important applications of these, is their use as a catalyst [3]. The acids of these compounds are known as heteropolyacids. One of the types of heteropolyacids is Preyssler, which has important features and having a large number of acidic protons [4]. The set of these properties has distinguished Preyssler from other structures of this group of mineral clusters, and its selection as a catalyst for this research project was based on these characteristics.

In recent decades, magnetic nanoparticles (MNPs) have been widely studied for to be promising supports for the immobilization of catalysts because magnetic catalysts can be easily separated from the reaction medium by an external magnet [5]. Recently, the synthesis of silica coated Fe_3O_4 and Fe_2O_3 MNPs for immobilizing heteropolyacids (HPAs) were reported [6]. In addition to Fe_3O_4 and Fe_2O_3, there are other iron oxides with the ferrite structure and general formula (AFe_2O_4), where A can be Mn, Co, Ni, Cu, and Zn [7]. So, in a continuation of our achievements in the preparation of novel catalysts [1, 4], we synthesized Preyssler HPA supported onto the silica coated $NiFe_2O_4$ (NFS-PRS) and $ZnFe_2O_4$ (ZFS-PRS) MNPs as new, efficient, separable and green solid acid catalyst, and applied these for one-pot synthesis of pyranopyrazoles from the condensation of aromatic aldehydes, hydrazine hydrate, ethyl acetoacetate and malononitrile at room temperature in water.

Experimental Section

Preparation of MFe_2O_4 Nanoparticles

A solution of the two aqueous metallic salts (1 M of $FeCl_3$, and 1 M of MCl_2 (M: Ni or Zn)) was poured as quickly as possible into one liter of a boiling aqueous solution of 1M NaOH under vigorous stirring using a mechanical stirrer.

Preparation of $MFe_2O_4@SiO_2$ Core-shell

The MFe_2O_4 NP (2.0 g) was ultrasonically dispersed in ethanol (25 mL) for 2 h at 60°C and then a 25% aqueous ammonia (10 mL) was added to the mixture and stirred at 60°C for 40 min. Then tetraethyl orthosilicate (1.0 mL) was added (as the silica source) to the mixture and stirring was continued at the same temperature for 24 h.

Preparation of $MFe_2O_4@SiO_2$-Preyssler (NFS-PRS & ZFS-PRS)

To a suspension of $MFe_2O_4@SiO_2$ (1.0 g) in water (50 mL) was added dropwise a solution of Preyssler HPA (0.75 g) in water (5 mL) and the mixture was stirred for 12 h at room temperature under N_2 atmosphere. Then the solvent was evaporated and the supported catalyst was collected and dried in vacuum overnight and the NFS-PRS or ZFS-PRS was calcinated at 250°C for 2 h.

General procedure for the synthesis of pyranopyrazole derivatives

A mixture of the aromatic aldehyde (1 mmol), ethyl acetoacetate (1 mmol), malononitrile (1 mmol), hydrazine hydrate (1 mmol) and NFS-PRS or ZFS-PRS (0.03 g) in water (10 ml) was stirred at room temperature for 20-30 min. Upon completion of the reaction, the magnetic catalyst was separated from the reaction mixture using an external magnet. The solvent was evaporated from the decanted solution obtained from the isolation of the catalyst to give the pure products.

22nd **Iranian Chemistry Congress (ICC22)**
Iranian Research Organization for Science and
Technology (IROST)
13-15 May 2024

03231-97589

IROST

Results and Discussion

The structure of NFS-PRS and ZFS-PRS were investigated by spectral methods such as XRD, FTIR, SEM, TEM, EDX and TGA. In order to investigate the catalytic activity of nanoparticles, the process of preparing of pyranopyrazole derivatives from the one-pot condensation were used (**Fig. 1**).
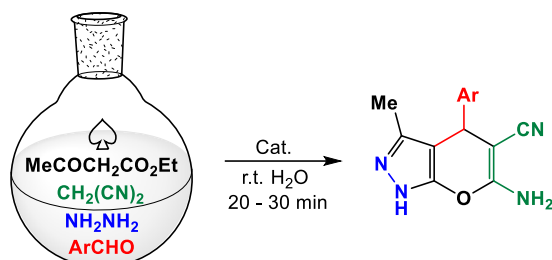

Fig.1: Synthesis of Pyranopyrazoles via one-pot reaction.

Based on the obtained results, the best reaction conditions are in the presence of 0.03 gr. of catalyst for 1 mmol of other reactants at room temperature, 20-30 minutes, and in the presence of water as a green solvent (**Table 1**). Also, after the end of the reactions, the catalyst could be recycled by a very simple workup (with the aid of an external magnet), washed, dried and reused at least four runs with no considerable change in its catalytic activity.

Table 1. Synthesis of Pyranopyrazoles using of MNP catalysts

Entry	Ar	Yield (%) Cat: Preyssler	Yield (%) Cat: NFS-PRS	Yield (%) Cat: ZFS-PRS
1	C_6H_5	68	86	87
2	$4\text{-}NO_2C_6H_5$	65	88	85
3	$3\text{-}NO_2C_6H_5$	59	84	84
4	$4\text{-}CNC_6H_5$	55	83	84
5	$2\text{-}ClC_6H_5$	60	87	85
6	$4\text{-}ClC_6H_5$	48	88	84
7	$4\text{-}MeOC_6H_5$	64	91	92
8	$4\text{-}MeC_6H_5$	61	87	88

Conclusions

In summary, NFS-PRS and ZFS-PRS have been used as an efficient and eco-friendly solid acid catalyst for the one-pot synthesis of pyranopyrazole derivatives. Mild reaction conditions at low temperature, high yields, short reaction times, re-usability of catalyst and absence of any hazardous organic solvents are some advantages of this method.

References

[1] Javid, A., Khojastehnezhad, A., Eshghi, H., Moeinpour, F. (2016) Synthesis of Pyranopyrazoles using a Magnetically Separable Modified Preyssler Heteropoly Acid, Organic Preparations and Procedures International, 48, 377-384. https://doi.org/10.1080/00304948.2016.1206424

[2] Busca, G., *Heterogeneous Catalytic Materials*, Amsterdam: Elsevier (2014).

[3] Kozhevnikov, I.V. (1998) Catalysis by Heteropoly Acids and Multicomponent Polyoxometalates in Liquid-Phase Reactions. Chemical Reviews, 98(1), 171–198. https://doi.org/10.1021/cr960400y

[4] Javid, A., Khojastehnezhad, A., Pombeiro, A. J. L. (2017) Preparation, Characterization, and Application of Preyssler Heteropoly Acid Immobilized on Magnetic Nanoparticles as a Green and Recoverable Catalyst for the Synthesis of Imidazoles. Russian Journal of General Chemistry, 87(12), 3000–3005. https://doi.org/10.1134/S1070363217120453

[5] Polshettiwar, V., Luque, R., Fihri, A., Zhu, H., Bouhrara, M., Basset, J.M. (2011) Magnetically Recoverable Nanocatalysts. Chemical Reviews, 111(5), 3036-3075. https://doi.org/10.1021/cr100230z

[6] Wang, S.G., Zhang, Z.H., Liu, B., Li, J.L. (2013) Silica coated magnetic Fe_3O_4 nanoparticles supported phosphotungstic acid: a novel environmentally friendly catalyst for the synthesis of 5-ethoxymethylfurfural from 5-hydroxymethylfurfural and fructose. Catalysis Science & Technology. 3(8), 2104-2112. https://doi.org/10.1039/C3CY00223C

[7] Hou, X.Y., Feng, J., Xu, X.D., Zhang, M.L. (2010) Synthesis and characterizations of spinel $MnFe_2O_4$ nanorod by seed–hydrothermal route. Journal of Alloys and Compounds, 491(1), 258-263. https://doi.org/10.1016/j.jallcom.2009.10.029

Investigation of the Crystallinity and Morphology of Copolymer-Templated Titanium Dioxide Layer

G. Kazemi[*], V. Mirkhani[*], R. Keshavarzi, M. Moghadam, S. Tangestaninejad, I. Mohammadpoor-Baltork

Corresponding Author E-mail: *ghazalekazemi13@gmail.com

Department of Chemistry, Catalysis Division, University of Isfahan, Isfahan 81746-73441, Iran.

Abstract: Titanium dioxide (TiO_2) is an attractive option for electron transport in optoelectronic devices due to its unique properties. In this study, the crystallinity and pores morphology of copolymer-templated titanium dioxide were investigated. Using the P123 block copolymer as a sacrificing template, a warm-like structure of mesoporous was formed. This mesoporous layer was characterized using XRD, UV-vis, and FE-SEM methods.

Keywords: Templated mesoporous TiO_2 layer; Electron-transport layer (ETL); TiO_2 crystallinity; P123 block copolymer.

Introduction

Research on semiconductors and their use in optical devices is a fundamental area of study in the field of chemistry. Inorganic oxides are popular electron transport materials, due to their suitable energy bandgap, high stability, and cost-effective fabrication methods. Among them, titanium dioxide is recognized as one of the most studied electron transport materials due to its transparency, high stability, and suitable energy bandgap (3.2 electron volts) [1]. The porosity of TiO_2 affects its performance in optoelectronic devices. Various methods exist for preparing mesoporous structures, with the simplest being the use of copolymers as template patterns. This method allows for the control of the morphology and pore size of TiO_2. In the present study, the triblock copolymer P123 was used as a template [2].

Experimental Section

To prepare a solution of titanium dioxide templated with the copolymer P123, 1 g of P123 copolymer is added to 9 g of butanol. Then, a mixture of 3.16 g of titanium isopropoxide and 2.42 g of hydrochloric acid is added. After optimizing several parameters, this layer is calcined at a temperature of 500℃ [3].

Results and Discussion

The X-ray diffraction pattern of this layer deposited on FTO is shown in Figure 1. The peak at (101) indicates the formation of TiO_2 crystals in the anatase phase
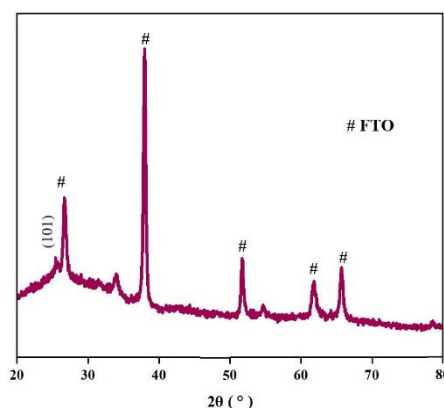
Fig.1: The X-ray diffraction pattern of titanium dioxide templated with the copolymer P123 on an FTO

The amount of light transmission through the electron transport layer can significantly impact the efficiency of optoelectronic devices. To assess the light transmission through this layer, the UV-vis technique was utilized, as shown in Figure 2. At a calcination temperature of 500℃, a 90% transmission was observed in the wavelength range of 500 to 600 nanometers.
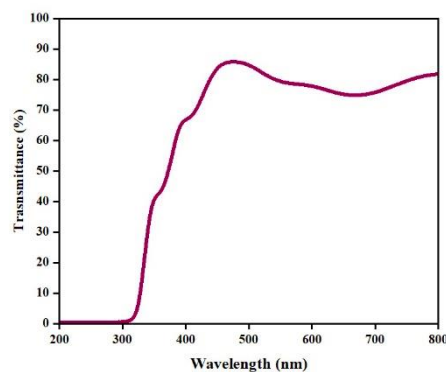
Fig.2 UV-vis transmittance spectra of a mesoporous templated TiO_2 layer

22nd Iranian Chemistry Congress (ICC22)
Iranian Research Organization for Science and Technology (IROST)
13-15 May 2024

03231-97589

IROST

In the FE-SEM image (Fig.3), the crystalline structure of the P123 copolymer can be observed after calcination. The image reveals a well-organized and consistent warm-like pore structure with high porosity, which is indicative of the successful templating process.
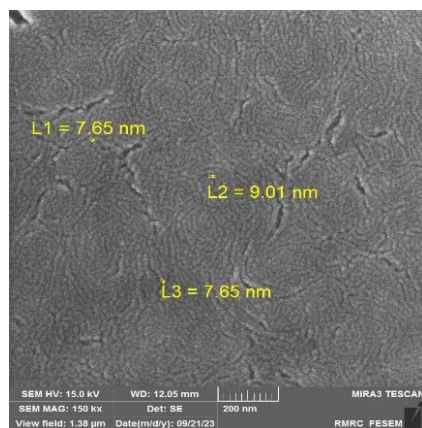
Fig.3 The FE-SEM image of the surface of the titanium dioxide layer templated with the P123 copolymer.

Conclusions

In this study, a mesoporous TiO_2 layer was prepared through various optimizations at a calcination temperature of 500℃. The analysis indicated that at this annealing temperature, the level of crystallinity and light transmittance were highly acceptable. Additionally, the FE-SEM image at this calcination temperature showed desirable grain size and porosity

References

[1] Shaikh, J. S., Shaikh, N. S., Mali, S. S., Patil, J. V., Pawar, K. K., Kanjanaboos, P., ... & Patil, P. S. (2018). Nanoarchitectures in dye-sensitized solar cells: metal oxides, oxide perovskites and carbon-based materials. *Nanoscale*, *10*(11), 4987-5034.

[2] Hoheisel, T. N., Hur, K., & Wiesner, U. B. (2015). Block copolymer-nanoparticle hybrid self-assembly. *Progress in Polymer Science*, *40*, 3-32.

[3] Keshavarzi, R., Jamshidvand, A., Mirkhani, V., Tangestaninejad, S., Moghadam, M., & Mohammadpoor-Baltork, I. (2018). The effect of the number of calcination steps on preparing crack free titania thick templated films for use in dye sensitized solar cells. *Materials Science in Semiconductor Processing*, *73*, 99-105.

Natural Halloysite Nanotubes as an Efficient Catalyst in Strecker Reaction: The Synthesis of α-Amino Nitriles Under Solvent-Free Conditions

Seyed Ali Mousavi-Mashhadi, Ali Shiri*

Corresponding Author E-mail: alishiri@um.ac.ir

Department of Chemistry, Faculty of Science, Ferdowsi University of Mashhad, Mashhad, Iran.

Abstract: In this work, a green and cost-effective method based on halloysite as natural catalyst for the synthesis of α-amino nitriles via Strecker three-component reaction is introduced. The chemical and physical structure of natural halloysite has characterized thoroughly, and then the effect of different parameters such as the amount of catalyst, solvent, and temperature were optimized in the synthesis of 2-phenyl-2-(phenylamino)acetonitrile as the model reaction.

Keywords: Natural catalyst; halloysite; Strecker reaction; α-amino nitrile

Introduction

Carbon-carbon bond formation reactions are one of the most important methods in the synthesis of drugs, natural products, and fine chemicals[1, 2]. α-Amino nitriles as the key valuable precursors have been used for the synthesis of various organic compounds, drugs, and bioactive scaffolds such as saframycin A and its derivative [3], anagliptin saxagliptin, vildagliptin[4], odanacatib, ecteinascidin, (±)-phthalascidin 622 , HCV NS3 serine protease inhibitors and clopidogrel . Moreover, α-amino nitriles can be converted to the corresponding α-amino acids, amines, enamines, ketones, α-amino amides, amino alcohols, and nitrogen-containing heterocyclic compounds, which have been reviewed by Enders and his coworkers [5].Herein, in continuation of our previous studies , a novel and green method are reported for the synthesis of α-amino nitriles starting from the appropriate substituted aldehydes, aromatic amines, and trimethylsilyl cyanide (TMSCN) in the presence of halloysite as a highly active natural catalyst as shown in Scheme 1.
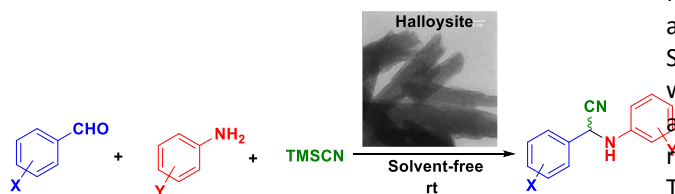
Scheme 1. Schematic pathway of the Strecker reaction.

Experimental Section

General procedure for the synthesis of α-amino nitriles:In a round bottom flask, a mixture of the appropriate aldehyde (1 mmol), amine (1 mmol), trimethylsilyl cyanide (TMSCN) (1.2 mmol), and halloysite (10 mg) was stirred in solvent-free condition at room temperature. The progress of the reaction was monitored by thin layer chromatography (TLC) using (n-hexane/ethyl acetate) as eluent (10/1). After the completion of the reaction, the mixture was diluted with dichloromethane.

Results and Discussion

The morphology of the natural halloysite was evaluated by transmittance electron microscopy (TEM). Most halloysite particles have cylindrical hollow tubular structures . Generally, halloysite tubes length is in the range of 200 to 1000 nm. Also, the outer diameter of tubes varies from 10 nm to 100 nm, and the lumen diameter ranges from 5 nm to 50 nm For further study of the natural halloysite structure, scanning electron microscopy (SEM) was used. SEM image and EDX analysis are represented . The SEM image indicates the poly-dispersity of halloysite particles in length. Also, the open-ended lumen of the cylindrically shaped tubes can be clearly observed . To recognize the elemental composition of halloysite, EDX analysis was also applied. In, the characteristic peaks of Si, Al, and O have been presented as the main elements of halloysite, which are attributed to the SiO_2 and Al_2O_3 composition of halloysite After structural characterization of the natural halloysite, the feasibility of a three-component reaction among aldehyde, amine, and trimethylsilyl cyanide known as Strecker reaction in the presence of halloysite catalyst was explored. The model reaction using benzaldehyde, aniline, and TMSCN was carried out under different reaction conditions to achieve the optimized procedure. The effectiveness of various factors, including the amount of catalyst, solvent, and reaction temperature, was investigated . The effect of the solvent on the reaction process was illustrated using polar and non-polar solvents such as DMSO, EtOH, n-hexane, and H_2O at room temperature/reflux conditions. In the progress of the reaction, the tested solvents were not significantly different from the solvent-free condition . Without any catalyst, the imine product was only detected, and the

22nd Iranian Chemistry Congress (ICC22)
Iranian Research Organization for Science and Technology (IROST)
13-15 May 2024

03231-97589

IROST

reaction did not further proceed to produce the desired α-amino nitrile even after 24 h in solvent-free conditions . This is concluded that the presence of a catalyst is necessary for this reaction. The model reaction with 10 mg of halloysite was completed in 1 h with 97% of product yield under solvent-free conditions. It is notable that no cyanohydrin was produced as byproduct in the model reaction. After the confirmation of the efficiency of halloysite in the model reaction, the effect of catalyst amount was evaluated. For this purpose, 15, 5, 2.5, and 1 mg of the catalyst were used . The yield of the final product was decreased to 95, 85, 60, and 30%, respectively. Therefore, 10 mg of the catalyst at room temperature under solvent-free conditions was selected as the optimized reaction conditions.

Conclusions

The natural halloysite is active for the one-pot synthesis of α-amino nitriles by a three-component condensation of various benzaldehydes, anilines, and TMSCN. This green natural catalyst can produce a variety of α-amino nitriles in a facile and cost-effective method in solvent-free condition at room temperature. Both electron-donating and electron-withdrawing substitutions on benzaldehyde and aniline substrates have been affected the reaction efficiency. Electron-withdrawing groups on benzaldehyde and electron-donating groups on aniline were converted to the desired α -amino nitriles in excellent yields. The catalyst was active for five consequent runs.The catalyst used for this reaction can cover the disadvantages of previous reports of catalytic work of this reaction and synthesize the desired products with the least amount of energy and cost.
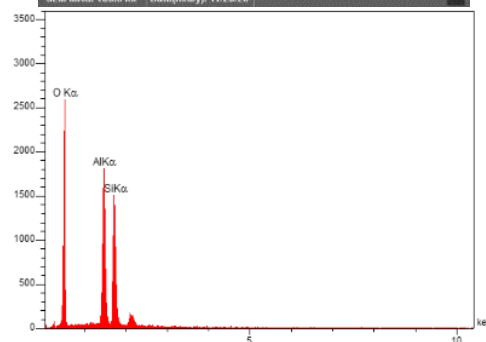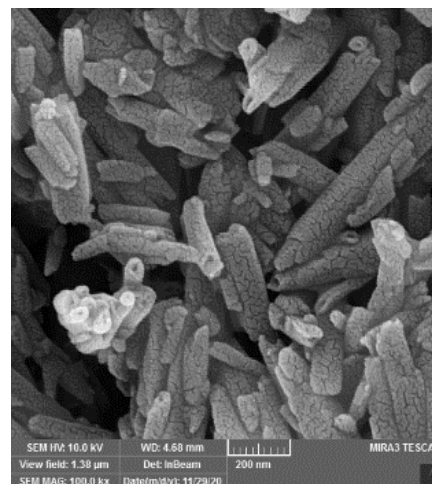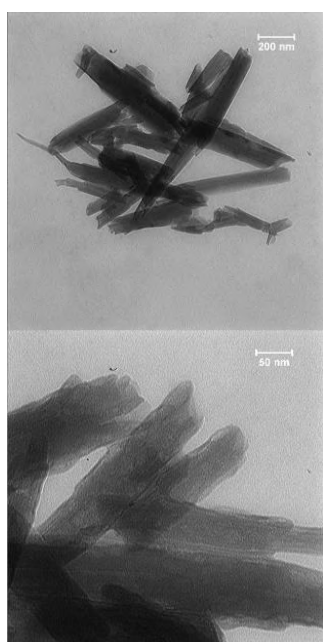
References

[1] Abdolmohammadi S, Rasouli Nasrabadi SR, Dabiri MR, Banihashemi Jozdani SM (2020) TiO2 Nanoparticles Immobilized on Carbon Nanotubes: An Efficient Heterogeneous Catalyst in Cyclocondensation Reaction of Isatins with Malononitrile and 4-Hydroxycoumarin or 3,4-Methylenedioxyphenol under Mild Reaction Conditions. Appl Organomet Chem 34:1–10.

[2] Chaghari-Farahani F, Abdolmohammadi S, Kia-Kojoori R (2020) A PANI-Fe3O4@ZnO nanocomposite: A magnetically separable and applicable catalyst for the synthesis of chromeno-pyrido[: D] pyrimidine derivatives. RSC Adv 10:15614–15621.

[3] Enders D, Shilvock JP (2000) Some recent applications of α-amino nitrile chemistry. Chem Soc Rev 29:359–373.

[4] Fleming FF, Yao L, Ravikumar PC, et al (2010) Nitrile-Containing Pharmaceuticals: Efficacious Roles of the Nitrile Pharmacophore. J Med Chem 53:7902–7917.

[5] Papoulis D, Somalakidi K, Todorova N, et al (2019) Sepiolite/TiO2 and metal ion modified sepiolite/TiO2 nanocomposites: synthesis, characterization and photocatalytic activity in abatement of NOx gases. Appl Clay Sci 179:105156.

22nd Iranian Chemistry Congress (ICC22)
Iranian Research Organization for Science and Technology (IROST)
13-15 May 2024

ISC
03231-97589

IROST

Investigation of Quantum Computing and Structural Characteristics of Deferiprone Drug

Hossein Shirani[a,b,*], Shiva Ghodsi[b]

Corresponding author. E-mail: hossein_shirani@iust.ac.ir
[a] Department of Chemistry, Iran University of Science and Technology, P.O. Box 16846-13114, Tehran, Iran.
[b] Department of Microbiology, Faculty of Biological Sciences and Technology, University of Science and Culture, Tehran, Iran.

Abstract: Quantum calculations were employed to examine the electronic and structural properties of Deferiprone, using the B3LYP/6-311+G computational method. Various geometric parameters such as bonding lengths, angles, dihedral angles, and the energy gap between the Highest Occupied Molecular Orbital (HOMO) and the Lowest Unoccupied Molecular Orbital (LUMO) were investigated and analyzed.
Keywords: Thalassemia; Deferiprone; HOMO-LUMO Gap; DFT; B3LYP/6-311+G

Introduction

Thalassemia major is a severe type of thalassemia that occurs when a child inherits two copies of the thalassemia gene. This particular form of the condition results in the presence of two mutated genes in the beta protein, leading to either a reduced production of beta protein or a complete absence of it in the body. As a consequence, the body compensates for this deficiency by overproducing alpha proteins, which ultimately leads to the destruction of red blood cells. The diagnosis of thalassemia major is typically confirmed through the identification of beta-globin deficiency. Patients suffering from this condition require regular blood transfusions followed by chelation therapy to eliminate the excess iron accumulated from the transfusions. Failure to address this iron overload can result in severe complications such as damage to the heart and liver, eventually leading to death. To remove the excess iron, subcutaneous administration of Deferoxamine is necessary, although this method can be quite painful. Alternatively, oral deferiprone can be used to facilitate the chelation process, making it a less uncomfortable option for patients. Deferiprone contains two chelating agents, 1,2-dimethyl-3-hydroxypyridin-4-one (DFP), which forms a complex with an iron atom possessing six empty orbitals. This complex is then excreted through the kidneys. In 2011, the drug deferiprone was approved by the FDA for use in the United States as a treatment for thalassemia major [1,2].

Methods

The drug's structure was initially visualized using the GaussView software before being optimized and calculated in the Gaussian program using the B3LYP/6-311+G input command. This process allowed for the extraction and analysis of essential information such as bond lengths, bond angles, IR spectra, and more.

Results and Discussion

Deferiprone, as shown in Fig. 1, has the chemical formula $C_7H_9NO_2$.
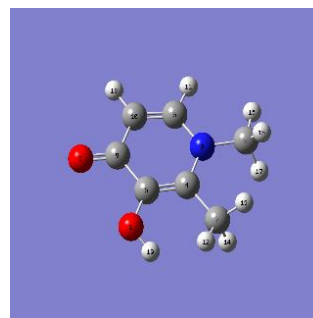
Fig. 1. 3D structures obtained from B3LYP/6-311+G calculations.

The distance between two atoms in a molecule, measured in angstroms, determines the strength of a particular bond. In general, a shorter bond indicates a higher electronegativity of the cation, resulting in increased strength and electron density. Thermodynamic values for drug hardening have been reported at the computational level of B3LYP/6-311+G: HF=-299521/381809546 Kcal, zero-point Energies=299425/27200144kcal, Cv=36.323 Cal/Mol-Kelvin, S= 95.734 Cal/Mol-Kelvin.

Table 1. B3LYP/6-311+G Optimized Values of bond length.

1-H19	C10-C6	O1-C5	C6-H11	C5-C9	C6-N3
0.97072	1.35792	1.39382	1.07963	1.46728	1.37998

When we obtain the shape of the charge distribution from the B3LYP/6-311+G calculations, atoms are visible in green, black and red that symbolize positive, neutral and negative charges, respectively.

Table 2. B3LYP/6-311+G optimized values of bond angles (°) for Deferiprone.

19H,1O,5C	9C,5C,4C	5C,9C,10C	2O,9C,5C	2O,9C,10C	9C,10C,6C
112.7	27.3	113.3	30.80	123.5	122.10

22nd Iranian Chemistry Congress (ICC22)
Iranian Research Organization for Science and Technology (IROST)
13-15 May 2024

03231-97589

IROST

Table 3. B3LYP/6 -311+G optimized values of bond dihedral for Deferiprone.

19H,1O,5C,9C	5C,9C,2O,10C	9C,10C,18H,6C	3N,8C,15H,17H	4C,7C,13H,14H	6C,3N,4C,7C
160.0	-179.4	-179.2	123.1	123.80	-177.6

Table 4. B3LYP/6-311+G Optimized Values of Atomic Charge for Dferiprone.

O1	O2	N1	H11
-0.570	-0.404	-0.667	0.118
C9	**C5**	**H13**	**C10**
0.310	0.042	0.210	-0.308

LUMO is higher in energy than the HOMO. Of the orbitals that have electrons, the HOMO is the highest in energy, and of the orbitals that don't, the LUMO is the lowest in energy. The HOMO-LUMO gap is where the most likely excitations can occur. The larger the aromatic system is, the smaller the HOMO-LUMO gap.

HOMO   LUMO

Fig. 2. Molecular orbital energy spacing including HOMO-LUMO gap for Deferiprone obtained from B3LYP/6-311+G calculations.

A high gap means less reactivity. So more gaps increase stability. According to the shape, Deferiprone has a smaller gap and high reactivity and is a soft molecule.
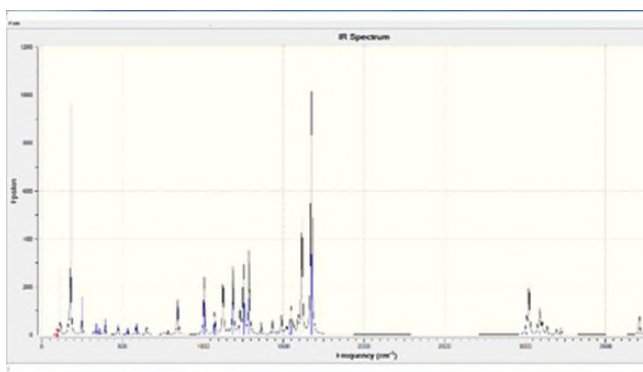
Fig. 3. IR spectrum for Deferprone optained from B3LYP/6-311+G calculations.

Infrared spectroscopy, also known as vibrational spectroscopy, involves analyzing the way infrared radiation interacts with molecules to identify and study chemical substances. Each compound has a unique IR spectrum, which reveals the frequencies of infrared radiation absorbed by the sample.

Conclusions

The primary objective of this research is to explore the intricate realm of quantum computing in order to analyze the distinctive characteristics of Deferiprone medication. Our goal is to uncover the molecular and electronic attributes of this therapeutic compound through a comprehensive investigation. Previous studies have suggested that Deferiprone exhibits promise in the treatment of various medical conditions. Specifically, Deferiprone is being researched for its potential to regulate elevated levels of iron in individuals with thalassemia, sickle cell disease, or anemia who receive frequent blood transfusions. It functions as an iron chelator, binding to excess iron in the blood and facilitating its elimination through the kidneys. The molecular structure of Deferiprone was simulated using Gaussian and View Gauss software, and then optimized structurally using B3LYP/6-311+G. Additionally, the atomic charges, IR spectrum, frequency and intensity, as well as the various energy levels of the molecule were thoroughly analyzed and assessed.

References
[1] Thein CL. (2013). The molecular basis of Betta Thalassemia. cold spring Harp Present Med,3(5). https://www.ncbi.nlm.nih.gov/pmc/articles/pmc3633182/
[2] Sadegh Kaviani, Mohammad Izadyar, & Mohammad Reza Housaindokht.(2020). A DFT study on the metal ion selectivity of deferiprone complexes.

A theoretical study on the interaction of cyclophosphamide drug with adenine, guanine, cytosine, thymine, and uracil

M. Rezaei-Sameti*, M. Talaei, F. Khazaei

Corresponding Author E-mail: mrsametimalayeru.ac.ir

Department of Applied Chemistry, Faculty of Science, Malayer University, Malayer, 65174, Iran.

Abstract: In this project, the interaction of cyclophosphamide (CYC) with DNA components is investigated using the density functional theory (DFT) at ωb97xd/6-31+G (d, p) level theory. The calculated results show that the amount of adsorption energy in the presence and absence of the electrical field is negative for all models and thermodynamically is exothermic, which is very favorable. The results of this study show the binding of CYC drugs to adenine and guanine is stronger than nucleobases.

Keywords: Nucleotide base, Cyclophosphamide drug, Density function theory, DNA
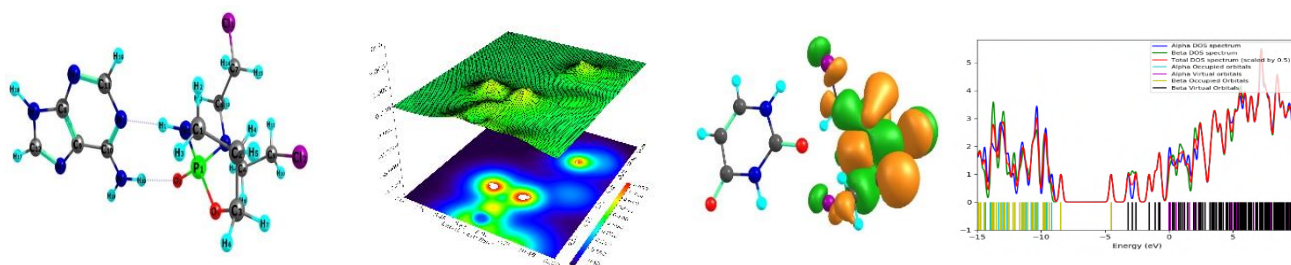
Fig.1: The optimized, DOS, ELF, and HOMO plots of the interaction of CYC drug with adenine

Introduction

DNA plays an important role in cell growth, transcription, and cell division. Since most interaction of anticancer drugs with the target cells occurs in the DNA region of the cell, therefore, studying the interaction of drugs with DNA nucleobases is biologically important to investigate the mechanism of action of the drugs and the smart binding of the drug to the target cells [1–2]. The binding mechanism of most anticancer drugs with DNA is covalent or non-covalent. The covalent bonds between the drug and DNA are irreversible and have high strength, so they cause complete inhibition of DNA processes and subsequent cell death, and because of the creation of additional compounds, they are also called alkylating agents*.* Non-covalent bonds are formed between the drug and the DNA grooves that do not form adducts, thus causing a less toxic effect, this agent causes structural disorders of DNA[3].

Results and Discussion

The E_ads values of all CYC-drug@ A, G, C, U, and T nucleobases complexes in all sites are listed in Table 1 in the absence and presence Eads' results prove that the binding of CYC-drug on guanine and adenine nucleobases is The E_HB for all studied configurations is the E_HB <12 kcal/mol, so the bonding between drug and nucleobases is a weak hydrogen bonds type. The MEP results proved

The details of the computational method

In this work, the interaction of CYC drugs from I, II, and III cities on the surface of adenine (A), cytosine(C), thymine(T), guanine(G), uracil(U) are investigated at the ωB97XD levels of DFT theory with 6-31+G(d,p) basis set. The Max Force and Max displacement for all calculations are 0.00045 (Ha), and 0.00015 Bohr, respectively. The adsorption energy (E_ads) of all studied complexes is computed by:

$$E_{ads} = E_{CYC@nucleobase} - (E_{CYC} + E_{nucleobases}) + BSSE \qquad (1)$$

The E_CYC@nucleobase, E_CYC, and E_nucleobase are the potential energy of the CYC-drug@nucleobases complexes, CYC-drug, and A, G, C, T, and U nucleobases respectively. BSSE is basis set superposition errors. The atom in molecule(AIM) parameters, Localized orbital locator (LOL) plots, reduced density gradient (RDG) scatter plots, electron spin potential (ESP), and density of states (DOS) for all CYC-drug@nucleobases complexes are determined.

that the areas around the drug complex with nucleobases are full of electrons and are suitable for the attack of electrophilic species.

22nd Iranian Chemistry Congress (ICC22)
Iranian Research Organization for Science and Technology (IROST)
13-15 May 2024

03231-97589

IROST

Conclusions

The computational results demonstrate that the binding of CYC-drug with guanine and adenine is stronger than other nucleobases and the nature of bonding is van der Waals and hydrogen bond type. With adsorbing CYC drugs the electrical, density of state (DOS) and electron localized function (ELF) plots of all complexes alter significantly from the original state. This information can be used both to describe the mechanism of the drug's effect and to comment on the interactions of CYC with other drugs.

References

[1] Guerra CF, Bickelhaupt FM (2006). Watson-Crick hydrogen bonds: Nature and role in DNA replication. Modern Methods for Theoretical Physical Chemistry of Biopolymers. 19: 79-97.

[2] Langkjæra N, Wengela J, Pasternak A (2015). Watson–Crick hydrogen bonding of unlocked nucleic acids. Bioorganic & Medicinal Chemistry Letters. 25 (22):5064-5066.

[3] Sirajuddin M, Ali S, Badshah A (2013). Drug–DNA interactions and their study by UV–visible, fluorescence spectroscopies and cyclic voltammetry. Journal of Photochemistry and Photobiology B: Biology. 124:1-19

Table 1. The adsorption energy and dipole moment of CYC@DNA complexes

	SEF+0		SEF+0.1		SEF+0.2		SEF+0.3		SEF+0.4		SEF+0.5	
	E_{ads}	μ	E_{ads}	μ	E_{ads}	μ	E_{ads}	μ	E_{ads}	μ	E_{ads}	μ
CA-a	-18.51	2.18	-16.11	6.11	-15.43	10.53	-16.44	15.05	-19.17	19.61	-23.64	24.25
CA-c	-21.65	2.31	-18.07	5.82	-16.49	10.30	-16.93	14.92	-19.43	19.64	-24.04	24.44
CA-d	-25.64	2.92	-16.61	6.09	-14.64	10.84	-15.82	15.86	-20.27	21.02	-28.15	26.32
Cc-a	-21.84	4.35	-16.86	6.45	-12.07	9.63	-7.54	13.16	-3.33	16.88	-0.41	20.80
Cc-b	-22.77	4.18	-9.92	3.33	-0.86	6.73	-9.52	11.00	-15.97	15.52	-20.07	20.20
CC-c	-22.77	4.18	-9.91	3.32	-0.87	6.72	-9.54	11.00	-15.99	15.52	-20.04	20.20
Cc-d	-17.30	4.32	-1.52	1.60	-12.67	4.91	-25.18	9.20	-35.89	13.66	-44.63	18.26
CG-a	-15.10	9.03	-14.37	10.99	-14.74	14.07	-16.22	17.69	-18.82	21.63	-22.59	25.78
CG-b	-15.98	5.94	-5.65	5.80	-2.83	8.68	-9.43	12.69	14.11	17.11	-16.79	21.75
CG-c	-20.28	8.21	-20.53	10.49	-21.90	13.81	-24.37	17.60	-27.96	21.65	-32.68	25.88
CG-d	-12.38	6.59	-3.79	4.93	-19.39	6.32	-34.34	9.54	-48.56	13.39	-61.97	17.53
CT-a	-17.42	2.75	-14.13	6.02	-12.65	10.42	-13.03	15.02	-15.35	19.73	-19.71	24.58
CT-c	-17.42	2.75	-14.13	6.02	-12.65	10.42	-13.03	15.02	-15.35	19.73	-19.72	24.58
CU-a	-19.08	7.45	-14.67	8.68	-10.60	11.15	-6.94	14.26	-3.81	17.76	-1.38	21.57
CU-d	-10.04	4.45	-13.39	8.42	-18.01	12.53	-23.91	16.70	-31.10	20.93	-39.64	25.23

pH Sensing Using Phenylene-diamine Derived Carbon Dots

Masoume Kaviani Darani [a], Shohre Rouhani [*b], Zahra Ranjbar [*a]

Corresponding Author E-mail: Rouhani@icrc.ac.ir / Ranjbar@icrc.ac.ir

[a] Department of Surface Coating and Corrosion, Institute for Color Science and Technology.
[b] Department of Organic Colorant, Institute for Color Science and Technology.

Abstract: This research explores a solvothermal method to synthesize carbon dots (CDs) using citric acid, Meta-phenylenediamine, and DMF. The resulting M-PDA-based CDs displayed uniform morphology with a size of around 3.2 nm. Characterization techniques confirmed the successful incorporation of nitrogen functionalities and various hydrophilic groups on the CD surface. These CDs exhibit pH-dependent fluorescence, making them suitable for application as a pH sensor.

Keywords: Carbon Dots; pH-sensitive fluorescence; Solvothermal Synthesis

Introduction

Carbon dots (CDs) have emerged as a fascinating class of nanomaterial due to their unique properties, including tunable photoluminescence, biocompatibility, and excellent chemical stability [1, 2]. Their synthesis methods are constantly evolving, with solvothermal techniques offering a simple and versatile approach [3, 4]. This study focuses on the development of pH-sensitive CDs synthesized via a solvothermal route using citric acid, Meta-phenylenediamine (O-PDA), and N,N-dimethylformamide (DMF) as precursors. Citric acid serves as a readily available carbon source, while m-PDA introduces nitrogen functionalities, potentially influencing the CDs' optical properties. DMF acts as the reaction solvent, facilitating the formation of CDs under controlled conditions [5, 6]..

Here, we report the successful synthesis of these m-PDA-based CDs and investigate their pH-dependent fluorescence response. We demonstrate that the CDs exhibit a significant change in fluorescence intensity with varying pH levels, making them promising candidates for application as pH sensors. This research contributes to the growing field of CD-based sensors by offering a simple and efficient method for creating a sensitive pH detection platform

Experimental Section

The preparation of carbon dots involved a solvothermal method that used Citric Acid (CA) as the carbon precursor, Meta-phenylene diamine (MPD) as the nitrogen source, and dimethylformamide (DMF) as the solvent. To prepare the precursor, a solution of 1.68 g citric acid and 40 ml DMF was mixed with 0.64 g of metaphenylenediamine (M-PDA). The mixture was thoroughly stirred to ensure homogeneity before being transferred to a Teflon-lined stainless steel autoclave. The autoclave was sealed and

heated in an oven at 200°C for 8 hours, resulting in the formation of carbon nanodots.

Results and Discussion

Meta-phenylene (M-CDots) were synthesized and examined in terms of their functional groups, size, morphology, and elemental analysis. The results were consistent with the references and demonstrated well-synthesized M-CDots (Fig. 1)
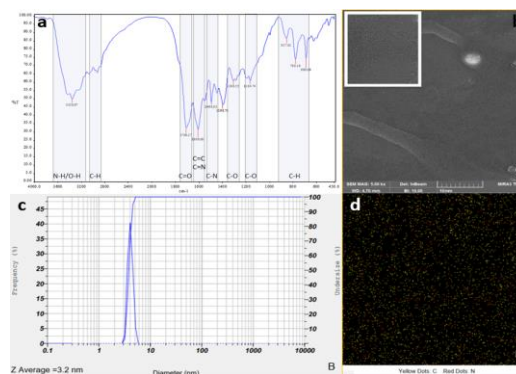
Fig.1: Characterization of synthesized and purified M-CDots. a) FTIR , b) SEM image, c) zeta sizer, and d) EDX

The M-CDots were characterized by FTIR to distinguish the vibrational characteristic peaks of the functional groups. The results showed that the M-CDs had numerous of hydrophilic groups on their surfaces, such as O−H and N−H (3200, 3358 cm−1), C−O−C/C−OH (1308 cm−1), and C=O (1708 cm−1) groups. These groups resulted in excellent solubility and stability of the M-CDs in water, which is important for their application.

The Scanning Electron Microscopy (SEM) technique was used to examine the morphology of the synthesized CDs under solvothermal conditions (see Fig.1b). The results indicate a uniform morphology of CDs. Additionally, the

22nd Iranian Chemistry Congress (ICC22)
Iranian Research Organization for Science and Technology (IROST)
13-15 May 2024

03231-97589

EDX analysis in Fig. 1d confirms the presence of nitrogen in the C-Dots, as expected. The Zeta sizer result shows that the diameter of C-Dots is 3.2 nm (Fig. 1c). These results are consistent with the references and demonstrate well-synthesized carbon nano dots [7, 8].

Fig. 2 displays the sensitivity of M-CDots to pH variations ranging from 1 to 13. The surface of carbon dots has abundant functional groups, such as amino (NH_2), carboxyl (COOH), and hydroxyl (OH) groups, which can exist in various protonation or deprotonation states based on pH [9]. The molecules' emission is determined by how they lose energy, either through the radiation path or non-radiative ways such as interaction with the solvent, hydrogen bonding, and energy transfer to the solvent. Hence, changing the pH of the environment and surface charge can alter the non-radiative paths and result in a pH-dependent emission, which can be useful in designing a pH sensor [10].
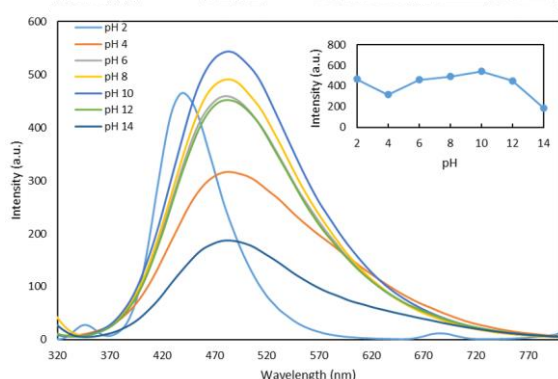
Fig.2: Emission spectra (ex=340 nm) of an aquas solution of M-CDs. Inset. emission at maximum intensity vs. pH.)

Conclusions

In summary, this study successfully synthesized pH-sensitive carbon dots (CDs) using a simple solvothermal method with citric acid, Meta-phenylenediamine (M-PDA), and N,N-dimethylformamide (DMF) as precursors. The synthesized O-PDA-based CDs exhibited uniform morphology and a size of approximately 3.2 nm. Characterization techniques confirmed the presence of nitrogen functionalities and various hydrophilic groups on the CD surface. Most importantly, the fluorescence intensity of the CDs displayed a significant response to varying pH levels. This pH-dependent fluorescence makes them promising candidates for applications in sensitive pH sensing. Our research contributes to the development of CD-based sensors by providing a straightforward and efficient approach for creating a reliable pH detection platform.

References

[1] Noun, F., J. Manioudakis, and R. Naccache, *Toward uniform optical properties of carbon dots.* Particle & Particle Systems Characterization, 2020. **37**(8): p. 2000119.

[2] Tian, X. and Z. Fan, *A design strategy of ratiometric probe based on dual-colored carbon dots for phosphate detection.* Dyes and Pigments, 2024: p. 111935.

[3] Zhang, W., et al., *Inhibition of mild steel corrosion in 1 M HCl by chondroitin sulfate and its synergistic effect with sodium alginate.* Carbohydrate Polymers, 2021. **260**: p. 117842.

[4] Pu, Z., et al., *Synthesis of diethylenetriamine-modified carbon quantum dots for dual sensing Fe3+ and Co2+ and its application.* Optical Materials, 2023. **146**: p. 114598.

[5] MP, A., S. Pardhiya, and P. Rajamani, *Carbon dots: an excellent fluorescent probe for contaminant sensing and remediation.* Small, 2022. **18**(15): p. 2105579.

[6] Xu, D., Q. Lin, and H.T. Chang, *Recent advances and sensing applications of carbon dots.* Small Methods, 2020. **4**(4): p. 1900387.

[7] Ji, C., et al., *Phenylenediamine-derived near infrared carbon dots: The kilogram-scale preparation, formation process, photoluminescence tuning mechanism and application as red phosphors.* Carbon, 2022. **192**: p. 198-208.

[8] Ye, Y., et al., *A high-efficiency corrosion inhibitor of N-doped citric acid-based carbon dots for mild steel in hydrochloric acid environment.* Journal of hazardous materials, 2020. **381**: p. 121019.

[9] Dutta Choudhury, S., et al., *pH-elicited luminescence functionalities of carbon dots: mechanistic insights.* The journal of physical chemistry letters, 2017. **8**(7): p. 1389-1395.

[10] Sui, L., et al., *Ultrafast carrier dynamics of carbon nanodots in different pH environments.* Physical Chemistry Chemical Physics, 2016. **18**(5): p. 3838-3845.

22nd Iranian Chemistry Congress (ICC22)
Iranian Research Organization for Science and Technology (IROST)
13-15 May 2024

03231-97589

IROST

Carbon Dots as Iron Ion Probes

Masoume Kaviani Darani [a], Shohre Rouhani [*b], Zahra Ranjbar [*a]

Corresponding Author E-mail: Rouhani@icrc.ac.ir / Ranjbar@icrc.ac.ir

[a] Department of Surface Coating and Corrosion, Institute for Color Science and Technology.
[b] Department of Organic Colorant, Institute for Color Science and Technology.

Abstract: This study explores metal-doped carbon dots (M-CDots) as probes for iron ion detection. M-CDots exhibited fluorescence quenching upon exposure to increasing Fe^{2+} and Fe^{3+} concentrations. UV-vis spectroscopy suggests an inner filter effect and energy transfer mechanism. The M-CDots displayed higher sensitivity towards Fe^{2+} ions compared to Fe3+ ions. These findings demonstrate the potential of M-CDots for selective iron ion detection.

Keywords: Carbon Dots; Iron ion Probe; Fluorescence Quenching

Introduction

Iron plays a vital role in numerous biological processes, but maintaining iron homeostasis is crucial. Iron dysregulation can lead to various health conditions, highlighting the need for efficient iron ion detection methods. Conventional techniques for iron ion detection often have limitations, such as complex procedures, high cost, or incompatibility with biological environments [1, 2].

In recent years, carbon dots (CDs) have emerged as a promising alternative for iron ion detection due to their unique properties [3, 4]. CDs are nanometer-sized carbon-based materials with exceptional photoluminescence (PL) properties, tunable surface functionalities, and good biocompatibility [5, 6]. These characteristics make them attractive candidates for developing sensitive and selective probes for iron ion detection in various environments.

Experimental Section
Synthesis

The synthesis of M-CDots was performed via a solvothermal method using citric acid (CA, 99%-Merck, Germany) as the carbon precursor, 1,3-phenylene diamine (MPD-Sigma-Aldrich, USA) as the nitrogen source, and dimethylformamide (DMF, Supelco, USA) as the solvent according to previous studies (different solvent and optimized temperature according to lab conditions) [7]. This method was chosen because of its ability to produce CDots with well-defined properties and controlled sizes. It should be noted that all the chemicals were used as received with no further purification.CA and MPD were weighed 1.68 gr and 0.64 gr respectively, and 40 ml DMF was added. The solution was thoroughly mixed to ensure homogeneity. The precursor solution was transferred to a Teflon-lined stainless-steel autoclave. The autoclave was sealed and heated in an oven at 200°C for

8 h. This high-temperature and high-pressure environment facilitated the formation of CDots. After the solvothermal reaction, the autoclave was allowed to cool to room temperature naturally. The resulting solution contained CDots in the DMF (Fig. 1).
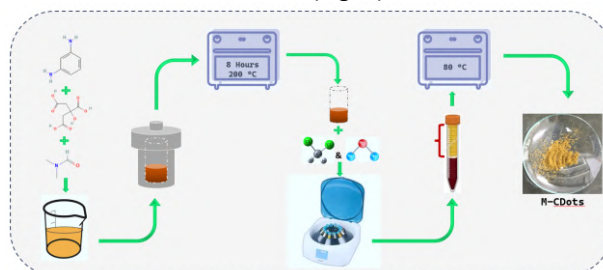
Fig.1: Schematic of M-CDots preparation process

Fluorescent detection of Fe^{2+} and Fe^{3+}

For iron ions detection, 2 mL M-CDots solution in DI water (0.04 Wt%) was prepared. Stock solutions of metal salts ($FeCl_3$ and $FeCl_2$, Merck) were dissolved in deionized water. Both solutions were diluted with different concentrations of DI water to obtain a series of Fe^{2+} and Fe^{3+} solutions with known concentrations. Upon adding the metal ions solution to the M-CDots solution, the fluorescence spectra of M-CDots at 340 nm excitation wavelength were measured to study the fluorescence response of CDs toward iron ions.

Results and Discussion

The fluorescence response of the CDs towards increasing iron ion concentration was investigated using fluorescence spectroscopy. Fig. 2 shows the PL emission spectra of the CDs upon excitation at 340 nm with increasing concentrations of iron ions.To examine the sensitivity of synthesized M-CDots toward iron ions, stock solutions of M-CDots were treated with various concentrations of iron ions. As a result, the photoluminescence of the M-CDots started quenching by

22nd Iranian Chemistry Congress (ICC22)
Iranian Research Organization for Science and Technology (IROST)
13-15 May 2024

03231-97589

IROST

increasing the concentration of iron ions. This may be due to the coordination between iron ions and hydroxyl groups on the surface of M-CDots [8-10]. As can be seen in Fig. 2, in both cases, increasing iron ion led to decrease in photoluminescence intensity, which makes these M-CDots a suitable probe for iron ion detection.
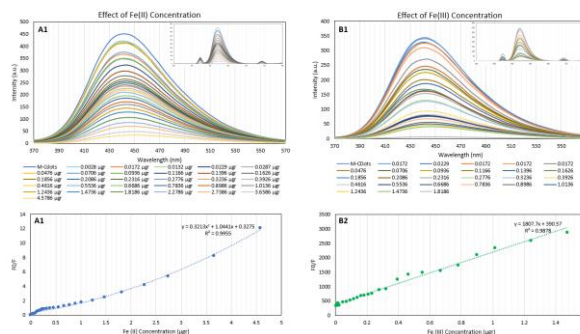

Fig.2: The dependence of M-CDots photoluminescence intensity to Fe^{2+} Concentrations (A1 and A2) and to Fe^{3+} concentrations (B1 and B2)

Overall, the graphs suggest that the carbon dots have the potential to be used as iron ion probes. The decrease in PL intensity with increasing iron ion concentration can be used to quantify the amount of iron ions present in a sample.

Quenching mechanism of photoluminescence in the presence of metal ions

To investigate the mechanism of photoluminescence quenching, the UV-vis absorption spectra of 0.4 wt% aqueous solution of carbon dots, aqueous solution containing Fe^{2+} ions, aqueous solution containing Fe^{3+} ions, M-CDots aqueous solution with Fe^{2+} ions, and M-CDots aqueous solution with Fe^{3+} ions were recorded. It was observed that the absorption spectrum of $Fe2+$ ions (green trace) and the absorption spectrum of Fe^{3+} ions (orange trace) overlap with the fluorescence emission of carbon dots (Figure 3). This overlap confirms that the sensor mechanism is of the inner filter effect and energy transfer type. This means that the mechanism of photoluminescence quenching of carbon dots in the presence of iron ions is also of the inner filter effect and energy transfer type. Therefore, it can be stated that the synergistic effect of the formation of non-photoluminescent aggregates and the inner filter effect causes the quenching of carbon dots against iron ions.
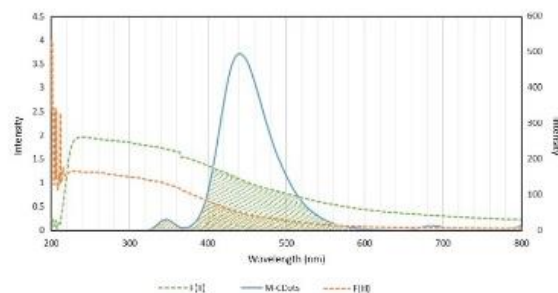
Fig.3: Overlap of the absorption spectra of aqueous solutions containing Fe^{2+} and Fe^{3+} ions with the photoluminescence emission spectrum of aqueous solution of carbon dots.

In the next step, to investigate the sensitivity of carbon dots to iron ions, equal concentrations of Fe^{2+} and Fe^{3+} ions were added to the solution of carbon dots. The photoluminescence spectra indicate a higher sensitivity of carbon dots to Fe^{2+} ions. As observed in Figure 4, the photoluminescence intensity of the sample of carbon dots containing Fe^{2+} ions (F(II)+M-Cdots) is lower than the photoluminescence intensity of the sample of carbon dots containing Fe^{3+} ions (F(III)+M-Cdots). Aqueous solutions containing Fe^{2+} ions (Fe(II)) and Fe3+ ions (Fe(III)) also show no photoluminescence.
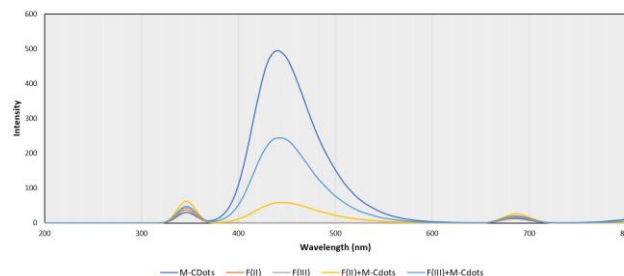
Fig.4: The photoluminescence spectra of Aqueous solution containing carbon dots (M-CDots), Fe^{2+} ions (Fe(II)), Fe^{3+} ions (Fe(III)), carbon dots and Fe^{2+} ions (F(II)+M-Cdots), and carbon dots and Fe^{3+} ions (F(III)+M-Cdots).

Conclusions

This study investigated the potential of metal-doped carbon dots as probes for iron ion detection. M-CDots exhibited a significant decrease in fluorescence intensity upon exposure to increasing concentrations of both Fe^{2+} and Fe^{3+} ions. Analysis of the quenching mechanism suggests a combination of inner filter effect and energy transfer between M-CDots and iron ions. Interestingly, the M-CDots displayed higher sensitivity towards Fe^{2+} ions compared to Fe^{3+} ions, indicating potential selectivity for ferrous iron. These findings demonstrate the promising application of M-CDots as a sensitive and selective probe for iron ion detection in various analytical settings.

22nd Iranian Chemistry Congress (ICC22)
Iranian Research Organization for Science and Technology (IROST)
13-15 May 2024

03231-97589

References

[1] Noun, F., J. Manioudakis, and R. Naccache, *Toward uniform optical properties of carbon dots.* Particle & Particle Systems Characterization, 2020. **37**(8): p. 2000119.

[2] Tian, X. and Z. Fan, *A design strategy of ratiometric probe based on dual-colored carbon dots for phosphate detection.* Dyes and Pigments, 2024: p. 111935.

[3] MP, A., S. Pardhiya, and P. Rajamani, *Carbon dots: an excellent fluorescent probe for contaminant sensing and remediation.* Small, 2022. **18**(15): p. 2105579.

[4] Xu, D., Q. Lin, and H.T. Chang, *Recent advances and sensing applications of carbon dots.* Small Methods, 2020. **4**(4): p. 1900387.

[5] Zhang, W., et al., *Inhibition of mild steel corrosion in 1 M HCl by chondroitin sulfate and its synergistic effect with sodium alginate.* Carbohydrate Polymers, 2021. **260**: p. 117842.

[6] Pu, Z., et al., *Synthesis of diethylenetriamine-modified carbon quantum dots for dual sensing Fe3+ and Co2+ and its application.* Optical Materials, 2023. **146**: p. 114598.

[7] Jiang, K., et al., *Red, green, and blue luminescence by carbon dots: full-color emission tuning and multicolor cellular imaging.* Angewandte chemie, 2015. **127**(18): p. 5450-5453.

[8] Sachdev, A. and P. Gopinath, *Green synthesis of multifunctional carbon dots from coriander leaves and their potential application as antioxidants, sensors and bioimaging agents.* Analyst, 2015. **140**(12): p. 4260-4269.

[9] Huang, H., et al., *Histidine-derived nontoxic nitrogen-doped carbon dots for sensing and bioimaging applications.* Langmuir, 2014. **30**(45): p. 13542-13548.

[10] Xu, Q., et al., *Preparation of highly photoluminescent sulfur-doped carbon dots for Fe (III) detection.* Journal of Materials Chemistry A, 2015. **3**(2): p. 542-546.

22nd Iranian Chemistry Congress (ICC22)
Iranian Research Organization for Science and Technology (IROST)
13-15 May 2024

03231-97589

IROST

Study of the enhanced visible-light-sensitive photocatalytic activity of the N,S-co doped carbon dots/CuBi2O4 micro particle composite for organic dye removal

Farhad Akhgari [a*], Anese Farhangi [b]

Corresponding Author E-mail: Farhad.akhgari@gmail.com

[a] Faculty of Materials and Manufacturing Technologies, Malek Ashtar University of Technology, Iran.

[b] Department of Chemistry, Payame Noor University, Urmia, Iran.

Abstract: Herein, we synthesis the Nitrogen, Sulfur co-doped fluorescent carbon dots/ $CuBi_2O_4$ micro particles composite and study their photocatalytic activity, which exhibits improved photocatalytic activity for organic dyes (methylene blue) under visible-light irradiation. The Nitrogen, Sulfur co-doped fluorescent carbon dots were synthesized from the mixture of glucose and thiourea by one step hydrothermal method and used for modification of $CuBi_2O_4$ micro particles.

Keywords: N,S-co doped carbon dots.; $CuBi_2O_4$; photocatalytic activity

Introduction

In recent years, considerable attention has been paid to the synthesis and application of carbon quantum dots (CDs), due to their outstanding tunable multi-color photoluminescence (PL) properties, high chemical stability, low toxicity, biocompatibility, and easy functionalization[1]. The unique PL property of CDs called by upconversion has been found, which could transfer low energy photon to high energy photon over CDs by sequential absorbing two or multiple longer wavelength photons.

Nowadays, nitrogen doped carbon nanomaterials (such as nanotubes, graphene, etc.) have received widespread attention, because nitrogen doping can effectively induce the delocalization of charges and regulate the overall function of carbon materials [2]. Consequently, the design of such a Nitrogen, Sulfur co-doped fluorescent carbon dots/$CuBi_2O_4$ (N,S-CDs/CBO) to construct a highly efficient composite photocatalyst is worth of expectation. To the best of our knowledge, few reports on the N,S-CDs/CBO composite have been reported.

Experimental Section

For the N,S-CDs/CBO composites, the 100 mg N,S-CDs powders were added into the hydrothermal fabricated process of CBO. In a typical procedure for synthesizing N,S-CDs/CBO, the 100 mg N,S-CDs solid powder was firstly mixed in 80 mL of distill water for 30 min, then 2.42 g of $Bi(NO_3)_3 \cdot 5H_2O$, 0.6 g $Cu(NO_3)_2 \cdot 2.5H_2O$ and 0.87 g NaOH were added and stirred for another 2.5 h. Subsequently,

the homogeneous precursor was transferred into 100 mL Teflon-lined stainless-steel autoclave, and kept at 180 °C for 24 h. After cooling to the room temperature, the product was collected, washed and dried.

Results and Discussion

The morphology of the synthesized samples was bserved by scanning electron microscope (SEM). As shown in Fig. 1, it is observed that the synthesized CBO is sepherical-like and the an average diameter of particles is about 200 nm. Fig. 1d shows the SEM image of N,S-CDs/CBO. It can be seen from the picture that the introduction of N-CDs does not change the morphology of CBO but increasing the surface area.

The dye molecule degradation, Methylene Blue (MB), study was also compared in the presence of N,S-CDs and without the presence of any photocatalyst. The results indicated that in the presence of the N,S-CDs showed the highest percentage of degradation rate compared to CDs and without the presence of photocatalyst.

The photocatalytic reaction kinetics of MB dyes were identified by the Langmuir-Hinshelwood (L-H) model, which is expressed by a first-order kinetics model. Graphs of $\ln (C_0/C_t)$ versus time were plotted in order to determine the apparent specific reaction rate (k). The linear plot indicated that the photo-kinetic degradation of MB dyes obey the first-order kinetics model. Fig. 3 shows the linear plot of $\ln C_0/C_t$ versus time for MB dye in the presence of N,S-CDs

22nd Iranian Chemistry Congress (ICC22)
Iranian Research Organization for Science and Technology (IROST)
13-15 May 2024

03231-97589

IROST
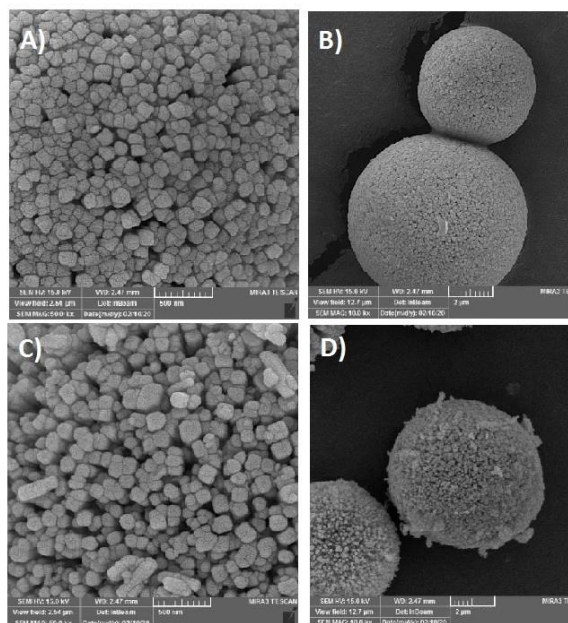
Fig.1: SEM images of (A,B) CBO and (C,D) N,S-CDs/CBO

Firstly, when N,S-CDs /CBO composite is irradiated by visible light, it can absorb photons and produce photo-induced electrons and holes, which are located on CB and VB of CBO, respectively. Secondly, because N,S-CDs exhibits better electron transport efficiency in composite photocatalytic materials, electrons located on CBO can be effectively transferred to N,S-CDs, thus the possible radical species ($°OH$ and $O_2°$) can be generated. These radical species could degrade the MB dye to form several intermediate products that finally decompose into several nontoxic side products such as NH_2, CH_4, NO_2, SO_3, CO_2, and H_2O.
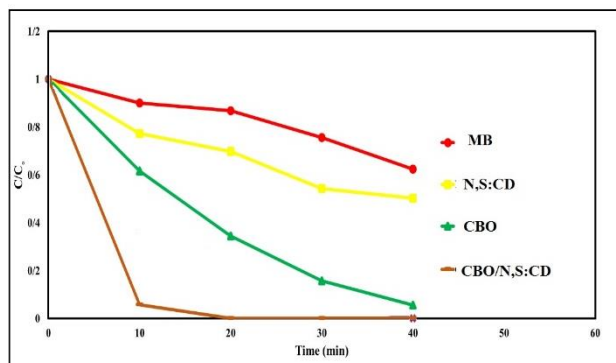
Fig.2: Comparison of the degradation rate of dyes in the presence and in the absence of N,S-CDs and CBO, versus sunlight irradiation exposure time
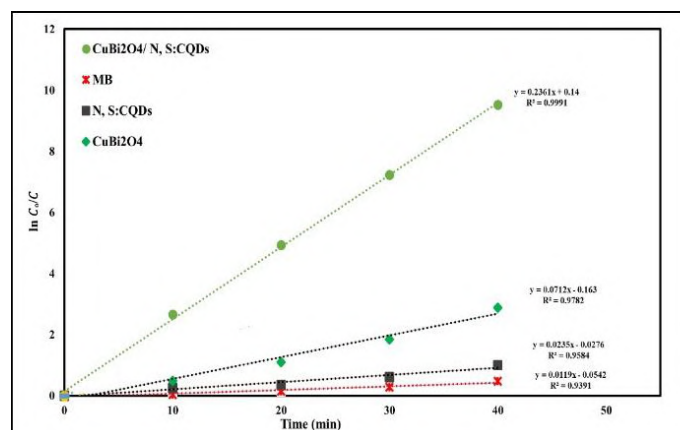
Fig.3: Graphs of ln (C_0/C_t) versus sunlight irradiation time for photocatalytic degradation of MB

Conclusions

A novel N,S-CDs modified $CuBi_2O_4$ photocatalyst was prepared through a facile hydrothermal method, and applied to the photocatalytic degradation of MB. Results exhibited the increased photocatalytic hydrogen production of N,S-CDs/ $CuBi_2O_4$ compared with pure $CuBi_2O_4$ and CDs/ $CuBi_2O_4$. The excellent photocatalytic performance of N,S-CDs/ $CuBi_2O_4$ composite was attributed to efficient synergistic effect between N,S-CDs and $CuBi_2O_4$, which increased light harvesting and electron transfer.

References

[1] Akhgari, F., Samadi, N., & Farhadi, kh. (2017). Fluorescent Carbon Dot as Nanosensor for Sensitive and Selective Detection of Cefixime Based on Inner Filter Effect. J. Fluorescence, 27(3):921-927. https://link.springer.com/article/10.1007/s10895-017-2027-0

[2] Akhgari, F., Samadi, N., Farhadi, kh. &Akhgari, M. (2017). A green one-pot synthesis of nitrogen and sulfur co-doped carbon quantum dots for sensitive and selective detection of cephalexin,Can. J. Chem. 95: 641–648. https://doi.org/10.1139/cjc-2016-0531

22nd Iranian Chemistry Congress (ICC22)
Iranian Research Organization for Science and Technology (IROST)
13-15 May 2024

03231-97589

IROST

A novel strategy for stabilization of Pd colloids on multi walled carbon nanotube as a robust catalyst for Stille coupling transformation

Kimiya Ghasemi, Nader Noroozi Pesyan, Hassan Alamgholiloo

Corresponding Author E-mail: nnp403@gmail.com

Department of Organic Chemistry, Faculty of Chemistry, Urmia University 57159, Urmia, Iran.

Abstract: Herein, we report nanoparticles of size-monodiperese Pd nanoparticles are effective catalysts for the Stille coupling reaction in polyethylene glycol-400 (PEG-400) at 90 °C. The SEM and TEM analysis confirmed that the catalyst was nano sized and high efficiency for the Stille C-C coupling reaction.
Keywords: Pd nanoparticles; Stille reaction; PEG

Introduction

The palladium-catalyzed cross-coupling reaction between organotin compounds and organic halides or triflates (the Stille reaction) is a widely used methodology for the formation of C-C bonds [1]. The distinction between homogeneous catalysis by molecular species and "heterogeneous" catalysis by soluble metal nanoparticles is especially relevant in carbon-carbon coupling reactions, which are often performed under conditions favorable for the formation of Pd(0) nanoparticles from molecular precursors. However, key experiments on Heck, Suzuki, Sonogashira, and other coupling reactions support currently that the true catalyst in these reactions consists of monomeric or dimeric [2].

Experimental Section

For the synthesis of Pd@ZnO/MWCNT, first, 0. 01 g Pd (OAc)$_2$ and 0.2 g CTAB in 50 ml deionized water was dispersed for 60 min. Then, 0.2 g NaBH$_4$ was added. Finally, the solution consisting of 25 ml of deionized water and 1 g ZnO was added. In the second step, the solution obtained from the previous step was was added to solution of MWCNT and 80 ml deionized water on the stirrer for 2 hours.

General procedure for Stille coupling reactions: In the model reaction, the mixture of aryl halides (1 mmol), triphenyltin chloride (0.3 mmol), Na$_2$CO$_3$ (1 mmol), PEG-400 (2 mL) was added to Pd@ZnO/MWCNT catalyst and allowed to stir at 90 °C for 1 h.

Results and Discussion

The FT IR spectrum confirmed the structure of Pd@ZnO/MWCNT (Fig. 1). The SEM image of nanocatalyst showed the rod like shape of MWCNT (Fig. 2).
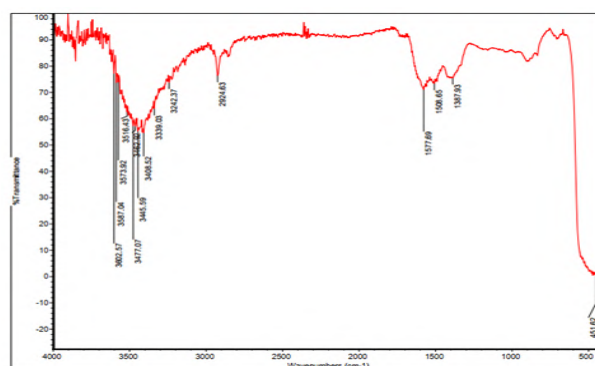
Fig.1: IR spectrum for Pd@ZnO/MWCNT.
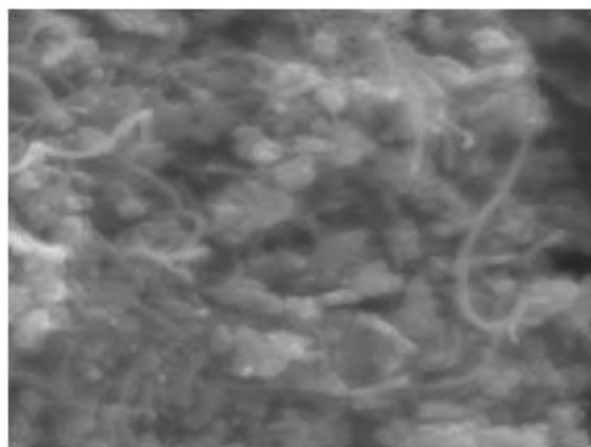
Fig. 2. SEM image of nanocatalyst.

It was also observed that aryl halides were found to be most reactive in high temperature (Table 1).

Table 1: Catalyst screening and reaction optimization for Stille coupling reaction

solvent	T (°C)	Time (h)
PEG-400	25°C	72
PEG-400	90°C	1

22nd Iranian Chemistry Congress (ICC22)
Iranian Research Organization for Science and Technology (IROST)
13-15 May 2024

03231-97589

IROST

Conclusions

We indicated that Pd@ZnO/MWCNT nanocatalyst an efficient protocol toward the economic synthesis of biaryls under sustainable conditions. This methodology revealed that this nanocatalyst has notable advantages such as excellent stability, large scalability, and eco-friendly nature, which could coincide with the concepts of green chemistry.

References

[1] Garcia Martinez, A., Osío Barcina, J., Colorado Heras, M. D. R., & de Fresno Cerezo, Á. (2001). Reactions of vinyl and aryl triflates with hypervalent tin reagents. Organometallics, 20(5), 1020-1023.

[2] Bernechea, M., de Jesús, E., López-Mardomingo, C., & Terreros, P. (2009). Dendrimer-encapsulated Pd nanoparticles versus palladium acetate as catalytic precursors in the Stille reaction in water. Inorganic chemistry, 48(10), 4491-4496.

22nd Iranian Chemistry Congress (ICC22)
Iranian Research Organization for Science and Technology (IROST)
13-15 May 2024

03231-97589

IROST

Selective Dehydration of Carbohydrate into 5-Hydroxymethylfurfural and Levulinic acid using Acidic Periodic Mesoporous Organosilicas (PMOs)

Hamzeh Hassanaki Veisi, Babak Karimi[*]

Corresponding Author E-mail: Karimi@iasbs.ac.ir

Institute for Advanced Studies in Basic Sciences (IASBS).

Abstract: Selective dehydration of fructose into 5-hydroxymethylfurfural and levulinic acid can be catalyzed by using the synergistic collaboration of active sites and plugging structures in Periodic Mesoporous Organosilicas (PMOs) at different solvents. Fructose can be converted into 5-Hydroxymethylfurfural with a 95% yield and 99% conversion in DMSO as a solvent using Plug-Ethyl-PMO at 140 ˚C. On the other hand, levulinic acid with a 90% yield can be produced from fructose (98% conversion) in GVL as a solvent using Unplug-Ethyl-PMO at 160 ˚C.

Keywords: Biomass; 5-Hydroxymethylfurfural; Levulinic acid; Periodic Mesoporous Organosilicas (PMOs); Acid catalyst

Introduction

Dehydration of carbohydrates into 5-hydroxymethylfurfural (5-HMF) and levulinic acid (LA), as two of the most important 12 bio-based principal molecules, has attracted huge interest due to its great potential to produce a broad diversity of valuable compounds such as dimethyl furan or gamma valerolactone as high-octane fuel additives, respectively. Several types of acid catalysts can successfully convert fructose to 5-HMF, but most catalyst systems for levulinic acid production typically require both Brnsted-Metal acid sites with complex structures. Considering the high surface acidic properties of SO_3H-PMOs and the possibility of hydrophobicity adjustment of channels by plugging, we were curious to test these materials in the dehydration of fructose. [1, 2]

Experimental Section

In a 25 mL home-designed high-pressure Teflon-lined reactor, a mixture of fructose (Merck) (30-100 mg), catalyst (10-30 mg), and a solvent (DMSO or GVL) was prepared. Then, the sealed reactor was placed in the oil bath (140 to 180 °C). Finally, the reaction mixture was filtered and examined by HPLC to calculate the 5-HMF yield and carbohydrate conversion.

Results and Discussion

First, using our reported method, we prepared ethyl-PMOs with plugged and unplugged channels as acidic catalysts. [3] The characterization of these catalysts by various analyses demonstrated the ordered mesoporous structures. (Fig. 1). Next, we investigated the use of these PMOs as acidic catalysts in fructose dehydration to determine whether our materials could also function as switchable catalysts.
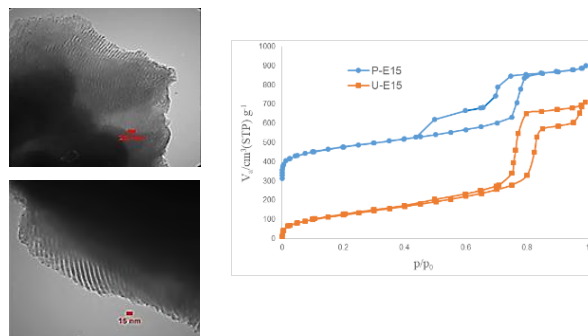
Fig.1: TEM and N_2 adsorption-desorption of of Periodic mesoporous organosilicas with plugged and unplugged channels

Results showed that 5-HMF can be the main product of unplugged PMOs, while levulinic acid can be produced from plugged PMOs. Indeed, the unplugged channels of PMOs provide a means of faster and more efficient mass transfer phenomena compared to the plugged structures of PMOs. In addition, plugged channels of PMOs with a silicon nature show hydrophilic properties. Hence, the main product of dehydration of fructose from unplugged PMO is 5-HMF (in DMSO as a solvent), while 5-HMF can be rehydrated into levulinic acid in plugged channels of PMO catalysts because of the hydrophilic nature of plugged structures (in GVL as a solvent) (Table 1).

Table1: Dehydration of Fructose with $SO_3H@U/P$-PMO in DMSO & GVL (U: Unplug channels, P: Plug channels)

Cat.	Solvent	T (˚C)	Time (min)	Conv. (%)	5-HMF Yield (%)	LA Yield (%)
$SO_3H@U$-PMO	DMSO	140	240	99	95	5
$SO_3H@P$-PMO	GVL	160	180	98	5	90

22nd Iranian Chemistry Congress (ICC22)
Iranian Research Organization for Science and
Technology (IROST)
13-15 May 2024

03231-97589

Conclusions

We designed and prepared two different types of PMOs as acid catalysts with plugged and unplugged channels. These catalysts demonstrated exceptional performance in dehydrating fructose into 5-HMF and levulinic acid. This study showed that the solvent and hydrophilicity of catalysts (plug and unplug PMOs) play a very important role in the dehydration of fructose. The idea investigated in this work, in our opinion, will pave the way for the future design and development of more suitable multifunctional materials with tuneable characteristics.

References

[1] Karimi, B., Mirzaei, H. M., Behzadnia, H., Vali, H. (2015). Novel Ordered Mesoporous Carbon Based Sulfonic Acid as an Efficient Catalyst in the Selective Dehydration of Fructose into 5-HMF: the Role of Solvent and Surface Chemistry. ACS Appl. Mater. Interfaces, 7, 19050-19059. https://doi.org/10.1021/acsami.5b03985.

[2] Veisi, H. H., Akbari, M., Karimi, B., Vali, H., Luque, R. (2023). One-pot acid–base catalysed tandem reactions using a bimodal N, S-doped cubic mesoporous carbon. Green Chem., 25, 4076-4089. https://doi.org/10.1039/D3GC00117B.

[3] Karimi B, Khorasani M, Vali H, Vargas C, Luque R. (2015). Palladium nanoparticles supported in the nanospaces of imidazolium-based bifunctional PMOs: The role of plugs in selectivity changeover in aerobic oxidation of alcohols. ACS Catal., 5 (7), 4189-200. https://doi.org/10.1021/acscatal.5b00237

Design and Synthesis of 2-Benzomidazolylmeyhyl Chalcone Hybrid Conjugates as potential Therapeutic Agents

Zahra Norouzi Makari , Mohammad Navid Soltani Rad

Corresponding Author E-mail: mozhdehn17@gmail.com

Department of Chemistry, Shiraz University of Technology, Shiraz 71555-313, Iran.

Abstract: This paper describes the design and synthesis of novel 2-benzimidazolylmethyl chalcone hybrid conjugates. The compounds were synthesized by coupling 2-chloromethylbenzimidazole with the desired chalcones. Due to the known beneficial biological properties of benzimidazole and chalcone derivatives, it is anticipated that these conjugate compounds may exhibit promising therapeutic properties.

Keywords: Synthesis**,** Benzimidazole; Chalcone; hybrid conjugate

Introduction

Chalcones, particularly 1,3-diphenylprop-2-en-1-one, as open-chain flavonoids with an α,β-unsaturated carbonyl group. They are essential structures in various natural compounds and serve as precursors for the biosynthesis of flavonoids and isoflavonoids. Chalcones exist in *trans* and *cis* forms, with the trans isomer being more stable. These compounds have attracted attention for potential therapeutic applications, with diverse biological activities such as anti-diabetic, anti-neoplastic, antihypertensive, anti-retroviral, and anti-inflammatory properties. Researchers have synthesized various chalcone derivatives, including those with N-heterocyclic compounds known for their significant biological effects [1] (Fig. 1).

The benzimidazoles are widely used in agriculture, veterinary medicine, and human medicine as antifungal, anticancer, antiparasitic, anti-hypertensive, antiviral, and anti-inflammatory agents. Figure 2 displays the structures of some well-known benzimidazole-based drugs along with their pharmaceutical characteristics [2].

The concept of hybrid conjugate compounds, which are artificial combinations of two or more pharmacophores belonging to known compound categories. These compounds are used to produce specific desired effects and play a significant role in chemistry, biology, and medicine. They have the potential to create novel chemotherapeutic agents that improve efficacy, activity, binding affinity, drug delivery, and reduce side effects [3].

Owing to beneficial biological profiles of benzimidazole and chalcone derivatives, hereby it is explained 2-benzomidazolylmeyhyl chalcone hybrid conjugates, the general structures of which are illustrated in Fig. 3.
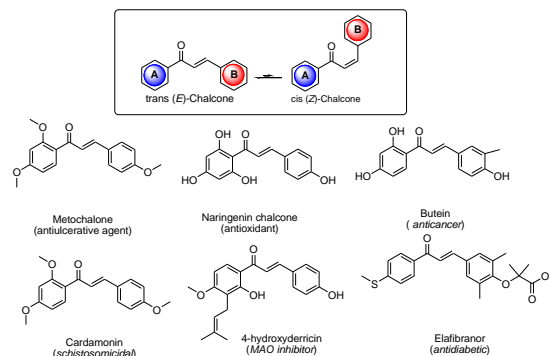
Fig.1: The structures of chalcone and some chalcone scaffold-based drugs
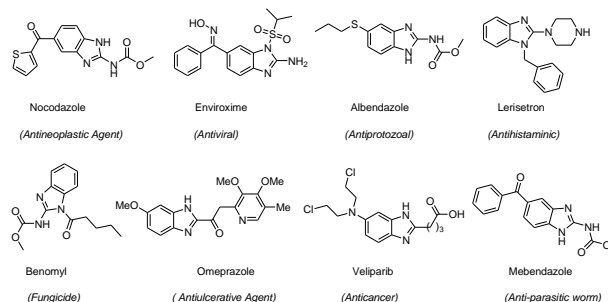
Fig. 2: The structure of well-known benzimidazole-based drugs
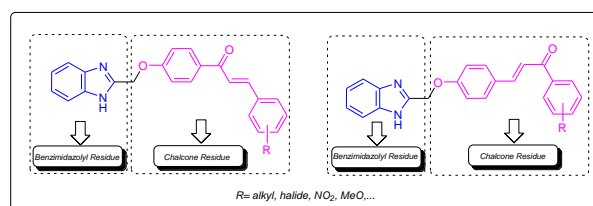
Fig. 3: General structure of novel 2-benzimidazolylmethyl chalcone hybrid conjugates

22nd Iranian Chemistry Congress (ICC22)
Iranian Research Organization for Science and Technology (IROST)
13-15 May 2024

03231-97589

IROST

Experimental Section

Synthesis of 2-chloromethyl-1H-benzoimidazole: This synthesis was carried out due to standard procedure [4].

Synthesis of chalcones: Chalcones were synthesized due to standard the Claisen-Schmidt condensation procedure [5].

Synthesis of 2-benzomidazolylmeyhyl chalcone hybrid conjugates: A 100 mL double-necked round bottom flask equipped with a condenser was charged with a mixture of desire chalcones (10 mmol), K_2CO_3 (1.38 g, 10 mmol) and 2-chloromethyl-1H-benzoimidazole (1.66 g, 10 mmol) in anhydrous DMF (30 mL). The mixture was heated to 100 °C and the progress of the reaction was monitored by TLC. When TLC monitoring indicated the completion of the reaction, the reaction was stopped and the solution was cooled to ambient temperature. The reaction media was diluted in 500 mL distilled water and the organic materials were extracted by 3×100 mL $CHCl_3$. The solvent was evaporated *in vacuo* and remaining crude product was purified by a short column chromatography on silica gel eluting with EtOAc/n-hexane.

Results and Discussion

The title compounds were synthesized according to Scheme 1. Scheme 1 illustrates a three-step reaction process. The synthesis commenced with the reaction of o-phenylenediamine with α-chloroacetic acid in a 5N HCl solution to produce 2-chloromethyl-1H-benzoimidazole (**I**). Subsequently, chalcones (**II**, **III**) were synthesized through a Claisen-Schmidt condensation reaction using 4-hydroxyacetophenone and selected aldehydes with various functional groups, or by employing 4-hydroxyaldehyde and acetophenone with diverse functionalities. The final step involved a coupling reaction of the respective 4-hydroxychalones with 2-chloromethyl-1H-benzoimidazole (I) via an S_N2-type reaction to obtain the corresponding products **VI** and/or **V**.

Having used the above procedure, several products bearing different functionalities were synthesized which some selected structures are illustrated in Fig.4.

Selected data for (E)-1-(4-((1H-benzo[d]imidazol-2-yl)methoxy)phenyl)-3-phenylprop-2-en-1-one: CC on SiO_2 eluted with n-hexane/EtOAc (1:6) afforded creamy foam (2.76 g, 78%), R_f (EtOAc/MeOH, 4:1): 0.39, ^1H NMR (DMSO-d_6, 400 MHz): δ_{ppm}= 6.01(s. 2H,OCH_2), 7.01-7.90(complex, 15H, aryl & venyl), 10.21(s, 1H, NH). ^{13}C NMR ($CDCl_3$, 100 MHz): δ_{ppm}= 71.5, 115.0,116.2, 122.5, 123.1, 126.3, 128.4, 130.9, 131.2, 135.3, 138.4, 141.6, 145.3, 162.6, 166.4, 190.1.

Conclusions

In conclusion, we have designed and synthesized novel 2-benzimidazolylmethyl chalcone hybrid conjugates through three steps in good to excellent yields.
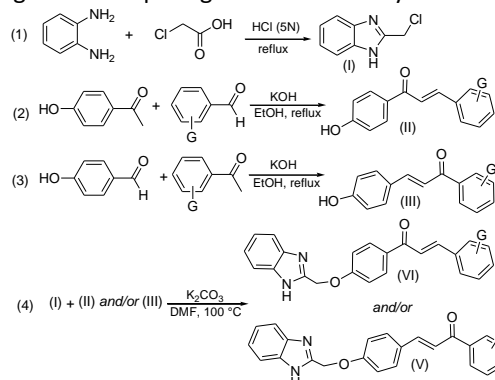
Scheme 1: General synthetic pathway for preparing novel 2-benzimidazolylmethyl chalcone hybrid conjugates
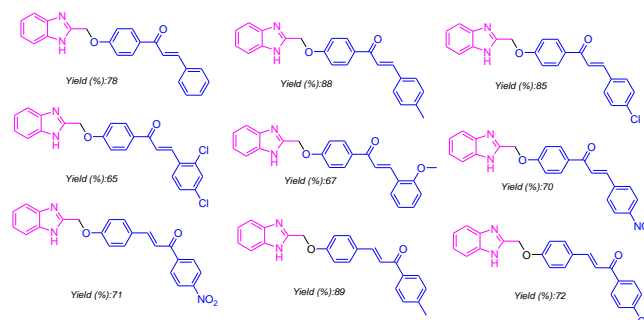
Fig. 4: Selected structures of some products

References

[1] Zhuang, C., Zhang, W., Sheng, C., Zhang, W., Xing, C. & Miao, Z. (2017). Chalcone: a privileged structure in medicinal chemistry. Chemical Reviews, 117, 7762–7810. https://doi.org/10. 1021/acs.chemrev.7b00020.

[2] Banerjee, S., Mukherjee, S., Nath P., Mukherjee, A., Mukherjee, S., Kumar, S.K. A., De, S.& Banerjee, S. (2023). A critical review of benzimidazole: Sky-high objectives towards the lead molecule to predict the future in medicinal chemistry. Results in Chemistry, 10, 101013. https://doi.org/10.1016/j.rechem.2023.101013.

[3] Alkhzem, A. H., Woodman, T. J. & Blagbrough, I. S. (2023). Design and synthesis of hybrid compounds as novel drugs and medicines. RSC Advances, 12, 19470. https://doi.org/10.1039/d2ra03281c.

[4] Petkar, K., Parekh, P., Mehta, P., Kumari, A.& Baro, A. (2013). Synthesis & evaluation of 2-chloromethyl-1h-benzimidazole derivatives as antifungal agents. International Journal of Pharmacy and Pharmaceutical Sciences, 5 (2), 115-119.

[5] Vogel, A. I. Vogel's Textbook of practical organic chemistry — 5th ed (1978).

ZnO-CdS heterostructure as a potential photocatalyst for preparing substituted chromenes and its anti-liver cancer activity

Reza Tayebee , Zahra Jalili*, Sedighe Abbaspour

Corresponding Author E-mail : m.jalili2011@yahoo.com

Department of Chemistry, Faculty of Science, Hakim Sabzevari University, Sabzevar, Iran.

Abstract: There are ongoing studies on the potential use of chromene derivatives in liver cancer therapy. They have shown promising results in preclinical studies for liver cancer, including inhibiting tumor growth and inducing apoptosis. Herein, the nanosized hybrid material ZnO-CdS is prepared using a green and ecofriendly procedure. The nanomaterial was characterized by FE-SEM, TEM , EDS and DRS The photocatalytic proficiency of ZnO-CdS was then scrutinized in the fabrication of some 4H-chromenes in a mild condition

Keywords: photocatalysis; ZnO-CdS; chromenes; HepG2; liver cancer

Introduction

Chromenes are a class of compounds with diverse biological activities, including anticancer properties.[1-2] The chromene family has gained attention for its potential anti-cancer properties, including its effectiveness against liver cancer.[3] Chromene derivatives have various biological functions including anti-cancer, anti-oxidant, and anti-inflammatory activities.[4] These compounds have been shown to possess cytotoxic and anti-proliferative properties, meaning they may inhibit the growth and division of liver cancer cells. While zinc is a necessary element, playing various functions in physiological routes, including immune function and DNA synthesis. Zinc oxide (ZnO) is an affordable and environmentally friendly semiconductor that possesses a large energy band gap of 3.38 eV. Recent studies show that heterojunction of ZnO with other semiconductors results in modification of new charge carriers with improved photocatalytic properties.[5] Cadmium sulfide (CdS) is also a compound used mainly in industrial applications, such as pigments, solar cells, and semiconductors. CdS plays a significant role in photocatalysis because of unique properties and effective band-gap energy that is around 2.20 eV, which positions it in the visible light spectrum

Experimental Section

Materials and Methods

The materials and solvents used in this study were provided commercially and used without additional purification. Morphology of nanoparticles conducted by using an FE-SEM instrument, TESCAN involving an energy dispersive x-ray (EDS) analyzer. Transmission electron microscopy (TEM) was performed on Philips-CM120 with a magnification of 200 K and voltage 200 kV.

Results and Discussion

FE-SEM ,TEM and EDS

The morphology and size of ZnO, CdS, and ZnO-CdS nanoparticles were examined using FE-SEM, as depicted in Figs. a-c. The analysis showed that the nanomaterials have consistent shape within the size range of ~45 nm. This finding was also approved by TEM (Fig. 1d).
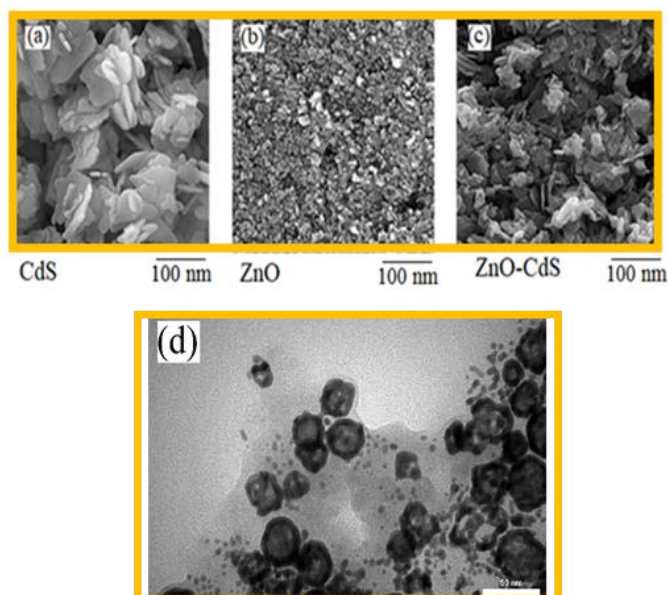
Fig. 1. FE-SEM images of ZnO (a), CdS (b), and ZnO-CdS (c) nanoparticles. TEM image of ZnO-CdS (d).

22nd Iranian Chemistry Congress (ICC22)
Iranian Research Organization for Science and
Technology (IROST)
13-15 May 2024

03231-97589

ISC
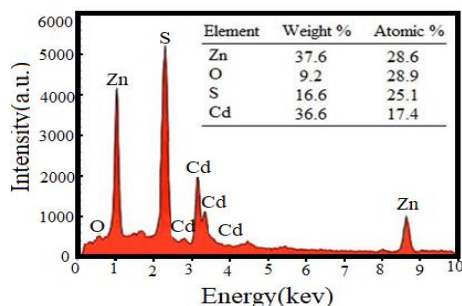
Fig. 2. EDS analysis of ZnO-CdS heterostructure.

The EDS spectrum of ZnO-CdS, displayed in Fig. 2, revealed the presence of specific elements Zn, S, Cd, and O atoms, confirming successful formation of ZnO-CdS nanoparticles .

DRS and optical properties
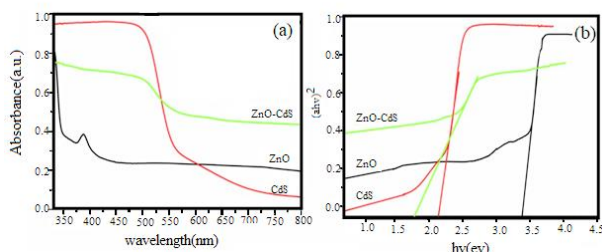
Fig. 3. (a) UV-Vis absorption spectra of ZnO, CdS, and ZnO-CdS; (b) Tauc plot of ZnO, CdS, and ZnO-CdS nanoparticles.

The optical characteristics of ZnO, CdS, and ZnO-CdS along with the Tauc plots of ZnO, CdS, and ZnO-CdS nanoparticles are provided in Figs. 3a-b.

Effect of some irradiation sources
To determine the role of irradiation source on the efficacy of the photocatalytic system, a distinctive reaction was carried out by utilizing 1 mmol of benzaldehyde, dimedone, and 4-hydroxycoumarin in the presence of ZnO-CdS (10 mg) in 10 mL ethanol at room temperature, based on the general reaction condition described in the experimental section (Table 1).

Table 1. Optimization of light source and presence of the photocatalyst

Entry	Light source	ZnO-CdS (mg)	Time (h)	Yield (%)
1	in dark	10	0.5	43
2	LED (Green), 25 W	10	0.5	95
3	LED (white), 20 × 1 W	10	0.5	58
4	LED (white), 20 × 1 W	-	0.5	15
5	–	-	0.5	7
6	LED (Green), 25 W	10	0.5	28

Conclusions

A novel method is established for the synthesis of chromeno[4,3-b]chromenes using visible light. The utilization of ZnO-CdS exhibits a superior green]alternative for driving the selected condensation reaction. We characterized the heterogeneous nanophotocatalyst through DRS, SEM, TEM, and EDS to unravel its properties. This innovative photocatalytic system exhibits several key attributes. Noteworthy advantages include mild reaction condition, broad substrate scope, cost-effective, and high yield.

References

[1] Raj V, Lee J. 2H/4H-Chromenes—A versatile biologically attractive Scaffold. Frontiers in Chemistry. 2020 .https://doi.org/10.3389/fchem.2020.00623

[2] . Eshghi H, Pirani F, Khoshnevis M. Recent Progress in the Synthesis and Biological Activity of Chromene and Its Derivatives. Frontiers in Natural Product Chemistry: Volume 8. 2021 Dec 6;8:239-304.

[3] . Nabeel AI, Mansour SZ, Mahdy ES, El-Mezayen HA, Mohamed SA. In vivo Study of a Newly Synthesized Chromen-4-one Derivative as an Antitumor Agent against HCC. Journal of Gastrointestinal Cancer. 2021 Sep 7:1-0.

[4] . Costa M, Dias TA, Brito A, Proença F. Biological importance of structurally diversified chromenes. European journal of medicinal chemistry. 2016 Nov 10;123:487-507. https://doi.org/10.1016/j.ejmech.2016.07.057

[5] . Dhiman P, Rana G, Kumar A, Sharma G, Vo DV, Naushad M. ZnO-based heterostructures as photocatalysts for hydrogen generation and depollution: a review. Environmental Chemistry Letters. 2022 Apr 1:1-35.

Novel green synthesis of Ni-NiO nanoparticles by licorice root extract towards photocatalytic synthesis of some substituted bis(indolyl)arylmethanes as anti-gastric cancer agents

Zahra Jalili*, Sedighe Abbaspour

Corresponding Author E-mail:m.jalili2011@yahoo.com

Department of Chemistry, Faculty of Science, Hakim Sabzevari University, Sabzevar, Iran.

Abstract: Indoles have shown promise as potential agents in the treatment of some cancers including gastric cancer. Herein, a new method is disclosed to prepare these important compounds by the mediation of green-biosynthesized Ni-NiO nanoparticles from licorice (Glycyrrhiza glabra) root extract. The prepared nanoparticles characterized by FT-IR, FE-SEM, and EDS analyzes.

Keywords: ： Ni-NiO nanoparticles, photocatalysis; bis(indolyl)methanes; gastric cancer; MKN-45 cell line

Introduction

Indoles are organic compounds that are found in numerous natural sources and plants [1-2]. Studies have demonstrated that certain indole derivatives may possess anticancer properties and can suppress tumor growth in gastric cancer cells [3-4]. Nickel-based heterogeneous catalysts, in particular, are commonly utilized in various industrially relevant reactions due to the low cost and abundance of nickel as an active metal [5] This study focuses on the development of a novel Ni-NiO nanophotocatalyst and its effectiveness in synthesizing bis(indolyl)arylmethanes.

Experimental Section

Preparation of Ni-NiO nanoparticles using licorice root extract. For this biogenic synthesis, highly pure hydrated nickel(II) nitrate ($Ni(NO_3)_2.6H_2O$) was used as the metal precursor. Therefore, 5 mL of the prepared extract was added drop-wise to the freshly prepared 0.1 M solution of nickel nitrate under vigorous stirring for 30 min until change the color of solution from green to yellow-green. After that, the solution was centrifuged and the obtained residue was calcined at 350 ºC for 1.5 h to provide a fine black-color material.
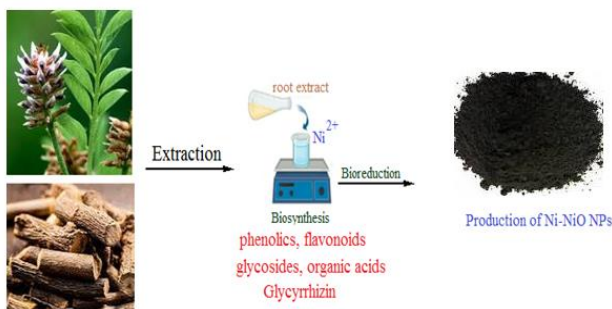
Fig. 1. Green biosynthesis of Ni-NiO nanoparticles from licorice root extract

Results and Discussion

FT-IR, FE-SEM and EDS

FT-IR spectroscopy was used as a tool to detect important functional groups and bonding in the prepared nanoparticles (Figs. 2a-b).
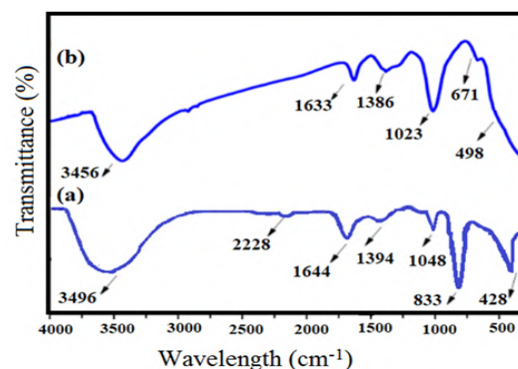
Fig. 2. FT-IR spectra of (a) NiO and (b) Ni-NiO nanoparticles..

The morphology of the prepared Ni-NiO nanoparticles is important because determines surface properties of the nanoparticles. Therefore, morphology of the biosynthesized nanomaterial was characterized through FE-SEM (Figs.3a-b).
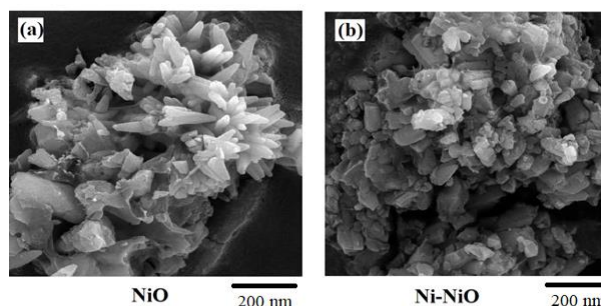
Fig. 3. FE-SEM images of (a) NiO and Ni-NiO nanoparticles (b).

22nd Iranian Chemistry Congress (ICC22)
Iranian Research Organization for Science and Technology (IROST)
13-15 May 2024

03231-97589

. Moreover, Fig. 4 depicts elemental composition of Ni-NiO based on EDS analysis, which confirmed presence of Ni and O in the sample .

Element	wt%	atomic%
O	43.8	73.4
Ni	56.2	26.6
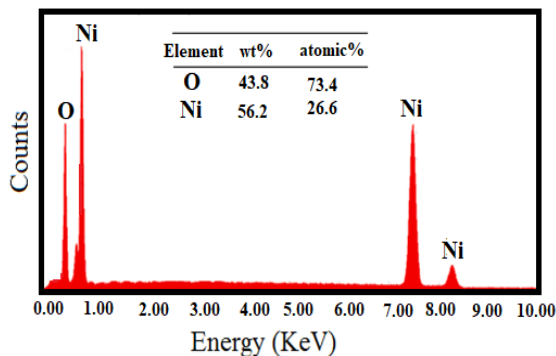
Fig. 4. EDS analysis of Ni-NiO nanoparticles

Table 1. Effect of experimental parameters. 1 mmol benzaldehyde reacted with 2 mmol indole in 10 mL ethanol.

Entry	Catalyst	Catalyst (mg)	Temperature (°C)	Time (min.)	Yield (%)
1	-	-	30	60	18
2	NiO	50	30	30	74
3	ZnO	50	30	30	54
4	Ni-NiO	10	30	30	68
5	Ni-NiO	20	25	60	86
6	Ni-NiO	20	50	60	92
7	Ni-NiO	50	30	30	98

Conclusions

In this research, we presented the results of our investigation into the properties of a unique binary photocatalyst called Ni-NiO. This photocatalyst exhibits remarkable efficiency in the synthesis of substituted bis(indolyl)arylmethanes under mild reaction conditions

References

[1]. Liu Y, Cui Y, Lu L, Gong Y, Han W, Piao G. Natural indole-containing alkaloids and their antibacterial activities. Archiv der Pharmazie. 2020 Oct; 353(10):2000120.https://doi.org/10.1002/ardp.202000120.

[2]. Omar F, Tareq AM, Alqahtani AM, Dhama K, Sayeed MA, Emran TB, Simal-Gandara J. Plant-based indole alkaloids: A comprehensive overview from a pharmacological perspective. Molecules. 2021 Apr 15; 26(8):2297. https://doi.org/10.3390/molecules26082297

[3].Sachdeva H, Mathur J, Guleria A. Indole derivatives as potential anticancer agents: A review. Journal of the Chilean Chemical Society. 2020 Sep;65(3):4900-7. http://dx.doi.org/10.4067/s0717-97072020000204900

[4]. Devi N, Kaur K, Biharee A, Jaitak V. Recent development in indole derivatives as anticancer agent: a mechanistic approach. Anti-Cancer Agents in Medicinal Chemistry (Formerly Current Medicinal Chemistry-Anti-Cancer Agents). 2021 Sep 1;21(14):1802-24. https://doi.org/10.2174/1871520621999210104192644

[5]. Helal A, Shaheen Shah S, Usman M, Khan MY, Aziz MA, Mizanur Rahman M. Potential Applications of Nickel-Based Metal-Organic Frameworks and their Derivatives. The Chemical Record. 2022. Jul;22(7):e202200055https://doi.org/10.1002/tcr.202200055

22nd Iranian Chemistry Congress (ICC22)
Iranian Research Organization for Science and Technology (IROST)
13-15 May 2024

03231-97589

IROST

Photoinduced synthesis of 2-substituted benzimidazoles as effective anti-cancer drugs mediated by new heterojunction Fe$_3$O$_4$/ZnO nanoparticles

Zahra Jalili*, Sedighe Abbaspour, Behnaz Abdi Aliabad

Corresponding Author E-mail : m.jalili2011@yahoo.com

Department of Chemistry, Faculty of Science, Hakim Sabzevari University, Sabzevar, Iran.

Abstract: Heterogeneous photocatalysts indeed offer a promising approach for conducting eco-friendly and sustainable organic transformations. The use of Fe$_3$O$_4$/ZnO as a photocatalyst for synthesizing 2-substituted benzimidazoles under illumination of a high pressure mercury lamp is innovative and efficient. The characterization techniques such as FT-IR, DRS, and VSM are used to identify the photocatalyst. Moreover, various parameters are evaluated on the photocatalytic performance of Fe$_3$O$_4$/ZnO throughout this research. It is realized that the protocol is successful to conduct the condensation reaction across different types of aromatic aldehydes with various substituents.

Keywords: 2-substituted benzimidazole, green chemistry, photocatalyst, UV-Vis light, Fe$_3$O$_4$/ZnO

Introduction

Benzimidazoles are important medications in ophthalmology primarily due to their ability to treat various eye conditions caused by parasitic infections [1]. These medications are effective against parasites such as nematodes and trematodes that can infect the eye and cause serious conditions like ocular larva migrans or toxocariasis [2]. Benzimidazoles work by disrupting the parasites ability to use glucose effectively, leading to their death [3-4]. Given the broad spectrum of applications for benzimidazoles, the synthesis of these compounds by efficient and environmentally friendly methods has gained significant attention in the last two decades. By consideration of all the existing literature, herein, we wish to disclose a new heterogeneous photocatalyst Fe$_3$O$_4$/ZnO biosynthesized from leaves extract of Petasites hybridus *rhizome* in the synthesis of 2-substituted benzimidazoles by the reaction of some o-substituted anilines with various aromatic aldehydes in the presence of air under the photocatalytic conditions.

Experimental Section

A general route for the synthesis of 2-substiyuted benzimidazoles from benzaldehydes and o-phenylenediamines

A mixture containing the calcined Fe$_3$O$_4$/ZnO nanomaterial (0.02 g) as a photocatalyst, benzaldehyde (1 mmol), and o-phenylenediamine (1.2 mmol) in ethanol (10 mL) was stirred at room temperature. The reaction mixture was then exposed to HP mercury light irradiation while monitoring the reaction progress using TLC. After completion of the reaction, the nanophotocatalyst was separated from the reaction mixture.

Results and Discussion

FT-IR, DRS and VSM The characterization of the prepared Fe$_3$O$_4$/ZnO nanocomposite using FT-IR analysis revealed the following key findings. (Fig. 1a-c).
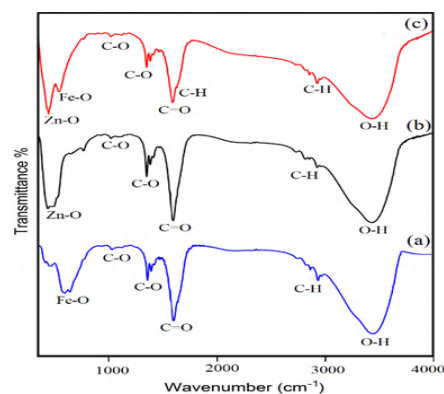
Fig. 1. FT-IR spectra of biosynthesized (a) Fe$_3$O$_4$, (b) ZnO, and (c) Fe$_3$O$_4$/ZnO nanoparticles

The optical band gap of Fe$_3$O$_4$/ZnO and ZnO were evaluated using diffuse reflectance spectra and Tauc plot analysis by extrapolating the linear slope to photon energy, as shown in Fig. 7. Therefore, diffuse reflectance spectra were recorded to assess the optical band gaps. The calculated band gap energy of Fe$_3$O$_4$/ZnO and ZnO were determined to be 3.07and 3.5 eV, respectively(Fig. 2).

22nd Iranian Chemistry Congress (ICC22)
Iranian Research Organization for Science and Technology (IROST)
13-15 May 2024

03231-97589

IROST
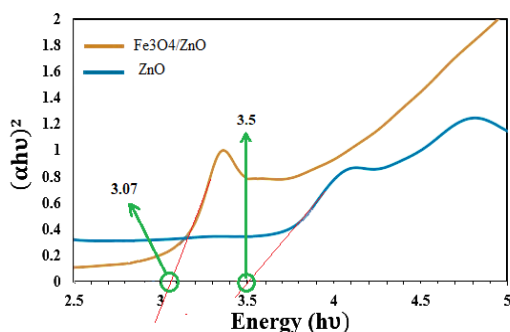
Fig. 2. DRS analysis of Fe_3O_4/ZnO and ZnO

Conclusions

In summary, we unveiled a novel and reusable heterogeneous nanophotocatalyst Fe_3O_4/ZnO for the one-pot multi-component photocatalytic synthesis of 2-substituted benzimidazoles, benzothiazoles, and benzoxazoles.

spite the reduction in magnetization observed in the Fe3O4/ZnO nanomaterial compared to bare Fe3O4 nanoparticles, the magnetic properties were still maintained (Fig3)

References

[1] Pardeshi VA, Chundawat NS, Pathan SI, Sukhwal P, Chundawat TP, Singh GP. A review on synthetic approaches of benzimidazoles. Synthetic Communications. 2021 Feb 16;51(4):485-513 https://doi.org/10.3389/fphar.2021.762807

[2] Padhi TR, Das S, Sharma S, Rath S, Rath S, Tripathy D, Panda KG, Basu S, Besirli CG. Ocular parasitoses: A comprehensive review. Survey of ophthalmology. 2017 Mar1;62(2):161-89
https://doi.org/10.1016/j.survophthal.2016.09.005

[3] parasites. ACS Infectious Diseases. 2021):1945 Mar 5;7(7-55) . Leshabane M, Dziwornu GA, Coertzen D, Reader J, Moyo P, van der Watt M, Chisanga K, Nsanzubuhoro C, Ferger R, Erlank E, Venter N. Benzimidazole derivatives are potent against multiple life cycle stages of Plasmodium falciparum malariahttps://doi.org/10.1021/acsinfecdis.0c00910

[4] Carvalho KP, Gadelha AP. Effects of three benzimidazoles on growth, general morphology and ultrastructure of Tritrichomonas foetus. FEMS microbiology letters. 2007 Oct 1;275(2):292-300.

https://doi.org/10.1111/j.1574-6968.2007.00897.x

Fig. 3. Magnetization curve for (a) calcined Fe_3O_4, (b) biosynthesized Fe_3O_4, (c) biosynthesized Fe_3O_4/ZnO, and (d) biosynthesized ZnO.

The notably elevated yield% in the presence of ZnO (65%) indicated that this particular photosensitizer can be the optimal choice for functionalizing Fe_3O_4 nanoparticles. It is evident that Fe_3O_4/ZnO displayed the most superior photocatalytic efficacy, achieving 97% product yield within 1.5 hours

Fig. 4. Comparison of the photocatalytic activity of ZnO and Fe_3O_4 with Fe_3O_4/ZnO under standard reaction conditions.

Studying the possibility of using covalent organic framework based on benzidine/triformylbenzene for temperature-sensitive release of doxorubicin by molecular dynamics simulation method

Elnaz Moghaddamfar [a], Rahim Ghadari [b]

Corresponding Author E-mail: rghadari@gmail.com

[a] Organic Chemistry Laboratory, Faculty of Chemistry, University of Tabriz, Iran.

[b] Department of Organic and Biochemistry, Faculty of Chemistry, University of Tabriz, 5166616471 Tabriz, Iran.

Abstract: Considering the importance of introducing new drug delivery systems, in this research, the use of drug delivery systems based on two-dimensional organic covalent frameworks (2D-COF) based on imine using the building blocks of 3,3-dimethoxybenzidine (DMB) and 1,3,5-triformylbenzene (TFB) and will be investigated using molecular dynamics simulation. In the first part of the study, one-layer COF structures are drawn, and then the 10-layer structure will be obtained using the Packmol program. The use of mentioned COFs for temperature sensitive drug delivery will be studied. In this study, the anticancer drug doxorubicin will be used as a model drug. The COF/drug system will be simulated at different temperatures in order to evaluate the ability to transport the drug in a temperature-sensitive manner by examining the behavior of the system at the studied temperatures. It is suggested that this simulation be done at four temperatures (25, 37, 42 and 50) degrees Celsius. The solvent used in this simulation will be water. The molecular dynamics simulation part will be done using the Amber program and the preparation of the structures for the molecular dynamics simulation will be done using the programs available in AmberTools. AmberTools and VMD programs will be used for data analysis. It is suggested that analyzes such as van der Waals interactions, electrostatics, hydrogen bonds and other cases be used if needed in order to analyze the results and interpret the data.

Keywords: COF; molecular dynamics simulation; temperature sensitive; smart drug delivery; anticancer

Introduction:

Covalent organic frameworks (COFs) are two- or three-dimensional organic solids with extended structures in which the blocks are connected by strong covalent bonds [1]. They are porous and crystalline and are composed entirely of light elements (H , B, C, N and O) are made[2]. These elements are known by creating strong covalent bonds in useful and widely used materials such as diamond, graphite and boron nitride. The construction of COF materials from molecular building blocks provides covalent frameworks that have various applications due to their light weight [3,4].Material characterization and computational simulation are required to identify the purity and quality of COFs. Bonding, crystal structure, crystallization process, porosity, thermal stability and surface morphology are evaluated with different instrumental analyzes. With diverse properties, COFs have been made for drug delivery, phototherapy, radiotherapy and immunotherapy [5].

Experimental Section

The structures designed to prepare COFs will be optimized using quantum mechanics programs. It is suggested to use programs such as Gaussian or GAMESS to optimize structures. In order to optimize the structures, DT-COF hypothesis level (DMB and TFB) will be used. AMBER program will be used in molecular dynamics stages. It is suggested to use the GAFF force field. In the results analysis section, programs such as VMD and AmberTools or other similar plans will be used based on necessity. Doxorubicin drug will be used as a model in this study(fig.1)
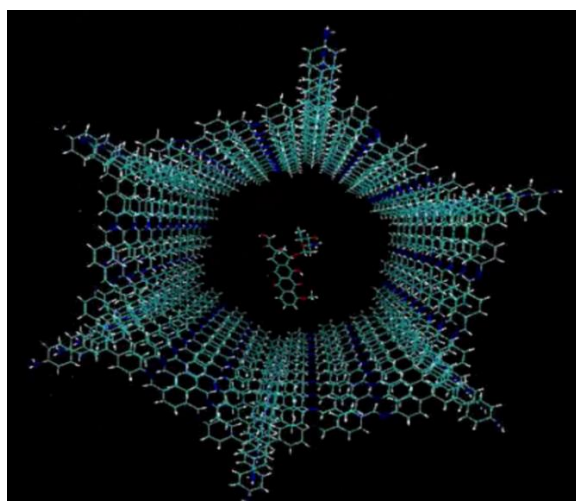

Fig.1: The MD simulation box contains 10 layers of COF with the drug in the middle

22nd Iranian Chemistry Congress (ICC22)
Iranian Research Organization for Science and
Technology (IROST)
13-15 May 2024

03231-97589

Results and Discussion

molecular dynamics (MD) study of a temperature-sensitive smart drug delivery system based on the two-dimensional as a carrier of the anticancer drug doxorubicin, was shown that the binding energy changes with the change of temperature (Fig. 2). Also, among the intermolecular interactions, van der Waals interactions contributed the most, and electrostatic interactions and hydrogen bonding had a small share in binding energy [6] Also, the results of the simulation of the 10- layer COF showed good stability even at a higher temperature, i.e. 323.15 K.

Conclusions

In this work, a molecular dynamics (MD) study of a temperature-sensitive smart drug delivery system based on the two-dimensional as a carrier of the anticancer drug doxorubicin, was performed. MD simulations were performed at 298.15, 310.15, 315.15, and 323.15 K, and it was shown that the binding energy changes with the change of temperature. Also, among the intermolecular interactions, van der Waals (vdw) interactions contributed the most, and electrostatic interactions and hydrogen bonding had a small share in binding energy, which makes this framework suitable for smart drug delivery, especially for lipophilic drug delivery.

References

[1] Diercks, C. S., & Yaghi, O. M. (2017). The atom, the molecule, and the covalent organic framework. Science, 355(6328), eaal1585.

[2] Garcia, J. C., Justo, J. F., Machado, W. V., & Assali, L. V. (2012). Functionalized adamantane: fundamental building blocks for nanostructure self-assembly. arXiv preprint arXiv:1204.2884.

[3] Cote, A. P., Benin, A. I., Ockwig, N. W., O'Keeffe, M., Matzger, A. J., & Yaghi, O. M. (2005). Porous, crystalline, covalent organic frameworks. science, 310(5751), 1166-1170.

[4] Marco, A. B., Cortizo-Lacalle, D., Perez-Miqueo, I., Valenti, G., Boni, A., Plas, J., ... & Mateo-Alonso, A. (2017). Twisted Aromatic Frameworks: Readily Exfoliable and Solution-Processable Two-Dimensional Conjugated Microporous Polymers. Angewandte Chemie, 129(24), 7050-7055.

[5] Yao, S., Wang, Z., & Li, L. (2022). Application of organic frame materials in cancer therapy through regulation of tumor microenvironment. Smart Materials in Medicine, 3, 230-242.

[6] Ghadari, R., Ghanbari, S., & Mohammadzadeh, Y. (2021). A computational study on the interactions between a layered imine-based COF structure and selected anticancer drugs. Journal of Molecular Modeling, 27, 1-10.
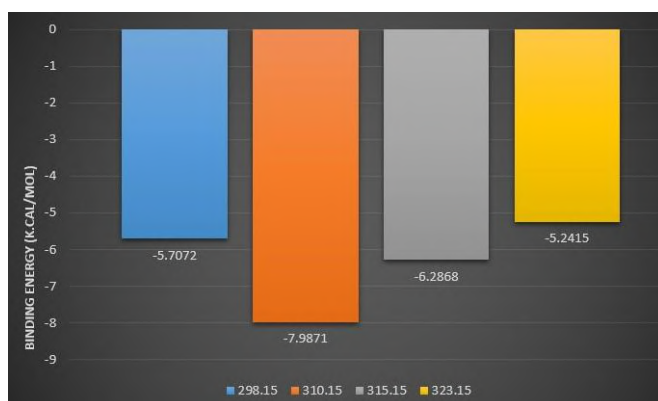
Fig.2: change of complex binding energy with changes of temperature

Effect of synthesis time on properties of Ce–UiO-66 MOF

Mohammad Sepehr Salimi, Hossein Molavi*

Corresponding Author E-mail: sepehrsalimi@iasbs.ac.ir, h.molavi@iasbs.ac.ir

Department of Chemistry, Institute for Advanced Studies in Basic Science (IASBS), GavaZang, Zanjan 45137-66731, Iran.

Abstract: Ce-UiO-66 MOF is one of the UiO-66 MOF derivatives with the exact structure and features of UiO-66 MOF with different metal nodes. It has the ability of synthesizing at room temperature, in water as solvent and lesser energy. Here Effect of time of synthesize, has been investigated for the features of this MOF. Then it is used for eliminating of chromium metal ion and organic dyes from water.

Keywords: Ce-UiO-66 MOF; Room temperature synthesis; water purification; chromium metal ion; malachite green; methylene blue; methyl orange; congo red

Introduction

One of the major solutions to the water scarcity problem is desalination and wastewater treatment. However, wastewater treatment includes many steps to produce usable water [1]. It is clear that water purification is a crucial issue and unfortunately according to new carcinogenic pollutants, this is becoming a dangerous problem for whole world. There are different methods for water treatment but among them, adsorption is one of the bests. In this project Ce-UiO-66 MOF is used as adsorbent to adsorb different pollutants. This MOF is synthesized at room temperature, at various 12, 18 & 24 hours, then different tests is done to investigate the properties of synthesized MOFs.

Experimental Section

The samples were prepared via a room temperature method. Briefly, $NaClO_4.H_2O$, terphetalic acid and $((NH_4)_2Ce(NO_3)_6)$ all were stirred vigorously at ambient condition in deionized water for 12, 18 and 24 hours. Finally, the prepared Ce-MOFs were separated form solution by centrifugation and washed with water, DMF and acetone many times. After washing, each sample was stirred in acetone at room temperature for three days, each day previous solvent was changed with fresh ones. After three days, samples were separated from solvent and dried at 90 degree C for 12 hours.

Results and Discussion
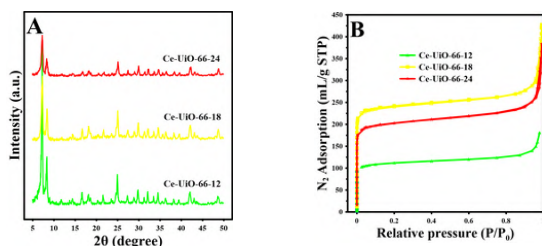
Fig.1: A) XRD pattern of different samples B) N_2 adsorption/desorption plot of different samples.

XRD results proofs that MOFs are successfully prepared with some differences in their structures. Furthermore, N_2 adsorption/desorption isotherm of samples show the isotherm type (IV) which indicates the existence of mesopores in the structure of these MOFs.

Based on the results obtained from N_2 adsorption/desorption, surface area, average pore diameter and total pore volume of samples are summerized in table 1. It is clear that different synthesis times changes the properties of samples.

Table1: BET surface area, average pore diameter and total pore volume of samples.

MOFs	Surface area (m^2/g)	Average pore diameter (nm)	Total pore volume (cm^3/g)
Ce-MOF-12	885	2	0.4663
Ce-MOF-18	968	2	0.6569
Ce-MOF-24	802	2	0.5805

Conclusions

Each sample is used to adsorb chromium metal ion, malachite green, methylene blue, methyl orange, and congo red dye. As it is obvious, this MOF can successfully adsorb these pollutants with different amounts. The adsorbed amounts are summarized in table 2.

Table2: Capacity of each sample after adsorption of different pollutants for 2 hours.

MOFs	Q MG (mg/g)	Q CR (mg/g)	Q MB (mg/g)	Q MO (mg/g)	Q Cr ion (mg/g)
Ce-MOF-12	131	268	200	122	53
Ce-MOF-18	115	260	258	128	51
Ce-MOF-24	113	255	243	135	55

References

[1] Elrasheedy, A., et al., *Metal organic framework based polymer mixed matrix membranes: Review on applications in water purification.* Membranes, 2019. **9**(7): p. 88.

22nd Iranian Chemistry Congress (ICC22)
Iranian Research Organization for Science and Technology (IROST)
13-15 May 2024

03231-97589

IROST

A Computational Investigation on Chain Structure and Thermoelectric Properties of Li(CaPd)₂ Based on DFT calculations

Amir Rahimpour Anghaneh [a,b], Jaber Jahanbin Sardroodi [a], Ebrahim Nemati-Kande * [b]

Corresponding Author E-mail: jsardroodi@azaruniv.ac.ir

[a] Department of Physical Chemistry, Faculty of Chemistry, Tabriz University of Shahid Madani, Tabriz, Iran.

[b] Department of Physical Chemistry, faculty of Chemistry, Urmia University, Urmia, Iran.

Abstract: The present study is aimed to investigate crystal structure of Li(CaPd)₂ alloy from a computational point of view. Quantum espresso package along with GG approximation was utilized in this study, and the obtained results demonstrated that the material can be regarded as conductive material.

Keywords: Density Functional Theory, Pseudo-potential, Quantum Espresso, Chain Structure.

Introduction

Invention of different materials in recent years has attracted wide attention due to their importance in energy storage and generation applications. The emergence of energy crisis in the world has motivated researchers across the world for development of Calcium and metal alloys [1]. The most potential application of these materials are in energy storage devices [2-4]. Considering the fact that experimental methods could be labour and time consuming, application of computational methods including dansity functional theory would be considered as an effective step for development of outsatnading materials. Therefore, the porpuse of this study is to employ DFT for investigation of the crystal structures of Li(CaPd)2 alloy.

Methodology

In this project, quantum espresso package based on the denisty functional theory was applied to calculate the crystal structure and electonic properties of Li(CaPd)2 alloy. In this computation, the generalized gradient approximation (GGA) of the Perdew, Burke and Ernzerhof (PBE) functional was implemented.

Results and Discussion

The Brillouin zone and the k-path of the proppsed compound has been visualized in Fig. 1.

The band plot of the alloy was also shown in Fig, 2. Based on this plot, the upper bands are indicated conduction bands and the lower bands are responcible for vallence bands, around the Fermi level, which is set to be zero in this figure. From Fig. 2 it can be observed that an overlap has been occurred between the curves, which means that the studied material exhibits a metalic nature.

oI (c largest):
Γ–X–F_2 | Σ_0–Γ–Y_0 | U_0–X | Γ–R–W–S–Γ–T–W
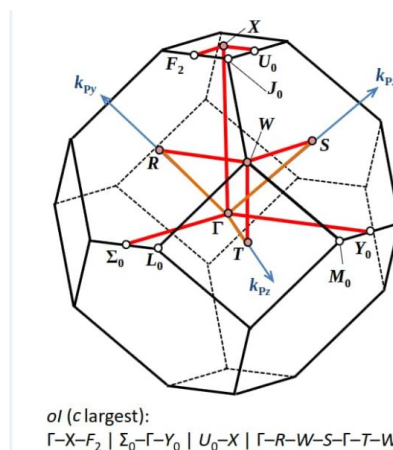
Fig.1: The optimized geometry of Li(CaPd)₂
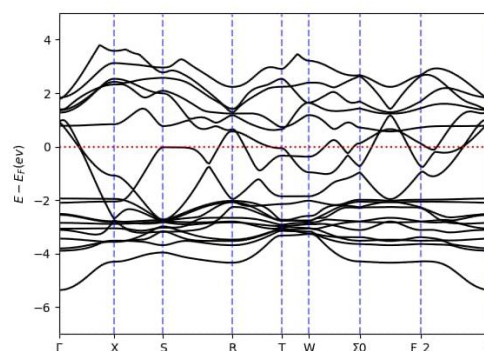
Fig.2: Band plot of allot material, depicted for investigation of chain structure

It is worth to note that the optimization for the structure of alloy material was performed and positive frequence is an indicator for stability of the material. The curves for frequency is presented in Fig. 3. which was obtained from the phonopy calculations.

22nd Iranian Chemistry Congress (ICC22)
Iranian Research Organization for Science and
Technology (IROST)
13-15 May 2024

03231-97589

IROST

a)

b)
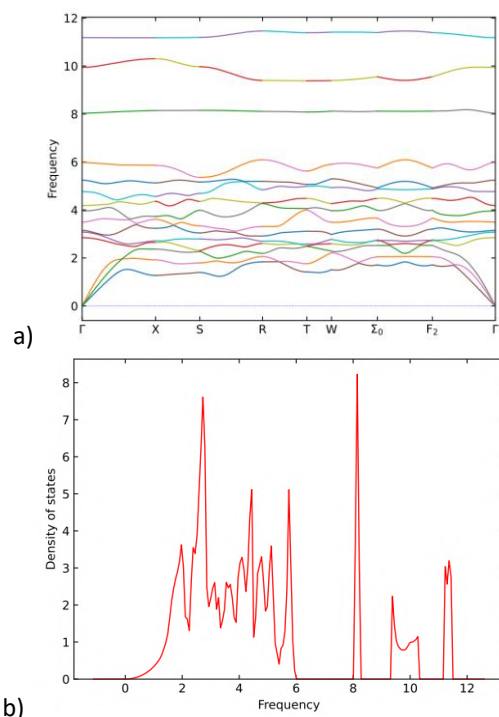
Fig. 3: Frequency band strcuture plots (a) and DOS plots for Li(CaPd)$_2$ alloys.

Conclusions

A new class of conductive material was proposed herein. In order to study the electronic property of this material, DFT was utilized for optimization of the structure and obtaining electronic properties. Based on the obtained results, the propossed material exhibited matalic nature with potential applicability in energy storage devices..

References

[1] Lao , Z., Hegde, V., Asporu, H. A., "Discovery of Calcium metal Alloys for Reversible Calcium Ion Bateries", 2019, htt[s://doi.org/10.1002/aenm.201802994

[2] D. lurcher, M. Trascon, Nat. Chem, 2015, 7, 19

[3] D. Aurbach, Z. Lu, A. Schechter, Y. Gafar, H. Gizbar, Nature, 2000, 407, 724.

[4] A. Pantouch, C. Frontera, F. Bardw, M. R. Palacin, Nat. Mater, 2015, 15, 169.

Electrochemical behavior of cobalt ferrite spinel in capacitive deionization

Fereshteh Mozardzadeh, Alireza Salehirad*, Sayed Ahmad Mozaffari, Fatemeh Ebrahimi

Corresponding Author E-mail: salehirad@irost.ir

Department of Chemical Technologies, Iranian Research Organization for Science and Technology (IROST), Tehran, Iran.

Abstract: The electrode materials play a significant role in determining the efficiency of the capacitive deionization (CDI) process. In the present study, the synthesis of $CoFe_2O_4$ ferrite and its electrochemical performance as a CDI electrode were investigated thorough cyclic voltammetry (CV) and electrochemical impedance spectroscopy (EIS) analysis. Finally, the CDI electrosorption capacity and salt removal efficiency of the $CoFe_2O_4$ electrode were investigated using Flow-through CDI cell configuration. Under optimized experimental conditions the highest electrosorption capacity of 19 mg/g was obtained.

Keywords: Capacitive deionization (CDI); Salt removal; Electrochemical properties; Flow-through CDI cell

Introduction
Spinel ferrite nanoparticles are widely studied due to their excellent magnetic and electrical properties. Spinel ferrite nanoparticles have a general formula MFe_2O_4, where M can be metals for example Mg, Ba, Cd, Zn, Fe, Mg, Co, Ni, Mn, etc. [1-2]. Owing to their high electrochemical activity, high surface area, natural abundance and low cost, iron ferrites are recognised as ideal materials for use in capacitive deionization. The summary of the studies showed that the electrodes consisting of ferrite nanoparticles can increase the salt absorption capacity due to the stability of the electrode and the speed of ion diffusion. Jie et al [3] used the capacitive deionization technique to remove NaCl from water by a zinc spinel ferrite (ZFO) nanoparticle electrode. The desalination capacity reached 136.6 mg/g of NaCl of ZFO under optimized conditions, a voltage range of −1.4 to 1.4 V, and an initial concentration of 100 mg L^{-1} [4].

Experimental Section
In order to electrode fabrication, specific amounts of activated carbon (AC), cobalt ferrite, and Polyvinylidene fluoride (PVDF) were combined, and then by adding the NMP solvent to the resulting mixture, a carbon slurry was obtained. After this step, the slurry was coated onto the carbon felt by a casting knife and was dried in an oven at $100°C$ for 4h to form $CoFe_2O_4$/AC electrode.

Results and Discussion
The electrochemical properties of the fabricated $CoFe_2O_4$/AC electrode was investigated using CV and EIS technique. Fig. 1 illustrates the CV curve of the electrode at a scan rate of 100 mV/s with a working potential range of (0-0.8) V in a 1.0 M NaCl solution. Evidently, this electrode exhibits a voltammogram with quasi-rectangular shapes, confirming the presence of inherent electrical double-layer properties in the fabricated electrode. The highly porous nanostructure and enhanced surface area, combined with the oxygen-rich surface functionality of $CoFe_2O_4$/AC, facilitate the easy intercalation and de-intercalation of electrolyte ions on the electrode surface.
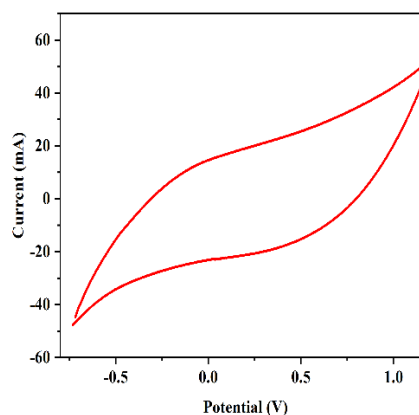
Fig.1. Cyclic voltammograms of the $CoFe_2O_4$ /AC electrode in a 1.0 M NaCl solution at the scan rate of 100 mV s^{-1}

Electrochemical impedance spectroscopy (EIS) was also studied for the $CoFe_2O_4$/AC electrode to examine its electrical conductivity. The Nyquist plot of electrode is shown in Fig. 2. As can be seen from the Nyquist diagram in Fig. 2, the electrode materials act as a resistor at high frequencies, following by the linear section of warburg impedance related to the diffusion process.
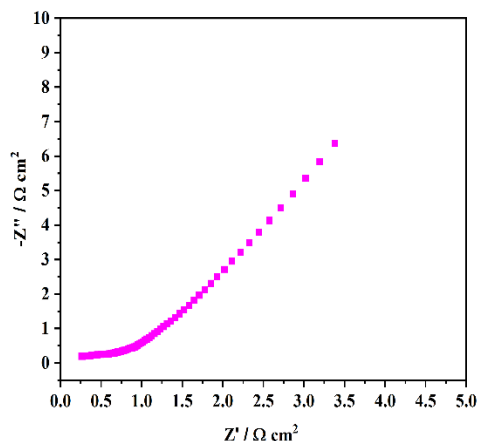
22nd Iranian Chemistry Congress (ICC22)
Iranian Research Organization for Science and Technology (IROST)
03231-97589
13-15 May 2024

IROST

Fig. 2. Nyquist plots of CoFe$_2$O$_4$ /AC at the V$_{OCP}$ and the frequency range of 100 KHz to 0.1 Hz in a 1.0 M NaCl solution

Fig. 3. shows the CDI performance based on the deionization behavior of the assembled CDI cell at a voltage of 1.2 V. The electrosorption performance was investigated by observing the variations in salt concentration in the CDI cell's outlet compared to the original NaCl feed solution. The decrease in the outlet NaCl concentration occurs rapidly in the first few minutes, and the reched a plateau. Under optimized condition the CoFe$_2$O$_4$/AC electrode showed the highest electrosorption capacity of 19 mg/g using the initial salt concentration of 1000 mgl^{-1}.

Conclusions

In summary, cobalt ferrite nanostructures/activated carbon nanocomposite (CoFe$_2$O$_4$ /AC) electrode has been successfully fabricated and its ion adsorption properties were investigated using electrochemical methods. The quasi-rectangular shape of the CV shows the capacitive behavior nature of the ion adsorption in the nanostructure of the fabricated CoFe$_2$O$_4$ /AC electrode. Also, the absence of the semicircle part in the Nyquist plot show that the electrochemical process at the electrode/electrolyte interface is mainly based on the ion adsorption desorption process rather than the redox reactions. The deionization efficiency of the fabricated electrode in a flow-through CDI cell were investigated using the initial salt concentration of 1000 mg l^{-1}. Under optimized conditions the CoFe$_2$O$_4$/AC electrode reaches the highest electrosorption capacity of 19 mg/g.

References

[1] Younes, H., Ravaux, F., El Hadri, N., & Zou, L. (2019). Nanostructuring of pseudocapacitive MnFe$_2$O$_4$/Porous rGO electrodes in capacitive deionization. Electrochimica Acta, 306, 1-8.

[2] Gholizadeh, A., & Beyranvand, M. (2020). Investigation on the structural, magnetic, dielectric and impedance analysis of Mg0. 3-xBa$_x$Cu0. 2Zn0. 5Fe$_2$O$_4$ nanoparticles. Physica B: Condensed Matter, 584, 412079.

[3] Ma, J., Xiong, Y., Dai, X., & Yu, F. (2020). Zinc spinel ferrite nanoparticles as a pseudocapacitive electrode with ultrahigh desalination capacity and long-term stability Environ. Sci. Technol. Lett, 7, 118.

Fig.3. The ion removal capacity using 1000 mg L^{-1}NaCl initial concentration at 1.2 V; flowrate: 3 ml min^{-1}.

22nd Iranian Chemistry Congress (ICC22)
Iranian Research Organization for Science and Technology (IROST)
13-15 May 2024

03231-97589

IROST

Fabrication of MgAl$_2$O$_4$/MnFe$_2$O$_4$/Zeolite 4A magnetic nanocomposite for methylene blue removal from aqueous solutions

Sania Sanjabi, Alireza Salehirad*

Corresponding Author E-mail: salehirad@irost.ir

Department of chemical Technologies, Iranian Research Organization for Science and Technology (IROST), Tehran, Iran.

Abstract: In this study, MgAl$_2$O$_4$/MnFe$_2$O$_4$/zeolite 4A nano composite was prepared as an adsorbent for methylene blue (MB) removal from aqueous solutions. The effect of adsorbent dosage, initial concentration of dye, time of contact and pH were studied in detail.To determine the characterization of nanoparticles several analyses such as BET, SEM, EDX, FT-IR, XRD and VSM were executed.

Keywords: MgAl$_2$O$_4$/MnFe$_2$O$_4$/zeolite 4A nano composite; methylene blue (MB); aqueous solutions.

Introduction

Organic dyes are widely used in textiles, papers, food, plastic, leather, and etc. [1]. Release colored wastes of these industries pose a toxic environmental hazard [2]. Various technologies have been used to treat polluted water [3]. Among these absorption has the advantages of effectiveness, comfort, easy operation, simple design and affordability [4]. So far, massive amounts of adsorbents have been investigated such as nanotubes of carbon, zeolite, polyoxometalates, graphene, … [5]. Magnetic ferrite (MFe$_2$O$_4$) nanoparticles have been of excellent interest, because they have proven to be beneficial in many applications. Ferrite-based nanocomposites provide a potential advantage for repeated magnetic separation purposes [6]. In this study, we synthesize magnetite MgAl$_2$O$_4$/ MnFe$_2$O$_4$/zeolite 4A nanocomposite as a low-cost adsorbents with high efficiency for the removal of MB from aqueous solutions.

Experimental Section

Preparation of ZnFe$_2$O$_4$ nano composites: Magnetic nanoparticles were synthesized by the co-precipitation method. The functional groups in the synthesized composites were identified by a Fourier Transform infrared spectroscopy (FTIR) was performed using a Nicolet 60-SXB spectrometer with a resolution of 4 cm^{-1} was used in 400 to 4000 cm^{-1} wavenumbers. So that the sample was degassed at 300 0C and the BELSORP Mini II instrument (as Brunauer-Emmett-Teller BET–BJH method) was used. Magnetic properties of the samples were characterized on a vibrating sample magnetometer (VSM, Mpms (squid) XL-7, Quantum, USA) at 25 0C.

The surface morphology of MgAl2O4/CuFe2O4/zeolite 4A nano composite was investigated by Field Emission Scanning Electron Microscope (Tuscan Mira II (FE-SEM, Czech Republic). The structure and crystallinity of samples were recorded on an (Powder XRD pattern was obtained on a Bruker D8 Advance instrument).

Results and Discussion

The BET analysis was studied the surface properties, size, and volume of pores on the surface of MgAl$_2$O$_4$/ MnFe$_2$O$_4$/zeolite4Ananocomposite.Thenitrogen adsorption-desorption isotherms and pore size distribution curves and the magnetic our sample were shown in Figure 1(a, b). The Langmuir specific surface area for synthesized composite were determined 113.1(m^2 g^{-1}) and the BET specific surface area for MgAl$_2$O$_4$/ MnFe$_2$O$_4$/zeolite 4A nanocomposite is 113.81(m^2 g^{-1}). The pores volume for nanocomposite specified 26.14 cm³/g. In addition, the mean size of pores of above nanocomposite is 14.816, which indicates the nano composite was mesoporous (2−50 nm).
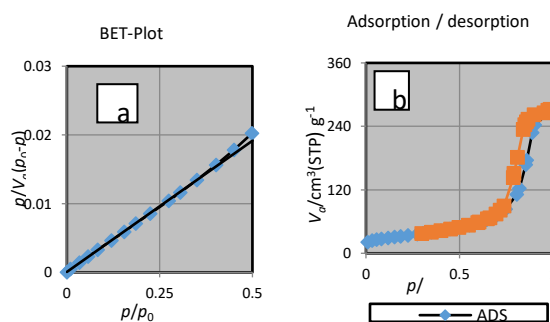

Fig1. N$_2$ adsorption isotherm (a) and BJH plot (b) for MgAl$_2$O$_4$/ ZnFe$_2$O$_4$/zeolite4A

Adsorption Kinetics
The adsorption kinetics give provide useful information about the adsorbate adsorption rate, which is a key factor

22nd Iranian Chemistry Congress (ICC22)
Iranian Research Organization for Science and Technology (IROST)
13-15 May 2024

03231-97589

IROST

in the sorption process. For studying the adsorption kinetics of MB, the initial concentration factor and contact time were used. The limited area of initial concentration changes (10-60 mg.L^{-1}) and the contact time (5-45min) were considered.

The curves of the adsorption kinetics of MB onto MgAl$_2$O$_4$/MnFe$_2$O /Zeolite 4A nanocomposite are shown in Fig. 2

The calculated kinetic parameters and the correlation coefficients (R^2) are given in Table 1.
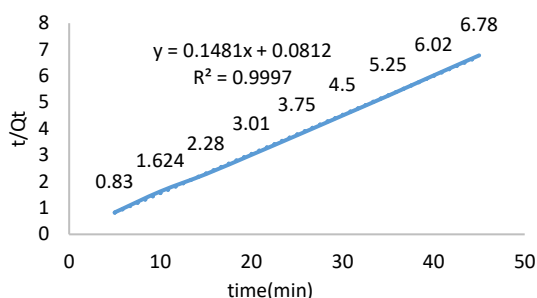
Fig.2.Linear plot for, (b) Pseudo Second order

Conclusions

In this work, the adsorption of MB from aqueous solutions by MgAl$_2$O$_4$/MnFe$_2$O$_4$/Zeolite4A magnetic nanocomposite was investigated. The best conditions for the adsorption of MB dye were taken at temperature of 30 °C, adsorbent dosage of 0.3 g/L, and initial dye concentration of 20 mg/l, contact time of 25 min and pH of 10. The removal efficiency was 99.8%.

The kinetic calculations show that the adsorption followed the pseudo-second-order model.

The cost-effective and abundance of this composite make this material particularly promising for the removal of cationic dyes in industrial wastewater treatment.

References

[1] Hajavazzade R., Kargar-Razi M., Mahjoub A. R., (2021),Synthesis and characterization of and their photocatalytic behaviors towards Congo red under UV light irradiation.Int. J. Nano Dimens. 2: 67-75.

[2] Rahimian A., Zarinabadi S., (2020), A review of studies on the removal of methylene blue dye from industrial wastewater using activated carbon adsorbents made from almond bark. Prog. Chem. Biochem. Res. 3: 251-268.

[3] Tran Hoang Tu, Le Tan Tai, Nguyen Tan Tien, Le Minh Huong, Doan Thi Yen Oanh, Hoang Minh Nam, Mai Thanh Phong, Nguyen Huu Hieu, (2020). Synthesis of Fe2O3/TiO2/graphene aerogel composite as an efficient Fenton-photocatalyst for removal of methylene blue from aqueous solution, Vietnam J. Chem. 58 (5) 697–704.

[4] Y. Wang, N. Lin, Y. Gong, R. Wang, X. Zhang, (2021) . Cu-Fe embedded cross-linked 3D hydrogel for enhanced reductive removal of Cr (VI): Characterization, performance, and mechanisms, Chemosphere 280 130663.

[5] Saeed Farhadi, Mansoureh Maleki, Ladan Nirumand, Farzaneh Moradabad. (2022). Keggin-type heteropoly acid H3PW12O40 supported on magnetic amine-grafted Graphene oxide: A new magnetically separable adsorbent for rapid and selective removal of cationic organic pollutants in aqueous solutions. Int. J. Nano Dimens. 13 (1): 40-53.

[6] Aparna M. L., Grace A. N., Sathyanarayanan P., Sahu N.K., (2018), A comparative study on the supercapacitive behaviour of solvothermally prepared metal ferrite (MFe$_2$O$_4$, M=Fe Co, Ni, Mn, Cu, Zn) nanoassemblies. J. Alloys Comp. 745: 385–395.

22nd Iranian Chemistry Congress (ICC22)
Iranian Research Organization for Science and Technology (IROST)
13-15 May 2024

03231-97589

Electrochemical Oxidation and Detection of Verbascoside and apigenin in etanolic leaf extract of *Aloysia Citriodora* (*Lemon verbena*)

Mohadese Mohtaji [a], Ameneh Amani [*,b], Sadegh Khazalpour[a]

Corresponding Author E-mail: Amani.iran@gmail.com

[a] Department of Analytical Chemistry, Faculty of Chemistry and Petroleum Sciences, Bu-Ali Sina University, Hamedan, Iran.

[b] Nahavand Higher Education Complex, Bu-Ali Sina University, Hamedan, Iran.

Abstract: Electrochemical oxidation of etanolic leaf extract of *Aloysia Citriodora* was studied using cyclic and differential pulse voltammetry. Antioxidant properties were assessed *via* DPPH radical-scavenging, correlated with redox potential. Verbascoside and apigenin as the main components in this extract, were purified using column chromatography (ethyl acetate/n-hexane 20/80) and characterized with IR, LC/MS, and UV/visible techniques.
Keywords: Antioxidant activity.; Cyclic voltammetry; *Lemon verbena*

Introduction

Antioxidants represent a wide class of chemical compounds that fight against the oxidative processes, including the degradation of nutrients found in diet, of materials such as rubber or plastic, of essential molecules found in biological media, etc [1]. Herbal teas, such as *lemon verbena*, contain high levels of polyphenols which have various health benefits. *Lemon verbena* is a popular herbal species found in South America and cultivated in North Africa and Iran. In countries, *lemon verbena* is used for both culinary and medicinal purposes, with its leaves known for their digestive and antispasmodic properties. *Lemon verbena* infusion is often used to treat colic, diarrhea, and indigestion, and is enjoyed as a flavored hot drink. *Lemon verbena* infusion is rich in polyphenols, including phenylpropanoid glycosides and flavone diglucuronides like verbascoside and apigenin. [2]. In this work, the electrochemical Oxidation of the etanolic leaf extract of Aloysia Citriodora (Lemon verbena) has been investigated by cyclic voltammetry and differential pulse voltammetry techniques in the different pHs at the surface of glassy carbon electrode at various concentrations and scan rates. In the next step, the separation and purification of verbascoside and apigenin as the main components in this extract has been carried out via column chromatography (ethyl acetate/n-hexane with volume ratio 20/80) and characterized with IR, LC/MS, and UV/visible. Also, the electrochemical approach has been used to analyze and detection the electroactive compounds in this extract and Antioxidant activities of this extract has been evaluated using the 2,2-diphenyl-2-picrylhydrazyl (DPPH) radical-scavenging method.

Experimental Section

All the reagents and chemicals utilized in the present study were of analytical reagent grade and purchased from E. Merck (Darmstadt, Germany). They were applied without any further purification. leave of Lemon verbena were collected from the Nahavand city in Hamedan province. They were then washed and dried at room temperature for 72 h. After proper drying, these herbs were ground in to a fine powder. In order to prepare the extract, 0.2 g of the powder was mixed with 50 ml of ethanol, then warmed to 50 °C, and finally maintained at room temperature for 24h. After that, the mixture was filtered with Whatman filter paper number 1 and allowed to be cooled. These extracts were considered as the etanolic leaf extract of *Lemon verbena* . The extract was dried and then concentrated. Obtained precipitate was purified by thin layer chromatography on silica gel chromatography (ethyl acetate/*n*-hexane with volume ratio 20/80). The most polar compound was corresponding to verbascoside and The yellow fraction was corresponding to apigenin. The separated components was characterized LC/MS. Isolation of verbascoide: IC/MS: $[M + H]^+$:624 Isolation of apigenin: : $[M + H]^+$:269

Results and Discussion

Electrochemical Investigations of *Lemon verbena* Extract The electrochemical behavior of *lemon verbena* extract was performed through cyclic voltammetry (CV) and DPV on a glassy carbon electrode at room temperature. As an example, these experimental observations were shown in a water (acetat buffer, c = 0.2 M, pH6.0)/ethanol mixture (70/30, V/V) (Figure.1). The CV and DPV response showed 2 oxidation peaks, the first peak related to verbascoside and the second peak related to apigenin.
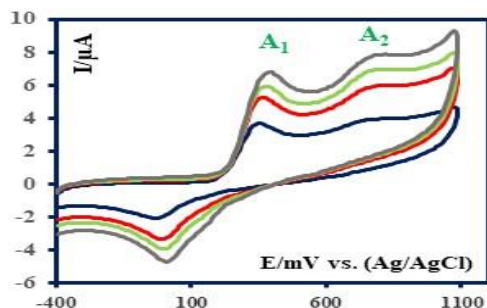
22nd Iranian Chemistry Congress (ICC22)
Iranian Research Organization for Science and
Technology (IROST)
13-15 May 2024

03231-97589

IROST

Fig.1: The CV response of Lemon verbena extract in water (acetate buffer, c = 0.2 M, pH 6.0)/ethanol mixture (70/30, v/v). at the various scan rates: 50, 100, 150 and 200 mv/s.

For depiction of pourbaix diagram (potential vs pH) and calculation the number of electron and proton in the oxidation process of the dominant compound Verbascoside in *lemon verbena* extract, CV plots have been carried out in different pH (from 1 to 12). Base on the isolation and characterization result of bioactive constituents in *lemon verbena* extract, we concluded that the oxidation peak (A1) is corresponds to the oxidation of verbascoside compound to oxidized form (VBOX). the potential of A_1 peak is shifted to a less positive value with increasing media's basicity. This phenomenon indicated that the proton has participated in the oxidation mechanism of verbascoside at glassy carbon electrode. The break point of the slopes at pH =9.68 observed in Fig2., indicates a pKa value between 9.0 and 10.0 for VB.
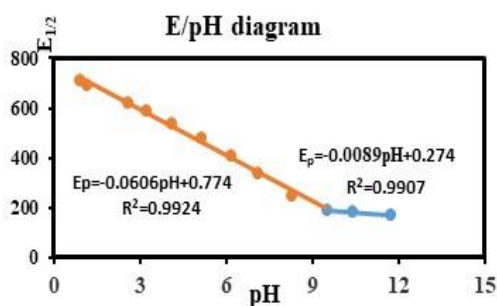
Fig.2: The E-pH diagram of VB

The available organic compounds in *lemon verbena* dried extract were separated and purified by column chromatography (silica gel) technique. The solvent system for column chromatography was ethyl acetate/n-hexane with volume ratio 20/80. After purification, the major isolated compound was characterized by IR, LC/MS, UV/visible spectra. Based on literature studies, two major types in *lemon verbena*. are verbascoside and apigenin. The spectroscopy data (IR, UV, and LC/MS) of the most polar compound in column chromatography were perfectly conformed with verbascosid and apigenin compounds. For more information, electrochemical

investigations of isolated compounds were carried out via the CV technique. The CV response of the polar compound is confirmed with the A_1 oxidation peak. The yellow compound is also oxidized in more positive potentials and is related to apigenin (Fig.3).
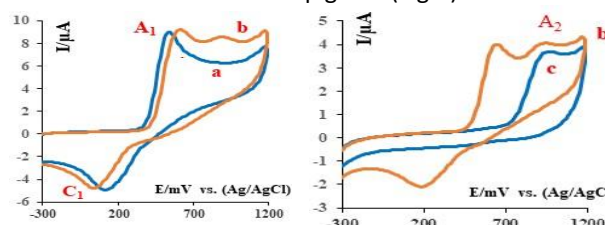
Fig.3: The CV response of (a) the most polar compound in column chromatography (b) *lemon verbena* extract (c) the yellow compound (d) lemon verbena extract in water (phosphate buffer, c = 0.2 M, pH2.0)/ethanol mixture (70/30, v/v).

Conclusions

In this study, the components of lemon verbena extract has been separated and isolated by column chromatography technique. Based on spectroscopy and electrochemical results, we concluded that the compounds Verbascoside and apigenin is the major constituent in lemon verbena . The number of electrons and protons was calculated based on pourbaix diagram (potential vs pH). This research work prepared a comprehensive electrochemical (green method) and biological investigations for lemon verbena extract.

References

[1] Felgines, C., Fraisse, D., Besson, C., Vasson, M. P., & Texier, O. (2014). Bioavailability of lemon verbena (Aloysia triphylla) polyphenols in rats: impact of colonic inflammation. *British Journal of Nutrition*, *111*(10), 1773-1781. https://doi.org/10.1017/S0007114514000026

[2] Jamshidi, M., Ranjbar, A., Khazalpour, S., Dastan, D., Vakili-Azghandi, M., Torabi, S., ... & Sedaghat, M. (2021). Characterization, electrochemical detection, biological evaluation and molecular modelling of 1, 5-Di-O-Caffeoylquinic acid from artichoke (Cynara scolymus L.) head extract. *Journal of the Electrochemical Society*, *168*(1), 016509. https://doi.org/10.1149/1945-7111/abdb45

22nd Iranian Chemistry Congress (ICC22)
Iranian Research Organization for Science and Technology (IROST)
13-15 May 2024

03231-97589

IROST

Green Synthesis of CuO -Ni Foam Heterojunction nanoparticles via Dip-Coating for Efficient Visible Light Photocatalytic Oxidation of Benzyl Alcohol to Benzaldehyde

Reza Taeybee*, Sedighe Abbaspour*ᴮ, Zahra Jalili, Farrokhzad Mohammadi Zonoz

Corresponding Author E-mail : 9814942014@hsu.ac.ir

Department of Chemistry, Faculty of Science, Hakim Sabzevari University, Sabzevar, Iran.

Abstract : The CuO-Ni foam heterojunction nanoparticles was prepared using a sustainable Green synthesis approach known as Dip-coating. This innovative method enabled the in-situ photocatalytic oxidation of benzyl alcohol (BA) to aldehydes when exposed to visible light. The CuO catalyst supported on a nickel foam bed played a crucial role in catalyzing the conversion of benzyl alcohol to benzaldehyde. Subsequently, the benzaldehyde underwent condensation with o-phenylenediamine, yielding a diverse array of 2-substituted benzimidazoles. These compounds serve as vital intermediates in pharmaceutical synthesis. The photocatalytic reaction occurred under green laser light with a wavelength of 535 nm. The reaction was conducted in water at 40°C for a duration of 60 minutes, resulting in an impressive efficiency of 89%. The nanocomposite was meticulously characterized using a range of analytical techniques including FT-IR, XRD, FESEM, and Matt Schottky analysis.

Keywords: heterojunction; photocatalytic oxidation; CuO-Ni foam

Introduction

Photocatalytic organic transformation is a versatile technique using light energy to convert organic substrates into valuable products, offering eco-friendly alternatives to traditional chemical methods. Scientists are continuously exploring new systems and approaches to improve efficiency and selectivity in these conversions. In recent years, researchers have been exploring alternative strategies to address limitations in photocatalytic organic transformations. One approach involves designing novel semiconductor materials to promote redox reactions, utilizing both photogenerated electrons and holes. By maximizing the potential of charge carriers, these systems aim for higher efficiencies and selectivities without sacrificial agents. This shift towards sustainable and cost-effective photocatalytic processes shows promise for green chemistry and environmental remediation [1]. Semiconductor photocatalysis uses semiconductor materials to convert light energy into chemical reactions, like degrading pollutants or producing clean fuel. This technology creates electron-hole pairs via light absorption to facilitate surface reactions. Through optimizing semiconductor properties and reaction conditions, photocatalysis offers a sustainable solution for worldwide pollution and energy issues [2]. CuO has good photocatalytic properties due to its band structure and bandgap. The internal electric field helps separate electron-hole pairs efficiently, enhancing its photocatalytic efficiency. Nickel foam has been investigated as a platform to improve the photocatalytic properties of materials. Wang et al. and other researchers have used nickel foam as a substrate to enhance the

photocatalytic activity of materials [3]. In this study, we synthesized an Ni foam-modified CuO nanocomposite structure using a (Green synthesis) Dip-coating method. When subjected to visible-light irradiation, the CuO-Ni foam nanolayer samples exhibited superior photocatalytic activity compared to pure Ni foam or CuO samples, with the CuO-Ni foam configuration demonstrating optimal performance.

Experimental Section

CuO nanoparticles synthesized on nickel foam involve optimizing copper chloride dihydrate and leaf extract ratios, heating at 80°C for 2 hours, adding sodium hydroxide drop-wise for nanoparticle formation, growing on nickel foam at 90°C, and air-drying at 80°C for 3 hours. Key stages include color change to brownish-black for CuO formation, growth on foam at 90°C, and washing/drying for residue removal. Resulting CuO-coated foam appears uniformly dark, ready for characterization and use in catalysis, sensors, and energy storage.

Results and Discussion

In Figure 1(A), CuO-Ni foam shows dense and uniform growth of fine-scale CuO-Ni foam on nickel foam surface, indicating strong mechanical adhesion. Synthesized nanoparticles have a particle size range of 28.82 to 64.86 nm (mean size: 43.42 nm), consistent with XRD results. CuO-Nifoam FT-IR spectrum peaks: 3000-3660 cm^{-1}: OH stretching vibrations of adsorbed water molecules, 1624 cm^{-1}: OH phenolic bending, 1390 cm^{-1}: CuO vibrations, - 996 cm^{-1}: Cu-O stretching vibrations, - 712 cm^{-1}: Cu-O

22nd Iranian Chemistry Congress (ICC22)
Iranian Research Organization for Science and Technology (IROST)
13-15 May 2024

03231-97589

IROST

stretching vibrations, 467 cm−1: Cu–O deformation vibrations, 3440.2 cm^{-1}: N–H stretching. These peaks indicate the presence of CuO, phenolic and flavonoid groups on the nanoparticle surface, and possibly amino acids as capping agents (Fig 1B).
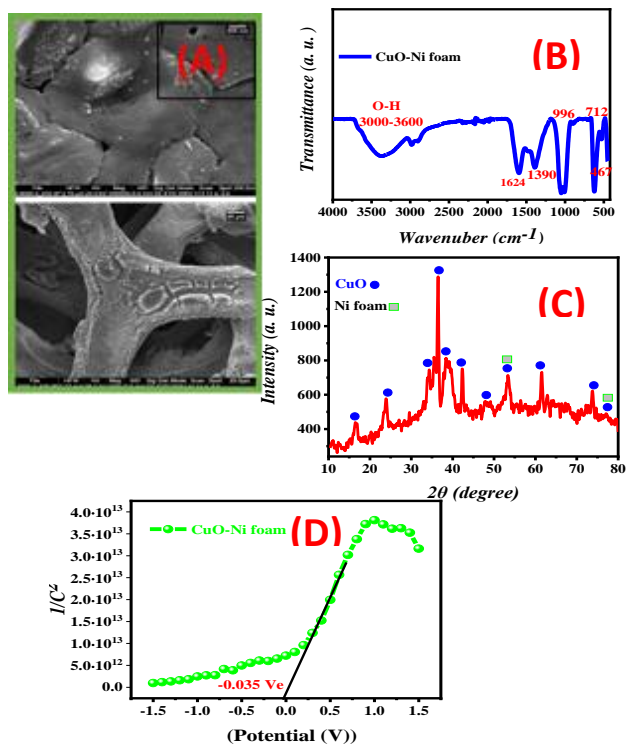

Fig. 2. Effect of common scavengers in the condensation reaction. BQ, EDTA, IPA. Studying recyclability of CuO-Ni foam photocatalyst.

Table1: Effect of different solvents on the condensation reaction

Entry	solvents	Yield%
1	Solvent free	80
2	H_2O	89
3	Ethanol	77)
4	CH_3CN	60

Fig.1: FE-SEM images and average height and width distribution of (A), FT-IR spectra of (B). Wide-angle XRD pattern of CuO-Ni foam (C) Mott–Schottky plots of (D).

Conclusions

A CuO-Ni foam p heterojunction was successfully developed using a Green synthesis method (Dip-coating). Copper oxide spherical nanoparticles were deposited on a nickel foam substrate and characterized using FT-IR, XRD, FESEM, and Matt Schottky measurements. Selective organic conversion experiments were carried out using water as a solvent. Photocatalyst oxidation performance tests indicated that the CuO-Ni foam photocatalyst exhibited optimal efficiency..

In Figure 1(C), CuO-Ni foam X-ray diffraction pattern showed sharp peaks at 2θ angles of 16.493, 23.943, 34.293, 35.593, 37.543, 38.443, 42.343, 48.57, 53.393, 61.493, 73.793, and 77.093, corresponding to various crystal planes of CuO phase (JCPDS card no. 01-089-2529). CuO-Ni foam showed lower impedance in Figure 1D, indicating better photon-to-electron conversion. Band positions (VB, CB) were analyzed for photocatalytic mechanism understanding. MS plots were used to examine flat-band potential and semiconductor properties. Negative slope indicates n-type, positive slope indicates p-type semiconductor. CuO-Ni foam was identified as a p-type semiconductor in Figure 1D.

References

[1] Jiang, K. B., Huang, W. Q., Song, T. T., Wu, P. X., Wang, W. F., Chen, Q. S., ... & Guo, G. C. (2023). Photobreeding heterojunction on semiconductor materials for enhanced photocatalysis. Advanced Functional Materials, 33(43), 2304351.https://doi.org/10.1002/adfm.202304351.

[2] Yao, S., He, J., Gao, F., Wang, H., Lin, J., Bai, Y., ... & Wang, M. (2023). Highly selective semiconductor photocatalysis for CO 2 reduction. Journal of Materials Chemistry A, 11(24), 12539-12558. DOI: 10.1039/D2TA09234D.

[3] Rahman, Z. U., Shah, U., Alam, A., Shah, Z., Shaheen, K., Khan, S. B., & Khan, S. A. (2023). Photocatalytic degradation of cefixime using CuO-NiO nanocomposite photocatalyst. Inorganic Chemistry Communications, 148, 110312. https://doi.org/10.1016/j.inoche.2022.110312

Optimization of *Ganoderma lucidum* mushrum growth in soild state bioreactor

Parisa Shirzadian, Seyed Ahmad Ataei

Corresponding Author E-mail: parisa@eng.uk.ac.ir

Chemaical Engineering Department, Shahid Bahonar University Of Kerman, Kerman, Iran.

Abstract: Biotechnological cultivation of G. lucidum mycelia has been established in bioreactors, both on solid substrates and in liquid environments, through submerged cultivation of fungal biomass. G. lucidum is rare in nature, and due to increasing demand in international markets for cultivated G. lucidum mycelial biomass, artificial cultivation holds significant importance.

Keywords: *Ganoderma lucidum, soild_state cultivation, optimazation*

Introduction

To enable a novel and fundamental approach to Ganoderma lucidum cultivation, many studies have focused on optimizing its growth. Kim investigated the phenolic compound concentration and antioxidant activity of ten mushroom species from Korea in 2008, meticulously assessing measurement methods [1]. Studies related to the cultivation and production of polysaccharides from Ganoderma lucidum mushrooms have been carried out in different cultivation conditions, including submerged and semi-solid cultivation [2-4]. In order to prepare the solid bioreactor, the researchers optimized the production process of inulinase from apple peel by utilizing the solid formatter method and the statistical response level approach [5]. Two-stage cultivation methods for Ganoderma have been optimised to produce high-quality pellets for use in the plant food industry [6]. This article seeks to optimise the mycelium growth of Ganoderma lucidum. It seeks to find the best method to increase the growth rate and improve the mushroom's mycelium quality by conducting different tests in different conditions.

Experimental Section

The mushroom mycelium is cultivated in a suitable culture medium and after breeding, it is transferred to sterilized corn or barley seeds. These colonized seeds, called spawn, are kept in the dark and at the optimal temperature until fully overtaken by the mycelium. The sterilised soil is then mixed with the spawn, and after the entire mixture is colonized, mushrooms are grown under indirect light. Once mature, the mushrooms can finally be harvested. Here are some key points to remember:

1. All cultivation steps must be done in sterile conditions.
2. Use LED lamps to illuminate the mushrooms.
3. Keep the ambient humidity at the right level (70 to 80 percent).

Results and Discussion

The best culture medium for Ganoderma mushroom mycelium growth is PDA with a pH of 7 and a temperature of 25°C. Absolute darkness and a temperature of 25°C are the best conditions for mycelium colonisation in corn and barley seeds. Corn is the best seed for Ganoderma mycelium colonization. These tests were conducted in laboratory conditions and the results may differ in real-world conditions. Ganoderma mushroom is sensitive to the pH and temperature of the culture medium. Direct and indirect light significantly reduces mycelium growth in corn and barley seeds. This research can be used for large-scale Ganoderma mushroom production.
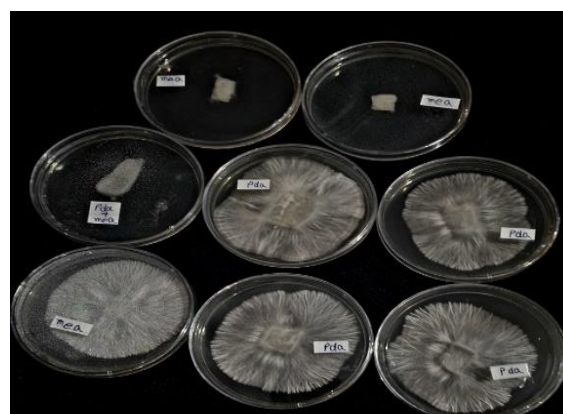

Fig.1: The growth of mycelium in different culture media (MEA، PDA، MEA+PDA)

22nd Iranian Chemistry Congress (ICC22)
Iranian Research Organization for Science and Technology (IROST)
13-15 May 2024

03231-97589

IROST

Table1: Mycelium colonization percentage in different seeds at 25 temperature

Day Cultivation environment	Day-5	Day-15	Day-25
Barley	10%	25%	50%
Corn	20%	35%	70%
sorghum	0%	0%	0%

Fig.2 Comparison of culture environments 1 and 2 at different temperatures and pH level.

Conclusions

This research provides valuable insights for the large-scale production of Ganoderma mushrooms. For optimal growth, the study suggests using Potato Dextrose Agar (PDA) culture medium with a neutral pH of 7 and maintaining a constant temperature of 25°C. The study also found that corn seeds were the most effective substrate for mycelium colonization, and complete darkness was the most favorable light condition. These findings hold significant promise for Ganoderma producers. By implementing these optimised conditions, cultivators can potentially streamline their production process, leading to increased yields and overall efficiency. Minimizing production costs and maximizing output results in greater economic benefits. However, it's important to acknowledge the limitations of this research. We conducted the study in a controlled laboratory environment, which may not accurately replicate real-world cultivation conditions. Factors like humidity, ventilation, and light exposure at various stages of growth might influence the results. Therefore, further research in field settings is crucial to confirm these laboratory findings and determine the optimal conditions across the entire Ganoderma production cycle. Furthermore, this research focused solely on the initial stage of mycelium growth. Future studies will delve deeper into the impact of various environmental factors on overall Ganoderma mushroom development, including fruiting body formation and yield.

References

[1] M.Kim, P. Seguin, J. Ahn, J. Kim, S. Chun, E. Kim, S. Seo, E. Kang, S. Kim, Y. Park, H. Ro, I. Chung. (2008). Phenolic Compound Concentration and Antioxidant Activities of Edible and Medicinal Mushrooms from Korea. Journal of Agricultural and Food Chemistry, 56, 7265-7270. https://doi.org/10.1021/jf8008553.

[2] F. P. Casciatori, C. L. Laurentino, S. R. Taboga, P. A. Casciatori, and J. C. Thomeo, Structural properties of beds packed with agro-industrial solid by-products applicable for solid-state fermentation: experimental data and effects on process performance, *Chemical Engineering Journal,*255,214-224,2014. https://doi.org/10.1016/j.cej.2014.06.040

[3] F. P. Casciatori, A. Bück, J. C. Thoméo, and E. Tsotsas, Two-phase and two-dimensional model describing heat and water transfer during solid-state fermentation within a packed-bed bioreactor, Chemical Engineering Journal, 287,103-116,2016. https://doi.org/10.1016/j.cej.2015.10.108.

[4] A. Ashok, K. Doriya, D. R. M. Rao, and D. S. Kumar, Design of solid state bioreactor for industrial applications: an overview to conventional bioreactors, Biocatalysis and Agricultural Biotechnology, 9, 11-18, 2017. https://doi.org/10.1016/j.bcab.2016.10.014.

[5] R. S. Singh, K. Chauhan, K. Kaur, and A. Pandey, Statistical optimization of solid-state fermentation for the production of fungal inulinase from apple pomace, Bioresource Technology Reports, 9, 100364, 2020. https://doi.org/10.1016/j.biteb.2019.100364.

[6] S. Bibi, Z.-L. Wang, C. Lin, S.-H. Min, and C.-Y. Cheng, Two-stage cultivation strategies for optimal production of Ganoderma pellets with potential application in the vegan food industry, Journal of Food Science and Technology, 60, 1793-1802, 2023. https://doi.org/10.1007/s13197-023-05719-x.

Synthesis, characterization and studies on host-guest interactions of inclusion complexes of metformin hydrochloride with sulfobutylether-β-cyclodextrin

Leila Yousefi, Nina Alizadeh*

Corresponding Author E-mail: n-alizadeh@guilan.ac.ir

Department of Chemistry, Faculty of chemistry, University of Guilan, Rasht, Iran.

Abstract: This study was to synthesize and characterization the host-guest complex of metformin. The host-guest interaction of metformin with SBE-β-CD in order to complexation drug in SBE-β-CD were investigated. The stability constant and solubility constant were obtained in this studty. Inclusion complexes were characterized by using FTIR, XRD, UV-Vis, DSC and [1] HNMR techniques.

Keywords: metformin; Inclusion complexation; SBE-β-CD; Solubility

Introduction

metformin hydrochloride (MF) is an oral antidiabetic drug is considered as the first line pharmacological therapy to treat high blood sugar levels in the management of type-2 diabetes. Poor wettability of drug leads to poor dissolution and hence, shows variation in bioavailability. The subsistence of host-guest interaction makes SBE-B-CD a suitable candidate for the enhancement of bioavailability of Metformin hydrochloride. Cyclodextrins are used to form host-guest inclusion complexes with various drugs in solution or a solid state have been recognized as pharmaceutical excipients .The inclusion complexes of drugs, metal ions or many organic ligands in cyclodextrins (CDs) represent a group of the simplest supramolecular structures widely studied for the last several decades. Such inclusion complexes have improved drug solubility, stability, dissolution and oral bioavailability . These are widely used and made to increase drug water solubility. in this study Inclusion complexes of Metformin hydrochloride with SBE-B-CD were prepared in solid and liquid state and they are characterized using spectroscopic method and also stability constant of the inclusion complex was calculated[1,2].

Experimental Section

Absorbance was done using UV-visible spectrophotometer model Shimadzu 1800 with quartz cells of 1 cm optical path length. IR was recorded using (FTIR) spectrometer 8400s (Shimadzu, Japan). Samples were pressed into KBr pellets and measured at frequencies from 4000 to 400 cm -1.

Results and Discussion

The results obtained in this work obviously demonstrate that SBE-B-CD react with metformin to form a 1:1 host-guest complex. Based on the improvement of the absorbance intensity of metformin resulted from complex formation, a sensitive and accurate method for determination of metformin in the presence of SBE-B-CD was proposed. The developed method is fully validated and successfully utilized for the determination of metformin pharmaceutical formulations. The formation constant was calculated by using a Benesi-Hildebrand equation to number of 28.33 M^{-1} (**Fig.1**).
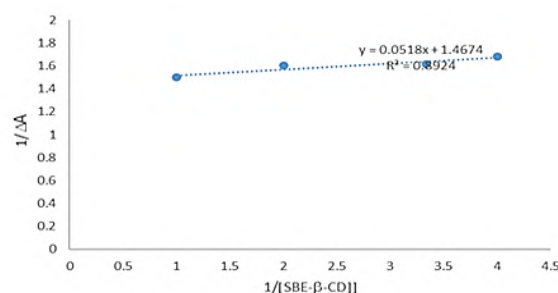

Fig. 1: Benesi Hildebrand diagram

The phase solubility plot of MF and SBE-β-CD binary system has been **Fig 2** . It has been clearly observed from the plot, the aqueous solubility of the MF drug increased linearly as a function of the SBE-β-CD. This type of phase solubility diagram of drug and SBE-β-CD can be considered as AL type according to Higuchi and Connor . The solubility constant value of the formed complex was obtained as 124.77 M^{-1} .

22nd Iranian Chemistry Congress (ICC22)
Iranian Research Organization for Science and
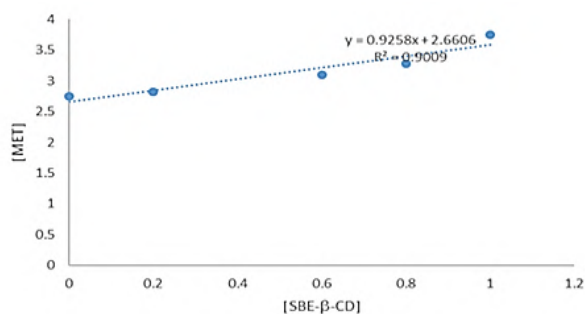Technology (IROST)
13-15 May 2024

03231-97589

Fig. 2: phase solubility diagram

The surface morphology of the SBE- β-CD, MF inclusion complexes of drug MF and SBE- β-CD is studied by scanning electron microscopy. The SEM images proved qualitatively the formation of new entities of inclusion complex from the drug MF and SBE-β-CD (**Fig.3**).
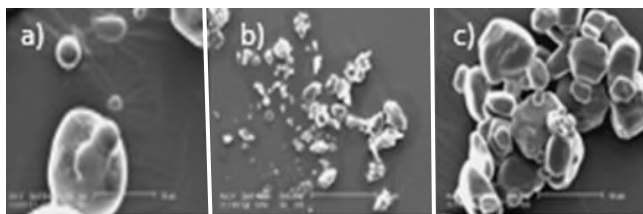

Fig. 3: SEM images of a)SBE-β-CD b)MET c)MET/SBE-β-CD

Conclusions

The results obtained in this work demonstrate that SBE-β-CD react with metformin to form a 1:1 host-guest complex.The Benesi Hildebrand plot shows the formation of inclusion complexes with 1:1 stoichiometry and stability constant of the formed inclusion complex.
The phase solubility studies of MF/SBE-β-CD revealed the solubility of MF is enhanced during the inclusion complex formation between MF and SBE-β-CD.

References

[1] Kaur, K., Jindal, R., & Jindal, D. (2019). Synthesis, characterization and studies on host-guest interactions of inclusion complexes of metformin hydrochloride with β–cyclodextrin. Journal of Molecular Liquids, 282, 162-168.

[2] Roselet, S. L., & Kumari, J. P. (2020). An investigation on host-guest complexation of Metformin hydrochloride with hydroxypropyl-α-cyclodextrin for enhanced oral bioavailability. Materials Today: Proceedings, 21, 514-518.

Electrochemical sensing of hydrazine and hydrogen peroxide based on copper oxide spheres decorated with flake-like CoFeS

Zahra Darvishmehr, Leila Naderi, Saeed Shahrokhian*

Corresponding Author E-mail: shahrokhian@sharif.edu

Department of Chemistry, Sharif University of Technology, Tehran 11155 9516, Iran.

Abstract: To prepare a dual-functional sensor to respond to hydrazine (N_2H_4) and hydrogen peroxide (H_2O_2), CoFeS/Cu2O nanocomposite synthesized by using electrodeposition method. The designed sensor exhibited very high sensitivity, low detection limit and fast response time. The sensor also displayed good recovery values towards interfering material and can reliably measure N_2H_4 and H_2O_2 concentrations in seawater sample.
Keywords: Amperometric sensor; Hydrazine; Hydrogen peroxide, nanocomposite

Introduction

N_2H_4 is a highly toxic substance because of its high solubility in water, and it can cause damage to the body and nervous system. H_2O_2 is a simple compound, but an increase in its amount in body fluids and tissues can cause oxidative stress and damage to DNA, RNA, and body proteins. For the detecting H_2O_2 and N_2H_4, analytical methods such as the chromatography, titrimetric, chemiluminescence, and spectrometry have been studied [1]. Among various techniques used to measure H_2O_2 and N_2H_4, the electrochemical technique is suitable due to high selectivity, sensitivity, and low price. Non-enzymatic sensors use electrocatalysts to accelerate the electro-oxidation/reduction. Transition metal sulfides display high conductivity, rich redox chemistry, and excellent thermal and mechanical stability. However, low electrocatalyst activity of mono metal sulfide has restricted their applications as the electroactive substances for energy and sensor -related fields. Thus, substitution of mono metal with binary metal sulfides is an effective rout to betterment electrocatalytic properties of metal sulfides [2]. These improvements are because of richer electrochemical reactions of metal ions and their contributions in the binary metal sulfides which result in higher catalytic activates relative to the mono metal sulfide. Besides, to direct grow of the sensing active substance on the electrode surface, electrochemical deposition stands out as a controllable technique that made relatively uniform films onto substrate surface with excellent adhesion and high reproducibility [3]. In this work, the FeCoS/Cu2O nanoarchitecture is designed as a non-enzymic amperometric detecting platform for H_2O_2 reduction and N2H4 oxidation. The structure characterization and electrocatalytic activity of the designed platform examined.

Experimental Section

To prepare of CoFeS/Cu2O on the GCE surface, Initially, Cu2O powder was synthesized via reduction of copper(II) chloride by ascorbic acid, and then prepared powder was dispersed in ethanol, and drop-casted onto the surface of the precleaned GCE. In the next step, flake-like CoFeS was deposited on Cu2O spheres by using cyclic voltammetry at potential range of -0.2 to -1.2 V (vs. Ag/AgCl) in equeous solution containg cobalt nitrate, iron sulfate and thiourea salts at a scan rate of 5 mV/s for 5 cycles.

Results and Discussion

Figures 1A-B display FE-SEM images of the Cu2O/GCE and FeCoS/Cu2O/GCE. Cu2O spheres are well covered surface of the GCE. After the electrodeposition of FeCoS, the spheres surface is decorated with FeCoS nanoflakes and created a nanocomposite architecture.
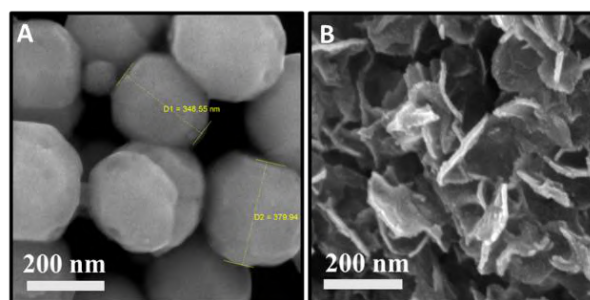

Fig. 1. of (A) The FE-SEM image of Cu_2O spheres and (B) flake-like CoFeS/Cu_2O composite.

The cyclic voltammetry was used to evaluate the electrocatalytic activities of bare, Cu2O, CoFeS, and CoFeS/Cu2O electrodes toward H2O2 sensing. As can be observed in Fig. 2A the best catalytic performance achieved for CoFeS/Cu2O/GCE. After every injection of H2O2 into alkaline media, increasing in reduction current response are observed (Fig 2B). Figure 2C exhibits amperogram of the CoFeS/Cu2O/GCE with the

22nd Iranian Chemistry Congress (ICC22)
Iranian Research Organization for Science and Technology (IROST)
13-15 May 2024

03231-97589

consecutive addition of H_2O_2 into 0.1 M NaOH solution at the optimized potential of -0.85 V. The calibration curve obtained from amperometric curve shows two linear ranges (Fig. 2D) of 1–30 µM, with a sensitivity of 12.31 mA mM^{-1} cm^{-2}, and 30 µM to 2.1 mM with a sensitivity of 3.96 mA mM^{-1} cm^{-2} as well as detection limit of 1.26 µM. The repeatability and reproducibility are two key parameters to evaluate the activity of the as-made platform, which were achieved 2.8% and 6%, respectively. Moreover, the feasibility of $CoFeS/Cu2O$ electrode was examined in seawater sample.
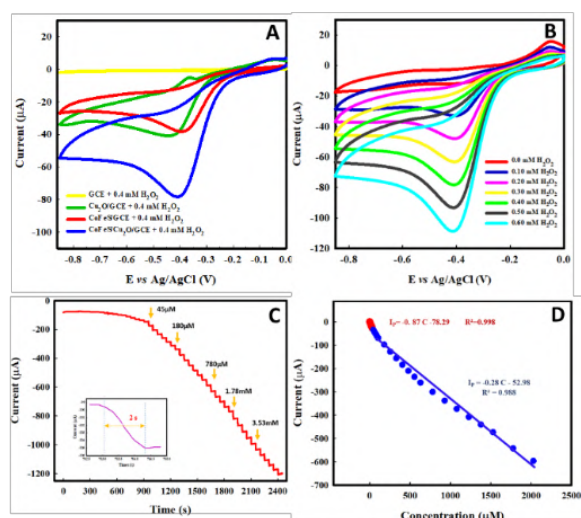
Fig. 2. (A) Comparison of CV plots of the as-made platforms, (B) CV plot of the $CoFeS/Cu_2O/GCE$ at various H_2O_2 concentrations, (C) Amperogram of the $FeCoS/Cu_2O/GCE$ after addition of H_2O_2 from 1 µM to 8.5 mM at potential of -0.85 V and (D) The linear calibration curve of H_2O_2.

The electrocatalytic properties of FeS, CoS, CoFeS, and $CoFeS/Cu_2O$ electrodes in the presence of 60 µM N_2H_4 exhibits that the oxidation current enhanced by injecting N_2H_4 (Fig. 3A), and the best catalytic activity achieved for $CoFeS/Cu_2O$ electrode. Figure 3B displays CV plot of the composite sample with successive addition of N_2H_4 from 0 to 60 µM into alkaline media. The amperograms of $CoFeS/Cu_2O/GCE$ are displayed in Fig. 3C. Addition of N_2H_4 at concentrations below 0.1 mm origins in a considerable enhancement in the electrocatalytic current response. A calibration curve with two linear ranges, I_P (µM) = 7.37 C_{HZ} (µM) + 3.43 (R^2 = 0.997) for concentration range of 0.1–20.5 µM and I_P (µM) = 1.56 C_{HZ} (µM) + 262.52 (R^2 = 0.989) for 20.5 µM to 1.77 mM were achieved, with sensitives of 104.35 and 22.04 mA mM^{-1} cm^{-2}, respectively (Fig 3D) and limit of detection of 0.12 µM (S/N =3). Repeatability and reproducibility of the sensor was evaluated, that the average relative standard deviation value was obtained

3.1 and 4%, respectively, and good recoveries was also achieved for this sensor in seawater sample.
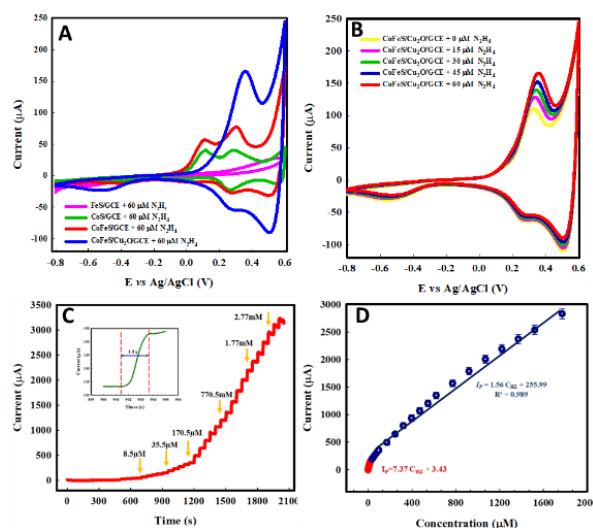
Fig. 3. (A) CV plots of the prepared sensors, B) CV plot of the $CoFeS/Cu_2O/GCE$ at different N_2H_4 concentrations, (C) Amperogram of the electrode after injection of N_2H_4 from 0.1 µM to 3.02 mM at potential of 0.50 V, and (D) Calibration curve of current versus N_2H_4 concentration.

Conclusions

The $CoFeS/Cu_2O$ nanocomposites were synthesized using fast, simple and cost-effective method and was used to measure hydrogen peroxide and hydrazine. The as-prepared composite exhibits excellent electrocatalytic activity in the amperometric detection of hydrazine and H_2O_2 with an excellent sensitivity, wide linear range, fast response time, low detection limit and good selectivity. The feasibility of the designed sensor was also examined in seawater sample.

References

[1] Han, N., Hu, S., Zhang, L., Yi, S., Zhang, Z., Wang, Y., ... & Gao, Y. (2022). CuCo-Cu@ CoCH stamen-like nanoarray prepared by co-reduction for electrochemical detection of hydrogen peroxide. *Applied Surface Science*, *576*, 151879.
[2] Naderi, L., & Shahrokhian, S. (2023). Metal-organic framework-assisted Co3O4/CuO@ CoMnP with core-shell nanostructured architecture on Cu fibers for fabrication of flexible wire-typed enzyme-free micro-sensors. *Chemical Engineering Journal*, *456*, 141088.
[3] Li, X., Wang, Y., Wang, J., Da, Y., Zhang, J., Li, L., ... & Hu, W. (2020). Sequential electrodeposition of bifunctional catalytically active structures in MoO3/Ni–NiO composite electrocatalysts for selective hydrogen and oxygen evolution. *Advanced Materials*, *32*(39), 2003414.

22nd Iranian Chemistry Congress (ICC22)
Iranian Research Organization for Science and Technology (IROST)
13-15 May 2024

03231-97589

IROST

Dyeing of wool fibers by aqueous extraction of Rhubarb stem using various mordants

Zaker Bahreini [a*], Afsaneh Behtash Oscoie[b]

Corresponding Author E-mail: bahreiniz@yahoo.com

[a] Department of Chemical Technologies, Iranian Research Organization for Science and Technology (IROST), Tehran, Iran.

[b] PhD in Inorganic Chemistry, Tehran, Iran.

Abstract: Dyeing of wool fibers with aqueous extract of Rhubarb stem, was studied, using mordants. The extract shows an absorbance at λ_{max} 436 nm. The dyed fibers were examined in term of K/S and CIELAB color difference values. Different shades (K/S =3.7-10.9) and acceptable wash and light fastness were achieved.
Keywords: Rhubarb, Rheum, Dyeing, Mordanting, Natural dyeing and Cherysophanic acid.

Introduction

There are many plant materials that can be used for dyeing yarns and materials: roots, burl, leaves, seeds, twigs, branches, tubers and nut hulls, each capable of producing a range of colours. In addition, when properly applied, natural dyes are fast, resisting fading due to exposure to sunlight. Natural dyestuffs produced by plants and insects have been used not only for dyeing fibers, but also as coloring agents in food and cosmetic industries [1]. Natural dyes are mostly non-substantive and must be applied on textiles by the help of mordants, usually a metallic salt, having an affinity for both the coloring matter and the fiber. It is possible to get hundreds of colors and shades by using different mordants with the same plant extract.

Rhubarb is a common name for *Rhenum rhabarbarum* L. it is a member of the buckwheat family and has large, thick and succulent stalks that are used as food. The root and stem of Rhubarb is the source of color which makes yellow, orange or red shades. Sometimes it is used for dyeing hair. The major constituents of the rhubarb sample (pink color, rhizome and root part) are anthraquinone and bianthrone derivatives, in which the main active components in rhubarb are 5-hydroxy anthraquinones (chrysophanic, emodin, physcion, aloe-emodin and rhein). Rhubarb root has chrysophanic acid, a yellow-pink dye, which will bind to fibers. The structures of the major components in rhubarb root are shown in Fig 1 [2].

Experimental

Commercially available scoured and bleached wool fibers were used. The fibers were washed with non-ionic detergent for 30 min at 50 ^{0}C to remove dirt and impurities followed by squeezing, rinsing and drying. Chemical substances used as mordant were of analytical grade, including, Alum (Potassium Aluminum Sulphate), KAl $(SO_4)_2.12H_2O$, Sodium Dichromate $Na_2Cr_2O_7.2H_2O$ and Cupric Sulphate $CuSO_4.5H_2O$.

Fresh rhubarbs were obtained from local market in Tehran, Iran. The rhubarbs stem was manually removed and washed with water. Distilled and deionized water was used as the extractant. The ratio of solid: liquid (plant dyestuff: Water) was 1: 10 (0.1 gr. per ml). The mixture was extracted at 70 ^{0}C for one hour. After cooling, the waste materials were separated by filtration, and the filtrate was used as the dyestuff solution [3]. Absorption spectra of the solution, were measured in the wavelength 200-700 nm is shown in Fig. 2. For mordanting, pots were prepared with the 5% on weight of fabric from each mordant with liquor ratio (LR) = 30:1. Wool fibers were introduced into the pot and then temperature of the bath was raised to boil and mordanting was continued for 45 minutes. The fibers were then removed, squeezed evenly and dyed in the respective dye solutions. The color depth of the dyed fibers were analyzed by measuring the K/S values of samples. colorimetric parameters (L^*, a^*, b^*) of each dyed and dried sample was measured, using a Colorgen Spectrophotometer under illuminant D65 at 10^0 observer. Wash fastness of the samples were determined by using grey scale according to EN ISO 105-A02 standard (ISO 105-A02:1996). For determining light fastness dyed samples were subjected to xenon arc fastness test according to EN ISO 105-B02 standard (table 1) [3].
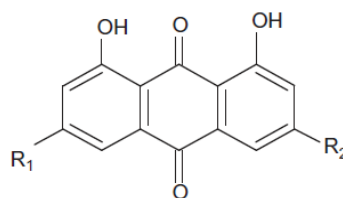
R_1=H,	R_2=CH_3;	Chysophanol
R_1=H,	R_2=CH_2OH;	Aloe-emodin
R_1=H,	R_2=COOH;	Rhein
R_1=CH_3,	R_2=OH;	Emodin
R_1=CH_3,	R_2=$OCH3$;	Physcion

Fig.1:   Active Component of *Rheum emodi.*

22nd Iranian Chemistry Congress (ICC22)
Iranian Research Organization for Science and Technology (IROST)
13-15 May 2024

03231-97589

IROST

Results and discussion

The visible absorption spectrum of dyestuff at pH 5 – 6, shows an absorption peak around 280 nm (Fig. 2) and the main peak at 436 nm arising from the extract red-orange dyestuff which belongs to cherysophanic acid component. unmordanted fibers produced yellow shade in wool dyeing, but different shades of tan in mordanting were obtained. especiallyusing alum as mordant produced green-yellow color. Depth of shade for mordanted fibers with cupric sulphate is 10.3 which is higher than other mordants used and is an indication of higher dye uptake and fixation. Dyeing of unmordanted fabric produced very weak yellow shade with a very low wash fastness and high wash fastness values were obtained in nearly all dyeing trials with pre-mordanting processes. High wash fastness values in pre-mordanting process are due to an insoluble complex forming between the dye and the mordants on the fiber substrate [4, 5].

Conclusions

The shades produced differed from mordant to mordant. Mordanting generally gave dull shades, while alum gave brighter shades. Alum show acceptable rate for lightfatsness (4). The wash fastness of all the dyeings with mordants were quite good (4-5). Natural dyes are able to produce strong, clear color that is fast to consumer use. It is potentially able to produce marketable natural dye. It produces good color and meets enough performance standards for color fastness to light and washing.

References

[1]. Kato, H., Hata, T., & Tsukada, M. (2004). Potentialities of natural dyestuffs as antifeedants against varied carpet beetle, Anthrenus verbasci. Japan Agricultural Research Quarterly: JARQ, 38(4), 241-251.

[2]. Chirikdjian, J. J., Kopp, B., & Beran, H. (1983). Über die laxative Wirkung eines neuen Anthrachinonglykosides aus Rhadix Rhei. Planta Medica, 48(05), 34-37.

[3]. Standard method for the determination of colour fastness of textiles and leather, 5th Edn. (Bradford: SDC, 1990).

[4]. Garg, A., Shinde, S., & Gupta, K. C. (1991). Effects of mordants on colour of natural dye extracted from tessue flowers (Butea mongsperma).

[5] Rama, S. J. et al., (1991)"Parijataka a Good source of Dye for Wollens" *Colourage* 38 (2), 55-56.

[6]. Li, W., Zhao, L., & Wang, Q. W. (2011). Research about the dyeing process design of the natural rhubarb dye on wool fabric. Advanced Materials Research, 332, 17-22.

Table 1: Effect of mordants on CIELAB values and fastness properties for dyeing of wool fibers with aqueous extraction of rhubarb stem.

Mordant	Shade	k/s	L^*	a^*	b^*	Light fastness	Wash fastness
Alum	amber	4.6	58.5	7.9	23	3	4/5
Sodium dicromate	Mustard tan	5.7	43.0	2.5	15.7	4	4/5
Cupric sulphate	beige	10.3	45.2	5.8	27.45	4	4/5
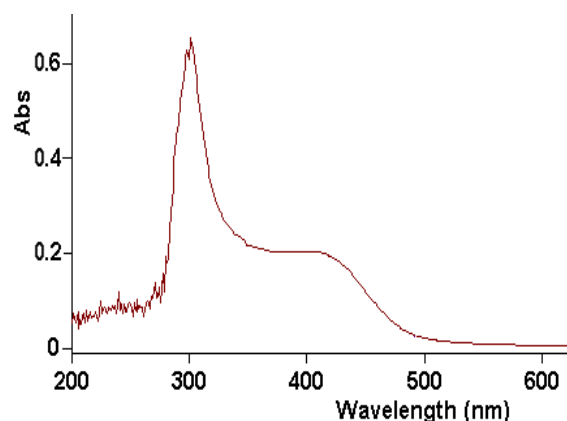
Fig.2: UV-vis absorption spectra of rhubarb extraction [6].

Streamlined Aerobic Synthesis of α-Aminophosphonates from Alcohols Using Tetrabutylammonium Tribromide (TBATB)

Milad Taghizadeh [a], Yadollah Shariati [a], Foad Kazemi [a,b]*

Corresponding Author E-mail: kazemi_f@iasbs.ac.ir

[a] Department of Chemistry, Institute for Advanced Studies in Basic Sciences (IASBS), Gava Zang, Zanjan, 45137-66731, Iran.

[b] Center for Climate and Global Warming (CCGW), Institute for Advanced Studies in Basic Sciences (IASBS), Gava Zang, Zanjan 45137-66731, Iran.

Abstract: A metal-free, one-pot method for synthesizing α-aminophosphonate from alcohols using tetrabutylammonium tribromide (TBATB) as a catalyst is reported. TBATB shows catalytic activity for alcohol oxidation and α-aminophosphonate synthesis from aldehydes. The method is optimized and works well for various alcohol and aniline derivatives

Keywords: α- Aminophosphonte; TBATB; Alcohol oxidation

Introduction

Organophosphorus chemicals, especially α-aminophosphonates, have diverse applications in agriculture, medicinal chemistry, and industrial chemistry.[1] They are structurally similar to α-amino acids and have antitumor and antimicrobial properties. The Kabachnik-Field method is commonly used for the synthesis of α-aminophosphonates.[2] Benzyl alcohols can be oxidized using visible light and molecular oxygen to produce benzaldehyde, a precursor in organic synthesis. One-pot tandem reactions allow for multiple conversions in a single vessel, reducing costs and waste generation. TBATB is a versatile reagent used in various reactions including the oxidation of benzyl alcohols and the synthesis of α-aminophosphonates.[3] The author's work focuses on two-step one-pot synthesis of α-aminophosphonates using TBATB as a catalyst in photocatalytic aerobic oxidation of alcohol.[4]

Experimental Section

In a 10 ml Pyrex flask, a reaction mixture containing alcohol (1 mmol), TBATB (10 mg, 0.01 mmol), and CH₃CN (8 ml) was subjected to blue LED light irradiation at room temperature while stirring under an air atmosphere. The reaction's progress was tracked by TLC. After reducing the solvent to 3 ml under vacuum, amine (1 mmol), diethylphosphite (1 mmol, 0.13 ml), and ethyl acetate (5 ml)

Results and Discussion

In our study, we aimed to optimize the one-pot synthesis of α-aminophosphonates, considering variables such as time, solvent, catalyst quantity, and energy sources. Benzyl alcohol served as the model compound. We discovered tha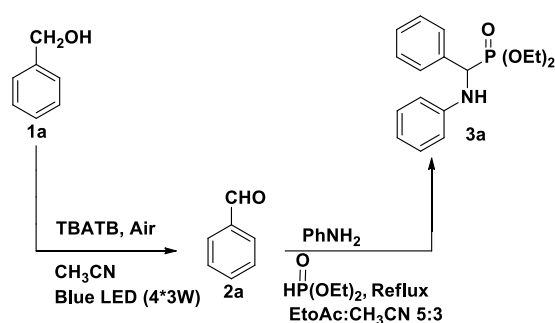t photooxidation of benzyl alcohol to benzaldehyde was most effective using 10 mg of TBATB in CH₃CN, achieving a 95% conversion under blue LED light after 3 hours. However, subsequent reactions under reflux conditions were less efficient, with a maximum yield of 52% in acetonitrile. Altering reaction parameters, such as increasing the amount of benzyl alcohol or the use of aniline and diethylphosphite, did not significantly improve yields. Continuous blue LED irradiation during reflux slightly enhanced conversion rates.

Further experiments explored various strategies to increase efficiency, including the use of P2O5, glacial acetic acid, tosyl chloride, and molecular sieves, but these modifications showed no substantial improvement. A solvent mixture of ethyl acetate and acetonitrile (5:3 ratio) proved to be the most effective, yielding an 82% conversion rate. Interestingly, initiating the reaction from benzyl alcohol rather than the corresponding aldehyde resulted in higher yields. TBATB was found to catalyze the reaction between aldehyde, diethylphosphite, and aniline under thermal conditions effectively. This suggests that TBATB can act as a synthetic equivalent to bromine, akin to iodine's role in similar reactions.
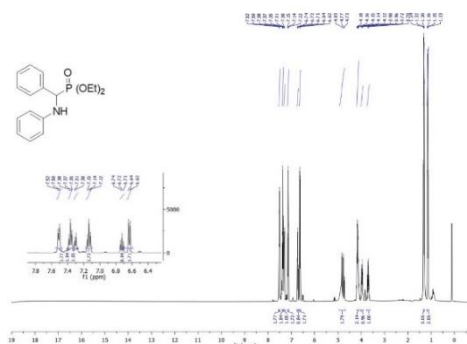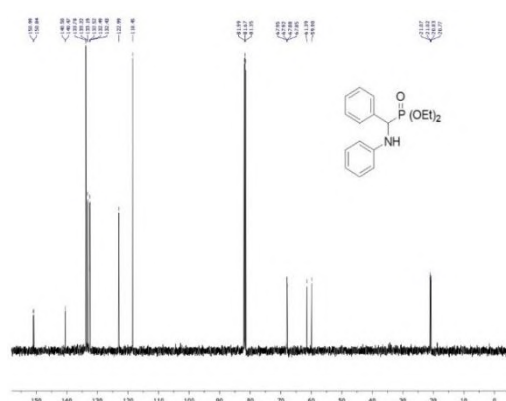
Optimized conditions involved oxidizing benzyl alcohol to benzaldehyde with a catalytic amount of TBATB under blue LED irradiation, followed by the addition of aniline and diethylphosphite under reflux to produce α-aminophosphonate with a 75% yield. This method was successfully applied to various benzyl alcohols and anilines, yielding moderate to good results.

22nd **Iranian Chemistry Congress (ICC22)**
Iranian Research Organization for Science and Technology (IROST)
13-15 May 2024

03231-97589

IROST

Table1: Optimization of one-pot two steps synthesis of α-aminophosphonate synthesis in the presence of TBATB.

Entry	PhCH$_2$OH (mmol)	Aniline (mmol)	Diethyl Phosphite (mmol)	Condition	Yield (%)
1	1	1	1	CH$_3$CN	52
2	2	1	1	CH$_3$CN	25
3	1	2	1	CH$_3$CN	50
4	1	1	2	CH$_3$CN	**20**
5	1	1	1	CH$_3$CN (+Light)	58
6	1	1	1	EtOAc: CH$_3$CN (5:3)	82
7	PhCHO 1 mmo	1	1	EtOAc: CH$_3$CN (5:3)	75
8	PhCH$_2$OH 1 mmol	1	1	EtOAc: CH$_3$CN (5:3) hv+hv	70

Fig.1: ^{1}H NMR Spectra of Diethyl phenyl (phenylamino) methyl phosphonate

Fig.2: ^{13}C NMR Spectra of Diethyl phenyl (phenylamino) methyl phosphonate

Scheme 1: synthesis of α-aminophosphonates derivatives

Conclusions

We have developed a streamlined, two-step, one-pot method for synthesizing α-aminophosphonates from alcohols, amines, and dialkylphosphite, catalyzed by Tetrabutylammonium Tribromide (TBATB). This catalyst efficiently drives both steps of the process. Initially, aldehydes with various substituents are synthesized via a photocatalytic, metal-free process under blue LED light in the presence of TBATB. Subsequently, these aldehydes are converted to α-aminophosphonates by reacting with aromatic amines and diethylphosphite under heat. Notably, starting the reaction with alcohols rather than aldehydes results in higher yields. This method offers advantages such as simplicity, ease of operation, and the use of readily available materials, making it superior to previous methods.

Our findings suggest that the radical nature of the reaction facilitates better outcomes for compounds with electron-withdrawing groups, both in benzyl alcohols and anilines. The study also explored the use of diisopropylphosphite, which, despite lower efficiency compared to diethylphosphite, still produced good results. However, aliphatic alcohols and amines did not yield satisfactory products, likely due to their instability in the imine intermediate stage. Overall, the research provides valuable insights into the synthesis of α-aminophosphonates and the factors influencing their production.

References

[1] B. B. Bonev, N. M. Brown, Bacterial Resistance to Antibiotics: From Molecules to Man, first ed., Wiley-Blackwell, Hoboken, New Jersey, 2019, 1–239.

[2] R. Lekkala, R. Lekkala, B. Moku, K. Rakesh, H. L. Qin, Eur. J. Org. Chem. 2019, 2019, 2769–2806

[3] A. Mardani, M. Heshami, Y. Shariati, F. Kazemi, M. A. Kakroudi, B. Kaboudin, J. Photochem. Photobiol. A 2020, 389, 112220.

[4] X. Y. Fu, Y. F. Si, L. P. Qiao, Y. F. Zhao, X. L. Chen, B. Yu, Adv. Synth. Catal. 2022, 364, 574–580

More natural more effective: introducing a new β-cyclodextrin and spermine polyamine based polymer

Zaynab Mokhtari *[a,b], Sedigheh Hashemnia [a]

Corresponding Author E-mail: Zmokhtari6559@yahoo.com

[a] Department of Chemistry, Faculty of Nano and Bio Science and Technology, Persian Gulf University, Bushehr 75169, Iran.
[b] Department of Chemical Industry, Technical and Vocational University (TVU), Bushehr, Iran.

Abstract: Considering that in many disorders, oxidative stress is an underlying cause, introduction of a new compound based on polyamines and β-cyclodextrin with antioxidant activity for medicinal, food additives and supplements applications would be valuable. After the preparation and characterization of the new spermine/β cyclodextrin polymer(SPM/β-CD), It was evaluated to examine the free-radical scavenging properties.
Keywords: Spermine; β-Cyclodextrin; Antioxidant

Introduction

High levels of free radicals including reactive oxygen species (ROS) and reactive nitrogen species has an important role in the oxidative damage of biomolecules such as DNA, proteins and membrane lipids and also in many of the chemical mechanisms associated to the degradation of food and chemical materials [1]. Accordingly, during the past years, there has been a growing request for natural antioxidants to act as functional additives that could provide biological systems with protection against free radicals. Cyclodextrin-based biopolymers are promising materials for therapeutic and medical applications due to their inherent synthetic versatility and nontoxicity. These compounds have a hydrophilic surface and a hydrophobic cavity that the guest molecules can be encapsulated in the cavity. Native cyclodextrins (α-CD, β-CD, and γ-CD) can be chemically modified to improve their solubility and hydrophilic/hydrophobic properties [2].

Polyamine compounds play essential role in many biological functions such as cellular replication and differentiation, metabolism regulation, and stabilization of membranes and nucleic acids. N,N'-bis(3-aminopropyl)-1,4-diaminobutane or spermine (SPM) is a natural and ubiquitous polyamine made during metabolic processes in all living cell, and also is essential to cell survival. Among the important biological functions of SPM, the antioxidant activity in the biological systems, membrane constituents, proteins and nucleic acids is considerable. the antioxidant mechanisms reported for polyamines are including free radical scavenging and transition metal chelation. Oxidation of lipids is one of the main causes of the many chronic diseases such as atherogenesis, and causes the various vascular complications of diabetes and aging. Polyamines with antioxidant activity have been shown to play an important role in the prohibition of inflammatory chronic diseases [3,4]. According to reports an increased polyamine intake can help with cardiovascular diseases prevention, promoting healthy aging and promotes longevity. The goal of our research involves two aspects: first, preparation of the spermine/β-cyclodextrin polymer (SPM/β-CD) and careful characterization. second, determination of the antioxidant capacity of β-CD, SPM and SPM/β-CD, to study the improvement of radical scavingering of the new synthesize SPM/β-CD.

Experimental Section

The SPM/CD polymer was prepared in two steps. carboxymethyl CD (CM-β-CD) was first synthesized, using cyclodextrin (CD) and monochloroacetic acid (MCA). then spermin/CD polymer was prepared using EDC/NHS (N-(3-dimethylaminopropyl)-N'-ethylcarbodiimide hydrochloride and N-hydroxysuccinimide) chemistry [5].
The Radical scavenging assay was done utilizing the 2, 2 diphenyl-1-picrylhydrazyl (DPPH) stable radicals. For this purpose, β-CD and SPM/β-CD with different concentrations was added DPPH solution and kept for 30 minutes at room temperature in the dark. then the absorbance of the solutions was measured at 517 nm [6].

Results and Discussion

Characterization of the synthesized SPM/ β-CD polymer
The physical nature of the developed polymer has been observed using XRD patterns (Fig.1).
SEM images could help us to demonstrate the formation of the SPM/β-CD polymer in the initial steps. As seen in Fig. 2, the difference between the β-CD and SPM/ β-CD morphologies can be an evidence of the SPM/ β-CD complex formation. The anti-radical properties of the SPM/CD polymer were evaluated and compared by SPM and β-CD. and the anti-radical activity was increased comparing to the β-CD and SPM alone.
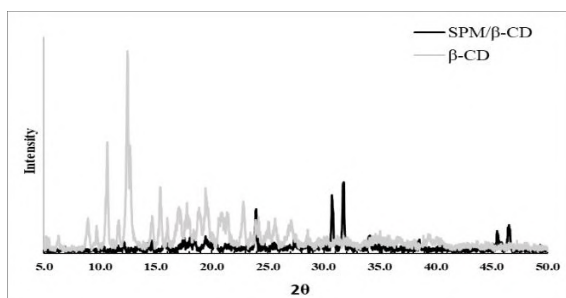
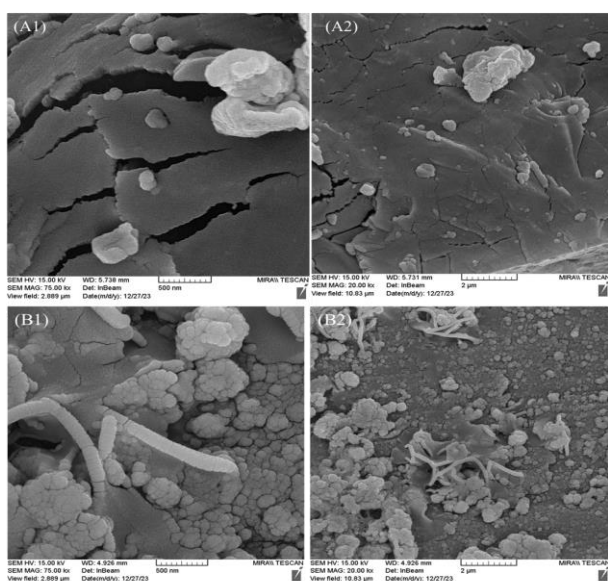**Fig.1:** XRD patterns of the β-CD and synthesize SPM/ β-CD.

Fig.2: SEM images of (A) β-CD and (B) the synthesize SPM/ β-CD by two magnetizations.

Conclusions

According to the Polyamine's antioxidant and anti-inflammatory properties to prevent cardiovascular disease, also the importantance of them for cell growth and proliferation, DNA stability, RNA transcription, protein synthesis, immune response modulation, it was thought worthwhile to propose new polymers based on the combinations of the SPM and β-CD. therefore this new SPM/CD polymer, which is synthesized by a safe method, can be used in food supplements and as drug carrier applications specially hydrophobic drugs.

Acknowledgment

References

[1] Jomova, K., Raptova, R., Alomar, S. Y., Alwasel, S. H., Nepovimova, E., Kuca, K., & Valko, M. (2023). Reactive oxygen species, toxicity, oxidative stress, and antioxidants: Chronic diseases and aging. Archives of toxicology, 97(10), 2499-2574.

[2] García-Padial, M., Martínez-Ohárriz, M. C., Navarro-Blasco, I., & Zornoza, A. (2013). The role of cyclodextrins in ORAC-fluorescence assays. Antioxidant capacity of tyrosol and caffeic acid with hydroxypropyl-β-cyclodextrin. Journal of agricultural and food chemistry, 61(50), 12260-12264.

[3] Toro-Funes, N., Bosch-Fusté, J., Veciana-Nogués, M. T., Izquierdo-Pulido, M., & Vidal-Carou, M. C. (2013). In vitro antioxidant activity of dietary polyamines. Food research international, 51(1), 141-147.

[4] Mozdzan, M., Szemraj, J., Rysz, J., Stolarek, R. A., & Nowak, D. (2006). Anti-oxidant activity of spermine and spermidine re-evaluated with oxidizing systems involving iron and copper ions. The international journal of biochemistry & cell biology, 38(1), 69-81.

[5] Kono, H., & Teshirogi, T. (2015). Cyclodextrin-grafted chitosan hydrogels for controlled drug delivery. International journal of biological macromolecules, 72, 299-308.

[6] Hashkavayi, A. B., Hashemnia, S., Osfouri, S., & Zarei, S. (2019). Electrochemical study of antioxidant capacity of gracilaria pygmaea macro-algae based on the green synthesis of gold nanoparticles: assessment of its cytotoxic effect on four cancer cell lines. Journal of The Electrochemical Society, 166(12), B969.

Integrating the Mn₂O₃ nanocubes and triangular Ag nanoplates as the green aptasensing platform for impedimetric detection of Penicillin G

Arshia Ghazian [a], Mahsa Ghanbarzadeh [a], Ali Ghaffarinejad [*a,b], Faezeh Shahdost-Fard [*c]

Corresponding Author's E-mail: ghaffarinejad@iust.ac.ir and F.Shahdost@cfu.ac.ir

[a] Research Laboratory of Real Samples Analysis, Faculty of Chemistry, Iran University of Science and Technology (IUST), Tehran 1684613114, Iran.
[b] Electroanalytical Chemistry Research Center, Iran University of Science and Technology (IUST), Tehran, 1684613114, Iran.
[c] Department of Chemistry Education, Farhangian University, P.O. Box 14665-889, Tehran, Iran.

Abstract: This study introduces the synergistic effect of the integration of the Mn₂O₃ nanocubes (Mn₂O₃NCs) and triangular Ag nanoplates (Tri-AgNPs) in the embedding of a green nanocomposite as the aptasensing platform for impedimetric detection of Penicillin G under a wide LDR (1 fM-2.7 μM) by an ultra-low LOD of 333.3 aM.

Keywords: Penicillin G; Impedimetric aptasensor; Triangular Ag nanoplates; Mn₂O₃ nanocubes; Non-invasive method.

Introduction

Penicillin G (Pen-G), one of the most important and effective β-lactam antibiotics, has been broadly implemented for preventing and/or treating various bacterial infections in humans, livestock, poultry, and aquaculture industries [1]. The excessive amounts of Pen-G in drinking water and food may enhance the antibiotic resistance of bacteria and its residues in animal-derived products may cause some allergenic and/or toxicological responses (even at 1 ppb) in sensitive individuals, thereby endangering people's health [2]. This study presents a novel impedimetric aptasensor for ultra-selective detection of Pen-G to overcome some challenges created by other reported sensors.

Thanks to the fantastic advantage of Mn₂O₃ nanocubes (Mn₂O₃NCs) and triangular Ag nanoplates (Tri-AgNPs) the synergistic effect both led to embedding the efficient nanocomposite to high-dense load the Apt (aptamer) sequence onto the glassy carbon electrode surface.
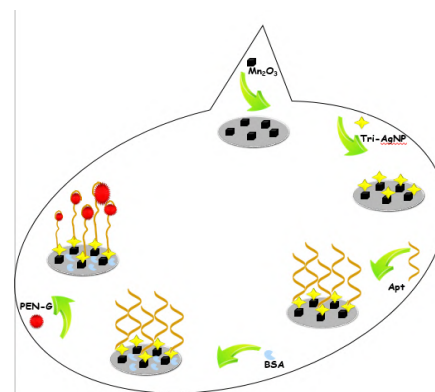
Experimental Section

An NH₂-Apt sequence specific to Pen-G was used [3]. Mn₂O₃NCs and Tri-AgNPs were easily synthesized by the green and non-toxic materials and integrated to pdovide the Tri-AgNPs@Mn₂O₃NCs nanocomposite. Some urine and saliva samples were collected from a healthy girl and diluted by 0.1 M PB (pH 7.4). Finally, 10 μL of each spiked Pen-G sample was separately dropped on the aptasensor surface to analyze Pen-G.

Results and Discussion

The steps of the fabrication process of the aptasensor is graphically provides in Fig. 1A. Nyquist plots in Fig. 1B indicate a semicircle domain with a R_{ct} value of 1298 Ω for the bare GCE (curve a). Attachment of the Mn₂O₃NCs on the GCE surface is verified by increasing the R_{ct} value to 11804 Ω (curve b). In the next step, the increase of R_{ct} value to 13416 Ω proves the covering of the Tri-AgNPs layer on Mn₂O₃NCs/GCE surface (curve c). A R_{ct} value increase (21191 Ω) is observed for NH₂-Apt/Tri-AgNPs@Mn₂O₃NCs/GCE surface, certifying NH₂-Apt attachment through binding NH₂ group in NH₂-Apt terminal to Tri-AgNPs layer (curve d). A further significant increasing in the R_{ct} value (31165 Ω) is achieved by incubating 300 nM of Pen-G on BSA/NH₂-Apt/Tri-AgNPs@Mn₂O₃NCs/GCE surface as the aptasensor, corroborating the successful tracing of Pen-G on the NH₂-Apt arm and NH₂-Apt/Pen-G complex formation on the sensing interface (curve e). These findings are in good agreement with the preceding results from the cyclic voltammograms (CVs) in Fig. 1C and both affirm the correctness of the electrochemical aptasensor fabrication principles.

The efficiency of the proposed sensing interface was confirmed by the aptasensor ability in the impedimetric measuring of Pen-G in a wide linear range from 1 fM to 2.7 μM with an ultra-low LOD of 333.3 aM with high sensitivity and selectivity.
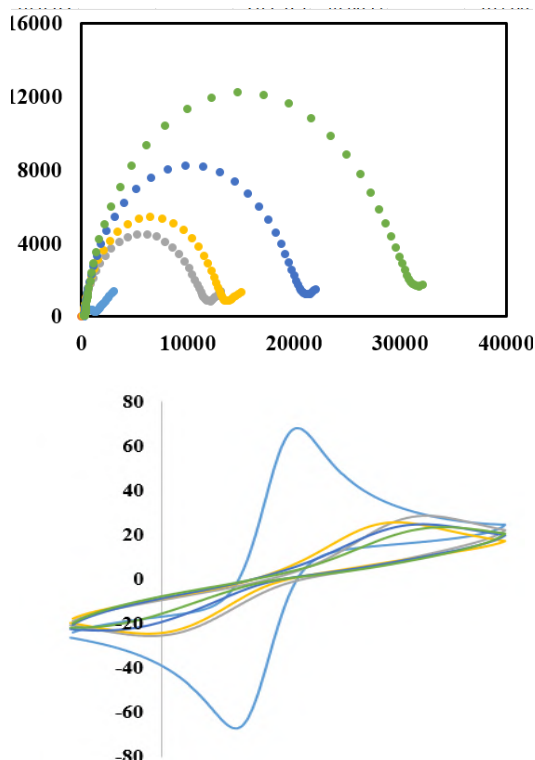
22nd Iranian Chemistry Congress (ICC22)
Iranian Research Organization for Science and Technology (IROST)
13-15 May 2024

03231-97589

IROST

https://doi.org/10.1007/s00604-018-3075-0.

[3] Zhao, J., Guo, W., Pei, M., & Ding, F. (2016). GR–Fe_3O_4 NPs and PEDOT–AuNPs composite based electrochemical aptasensor for the sensitive detection of penicillin. *Analytical methods*, *8*(22), 4391-4397.

https://doi.org/10.1039/D4AY00018H.

Fig.1: (A) Step–by–step processes of Pen-G aptasensor fabrication, (B) Nyquist plots (inset (B): the equivalent circuit) and (C) The CVs in 0.1 M PB containing 5 mM $[Fe(CN)_6]^{3-/4-}$ and 0.1 M KCl as the redox probe.

Conclusions

The proposed Mn_2O_3NCs@Tri-AgNPs nanocomposite presented many advantages in the fabrication of the impedimetric aptasensor for the rapid and ultrasensitive detection of Pen-G in human biofluids. Besides, the greenness of the applied methodology was satisfactorily evaluated by the complimentary green analytical procedure index (ComplexGAPI) and the analytical greenness approach (AGREE) as the international criteria in green chemistry technology. These findings promise the cost-effective nanocomposite ability for other electrochemical applications, especially (Apta)sensor fabrication technology.

References

[1] Wang, J., Zhuan, R., & Chu, L. (2019). The occurrence, distribution and degradation of antibiotics by ionizing radiation: an overview. *Science of the total environment*, *646*, 1385-1397.

https://doi.org/10.1016/j.scitotenv.2018.07.415.

[2] Zarei, S. S., Soleimanian-Zad, S., & Ensafi, A. A. (2018). An impedimetric aptasensor for Shigella dysenteriae using a gold nanoparticle-modified glassy carbon electrode. *Microchimica Acta*, *185*, 1-9.

22nd Iranian Chemistry Congress (ICC22)
Iranian Research Organization for Science and Technology (IROST)
13-15 May 2024

03231-97589

IROST

MOF/MSN Composite as an Effective Adsorbent for Solid-Phase Microextraction Sampling of PAHs from Soil Samples

Sara Maleki, Payman Hashemi*

Corresponding Author E-mail: Hashemi.p@lu.ac.ir

Department of Chemistry, Faculty of of Chemistry, Lorestan University, Khorramabad, Iran.

Abstract: In this work, a new composite of MOFs (MIL-88(Fe)) and MSNs (mesoporous silica materials) were synthesized and characterized by FE-SEM, XRD, BET, TGA and FTIR techniques. The HS-SPME method is evaluated for sampling PAHs (Polycyclic aromatic hydrocarbons) compounds from polluted soil samples using the MOF/MSN fiber. Optimization of the extraction parameters including extraction temperature, extraction time, moisture content of the sample, desorption time and desorption temperature was carried out using a GC-FID instrument and a Box-Behnken design (BBD) method.
Keywords: Headspace solid-phase microextraction; Metal organic frameworks; Mesoporous silica materials

Introduction

Headspace solid-phase microextraction (HS-SPME) is a simple, rapid, solvent free and cost effective sample preparation method [1]. The key factor affecting the selectivity, extraction efficiency and sensitivity of analytes in SPME technique is choosing a suitable coating on the SPME fiber. Various porous materials with different physical, chemical, thermal, and mechanical properties have been reported as fiber coating for the analysis of different samples in recent years. One of the most recent coatings is MOF/MSN. Nanoporous materials have attracted broad attention due to their unique properties including large specific surface areas, adjustable pore sizes, controllable compositions and structures, and ease of modification [2]. In particular, metal organic frameworks (MOFs) with a hybrid structure consisting of inorganic nodes interconnected by organic ligands, have been applied in various fields.

As another family of nanoporous materials, mesoporous materials with pore sizes ranging from 2 to 50 nm are more favourable for carrying large molecules.

Among them, mesoporous silica materials (MSMs), especially mesoporous silica nanoparticles (MSNs), have been widely studied due to their good stability, excellent biocompatibility and tunable particle/pore sizes [3]. Nevertheless, the plain chemistry of silica may limit its functions and applications. Therefore, combining MOFs and MSMs/MSNs is a promising approach to integrating the advantageous properties of two components in one composite.

Experimental Section

Preparation of MOF/MSN

Firstly, DMSN (dendritic mesoporous silica nanosphere) was synthesized, for this purpose, 0.082 g of TEOA was dissolved in 30 mL of deionized water and the solution was stirred for 30 min at 80 °C in a water bath. Subsequently, 40.456g CTAB and 0.202 g NaSal were separately added into the above solution under stirring, and then the solution was stirred for another hour. Thereafter, 4.8 g TEOS was slowly added into the solution and stirring was continued for 1.5 h. Then, the mixture was placed in a Teflon-lined autoclave (50 mL) and crystallized for 4 h at 100 °C. Finally, DMSNs were obtained after the final solid product was repeatedly extracted 3 times in ethanol and then roasted for 4 h at 550 °C. Then, composite material (MOF/MSN) was prepared using the solvothermal technique, but during the synthesis of MIL-88(Fe), in order to prepare MOF/MSN composite, some DMSN compound was added to the reaction.

SPME Method

The extraction of PAHs were operated in a 10 mL vial containing 2 g of soil. Then the MOF/MSN coated fiber was exposed to the headspace above the soil when the temperature was held at 80 °C for 9 min. Finally, the fiber was removed from the vial and inserted into the GC inlet followed by GC-FID analysis.

Results and Discussion

The structure and morphology of the nanocomposite was characterized using Fourier transform infrared spectroscopy (FT-IR), scanning electron microscopy (SEM), and X-ray diffraction (XRD) techniques that shown in Fig. 1, 2 and 3, respectively. Then Response surface methodology (RSM) involving Box-Behnken design (BBD) was implemented to evaluate the effective experimental variables such as extraction time, extraction temperature and humidity were studied using the MOF/MSN fiber in HS-SPME. The statistical model predicted 80 °C, 9 min,

22nd Iranian Chemistry Congress (ICC22)
Iranian Research Organization for Science and Technology (IROST)
13-15 May 2024

03231-97589

and 0 μL, as the optimal values for sampling temperature, sampling time, and sample's moisture content, respectively. Under the optimum conditions, the proposed method showed low limits of detection (LODs, 0.5–0.8 ng g^{-1}), wide linear ranges (1–9000 ng g^{-1}), and good repeatability with relative standard deviations (RSDs) of 2–5.4% for single fiber and 5.3%–9.1% for fiber-to-fiber. The developed MOF/MSN fiber –GCFID method was successfully applied for the extraction and determination of PAHs in contaminated soil samples.
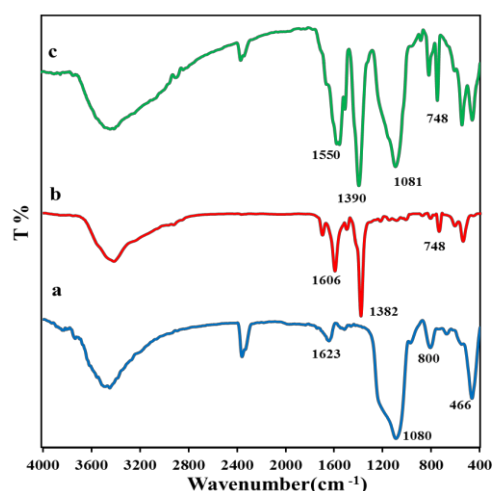
Fig. 1: FT-IR spectra of (a) DMSN, (b) MIL-88(Fe) and (c) MOF/DMSN
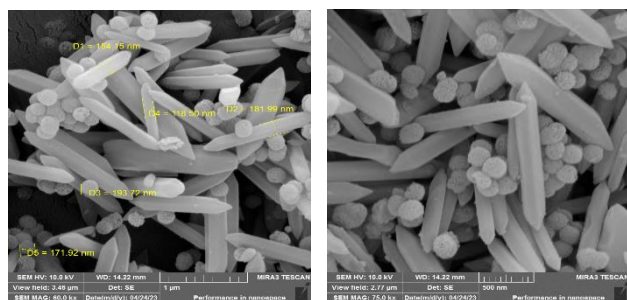
Fig. 2: SEM images of MOF/DMSN
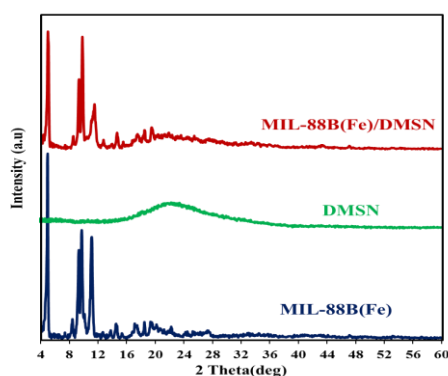
Fig. 3: XRD patterns of MIL-88(Fe), DMSN and MOF/DMSN.

Conclusions

A MOF/DMSN Composite coated stainless steel fiber was fabricated by a physical adhesion approach for extracting trace amounts of PAHs prior to GC-FID analysis. The prepared coating possessed good thermal stability, long lifetime, as well as excellent extraction efficiency due to its high surface area, porous structure, and conjugated system. Under the optimized condition, the developed HS-SPME method showed wide linear range, low LODs, good repeatability and reproducibility. The method was successfully applied to analysis of PAHs in soil samples with satisfactory recoveries. All those results show that MOF/DMSN Composite is a promising adsorbent for analysis of compounds with large conjugation structure.

References

[1] Ma, Q.L., et al. (2013). Optimization of headspace solid phase microextraction (HS-SPME) for gas chromatography mass spectrometry (GC–MS) analysis of aroma compounds in cooked beef using response surface methodology. Microchem. J., 111, 16-24. https://doi.org/10.1016/j.microc.2012.10.007.

[2] J. Liang, Z. Liang, R. Zou, Y. Zhao, Adv. Mater. (2017). Heterogeneous Catalysis in Zeolites, Mesoporous Silica, and Metal–Organic Frameworks. Advanced Materials, 29, 1701139, https://doi. org/10.1002/adma.201701139.

[3] V.B. Cashin, D.S. Eldridge, A. Yu, D. Zhao, Environ. Sci. (2018). Surface functionalization and manipulation of mesoporous silica adsorbents for improved removal of pollutants: a review Water Research. Technol. 4, 110–128, https://doi.org/10.1039/C7EW00322F.

22nd Iranian Chemistry Congress (ICC22)
Iranian Research Organization for Science and Technology (IROST)
13-15 May 2024

03231-97589

IROST

Improving Cell Adhesion and Differentiation in cell delivery: The Innovation of Gelatin-Coated Whitlockite Microcarriers

Marziye Gholami, Roya Sedghi*

Corresponding Author E-mail: r_sedghi@sbu.ac.ir

Department of Polymer and Materials Chemistry, Faculty of Chemistry and Petroleum Sciences, Shahid Beheshti University, G.C, 1983969411, Tehran, Iran.

Abstract: Bone's regenerative capacity is limited for critical defects, necessitating therapeutic cell delivery for enhanced bone healing. Various mesenchymal stem cells sources and scaffold delivery expedite bone repair, offering tailored, low-risk treatment for efficient bone regeneration. Whitlockite microcarriers enhance cell attachment and survival, reducing shear pressure during delivery.

Keywords: Whitlockite; cell-laden microcarriers; bone defects.

Introduction

Bone possesses innate regenerative abilities for minor injuries, yet critical-sized defects require therapeutic intervention to stimulate regeneration. Cell delivery for bone defect treatment involves targeted administration of therapeutic cells, such as mesenchymal stromal cells (MSCs), to enhance bone regeneration. Techniques encompass local injection and biomaterial-based methods. While combining cells with biomaterials can enhance bone formation, challenges persist. Local MSC injection shows promise in addressing conditions like osteonecrosis. Diverse MSC sources have been studied for fracture repair, with controlled delivery via scaffolds expediting bone healing. This approach offers tailored, low-risk treatment, fostering accelerated and more efficient bone tissue regeneration, with potential for improved patient outcomes in regenerative medicine [1]. The whitlockite microcarriers (WHMCs) facilitate cell attachment, homing, and survival due to their high specific surface area for cell proliferation, while reducing shear pressure during delivery. Previous research indicates superior osteogenic differentiation of whitlockite (WH) microparticles compared to hydroxyapatite [2]. This study aims to develop cell microcarriers using whitlockite and gelatin, with WHMCs designed as a localized cell delivery system for bone defect treatment in patients.

Experimental Section

The synthesis of WH microcarriers began with heating a solution containing 0.13 moles of magnesium hydroxide and 0.37 moles of calcium hydroxide in 1000 mL of water to 85 °C for 1 hour. Phosphoric acid (0.5 M) was added dropwise at 12 ml/min. After 20 hours of aging, the resulting milky white precipitates were centrifuged, washed to neutral pH, and dried at 100 °C overnight to yield highly crystalline WH particles.

In a separate process, 0.15 g of dopamine was dissolved in 100 mL of deionized water to create a dopamine aqueous solution. Subsequently, 2.6 g of WHMCs were introduced into the dopamine solution to form the WHMCs/dopamine suspension. The mixture was vigorously stirred for 5 hours to facilitate dopamine intercalation and oxidation, resulting in the formation of polydopamine-coated WHMCs. The gray precipitates were then centrifuged, washed, and combined with a 5% w/w gelatin solution, followed by stirring for 8 hours to produce gelatin-coated microcarriers.

Results and Discussion

The crystalline nature of synthesized WHMCs was examined by the X-ray diffraction (XRD) spectroscopy and shown in Fig.1. The results of the XRD spectrum coincide with major peaks at 2θ of 26.05°, 28.13°, 31.30°, 32.81°, and 34.78° that corresponds to the plane (1 0 10), (2 1 4), (0 2 10), (1 2 8), and (2 2 0) respectively.
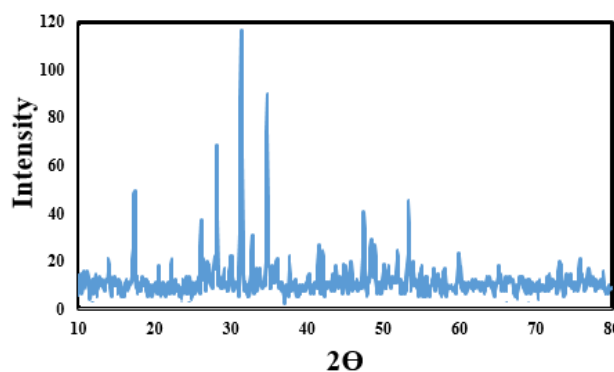

Fig.1: XRD spectrum of WHMCs

Field emission Scanning Electron microscopy (FESEM, TESCAN MIRA 3) was used to investigate the morphology of WHMCs. FESEM image confirms the semispherical

22nd Iranian Chemistry Congress (ICC22)
Iranian Research Organization for Science and Technology (IROST)
13-15 May 2024

03231-97589

morphology with an average MCs size of 4.5 ± 0.6 µm (Fig.2).

Also, the energy-dispersive X-ray spectroscopy (EDS) data confirm the presence of C, N, O, Ca, and Mg in the gelatin-coated WHMCs, as shown in Fig.3.
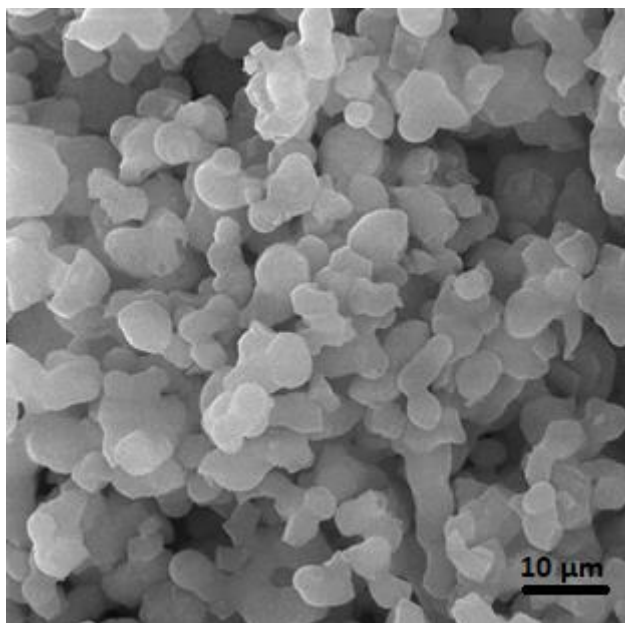

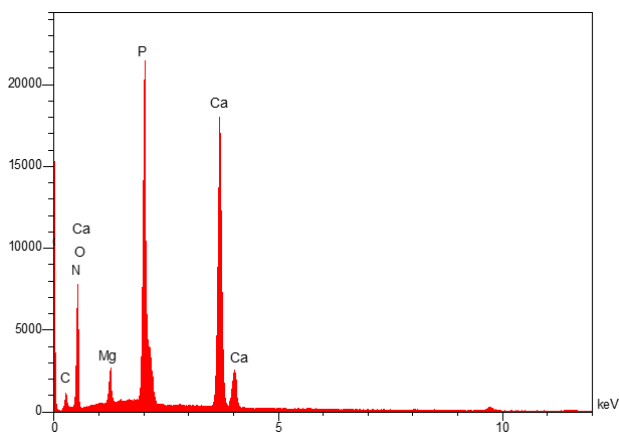**Fig.2:** FESEM image of gelatine-coated microcarriers

Fig.3: EDS pattern of gelatine-coated microcarriers

The formation of a calcium mineralized matrix was evaluated using Alizarin Red S (ARS) staining on days 7, 14, and 21 in 3D bioprinted hydrogels incorporating alginate and human adipose-derived mesenchymal cells (AD-MSCs) loaded with gelatin-coated WHMCs. The results depicted in Fig. 4 demonstrate a higher degree of mineralization in 3D printed hydrogels with increased WHMCs components on the day7, day 14 ,and day 21. According to results, the presence of the WHMCs component influenced the osteogenic differentiation of AD-MSCs.

Furthermore, the findings suggest that gelatin plays a pivotal role in improving the mechanical characteristics of hydrogels by facilitating cross-linking between alginate and gelatin.
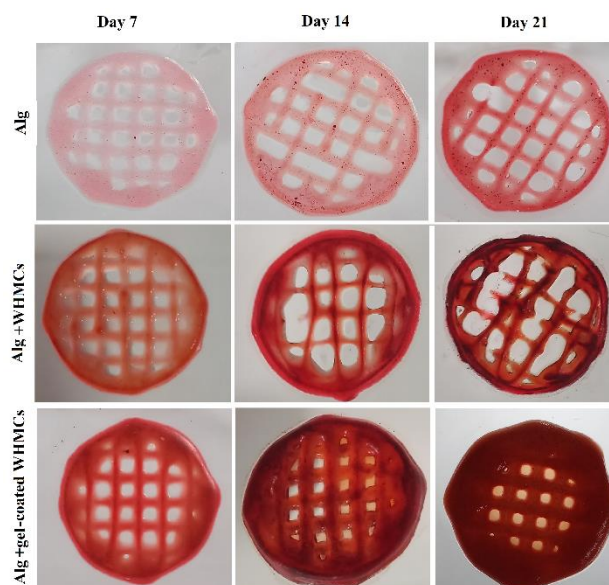
Fig.4: ARS staining of 3D bioprinted alginate, alginate/WHMCs, and alginate/gelatin-coated WHMCs at 7, 14, and 21 days

Conclusions

Leveraging microcarrier technology enables the substantial proliferation of cells as they develop multicellular clusters, with the ability to regulate their phenotype. This study involved the delivery of living constructs using cell-laden microcarriers. Additionally, enhancing the mechanical properties of hydrogels and promoting cell differentiation was achieved through surface modification of bioactive WH particles. These results highlight the promise of this innovative microcarrier-based biofabrication method for creating bone and osteochondral constructs.

References

[1] Zhou, Z., Wu, W., Fang, J., & Yin, J. (2021). Polymer-based porous microcarriers as cell delivery systems for applications in bone and cartilage tissue engineering. International Materials Reviews, 66(2), 77-113.

[2] Pouraghaei Sevari, S., Kim, J. K., Chen, C., Nasajpour, A., Wang, C. Y., Krebsbach, P. H., ... & Moshaverinia, A. (2021). Whitlockite-enabled hydrogel for craniofacial bone regeneration. ACS Applied Materials & Interfaces, 13(30), 35342-35355.

Unveiling the Secrets of Quantum Mechanics in the Thermal Formation of Pyrrole and Furan

Hossein Shirani[a,b,*], Mohanna Badri[b] and Peyvand Ghanbarpour[c]
Corresponding Author E-mail: hossein_shirani@iust.ac.ir

[a] Department of Chemistry, Iran University of Science and Technology, P.O. Box 16846-13114, Tehran, Iran.
[b] Department of Microbiology, Faculty of Biological Sciences and Technology, University of Science and Culture, Tehran, Iran.
[c] Water safety research center, food and drug administration, ministry of health and medical education, Tehran, Iran.

Abstract: The prediction of polyfuran and polypyrrole heat of formation was done using MP2 quantum calculations and DFT computations at the B3LYP/6-311+G** levels. The outcomes of the ab initio calculations demonstrated a remarkable correlation between the anticipated heat of formation for furan and pyrrole and the results derived from experimental trials.
Keywords: polyfuran, polypyrrole, ab initio, density functional theory

Introduction

The study conducted here focused on determining the heats of formation in the gas phase of pyrrole monomer, pyrrole dimer, and furan using the MP2 level of theory with relative success. However, it was noted that this approach lacks correlation energy, which may not provide accurate results for conjugated molecules like PF and PPy. To address this, DFT calculations were employed, showing promise as a superior method compared to Hartree-Fock, especially for more complex systems. The Asian Committee for Future Colliders (ACFA) has proposed the development of the Joint Linear Collider (JLC) to investigate the elusive Higgs boson, the last remaining unobserved particle in the Standard Model of particle physics. A key component of the JLC is the vertex detector, crucial for precisely tracking particle trajectories near the interaction point and distinguishing genuine vertex tracks from background noise. Traditionally, vertex detectors are constructed using inorganic semiconductors like silicon (Si). However, limitations in producing large Si crystals have led to high fabrication costs for semiconductor detectors. To address this issue, a collaborative effort between Niigata University in Japan and MSU-Iligan Institute of Technology in the Philippines is exploring the feasibility of utilizing conducting polymers as radiation sensors for a cost-effective alternative to Si detectors [1-4].

Methods

The initial step in the Gaussian calculations involved the use of MP2 techniques to optimize geometry at the HF/6-31G* level and determine vibrational frequencies. Subsequently, the geometry is reoptimized at the MP2/6-31G* level as the standard reference. A further MP2/6-311+G calculation was performed to obtain the corresponding HF energy. The ab initio and density functional theory (DFT) calculations were conducted using the Gaussian 94 suite of quantum chemistry software, employing MP2 and B3LYP/6-311+G** methods. The calculations were executed on a DEC Alpha Machine and Windows 2000 workstations [5-7].

Results and Discussion

The heats of formation were calculated using the MP2 method and are presented in Table 1. This table also includes the heat of formation data derived from DFT calculations.
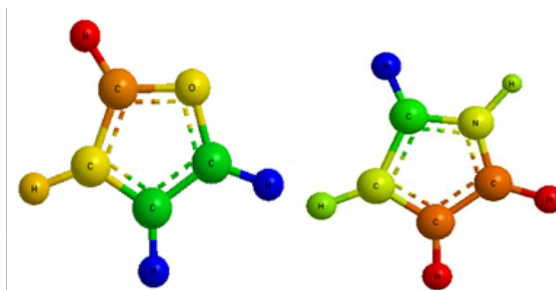

Fig. 1. Structure of (a) furan and (b) pyrrole monomer optimized using 6-311+G** basis set.

As anticipated, the ab initio MP2 calculations yielded highly satisfactory outcomes. We analyzed the molecular structures of pyrrole, dipyrrole, furan, and difuran in a gaseous state. Experimental data for pyrrole and furan were available, as well as the findings from MP2 and DFT calculations for comparison. The results from MP2 closely matched the experimental data within a margin of error of less than ±1 kcal/mol for furan and less than ±3 kcal/mol for pyrrole. The calculations for difuran and dipyrrole are still ongoing, with expectations of even more accurate results once the experimental data is obtained.

22nd Iranian Chemistry Congress (ICC22)
Iranian Research Organization for Science and
Technology (IROST)

13-15 May 2024

03231-97589

IROST

Table 1. Calculated Energies of Compounds with zero point correctiona (MP2) and B3LYP/6-311+G**).

Compound	Total Energy MP2	Total Energy B3LYP
Furran	-453.6895267	-455.7652755
Difuran	-440.9835679	-457.9723957
Pyrrole	-437.9736594	-451.9030693
Dipyrrole	-438.9384833	-424.9857434

Computational simulations with the B3LYP/6-311+G** method yielded energy values of 14.237 kcal/mol for furan and 10.868 kcal/mol for pyrrole. Unfortunately, the DFT calculations did not produce satisfactory results for conjugated polymers based on furan and pyrrole, even after accounting for electron correlation energy. Due to significant deviations exceeding ±5 kcal/mol in the monomers, further calculations for difuran and dipyrrole were abandoned. It was concluded that pursuing these calculations would not yield meaningful results.

Conclusions

Novel conducting polymers have garnered significant attention from researchers due to their potential applications as biosensors, organic semiconductors, and various other fields. The need for energy efficiency and consideration of environmental impact has brought focus to key factors like heats of formation of these compounds. However, conducting experiments to measure such quantities is not straightforward, leading to limited reported results in this area. Overcoming this lack of experimental data can be achieved by utilizing reliable computational models, which can also facilitate exploration into new compound classes. For the development of effective vertex detectors, studying the heats of formation of conducting polymers is crucial. These heats of formation represent the energies of compounds in their standard states, providing fundamental insights. Yet, accurately measuring these quantities through experiments is both challenging and time-consuming, demanding precise design and controlled measurement conditions.

References

[1] http://preprint.chemweb.com/physchem/0103028

[2] C.S. Belotindos, "An Ab Initio Study on the Determination of Heats of Formation for the Reaction of Fe+ and Co+ With Acetone", Undergraduate Thesis, MSU-IIT, Iligan, Unpublished (2001).

[3] C. D. Gutsche and D. J. Pasto, Fundamentals of Organic Chemistry, Copyright © 1975 Prentice- Hall Inc., Englewood Cliffs, New Jersey.

[4] Hyperchem TMRelease3. Windows Molecular Modelling System, © 1993, HyperCube, Inc. and Autodesk, Inc. Developed by HyperCube, Inc.

[5] P. Walters and M. Stahl, BABEL Program (version 1.1) Copyright © 1992, 93, Dolota

Research Group, Department of Chemistry, University of Arizona.

[6] J. B. Foresman and Æ. Frisch, Exploring Chemistry With Electronic Structure Methods, 2nd ed. Gaussian, Inc., Pittsburgh, P. A. 1995. [1] J. Labannowski, L. Schmitz, K.H. Chen, and N. L. Allinger, "Heats of Formation of Organic Molecules by Density Functional Theory: II. Alkanes", Journal of Computational Chemistry, Vol. 19, No. 12, 1421-1430 (1998), © 1998 John Wiley & Sons, Inc.

[7] R.J. Berry, C.J. Ehlers, D.R. Burgess Jr., M. R. Zachariah, M. R. Nyden, and M. Schwartz, "Halon thermochemistry: ab initio calculations of the enthalpies of formation of fluoroethanes", Journal of Molecular Structure (Theochem), 422, 89-98, © 1998 Elsevier Science B. V.

22nd Iranian Chemistry Congress (ICC22)
Iranian Research Organization for Science and Technology (IROST)
13-15 May 2024

03231-97589

IROST

The Use of Fullerenes in Cancer Therapy: A Promising Advancement

Peyvand Ghanbarpour[a], Hossein Shirani[b,c,*] and Mohanna Badri[c]

Corresponding Author. E-mail: hossein_shirani@iust.ac.ir

[a] Water safety research center, food and drug administration, ministry of health and medical education, Tehran, Iran.
[b] Department of Chemistry, Iran University of Science and Technology, P.O. Box 16846-13114, Tehran, Iran.
[c] Department of Microbiology, Faculty of Biological Sciences and Technology, University of Science and Culture, Tehran, Iran.

Abstract: Cancer remains a significant contributor to mortality rates across the globe. Existing drugs often have adverse side effects because they are not specific enough in their targeting. This article explores the functionalization, diverse characteristics, and potential uses of C60 fullerenes in cancer treatment through Quantum mechanics calculations and DFT techniques.
Keywords: Nanotechnology, Cancer, Drug Delivery, C60 fullerenes, density functional theory

Introduction

In recent years, nanoparticles (NPs) have become increasingly important in the field of cancer treatment, alongside traditional treatments like chemotherapy, surgery, radiation therapy, immunotherapy, and hormone therapy. Chemotherapy drugs face challenges such as poor stability and solubility, as well as toxicity to healthy cells leading to side effects like hair loss, appetite loss and nerve damage. Another obstacle in cancer treatment is multidrug resistance (MDR), where cancer cells become resistant to multiple anti-cancer drugs. Nanotechnology offers a promising solution to these issues by targeting specific tissues and reducing systemic toxicity. This approach can also help overcome MDR by evading drug resistance mechanisms. Furthermore, nanoparticles have potential not only as treatments but also as diagnostic tools [1-3]. A wide range of nanotechnology-based products have been successfully employed in the realm of cancer therapy, including liposomes, dendrimers, colloidal silica nanoparticles, magnetic nanoparticles, polymeric micelles, and solid-lipid nanoparticles (SLNs). Cutting-edge nanomedicine and nanodevices such as quantum dots, nanowires, nanotubes, nano cantilevers, nanopores, nano-shells, and nanoparticles hold immense promise for a variety of cancer treatments. Carbon-based nanomaterials, like carbon nanotubes (CNTs), graphene oxide (GO), nano diamonds, graphene quantum dots (GQDs), and fullerenes, are renowned for their exceptional inherent properties [4-6].

Methods

At the outset, DOX-nanocarrier's molecular structure (Fig. 1) was crafted through the utilization of GaussView software, then proceeded with quantum mechanical estimations at the B3LYP/6–31G theoretical method via Gaussian09 software.

Results and Discussion

Properties of fullerenes

Fullerenes demonstrate distinctive structural qualities that have solidified their importance across multiple industries. Resembling a soccer ball in shape, they are comprised of 60 carbon atoms organized into 12 pentagons linked by single C5-C5 bonds and 20 hexagons linked by double C5-C6 bonds. These compounds are made up of fused rings and conjugated bonds, showcasing a mixture of sp2 and sp3 bond hybridization, with an average bond length of 0.145 nm for single bonds and 0.141 nm for double bonds.

Fullerenes display a geometric shape known as a truncated icosahedron, where each carbon atom is surrounded by an identical arrangement. Among these fullerenes, C60 is distinguished by its smallest cage structure, making it both reactive and stable due to adherence to the isolated pentagon rule. This rule stipulates that each pentagon within the structure must be surrounded by exactly 5 hexagons. Because of their electron deficiency caused by poor electron delocalization, fullerenes possess strong antioxidant properties and are commonly used in cancer treatment. Their hydrophobic nature results in low solubility in polar solvents but high solubility in organic solvents such as benzene, toluene, and chloroform. To increase solubility in polar solvents, fullerenes can be modified with polar groups. These molecules are highly reactive as electron acceptors and can undergo a wide range of chemical reactions. Additionally, their inertness allows them to encapsulate various ionic species within their cage-like structure. The diverse properties of fullerenes, including high hydrophobicity, strong intermolecular cohesion, photo-activity, reactivity, and electron acceptance and release capabilities, make them suitable for a variety of chemical modifications and biomedical applications.

22nd Iranian Chemistry Congress (ICC22)
Iranian Research Organization for Science and Technology (IROST)
13-15 May 2024

03231-97589

Fullerenes in Tumor Therapy

Regular cellular activities and unusual occurrences within mitochondria can lead to the production of free radicals. An excess of these reactive oxygen species, including peroxides like ROS, hydroxyl radicals, superoxide radicals, and singlet oxygen, can cause damage to cells and potentially contribute to cancer development. Numerous research studies have demonstrated the harmful effects of these reactive oxygen species. Fullerene's natural ability to scavenge free radicals represents a significant advancement in cancer treatment. Due to their small size, fullerenes exhibit enhanced permeability and retention effect (EPR) in tumor tissues, reducing the concentration of ROS without being depleted and acting as a sponge for free radicals. Additionally, fullerene inhibits the activation of proto-oncogenes, limits tumor growth, and suppresses angiogenesis, thereby promoting anti-cancer activity.

Because of their electron-deficient nature and limited electron delocalization, fullerenes exhibit high reactivity towards free radicals. The carbon bonds within the fullerene structure have the ability to abstract electrons, providing it with antioxidant qualities. The interaction between fullerenes and reactive oxygen species (ROS) involves an exchange of electrons on the outer shell, resulting in radical scavenging capabilities. This antioxidant mechanism is vital in the potential applications of fullerene in cancer therapy. Additionally, fullerenes, which are hydrophobic in nature, can be altered with polar groups to enhance their antioxidant properties. This modification allows for increased antioxidant activity by improving the solubility of fullerenes in aqueous environments. These distinct characteristics make fullerenes a viable option for addressing diseases related to oxidative stress.
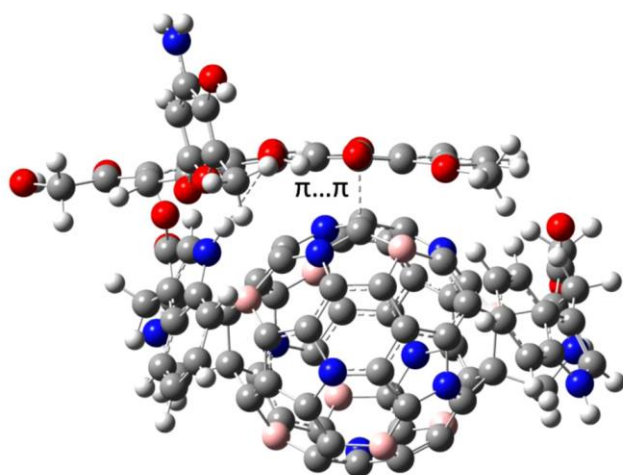
Fig. 1. Structure of trans1 isomer of DOX-nanocarrier optimized using 6-31G basis set.

Conclusions

Recent developments in cancer nanotechnology show great potential in transforming how early cancer detection is done, leading to more precise diagnosis and treatment. Conventional imaging methods carry the risk of harming healthy cells and lack the ability to target cancerous tumors accurately. However, advancements in the manufacturing of fullerenes and their variants have pushed forward research into their use in fighting cancer. Studies indicate that fullerenes derivatives possess various properties that can effectively combat tumor growth and spread. These properties include boosting the immune system, reducing oxidative stress, blocking the spread of cancer cells, stopping cell division, inhibiting the formation of new blood vessels to tumors, and overcoming drug resistance. Despite these encouraging results, there remain obstacles in utilizing fullerene derivatives as efficient anti-cancer agents.

It is crucial to address these challenges to fully harness the potential of fullerenes in controlling tumor growth and preventing metastasis. The exceptional and captivating features of fullerene derivatives, such as their optical, electrical, and magnetic properties, are greatly influenced by the methods used for their production and refinement. In order to fully leverage these characteristics, a thorough understanding of the fundamental traits that dictate their behavior and precise synthesis techniques for controlling their size and shape is crucial. Despite these challenges, the rapid advancement of technology and the drive for innovation ensure that the field of nanomedicine will continue to evolve, with fullerene nanoparticles set to transform therapeutic approaches.

References

[1] Alargova RG, Deguchi S, Tsujii K (2001) Stable colloidal dispersions of fullerenes in polar organic solvents. J Am Chem Soc 123(43):10460–10467

[2] Awasthi R, Roseblade A, Hansbro PM, Rathbone MJ, Dua K, Bebawy M (2018) Nanoparticles in cancer treatment: opportunities and obstacles. Curr Drug Targets 19:1696–1709

[3] Azami T, Kasuya D, Yuge R, Yudasaka M, Iijima S, Yoshitake T, Kubo Y (2008) Large-scale production of single-wall carbon nanohorns with high purity. J Phys Chem C 112:1330–1334

[4] Bai Y, Wu X, Ouyang P, Shi M, Li Q, Maimaiti T, Lan S, Yang ST, Chang XL (2021) Surface modification mediates the interaction between fullerene and lysozyme: protein structure and antibacterial activity. Environ Sci Nano 8:76–85

[5] Bakry R, Vallant RM, Najam-ul-Haq M, Rainer M, Szabo Z, Huck CW, Bonn GK (2007) Medicinal applications of fullerenes. Int J Nanomed 2(4):639–649

[6] Bezmelnitsin VN, Eletskii AV, Schepetov NG, Avent AG, Taylor R (1997) Isolation and characterisation of C 70 O. J Chem Soc Perkin Trans 2(4):683–686

22nd Iranian Chemistry Congress (ICC22)
Iranian Research Organization for Science and Technology (IROST)
13-15 May 2024

03231-97589

IROST

Synthesis, Characterization and Solvatochromism Studies of a New Mixed-Chelate Copper(II) Complex

Mohsen Javadian, Hamid Golchoubian*

Corresponding Author E-mail: golchobian@gmail.com

Department of Chemistry, University of Mazandaran, Babolsar, Iran.

Abstract: A new mixed-chelate copper(II) complex, $[Cu(L)(acac)(ClO_4)]ClO_4$ (L = 2-[(2-diisopropylamino-ethylamino)-methyl]-pyridine), was synthesized and thoroughly characterized. X-ray diffraction confirmed its unique, distorted square pyramidal geometry. The complex exhibited solvatochromism, with its visible absorption band shifting red (bathochromic shift) in different solvents. This sensitivity to solvent polarity suggests interactions between the solvent and the weakly bound perchlorate ion. Statistical analysis (stepwise multiple linear regression) revealed the Gutmann donor number (DN) as the key factor influencing the shift. Higher DN solvents caused a larger red shift, suggesting stronger interactions. This opens potential applications for this complex as a chromogenic sensor for solvent polarity determination.

Keywords: Mixed-Chelate; acetylacetonate; diamine ligand; copper(II); solvatochromism

Introduction

The development of advanced sensor materials is crucial for various fields like medical diagnostics and environmental monitoring [1]. Transition metal complexes, especially copper(II) complexes, are promising candidates due to their tunable properties. One particularly useful property is solvatochromism, where a material's color changes based on the surrounding solvent [2]. In transition metal complexes, solvatochromism is influenced by factors like the metal ion and the ligands. Mixed-chelate copper(II) complexes, with a combination of ligand types, offer a unique way to control this behavior [3]. By strategically designing these complexes, scientists can create highly responsive and selective color-changing materials for sensor applications [4]. This paper builds on previous research by presenting a new mixed-chelate copper(II) complex. We explore how the carefully chosen ligands affect the complex's solvatochromic behavior in various solvents. We will investigate the complex's response to light and the mechanism behind its color change.

Experimental Section

The reaction between 2-[(2-diisopropylamino-ethylamino)-methyl]-pyridine (L), acetylacetone, copper(II) perchlorate, and sodium carbonate in ethanol yielded a green complex. Recrystallization from nitrobenzene with diethyl ether vapor diffusion provided suitable crystals for X-ray analysis (yield: 28%).. Selected IR data (υ/cm^{-1} using KBr): 3102 (m, N–H str.), 2679 (m, N–H+ str.), 1579 (s, C=O str.),1522 (s, C=C str.),1434 (s, –CH2– bend.), 1087 (s, C–O str.), 629 (m, C–O bend.). Anal.

Calcd. For $C_{19}H_{33}N_3Cl_2O_{10}Cu$ (MW=615.9 g.mol-1): C, 38.17; H, 5.56; N, 7.03; Found: C, 38.27; H, 5.27; N, 7.09%. Molar conductance ($\Lambda_M /\Omega^{-1} cm^2 mol^{-1}$): 283 in AN

Results and Discussion

This mixed-chelate complex contains a diamine group and an acetylacetonate ligand. The amine moiety of ligand L in the complex acts as a base, accepting a proton from the reaction medium and converting to -NH+ (scheme 1)
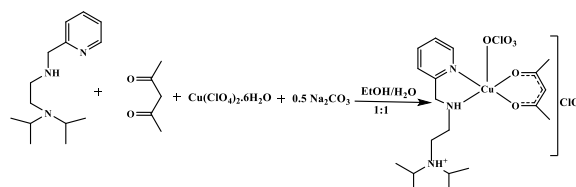
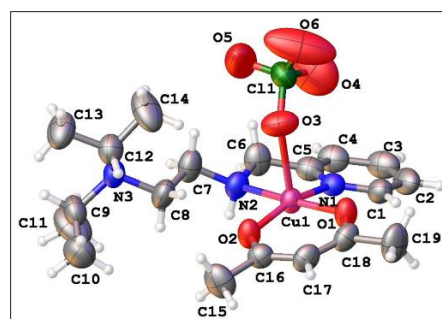**Scheme 1:** Synthetic outline of the complex

Fig.1: An ORTEP view of the complex

X-ray analysis reveals the complex structure (Fig 1). Copper(II) sits in a distorted square pyramidal geometry, coordinated by a diamine ligand, an acetylacetonate, and two perchlorates (details in Table 3). The remaining

22nd Iranian Chemistry Congress (ICC22)
Iranian Research Organization for Science and
Technology (IROST)
13-15 May 2024

03231-97589

IROST

nitrogen atom in the ligand forms a hydrogen bond with a perchlorate anion.

The copper complex is highly soluble and displays solvatochromism, changing color from green to blue in different solvents (Fig 3). This is due to shifts in the absorption band (Table 4) caused by interactions between the complex and the solvent molecules.
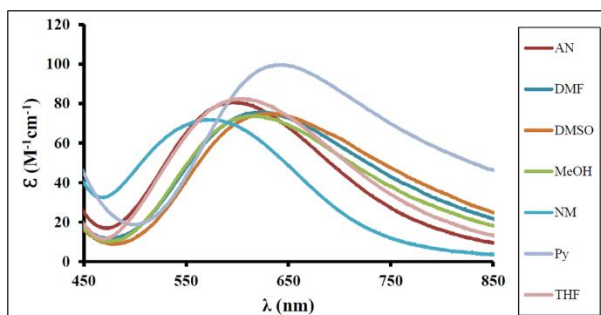

Fig. 2: Absorption spectra of the complex in selected solvents

Stepwise multiple linear regression (SMLR) analysis identified the Gutmann donor number (DN) as the primary factor influencing solvatochromism (Table 1). A positive coefficient for DN indicates a red shift with increasing solvent donor ability (better donors). This is further confirmed by the linear trend between λ_{max} (absorption wavelength) and DN (Fig. 3). In addition, the proposed mechanism involves the dissociation of a weakly bound perchlorate anion from the complex due to stronger interactions with high DN solvents. This dissociation allows solvent molecules to approach the complex more effectively, influencing its electronic transitions and leading to the color change.

Table1: The equation resulted from the linear correlation of the λ_{max} values with DN of the solvents for complex.

Equation	F	R	S.E.	$\Delta\lambda$ (nm)
λ_{max}= 2.11(±0.06) $DN_{solv.}$ + 564.31(±1.26)	1443	0.996	2.42	87
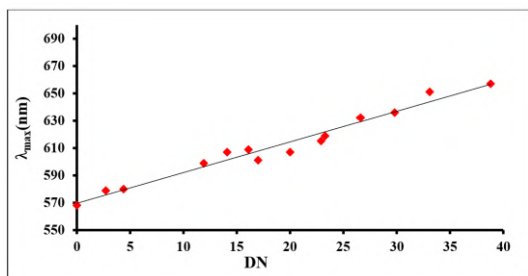
Fig. 3: Dependence of λ_{max} values of the complex on the solvent DN values.

The observed solvatochromism can be attributed to the interaction of solvent molecules with the weakly bound perchlorate (ClO_4^-) anion in the axial positions of the complex. This interaction facilitates the displacement of the ClO_4^- anion, leading to the solvation of the metal center (Cu(II)) at the axial sites. As the solvent polarity increases (indicated by higher Gutmann donor number, DN), the polar solvent molecules interact more favorably with the Cu(II) ion. This interaction can be visualized as the dxy, dyz, and dxz orbitals of the copper ion being "pushed up" in energy due to their interaction with the approaching solvent molecules positioned above and below the molecular plane (Figure S3) . Consequently, the energy gap between the ground state and the excited state involved in the d-d transition decreases. This decrease in energy gap results in a red shift (bathochromic shift) of the broad d-d transition band observed in the complex's visible absorption spectrum.

Conclusions

A novel copper(II) complex was synthesized and characterized, exhibiting a tunable electronic structure due to its mixed-ligand environment. The complex was found to be solvatochromic, with a red shift observed upon increasing solvent donor ability. This behavior, attributed to solvent interaction with the weakly bound perchlorate anion, was statistically confirmed using the Gutmann donor number model. These findings suggest the potential of the complex as a chromotropic sensor for solvent polarity, opening doors for the development of advanced materials in sensing applications..

References

[1]. Ebralidze, I. I., Laschuk, N. O., Poisson, J., & Zenkina, O. V. (2019). Colorimetric sensors and sensor arrays. In Nanomaterials design for sensing applications (pp. 1-39). Elsevier.

[2] Pierpont, C. G., & Kitagawa, S. (2007). Inorganic Chromotropism

[3] Ghaseminasab, F., Golchoubian, H., & Shirvan, A. (2024). Solvatochromism in mixed-chelate of copper (II) with tetramethyl ethylenediamine and 2, 4-dihydroxybenzophenone, experimental and computational study. Journal of Molecular Structure, 1295, 136623.

[4] Klymchenko, A. S. (2017). Solvatochromic and fluorogenic dyes as environment-sensitive probes: design and biological applications. Accounts of chemical research, 50(2), 366-375.

22nd Iranian Chemistry Congress (ICC22)
Iranian Research Organization for Science and Technology (IROST)
13-15 May 2024

03231-97589

IROST

Green in-situ preparation of pectin/zeolitic imidazolate metal-organic framework nanocomposite hydrogel beads as an antibacterial agent

Hanieh Hamedi Hagi, Siamak Javanbakht and Reza Mohammadi*

Corresponding Author E-mail: r.mohammadi@tabrizu.ac.ir

Polymer Research Laboratory, Faculty of Chemistry, University of Tabriz, Tabriz, Iran.

Abstract: Antibacterial medications have always carried a significant risk of becoming less effective against bacteria. This work developed zeolitic imidazolate metal-organic framework (ZIF-8), which has antibacterial properties, to improve the biological efficiency of pectin (Pec) hydrogel beads. According to antibacterial studies, the Staphylococcus aureus bacteria had an inhibition zone measuring 14 ± 0.5 mm. The produced nanocomposite hydrogel beads have a good chance of being used as an antibacterial bio-platform, based on the results that were obtained.

Keywords: Antibacterial, Pectin, Nanocomposite, Metal-Organic Frameworks, Zeolitic Imidazolate

Introduction

In recent years, antibacterial resistance has become one of the most important global health concerns. However, one of the main problems restricting the benefits of antibiotics in infection control is the widespread development of antimicrobial resistance. This issue is now the second greatest cause of death worldwide. Because antibacterial agent delivery systems can inhibit the growth of bacteria and increase the effectiveness of drugs, they have garnered a lot of attention. Biopolymers are present in natural polymers and polymer-based composites that are sourced from flora, animals, bacteria, and fungi. Pectin has unique characteristics because of the presence of hydroxyl and carboxyl functional groups in its structure [1]. Studies have shown that the performance of biopolymer matrices can be enhanced by the addition of various elements, including carbon nanotubes, metal organic frameworks, double layer hydroxides, and nanoparticles [2]. Because of their large pore volumes, high surface areas, and adjustable pore sizes, porous materials make excellent candidates for biomedical applications [3]. Their non-toxicity, high pseudoenzymatic activity, high specific surface, continuous release of metal ions, and bioactive ligands make them appropriate for use in the antimicrobial field as well. To our knowledge, polysaccharide/MOF nanocomposite materials have only infrequently been synthesized using the in situ synthesis method. The in situ method was employed in this work to synthesis bioactive ZIF-8 [4].

Experimental Section

The proper proportions of Pec, Zn, and IMZ were used to create the beads. The initial mixture was made by combining IMZ, Pec, and glycerol in an aqueous solution and stirring it at 300 revolutions per minute. After creating a second mixture with 50% ethanol and water, a specific amount of Zn $(NO_3)_2.6H_2O$ and $CaCl_2.2H_2O$ as a cross-linker was added. To generate beads, the last step was to gradually add drops of the first mixture to the second mixture, as shown in the (scheme). To create the Pec/ZIF-8 nanocomposite hydrogel bead, ZIF-8 crystals are in-situ generated inside the Pec network's pores by diffusion of Zn^{2+} into the Pec matrix containing IMZ [4].
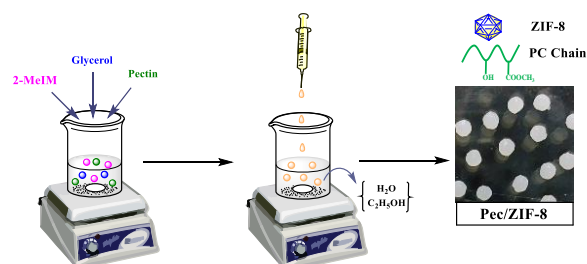
Results and Discussion

To understand the interactions between substances, the in-situ synthesis of ZIF-8 into the Pec polymeric matrix, the FT-IR analysis was considered. shoulder peaks at 688 cm^{-1} and in the region of 757 cm^{-1} related to the vibrations of the Zn-N and Zn-O of ZIF-8, respectively, appeared [5], confirming the in-situ forming ZIF-8 in the network of Pec hydrogel (Fig. 1). The microstructure Pec network is related to a typical amorphous polysaccharide peak at 2 around 20° visible in the XRD patterns of synthetic hydrogel beads (Fig. 2). Pec biopolymer's amorphous structure is not significantly impacted by the crystalline structure of ZIF-8. This is most likely caused by the nanocomposite structure's low aggregate and good dispersion of zif-8 nanoparticles. Fig. 3 shows the release profiles of Zn^{2+} from nanocomposite hydrogel beads at pH (1.2, 6.8, and 7.4) and 37 °C. The release curve of Zn^{2+} shows an initial low burst release for up to 1 h, followed by a controlled and prolonged release for up to 8 h. One of the main features affecting the release profile of the

22nd Iranian Chemistry Congress (ICC22)
Iranian Research Organization for Science and Technology (IROST)
13-15 May 2024

03231-97589

ISC

IROST

drug carrier is its morphology. Fig. 4 shows Pec hydrogel beads with a spherical morphology and a porous and wrinkled surface structure. As can be observed in Fig, ZIF-8 nanoparticles changed the surface morphology of the beads.
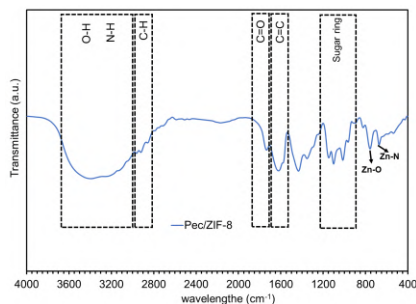

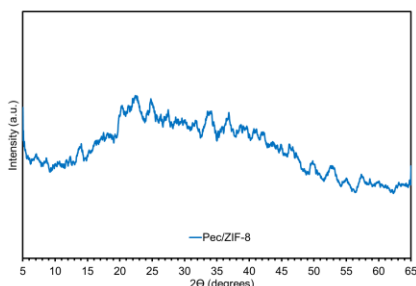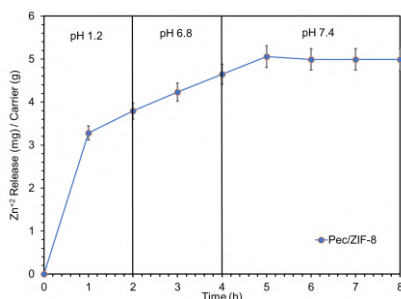**Fig.1:** FT-IR spectra for Pec-ZIF-8.

Fig.2: The XRD pattern of Pec/ZIF-8.

Fig.3: Zn^{2+} release behavior of Pec/ZIF-8 at pH (1.2, 6.8, and 7.4) and 37 °C. The values are reported as mean ± SD of three experiments.
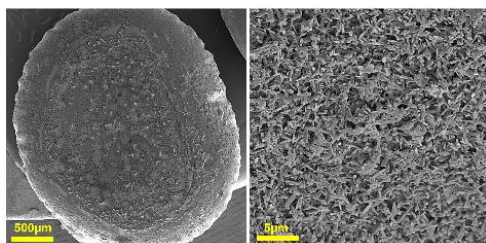
Fig.4: SEM image of the Pec/ZIF-8.

Conclusions

This research explores a novel method for producing highly productive antibacterial hydrogel beads based on Pec hydrogel. Through in situ synthesizing, the ZIF-8 was

successfully incorporated into the Pec matrix. Due to the use of a green method, i.e. e., in situ straightforward synthetic techniques, and the accessibility of raw materials. The rigidity and release performance of the Pec beads' biopolymeric network were effectively controlled by the integration of the ZIF-8. The hydrogel bead containing ZIF-8 showed a minor initial burst release and controlled release over 8 h in the release profile of Zn^{2+}. Surprisingly, the Pec/ZIF-8 hydrogel beads demonstrate a strong antibacterial property in comparison to. Additionally, S. aureus bacteria show compatibility with HT29 cell lines. The findings demonstrated that the prepared hydrogel beads can be used to develop a safe (over about 85% cell viability) and simple system using a green technique, with potential use as an antibacterial agent.

References

[1] J.-q. Zhang, H.-c. Li, J. Wang, S.-s. Liu, J. Li, D.-q. Li, Dopamine-functionalized pectin-based Pickering emulsion as an oral drug delivery system, Colloids and Surfaces A: Physicochemical and Engineering Aspects (2023) 131807.

[2] M.S. Islam, M.M. Islam, in Physical and chemical properties of sustainable polymers and their blends, pp. 37-57, Elsevier, (2021).

[3] S. Mallakpour, M. Hatami, International journal of biological macromolecules, 122 (2019)

[4] L. Wang, H. Xu, J. Gao, J. Yao, Q. Zhang, Coordination Chemistry Reviews, 398 (2019) 213016.

[5] C. Wu, Q. Liu, R. Chen, J. Liu, H. Zhang, R. Li, K. Takahashi, P. Liu, J. Wang, Fabrication of ZIF-8@ SiO₂ micro/nano hierarchical superhydrophobic surface on AZ31 magnesium alloy with impressive corrosion resistance and abrasion resistance, ACS applied materials & interfaces 9(12) (2017) 11106-11115.

Mononuclear copper(II) complexes containing chelating ligand of N-(pyridin-2-ylmethyl)butan-2-amine as chromotropic probe

Reyhaneh Hamedani*, Hamid Golchoubian, Ati Shirvan

Corresponding Author E-mail: reyhanehhamedani.313@gmail.com

Department of Inorganic Chemistry, Faculty of Chemistry, University of Mazandaran, Babolsar, Iran.

Abstract: The synthesis of a mononuclear copper(II) complexes of formula [LCuBr$_2$] where L is a bidentate ligand of *N*-(pyridin-2-ylmethyl)butan-2-amine is reported. The complex is fully characterized by physic chemical techniques. The structure of the complex is a distorted square-planar arrangement around copper(II) ion. The chromotropism behavior of the complex, including thermo- and solvatochromism, was investigated.

Keywords: Copper(II) complex; Chromotropism; Mononuclear complex

Introduction

Chromotropism refers to a material's ability to change color in response to external stimuli, including temperature (thermochromism), solvent (solvatochromism), light (photochromism), pressure (piezochromism), electric field (electrochromism), pH (halochromism), and specific ions (ionochromism) .The study of chromotropic behavior in inorganic compounds, particularly transition metal complexes, has gained significant interest in recent decades due to its potential applications in various fields [1]. Copper(II) complexes are particularly attractive candidates for chromogenic materials since Copper(II) possesses a d^9 electron configuration, leading to characteristic d-d electronic transitions that often fall within the visible region of the electromagnetic spectrum, resulting in colored complexes. It can adopt various coordination numbers (e.g., 2, 3, 4, 6) and geometries (e.g., tetrahedral, square planar, octahedral) depending on the ligands, influencing the d-orbital splitting and ultimately the observed color. Many Cu(II) complexes exhibit the Jahn-Teller effect, a phenomenon where the distortion of the coordination environment around the metal ion lowers the overall energy of the complex. This effect can further influence the electronic transitions and color. By strategically selecting appropriate ligands, researchers can design Cu(II) complexes with tailored chromotropic properties. Multidentate ligands, with multiple donor atoms chelating the metal center, enhance the stability of these complexes through the chelate effect. Herein, the synthesis of a mononuclear copper(II) complexes of formula [LCuBr$_2$] where L is a bidentate ligand of N-(pyridin-2-ylmethyl)butan-2-amine is reported and its chromotropic behaviors including thermochromism, solvatochromism, and halochromism is investigated.)

Experimental Section

The ligand L was prepared following a previously reported procedure [2]. To a solution of the ligand (0.328 g, 2 mmol) in ethanol (6 mL), a solution of copper(II) bromide (0.447 g, 2 mmol) in ethanol (10 mL) was gradually added. The reaction mixture was stirred at room temperature for 2 hours. The desired copper(II) complex subsequently precipitated as a green solid. Recrystallization was achieved by diffusing diethyl ether into an acetonitrile solution of the crude product. The final yield was 54% (0.418 g).

Results and Discussion

The ligand was characterized by NMR and IR spectroscopy and the complex was fully characterized by elemental analysis, spectroscopic techniques (IR, UV-Vis,), thermal analysis, and computational study conductance measurements. The structure of the complex is a distorted square-planar arrangement around copper(II) ion.
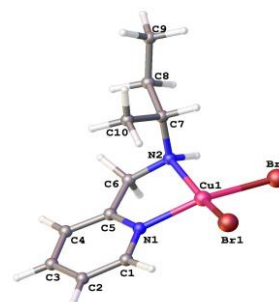

Fig.1: A plot of [LCuBr$_2$]

The complex exhibits thermochromism in high-boiling-point solvents such as DMSO and DMF. The visible spectra of the compound were examined over a temperature range of 25 to 170 °C in DMSO (Fig. 2). The complex displays reversible thermochromism, with the initial green color of the solution gradually shifting to blue up to

22nd Iranian Chemistry Congress (ICC22)
Iranian Research Organization for Science and Technology (IROST)
13-15 May 2024

03231-97589

90 °C and becoming light brown as the temperature reaches 160 °C. The light brown color change is likely due to the substitution of DMSO molecules with coordinated diamine and bromide ligands ([Cu(DMSO)$_n$]Br$_2$), as depicted in Scheme 1.
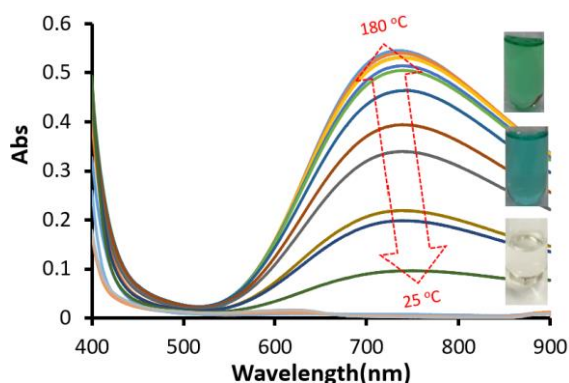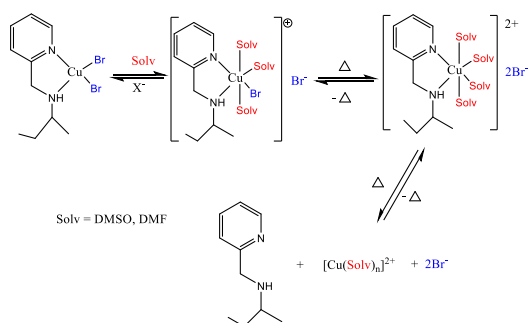

Fig.2: Thermal behavior of the complex in DMSO.

Scheme 1: Mechanistic insights into the complex in DMSO and DMF at elevated temperatures.

The complex exhibits solubility in a wide range of solvents and demonstrates solvatochromism. When dissolved in various organic solvents, the solution color of the complex shifts from green to blue, as illustrated in Fig. 3. The color variations originate from changes in the d–d band of the Cu(II) center. The shift in the d–d band of the complex due to solvent variation may be attributed to structural changes in solvents with different polarity and the donor/acceptor interaction between solute and solvent (Routes 1 and 2 in Scheme 2).
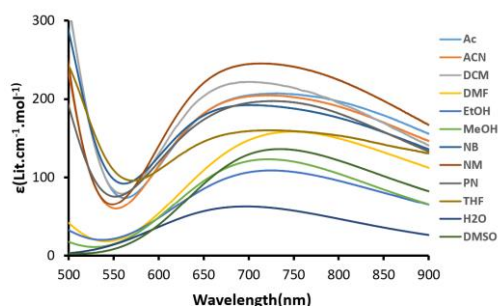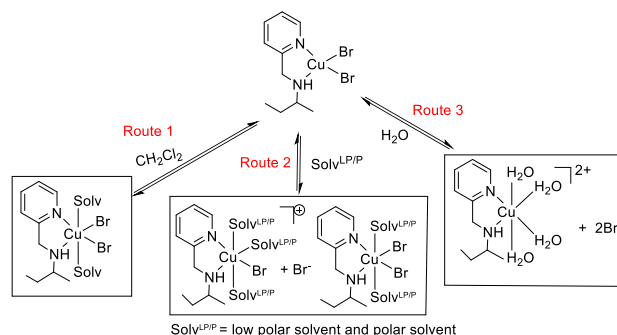

Fig.3: Visible absorption spectroscopic analysis of the complex in selected solvents.

Scheme 2: Structural response of the complex to solvent polarity

Conclusions

A distorted square-planar complex, [CuLBr$_2$], was characterized, and its geometric structure, electronic properties, and spectroscopic features were extensively examined. Heating the complex in DMSO and DMF solvents results in the removal of ligands and subsequent coordination of solvent molecules, leading to changes in the copper(II) coordination geometry and the color of the solution. Additionally, the complex exhibits solvatochromism in solvents with varying polarities, with the observed solvatochromism stemming from structural alterations and solvation effects in different solvents. These complexes demonstrate responsiveness to combinations of stimuli (solvent, and heat), primarily driven by structural modifications within the complex.

References

[1] Linert, W., Fukuda, Y., & Camard, A. (2001). Chromotropism of coordination compounds and its applications in solution. Coordination Chemistry Reviews, 218, 113-152. https://doi.org/10.1016/S0010-8545(01)00359-9

[2] Nazari, R., Golchoubian, H., & Bruno, G. (2019). Mononuclear copper (II) complexes containing chelating ligand of 2-methyl-N-(pyridine-2-yl-methyl) propane-2-amine as chromotropic probes. Journal of the Iranian Chemical Society, 16, 1041-1052. https://doi.org/10.1007/s13738-018-01577-z

[3] Nadarkhani, S., Golchoubian, H., & Shirvan, A. (2023). Synthesis, crystal structure, and chromotropism properties of Dihalo N-2-ethanolpicolylamine copper (II). Journal of Molecular Structure, 1276, 134801. ttps://doi.org/10.1016/j.molstruc.2022.134801

22nd Iranian Chemistry Congress (ICC22)
Iranian Research Organization for Science and Technology (IROST)
13-15 May 2024

03231-97589

ISC

IROST

Metal-organic framework Cu-BDC/SS electrocatalyst for efficient oxygen evolution reaction

Afsaneh Ahmadi[a], Mohammad Chahkandi*[a], Mahboobeh Zargazi [b]

Corresponding Author E-mail: chahkandimohammad@gmail.com

[a] Department of Chemistry, Faculty of Science, Hakim Sabzevari University, Sabzevar, Iran.

[b] Sonochemical Research Center, Department of Chemistry, Faculty of Science, Ferdowsi University of Mashhad, Mashhad, Iran.

Abstract: The intrinsic features of 2D metal-organic frameworks (MOFs), including efficient charge transfer and an abundance of coordination unsaturated active sites, have made them attractive candidates for electrocatalytic oxygen evolution reactions (OER). Herein, a novel thin film of Cu-BDC/SS fabricated on stainless steel mesh (SS) using electrophoretic deposition. The electrocatalyst Cu-BDC/SS exhibits an excellent OER performance with an incredibly low overpotential of 180 mV at 50 mA cm^{-2} and a tinyTafel slope of 40 mV·dec^{-1} in 1 M KOH solution.

Keywords: electrocatalyst; oxygen evolution reaction; Cu-BDC/SS

Introduction

The Oxygen Evolution Reaction (OER) is crucial for energy conversion in devices like fuel cells and metal-air batteries. Despite the development of numerous high-performance OER catalysts, achieving efficient OER at low overpotentials remains challenging [1]. The Oxygen Evolution Reaction (OER) involves a 4-electron transfer process, leading to high overpotentials. Noble metal oxides and their derivatives are currently the most effective catalysts for water oxidation, but their high cost limits widespread commercial use. Recent research has focused on finding noble-metal-free OER catalysts, such as 3d transition metal chalcogenides, phosphates, perovskite oxides, and metal-organic frameworks (MOFs) [2]. MOFs are promising electrochemical catalysts due to their high surface area, tunable pore size, and easy functionalization. However, they often have few active sites and low conductivity, limiting their practical application. Researchers are exploring ways to enhance their performance by coupling them with other materials that possess complementary properties [3]. Composite materials combining MOFs with other substances are being explored to leverage synergistic effects. Cu-BDC, a MOF with copper nodes connected by benzene-1,4-dicarboxylate linkers, shows promise for OER catalysis due to its active Cu sites. However, its low conductivity hinders its practical use as an OER catalyst [4]. In this work, the first step is the synthesis of Cu-BDC MOF by a solvothermal method using Cu metal ion and BDC organic linker. Then, by the EPD process, Cu-BDC MOF was deposited on a stainless steel mesh substrate. The synthesized Cu-BDC MOF was characterized by different characterization FT-IR, SEM, and XRD. Cu-BDC/SS electrocatalyst displayed OER performance, with a lower onset potential of 1.4 V vs RHE and a tafel slope of 40 mV dec^{-1}.

Experimental Section

Copper nitrate trihydrate and terephthalic acid were dissolved in DMF and heated in an autoclave at 120°C for 24 hours. After cooling, the blue precipitate was washed with DMF and dried at 60°C. A Cu-BDC MOF film was formed on stainless steel (Cu-BDC MOF/SS) using the electrophoretic deposition method. An electrolyte solution was prepared by sonicating Cu-BDC MOF in acetone and methanol. The film was deposited on the working electrode using a constant DC voltage for 2 minutes. After washing and drying, the Cu-BDC MOF film was ready for further use.

Results and Discussion

The morphology of the synthesized Cu-BDC MOF was examined by scanning electron microscopy (SEM). A SEM image (Fig. 1a) reveals that the resulting MOF takes a cubic morphology. Fig. 1b shows the FT–IR spectra of the synthesized MOF powder. The absorption peaks at about 1617, 1508, and 1395 cm^{-1} could be assigned to the characteristic vibrations of C=O, and the peaks at about 674 cm^{-1} belonged to the stretching vibrations of the Cu–O. To further verify the structure of the synthesized Cu-BDC MOF, the powder XRD pattern of the as-prepared MOF is presented in Fig. 1c. The peaks in the powder diffraction scans were compared against the predicted peaks from the literature. The main diffraction peaks of the as-synthesized Cu-BDC were consistent with those previously reported in the literature [5].
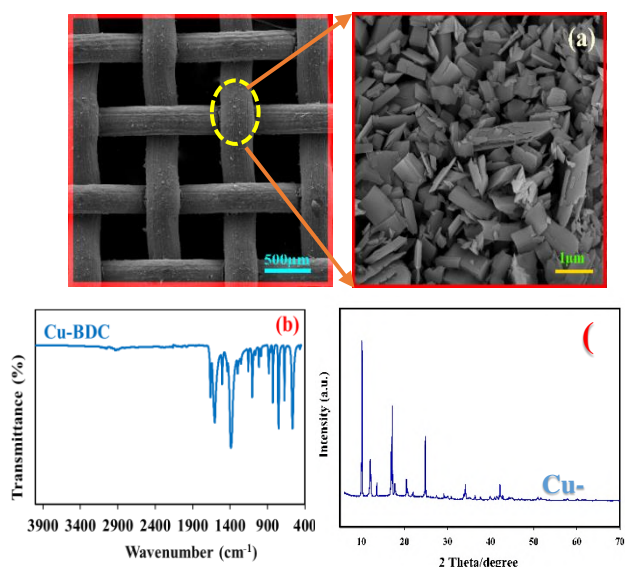
22nd Iranian Chemistry Congress (ICC22)
Iranian Research Organization for Science and Technology (IROST)
13-15 May 2024

03231-97589

IROST

Fig.1. (a) SEM image of Cu-BDC/SS, (b) FTIR spectroscopy, and (c) XRD pattern of powder Cu-BDC.

As can be exported from Fig. 6b, the Cu-BDC/SS electrode compared to the bare SS exhibited the best OER performance with the lowest overpotential of 180 mV to achieve anodic current densities of 50 mA cm^{-2} (Fig.2a). The favorable understanding of the reaction's kinetics was earned through the calculated Tafel plots based on the corresponding LSV curves. Cu-BDC/SS and bare SS have Tafel slopes of 43 and 96 mV dec^{-1}, respectively.
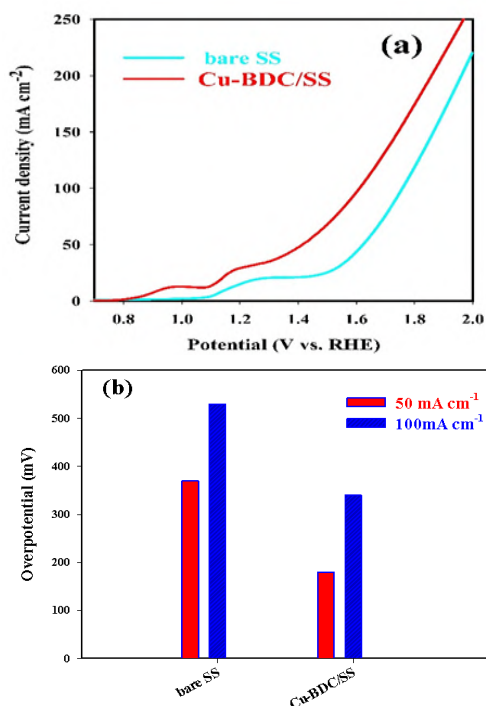
Fig.2. (a) LSV curves, and (b) the overpotential of Cu-BDC/SS and bare SS.

Conclusions

In summary, the Cu-BDC was synthesized via a straightforward solvothermal process. Subsequently, a thin film, formulated as Cu-BDC/SS, was fabricated on SS using a method through electrophoretic deposition. Cu-BDC/SS exhibits remarkable OER activity in alkaline electrolytes, requiring overpotentials of 180 and 340 mV to achieve current densities of 50 and 100 mA cm^{-2}, respectively, accompanied by a small Tafel slope of 40 mV dec^{-1} and long-term stability of at least 20 hours.

References

[1] Li, J. (2022). Oxygen evolution reaction in energy conversion and storage: design strategies under and beyond the energy scaling relationship. *Nano-Micro Letters*, *14*(1), 112..

[2] Han, N., Zhang, W., Guo, W., Pan, H., Jiang, B., Xing, L., ... & Fransaer, J. (2023). Designing oxide catalysts for oxygen electrocatalysis: insights from mechanism to application. *Nano-Micro Letters*, *15*(1), 185.

[3] Zhang, X., Zhang, S., Tang, Y., Huang, X., & Pang, H. (2022). Recent advances and challenges of metal-organic framework/graphene-based composites. *Composites Part B: Engineering*, *230*, 109532.

[4] Ahsan, M. A., Jabbari, V., El-Gendy, A. A., Curry, M. L., & Noveron, J. C. (2019). Ultrafast catalytic reduction of environmental pollutants in water via MOF-derived magnetic Ni and Cu nanoparticles encapsulated in porous carbon. *Applied Surface Science*, *497*, 143608.

[5] Shete, M., Kumar, P., Bachman, J. E., Ma, X., Smith, Z. P., Xu, W., ... & Tsapatsis, M. (2018). On the direct synthesis of Cu (BDC) MOF nanosheets and their performance in mixed matrix membranes. *Journal of membrane science*, *549*, 312-320.

Elimination of Cyanide by native bacterial strain

Sanaz Fotuhi [a], Fereshteh Jookar Kashi [*b], Zohreh Boroumand [c]

Corresponding Author E-mail: jookar@kashanu.ac.ir

[a, b] Department of Cell and Molecular Biology, Faculty of Chemistry, University of Kashan, Kashan, Iran.
[c] Head of NanoBioEarth department, applied research center of geological survey of Iran.

Abstract: Cyanide and combinations dependent on it are considered contaminants of sewage in different industries, such as photography, pharmacy, electrotyping, gilding, and especially mines, so its elimination is of special importance. There are three methods of purifying sewage containing cyanide: physical, chemical, and biological. The biological method is more cost-effective than the other methods. In this research, the capability of eliminating cyanide is considered by a biological strain isolated from the Sangan mine. This strain could eliminate 53% of the cyanide in the medium with an alkaline pH at 30 ^{0}C after 72 hours.

Keywords: Cyanide; Biological elimination; Bacterial strain

Introduction

Cyanide is a toxic combination that has very serious dangers for the health of humans and the environment. Drinking and inhaling it can influence the heart and brain and cause coma and death in a short time [1]. Methods of eliminating cyanide are divided into three physical, chemical, and biological categories. Common chemical methods for decomposing cyanide, alkaline chlorination, ozonation, oxidation of wet weather, and sulfur-based technology can be named [2]. Although various chemical and physical methods exist, they are very complicated and expensive and require a lot of equipment and reagents [3-5]. Various species of bacteria, fungi, ferments, and plants perform biological elimination of cyanide. Microorganisms can use cyanide as a source of nitrogen and change it to combinations with less toxic and harmless combinations [3-5].

Among cyanide elimination methods, the biological elimination method is preferred because it is cheaper, has the possibility of simultaneous production of biogas, and is harmless [6,7].

Materials and methods

Bacterial strains were isolated from sewage samples of Sangan iron mine and were cultured in Luria-Bertani Agar. Colonies were selected and cultured several times so that their purity was assured in agar culture medium. Samples were incubated at 30 ^{0}C for 72 hours. To cyanide elimination, 100 ml of bacterial suspension was adjusted to 0.5 McFarland. Then, in 100 ml Erlenmeyer flasks containing 10, 25, 100, 200, and 500 ppm density of cyanide, 20 ml of the bacterial suspension was added, and then the solutions were incubated at 30 ^{0}C, and 150 revolutions per minute (rpm). Then, after 48 and 72 hours, samples were taken from solutions, and amount of consumed cyanide was evaluated by titration method. Titration was performed with silver nitrate and potassium

iodide reagents, and the percent of elimination by strains was obtained through the following equation:

$$\text{Elimination Percent} = \frac{\text{Primary density} - \text{Secondary density}}{\text{primary density}} \times 100 \quad (1)$$

Result

This study was performed to determine the capability of bacteria to eliminate cyanide. After 72 hours, the efficacy of elimination hours was calculated as 53%, and Figure 1 demonstrates elimination efficacy in different densities.
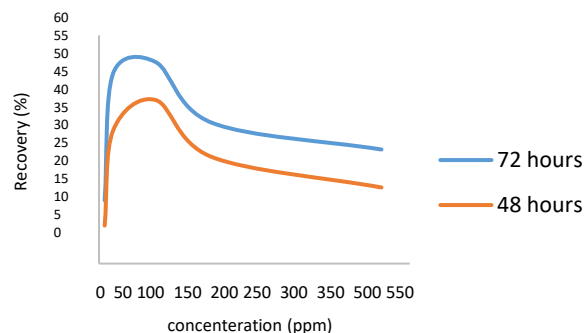

Fig.1: Removal efficiency in different cyanide concentrations

Refrences

[1] Deveci, H. A. C. I., Yazıcı, E. Y., Alp, I., & Uslu, T. U. N. C. A. Y. (2006). Removal of cyanide from aqueous solutions by plain and metal-impregnated granular activated carbons. International Journal of mineral processing, 79(3), 198-208 .

[2] Luque-Almagro, V. M., Blasco, R ,. Martínez-Luque, M., Moreno-Vivián, C., Castillo, F., & Roldán, M. D. (2011). Bacterial cyanide degradation is under review: Pseudomonas pseudoalcaligenes CECT5344, a case of an alkaliphilic cyanotroph. Biochemical Society Transactions, 39(1), 269-274.

[3] Dubey, S. K., & Holmes, D. S. (1995). Biological cyanide destruction mediated by microorganisms. World Journal of Microbiology and Biotechnology, 11, 257-265.

[4] Gupta, N., Balomajumder, C., & Agarwal, V. K. (2010). Enzymatic mechanism and biochemistry for cyanide degradation: a review. Journal of hazardous materials, 176(1-3), 1-13 .

[5] Dash, R. R., Balomajumder, C., & Kumar, A (2008). Treatment of metal cyanide bearin wastewater by simultaneous adsorption an biodegradation (SAB). Journal of Hazardou Materials, 152(1), 387-39

[6] Ebbs, S. (2004). Biological degradation of cyanide compounds. Current opinion in Biotechnology, 15(3), 231-236.

22nd Iranian Chemistry Congress (ICC22)
Iranian Research Organization for Science and Technology (IROST)
13-15 May 2024

03231-97589

IROST

Synthesis of allyl acrylate and 1,2-ethanedithiol copolymers via Thiol-Ene click reaction and investigating the effect of initiator on polymerization

Arezoo Sabri, Reza Najjar*

Corresponding Author E-mail: najjar@tabrizu.ac.ir

Polymer Research Laboratory, Faculty of Chemistry, University of Tabriz, 5166616471, Tabriz, Iran.

Abstract: Sulfur-containing polymers have many important useful characteristics, such as mechanical, electrical, and optical properties. Thiol-ene photopolymerization is a fast, controllable, and easy method in mild reaction conditions with no or minimal side products formation for the synthesis of sulfur-containing polymers. In this study, sulfur-containing polymers with linear and cross-linked structures were successfully synthesized using thiol-ene reactions, and it was discovered that the presence of a radical initiator has caused the polymer chains to form cross-links.

Keywords: Sulfur-containing polymers; thiol-ene polymerization; linear polymer; cross-linked polymer; radical initiator.

Introduction

Polymer materials play an incredibly important role in modern life. After development of polymer chemistry in the last century, sulfur and sulfur-containing moieties have been increasingly involved in the construction of various polymers. The presence of sulfur atoms in polymer structure, depending on the functional group types, can bring some important properties, such as mechanical, electrical, optical, and then adhesion to metals, resistance to heat, chemicals, radiation, bacteria, biocompatibility, and so on. Sulfur-containing polymers possess various classes and cover a broad range of properties, such as excellent thermal stability, high refractivity, selective absorption of some heavy metal ions, self-healing properties, enhanced dielectrical properties, and unique electrochemical properties [1]. Although the widely studied sulfur-containing polymers are still quite limited, sulfur-containing polymers with new and complex structures remain rare, and their design and synthesis still face many challenges, such as complicated and unstable monomer structures, poor solubility of polymers, chaotic product structures, etc [2].

Nowadays, plentiful synthetic techniques, such as polymerizations based on elemental sulfur, CS_2, and carbonyl sulfide (COS), have been developed for preparation of sulfur-containing polymers with diverse structures and functional properties. Since it was coined by Sharpless and coworkers in 2001, click chemistry had served as inspiration in most of the areas [3, 4].

Owing to the high efficiency of click chemistry, a variety of click reactions can be utilized including thiol-ene, thiol-yne, thiol-epoxy, thiol-isocyanate, and thiol-halogen clicks. Polymerization based on these click reactions have yielded various sulfur-containing polymers. Thiol-ene polymerisation is considered as a click-chemistry reaction for it can be carried out under mild conditions and normally provides a high yielding and the generation of inoffensive by-products [5].

Thiol-ene polymerisation proceeds as the traditional free-radical polymerisation, featuring three steps: initiation, propagation, and termination, plus a chain transfer step. In the mechanistically fundamental chain-transfer pace a carbon-centred radical transfers its electron to a thiol group. Generally, it is used a thiol:ene ratio of 1:1 in order to avoid side-reactions. It is important to notice that a proper copolymerisation between olefin and thiol molecules will only take place if the first is a diene and the latter a dithiol[6].

Experimental Section

Allyl acrylate (Fluka, 99%) 1,2-Ethanedithiol (Merck, 99%) were purchased and used without further purification. Azobisisobutyronitrile (AIBN) was purchased from Merck and was used after recrystallization from methanol.

In order to synthesize sulfur-containing polymers in this research, first allyl acrylate and 1,2- ethanedithiol monomers at a ratio of 1:1 and AIBN at a ratio of 0.01:1 were mixed together in 1 ml of toluene in a round bottomed flask equipped with a magnetic stir bar. The reaction mixture was deoxygenated by purging with nitrogen, then it was exposed to 70 °C and LED light irradiation until the completion of the reaction.

Results and Discussion

According to the obtained results, thiyl radicals are formed in these reactions due to the decomposition of S-

22nd Iranian Chemistry Congress (ICC22)
Iranian Research Organization for Science and Technology (IROST)
13-15 May 2024

03231-97589

IROST

H bonds in 1,2-ethanedithiol, which occurs through heat and light. Furthermore, AIBN initiator breaks down in the presence of heat and produces free radicals. The produced radicals target and adhere to the C=C bonds and the reaction continues until the monomers are used up.

The overall mechanism of these polymers is shown in Fig. 1 , that A and B represented linear copolymer and networked polymer, respectively. There is relatively little chance of allyl acrylate homopolymerization and the formation of cross-links between polymer chains when the reaction environment is free of AIBN because the generated thiyl radicals are weak, so the majority of the chains will be linear copolymers (A in **Fig. 1**). The addition of AIBN causes the homopolymerization of allyl acrylate so cross-links are formed between the polymer chains, and the polymer structure to be networked (B in **Fig. 1**)
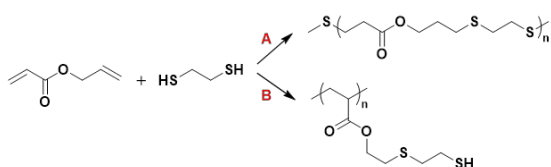
Fig. 1: General mechanism of allyl acrylate and 1,2ethanedithiol copolymers

The ^{1}H-NMR spectrum of the allyl acrylate and 1,2-ethandithiol copolymer in **Fig. 2** confirms the successful synthesis of allyl acrylate and 1,2-ethanedithiol copolymer.
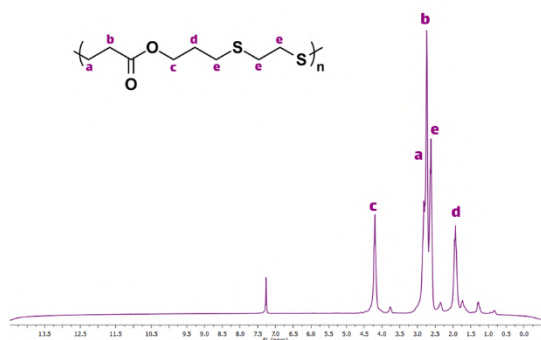

Fig. 2: ^{1}H-NMR spectrum of the allyl acrylate and 1,2-ethan dithiol copolymer

In the **Fig. 3** for the sake of easy comparison the FT-IR spectra of A and B polymers are plotted in one frame. As it can be seen, polymer B has sharper absorption bands in the 3400 cm^{-1} area, that proves the homopolymerization of allyl acrylate monomers.
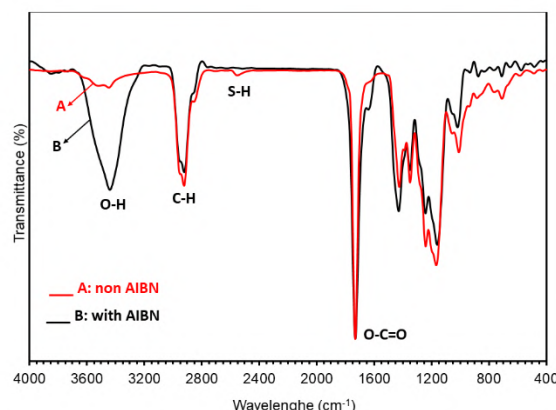

Fig.3: FTIR spectra of the allyl acrylate and 1,2-ethan dithiol copolymers

The product from reaction A with a paste like appearance has been soluble in solvents such as THF and DMSO, while the product obtained from reaction B have been rubbery and insoluble in all solvents. This outcome provides additional evidence that crosslinks exist in polymer B.

Conclusions

According to the obtained results, sulfur-containing polymers were successfully synthesized using thiol-ene reactions. Without a radical initiator, the structure of the synthesized polymers was linear; however, the addition of a radical initiator was resulted to the formation of cross-links between the polymer chains.

References

[1] T.J. Yue, W.M. Ren, X.B. Lu, Copolymerization Involving Sulfur-Containing Monomers, Chem Rev, 123 (2023) 14038-14083.

[2] H. Mutlu, E.B. Ceper, X. Li, J. Yang, W. Dong, M.M. Ozmen, P. Theato, Sulfur Chemistry in Polymer and Materials Science, Macromol Rapid Commun, 40 (2019) e1800650.

[3] C.E. Hoyle, A.B. Lowe, C.N. Bowman, Thiol-click chemistry: a multifaceted toolbox for small molecule and polymer synthesis, Chem Soc Rev, 39 (2010) 1355-1387.

[4] Z. Geng, J.J. Shin, Y. Xi, C.J. Hawker, Click chemistry strategies for the accelerated synthesis of functional macromolecules, Journal of Polymer Science, 59 (2021) 963-1042.

[5] X.-H. Zhang, and Patrick Theato, eds. Sulfur-containing polymers: from synthesis to functional materials. John Wiley & Sons, 2021.

[6] D.S. Kazybayeva, G.S. Irmukhametova, V.V. Khutoryanskiy, Thiol-Ene "Click Reactions" as a Promising Approach to Polymer Materials, Polymer Science, Series B, 64 (2021) 1-16.

Investigating the condition of the clarified water of Ramin power plant and providing corrective solutions to improve the quality

Mohsen Esmaeilpour, Morteza Faghihi*, Abbas Yousefpour

Corresponding Author E-mail: mfaghihi@nri.ac.ir

Chemistry and Process Research Department, Niroo Research Institute, Tehran, Iran.

Abstract: The situation of the clarified water of Ramin Ahvaz power plant is discussed. For this purpose, the condition of the water catchment pond, sedimentation tank and clarifier has been investigated. The results of the investigations show that the condition of the water catchment pond as well as the chemical injection in the clarifier stage of the Ramin power plant needs correction. In this regard, the preparation of a new water catchment pond and the use of coagulant aid in the clarifier of Ramin Ahvaz power plant are suggested.

Keywords: Power plant; chemical injection; water catchment pond; coagulation; clarifier

Introduction

Ramin power plant is the largest heating power plant in the country, which supplies a major part of the electricity of Khuzestan province. The input water of this power plant is from the Karun River, and due to the problems of lack of rainfall and drought, the importance of water consumption and various operations of pre-treatment and purification of the input water has become very important in recent years. In this article, the condition of the incoming water was examined, especially from the perspective of the clarifier's performance in the power plant. Water, as the main fluid in heating power plants, acts as a substrate for energy transfer in heating power plants. The discussion of energy transfer by water is important from two aspects inckuding as steam cycle and act as a cooling fluid. Therefore, the issue of water quality and its consumption in power plant industries is very important [1-3].

Power Plant Water Condition

The age of the Ramin power plant and the climate of the region have caused various problems in the power plant over the past years. Harsh environmental conditions, unforeseen problems in operation and other issues caused by the country's conditions (such as sanctions, funding, etc.) have caused us to face power loss in Ramin power plant over the years. One of the important roots in the occurrence of power plant problems is the water supply issue of the power plant that lead to a series of problems in other parts of the unit. Due to the change in the percentage of the chemical composition of Karun water and its quality decline during the past decades (caused by environmental issues) and serious challenges have been created in the water chemistry of the power plant and consequently in other parts of the power plant. Therefore, in this study, an attempt has been made to check the condition of the clarifier and its inlet water and propose corrective solutions.

Results and Discussion

Observations of the power plant showed that in the chemical treatment plant, chemicals are not injected into the clarifiers, and coagulant injection is done only in the coastal facilities and in the sedimentation tank, during which the turbidity of the river water is reduced to about 25 NTU and the alkalinity of the water is also reduced to 0.1-0.3 meq/l. **Fig. 1** shows the water catchment pond which transfer raw water from Karun river to sedimentation tank by usuing tranferring pumps.

Fig.1: A view of the water catchment pond and its equipment

The pre-purified water enters the clarifiers of the chemical treatment plants and after passing through the ion exchange filters, the sodium form of the water hardness is reduced to below 10 μeq/l (equivalent to 0.5 ppm as $CaCO_3$). One of the major problems of the Ramin power plant water catchment pond is that due to its design and special conditions, it is not able to prevent the entry of high amounts of suspended substances in the

22nd Iranian Chemistry Congress (ICC22)
Iranian Research Organization for Science and Technology (IROST)
13-15 May 2024

03231-97589

water. As a result, the suspended materials settled in the sedimentation tank as well as the suspended materials greatly increased during rains and floods are stored in the sedimentation tank and then transferred to the power plant's water purification devices by the feeding pumps installed in that section. For this reason, all the equipment in the water path have been affected in such a way that the existing facilities, especially in times of rain and flood, cannot provide the water required by the power plant according to acceptable standards for feeding the units and cooling towers. **Fig. 2** shows the sedimentation tank of Ramin power plant.

Fig.2: A view of sedimentation tank in operation

In order to improve the quality of incoming water to Ramin power plant, it is needed a better design for the water catchment pond. For this purpose, it is necessary to create barrier to reduce the turbulence of the water flow in the water catchment pond. These barriers prevent the entry of mud and small and suspended objects into the sedimentation tank, especially during rains. Due to the continuous flow of water from the Karun River into the water catchment pond, the capacity of the water catchment pond should be at least four times the water collected from the water catchment pond. According to the existing conditions of Ramin power plant, it is necessary to install a water catchment pond with appropriate dimensions and equipment in the water intake area of the power plant, which can reduce the chemical consumptions and the cost of repairs and corrosion of parts. In **Fig. 3**, a proposed design for a c water catchment pond is shown.

Another issue of Ramin power plant is the update of chemical water injection. In the initial design of Ramin power plant, ferric chloride ($FeCl_3$) is injected into the sedimentation tank as a coagulant and polyacrylamide (PAM) as a coagulant aid along with sodium hydroxide (NaOH) in order to increase the pH of the water for maximum sedimentation of suspended substances. But currently, only $FeCl_3$ is injected into raw water. Since the $FeCl_3$ brings the water turbidity to an acceptable value of 25 NTU, PAM and NaOH are not currently injected in the power plant. It is important to note that clarification will

be fully effective when all its steps are fully implemented. Also, the lower the turbidity of the water in the initial stages of treatment, the lower the load of the treatment plant will be in the later stages. All these things reduce suspended particles and ions in water, and as a result, equipment corrosion is reduced. Therefore, it is recommended to use PAM and naOH in addition to $FeCl_3$ to complete the pretreatment process in the power plant.
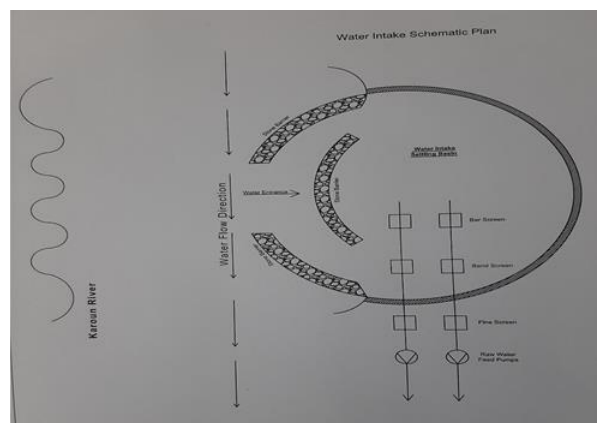

Fig.3: Schematic of proposed plan of water catchment pond

Conclusions

Observations and investigations showed that completing the coagulation process and also modifying the design of the water catchment pond will greatly help the pre-treatment and clarification process of the power plant. It was suggested to achieve the maximum sedimentation and bring the water turbidity to the minimum possible amount, based on the manufacturer's instructions, in addition to FeCl3 coagulant, PAM (as a coagulant aid) and NaOH should also be used. Also, considering the amount of incoming water to power plant from Karun river, increasing the capacity of the water catchment pond, constructing barriers and modifying the incoming water path should be included in the agenda of the power plant.

References

[1] Afshari, F., & Dehghanpour, H. (2019). A review study on cooling towers; types, performance and application. ALKÜ Fen Bilimleri Dergisi, 1-10.

[2] amel, M., Abd Rahman, A., & Shamsuddin, A. (2013). Advances in the integration of solar thermal energy with conventional and non-conventional power plants. Renewable and Sustainable Energy Reviews, 20, 71-81.

[3] Gorjian, S., Zadeh, B. N., Eltrop, L., Shamshiri, R. R., & Amanlou, Y. (2019). Solar photovoltaic power generation in Iran: Development, policies, and barriers. Renewable and Sustainable Energy Reviews, 106, 110-123.

22nd Iranian Chemistry Congress (ICC22)
Iranian Research Organization for Science and Technology (IROST)
13-15 May 2024

03231-97589

IROST

A Large Scale HTL-Free Carbon-Based Perovskite Solar Cell

Elaheh Noha, Reza Keshavarzi*

Corresponding Author E-mail: r.keshavarzi85@gmail.com

Abstract: This paper presents the successful scaling up and optimization of HTL-free carbon-based perovskite solar cells, resulting in an efficiency of 11.45% for 1 cm2 active area, 15.05% for 0.09 cm2 active area and long-term stability with the cell configuration of Glass /FTO /Dense TiO2 /Mesoporous TiO2 /Perovskite /Carbon. Various analyses were conducted to understand the performance of the cells, paving the way for their commercial practicality in solar panel applications.

Keywords: Perovskite Solar Cells; Carbon; Hole Transport Layer; Large Scale

Introduction

The depletion of fossil fuels and the urgent need for sustainable energy sources have fueled the development of photovoltaic technologies, with perovskite solar cells (PSCs) emerging as a promising solution. However, the high cost of Au based perovskite solar cells hampers their widespread adoption [1]. To address this, researchers have explored the use carbon-based materials in PSCs, aiming to enhance stability and reduce costs. Moreover, Carbon-based materials can replace expensive hole-transporting layers (HTLs), reducing overall device costs [2]. This paper investigates the role of carbon electrode in PSCs, highlighting the challenges in carbon paste deposition and the need for improved uniformity in large-scale applications. By addressing these issues, the efficiency and scalability of PSCs can be enhanced, paving the way for their wider implementation in renewable energy systems.

Experimental Section

Deposition of Dense and Mesoporous titanium dioxide (TiO2) layers: In the first part, a dense TiO2 layer was prepared by mixing ethanol solvent with acetylacetone and titanium isopropoxide (TTIP). The solution was filtered and ready for deposition. The glass substrate was placed on a hot plate, and the prepared solution was sprayed onto the surface. The coated substrate is then baked at a specific temperature. In the second part, a mesoporous TiO2 layer was prepared by diluting a TiO2 paste in ethanol. The diluted solution was spin-coated onto the substrate surface. The coated substrate was then baked according to a temperature program.

Deposition of Perovskite and Carbon: The perovskite solution was prepared using PbI2, MAI, DMF, and DMSO solvents through a one-step method. This solution was prepared by dissolving lead iodide in DMF and DMSO solvents. Methylammonium was added to the cooled solution. The perovskite solution was then spin-coated onto the mesoporous TiO2 surface and excess solvent was removed.

Next, a carbon electrode layer was deposited using the doctor blade method. Scotch tape is placed on the cell surface, leaving an exposed area. Carbon paste was spread on the surface using a blade at a 45-degree angle. The cell was then baked and ready for performance analysis using a solar simulator.

Results and Discussion

The configuration and thickness of different layers in the manufactured solar cell is showed in figure 1. Optimizing the thickness of the carbon electrode resulted in better photovoltaic performance with a 2-layer scotch tape. As can be seen the quality of the perovskite layer and improved contact with carbon is high, leading to improved charge transfer and power conversion efficiency.

The photovoltaic performance of the carbon based perovskite solar cells in the absence of a hole transporting layer were evaluated through current-voltage (IV) analysis. The J-V curve of the PSCs are shown in Figure 2, and the measured photovoltaic parameters under light illumination are presented in Table 1. These samples exhibited high repeatability. The results indicate that the perovskite solar cells prepared in this study exhibited good photovoltaic behavior with a reproducible efficiency of around 11% in a large area of 1 cm^2 and 15.05% in 0.09 cm^2 active area.

Furthermore, the carbon-based perovskite solar cell demonstrated superior stability, retaining 90% of its efficiency after 31 days, while the gold-based counterpart lost its performance after 10 days (Figure 3). Overall, the prepared carbon-based perovskite solar cell showed optimal photovoltaic performance and stability, making it a suitable option for high-efficiency and stable solar cells.
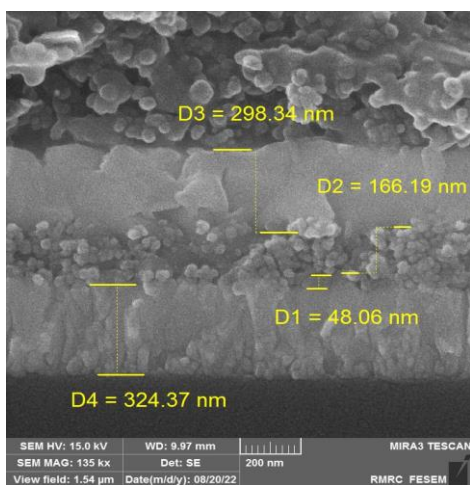
22nd Iranian Chemistry Congress (ICC22)
Iranian Research Organization for Science and
Technology (IROST)
13-15 May 2024

03231-97589

IROST

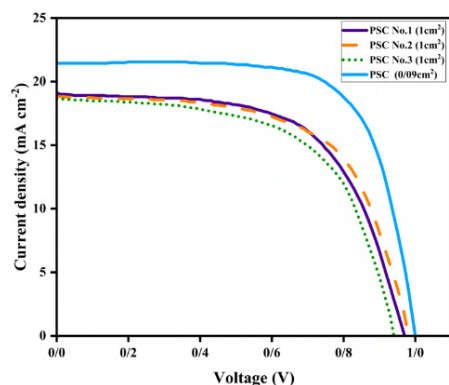**Fig.1:** cross section FE-SEM image of C-PSC

Fig.2: Current-voltage curve of carbon-based perovskite solar cells without HTL with the active areas of 1cm^2 and 0.09 cm^2 prepared at different times.
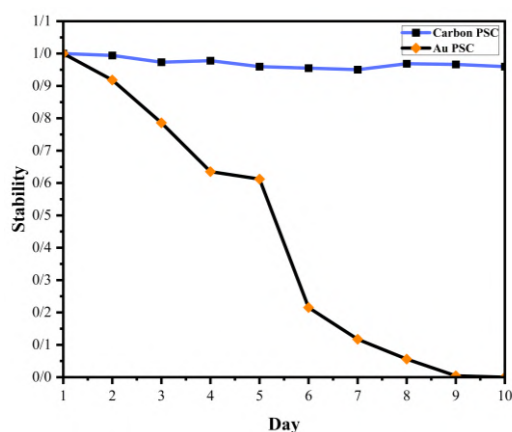

Fig.3: Comparison of the photovoltaic stability of a carbon-based perovskite solar cell without a hole transporting layer (dimensions: 1 cm^2) with a gold-based perovskite solar cell over a period of 10 days.

Table1: The photovoltaic performance of HTL-free C-PSC

C-PSC	J_{SC} (mA)	V_{OC} (V)	FF	η (%)
Active Area (0.09 cm^2)	21.43	1	0.7	15.05
Active Area (1cm^2)	18.82	0.98	0.62	11.45

Conclusions

In conclusion, we have successfully developed a carbon-based perovskite solar cell without a hole-transporting layer, demonstrating long-term stability with the cell configuration of Glass /FTO /Dense TiO$_2$ /Mesoporous TiO$_2$ /Perovskite /Carbon.

Initially, a small-scale cell with an area of 0.09 cm^2 achieved an impressive efficiency of 15.05%. To move towards industrial-scale production, we scaled up the fabrication process to a 1 cm^2 area.

By eliminating the hole-transporter layer and utilizing carbon as the counter electrode, we achieved remarkable results. The optimized solar cell delivered a short-circuit current of 18.82 mA, an open-circuit voltage of 0.98 V, a fill factor of 0.621%, and an efficiency of 11.45% for the 1 cm^2 active area.

These findings highlight the potential of carbon-based perovskite solar cells as a viable and efficient alternative to conventional devices with hole-transporting layers. The elimination of the hole-transporting layer simplifies the fabrication process and enhances the overall stability of the cell. Further research and optimization efforts may lead to even higher efficiencies and improved scalability, making these carbon-based perovskite solar cells suitable for practical applications in the field of solar energy.

Acknowledgements

References

[1] Lewis, N. S. (2016). Research opportunities to advance solar energy utilization. *Science*, *351*(6271), aad1920.

[2] Keshavarzi, R., Molabahrami, N., Afzali, N., & Omrani, M. (2020). Improving efficiency and stability of carbon-based perovskite solar cells by a multifunctional triple-layer system: antireflective, uv-protective, superhydrophobic, and self-cleaning. *Solar RRL*, *4*(12), 2000491.

22nd Iranian Chemistry Congress (ICC22)
Iranian Research Organization for Science and Technology (IROST)
13-15 May 2024

03231-97589

IROST

FeCoNi oxide derived from MIL-88 as an efficient electrocatalyst for oxygen evolution reaction

Ali Akbar Asgharinezhad*, Afsanehsadat Larimi*, Morteza Faghihi

Corresponding Author E-mail: aasgharinezhad@nri.ac.ir (A.A. Asgharinezhad); alarimi@nri.ac.ir (A. Larimi)

Chemistry and Process Research Department, Niroo Research Institute, Tehran, Iran.

Abstract: Herein, FeCoNi-MOF based on MIL-88 was synthesized by a hydrothermal method. Then, the performance of the catalyst was investigated and improved by calcination in the range of 250-450 ℃. The (FeCoNi)-O250 ℃ electrocatalyst, exhibited an overpotential of 313 mV (J= 10 mA.cm^{-2}) and a Tafel slope of 31.5 mV.dec^{-1}.

Keywords: Electrocatalyst; Oxygen evolution reaction; Metal-organic frameworks.

Introduction

Energy demand is increasing as a result of population growth and technological advances, so it is important to find renewable and affordable energy sources to replace fossil fuels [1]. As a carbon-free, renewable, and environmentally friendly energy source, hydrogen has high conversion efficiency and energy density [2]. Hydrogen contains more energy than natural gas, gasoline, and oil. Currently, the majority of all hydrogen consumed worldwide is derived from fossil fuels, through superheated steam [2]. Utilizing water electrolysis, encompassing the processes of the oxygen evolution reaction (OER) and the hydrogen evolution reaction (HER), holds potential as a viable method for producing environmentally friendly and highly efficient hydrogen [3].

In this work, (FeCoNi)-MOF based on Mil-88 was synthesized using the hydrothermal method. The synergy between Fe, Co, and Ni within the MOF structure enhances its electrochemical activity, making it a promising material for applications such as the oxygen evolution reaction (OER).

Experimental Section

FeCoNi-MOF nanorods were prepared through a conventional hydrothermal method. Typically, a mixture of 724 mg of $FeCl_3 .6H_2O$, 192 mg of $Co (NO_3)_2 .6H_2O$, 192 mg of $Ni (NO_3)_2.6H_2O$, and 664 mg H_2DBC were dissolved in 40 mL DMF. The mixture was ultrasonicated to make sure of complete dissolution. Then, 8 mL of 0.4 M KOH solution was added dropwise to the mixture solution under stirring. The solution was transferred to a 110 mL Teflon-lined stainless-steel autoclave. The autoclave was heated in the normal oven at 110 ℃ for 48 h, later cooling to room temperature. The product was washed with DMF and distilled water three times and finally dried at 100 ℃ overnight to obtain a brown powder of FeCoNi-MOF.

To synthesis $FeCoNi-O_x$ (X: 250-450 ℃), appropriate amount of FeCoNi-MOF was taken in a crucible and heated at different temperatures for 4 h.

Results and Discussion

Characterization of the synthesized materials

XRD analysis was performed to study the crystal structure and phase purity of the prepared FCN-MOF and $(FCN)-O_x$. Fig. 1 shows the XRD diffraction peaks of (FCN)-MOF and (FCN)-Ox (x=250 ℃, 350 ℃, 450 ℃) in the 2θ range of $20° - 30°$. According to the MIL-88B (Fe) substrate the peaks situated at the 2θ values of $17.4°, 19.3°, 21.6°, 22.1°, 26.4°, 28.2°$ assigned to MIL-88B (Fe) [4]. For calcined samples the peaks at 35.7° and 57.4° are assigned to (311) and (5 1 1) diffractions of $NiCo_2O_4$ and $CoFe_2O_4$ [5]. This peak also increases with increase of calcination temperature. The peak situated at 43.4° correspond to the (2 0 0) plate of NiO. The peaks observed at 33.1° and 40.6° are related to (1 0 4) and (1 1 3) diffractions of Fe_2O_3. Also the peaks situated at 30.2°, 53.8° and 62.9° are related to (2 2 0), (1 1 6) and (4 4 0) diffractions of Fe_3O_4 increased with increase temperature.
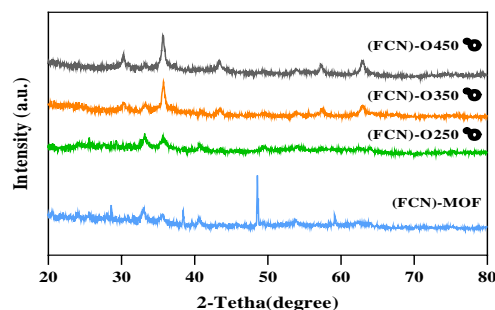

Fig. 1: XRD patterns of (FCN)-MOF and $(FCN)-O_x$.

The FTIR spectroscopy (Fig. 2) used to identify the functional groups of (FCN)-MOF and $(FCN)-O_x$ samples. The deep absorbance bands around 3400 cm^{-1} are associated to O-H stretching vibration of the carboxylic acid group,

22nd Iranian Chemistry Congress (ICC22)
Iranian Research Organization for Science and Technology (IROST)
13-15 May 2024

03231-97589

IROST

and the bands around 1725 cm^{-1} are corresponding to the stretching vibration of the C=O, The C=C stretching vibration of the aromatic ring generally was observed the range of 1600-1450 cm^{-1}.
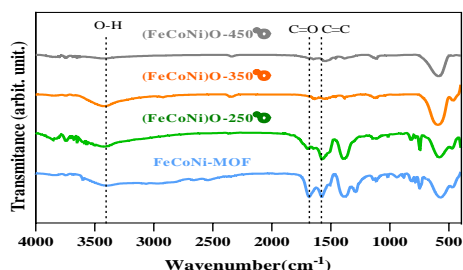

Fig. 2: FTIR spectra of (FCN)-MOF and (FCN)-O$_x$.

FESEM analysis was used to study the morphology and structure of the synthesized samples. The morphology of (FCN)-MOF composites is shown in Fig. 3-a FESEM micrographs show that the structure and morphology of the particles (FCN)-MOF were rod nanostructures with a diameter ranging from 98 nm to 140 nm. The results of heat treatment on the sample (FCN)-MOF at temperatures of 250 ℃, 350 ℃ and 450 ℃ are shown in Fig. 3-(b-d) it is noted that the micrographs describe the porous morphology and homogeneous and uniform non-bonded structure of the synthesized samples. In the first temperature gradient at 250 ℃, while maintaining the rod structure, oxide granular particles start to grow on the surface of the structure.
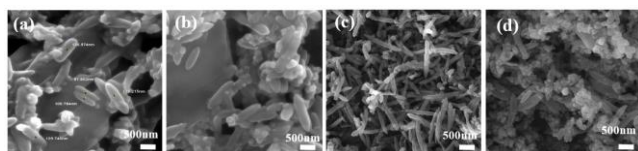

Fig. 3: FESEM micrographs of (a) (FCN)-MOF, (b) (FCN)-O250 ℃, (c) (FCN)-350 ℃, (d) (FCN) - O 450 ℃.

Electrocatalytic activity studies

To compare the activity and efficiency of the synthesized electrocatalysts in the OER reaction, various electrochemical tests have been designed. Firstly, the activity of the as-prepared electrocatalysts in the process of oxygen release was investigated using LSV with a scan rate of 1 mV.s^{-1} and in a 1.0 M KOH solution. All calculated potentials were reported in terms of reversible hydrogen electrode (RHE).

The electrocatalytic performance of the prepared electrodes was compared under the same conditions. The overpotential for each of the NF, (FCN)-MOF/NF electrodes were 432 mV and 322 mV at a current density of 10 mA.cm^{-2}, which decreased with the electrocatalyst layer deposited on the nickel foam (NF). Additionally, the overpotential for each of the (FCN)-O$_x$/NF electrodes at 250 °C, 350 °C, and 450 °C was 313 mV, 342 mV, and 352 mV, respectively. The (FCN)-O250 °C /NF has the lowest overpotential among fabricated oxides.

The Tafel slope for NF electrode and (FCN)-MOF/NF electrode is 97.1 mV.dec^{-1} and 50 mV.dec^{-1}, respectively. Additionally, the Tafel slope for (FCN)-O$_x$/NF electrodes at 250°C, 350°C, and 450°C are 47.7 mV.dec^{-1}, 79 mV.dec^{-1}, and 84 mV.dec^{-1}, respectively. As a result of calcination, regular and stable crystal networks are formed. Also, the heating operation causes the removal of impurities and volatile species and the formation of a homogeneous substance with a higher degree of purity.

Conclusions

In this study, a FeCoNi-MOF was synthesized using the hydrothermal method. The synthesized catalyst was then subjected to calcination at three different temperatures (250℃, 350℃, and 450℃) to investigate its electrocatalytic properties and effects on the OER process. By loading the synthesized samples onto a NF and testing the prepared electrodes under the same conditions in a 1.0 M KOH solution at room temperature, the (FeCoNi)-O$_{250}$ electrocatalyst showed a nanorod-like structure and exhibited an overpotential of 313 mV at a current density of 10 mA/cm².

References

[1] Kannan, N., & Vakeesan, D. (2016). Solar energy for future world:-A review. *Renewable and sustainable energy reviews*, *62*, 1092-1105.

[2] Chouhan, K., Sinha, S., Kumar, S., & Kumar, S. (2021). Simulation of steam reforming of biogas in an industrial reformer for hydrogen production. *International Journal of Hydrogen Energy*, *46*(53), 26809-26824.

[3] Du, J., Li, F., & Sun, L. (2021). Metal–organic frameworks and their derivatives as electrocatalysts for the oxygen evolution reaction. *Chemical Society Reviews*, *50*(4), 2663-2695.

[4] Zorainy, M. Y., Kaliaguine, S., Gobara, M., Elbasuney, S., & Boffito, D. C. (2022). Microwave-Assisted Synthesis of the Flexible Iron-Based MIL-88B Metal–Organic Framework for Advanced Energetic Systems. *Journal of Inorganic and Organometallic Polymers and Materials*, *32*(7), 2538-2556.

[5] Khalid, S., Cao, C., Wang, L., & Zhu, Y. (2016). Microwave assisted synthesis of porous NiCo2O4 microspheres: application as high performance asymmetric and symmetric supercapacitors with large areal capacitance. *Scientific reports*, *6*(1), 22699.

22nd Iranian Chemistry Congress (ICC22)
Iranian Research Organization for Science and Technology (IROST)
13-15 May 2024

03231-97589

Highly efficient electrocatalytic oxygen evolution reaction on a trimetallic zeolitic-imidazolate framework/nickel foam electrode

Ali Akbar Asgharinezhad*, Afsanehsadat Larimi*

Corresponding Author E-mail: aasgharinezhad@nri.ac.ir (A.A. Asgharinezhad); alarimi@nri.ac.ir (A. Larimi)

Chemistry and Process Research Department, Niroo Research Institute, Tehran, Iran.

Abstract: Herein, we prepared a series of monometallic (ZIF-67), bimetallic (ZIF-CoCu), and novel trimetallic zeolitic imidazolate frameworks (ZIF-CoCuNi) via a facile one-step room-temperature solution precipitation method. The ZIF-CoCuNi exhibited an overpotential of 325 mV and a Tafel slope of 118 mV.dec^{-1}. The ECSA of ZIF-CoCuNi is 2.74 times higher than ZIF-67.

Keywords: Zeolitic-imidazolate framework; Oxygen evolution reaction (OER); Water splitting.

Introduction

The energy is one of the most important and necessary demands for today's society and a key source of economic growth [1]. Hydrogen can be used in fuel cells for transportation, and for generation of electricity. Currently, most hydrogen production is from fossil fuel through reforming method [2]. However, in recent years, the production of hydrogen from clean and renewable sources has received much attention. In this regard, various processes including reforming and decomposition of biomass, photochemical water splitting, electrochemical water splitting 8, and pyrolysis of plastics have been proposed [3].

Water splitting consists of OER and hydrogen evolution reaction (HER), which produce oxygen at the anode surface and hydrogen at the cathode surface. The OER process requires more additional potential compared to the HER. In this regard, many efforts have been made to identify and synthesize electrocatalysts with suitable performance and stability.

Herein, based on the abovementioned considerations, we synthesized CoNiCu-ZIF, CoCu-ZIF, and ZIF-67, as trimetallic, bimetallic, and monometallic ZIF, respectively, by a facile one-step room-temperature solution precipitation method. It was investigated that Ni and Cu modify the Co active sites in order to decrease the energy barrier associated with the rate-limiting step.

Experimental Section

In a standard synthesis [4], a solution containing 3.0 mmol of $Co(NO_3)_2 \cdot 6H_2O$ and a combined total of 1.0 mmol of X (either 1.0 mmol $Cu(NO_3)_2 \cdot 3H_2O$ or 0.5 mmol $Cu(NO_3)_2 \cdot 3H_2O$ and 0.5 mmol $Ni(NO_3)_2 \cdot 6H_2O$) was prepared by dissolving them in 46 mL of methanol. Furthermore, 16.0 mmol of 2-MIM was dissolved in 46 mL of methanol. During the stirring process, the solution containing 2-MIM was slowly introduced into the metal salt solution. After 15 minutes of stirring, the mixture was left to age at room temperature for 24 hours. The final step involved subjecting the resulting products to centrifugation, followed by a wash with methanol, and finally drying at 60°C for 8 hours. The resultant product was named CoX-ZIF (where X could be either Cu or CuNi). For the sake of comparison, ZIF-67 was also synthesized under the same conditions, but without the inclusion of $Cu(NO_3)_2 \cdot 3H_2O$, and $Ni(NO_3)_2 \cdot 6H_2O$.

Results and Discussion

Characterization

Fig.1 illustrates the XRD results of all prepared electrocatalysts, providing insight into their respective phase compositions. The main six typical peaks of ZIF-67 are observed at 2θ of 7.34°, 10.39°, 12.72°, 14.71°, 16.47°, and 18.03°, which correspond to the (011), (002), (112), (022), (013), and (222) crystalline planes, respectively (Fig. 1a). The XRD patterns of as-prepared ZIF-67 are well-matched to the simulated ZIF-67 peaks that have been documented in existing literature [5]. It is observed that the XRD patterns of ZIF-CoX samples have identical diffraction peaks as ZIF-67.
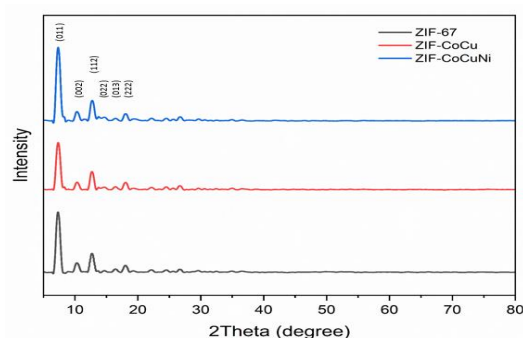

Fig. 1: XRD patterns of fabricated electrocatalysts.

FESEM, and TEM were employed to determine the morphology of ZIF-CoCuNi. Fig. 2a show the FESEM

22nd Iranian Chemistry Congress (ICC22)
Iranian Research Organization for Science and Technology (IROST)
13-15 May 2024

03231-97589

IROST

micrograph of ZIF-CoCuNi. In agreement with the previous report, ZIF-CoCuNi exhibits a regular rhombic dodecahedron structure with smooth surface. TEM micrograph (Fig. 2b) reveals that ZIF-CoCuNi crystals have well-defined rhombic dodecahedral shapes with smooth surfaces.
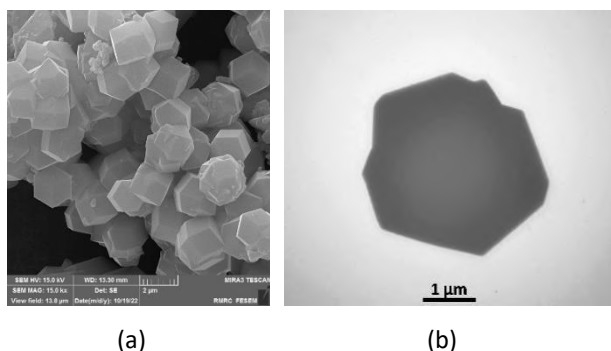

(a)   (b)

Fig. 2: (a) FESEM and (b) TEM micrographs of ZIF-CoCuNi.

Electrocatalytic activity studies

The OER performances of the electrodes that were prepared were studied in 1 $mol.L^{-1}$ KOH solution using a three-electrode configuration. The overpotentials of ZIF-67, ZIF-CoCu, and ZIF-CoCuNi, at a current density of 10 $mA.cm^{-2}$ are 418, 390, and 325, respectively. The OER catalytic performance of ZIF-67 is significantly improved through the substitution of cobalt by copper and nickel in bimetallic, and trimetallic ZIFs. It has been demonstrated that the presence of multiple elements improves the catalytic performance of electrodes.

The Tafel slops were evaluated to investigate the reaction kinetics. Meanwhile, the results revealed that ZIF-CoCuNi has a smaller Tafel slope of 118 $mV.dec^{-1}$ compared to ZIF-67 (131 $mV.dec^{-1}$), ZIF-CoCu (122 $mV.dec^{-1}$). This difference indicates that CoCuNi-ZIF exhibits excellent kinetics for the OER and facilitates efficient electron transfer.

The charge transfer resistance (R_{ct}), and solution resistance between the working electrode and reference electrode (R_s) values of all catalysts are listed in Table 1. Among all ZIF samples tested, the trimetallic ZIF has the fastest charge transfer capability. Thus, the synergy of multiple elements can enhance the rate of charge transfer.

Table 1. The R_s and R_{ct} values of the prepared electrodes.

Electrode	R_s (Ω)	R_{ct} (Ω)
ZIF-67	4.21	35.65
ZIF-CoCu	4.006	33.36
ZIF-CoCuNi	3.581	31.29

The electrochemically active surface area (ECSA) of synthesized electrocatalysts was estimated by determining the double-layer capacitance (C_{dl}) measured in the non-Faraday potential region. As depicted in Table 2, the C_{dl} and ECSA of ZIF-CoCuNi are significantly greater compared to ZIF-CoCu and ZIF-67.

Table 2. The Cdl and ECSA values of the prepared electrodes.

Electrode	C_{dl} ($mF.cm^{-2}$)	ECSA (cm^{-2})
ZIF-67	0.41	10.34
ZIF-CoCu	1.02	25.49
ZIF-CoCuNi	1.13	28.29

Conclusions

In summary, ZIF-67, ZIF-CoCu, and ZIF-CoCuNi were successfully synthesized via a facile one-step room-temperature solution precipitation method. ZIF-CoCuNi exhibits superior electrochemical performance compared to ZIF-CoCu and ZIF-67, mainly due to the synergistic effect of cobalt, copper, and nickel. This combination amplifies the electrocatalytic activity, leading to an enhancement in the overall performance.

References

[1] Pan, X., Wang, Y., & He, S. (2021). The evidential reasoning approach for renewable energy resources evaluation under interval type-2 fuzzy uncertainty. *Information Sciences*, *576*, 432-453.

[2] Khodabandehloo, M., Larimi, A., & Khorasheh, F. (2020). Comparative process modeling and techno-economic evaluation of renewable hydrogen production by glycerol reforming in aqueous and gaseous phases. *Energy conversion and management*, *225*, 113483.

[3] Chi, J., Jiang, Z., Yan, J., Larimi, A., Wang, Z., Wang, L., & Shangguan, W. (2022). Recent advancements in bismuth vanadate photoanodes for photoelectrochemical water splitting. *Materials Today Chemistry*, *26*, 101060.

[4] Wang, Y. L., Yang, S. H., Wang, H. Y., Wang, G. S., Sun, X. B., & Yin, P. G. (2020). Hollow porous CoNi/C composite nanomaterials derived from MOFs for efficient and lightweight electromagnetic wave absorber. *Carbon*, *167*, 485-494.

[5] Qian, J., Sun, F., & Qin, L. (2012). Hydrothermal synthesis of zeolitic imidazolate framework-67 (ZIF-67) nanocrystals. *Materials Letters*, *82*, 220-223.

Physico-Chemical and organoleptic Properties of Biscuits enriched with pomegranate seed powder

Mansure Shafie [a], Alireza Bassiri *[b], Babak Ghiassi [a]

Corresponding Author E-mail: Bassiri@irost.ir

[a] Department of Food Science and Technology, Science and Research branch, Islamic Azad University, Tehran, Iran.

[b] Department of Food Science and processing, Institute of Chemical Technologies, Iranian Research Organization for Science and Technology (IROST), Tehran, Iran.

Abstract: The aim of the present study was to investigate the effects of pomegranate seed powder (PSP) on physico-chemical and organoleptic properties of enriched Biscuits. Different concentrations of pomegranate seed powder have been fortified in Biscuits formulations by replacement of refined wheat flour. The study demonstrated that Biscuits with good sensory and quality characteristics could be produced by substituting wheat flour with 5% of pomegranate seed powder.
Keywords: Pomegranate seed powder, Biscuits, Quality characteristics, Enrichment

Introduction

Pomegranate (*Punica granatum L.*) is an important fruit from tropical and subtropical regions. Iran is one of the world leading countries in pomegranate production. Pomegranate seed is a major byproduct from pomegranate fruit juice industries which goes unused most of the time. Pomegranate seeds, are a valuable source of bioactive phytochemicals and can be used as ingredients for the production of functional foods. (Liu et al., Citation2009). Seeds contribute about 3–5% of the total fruit weight are the major by-product from the pomegranate juice industry, which have a major potential to be converted into value-added products. Pomegranate seed, a byproduct of juice processing industries was reported to contain a series of bioactive compounds, minerals and fibres for a wide range of dietary requirements (Paul et al, 2015). Recycling byproducts or processing waste is of great importance from environmental point of view as well as the health benefits derived from the extracted bioactive compounds. This product may be used as such or after further value addition. Waste recycling is emerging as one of the important areas in research for achieving efficiency in utilization of all the raw material or inputs so as to reduce the cost of production. Functional foods are the food components that benefits health beyond the basic nutrition. Conventional foods, enriched or enhanced foods, dietary supplements and fortified foods are some of the examples of functional foods. Baking Industry is considered to be one of the major segments of food processing in Iran. Baked products have popularities in the populace because of their availability, ready to eat convenience and reasonably good shelf life. Biscuits are different from other baked products because of their low moisture content which ensures less chance of microbial spoilage to provide a longer shelf life, making large scale production and distribution possible (Ajila, 2008).

Experimental Section

Pomegranate fruits of optimum maturity were purchased from local market. After washing with tap water, fruits were cut into two parts and the juice was extracted. Seeds were separated manually. The pomegranate seeds were dried in a tray drier at 40°C for 48 hr until the seeds reached below 10% moisture content. The dried pomegranate seeds were ground to a fine powder. The powder obtained was passed through a 0.5 mm size mesh sieve. Pomegranate seed powder was stored in LDPE bags for further chemical analysis and for biscuit fortification. For production of Biscuits, all the ingredients were mixed for 5 min. and the obtained dough was rolled out approximately 2 cm thick with a dough roller and cut into 5x5 cm squares. The shaped biscuit doughs were baked at 200°C for 10 min. in an oven. After cooling in room temperature, samples were packed in LDPE bags for further analyses. The breaking strength was measured using the triple beam snap technique of Gaines (1991) using Instron Universal Testing machine (Model 4301, Instron Ltd., High Wycombe, England). The force required to break a single cookie was recorded, and the average value of five replicates is reported. Colour parameters (L^*, a^* and b^*) were measured on five different points on the surface of samples. A colorimeter (Minolta Chroma Meter CR-400, Osaka, Japan) equipped with D65 illuminant, in the reflectance mode and in the CIE L^* a^* b^* colour scale was used. Colour values of cookies were recorded as "L^*" (lightness), "a^*" (redness) and "b^*" (yellowness). The crude ash, Moisture, Protein, Fat and Fiber contents of cookies were determined as per the standard methods (AACCI 1999). The antioxidant activity of the extracted betalain samples was determined by DPPH method. The

22nd Iranian Chemistry Congress (ICC22)
Iranian Research Organization for Science and Technology (IROST)
13-15 May 2024

03231-97589

sensory evaluation of baked cookies was performed according to Hosmani et al. (2016) by panel of 10 judges using five-point hedonic scale (5 – most liked, 1 – most disliked). All of the tests were performed at least in triplicate. Experimental data were processed by one-way analysis of variance using SPSS Statistics 20 (IBM, NY, USA) with Duncan's multiple range test (p < 0.05).

Results and Discussion

The data revealed significant differences among the treatments with respect to moisture content of samples. The minimum moisture content was recorded in control sample and the maximum moisture was recorded in samples with 10% PSP. The increase in moisture content of samples containing PSP might be due to increased water absorption of dietary fibre present in PSP. The total ash content was significantly higher in treatments with higher PSP. This might be attributed to the higher amounts of mineral present in the PSP. The fat, protein and fibre contents of samples were influenced by PSP content. By increasing the amount of PSP in the formulation, the fat, protein and fibre contents in the produced samples increased significantly (P<0.05). With the increase of amounts of PSP, the colour index (L*) of the samples decreased significantly. The addition of PSP has increased the colour indexes (a*) and (b*) in the samples compared to the control sample. Total colour changes were influenced by PSP content. The total colour changes were significantly higher in treatments with higher PSP. Hardness of samples containing PSP was significantly ($p < 0.05$) higher than that of the control. Increasing level of PSP resulted in increasing biscuit hardness. This effect could be explained by the high fibre content of PSP. According to Ajila et al. (2008), increase in hardness of biscuits enriched with fibres may be due to the higher water content in corresponding doughs. Ajila et al. (2008) and Gaines (1991) reported that doughs with higher water content produce an extensive gluten structure, which give harder biscuits. The chemical compositions of wheat flour, and pomegranate seeds powder are presented in Table 1.

Table 1 Chemical composition of wheat flour and Pomegranate seeds powder

	Wheat flour	Pomegranate seed powder
Moisture content (%)	13.81	5.67
Ash content (%)	0.47	2.75
Protein content (%)	9.14	15.51
Fat content (%)	0.7	18.32
Fiber content (%)	0.32	33.63

Examining the trends of the results, PSP content tended to increase both Total Phenolic Content and antioxidant capacity of biscuits enriched PSP. The statistical results showed a significant increase in Total Phenolic Content and antioxidant capacity for biscuits containing PSP at the 10% compared to the control. Biscuits without addition of PSP (control sample) contained the highest volume. The volume of samples decreased significantly with increasing of PSP content. The biscuits prepared from PSP were evaluated for their colour and appearance, texture, flavour, taste and overall acceptability using 5-point hedonic scale. The sensory quality of the biscuit was best in the control sample and gradually decreased with the increment of PSP content in the formulation. This may be due to the lower lightness, higher yellowness, and redness values of PSP. The colour and appearance of the product make the first impression in the consumer's mind.

Conclusions

Pomegranate seeds powder (PSP) is a rich source of macro, micronutrient and bioactive compounds and minerals. In this study, it was aimed to determine the Physico-Chemical and sensorial properties of biscuits enriched with PSP, which is edible but considered as waste. PSP positively affected the Physico-Chemical and antioxidant characteristics of biscuits. Sensory analysis like color, texture, taste and overall acceptability of the cookies although decreased, however, the cookies were in the acceptable to the consumer's panel. PSP addition of 5% was found the best among the other concentrations in terms of sensory evaluations. As a result, enriching biscuits with PSP in terms of making functional biscuits goal was met.

References

[1] Ajila CM, Leelavathi K, Prasada Rao UJS. 2008. Improvement of dietary fiber content and antioxidant properties in soft dough biscuits with the incorporation of mango peel powder. J Cereal Sci. 48:319–326.

[2] Gaines CS. 1991. Instrumental measurement of the hardness of cookies and crackers. Cereal Foods World 36(12):989–996.

[3] Hosmani, R., Jagadessh, S. L., Suresha, G. J. and Tummaramatti, S., 2016, Fortification of carrot, jackfruit and aonla powder to enhance nutritional and sensory qualities of sweet biscuits. J. Nutri. Health Food Eng., 4(3): 130-135.

[4] Paul, P., and Bhattacharyya, S., 2015, Antioxidant profile and sensory evaluation of cookies fortified with juice and peel powder of fresh pomegranate (Punica granatum). International J. Agri. Food Sci., 5(3): 85-91.

Effect of sourdough addition on qualitative and sensory characteristics of brown rice-based gluten-free bread

Nilufar Roushandel [a], Alireza Bassiri *[b], Majid Javanmard [b]

Corresponding Author E-mail: Bassiri@irost.ir

[a] Department of Food Science and Technology, Science and Research branch, Islamic Azad University, Tehran, Iran.
[b] Department of Food Science and processing, Institute of Chemical Technologies, Iranian Research Organization for Science and Technology (IROST), Tehran, Iran.

Abstract: The gluten-free alternative flours and the application of natural fermentation in the breads production are promising technologies to improving quality and sensory properties. The aim of this study was to evaluate the effect of sourdough addition on qualitative and sensory characteristics of brown rice-based gluten-free bread during the 6-day storage period compared to control sample.

Keywords: Gluten free bread, Brown rice, Sourdough, Quality characteristics, Organoleptic properties, Shelf-life

Introduction

Celiac disease is an autoimmune disorder that occurs in genetically predisposed individuals who develop an immune reaction to gluten. Due to the growing prevalence of Celiac disease, interest in the development of gluten-free breads has significantly increased. At present, the only effective and safe treatment for patients with celiac disease is to follow a strict gluten-free diet for life. Among gluten-free foods, bread is the most consumed; globally, it represents an important staple food product. Generally, gluten-free bread is a product with unsatisfactory sensory properties and a poor nutritional quality. However, producing high-quality gluten-free bread is still a technical challenge due to the absence of gluten. Gluten plays a vital role in bread making because it is responsible for forming a sticky, stretchable and elastic dough, which helps gas retention and structure formation. The absence of gluten significantly reduces the retention rate of carbon dioxide produced by yeast, resulting in gluten-free bread with a rough and firm texture and low specific volume. The production and improvement of gluten free bread have been widely studied, and some innovative technologies were applied to improve the quality of gluten-free bread, including sourdough fermentation. Sourdough is a mixture of flour and water fermented with starter cultures of lactic acid bacteria (LAB) and yeasts. It has been well recognized that sourdough fermentation enhances dough properties; it improves volume, texture, flavour, and nutritional value of the bread, retards the staling process and protects bread from Mold and bacterial spoilage. In recent years, research into gluten-free bread production has increased significantly. Rice flour is one of the most commonly utilized flours in commercial gluten-free loaves due to its accessibility, cost-effectiveness and neutral flavour. Gluten-free bread made with polished rice is likely to be nutritionally deficient due to the removal of the bran layer during processing. On the contrary, gluten-free bread produced from brown rice contains better nutritional profiles. This is because the bran layer of rice contains a greater concentration of dietary fibre, minerals, and bioactive components, improving gluten-free bread's nutrient deficiencies. The purpose of this study was to investigate the potential interactions of sourdough fermentation on key characteristics of gluten-free sourdough breads prepared from brown rice flour.

Experimental Section

Material used in bread making, brown rice grains, instant dried yeast, salt and sugar were procured from a local market. Brown rice grains were ground and sieved to produce rice flour which could pass through a 250-micron sifter. Four types of dough formulations were prepared by adding 0 (control), 10, 20, and 30% sour dough (based on the weight of brown rice flour). After kneading, the dough was rested at room temperature for 40 min. Then, the dough was cut into 200 g pieces, rolled by hand, and placed on baking pans. Fermentation was done at 30°C for 4 h at 80% relative humidity. The doughs were baked at 180 ± 5°C for 50±5 min. The loaves were rested 1h to cool at room temperature. The moisture content was measured according to the AACCI (2010) standard guideline. A colorimeter (Minolta Chroma Meter CR-400, Osaka, Japan) equipped with D65 illuminant, in the reflectance mode and in the CIE L* a* b* colour scale was used. Colour values of cookies were recorded as "L*" (lightness), "a*" (redness) and "b*" (yellowness). To analyses the texture characteristics a Instron Universal Testing machine (Model 4301, Instron Ltd., High Wycombe, England) was used. A 20 mm diameter plate as probe was used. The initial speed of the measuring probe

22nd Iranian Chemistry Congress (ICC22)
Iranian Research Organization for Science and Technology (IROST)
13-15 May 2024

03231-97589

IROST

was 1 mm/s, the text speed was 5 mm/s. The measurements were done 5 times. From the measured curves the software calculated the hardness, cohesiveness, springiness, and chewiness. The sensory evaluation of baked cookies was performed according to Hosmani et al. (2016) by panel of 10 judges using five-point hedonic scale (5-most liked, 1-most disliked). All of the tests were performed at least in triplicate. Experimental data were processed by one-way analysis of variance using SPSS Statistics 20 (IBM, NY, USA) with Duncan's multiple range test (p < 0.05).

Results and Discussion
The chemical composition of the brown rice flour on a wet basis was 1.1% ash, 13.65% proteins, 0.7% lipids, and 8.38% moisture, 6.94 pH and 0.93 dietary fibre. Increasing the sourdough content caused a significant increase of moisture content of the bread compared to control sample (P<0.05). ANOVA analysis showed that storage time had a significant effect on moisture content. The moisture content decreased significantly by storage time at all treatments during storage period. Addition of sourdough delayed a fast decrease of moisture content (P<0.05). The bread colour value L* were significantly affected (p < 0.05) by sourdough content. The L values (which represent the lightness of the bread samples) were lower with the increased of sourdough content. Increasing of sourdough content has no significant effect on a* (which indicates greenness to redness) and b* (which represent the degree of blueness to yellowness) values. Results demonstrate that storage time has a significant effect on bread colour values. During storage, the a* value bread samples was significantly (p < 0.05) increased, however, the b* value and L* value were decreased. The decreased L* value was an indication of darkening of the breads during the storage period. ANOVA results showed a significant effect of sourdough content on bread hardness; Increasing of sourdough content caused a significant decrease of bread hardness because the sourdough improved gas retention in the bread dough. Moreover, acidification caused by the sourdough impacted on the solubility of the structure-forming components. The sample containing 30% sourdough had the lowest hardness value. The hardness of the Breads decreased significantly with extended storage time. The springiness and cohesiveness of samples increased significantly (P<0.05) with the increased sourdough content because sourdough created a spongy structure in the bread which was reflected in the increased springiness and cohesiveness. With the increase of storage time, the springiness and cohesiveness of bread decreased significantly. Sourdough content has a significant effect on chewiness of the samples (P>0.05). By increasing of sourdough content, the

chewiness of samples increased significantly. The results showed that with the increase of storage time, the chewiness of bread increased significantly (P<0.05). The three-color indexes decreased as the sourdough level increased in the bread formula, indicating a darker (lower L*), less red (lower a*), and yellow (lower b*) compared to control sample (P>0.05). Storage time hat a significant effect of colour indexes of all samples. Decrease of L* and b*-value and increase a*-value during storage time may be related to the migration of some water from the crumb to the crust. Increasing the moisture content of bread crust as a result of staling can affect the colour parameters of the sample. The sensory quality of samples was best in the sample with 10% sourdough in the formulation.

Conclusions
The possibilities of a gluten-free sourdough bread development based on brown rice flour were examined. Four types of dough formulations were prepared by adding 0 (control), 10, 20, and 30% sour dough (based on the weight of brown rice flour). The results of qualitative and sensory characteristics of samples showed that sourdough with a concentration of 10% was the most preferred bread.

References
[1] AACCI. (2010). American Association of Cereal Chemists International. Approved Methods of American Association of Cereal Chemists. AACC, St. Paul.
[2] Arendt, E. K., & Moroni, A. V. 2013. Sourdough and Gluten-Free Products. In Handbook on Sourdough Biotechnology (p. 245–264). Springer US.
[3] Gaines CS. 1991. Instrumental measurement of the hardness of cookies and crackers. Cereal Foods World 36(12):989–996.
[4] Hosmani, R., Jagadessh, S. L., Suresha, G. J. and Tummaramatti, S., 2016, Fortification of carrot, jackfruit and aonla powder to enhance nutritional and sensory qualities of sweet biscuits. J. Nutri. Health Food Eng., 4(3): 130-135.

Enhancing Nanofiber Stability for Drug Delivery: Novel Crosslinking Strategy between Thiocarbonyl and Amine Groups in Polymer Chemistry

Marziye Gholami, Roya Sedghi*

Corresponding Author E-mail: r_sedghi@sbu.ac.ir

Department of Polymer and Materials Chemistry, Faculty of Chemistry and Petroleum Sciences, Shahid Beheshti University, G.C, 1983969411, Tehran, Iran.

Abstract: Local recurrence of breast cancer is a significant contributor to post-surgery mortality in females. Nanofibers show promise in reducing cancer recurrence by targeting residual cells. Research aims to create efficient chitosan and polyvinyl alcohol nanofibers for post-surgery cancer prevention, utilizing novel chitosan derivatives and crosslinking methods to increase water stability.

Keywords: Anticancer nanofibers; cross-linker free; heat treatment.

Introduction

The most recent publication from the International Agency for Research on Cancer (IARC) highlights breast cancer as the leading cause of cancer-related fatalities among women. A critical factor influencing breast cancer mortality is the occurrence of local recurrence, which significantly impacts survival rates post-surgery [1]. To address the challenges posed by anticancer drugs and prevent cancer recurrence, the investigation into innovative local drug delivery systems has gained prominence. Particularly, the utilization of local drug delivery systems like nanofibers has shown promise in improving treatment outcomes for localized diseases by targeting residual cells at the tumor site post-surgery, thereby reducing the risk of cancer recurrence [2].

Notably, commercially available nanofibers often consist of combinations like chitosan with polyvinyl alcohol (PVA). However, PVA, essential in the electrospinning process, face limitations hindering its practical application. PVA's high hydrophilicity and water absorption lead to swelling, impeding cell adhesion and restricting its use to non-adhesive dressings. Despite extensive research on nanofibers made from this synthetic polymer, its internal use for local drug delivery remains non-commercialized.

This research article aims to develop electrospun nanofibers using chitosan derivatives and PVA. These nanofibers, characterized by hydrophilicity and stability in aqueous environments, are intended for implantation as a local drug delivery system post-tumor excision surgery to prevent breast cancer recurrence in patients.

Experimental Section

The synthesis of thiosemicarbazide carboxymethyl chitosan involved combining carboxymethyl chitosan and ammonium hydroxide in ethanol, followed by the gradual addition of carbon disulfide, sodium chloroacetate, and hydrazine hydrate. The resulting mixture was filtered, washed with ethanol, and dried. For electrospinning, a chitosan derivative and PVA solution were prepared using formic acid, acetic acid, and water. The solutions were mixed in a 3:7 ratio and electrospun at specific parameters. Drug-loaded nanofibers were prepared by adding curcumin to the electrospinning solution. Heat treatment was then applied to cross-link the nanofibers in chitosan derivative at 70°C for 24 h.

Results and Discussion

The Eager 300 elemental analysis device model EA1112 was utilized to monitor the substitution percentage at various stages of the reactions. To assess the substitution efficiency of thiosimicarbazoid carboxymethyl chitosan, the carbon-to-oxygen ratio was employed, indicating a substitution range of 60.98%. The successful cross-linking of thiocarbonyl and amine groups is indicated by the reduction in sulfur content, enhancing reaction efficiency. This reaction aims to form cross-links without additional connectors to avoid residual binder issues. The decrease in sulfur content signifies successful completion, with a substitution efficiency of 49.16% due to solvent absence and sole heat utilization, ensuring a favorable yield.

To study drug release from nanofibers, a phosphate buffer solution and dimethyl sulfoxide mixture (9:1 ratio) were utilized in an oil bath at 37 °C.

Fig.1 illustrates that in non-crosslinked nanofibers, 69% of the drug is released within 24 h. In contrast, crosslinking after heating reduces initial drug release, with only 27% released in the first day. Over 24 days, heated nanofibers exhibit an 81% release rate, while unheated nanofibers reach 94% release within 2 days. This demonstrates the impact of crosslinking on controlling drug release kinetics from the nanofiber structure.
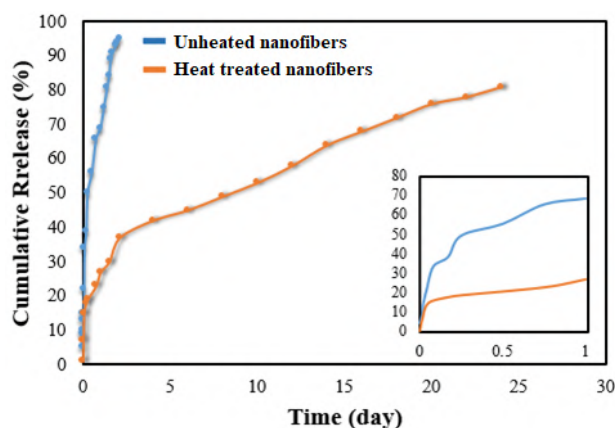
22nd Iranian Chemistry Congress (ICC22)
Iranian Research Organization for Science and Technology (IROST)
13-15 May 2024

03231-97589

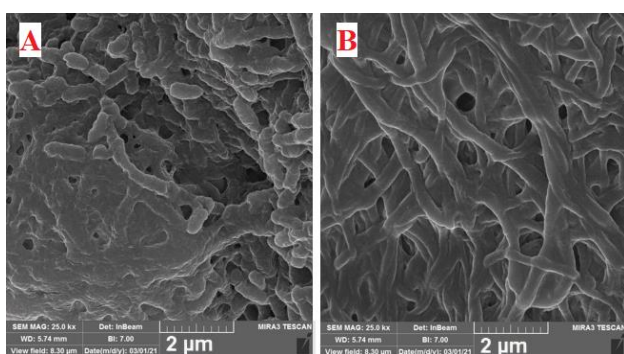**Fig.1:** Drug release profile from heated and unheated nanofibers

Fig.2: Degradation of A) unheated and B) heated nanofibers

Degradation analysis was performed on nanofibers with and without drugs, both before and after heat treatment, in plastic vials containing PBS at 37°C for varying durations from 1 to 3 days and intervals up to 6 months. Fig.2 illustrates the experimental procedure where drug-loaded nanofibers underwent hydrolytic degradation for a continuous 24-hour period both before and following a heat treatment regimen. Notably, the degradation kinetics within a single day exhibited a significant disparity between the unheated nanofibers, which experienced a rapid degradation rate, and the heated nanofibers, where no discernible degradation was detected. This observation underscores the contrasting effects of heat treatment on the degradation behavior of drug-containing nanofibers, emphasizing the critical role of thermal processing in influencing the structural stability of such materials. As shown in Fig.3, unheated nanofibers showed significant degradation within a day, with drug-free and drug-loaded nanofibers retaining 26.2% and 29.6% of their weight, respectively. The hydrophilic nature of unheated nanofibers caused surface erosion. Heated nanofibers exhibited swelling behavior, minimal erosion, and prolonged degradation up to 6 months. Cross-linking reduced the degradation rate of highly hydrophilic polymer-containing nanofibers, aligning their behavior with water-repellent counterparts.
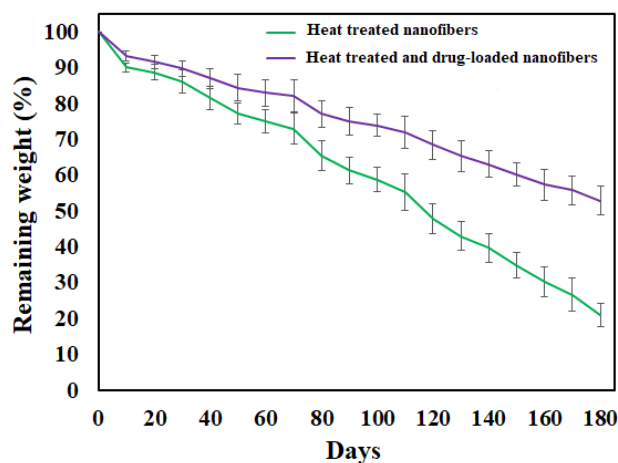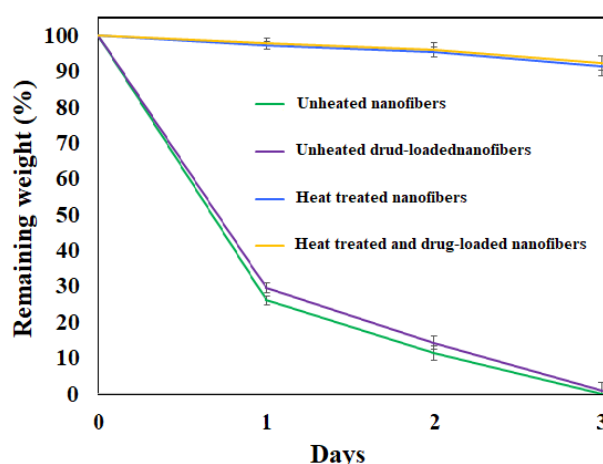

Fig.3: Degradation of nanofibers through 3 and 180 days

Conclusions

Novel nanofibers for drug delivery were developed using thiosimicarbazide carboxymethyl chitosan and PVA to enhance stability in local drug delivery systems. The fabrication method is cost-effective and utilizes readily available materials, aiding future commercialization. Crosslinking thiocarbonyl and amine groups in the nanofibers represents an innovative polymer chemistry approach, eliminating the need for a separate crosslinker, enabling heat-based reactions, and avoiding solvent requirements, promising improved drug delivery efficiency.

References

[1] Arnold, M., Morgan, E., Rumgay, H., Mafra, A., Singh, D., Laversanne, M., ... & Soerjomataram, I. (2022). Current and future burden of breast cancer: Global statistics for 2020 and 2040. The Breast, 66, 15-23.

[2] Sedghi, R., Gholami, M., Shaabani, A., Saber, M., & Niknejad, H. (2020). Preparation of novel chitosan derivative nanofibers for prevention of breast cancer recurrence. European Polymer Journal, 123, 109421.

22nd Iranian Chemistry Congress (ICC22)
Iranian Research Organization for Science and Technology (IROST)
13-15 May 2024

03231-97589

IROST

3D bioprinting of waterborne polyurethane scaffolds for the regeneration of bone defects

Alireza Shaabani, Marziye Gholami, Nahid Salimiyan, Roya Sedghi *

Corresponding Author E-mail: r_sedghi@sbu.ac.ir

Department of Polymer & Materials Chemistry, Faculty of Chemistry and Petroleum Sciences, Shahid Beheshti University, G.C, 1983969411, Tehran, Iran.

Abstract: This study employs bioprinting to engineer bone tissue based on chitosan sulfonate waterborne polyurethane and alginate, resulting in high cell viability and osteoblast differentiation. In addition, according to alizarin red S staining and alkaline phosphatase activity results, the cells were able to differentiate into osteoblasts and produce an extracellular matrix.

Keywords: 3D-Print; Waterborne polyurethane; Chitosan; Bone tissue engineering

Introduction

Polyurethane-based inks present various benefits for bone tissue engineering. They are biocompatible, supporting cell viability and growth without adverse reactions. Their mechanical properties can be tailored to imitate natural bone, offering required rigidity and flexibility. These inks are biodegradable, enabling natural tissue replacement, and water-based, simplifying handling and being eco-friendly[1, 2]. In this research, a chitosan sulfonate-based waterborne polyurethane/alginate bio-ink was optimized to promote cell viability and proliferation. It was utilized to encapsulate BMP-2 protein for functional bone tissue generation. Additionally, in vitro assessments were conducted on bioprinted scaffolds to evaluate bone regeneration efficiency.

Experimental Section

Chitosan sulfonate (CSS) was synthesized from the reaction between 1,4-BS (4 g) and CS solution (2 wt%) in 1 wt% acetic acid solution at 60 °C for 10 h. The product is precipitated in cold acetone. Then, the resulting product is dried in a vacuum oven at 30 °C for 24 h [3].

The chitosan sulfonate-based waterborne polyurethane (WPU) was prepared through a one-pot synthesis using the required amounts of polycaprolactone diol 2000 Da, isophorone diisocyanate, 2,2-bis(hydroxymethyl)propionic acid, and chitosan sulfonate[4].

The bio-inks were prepared by using different ratios of WPU and alginate solutions. Initially, the WPU and sodium alginate were added to the deionized water in concentrations of 30% and 5% w/v, respectively. All bio-inks contained BMP-2 with respect to the dry WPU and alginate polymers (Table 1).

Table1: Different ratios of materials in bioink composition

Sample	Sodium alginate (%)	Waterborne polyurethane (%)
WPU0	100	0
WPU20	80	20
WPU40	60	40

a Respect to the dry WPU and alginate (%wt/wt)

Results and Discussion

As can be seen in Fig. 1, CS shows absorption bands in the wavenumbers 3440 cm^{-1}, 2920 cm^{-1}, 2846 cm^{-1}, 1659 cm^{-1}, 1594 cm^{-1}, and 1048 cm^{-1}, which are related to the stretching vibrations of amine, hydroxyl, symmetrical and asymmetrical $-CH_x-$, amide I, amide II, and C-O ether groups [1].
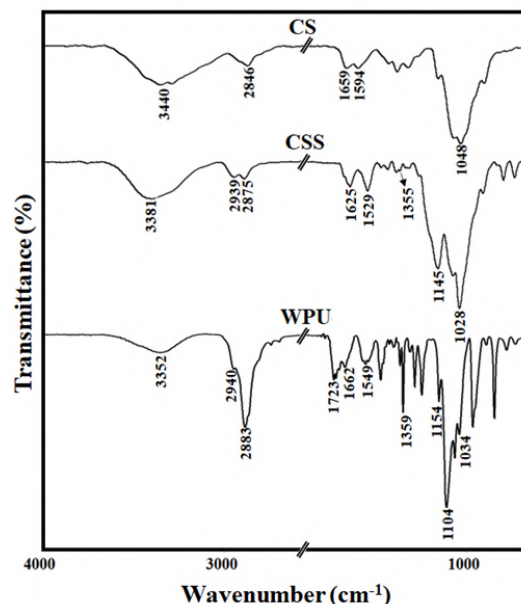

Fig.1: FT-IR spectrum of CS, CSS, and WPU

In the FT-IR spectrum of CSS, the absorption bands at 1028 cm^{-1}, 1145 cm^{-1}, and 1355 cm^{-1} are related to the stretching vibrations of the S=O group, which indicates

22nd Iranian Chemistry Congress (ICC22)
Iranian Research Organization for Science and Technology (IROST)
13-15 May 2024

03231-97589

the successful synthesis of CSS. Moreover, in WPU sample, the combination of WPU-CSS absorption peaks at 3352 cm^{-1} (stretching vibrations of -NH$_x$- groups (CSS, urethane and urea), 1723 cm^{-1} (stretching vibration of the carbonyl group of the PCL), 1104 cm^{-1} (stretching vibration of C-O-C bond of the PCL), 1028 cm^{-1}, 1145 cm^{-1}, and 1355 cm^{-1} (S=O group of the CSS), 1662 cm^{-1} (carbonyl urethane), and 1549 cm^{-1} (-NH- bending of urethane and urea).
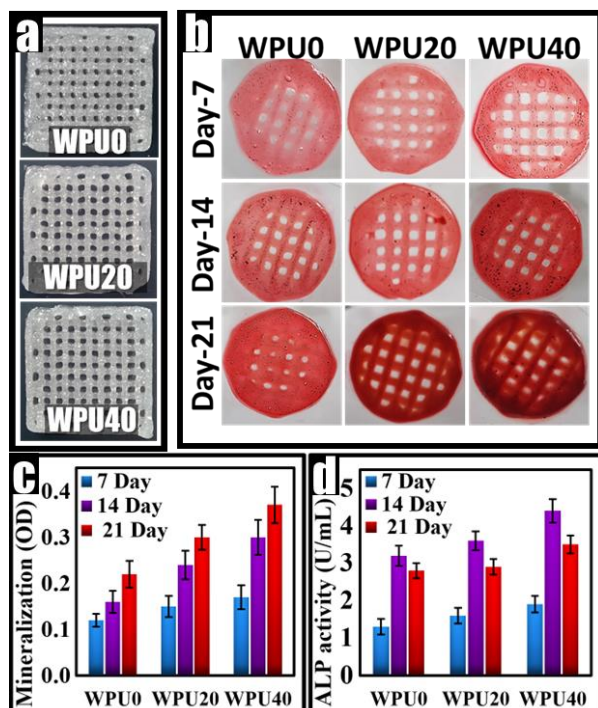
Fig.2: a) Optical image of scaffolds, b) qualification of alizarin red s staining, c) quantification of alizarin red s staining, and d) Alkaline phosphatase activity on day 7, 14, and 21.

The images in Fig. 2a demonstrate the ability of hydrogels to form 3D scaffolds with high precision and integrity, showing minimal defects in the patterns.

The effectiveness of scaffolds containing BMP-2 was evaluated through alizarin red s activity at different time points. Results in Fig. 2 (b &c) indicate that the osteogenic differentiation and mineralization of adipose-derived mesenchymal stem cells were more prominent in scaffolds with a higher WPU component on days 14 and 21. Studies have revealed that CSS can enhance the mineralization process necessary for bone tissue formation by depositing hydroxyapatite[5].

ALP activity, a marker of osteogenesis, was used to assess cell proliferation and differentiation on bioprinted scaffolds over various time points. Fig. 2d shows that ALP activity increased as the culture time extended from day 7 to day 21, with all scaffolds exhibiting higher activity compared to WPU0. Scaffolds incorporating WPU showed significantly enhanced ALP activity, indicating WPU's

positive impact on osteoconductivity. Notably, WPU40 displayed the highest ALP activity consistently. These results align with previous studies suggesting that CSS incorporation in scaffolds improves cell attachment, protein adsorption, and osteogenic differentiation[5].

Conclusions

In summary, employing bioprinting technology to fabricate bone tissue with 3D structured scaffolds containing BMP-2 in a waterborne polyurethane-based bio-ink holds potential in creating bone grafts for critical defects. The capability to produce intricate structures with controlled porosity using 3D bioprinting provides an edge over conventional tissue engineering methods. Further enhancements in ink composition and printing settings could advance tissue engineering tactics for bone regeneration.

References

[1] Hung, K. C., Tseng, C. S., Dai, L. G., & Hsu, S. H. (2016). Water-based polyurethane 3D printed scaffolds with controlled release function for customized cartilage tissue engineering. Biomaterials, 83, 156-168.

[2] Hung, K. C., Tseng, C. S., & Hsu, S. H. (2014). Synthesis and 3D printing of biodegradable polyurethane elastomer by a water-based process for cartilage tissue engineering applications. Advanced healthcare materials, 3(10), 1578-1587.

[3] Rwei, S. P., & Lien, C. C. (2014). Synthesis and viscoelastic characterization of sulfonated chitosan solutions. Colloid and Polymer Science, 292, 785-795.

[4] Shaabani, A., & Sedghi, R. (2021). Preparation of chitosan biguanidine/PANI-containing self-healing semi-conductive waterborne scaffolds for bone tissue engineering. Carbohydrate Polymers, 264, 118045.

[5] Chen, H., Yu, Y., Wang, C., Wang, J., & Liu, C. (2019). The regulatory role of sulfated polysaccharides in facilitating rhBMP-2-induced osteogenesis. Biomaterials science, 7(10), 4375-4387.

The effect of Si/Al ratio in the synthesis of B/H- ZSM-5 catalyst in methanol to Propylene

M.Hamidzadeh*, Solmaz Shifte, Ali Abdolali
Corresponding Author E-mail: Hamidzadeh@nipc.ir
National Petrochemical Company, Petrochemical Research and Technology Company, P.O. Box: 1435884711, Tehran, Iran.

Abstract: A series of boron-containing H-ZSM-5 zeolites with different Si/Al ratios between 112 and 152 were prepared employing the hydrothermal method. The evaluation of catalytic performance in the methanol-to-propylene (MTP) reaction shows that the catalyst with Si/Al equal 132 illustrated the best lifetime and selectivity to propylene.

Keywords: Methanol, propylene, H-ZSM-5, Si/Al ratio.

Introduction

ZSM-5 zeolite is composed of straight channels, sinusoidal channels, and tunable acidity sites. It has been used in fixed-bed methanol-to-propylene reactors; however, this use faces two notable challenges: increasing the catalyst lifetime and enhancing the propylene selectivity [1]. therefore in our approach in this research, the coke formation can be controlled by the number of strong acid sites and Si/Al ratio in synthetic gel.

Experimental Section

A series of B/ZSM-5 hierarchical zeolites with a molar ratio of silicon to aluminum between 112 and 152 were synthesized through the hydrothermal crystallization method. The product was filtered, washed, dried, and calcined in air at 583 K for 6 h to remove the template Then B/HZSM-5 was formed by an ion exchange process. Catalyst evaluation was carried out on a fixed bed reactor at 480°C and atmospheric pressure. We used aqueous methanol as a feed with a methanol mass content of 72% and a WHSV of 8.0 h-1 methanol in the feed.

Results and Discussion

According to Table 1, the surface characteristics of the three catalysts are the same, and changing the Si/Al ratio in the gel in the range of 112 to 152 does not change the micro surface, meso surface, total surface area, and pore volume. According to XRD, the decrease in the intensity of the diffraction in 2theta equals 7.8 compared to the diffraction in 2theta equals 9 indicates a decrease in the number of diffraction planes in straight channels compared to zigzag, so the diffusion limit resistance in this catalyst is low. The relative intensity of this diffraction is the lowest in catalyst 2, so as we expected, this catalyst showed a longer lifetime (113 hours) and at the same time produced more propylene, as confirmed in Table 1.
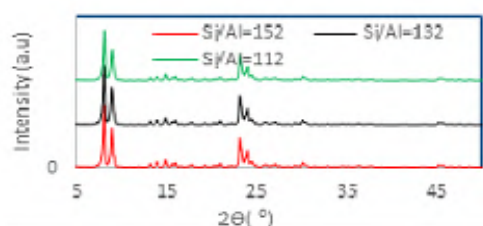

Fig.1:X-ray diffraction of catalysts

On the other hand, comparing the results of surface elemental analysis (EDX) with bulk analysis (XRF) shows that the amount of surface aluminum compared to bulk [2] aluminum in catalyst 3 is higher than other catalysts. Therefore, there are more strong acid sites (Brønsted) on the surface of catalyst 3. Therefore, more coke is formed on the surface of this catalyst and covers the surface pores. Strong acidic sites in bulk can convert methanol and dimethyl ether to olefins, but these sites on the catalyst surface cause coke formation and block surface pores.

Table1: properties and performance of catalysts

Properties	Unit	Cat1 Si/Al=152	Cat2 Si/Al=132	Cat3 Si/Al=112
S_BET	m²/g	361	369	355
V Micro-pore	cc/g	0.08	0.09	0.09
S Micro-pore	m²/g	162	187	194
HF		0.23	0.24	0.24
Si/Al (EDX)		182	173	122
Si/Al (XRF)		222	211	182
Mol Pr/g cat		3.03	3.65	2.3
Life time		96	113	78
g pr/g cat in h		1.33	1.36	1.23

Conclusions

the catalyst with Si/Al equal 132 illustrated the best lifetime(about 113 h) and selectivity to propylene(45%) and the most mol of propylene in one hour. In this catalyst, the decrease in the intensity of the 7.8 line in XRD indicates the decrease in the number of plates in the straight channels, so the emission limit resistance in this catalyst is reduced and the lifetime is increased.

References

[1] Feng R., Zhou P., Liu B., Yan X., Hu X., Zhou M. (2022). Direct synthesis of HZSM-5 zeolites with enhanced catalytic performance in the methanol-to-propylene reaction. Catalysis Today Vol. 405–406, 299-308 https://doi.org/10.1016/j.cattod.2022.04.023

[2] Yuan K., Jia X.,Wang S., Fan Sh.,He Sh.,, Wang P., QinZ., Dong M., Fan W., Wang J.(2022) Regulating the distribution of acid sites in ZSM-11 zeolite with different halogen anions to enhance its catalytic performance in the conversion of methanol to olefins, Microporous and Mesoporous Materials 341 112051, https://doi.org/10.1016/j.micromeso.2022.112051

22nd Iranian Chemistry Congress (ICC22)
Iranian Research Organization for Science and Technology (IROST)
13-15 May 2024

03231-97589

IROST

Green synthesis of silver nanoparticles using Olive Leaf aqueous extract and its encapsulation with β-CD

Reza Allahyari, Mehrdad Hadadian, Behnam Mahdavi*

Corresponding Author E-mail:b.mahdavi@hsu.ac.ir

Department of Chemistry, Faculty of Science, Hakim Sabzevari University, Sabzevar.

Abstract: Silver nanoparticles (AgNPs) have antibacterial, antifungal, and antiviral properties. This study aims to synthesize AgNPs using olive leaf extract and forming an inclusion complex between AgNPs and β-CD to enhance the physicochemical properties of AgNPs. In this way, UV-Vis spectroscopy, FT-IR, DLS, and XRD analyses were performed to characterize the prepared silver nanoparticles and inclusion complex.

Keywords: Cyclodextrin; Olive leaf; Silver nanoparticle; inclusion complex

Introduction

Silver nanoparticles (AgNPs) have been attracting the attention of researchers due to their diverse applications in various fields notably in biomedicine [1]. AgNPs have anti-inflammatory, antiviral, antiangiogenic, and anti-platelet activity and cytotoxicity against cancer [2]. While many methods for synthesizing AgNPs are so costly and require hazardous chemical materials, it is crucial to focus on developing environmentally friendly approaches such as biosynthesis using natural agents like plant extracts [3]. The olive leaf extract is a promising candidate for the green synthesis of nanoparticles due to its antioxidant properties [4].

Cyclodextrins (CDs) are natural cyclic carbohydrates that are derived from starch degradation by glycosyl transferase enzyme (GCTase). The commonly known CDs include αCD, βCD, and γCD forms, consisting of 6, 7, and 8 glucose units, respectively. These CDs have a hydrophobic interior and a hydrophilic outer surface, providing a straightforward system for the encapsulation of diverse organic and inorganic compounds [5]. CDs enhance the solubility of insoluble compounds, regulate volatility and sublimation, protect labile guests from oxidation, mask off-flavors to modify taste, and moderate the release of drugs [6]. Among CDs, βCD is extensively utilized due to its optimal cavity size, cost-effectiveness, accessibility, biodegradability, and non-toxic nature [7].

This study aims to synthesize AgNPs using Olive leaf extract and form a β-CD/AgNPs inclusion complex to improve the physicochemical properties of AgNPs. Characterization of β-CD/AgNPs inclusion complex was performed by Fourier-transform infrared (FT-IR) spectroscopy, Dynamic light scattering (DLS), and X-ray diffractometry (XRD).

Experimental Section

Material

Olive leaf was collected from Sabzevar, Khorasan Razavi province. AgNO₃ salt and β-cyclodextrin were purchased from Sigma-Aldrich. Sodium hydroxide (NaOH) and hydrochloric acid (HCL) were purchased from Merck.

Preparation of aqueous extract

The olive leaves were collected, rinsed with deionized water to remove contamination, and kept in a dark environment. Then, powdered plant samples (10% V/W) were placed into an Erlenmeyer comprising deionized water. The mixture was heated to 80°C with continuous stirring for 30 min.

Synthesis of silver nanoparticles with Olive leaf extract

Initially, the pH of the plant extract was assessed. The extract was mixed with AgNO₃ at 1 to 3 mM concentrations to synthesize AgNPs. Hence, the reaction mixture was stirred for 220 minutes at 180 rpm at 60°C. therefore, the solution's color changed from brownish-yellow to dark brown within 20 *minutes*, indicating the synthesis of silver nanoparticles. Subsequently, the obtained nanoparticles were centrifuged at 12,000 rpm for 20 minutes to separate the brown residue.

Preparation of β-CD/AgNPs inclusion complex

The β-CD/AgNPs inclusion complex was prepared following the co-precipitation method with some modifications [8]. Briefly, 0.1g of AgNPs was dispersed in 50 mL of deionized water. Then, 0.6g of β-CD was added to the mixture and stirred at RT for 24h. Consequently, the reaction mixture was placed in an ultrasonic bath for 30min at 30°C and refrigerated at 4°C for 12h. Finally, the precipitated β-CD/AgNPs inclusion complex was separated, rinsed, and dried for further studies.

Results and Discussion

the UV-Vis method was used and the highest absorption peak was observed at 426 nm for nanoparticle biosynthesis analysis, (Fig. 1). Different factors can influence the morphology of AgNPs. In this study, the effect of pH, AgNO₃ concentration, temperature, and time were investigated. Based on the results, the mobility of silver ions was increased at higher temperatures. Besides,

22nd Iranian Chemistry Congress (ICC22)
Iranian Research Organization for Science and Technology (IROST)
13-15 May 2024

03231-97589

IROST

optimal synthesis was done at pH = 8, and the best UV-Vis peak was obtained at a 2 mM concentration of AgNO$_3$ at 426 nm.
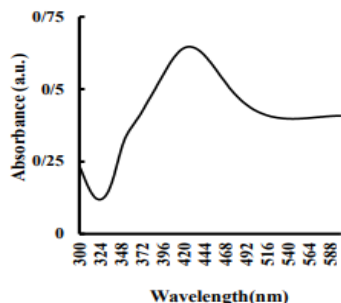

Fig.1: UV-visible spectra of synthesized AgNPs.

XRD analysis

X-ray diffraction is a useful method for the detection of CDs and their complexes. The appearance, disappearance, shift, and diffraction of peaks are evidence of interaction between components confirming the synthesis of the inclusion complex. As indicated in Fig. 2. AgNPs has a crystalline nature with two broad peaks at a range of 2θ ~15-25°, also at angles of 2θ ~38.12°, 44.32°, 64.73°, and 64.79°. The XRD pattern of β-CD/AgNPs shows characteristic peaks of AgNPs with small shifts at angels of 2θ ~ 38.19°, 44.37°, 64.79°, and 77.76°. In addition, two broad peaks of AgNPs at the range of 2θ~15-25° disappeared in the XRD pattern of β-CD/AgNPs which indicates the inclusion complex was formed successfully.
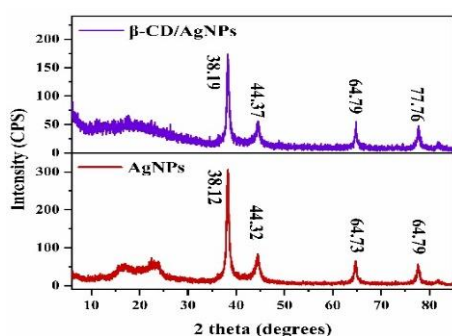
Fig.2: XRD patterns of AgNPs, and β-CD/AgNPs complex.

DLS analysis

Fig. 3 shows the DLS pattern of the biosynthesized AgNPs using olive leaf extract and β-CD/AgNPs inclusion complex. The AgNPs and β-CD/AgNPs show an average size of 22 and 51 nm, respectively. Besides, the inclusion complex recorded a narrow particle size distribution.
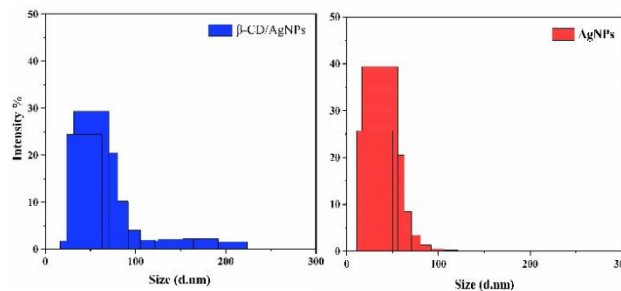
Fig.3: Particle size distribution analysis of synthesized AgNPs and β-CD/AgNPs complex.

Conclusions

Synthesizing nanoparticles using plants offers cost-effectiveness, minimal risk, and low toxicity. Additionally, CDs can enhance the physicochemical properties of AgNPs such as, stability, solubility, dissolution rate, and control release. In this study, the AgNPs were synthesized using olive leaf extract with the best result at pH=8 at high temperature at the concentration of 2 mM. Furthermore, the inclusion complex of AgNPs with β-CD was prepared and characterized using XRD and DLS techniques.

References

[1] Nadagouda, M.N., et al., *Green synthesis of Au nanostructures at room temperature using biodegradable plant surfactants.* Crystal Growth & Design, 2009. **9**(11): p. 4979-4983.

[2] Safaepour, M., et al., *Green synthesis of small silver nanoparticles using geraniol 164.* Avicenna journal of medical biotechnology, 2009. **1**(2): p. 111.

[3] Duan, H., D. Wang, and Y. Li, *Green chemistry for nanoparticle synthesis.* Chemical Society Reviews, 2015. **44**(16): p. 5778-5792.

[4] Alhajri, H.M., et al., *Olive leaf extracts for a green synthesis of silver-functionalized multi-walled carbon nanotubes.* Journal of Functional Biomaterials, 2022. **13**(4): p. 224.

[5] Di Cagno, M.P., *The potential of cyclodextrins as novel active pharmaceutical ingredients: a short overview.* Molecules, 2016. **22**(1): p. 1.

[6] Jin, Z.-Y., *Cyclodextrin chemistry: preparation and application.* 2013: World Scientific.

[7] Astray, G., J. Mejuto, and J. Simal-Gandara, *Latest developments in the application of cyclodextrin*, 2020. **106**: p. 105882.

[8] Kaur, K., R. Jindal, and D. Jindal, *Synthesis, characterization and studies on host-guest interactions of inclusion complexes of metformin hydrochloride with β–cyclodextrin.* Journal of Molecular Liquids, 2019. **282**: p. 162-168.

22nd Iranian Chemistry Congress (ICC22)
Iranian Research Organization for Science and
Technology (IROST)
13-15 May 2024

03231-97589

IROST

Bio-base pigment based on waste pomegranate peels for Natural Ink

Shohre Rouhani [a]*, Poua Jahanshahi[b], Mozhgan Hosseinnezhad [a], Kimiya Rastgou Moghadam[c]

Corresponding Author E-mail: Rouhani@icrc.ac.ir

[a] Department of Organic Colorant, Institute for Color Science and Technology, Iran.
[b] Department of Graphic Design, Oklahoma State University, USA.
[c] Fin Art institute, University of Applied Arts Vienna, Austria.

Abstract: Today natural pigments are attracted much attention because of environmental accepts and human health in all area of related industries. In this work we reported extraction of dyes from waste of pomegranate peel to prepare an aluminum lake pigment for ink formulation, the extraction process was studied by the use of the response surface methodology (RSM). Preparation of lake pigments of different metal content were studied by uv-vis spectrophotometry, FTIR, SEM and DSC analysis. The results suggest that obtained lake pigments have good potential for use in ink formulation.
Keywords: Pomegranate, natural Ink, peel extract

Introduction

For centuries, ink is made from natural products such as berries, barks, and extracts of leaves. These have been used as raw materials to create various colors and to produce ink, dye, or paint when mixed with other substances [1]. Ink has been studied in a wide area of applications including artwork, inkjet printing [2,3] and bio-ink [4]. Inks are commonly made today from non-renewable synthetic resources such as petroleum- and chemical-based solvents, which are harmful to both users and the environment. Unprotected contact with ink may cause severe headaches, skin irritation, or damage to the nervous system likely due to the effects of solvents or pigment, in the ink. The preparation of a dye lake could be an economically and ecologically useful route leading to a sustainable plant-based pigment. These pigments then could be applied in mass coloration of plastics, textile, ink and paint, with biodegradation of the polymer matrix the dye lake will be released into the environment [5-8].

In this work we have reported extraction of dyes from waste pomegranate peel to prepare an aluminum lake pigment for ink formulation, the extraction process is optimized and the lake pigment preparation ad characterization is reported.

Experimental Section

Extraction of dye

0.5 g of the powdered sample was added to 50 ml of the solvent and shaken for 50 minutes at a constant incubation shaker (250 rpm) at 40 ° C. The final mixture was filtered through filter paper and the absorbance of the solution was measured by spectrophotometer.

Preparation of lake pigment

The pre-dissolved 10% solution of 25 mL $Al_2(SO4)_3$ at $50°C$ was added to a solution containing a mixture of 50 mL extracted dye 10% W/V .Then 10 mL NaOH(0.1 M) solution was added to adjust the pH of the mixtures to -7.

The mixture was cooled to room temperature to allow the precipitation of the aluminum-pmegranate-dye lake pigment. After settling down, the mixture was filtered and the precipitates were washed with ultra-pure water and dried on a filter paper at $100°C$ for 2 hr. The dried lake pigment precipitates were then powdered. The same process was repeated to precipitate the lake pigments by using ferrous sulfate:Alum ratios solution[19,20].

Result and discussion

The practical model in the response surface method is usually a quadratic relationship. In this method, a model is defined as each dependent variant, which expresses the main factors and reciprocal impressions on each variant, singly. The variance resolution results show the higher the regression coefficient and the lower the response variant amount (P<0.0001), the more significant impression on tests parameters, which means if the variant's response is higher (P>0.05) the parameter is not possible to exert a significant impact on the entire tests [8]. To present the linear impressions on the model and reciprocal impressions, a linear graph (Figure 1), and a three-dimensional response surface graph were depicted by model, respectively (Figure 2).
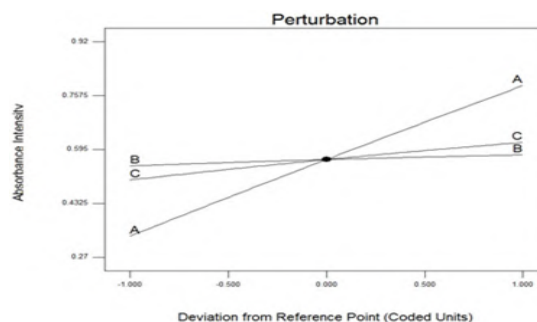

Fig. 1 Linear effects of the extraction parameters on absorptions of the pomegranate peel extracts. pH (A); Time (B); Temperature (C).

22nd Iranian Chemistry Congress (ICC22)
Iranian Research Organization for Science and Technology (IROST)
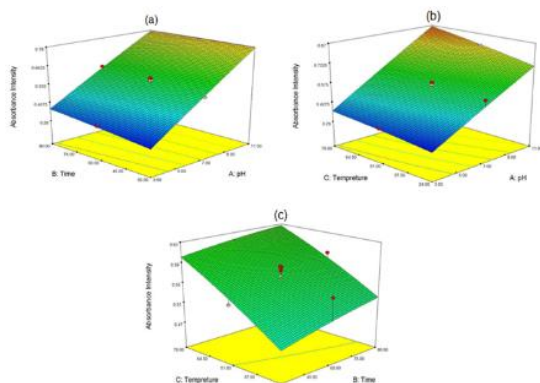13-15 May 2024

03231-97589

IROST

Fig. 2 Response surface plots (3D) showing the effects of the extraction parameters on absorptions intensity of pomegranate skin extracts. (a) pH and time; (b) pH and temperature; (c) time and temperature.

In this study, response surface methodology was used to optimize the extraction conditions of dyes in pomegranate peel. The data shows that the values of the obtained sorption intensities in extracted solutions through experimental experiments are in good agreement with the results predicted by the model. The difference between the absorption values for the experimental tests and the model prediction is about 3.915% (Table 1).

Table 1 Experimental and predicted values of response variables on numerical optimum conditions

	Optimum Extraction			Absorbance		
Response	pH	t (min)	T (℃)	Exp.	Pred.	CV (%)
Y_1	10.62	53.32	47.79	0.908	0.945	3.915

Lake pigment

The resulting Al-lake pigment were dark- yellow. The alum-Fe lake get more dark-yellow to dark-green to black at higher percentages of iron salt (Fig. 3). lake pigments prepared using alum were relatively high in yield, showed smooth and fine textures. Fig.3 shows the photograph and color appearerances of Al-Fe pomegranate pigments. Color cherecteristics of pigments obtained by reflectance spectrophotometry ($l^*a^*b^*$). The FTIR analysis of pigments confirm the complexation of extracted dye with metal salts. As shown in Fig. 4 vibrational peaks of -C=O and OH of anthocyanine were shifted by addition of metal ion. Thermal analysis was performed for dried powder dye, Al and Al-Fe pigments. Results showed the lake pigments have higher thermal stability up to $250°C$ against pure dye.

Fig. 3 photograph and color appearerances of Al-Fe pomegranate pigments

Conclusions

The response surface method of central composite design model by design expert software was used to optimize the extraction of dyes in the pomegranate skin. The optimum conditions in the extraction of dyes for pH, time and temperature were 10.62, 53.32 min and 47.79 °C, respectively. Preparation of lake pigments of different metal content resulted different colours. Prepared pigments showed different hue and appearanc with high thermal stability and indicated, they have good potential for aplication in ink formulation as a green source.

References

[1]Robert T. "Green ink in all colors" - printing ink from renewable resources. Prog Org Coat. 2015;78:287-292.

[2]Tutak D. Modified deinking of digitally printed paper with water based inkjet ink. Cellul Chem Technol. 2017;51(5–6): 483-488.

[3] Ozcan A. Investigation of the effect of para-amino benzoic acid (PABA) added starch-coated chemicals on the printability properties of paper. J Appl Biomater Funct Mater.2019;17(1).

[4]Carlyle, L. & Witlox, M. 2005. Historically Accurate Reconstructions of Artists' Oil Painting Materials. In: M. Clarke, J. Townsend & A. Stijnman, eds. Art of the Past – Sources and Reconstructions. London: Archetype Publications, pp. 53–59

[5]Kirby, J., Nash, S. & Cannon, J. eds. 2010. Trade in Artists' Materials – Markets and Commerce in Europe to 1700. London: Archetype Publications. Kirby, J., Spring, M. & Higgitt, C. 2005. The Technology of Red Lake Pigment Manufacture: Study of the Dyestuff Substrate. National Gallery Technical Bulletin, 26: 71–87.

22nd Iranian Chemistry Congress (ICC22)
Iranian Research Organization for Science and Technology (IROST)
13-15 May 2024

03231-97589

IROST

Synthesis and antibacterial activity evaluation of some new sulfonamide derivatives

Parisa Rezavandi Jamalouei, Ahmad Reza Massah

Corresponding Author E-mail: massahre@yahoo.com

Department of Medicinal Chemistry, Shahreza Branch, Islamic Azad University, P.O. Box 311-86145, Shahreza, Isfahan, Iran.

Abstract: A few new azomalontrile sulfonamide derivatives have been synthesized under solvent-free conditions and confirmed by FT-IR, ^{1}H NMR, and ^{13}C NMR. The antibacterial potential of synthesized sulphonamides was also studied against Staphylococcus aureus and Escherichia coli.

Keywords: sulfonamide hybrides; azomalononitrile; anti-bacterial activity

Introduction

Sulfonamides are a class of compounds that show a wide range of biological activities, including antibacterial [1], antitumor [2], antifungal [3], anti-inflammatory[4]. Azo sulpha drug and its derivatives are among the most common precursors in chemistry due to both their synthetic versatility and great potential for synthesis of compounds with intrinsic biological and pharmacological activities and these molecules constitute a part of the many commercialized drugs, such as Prontosil rubrum and Sulfasalazine [5]. Azo compounds which are produced one million tons per year in the world [6] have a wide range of applications in the dyeing of textile tissue [7]. Additionally, heteroaryl based azo dyes have been studied for their potent biological applications such as antioxidant, antimicrobial, antitumor, antidiabetics and antiviral activities [8]. As part of our ongoing study in this area, we report here the synthesis of some novel sulphonamide hybrid. The antibacterial activities of the synthesized sulfonamide are also reported.

Experimental Section

At first, acetic anhydride was added to p-anisidine and stirred. After completion of the reaction, sulfonation of N-(4-methoxyphenyl) acetamide was done by the reaction with chlorosulfonic acid. The synthesis of sulfonamides was done through the reaction of the sulfonated product of the previous step with different amines in solvent-free conditions. Then hydrolysis was done. In the next step, the obtained product was added to solution of hydrochloric acid and water, and for completion of the diazotisation, a solution of sodium nitrite was added portionwise. Finally, The reaction of azo sulfonated product with malononitrile and sodium acetate can be done in the presence of H$_2$O.

Results and Discussion

The main target for this project is the synthesis of azomalontrile sulfonamide derivatives according to green chemistry and under solvent-free conditions.

Firstly, N-(4- methoxy phenyl) acetamide was prepared by the acetylation of *p*-anisidine with acetic anhydride under solvent-free conditions.
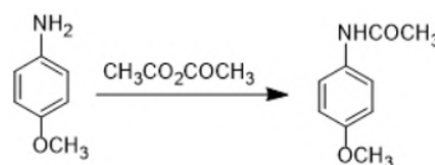

In the next step, chlorosulfonation of the formed N-(4-methoxyphenyl) acetamide was done using chlorosulfonic acid as a sulfonating agent.


The next step is the synthesis of sulfonamide derivatives through the reaction of the product of the previous step with different amines that were performed under solvent-free conditions.
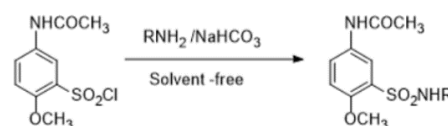

Then hydrolysis in acidic condition is done to obtain the corresponding sulfonamide-amines.
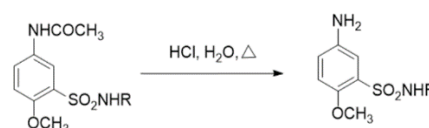
The product in the previous step is added to a solution of hydrochloric acid and sodium nitrite.
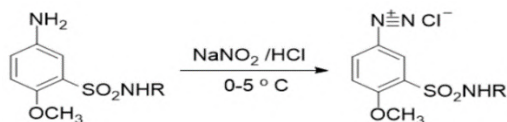
Finaly, the synthesis of azomalono nitrile sulfonamide derivatives through the reaction of the malononitrile and sodium acetate was performed in the presence of H_2O. New sulfonamide hybrids with good synthesis efficiency were identified by different techniques such as IR, ^{1}H NMR, ^{13}C NMR, and melting point.
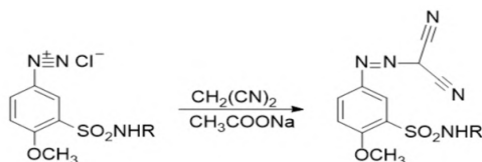
At the end of this research, the antibacterial activity of the synthesized sulfonamide hybrids was also investigated.

Conclusions

Environmentally friendly methods for producing compounds are very important. In this project, we have tried to present a method according to green chemistry under solvent-free conditions. All of the synthesized compounds were obtained in good to high yield and purity. The synthesized sulfonamides showed good antibacterial activity.

References

[1] Beheshti-Maal, K., Khazaeili, T., Asakere, N., Mousavi, F., & Massah, A. (2018). Synthesis of some novel sulfonamide-imines as potential antimicrobial agents. Letters in Organic Chemistry, 15(2), 111-117. https://doi.org/10.2174/1570178614666170707152357

[2] Faidallah, H. M., Al-Saadi, M. S., Rostom, S. A., & Fahmy, H. T. (2007). Synthesis of some sulfonamides, disubstituted sulfonylureas or thioureas and some structurally related variants. A class of promising antitumor agents. Medicinal Chemistry Research, 16, 300-318. https://doi.org/10.1007/s00044-007-9033-8

[3] Szafrański, K., Sławiński, J., Kędzia, A., & Kwapisz, E. (2017). Syntheses of novel 4-substituted N-(5-amino-1 H-1, 2, 4-triazol-3-yl) pyridine-3-sulfonamide derivatives with potential antifungal activity. Molecules, 22(11), 1926. https://doi.org/10.3390/molecules22111926

[4] Ning, X., Guo, Y., Ma, X., Zhu, R., Tian, C., Zhang, Z., Wang, X., Ma, Z., & Liu, J. (2013). Design, synthesis and pharmacological evaluation of (E)-3, 4-dihydroxy styryl sulfonamides derivatives as multifunctional neuroprotective agents against oxidative and inflammatory injury. Bioorganic & medicinal chemistry, 21(17), 5589-5597. https://doi.org/10.1016/j.bmc.2013.05.043

[5] Ghasemi, Z., Azizi, S., Salehi, R., & Kafil, H. S. (2018). Synthesis of azo dyes possessing N-heterocycles and evaluation of their anticancer and antibacterial properties. Monatshefte für Chemie-Chemical Monthly, 149, 149-157. https://doi.org/10.1007/s00706-017-2073-y

[6] Batool, S., Khalid, A., Jalal, K. C. A., Sarfraz, M., Balkhair, K. S., & Ashraf, M. A. (2015). Effect of azo dye on ammonium oxidation process and ammonia-oxidizing bacteria (AOB) in soil. RSC Advances, 5(44), 34812-34820. https://doi.org/10.1039/C5RA03768A

[7] Zheng, Z., & Shetty, K. (2000). Azo dye-mediated regulation of total phenolics and peroxidase activity in thyme (Thymus vulgaris L.) and rosemary (Rosmarinus officinalis L.) clonal lines. Journal of agricultural and food chemistry, 48(3), 932-937. https://doi.org/10.1021/jf9909306

[8] Prakash, S., Somiya, G., Elavarasan, N., Subashini, K., Kanaga, S., Dhandapani, R., ... & Sujatha, V. (2021). Synthesis and characterization of novel bioactive azo compounds fused with benzothiazole and their versatile biological applications. *Journal of Molecular Structure*, 1224, 129016. https://doi.org/10.1016/j.molstruc.2020.129016

Activation of the carbon-hydrogen bond of phenols

Mehdi Sheykhan*, Parvaneh Taghizadeh

Corresponding Author E-mail: sheykhanmehdi@gmail.com, Parvanehorgchem@gmail.com,

University of Guilan, Rasht, Iran.

Abstract: A method was proposed for the activation of the Carbon-Hydrogen bond of phenols and activation of molecular oxygen and the subsequent of the phenol substrate without the use of halides or external oxidants. According to this method, phenols are oxidized to quinones and then ortho-amination through an atomic-economical and most sustainable dehydrogenative oxidation and the amination method. This oxidation occurs through a radical activity of copper and oxygen gas under mild reaction conditions and with a broad substrate scope.

Keywords: Phenols, Activation of Carbon-Hydrogen bond, Quinones, Ortho amination.

Introduction

In the past decade, direct transition-metal-catalyzed C-H bond functionalization has emerged as an important tool for the construction of various C-N bonds [1]. The quinones compounds are exist in chemistry, nanotechnology, material science and medicine [2]. They play an important role in cell respiration [3]. recent reports on the conversion of phenols to quinones have been made through a series of reaction steps [4]. In our proposed project, activated C-H bond of phenols and then oxidized to quinones and and they are amination in 2-position in the reaction path with tertiary amines, by using inexpensive metal copper and without using any kind of external oxidant polluting the environment.

Experimental Section

We used from copper as promoter.oxygen gas used to oxidation phenol to benzoquinone. In order to check the experimental data, the reaction was tracked with thin layer chromatography (TLC).he product obtained was separated with columns chromatography.checking the result of NMR analysis data in deuterochloroform (CDCl3) confirmed the obtained product [figure 1]. The desired product was obtained as semi-solid with 85% yield and crimson color.

Results and Discussion

According to classical organic chemistry, position number 2 in phenols is nucleophilic and reacts with electrophiles, and aromatic electrophilic substitution reactions are not selective and other than position number 2, position 4 is also involved.Therefore, it is important to find a way to selectively activate only the 2-position in phenol, without involving the 4-position, and also to be able to react phenols with nucleophiles instead of electrophiles, and the example of Amplang in organic chemistry is.

In the method presented in this project, the position of ortho phenols by tertiary amines, nucleophile and not electrophile - amplang - in only one step and without using expensive metal or chemical oxidant that pollutes the environment and is expensive, without involving the para position. has been activated. In this method, phenolic compounds are oxidized to benzoquinone and it is selectively aminated in position 2.
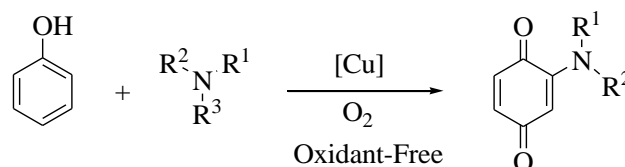

Fig. 1: Amination of benzoquinone

Conclusions

In summary this project opened a new window in the field of activation of C-H bond of ohenols, oxidation them to quinones and then amination of quinones. In fact the ortho position of phenols, which itself is a nucleophil, react with amines that have nucleophilic properties.

References

[1] Louillat-Habermeyer, M. L., Jin, R., & Patureau, F. W. (2015). O2-mediated dehydrogenative amination of phenols. Angewandte Chemie International Edition, 54(13), 4102-4104.

[2] Patai, S. (1974). The chemistry of the quinonoid compounds. (No Title).

[3] C. E. Price, A. J. M. Driessen, Biochim. Biophys. Acta Mol. Cell Res. 2010, 1803, 748 – 766 and references therein.

[4] Angew. Chem. Int. Ed. 2019, 58, 18530 –18534

Synthesis and antibacterial activity evaluation of some new Triazole methyl salicylate sulfonamide derivatives

Hossein Babaei, Ahmad Reza Massah

Corresponding Author E-mail : massahar@yahoo.com

Department of Chemistry, Shahreza Branch, Islamic Azad University, P.O. Box 311-86145, Shahreza, Isfahan, Iran.

Abstract: A few new 1,2,3-triazole sulfonamide derivatives have been synthesized under solvent-free conditions using different amines and confirmed by FT-IR, ^{1}H NMR, and ^{13}C NMR. The antibacterial potential of the synthesized sulfonamides was also studied against Escherichia coli and Staphylococcus aureus.

Keywords: Sulfonamide hybrids; 1,2,3-triazole; anti-bacterial activity

Introduction

Sulfonamides have received considerable attention in recent years due to their wide range of biological properties. Sulfonamide derivatives are known to exhibit various pharmacological activities such as anticonvulsants [1], anticancer [2], antibacterial [3], anti-inflammatory [4] and antitumor [5] agents. Pharmaceutically important examples include the protease inhibitor amprenavir, analgesic celecoxib and antimigraine agent sumatriptan [6]. Although many efforts have been made toward the development of novel sulfonamides, the conventional synthesis method involves the reaction of amino compounds with sulfonyl chlorides [7]. In the past few decades, heterocyclic chemistry has been one of the most important disciplines in organic synthesis and pharmaceutical chemistry [8]. The most promising heterocyclic compounds are azoles which are five-membered nitrogen heterocycles [9].

Triazoles are found in the structure of some drugs such as Anastrozole and Fluconazole. Other pharmacutical properties of triazole-containing compounds are antifungal [10], anticancer [11], antibacterial [12], and anti-inflammatory [13] activities.

As part of an ongoing study in this field, we are going to report the synthesis of some novel sulfonamide hybrid. The antibacterial activities of the synthesized sulfonamide are also reported.

Experimental Section

At first, the reaction of methyl salicylate and propargyl bromide can be done in the presence of DMF (dimethylformamide) solvent. Then the triazole ring was formed through the reaction of the product of the previous step with sodium azide, benzyl bromide, sodium ascorbate and copper sulfate. Sulfonation of triazole methyl salicylate was done by reaction with chlorosulfonic acid. The synthesis of new sulfonamides was done through the reaction of the sulfonated product of the previous step with different amines in solvent-free conditions.

Results and Discussion

In this regard, the synthesis of triazole methyl salicylate sulfonamide derivatives under solvent-free and suitable conditions and according to green chemistry is the main target of this project. Firstly, the reaction between methyl salicylate and propargyl bromide was carried out in DMF (dimethylformamide) as solvent.
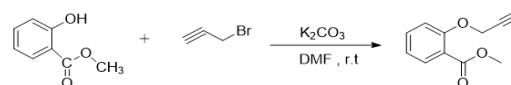
Then, benzyl bromide, sodium azide, sodium ascorbate, and copper sulfate were added to the product of the first step in water and DMF as a mixed solvent in a ratio of one to one.
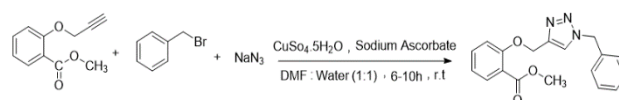
In the next step, sulfonation of the formed triazole methyl salicylate ring through reaction with chlorosulfonic acid was done.
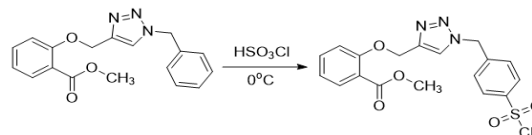
The last step is the synthesis of triazole methyl salicylate sulfonamide derivatives through the reaction of the product of the previous step with different amines that were performed under solvent-free conditions. New sulfonamide hybrids with good synthesis efficiency were identified by different techniques such as IR, 1H NMR, 13C NMR, and melting point.

22nd Iranian Chemistry Congress (ICC22)
Iranian Research Organization for Science and Technology (IROST)
13-15 May 2024

03231-97589

At the end of this research, the antibacterial activity of the synthesized sulfonamide hybrids was investigated.

IR (KBr, cm^{-1}) = 3262 (N-H), 2952 (C-H), 1727(C=O), 1597(N=N), 1510 (C=C), 1336,1159 (SO2).
^{1}H NMR (400 MHz, DMSO) δ (ppm) = 9.96 (s, 1H, N-H), 8.51 – 7.21 (m, 9H, Ar-H), 7.01 (s, 2H, Ar-H), 6.93 – 6.80 (m, 2H), 5.76 (s, 2H), 5.36 (s, 2H), 3.88 (s, 6H).

Conclusions

In this research, an environmentally friendly method was presented for the synthesis of new sulfonamide derivatives under solvent-free conditions. Good to high yield of products, easy separation, and green conditions are some of the advantages of this synthetic method. The synthesized sulfonamides showed good antibacterial activity.

References

[1] Li, J., Lou, J., Wang, Z., Wang, T., Xiao, Y., Hu, X., Liu, P., & Hong, X. (2015). Design, synthesis and pharmacological evaluation of novel N-(2-(1, 1-dimethyl-5, 7-dioxo-4, 6-diazaspiro [2.4] heptan-6-yl) ethyl) sulfonamide derivatives as potential anticonvulsant agents. European Journal of Medicinal Chemistry, 92, 370-376.
https://doi.org/10.1016/j.ejmech.2015.01.008

[2] Reddy, N. D., Shoja, M., Biswas, S., Nayak, P. G., Kumar, N., & Rao, C. M. (2016). An appraisal of cinnamyl sulfonamide hydroxamate derivatives (HDACáinhibitors) for anti-cancer, anti-angiogenic and anti-metastatic activities in human cancer cells. Chemico-biological interactions, 253, 112-124.
https://doi.org/10.1016/j.cbi.2016.05.008

[3] Zoumpoulakis, P., Camoutsis, C., Pairas, G., Soković, M., Glamočlija, J., Potamitis, C., & Pitsas, A. (2012). Synthesis of novel sulfonamide-1, 2, 4-triazoles, 1, 3, 4-thiadiazoles and 1, 3, 4-oxadiazoles, as potential antibacterial and antifungal agents. Biological evaluation and conformational analysis studies. Bioorganic & medicinal chemistry, 20(4), 1569-1583.
https://doi.org/10.1016/j.bmc.2011.12.031

[4] Ning, X., Guo, Y., Ma, X., Zhu, R., Tian, C., Zhang, Z., Wang, X., Ma, Z., & Liu, J. (2013). Design, synthesis and pharmacological evaluation of (E)-3, 4-dihydroxy styryl sulfonamides derivatives as multifunctional neuroprotective agents against oxidative and inflammatory injury. Bioorganic & medicinal chemistry, 21(17), 5589-5597.
https://doi.org/10.1016/j.bmc.2013.05.043

[5] Yoshino, H., Ueda, N., Niijima, J., Sugumi, H., Kotake, Y., Koyanagi, N., Yoshimatsu, K., Asada, M., Watanabe, T., & Nagasu, T. (1992). Novel sulfonamides as potential, systemically active antitumor agents. Journal of medicinal chemistry, 35(13), 2496-2497.
https://doi.org/10.1021/jm00091a018

[6] Pandya, R., Murashima, T., Tedeschi, L., & Barrett, A. G. (2003). Facile one-pot synthesis of aromatic and heteroaromatic sulfonamides. The Journal of organic chemistry, 68(21), 8274-8276.
https://doi.org/10.1021/jo034643j

[7] Tang, X., Huang, L., Qi, C., Wu, X., Wu, W., & Jiang, H. (2013). Copper-catalyzed sulfonamides formation from sodium sulfinates and amines. Chemical communications, 49(54), 6102-6104.
https://doi.org/10.1039/C3CC41249K

[8] Sayyafi, M., Seyyedhamzeh, M., Khavasi, H. R., & Bazgir, A. (2008). One-pot, three-component route to 2H-indazolo [2, 1-b] phthalazine-triones. Tetrahedron, 64(10), 2375-2378.
https://doi.org/10.1016/j.tet.2008.01.006

[9] Ayati, A., Emami, S., & Foroumadi, A. (2016). The importance of triazole scaffold in the development of anticonvulsant agents. European Journal of Medicinal Chemistry, 109, 380-392.
https://doi.org/10.1016/j.ejmech.2016.01.009

[10] Bitla, S., Sagurthi, S. R., Dhanavath, R., Puchakayala, M. R., Birudaraju, S., Gayatri, A. A., Bhukya, V. K., & Atcha, K. R. (2020). Design and synthesis of triazole conjugated novel 2, 5-diaryl substituted 1, 3, 4-oxadiazoles as potential antimicrobial and anti-fungal agents. Journal of Molecular Structure, 1220, 128705.
https://doi.org/10.1016/j.molstruc.2020.128705

[11] Lønning, P. E., Geisler, J., & Dowsett, M. (1998). Pharmacological and clinical profile of anastrozole. Breast cancer research and treatment, 49, S53-S57.
https://doi.org/10.1023/A:1006000806630

[12] Gao, F., Wang, T., Xiao, J., & Huang, G. (2019). Antibacterial activity study of 1, 2, 4-triazole derivatives. European Journal of Medicinal Chemistry, 173, 274-281.
https://doi.org/10.1016/j.ejmech.2019.04.043

[13] Mullican, M. D., Wilson, M. W., Conner, D. T., Kostlan, C. R., Schrier, D. J., & Dyer, R. D. (1993). Design of 5-(3, 5-di-tert-butyl-4-hydroxyphenyl)-1, 3, 4-thiadiazoles,-1, 3, 4-oxadiazoles, and-1, 2, 4-triazoles as orally active, nonulcerogenic antiinflammatory agents. Journal of medicinal chemistry, 36(8), 1090-1099.
https://doi.org/10.1021/jm00060a017

22nd Iranian Chemistry Congress (ICC22)
Iranian Research Organization for Science and Technology (IROST)
13-15 May 2024

03231-97589

IROST

Electrochemical Study of 3,5-Dinitrosalicylic Acid and Its Use in Paired Electrosynthesis

Samaneh Moradi Chaghamarani [a], Sadegh Khazalpour [*a], Ameneh Amani [b], Maryam Mehrdadian [a]

Corresponding Author E-mail: S.khazalpour@basu.as.ir

[a] Department of Analytical Chemistry, Faculty of Chemistry and Petroleum Science, Bu-Ali Sina University, Hamedan, Iran.

[b] Nahavand Higher Education Complex, Bu-Ali Sina University, Hamedan 65178-38683, Iran.

Abstract: In this study, the electrochemical behavior of 3,5-dinitrosalicylic acid (DNS) at different pH was investigated using cyclic voltammetry (CV) and coulometry with controlled potential, and by cyclic voltammogram analysis, intermediates and products synthesized, the governing mechanism of the system was determined.

Keywords: 3,5-dinitro salicylic acid; Cyclic voltammetry; Controlled potential coulometry

Introduction

One of the main uses of the nitro group in organic chemistry reactions is its production and conversion to other functional groups, especially amines.

Among the most abundant organic molecules are amines and compounds containing nitrogen. These substances are very important in biochemistry as components of producing proteins and peptides [1]. Nitroarenes can simultaneously form intermediate hydroxyamines and nitroarenes in the coupling process. [2]. 3,5-dinitrosalicylic acid has two nitro functional groups and two acidic functional groups (carboxylic acid and hydroxide). It can react with reducing sugars and other reducing molecules to form 3-amino-5-nitrosalicylic acid, which strongly absorbs light at 540 nm [3]. Also, this substance can form complexes with many divalent and trivalent metal ions such as Ni (II), Co (II). In addition, **DNS** is a very important pharmaceutical intermediate in the analysis of many enzymes and drug synthesis [4]. On the other hand, the electrochemical method is known as a green method. This method allows the oxidation/reduction of organic compounds without using stoichiometric amounts of toxic and dangerous reagents. Also, the conversion of the raw material to the product is usually done close to ambient temperature and pressure. The method has good selectivity, too [5]. because of the mentioned advantages and since there has been no report on an electrochemical study of **DNS**, in this study, the electrochemical behavior of 3,5-dinitrosalicylic acid at different pHs was investigated.

Experimental Section

Electrochemical measurements of DNS were performed using an Autolab PGSTA30 (Eco Chemie, The Netherlands). For voltammetric measurement, a three-electrode system including a reference electrode (Ag/AgCI), an auxiliary electrode (platinum wire) and a glassy carbon electrode was used as the working electrode.

3.5 dinitrosalicylic acid, ethanol, sodium bicarbonate, sodium hydroxide, HCl were used without purification.

Results and Discussion

The electrochemical reduction of 3,5-dinitrosalicylic acid was investigated using the cyclic voltammetry technique. The voltammogram of 1.0 mM **DNS** in 20:80 ethanol/buffer solution, pH: 4.01, is shown in Figure 1. CV curves were recorded at potentials from +0.6 to -1.1 volt with different scan rates (25 to 1000 mV.s^{-1}).

As shown in Fig.1, there are 4 cathodic and 2 anodic peak (C_{N1}, C_{N2}, C_1, C_2, A_1, and A_2) that strongly depend on the pH and potential scan rate.

By increasing the scan rate, the appearance of voltammograms changed due to the existence of a chemical reaction involved.
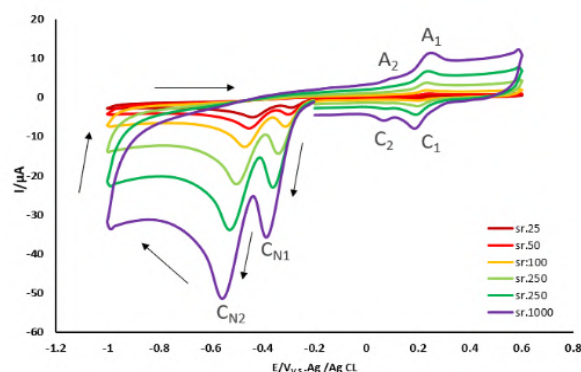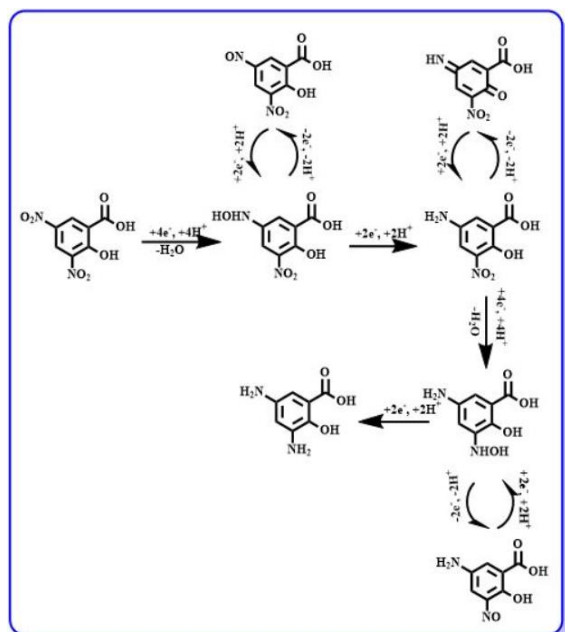

Fig.1: Cyclic voltammograms of a solution of 1.0 mM **DNS** at glassy carbon electrode in a mixture of buffer (pH: 4.01) / ethanol (80/20 v/v) at different potential scan rate: 25-500 mV/s. Room temperature.

22nd Iranian Chemistry Congress (ICC22)
Iranian Research Organization for Science and Technology (IROST)
13-15 May 2024

03231-97589

IROST

Scheme 1 Electrochemical behaviour of **DNS**.

Moreover, as clear in Fig 2, by increasing the pH, voltammograms will shift to less positive potentials and the colour of the solution changes from colourless to rich yellow. In addition, the current of all the anodic and cathodic peaks decreases, so no anodic and cathodic peaks are observed in an alkaline environment.
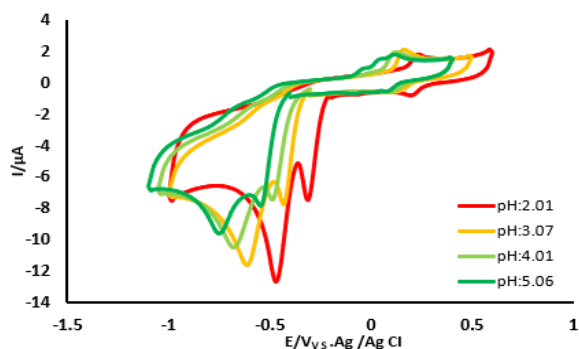
Fig 2: Cyclic voltammograms of **DNS** (1.0 mM) at the surface of glassy carbon electrode in buffered solutions with various pHs and same ionic strength (c = 0.25 M)/ethanol (80/20 v/v). Potential scan rate: 100 mV/s. Room temperature.

Electrolysis at controlled potential was investigated to investigate the number of exchanged electrons on both CN1 and CN2 cathodic peaks and the development method was evaluated by CV. As we can see in Figure 3, when we scan the potential to 0.3, the CN1 peak disappears after consuming 200 clones with the passage of eight electrons, but if we set the potential to 0.8, both CN1, CN2 peaks simultaneously are reduced.
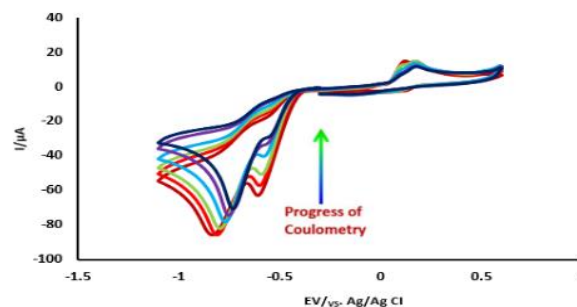

Fig 3: Cyclic voltammograms of DNS during controlled-potential coulometry: I) DNS (1.0 mmol) at the surface of working electrode; glassy carbon. Solvent/ ethanol (80/20 v/v) aqueous solution containing phosphate buffer (c = 0.25 M, pH : 4.01). Scan rate: 100 mV s^{-1}; Temperature: 25 ± 1 °C.

Conclusion

In this study, the electrochemical behavior of 3,5-dinitrosalicylic acid at different pH was investigated using the electrochemical method. The results show that reduction of **DNS** is highly dependent on pH and potential scan rate. The use of the **DNS** for the synthesis of intermediate compounds was carried out using a simple cell, at room temperature, without the need for a catalyst, using a carbon electrode. In addition to its simplicity, this method can be used for most nitroarenes. By using the ability to adjust the potential in this electrochemical method, we reduced the side reactions and optimized the electrolysis conditions, which finally increased the reaction efficiency so that by adjusting the potential, the desired product can be selectively synthesized.

References

[1] Kanazawa H, Higuchi M., Yamamoto K., (2005) An Electric Cyclophane: Cavity Control Based on the Rotation of A Paraphenylene by Redox Switching," Journal of the American Chemical Society, 127: pp. 16404-16405 https://doi.org/10.1021/ja055681i

[2] Casademunt Raghupathi, D. N. (2023). Yeast microencapsulation in coaxial systems (Bachelor's thesis, Universitat Politècnica de Catalunya).

[3] McKee, L. S. (2017). Measuring enzyme kinetics of glycoside hydrolases using the 3, 5-dinitrosalicylic acid assay. Protein-carbohydrate interactions: methods and protocols, 27-36. https://doi.org/10.1007/978-1-0716-3151-5_2

[4] Athmani, A. S., Madi, F., Laafifi, I., Cheriet, M., Issaoui, N., Nouar, L., & Merdes, R. (2019). DFT Investigation of a Charge-Transfer Complex Formation Between p-Phenylenediamine and 3, 5-Dinitrosalicylic Acid. Journal of Structural Chemistry, 60, 1906-1916. https://doi.org/10.1134/S0022476619120060

[5] Pletcher, D. (2018). Organic electrosynthesis–A road to greater application. A mini review. Electrochemistry Communications, 88, 1-4. https://doi.org/10.1016/j.elecom.

Synthesis and antibacterial activity evaluation of some new sulfonamide derivatives

Mohadeseh Ghaed Amini, Parisa Rezavandi Jamalouei, Ahmad Reza Massah

Corresponding Author E-mail: massahar@yahoo.com

[a]Islamic Azad University Isfahan Branch,Iran.

[b]Department of Medicinal Chemistry, Shahreza Branch, Islamic Azad University, P.O. Box 311-86145, Shahreza, Isfahan, Iran.

Abstract: A few new thiosemicarbazone sulphonamide derivatives have been synthesized under solvent-free conditions using different amines and confirmed by FT-IR, ^{1}H NMR, and [13] C NMR. The antibacterial potential of synthesized sulphonamides was also studied against Staphylococcus aureus and Escherichia coli.

Keywords: sulfonamide hybrides; thiosemicarbazone; anti-bacterial activity

Introduction

Sulfonamides are important scaffolds for the development of biologically relevant molecules because they display a wide variety of pharmacological properties including anti-inflammatory, antimicrobial, anticancer, antiviral, diuretic, and hypoglycemic [1]. The chemistry of sulfur-containing substances such as thiosemicarbazones (TSCs) has been receiving considerable attention in the area of medicinal chemistry because of their promising biological implications and remarkable pharmacological properties [2]. When thiosemicarbazones bind with metal ions, they have shown an array of potential anticancer, antimicrobial, and antioxidant activities [3]. Thiosemicarbazones are found in the structure of some drugs such as Triapine [4] and Methisazone [5]. As part of our study in this field, we report here the synthesis of some novel sulphonamide-thiosemicarbazones hybrids. The antibacterial activities of the synthesized compounds are also studied.

Experimental Section

Firstly, Sulfonation of 4-Methoxyacetophenone was done by the reaction with chlorosulfonic acid. The synthesis of new sulfonamides was done through the reaction of the sulfonated product of the previous step with different amines under solvent-free conditions. In the next step, The reaction of the obtained product with thiosemicarbazone can be done in the presence of ethanol as a solvent which produces sulphonamide-thiosemicarbazones hybrids.

Results and Discussion

The synthesis of thiosemicarbazone sulfonamide derivatives under solvent-free and according to green chemistry is the main target of this project.
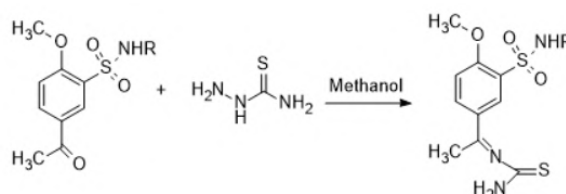
At first, chlorosulfonation of the 4-Methoxyacetophenone was done using chlorosulfonic acid as a sulfonating agent.
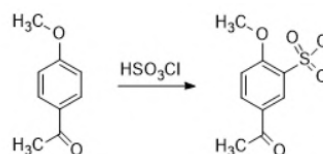
The next step is the synthesis of sulfonamide derivatives through the reaction of the product of the previous step with different amines that were performed under solvent-free conditions.

Finally, the synthesis of thiosemicarbazone sulfonamide derivatives through the reaction of the thiosemicarbazone with the synthesized sulfunyl chloride was performed in ethanol as solvent. New sulfonamide hybrids with good synthesis efficiency were identified by different techniques such as IR, ^{1}H NMR, ^{13}C NMR, and melting point.

At the end of this research, the antibacterial activity of the synthesized sulfonamide hybrids was also investigated.

22nd Iranian Chemistry Congress (ICC22)
Iranian Research Organization for Science and Technology (IROST)
13-15 May 2024

03231-97589

Conclusions

In this research, an environmentally friendly method was used for the synthesis of new sulfonamide derivatives under solvent-free conditions. All of the synthesized compounds were obtained in good to high yield and purity. The synthesized sulfonamides showed good antibacterial activity.

References

[1] Castaño, L. F., Cuartas, V., Bernal, A., Insuasty, A., Guzman, J., Vidal, O., ... & Insuasty, B. (2019). New chalcone-sulfonamide hybrids exhibiting anticancer and antituberculosis activity. *European journal of medicinal chemistry*, *176*, 50-60. https://doi.org/10.1016/j.ejmech.2019.05.013

[2] Ebrahimi, H. P., Hadi, J. S., Alsalim, T. A., Ghali, T. S., & Bolandnazar, Z. (2015). A novel series of thiosemicarbazone drugs: from synthesis to structure. *Spectrochimica Acta Part A: Molecular and Biomolecular Spectroscopy*, *137*, 1067-1077. https://doi.org/10.1016/j.saa.2014.08.146

[3] Siddiqui, E. J., Azad, I., Khan, A. R., & Khan, T. (2019). Thiosemicarbazone complexes as versatile medicinal chemistry agents: a review. *Journal of drug delivery and therapeutics*, *9*(3), 689-703. https://doi.org/10.22270/jddt.v9i3.2888

[4] Mrozek-Wilczkiewicz, A., Malarz, K., Rejmund, M., Polanski, J., & Musiol, R. (2019). Anticancer activity of the thiosemicarbazones that are based on di-2-pyridine ketone and quinoline moiety. *European Journal of Medicinal Chemistry*, *171*, 180-194. https://doi.org/10.22270/jddt.v9i3.2888

[5] Song, G. Q., Wang, W. M., Li, Z. S., Wang, Y., & Wang, J. G. (2018). First identification of isatin-β-thiosemicarbazones as novel inhibitors of New Delhi metallo-β-lactamase-1: Chemical synthesis, biological evaluation, and molecular simulation. *Chinese Chemical Letters*, *29*(6), 899-902. https://doi.org/10.1016/j.cclet.2017.09.035

22nd Iranian Chemistry Congress (ICC22)
Iranian Research Organization for Science and Technology (IROST)
13-15 May 2024

03231-97589

IROST

Isotherm, Kinetic, and Thermodynamic Study of Nickel Adsorption from Synthetic Sample Using Aminated Magnetic Mesoporous Silica

Fahime Salari Goharrizi[a], S. Yousef Ebrahimipour[a,*], Hadi Ebrahimnejad[b], S. Jamiladin Fatemi[a]

Corresponding Author E-mail: Ebrahimipour@uk.ac.ir

[a,c] Department of Chemistry, Faculty of Science, Shahid Bahonar University of Kerman, Kerman, Iran.

[b] Department of Food Hygiene and Public Health, Faculty of Veterinary Medicine, Shahid Bahonar University of Kerman, Kerman, Iran.

Abstract: Aminated magnetic mesoporous silica (MMS-NH$_2$) effectively removes nickel from water (synthetic and Arvand River). Amine modification boosted efficiency (64% to 90%) and capacity (165 to 237 mg/kg). Different adsorption mechanisms were observed for unmodified and amine-modified MMS. This reusable material shows promise for real-world nickel remediation

Keywords: Nickel adsorption, magnetic mesoporous silica, amine functionalization, isotherm, kinetic, thermodynamic study, Arvand River water

Introduction

Nickel (Ni) contamination in water poses a significant threat to human health and ecosystems [1, 2]. This study explores the use of amine-functionalized magnetic mesoporous silica (MMS-NH$_2$) for Ni removal from water. MMS offers advantages like high surface area and magnetic separation. Amine functionalization aims to improve adsorption capacity by providing additional binding sites for Ni(II) ions .

2. Experimental

2.1 Materials and Synthesis

At first, Fe$_3$O$_4$ nanoparticles were synthesized by co-precipitation method . Then, the fibrous nano-silica (KCC-1) were deposited with hydrothermal on their surface followed by amine functionalization with APTES [3, 4]. Various characterization techniques, including VSM, FESEM, EDX, XRD, and FTIR, were employed to analyze the morphology, structure, and surface properties of the synthesized materials.

2.2 Adsorption Experiments

Batch adsorption experiments were conducted to investigate the Ni adsorption capacity of MMS and MMS-NH$_2$. The effects of solution pH, contact time, and initial Ni concentration were studied. Flame atomic absorption spectroscopy (AAS) determined the residual Ni concentration after contacting the adsorbents with Ni solutions.

2.3 Isotherm, Kinetic, and Thermodynamic Studies

Langmuir, Freundlich, and Temkin isotherm models were used to analyze the equilibrium data and understand the adsorption mechanism. Kinetic studies employed pseudo-first-order and pseudo-second-order models to investigate the rate of Ni adsorption [5]. Thermodynamic parameters, including Gibbs free energy, were calculated to assess the feasibility and nature of the adsorption process.

2.4 Regeneration Experiments

The reusability of the synthesized materials was evaluated by performing five adsorption-desorption cycles. The effectiveness of 0.1 M HCl washing for regeneration compared to a soda solution was also investigated.

3. Results and Discussion

The results confirmed the successful synthesis and characterization of MMS and MMS-NH$_2$. Amine functionalization significantly improved the adsorption efficiency and capacity for Ni removal. Isotherm studies revealed the presence of different types of adsorption sites on the surface of MMS and MMS-NH$_2$. Kinetic studies suggested different adsorption mechanisms for unmodified and amine-modified MMS. Thermodynamic parameters indicated a favorable and endothermic process for Ni adsorption. The synthesized MMS-NH$_2$ effectively removed Ni from Arvand River water despite the presence of interfering contaminants. Additionally, the successful regeneration using 0.1 M HCl washing highlights the reusability of these nanomaterials.

4. Conclusion

This study demonstrates the potential of amine-functionalized magnetic mesoporous silica (MMS-NH$_2$) for efficient Ni removal from both synthetic solutions and real water samples. The enhanced adsorption capacity, reusability, and effectiveness against interfering contaminants make MMS-NH$_2$ a promising candidate for practical applications in Ni remediation.

22ⁿᵈ Iranian Chemistry Congress (ICC22)
Iranian Research Organization for Science and Technology (IROST)
13-15 May 2024

03231-97589

References:

[1] Genchi, G., et al., *Nickel: Human Health and Environmental Toxicology.* Int J Environ Res Public Health, 2020. **17**(3).

[2] Ahmad, M.S.A. and M. Ashraf, *Essential Roles and Hazardous Effects of Nickel in Plants*, in *Reviews of Environmental Contamination and Toxicology*, D.M. Whitacre, Editor. 2011, Springer New York: New York, NY. p. 125-167.

[3] Emrani, S., et al., *Magnetic fibrous silica mesoporous as a selective and efficient system for removal of Cd (II) ions with a focus on optimization by response surface methodology.* International Journal of Environmental Analytical Chemistry, 2023. **103**(4): p. 849-867.

[4] Moradi, M., J. Soleymani, and A. Jouyban, *A combination of amino-functionalized fibrous silica (KCC-1-NH2)/effectively and efficiently oxidized graphene oxide (EEGO) nanocomposite for dispersive solid-phase extraction, pre-concentration and fluorescence determination of total para-cresol in plasma samples of chronic kidney disease patients.* Journal of Pharmaceutical and Biomedical Analysis, 2022. **214**: p. 114746.

[5] Revellame, E.D., et al., *Adsorption kinetic modeling using pseudo-first order and pseudo-second order rate laws: A review.* Cleaner Engineering and Technology, 2020. **1**: p. 100032. https://doi.org/10.1016/j.clet.2020.100032

Photocatalytic degradation of acetaldehyde from polluted air by Ag/LaCoO₃ nanoperoviskite

Parvaneh Nakhostin Panahi*, Fatemeh Norouzi

Corresponding Author E-mail: panahi@znu.ac.ir

Department of Chemistry, Faculty of Science, University of Zanjan, Zanjan, 4537138791, Iran.

Abstract: In this study, LaCoO₃ nanoperoviskite was prepared by sol–gel method and then Ag cocatalyst was loaded on LaCoO₃ by the impregnated method. The physicochemical properties of the perovskites were analyzed by XRD and SEM. The photocatalytic activity of the perovskites was evaluated for the decomposition of acetaldehyde from polluted air.

Keywords: photocatalyst; Ag/LaCoO₃; acetaldehyde removal

Introduction

Since 1950, researchers identified volatile organic compounds (VOCs) as the constituents of petrochemical fog, leading to a tremendous increase in knowledge and awareness of their environmental functions. The VOCs generally are hydrocarbons whose boiling point is 50–260 °C at normal temperature (25 °C) and atmospheric pressure, and they evaporate easily. Considering the problems that VOCs pose on the environment and human health, it is necessary to prevent the release of these compounds into the environment. The high efficiency of the photocatalytic oxidation process has led to its application in the removal of various types of pollutants. This process uses a photocatalyst and a suitable light source to degrade pollutants. Commercial photocatalysts such as TiO₂ and ZnO are active in the UV region because of have a high energy gap. The UV light constitutes only 4% of sunlight. Therefore, it is necessary to use photocatalysts that are active in the range of visible light. Mixed metal oxides with perovskite structures are active photocatalysts in visible light [1].

Consequently, in the present paper, LaCoO₃ nanoperovskites with different loadings of silver (Ag/LaCoO₃) were synthesized and their photocatalytic activity was investigated for degradation of acetaldehyde pollutant under UV and visible light radiation.

Experimental Section

2.1. Preparation of photocatalysts

The sol-gel method was used for the preparation of LaCoO₃ nanoperoviskite. In this method, citric acid was used as a complexing agent, and ethylene glycol was used as an esterification and polymerization reaction agent. The specified amount of metals salt was dissolved in distilled water and then citric acid and ethylene glycol were added. The suspension was stirred with a magnetic stirrer and the temperature was raised to evaporate the solvent and form a gel. Then the resulting gel was heated at 200°C to decompose and burn the existing organic species. Finally, the obtained solid particles were powdered and calcined at 700 °C to form the perovskite structure [2].

In the next step, different amounts of silver were loaded onto LaCoO₃ by the impregnated method. In this method, a specific amount of LaCoO₃ perovskite powder and the required amount of silver were added to distilled water and stirred. The temperature was raised to evaporate the solvent. Next, the resulting material was dried in an oven at 80 °C and then calcined at 450°C.

2.2. Photocatalytic tests

For photocatalytic tests, a certain amount of the photocatalyst was placed inside the photoreactor, and it was sealed. Then, acetaldehyde was injected into the photoreactor using a micro syringe. The photoreactor was placed in the dark for 1 h to evaporate acetaldehyde and to achieve the absorption-desorption equilibrium of acetaldehyde on the photocatalyst, after which the lamp was turned on. At fixed time intervals of irradiation, the air inside the reactor was sampled using a gastight syringe and injected into the gas chromatography (Agilent GC) equipped with an OV-1 capillary column and flame ionization detector (FID). Finally, the degradation efficiency of acetaldehyde was calculated by the following equation:

$$\% \ degradation \ efficiency = \frac{C_0 - C_t}{C_0} \times 100 \qquad (1)$$

Where C_0 and C_t are the initial and final concentrations of acetaldehyde, respectively.

Results and Discussion

3.1. XRD and SEM

The XRD patterns of LaCoO₃ and Ag(4%)/LaCoO₃ are shown in Fig. 1. The XRD spectrum of the synthesized perovskites is in perfect agreement with the standard reference (JCPDS card 00-025-1060). This shows that LaCoO₃ was crystallized as a perovskite structure and

22nd Iranian Chemistry Congress (ICC22)
Iranian Research Organization for Science and Technology (IROST)
13-15 May 2024

03231-97589
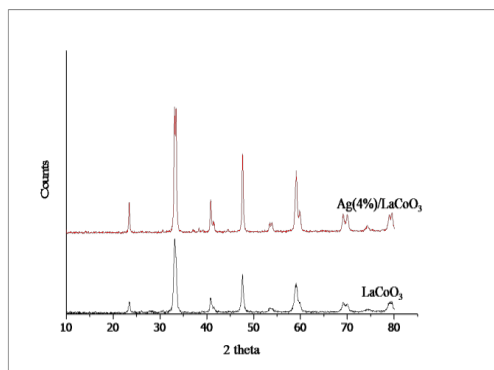
IROST

also the silver loading does not destroy the perovskite structure.

Fig.1: XRD patterns of $LaCoO_3$ and $Ag(4\%)/LaCoO_3$

Fig. 2 displays the SEM images of $LaCoO_3$ and $Ag(4\%)/LaCoO_3$ perovskites. According to this shape, the synthesized perovskite is spherical, and the particle size is in the range of 40–60 nm.
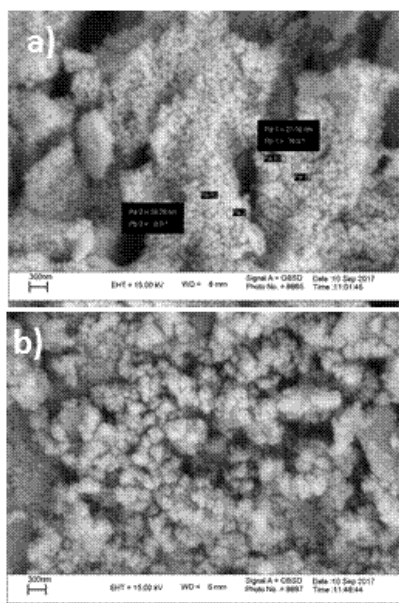

Fig.2: SEM images of (a) $LaCoO_3$ and (b) $Ag(4\%)/LaCoO_3$

3.2. Photocatalytic activity

The activity of synthesized nanoperovskites ($LaCoO_3$ and $Ag/LaCoO_3$) for degradation of acetaldehyde under visible and UV radiation is shown in Figs. 3 a and b. The removal efficiency of acetaldehyde in UV light is greater than visible because of the high energy of UV light. Fig. 3 shows that silver loading on $LaCoO_3$ improves its photocatalytic activity and acetaldehyde degradation. The photocatalytic activity increases with the increase of silver loading and finally, $Ag(4\%)/LaCoO_3$ removed 90% of acetaldehyde pollutant under UV light irradiation. The metallic silver particles (Ag^0) on the surface of $LaCoO_3$

trap the photoelectrons generated in $LaCoO_3$ and consequently, the recombination of photoelectron and hole is prevented. As a result, the photocatalytic performance and removal efficiency of pollutant increase [3].
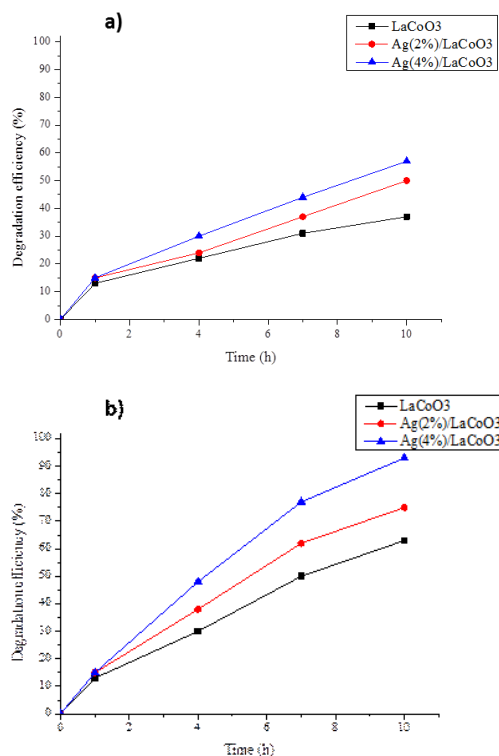

Fig.3: The degradation efficiency of acetaldehyde by photocatalytic processes using LaCoO3 and Ag/LaCoO3 under (a) visible and (b) UV radiation

Conclusion

In this project, $Ag/LaCoO_3$ nanoperoviskites with different amounts of silver were synthesized. The results of photocatalytic test showed that silver loading on $LaCoO_3$ improves photocatalytic activity and degradation of acetaldehyde pollutant.

References

[1] Nakhostin Panahi, P., Mohajer, S., Rasoulifard, M. H., & Farajmand, B. (2022). Synthesis of Ag/AgCl/TiO2 nanocomposite and study of photocatalytic activity in VOCs removal from gas phase. *International Journal of Environmental Analytical Chemistry*, *102*(9), 2195-2211.

[2] Nakhostin Panahi, P., Rasoulifard, M. H., & Babaei, S. (2020). Photocatalytic activity of cation (Mn) and anion (N) substitution in LaCoO3 nanoperovskite under visible light. *Rare Metals*, *39*(2), 139-146.

[3] Panahi, P. N., Babaei, S., & Rasoulifard, M. H. (2020). Synthesis and visible-light photocatalytic activity of nanoperovskites and exploration of silver decoration to enhance photocatalytic efficiency. *Desalination and Water Treatment*, 194-202.

Synthesis of La₂MnTiO₆ double perovskite loaded with graphene and study of photocatalytic activity for removal of toluene in the gas phase

Parvaneh Nakhostin Panahi*, Fatemeh Norouzi

Corresponding Author E-mail: panahi@znu.ac.ir

Department of Chemistry, Faculty of Science, University of Zanjan, Zanjan, 4537138791, Iran.

Abstract: The La₂MnTiO₆ double peroviskite was prepared by sol–gel method and its structure and morphology were characterized by XRD and SEM. In the following, graphene/La₂MnTiO₆ nanocomposite was also synthesized by a facile impregnated method. The photocatalytic activity of the catalysts was evaluated for the decomposition of toluene in the gas phase.

Keywords: photocatalyst; graphene/La₂MnTiO₆; toluene removal

Introduction

Volatile organic compounds (VOCs) are hydrocarbons whose vapor pressure is more than 10.3 kPa at normal temperature and pressure, and they evaporate easily. Most VOCs are toxic and contribute to the formation of secondary pollution in the atmosphere of the chemical and petrochemical industries. Researchers are trying to find effective and economical techniques to remove VOCs in the chemical and petrochemical industries. One of the most effective methods to remove these compounds is the photocatalytic process. In this process, a photocatalyst (such as TiO_2 and ZnO) and a suitable light source are used to degrade pollutants, and pollutants are decomposed into carbon dioxide and water or other harmless substances. The TiO_2 is the most usual photocatalyst but its activation requires the providing of ultraviolet radiation which covers only 3–5% of the total solar spectrum. Hence, the development of visible-light-responded photocatalysts for the effective use of sunlight is necessary for the field of photocatalysis. Mixed metal oxides with perovskite structures are active photocatalysts in visible light [1].

In this project, firstly, La₂MnTiO₆ double perovskite is synthesized using the sol-gel method, which is the most common method for the synthesis of nanoparticles in the solution phase, and then, its photocatalytic activity is investigated in the removal of toluene pollutant under ultraviolet and visible light radiation. Next, the effect of graphene loading on La₂MnTiO₆ in toluene removal will be investigated.

Experimental Section

2.1. Preparation of photocatalysts

The La₂MnTiO₆ double perovskite was synthesized by the sol-gel method. In this method, citric acid was used as a complexing agent, and ethylene glycol was used as an esterification and polymerization reaction agent. The specified amount of metals salt was dissolved in distilled water and then citric acid and ethylene glycol were added. The suspension was stirred with a magnetic stirrer and the temperature was raised to evaporate the solvent and form a gel. Then the resulting gel was heated at 200°C to decompose and burn the existing organic species. Finally, the obtained solid particles were powdered and calcined at 700 °C to form the perovskite structure [2].

The graphene (G) was loaded with 50 wt% on La₂MnTiO₆ and the impregnation method was used for loading. In this method, the required amount of graphene was added to distilled water and exposed to ultrasonic for uniform distribution. Then, a certain amount of La₂MnTiO₆ was added to the suspension. In the next step, the temperature was increased to 80 °C during stirring until all the water evaporated, and as a result, graphene was deposited on the La₂MnTiO₆. Finally, the obtained composite was dried at 80 °C for 12 h in an oven.

The synthesized photocatalysts were fixed to glass lamps by the thermal method.

2.2. Photocatalytic tests

To study the photocatalytic activity of La₂MnTiO₆ and graphene/La₂MnTiO₆ composite in the removal of toluene, a photoreactor (volume 1.5 L) equipped with a light source was utilized. For photocatalytic tests, the photocatalyst was placed inside the photoreactor, and it was sealed. Then, toluene was injected into the photoreactor using a micro syringe. The photoreactor was placed in the dark for 1 h to evaporate toluene and to achieve the absorption-desorption equilibrium of toluene on the photocatalyst, after which the lamp was turned on. At fixed time intervals of irradiation, the air inside the reactor was sampled using a gastight syringe and injected into the gas chromatography (Agilent GC) equipped with an OV-1 capillary column and flame ionization detector (FID). Finally, the degradation efficiency of toluene was calculated by the following equation:

$$\% \, degradation \, efficiency = \frac{C_0 - C_t}{C_0} \times 100 \qquad (1)$$

Where C_0 and C_t are the initial and final concentrations of toluene, respectively.

22nd Iranian Chemistry Congress (ICC22)
Iranian Research Organization for Science and
Technology (IROST)
13-15 May 2024

03231-97589

IROST

Results and Discussion

3.1. XRD and SEM

The XRD patterns of La_2TiMnO_6 and $G(50\%wt)/La_2TiMnO_6$ composite are shown in Fig. 1. In the XRD pattern of La_2TiMnO_6, only peaks related to perovskite are observed (standard JCPDS 50-0297) and it indicates that perovskite was purely synthesized. Also, due to the loading of graphene, the perovskite structure has not been destroyed.
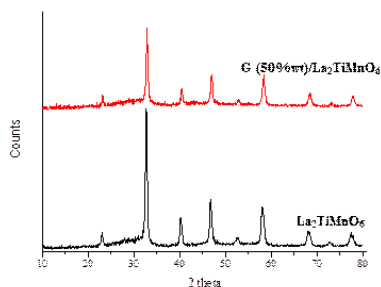

Fig.1: XRD patterns of La_2TiMnO_6 and $G(50\%wt)/La_2TiMnO_6$

Fig. 2 shows the SEM images of La_2TiMnO_6 and $G(50\%wt)/La_2TiMnO_6$ composite. According to Fig. 2, La_2TiMnO_6 has a porous structure, and the particle size is in the range of 40–60 nm. In the $G(50\%wt)/La_2TiMnO_6$ composite, La_2TiMnO_6 particles and graphene were completely distributed among each other. Adding graphene with a high specific surface area increases the specific surface area of the photocatalyst, and this increases the contact surface of the photocatalyst with the pollutant. As a result, it expectes that the removal efficiency of pollutant will increase.
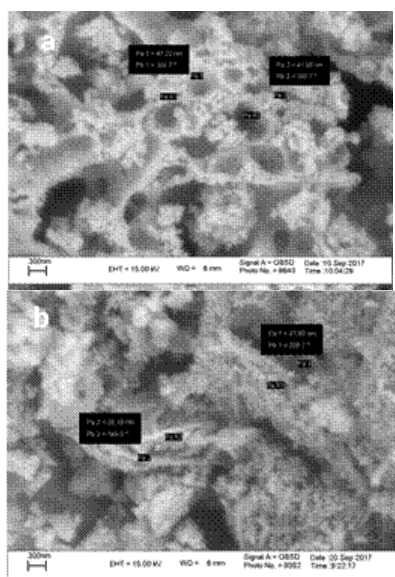

Fig.2: The SEM images of (a) La_2TiMnO_6 and (b) $G(50\%wt)/La_2TiMnO_6$

3.2. Photocatalytic activity

The activity of La_2TiMnO_6 double perovskite and $G(50\% wt)/La_2TiMnO_6$ nanocomposite to remove toluene under visible and UV radiation is shown in Figs. 3 a, b. According to Fig. 3, the photocatalytic performance of $G(50\%wt)/La_2TiMnO_6$ is higher than La_2TiMnO_6 in both the visible and UV regions and the $G(50\%wt)/La_2TiMnO6$ nanocomposite was able to remove 96% of the toluene pollutant under UV light irradiation. The synergistic effect between graphene and La_2TiMnO_6 improves the photocatalytic performance. The graphene acts as an electron acceptor and transporter, and with the fast transfer of photoelectrons produced in La_2TiMnO_6, causes a better separation of charge carriers (photoelectron and hole). Consequently, photocatalytic performance and the removal efficiency of pollutant increase [3].
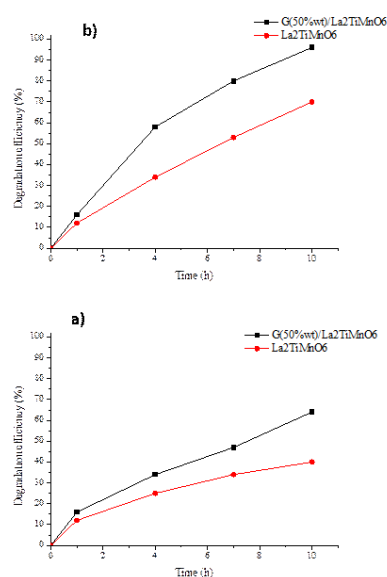

Fig.3: The degradation efficiency of toluene by photocatalytic processes using La_2TiMnO_6 and $G(50\%wt)/La_2TiMnO_6$ under (a) visible and (b) UV radiation

Conclusions

The La_2MnTiO_6 double perovskite was synthesized by the sol-gel method. The graphene was loaded with 50 wt% on La_2MnTiO_6 with the impregnation method. Experimental results showed that the photocatalytic activity and the toluene removal efficiency of graphene/La_2MnTiO_6 is much higher than that of La_2MnTiO_6.

References

[1] Wang, L. K., Pereira, N. C., Hung, Y. T., & Li, K. H. (Eds.). (2004). Air pollution control engineering. *Totowa, NJ: Humana press*, 1-495.

[2] Nakhostin Panahi, P., Rasoulifard, M. H., & Babaei, S. (2020). Photocatalytic activity of cation (Mn) and anion (N) substitution in LaCoO3 nanoperovskite under visible light. *Rare Metals*, *39*(2), 139-146.

[3] Nakhostin Panahi, P., Rasoulifard, M. H., & Hekmati, F. (2019). Photocatalytic discoloration of an azo-dye using LaMn 0.5 Ti 0.5 O 3 double perovskite under visible light irradiation and enhancement of photocatalytic activity by using graphene. *Reaction Kinetics, Mechanisms and Catalysis*, *128*, 539-554.

22nd Iranian Chemistry Congress (ICC22)
Iranian Research Organization for Science and Technology (IROST)
13-15 May 2024

03231-97589

IROST

Synthesis and characterization of 3,5-dinitrobenzoate salts of transition metals (Pb, Mn, Fe, Zn, Cr, Co, La and Ce)

Maryam Korivand[a], Mehdi Zamani[a,*], Razieh Habibpour[b]

Corresponding Author E-mail: m.zamani@du.ac.ir

[a] School of Chemistry, Damghan University, Damghan, Iran.

[b] Iranian Research Organization for Science and Technology (IROST), Tehran, Iran.

Abstract: In this study, the 3,5-dinitrobenzoate salts of transition metals (3,5-MDB$_Z$) with the general formula of $M(C_7H_3N_2O_6)_m.nH_2O$ in which M= Pb, Mn, Fe, Zn, Cr, Co, La and Ce have been synthesized and characterized by infrared spectroscopy (IR) and X-ray diffraction (XRD).

Keywords: Dinitrocarboxylate salts; Transition metals; Ammonium 3,5-dinitrobenzoate

Introduction

3,5-Dinitrobenzoic acid (3,5-DNB) is a white crystalline solid that is slightly soluble in water. This compound is an important precursor for the synthesis of many other organic substances. The salts of this compound with various metal cations such as Hg^{2+}, Y^{3+}, La^{2+}, Ce^{3+}, Mn^{2+} and Ni^{2+} have been prepared. All of dinitrobenzoates are crystalline and colorful. Their color depend on the position of the NO_2 group. If the NO_2 group is not associated with another substituent in the benzene ring and the molecule is stable, the electrons of the NO_2 group will combine with π conjugated electrons, causing a decrease in the electron density in the benzene ring and a bathochromic change. In these molecules, d→d electron transfers of central ions have the lowest energy and absorption occurs at relatively high wavelengths [1-3]. The unique structural properties of metal carboxylates and their use as catalysts in extraction systems, dispersants in water, polymer dispersants, fertilizers, pigments and materials have been reported which cause them interesting for researchers [4]. The aim of this work is to produce the 3,5-dinitrobenzoate salts of transition metals of Pb, Mn, Fe, Zn, Cr, Co, La and Ce from ammonium 3,5-dinitrobenzoate ($NH_4^+.C_7H_3N_2O_6^-$) [4].

Experimental Section

Dinitrobenzoicacid, hydrated nitrate salts of Pb(II), Mn(II), Fe(III), Zn(II), Cr(III), Co(II), La(III) and Ce(III), ammonium hydroxide and ethanol were purchased from Merck.

Synthesis of the ammonium 3,5-dinitrobenzoate

3,5-Dinitrobenzoic acid reacts with concentrated ammonia at a molar ratio of 1:1. Concentrated ammonia is slightly excessive for the purpose of complete reaction of benzoic acid. A certain amount of benzoic acid was firstly put into a 250 mL beaker. Then excess concentrated ammonia and appropriate amount of distilled water were successively added into the beaker with stirring to obtain a clear solution. The above solution was heated and condensed on the electric furnace until a crystal membrane appeared. The final solution was cooled naturally to room temperature and filtered; the crude product was washed with anhydrous ethanol three times. The white solid product was recrystallized using anhydrous ethanol, and white crystals were obtained. Finally, the sample was placed in a vacuum desiccator at 60 °C to vacuum dry for 6 h.

Synthesis 3,5-dinitrobenzoate salts

3,5 dinitrobenzoate salts of transition metals of Pb, Mn, Fe, Zn, Cr, Ni, Co, La and Ce were prepared by addition of equivalent amounts of 0.2 M ammonium dinitrobenzoate (pH≈ 5) to a hot solution containing divalent ions of Co, Ni, Mn and Cd nitrates and by crystallization at 293 K. The solids formed were filtered off, washed with hot water to remove ammonium ions and dried at 303 K to constant mass.

Results and Discussion

The IR spectra of the prepared salts were recorded over the range 400-4000 cm^{-1}. The characteristic absorption vibration of the main groups obtained from the IR spectra of 3,5-dinitrobenzoic acid, ammonium 3,5-dinitrobenzoate and their transition metal salts are listed in Tables 1 and 2.

The XRD technique was used to investigate crystallinity and determine whether the new synthesized compounds are novel. XRD patterns of 3,5-dinitrobenzoic acid, ammonium 3,5-dinitrobenzoate and their transition metal salts have been plotted in Fig. 1.

Table1: Characteristic vibration absorptions of main groups obtained from IR spectra of 3,5-dinitrobenzoic acid and ammonium 3,5-dinitrobenzoate (cm^{-1}).

Compound	$\upsilon_{C=O}$	υ_{-OH}	$\upsilon_{C=C}$	υ_{NO2}	υ_{NO2}	υ_{N-H}
(3,5-DNB)	1706	3095	1634	1350	1550	-
NH_4 (3,5-DNB)	-	3098	1627	1351	1548	3390

L=$C_7H_3N_2O_6$

22nd Iranian Chemistry Congress (ICC22)
Iranian Research Organization for Science and Technology (IROST)
13-15 May 2024

03231-97589

IROST

Table2: Characteristic vibration absorptions of main groups obtained from IR spectra of 3,5-dinitrobenzoate salts of transition metals (cm^{-1}).

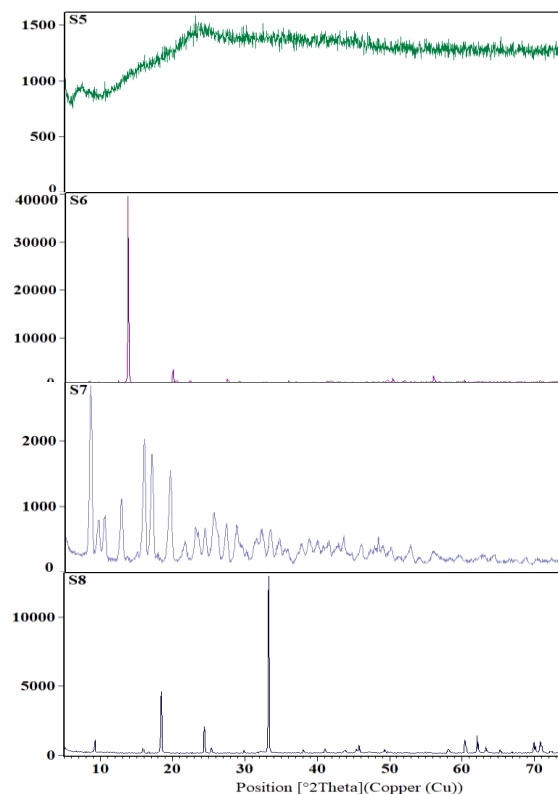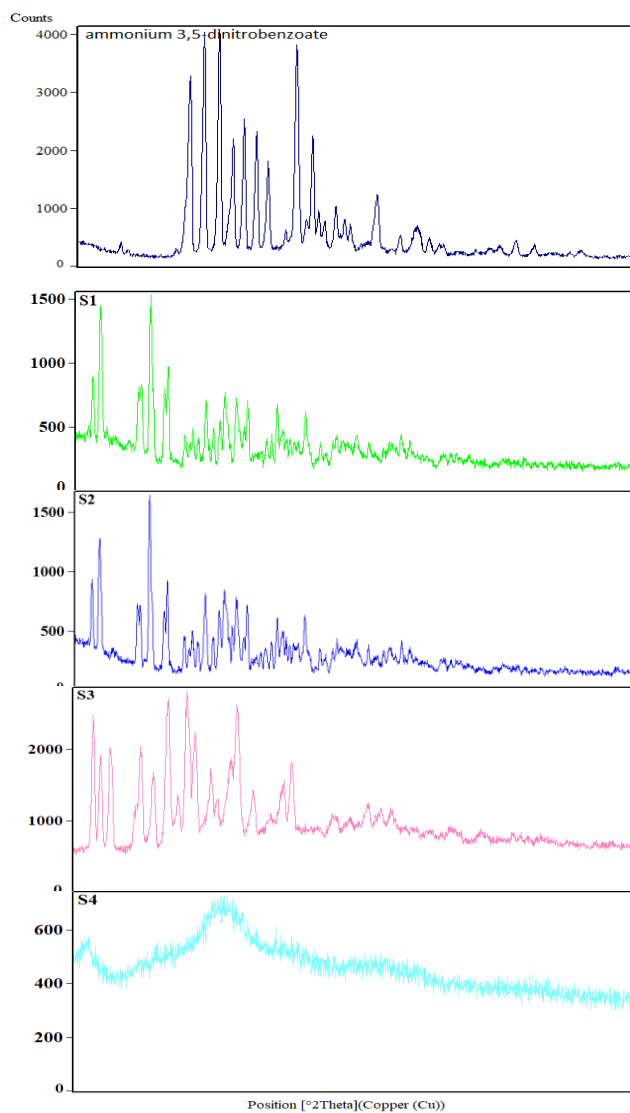| Compound	asν–OCO	symνOCO	asνNO2	symνNO2
(S1) PbL$_2$.3H$_2$O	1606	1410	1548	1348
(S2) MnL$_2$.5H$_2$O	1624	1426	1532	1344
(S3) FeL$_3$.9H$_2$O	1628	1412	1552	1342
(S4) ZnL$_2$.6H$_2$O	1610	1418	1550	1346
(S5) CrL$_3$.9H$_2$O	1612	1420	1552	1352
(S6) CoL$_2$.6H$_2$O	1616	1390	1536	1350
(S7) LaL$_3$.6H$_2$O	1606	1410	1546	1344
(S8) CeL$_3$.6H$_2$O	1602	1412	1546	1342

Fig 1. XRD patterns of ammonium 3,5-dinitrobenzoate and samples S1–S8.

References

[1] Ferenc, W. (1995). 2, 4-and 3, 5-dinitrobenzoates of Cd, Mn, Ni and Co. *Croatica Chemica Acta*, *68*(2), 383-392. https://hrcak.srce.hr/136759

[2] Ferenc, W. (1989). Preparation and properties of yttrium, lanthanum, and lanthanide 3, 5-dinitrobenzoates. Monatshefte fuer Chemie;(Austria), 120.

[3] Yang, W. W., Di, Y. Y., Kong, Y. X., Guo, X. Y., & Tan, Z. C. (2010). Synthesis, characterization, and thermodynamic study of ammonium benzoate C7H5O2NH4 (s). *Thermochimica acta*, *502*(1-2), 14-19. https://doi.org/10.1016/j.tca.2010.01.021

[4] Rosen, M. J., & Kunjappu, J. T. (2012). Surfactants and interfacial phenomena. John Wiley & Sons.

Synthesis of new polysubstituted chromenone-based imidazoles *via* Knoevenagel reaction

Somayeh Rashtabad Jadidi, Zarrin Ghasemi*

Corresponding Author E-mail: z.ghasemi@tabrizu.ac.ir

Organic Chemistry Laboratory, Faculty of Chemistry, University of Tabriz, Tabriz, Iran.

Abstract: a series of polysubstituted imidazole-based coumarin derivatives have been synthesized by Knoevenagel reaction of polysubstituted imidazole-based salicylaldehydes with ethyl acetoacetate in the presence of piperidine as catalyst. Polysubstituted imidazole-based salicylaldehydes were synthesized from corresponding polysubstituted imidazole-based phenols using hexamethylenetetramine via duff reaction. The newly synthesized compounds were confirmed by spectroscopic techniques and their optical properties were studied by UV and fluorimetry spectroscopies.

Keywords: polysubstituted imidazole; Knoevenagel reaction; Duff reaction; coumarin

Introduction

Coumarin derivatives have attracted significant attention due to their diverse medicinal properties and biological activities. Their potential for anti-inflammatory, anticancer, antioxidant, and antituberculosis effects has made them the subject of recent comprehensive reviews and studies [1-4]. Numerous methods, such as the Reformatsky, Perkin, Knoevenagel, Pechmann, and Wittig reactions, can be used to synthesize coumarins [5]. However, the Knoevenagel reactions are very helpful for synthesizing coumarins because they have straightforward reaction conditions and a high product yield [6]. The synthesis and development of fluorescent organic compounds have always been studied by many scientists due to their technological applications [7]. On the other hand, 1,2,4,5-tetraarylimidazoles, which can be prepared via four-component condensation of 1,2-diketones, aryl aldehydes, primary amines, and ammonium acetate, are an important part of many bioactive molecules, conjugated and fluorescent materials, and metal-coordinating ligands [8]. Considering these, herein we report the design and synthesis of new 4-(triarylimidazolyl) salicylaldehydes from Duff reaction of 4-(triarylimidazolyl)phenol with hexamethylenetetramine (HMTA) and corresponding 4-(triarylimidazolyl) coumarins via Knoevenagel reaction. The newly synthesized imidazolyl based salicylaldehydes and coumarin compounds can strongly possess optical properties.

Experimental Section

General procedure for the synthesis of 4-(triarylimidazolyl)salicylaldehydes

A mixture of 4-(triarylimidazolyl)phenols (1.0 mmol) and HMTA (3.0 mmol) in acetic acid (20 mL) was refluxed for about 36h. The reaction mixture was cooled to ro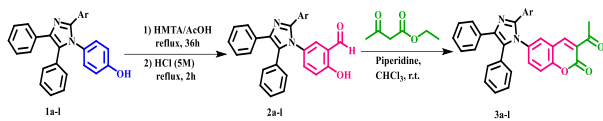om temperature and then added HCl (5M, 10 mL)to it. The reaction mixture was heated to 115 °C for another 2h. After cooling the reaction mixture was diluted with distilled water, and the precipitates formed were filtered, washed with water and dried in air. The crude product was purified via column chromatography using EtOAc:Hexane (3:7) as eluent to afford 4-(triarylimidazolyl)salicylaldehydes.

General procedure for the Synthesis of coumarins

The mixture of ethyl acetoacetate (1 mmol) and salicylaldehyde (1 mmol) in dichloromethane (3 mL) was stirred at room temperature. Piperidine (5 mol %) was added to it, and the mixture was stirred at room temperature for the appropriate time as indicated in Table 4. After the reaction was completed (as monitored by TLC), the reaction was concentrated in vacuo and purified by column chromatography using EtOAc:Hexane (4:6) as eluent to give the desired products.

Results and Discussion

To the synthesis of polysubstituted imidazolyl-based coumarin derivatives, first, 4-(triarylimidazolyl)phenol compounds **1a-l** were prepared by condensing aromatic aldehydes, anilines, benzil, and ammonium acetate using *p*-toluene solfunicacid as catalyst according to the literatures [9]. Then *ortho*-formilation of **1a-l** via Duff reaction in the presence of HMTA and acetic acid at 115 °C provided the desired salicylaldehyde derivatives **2a-l**. Finally, coumarin compounds **3a-l** were prepared *via* Knoevenagel reaction of salicylaldehydes with ethylacetoacetate using dichloromethane as the reaction medium in the presence of piperidine as catalyst. After 4 h of stirring at ambient temperature, the desired product **3a** was obtained in 89% isolated yield (**Scheme 1, Table 1**).

22nd Iranian Chemistry Congress (ICC22)
Iranian Research Organization for Science and
Technology (IROST)
13-15 May 2024

03231-97589

Scheme 1: Synthesis of imidazolyl-based salicylaldehyde derivatives (**2a-l**) and corresponding coumarins (**3a-l**)

Table1: The synthesized imidazolyl-based salicylaldehydes (**2a-l**) and corresponding coumarins (**3a-l**)

Entry	Phenol	Ar	Salicylaldehyde (yield %)	Coumarin (yield %)
1	**1a**	C_6H_5	**2a** (55)	**3a** (89)
2	**1b**	$4\text{-}ClC_6H_4$	**2b** (53)	**3b** (88)
3	**1c**	3-thienyl	**2c** (49)	**3c** (79)
4	**1d**	$3\text{-}NO_2C_6H_4$	**2d** (49)	**3d** (79)
5	**1e**	$4\text{-}MeC_6H_4$	**2e** (58)	**3e** (93)
6	**1f**	$4\text{-}FC_6H_4$	**2f** (59)	**3f** (89)
7	**1g**	$4\text{-}OMeC_6H_4$	**2g** (65)	**3g** (87)
8	**1h**	5-MeFuryl	**2h** (57)	**3h** (83)
9	**1i**	$4\text{-}iPrC_6H_4$	**2i** (51)	**3i** (87)
10	**1j**	$3\text{-}BrC_6H_4$	**2j** (50)	**3j** (84)
11	**1k**	$4\text{-}BrC_6H_4$	**2k** (53)	**3k** (91)
12	**1l**	2-thienyl	**2l** (49)	**3l** (80)

Conclusions

In summary, we report the synthesis of some new 4-(triarylimidazolyl)phenol compounds and their related salicylaldehyde derivatives *via* Duff reaction. The obtained salicylaldehyde derivatives were converted to the new polysubstituted imidazole-based coumarin derivatives *via* Knoevenagel reaction.

References

[1] Emam, S.H., Sonousi, A., Osman, E.O., Hwang, D., Kim, G.D. and Hassan, R.A., (2021). Design and synthesis of methoxyphenyl-and coumarin-based chalcone derivatives as anti-inflammatory agents by inhibition of NO production and down-regulation of NF-κB in LPS-induced RAW264. 7 macrophage cells. *Bioorganic Chemistry*, *107*, p.104630. https://doi.org/10.1016/j.bioorg .2021.104630

[2] Shaik, B.B., Katari, N.K., Seboletswe, P., Gundla, R., Kushwaha, N.D., Kumar, V., Singh, P., Karpoormath, R. and Bala, M.D., (2023). Recent Literature Review on Coumarin Hybrids as Potential Anticancer Agents. *Anti-Cancer Agents in Medicinal Chemistry*, *23*(2), pp.142-163. https://doi.org/10.2174/1871 520622666220418143438

[3] Todorov, L., Saso, L. and Kostova, I., (2023). Antioxidant Activity of Coumarins and Their Metal Complexes. *Pharmaceuticals*, *16*(5), p.651. https://doi.org/10.3390/ph16050651

[4] Mujeeb, S., Singh, K., Yogi, B., Ansari, V. and Sinha, S., (2022). A review on coumarin derivatives as potent anti-tuberculosis agents. *Mini Reviews in Medicinal Chemistry*, *22*(7), pp.1064-1080. https://doi.org/10.2174/1389557521666210927124511

[5] Mustafa, Y.F., Bashir, M.K. and Oglah, M.K., (2020). Original and innovative advances in the synthetic schemes of coumarin-based derivatives: A review. *Systematic Reviews in Pharmacy*, *11*(6), pp.598-612. https://www.researchgate.net/publication/342344634

[6] Adimule, V.M., Nandi, S.S., Kerur, S.S., Khadapure, S.A. and Chinnam, S., (2022). Recent advances in the one-pot synthesis of coumarin derivatives from different starting materials using nanoparticles: a review. *Topics in Catalysis*, pp.1-31. https://doi.org/10.1007/s11244-022-01571-z

[7] Jie, B., Lin, H., Zhai, Y., Ye, J., Zhang, D., Xie, Y., Zhang, X. and Yang, Y., (2023). Mechanism, design and application of fluorescent recognition based on metal organic frameworks in pollutant detection. *Chemical Engineering Journal*, *454*, p.139931.

[8] Jadhav, C.K., Nipate, A.S., Chate, A.V., Kamble, P.M., Kadam, G.A., Dofe, V.S., Khedkar, V.M. and Gill, C.H., (2021). Room temperature ionic liquid promoted improved and rapid synthesis of highly functionalized imidazole and evaluation of their inhibitory activity against human cancer cells. Journal of the Chinese Chemical Society, 68(6), pp.1067-1081.

[9] Ghasemi, Z., Fathi, Z., Alipour, E. and Shahabi, H., (2023). Wittig Synthesis, Optical Properties and Electrochemical Behaviors of Some Conjugated Derivatives of 4-Pyrones. Polycyclic Aromatic Compounds, pp.1-9.

22nd Iranian Chemistry Congress (ICC22)
Iranian Research Organization for Science and Technology (IROST)
13-15 May 2024

03231-97589

IROST

A convenient ultrasound-promoted synthesis of polysubstituted imidazole-linked benzoxazole derivatives

Somayeh Rashtabad Jadidi, Zarrin Ghasemi*

Corresponding Author E-mail: z.ghasemi@tabrizu.ac.ir

Organic Chemistry Laboratory, Faculty of Chemistry, University of Tabriz, Tabriz, Iran.

Abstract: To synthesize novel polysubstituted imidazole-based benzoxazole derivatives with high yields, short reaction times from benzoic acid derivatives and polysubstituted imidazole-based 2-aminophenols, ultrasound was explored as a green technique and alternative energy source. FT-IR, ^{1}H NMR, ^{13}C NMR, and elemental analysis have all been used to characterize these benzoxazole compounds.

Keywords: polysubstituted imidazole; ultrasound; benzoxazole

Introduction

Ultrasound-mediated reactions have been a popular and effective approach for chemical synthesis over the past decades. In comparison to traditional procedures, these reactions offer higher product yields, milder temperatures, shorter reaction times, and overall greater convenience and benefits [1,2].

Benzoxazole play an essential role among diverse aromatic heterocyclic compounds due to its versatile biological activities, such as anti-cancer [3], anti-microbial [4] anti-fungal [5], anti-oxidant. Because of their fluorescent properties, benzoxazole derivatives are also used in a variety of dyes and pigments [6,7]. On the other hand, polysubstituted imidazole derivatives with extended π-conjugation possess good photophysical properties, which result in their potential application in materials chemistry such as electroluminescent devices and organic light emitting diodes (OLEDs) [8,9]. Therefore, herein we report the synthesis of new imidazolyl-based o-aminophenols from the reduction of imidazolyl-based o-nitrophenols with Fe powder and corresponding imidazolyl-based benzoxazoles *via* a cycloaddition reaction between imidazole-based o-aminophenols and different benzoic acids in polyphosphoric acid PPA ultrasound irradiation.

Experimental Section

General procedure for the synthesis of o-nitrophenol compounds (2a-b)

Nitric acid (65%, 0.78 mL) was slowly added to a stirred solution of 1,2,4,5-tetraaryl imidazole (**1a** or **1b**, 2 mmol) in acetic acid (10 mL) at 38 °C. The obtained mixture was stirred for further 4 hours at 38 °C. After completion of the reaction, the mixture was allowed to cool at room temperature, poured into water (100 mL) and filtered to collect a solid which was washed with chloroform and methanol (1:1, 25 mL).

### General procedure for the preparation of o-aminophenol compounds (3a-b)

o-Nitrophenol (1.0 mmol) was suspended in aceticacid (6 mL) and ethanol (8 mL). To this, Fe powder (4 equiv) was slowly added at 60 °C and the obtained mixture was stirred for 4 h at 90 °C. After completion of the reaction, the mixture was allowed to cool at room temperature, poured into water (30 mL), filtered, dried and purified by column chromatography on silica gel (n-hexane: EtOAc 17:3 v/v) to afford pure o-aminophenol (**3a-b**).

General procedure for the preparation of benzoxazole compounds (4a-o)

A mixture of polysubstituted imidazole linked o-Aminophenols (**3a-b**) (1.0 mmol), benzoic acid derivatives (1.0 mmol) in polyphosphoric acid (0.5 g) was sonicated at amplitude 40% for 2 min. After adding ammonia solution (5 mL, 6% in H$_2$O), the solid product was separated, washed with ammonia solution, dried, and purified by column chromatography on silica gel (n-hexane: EtOAc 17:3 v/v) to afford pure benzoxazoles (**4a-o**).

Results and Discussion

The starting materials, polysubstituted imidazole-based phenols **1a-b** were prepared by four-component reaction of benzil, ammonium acetate, p-aminophenol, and benzaldehyde derivatives in the presence of p-toluene sulfonic acid as catalyst. Nitration of this compounds with nitric acid in acetic acid gave o-nitrophenols **2a-b**. Next, iron in acetic acid and ethanol was used to reduce the obtained compounds to the corresponding o-aminophenols **3a-b**. In the following, o-aminophenol compounds reacted with benzoic acid derivatives under ultrasound in polyphosphoric acid and created benzoxazole products **4a-o** (Table 1, Scheme 1).
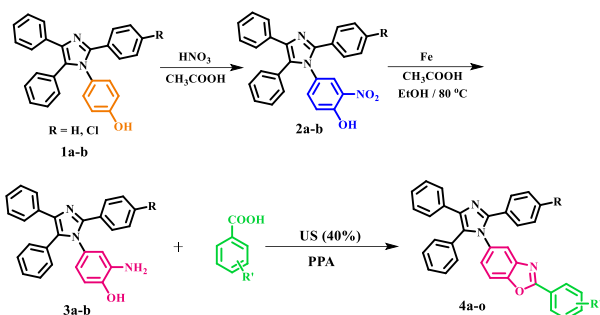
Scheme 1: synthesis steps of compounds **4a-o**

Table1: The synthesized imidazolyl-based benzoxazoles (**4a-o**)

Entry	R	R'	Benzoxazole (Yield %)
1	H	H	**4a** (89)
2	Cl	H	**4b** (79)
3	H	4-Me	**4c** (81)
4	H	4-Br	**4d** (78)
5	H	4-Cl	**4e** (74)
6	H	4-NO$_2$	**4f** (83)
7	H	4-F	**4g** (89)
8	Cl	4-F	**4h** (92)
9	H	4-iPr	**4i** (90)
10	Cl	4-iPr	**4j** (89)
11	Cl	4-Br	**4k** (76)
12	Cl	4-NO$_2$	**4l** (77)
13	Cl	4-Cl	**4m** (80)
14	H	2-Cl	**4n** (71)
15	Cl	2-C	**4o** (72)

Conclusions

In conclusion, a mild and efficient approach for synthesizing polysubstituted imidazole-baseds benzoxazoles ultrasonic irradiation has been successfully developed. Faster conversion using ultrasonic irradiation energy sources without catalyst makes this protocol attractive to chemists.

References

[1] Nasuhipur, F., Ghasemi, Z., Shahrisa, A. and Arsalani, N., 2023. Ultrasound promoted three-component synthesis of dihydroindeno [1, 2-b] pyrrole derivatives. Journal of Heterocyclic Chemistry, 60(1), pp.106-115.

[2] Maury, S.K., Kumar, D., Kamal, A., Singh, H.K., Kumari, S. and Singh, S., 2021. A facile and efficient multicomponent ultrasound-assisted "on water" synthesis of benzodiazepine ring. Molecular diversity, 25, pp.131-142.

[3] European Journal of Medicinal Chemistry, 210, p.112979. Jiang, Y., Yang, W., Wang, F. and Zhou, B., 2023. In silico studies of a novel scaffold of benzoxazole derivatives as anticancer agents by 3D-QSAR, molecular docking and molecular dynamics simulations. RSC advances, 13(22), pp.14808-14824.

[4] Alheety, N., 2019. Synthesis, characterization and antimicrobial activity study of some new substituted benzoxazole derivatives. Baghdad Science Journal, 16(3), pp.616-616.

[5] Wang, R., Kang, R., Yang, X., Cheng, Y., Bai, H. and Du, Z., 2022. Design, Synthesis, and Anti-Fungal Evaluation of Heterocyclic Benzoxazole Derivatives. Molecules, 27(23), p.8375.

[6] Le Guennic, B., Chibani, S., Charaf-Eddin, A., Massue, J., Ziessel, R., Ulrich, G. and Jacquemin, D., 2013. The NBO pattern in luminescent chromophores: unravelling excited-state features using TD-DFT. *Physical Chemistry Chemical Physics*, *15*(20), pp.7534-7540.

[7] Xue, P., Chen, P., Jia, J., Xu, Q., Sun, J., Yao, B., Zhang, Z. and Lu, R., 2014. A triphenylamine-based benzoxazole derivative as a high-contrast piezofluorochromic material induced by protonation. *Chemical communications*, *50*(20), pp.2569-2571.

[8] Kula, S., Ledwon, P., Maroń, A.M., Siwy, M., Grzelak, J., Szalkowski, M., Maćkowski, S. and Schab-Balcerzak, E., 2021. Synthesis, photophysical properties and electroluminescence characterization of 1-phenyl-1H-phenanthro [9, 10-d] imidazole derivatives with N-donor substituents. Dyes and Pigments, 192, p.109437.

[9] Islam, A., Usman, K., Wattoo, A.G., Shahid, T., Abbas, N., Sharif, H.M.A., Siddique, A.H., Ahmed, M., Ge, Z. and Ouyang, X., 2019. Meta-substituted bipolar imidazole-based emitter for efficient non-doped deep blue organic light emitting devices with a high electroluminescence. Journal of Photochemistry and Photobiology A: Chemistry, 379, pp.72-78.

Designing some new effective inhibitors for SARS-CoV-19 main protease enzyme using molecular docking studies

Bagher Mohammadi*, Shahram Babadoust*, Saeid Azimi

Corresponding Author E-mail: bagher.mohammadi@yahoo.com & s.babadoust@gmail.com

Department of Chemistry, Payame Noor University (PNU), P. O. Box 19395-3697, Tehran, Iran.

Abstract: To design a new therapeutic agent for SARS-CoV-19, analysis of ligand-based pharmacophore modeling, molecular docking studies were performed. A series of 10 molecules with different molecular scaffolds was collected. A comparative analysis of the selected molecules and the main ligand was performed for binding the ligand receptor in the target enzyme. The docking results and prediction of ADMET related properties helped us to find the effective molecule to inhibit the main protease enzyme of SARS-CoV-19.

Keywords: Docking; SARS-CoV-19; Protease enzyme; ADMET

Introduction

The main protease enzyme of the corona virus is one of the most interesting enzymes in the virus. In recent years, a lot of research has been done in the field of designing inhibitory compounds for this enzyme using molecular docking studies [1]. Epirubicin, Vapreotida, Saquinavir [2] Boceprevir, Telaprevir can be mentioned among the investigated inhibitory compounds. Many of the compounds that have been studied, have effective functional groups such as aldehyde, ketone, alpha ketoamide, ester, alpha haloacetamide, nitrile, α,β-unsaturated ketones, sulfide, and selenide [3]. In addition to chemical compounds, scientists have also conducted studies on plant compounds. The terpenoid glycyrrhizic acid, withafrin, polyphyllin, cicosaponin, chlorogenic acid, silibinin, and rosmarinic acid, anthocyanin, procyanidin, and proanthocyanidin are among the plant compounds that have been studied as inhibitors of the main protease enzyme of the Sars-Covid-2 virus [4].

Experimental Section

First, the 3D structure of the main protease enzyme (6y3f) was downloaded from the protein database. According to the ligands in the structure of the main enzyme and the size of the available cavities as well as the effective functional groups, 10 ligands were selected to investigate the effective interactions.

Results and Discussion

In this research, 10 ligands were selected and each one was named with the symbols L1, L2, L3, …, L10. All ligands are stored in the database with their position, orientation and formation to place the primary substitute in the active site of the protein. The ligands interacted with the protein one by one and placed the best ligand in the active site so that we could design the best drug. The structures of the studied ligands and the complex total energy are shown in Table 1.
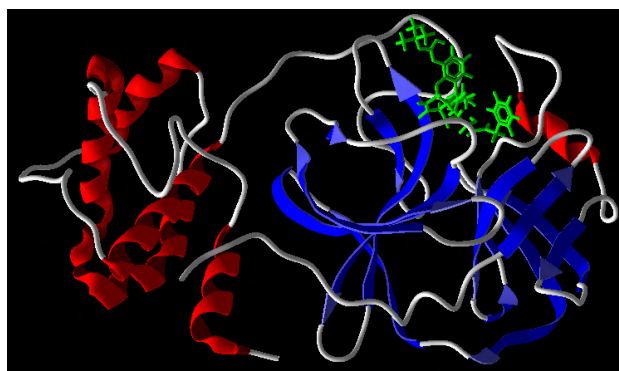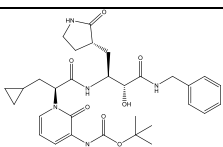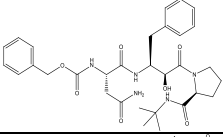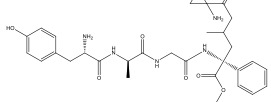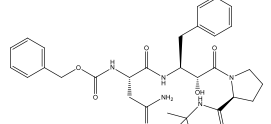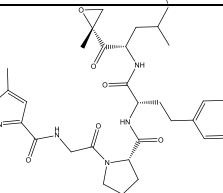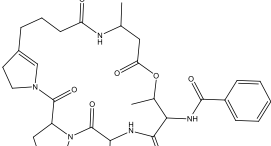

Fig.1: 3D image of SARS-CoV-19; Protease enzyme (6y2f) in complex with inhibitor ligand.

Conclusions

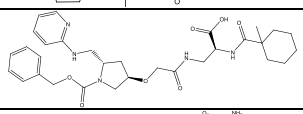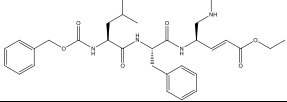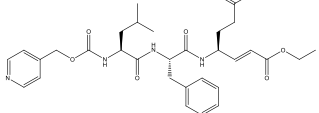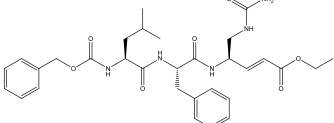In conclusion, the in silico study was performed to investigate and evaluate new potent inhibitors for main protease enzyme of SARS-CoV-19. Active site of the enzyme was studied and newly selected ligands were applied to molecular docking simulation in active site and other active cavities in target protein. The results were evaluated and low quantities in total energies were selected as candidate ligands. Then prediction of ADMET related properties occurred using ADMETLab 2.0 and prediction results were compared with molecular docking results. Finally, indicated that 5-methyl-N-[2-[(2S)-2-[[(2S)-1-[[(2S)-4-methyl-1-[(2R)-2-methyloxiran-2-yl]-1-oxopentan-2-yl]amino]-1-oxo-4-phenylbutan-2-yl]carbamoyl]pyrrolidin-1-yl]-2-oxoethyl]-1,2-oxazole-3-

carboxamide (L5 Table 1) had best results and must be considerate as potent inhibitorof main protease enzyme of SARS-CoV-19.

Table1: The chemical structure, PubChem codes and complex total energies of compounds applied as ligands.

Ligand (PubChem code)	Structure	Total energy
L1(146018708)		2254.15
L2(65004)		2278.49
L3(5492417)		8578.22
L4()469380		2259.64
L5(138665783)		1429.78
L6()102145497		
L7(11721315)		7154.92
L8(10627333)		7389.99
L9(6478286)		2178.14
L10(6478240)		3143.63

References

[1] Choudhary, M. I., Shaikh, M., tul-Wahab, A., & ur-Rahman, A. (2020). In silico identification of potential inhibitors of key SARS-CoV-2 3CL hydrolase (Mpro) via molecular docking, MMGBSA predictive binding energy calculations, and molecular dynamics simulation. Plos one, 15(7), e0235030. https://doi.org/10.1371/journal.pone.0235030

[2] De Jesús-González, L. A., Osuna-Ramos, J. F., Reyes-Ruiz, J. M., Farfan-Morales, C. N., Palacios-Rápalo, S. N., Cordero-Rivera, C. D., Del Ángel, R. M. (2020). Flavonoids and Nucleotide Analogs Show High Affinity for Viral Proteins of SARS-CoV-2 by in silico Analysis: New Candidates for the Treatment of COVID-19. https://doi.org/10.21203/rs.3.rs-67272/v1

[3] Khan, M. A., Mahmud, S., Alam, A. R. U., Rahman, M. E., Ahmed, F., & Rahmatullah, M. (2021). Comparative molecular investigation of the potential inhibitors against SARS-CoV-2 main protease: a molecular docking study. Journal of Biomolecular Structure and Dynamics, 39(16), 6317-6323. https://doi.org/10.1080/07391102.2020.1796813

[4] La Monica, G., Bono, A., Lauria, A., & Martorana, A. (2022). Targeting SARS-CoV-2 main protease for treatment of COVID-19: Covalent inhibitors structure–activity relationship insights and evolution perspectives. Journal of medicinal chemistry, 65(19), 12500-12534. https://doi.org/10.21203/rs.3.rs-67272/v1

Design and Synthesis of Graphene Oxide Aerogel (GOA)/Vanadium Oxide (VOX) Nanocomposite for Supercapacitor Applications

Ghazal Lolo, Fatemeh Rahnemaye Rahsepar*

Corresponding Author E-mail: frahsepar@ut.ac.ir

Department of chemistry, University of Tehran, Tehran, 1417614411, Iran.

Abstract: This study investigates the synthesis and evaluation of rGO-VO$_2$ aerogel as a supercapacitor electrode material, demonstrating a specific capacitance of 183.65 F.g^{-1} from CV tests and 36.36 F.g^{-1} from GCD tests. Equivalent circuit analysis from EIS data provided important resistances, and essential identification tests, including XRD, BET, and FESEM, were performed.

Keywords: hybrid supercapacitor, aerogel nanocomposite, rGO-VO$_2$ Aero

Introduction

The growing recognition of the necessity to utilize renewable resources has underscored the significance of conducting research on energy storage devices, particularly electrochemical storage [1]. Hybrid supercapacitors have emerged as a crucial component in addressing the challenges within this domain [2]. The objective of the researchers is to develop materials with a high power density and energy density. Hybrid materials in supercapacitors, along with other energy storage devices, offer promising potential for achieving this goal [3].

Experimental Section

In summary, the process of synthesizing the nanocomposite aerogel involved four main steps. Initially, reduced graphene oxide sheets were produced using an enhanced version of the Hummer method (Improved Hummer). Vanadium dioxide nanobelts were then synthesized via the hydrothermal method. rGO-VO$_2$ nanocomposite was subsequently created through a straightforward synthesis technique employing hydrazine. The nanocomposite's morphology was transformed into aerogel form using the polymer assisted technique, and ultimately, rGO-VO$_2$ aerogel (rGO-VO$_2$ Aero) nanocomposite was successfully synthesized utilizing polyvinyl alcohol polymer (PVA).

Results and Discussion

The synthesized rGO-VO$_2$ aerogel nanocomposite has been confirmed through characteristic tests such as XRD and BET, as well as morphological studies. Additionally, electrochemical tests including CV, EIS, and GCD have further confirmed the enhanced supercapacitor behavior of the synthesized material in a three-electrode system. This system consists of 0.5 M K$_2$SO$_4$ as the electrolyte, Ag/AgCl as the reference electrode, platinum as the counter electrode, and glassy carbon as the working electrode substrate. In Fig.1, The XRD pattern of the

synthesized aerogel nanocomposite reveals peaks corresponding to rGO and VO$_2$ samples, corroborated by FESEM images, confirming the presence of VO$_2$ nanobelts on the rGO sheets. Furthermore, analysis of the BET data shows a residual loop shape (IV) and type (H$_4$), indicating the material is composed of a combination of micro and mesopores, particularly in the form of slit-like pores.
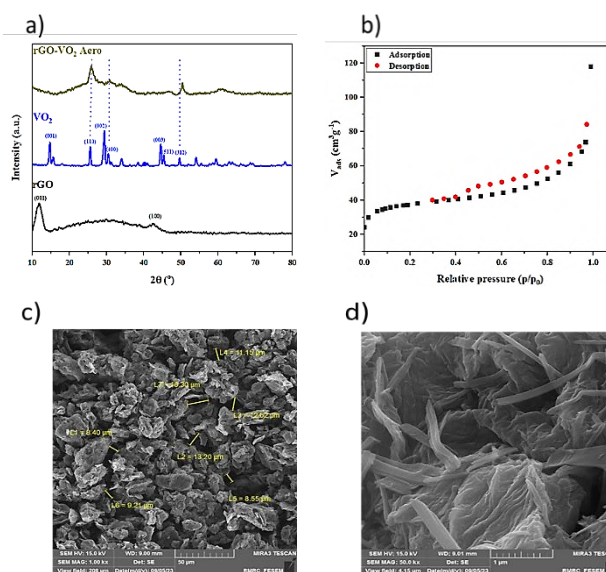
Fig.1: a) The powder XRD pattern of rGO, VO$_2$ and rGO-VO$_2$ Aero, b) BET adsorption -desorption isotherm and c,d) FESEM images of rGO-VO$_2$ Aero

Table1: Specific surface area and average pore size of rGO-VO$_2$ Aero

Material	Sepecific surface area (m^2/g)	Average pore size (nm)
rGO-VO$_2$ Aero	142.07	5.0987

In fig.2, The synthesized aerogel nanocomposite demonstrates enhanced energy storage performance

22nd Iranian Chemistry Congress (ICC22)
Iranian Research Organization for Science and
Technology (IROST)
13-15 May 2024

03231-97589

compared to its constituent materials, as indicated by the larger area under the curve in the CV test and the extended discharge time obtained from the GCD test, resulting in an increase in specific capacity (C_s). In contrast, the analysis of equivalent circuit through the use of EIS data provided valuable insights into the resistances, such as the internal resistance of the electrolyte (R_s) and the charge transfer resistance of the electrodes (R_{ct}).
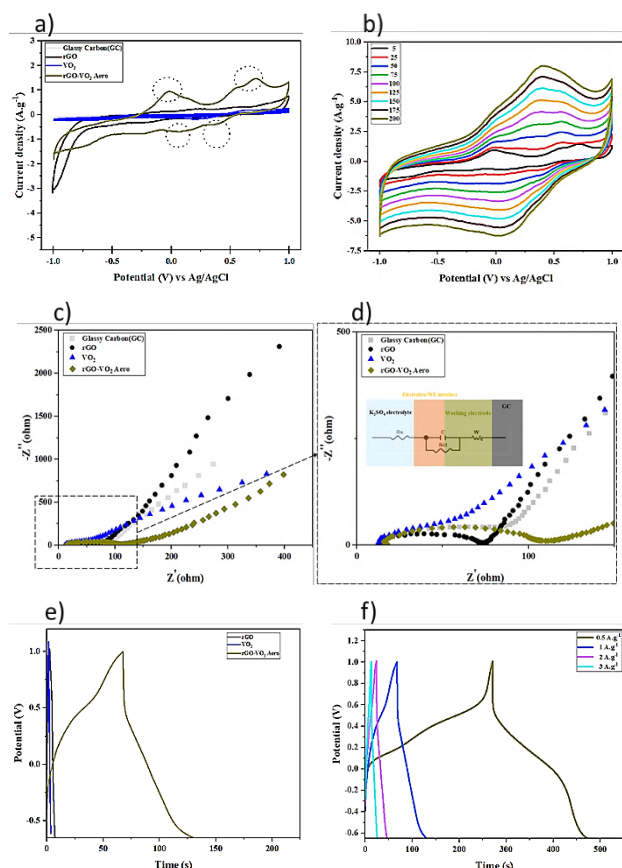

Fig.2: CV curves of a) rGO, VO₂ and rGO-VO₂ Aero at 0.005 V.s⁻¹, b) rGO-VO₂ Aero at various scan rates (5 to 200 mV s⁻¹), c,d) Nyquist plot of impedance from 0.1 Hz to 100 kHz, inset shows corresponding equivalent circuit of rGO-VO₂ Aero, e) GCD curves of rGO, VO₂ and rGO-VO₂ Aero at 1 A.g⁻¹ and b) GCD curves of rGO-VO₂ Aero at different current densities rangingfrom 0.5 to 3 A.g⁻¹

Table 2: Electrochemical Performance Evaluation

	CV 0.005 V.s⁻¹		EIS 20 mV		GCD 1 A.g⁻¹		
	C_S	E_S	R_S	R_{ct}	C_S	E_S	P_S
	F.g⁻¹	Wh.g⁻¹	Ω	Ω	F.g⁻¹	Wh.g⁻¹	W.g⁻¹
rGO-VO₂ Aero	183.65	0.204	17.31	91	36.36	3.43	205.8

Conclusions

The primary objective of this study was to synthesize advanced materials for application as the working electrode in hybrid supercapacitors. This involved the selection of materials from the carbon family (specifically reduced graphene oxide), metal oxides (such as vanadium dioxide nanobelts), and conductive polymers (polyvinyl alcohol). A novel approach was employed to utilize polyvinyl alcohol to alter the morphology of the final nanocomposite to an aerogel structure, resulting in the synthesis of the rGO-VO₂ aerogel nanocomposite (rGO-VO₂ Aero). Various identification tests including XRD, BET, and FESEM were conducted to confirm the synthesis of reduced graphene oxide sheets, vanadium dioxide nanobelts, and the rGO-VO₂ aerogel nanocomposite, characterized by micro, meso, and macro holes. Furthermore, electrochemical tests such as CV, EIS, and GCD were performed on the synthesized nanocomposite to assess its suitability as a working electrode for supercapacitors. The results of these tests validated the synthesized nanocomposite for this application.

References

[1] J. M. Lim *et al.*, 'Advances in high-voltage supercapacitors for energy storage systems: materials and electrolyte tailoring to implementation', *Nanoscale Adv*, vol. 5, no. 3, pp. 615–626, Jan. 2023, doi: 10.1039/D2NA00863G.

[2] P. Ragupathy, S. D. Bhat, and N. Kalaiselvi, 'Electrochemical energy storage and conversion: An overview', *Wiley Interdiscip Rev Energy Environ*, vol. 12, no. 2, p. e464, Mar. 2023, doi: 10.1002/WENE.464.

[3] A. E. Karaca and I. Dincer, 'Overview of Canada's energy storage related research activities: A perspective', *Int J Energy Res*, vol. 45, no. 12, pp. 17450–17460, Oct. 2021, doi: 10.1002/ER.6842.

Deep eutectic solvents and their application in food analysis

Mohsen Shahrokhi Nezhad*, Elaheh Maleki

Corresponding Author E-mail:shahrkhynzhad@gmail.com

Department of Food Science and Technology, Science and Research Branch, Islamic Azad University, Tehran, Iran.

Abstract: Deep Eutectic Solvents are new green solvents to replace conventional organic solvents. they are non-volatile hydrophilic and hydrophobic than common organic solvents and they can be used to extract and separate heavy metals, antibiotics, aflatoxins, artificial colors, phenolic compounds, flavonoids, sugars and aromatic amines, and proteins from food samples.

Keywords: Green solvents ; Deep eutectic solvents ; Application

Introduction

Food analysis has become one of the most important methods in controlling safety and quality during the manufacture of food products. It is an important part of food production, quality control, and safety testing. The development of various new instrumental techniques using ultra-high performance liquid chromatography and liquid chromatography coupled with sequential mass spectrometry and various new preparation technologies with low cost and high efficiency are essential for food analysis [1].

1-Deep eutectic solvents for extracting synthetic phenolics

Phenolic compounds are used as antioxidants to delay the rancidity of edible oils. TBHQ is at most 0.02% in many countries such as China, the United States, and Australia. allowed in foods. Liu et al. developed an ultrasonic-assisted liquid-liquid microextraction technique based on deep eutectic solvents combined with high-performance liquid chromatography to extract TBHQ, developed from edible oils [2].

2-Deep eutectic solvents for extraction of natural phenolics

Plant-derived foods contain a variety of phenolic compounds, which are mainly influenced by cultivated varieties, food processing, and food storage. It was found that the deep eutectic solvent consisting of choline chloride and ethylene glycol was efficient for the microextraction of sesamol from different sesame oil samples, and the detected results were close to the results of conventional liquid-liquid extraction with methanol as solvent. The concentration of curcumin in the deeply enriched eutectic solvent phase can be analyzed by UV-visible spectrophotometer at 425 nm [3].

3-Deep eutectic solvents for extraction of flavonoids

The extraction efficiency of the natural deep eutectic solvent based on choline chloride, acetylcholine chloride, choline tartrate, betaine, and carnitine with different compounds was evaluated and it was found that the eutectic solvent Natural deep concentrate consisting of acetylcholine chloride and lactic acid diluted with 30% water had the highest recovery of flavonoids [4].

4-Deep eutectic solvents for extracting other polar organic compounds

Aflatoxins are highly toxic and carcinogenic mycotoxins produced by the secondary metabolism of certain Aspergillus species. Considering their threat to food safety, the accurate and sensitive determination of aflatoxins is an important requirement to comply with official regulations. A deep eutectic solvent-based matrix solid-phase dispersion method for the determination of aflatoxins in different products was established using high-performance liquid chromatography combined with a fluorescence detector [5].

5-Deep eutectic solvents for extracting antibiotics

used hydrophobic deep eutectics to extract tetracyclines in milk. In this study, eleven hydrophobic deep eutectic solvents based on some natural fatty acids, alcohols, and choline chloride were synthesized and evaluated as green extractants in dispersive liquid microextraction of oxytetracycline, tetracycline, and doxycycline [6].

6-Deep eutectic solvents for extraction and pre-concentration of metals

Food samples may be contaminated by trace amounts of metals originating from various sources or introduced during storage and purification processes. Quality and safety of material samples Food is directly related to the concentration of trace metals, especially toxic metals.

22nd Iranian Chemistry Congress (ICC22)
Iranian Research Organization for Science and Technology (IROST)
13-15 May 2024

03231-97589

IROST

Therefore, the determination of trace metals in food samples is directly related to the concentration of trace metals, especially toxic metals. Therefore, the determination of trace metals in different food samples is very important from a health point of view [7].

7-Deep eutectic solvents for protein extraction

Deep eutectic solvents can also be used in protein extraction. An effective method for gluten extraction was developed using deep eutectic solvents based on tuberculin chloride. The important point is that by using these deep eutectic solvents, a high recovery was found compared to water-ethanol solvent [8].

8-Deep hydrophobic eutectic solvents for extracting food samples

A typical deep eutectic solvent is made from a quaternary ammonium salt and a hydrogen bond donor to form a hydrophilic deep eutectic solvent. Therefore, the development of hydrophobic deep eutectic solvents is very desirable. By using deep hydrophobic eutectic solvents as extraction solvents, a dispersive liquid microextraction method was developed for the extraction of pyrethroids in tea drinks and fruit juices.

9-General considerations of using deep eutectic solvents as extraction solvents

Deep eutectic solvents combined with liquid-liquid extraction or liquid-liquid microextraction are suitable for extracting liquid food samples, while Deep eutectic solvents are suitable for solid-liquid extraction for solid food samples. Hydrophobic deep eutectic solvents are suitable for extracting organic and mineral analytes from aqueous food samples via liquid-liquid extraction or liquid-liquid microextraction methods, while hydrophilic deep eutectic solvents are suitable for extracting analytes from samples Low polarity food, such as edible oils, are sufficient. Since deep eutectic solvents have low volatility and are non-flammable, microextraction based on deep eutectic solvent extracts can be combined with high-performance liquid chromatography and other detection methods to determine the target.

Conclusions

Deep eutectic solvents are a promising alternative to traditional solvents in various fields including food analysis. Hydrophilic and hydrophobic deep eutectic solvents were selected according to the characteristics of extraction targets and food samples . The properties of deep eutectic solvents can be determined by mixing hydrogen bond acceptor and hydrogen bond donor in molar ratios. compared to conventional organic solvents, deep eutectic solvents are non-volatile hydrophilic, and hydrophobic, so they can be combined with high-

performance liquid chromatography and UV-visible spectrophotometry for rapid analysis. deep eutectic solvents with Different microextraction technologies, including liquid-liquid microextraction and solid-liquid microextraction, are the main point in the development of food analysis.

References

[1] Hansen, B. B., Spittle, S., Chen, B., Poe, D., Zhang, Y., Klein, J. M., ... & Sangoro, J. R. (2020). Deep eutectic solvents: A review of fundamentals and applications. Chemical reviews, 121(3), 1232-1285.

[2] Liu, W., Zhang, K., Chen, J., & Yu, J. (2018). Ascorbic acid and choline chloride: A new natural deep eutectic solvent for extracting tert-butylhydroquinone antioxidant. Journal of Molecular Liquids, 260, 173-179.

[3] Jeong, K. M., Jin, Y., Han, S. Y., Kim, E. M., & Lee, J. (2018). One-step sample preparation for convenient examination of volatile monoterpenes and phenolic compounds in peppermint leaves using deep eutectic solvents. Food chemistry, 251, 69-76.

[4] Xu, M., Ran, L., Chen, N., Fan, X., Ren, D., & Yi, L. (2019). Polarity-dependent extraction of flavonoids from citrus peel waste using a tailor-made deep eutectic solvent. Food Chemistry, 297, 124970.

[5] Wu, X., Zhang, X., Yang, Y., Liu, Y., & Chen, X. (2019). Development of a deep eutectic solvent-based matrix solid phase dispersion methodology for the determination of aflatoxins in crops. Food chemistry, 291, 239-244.

[6] Sereshti, H., Jazani, S. S., Nouri, N., & Shams, G. (2020). Dispersive liquid–liquid microextraction based on hydrophobic deep eutectic solvents: application for tetracyclines monitoring in milk. Microchemical Journal, 158, 105269.

[7] Huang, Y., Feng, F., Chen, Z. G., Wu, T., & Wang, Z. H. (2018). Green and efficient removal of cadmium from rice flour using natural deep eutectic solvents. Food chemistry, 244, 260-265.

[8] Grudniewska, A., de Melo, E. M., Chan, A., Gniłka, R., Boratynski, F., & Matharu, A. S. (2018). Enhanced protein extraction from oilseed cakes using glycerol–choline chloride deep eutectic solvents: a biorefinery approach. ACS sustainable chemistry & engineering, 6(11), 15791-15800.

Synthesis and identification of heterogeneous molybdenum catalyst supported on graphene oxide and investigation of its catalytic performance in the oxidation reaction of alcohols.

Tahere Mohammadi*, Valiollah Mirkhani*, Mehrnaz Bahadori, Majid Moghadam, Shahram Tangestaninejad, Iraj Mohammadpoor-Baltork, Shakila Mohammadzade-Darshuri

Corresponding Author E-mail: tahereh123mohammadi@gmail.com

Department of Chemistry, University of Isfahan, Isfahan, Iran.

Abstract: In this research, graphene oxide was used as a suitable substrate for the synthesis of heterogeneous molybdenum catalysts. The stabilization of the molybdenum acetonate complex on the functionalized graphene oxide substrate was carried out by Base-Schiff to be used in the oxidation reaction of alcohols.
Keywords: functionalized graphene oxide; molybdenum complex; alcohol oxidation.

Introduction

Catalysts are important in science and technology because they make reactions more efficient and faster. There are two main types of catalysts: homogeneous, which is in the same phase as the reactants, and heterogeneous, which is in a different phase. Heterogeneous catalysts can perform reactions on their surface. [1].

The oxidation of alcohols is traditionally carried out using stoichiometric inorganic oxidants such as permanganate-, bromate- or chromium (VI)-based reagents, which produce large amounts of heavy metal waste [2, 3].

Many challenges exist in the oxidation of alcohols, including the presence of mixtures of organic substrates, products, solvents, and molecular oxygen which may lead to explosion. Additionally, harsh conditions such as high temperature and high oxygen pressure, as well as the use of unfavorable environmental solvents like chlorinated hydrocarbons, require careful consideration. As a result, there is a growing interest in developing a safe catalytic pathway for alcohol oxidation using dioxygen or hydrogen peroxide as an oxidant, preferably without the need for solvents [2]. Among transition metal complexes, molybdenum (VI) complexes have functional and structural similarities with molybdenum of enzymes and the ability to catalyze various oxidation reactions [4].

In this work, we prepared the catalyst GO@-Schiff base-Mo (VI) and used it in the oxidation reaction of alcohols.

Experimental Section

To make this catalyst, graphene oxide is first prepared using Hammer's method and then the surface is chlorinated [5]. Next, a ligand is applied to the graphene oxide substrate, followed by the addition of Molybdenum acetylacetonate complex to complete the catalyst synthesis. To verify the proper execution of these steps,

the compounds obtained from each stage are identified using various analyses. In this study, identification and examination of the synthesized compounds have been conducted using techniques such as SEM (Figure 2), XRD, IR-FT (Figure 1), TGA, and ICP.
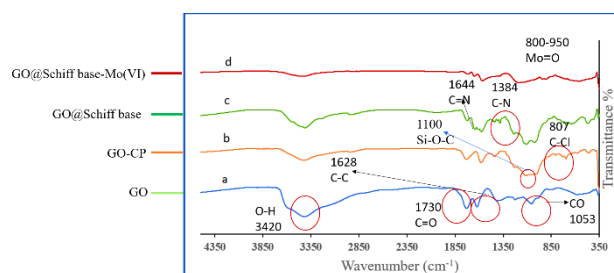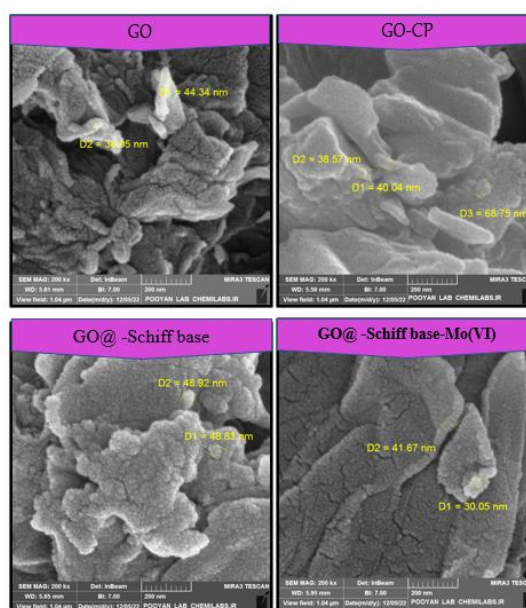

Fig. 1: IR spectroscopy

Fig. 2: SEM images

22nd Iranian Chemistry Congress (ICC22)
Iranian Research Organization for Science and Technology (IROST)
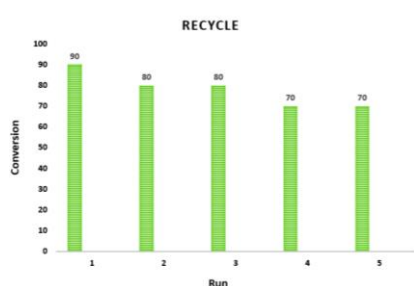**13-15 May 2024**

03231-97589

Fig 3. Recycle of catalyst

To optimize the reaction conditions in the oxidation of alcohols, by changing one of the reaction factors and the look constant having other parameters, the desired factor was optimized. During the optimization process, the parameters of solvent, amount of catalyst, type of oxidant, amount of oxidant, type of base, and temperature were investigated by gas chromatography (GC).

Results and Discussion

We checked the parameters of solvent, amount of catalyst, type of oxidant, amount of oxidant, type of base, and temperature and obtained the following results.

Investigating the effect of catalyst amount: To optimize the amount of catalyst in the oxidation process of 4-methoxybenzyl alcohol, catalytic systems were installed and amounts of 5, 10, 20, 30, and 40 mg of catalyst were used. Other parameters were considered constant. Finally, by comparing the results, the amount of 10 mg of catalyst was chosen as the optimal amount.

To optimize the temperature in the oxidation process of 4-methoxybenzyl alcohol, catalytic systems were installed and different temperatures were used. Other parameters were considered constant. Finally, by comparing the results, the temperature of 100 degrees Centigrade was chosen as the optimal temperature.

Ultimately, the catalyst's effectiveness in catalyzing the oxidation of various alcohols was examined (Table1).

Table 1. Various alcohols

Entry	Alcohol	Conversion(min)			
		10	20	30	50
1	4-Methoxybenzyl alcohol	70	80	80	90
2	4-Bromobenzyl alcohol	70	80	80	80
3	2-Nitrobenzyl alcohol	10	10	30	30
4	4-Chlorobenzyl alcohol	70	80	80	80
5	Benzyl alcohol	80	90	90	90
6	3-Methoxybenzyl alcohol	70	80	80	80
7	4-Nitrobenzyl alcohol	5	20	20	30

To assess the functionality and regeneration potential of the GO@-Schiff base-Mo(VI) catalyst, researchers implemented catalytic systems for the oxidation of 4-methoxybenzyl alcohol and subsequently assessed the catalyst's performance (Figure3).

Conclusions

Considering the disadvantages of homogeneous catalytic systems and the properties of graphene oxide that were mentioned, in this research, a homogeneous complex of molybdenum on a modified graphene oxide substrate was stabilized and a heterogeneous catalyst was synthesized from this metal. Reaction conditions such as temperature, solvent, the amount of catalyst, type of oxidant, etc. were optimized and the recovery of the catalyst was done under the same optimal conditions. In this work, the heterogeneous catalyst of molybdenum in the oxidation reaction of alcohols, its performance, and catalytic activity was investigated, according to the results of the reactions, it was observed that the catalyst has good activity and the products were obtained with good efficiency. Also, the catalyst shows a good ability to recover and reuse, which indicates that the catalyst is stable in the reaction environment.

References

[1]. Philipse, A. P., Heterogeneous catalysis: On bathroom mirrors and boiling stones. *Journal of Chemical Education* **2011,** *88* (1), 59-62.

[2]. Veitch, G. E.; Boyer, A.; Ley, S. V., The azadirachtin story. *Angewandte Chemie International Edition* **2008,** *47* (49), 9402-9429.

[3]. Ma, X.-T.; Lu, X.-H.; Wei, C.-C.; Zhao, Z.-S.; Zhan, H.-J.; Zhou, D.; Xia, Q.-H., Catalytic epoxidation of cyclic alkenes with air over CoOx/zeolite heterogeneous catalysts. *Catalysis Communications* **2015,** *67*, 98-102.

[4]. Biradar, A. V.; Dongare, M. K.; Umbarkar, S. B., Selective oxidation of aromatic primary alcohols to aldehydes using molybdenum acetylide oxo-peroxo complex as catalyst. *Tetrahedron Letters* **2009,** *50* (24), 2885-2888.

[5]. Zarnegaryan, A.; Pahlevanneshan, Z.; Moghadam, M.; Tangestaninejad, S.; Mirkhani, V.; Mohammdpoor-Baltork, I., Copper (II) Schiff base complex immobilized on graphene nanosheets: a heterogeneous catalyst for epoxidation of olefins. *Journal of the Iranian Chemical Society* **2019,** *16*, 747-756.

Synthesis of Co-Mg-Al/layered triple hydroxide@ZIF-8 nanocomposite as an efficient adsorbent for the removal of diazinon pesticide from aqueous media

Sahar Abaskhani Davanlo [a], Abdolraouf Samadi-Maybodi [b], Hashem Ghezel-Sofla*[c]

Corresponding Author E-mail: h.ghezelsofla@mazums.ac.ir

[a & b] Analytical division, Faculty of Chemistry, University of Mazandaran, Babolsar, Iran

[c] PhD in Analytical Chemistry, Mazandaran University of Medical Sciences, Sari, Iran.

Abstract: A Co-Mg-Al/LTH@ZIF-8 nanocomposite was synthesized to eliminate the pesticide diazinon from an aqueous solution. The results showed that 95.5% of diazinon was removed under optimized conditions (initial concentration of diazinon = 9.7 mg·L^{-1}, pH = 7.7, adsorbent dose = 16.9 mg, and contact time = 25 min).

Keywords: Layered triple hydroxide; absorbent; diazinon.

Introduction

Pesticide overuse is a major issue in agriculture. diazinon (DIZ) is a potent pesticide increasingly used because of its low cost and accessibility [1]. Overuse of pesticides leads to their accumulation in the environment and underground water sources, posing a threat to human health and agricultural soil stability. Limiting pesticide use is the best option to minimize these risks, but practical methods for their removal are necessary because of high demand [2]. Among the various methods used to remove agricultural pesticide residues from water sources, the adsorption method has received more attention because of its simplicity, cost, and higher efficiency [3].
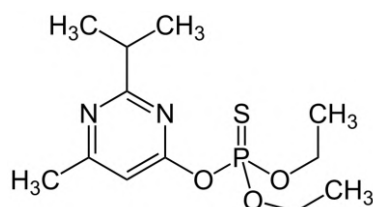

Fig.1: Chemical structure of diazinon (Chemical name: O, O-Diethyl O-[4-methyl-6-(propan-2-yl)pyrimidin-2-yl] phosphorothioate).

Experimental Section

The hydrothermal technique was employed to create three nanocomposites - Co-Mg-Al/LTH, ZIF-8, and Co-Mg-Al/LTH@ZIF-8. These nanocomposites were then put to the test to determine their ability to remove diazinon from aqueous solutions. The nanocomposites were characterized using several methods such as Fourier transform infrared spectroscopy, X-ray diffraction, field emission scanning electron microscopy, and energy-dispersive X-ray spectroscopy to ensure their effectiveness.
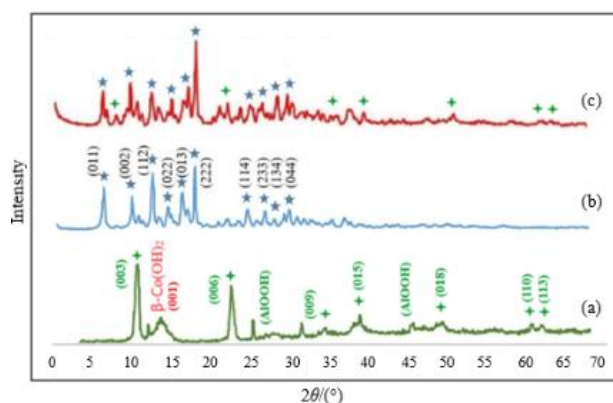

Fig.2: Patterns of X-ray diffraction for Co–Mg–Al/LTH (a), ZIF-8 (b), and Co–Mg–Al/LTH @ ZIF-8 (c) nanoparticles.

The experiment utilized the central composite design to evaluate statistics and determine the factors that affect the absorption process. The response level method was also used to optimize these factors.

Table1: Levels of effective factors in central composite design

Factor	Level				
	(−1)	(0)	(+1)	(−α)	(+α)
Initial concentration/mg·L^{-1}	20	35	50	5	65
Adsorbent dose/mg	10	15	20	5	25
pH	5	7	9	3	11
Contact time/min	20	30	40	10	50

The results showed that under optimized conditions (initial concentration of DIZ = 9.7 mg·L^{-1}, pH = 7.7, adsorbent dose of Ni/Al-LDH@ZIF-8 = 16.9 mg, and contact time = 25 min). Results showed that 94.5% of DIZ was removed. According to the model of isotherms parameters, the adsorption process is more consistent with the Freundlich model, with an absorption capacity of 87.6 mg·g^{-1}.
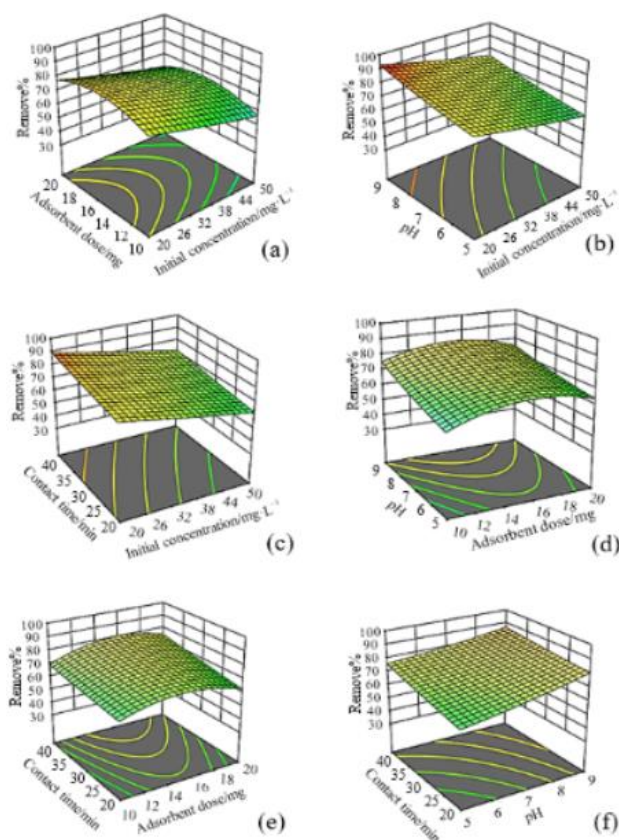
22nd Iranian Chemistry Congress (ICC22)
Iranian Research Organization for Science and
Technology (IROST)
13-15 May 2024

03231-97589

Fig.3: Interactions between (a) adsorbent dose (mg) and initial concentration (mgL^{-1}), (b) pH and initial concentration, (c) contact time (min) and initial concentration, (d) pH and adsorbent dose, (e) contact time and adsorbent dose, and (f) contact time and pH are shown in 3D response surfaces and contour plots.

Conclusions

Studies have shown that 3D structures have more adsorption sites and a higher specific surface area compared to 2D structures [4]. LDHs are excellent support materials for the growth of metal complexes. By combining the advantages of the 3D nanosheets of LDHs and the hydrophobic/π-conjugated surfaces of MOFs, functional composites can be designed to make full use of the functional surfaces. This can lead to significant improvements in the removal of organic compounds. The nanocomposite consisting of Co–Mg–Al/LTH and ZIF-8 showed a removal efficiency of 94.5% for diazinon in optimal conditions, which is significantly higher than LTH and ZIF-8 alone. Langmuir and Freundlich isotherm models with $R^2 > 0.99$ showed that DIZ absorption is possible as one or multiple layers on the adsorbent. The pseudo-second-order model described the adsorption kinetics data and the maximum adsorption capacity of DIZ on the adsorbent was 87.20 mg·g^{-1}. The thermodynamic studies of adsorption showed this process to be spontaneous, endothermic, and with increasing disorder

during absorption. Several mechanisms for the adsorption process of these nanocomposites have been proposed, including the adsorbent composite's hydrophobic effects, π–π interactions, pollutant penetration into the pores and layers of the composite, and the possibility of forming H-boning. The synthesis of these compounds as an adsorbent is quick, easy, cheap, and efficient, making their wider use promising for removing pesticides from wastewater.

References

[1] Samadi-Maybodi, A., Ghezel-Sofla, H., & BiParva, P. (2023). Co/Ni/Al-LTH layered triple hydroxides with zeolitic imidazolate frameworks (ZIF-8) as high efficient removal of diazinon from aqueous solution. *Journal of Inorganic and Organometallic Polymers and Materials*, *33*(1), 10-29.

[2] Zhang, R., Ai, Y., & Lu, Z. (2020). Application of multifunctional layered double hydroxides for removing environmental pollutants: recent experimental and theoretical progress. *Journal of Environmental Chemical Engineering*, *8*(4), 103908.

[3] Shi, J., Zhang, H., Yu, Y., Zou, X., Zhou, W., Guo, J., Ye, Y. and Zhao, Y. (2020). Adsorption properties of calcium alginate-silica dioxide hybrid adsorbent to methylene blue. *Journal of Inorganic and Organometallic Polymers and Materials*, *30*(6), 2114-2125.

[4] Zhan, W., Yuan, Y., Sun, L., Yuan, Y., Han, X., & Zhao, Y. (2019). Hierarchical NiO@ N-Doped Carbon Microspheres with Ultrathin Nanosheet Subunits as Excellent Photocatalysts for Hydrogen Evolution. *Small*, *15*(22), 1901024.

Intermolecular Interactions between Sacubitril and Valsartan in Entresto: A QTAIM Study

T. Hassani Saadi [a,b], S. Pourestarabadi [a,b], M. Dehestani *[a]

Corresponding Author E-mail: dehestani@uk.ac.ir

[a] Department of Chemistry, Shahid Bahonar University of Kerman, Kerman, Iran.

[b] Young Researchers Society, Shahid Bahonar University of Kerman, Kerman, Iran.

Abstract: In this study, we used quantum theory of atoms in molecules (QTAIM) to investigate the sacubitril/valsartan complex as a double-acting drug (Entresto) used for treating heart failure. Our findings show no covalent interaction between valsartan and the carboxylate groups and amide group of sacubitrilat which may decrease the effectiveness of treatment of sacubitrilat.

Keywords: Sacubitril; Valsartan; Antihypertensive drug; QTAIM

Introduction

Sacubitril/valsartan, as a double-acting drug with the brand name Entresto, is used for heart failure treatment. Sacubitril is a neprilysin inhibitor prodrug, while valsartan is an angiotensin receptor blocker. Therefore, the combination sacubitril/valsartan blocks the renin-angiotensin-aldosterone path [1-2]. Studies comparing the sacubitril/valsartan to other antihypertensives have shown that sacubitril/valsartan reduces the risk of cardiovascular death [3].

Jovanović et al. studied the inhibitory effects of sacubitril/ valsartan on neprilysin and angiotensin receptor using simulation methods. In these studies, the interactions of valsartan with the angiotensin receptor and sacubitril with neprilysin were determined [4]. However, akey factor that has not been considered in these studies is that the presence of hetero-atoms in this drug combination can affect the function of valsartan in the active site of the angiotensin receptor and sacubitril in neprilysin. In this study, we have studied the interaction between valsartan and sacubitril for the first time to determine if the binding of sacubitril to amino acids of neprilysin is disrupted by valsartan.

Computational Section

In this research, we used Gaussview software to draw the structures of valsartan and sacubitrilate, the active metabolite of sacubitril. Then, we performed computations using the Materials Studio software with the DMol3 modules and GGA/PW91 functional method. The optimized structures of valsartan and sacubitrilate were obtained, as shown in **Fig.1**. The interaction energy between two molecules was calculated for different orientations, and the most stable system was selected.

QTAIM properties and QTAIM graph for most stable sacubitrilate/valsartan system were obtained by AIM2000 software.
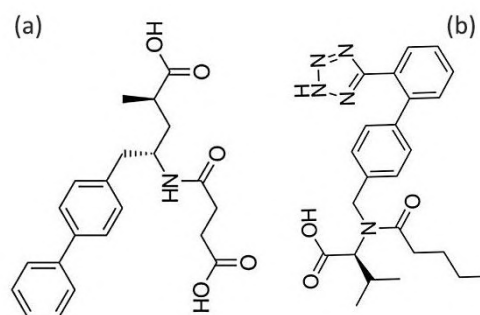

Fig.1: Structures of (a) Sacubitrilate and (b) Valsartan

Results and Discussion

QTAIM was used as a computational method to study the nature of chemical interactions between the atoms of sacubitrilat and valsartan, based on the electron density at the critical points between the atoms. The QTAIM graph of the most stable sacubitrilate/valsartan system (**Fig.2**) was obtained based on the bond critical points (BCPs) that form between sacubitrilate and valsartan to predict the nature of these interactions. The density (ρ) at these BCPs and other parametres, such as the Laplacian of the density ($\nabla^2\rho$), kinetic energy density (G) and potential energy density (V), that can help analyze the interaction between the atoms of sacubitrilate and valsartan for both valsartan and sacubitrilate systems were computaed and listed in **Table1**.

22nd Iranian Chemistry Congress (ICC22)
Iranian Research Organization for Science and Technology (IROST)
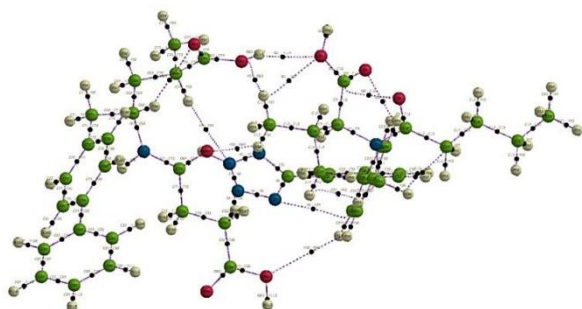**13-15 May 2024**

03231-97589

Fig.2: QTAIM graph Sacubitrilate/valsartan

Molecular docking simulations by Jovanović et al. show that the inhibitory effect of sacubitrilat is related to the interactions of carboxylate groups with Arginine (Arg102, Arg110 and Arg717), amide group with Histidine (His711), Alanine (Ala54) and Asparagine (Asn542) benzene rings with Histidine (His587) and Tyrosine (Tyr545) [4]. *QTAIM* results in **Table1** show no-covalence interaction (with $\rho \geq 0.20$ a.u. is for shared-shell interactions or covalent bonds, and $\rho \leq 0.10$ a.u. for closed-shell interactions or ionic, van-der-Waals and hydrogen bond [5]) between valsartan and the carboxylate groups and amide group of sacubitrilat. The blocking of these groups prevents the connection of sacubitrilat functional groups with the corresponding amino acids, therefore the presence of valsartan can affect the effectiveness of sacrobitrilat.

Table1: QTAIM properties (a.u.) of the sacubitrilate/valsartan system based on BCP (sacubitrilate atom…valsartan atom) .

BCPs	ρ	$\nabla^2\rho$	H=G+V
O(63)… H(90)	0.00980	0.0383	0.0014
H(93)… N(7)	0.00031	0.0014	0.0001
H(106) …N(8)	0.00970	0.0301	0.0009
C(24) …N(6)	0.01050	0.0368	0.0016
O(65)… H(50)	0.00260	0.0108	0.0007
H(42) …H(35)	0.00700	0.0267	0.0016
C(15) …H(36)	0.01370	0.0605	0.0029
O(3) …H(49)	0.01200	0.0391	0.0007
O(2) …C(16)	0.01800	0.0707	0.0022
H(37)… O(1)	0.01270	0.0468	0.0013
H(37) …O(62)	0.00270	0.0112	0.0007
O(1) …H(114)	0.00330	0.0149	0.0009
H(38) …O(64)	0.01740	0.0601	0.0008

Conclusions

One of new drug for heart failure treatment, is sacubitril/valsartan combination drug. This combination blocks the renin-angiotensin-aldosterone pathway

sacubitril/valsartan. Molecular docking simulations by Jovanović et al. on the binding of sacubitrilat to amino acids of neprilysin, show that the inhibitory effect of sacubitrilat is related to the interactions of carboxylate groups with Arginine, amide group with Histidine, Alanine and Asparagine benzene rings with Histidine, and Tyrosine. *QTAIM* results show no covalence interaction between valsartan and the carboxylate groups and amide group of sacubitrilat. The blocking of these groups prevents the connection of sacubitrilat functional groups with the corresponding amino acids, so the presence of valsartan can be affected on the effectiveness of sacrobitrilat.

References

[1] N.H. Mustafa, J. Jalil, S. Zainalabidin, M.S. Saleh, A.Y. Asmadi, Y. Kamisah, "Molecular mechanisms of sacubitril/valsartan in cardiac remodeling, " Front. pharmacol, 13 (2022) 892460. https://doi.org/10.3389/fphar.2022.892460

[2] Docherty, K. F., Vaduganathan, M., Solomon, S. D., & McMurray, J. J. (2020). Sacubitril/valsartan: neprilysin inhibition 5 years after PARADIGM-HF. *Heart Failure*, *8*(10), 800-810. https://doi.org/10.1016/j.jchf.2020.06.020

[3] Dargad, R. R., Prajapati, M. R., Dargad, R. R., & Parekh, J. D. (2018). Sacubitril/valsartan: a novel angiotensin receptor-neprilysin inhibitor. *Indian heart journal*, *70*, S102-S110. https://doi.org/10.1016/j.ihj.2018.01.002

[4] Jovanović, J. Đ., Antonijević, M., Vojinović, R., Filipović, N. D., & Marković, Z. (2022). In silico study of inhibitory capacity of sacubitril/valsartan toward neprilysin and angiotensin receptor. *RSC advances*, *12*(46), 29719-29726. https://doi.org/10.1039/D2RA04226F

[5] Pilme, J., Renault, E., Bassal, F., Amaouch, M., Montavon, G., & Galland, N. (2014). QTAIM analysis in the context of quasirelativistic quantum calculations. *Journal of Chemical Theory and Computation*, *10*(11), 4830-4841. https://pubs.acs.org/doi/abs/10.1021/ct500762n

22ⁿᵈ Iranian Chemistry Congress (ICC22)
Iranian Research Organization for Science and Technology (IROST)
13-15 May 2024

03231-97589

IROST

Two-step, Three-component Process, for One-pot Synthesis of 2-methyl alkyl thioether benzimidazole Derivatives as Potential Therapeutic Agents

Haniyeh Zare, Mohammad Navid Soltani Rad

Corresponding Author E-mail: hanizare16@gmail.com

Department of Chemistry, Shiraz University of Technology, Shiraz 71555-313, Iran.

Abstract: This paper presents the synthesis and characterization of novel 2-methyl alkyl thioether benzimidazole derivatives using a two-step, three-component one-pot synthesis involving 2-chloromethylbenzimidazole, thiourea, and selected alkyl halides. Given the well-documented beneficial biological properties associated with benzimidazole derivatives, it is expected that these hybrid compounds could demonstrate significant therapeutic potential.

Keywords: Benzimidazole; One-pot; Three-component; Thioether; Alkyl halide

Introduction

The largest and most diverse family of organic compounds is formed by heterocyclic compounds, which are ring-shaped and contain at least one heteroatom, with nitrogen, oxygen, and sulfur being the most common. Among these, compounds containing nitrogen have garnered more attention from scientists. The increasing microbial resistance and emergence of new pathogens pose serious challenges to public health. Efforts are underway to develop new antimicrobial agents with mechanisms different from those of known drugs, owing to the widespread clinical use of azole-based drugs. Extensive research is being conducted on these compounds to create efficient derivatives with high biological activity and low toxicity. Azoles readily interact with enzymes and various receptors in organisms through non-covalent interactions, exhibiting a wide range of biological activities. Benzimidazoles, a subset of azoles containing a benzene ring fused with a five-membered imidazole ring, are crucial heterocycles known for their pharmaceutical properties [1]. The NH group present in benzimidazole is both acidic and weakly basic (Fig.1).

Benzimidazole

Fig. 1: Structure of Benzimidazole

Various chemical modifications have been implemented on the substituents connected to the benzimidazole core to enhance its diverse biological activities. These modifications have demonstrated that alterations in substituents can result in either increased or decreased activities. Recent studies suggest that compounds containing benzimidazole exhibit lower toxicity in humans. The incorporation of groups onto the benzimidazole core imparts a broad spectrum of therapeutic properties. Examples of drugs containing benzimidazole are albendazole and mebendazole used as anthelmintics, enveradine as an antiviral agent, carbendazim as a fungicide, amperazole and pantoprazole as proton pump inhibitors, candesartan as an antihypertensive medication, and astemizole as an antihistamine [2] (Fig. 2).
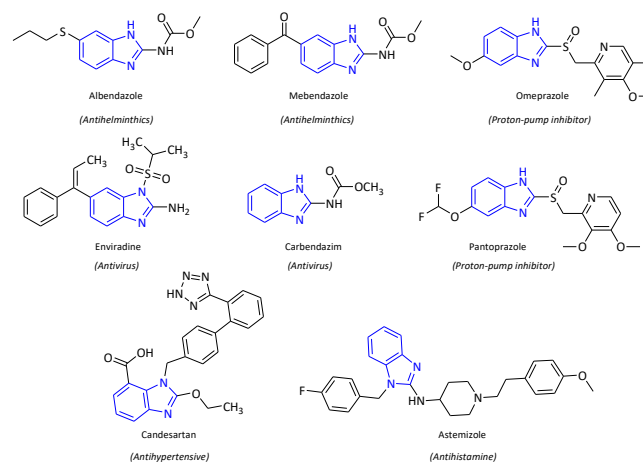

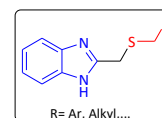**Fig. 2**: The structure of some benzimidazole-based drugs

Fig.3: General structure of 2-methyl alkyl thioether Benzimidazole

Having realized the pharmaceutical significance of benzimidazole derivatives; hereby, we described the synthesis and characterization 2-methyl alkyl thioether benzimidazole derivatives through a two-step, three-component, and one-pot synthesis process. The general structure of title compounds is depicted in Fig.3.

22nd Iranian Chemistry Congress (ICC22)
Iranian Research Organization for Science and Technology (IROST)
13-15 May 2024

03231-97589

IROST

Experimental Section

Synthesis of 2-chloromethyl-1*H*-benzoimidazole (CMB): This synthesis was carried out due to standard procedure [3].
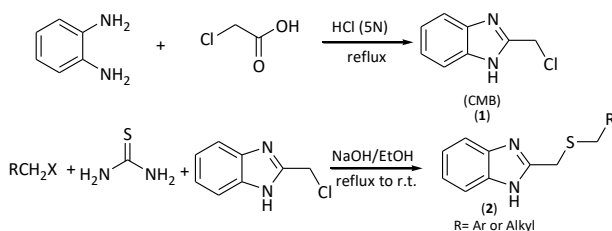
Synthesis of 2-methyl alkyl thiouther benzimidazoles:

In a 100 mL double-necked round bottom flask containing 30 mL EtOH, it was charged with thiourea (0.76 g, 10 mmol) and desired alkyl halide (10 mmol). The reaction media was refluxed until TLC indicate the full consumption of thiourea. Afterward, NaOH (0.8 g, 20 mmol) in distilled water (2 mL) was added dropwise to the reaction vessel. Then the reaction was set to ambient temperature and CMB (1.66 g, 10 mmol) was added to the reaction vessel. After completion of reaction (TLC check), solvent was evaporated and the reaction media was diluted in 500 mL distilled water and the organic materials were extracted by 3×100 mL CHCl3. The solvent was evaporated *in vacuo* and the remaining crude product was purified by a short column chromatography on silica gel eluting with EtOAc/*n*-hexane.

Results and Discussion

The title compounds were synthesized according to Scheme 1. The synthesis commenced with the reaction of *o*-phenylenediamine with α-chloroacetic acid in 5N hydrochloric acid solvent at reflux to produce CMB (**1**). In the next step, thiourea is reacted with the desired alkyl halide under reflux condition, and then it was quenched by NaOH. Susequently, CMB was added to reaction media at RT to acquire the products.

Having used the above procedure, several products bearing different functionalities were synthesized which some selected structures are illustrated in Fig.4.

Scheme 1: General procedure for synthesis of 2-methyl alkyl thioether Benzimidazole

Selected data for **2d**: CC on SiO2 eluted with *n*-hexane/EtOAc (16:1) afforded yellow foam (2.33 g, 87%), Rf (*n*-hexane/EtOAc):0.45; ^{1}H-NMR (CDCl3, 400 MHz): δ_{ppm} = 2.78-2.86 (m, 4H,SCH2, PhCH2), 4.05 (s, 2H, =CCH2), 7.09 (d, *J*=4.0 Hz, 2H,Ar), 7.17-7.33 (m, 5H, Ar), 7.58-7.62 (m, 2H, Ar), 9.24 (s, 1H, NH). ^{13}C-NMR (CDCl3, 100 MHz): δ_{ppm} = 29.26, 33.74, 35.47, 114.94, 123.18, 126.50, 128.47, 128.56, 137.51, 139.77, 1501.76.
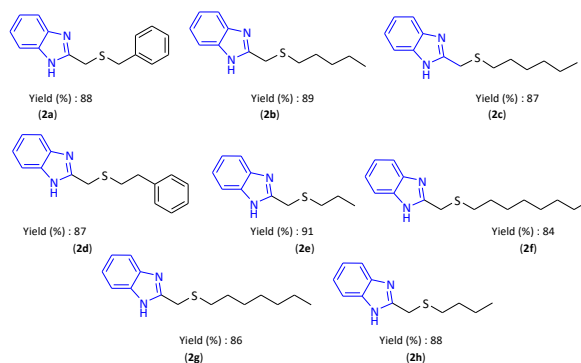

Fig. 4: Selected structures of some products

Conclusions

In conclusion, we have synthesized and characterized some novel 2-methyl alkyl thioether benzimidazole derivatives using a two-step, three-component one-pot synthesis by reaction of 2-chloromethylbenzimidazole, thiourea, and selected alkyl halides to afford products in good to excellent yields.

References

[1] Banerjee, S., Mukherjee, S., Nath P., Mukherjee, A., Mukherjee, S., Kumar, S.K. A., De, S. & Banerjee, S. (2023). A critical review of benzimidazole: Sky-high objectives towards the lead molecule to predict the future in medicinal chemistry. Results in Chemistry, 10, 101013. https://doi.org/10.1016/j.rechem.2023.101013.

[2] Kleemann, A. & Engel, J. (2009). Pharmaceutical Substances. 5th edn, Thieme, Germany. https://doi.org/ 10.1055/b-003-108611.

[3] Petkar, K., Parekh, P., Mehta, P., Kumari, A. & Baro, A. (2013). Synthesis & evaluation of 2-chloromethyl-1h-benzimidazole derivatives as antifungal agents. International Journal of Pharmacy and Pharmaceutical Sciences, 5 (2), 115-119.

22nd Iranian Chemistry Congress (ICC22)
Iranian Research Organization for Science and Technology (IROST)
13-15 May 2024

03231-97589

Comparison of Curcumin Microencapsulation Using Maltodextrin, Whey protein, and Arabic gum

Elaheh Maleki *, Mohsen Shahrokhi Nezhad

Corresponding Author E-mail: malekielaheh1998@gmail.com

Department of Food Science and Technology, Science and Research Branch, Islamic Azad University, Tehran, Iran.

Abstract: The aim of the present work was to microencapsulate curcumin in three different substances and investigate the physicochemical properties of those particles. Fluidized bed coating method was used for microencapsulation. Maltodextrin, whey protein, and Arabic gum were coating materials and curcumin was the main core.

Keywords: microencapsulation; curcumin; fluidized bed dryer

Introduction

Curcumin, is a natural polyphenol compound, that extracted from the turmeric. It is also employed as a traditional natural food dye. It has been reported that curcumin has antioxidant, anticancerous, anti-inflammatory, and antimicrobial activities [1]. Despite the unique properties of curcumin, it has low bioavailability [2]. Therefore, one of the strategies used in several research to increase its bioavailability is to microencapsulate it in different combinations as a carrier.

Materials and Methods

Materials

Curcomin was obtained from merck (Darmstadt, Germany). All chemicals used in this research were of hplc grade and were obtained from reputable Iranian companies.

Methods

Encapsulation of curcumin

The mothod for microencapsulating of curcumin was carried out as described by zaghari et al., with some modifications[3]. 1 gr of curcumin was dissolved in 10 cc of distilled water as the core. It was stirred for 10 minutes for better dissolution. To prepare the shells, we proceeded as follows: 3 gr of wpc (whey protein concentrated) were dissolved in 10 gr of distilled water(wpc 30%), 5 gr of maltodextrin were dissolved in 10 cc of distilled water and stirred frequently for complete dissolution(maltodextrin 50%), 0.1 grams of Arabic gum was poured into 10 cc of distilled water and placed under heat at 50°c for 10 minutes for complete dissolution (arabic gum 1%).

For microencapsulation by a fluidized bed device, the following procedure was performed: (1) The temperature of the device was set to 40 degrees. (2) the carrier material, which is microcrystalline cellulose in this research, was introduced into the dryer. (3) the core is injected and takes a few minutes to dry. (4) The shell solution is injected and dried. Finally, the microencapsulated curcumin powder is obtained. The operation of the device is shown in Figure 1.

Encapsulation efficiency

EE was calculated by dividing the amount of encapsulated curcumin by the total amount used. Microencapsulated curcumin was centrifuged at 10000 rpm for 20 minutes, then supernatant was mixed in acetone. The absorbance of the solution was measured at 426 nm using a UV-vis spectrophotometer [5]. The following formula was used to calculate the EE:

$$EE \% = \frac{\text{Encapsulated curcumin}}{\text{The total content of curcumin}} x\ 100$$

Release of curcumin

6 mg of sample was heated in 10 ml of distilled water at pasteurization temperature for 30 minutes and finally the solution was filtered. The wavelength of the filtered solution after preparation was read at 470 nm in a spectrophotometer and compared with the curcumin standard curve [6].

Anti-oxidant activity

The anti-oxidant activity was determined through DPPH (2, 2- diphenyl-1-picryl-hydrazyl) free radical scavenging activity. After preparing samples, the absorbance of each test was measured at 517 nm using UV spectrophotometer [7].
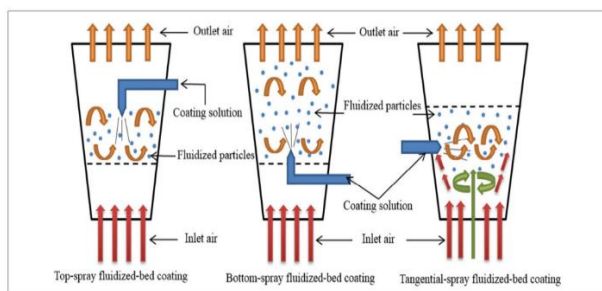
22nd Iranian Chemistry Congress (ICC22)
Iranian Research Organization for Science and Technology (IROST)
13-15 May 2024

03231-97589

Fig.1 Schematic illustration to show top, bottom, and tangential-spray fluidized-bed coating [4]

Results and Discussion

The results of the tests are summarized in Table 1. Encapsulation efficiency plays a crucial role in assessing the encapsulation procedure. A high EE ensures the good bioavailability of bioactive substances. Based on the previous studies, the EE of curcumin in protein matrices is near to 90%. For example, an EE of 96% was reported for microencapsulation of curcumin by β-lactoglobulin [8]. microcapsule release potential is necessary for predicting carrier behaviours during consumption in the body. This property is also important for evaluating the bioavailability of encapsulated compounds. Microcapsules with wpc shells are very stable [9]. The highest release rate in in-vitro test was related to maltodextrin and the lowest for wpc. Antioxidant activity is affected by factors such as pH, concentration and temperature, which were not among the parameters investigated in this research, and therefore this value is almost similar in 3 samples.

Conclusions

In this research, a new technique was used to microencapsulate curcumin with different shells. The encapsulation system could significantly improve the oxidation stability and control releasing of curcumin. Due to the unique properties of curcumin, microencapsulating of it, helps to preserve and better transfer this valuable compound. This technique can be used in the treatment of diseases such as cancer.

Table1: analysis results

	Maltodextrin	Arabic Gum	WPC
Antioxidant activity (%)	66.9%	67.12%	67.27%
Encapsulation efficiency (%)	67%	84%	95%
Curcumin release (%)	30%	26.1%	21%

References

[1] Bhawana, Basniwa, R. K., Buttar, H. S., Jain, V. K., & Jain, N. (2011). Curcumin nanoparticles: Preparation, characterization, and antimicrobial study. Journal of Agricultural and Food Chemistry, 59, 2056–2061. https://doi.org/10.1021/jf104402t

[2] Lin, J.-K., Pan, M.-H., & Lin-Shiau, S.-Y. (2000). Recent studies on the biofunctions and biotransformations of curcumin. BioFactors, 13, 153–158. https://doi.org/10.1002/biof.5520130125

[3] Leila Zaghari, Alireza Basiri and Somayeh Rahimi, Preparation and characterization of doublecoated probiotic bacteria via a fluid-bed process: a case study on Lactobacillus reuteri., Int. J. Food Eng. 2020; 16(9): 20190384, https://doi.org/10.1515/ijfe-2019-0384

[4] Bakry, A. M., Abbas, S., Ali, B., Majeed, H., Abouelwafa, M. Y., Mousa, A., et al. (2016). Microencapsulation of oils: A comprehensive review of benefits, techniques, and applications. Comprehensive Reviews in Food Science and Food Safety, 15(1), 143–182. https://doi.org/10.1111/1541-4337.12179

[5] Zou, L., Zheng, B., Zhang, R., Zhang, Z., Liu, W., Liu, C., … McClements, D. J. (2016). Enhancing the bioaccessibility of hydrophobic bioactive agents using mixed colloidal dispersions: Curcuminloaded zein nanoparticles plus digestible lipid nanoparticles. Food Research International, 81, 74–82. https://doi.org/10.1016/j.foodres. 2015.12.035

[6] Jain A, Thakur D, Ghoshal G, Katare O, Shivhare U. Characterization of microcapsulated β -carotene formed by complex coacervation using casein and gum tragacanth. International Journal of Biological Macromolecules. 2016; 87:101 -13.

[7] Khatun, M., Nur, M. A., Biswas, S., Khan, M., & Amin, M. Z. (2021). Assessment of the anti-oxidant, anti-inflammatory and anti-bacterial activities of different types of turmeric (Curcuma longa) powder in Bangladesh. *Journal of Agriculture and Food Research*, *6*, 100201.

[8] Sneharani, A. H., Karakkat, J. V., Singh, S. A., & Rao, A. A. (2010). Interaction of curcumin with β-lactoglobulin stability, spectroscopic analysis, and molecular modeling of the complex. Journal of Agricultural and Food Chemistry, 58, 11130–11139. https://doi.org/10.1021/jf102826q

[9] Solghi, S., Emam-Djomeh, Z., Fathi, M., & Farahani, F. (2020). The encapsulation of curcumin by whey protein: Assessment of the stability and bioactivity. *Journal of Food Process Engineering*, *43*(6), e13403.

22nd Iranian Chemistry Congress (ICC22)
Iranian Research Organization for Science and Technology (IROST)
13-15 May 2024

03231-97589

IROST

Comparison of the enzymatic extraction efficiency of chicken abdominal waste fat using 3 different proteases

Elaheh Maleki [A], Majid Javanmard Dakheli *[B]

Corresponding Author E-mail: javanmard@irost.ir

[a] Department of Food Science and Technology, Science and Research Branch, Islamic Azad University, Tehran, Iran.

[b] Associate Professor of Food Hygiene & Quality Control, Iranian Research Organization for Science and Technology, Tehran, Iran.

Abstract: Considering the high amount of waste in poultry industry and also considering the potential value of these wastes, it is necessary to find a way to revalue these products. The aim of this work was to extract fat from chicken abdominal fat waste and compare the efficiency of different proteases.

Keywords: enzymatic extraction; chicken fat; food waste

Introduction

Today, due to the increasing population growth, it seems that the need for new resources to meet human food needs is essential, and in the meantime, the use of food industry wastes has been the focus of many food producers and activists. Among the food products that have a high amount of waste, we can mention chicken.

Material and method

Materials

Chicken fat was obtained from a chicken slaughterhouse in Karaj, Iran and was used for the extraction process. For water extraction, enzymes donated by Novozyme (Denmark) in Tehran were used, which included Alcalase 2.4L, Flavourzyme 1000L, and Protamex.

Methods

Fat enzymatic extraction

The abdominal chicken fat was transferred to the laboratory and cleaned. Then it was finely chopped and homogenized by a meat grinder. In order to extract fat, tissue was mixed with water at a ratio of 1:2 (water: fat) and its pH was adjusted to the optimal point for each enzyme with buffer. The desired enzymes are also added with ratios of 2, 2.5 and 3% (weight/weight) of the total protein in the raw chicken fat sample, and finally, considering the optimal temperature, the samples are incubated in a shaker at 200 rpm for 120, 150 and 180 minutes were placed. After finishing the enzymatic hydrolysis process, it was transferred to water bath with a temperature of 90°C to inactivate the enzymes. After 15 minutes, the suspension was filtered to separate the excess solids that were not hydrolyzed by the enzyme, and then the solution was placed in the decanter. In this step, we separated the aqueous and oily phases by slowly removing the aqueous phase from the bottom of the decanter. The oil obtained from the extraction was centrifuged for the final separation of suspended and dispersed particles as well as possible water removal [1].

Extraction efficiency

After oil extraction, the extraction yield in gram was calculated by the following formula and expressed as percentage [2]:

$$EE\ (\%) = \frac{Weight\ of\ extracted\ oil\ in\ gram}{fat\ tissue\ weight} \times 100$$

statistical analysis

The design of the experiments and the analysis of the data obtained from the research were carried out using the response level method using the Design Expert software. The independent variables are the type of enzyme, the time of reaction and the ratio of the enzyme to the substrate, and the dependent variable is the percentage of extraction.

Results

Fat extraction efficiency

The results of the analysis of variance showed that the process variables, including enzyme type, enzyme-to-substrate ratio, and process time, have a significant effect (P≤0.05) on the extraction efficiency. As the extraction time increases and the percentage of the enzyme used increases, the extraction efficiency increases. Among the enzymes used, Flourzyme was the first in extraction efficiency, followed by Protamax and with a long distance, Alkalase showed lower amounts of extraction efficiency. The highest efficiency of fat extraction was 86% (P≤0.05), which was related to the Flourzyme enzyme, the ratio of enzyme to substrate was 3:100, and the extraction time was 180 minutes. The exact values of the extraction efficiencies are shown in Table 1.

22nd Iranian Chemistry Congress (ICC22)
Iranian Research Organization for Science and Technology (IROST)
13-15 May 2024

03231-97589

IROST

Table 1. Exact values of extraction efficiency

Enzyme	Enzyme-substrate ratio	Reaction time	EE (%)
Protamex	3	180	76.6
Flavourzyme	2.5	180	83
Flavourzyme	2.5	180	83.6
Flavourzyme	3	150	82.4
Protamex	3	150	79.4
Protamex	2	120	69.8
Flavourzyme	2	150	81.2
Alcalase	2	150	68.2
Alcalase	3	180	67
Protamex	2.5	150	83.2
Protamex	2	180	80.6
Protamex	2.5	180	80.4
Alcalase	3	120	80
Protamex	2.5	150	73.8
Alcalase	2	150	69.2
Protamex	2	150	81.4
Flavourzyme	3	150	86
Flavourzyme	2	150	79
Alcalase	2.5	120	68
Flavourzyme	2.5	120	82
Alcalase	2	120	76
Protamex	3	120	84

The results of this research were much more than other similar researches. For example, Su et al.,[3] treated black soldier fly larvae using Protamax enzyme, and the maximum fat yield was 36%. Also, in the research of Safarrazavizadeh et al.,[4] the efficiency of enzymatic extraction from chicken skin was 19 to 32%, which was much lower than the current research.

Conclusions
The special combination of fatty acids of chicken fat in terms of saturation, suitable content of palmitic acid and high amount of unsaturated fatty acids such as oleic and linoleic acid makes this fat a suitable source for the production of biodiesel, cosmetic products, soaps and even edible products such as margarines [5]. According to the contents stated in this study, fat extraction was done using protease enzymes, which as is evident, the extraction efficiency increased significantly.

References
[1] Mostafa Fallah-Delavar , Jamshid Farmani(2018) Recovery and Characterization of Enzymatic Protein Hydrolyzates and Fat from Chicken Skin, Journal of the American Oil Chemists' Society, Volume95, Issue9 ,September 2018, Pages 1151-1161.

[2] Rebolleda, S., Beltrán, S., Sanz, M. T., & González-SanJosé, M. L. (2014). Supercritical fluid extraction of wheat bran oil: Study of extraction yield and oil quality. *European Journal of Lipid Science and Technology*, *116*(3), 319-327.

[3] Su, C., Nguyen, H. C., Bui, T. L., & Huang, D. (2019). Enzyme-assisted extraction of insect fat for biodiesel production. *Journal of Cleaner Production*, *223*, 436-444.

[4] Rahimeh Safar Razavizadeh , Jamshid Farmani , Ali Motamedzadegan(2022). Enzyme-assisted extraction of chicken skin protein hydrolysates and fat: Degree of hydrolysis affects the physicochemical and functional properties, Journal of the American Oil Chemists' Society, Volume99, Issue7 ,July 2022, Pages 621-632

[5] Shi W, Li J, He B, Yan F, Cui Z, Wua K, Lin L, Qian X, Cheng Y, (2013). Biodiesel production from waste chicken fat with low free fatty acids by an integrated catalytic process of composite membrane and sodium methoxide. Bioresour Technol 139, 316–322.

Evaluating the effectiveness of Eucalyptus-based nanoherbicide on preventing the growth and germination of Amaranthus retroflexus seeds

Fatemeh Ahmadzadeh [a], Shima Kaviani [a], Farzaneh Jokarshoorijeh [b], Leila Ma'mani [*b]

Corresponding Author E-mail: leila.mamani@abrii.ac.ir

[a] Department of Biology, Faculty of Basic Sciences, Ale Taha Institute of HigherEducation, Tehran, Iran.

[b] Department of Nanotechnology, Agricultural Biotechnology Research Institute of Iran (ABRII), Agricultural Research Education and Extension Organization (AREEO), Karaj, Iran.

Abstract: The effect of nanoherbicide based on eucalyptus essential oil on the seed germination of redroot pigweed was investigated. To investigate its germination and growth, an experiment was conducted in the form of a completely randomized design with three concentrations on the redroot pigweed `seeds`. At a concentration of 5% of nano-herbicide, growth inhibition occurred completely.

Keywords: Allelopathy; Pesticides; Germination; Weed

Introduction

Redroot pigweed seeds (Amaranthus retroflexus L.) is an important and widespread weed found in fields and gardens, with a wide distribution in Iran, causing damage to agricultural products [1]. To combat this weed, using different herbal compounds instead of chemical herbicides, which can be harmful to humans and the environment, is a viable option. Eucalyptus is a plant known for its herbicidal properties. Various reports have highlighted the antioxidant, antimicrobial, insecticidal, antibacterial, herbicidal, and fungicidal effects of eucalyptus essential oil [2]. Eucalyptus is considered an allelopathic plant, with its effective ingredients interfering with the growth of other plants. These effective ingredients protect agricultural products without harming the environment or causing pollution, making them a suitable alternative to chemical herbicides [3]. To investigate the effect of an herbal nanoherbicide based on eucalyptus essential oil, a germination test was conducted using concentrations of 1.25%, 2.5%, and 5% along with a control (distilled water) with three replications.

Experimental Section

Materials: Herbal oil; Organic solvent; Eucalyptus essential oil; Distilled water; Polysorbate 80; Span 80

Method: The listed materials were combined in a laboratory tube. Then it was stirred with the help of a magnetic stirrer at a temperature in the range of 25-35°C and at a speed of 100-500 rpm for 2 h. Finally, it was kept in the dark and away from temperature and humidity [4].

Germination test: The germination test was used to evaluate the effect of the herbal nanoherbicide. In this test, three concentrations of 1.25%, 2.5%, 5% and control (distilled water) were used with three replications. In each replication, 20 seeds of redroot pigweed were placed in the dark and at a temperature of 25°C, and their germination and growth were examined (Fig .1).
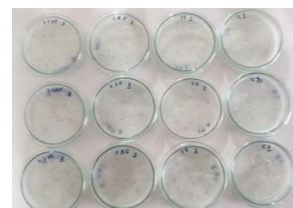

Fig.1: Germination test with concentrations of 1.25%, 2.5%, 5% and control with three replications.

2.5 mL of the desired concentration was applied to all treatments and in the control treatment, distilled water was used as a negative control. The treatments were applied only once and in the subsequent stages, only water was used for irrigation. The seeds were examined for germination and growth after every 24 hours.

The DLS test was used to check the size of formulation particles. According to the results of this test, the size of nanoparticles is below 100 nm (Fig .2)
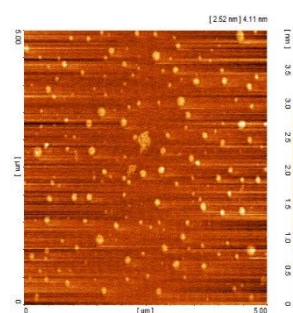

Fig.2: AFM image of nanoherbicide

22nd Iranian Chemistry Congress (ICC22)
Iranian Research Organization for Science and Technology (IROST)
13-15 May 2024

03231-97589

IROST

Statistical analysis

The test was performed as a completely randomized design. Excel 2013 software was used to draw the charts. Also SAS 9.4 software was used for statistical analysis.

Results and Discussion

Based on the results obtained, the herbal herbicide at concentrations of 5% and 2.5% inhibited the germination of redroot pigweed weed seeds. Additionally, the formulation had a significant effect on reducing the stem length at a concentration of 1.25% of the nanoherbicide (Fig .3).
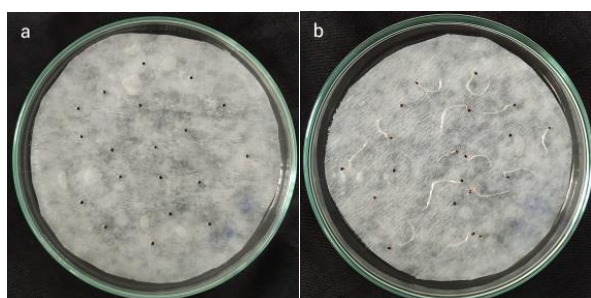

Fig.3: (a) Inhibition of germination and seed growth at a 5% herbicide concentration. (b) Germination and growth of seeds in the negative control treatment.

The lowest percentage of germination was observed at concentrations of 5%, and 2.5%, while the highest percentage of germination (58.3%) was observed in the negative control (Fig .4).
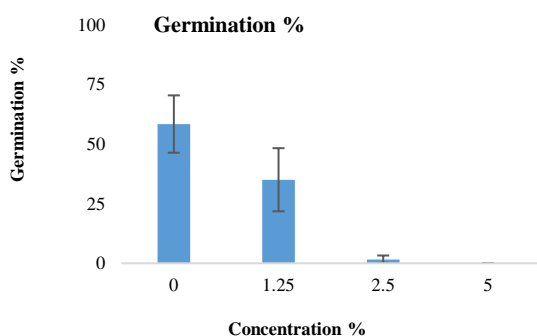

Fig.4: Percentage of germination in seeds treated with three concentrations of herbicide (5%, 2.5%, and 1.25%) and negative control.

The lowest germination rate was observed at the 5% concentration, while the highest germination rate was observed in the negative control treatment (Fig .5)
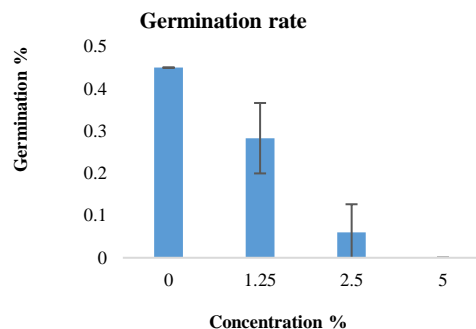

Fig.5: Germination rate of seeds after treatment with three concentrations of herbicide (5%, 2.5%, and 1.25%) and negative control.

In a study conducted in 2021 on redroot pigweed weed, an herbal formulation containing Asafoetida essential oil and Castor oil at a concentration of 1% showed about 30% germination [5]. Meanwhile redroot pigweed retroflexus at a concentration of 5%.

Conclusions

The results of this research indicate that the herbicide made from eucalyptus essential oil, at a concentration of 5%, completely (~100%) inhibited the germination and growth of redroot pigweed seeds. At a concentration of 2.5%, germination was inhibited to a great extent (99.6%), and at 1.25%, there was a decrease in stem growth, with the maximum length of the stem at this concentration being 11 mm. In the negative control, stem length reached about 20 mm. Additionally, according to the DLS test, the particles of this herbicide are in nano dimensions. Another advantage of this herbicide is its pleasant smell.

References

[1] Hamidzadeh Moghadam, S., Alebrahim, M. T., Mohebodini, M., & MacGregor, D. R. (2023). Genetic variation of Amaranthus retroflexus L. and Chenopodium album L. (Amaranthaceae) suggests multiple independent introductions into Iran. Frontiers in Plant Science, 13, 1024555.

[2] Almas, I., Innocent, E., Machumi, F., & Kisinza, W. (2021). Chemical composition of essential oils from Eucalyptus globulus and Eucalyptus maculata grown in Tanzania. Scientific African, 12, e00758.

[3] Jokar-shorijeh, F., Ma'mani, L., Sheikhi Garjan, A., Hosseini, R., Mahdavi, V. and Heidary Alizadeh, B., 2020. Repellency and control of nymph of greenhouse whitefly (Trialeurodes Vaporariorum) using nanobiopesticide. *Journal of Biosafety*, *12*(4), pp.97-110.

[4] El-Rokiek, K. G., & Eid, R. A. (2009). Allelopathic effects of Eucalyptus citriodora on amaryllis and associated grassy weed. Planta daninha, 27, 887-899.

[5] Tarassoli, Z., Labbafi, M. and Jokar Shoorijeh, F., 2021. Allelopathic effect of herbal formulation containing Ferula assa-foetida L. essential oil and castor oil (Ricinus communis L.) as an herbicide on Amaranthus retroflexus L. seed germination. Journal of Medicinal Plants, 20(80), pp.69-82.

Facile electrodeposition synthesis and electrochemical investigation of MnO$_2$ nano structure on conductive carbon fiber substrate used as supercapacitor electrode material

G. Alaei, M. Mazloum, F. Ebrahimi

Corresponding Author E-mail: alaeeghazale147@gmail.com

Department of Chemistry, Faculty of Science, Yazd University, Yazd, 8915818411, Iran.

Abstract: in this work electrochemical deposition of MnO$_2$ nanoparticles on the carbon fiber substrate as an electrode for energy storage devices was reported. The results showed a High capacitance of 545.641 F.g^{-1} at 1 A.g^{-1} for the MnO$_2$/CFS electrode. So MnO$_2$ can be used as a promising electrode material for supercapacitors.

Keywords: Supercapacitor; Electrochemical deposition; Manganese oxide nanostructure

Introduction

To date, for supercapacitors, there has been great interest in the development of commercial high-conductivity intermediate metal oxide electrodes such as CuO, Fe$_3$O$_4$, NiO, Co$_3$O$_4$, MnO$_2$, etc.[1]. Mn-based oxides have emerged as a promising electrode material for supercapacitor applications due to abundance and diversity in oxidation number, high theoretical Specific capacitance and compatibility with the standards of green chemistry [2]. It is important to obtain an easy and fast electrochemical method for preparing MnO$_2$ nanoparticles.

Experimental Section

Synthesis:

A carbon fiber substrate with dimensions (1 × 2 cm^2) was wetted several times with deionized water. Then electrochemical deposition was performed in a three-electrode cell consisting of a working electrode (carbon fiber substrate), a counter electrode (platinum electrode) and a reference electrode (Ag/AgCl). The surface of the carbon electrode placed in the solution (1x1 cm^2) square meters). MnO$_2$ nanoparticles were placed on a carbon felt substrate with a voltage of 0.9 V and for 10 minutes in a solution containing 20 ml of MnCl$_2$.4H$_2$O 0.05 M + 0.1 M KCl. After that, the products were washed with deionized water and absolute ethanol, and then the sediment obtained was dried in a vacuum oven at 60°C for 4 hours. The mass of the deposited MnO$_2$ nanomaterials is (0.0005g) that obtained from the difference in the mass of the carbon electrode before and after the electrochemical deposition[2].

The electrochemical properties of the electrode were analyzed by a three-electrode system and CV, GCD and EIS electrochemical tests in the presence of 3M KOH electrolyte.

Results and Discussion

Electrochemical characterization of MnO$_2$/CFS electrode:

Cyclic voltammetry (CV) was performed at -0.3-0.6 V at different scan rates for the MnO$_2$/CFS electrode (Fig. 1a) .The redox peaks observed in the curve of (Fig.1a) correspond to the reduction and oxidation of manganese oxidation numbers(Mn^{4+}/Mn^{3+}/Mn^{2+}). Using galvanostatic charge-discharge (GCD) for different current densities, the capacitance of the electrode MnO$_2$/CFS can be obtained for each current density (Fig. 1b) (Table 1). According to (Table 1), the specific capacitance decreases with the increase in current density. Fig. 1c shows the galvanostatic charge-discharge (GCD) curves of the CFS and MnO$_2$/CFS electrodes measured at 0 to 0.4 V at 1 A.g^{-1}. The discharge time of MnO2/CFS at 1 A.g^{-1} was determined to be (381.949 s), which is longer than the discharge time of the CFS electrode (6.61 s). In addition, electrochemical impedance spectroscopy (EIS) was performed to compare the charge transfer resistance(R$_{ct}$) of the two surfaces(MnO$_2$/CFS and CFS) (Fig. 2)[3]. CV obtained from the MnO$_2$/CFS electrode under different scan rates as shown in (Fig. 1a), with increasing scan rate from 0.01 to 0.1 V.s^{-1}, in the potential window of -0.3 to 0.6 V, The CV remains almost rectangular indicating excellent electrochemical reversibility.As shown in (Table 2), the MnO$_2$/CFS electrode materials were compared with other electrodes with different synthesis methods or different compositions previously reported.
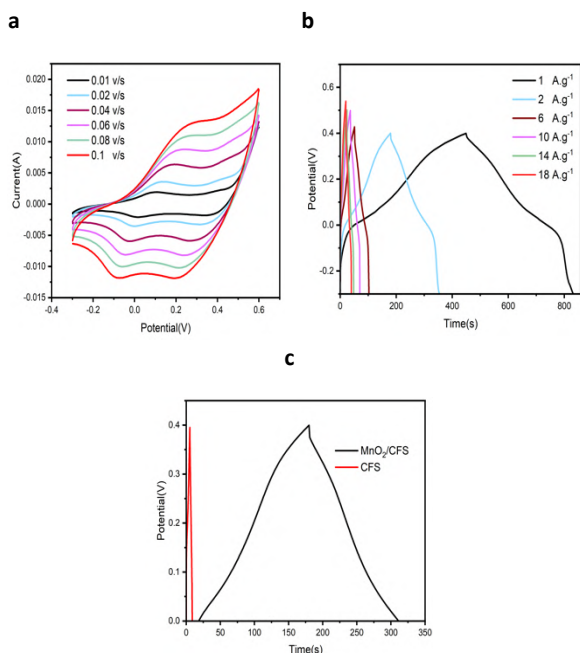
22nd Iranian Chemistry Congress (ICC22)
Iranian Research Organization for Science and Technology (IROST)
13-15 May 2024

03231-97589

IROST

Table 2: Performance of supercapacitor electrode materials of different synthesis and compositions of MnO_2.

Electrode material	Synthesis method	Specific capacitance $(F.g^{-1})$	Ref.
CuO@MnO_2/N-MWCNT	Hydrothermal	184 $F.g^{-1}$ at 0.5 $A.g^{-1}$	[5]
MnO_2/ graphite paper	Electrochemical deposition	261 $F.g^{-1}$ at 1 $A.g^{-1}$	[2]
MnO_2nanocage/ Ni foam	Hydrothermal Synthesis	278 $F.g^{-1}$ at 0.1 $A.g^{-1}$	[3]
MnO_2/CFS	Electrochemical deposition	545.641 $F.g^{-1}$ at 1 $A.g^{-1}$	This work

Fig.1: (a) CV curves of the MnO_2/CFS electrode at different scan rates. (b) GCD curves of the MnO_2/CFS electrode at different current densities. (c) GCD of CFS and MnO_2/CFS electrodes at $1A.g^{-1}$.
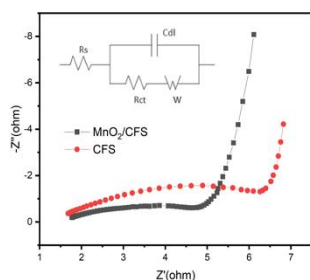
Conclusions

According to the results obtained from the electrochemical investigations, the synthesized electrode (MnO_2/CFS) has good specific capacitance (545.641$F.g^{-1}$ at 1 $A.g^{-1}$) and high reversibility and low charge transfer resistance. So these results show MnO_2 is a promising material for supercapacitor electrodes.

Fig.2: EIS spectra comparison of the MnO_2/CFS and CFS electrode.

Table 1: Relation between specific capacity and scan rates of MnO_2/CFS electrode.

Current density ($A.g^{-1}$)	Specific capacitance ($F.g^{-1}$)
1	545.641
2	499.065
6	423.287
10	420.1125
14	419.3175
18	414.021

References

[1] Aghazadeh, M. (2017). Synthesis, characterization, and study of the supercapacitive performance of NiO nanoplates prepared by the cathodic electrochemical deposition-heat treatment (CED-HT) method. *Journal of Materials Science: Materials in Electronics*, *28*, 3108-3117.

[2] Rakhi, R. B., Chen, W., Cha, D., & Alshareef, H. N. (2012). Substrate dependent self-organization of mesoporous cobalt oxide nanowires with remarkable pseudocapacitance. *Nano letters*, *12*(5), 2559-2567.

[3] Yang, P., Li, Y., Lin, Z., Ding, Y., Yue, S., Wong, C. P., ... & Mai, W. (2014). Worm-like amorphous MnO 2 nanowires grown on textiles for high-performance flexible supercapacitors. *Journal of Materials Chemistry A*, *2*(3), 595-599.

[4] Li, W., Xu, J., Pan, Y., An, L., Xu, K., Wang, G., ... & Hu, J. (2015). A facile synthesis of α-MnO2 used as a supercapacitor electrode material: The influence of the Mn-based precursor solutions on the electrochemical performance. *Applied Surface Science*, *357*, 1747-1752.

[5] Zheng, Y., & Zheng, X. (2020). Hydrothermal synthesis of MnO2 with different morphological characteristics as electrode material for high electrochemical performance supercapacitors. *International Journal of Electrochemical Science*, *15*(2), 1465-1473.

22nd Iranian Chemistry Congress (ICC22)
Iranian Research Organization for Science and Technology (IROST)
13-15 May 2024

03231-97589

IROST

Design and synthesis of covalent organic framework by sulfonic acid tags as a catalyst for the preparation of imidazoles

Erfan Abdoli, Morteza Torabi, Mohammad Ali Zolfigol[*], Meysam Yarie

Corresponding Author E-mail: mzolfigol@yahoo.com

Department of Organic Chemistry, Faculty of Chemistry and Petroleum Sciences, Bu-Ali Sina University, Hamedan, Iran.

Abstract: In this study, new covalent organic framework by sulfonic acid tags namely $COF@(CH_2)_3SO_3H$ was designed and synthesized via post modification of imine-linked COF. After precisely characterization of $COF@(CH_2)_3SO_3H$, it was used as highly active and effective catalyst for the preparation of imidazole derivatives.

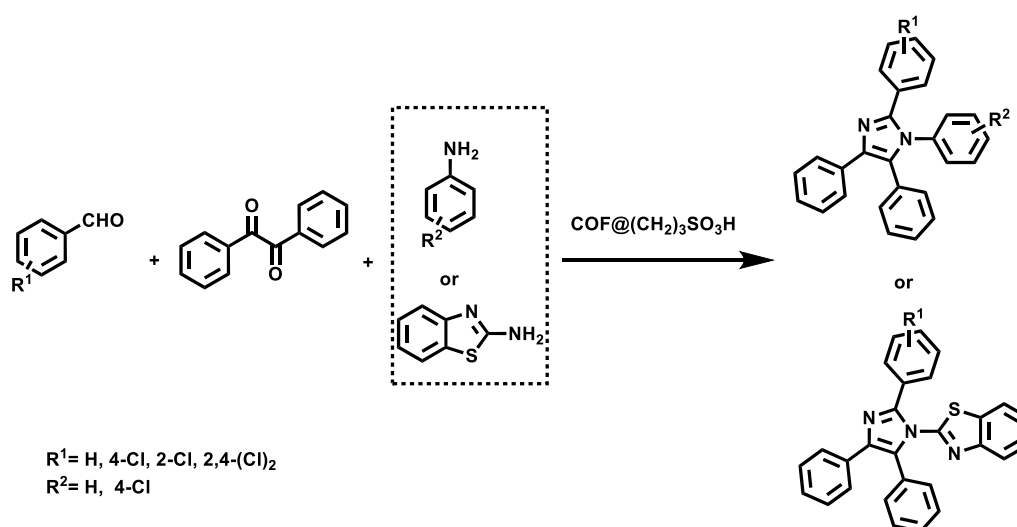**Keywords:** Covalent organic framework; Catalyst; Imidazole;

Introduction

COF-based materials are synthesized by the strong covalent linkages in a repeating patterns to form a porous crystal structure that is ideal candidate for various fields such as gas adsorption and storage, energy storage such as supercapacitors, and batteries, energy conversion in solar cells, catalytic transformations, electrochemical applications and dug delivery. [1-2]. There are several catalytic applications for COFs such as photocatalytic transformations, oxidation/reduction reaction, coupling reactions, multicomponent reactions and click reactions. Imidazole rings, which is widely found in natural products and medical molecules, is one of the most prominent, five-membered, nitrogen-containing, heterocyclic scaffolds. Furthermore, imidazole-based heterocyclic compounds, which possess a vital position in medicinal chemistry, have been playing a central role in the treatment of numerous types of diseases [3]. Nevertheless, synthesis of these chemical by simple methodologies deserved more attentions.

Experimental Section

In this methodology, we were able to synthesis imidazoles by using $COF@(CH_2)_3SO_3H$ catalyst and benzyl, ammonium acetate, aromatic andaldehydes and aniline derivatives under solvent-free conditions at 110 ℃ (Scheme 1). To find optimal conditions, several parametes such as temperature, solvent and the amount of catalyst was investigated.

R^1= H, 4-Cl, 2-Cl, 2,4-$(Cl)_2$
R^2= H, 4-Cl

Scheme 1: preparation of imidazoles using $COF@(CH_2)_3SO_3H$ as a catalyst

22nd Iranian Chemistry Congress (ICC22)
Iranian Research Organization for Science and Technology (IROST)
13-15 May 2024

03231-97589

IROST

Results and Discussion

We characterized the catalyst by SEM, TEM, EDS, TGA,BET and XRD methods. The SEM image and XRD pattern of catalyst are illustrated in below (Figure 1).
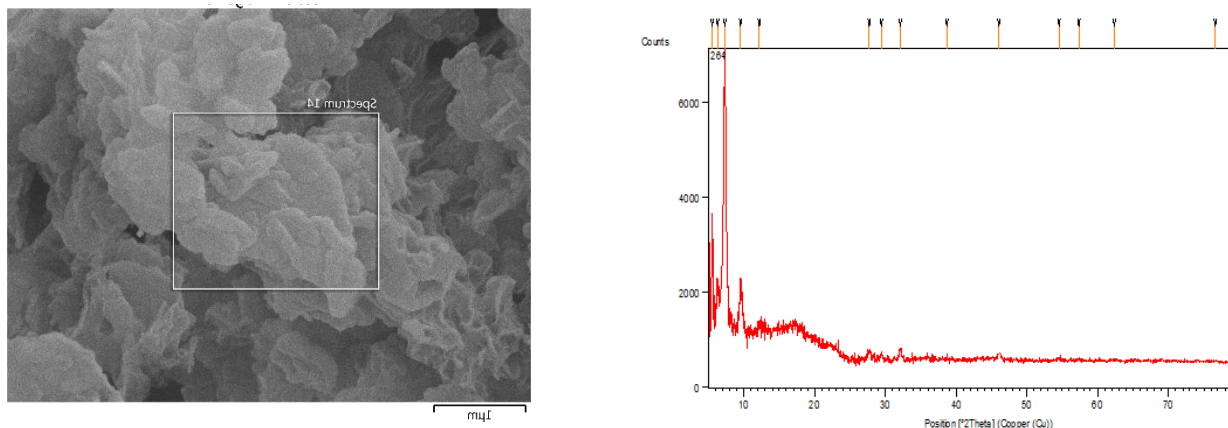

Figure 1: SEM image and XRD pattern of COF@$(CH_2)_3SO_3H$

Conclusions

As a result, we designed and synthesized SO3H@AFB-COF as a catalyst. This catalyst was successfully used in the synthesis of new imidazols derivatives. All derivatives have short reaction times and were prepared in mild and solvent-free conditions.

References

[1] Ozdemir, J., Mosleh, I., Abolhassani, M., Greenlee, L. F., Beitle Jr, R. R., & Beyzavi, M. H. (2019). Covalent organic frameworks for the capture, fixation, or reduction of CO2. *Frontiers in Energy Research*, *7*, 77.

[2] Zhao, X., Pachfule, P., & Thomas, A. (2021). Covalent organic frameworks (COFs) for electrochemical applications. *Chemical Society Reviews*, *50*(12), 6871-6913.

[3] Zheng, X., Ma, Z., & Zhang, D. (2020). Synthesis of imidazole-based medicinal molecules utilizing the van leusen imidazole synthesis. *Pharmaceuticals*, *13*(3), 37.

Evaluation of the Anti-Oxidant Activity and Total Phenolic and Flavonoid Contents of *Hippophae rhamnoides*

Pegah Amini[*], Mehdi Fatehi, Mahdi Abbas-Mohammadi

Corresponding Author E-mail: pegah_amini78@yahoo.com

Department of Phytochemistry, Faculty of Chemistry, University of Kashan, Kashan, Iran.

Abstract: Plant phenolics and flavonoids have a great role in eliminating free radicals in the body and act as antioxidants. This research aims to determine the primary phytochemical content of total phenolics and flavonoids of differnet extracts of *Hippophae rhamnoides* from the Elaeagnaceae family. Total flavonoid content was measured using the aluminum chloride colorimetric method and total phenol content was measured by Folin-Ciocalteu assay. Then, the antioxidant activity of the extracts was assessed by DPPH method. According to the obtained results, the highest level of inhibition of free radicals was related to the methanolic extract of the stem with an IC50 value of 166 µg/mL.

Keywords: phenolic content; flavonoid content; antioxidant activity

Introduction:

Hippophae rhamnoides, also known as sea-buckthorn is a species of flowering plant in the family of Elaeagnaceae, native to the cold-temperate regions of Europe and Asia. It is a spiny deciduous shrub. The plant is used in the food and cosmetics industries, in traditional medicine, as animal fodder, in horticulture, and for ecological purposes. This study aimed to screen total phenolic and flavonoid contents of various extracts of different parts of the *Hippophae rhamnoides* species in order to discovery of novel natural antioxidants for using in food and pharmaceutical formulations. Phenols and flavonoids are plant secondary metabolites that have an aromatic ring with at least one hydroxyl group. According to the several reports, phenolic compounds in biological systems exhibit free radical scavenging, peroxide decomposition, metal inactivation, or oxygen scavenging and prevent oxidative diseases.

Experimental Section

Plant Material:

Firstly, the plant material of *Hippophae rhamnoides* was collected in late October 2023 from Alborz province, and after separation of stems, leaves, and fruits from each other, they were dried in the shade and away from direct sunlight. Then, the soil and impurities of the plant were cleaned and the seeds and fruits were separated from each other the organs were crushed by a grinder and the seeds were pounded with a porcelain mortar.

Extraction:

To extract different organs and according to the reports of different compounds in fruit and seeds, the seeds were separated from the fruit and 8 grams of seeds were obtained from 20 grams of fruit (Fig1). Then 20 grams of leaves and stems of the plant were also weighed and in order to separate the different compounds of the plant with different polarities, extracting from the organs was done with hexane, ethyl acetate, and methanol solvents by soaking method, and the amount of washing and extract the results obtained in each step are shown in Table 1.

Table1: Details of different extracts of *H. rhamnoides*

organ		Time of extract	Solvent(cc)		g
leaf	20 g	2*19 h	Hexane:	350	1.45
		2*19 h	Ethyl acetate:	320	0.59
		2*19 h	Methanol:	250	0.87
stem	20 g	2*19 h	Hexane:	360	0.3
		2*19 h	Ethyl acetate:	300	0.27
		2*19 h	Methanol:	250	0.12
fruit	20 g	2*19 h	Hexane:	300	3.15
		2*19 h	Ethyl acetate:	250	1.11
		2*19 h	Methanol:	250	1.01
seed	8 g	2*19 h	Hexane:	150	0.17
		2*19 h	Ethyl acetate:	150	0.13
		2*19 h	Methanol:	150	0.09

Total phenol analysis:

Phenolic compounds are important plant components with redox properties that are responsible for antioxidant activity [1]. Hydroxyl groups present in plant extracts are responsible for facilitating the scavenging of free radicals. In this research, phenolic content was measured using the Folin-Ciocalteu reagent in each extract. The results were extracted from a calibration curve (y = 0.0016x − 0.0597, R2 = 0.9643) of gallic acid (0-250 µg/ml) and expressed in

22nd Iranian Chemistry Congress (ICC22)
Iranian Research Organization for Science and Technology (IROST)
13-15 May 2024

03231-97589

IROST

gallic acid equivalents (GAE) per gram of dry extract weight (Table 2). According to the results, the methanolic extract of the seed with the amount of 278 (mg GAE/g dry extract wt) has the highest amount of phenolic compounds.

Total flavonoid analysis:

Flavonoids are secondary metabolites with antioxidant activity whose potency depends on the number and position of free OH groups [2]. After analyzing all the extracts, Table 2, it was found that the hexane extract of the leaf has the highest amount of flavonoid compounds.

DPPH Radical Scavenging Activity

The DPPH assay is a simple, acceptable, and most widely used technique to evaluate the radical scavenging potency of plant extracts. The antioxidants are the components of the plants that are capable of enacting the visually noticeable quenching of the stable purple-colored DPPH radical to the yellow-colored DPPH [3]. According to the results, the highest amount of 50% inhibition (IC50) was seen in the methanolic extract of stem. with the amount of 165.7792 µg/mL. (Table2)

Results and Discussion

Considering that the seeds and leaves of the plant had the highest amount of phenolic and flavonoid contents, it is suggested that other researches should be conducted on the isolation of the compounds in the seeds and leaves in order to identify the antioxidant contents of the plant.
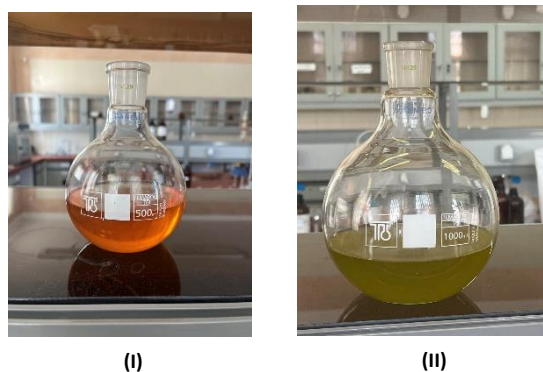

(I)   **(II)**

Fig.1: I: Methanolic extract of seeds, II: Hexane extract of leaves

Conclusions

After comparing the data, it can be hypothesized that the phenolic and flavonoid contents in the plant contribute to its antioxidant activity and can be used as a promising plant species for free radical scavenging activity to treat many diseases. considered life-threatening. This plant can be used as a medicinal plant in the treatment of vascular diseases. Further investigation is necessary to purify and identify the effective compounds of this plant for herbal treatments.

Table2: Results of anti-oxidant and total phenolic and flavonoid of *H. rhamnoides*

Solvent	Organ	TPC (mg GAE/g dry extract wt)	TFC (mg QE/g dry extract wt)	DPPH scavenging IC50 (µg/mL)
n-hexane	Seed	13.54167	13.32857	
	Fruit	2.680556	146.4357	
	Stem	15.63889	58.71667	
	Leaf	31.01389	174.6571	
Ethyl acetate	Seed	24.26389	4.17381	
	Fruit	19.56944	14.81905	
	Stem	74.56389	69.3	
	Leaf	36.86111	140.3333	
Methanol	Seed	318.2222	2.242857	224.9688
	Fruit	32.98611	4.666667	1134.7611
	Stem	280.8889	8.604762	165.7792
	Leaf	132.5556	31.95714	243.8068

TPC: total phenol content; TFC: total flavonoid content; GAE: gallic acid equivalents; QE: quercetin equivalents; wt: weight; DPPH: DPPH radica

References

[1] Soobrattee, M.A.; Neergheen, V.S.; Luximon-Ramma, A.; Aruoma, O.I.; Bahorun, T. Phenolics as potential antioxidant therapeutic agents: Mechanism and actions. Mutat. Res.-Fund. Mol. Mutagen. 2005, 579, 200–213.

[2] Panche, A.N.; Diwan, A.D.; Chandra, S.R. Flavonoids: An overview. J. Nutr. Sci. 2016, 5, e47.

[3] Chang, L.-W.; Yen, W.-J.; Huang, S.C.; Duh, P.-D. Antioxidant activity of sesame coat. Food Chem. 2002, 78, 347–354.

Synthesis of ethyl 5-aryl-1*H*-tetrazole-1-carboxylate and ethyl 5-aryl-2*H*-tetrazole-2-carboxylate through the reaction of tetrazole derivatives with ethyl chloroformate in the presence of *N,N*-diisopropylethylamine

Zeinab Motamedi[a], Nader Noroozi Pesyan[*a] Mahmoud Nasrollahzadeh [*b]

Corresponding Author E-mail: nnp403@gmail.com, mahmoudnasr81@gmail.com[b]

[a] Department of Organic Chemistry, Faculty of Chemistry, Urmia University, 57159 Urmia, Iran.

[b] Department of Organic Chemistry, Faculty of Chemistry, Qom University, 37185-359 Qom, Iran.

Abstract: Increasing interest in tetrazoles and tetrazole-based materials in the recent century has been followed by enormous research efforts devoted to synthesizing various materials based on these five-membered heterocyclic compounds, which basically contain four nitrogen atoms. The wide field of tetrazole applications as efficient, air-stable, and inexpensive materials has drawn attention to the methods to synthesize various kinds of tetrazoles and their derivatives. In this project, 5-phenyl-1*H*-tetrazole-1-carboxylate and 5-phenyl-2*H*-tetrazole-2-carboxylate are synthesized by the reaction of 5-aryl(aryloxy)tetrazole (or 5-aryl 1*H*-tetrazole) with ethyl chloroformate in tetrahydrofuran through N-H bond activation in the presence of DIPEA (*N,N*-Diisopropylethylamine). All the synthesized compounds are characterized by FT-IR, ^{1}H and ^{13}C NMR.
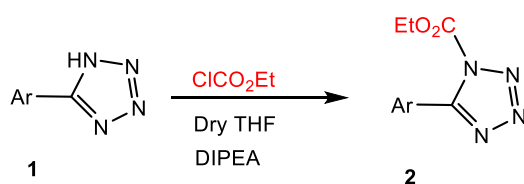
Keywords: Ethyl 5-aryl-1*H*-tetrazole-1-carboxylate; Ethyl 5-aryl-2*H*-tetrazole-2-carboxylate; DIPEA; Ethyl chloroformate; Tetrahydrofuran

Introduction

Tetrazoles constitute a privileged class of heterocycles with attractive characteristics such as nitrogen atoms, high acidity, low basicity, maximum dipole moment, good stability, high formation enthalpy, etc [1]. Tetrazole derivatives attained remarkable attention as prime heterocycles due to extensive utilization in numerous fields such as medicine, pharmacology, photography and as potential explosives and rocket propellant components based on their high energy properties [2]. Tetrazoles undergo various reactions such as alkylation and acylation, complex formation with metals, thermolysis, photolysis, decomposition with formation of nitrenes, etc [3].

Experimental section

In this study, the reaction of 5-aryloxy 1*H*-tetrazole or 5-aryl 1*H*-tetrazole (1.46 g, 10 mmol) was treated with ethyl chloroformate (1.36 g, 10 mmol) in THF as solvent and 100 mL of DIPEA (1 mL) as a catalyst (Scheme 1). The reaction was refluxed at 80°C for 16 hours, and two products were formed.

Scheme 1: Synthesis of ethyl 5-aryl-1*H*-tetrazole-1-carboxylate and ethyl 5-aryl-2*H*-tetrazole-2-carboxylate.

Results and discussion

The products were characterized by ^{1}H NMR, ^{13}C NMR, FT-IR (Figs. 1-3), and melting points. The disappearance of one strong and sharp absorption band (CN stretching band) and the appearance of a NH stretching band in the FT-IR spectra provided clear evidence for the formation of aryloxy tetrazoles (Fig. 1).
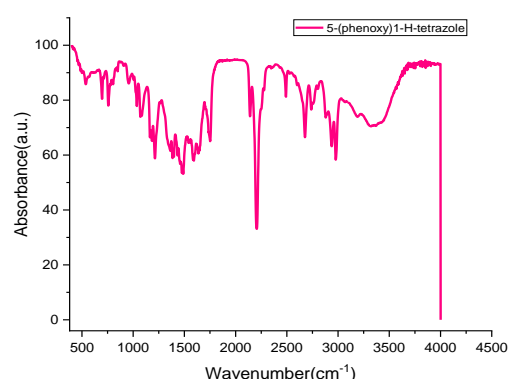

Fig. 1: FT-IR spectrum (KBr) of 5-phenoxy 1*H*-tetrazole.

^{13}C NMR spectra displayed signals at δ = 154-157.5 ppm, indicating C$_5$ in the tetrazole ring. The free N-H bond of tetrazoles (NH) makes them acidic molecules, and not surprisingly, it has been shown that both the aliphatic and aromatic heterocycles have pKa values that are similar to the corresponding carboxylic acids due to the ability of the moiety to stabilize a negative charge by electron

22nd Iranian Chemistry Congress (ICC22)
Iranian Research Organization for Science and
Technology (IROST)
03231-97589
13-15 May 2024

IROST

delocalization. In general, tetrazolic acids exhibit physical characteristics similar to carboxylic acids. Thus, the signal of the NH proton of the tetrazole ring (NH) shifted downfield.

Fig. 2: ^{1}H NMR spectrum (400 MHz, DMSO-d_6) of 5-phenyl-1H-tetrazole.
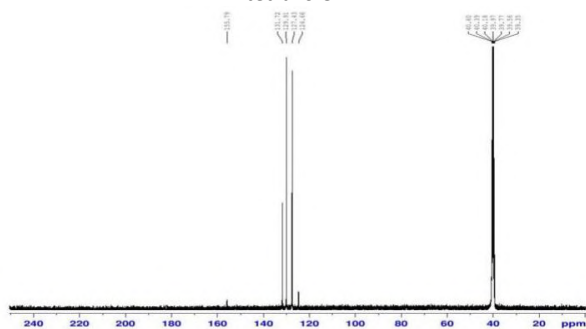
Fig. 3: ^{13}C NMR spectrum (100 MHz, DMSO-d_6) of 5-phenyl-1H-tetrazole.

Conclusions

The reaction of 5-aryloxy 1H-tetrazole (or 5-aryl 1H-tetrazole) with ethyl chloroformate and DIPEA in THF activates the N-H bond, synthesizing two compounds. All the synthesized compounds were characterized by FT-IR, ^{1}H and ^{13}C NMR. This reaction can lead to the production of new compounds with different properties that are used chemically and biologically.

References

[1] Sajjadi, M., Nasrollahzadeh, M., & Ghafuri, H. (2021). Cu (II)-N-benzyl-amino-1H-tetrazole complex immobilized on magnetic chitosan as a highly effective nanocatalyst for CN coupling reactions. Journal of Organometallic Chemistry, 950, 121959.

[2] Abdessalam, M., Sidhoum, M. A., Zradni, F. Z., & Ilikti, H. (2021). Synthesis of 1,5-disubstituted tetrazoles in aqueous micelles at room temperature. Molbank, 2021(1), M1194.

[3] Dabbagh, H. A., Noroozi Pesyan, N., Bagheri, A., Takemo, S., & Hayashi, H. (2005). Reaction of 5-aryloxytetrazoles with dimethyl sulfoxide and DMSO-acetic anhydride. structure and quantum-chemical calculations of 1-methylsulfanylmethyl-5-(4-nitrophenoxy) tetrazole. Russian journal of organic chemistry, 41, 1055-1063.

22nd Iranian Chemistry Congress (ICC22)
Iranian Research Organization for Science and Technology (IROST)
13-15 May 2024

03231-97589

IROST

Comparison of the effect of treated kaolin and metakaolin as the matrices in the SAPO-34 spray-dried catalyst for converting methanol to light olefins

Farahnaz Aflatooni [a,b], Iman Akbari Dahoui [a], Sima Askari [a], Marzieh Hamidzadeh [b]
Corresponding Author E-mail: askari.sima@gmail.com
[a] Chemical Engineering Department, Science and research Branch University.
[b] National Petrochemical Company, Petrochemical Research and Technology Company, P.O. Box: 1435884711, Tehran, Iran.

Abstract: With using kaolin and metakaolin treated as matrix in the formation of SAPO-34 catalyst for the reaction of methanol to light olefins[1], the metakaolin-based SAPO-34 catalyst outperformed the kaolin-based catalyst with 82% selectivity in MTO conversion. The selectivity of propene and ethane in both catalysts was around 72%. Both catalysts were stable for 1200-150 minutes.

Keywords: Methanol, kaolin, metakaolin, light olefin, matrix, SAPO-34

Introduction

Due to rising crude oil prices and increased demand for ethylene and propylene, Methanol-to-Olefins (MTO), a non-petroleum method, is used to produce light olefins.

The SAPO-34 framework is a suitable shape-selective catalyst due to its moderate acid strength to control selectivity. Despite the high methanol conversion and the selection of suitable light olefins compared to SAPO-34, rapid deactivation of this catalyst through coke precipitation is an unavoidable drawback in this reaction [1,2]. By using spray drying, controlling the particle size and morphology enhances the selectivity and lifetime. The slurry used to form the catalyst includes filler or matrix, zeolite, and binder[3]. Kaolin is a clay type with a content of Si-Al, which has various industrial applications. It is used as a raw material for synthesizing zeolites and for catalysis purposes. As a filler, it provides silica and alumina, which enhance the physical properties and dilute the catalyst body. To use industrial kaolin as a filler, it is crucial to have high reactivity and enhance the surface. Mixing kaolin with chemical raw materials for use as a filler can be difficult due to its low dispersion. However, by heating kaolin to a temperature above 400 degrees, it transforms into metakaolinite, creating a chemically stable and active environment. As a result, active kaolin is treated in a way that enhances various coordination structures and enriches Si-Al.Kaolin as a matrix has good thermodynamic stability and has a significant beneficial effect on the stability of SAPO-34 catalysts but it has undeseraible effect on selectivity of catalyst.[4,5,6]

Previous studies have focused on only calcined kaolin and it was used to investigate the impact of temperature variations on the performance of the SAPO-34 catalyst in the MTO process. However, this study focuses on preparing the SAPO-34 catalyst slurry for the MTO process by using spraydrying method and innovative techniques to increase its selectivity and longevity.In this project , The influence of treated kaolin and metakaolin on performance of final shaping SAPO-34 catalyst for MTO reaction investigated.

Experimental Section

30 grams of kaolin or metakaolin was mixed with 8.5 moles of water, 0.28 moles of morphine, 0.23 moles of phosphoric acid, and 3Wt% of SAPO-34 seeds. The mixture placed in a hydrothermal reactor at a temperature of 190 degrees for 36 hours. Each was mixed separately with Boehmite Sol and SAPO-34 in a ratio of 40:20:40, and the slurry containing 30% of solids in water was synthesized. The pH of this slurry reached to 3 by adding HCl. the slurry was sprayed and calcined by spray dryer (Catalyst FK1 and FMK2). FTIR XRD, BET, FESEM, NH3-TPD determined the properties of the compounds, and the amount of catalysts efficiency in the reaction was determined in fixed bed reactor.

Results and Discussion

For aluminosilicates, functional groups Al-OH and Si-OH are responsible for NH3 adsorption . TPD-NH3 profiles of ammonia desorption for kaolin treated at 662 and metakaolin at 655 are visible due to the presence of Brønsted sites. In metakaolin, the lower temperature peaks at 246 and 436 are also observed corresponding to Lewis and Bronsted acid sites. In the case of metakaolin, the thermal process in the preparation can prevent the collapse of the layers of its structure, and the total acidity of metakaolin and kaolin is 593 and 108 µmol/g, respectively. Both of these aluminosilicates produce dimethyl ether under the reaction conditions of methanol to light olefin with a high selectivity of 90%. The results of the catalytic reaction of samples FK1 and FMK2 in fig 1. show that the synthetic catalyst with kaolin and metakaolin shows the maximum selectivity to light olefins

---

[1] MTO

22nd Iranian Chemistry Congress (ICC22)
Iranian Research Organization for Science and Technology (IROST)
13-15 May 2024

03231-97589

IROST

equal to 75 and 82%, respectively, but the lifetime of catalyst FK1 is longer.
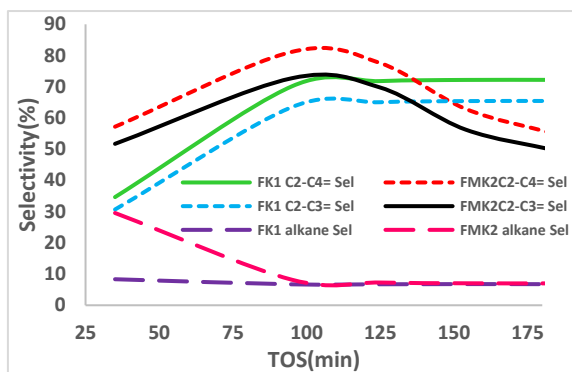

Fig.1: Catalytic selectivity to alkanes, light olefins and $C_2=+C_3=$

Table 1 shows the BET surface area and average pore diameter of these catalysts. As expected, the total pore volume and the average pore diameter value of the final catalyst become smaller as a result of adding kaolin compound instead of metakaolin to the composition of the shaping slurry. A higher external surface area to total surface area ratio indicates greater stability of the FMK2 catalyst. A larger pore diameter makes it easier to remove the product from the catalyst surface and delays coking. The presence of only one strong acid peak at around 439°C in FK1 catalyst and the presence of two strong and very strong acid peaks in FMK2 catalyst at 429°C and 631°C, respectively, also confirms the formation of less coke in catalyst FK1.Therefore, we expected to this catalyst illustrated lower selectivity and higher stability. These results are consistent with the reactor test results.

Table 1: BET specific surface area and average pore size of samples

		MF11	FMK2
Total Pore Volume	cc/g	0.16	0.21
Multipoint BET	m²/g	90.46	98.25
External Surface Area	m²/g	63.78	67.35
Average Pore Diameter	Å	64.46	73.59

Conclusions
The results showed that metakaolin increases the selectivity towards light olefins in the reaction product and increases the surface area and average size of the pores, so the coke on the catalyst surface was easily removed. According to TPD-NH3, in the presence of metakaolin, new Bronsted acidic sites are created on the catalyst surface, which are prone to coke formation and cause catalyst instability. These very strong acid sites do not exist in the presence of kaolin. They accelerate the formation of coke in the FMK2 catalyst and reduce the stability of the catalyst.

References

[1] Jiang, T., Bai, Y., Li, L., Tai, W., Wang, Y., Wang, H., & Sun, N. (2023). The effects of templates and seeds on the properties of nanosheet SAPO-34 molecular sieves and their catalytic performance in the MTO reaction. *Australian Journal of Chemistry*, *76*(2), 81-87. https://doi.org/10.1071/CH22238

[2] Mousavi, Y. S., Akbari, A., Omidkhah, M., & Safari, P. (2024). Formulated Mn-promoted SAPO-34/kaolin/alumina sol micro-size catalyst with a superior performance for methanol to light olefins conversion in a fluidized bed reactor. *Journal of Industrial and Engineering Chemistry*, *129*, 403-412. https://doi.org/10.1016/j.jiec.2023.08.053

[3] Lee, U. H., Valekar, A. H., Hwang, Y. K., & Chang, J. S. (2016). Granulation and shaping of metal–organic frameworks. *The Chemistry of Metal–Organic Frameworks: Synthesis, Characterization, and Applications*, *2*, 551-572. https://doi.org/10.1002/9783527693078.ch18

[4] Wang, Q., Gao, Z., Ding, Z., Zhang, J., Liu, W., He, Q., ... & Liu, C. (2024). Effect of kaolin calcined temperature on the preparation and crystallization mechanism of SAPO-34 molecular sieve for methanol-to-olefins performance. *Microporous and Mesoporous Materials*, 113037. https://doi.org/10.1016/j.micromeso.2024.113037

[5] Xu, S., Zhang, Q., Feng, Z., Meng, X., Zhao, T., Li, C., ... & Shan, H. (2012). A high-surface-area silicoaluminophosphate material rich in Brönsted acid sites as a matrix in catalytic cracking. *Journal of natural gas chemistry*, *21*(6), 685-693. https://doi.org/10.1016/S1003-9953(11)60420-9

[6] El-Aal, M. A., Said, A. E. A. A., Abdallah, M. H., & Goda, M. N. (2022). Modified natural kaolin clay as an active, selective, and stable catalyst for methanol dehydration to dimethyl ether. *Scientific Reports*, *12*(1), 9407. https://doi.org/10.1038/s41598-022-13349-0

Thin-Film Composite Membrane Containing Nanoparticles and Covalent-Organic Framework for Diminishing Dye

Samaneh Bagheri, Simin Asadabadi*

Corresponding Author E-mail: s.asadabadi@basu.ac.ir

Department of Applied Chemistry, Faculty of Chemistry and Petroleum Sciences, Bu-Ali Sina University, Hamedan, Iran.

Abstract: In this study, a thin-film composite membrane was fabricated with polyethersulfone/chitosan-EDTA/covalent-organic framework in order to diminishing dye from aqueous solution. Polyethersulfone-based mixed matrix membrane containing hydrogel of chitosan and EDTA was modified by covalent-organic framework. In this condition, dye removal reached 86.88%.

Keywords: Water treatment; Polyethersulfone; Mixed matrix membrane; Thin-film composite; Covalent-organic framework; Chitosan; EDTA; Dye Removal

Introduction

The acceleration of population growth and industrialization has intensified the consumption of freshwater and the release of significant volumes of wastewate. Membrane technology, renowned for its superior separation capabilities and comparatively affordable expenses, emerges as a pivotal method for the effective reclamation of freshwater amidst various technological options [1].

Selection of membrane matrial is the first issue in the design of any membrane process. Among different membranes, the polyethersulfone (PES) membrane holds particular significance due to its distinctive properties, including mechanical, thermal, and chemical stability. However, its separation efficiency is inherently limited by the absence of effective adsorptive functional groups in its structure. Additionally, rapid fouling caused by removed pollutants significantly diminishes its separation performance, resulting in a substantial increase in energy consumption and maintenance costs. Thus, to improve its separation efficiency, enhance pure water flux, and reduce fouling tendencies, the PES matrix must undergo modification through the incorporation of effective nanocomposites into its structure. Chitosan (CH) and ethylenediaminetetraacetic acid (EDTA) can increase the efficiency of the membrane [2].

Covalent-organic frameworks (COFs) are a class of polymeric organic materials characterized by covalent bonds linking their molecular components, which primarily include hydrogen, boron, carbon, nitrogen, and oxygen. Often referred to as organic zeolites, COFs represent a novel group of crystalline substances utilized for pollutant separation. Their utility stems from attributes such as lower density compared to conventional polymers, extensive surface area,

exceptional chemical and thermal stability, and modifiable pore structures, enabling precise control over separation processes [3]. Thin-film composite membranes comprised of an ultrathin active layer and a porous substrate have been dominating the membrane market, due to their merits of relatively high water permeability. The aim of this study was to study the effect of thin layer of COF prepared on the polyethersulfone substrate containing CH-EDTA on the flux and dye removal.

Experimental Section

Polyethersulfone membrane (PES-) and PES containing pore-forming (PES-PVP) were fabricated using phase inversion method. The third membrane was fabricated with PES, pore forming and CH-EDTA (CH-EDTA). Then, COF layer was formed on the surface of CH-EDTA and the membrane was demonstrated by CH-EDTA/COF. The cross-flow setup was used for examining the performance of the membranes. Relevantly, pure water flux was calculated by the following equation:

$$Flux = \frac{m}{A\Delta t} \qquad (1)$$

where, m, A and Δt were the mass of permeate, the effective surface area and time for collecting permeate, respectively.

Also, methyl violet 2B (MV 2B) rejection was calculated according the following equation [4]:

$$Re\% = \frac{C_0 - C_{res}}{C_0} \times 100\% \qquad (2)$$

in which, C_0 and C_{res} were initial and residual concentration of MV 2B, respectively.

22nd Iranian Chemistry Congress (ICC22)
Iranian Research Organization for Science and Technology (IROST)
13-15 May 2024

03231-97589

ISC

IROST

Results and Discussion

The morphology of the synthesized membrane was evaluated with FE-SEM images taken from the surface of membranes and the results are shown in Fig. 1.
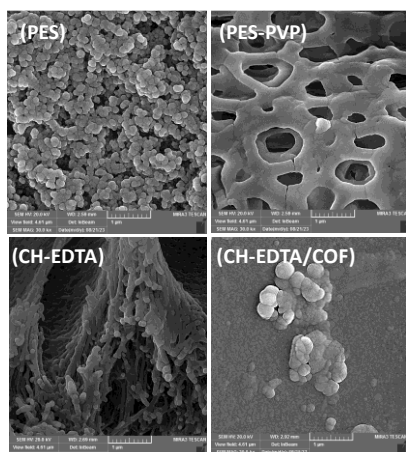

Fig.1: FE-SEM images for PES, PES-PVP, CH-EDTA and CH-EDTA/COF membranes

It can be seen in Fig. 1 that the morphology was changed from PES to CH-EDTA/COF. The last one has a smoother surface with small pores.

As can be seen in Fig. 2, the PES had a little pure water flux, and its value increased when PVP was added to the polymer solution. It was due to the pore formation. By adding CH-EDTA, the flux suprisingly inclined because of hydrophilic nature of nanoparticles [2]. However, the presence of COF (CH-EDTA/COF) caused a slight decrease in the flux since an uniform layer was created on the top layer of membrane.
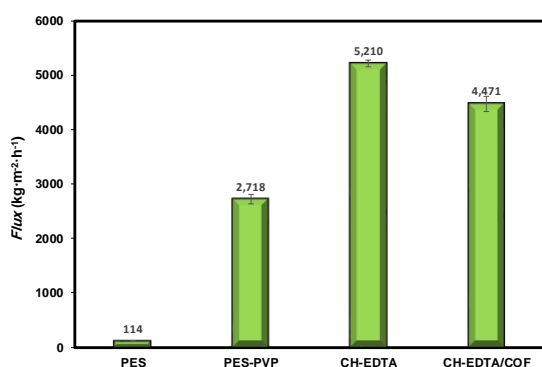

Fig.2: Pure water flux obtained for PES, PES-PVP, CH-EDTA and CH-EDTA/COF membranes

Fig. 3 presents MV 2B rejection by PES, PES-PVP, CH-EDTA and CH-EDTA/COF membranes. The two first ones were not able to romve dye molecules from aqueous solution effectively. However, dye was rejected by CH-EDTA about 567.47% due to intercations between molecules of MV 2B and CH-EDTA functional groups. The presence of COF layer caused to rejection of 86.88%.
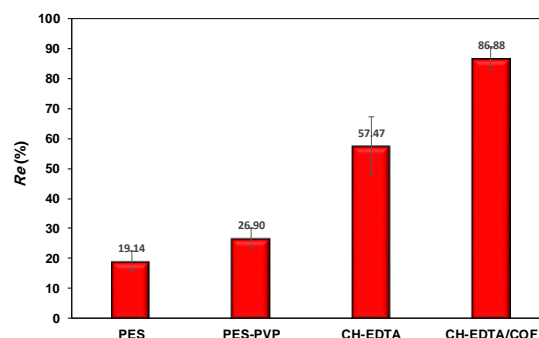

Fig.3: Dye rejection obtained for PES, PES-PVP, CH-EDTA and CH-EDTA/COF membranes

Conclusions

This study involved the fabrication of a thin-film composite membrane for the removal of dye from aqueous solutions. The membrane was composed of a polyethersulfone/chitosan-EDTA/covalent-organic framework blend. Initially, a polyethersulfone-based mixed matrix membrane incorporating a hydrogel composed of chitosan and EDTA was prepared. Subsequently, this membrane was further modified by incorporating a covalent-organic framework. Under these conditions, the membrane demonstrated a dye removal efficiency of 86.88%.

References

[1] Peydayesh, M., Bagheri, M., Mohammadi, T., Bakhtiari, O., (2017). Fabrication optimization of polyethersulfone (PES)/polyvinylpyrrolidone (PVP) nanofiltration membranes using Box-Behnken response surface method, RSC Adv. 7, 24995. https://doi.org/10.1039/c7ra03566g.

[2] Saheed, I. O., Oh, W. Da, Suah, F. B. M. (2021). Chitosan modifications for adsorption of pollutants – A review. J. Hazard. Mater. 408, 124889. https://doi.org/10.1016/j.jhazmat.2020.124889.

[3] Jiang, Y., Li, S., Su, J., Lv, X., Liu, S., Su, B. (2021). Two dimensional COFs as ultra-thin interlayer to build TFN hollow fiber nanofiltration membrane for desalination and heavy metal wastewater treatment. J. Memb. Sci. 635, 119523. https://doi.org/10.1016/j.memsci.2021.119523.

[4] Liu, Q., Basel, N., Li, L., Xu, N., Dong, Q., Fan, L., Wang, Q., Ding, A., Wang, T. (2022). Interfacial polymerization of a covalent organic framework layer on titanium dioxide@ graphene oxide/polyacrylonitrile mixed-matrix membranes for high-performance dye separation. J. Memb. Sci. 647, 120296. https://doi.org/10.1016/j.memsci.2022.120296.

Design and synthesis of a quinoline-4-carboxilic acid-linked covalent organic framework as a catalyst in the synthesis of new pyridine-sulfonamide hybrids

Narges Zarei, Zahra Alishahi, Morteza Torabi, Meysam Yarie, Mohammad Ali Zolfigol[*]

Corresponding Author E-mail: mzolfigol@yahoo.com

Department of Organic Chemistry, Faculty of Chemistry and Petroleum Sciences, Bu-Ali Sina University, Hamedan, Iran.

Abstract: In this study, a quinoline-4-carboxilic acid-linked covalent organic framework was designed and synthesized as a heterogeneous and active catalyst. Then, this catalyst was used for the synthesis of new pyridine-sulfonamide hybrids. High yield of products and short reaction times are some advantages of this protocol.

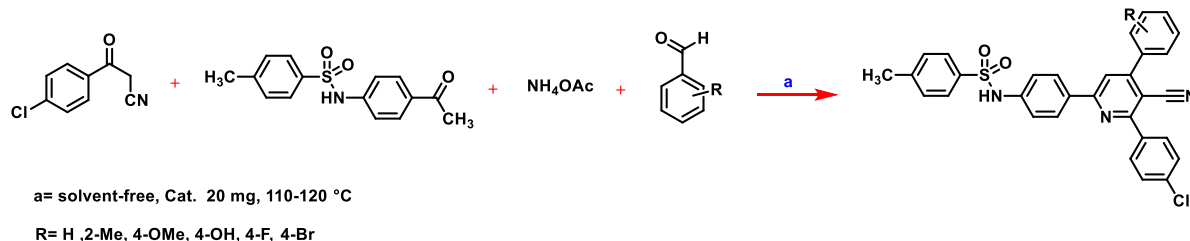**Keywords:** Covalent Organic Framework; Pyridine; Sulfonamide

Introduction

Covalent organic frameworks (COFs) are considered as a class of crystalline porous polymers. High surface area, chemical and thermal stability, and adjustabe pore size are among the characteristic propertes of COFs that facilitate their application as catalysts [1-2]. Pyridine-bearing heterocycles show several biological activities and are used as antitumor, antioxidant, and antibacterial drugs [3-4]. In addition, sulfonamide families have a lot of medicinal and biological applications and their extraordinary applications in antibiotic drugs is undeniable.

Experimental Section

Herein, we report the synthesis and catalytic application of a quinoline-4-carboxilic acid-linked COF in the synthesis of new pyridine-sulfonamide hybrids via multicomponent strategy (Scheme 1).

a= solvent-free, Cat. 20 mg, 110-120 °C

R= H ,2-Me, 4-OMe, 4-OH, 4-F, 4-Br

Scheme 1: Synthesis of new pyridines using a covalent organic framework as a catalyst

Results and Discussion

Then, For characterization of catalyst, varied techniques including Fourier transform infrared (FT-IR) spectroscopy, energy dispersive X-ray (EDX) analysis, thermo gravimetric analysis/differential thermal analysis (TGA/DTA), scanning electron microscopy (SEM) and transmission electron microscopy (TEM) have been applied. SEM and TEM analysis are shown in the figures below.
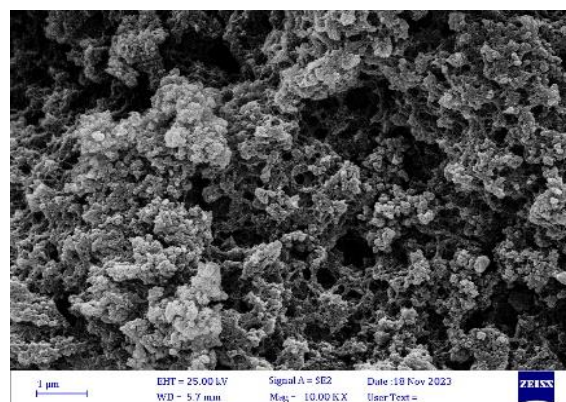

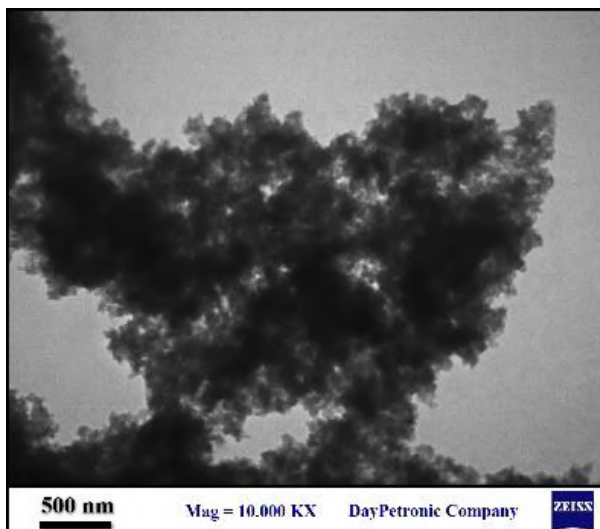**Fig.1:** SEM images of quinoline-4-carboxilic acid-linked COF

22nd Iranian Chemistry Congress (ICC22)
Iranian Research Organization for Science and Technology (IROST)
13-15 May 2024

03231-97589

Fig.2: TEM images of quinoline-4-carboxilic acid-linked COF

Conclusions

As a result, we designed and synthesized quinoline-4-carboxilic acid-linked COF as a catalyst. This catalyst was successfully used in the synthesis of new sulfonamide-containing pyridine derivatives. All derivatives have short reaction times and were prepared in mild and solvent-free conditions.

References

[1] Yusran, Y., Li, H., Guan, X., Fang, Q., & Qiu, S. (2020). Covalent organic frameworks for catalysis. *EnergyChem*, 2(3), 100035.

[2] Ma, D., Wang, Y., Liu, A., Li, S., Lu, C., & Chen, C. (2018). Covalent organic frameworks: Promising materials as heterogeneous catalysts for CC bond formations. *Catalysts*, 8(9), 404.

[3] Raja, R., Sivasubramaniyan, A., Murugan, D., Subbaiah, N., George, J., Poovan, S., ... & Manivachagam, C. (2016). A green synthesis of 1, 2, 3-triazolyl-pyridine hybrids and evaluation of their antibacterial activity. *Research on Chemical Intermediates*, 42, 8005-8021.

[4] Mrozek-Wilczkiewicz, A., Malarz, K., Rejmund, M., Polanski, J., & Musiol, R. (2019). Anticancer activity of the thiosemicarbazones that are based on di-2-pyridine ketone and quinoline moiety. *European Journal of Medicinal Chemistry*, 171, 180-194.

22nd Iranian Chemistry Congress (ICC22)
Iranian Research Organization for Science and Technology (IROST)
13-15 May 2024

03231-97589

IROST

NLO properties of newly designed molecular switches using C20&C40 nanowires

Elham Gravand Tabar,* Hamid Reza Shamlouei, Zeinab Biglari

Corresponding Author E-mail: elhamtabar540@yahoo.com

Department of Chemistry, Faculty of of Chemistry, Lorestan University, Khorramabad, Iran.

Abstract: In this research, the non-linear electrical and optical properties of the molecular switches formed by the nano bud obtained from the hybridization of C20 and C40 fullerenes have been investigated using DFT calculation methods. Also, the effect of different electric fields on the nonlinear structural, electrical and optical properties was investigated. It was observed that due to the increase of the applied electric field, the distance between HOMO and LUMO has decreased drastically and therefore its electrical conductivity has increased well, which exactly corresponds to the molecular switch being turned on.

It was also observed that due to the increase of the field intensity, the nonlinear optical properties of the molecular switch have also been improved. Thus, with the increase in the intensity of the electric field, the amount of polarizability and the first hyperpolarizability obtained in different fields increased greatly.

Keywords: Nanobud, NLO, Molecular Switches, NBO

Introduction

Materials that produce a nonlinear response due to interaction with light can be classified as nonlinear optical (NLO) materials, which is related to another branch of optics called second-order nonlinear optics (NLO) and when trying to explain the first practical laser invented by Meimann in 1960 with linear optics [1]. Wide applications of these high NLO materials include use in photonic systems including high-speed optical modulators, ultrafast optical switches, and high-density optical storage media [2]. Many factors such as the use of electron donor and acceptor groups and doping atoms in pristine nanoclusters, Decoration of nanocluste r with alkali metal atoms and etc.have been used to improve the NLO response of materials for use as high NLO materials. In the current research, the possibility of using C20&C40 nanobuds as a π electron source in molecular switch will be investigated. Also, the effect of the electric field on the structural and electrical properties of the designed molecular switch will be investigated. Molecular switches are one of the most important components in nanoelectronic systems which convert into two reversible stable, on and off states. these two on and off states have different optical, electrochemical or magnetic properties, which a switch under the influence of environmental factors such as light, pH, solvent type and presence of an ion and electric field may be on or off [3-4].

COMPUTATIONAL DETAILS

electric fields of (0, 0.002, 0.0025, 0.003, 0.004 and 0.006a.u.), Gaussian09 package using the B3LYP and GaussSum03 program. 6-31G (d) basis set for Au, S and C atoms and others atoms .

E_{HOMO}, E_{LUMO} and E_g was calculated.

The polarizability (α_o) and first hyperpolarizability (β_o) was calculated with Multiwfn programs.

NBO charge of left and right Au, S and catoms was calculated. the electronic densities of states (DOS and TDOS) and MEP Structures was draw.

Results and Discussion

First, the effect of the electric field on the structural, electrical and optical properties of the designed switch was investigated in different electric fields (0, 0.002, 0.0025, 0.003, 0.004, and 0.006 a.u.) and the possibility of using fullerene nanobuds as a molecular switch was investigated by B3LYP method.
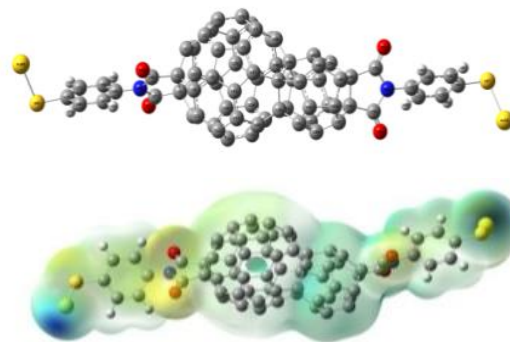

Fig.1 the structures of molecules in Electric Fiels= 0

22nd Iranian Chemistry Congress (ICC22)
Iranian Research Organization for Science and Technology (IROST)
13-15 May 2024

03231-97589

IROST

Table1: The UV and visible absorption data in electrical fields

|	00a.u		0.002a.u		0.004a.u		0.006 a.u	
	λ	f	λ	f	λ	f	λ	f
1	3159.68	0.0160	6247.93	0.0024	7700.30	0.0132	5069.99	0.0367
2	2085.31	0.0116	3114.65	0.0144	3616.29	0.0086	4597.19	0.0367
3	1764.33	0.0190	2092.38	0.0168	2086.02	0.0359	2234.64	0.0006
4	1633.69	0.0068	1814.42	0.0137	1755.20	0.0066	1946.09	0.0445
5	1544.67	0.0062	1688.74	0.0140	1641.99	0.0035	1691.55	0.0091
6	1521.52	0.0223	1523.94	0.0179	1551.95	0.0188	1651.39	0.0002
7	1340.65	0.0067	1432.69	0.0009	1464.67	0.0109	1584.29	0.0011
8	1264.03	0.0109	1368.67	0.0065	1419.37	0.0014	1505.77	0.0158
9	1155.89	0.0033	1286.44	0.0002	1304.18	0.0003	1336.72	0.0037
10	1044.67	0.0024	1196.87	0.0019	1266.60	0.0070	1312.93	0.0092
11	955.52	0.0025	1132.72	0.0028	1199.26	0.0021	1292.86	0.0003
12	926.82	0.0008	1092.54	0.0017	1163.27	0.0014	1210.22	0.0068
13	859.52	0.0003	974.79	0.0027	1087.51	0.0017	1194.62	0.0052
14	813.23	0.0011	934.70	0.0002	1057.85	0.0013	1138.83	0.0002
15	783.84	0.0004	918.73	0.0020	1015.54	0.0087	1082.29	0.0015
16	782.50	0.0169	801.89	0.0012	918.50	0.0003	1053.15	0.0048
17	779.27	0.0119	792.48	0.0303	904.48	0.0008	1022.66	0.0051
18	775.01	0.0004	771.98	0.0012	852.43	0.0013	996.14	0.0025
19	770.11	0.0333	768.54	0.0288	848.46	0.0064	986.87	0.0093
20	728.69	0.0018	752.13	0.0001	810.36	0.0425	908.13	0.0417
21	725.41	0.0030	736.21	0.0057	794.19	0.0005	892.03	0.0007
22	687.69	0.0032	670.03	0.0050	744.88	0.0034	888.43	0.0005
23	653.94	0.0010	646.78	0.0018	724.15	0.0122	780.17	0.0006
24	623.39	0.0123	632.87	0.0119	713.08	0.0011	746.59	0.0104
25	610.59	0.0027	627.34	0.0007	712.29	0.0024	737.89	0.0012
26	606.57	0.0019	626.68	0.0003	701.28	0.0055	727.37	0.0004
27	588.33	0.0040	623.93	0.0072	682.20	0.0010	713.25	0.0036
28	566.26	0.0149	598.89	0.0011	674.85	0.0063	699.83	0.0008
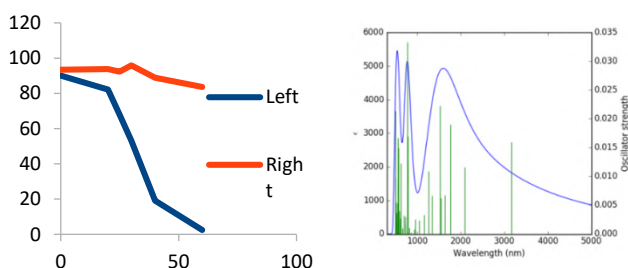
Fig.2 Designed structures for moleculares

Coclusions:

In this research, the feasibility of using C20@C60 nanobud as a molecular switch was investigated and and the structural, electrical, and optical properties were calculated DFT using. it was shown that with increasing electric field strength, the distance between HOMO and LUMO orbitals decreases. In the same electric field as the HLG approaches zero, the dihedral angle changes are also intense, which can be the reason for the molecular switch to turn on. In addition, it was shown that with increasing electric field strength, increases the optical properties of the molecular switch this increase increase is more severe in the range of the electric field that turns on the molecular switch.

References:

[1] T.H. Maiman, Stimulated optical radiation in ruby, Nature 187 (1960) 493–494.

[2] D. Arivuoli, Fundamentals of nonlinear optical materials, Pramana- Journal of Physics, 57 (5) (2001) 871–883

[3] Harismah K, Dhumad A.M, Ibraheem H.S, Zandi H, Majeed H.J, 2021, Jour. of Molec. Liqu., 334 : 116018.

[4] Zahedi E, Mozaffari M, Karimi F.S, Nouri A, 2014, Can. J. Chem., 92: 317–323.

Photoelectrochemical investigation of synthesized Echinops shape nanocomposite of cupreous oxide/carbon nitride/ZnO towards water splitting

Seyedeh Fatemeh [a], Javad Tashkhourian [*,a], Mojtaba Shamsipur[b]

Corresponding Author E-mail: Tashkhourian@shirazu.ac.ir

[a] Shiraz University.

[b] Razi University.

Abstract: A new composite with special morphology of copper (I) and zinc oxide was synthesized electrochemically on fluoride-doped tin oxide electrodes (FTO). Then, its photoelectrochemical behavior at negative and positive bias potentials was investigated. The composite showed good photoelectrochemical behaviour at both positive and negative potentials and also for water oxidation.
Keywords: Photoanode; Photoelectrochemistry; Water Oxidation.

Introduction

The cost-effective, robust, and efficient electrocatalysts for photoelectrochemical (PEC) water-splitting has been extensively studied over the past decade to address a solution for the energy crisis [1]. For photoelectrochemical (PEC) water splitting, the utilization of semiconductor heterojunctions as building blocks for photoanodes allows for high light absorption, effective charge separation, and superior redox capability, greatly boosting the solar energy conversion efficiency [2]. In addition to nanostructure engineering, the surface modification of photoelectrodes is also important for achieving high PEC performance. As the surfaces of the photoelectrode materials are active sites for redox reaction, the surface states are closely related to photon energy absorption properties and surface charge transfer ability of the semiconductors. Doping is one common strategy to improve the conductivity of semiconductors and extend the lifetime of charge carriers by reducing recombination of the photogenerated electron–hole pairs [2]. In the last 20 years, solar cells based on inorganic materials have been extensively investigated due to their excellent photovoltaic properties. Cuprous oxide (Cu_2O) is a promising candidate material for low-cost solar cell production owing to its good photocatalytic behavior, low cost, non-toxicity and long-term stability. Here ZnO and Cu_2O was synthesized by electrodeposition and also investigation of photoelectrochemical behavior at negative and positive bias potential was done. It was tried to synthesize nanocomposite that have good photocurrent stability and also have photocurrent behavior at negative and positive potential so that can be applicable to use in photoelectrochemical water splitting. At first ZnO and Cu_2O was individually investigated. After that, the surface of ZnO nanorod was covered by casting carbon nitride and then electrodeposition Cu_2O was done on that surface composed of ZnO and carbon nitride. After characterization the photo electrochemical behavior and stability towards photobleaching was studied.

Experimental Section

The electrochemical deposition experiments were carried out in a three-electrode glass cell immersed in a paraffin oil bath held at 70 °C. The working electrode was single-sided polished fluorine-doped tin oxide, SnO_2:F (FTO). The FTO coated glass substrates were ultrasonically cleaned. The aqueous deposition bath solution included 5 and 10 mM ($Zn(NO_3)_2 \cdot 4H_2O$). A potentio/galvanostat electrochemical workstation was used to deposit the nanostructures by amperometry at -0.8 V (relative to the Ag/AgCl reference electrode). Cu_2O nanostructure were electrodeposited from the electrolytic bath containing 1 M $CuSO_4$ and 6.0 M lactic acid by reduction of alkaline aqueous solution of cupric lactate. After growing of ZnO nanorode graphitic carbon nitride casted and then cuprous oxide was deposited.

Results and Discussion

The photograph of Synthesized Cu_2O was shown in Figure 1. A specific preferred orientation developed to present a texture with large grains and morphology of the stable phase, pyramids was formed which is the specific preferred orientation was confirmed that the importance of crystallographic orientation in getting high performance in electrical rectification and photosensitivity. Effect of Time and potential and temperature was optimized.
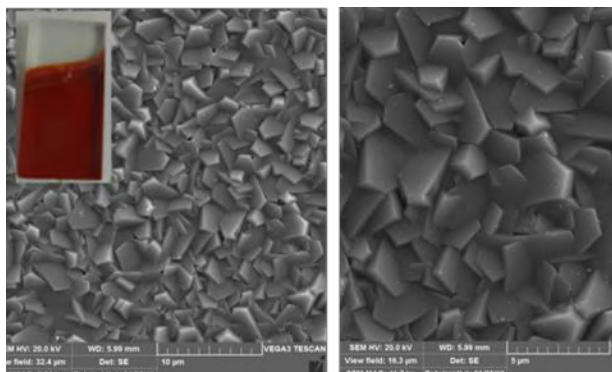
22nd Iranian Chemistry Congress (ICC22)
Iranian Research Organization for Science and Technology (IROST)
13-15 May 2024

03231-97589

IROST

Fig.1: The SEM image of Cu₂O at -0.9 V vs. Ag/AgCl, 1800s, 65°C.

The photoelectrochemical of the synthesized electrodeposited Cu_2O, ZnO, $g-C_3N_4$ and their composites were investigated. The transient photocurrent responses performed in 0.5 M Na_2SO_3 solution and photocurrent variations was recorded under different applied potential of 0, 0.2, 0.4 and 0.6 v vs.ag/AgCl. Figure 2 showing the photo current behavior by switching on/off of light. It shows the photocurrent enhances by increasing the potential showing the good response of synthesized composite.
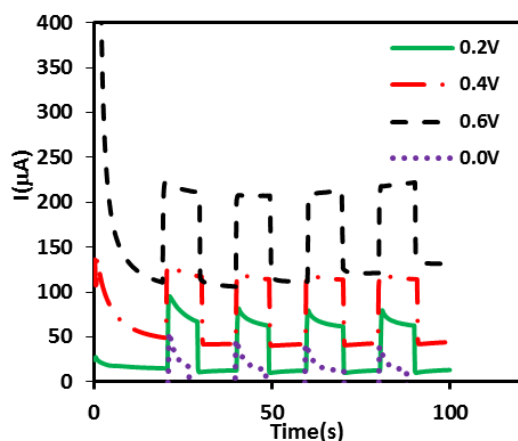
Fig.2: Photoelctrochemical behavior for Cu_2O electrodeposited at 1000s and 1200s at applied potential of 0.0, 0.2, 0.4 and 0.6 V vs. Ag/AgCl. Wight LED light, 1.2W/cm2. 0.5M Na_2SO_3.

Figure 3 compare the behavior of individual constituent of the synthesized composits, as it is obvious, the lowest photoelectrooxidation current was obtained for $g-C_3N_4$ and slightly increased at ZnO. For Cu_2O it shows a good enhancement than that individual ZnO or $g-C_3N_4$, however for Cu_2O that electrodeposited on the surface of ZnO covered by $g-C_3N_4$ the photooxidation current improved significantly that all those three components and also show good stability even for each cycle on- off light.
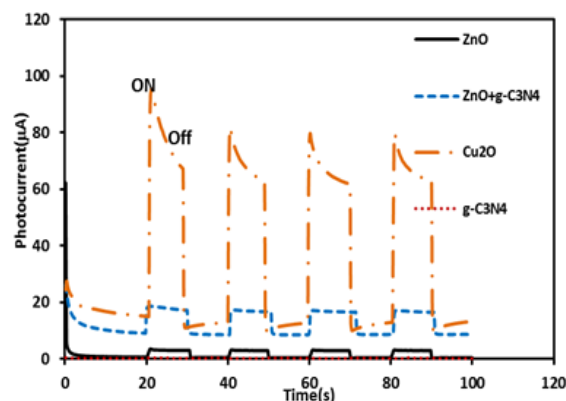

Fig.3: Comparison of photoelctrochemical behavior for Cu_2O, ZnO, $g-C_3N_4$ and $Cu_2O-ZnO-g-C_3N_4$, +0.6Vapplied potential vs. Ag/AgCl; Wight LED light, 1.2W/cm². 0.5M Na_2SO_3.

Conclusions

A nanocomposite of Cu_2O with new morphology of Echinops like are successfully fabricated by electrochemical depositing of Cu_2O on the surface of ZnO nanorods, which was covered by $g-C_3N_4$. The photoelectrochemical behavior at different applied potentials was investigated and showed a good photocurrent production in reductive and the oxidative poetical scans. photoelectrochemical behavior of Cu_2O nanocomposite for photoelectrochemical water splitting.

References

[1] Roozbeh, S. M., Hosseini-Hosseinabad ,S. M., Masudy-Panah, S, A., Seza, S., Jalali, M., Hesam Fallah-Arani, Dabir, F., & so on. (2021) Photoelectrochemical Water-Splitting Using CuO-Based Electrodes for Hydrogen Production: A Review, 33(33), 2007285. https://doi.org/10.1002/adma.202007285.

[2] Li, Sh., Xu, W., Meng, L., Tian, W., Li, L., (2022), Recent Progress on Semiconductor Heterojunction-Based Photoanodes for Photoelectrochemical Water Splitting, 2(5), 2100112. https://doi.org/10.1002/smsc.202100112 .

Investigation of the effects of the cobalt-doped tin diselenide nanostructures for high-performance electrochemical supercapacitors

Homa madadi Gholipour*, Mohammad Barazandeh, Sayed Habib Kazemi*

Corresponding Author E-mail : habibkazemi@iasbs.ac.ir, homamadadi@iasbs.ac.ir

Abstract: Supercapacitors and batteries face technical challenges that need to be addressed to meet the growing demand for clean energy technologies. Also, two-dimensional nanolayered transition metal dichalcogenides (2D TMDs) have attracted great attention to enhancing capacitive behaviors due to their ultrathin structure, large surface area, and concurrently "Faradaic" and "double layer" energy storage mechanisms. The maximum capacity of 316.4 Fg^{-1} was obtained at the current density of 4.5 A g^{-1} for the prepared Co-$SnSe_2$@NF electrode. Also, this electrode showed very good cyclic stability, so after 13000 cycles, it exhibited about 124% of its initial capacitance, which indicates the effect of the cobalt doping to increase the mechanical strength of the tin diselenide nanostructure.

Keywords: Supercapacitor; doping; dichalcogenides; tin diselenide

Introduction

In recent years, the adoption of renewable energy sources such as solar or wind power has accelerated, necessitating intelligent and dependable energy storage solutions.[1] As a result, energy storage has become a hot topic in energy production. Today's alternative energy storage systems have been developed and exhibited distinct qualities.[2]Supercapacitors (SCs) have become a topic of interest for future self-powered devices due to their high energy and power density.[3] Transition metal dichalcogenides (TMDCs) are important electrode materials for energy storage. They can be transformed into 2D layered nanomaterials, which are useful in scientific and industrial applications.[4] These materials have been employed in various fields including optoelectronics, electronics, mechanical, optical, catalytical, and energy storage devices.[5]

Experimental Section

The Co-$SnSe_2$ was synthesized with the Sol-Gel method and its electrochemical behaviors were studied as novel electrode materials for supercapacitors. The electrochemical performance of the Co-$SnSe_2$ electrode on nickel foam substrate was investigated with galvanostatic charge-discharge (GCD), cyclic voltammetry, and electrochemical impedance spectroscopy methods. Also, the morphology and crystal structure of the desired material were examined with SEM, FTIR, TGA, XRD, BET, and EDX methods.
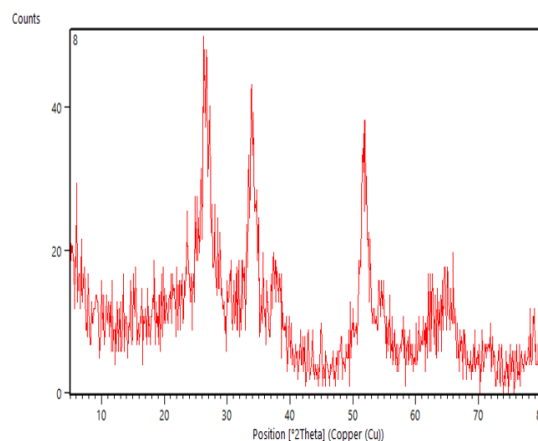
Results and Discussion

Fig.1: A) X-ray diffraction pattern related to Co-$SnSe_2$ nanostructure. B) Co-$SnSe_2$@NF electrode, at a scanning speed of 100 mVs^{-1}

The structural properties of the Co-SnSe2 nanostructure were examined using X-ray diffraction (XRD) analysis. Fig.1) indicates all the peaks associated with the tin diselenide nanostructure. As seen, peaks at 2θ values 30 and 58, corresponding to (011) and (310) respectively, suggest that cobalt doping has effectively occurred in the tin diselenide nanostructure.
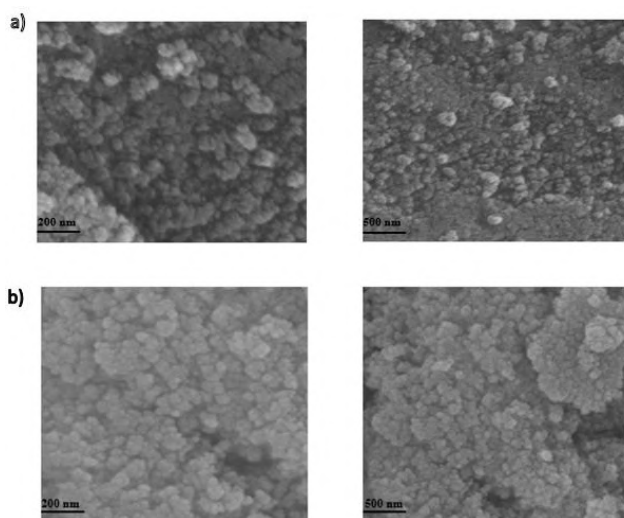
22nd Iranian Chemistry Congress (ICC22)
Iranian Research Organization for Science and Technology (IROST)
13-15 May 2024

03231-97589

Fig.2: Typical FESEM images of surface morphology of a) $SnSe_2$ nanostructure, b) Co-$SnSe_2$ nanostructure.

The SEM analysis was used to examine the synthesized SnSe2 and Co-SnSe2 nanostructures at magnifications of 500 nm and 200 nm. Fig.3 a) shows the spongy state of the tin diselenide nanostructure with an average particle size of approximately 20 nm. On the other hand, Fig.3 b) displays the cobalt-doped tin diselenide nanostructure, which has a similar spongy structure, with more uniform and reproducible synthesized nanoparticles placed on the nickel foam substrate. Additionally, the particle size is slightly reduced to increase the surface area, which is a valuable feature for providing high capacity in supercapacitors.
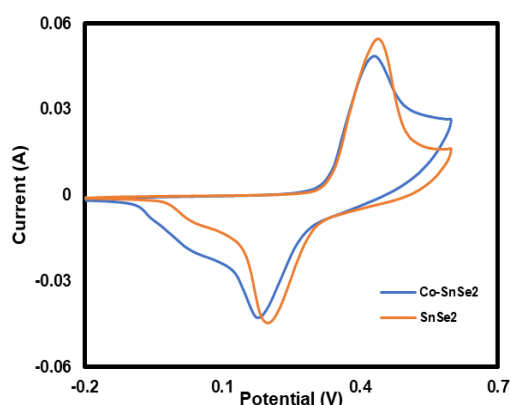

Fig.3: Co-$SnSe_2$@NF electrode, at a scan rate of 100 mVs^{-1}

To investigate the capacitive performance of tin diselenide nanostructure and cobalt doping in tin diselenide nanostructure, cyclic voltammetry measurements were performed in potassium hydroxide solution, in the potential range of -0.2 to 0.6 V. To investigate the supercapacitor effects of tin diselenide nanostructures and tin diselenide doped with cobalt, the comparative electrochemical behavior of these 2 electrodes is presented.

According to Fig.3, the electrode containing cobalt doping in the tin diselenide nanostructure has a higher surface area under the voltammetric peaks and produces more current compared to the tin diselenide electrode, thus, it provides better supercapacitor behavior and greater capacity.

Conclusions

In this research, The electrode achieved a maximum capacity of 316.4 Fg^{-1} at a current density of 4.5 A g^{-1}. Moreover, after 13000 cycles, the electrode demonstrated outstanding cycle stability and retained 124% of its initial capacitance.

References

[1] M. Sarno, "Nanotechnology in energy storage: The supercapacitors," in *Studies in surface science and catalysis*, vol. 179, Elsevier, 2020, pp. 431–458.

[2] L. Zhang, D. Shi, T. Liu, M. Jaroniec, and J. Yu, "Nickel-based materials for supercapacitors," *Mater. Today*, vol. 25, pp. 35–65, 2019.

[3] F. Yu, "Design and synthesis of materials for supercapacitors with enhanced energy storage performance." Queensland University of Technology, 2020.

[4] J. Theerthagiri *et al.*, "Recent advances in metal chalcogenides (MX; X= S, Se) nanostructures for electrochemical supercapacitor applications: a brief review," *Nanomaterials*, vol. 8, no. 4, p. 256, 2018.

[5] H. L. Zhao, D. D.; Bao, S. J.; Zhou, W. H.; Li, "Preparation of hexagonal nanoporous nickel hydroxide film and its application for electrochemical capacitor," *Electrochem. Commun*, vol. 9, no. 5, pp. 869–874, 2007.

Nanostructured Ni oxide electrocatalyst modified with Fe to enhance oxygen evolution reaction

Maryam Soltani, Omran Moradlou[*], Maryam Ostadebrahim

Corresponding Author E-mail:moradlou@alzahra.ac.ir

Department of Analytical Chemistry, Faculty of Chemistry, Alzahra University, Tehran 1993893973, Iran.

In this research, we synthesized an effective NiFeOxHy electrocatalyst by a two-step procedure of hydrothermal and calcination on the Ni foam (NF) substrate. The NiFeOxHy/NF electrode exhibited remarkable oxygen evolution reaction (OER) activity with a small value of the Tafel slope and a low overpotential in 1.0 M KOH.

Keywords: Electrocatalyst, Oxygen evolution reaction, Nickel Iron oxide, Water splitting, Electrochemical impedance spectroscopy.

Introduction

The increasing demand for low-cost, efficient, stable, eco-friendly, and earth-abundant electrocatalysts, which are compatible for producing renewable, clean energy, is a critical issue for modern society. Water splitting reaction is a promising and sustainable approach for storing energy. Water splitting reactions consist of two half reactions: the anodic oxygen evolution reaction (OER) and the cathodic hydrogen evolution reaction (HER). Kinetic of OER is more sluggish than HER, as it takes place in a multi-step reaction with single-electron transfer at each step. The role of electrocatalyst is increasing the kinetic of OER by decreasing overpotential. Most commercial catalysts for OER are RuO_2 and IrO_2. However, these catalysts are expensive and scarce so they are hindered to be used in industrial applications[1-6].

Ni oxide is a poor catalyst. Introducing Fe into this catalyst, significantly decreases the overpotential of OER of Ni oxide. Fe ions decrease the electrochemical capacity of Ni oxide. Najafpour et al. studied the effect of Fe impurity $[FeO4]^{2-}$ into Ni_2O_3. In the presence of K_2FeO_4 and Ni(II)hydroxide, significant OER is observed[1]. Chen J. et al. have used Fe/Ni dual dopants to promote OER reaction of MoO_2 catalyst. Fe doping can enhance the oxygen vacancies and Ni impurity improve the adsorption of OER intermediates and decrease the onset potential [7].

Herein, OER by hierarchical NiO microsphere electrocatalyst developed along with Fe^{3+} supported on Ni foam (NF) using two steps including hydrothermal and calcination steps is reported. In the next step, prepared electrodes developed by a simple immersing method to decorate with NiFeOxHy layer, which provides more active sites to electrochemical reactions [8].

Experimental Section

Preparation of the NiO/NF electrode. The hierarchical NiO microspheres are synthesized through two steps consisting of hydrothermal and calcination steps. $Ni(NO_3)_3.9H_2O$ and urea was selected as raw material. A piece of Ni foam (1×3 cm^2) used as substrate in a hydrothermal process. Calcination was performed in 400^0C.

Preparation of the $NiFeO_xH_x$/NiO/NF electrode. Fabricated NiO/NF electrodes were immersed in $Fe(NO_3)_3$ solution for 30 min. Final electrode rinsed with deionized (DI) water and dried in 60 ^0C for 2h. Then, the prepared electrode was used as an anodic OER electrode in water splitting.

Results and Discussion

Ni oxides have long been investigated as OER electrocatalysts in alkaline media. Fe dopants significantly boost Ni oxides OER activity. Resulting electrocatalyst ($NiFeO_xH_y$) is considered as a benchmark OER electrocatalyst [9, 10]. NiO was grown on Ni foam.

The morphology of the samples was studied by a field-emission scanning electron microscope (FE-SEM; MIRA3 TESCAN and Philips XL-30), as shown in Fig. 1 (a-c). According to the FE-SEM images, it is evident that the NF surface uniformly was covered by microsphere NiO based on nanorods with hierarchical urchin-like morphology.

The electrocatalytic OER performance of the prepared electrodes were measured using an Autolab PGSTAT 302 N electrochemical analyzer (Metrohm/Autolab) in a three-electrode cell which were immersed in 1.0 M KOH electrolyte. LSV curves in Fig. 1 (d) show final catalyst remarkably enhanced OER activity, and overpotential are 360 and 470 mV at current density of 10 and 100 mA cm^{-2}, respectively.

Also, Electrochemical impedance spectroscopy (EIS) was carried out to investigate resistance of charge-transfer among electrolyte and electrocatalyst (Fig. 1 (e)). EIS analysis shows the Fe/NiO/NF have low charge-transfer resistance (Rct).
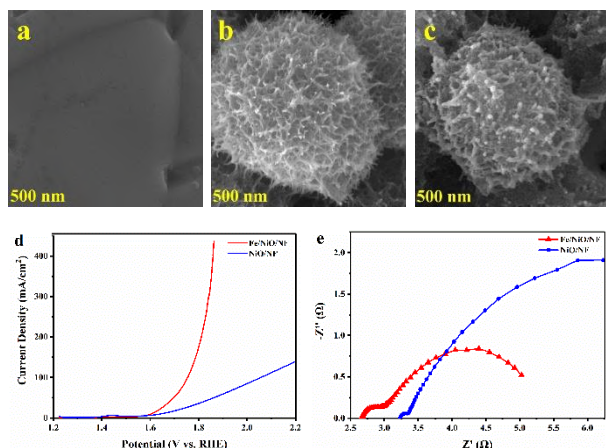
22nd Iranian Chemistry Congress (ICC22)
Iranian Research Organization for Science and Technology (IROST)
13-15 May 2024

03231-97589

Fig. 1. FESEM images of the NF (a), NiO/NF (b), and Fe/NiO/NF (c) electrodes. OER LSV (d) and Nyquist curves (e) of the NiO/NF and Fe/NiO/NF electrodes in alkaline media (1.0 M KOH).

Conclusions

In summary, the NiO microsphere was assembled on Ni foam by using a two step hydrothermal and calcination method. In the next step, the prepared electrocatalyst was immersed in Fe nitrate salt to decorate NiO/NF along with NiFeO$_x$H$_y$ layer. The NiFeO$_x$H$_y$/NiO/NF was shown significant OER activity with low overpotential (360 and 470 mV at current density of 10 and 100 mA cm^{-2}, respectively). Fe played a synergistic role and composed an active site of a Ni-Fe-O coordinated chemical structure.

References

[1] Ali Akbari, M. S., Bagheri, R., Song, Z., & Najafpour, M. M. (2020). Oxygen-evolution reaction by nickel/nickel oxide interface in the presence of ferrate (VI). Scientific reports, 10(1), 8757.

[2] Hemmati, K., Kumar, A., Jadhav, A. R., Moradlou, O., Moshfegh, A. Z., & Lee, H. (2023). Nanorod array-based hierarchical NiO microspheres as a bifunctional electrocatalyst for a selective and corrosion-resistance seawater photo/electrolysis system. ACS Catalysis, 13(8), 5516-5528.

[3] Acharya, P., Nelson, Z. J., Benamara, M., Manso, R. H., Bakovic, S. I. P., Abolhassani, M., ... & Greenlee, L. F. (2019). Chemical structure of Fe–Ni nanoparticles for efficient oxygen evolution reaction electrocatalysis. ACS omega, 4(17), 17209-17222.

[4] Qazi, U. Y., Yuan, C. Z., Ullah, N., Jiang, Y. F., Imran, M., Zeb, A., ... & Xu, A. W. (2017). One-step growth of iron–nickel bimetallic nanoparticles on FeNi alloy foils: Highly efficient advanced electrodes for the oxygen evolution reaction. ACS applied materials & interfaces, 9(34), 28627-28634.

[5] Kajbafvala, M., Rahimi, K., Eshqi, B., Moradlou, O., Sarikhani, N., & Moshfegh, A. Z. (2023). MoS2–MoO2/Ni3S2/Nickel Foam Electrocatalysts Decorated with NiFeO x H y for Energy-Saving Hydrogen Evolution via Urea Oxidation Reaction-Assisted Water Splitting. ACS Applied Nano Materials, 6(23), 21556-21570.

[6] Zhu, G., Xi, C., Shen, M., Bao, C., & Zhu, J. (2014). Nanosheet-based hierarchical Ni2 (CO3)(OH) 2 microspheres with weak crystallinity for high-performance supercapacitor. ACS applied materials & interfaces, 6(19), 17208-17214.

[7] He, H., Chen, H., Chen, J., Jia, C., Chen, J., Liang, J., ... & Wen, Z. (2022). Dual sites modulating MoO2 nanospheres for synergistically enhanced electrocatalysis of water oxidation. Chemical Engineering Journal, 443, 136339.

[8] Yin, H., Jiang, L., Liu, P., Al-Mamun, M., Wang, Y., Zhong, Y. L., ... & Zhao, H. (2018). Remarkably enhanced water splitting activity of nickel foam due to simple immersion in a ferric nitrate solution. Nano Research, 11, 3959-3971.

[9] Li, Y., Wu, Z. S., Lu, P., Wang, X., Liu, W., Liu, Z., ... & Bao, X. (2020). High-valence nickel single-atom catalysts coordinated to oxygen sites for extraordinarily activating oxygen evolution reaction. Advanced Science, 7(5), 1903089.

[10] Lee, S., Banjac, K., Lingenfelder, M., & Hu, X. (2019). Oxygen isotope labeling experiments reveal different reaction sites for the oxygen evolution reaction on nickel and nickel iron oxides. Angewandte Chemie, 131(30), 10401-10405.

Evaluation of the efficiency of chemical precipitation method in removing organic load from urea formaldehyde glue wastewater

A. Eshraghi Khah [a], A. Pendashteh [a, b], s. Niazi [b]

Corresponding Author E-mail:Eshraghikhaha@gmail.com

[a] Departeman of Chemical Engineering, Facuty of Engineering, Univercity of Guilan, Rasht, Iran.

[b] The Caspian Sea Research Center, Univercity of Guilan, Rasht, Iran.

Abstract: Urea formaldehyde (UF) resin is commonly utilized in the production of adhesives for wood-based pane , which is hazardous. This study evaluated the treatability of UF resin wastewater via chemical coagulation. Ferric chloride at 100 mg/L and pH 7 demonstrated the highest chemical oxygen demand removal, achieving approximately 20% efficiency.
Keywords: adhesive; wastewater treatment; chemical coagulation

Introduction

The adhesives used in furniture and MDF board factories for manufacturing laminated boards and furniture panels are derived from urea formaldehyde (UF) resins.
UF resin is a primary resin synthesized from urea and formaldehyde (FA) [1].
The UF wastewater generated during UF preparation and use contains formaldehyde and urea. Formaldehyde is harmful to humans and animals, and has been identified as carcinogenic by the IARC[2, 3]. UF wastewater with high toxicity (4000-7 mg/L FA), high chemical oxygen demand (400-4000 mg/L COD), and high nitrogen levels (56-800 mg/L TKN), has attracted the attention of many researchers [4].
Since the direct discharge of chemical wastewater containing formaldehyde threatens aquatic life, effective treatment systems are imperative[5]. Treatment of industrial formaldehyde-containing wastewater may be accomplished via chemical, advanced oxidation, or biological methods [6].

Experimental Section

In this method, three coagulants, polyaluminum chloride, aluminum sulfate, and ferric chloride were prepared in a stock of 50,000 ppm to treat this wastewater. Also, polyelectrolyte was used as flocculant in 400 ppm stock. Also, 98% sulfuric acid and Merck sodium hydroxide in 5 M stock were used to adjust the pH. Coagulation processes were performed using a Zag Chemi brand six-cell jartest device. The initial rapid mixing stage at 120 rpm for 5 minutes, slow mixing for 20 minutes at 30 rpm and the final sedimentation stage lasted for 30 minutes. Finally, the clear effluent was sampled to determine its COD parameter.

Wastewater Characteristics

Wastewater samples were collected from the urea-formaldehyde adhesive unit of vina fiberboard factory and transferred to the water and wastewater treatment laboratory of Gilan University. The samples were collected from the top of the beakers, and then were analyzed for the determination of COD removal [7].
The characteristics of adhesive wastewater are shown in Table 1.

Table 1: Physical and chemical characteristics of raw wastewater

pH	5.5
COD (ppm)	6240
BOD (ppm)	3120
TSS (ppm)	3355
TDS (ppm)	4276.67

Results and Discussion

The results of the analyses for comparing the performance of coagulants at different pH values and concentrations on COD reduction are as follows:
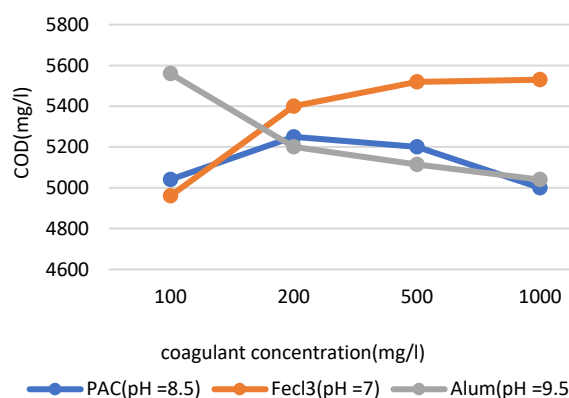

Fig.1: Effects of coagulants dosage and pH on COD reduction

22nd Iranian Chemistry Congress (ICC22)
Iranian Research Organization for Science and Technology (IROST)
13-15 May 2024

03231-97589

In figure 1, the lowest COD was obtained at a concentration of 100 mg/l of FeCl3 coagulant at pH = 7.The normal pH of iron chloride solution is acidic, and the coagulation process works well when the pH is in the neutral range, because at lower pH, there are more positive iron ions that may interfere with the coagulation and flocculation process.

In the case of alum coagulant, the lowest COD was obtained at pH=9.5 with a concentration of 1000 mg/l. Alum has acidic properties, but at higher pH, aluminum ions have a greater tendency to form aluminate precipitates, which causes better removal of organic materials.

Also, in the case of polyaluminum chloride (PAC) coagulant, the lowest COD was obtained at pH = 5.5 and at a concentration of 1000 mg/L. Because at lower pH, the positive charge of aluminum ions increases and they have a better ability to neutralize the negative charges of colloidal particles.

Conclusions

In this study, the efficiency of the chemical coagulation process using different coagulants, including polyaluminum chloride, aluminum sulfate, and ferric chloride, was investigated by changing the pH to remove the organic load from the wastewater resulting from the production of urea formaldehyde adhesive.

The results showed that the use of ferric chloride at neutral pH (about 7) and a concentration of 100 mg/l had the highest COD removal efficiency (about 20 percent). Therefore, it can be concluded that the chemical coagulation process using ferric chloride can be used as an economical and effective pre-treatment for removing a part of the organic load from wastewater containing urea formaldehyde.

References

[1] Dubina, A. and V. Martsul, *Treatment of wastewater containing formaldehyde from wood processing enterprises.* 2015.

[2] Du, L., et al., *Oxidative degradation of formaldehyde in wastewater by MgO/O3/H2O2 in a rotating packed bed.* Chemical Engineering and Processing-Process Intensification, 2020. 155: p. 108053.

[3] Hauptmann, M., et al., *Mortality from solid cancers among workers in formaldehyde industries.* American journal of epidemiology, 2004. 159(12): p. 1117-1130.

[4] Mei, X., et al., *A novel clean and energy-saving system for urea-formaldehyde resin wastewater treatment: Combination of a low-aeration-pressure plate membrane-aerated biofilm reactor and a biological aerated filter.* Journal of Environmental Chemical Engineering, 2021. 9(5): p. 105955.

[5] Vossoughi, M., et al., *Combined chemical and biological processes for the treatment of industrial wastewater containing formaldehyde.* Scientia Iranica, 2001. 8(3): p. 223-227.

[6] Marco, A., S. Esplugas, and G. Saum, *How and why combine chemical and biological processes for wastewater treatment.* Water Science and Technology, 1997. 35(4): p. 321-327.

[7] Azimi, S.C., F. Shirini, and A. Pendashteh, *Treatment of wood industry wastewater by combined coagulation–flocculation–decantation and fenton process.* Water environment research, 2021. 93(3): p. 433-444.

Perovskite based-oxides: LaCrO₃, LaMnO₃ and LaFeO₃; synthesis and electrochemical study

Maryam Pedram, Omran Moradlou*, Maryam Ostadebrahim

Corresponding Author E-mail:moradlou@alzahra.ac.ir

Department of Analytical Chemistry, Faculty of Chemistry, Alzahra University, Tehran 1993893973, Iran.

Abstract: In this study, nano-sized perovskite-based oxides, LaCrO₃, LaMnO₃ and LaFeO₃ were synthesized via a single-phase sol-gel route. Crystallinity and morphology of synthesized samples were studied by X-ray diffraction (XRD) and field-emission scanning electron microscope (FE-SEM). Moreover, capacitive behaviors of the synthesized samples were studied and compared with each other.
Keywords: Perovskite, Sol-gel, Capacitive, Supercapacitor, Quasireversible behaviour, Battery type

Introduction

Supercapacitors (SCs) are energy storage devices (ESD) with high power density. SCs storage energy by means of two mechanisms. On first mechanism, charges store in a form of electric double layer on SC`s plates. These SCs, is called electric double layer capacitors (EDLC). On second mechanism, Charges store by fast reversible redox reactions on the surface. These SCs, are nominated pseudocapacitors. SCs are ESDs as providing high-rate cycling, large cycle life and high specific capacitance [1,2]. Nevertheless, SCs have low energy density rather than batteries. Therefore, many researchers, focused on developing new materials with high porosity and conductivity, which could have high energy density. Up to now, various materials are developed and investigated as electrode materials such as, metal oxides, nitrides, sulfides [1,3]. Perovskites based oxides (PBO) with general formula ABO₃ are considered as encouraging compounds for SCs electrode materials, which A is rare earth metal in center of the cube, B is a transition metal cation in vertices of the cube, and Oxygen anions are placed in middle of the edges [3,4]. PBOs, are applied as electrode materials in SCs since they have useful characteristics such as lattice defects, unvarying surface morphology, nano size and high surface area [3]. In this study, nanostructures of LaCrO₃, LaMnO₃ and LaFeO₃ were synthesized via a single-phase sol-gel route and then were calcinated in 900℃ for 5 hours. Further, the electrochemical behaviour of the samples was studied and compared with each other.

Experimental Section

In this study, nano-sized perovskites, LaCrO₃, LaMnO₃ and LaFeO₃ were synthesized by sol-gel route according to the Ref. [5]. Briefly, a 20 ml aqueous solution contains of La(NO₃).6H₂O and Cr(NO₃)₃.9H₂O in molar ratio of 1:1 was stirred to form of a homogeneous solution. Afterward, a certain amount of citric acid (C₆H₆O₆) slowly was added to the previous solution and was stirred about 2 h. The final homogeneous solution was kept at 60 ℃ for 24 h to evaporate the solvent gradually. Then, the temperature

of the viscose compound was raised up to 80 ℃ for 24 h to form a spongy substance. The resulting material was heated for 24 h at 150 ℃. In the last stage the brittle substance was heated at 200 ℃ for 24 h. When the temperature' compound reaches ambient temperature, it is entirely powdered, followed by calcination at optimum temperature of 900 ℃ for 5 h. LaMnO₃ and LaFeO₃ were synthesized in a same route by adding their own metal nitrate precursors i.e. Mn(NO₃)₂.4H₂O and Fe(NO₃)₃.9H₂O, respectively. The crystallinity of nano-sized synthesized perovskites was characterized using an X-ray diffraction (XRD; Rigaku Ultima IV (Japan)) equipped with a Cu Kα radiation source (λ = 1.54187 Å) with a scanning rage of 0-140° Bragg angle. The morphology of the synthesized samples was determined using a field-emission scanning electron microscope (FE-SEM; MIRA3 TESCAN and Philips XL-30). Lastly, Electrochemical analysis of synthesized perovskites was performed via the Autolab PGSTAT 302 N electrochemical analyzer (Metrohm/Autolab).

Results and Discussion

Crystallinity of synthesized perovskites were studied via XRD technique. Fig. 1 (a) demonstrates XRD patterns of the LaCrO₃ (1), LaMnO₃ (2) and LaFeO₃ (3) samples. Fig. 1. (a, a) indicates 11 diffraction peaks at 2θ values of 22.8°, 32.5°, 40.0°, 46.7°, 52.6°,58.0°, 68.0°, 73.0°, 77.6°, 82.0°, and 86.7° which were matched with the (100), (110), (111), (200), (210), (211), (220), (221), (310), (311), and (222) lattice planes of the LaCrO₃ cubic structure which is corresponding to JCPDS Card No. 01–074-1961. Fig. 1. (a, b) represents the diffraction peaks at 2θ values of 22.9°, [32.6°, 32.7°], [40°, 40.3°], [46.7°, 46.8°], [52.7°, 52.8°], 58.0°, 58.3°, 68.3°, 68.5°, [77.7°, 77.8°], and 86.6° are related to (101), [(121), (200)], [(022), (220)], [(202), (040)], [(222), (301)], (042), (240), (242), (400), [(323), (161)], and (044) lattice planes of the orthorhombic structure of LaMnO₃ which is correlating with JCPDS Card No. 01-089-2470. Fig. (a, C) attendance of the diffraction peaks at 2θ values of 22.6°, 32.0°, 39.7°, 46.0°, 47.6°,

22nd Iranian Chemistry Congress (ICC22)
Iranian Research Organization for Science and Technology (IROST)
13-15 May 2024

03231-97589

52.0°, 53.3°, 57.4°, 67.3°, 76.5°, and 85.5° are owing to the reflections of the (002), (112), (022), (004), (023), (114), (131), (204), (040), (116), and (404) lattice planes in the orthorhombic structure of LaFeO$_3$ and correspond to JCPDS Card No. 01-074-2203. For determination of morphology and size of the prepared nano crystals FE-SEM method was carried out. Fig. 1. (b-d) illustrated FE-SEM images of nano-sized perovskites. General evaluation confirm that LaFeO$_3$ sample (Fig.1 (d)) has more uniformity in grain particles and average grain size is smaller (~70 nm) than LaCrO$_3$ and LaMnO$_3$ grain size which are apprised approximately 83 and 75 nm, respectively. In addition, capacitive behaviour of the nanostructures was evaluated and compared with each other via electrochemical analysis such as cyclic voltammetry (CV) technique. CVs are performed in a three-electrode system, which a Pt plate was as counter electrode and the reference electrode was Ag/AgCl (KCl 3.0 M). Also, working electrode was 1×1 cm^2 nickel foam which was coated with synthesized samples. It is worth mentioning that electrochemical studies were performed in 1 M KOH as electrolyte. Fig. 2. (a-c), indicates the voltammograms of synthesized perovskites at scan rates of 5-100 mV s^{-1}. In general, all samples show redox peaks, having battery-type CV curves.
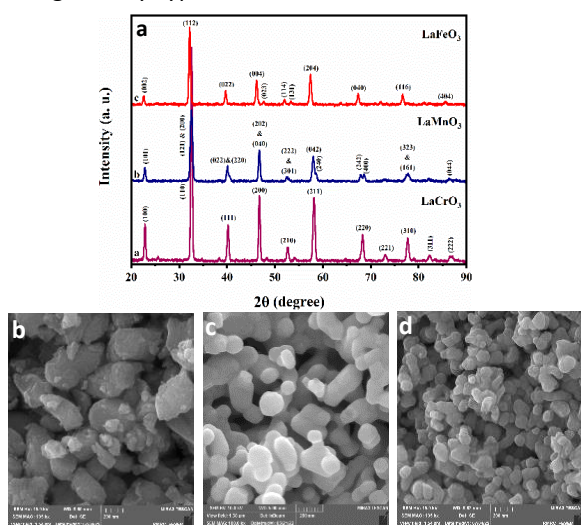
Despite having no change in voltammograms' shape, the peak potentials were shifted by increasing in scan rates, illustrating the quasireversible behaviour of the electrode reactions.

Conclusions

Nano-sized perovskites were synthesized via a single-phase sol-gel route. Then, the synthesized sample were calcined in 900 °C for 5 h. to study characterization the crystal structures and morphologies of synthesized perovskites, XRD and FE-SEM techniques were applied. As a result, LaFeO$_3$ and LaMnO$_3$ crystals have orthorhombic structure and LaCrO$_3$ has cubic crystal. Moreover, nano-sized particles of LaFeO$_3$ not only are smaller in comparison with LaMnO$_3$ and LaCrO$_3$ but also have more uniformity. Electrochemical behaviours of synthesized perovskites were studied that voltammograms showed quasireversible behaviour of the electrode reactions.

References

[1] Raza, W., Ali, F., Raza, N., Luo, Y., Kim, K. H., Yang, J., ... & Kwon, E. E. (2018). Recent advancements in supercapacitor technology. Nano Energy, 52, 441-473.

[2] Zhang, Y., Mei, H. X., Cao, Y., Yan, X. H., Yan, J., Gao, H. L., ... & Gui, Y. H. (2021). Recent advances and challenges of electrode materials for flexible supercapacitors. Coordination Chemistry Reviews, 438, 213910.

[3] Goel, P., Sundriyal, S., Shrivastav, V., Mishra, S., Dubal, D. P., Kim, K. H., & Deep, A. (2021). Perovskite materials as superior and powerful platforms for energy conversion and storage applications. Nano Energy, 80, 105552.

[4] Monama, G. R., Ramohlola, K. E., Iwuoha, E. I., & Modibane, K. D. (2022). Progress on perovskite materials for energy application. Results in Chemistry, 4, 100321.

[5] Ostadebrahim, M., & Moradlou, O. (2023). Electrochemical hydrogen storage in LaMO3 (M= Cr, Mn, Fe, Co, Ni) nano-perovskites. Journal of Energy Storage, 72, 108284.

Fig. 1. (a) XRD patterns of the LaCrO$_3$, LaMnO$_3$ and LaFeO$_3$ samples. (b-d) FE-SEM images of the LaCrO$_3$, LaMnO$_3$ and LaFeO$_3$ perovskites.

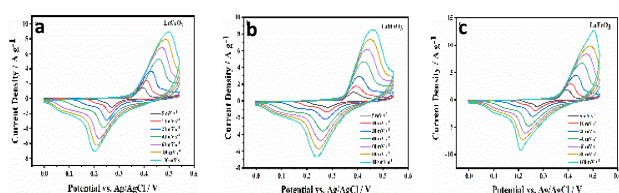**Fig. 2.** CV curves of the (a) LaCrO$_3$, (b) LaMnO$_3$ and (c) LaFeO$_3$ perovskites at the scan rates of 5-100 mV/s in 1.0 M KOH solution.

22nd Iranian Chemistry Congress (ICC22)
Iranian Research Organization for Science and Technology (IROST)
13-15 May 2024

03231-97589

IROST

Enhanced Data Point Importance for Subset Selection in Partial Least Square Regression: A Comparative Study with Kennard-Stone Method

Mahya Vazifeh Solout [a], Somaye Vali Zade [b], Hamid Abdollahi [c], Jahan B. Ghasemi [*a]

Corresponding Author E-mail : jahan.ghasemi@ut.ac.ir

[a] Chemistry Faculty School of Sciences University of Tehran, Tehran POB 14155-6455, Iran.

[b] Halal Research Center of IRI, Food and Drug Administration, Ministry of Health and Medical Education, Tehran, Iran.

[c] Faculty of Chemistry, Institute for Advanced Studies in Basic Sciences, 45195-1159, Zanjan, Iran.

Abstract: A new method called EDPI has been proposed for selecting a subset of data samples. It is based on the DPI concept and ranks all data points in order of importance. The performance of this method has been compared with the Kennard-Stone method in developing PLS calibration models.

Keywords: subset selection; PLS regression; Kennard-Stone method

Introduction

When developing a model for a multivariate dataset, whether for regression or classification purposes, it is crucial to split the dataset into a calibration (training) set and a test set. This process is known as subset selection. The calibration set is utilized to construct the model, while the test set is used to assess the model's performance. The subset chosen for the calibration set should be a representative portion of the entire dataset, capturing the various patterns, trends, and variations present in the data. Therefore, selecting a subset during the model development process is critical.

In this study, we proposed a method for subset selection based on Data Point Importance(DPI) in partial least squares regression. In PLS space, data points can be categorized into essential and non-essential points. Essential points (EP) represent convex hull vertices built from data points in a normalized space, forming a representative data set. On the other hand, non-essential points are located inside the convex hull. Recently, an algorithm called Data Point Importance (DPI) [1] has been introduced to determine the order of importance of EPs, enabling the sorting of information and selection of samples within the dataset. DPI provides an easily calculable value that reflects the impact of each data point on preserving the data structure's pattern. This research extends the concept of DPI to non-essential points, establishing the sequence of importance for all data points and sorting information for each.

This study proposes the Enhanced DPI (EDPI) method and its application in subset selection. The EDPI ranks and assesses the importance of data points through the layered convex hull concept. Its ability to select a representative subset is compared with the Kennard-Stone method [2], which selects data points using Euclidean distance.

Experimental Section

When choosing a calibration set, selecting informative samples that accurately reflect the variations within the dataset is crucial. The EDPI method provides a solution by assessing and ranking data points based on their importance using the DPI principle and layered convex hulls. This technique includes computing the DPI values for each vertex of the original convex hull in an abstract space, organizing them, and then removing those vertices from the dataset. The procedure is then repeated with the remaining data points until a sequence of data points is obtained, arranged in order of importance, with the most important ones at the start of the sequence.

The widely used Kennard-Stone method [2] is used to assess the effectiveness of the EDPI method. The Kennard-Stone method employs Euclidean distance to cover the spectral space to select a representative set uniformly. This process begins with identifying the central sample, proceeds to select samples near the border of the sample space, and finally, fills the remaining space with samples in an orderly manner.

This study aims to compare the selection capabilities of the mentioned methods. For this purpose, an independent test set has been employed to assess the performance of the PLS calibration models developed by each strategy. The model's performance was evaluated by calculating the Root Mean Square Error of Prediction (RMSEP) values.

Results and Discussion

To evaluate the performance of EDPI and compare it with the Kennard-Stone method, ^{1}H NMR spectra of

22nd Iranian Chemistry Congress (ICC22)
Iranian Research Organization for Science and Technology (IROST)
13-15 May 2024

03231-97589

mixtures of three linear alcohols were used. The data set includes the pure spectra of alcohols. Figure 1 depicts the raw spectra of samples, and the layered convex hulls in abstract space as the result of the EDPI method. Seven PLS models were developed for each approach to assess the effectiveness of these sample subset selection methods.

Prediction results of the models are provided in Table 1. Analysis of the RMSEP values reveals that the EDPI method outperforms the Kennard-Stone method in calibration models with fewer samples. This is because the EDPI method starts by selecting the most informative points within the dataset, leading to improved performance with fewer samples. Conversely, in models with more samples, the Kennard-Stone method selects more points, resulting in a broader coverage of the variable space, which includes essential data points. As a result, the difference in RMSEP values between the two methods decreases, and their performance becomes comparable.
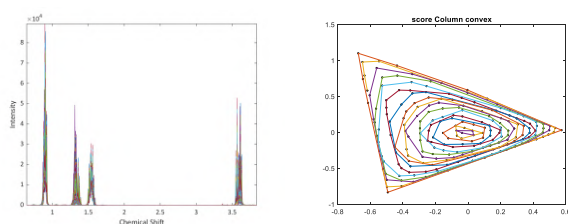
widely used Kennard-Stone method, which selects subsets based on Euclidean distance. The study assesses the effectiveness of both methods in developing PLS models and compares the predictive performance of the models produced by each technique. The findings indicate that the models generated using EDPI demonstrate comparable or superior performance to those created through the Kennard-Stone method. This highlights the potential of the EDPI approach in enhancing predictive accuracy within multivariate data analysis.

References

[1] Zade, S. V., Neymeyr, K., Sawall, M., Fischer, C., & Abdollahi, H. (2023). Data point importance: Information ranking in multivariate data. *Journal of Chemometrics*, *37*(1), e3453.

https://doi.org/10.1002/cem.3453

[2] Kennard, R. W., & Stone, L. A. (1969). Computer aided design of experiments. *Technometrics*, *11*(1), 137-148.

https://doi.org/10.1080/00401706.1969.10490666

Fig.1: a)The raw spectra of the alcohol mixtures, b) the layered convex hulls resulting from the EDPI approach.

Table1: Prediction results of the PLS models developed using the EDPI and Kennard-Stone method.

Method	Number of samples	RMSEP	R_p^2
EDPI	20	0.63	1.0
	41	0.62	1.0
	62	0.62	1.0
	83	0.63	1.0
	104	0.62	1.0
	124	0.62	1.0
	145	0.62	1.0
Kennard-Stone	20	1.2	1.0
	41	0.77	1.0
	62	0.64	1.0
	83	0.64	1.0
	104	0.65	1.0
	124	0.65	1.0
	145	0.66	1.0

Conclusions

This study introduces a novel approach, EDPI, for selecting a representative subset from a multivariate dataset aimed at developing a model to predict a specified property of interest. This method's efficiency is compared to the

Interaction of Trofinetide with C60 Fullerene; A Quantum Calculation Study

Hossein Shirani[a,b], Mahdi Nasabizadeh[b]

Corresponding Author E-mail: hossein_shirani@iust.ac.ir
[a] Department of Chemistry, Iran University of Science and Technology, P.O. Box 16846-13114, Tehran, Iran.
[b] Department of Biotechnology, Faculty of Biological Sciences and Technology, University of Science and Culture, Tehran, Iran.

Abstract: This study utilizes quantum mechanical calculations with the B3LYP/6-311+G approach to analyze Trofinetide's structural and electronic properties for treating Rett syndrome. We examine molecular geometry, vibrational frequencies, and electronic structure, revealing insights into its chemical properties. Analysis of bond lengths, angles, dipole moments, and the HOMO-LUMO gap aids drug discovery for neurological disorders.
Keywords: Rett syndrome; Trofinetide; HOMO-LUMO Gap; DFT; B3LYP/6-311+G; Fullerene

Introduction

Rett syndrome (RTT), a rare genetically driven neurological disorder, predominantly affects females, typically becoming noticeable after 6–18 months of age [1]. It is characterized by severe cognitive and physical impairments, notably the loss of intentional hand skills superseded by repetitive hand motions. The observed incidence ranges between 1 in 10,000 to 1 in 15,000 live female births [2].) While no definitive cure currently exists for Rett syndrome, the focus of therapeutic interventions remains on enhancing the quality of life for those affected [3].

In this context, a breakthrough emerged with the FDA's sanctioning of Daybue (trofinetide) oral solution, marking it as the first treatment specifically for Rett syndrome [4]. This novel drug represents a beacon of hope for those affected by RTT, signifying a monumental step forward in the realm of targeted therapies. Trofinetide is a novel synthetic analog of the amino-terminal tripeptide glycine-proline-glutamate (GPE) which plays key roles in modulating excitatory/inhibitory balance and neuroinflammation [5]

Methods

In the initial stage, the molecular structure of Trofinetide was designed using GaussView software, followed by quantum mechanical calculations at the B3LYP/6–311+G theoretical level using Gaussian09 software.

Results and Discussion

Molecular calculations of the drug Tolterodine were performed using the GaussView software at the B3LYP/6–311+G theoretical level, and the structural parameters wer reported.Using the GaussView software, the molecular structure of interest was initially designed in this software (Fig.1).
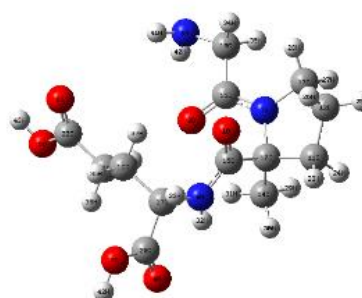

Fig.1. The optimized structure of Trofinetide at the B3LYP/6–311+G level.

Thermodynamic values for the structure of Trofinetide at the B3LYP/6–311+G computational level are reported: Total Energy: 236.840 kcal/mol; Zero-Point Energy: -704,884.0286826 kcal/mol; Gibbs Free Energy: 187.23894384 kcal/mol.

Table 1. Calculated Bond Length Values for Trofinetide Molecule using B3LYP/6-311+G Computational Method.

N8-C15	N7-C16	C17-C20	C19-C21	C22-O5	C20-O4
1.35602	1.36176	1.51000	1.53306	1.38462	1.23362

Table 2. Calculated Bond Angles Values for Trofinetide Molecule using B3LYP/6-311+G Computational.

N8-C15-C17	O1-C15-C10	C13-N7-C15	C14-C10-C11	O2-C16-C18	O5-C22-O6
30.3	119.9	125.4	111.2	120.6	121.5

22nd Iranian Chemistry Congress (ICC22)
Iranian Research Organization for Science and
Technology (IROST)
13-15 May 2024

03231-97589

IROST

Table 3. Calculated Dihedral Angle Values for Trofinetide
Molecule using B3LYP/6-311+G Computational.

N7-C16-C18-N9	C19-C21-C22-O5	O3-C20-C17-N8	C14-C10-N7-C13	N9-C18-C16-O2	C17-C19-C21-C22
175.3	-162.1	170.7	-122.9	-4.6	-178.5

Table 4. Calculated Dipole Moments Values for Trofinetide
Molecule using B3LYP/6-311+G Computational.

μ_x	μ_y	μ_z	μ_{tot}
-1.6692	-3.4437	1.9978	4.3171

Table 5: Calculated HOMO-LUMO Energy Gap Values for
Trofinetide Molecule using B3LYP/6-311+G Computational.

Table 5: HOMO-LUMO Energy Gap

E_{HOMO}	HLG	E_{LUMO}
-0.23741	-0.19089	-0.04652

HLG = 0.19 V
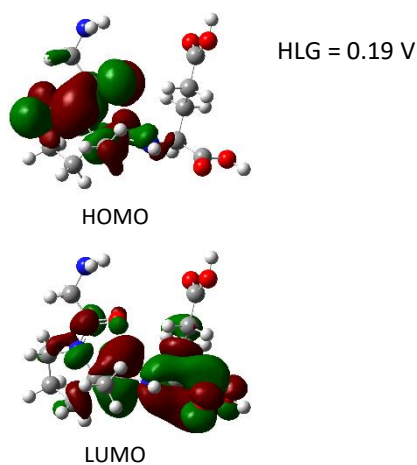
HOMO

LUMO

Fig2. The molecular orbital shapes of the HOMO and LUMO of
the Trofinetide molecule at the B3LYP/6–311+G level.

IR Spectrum Vibrational Frequencies
The IR spectrum, known for its heightened sensitivity in
discerning molecular chemical and structural traits, finds
extensive applications in chemistry, physics,
biochemistry, and pharmaceuticals. In the presented
spectrum, the most prominent peak at ١١٠٨,١٧ signifies
oscillations per second, positioned on the left side of the
chart. The value 683.632 on the right denotes the
dielectric constant. Notably, three distinct peaks are
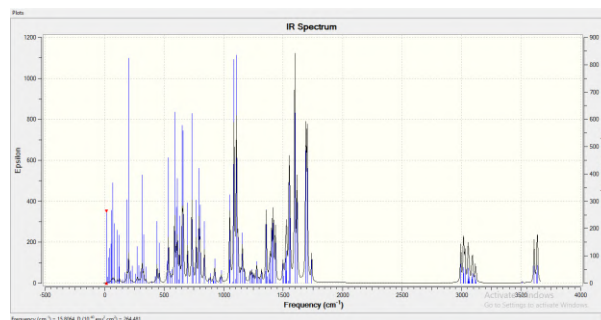discernible in this IR spectrum.

Fig 3. Vibrational Frequency in IR Spectrum for Trofinetide Molecule at
B3LYP/6–311+G Level. without encountering negative frequencies.

Trofinetide Delivery with C60 Fullerene Nanocarriers: This
study investigates the use of C60 fullerene nanocarriers
for delivering Trofinetide, a potential treatment for Rett
syndrome. By analysing their interaction computationally,
researchers aim to understand how nanotechnology can
enhance Trofinetide's pharmacokinetics and efficacy. This
exploration sheds light on the potential of nanocarriers in
improving therapeutic interventions for neurological
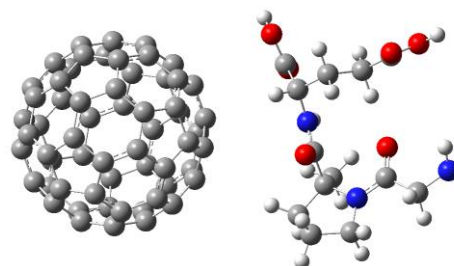disorders like Rett syndrome.

Fig 4. The optimized structure of Trofinetide and C60 at
the B3LYP/6–311+G level.

Conclusions
our study explored Trofinetide's chemical properties
through quantum mechanical calculations, revealing its
potential for treating Rett syndrome. Additionally,
investigating C60 fullerene nanocarriers for Trofinetide
delivery presents promising opportunities for advancing
neurological disorder therapies. These insights contribute
to ongoing efforts in drug discovery and design for
conditions such as Rett syndrome.

References
[1] Borloz, E., Villard, L., & Roux, J. C. (2021). Rett syndrome: think outside the (skull) box. Faculty reviews, 10, 59. https://doi.org/10.12703/r/10-59
[2] Sarajlija, A., Kisic-Tepavcevic, D., Nikolic, Z., Savic Pavicevic, D., Obradovic, S., Djuric, M., & Pekmezovic, T. (2015). Epidemiology of Rett syndrome in Serbia: prevalence, incidence and survival. Neuroepidemiology, 44(1), 1–5. https://doi.org/10.1159/000369494
[3] Smeets, E., Pelc, K., & Rutherford, M. A. (2011). Rett Syndrome. Molecular Syndromology, 2(3–5), 113–127. https://doi.org/10.1159/000337637
[4] Simon, J, Pytkowicz, J, and... (2016). Incorporation of Trifluoromethylated Proline and Surrogates into Peptides: Application to the Synthesis of Fluorinated Analogues of the Neuroprotective Glycine-Proline-Glutamate (GPE) Tripeptide. The Journal of organic chemistry, 81(13), 5381–5392. https://doi.org/10.1021/acs.joc.6b00704

Quantum Mechanics Computations on fostemsavir Drug

Hossein Shirani[a,b,*], Mahdi Nasaizadeh[b]

Corresponding Author E-mail: hossein_shirani@iust.ac.ir
[a] Department of Chemistry, Iran University of Science and Technology, P.O. Box 16846-13114, Tehran, Iran.
[b] Department of Biotechnology, Faculty of Biological Sciences and Technology, University of Science and Culture, Tehran, Iran.

Abstract: The research utilizes quantum mechanics calculations with the B3LYP/6-311+G computational method to assess the structural and electronic features of fostemsavir. A thorough investigation offers valuable information about its chemical attributes, which can assist in the development of medications for hereditary angioedema, an uncommon genetic condition that leads to repeated and intense inflammation.
Keywords: Hereditary angioedema; fostemsavir; B3LYP; Density Functional Theory

Introduction

Fostemsavir, a novel antiretroviral drug, has gained prominence as a potential treatment for HIV/AIDS, particularly in individuals with multidrug-resistant HIV-1 infection. [1] Through quantum mechanical calculations utilizing the B3LYP/6-311+G computational approach, we aim to unveil the molecular intricacies underlying fostemsavir's pharmacological profile. Recognized by the U.S. Food and Drug Administration (FDA) as a first-in-class medication [2], fostemsavir, marketed as Rukobia, addresses the therapeutic needs of adults living with HIV/AIDS who face challenges with existing treatment options due to resistance, intolerance, or safety concerns. Our study offers insights into fostemsavir's structural and electronic properties, shedding light on its potential as a valuable addition to HIV therapy.

Fostemsavir may cause a serious condition called immune reconstitution syndrome, akin to other approved drugs for HIV-1 treatment. [3] This phenomenon may occur at the initiation of HIV-1 therapy, as the immune system strengthens and begins to combat latent infections within the body.[3] Additionally, patients may experience heart rhythm disturbances attributable to QT prolongation, as well as elevated liver enzyme levels in those co-infected with hepatitis B or C viruses. These potential adverse effects underscore the importance of close monitoring and healthcare provider supervision during fostemsavir treatment. [3]

Methods

In the initial stage, the molecular structure of fostemsavir was designed using GaussView software, followed by quantum mechanical calculations at the B3LYP/6–311+G theoretical level using Gaussian09 software.

Results and Discussion

Molecular calculations of the drug fostemsavir were performed using the GaussView software at the B3LYP/6–311+G theoretical level, and the structural parameters were reported. Using the GaussView software, the molecular structure of interest was initially designed in this software (Fig.1).
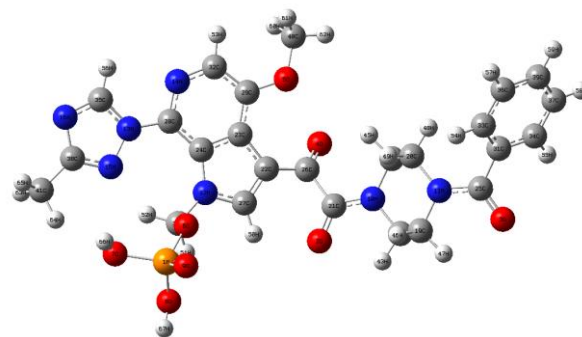

Fig. 1. The optimized structure of fostemsavir at the B3LYP/6–311+G level.

Table 1. Calculated Bond Length Values for fostemsavir Molecule using B3LYP/6-311+G Computational Method.

P1 – O6	N12 – C27	N10-C21	N13-C28	C40-O5	C25-O3
1.72653	1.37915	1.36403	1.42706	1.45788	1.25702

Table 2. Calculated Bond Angles Values for fostemsavir Molecule using B3LYP/6-311+G Computational.

O8-P1-O7	P1-O6-C30	O2-C21-C25	C48-O5-C29	O3-C25-N11	41C-38C-15N
39.5	122.8	118.9	119.4	121.0	123.6

22nd Iranian Chemistry Congress (ICC22)
Iranian Research Organization for Science and Technology (IROST)
13-15 May 2024

03231-97589

IROST

Table 3. Calculated Dihedral Angle Values for fostemsavir Molecule using B3LYP/6-311+G Computational.

C8-P1-O6-C30	N12-C27-C22-C26	N13-N15-C38-C41	C40-O5-C29-C32	O3-C25-N11-C20	O2-C21-N10-C18
37.1	-173.6	-178.9	-7.43	-160.25	-176.5

Table 4. Calculated Dipole Moments Values for fostemsavir Molecule using B3LYP/6-311+G Computational.
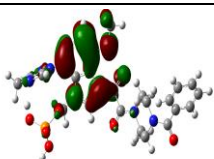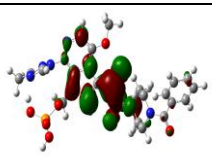
μx	μy	μz	μtot
0.7138	5.1929	0.2437	5.2474

Table 5. Calculated Mulliken Charge Values for fostemsavir Molecule using B3LYP/6-311+G Computational Method.

P1	O5	N13	C21	C30	C41
1.43	-0.53	-0.57	0.51	0.13	-0.45

Table 6. Calculated HOMO-LUMO Energy Gap Values (ev) for fostemsavir Molecule using B3LYP/6-311+G Computational.

EHOMO	HLG	ELUMO
-0.23827	0.15	-0.08288

The molecular orbital shapes of the HOMO and LUMO of the fostemsavir molecule at the B3LYP/6–311+G level have also been presented.

Conclusions

our study utilized quantum mechanical calculations to analyze the structural and electronic properties of Berotralstat, a potential treatment for Rett syndrome. By examining molecular geometry, vibrational frequencies, and electronic structure, we gained valuable insights into its chemical properties. Our findings contribute to drug discovery efforts for neurological disorders like Rett syndrome. Additionally, exploring innovative delivery methods such as C60 fullerene nanocarriers holds promise for advancing therapeutic options in this field.

References

[1] Office of the Commissioner. (2020, July 2). FDA approves new HIV treatment for patients with limited treatment options. U.S. Food And Drug Administration. https://www.fda.gov/news-events/press-announcements/fda-approves-new-hiv-treatment-patients-limited-treatment-options

[2] Research, C. F. D. E. A. (2021, January 8). New Drug therapy Approvals 2020. U.S. Food And Drug Administration. https://www.fda.gov/drugs/new-drugs-fda-cders-new-molecular-entities-and-new-therapeutic-biological-products/new-drug-therapy-approvals-2020

[3] Research, C. F. D. E. A. (2020, July 14). Drug trials snapshots: RUKOBIA. U.S. Food And Drug Administration. https://www.fda.gov/drugs/drug-approvals-and-databases/drug-trials-snapshots-rukobia

Experimental and computational studies on some thiazole derivatives as corrosion inhibitors for mild steel in HCl medium

Afsaneh Amiri, A-Reza Nekoei*

Corresponding Author E-mail: nekoei@sutech.ac.ir

Department of Chemistry, Shiraz University of Technology, Shiraz, Iran.

Abstract: Steel corrosion inhibitory performance of 5 samples of thiazole derivatives was examined in 1 M HCl solution by potentiodynamic polarization method at different inhibitor concentrations. Also, the inhibition mechanism at the atomic level was investigated by combining quantum mechanics and molecular dynamics studies. Simulations have been used to reveal the relationship between chemical structure and performance of inhibitors. Analyses of experimental observations, theoretical adsorption energy, frontier orbitals, reactivity and radial distribution function showed that inhibitor II (having a naphthalene ring) has the best performance against steel corrosion in HCl environment.

Keywords: Inhibitor; Corrosion; DFT; Simulation.

Introduction

Corrosion control, also methods of decreasing it, are very essential in a wide range of industries. Among different methods, the use of proper inhibitor substances is one of the economic and efficient methods [1]. Inhibitors are added in small amounts to the corrosive environment to reduce metal corrosion. Corrosion inhibitors are usually organic compounds with some functional groups or double and triple bonds, π electrons, heteroatoms of high electron density such as oxygen, nitrogen, or sulfur, which can be adsorbed by donating an electron to an empty orbital of the metal surface [2]. Since checking the effectiveness of inhibitors by experimental methods is time-consuming and expensive, in recent years, theoretical methods such as simulation and modeling by quantum methods have also been used to predict the behavior of inhibitors [3].

In this research, the inhibitory effects of 5 thiazole derivatives (Fig. 1), in different concentrations, on the prevention of steel corrosion in 1M HCl solution have been investigated experimentally and theoretically.

Method Section

In the experimental part, potentiodynamic polarization studies on corrosive environment in 1M HCl, containing 0.1, 0.5, 2.0 and 5.0 mM of inhibitors were performed using a Potantiostat/Galvanostat device. Also, quantum mechanics DFT calculations were performed at B3LYP/6-311++G(d,p) level by using Gaussian 16 program, and GGA/DNP level by using Material Studio 20 software, which was also used for Monte Carlo (MC) and molecular dinamics (MD) simulations. MC simulation has been done with the adsorption locator module and the COMPASS force field and considering the periodic boundary conditions. The MD simulations were performed by the COMPASS force field under NVT ensemble at temperature of 298K with a time step of 0.1fs and a simulation time of 1000ps.

Results and Discussion

By examining the results of electrochemical potentiodynamic polarization, it was observed that after adding inhibitors to the corrosive environment, the intensity of the corrosion current significantly decreased. Also, as collected in Table 1, the inhibition percentage increases by increasing the inhibitor concentration.

Table 1: Inhibition efficiency (%)

concentration	I	II	III	IV	V
0.1 (mM)	67	67	62	60	60
0.5 (mM)	71	87	73	65	68
2.0 (mM)	76	93	84	77	77
5.0 (mM)	83	99	97	87	80
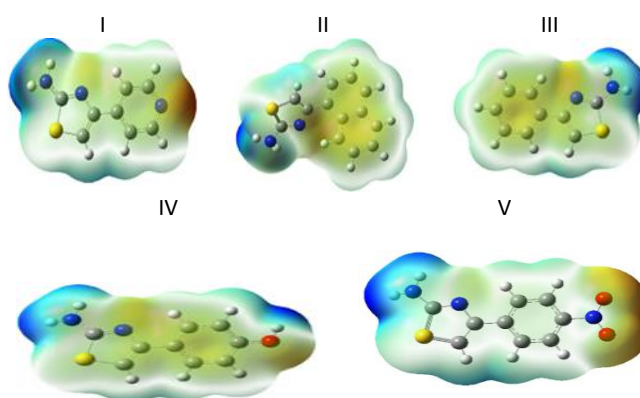
Fig. 1: Molecular Electrostatic Potential (MESP) surface

22nd Iranian Chemistry Congress (ICC22)
Iranian Research Organization for Science and
Technology (IROST)
13-15 May 2024

03231-97589

According to the previous research, an inhibitor is useful when it interacts strongly with the surface by donating and withdrawing electrons. For this reason, frontier molecular orbitals were used to check the reactivity of these items. HOMO-LOMO gap (Table 2) is a function of the reactivity of the inhibitor molecule for adsorption on the metal surface. The lowest value of the gap for II indicates that this molecule could simply adsorbed on the metal surface, and as a result, the ability of the inhibitor II to form a complex with the metal surface is the highest, which increases its inhibition efficiency [3], in the best agreement with the experimental observasions (Table 2)

Table 2: Computed global electronic parameters*

Sample	E_{HOMO}	E_{LUMO}	Gap	IP	EA	X
I	-6.16	-1.66	4.50	6.16	1.66	3.91
II	-5.75	-1.44	4.30	5.75	1.44	3.60
III	-5.77	-1.18	4.60	5.77	1.18	3.47
IV	-5.55	-1.02	4.53	5.55	1.02	3.29
V	-6.32	-2.82	3.50	6.32	2.82	4.57

*Energies, ionization potential and electron affinity in eV; X, absolute electronegativity

Fig. 2, for instance, shows the equilibrium state of inhibitor II on the steel surface by molecular dynamics simulation. It shows that, after the simulation period, in the corrosive environment, the inhibitor molecule is adsorbed on the metal surface, and protects it from corrosive species.
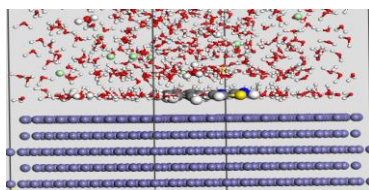
Fig.2: Inhibitor II on the steel surface (MD simulation)

The amount of adsorption energy obtained from MC and MD simulations is reported in Table 3. According to the results, inhibitor II has a higher adsorption energy than other thiazole derivatives, again in the best agreement with the experimental observations in Table 1.

Table 3: Adsorption energy in kj/mol

Inhibitor	E_{ads} (MD)	E_{ads} (MC)
I	-732.09	-378.55
II	-960.65	-498.26
III	-754.75	-384.08
IV	-848.24	-332.13
V	-804.37	-435.03

According to the previous studies reported on the radial distribution function (RDF) diagram, the peaks observed

in the distance range of 1-3.5 Å indicate the chemical bonding between the inhibitor and the metal surface, while the peaks outside this range are mainly due to Coulomb and van der Waals interactions [4]. According to Figure 3, all studied inhibitors with the first peak in the range of 1 Å, have the ability to form a chemical bond with the metal surface, to the same extent.
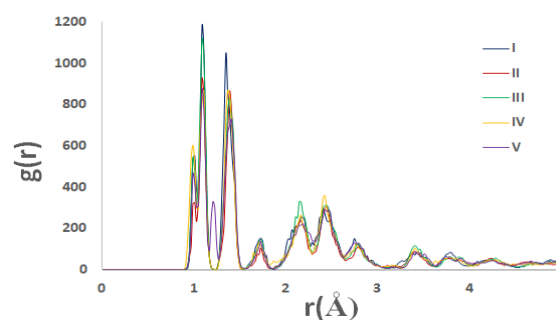

Fig.3: Radial Distribution Function (RDF) diagram

Conclusions

Based on the experiment and quantum results, all studied inhibitors have the ability to interact with the steel surface by donating electrons. The experimental results showed a significant advantage for inhibitor II, which is well predicted by simulation results of gap energy, adsorbtion energy and charge transfer.

References

[1] Tan, B., Zhang, S., Qiang, Y., Li, W., Li, H., Feng, L., & Zhang, G. (2020). Experimental and theoretical studies on the inhibition properties of three diphenyl disulfide derivatives on copper corrosion in acid medium. *Journal of Molecular Liquids*, *298*, 111975.

[2] Ghaderi, M., Ramazani SA, A., Kordzadeh, A., Mahdavian, M., Alibakhshi, E., & Ghaderi, A. (2022). Corrosion inhibition of a novel antihistamine-based compound for mild steel in hydrochloric acid solution: Experimental and computational studies. *Scientific Reports*, *12*(1), 13450.

[3] Chugh, B., Singh, A. K., Thakur, S., Pani, B., Lgaz, H., Chung, I. M., & Ebenso, E. (2020). Comparative investigation of corrosion-mitigating behavior of thiadiazole-derived bis-schiff bases for mild steel in acid medium: experimental, theoretical, and surface study. *ACS omega*, *5*(23), 13503-13520.

[4] Guo, L., Tan, J., Kaya, S., Leng, S., Li, Q., & Zhang, F. (2020). Multidimensional insights into the corrosion inhibition of 3, 3-dithiodipropionic acid on Q235 steel in H_2SO_4 medium: a combined experimental and in silico investigation. *Journal of colloid and interface science*, *570*, 116-124.

22nd Iranian Chemistry Congress (ICC22)
Iranian Research Organization for Science and Technology (IROST)
13-15 May 2024

03231-97589

Cyclometalated piano-stool Iridium(III) complexes: structural Characterization and theoretical calculations

Mahya Ghaffari, Mahshid Nikravesh, Hamid R. Shahsavari*

Corresponding Author E-mail: shahsavari@iasbs.ac.ir

Department of Chemistry, Institute for Advanced Studies in Basic Sciences (IASBS), Zanjan 45137-66731, Iran.

Abstract: This study aims to synthesize and characterize new Ir(III) complexes based on the 2-(2,4-difluorophenyl)pyridine (dfppy) cyclometalated ligand. Various analytical techniques, including HR ESI-MS, NMR spectroscopy, and X-ray diffraction crystallography were employed to characterize the complexes. Additionally, UV-Vis absorption spectra were recorded and compared with theoretical calculations using DFT and TD-DFT methods. The results provide insights into the electronic transitions and photophysical properties of the complexes.

Keywords: Cyclometalated iridium compounds; half-sandwich; Computational.

Introduction

Studying the chemistry and applications of half-sandwich cyclometalated complexes has grown to be one of the most active and intriguing fields of organometallic chemistry due to their air stability, accessibility, robustness, and water solubility [1]. In Cp*Rh(III)/Ir(III) complexes, one face of the octahedron (three coordination sites) is occupied by the π-bound negatively charged pentamethylcyclopentadiene (Cp*) ligand. The remaining positions of the coordination sphere may accept the chelating L'L' ligands to create a variety of complexes, adding to the complex's stability and modifying the rhodium and iridium center's electrical characteristics [2]. Due to their accessibility *via* sodium-acetate-promoted C–H activation of [Cp*Ir(μ-Cl)(Cl)]$_2$ as a precursor, the synthesis of cyclometalated [Cp*Ir(Y)(C^D)] complexes has attracted a lot of interest in the past ten years [3]. Since the synthesis and reactivity of cyclometalated Cp*Ir complexes, as well as their applications as supramolecular building blocks [4], have been only marginally studied to date, this study will focus on isolated and well-defined complexes that contain a Cp*Ir–C bond stabilized by the intramolecular coordination of neutral donor atoms.

Experimental Section

[Cp*IrCl(dfppy)], 1, A solution of [Cp*Ir(μ-Cl)(Cl)]$_2$, **A**, (48 mg, 0.06 mmol), 2-(2,4-difluorophenyl)pyridine (23 mg, 0.12 mmol), and sodium acetate (20 mg, 0.24 mmol) in CH$_2$Cl$_2$ was stirred for 24 h at ambient temperature. The solution was filtered through Celite. The filtrate was evaporated to dryness on a rotary evaporator and washed with cold n-Pentane. The product was recrystallized from CHCl$_3$/hexane.

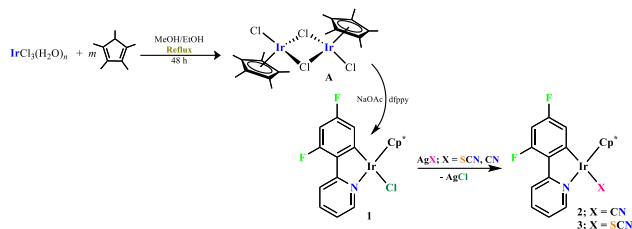**[Cp*Ir(CN)(dfppy)], 2,** To a solution of **1** (200 mg, 0.37 mmol) in CH$_2$Cl$_2$ (20 mL) was added silver cyanide (50 mg, 0.37 mmol). Under dark conditions and an argon atmosphere, the resulting mixture was stirred at room temperature for 12 h. The reaction mixture was filtered on a Celite to separate the AgCl precipitate. The filtrate was evaporated to dryness on a rotary evaporator and washed with hexane. The product was recrystallized from CHCl$_3$/n-hexane.

[Cp*Ir(SCN)(dfppy)], 3, To a solution of **1** (200 mg, 0.35 mmol) in CH$_2$Cl$_2$ (20 mL) was added silver thiocyanate (50 mg, 0.30 mmol). Under dark conditions and an argon atmosphere, the resulting mixture was stirred at room temperature for 12 h. The reaction mixture was filtered on a Celite to separate the AgCl precipitate. The filtrate was evaporated to dryness on a rotary evaporator and washed with hexane. The product was recrystallized from CHCl$_3$/n-hexane.

Results and Discussion

The synthesis route for the new complexes is displayed in Scheme 1. Among the several methods for generating cyclometalated Cp*Ir complexes, the direct chelation-assisted activation of C–H bonds are the most straightforward. An efficient sodium-acetate-promoted C–H activation was developed using [Cp*Ir(μ-Cl)(Cl)]$_2$, **A**. In the presence of sodium acetate acting as both catalyst and base, the C–H bonds were cleaved for specific substrates at room temperature, and the expected cyclometalated complexes were formed almost quantitatively. The effective C–H bond activation is a heteroatom-assisted process. The reaction of **A** with 2-(2,4-difluorophenyl)pyridine, dfppy, in the presence of sodium acetate gave the cyclometalated complexes [Cp*Ir(Cl)(dfppy)], **1**, (Scheme 1). The treatment of **1** with AgCN and AgSCN under dark conditions at room temperature, through chloride abstraction, led to the formation of the complexes [Cp*Ir(CN)(dfppy)], **2**, and

22nd Iranian Chemistry Congress (ICC22)
Iranian Research Organization for Science and
Technology (IROST)
13-15 May 2024

03231-97589

IROST

[Cp*Ir(SCN)(dfppy)], **3**, respectively. Products were isolated as pure and stable solids.

Scheme 1. Synthetic pathway for the iridium complexes.

The HSQC NMR spectrum of **2** is shown in Fig. 1. Methyl protons of Cp* ligand appear as a singlet peak at δ = 1.8 ppm. The signals in the range of δ = 6.5-8.6 ppm are related to the hydrogens of the dfppy ligand. The triplet of doublet signal at δ = 6.5 ppm is related to H[11] of the dfppy ligand due to its coupling with fluorine and H[9] atoms ($^4J_{HH}$ = 2.29 Hz, $^3J_{FH}$ = 9.84 Hz). Also, a doublet signal at δ = 8.6 ppm is related to H[6] of the dfppy ligand due to its coupling with vicinal hydrogen ($^3J_{HH}$ = 5.26 Hz).
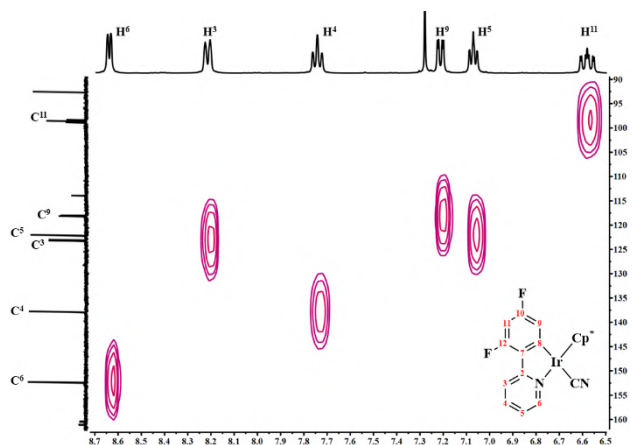
Fig. 1. HSQC spectrum (aromatic region) of **2** in CDCl$_3$.

The crystal structure of complexes **1–3** was identified by X-ray diffraction crystallography (Fig. 2). These complexes contain a metal center, the surrounding structure of which is pseudo-octahedral, whose coordination sphere is completed with the cyclopentadienyl group, nitrogen and carbon atoms of the dfppy ligand, and the cyanide/thiocyanate group, chiral-at-metal complexes. The complexes show a piano-stool type geometry which is a typical geometry for the half-sandwich complexes, and the metal center has the expected pseudo-octahedral arrangement due to the angles around the metal centers being relatively close to the ideal angles of an octahedral complex [5].

The UV-Vis absorption spectra were acquired for all complexes in CH$_2$Cl$_2$ and show high-energy intense absorption bands (λ < 300 nm) that can be assigned to intraligand transitions. There is also a broad weak absorption at λ values ranging from 350 to 400 nm, typically ascribed to charge transfer transitions. Accordingly, density functional theory (DFT) and time-dependent (TD-DFT) calculation methods were used to understand better the nature of electronic transitions.
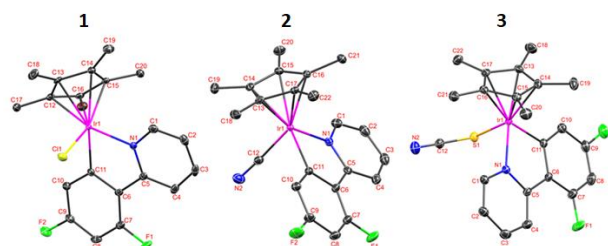

Fig. 2. ORTEP plots of **1–3**.

Conclusions

In summary, we report three complexes of Cp*Ir(III) based on functional dfppy ligand; **1–3**. All complexes are non-emissive, which can be related to d-d transitions, and those are forbidden by Laporte's rule. DFT and TD-DFT calculation methods were used to understand better the nature of electronic transitions for all complexes. The HOMO is mainly localized on the Ir (42%), dfppy (27%), and Cp* (23%) fragments in **2**. Still, the LUMO is notably centered on the dfppy ligand (90%). In the complex **3**, the SCN ligand also plays a role in HOMO contribution (25%), and the LUMO delocalized over all fragments.

References

[1] Gao, W.-X.; Cui, P.-F.; Cui, Z.; Jin, G.-X., 8.02 - Half-Sandwich Rhodium and Iridium Complexes. In *Comprehensive Organometallic Chemistry IV*, Parkin, G.; Meyer, K.; O'hare, D., Eds. Elsevier: Oxford, 2022; pp 55-187.

[2] Liu, J.; Wu, X.; Iggo, J. A.; Xiao, J., Half-sandwich iridium complexes—Synthesis and applications in catalysis. *Coord. Chem. Rev.* **2008,** *252*, 782-809.

[3] Ackermann, L., Carboxylate-Assisted Transition-Metal-Catalyzed C–H Bond Functionalizations: Mechanism and Scope. *Chem. Rev.* **2011,** *111*, 1315-1345.

[4] Song, G.; Wang, F.; Li, X., C–C, C–O and C–N bond formation via rhodium(III)-catalyzed oxidative C–H activation. *Chem. Soc. Rev.* **2012,** *41*, 3651-3678.

[5] Nahaei, A.; Mandegani, Z.; Chamyani, S.; Fereidoonnezhad, M.; Shahsavari, H. R.; Kuznetsov, N. Y.; Nabavizadeh, S. M., Half-Sandwich Cyclometalated Rh^{III} Complexes Bearing Thiolate Ligands: Biomolecular Interactions and In Vitro and In Vivo Evaluations. *Inorg. Chem.* **2022,** *61*, 2039-2056.

22nd Iranian Chemistry Congress (ICC22)
Iranian Research Organization for Science and Technology (IROST)
13-15 May 2024

03231-97589

Fabrication of novel efficacious nanocomposites on the basis of modified graphic carbon nitride for wastewater detoxification upon visible light

Paria Hemmati-Eslamlu[*], Aziz Habibi-Yangjeh

Corresponding Author E-mail: p.hemmati@uma.ac.ir.

Department of Chemistry, Faculty of Science, University of Mohaghegh Ardabili, Ardabil, Iran.

Abstract: The presence of various pollutants, including pharmaceuticals and heavy metals in the aquatic environment, has resulted in appearance of widespread diseases. In this presentation, photocatalytic performance of novel materials fabricated based on modified $g\text{-}C_3N_4$ (abbreviated as MCN) and used for detoxification of the solutions polluted with antibiotics will be compared.

Keywords: Modified $g\text{-}C_3N_4$; Antibiotics; Wastewater pollutants; Photocatalyst.

Introduction

During the last decades, with the rapid increase in population and fast economic development, the water pollution has tremendously increased. The presence of various pollutants, including pharmaceuticals, organic dyes, pesticides, and inorganic compounds in the aquatic environment has led to rapid deterioration of environment, which resulted in appearance of widespread diseases. Consequently, many researchers are looking for effective and affordable technologies to tackle the environmental pollution. In general, the methods of removing these pollutants can be summarized as adsorption, electrolysis, biological, reverse osmosis, chemical precipitation, and advanced oxidation processes (AOPs) [1-3].

In recent decade, nanomaterials on the basis of graphitic carbon nitride ($g\text{-}C_3N_4$)-based have been extensively considered due to their facile fabrication, excellent chemical and thermal stability, ideal band edge positions, ability for absorb light up to 460 nm, and unique structure. Despite these advantages, the high recombination rate, the absence of enough active sites, and limited response to visible light are the bottlenecks of the pristine $g\text{-}C_3N_4$. To overcome these inherent limitations, various advanced modification strategies were proposed, including morphological adjustment, modification of functional group, elemental doping, and developing homo/hetero junctions [2]. Regarding the above discussions, the photocatalytic activity of the fabricated nanocomposites based on modified $g\text{-}C_3N_4$ upon visible-light will be compared, including MCN/Sb_2MoO_6, $MCN/Ag/Ag_2WO_4/AgI$, $MCN/NiCr_2O_4$, MCN/Cu_3BiS_3, and MCN/Ce_2S_3 [4-9].

Experimental Section

The detailed preparation methods of the MCN/Sb_2MoO_6, $MCN/Ag/Ag_2WO_4/AgI$, $MCN/NiCr_2O_4$, MCN/Cu_3BiS_3, and MCN/Ce_2S_3 were reported elsewhere [4-8].

Results and Discussion

The crystal structure information of the catalysts were identified with X-ray diffraction pattern [4-9]. To study the surface microstructure and morphology of the samples, FE-SEM analyses were conducted. As shown in Figs, 1(a-f), the particles of Sb_2MoO_6, $Ag/Ag_2WO_4/AgI$, $NiCr_2O_4$, Cu_3BiS_3, and Ce_2S_3 have located on the modified $g\text{-}C_3N_4$.

In Figure 2, the photocatalytic performance was evaluated using tetracycline degradation rate constants. As noticed, the rate constant corresponds to the MCN/Sb_2MoO_6 (30%), $MCN/Ag/Ag_2WO_4/AgI$ (20%), $MCN/NiCr_2O_4$ (20%), MCN/Cu_3BiS_3 (30%), and MCN/Ce_2S_3 (20%) photocatalysts with a values of 884.7×10^{-4}, 457×10^{-4}, 668.2×10^{-4}, 276.7×10^{-4}, and 401×10^{-4} min^{-1} were 95.0, 49.0, 71.7, 29.7, and 43.1 folds of $g\text{-}C_3N_4$, respectively. Also, the MCN/Sb_2MoO_6 (30%), $MCN/Ag/Ag_2WO_4/AgI$ (20%), $MCN/NiCr_2O_4$ (20%), MCN/Cu_3BiS_3 (30%), and MCN/Ce_2S_3 (20%) nanocomposites presented superior performance upon visible light, which was 7.12, 3.70, 5.40, 2.23, and 3.23 premier than modified $g\text{-}C_3N_4$ in the degradation of tetracycline, respectively [4-8].

Conclusions

In summary, the deposited Sb_2MoO_6, $Ag/Ag_2WO_4/AgI$, $NiCr_2O_4$, Cu_3BiS_3, and Ce_2S_3 nanoparticles over the modified $g\text{-}C_3N_4$ boosted charges separation/transfer within $g\text{-}C_3N_4$, enhanced surface area, and improved the visible-light harvesting capability. Finally, regarding facile synthesis route, impressive activity, and high stability, the fabricated photocatalysts are promising materials for addressing energy and enviromental issues.
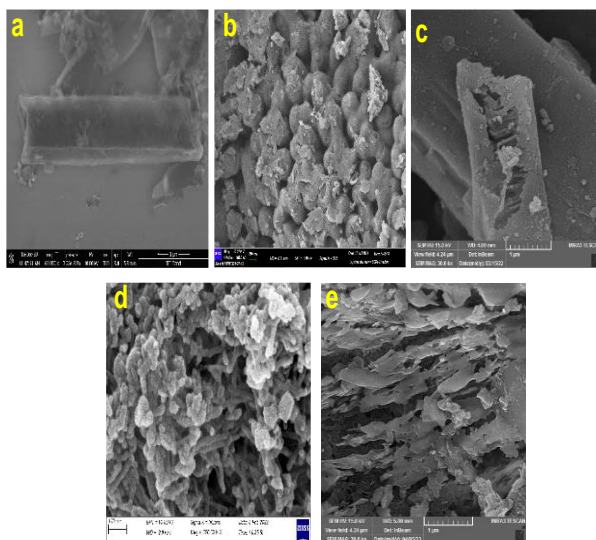
22nd Iranian Chemistry Congress (ICC22)
Iranian Research Organization for Science and Technology (IROST)
13-15 May 2024

03231-97589

Fig.1: FE-SEM images of (a) MCN/Sb$_2$MoO$_6$ (30%), (b) MCN/Ag/Ag$_2$WO$_4$/AgI (20%), (c) TCN/NiCr$_2$O$_4$ (20%), (d) MCN/Cu$_3$BiS$_3$ (30%), and (e) TCN/Ce$_2$S$_3$ (20%) systems.
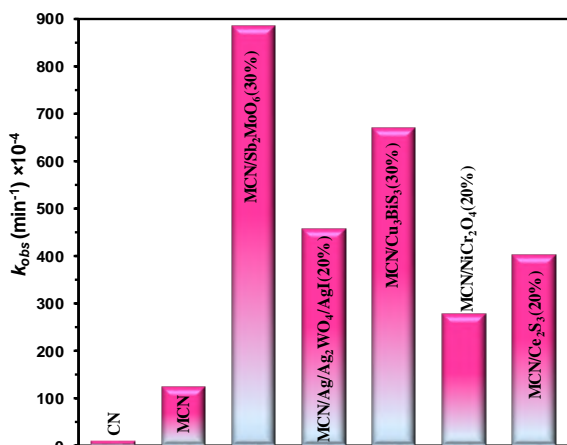

Fig.2: The removal rate constants of the studied systems.

References

[1] Habibi-Yangjeh, A., Pournemati, K., 2024. A review on emerging homojunction photocatalysts with impressive performances for wastewater detoxification. Critical Reviews in Environmental Science and Technology, 54, 290-320.
https://doi.org/10.1080/10643389.2023.2239125.

[2] Hemmati-Eslamlu, P., Habibi-Yangjeh, A., 2023. A review on impressive Z-and S-scheme photocatalysts composed of g-C$_3$N$_4$ for detoxification of antibiotics. FlatChem, 43, 100597.
https://doi.org/10.1016/j.flatc.2023.100597.

[3] Seifikar, F., Habibi-Yangjeh, A., 2024. Floating photocatalysts as promising materials for environmental detoxification and energy production: A review. Chemosphere (2024).
https://doi.org/10.1016/j.chemosphere.2024.141686.

[4] Hemmati-Eslamlu, P., Habibi-Yangjeh, A., Asadzadeh-Khaneghah, S., Chand, H., & Krishnan, V. (2021). Integration g-C$_3$N$_4$ nanotubes and Sb$_2$MoO$_6$ nanoparticles: impressive photoactivity for tetracycline degradation, r (VI) reduction, and organic dyes removals under visible light. Advanced Powder Technology, 32(7), 2322-2335.
https://doi.org/10.1016/j.apt.2021.05.007

[5] Hemmati-Eslamlu, P., Habibi-Yangjeh, A., Xu, X., Wang, C., & Khataee, A. (2022). Ultrasonic-assisted decoration of Ag$_2$WO$_4$, AgI, and Ag nanoparticles over tubular g-C$_3$N$_4$: Plasmonic photocatalysts for impressive removal of tetracycline under visible light. Photochemical & Photobiological Sciences, 21(7), 1201-1215.
https://doi.org/10.1007/s43630-022-00209-z

[6] Hemmati-Eslamlu, P., Habibi-Yangjeh, A., & Khataee, A. (2023). Anchoring spinel NiCr$_2$O$_4$ nanoparticles on tubular g-C$_3$N$_4$: Efficacious pn heterojunction photocatalysts for removal of tetracycline hydrochloride under visible light. Journal of Alloys and Compounds, 932, 167571.
https://doi.org/10.1016/j.jallcom.2022.167571

[7] Hemmati-Eslamlu, P., Habibi-Yangjeh, A., Akinay, Y., & Cetin, T. (2023). Novel g-C$_3$N$_4$ nanorods/Cu$_3$BiS$_3$ nanocomposites: Outstanding photocatalysts with pn heterojunction for impressively detoxification of water under visible light. Journal of Photochemistry and Photobiology A: Chemistry, 443, 114862.
https://doi.org/10.1016/j.jphotochem.2023.114862

[8] Hemmati-Eslamlu, P., Habibi-Yangjeh, A., & Khataee, A. (2024). S-scheme g-C$_3$N$_4$/Ce$_2$S$_3$ nanocomposites for visible-light activation of persulfate ions: Photocatalytic degradations of antibiotics and dyes. Journal of Photochemistry and Photobiology A: Chemistry, 453, 115622.
https://doi.org/10.1016/j.jphotochem.2024.115622

Professional approaches to synthesizing WZnO and TiO$_2$ materials for Photocatalytic activity and Catalytic

Parisa Sang Sefidi, Mohammad Zirak, Reza Tayebee[*], Zahra Jalili, Hossein Mohammadi Arakhlo

Corresponding Author E-mail : parisa.sss2020@gmail.com

Department of Chemistry, Faculty of Science, Hakim Sabzevari University, Sabzevar, Iran.

Abstract: This paper reviews professional approaches for the synthesis of WZnO and TiO$_2$ materials tailored for enhanced photocatalytic and catalytic activities. Various synthesis methods, including Hydrolysis, core-shell techniques, are discussed in detail. The impact of different parameters such as precursor concentration, reaction temperature, and post-treatment processes on the properties of WZnO and TiO2 materials is evaluated. Furthermore, the synergistic effects of combining WZnO and TiO$_2$ in composite structures for improved photocatalytic and catalytic performance are highlighted. This review aims to provide insights into the design and fabrication of advanced materials for sustainable environmental applications.
Keywords: Hydrolysis, core-shell , photocatalyst WZnO and TiO$_2$.

Introduction

Hydrolysis is a versatile method for synthesizing a wide range of products by reacting compounds with water. Researchers can control the properties of the final product through this process, making it a powerful tool in chemistry for creating simple molecules and complex polymers [1]. Core-shell synthesis involves coating a core material with a shell material to create a composite structure, commonly used in nanotechnology, catalysis, and drug delivery [2]. TiO2 and ZnO are semiconductor materials with unique properties - TiO2 is known for its photoactivity and stability, while ZnO has distinctive electronic and optical properties. When combined in a composite, TiO$_2$-WZnO exhibits enhanced photocatalytic activity and improved charge separation, showing promise for environmental and energy applications. Various synthesis methods like sol-gel, hydrothermal, and solvothermal are used to prepare TiO$_2$ nanoparticles with controlled properties, while techniques such as sol-gel, hydrothermal, and chemical precipitation are employed for ZnO nanoparticles to achieve tunable characteristics [3-4]. These methods enable control over the structural and morphological properties of TiO2 and ZnO nanoparticles for diverse applications. In this study, hydrolysis and core-shell methods produced the best results.

Experimental Section

1. "Preparation of TiO$_2$ Nanoparticles by Hydrolysis Method"

5 mL of titanium isopropoxide was dissolved in 50 mL of orange-colored isopropanol and stirred at room temperature for an hour. The initial pH was 2.70, increased to 8.3 with ammonia. After adding more ammonia to reach pH 8, 75 mL of deionized water was added, resulting in a slightly yellow solution. The mixture aged for three hours, then centrifuged, washed with deionized water and ethanol, and air-dried for four days, yielding a pale yellow deposit. Finally, it was oven-dried at 450 degrees for 2 hours.

2. The preparation of WZnO nanoparticles.

4.799g NaOH + 30ml deionized water, 4.39g zinc acetate + 20ml deionized water, 0.32986g Na2WO4.2H2O + 2ml deionized water. Colorless solutions. Mix Na2WO4.2H2O with zinc acetate, add NaOH dropwise. Stir suspension at room temp for 3 hours. Transfer to 250ml flask, heat at 95°C for 10 hours. Collect, wash, dry precipitate.

- Synthesis of particles by core-shell method.

Initially, 0.5487g of zinc acetate dihydrate (Zn(C2H4O2)2.2H2O) at a concentration of 10 mM was dissolved in 250mL of deionized water and stirred for 10 minutes. Then, 0.1997g of pre-synthesized TiO$_2$ nanoparticles, a mixture of 0.2g Zn(OAC)$_2$, 100mL deionized water, and 0.01g Na$_2$WO$_4$ were added and stirred for 30 minutes. The colorless initial solution was combined with the white second solution. Subsequently, 250mL of 0.1M NaOH solution was slowly added to the mixture, which was vigorously stirred for 5 hours. The resulting solution was heated at 97°C for 3 hours. The precipitate was separated via centrifugation, and any unreacted substances were removed using deionized water and acetone.

3. Composite synthesis.

2.5 ml titanium isopropoxide + 50 ml isopropanol, stirred for 1 hour. Then, mix 0.1 g zinc acetate + 0.005 g Na$_2$WO$_4$ + 50 ml deionized water for 30 mins. Dissolve 0.4999 g sulfur in 125 ml deionized water. Mix solutions, adjust pH from 3.56 to 8 with sulfur. Stir 5 hours, stand 3 hours, centrifuge. Heat at 125°C for 1 hour, then at 450°C for 2 hours.

22ⁿᵈ Iranian Chemistry Congress (ICC22)
Iranian Research Organization for Science and
Technology (IROST)
13-15 May 2024

03231-97589

IROST

Results and Discussion

The Raman spectrum of TiO2 shows peaks at 645 cm-1, 531 cm-1, and 410 cm-1 indicating anatase structure (Fig 1a). WZnO spectrum displays peaks at 324 cm-1 and 426 cm-1 for ZnO modes and 381 cm-1 for W-OH 2bond Fig 1b). TiO2-ZnO spectrum exhibits peaks at 145 cm-1, 398 cm-1, 517 cm-1, 641 cm-1 due to TiO_2 modes with slight shifts from ZnO (1c). The composite sample spectrum in Figure 1d lacks clear peaks, providing limited information.
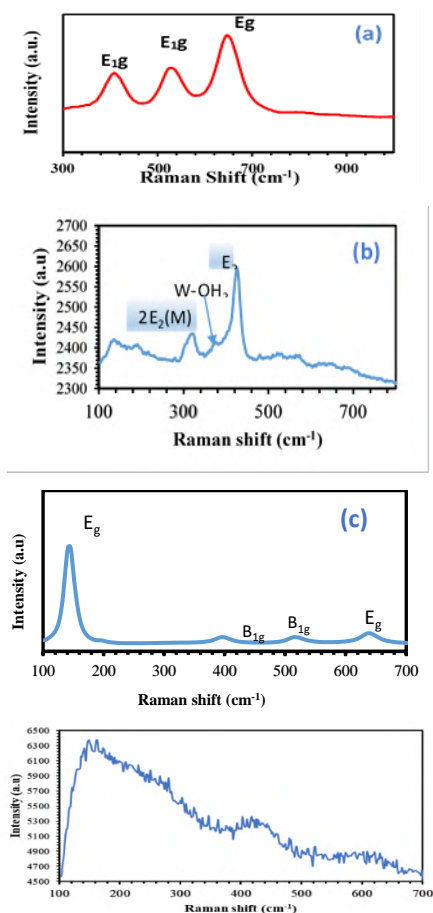
Fig. 1. The Raman spectrum belongs to a TiO_2 [a], WZnO [b], (TiO_2-WZnO) composite sample [d].

The XRD patterns of synthesized nanoparticles were analyzed as follows: WZnO nanoparticlesPeaks at 31.69, 34.36, 36.22, 47.45, 56.54, 62.78, 69.10 correspond to ZnO (Fig 2a). These peaks appear sharp and narrow.TiO_2 nanoparticles: Peaks at 25.37, 48.16 belong to TiO_2 in the anatase phase (Fig 2b). Core-shell sample: Peaks at 25.31, 33.25, 48.23, 55.34, 63.13 belong to TiO2 (Fig 2b). Peaks at 38.05, 59.90 belong to WO_3/ZnO (Fig 2b).These results confirm the successful synthesis of the desired samples. (Fig. 2).
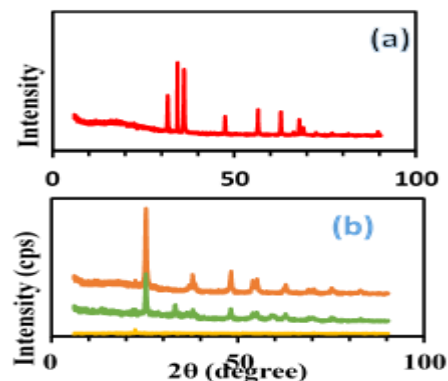
Fig. 2. XRD analysis of WZnO (a), TiO_2 Core-shell and composite, TiO_2-WZnO (b).

Conclusions

This review emphasizes professional synthesis strategies for enhancing the photocatalytic and catalytic activities of WZnO and TiO_2 materials. Various synthesis methods, including hydrolysis and core-shell techniques, are explored, along with the impact of parameters like precursor concentration and reaction temperature. The synergistic benefits of combining WZnO and TiO_2 in composite structures for superior performance are highlighted, offering valuable insights for developing advanced materials for sustainable environmental applications.

Acknowledgments

References

[1] Yan, P., Zhang, Y., & Zheng, S. Microscale spherical TiO2 powder prepared by hydrolysis of TiCl4 solution: Synthesis and kinetics. Particuology, 84, (2024). 60-71. https://doi.org/10.1016/j.partic.2023.03.004.

[2] Lv, Y., Liu, J., Zhang, Z., Zhang, W., Wang, A., & Tian, F.. Two-step liquid phase synthesis of ZnO@ CuO core–shell heterojunction nanorods arrays composites photodetectors with the enhanced UV photoelectric performances. Optics & Laser Technology, 168, (2024). 109958.https://doi.org/10.1016/j.optlastec.2023.109958

[3] Kanmani, S.S. Ramachandran, Synthesis K. and characterization of TiO2/ZnO core/shell nanomaterials for solar cell applications, Renewable Energy, 43 (2012) 149-156,https://doi.org/10.1016/j.renene.2011.12.014.Reader J.

Synthesis of sulfuric acid nanocatalysts stabilized on the Nanostructures of carbon and its catalytic property in the esterification process.

Samaneh Taheri, Farhad Kabiri esfahani, Babak Karimi[*]

Corresponding Author E-mail: karimi@iasbs.ac.ir

Abstract: Sulfuric acid plays a direct or indirect role in the production of almost all manufactured goods that humans use today. As a result of such widespread industrial use, large volumes of sulfuric acid waste are generated annually, posing severe environmental hazards. Although sulfuric acid recovery is technically possible and even used on an industrial scale, such processes are very expensive and therefore cannot be considered as a long-term solution as green chemistry. The aim of this study was to stabilize sulfonic acid on the carbon surface and after initial studies on the acidity and surface stability by various techniques, its catalytic properties as a solid acid in the process of esterification of carboxylic acid with various alcohols, which is of great importance in the industry, to be examined. Based on this, the GIOMC-SO₃H catalyst was synthesized and then obtained by various techniques such as porosity, scanning electron microscopy, Fourier-transform infrared spectroscopy and its acidic was obtained by titration of acid and base. The synthesized nanoparticles were examined in the process of esterification under solvent-free conditions at a temperature of 50 ° C.

Keywords: Green Chemistry; Ordered Mesoporous Carbon; Heterogeneous Acid Catalyst; Esterification

Introduction

Sulfuric acid, with an annual production of nearly 290 million tons, is the most important industrial chemical produced so far. The main consumers of H_2SO_4 are chemical industries, fertilizer production, followed by oil refineries, metal processing, and fiber and pulp industries. Due to the low cost of H_2SO_4, it has been used in chemical and metallurgical industries for various reactions and operations (as a catalyst) such as nitration, sulfonation, esterification and organic alkylation, as well as electrolysis, electroplating (H^+ conductor). In summary, H_2SO_4 plays a direct or indirect role in the production of almost all manufactured goods that we use today. As a result of such extensive industrial use, a large amount of H_2SO_4 waste is also produced annually (about 15 million tons of H_2SO_4 are consumed annually as non-recyclable sulfates), which causes severe environmental hazards and disposal problems.

Although the recovery of H_2SO_4 is technically possible and even used on an industrial scale, such processes are very expensive due to the energy consumption of distillation and regeneration processes, and therefore cannot be considered as a long-term solution and as green chemistry. The biggest drawback is the use of liquid acids as catalysts in chemical processes that complicate downstream product recovery as additional separation, purification, and detoxification measures to remove inactivated acids from the products. The study of recyclable solid acids as an environmentally friendly and "green" alternative to "non-recyclable liquid acids" such as H_2SO_4 is of great importance.

Until recently, one of the most important obstacles to the progress of research in the field of solid acid catalysis is the lack of a cost-effective material whose acid activity (strength, acid site concentration, H^+ conductivity, etc.), stability and Its cost is the same as liquid H_2SO_4.

Carbonic acid materials with functionality SO_3H or "sulfonite carbons" are a new member for the family of solid protonic acids, characterized by low production cost and high Brønsted acidity ($H_0 \leq -11$) at a level similar to concentrated H_2SO_4. These materials are considered by many experts as ideal alternatives to liquid H2SO4 in applications such as catalysis, electrocatalysis, water treatment, CO_2 absorption and energy storage due to features such as high chemical, mechanical and thermal stability, adjustable pore structure, and also having chemistry. The high level, especially the catalysis of large molecules and biomolecules, is one of the most interesting features in which sulfonated carbons are better than homogeneous mineral acids and solid acid catalysts (zeolites, ion exchange resins, sulfated metal oxides, etc.) [1].

Among various metal-free carbocatalysts, "sulfonated carbons (or sulfated carbons") are the most comprehensively studied carbocatalysts. Since their introduction in 2004 as solid acids by Hara et al., who obtained these materials. They have received considerable attention as a low-cost alternative catalyst for various organic transformations. This can be recognized by the rapid growth of the number of articles and patents filed in the preparation, description and

22nd Iranian Chemistry Congress (ICC22)
Iranian Research Organization for Science and Technology (IROST)
13-15 May 2024

03231-97589

ISC

IROST

applications of such acidic carbonic materials containing SO_3H since 2004. sulfonated carbons are generally prepared via sulfonation of incompletely carbonized organic matter or via semicarbonization of organic/carbon matter in strong sulfonating agents like concentrated H_2SO_4 [2].

Experimental Section

Preparation of Ordered Mesoporous Carbon (GIOMC): First, guanine (0.4 g) was slowly added to the ionic liquid 1-methyl-3-phenylethylimidazolium hydrogen sulphate (MPIHS) (2 g) until it was completely dissolved. Add guanine solution and ionic liquid (1ml) to SBA-15 (1g) to obtain a paste-like mixture. Then the silica/ionic liquid/guanine composite was heated to 900°C under argon atmosphere for 2 hours. In order to remove the hard template, the produced black powder was stirred in 50 ml of two molar sodium hydroxide solution at 50°C for 24 hours. Finally, after separating the mesoporous carbon, the product was first treated with sodium hydroxide solution (2 M, 20 ml) and then several times with deionized water and ethanol. Washed and dried under vacuum conditions [3].

Preparation of GIOMC-SO$_3$H catalyst:
In order to activate GIOMC Ordered mesoporous carbon, a 250 ml flask containing 0.04 grams of Ordered mesoporous carbon; 5 ml of concentrated sulfuric acid (98%) was added and the obtained mixture was stirred for 5 days at a temperature of 150°C on a magnetic stirrer under an argon atmosphere. After the completion of the reaction and cooling the contents of the balloon to room temperature, the reaction mixture was washed with warm distilled water (80°C) until the pH was almost neutral. After all impurities were removed, the catalyst was placed in an oven at 80°C for drying.

Results and Discussion

From the comparison of related to Figure 1: Nitrogen adsorption-desorption diagram data, it can be concluded that the structure of carbon mesopores did not change during sulfonation. As a result, sulfonation took place at a temperature of 150° while maintaining the original structure.
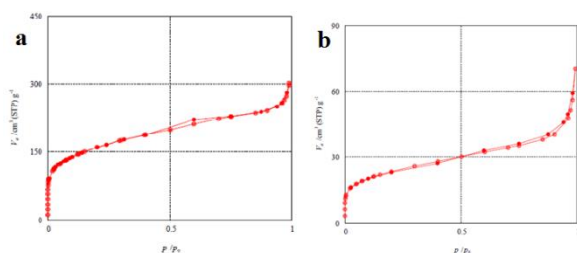
According to the BET calculations, the effective surface area of this composition was 82.0 m^2/g and its total pore volume was 0.11 m^3/g. From the comparison of the data related to GIOMC and GIOMC-SO$_3$H, it can be concluded that acidic groups are placed on the structure of the supported and have caused the surface area and volume of pores to decrease. The results of BJH calculations also show that the synthesized structure has uniform pores with a uniform distribution and an average diameter of 2.42 nm, which is the lower border region of mesoporous compounds. In order to determine the acid capacity of GIOMC-SO$_3$H catalyst, the titration method has been used. After confirming the synthesis of GIOMC-SO$_3$H compound, the catalytic property of this material was investigated in the process of esterification of benzyl alcohol and acetic acid.

Conclusions

The catalyst synthesized in this project "sulfonic acid stabilized on the surface of Ordered Mesoporous Carbon " has unique properties such as high surface chemistry, presence of Ordered pores, high density of acidic sites, high thermal, chemical, and mechanical stability. This catalyst is used in the esterification process of carboxylic acid and benzyl alcohol. The use of heterogeneous, metal-free carbocatalysts in organic reactions as well as electrochemical processes, in the realization of green chemical processes, and also in part as a result of reducing the sources of rare metals and rare alkalis, which are usually used as catalysts in industrial processes. It will have a bright future for this type of catalysts.

References

[1] *Chem. Rev.* 2019, 119, 22, 11576–11630. https://doi.org/10.1021/acs.chemrev.9b00199

[2] Angew. Chem. Int. Ed. 2004, 43, 2955 –2958. DOI: 10.1002/anie.200453947

[3] *ACS Appl. Mater. Interfaces* 2015, 7, 34, 19050–19059. https://doi.org/10.1021/acsami.5b03985

Fig. 2: Nitrogen adsorption-desorption diagram of GIOMC (a) and GIOMC-SO$_3$H (b)

Investigation of electronic and structural properties of B$_6$C$_6$ boron- graphyne

Forouzan Arashnezhad, Zabiollah mahdavifar*, Morteza Zare
Corresponding Author E-mail: z.mahdavifar@scu.ac.ir
Department of Chemistry, Faculty of Science, Shahid Chamran University of Ahvaz, Ahvaz, Iran.

Abstract: In this study, the stability and electronic properties of B$_6$C$_6$boron-graphyne structure was analyzed. Thermal stability was assessed through AIMD (Ab initio molecular dynamics) at the specified temperature. Electronic properties were evaluated via band structure analysis.

Keywords: Graphyne; boron; AIMD; band structure

Introduction

Graphene is an excellent and interesting nanomaterial due to its extraordinary properties, but its application has been limited because it does not have a bandgap[1]. Scientists have turned to graphyne and graphdiyne because they have a limited bandgap. Recent advances in the fabrication of layered materials from graphyne and graphdiyne have opened up new opportunities for scientific applications of these materials. In this work, we intend to investigate the combination of graphyne with boron and perform various analyses[2].

Computational Details

All the calculations in this study were performed with VASP. First, we optimized l structure by VASP at PBE level of theory. After optimization, other calculation was being done.

Results and Discussion

1: **AIMD simulations**: In the present work, *Ab initio* molecular dynamics (AIMD) simulations with canonical ensemble using the Nosé heat bath scheme were performed to evaluate the thermal stability of specific phases up to 300 K for 12 ps, see Figure 1. Radial distribution function (RDF) of sstructure is also presented, which reveal if the contacts between atoms .
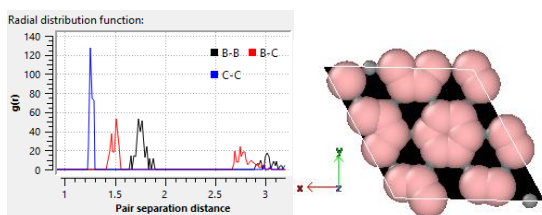

Fig.1: RDF (left panel) and snapshots (right panel) of the B6C6 at 0 GPa with 2 × 1 × 1 supercell (61 atoms) after 12 ps AIMD simulations at 300 K respectively. Large pink spheres are B atoms, and small gray spheres are C atoms. The single bonds C-C under 0 GPa are indicated by blue arrows in RDF

2: Electronic properties: Projected band structures and density of states (DOS) at PBE level. The colored bands of band structures indicate the atomic contributions to the band structure, from gold (high B contributions) to blue (high C contribution) see figure 2.

As it can see in Figure 2 The valence band maximum (VBM) and conduction band minimum (CBM) of B$_6$C$_6$ are -3.25 and -3.55 ev. Fermi level crosses the conductive bands, indicating that B6C6 is metallic at 0 GPa. The calculated metallic behaviour of B6C6 at 0 GPa has good agreement with the previous experimental report [3].
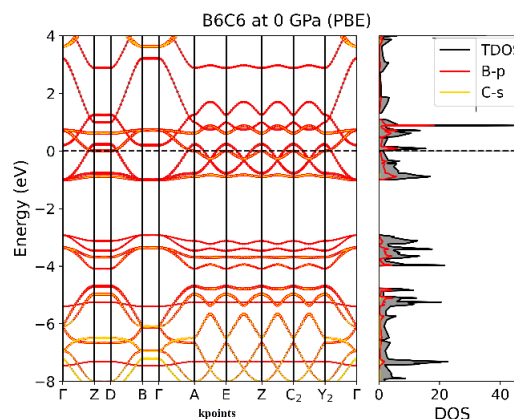

Fig.2: Band structure and DOS for *B$_6$C$_6$* at 0 GPa

Conclusions

We have extensively studied the B6C6 system at 0 GPa pressure.
The results suggest that the bonds in boron-graphyne compound are stable at 300K and have been preserved. Therefore, our compound is thermally stable. These results indicate a route to the design and stabilize of the boron- graphyne. The evaluation of the structure shown boron-graphyne is metallic.

References

[1] Ortega, I.F., Arellano, J.S, Gomez, T.N,. Ruiz, G.A, Garcia, V.A, (2022). DFT study for hydrogen storage on γ-Boron-Graphyne decorated with Li atoms ,*Computational and Theoretical Chemistry*,1214, 113764. https://doi.org/ 10.1016/j.comptc.2022.113764
[2] Mortazavi.B (2023). Electronic, Thermal and Mechanical Properties of Carbon and Boron Nitride Holey Graphyne Monolayers, *Materials*, 16(20)6642. https://doi.org/ 10.3390/ma16206642.
[3] Rao, C.N.R , Gopalakrishnan, A, (2014). Synthesis, properties and application of graphene doped with boron, nitrogen and other elements, *Nano Today*, 9(3) 324.

22nd Iranian Chemistry Congress (ICC22)
Iranian Research Organization for Science and Technology (IROST)
13-15 May 2024

03231-97589

IROST

Overcoming Limitations in CO₂ Conversion by Ethaline -Based Electrolyte

Afsaneh Azhdeh *[a], Ali Reza Harifi-Mood [b]

Corresponding Author E-mail: afsaneh.azhdeh@gmail.com

[a] Research and development, Sanat Afarin Mahan Asia Co., Alborz, Iran.

[b] Department of Physical Chemistry, Faculty of Chemistry, Kharazmi University, Tehran, Iran.

Abstract: Deep Eutectic Solvents (DES) offer innovative solutions to address major constraints in electrochemical reduction. They make it easier for carbon dioxide to dissolve, make it easier to choose the right product, and stop the competing electrochemical reaction of hydrogen evolution in the range of potentials for carbon dioxide reduction. Ultimately, these limitations enhance the energy efficiency of carbon dioxide conversion. Ethaline (a mixture of choline-chloride ([Ch] Cl) and ethylene glycol (EG) in a 1:2 ratio) as an electrolyte has observed a highly selective conversion of CO_2 to CO with a faradaic efficiency of 95 ± 5% at -1.4 V vs. Ag/AgCl. Using Ethaline as an electrolyte, the CO_2 conversion is increased by about 45% compared to 0.5 M $KHCO_3$ media.

Keywords: CO₂ Conversion.; Ethaline; Electrolyte

Introduction

Global warming and climate change are caused by excessive anthropogenic activities and fossil fuel combustion, which release greenhouse gases (mostly CO_2). Environmentally beneficial technologies, including CO_2 collection, utilization, and storage (CCUS), are investigated by researchers [1]. Electrochemical reduction of carbon dioxide is a viable solution to climate change caused by greenhouse gas emissions. Carbon dioxide (CO_2) doesn't dissolve easily in either water or organic electrolytes, so it can't get to the electrode surface to be captured and changed. Hydrogen evolution reaction (HER) is one of the key competitive (often simultaneous) processes limiting electrochemical CO_2 reduction (ERCO₂) performance. This competition between ERCO₂ and H_2O/H^+ (HER) decreases the energy efficiency of CO_2 conversion, reaction product selectivity, and industrial application [2]. Modifying the electrolyte composition is a primary strategy to reduce the overpotential and enhance the selectivity of the ERCO₂ reaction. Deep eutectic solvents (DESs) have demonstrated potential in the absorption of greater quantities of carbon dioxide (CO_2) compared to the standard solvents employed for CO_2 sequestration. Deep eutectic solvents (DESs) are made by mixing a hydrogen bond donor (HBD) and a hydrogen bond acceptor (HBA) component in the right amount to make sure there are no unwanted by-products that need to be cleaned up even more [3].

Experimental Section

Ethaline ([Ch] Cl/EG) electrolyte was prepared in a round-bottomed flask by combining them in a 1:2 molar ratio. The mixture was then heated at 65 °C with continuous stirring until a uniform electrolyte solution was obtained.

In the cathodic chamber, after immersing Ag/AgCl (3 M KCl) reference, the Ag plate (1×1 cm) working electrode was immersed in 5 mL Ethaline. In the anodic chamber, the counter electrode is in a 5 mL 0.5 M KHCO3 electrolyte solution. The following cell was saturated by expelling CO_2 gas for 30 minutes. The cyclic voltammetry (CV) on the Ag electrode was recorded in Ar and CO_2 at 0.0 to -1.7 V vs. Ag/AgCl for 0.5 M $KHCO_3$ aqueous solution and Ethaline at 100 mV/s. All experiments were performed at room temperature.

Faradaic efficiency (FE CO%) was obtained by using the following formula:

$$(FE\ CO\%) = \frac{znF}{It} \times 100 \tag{1}$$

G where z represents the number of electrons and n represents the number of carbon moles that are obtained from GC, the Faradaic constant (C/mol), and the total current density at the time of sample collection (mA/cm2), the time for sample collection from the electrochemical cell(s). as products (CO) were analyzed at the end of steady-state potentiation CO_2 electrolysis at electrolytes.

Results and Discussion

Figure 1 displays the cyclic voltammetry (CV) results of the Ag working electrode in 0.5 M $KHCO_3$ aqueous solution and Ethaline electrolyte solution that were saturated with argon (Ar) and CO_2 for duration of 30 minutes. The cathodic current density in ethyl ether saturated with argon is around -1.1 mA/cm², and the current density rises to nearly three times that amount (-6.5 mA/cm²) when ethyl ether is saturated with CO_2 at a potential of -1.7 V versus Ag/AgCl. It's possible that the Ag electrode can help reduce CO_2 because it caused a big rise in the

22nd Iranian Chemistry Congress (ICC22)
Iranian Research Organization for Science and Technology (IROST)
13-15 May 2024

03231-97589

ISC

IROST

cathodic current in Ethaline after CO_2 was removed. The onset potentials of two experimental electrolytes were compared. They were CO_2 saturated 0.5 M $KHCO_3$ and Ethaline. Ethaline has a much higher selectivity at -1.4 V compared to Ag/AgCl. Indeed, its selectivity is 45% higher than that of 5 M $KHCO_3$. The appearance of this adsorption peak not only shows that the current density has gone up, but it also shows that CO_2 is being reduced effectively in the electrochemical system by making CO.

electrolyte to expedite the conversion of CO_2 into other valuable fuel materials.

References

[1] Lee, G., Li, Y.C., Kim, JY. et al. Electrochemical upgrade of CO2 from amine capture solution. Nat Energy 6, 46–53 (2021). Doi:10.1038/s41560-020-00735-z.

[2] Maniam KK, Paul S. Ionic Liquids and Deep Eutectic Solvents for CO2 Conversion Technologies- A Review. Materials (Basel) 14(16):4519 (2021). Doi:10.3390/ma14164519.

[3] Ahmed Halilu, Mohamed Kamel Hadj-Kali, Mohd Ali Hashim, Rozita Yusoff, Mohamed Kheireddine Aroua. Bifunctional Ionic Deep Eutectic Electrolytes for CO2 Electroreduction. ACS Omega 7 (42), 37764-37773 (2022). Doi: 10.1021/acsomega.2c04739.

s

Fig.1. Cyclic voltammograms; saturated with (black line) and CO_2 (green line) for 30 min electrolyte (a) Ethaline ([Ch] Cl/EG (1:2)), (b) 0.5 M $KHCO_3$, Insets: Faradaic efficiency of CO obtained during potentiation electrolysis in the presence of CO_2 in each case.

Table1: Summary reduction potentials for the CO_2RR and FE% CO of DES and $KHCO_3$ as electrolytes

Cathodic Electrolyte	E (V vs. Ag/AgCl)	FE CO%
Ethaline ([Ch] Cl/EG)	-1.4	95%
$KHCO_3$	-1.4	56%

Conclusions

Basically, choline ions at the catalyst-electrolyte interface stop the release of hydrogen by blocking the sources of protons, which is not what you want. In addition, DESs improve the product's selectivity (with a 95 ± 5% FE CO%) and boost the current density in the CO_2 process compared to an aqueous solution. By altering the electrode with catalysts, we may utilize the benefits of the

Theoretical Study of the Structure of Pyridine-2-methylene Isonicotinohydrazide Based on DFT Function

Mirtamizdoost Babak, Latifi Fatemeh[*]

Corresponding Author E-mail: Latifi.1995.fl@gmail.com

Department of Chemistry, Faculty of Science, University of Qom, Qom, Islamic Republic of Iran.

Abstract: In this research, the structure of pyridine-2-methylene-isonicotinoic hydrazide compound is optimized using Gaussian and Gaussian software, and then orbital calculations and energy levels and its absorption spectra will be performed and optimized using the density function theory and practical suggestions for its coordination method will be proposed to the metal centers.

Keywords: structure study; pyridine-2-methylene-isonicotinoo hydrazide; density function theory; organic compound; theory study; Schiff base

Introduction

Theoretical studies on organic and inorganic compounds are a suitable method for predicting the synthesis and behavior of these compounds. One of the common methods for investigating the structure and predicting the behavior of structures is the use of computational chemistry and DFT density functional theory[1]. The importance of choosing the DFT method is that this method is not just a method to solve the Schrödinger equation or to parametrize the experimental results, but it is different from other methods and by assuming a simpler problem of non-interacting systems and generalizing it to interacting systems, it is solved issues[2]. In this research, the structure of pyridine-2-methylene-isonicotino hydrazide compound is discussed. At first, the structure of the compound is optimized using Gaussian and Gaussian software, and then orbital calculations and energy levels and its absorption spectra will be performed[3]. The reason for choosing this material is due to its use as models for biological systems, its antimicrobial property, as well as its ease of preparation and structural diversity. The compound in question is a Schiff base which is formed from the condensation reaction between an amine of the first type and a carbonyl compound[4]. These compounds are stable compounds due to coordination with metals[5]. Another reason for the attention of these compounds is their ability to absorb and de-absorb oxygen, the ability to form complexes with some toxic metals, catalytic activity in the hydrogenation of alkenes, antiviral activity, anti-tuberculosis, anti-bacterial, anti-viral acquired immunodeficiency properties. photochromism and thermochromism and other applications in many fields such as oxidation and electrochemistry[6]. Finally, the structure of the compound will be optimized using the density function theory and practical suggestions for its

coordination method will be proposed to the metal centers[7].

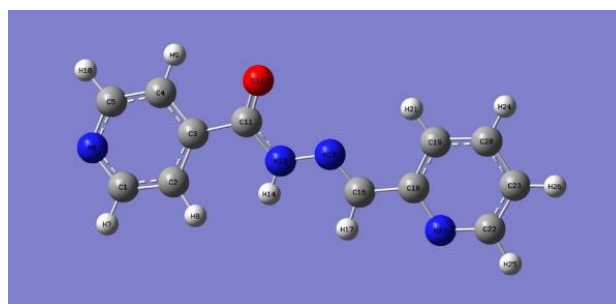## The Results of the Software and Discussion
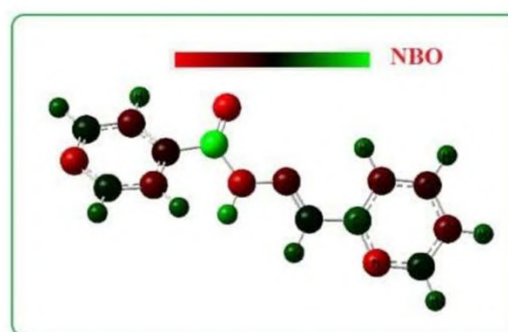

Fig1: Optimized structure of the molecule

Fig2: Graphical image of electron delocalization in the molecule

The results of NBO analysis have been performed using B3LYP/6-31G theoretical level calculations to investigate the structural behavior of the compound. In fact, NBO performs the analysis of multi-electron wave functions in the form of bond pairs. In the calculations of this method, the first order matrix of reduced density of wave functions is used. For this reason, this method is used in general mathematical forms of wave functions. In the NBO

22nd Iranian Chemistry Congress (ICC22)
Iranian Research Organization for Science and Technology (IROST)
13-15 May 2024

03231-97589

IROST

method, electron wave functions are discussed in terms of a group of occupied Lewis orbitals and a group of unoccupied Lewis orbitals. Because the lack of non-covalent destabilization between the electron donor and acceptor orbitals are combined, therefore Lewis acid or Lewis base is used to explain them.

Changes in the local electron kinetic energy and its Laplacian represent the local changes of the density gradient vector and the local redistribution of charge and energy in the proposed systems. The charge density around each atom causes the lines to be condensed.
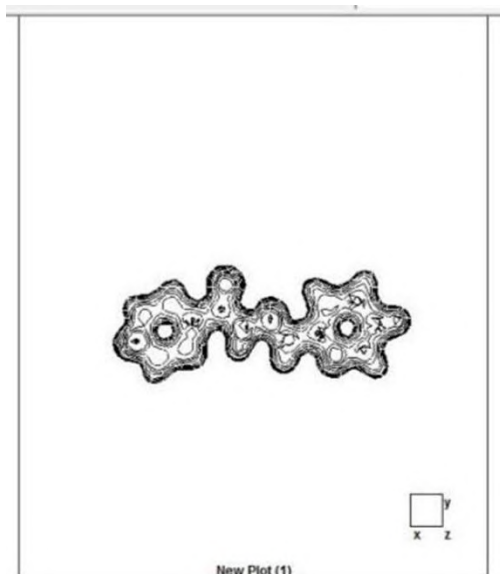
Fig3: Kinetic energy
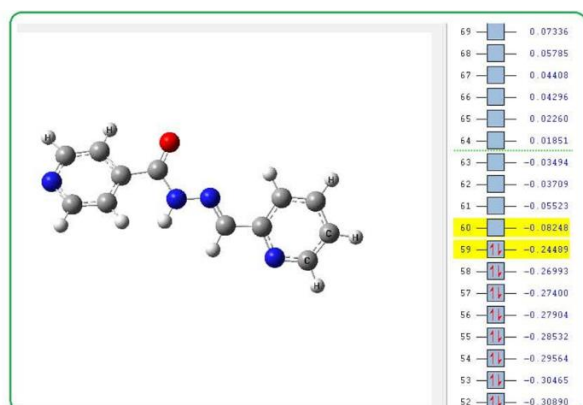
Fig4: HOMO and LUMO energy levels of the molecule

The HOMO orbital, which is actually the highest occupied molecular orbital, and the LOMU orbital, which is the lowest molecular orbital that is not occupied, are of particular importance, because the HOMO orbital, as an ionization potential, has the ability to give electrons in the molecule, and the LUMO orbital, as an electron-withdrawing potential, has the ability captures electrons

in the molecule. Therefore, according to the definition, electron donor and electron acceptor molecules can be identified from each other.

References

[1] Gu¨tlich P, Ensling J (1999) Inorganic electronic structure and spectroscopy. Wiley, New York

[2] Jaszewski AR, Stranger R, Pace RJ (2008) Time-dependent DFT studies of metal core-electron excitations in Mn complexes. J Phys Chem A

[3] Seth M, Ziegler T, Banerjee A, Autschbach J, van Gisbergen SJA, Baerends EJ (2004) Calculation of the A term of magnetic circular dichroism based on time dependent-density functional theory I. Formulation and implementation. J Chem Phys

[4] Neese F (2008a) Calculation of molecular spectra and molecular properties with density functional theory: from fundamental theory to exchange coupling. Coord Chem Rev

[5] Neese F (2004) Definition of corresponding orbitals and the diradical character in broken symmetry DFT calculations on spin coupled systems. J Phys Chem Solids

[6] Koch W, Holthausen MC (2000) A chemist's guide to density functional theory. Wiley-VCH, Weinheim

[7] Stratmann RE, Burant JC, Scuseria GE, Frisch MJ (1997) Improving harmonic vibrational frequencies calculations in density functional theory. J Chem Phys

22nd Iranian Chemistry Congress (ICC22)
Iranian Research Organization for Science and Technology (IROST)
13-15 May 2024

03231-97589

IROST

Ultrasound-Based Nano-Encapsulation of Geranium Essential Oil in Alginate Biopolymer: A Controlled Release system

Soraya Ghayempour

Corresponding Author E-mail: s,ghayempour@yazd.ac.ir

Department of Textile Engineering, Faculty of Engineering, Yazd University, Yazd, Iran.

Abstract: In this work, an ultrasound-based method was used for encapsulation of Geranium essential oil in alginate biopolymer to increasing their durability and controlling release. The encapsulation efficiency of 94.5 %, the loading percentage of 17 % and controlled release of essential oil during 13 h stirring are the important results of the prepared drug delivery system.

Keywords: Encapsulation; Geranium essential oil; Alginate; Controlled release

Introduction

Geranium, an annual or biennial herb belongs to the Geraniaceae family, is flowering plant native to South Africa but is also grown in many regions of world. It is composed from phenolic constituents, tannins, flavonoids and phenolic acids [1]. Geranium essential oil is an important agent in the cosmetic, aromatherapy, and food industries. It also has been used as a traditional medicine due to its anti-inflammatory, antibacterial and antioxidant properties [2]. Application of volatile essential oils is difficult due to uncontrollable dosage and instability against environmental factors such as air, light and high temperatures. They can be encapsulated in a polymeric wall to increasing durability and controlling release of them [3, 4]. In this work, Geranium essential oil was encapsulated in alginate biopolymer an ultrasound-based method in presence of emulsifier and cross-linking agent.

Experimental Section

The encapsulation process was started through prepare a mixture of sodium alginate, Geranium essential oil and Triton X-100 and sonicate with a 400 W and 24 kHz ultrasonic homogenizer (UP400S, Hielscher, Germany) coupled to a 7 mm sonotrode. Calcium chloride as the cross-linking agent was added to the prepared microemulsion and sonication was continued to obtain nanocapsules containing Geranium essential oil. The prepared nanocapsules were centrifuged using a Iranian RST 24&16 centrifuge. Finally, they were washed with deionized water and dried at room temperature. The surface morphology of the prepared nanocapsules was investigated by a VEGA2-TESCAN Field emission scanning electron microscope (FESEM) device.

Results and Discussion

The FESEM image of the alginate nanocapsules containing Geranium essential oil is showed in Figure 1. The prepared nanocapsules indicated spherical shape with smooth surface and average size of 90 nm.

In order to determine the encapsulation efficiency (EE), the weight of the obtained nanocapsules ($W_{Nanocapsules}$) and the raw materials including sodium alginate, Geranium essential oil and cross-linking agent ($W_{Raw\ materials}$) were measured and the efficiency was calculated using the equation 1.

$$EE\ (\%) = \frac{W_{Nanocapsules}}{W_{Raw\ materials}} \times 100 \qquad (1)$$

The results showed the Geranium essential oil was successfully encapsulated in the alginate biopolymer with the encapsulation efficiency of 94.5 %.
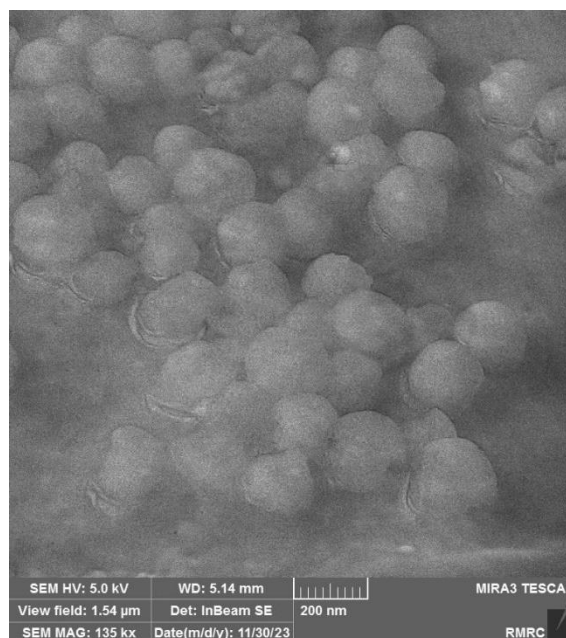

SEM HV: 5.0 kV	WD: 5.14 mm		MIRA3 TESCAN
View field: 1.54 µm	Det: InBeam SE	200 nm	
SEM MAG: 135 kx	Date(m/d/y): 11/30/23		RMRC

Fig.1: FESEM image of the alginate nanocapsules containing Geranium essential oil

The release of Geranium essential oil from nanocapsules was studied by measuring the UV spectra of their solution during different stirring times. For this purpose, the

22nd Iranian Chemistry Congress (ICC22)
Iranian Research Organization for Science and Technology (IROST)
13-15 May 2024

03231-97589

intensity of absorption peaks at 238 nm as the maximum peak were measured at different times of stirring. Figure 2 indicates the changes of intensity versus various stirring times.
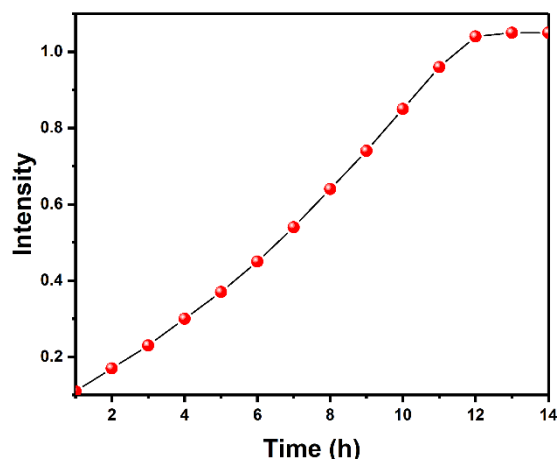

Fig.2: The changes of intensity versus various stirring times

As observed, the absorption peak intensity increases regularly with increasing stirring time and become constant after 13 hours. The released essential oil from nanocapsules can be calculated according to the amounts of intensity. As seen in Table 1, Geranium essential oil was controlled released from the nanocapsules into soultion during a relative long stirring time of 13 h.

Table1: The release of Geranium essential oil from nanocapsules

Time (h)	Intensity	Released essential oil (%)
1	0.11	10.5
2	0.17	16.2
3	0.23	21.9
4	0.30	28.6
5	0.37	35.2
6	0.45	42.9
7	0.54	51.4
8	0.64	61.0
9	0.74	70.5
10	0.85	81.0
11	0.96	91.5
12	1.04	99.0
13	1.05	100
14	1.05	100

In order to determine the loading percentage (LP) of Geranium essential oil in nanocapsules, a certain weight of nanocapsules (W_1) was dissolved in acetone. Then it was stirred for 1 hour and dried after water evaporation. Finally, after measuring the weight of the resulting powder (W_2), the loading percentage of Geranium essential oil in nanocapsules was calculated using equation 2.

$$LP\ (\%) = \frac{W_1 - W_2}{W_2} \times 100 \qquad (2)$$

The loading percentage of Geranium essential oil in alginate nanocapsules was 17 % indicating an appropriate loading percentage for a volatile essential oil.

Conclusions

The proposed solution for increasing durability and controlling release of volatile essential oils is their encapsulation in a polymeric wall. For this purpose, Geranium essential oil was encapsulated in sodium alginate as a biopolymer. The results indicated the prepared nanocapsules successfuly synthesized with encapsulation efficiency of 94.5 %. Also, they can be used as the delivery system due to the good controlled release of essential oil during 13 h.

References

[1] Graça, V. C., Barros, L., Calhelha, R. C., Dias, M. I., Carvalho, A. M., Santos-Buelga, C., ... & Santos, P. F. (2016). Chemical characterization and bioactive properties of Geranium molle L.: from the plant to the most active extract and its phytochemicals. *Food & function*, *7*(5), 2204-2212.

[2] Kobayashi, Y., Sato, H., Yorita, M., Nakayama, H., Miyazato, H., Sugimoto, K., & Jippo, T. (2016). Inhibitory effects of geranium essential oil and its major component, citronellol, on degranulation and cytokine production by mast cells. *Bioscience, Biotechnology, and Biochemistry*, *80*(6), 1172-1178.

[3] Ghayempour, S., Montazer, M., & Rad, M. M. (2016). Encapsulation of Aloe Vera extract into natural Tragacanth Gum as a novel green wound healing product. *International journal of biological macromolecules*, *93*, 344-349.

[4] Ghayempour, S., & Mortazavi, S. M. (2015). Preparation and investigation of sodium alginate nanocapsules by different microemulsification devices. *Journal of Applied Polymer Science*, *132*(17).

22nd Iranian Chemistry Congress (ICC22)
Iranian Research Organization for Science and Technology (IROST)
13-15 May 2024

03231-97589

IROST

Trapping Formic Acid from Ether As a Degradation Intermediate and Its Unique Applications

Hadi Yari [a], Mousa Ramdar [a], Foad Kazemi[*a,b]

Corresponding Author E-mail : kazemi_f@iasbs.ac.ir

[a] Department of Chemistry, Institute for Advanced Studies in Basic Sciences (IASBS), Gava Zang, 49195-1159 Zanjan, Iran.

[b] Center for Climate and Global Warming (CCGW), Institute for Advanced Studies in Basic Sciences (IASBS), Gava Zang, 45137-66731 Zanjan, Iran.

Abstract: This study explores the use of ethers, as novel formylating agents under various photocatalytic , photochemical, and non-photo-induced conditions. The research focuses on trapping and utilizing formic acid as a photodegradation intermediate, presenting a fresh approach to transform degradation byproducts into value-added products. The reactions resulted in the production of the respective formamides with high yields, all achieved under straightforward and gentle operating conditions.

Keywords: Formic Acid;Amines; Photochemistry; Formylation

Introduction

Utilizing photochemical and photocatalytic synthesis is considered an effective strategy to address environmental pollution and the global energy crisis, as it efficiently converts solar energy into chemical energy (1) . Within the realm of photocatalysis research, significant efforts are directed towards developing environmentally friendly photocatalytic materials exhibiting superior activity. Among these, TiO2 stands out as a highly promising catalyst with diverse applications in chemical reactions (2). It has been employed as a catalyst in oxidative ,reductive and radical reactions. Literature analysis indicates that ethers can engage in photocatalytic radical reactions in the presence of TiO2 (3). Specifically, sunlight-induced reactions of ethers with heterocyclic bases in the presence of TiO2 have been conducted (4) . Furthermore, three-component coupling reactions involving cyclic and noncyclic ethers, aldehydes, and amines using TiO2–(NH4)2S2O8 as a catalyst under UV light irradiation have also been documented (5). N-formylation of amines holds significant importance as a pivotal reaction in organic synthesis . Formamides serve as essential chemical feedstock for the production of valuable heterocycles, drug molecules, materials, agrochemicals, and various natural products (6).

Experimental Section

The photocatalytic reactions were conducted in a round-bottom Pyrex flask and exposed to sunlight or 400 nm LED light, while being stirred using a magnetic stirrer. The reactions took place in the presence of TiO2–P25 (30 mg) in 5 ml of dioxane and 0.05 mmol of an aromatic amine, with irradiation lasting between 6 to 24 hours under varying conditions. The reactions were carried out in an oxygen atmosphere using an oxygen balloon. Product yields were assessed by monitoring using gas chromatography.

Results and Discussion

In our assessment, the in situ formed formic acid during the photocatalytic degradation of ethers could serve as a formylating agent for amines. Accordingly, aniline, sunlight, and titania were selected as the aromatic compound, light source, and catalyst, respectively, in an aerobic oxidation model reaction. Initially, to achieve environmentally friendly conditions based on our unpublished findings and in line with green principles, diglyme was employed as a green ethereal solvent in the reaction. Aniline (0.1 mmol) was dissolved in 5 ml of diglyme, and the reaction was conducted in the presence of 40 mg of TiO2 under aerobic conditions. The reaction was carried out under sunlight irradiation for 6 hours. Under these conditions, two products were obtained, as confirmed by TLC, NMR, CHN, and GC analyses, revealing the surprising formation of formanilide and nitrobenzene as products with yields of 23% and 4%, respectively.

In order to expand substrate scopes after obtaining optimized condition, other aniline derivatives were successfully used in the reaction (Table 2). The best yields were observed for halogenated anilines. 4-Bromoaniline (Table 2, entry 4), 3-chloro-2-methylaniline (Table 2, entry 5), 3-chloro-4-flouroaniline (Table 2 entry 6) and 3-chloroaniline (Table 2,entry 9) were successfully used in the reaction. 3-Chloro-4-flouroaniline showed the highest conversion (99 %) and selectivity (98 %) (Table 2, entry 6). 2-Nitroaniline didn't show any conversion at these conditions (Table 2, entry 10). For 4-nitroaniline, there was just 28 % conversion and 86 % selectivity (Table 2,

entry 11). N-Methylaniline and diphenylamine as secondary amines were also used in the optimized condition. Interestingly, oxidation of methyl group was done for N-methylaniline and, formanilide was produced as major product in this condition (Table 2, entry 12).

In order to consider the mechanism of the photochemical condition and to study the existence of $O_2^{-\bullet}$ intermediate in the reaction mechanism, 0.1 mmol benzoquinone was used in the photochemical reaction, in the presence of 400 nm LED to trap the $O_2^{-\bullet}$ (7) . After the reaction,formamide was produced and it can be concluded that no $O_2^{-\bullet}$ has beenproduced in the reaction. These results may be caused through 1,4-dioxane radical formation in this condition and this radical can react with oxygen and produce 1,4-dioxan-2-hydroperoxide . (8) (9)

Table 1. Photocatalytic and photochemical synthesis of formamides in dioxane.

Ent.	R^1	R^2	Yield(%)	Con.(%)	Sel.(%)
1	H	H	87	100	87
2	4-Me	H	70	85	81
3	4-OMe	H	73	86	85
4	4-Br	H	78	82	95
5	3-Cl-2-Me	H	87	93	94
6	3-Cl-4-F	H	97	99	98
7	2-Me	H	74	86	88
8	3-OMe	H	62	69	90
9	3-Cl	H	81	89	92
10	2-NO$_2$	H	0	0	-
11	4-NO$_2$	H	24	28	86
12	H	Me	37	38	98

Conclusions

In summary, the synthesis of formamides was carried out under various conditions using ethers as the formylating agent through the trapping of in situ formed formic acid. In a groundbreaking study, TiO2 was utilized as a photocatalyst, enabling the formylation of different amines with both electron withdrawing and electron donating groups under sunlight irradiation. The capture of photodegradation intermediates of ethers offers a promising approach for converting these intermediates into value-added products under mild conditions, employing sunlight as the primary energy source. Successful utilization of diglyme, dioxane, and THF as solvents and formylating agents was demonstrated. Moreover, in a significant advancement, the first-ever photochemical formylation reaction of amines was achieved under visible 400 nm LED irradiation in dioxane. Finally, in the exploration of peroxide radical intermediates, the successful formylation of amines in non-photochemical conditions was achieved using APS.

References

[1] R. Daghrir, P. Drogui, D. Robert, Modified TiO2 for environmental photocatalytic. applications: a review, Ind. Eng. Chem. Res. 52 (2013) 3581–3599.

[2] T. Caronna, C. Gambarotti, L. Palmisano, C. Punta, F. Recupero, Sunlight-induced. reactions of some heterocyclic bases with ethers in the presence of TiO2: a green route for the synthesis of heterocyclic aldehydes, J. Photochem. Photobiol. A: Chemistry 171 (2005) 237–242.

[3] M. Behpour, V. Atouf, Study of the photocatalytic activity of nanocrystalline S, N-. codoped TiO2 thin films and powders under visible and sun light irradiation, Appl. : Surf. Sci. 258 (2012) 6595–6601.

[4] M.A. Kakroudi, F. Kazemi, B. Kaboudin, β-cyclodextrin–TiO2: green nest for. reduction of nitroaromatic compounds, RSC adv. 4 (2014) 52762–52769.

[5] M. Hosseini-Sarvari, H. Sharghi, ZnO as a new catalyst for N-formylation of amines. under solvent-free conditions, J. Org. Chem. 71 (2006) 6652–6654.

[6] B. Alcaide, P. Almendros, C. Aragoncillo, β-Lactams: versatile building blocks for. he stereoselective synthesis of non-β-lactam products, Chem. Rev. 107 (2007) : 4437–4492.

[7] Rodriguez, E. M., Marquez, G., Tena, M., Álvarez, P. M., & Beltrán, F. J. (2015). Determination of main species involved in the first steps of TiO2 photocatalytic degradation of organics with the use of scavengers: The case of ofloxacin. Applied Catalysis. B: Environmental, 178, 44-53.

[8] Zhang, Y., Wang, Z., & Lang, X. (2017). Merging visible light photocatalysis of dye-sensitized TiO 2 with TEMPO: the selective aerobic oxidation of alcohols. Catalysis Science & Technology, 7(21), 4955-4963.

[9] Xia, X., Zhu, F., Li, J., Yang, H., Wei, L., Li, Q., ... & Zhao, Q. (2020). A review study on sulfate-radical-based advanced oxidation processes for domestic/industrial wastewater treatment: degradation, efficiency, and mechanism. Frontiers in Chemistry, . 8, 592056.

Synthesis of 6',8'-diisocyano-7'-phenyl-3'H-spiro [indene-2,2'- [1,2,4] triazolo[1,5-a] pyridine]-1,3,5'(1'H)-trione derivatives under microwave irradiation

Shahrzad Mahdavi Aliabad, Ali Darehkordi *, Abbas Ebrahimi marj

Corresponding Author E-mail: darehkordi@vru.ac.ir

Department of Organic Chemistry, Faculty of Chemistry, Vali-e-Asr University, Rafsanjan, Iran.

Abstract: In this research, Spiro triazole molecules using 6,1-diamino-4-aryl-2-oxo-2,1-dihydropyridine-5,3-dirbonitrile and ninhydrin derivatives under high efficiency microwave irradiation, short duration and high purity were synthesized. Determination of the new structure was done using FT-IR and NMR spectral data.

Keywords: Spiro.; Microwave irradiation; Triazole
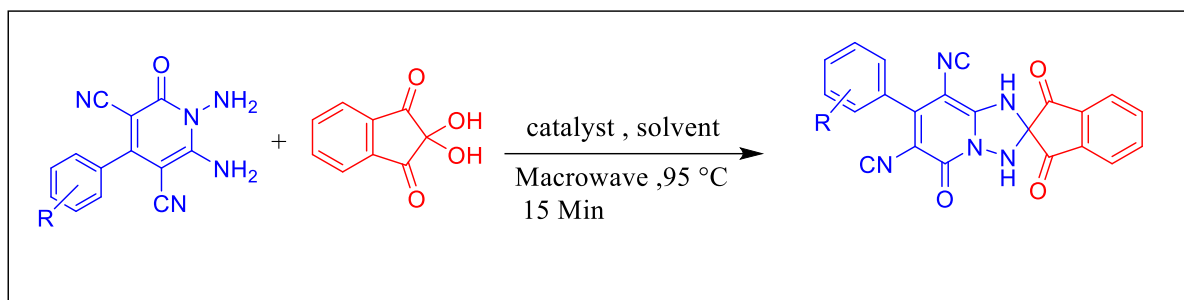
Introduction

Antibiotic resistance is a global challenge that requires new solutions, such as azoles. Azoles are remarkable compounds with diverse applications in medicine, including antifungal, antiviral, antibacterial and antitumor properties. The azole molecule exists in two spatial isomers, and 1,2,4-triazole is considered more important in pharmacology due to its synthetic application and broad biological activity. Several commercial drugs, such as triazolam, sitagliptin, maraviroc and defrasirox contain triazole ring [1-3]. Spiro compounds have attracted the attention of chemists due to their cyclic structure and unique biological properties, including antibacterial, antifungal and anticancer activity. Also, Spiro triazole derivatives have received much attention due to their specific structure and biological activity [4-6]. The use of microwave radiation in the synthesis of biologically active skeletons is a new and powerful method with several advantages over traditional heating methods. This method can produce products with high efficiency, greater purity, and low environmental impact. It also facilitates the development of methods new and more stable methods for producing important molecules [7-9]

Experimental Section

From the reaction of ninhydrin with 6,1-diamino-2-oxo-4-phenyl-2,1-dihydropyridine-5,3-dicarbonitrile derivatives in the presence of trifluoroacetic acid catalyst in the water as solvent for 15 minutes at 95 °C under microwave rradiation 8,6-diisocyano-7-(aryl)-1H-spiro[[4,2,1]triazolo[5,1-a]pyridine-2,2'-indene]-1' derivatives, 3',5(3H)-trione have been synthesized. The structure of these compounds was confirmed using different spectroscopic methods. For example:

6',8'-diisocyano-7'-(4-methoxyphenyl)-3'H-spiro[indene-2,2'-[1,2,4]triazolo[1,5-a]pyridine]-1,3,5'(1'H)-trione:
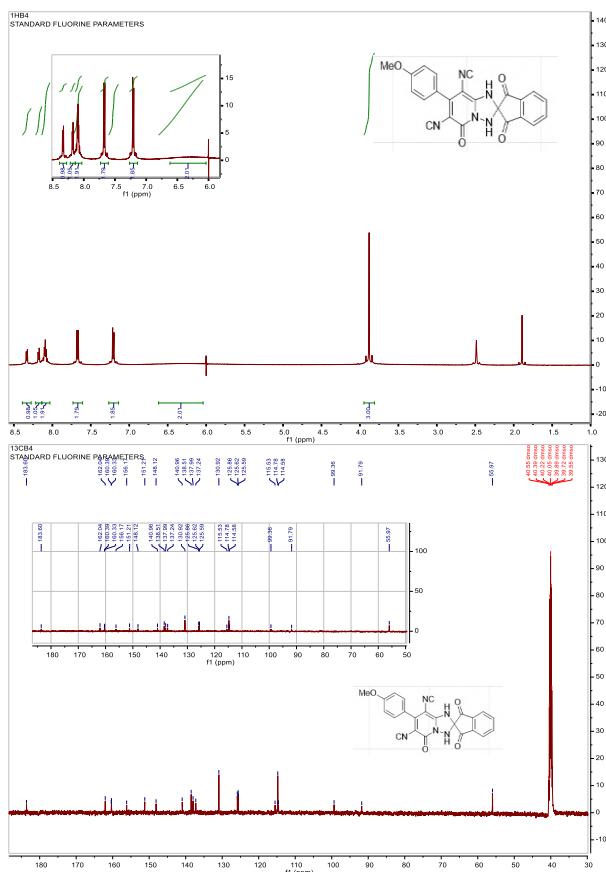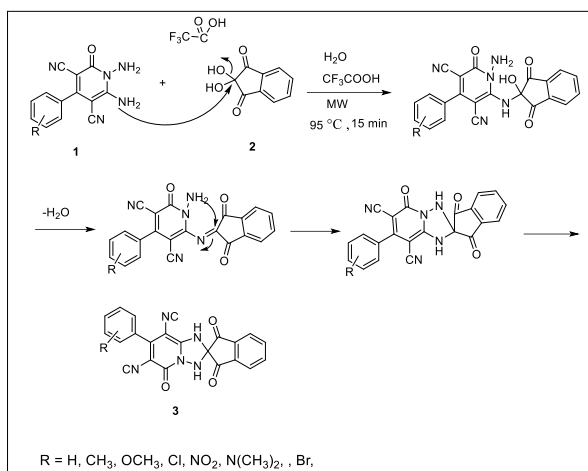
FT-IR(KBr, cm-1)vmax =1152(C-O),1462 (C=C), 1689, 1741.(C=O),2217(CN).

^{1}H-NMR (500 MHz, DMSO-d$_6$) δ= 6.41(s, 1H, NH), 3.88(S, 3H, OMe), 8.10-8.16(m, 2H, H$_{Ar}$), 8.21-8.24(m, 1H. H$_{Ar}$), 8.36-8.40 (m, 1H, H$_{Ar}$) ppm

13C-NMR(125 MHz, DMSO-d6) δ= 91.80 , 99.83 (CN), 114.90 ,115.37 ,124.89,125.71,125.99,128.67,129.42, 131.67,137.22, 137.78 ,138.13, 138.96 ,141.04 ,148.40, 151.30 (Ar), 156.22, 160.52 (CN) 160.76, 183.67(C=O)ppm

Results and Discussion

At the first, 6,1-diamino-4-aryl-2-oxo-2,1-dihydropyridine-5,3-dicarbonitrile derivatives have been synthesiszed from the reaction of 2-cyanoacetohydrazide and benzylidene malonitrile derivatives in the presence of pyridine as catalyst and ethanol solvent under reflux conditions. These 1,2 diamino compounds are very interesting for ring closing reactions. Then, from the reaction of these compounds with ninehydrin in the presence of trifluoroacetic acid catalyst and under microwave radiation, 8,6-diisocyano-7-(aryl)-1H-spiro[[4,2,1]triazolo[5,1-a] pyridine-2,2'-indene]-1',3',5(3H)-trione were synthesized in a very short time with high efficiency. The proposed mechanism for the reaction is as follows.

22nd Iranian Chemistry Congress (ICC22)
Iranian Research Organization for Science and Technology (IROST)
13-15 May 2024

03231-97589

R = H, CH₃, OCH₃, Cl, NO₂, N(CH₃)₂, , Br,

Conclusions

In the result, we have successfully synthesized a new series of 6',8'-diisocyano-7'-aryl-3'H-spiro[indene-2,2'-[1,2,4]triazolo[1,5-a] derivatives in excellent yield in the short time under Microwave irradiation. These new triazine drivatives can be have biological activities such as anti-cancer, muscle relaxant, hypnotic, anti-inflammatory and anti-hypertensive.

References

[1] Dixit, D., Verma, P. K., & Marwaha, R. K. (2021). A review on 'triazoles': Their chemistry, synthesis and pharmacological potentials. *Journal of the Iranian Chemical Society*, *18*(10), 2535-2565. https://doi.org/10.1007/s13738-021-02231-x

[2] Aggarwal, R., & Sumran, G. (2020). An insight on medicinal attributes of 1, 2, 4-triazoles. *European journal of medicinal chemistry*, *205*, 112652. https://doi.org/10.1016/j.ejmech.2020.112652

[3] Kharb, R., Sharma, P. C., & Yar, M. S. (2011). Pharmacological significance of triazole scaffold. *Journal of enzyme inhibition and medicinal chemistry*, *26*(1), 1-21. https://doi.org/10.3109/14756360903524304

[4] Ahsan, M. J., Ali, A., Ali, A., Afzal, O., Yusuf, M., Altamimi, A. S. A., ... & Bakht, M. A. (2023). Synthesis of New 4'-(Substituted phenyl) spiro [indoline-3, 3'-[1, 2, 4] triazolidine]-2, 5'-diones as Antimicrobial, Antitubercular, and Antifungal Agents: An Insight into the ADME and Toxicity Prediction as well as in-silico Molecular Docking Studies. *Journal of Molecular Structure*, *1290*, 135846. https://doi.org/10.1016/j.molstruc.2023.135846

[5] Dandia, A., Singh, R., Sachdeva, H., & Arya, K. (2001). Microwave assisted one pot synthesis of a series of trifluoromethyl substituted spiro [indole–triazoles]. *Journal of Fluorine Chemistry*, *111*(1), 61-67. https://doi.org/10.1016/S0022-1139(01)00429-8

[6] Maheswari, S. U., Balamurugan, K., Perumal, S., Yogeeswari, P., & Sriram, D. (2010). A facile 1, 3-dipolar cycloaddition of azomethine ylides to 2-arylidene-1, 3-indanediones: synthesis of dispiro-oxindolylpyrrolothiazoles and their antimycobacterial evaluation. *Bioorganic & medicinal chemistry letters*, *20*(24), 7278-7282. https://doi.org/10.1016/j.bmcl.2010.10.080

[7] Giofre, S. V., Romeo, R., Mancuso, R., Cicero, N., Corriero, N., Chiacchio, U., ... & Gabriele, B. (2016). A new microwave-assisted thionation-heterocyclization process leading to benzo [c] thiophene-1 (3 H)-thione and 1 H-isothiochromene-1-thione derivatives. *RSC advances*, *6*(25), 20777-20780. https://doi.org/10.1039/C6RA01329E

[8] Yadagiri, D., Rivas, M., & Gevorgyan, V. (2020). Denitrogenative transformations of pyridotriazoles and related compounds: Synthesis of N-containing heterocyclic compounds and beyond. *The Journal of organic chemistry*, *85*(17), 11030-11046. https://doi.org/10.1021/acs.joc.0c01652

[9] Bandyopadhyay, D., & Banik, B. K. (2017). Synthesis of medicinally privileged heterocycles through dielectric heating. Current Medicinal Chemistry, 24(41), 4596-4626. https://doi.org/10.2174/0929867324666170223152137

Formamidine sulfonic acid Functionalized Fe₃O₄@SiO₂: Organocatalyzed Paal-Knorr pyrrole synthesis

Leila Ghandi[a]*, Mahsan zarghari[a], Ghodsi Mohamadi Ziarani[a], Akbar Heydari[b]

Corresponding Author E-mail: L.Ghandi@alzahra.ac.ir

[a] Department of Chemistry, Alzahra University, Tehran, Iran.

[b] Department of Chemistry, Tarbiat Modares University, Tehran, Iran.

Abstract: Today, due to the environmental toxicity of metal nanoparticles, the use of organic catalysts has received much attention in many industries. In this paper, Formamidine sulfonic acid placed on the surface of magnetic nanoparticles has been used. This catalyst was evaluated in the synthesis of substituted pyrroles using condensation of amines and the desired product was achieved in high yields. Fe₃O₄@SiO₂@Formamidin sulfonic acid showed a typical superparamagnetic behavior so we could separate this catalyst from the reaction vessel by an external magnet. Formamidine sulfonic acid is a suitable catalytic agent because it is Cheap, has minimal toxicity, and can create hydrogen bonds which is a good reason to use it. This catalyst was prepared and XRD, SEM, and VSM analyses were done to check its structure and dimensions.

Keywords: Paal-Knorr; Formamidine sulfonic acid; superparamagnetic; nano Catalyst

Introduction

Organocatalyst is a form of catalyst that consists of carbon, hydrogen, sulfur, and other nonmetal elements. Organocatalysts get confused with enzymes because of their effects on the reaction rates.[1] Formamidine sulfonic acid as an organic catalyst makes it hard to separate the homogenous catalyst from the reaction mixture, thus numerous efforts to anchor catalysts to solids were made. Immobilized catalysts exhibit advantages over their homogeneous analogs.

Pyrroles are biologically active compounds and are used as antimalarial, anti-inflammatory antiasthmatic, antibacterial, antihypertensive, and tyrosine kinase inhibiting agents.[2] The Paal–Knorr reaction is an undeviating way for the preparation of N-substituted pyrroles. It is known that 1, and 4-diketones do not react with amines without the catalyst.[3] Certain applied catalysts for this synthesis include zirconium Compounds, montmorillonite-KSF, Sc(OTf)3, and Silica compounds. We have developed a prosperous procedure to tether Formamidine sulfonic acid on silica-encapsulated Fe3O4 nanoparticles. Formamidine sulfonic acid was covalently interconnected to the MNPs, which provided a highly efficient and magnetically reusable catalyst for the synthesis of the substituted pyrrole. Supported Formamidine sulfonic acid can keep its stable catalytic activity after recovery.

Experimental Section

According to the reported instructions, a Formamidine sulfonic acid catalyst coated on the surface of magnetic nanoparticles was prepared. [4]

To a mixture of amine (1 mmol) and 1, 4-diketone (1 mmol) was added Fe₃O₄@SiO₂ @FSA. The mixture was stirred for 4 h at RT (liquid amines). The reaction progress was monitored by Using TLC. After completion of the reaction, CH₂Cl₂ was added to solve and dilute the mixture. The catalyst was separated by using a permanent magnet.

Pure products were obtained in good yields after further purification by plate chromatography using ethyl acetate/hexane (1:4) as the eluent.
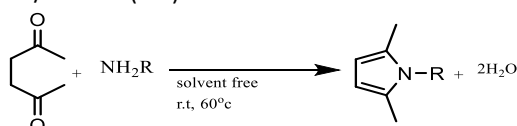
Results and Discussion

The FT-IR spectra of magnetic NPs (Fe₃O₄@SiO₂), magnetic NPs coated by Formamidine sulfonic acid are shown in Fig.1.
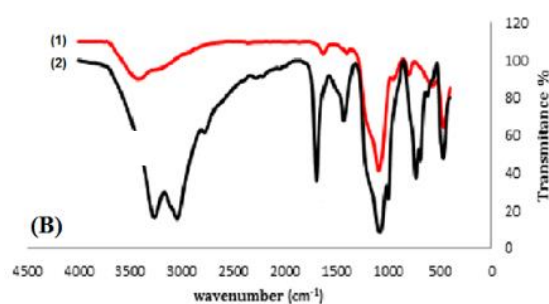

Fig.1: FT-IR pattern

22nd Iranian Chemistry Congress (ICC22)
Iranian Research Organization for Science and Technology (IROST)
13-15 May 2024

03231-97589

IROST

In the XRD pattern, there are six characteristic peaks for Fe_3O_4 (2θ = 21.25°, 37.29°, 43.73°, 52.56°, 65.09°, 69.73°, 76.81°). These are related to six crystal faces. As shown in Fig.2, the XRD pattern of $Fe_3O_4@SiO_2$ (Fig.2(2)) and $Fe_3O_4@SiO_2@FSA$ (Fig2(3)) matches with the peaks of Fe_3O_4 and this shows that after surface modification of Fe_3O_4, the crystalline structure of Fe_3O_4 does not change.
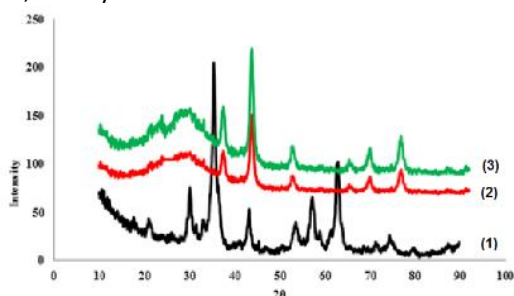
Fig.2: XRD pattern

The synthesized core-shell catalyst possesses sufficient superparamagnetic characteristics for practical applications. The magnetic saturation value of Formamidine sulfonic acid functionalized is 4emu/g (Fig.3).
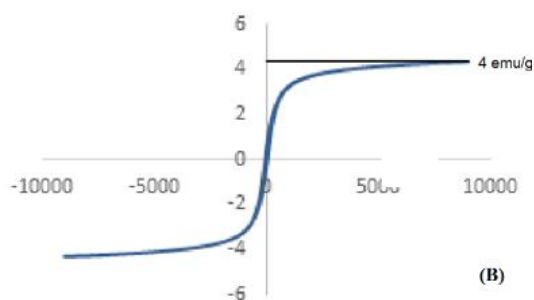
Fig.3: VSM pattern

As illustrated in Fig, the morphology of MNPs@SiO₂@FSA was studied by scanning electron microscopy (SEM) images. It was confirmed that the catalyst was made up of nanometer-sized particles (Fig.4).
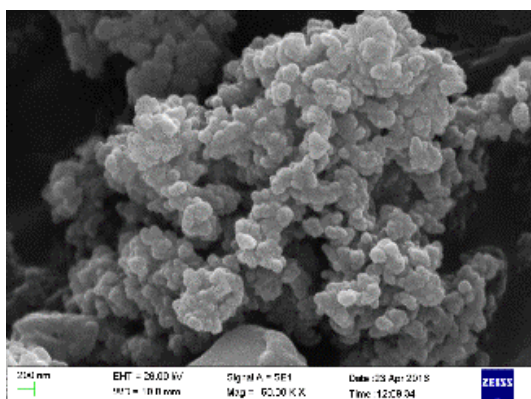
Fig.4: SEM pattern

At first, the reactions were performed without catalysts and with Fe_3O_4, $Fe_3O_4@SiO_2$, and $Fe_3O_4@SiO_2@FSA$ catalysts under the above conditions, and the following results were obtained. The high yield was obtained with FSA-functionalized Fe_3O_4 nanoparticles.

Entry	Cat.	Cat. (mg)	Yield (%)
1	-	-	24
2	Fe_3O_4	20	40
3	$Fe_3O_4@SiO_2$	20	52
5	$Fe_3O_4@SiO_2@FSA$	20	87

Conclusions

In conclusion, we have developed the first tethered Formamidin sulfonic acid on the magnetic surface as an active catalyst in Paal–Knorr pyrrole synthesis. This reaction proceeded in the one-pot reaction from various amines and 1, 4-diketone with good yield. Fe3O4@SiO2@FSA possesses the advantage of being magnetically recoverable, eliminating the requirement of catalyst filtration after the reaction.

References

[1] T. Akiyama, Chem. Rev. 2007, 107, 5744.
[2] A. R. Manning, D. J. Davis, Drug Discovery 2003, 2, 554.
[3] K. D. Surya, Synth Commun. 2008, 38, 803.
[4] L. Ghandi, ChemistrySelect. 2018, 3, 1787.

22ⁿᵈ Iranian Chemistry Congress (ICC22)
Iranian Research Organization for Science and Technology (IROST)
13-15 May 2024

03231-97589

Comparative Analysis of Thin Layer Fabrication Methods in UiO-66 and Synthesis of Ag2O@UiO-66 Thin Composite Layer for Photocatalytic Reactions

Mohammad Chahkandi, Sara Amiri*

Corresponding Author E-mail : sara.amirii@yahoo.com

Department of Chemistry, Faculty of Science, Hakim Sabzevari University, Sabzevar, Iran.

Abstract : In this study, we conducted a comprehensive comparative analysis of various thin layer fabrication methods utilized in UiO-66, a prominent metal-organic framework. We assessed the efficacy and efficiency of different techniques in producing thin UiO-66 layers and scrutinized their influence on material characteristics. Additionally, we introduced a novel synthesis approach for generating a thin composite layer of $Ag_2O@UiO-66$ tailored for photocatalytic reactions. We delved into the distinct properties of this composite layer, elucidating its potential in augmenting photocatalytic efficiency. This investigation contributes to the progression of thin layer fabrication methods in UiO-66 and provides valuable insights into the innovation of composite materials for catalytic applications. Furthermore, our investigation revealed the limitations of previous methods when depositing films on FTO substrates, prompting the transition to stainless steel mesh for improved stability and layer formation.

Keywords: metal-organic frameworks; UiO-66; $Ag_2O@UiO-66$; photocatalytic

Introduction

Metal-organic frameworks (MOFs) are a class of materials with highly ordered structures composed of metal ions or clusters linked by organic ligands [1]. Optical thin films are thin layers of material deposited on a substrate to modify the transmission, reflection, or absorption of light. These films are typically on the order of a few wavelengths of light thick, allowing for precise control over optical properties. By carefully selecting the thickness and refractive index of the thin film, interference effects can be utilized to achieve desired optical characteristics, such as anti-reflection coatings or optical filters [2]. To date, several strategies have been developed for preparing thin films. Some of the most common methods spin-coating, dip-coating, self-assembly, direct growth, the stepwise layer by layer growth, and electrophoretic deposition (EPD) method. Each method has its own advantages and limitations, making it important to choose the most suitable technique based on the specific requirements of the desired MOF thin film [3]. In this study, the intended thin films of $Ag_2O@UiO-66$ were coated on polished commercial steel mesh substrates (2 cm²) using by the prepared suspension through electrophoretic deposition (EPD) process.The EPD process allowed for a uniform and controlled deposition of the $Ag_2O@UiO-66$ thin films onto the steel mesh substrates, ensuring good adhesion and coverage. The resulting coated substrates exhibited promising properties for potential applications in catalysis and sensing..The morphology and composition of the coated steel mesh substrates were characterized using scanning electron microscopy (SEM), FT-IR spectra, and Wide-angle XRD pattern, confirming the presence of Ag2O@UiO−66 thin films with a uniform distribution. The catalytic activity of the coated substrates was evaluated using model reactions, demonstrating enhanced performance compared to uncoated substrates. Additionally, the sensing capabilities of the coated substrates were tested for various analytes, showing high sensitivity and selectivity. Overall, the $Ag_2O@UiO-66$ thin films deposited on steel mesh substrates via EPD show great potential for practical applications in catalysis and sensing.

Experimental Section

UiO-66 loading methods on FTO substrate

1.Solvent-thermal method

The FTO substrate was cleaned with water, ethanol, and acetone under ultrasonic waves. It was then immersed in a terephthalic acid solution in dimethylformamide for 17 hours. After drying, a benzoic acid solution with ZrCl4 was prepared and subjected to ultrasonic waves, followed by heating. Terephthalic acid was added, and the substrate was immersed in the solution for 20 hours. It was then washed with dimethylformamide and immersed in acetone for 24 hours. However, the resulting film lacked adhesion and stability.

2. Rotational coverage method

In the spin coating method, 200 microliters of the synthesized UiO-66 alcohol suspension (4.3% by weight) was placed on the FTO substrate at 3000 rpm for 60 seconds . But the film obtained from this method did not have enough adhesion and stability to continue working and placing the second layer.

3. Self-assembly method

22nd Iranian Chemistry Congress (ICC22)
Iranian Research Organization for Science and Technology (IROST)
13-15 May 2024

03231-97589

IROST

The self-assembly method used to place UiO-66 on the substrate involved the following steps:1. Fill the flask with deionized water. 2. Slowly drip 10 microliters of UiO-66 alcohol suspension onto the surface of the water. 3. After 5 minutes, add a few drops of sodium lauryl sulfate solution. 4. Transfer the layer formed on the surface of the water to the clean and ready FTO substrate.Despite following these steps, the resulting film was still unstable.

4. Electrophoretic method

In this method, 10 milligrams of UiO-66 synthesized by the solvothermal method were dispersed in 20 milliliters of toluene solvent for 30 seconds under ultrasonic waves. Two FTO substrates were placed one centimeter apart from each other in the solution containing UiO-66, and a voltage of 90 volts was applied to them. After three hours, a visible film was observed. However, the film obtained from this method also did not have sufficient adhesion and stability.

5. Changing the platform to load UiO-66

In all previously mentioned methods, the films deposited on the FTO substrate were unstable and lacked the ability to form a second layer. Therefore, the substrate was changed to stainless steel mesh for depositing the UiO-66 film to enhance photocatalytic chromium reduction. Experimentation revealed that finer mesh sizes resulted in better deposition and more stable films. Subsequently, a stainless steel mesh substrate coated with UiO-66 (prepared by the method of electrophoretic deposition described in section 4) was used for depositing a second layer with photocatalytic properties.

Results and Discussion

SEM images were utilized to investigate the particle size and surface morphology of the prepared $Ag_2O@UiO-66$ NPs (Fig.1). FTIR is a method based on atom vibrations in a molecule to analyze functional groups. The FTIR spectra of Ag_2O, UiO-66, and $Ag_2O@UiO-66$ show vibrations in the range 500-4000 cm^{-1}. Benzene rings and carboxylate groups in UiO-66 are confirmed. Peaks at 3000-3600 cm^{-1} correspond to O–H vibrations, 1700 cm^{-1} to C=O stretching, 1590 cm^{-1} to C=O stretching, 1420 cm^{-1} to benzene C-C stretching, 745 cm^{-1} to Zr node bending, 670 cm^{-1} to Zr-O stretching, and 510 cm^{-1} to Zr-O-Zr stretching. X-ray diffraction is a non-destructive technique that identifies crystal structures and nanoparticle purity based on unique diffraction patterns, serving as a fingerprint for crystal structure recognition and successful synthesis.
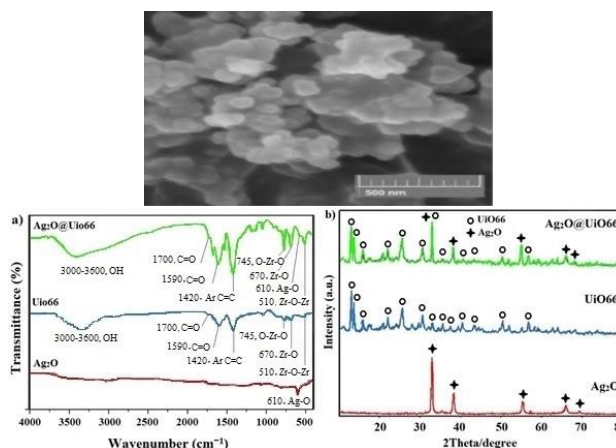

Fig.1: FE-SEM images and average height and width distribution of ($Ag_2O@UiO-66$), FT-IR spectra of ($Ag_2O@UiO-66$). Wide-angle XRD pattern $Ag_2O@UiO-66$

Conclusions

In summary, our study provides a thorough analysis of thin layer fabrication techniques in UiO-66, a prominent metal-organic framework. We evaluated the efficiency of these methods in producing thin UiO-66 layers and their impact on material properties. Introducing a novel synthesis approach for $Ag_2O@UiO-66$ composite layer tailored for photocatalytic reactions signifies a significant advancement. Transitioning to stainless steel mesh from FTO substrates improved stability and layer formation, with optimized mesh sizes enhancing deposition results and film stability. Coating a stainless steel mesh substrate with UiO-66 for a second layer with photocatalytic properties demonstrates innovative potential in catalytic applications..

References

[1] Rao, R., Ma, S., Gao, B., Bi, F., Chen, Y., Yang, Y., ... & Zhang, X. (2023). Recent advances of metal-organic framework-based and derivative materials in the heterogeneous catalytic removal of volatile organic compounds. Journal of Colloid and Interface Science, 636, 55-72. https://doi.org/10.1016/j.jcis.2022.12.167.

[2] Sathya, M., Selvan, G., Karunakaran, M., Kasirajan, K., Usha, S., Logitha, M., ... & Baskaran, P. (2023). Synthesis and characterization of cadmium doped on ZnO thin films prepared by SILAR method for photocatalytic degradation properties of MB under UV irradiation. The European Physical Journal Plus, 138(1), 1-12. https://doi.org/10.1140/epjp/s13360-023-03667-1

[3] Huang, Y., Tao, C. A., Chen, R., Sheng, L., & Wang, J. (2018). Comparison of fabrication methods of metal-organic framework optical thin films. Nanomaterials, 8(9), 676. https://doi.org/10.3390/nano8090676.

22nd Iranian Chemistry Congress (ICC22)
Iranian Research Organization for Science and Technology (IROST)
13-15 May 2024

03231-97589

Removal of benzene and toluene in gas phase by activated carbon fabrics

Razieh Salehi[a], Mohammad Abedi*[b], Fatemeh Dadashian[c]

Corresponding Author E-mail: mabedi50@yahoo.com

[a] Department of Textile Engineering, Amirkabir University of Technology, Tehran, Iran.

[b] Department of Chemical Technologies, Iranian Research Organization for Science and Technology (IROST), Tehran, Iran.

[c] Department of Textile Engineering, Amirkabir University of Technology, Environmental Research Center of Amirkabir University of Technology, Tehran, Iran.

Abstract: The application of activated carbon fabrics (ACFs) for removal of gas phase benzene and toluene was performed. The effect of process parameters such as initial inlet concentration, flow rate, and adsorbent mass on the removal efficiency was evaluated. The dynamic of the adsorption process was evaluated using Thomas model.

Keywords: Activated Carbon Fabrics, Removal, Benzene, Toluene, Dynamic model

Introduction

The environment is constantly contaminated with benzene, toluene, and xylenes (BTX) as a result of industrial development, combustion of fossil fuels, unintentional spills, and leaks from chemical facilities and disposal sites[1]. Because of their hazardous specifications, BTX compounds have been designated as significant pollutants by the USEPA. Since the presence of volatile organic compounds (VOCs) is harmful to the environment and human health even at extremely low concentrations, removal of these pollutants has received a lot of attention. Many studies have been focused on using activated carbons (ACs) for remove of benzene and toluene in liquid and gas phase [2]. In the recent years, activated carbon fabrics (ACFs) have gained increasing attention due to the comparative advantages over the traditional forms. The advantages of activated carbon fabrics (ACFs) are faster adsorption kinetics, higher efficiency, and larger capacity for adsorption of different molecules and species [3]. The main purpose of this work is to evaluate the efficiency of activated carbon fabrics (ACFs) on the removal of benzene, toluene compounds in gas phase.

Experimental Section

The adsorption experiments of the benzene and toluene in gas phase onto ACFs adsorbent were performed in the fixed bed of a Pyrex-glass reactor. To determine the optimum adsorption conditions, the study was carried out under atmospheric pressure at different N_2 flow rates (0.25–0.6 L min^{-1}) as a benzene and toluene in gas phase carrier, activated carbon amounts (0.05-0.2 g), the concentrations of benzne and toluene in gas phase at the inlet (300 ppm) and adsorption temperatures 298°K. N_2 gas flow rate during the adsorption process was measured using a volumetric flowmeter. The concentrations of toluene and benzene in gas phase at the inlet and outlet were measured by a Gas Chromatograph equipped with a Flame Ionization Detector (model YL Instrument 6500 GC system with TRB-G43 column (30m*0.53mm*3μm) Teknokroma company), and were recorded by a computer.

Results and Discussion

The breakthrough curves at different adsorbent masses have been given in Fig. 1 and Fig. 2. The breakthrough time, maximum adsorption capacity, and equilibrium adsorption capacity for different conditions listed in Table 1. The increase in mass of the adsorbent shows that the breakthrough time and the area under the graph increase, and as a result, the adsorption capacity increases. In fact, increasing the mass of the adsorbent causes an increase in the specific surface area and the number of binding sites for the adsorption of adsorbed molecules to the adsorbent. For two samples E and F, considering that the amount of absorbent in sample F was greater than that of sample E, sample F has a higher adsorption capacity and breakthrough time than sample E.

Experimental conditions for samples G and H were also carried out for nitrogen gas-carrying benzene. Sampling was done at different time intervals. The result showed the G sample with a higher amount of absorbent had a higher adsorption capacity than the H sample. However, the equilibrium adsorption capacity of sample H is lower compared to sample G. Increasing the amount of adsorbent has caused a decrease in the amount absorbed; perhaps the reason is the volatility of benzene, which has caused a laboratory error.
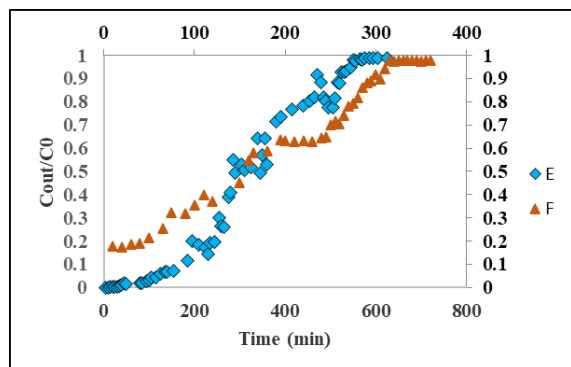
Fig 1: Breakthrough curves for adsorption of toluene on ACF at different experimental conditions: initial concentration = 300 mgL^{-1}. flow rate = 0.25 Lmin^{-1}
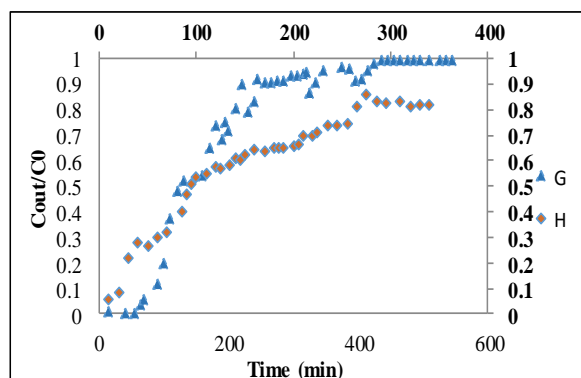

Fig 2: Breakthrough curves for adsorption of benzene on ACF at different experimental conditions: initial concentration = 300 mgL^{-1}. flow rate = 0.25 Lmin^{-1}

In all samples, the absorption capacity of toluene is always higher than that of benzene, which is consistent with previous articles [4] and it can be explained that the higher relative pressure of toluene compared to benzene (4.5 x 10^{-3} and 1.6 x 10^{-3}) has increased the absorption capacity. Although in both cases, constant conditions have been used, when comparing samples E and G, it can be seen that the absorption capacity of toluene is higher than that of benzene.

Table 1: breakthrough parameters for removal of toluene and benzene by ACF

Sample	Adsorbent mass (g)	Breakthrough Time (min)	q eq (mg/g)	q total (mg)
E	0.1	340.0	24.2	242
F	0.05	147.3	11.2	224
G	0.1	182.7	10.9	109
H	0.05	134.7	10.0	200

The Thomas model assumes a plug flow behavior in the bed. This model is one of the most general and widely used to describe the performance theory of the sorption process in fixed beds. Moreover, the model assumes Langmuir kinetics of adsorption–desorption and no axial dispersion derived with the adsorption such that the rate driving force obeys second-order reversible reaction kinetics. As Table 2 shows the calculated parameters k_{Th} and q_0, obtained from the linear regression analysis of Thomas Equation and observed that the k_{Th} values decrease and the q_f values increase with the increase in the bed mass. The use of a larger adsorbent mass increases the active surface area for the adsorption of absorbed molecules to the adsorbent, and as a result, increases the absorption capacity.

Table 2: Thomas **model** parameters at different experimental conditions

Different experimental conditions		Thomas model parameters		
sample	Adsorbent mass (g)	K_{Th} (L mg min^{-1})	q_F (mg g^{-1})	R^2
E	0.1	5.20×10^{-2}	255	0.952
F	0.05	5.27×10^{-2}	221	0.893
G	0.1	5.93×10^{-2}	137	0.867
H	0.05	3.43×10^{-2}	202	0.842

Conclusions

The application of activated carbon fibers (ACFs) for removal of benzene and toluene in gas phase was evaluated using an adsorption fix bed. According to the results, the amounts of adsorbent and the initial concentration have a significant effect on the adsorption process and the breakthrough curve. The experimental results was fitted in Thomas adsorption model with appropriate correlation coefficient.

References

[1] Memetova, A.E., et al. (2023) Effective adsorption of toluene and benzene on coconut activated carbon modified with carbon nanotubes: kinetics, isotherms and thermodynamics. Adsorption, 29(5), 335-349.

[2] Salehi, R., Dadashian, F., Abedi, M., & Hasani, B. (2018). Optimization of chemical activation of cotton fabrics for activated carbon fabrics production using response surface methodology. The journal of the Textile Institute, 109(12), 1586-1594.

[3] Isinkaralar, K., (2022) High-efficiency removal of benzene vapor using activated carbon from Althaea officinalis L. biomass as a lignocellulosic precursor. Environmental Science and Pollution Research, 29(44), 66728-66740.

[4] Lillo-Ródenas, M.A., et al., (2006) Competitive adsorption of a benzene–toluene mixture on activated carbons at low concentration. Carbon, 44(8), 1455-1463.

22nd Iranian Chemistry Congress (ICC22)
Iranian Research Organization for Science and
Technology (IROST)
13-15 May 2024

03231-97589

IROST

Cauliflower-Like nanostructured mixed Mo-Zr-Fe oxide: Synthesis, characterization, and application as heterogeneous catalyst for selective oxidation of benzyl alcohols

Hoda Haghi, Alireza Sedrpoushan

Corresponding Author E-mail: sedrpoushan@irost.ir

Department of Chemical Technologies, Iranian Research Organization for Science and Technology (IROST), P.O.Box 33535111, Tehran, Iran.

Abstract: A ternary metal oxide was developed using of Zr, Mo, Fe as inexpensive, non-toxic metals. XRD, SEM, EDS and EM were used to characterize the composite. The use of composite in the oxidation of alcohols to the aldehydes as a green heterogeneous catalyst with yield of 75 percent was examined.

Keywords: Metal oxide; Catalyst; Oxidation; Alcohol

Introduction

Environment-friendly technologies in chemical reactions in industry, catalytic processes (e.g. toxic and expensive reagents removal, minimization of by-products, and simplifying of workup procedures) have drawn a great deal of attention [1]. One of the most complex challenges in organic chemistry is the selective oxidation of alcohols to aldehydes [2]. Transition group metals are typically employed as catalysts and their activity is rooted in their outer electron configuration [3]. Some of the metal oxide catalysts, including transition metals, are highly important given their advantages like inexpensive production, ease of regeneration and selective reactivity. Evidently, ternary metal oxide nanostructures have profound scientific features (as optical, electronic, and catalytic properties) and contain a wide range of technological applications (e.g. transistors and computational devices). Hence, we reported here an inexpensive mixed nano-metal oxides of Mo-Zr-Fe catalyst with increased surface area and physical-chemical interaction and without an additional support as a highly active. Also, we studied selective heterogeneous catalyst for our reactions employing hydrogen peroxide as a sustainable co-oxidant.

Experimental Section

Catalysis preparation: The precursors of the metals in the proper quantities, $MoCl_5$ (1 mmol, 0.273g), $ZrCl_4$ (1 mmol, 0.233g), $FeCl_3.6H_2O$ (1 mmol, 0.270g), NH_4F (6 mmol, 0.253g) and urea (15 mmol) were dissolved at room temperature in distilled water (70 mL). Then, the solution was transferred into the autoclave and heated to 100 °C for 24 hours. After cooling the autoclave to room temperature, the resulting precipitate was washed with water and ethanol and dried for 12 hours. The resulting material was then calcinated at 350 °C to give the ternary metallic nano catalyst.

Catalyst testing for benzylic alcohols: Catalytic oxidation of alcohols to corresponding aldehydes, was investigated at 80 °C using a catalyst (15 mg), 30% H_2O_2 (4 mmol) as oxidant, and benzylic alcohol (0.5 mmol) in acetonitrile (5 mL) for 6 hours. The reactions were achieved to get the optimal point in different solvents, temperatures, and the molar ratios of substrate/oxidant. We were performed the oxidation reactions of benzylic alcohols in reflux conditions using thin-layer chromatography (TLC) (EtOAc/n-hexane)) monitoring. Finally, the catalysis was filtered, washed with hot acetone, and dried in a vacuum desiccator to reuse and test the recycling capability

Results and Discussion

We have the foundations for using XRD analysis to determine the structures of these compounds. The prepared ternary oxide's powder X-ray diffraction showed overlapping diffraction peaks (Fig. 1).
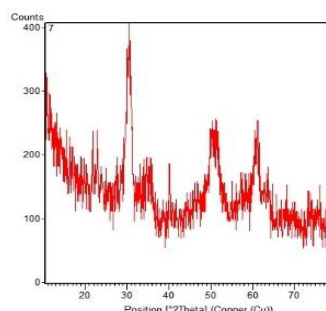

Fig.1: X-ray diffraction (XRD) pattern of Mo-Zr-Fe

We were used the FESEM image at higher magnification to examine the shape and dimensions of the ternary Mo-Zr-Fe oxide catalyst (Fig. 2). The layers of the cauliflower-like structure, are spaced at a distance of 200 nm to 1 μm. Also, the sample includes cauliflower-like spherical particles with a diameter in the μm range. cauliflower-like made of mixed metal oxide have about 20 nm thickness.
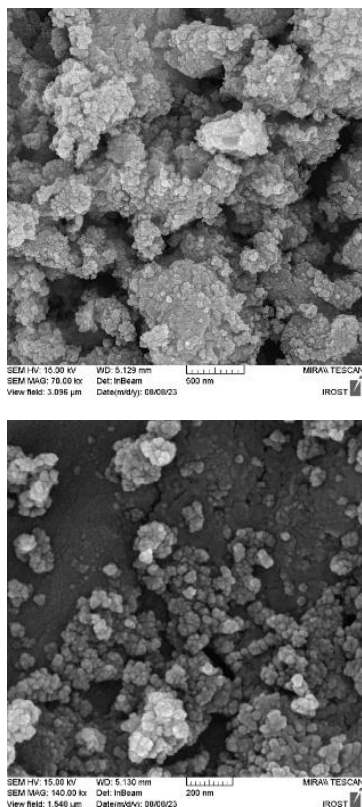
22nd Iranian Chemistry Congress (ICC22)
Iranian Research Organization for Science and Technology (IROST)
13-15 May 2024

03231-97589

IROST

Fig.2: SEM images of Mo-Zr-Fe at 200 and 500 nm

Additionally, EDS analysis proves the presence of all three elements molybdenum, zirconium and iron in the synthetic composition (Fig. 3).
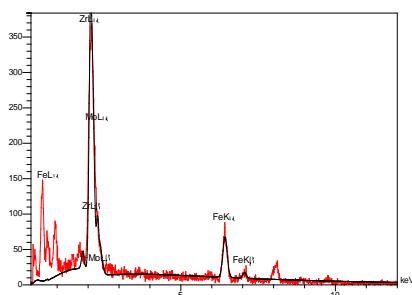

Fig.3: EDS of Mo-Zr-Fe

The presence of all three elements molybdenum, zirconium and iron has been proven with colour images. Also, a higher percentage of zirconium than other metal elements in the metal oxide structure can be seen through EM (Fig. 4).
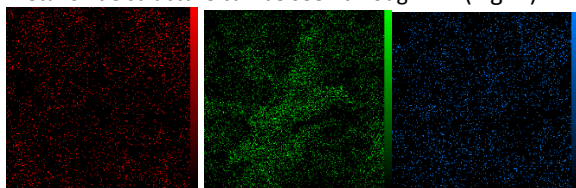
Fig.4: Elemental mapping images of Mo-Zr-Fe

Different types of alcohols were oxidized to aldehydes with good yields under the optimized conditions (Table 1).

Table 1. Oxidation of different alcohols to aldehydes using Mo-Zr-Fe

Alcohol	Product	Time (h)	Yield (%)
		6	68
		6	75
		6	75
		6	70
		6	72
		6	68

Conclusions

A new heterogeneous mixed Mo-Zr-Fe nano-metal oxide catalyst was synthesized from commercially available raw materials, characterized by various techniques and proven highly successful for the selective mono- oxidation of benzylic alcohols to the corresponding aldehydes with outstanding yields employing H_2O_2 as an environment-friendly oxidant under mild reaction conditions.

References

[1] Nur, H., Ikeda, S., & Ohtani, B. (2001). Phase-Boundary Catalysis of Alkene Epoxidation with Aqueous Hydrogen Peroxide Using Amphiphilic Zeolite Particles Loaded with Titanium Oxide. Journal of Catalysis, 204(2), 402–408. https://doi.org/10.1006/JCAT.2001.3386

[2] Cui, C., Zhao, X., Su, X., Gao, W., Zhan, J., Zhang, X., Li, G., Zhang, X. L., Sang, Y., & Liu, H. (2021). Selective oxidation of benzyl alcohol using a Ni(OH)2-modified CdS-MoS2 composite photocatalyst under ambient conditions. Journal of Environmental Chemical Engineering,9(6),106416.https://doi.org/10.1016/j.jece.2021.106416

[3] Bond, G. C. (Geoffrey C. (1974). Heterogeneous catalysis: principles and applications /. Clarendon Press

Investigation of the impact of operational parameters on the performance of a tubular reactor in removing organic dye pollutant from water using photocatalyst and persulfate

Seyedeh Narges Saeedi, Rahmatollah Pourata*, Hanieh Feizollahnezhad, Mohammad Hossein rasoulifard

Corresponding Author E-mail: pourata@znu.ac.ir

Applied Chemistry Research Laboratory, Department of Chemistry, Faculty of Science, University of Zanjan.

Abstract: In this study, the removal of Reactive Black 5 contamination from polluted water using a tubular reactor with immobilized titanium dioxide photocatalyst is investigated. The photocatalyst is activated by an 8-watt UV lamp and is used in conjunction with persulfate oxidants. Parameters such as dye concentration, persulfate dosage, and flow rate in the process of contaminant removal from water are examined.

Keywords: Tubular reactor; Dye removal; AOP; TiO_2

Introduction

The removal of pollutants from water is of utmost importance to ensure the availability of clean and safe water for human consumption and environmental protection [1]. Organic dyes, commonly used in various industries, pose a significant threat to water quality due to their persistence and potential toxicity. Advanced oxidation processes (AOPs) have emerged as effective methods for the degradation of organic pollutants in water [2]. These processes involve the generation of highly reactive hydroxyl radicals that can efficiently break down complex organic molecules. Among AOPs, photocatalyst and persulfate-based oxidation have gained attention for their high efficiency and versatility in treating a wide range of pollutants [3]. The use of a tubular reactor in photocatalyst and persulfate-based oxidation processes offers enhanced mass transfer, improved reaction kinetics, and better control over operational parameters, leading to optimized pollutant removal efficiency [4]. This study aims to investigate the impact of various operational parameters on the performance of a tubular reactor in removing organic dye pollutants from water using persulfate as the oxidant, contributing to the advancement of sustainable water treatment technologies.

Experimental Section

A continuous tubular photoreactor was designed and constructed for this project.

The reactor consisted of two concentric tubes with diameters of 28 and 36 mm, the inner and outer tube were made of quartz and PVC, respectively.Titanium dioxide powder was immobilized by silicone adhesive the inner surface of the outer tube. The length of the reactor was 21 cm. The contaminated water was passed through the space between the two pipes by a peristaltic pump. An 8-watt UV-C lamp located in the center of the quartz tube supplied the photoreactor light.

Results and Discussion

Fig. 1a shows that the photolysis and surface adsorption of dye by the catalyst in darkness are very negligible compared to the photocatalytic degradation of dye. As the graphs demonstrate, the maximum removal is related to the photocatalyst activity in the presence of UV light

Operating parameters' impact on a tubular photoreactor's photocatalytic degradation:

- Impact of the initial dye concentration:

It is clear from figure1.b the degradation efficiency was highest at 5 mg/L of dye and thereafter declined as the dye concentration increased. Therefore, a lower starting dye concentration may increase the dye's removal effectiveness. In this work, the concentration of 15 mg/L was chosen as the optimal concentration [5].

- Effect of persulfate concentration:

The concentration of persulfate is one of the key factors in the dye removal process. A higher concentration of persulfate can lead to more effective dye removal, but it should be noted that increasing the concentration too much may result in other issues, such as increased costs or additional side pollutants. According to Fig. 1.c, increasing persulfate increases the amount of dye removal. Here, the concentration value of 0.1 mM was chosen as the optimal concentration [6].
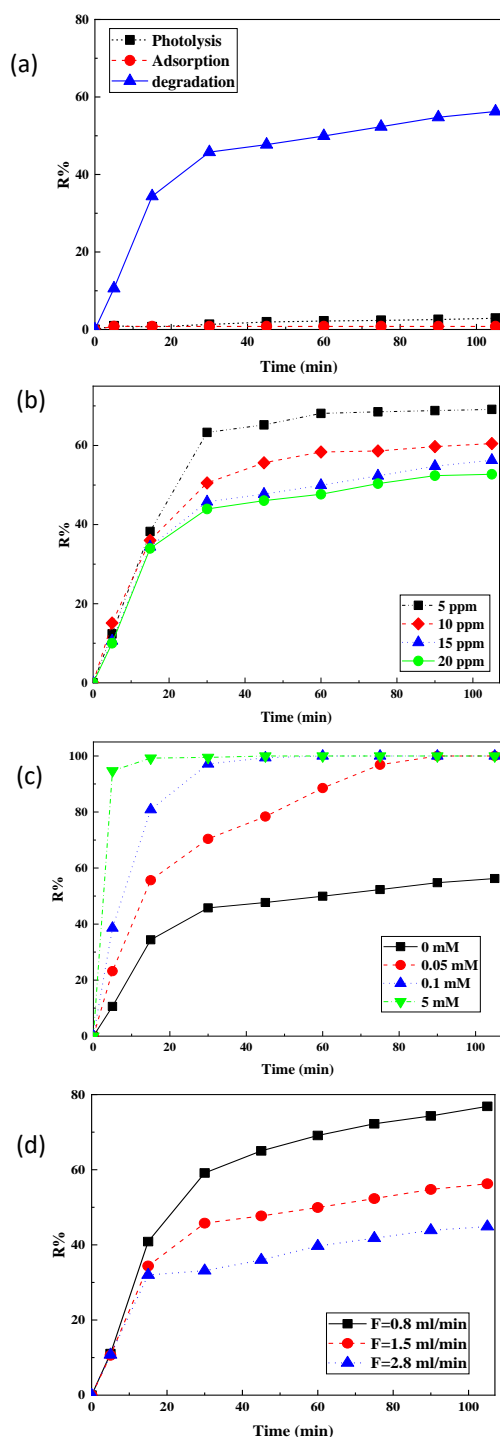
22nd Iranian Chemistry Congress (ICC22)
Iranian Research Organization for Science and Technology (IROST)
13-15 May 2024

03231-97589

IROST

Fig. 1: (a) Investigating the effects of photolysis, surface absorption, and photocatalytic degradation. (b) Effect of initial dye concentration. (c) Effect of persulfate concentration. (d) Effect of flow rate.

Effect of flow:

As can be seen in the graphs in Figure 1.d, with the increase in the flow rate, the amount of dye removal has decreased. The increase in the flow rate may lead to a decrease in the contact time between the pollutant and the photocatalyst. In this study, the flow rates of 0.8 ml/min, 1.5 ml/min, and 2.8 ml/min were checked, and based on the amount of removal and energy consumption, the flow rate of 1.5 ml/min was chosen as the optimal flow rate [7].

Conclusions

This study investigated the effect of various parameters, such as initial dye concentration, flow rate, and persulfate concentration, on dye removal in a tubular photoreactor. According to the results obtained in the experiments, increasing the dye concentration leads to a decrease in dye removal. Also, increasing the persulfate concentration led to an increase in the dye removal efficiency. Increasing the flow rate also reduces the efficiency of the dye removal process. It is better to optimize the process conditions, including the balance between dye and persulfate concentrations and the flow rate. Investigating the effect of pH, UV intensity, and simultaneous and competitive degradation of chemicals in the future can help to improve the dye removal process.

References

[1] Zhang, Y., Wang, Y., Xie, R., Huang, H., Leung, M. K., Li, J., & Leung, D. Y. (2022). Photocatalytic oxidation for volatile organic compounds elimination: from fundamental research to practical applications. Environmental Science & Technology, 56(23), 16582-16601.

[2] Yu, T., Chen, H., Hu, T., Feng, J., Xing, W., Tang, L., & Tang, W. (2024). Recent advances in the applications of encapsulated transition-metal nanoparticles in advanced oxidation processes for degradation of organic pollutants: A critical review. *Applied Catalysis B: Environmental*, *342*, 123401.

[3] Li, S., Yang, Y., Zheng, H., Zheng, Y., Jing, T., Ma, J., ... & Chang, J. S. (2022). Advanced oxidation process based on hydroxyl and sulfate radicals to degrade refractory organic pollutants in landfill leachate. *Chemosphere*, *297*, 134214.

[4] Mosleh, S., & Ghaedi, M. (2021). Photocatalytic reactors: technological status, opportunities, and challenges for development and industrial upscaling. *Interface Science and Technology*, *32*, 761-790.

[5] Nayagam, J. O. P., & Prasanna, K. (2022). Utilization of shell-based agricultural waste adsorbents for removing dyes: A review. *Chemosphere*, *291*, 132737.

[6] Brillas, E., & Oliver, R. (2024). Development of persulfate-based advanced oxidation processes to remove synthetic azo dyes from aqueous matrices. *Chemosphere*, 141766.

[7] Abd Rahman, N., Choong, C. E., Pichiah, S., Nah, I. W., Kim, J. R., Oh, S. E., & Jang, M. (2023). Recent advances in the TiO₂ based photoreactors for removing contaminants of emerging concern in water. *Separation and Purification Technology*, *304*, 122294.

The effect of silica and aluminum hydroxide fillers on the insulating properties of Epiran_06SPL epoxy resin

Fatemeh Safari Oori[a], Rahmatullah Pourata[a,*], Farhad Kabiri Esfahani[a], Seyed Hadi Hosseini[b]

Corresponding Author E-mail: pourata@znu.ac.ir

[a] Department of Chemistry, Faculty of Science, University of Zanjan.

[b] Department of Electrical Engineering, Faculty of Engineering, University of Zanjan.

Abstract: Epoxy resins are inherently very good electrical insulators that are used as insulating materials in electrical applications. In this study, the insulating properties of Epiran-06spl epoxy resin and the effect of various factors such as type of filler, filler content and curing temperature were investigated. The results showed that utilization of filler had a negligible effect on the electrical properties, but the $Al(OH)_3/SiO_2$ ratio was effective on the dielectric breakdown strength .

Keywords: Epoxy resin, Electrical insulation, Dielectric breakdown strength, $Al(OH)_3$, SiO_2

Introduction

Insulators are one of the most widely used materials in the electrical power transmission and distribution industry. Insulators, in addition to insulating properties, must also have appropriate thermal and mechanical properties [1].

Epoxy resins were first synthesized in 1891, but their commercialization began in the 1940s [2]. Diglycidyl ethers of bisphenol A (DGEBPA) is a widely used epoxy resin in various utilization such as electrical & electronics, paints & coatings, adhesives, composites, and other applications [3-4].

Epoxy resin is used in the electrical industry in a wide range of equipment including motors, generators, transformer switchboards, bushings as insulators. The epoxy resins provide excellent electrical insulation properties and effectively protect electrical components from potential problems such as short circuits, dust ingress, and moisture exposure [5].

Dielectric breakdown strength is an important parameter for electrical insulating materials. The dielectric breakdown strength of the insulation is the voltage that makes a part of the insulator conductor and an electric current passes through it [6].

The main purpose of this study is to investigate the insulating properties of epoxy resin composite with fillers such as silica and aluminium hydroxide.

.2. Experimental Section

2.1. Materials

Epiran-06SL epoxy resin (produced by Khuzestan Petrochemical), polyamine hardener (produced by Huntsman) and commercial silica and aluminium hydroxide fillers were used to prepare the electrical insulation composite.

2.2. Sample preparation

To perform the dielectric breakdown strength test, a polyethylene mold was made in the shape of a rectangular cube. The mold consisted of six pieces of polyethylene, which could be separated after curing and removing the sample. Also, there were two holes in the two pieces facing each other, where the electrodes were placed. The electrodes were located with a distance of 1 mm. Figure 1 shows the electrodes and the prepared sample.

Fig.1: Electrodes and the prepared sample fore dielectric breakdown strength test

2.3. Dielectric breakdown strength measurement

The dielectric breakdown strength test of the prepared samples was performed using an alternating high pressure test device (20KVA, (220KV)) and a recording and control system (operator panel OP17, SIEMENS). The sample prepared using needle-plate electrodes was placed in the oil bath at ambient temperature and the breakdown voltage was recorded.

3. Results and Discussion

3.1. Effect of SiO_2 filler on dielectric breakdown strength

Figure 2 shows the effect of silica (as a filler) in different percentages on dielectric breakdown strength. According to the results, filler content had little effect on dielectric breakdown strength. On the other hand, the higher the amount of filler, the cheaper the product, but using more than 350% makes the resin and filler mixture too viscous, so it was considered as the optimal amount.
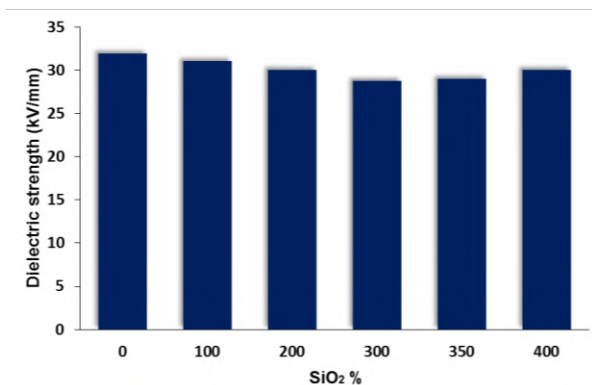
22nd Iranian Chemistry Congress (ICC22)
Iranian Research Organization for Science and Technology (IROST)
13-15 May 2024

03231-97589

IROST

Fig.2: The effect of SIO₂ filler on dielectric breakdown strength. Post-curing temperature: 130°C, Post-curing time: 6 h.

3.2. Investigating the influence of the ratio of silica filler to aluminum hydroxide on dielectric breakdown strength

Figure 3 shows the effect of silica to aluminum hydroxide ratio on dielectric breakdown strength. According to the figure, the ratio of 70 to 30 silica to aluminum hydroxide showed the best dielectric breakdown strength and insulation properties.
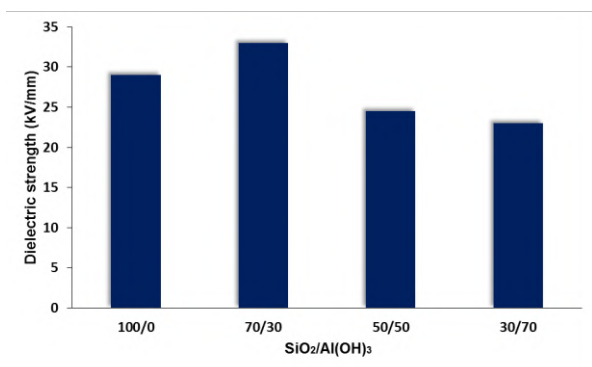
Fig.3: Effect of silica to aluminum hydroxide ratio on dielectric breakdown strength. Post-curing temperature: 130°C, Post-curing time: 6 h, Filler content: 350%.

3.3 Effect of post-curing temperature on dielectric breakdown strength

Figure 4 shows the effect of post-curing temperature on dielectric breakdown strength. The samples were first cured at 130°C for 12 hours and then post-cured for 6 hours at different temperatures. It can be seen that the dielectric breakdown strength of the sample that was post-cured at 150°C was higher than the others.
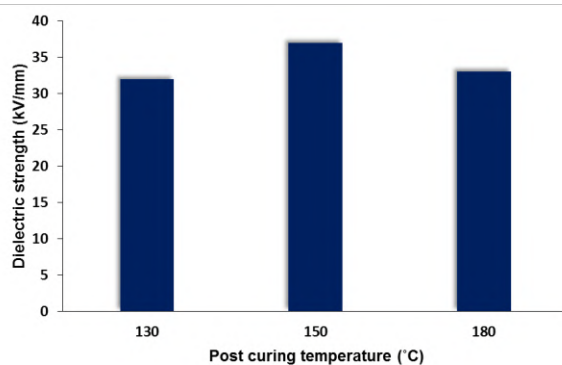
Fig.4: Effect of the post-curing temperature on the dielectric breakdown strength. Filler percentage 350%, silica to aluminum hydroxide ratio 70/30, Post-curing time: 6 h.

Conclusions

It can be concluded that Epiran-06SPL epoxy resin has good dielectric strength and its composites can be used as insulation in electrical equipment. According to the results obtained from the analysis of the samples, it was concluded that although the use of fillers such as silica and aluminum hydroxide did not have a significant effect on increasing the insulation property of epoxy resin, it can reduce the cost of insulation. Also, replacing aluminum hydroxide instead of 30% of silica improves insulation properties. Post curing also had a positive effect on the insulating properties of the epoxy composite.

References

[1] TS, Karthik, et al. "Investigation on Dielectric Properties of Press Board Coated with Epoxy Resin, Quartz, and Rice Husk Ash." Advances in Materials Science and Engineering 2021 (2021): 1-7.

[2] Rehim, Mona Abdel, and Gamal Turky. "Epoxy resin reinforced with graphene derivatives: physical and dielectric properties." Journal of Polymer Research 29.4 (2022): 120.

[3] Sienkiewicz, Natalia, Midhun Dominic, and Jyotishkumar Parameswaranpillai. "Natural fillers as potential modifying agents for epoxy composition: A review." Polymers 14.2 (2022): 265.

[4] Guo, Yuntian. "Study on the electrical properties of itaconic acid-based epoxy resin." Journal of Physics: Conference Series. Vol. 1986. No. 1. IOP Publishing, 2021.

[5] Dallaev, Rashid, et al. "A Brief Overview on Epoxies in Electronics: Properties, Applications, and Modifications." Polymers 15.19 (2023): 3964.

[6] Adnan, Mohammed Mostafa, et al. "Epoxy-based nanocomposites for high-voltage insulation: a review." Advanced Electronic Materials 5.2 (2019): 1800505.

Preparation and investigation of mechanical properties of composite based on epoxy resin and cellulose fibers functionalized by amine groups

Mohadese Mirzakhani, Rahmatullah Pourata[*], Mohammad Hossain Rasoulifard

Corresponding Author E-mail: pourata@znu.ac.ir

Department of Chemistry, Faculty of Science, University of Zanjan.

Abstract: Cellulose is one of the biofibers that can be used to improve the mechanical properties of polymer materials to make composite materials with high stability and performance. The biggest challenge that prevents the use of cellulose as a reinforcement in polymer composites is its poor compatibility due to the inherent hydrophilicity of cellulose and the hydrophobic nature of polymer matrices. In the present study, the surface of cellulose was modified with amine groups. The composite obtained from modified cellulose and epoxy resin showed 25% higher tensile strength than pure epoxy resin.

Keywords: Epoxy resin Composite; cellulose; surface treatment

Introduction

Epoxy resins are one of the most widely used polymer matrices, which have been used in various industries such as aerospace, automotive, and marine due to their physical, mechanical, thermal, and chemical resistance characteristics [1-2].

The improvement of properties of epoxy composites strongly depends on the type, shape, content, size distribution and chemical groups on the filler surface [3-4]. Surface treatment of filler with different chemical groups that can interact with epoxy matrix is an effective method to achieve uniform dispersion of particles in epoxy matrix. In addition, some functional groups on the surface of fillere can chemically react with matrix epoxide groups [2].

Cellulose is very suitable as a biofiller for polymer materials and provides the possibility of making composite materials with high stability and performance. However, cellulose is inherently incompatible with hydrophobic polymers and as a result creates poor surface adhesion between fillers and polymer matrices [5]. Due to the abundance of hydroxyl groups on the surface of cellulose, various methods such as acidification, esterification, etherification, urethane, silane coupling and chemical bonding through radical polymerization have been used to modify the surface of cellulose fibers [5].

In the present study, the surface of cellulose fibers was modified with amine groups using a water-based method. Epoxy composites were prepared using the modified fibers and their mechanical properties were investigated.

Experimental Section

E06 epoxy resin (Khuzestan Petrochemical Company) and PC205 polyamine hardener were used to prepare the composite. To prepare cellulose fibers, used paper was shredded and turned into a paste in water.

To functionalize cellulose, 3 grams of cellulose pulp and 1.5 grams of triethanolamine were refluxed in 100 cc of distilled water for 24 hours. After that, the solution was filtered and the remaining cellulose was washed with distilled water and then with acetone.

To prepare the composite, certain amount of modified cellulose was mixed with 5 g of epoxy, and then heated in an oil bath for 40 minutes while stirring. After cooling, it was mixed with 2.5 grams of hardener and poured into the mold. The resin curing process was carried out for 24 hours at ambient temperature and then the curing process was completed for 4 hours at 80°C.

To study of the tensile strength of the prepared composites, samples were prepared in dumbbell-shaped molds according to ISO 527-1. The stress-strain curve of the samples was plotted using Santam STM50 universal testing machine. Tensile strength, Young's modulus and elongation at break of the samples were calculated from the obtained curves.

Results and Discussion

FTIR of unmodified cellulose and modified cellulose by triethanolamine illustrated in figure 1. After modification of cellulose a weak peak has been appeared at 1315 cm^{-1} indicated the C-N bond of amine.

22nd Iranian Chemistry Congress (ICC22)
Iranian Research Organization for Science and Technology (IROST)
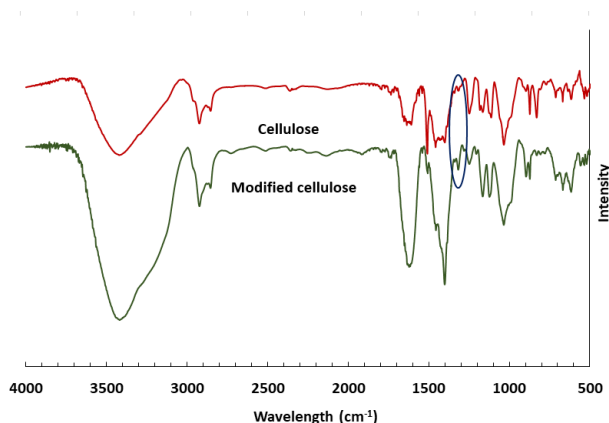**13-15 May 2024**

03231-97589

IROST

Fig.1: FTIR of unmodified cellulose and modified cellulose by triethanolamine.

It is clear from Figure 2, the tensile strength value of the modified cellulose samples was significantly increased compared to the unmodified state. The modification of the cellulose surface and the presence of amino groups on the surface of the cellulose fibers improved the physical or chemical interaction between the fibers and the epoxy resin matrix.
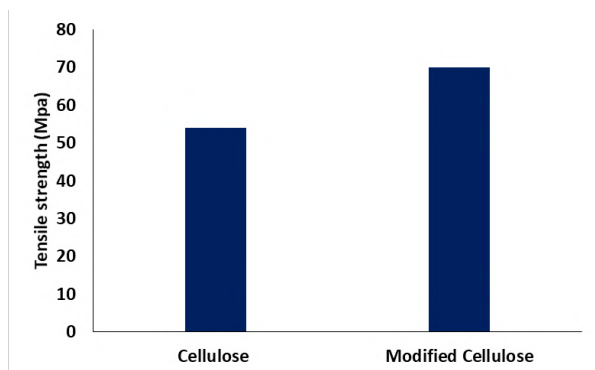
Fig.2: FTIR of unmodified cellulose and modified cellulose by triethanolamine.

As illustrated in figure Figure 2, with the increase in concentration up to 1.5%, the tensile strength also increased, and after 1.5%, the tensile strength of the composite decreased due to agglomeration and not properly spreading the cellulose fibers. Therefore, the optimal concentration of cellulose fibers was obtained as 1.5%.

figures and tables at the top and bottom of columns. Avoid placing them in the middle of columns. Large figures and tables may span across both columns. Figure captions should be below the figures; table heads should appear above the tables. (Font: Calibri 10)
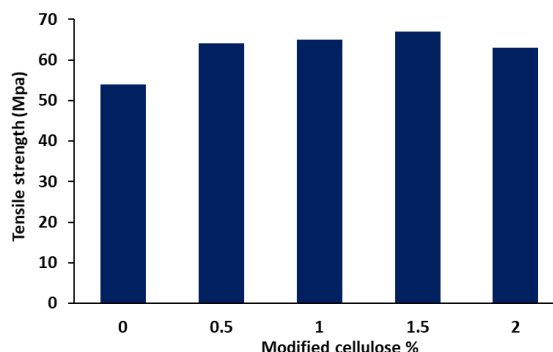
Fig.3: The effect of the concentration of modified cellulose on the tensile strength of epoxy resin composite (mixing temperature 80°C).

Conclusions

The method presented in this study provided a simple approach to modify the surface of cellulose fibers without using organic solvents. Modified cellulose as a modifier could improve the mechanical properties of epoxy by about 25%. The results showed that the use of cellulose up to 1.5% increased the tensile strength of the epoxy-cellulose composite, but after that it decreased due to the agglomeration of cellulose fibers. In general, the results of this research can be concluded that cellulose fibers recovered from used paper can be used as a reinforcement in polymer composites with surface modification.

References

[1] Ahmadi, Z., Nanostructured epoxy adhesives: A review. Progress in Organic Coatings 135 (2019) 449–453.

[2] Chang, K.C., Lin, C.Y., Lin, H.F., Chiou, S.C., Huang, W.C., Yeh, J.M., Yang, J.C., Thermally and mechanically enhanced epoxy resin–silica hybrid materials containing primary amine-modified silica nanoparticles. J Appl Polym Sci. 108 (2008) 1629–1635

[3] Maity, T., Samanta, B.C., Dalai, S., Banthia, A.K., Curing study of epoxy resin by new aromatic amine functional curing agents along with mechanical and thermal evaluation. Materials Science and Engineering A 464 (2007) 38–46

[4] Domun, N., Hadavinia, H., Zhang, T. and et al, Improving the fracture toughness properties of epoxy using graphene nanoplatelets at low filler content, Nanocomposites (2017) 85-96

[5] Cui, X., et al., Cellulose modified by citric acid reinforced polypropylene resin as fillers. Carbohydrate polymers. 230 (2020) 115662.

22nd Iranian Chemistry Congress (ICC22)
Iranian Research Organization for Science and Technology (IROST)
13-15 May 2024

03231-97589

IROST

Application of N, S-doped ordered mesoporous carbons as solid acid-base bifunctional catalyst in one-pot cascade Biginelli reaction

Nahid Moghaddam [a], Babak Karimi*[a,b]

Corresponding Author E-mail: karimi@iasbs.ac.ir, nahidmoghaddam@iasbs.ac.ir

[a] Department of Chemistry, Institute for Advanced Studies in Basic Sciences (IASBS), Prof. Sobouti Boulevard, Zanjan 45137-66731, Iran.

[b] Research Center for Basic Sciences & Modern Technologies (RBST), Institute for Advanced Studies in Basic Sciences (IASBS), Prof. Sobouti Boulevard, Zanjan 45137-66731, Iran.

Abstract: A novel bifunctional acid-base ordered mesoporous carbon, denoted Ionic liquid derived Bimodal cubic Ordered Mesoporous Carbon (IBOMC), was prepared using a nanocasting protocol with KIT-6 as a hard template. The dual acid-base activity of our catalyst was verified in the Biginelli reaction.

Keywords: Ordered mesoporous carbon; nanocasting; ionic liquids; acid-base bifunctional catalyst; Biginelli reaction.

Introduction

A novel bifunctional acid-base ordered mesoporous carbon, denoted Ionic liquid derived Bimodal cubic Ordered Mesoporous Carbon (IBOMC), was prepared using a nanocasting protocol with KIT-6 as a hard template and a mixture of an of 1-methyl-3-phenethyl-1H-imidazolium hydrogen sulfate (MPIHS) and guanine as ionic liquid as the main organic precursor. The resulted template and carbon samples were characterized by various detection techniques. The coexistence of acidic and basic sites on this carbocatalyst made it suitable for one-pot cascade reactions that require both acid and base, such as the Biginelli reaction.[1] Cascade or tandem reactions where two or more individual reactions are carried out in one pot constitute. In catalytic reactions, cascade processes require bifunctional catalysts containing different classes of active sites.[2] Therefore, it is very important to develop acid-base bifunctional catalysts that can combine two or more steps of a chemical reaction in one vessel and thus improve the reaction efficiency and simplify the work process.[3] It is crucial to create acid-base bifunctional catalysts that can merge multiple steps of a chemical reaction into a single vessel, thereby enhancing reaction efficiency and simplifying the work process. Carbon-based materials can catalyze a wide variety of reactions, but most are less active compared to metal-based catalysts. To solve this problem, chemists have focused on materials with a high surface area.[4] Carbon nanomaterials exhibit great potential for use in creating environmentally friendly catalysts for sustainable chemistry practices.[5] In this study, bifunctional acid-base ordered mesoporous carbon was prepared and used for one-pot cascade Biginelli reactions of acetls.The bifunctional nature of our catalyst was confirmed in the Biginelli reaction, where basic groups facilitate the deprotonation of ethyl acetoacetate, while acidic sites enable the conversion of acetals to aldehydes, activation of aldehydes, and aldol condensation necessary for the synthesis of the Biginelli product.

Experimental Section

Synthesis of the KIT-6 silica template

In a typical synthesis batch,triblock copolymer P123 (6 g) was disolved in water (220 g) and hydrochloric acid (12 g, 37 wt%) with stirring at 35 °C for 6 h. Following complete dissolution, n-butanol (6 g) was added into the solution, and after 1 h of stirring, TEOS (12.48 g) was added to it.The reaction mixture was stirred for 24 h at 35 °C. Then, the mixture was placed under static conditions for 24 h at 100 °C. Finally, the KIT-6 product was obtained after calcination of the solid material at 550°C for 5 h in air.

Synthesis of the IBOMC catalyst

2 g of the MPIHS ionic liquid and 0.3 g of guanine were added to a HCl solution (5 mL, 2 M). This mixture was combined with 2 g of the KIT-6 template and then stirred for 3 h. The composite was then carbonized under a flow of argon at 900 °C for 3 h. The resulting black powder was stirred overnight in a HF (3 M) solution to remove the template. The resulting black powder was stirred overnight in a HF (3 M) solution to remove the template. The filtered mesoporous carbon was washed with water and acetone, and then dried at 100 °C.

22nd Iranian Chemistry Congress (ICC22)
Iranian Research Organization for Science and
Technology (IROST)
13-15 May 2024

03231-97589

ISC

IROST

General procedure for the Biginelli reaction using IBOMC nanocatalyst

In a typical procedure, a mixture of acetal (1.0 mmol), ethyl acetoacetate (1.0 mmol), and urea or Thiourea (1.2 mmol) was stirred at 80 °C, utilizing IBOMC (5,10 mg) under solvent-free conditions for the appropriate time until the reaction was complete (monitored by TLC). After the addition of hot ethanol and after the mixture was centrifuged and filtrated, the formed precipitate was collected. (Table1)

Results and Discussion

The N2 adsorption–desorption isotherm of the KIT-6 showed type IV isotherm with hysteresis loop at the relative pressure of 0.6–0.8 (fig. 1a). BET surface area of 747m^{2}g^{-1}(fig. 1b) , and total pore volume of 0.856 cm^3 g^{-1}. The nitrogen adsorption–desorption isotherm of the IBOMC sample showed a type IV curve with two-step capillary condensation at a relative pressure range of 0.4–0.9 , corresponding to an ordered mesoporous structure with a bimodal mesoporous structure. Ordered mesoporous carbon with many advantages such as large surface area, high ordered pore structure, narrow pore size distribution, has been successfully synthesized by a facile template assisted method. This mesoporous carbon has exhibited its capability in facilitating the multicomponent Biginelli reaction under mild reaction conditions,simple experimental procedure and elimination of solvents.

Conclusions

The nitrogen sorption experiment, small-angle powder XRD, and TEM analyses of the IBOMC significantly confirmed a cubic mesostructure with high regularity and uniform pore-size distribution for the catalyst. Characterization of this carbon by various analyses demonstrated the uniform distribution of N, S, and O-containing functional groups in its framework. This study also revealed the crucial role of topology and a balance between the strength of acid–base functional groups for catalysts in tandem reactions. This catalyst was then successfully applied in the Biginelli reaction of a wide range of acetals with alkylacetoacetates and urea and delivered excellent yields of the corresponding dihydropyrimidinone products.
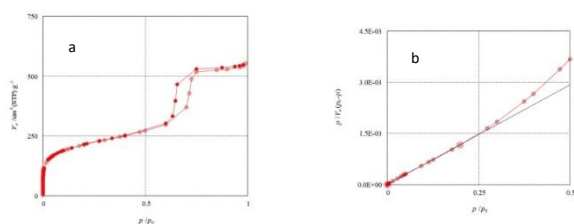

Fig.1: (a) N2 sorption isotherm and, (b) BET surface area

Table1: Preparation of dihydropyrimidinone derivatives in the presence of IBOMC nanocatalyst

Entry	Acetal	Time(h)	T (°C)	Yield (%)
1	Benzaldehyde dimethyl acetal	36	80	81
2	Phenyl Acetaldehyde Dimethyl Acetal	36	80	63
3	4-methylbenzaldehyde diethyl acetal	36	80	82
4	3- methylbenzaldehyde diethyl acetal	36	80	57
5	4-chlorobenzaldehyde diethyl acetal	36	80	80
6	4-nitrobenzaldehyde diethyl acetal	36	80	92
7	4-methyl benzaldehyde dimethyl acetal	36	80	65
8	4-chlorobenzaldehyde dimethyl acetal	36	80	72
9	4-chlorobenzaldehyde diethyl acetal + Thiourea	36	80	40

References

[1] Veisi, H. H., Akbari, M., Karimi, B., Vali, H., & Luque, R. (2023). One-pot acid–base catalysed tandem reactions using a bimodal N, S-doped cubic mesoporous carbon. Green Chemistry, 25(10), 4076-4089. https://doi.org/10.1039/D3GC00117B

[2] Dhakshinamoorthy, A., & Garcia, H. (2014). Cascade reactions catalyzed by metal organic frameworks. ChemSusChem, 7(9), 2392-2410. https://doi.org/10.1002/cssc.201402148

[3] Shi, X. L., Jiang, L., Sun, B., Liu, S., Du, M., Hu, Q., ... & Liu, B. (2021). Tuning acid–base cooperativity to create bifunctional fiber catalysts for one-pot tandem reactions in water. Reaction Chemistry & Engineering, 6(12), 2280-2291. https://doi.org/10.1039/D1RE00352F

[4] Ahmad, M. S., & Nishina, Y. (2020). Graphene-based carbocatalysts for carbon–carbon bond formation. Nanoscale, 12(23), 12210-12227. https://doi.org/10.1039/D0NR02984J

[5] Wang, J., Zhang, Z., Jin, S., & Shen, X. (2017). Efficient conversion of carbohydrates into 5-hydroxylmethylfurfan and 5-ethoxymethylfurfural over sufonic acid-functionalized mesoporous carbon catalyst. Fuel, 192, 102-107. https://doi.org/10.1016/j.fuel.2016.12.027

22nd Iranian Chemistry Congress (ICC22)
Iranian Research Organization for Science and Technology (IROST)
13-15 May 2024

03231-97589

IROST

Application of carbon quantum dots for fluorescence imaging and drug delivery: a DFT study

Soode Amigh

Corresponding Author E-mail: s.amigh@shirazu.ac.ir, s.amigh541@gmail.com

Department of Chemistry, College of Sciences, Shiraz University, Shiraz, Iran.

Abstract: There has been a perpetual interest in finding appropriate nanocarriers for drug delivery. Carbon-based two-dimensional materials have emerged as promising candidates for drug carriers. In this paper, we have investigated the adsorption characteristics of a widely used anticancer drug, doxorubicin (DOX), on the coronene-based quantum dots by density functional theory (DFT) calculations and fluorescence spectroscopy. After the DOX adsorption on the coronene, simultaneous quenching and red-shift in the fluorescence spectrum of the carriers imply that the designed drug delivery systems can be tracked by fluorescence imaging.

Keywords: Coronene; Doxorubicin; fluorescence imaging; Drug delivery

Introduction

Doxorubicin (DOX) is a potent anticancer drug, so developing an effective drug delivery system (DDS) is essential to enhance targeted and controlled delivery to maximize therapeutic outcomes while minimizing side effects [1].

To accomplish optimal therapeutic efficacy, the spatial and temporal tracking of DDSs is vital for drug delivery. Except for magnetic nanoparticle-based drug delivery systems that can be tracked by magnetic resonance imaging (MRI) techniques, the other DDSs are often non-fluorescent and non-tracking [2]. Therefore, it is advised to use fluorescent carriers to make drug delivery systems visually traceable. In preclinical research, fluorescence imaging has become one of the most commonly used powerful imaging tools [3]. This technique is non-destructive and non-invasive to samples. They can be performed in real-time at ambient or physiological temperatures [4]. Coronene-based nano-carriers have stimulated great research interest in bio-imaging, especially in fluorescent probes [5]. Therefore, these nanomaterials are the appropriate choice in order to real-time monitoring of drug delivery and release in vivo and in vitro [6].

In this paper, a fluorescent drug delivery system (CC/DOX) was designed and studied with DOX as the fluorescent antitumor drug and coronene (CC) as the self-fluorescent carrier.

Computational details

Density-functional theory (DFT) and time-dependent DFT (TD-DFT) calculations were employed to optimize the geometries of the ground and excited states of the studied carriers, respectively. All geometry optimizations were carried out with B3LYP three-parameter hybrid functional form in conjugation with 6-31G(d) basis set as implemented in the ORCA molecular code [7]. The polarizable continuum model (PCM) has been employed to take into account the impact of water solvent on the

interaction between coronene-based carriers (CC) and DOX [8].

Results and Discussion

The coronene incorporating amine (CC) was selected as potential carrier for the delivery of DOX drug. The optimized structures for the DOX/CC complex in their lowest energy configurations are shown in Fig. 1.
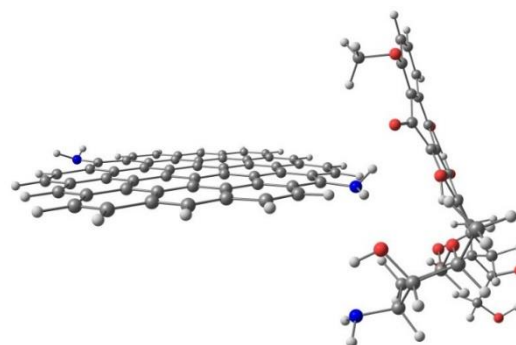

Fig.1: Optimized structures for the most stable configuration of DOX/CC complex.

Then, we turn our attention toward visualization and quantification of the fluorescence emission for the DOX/CC as a part of the delivery system in Fig. 2.
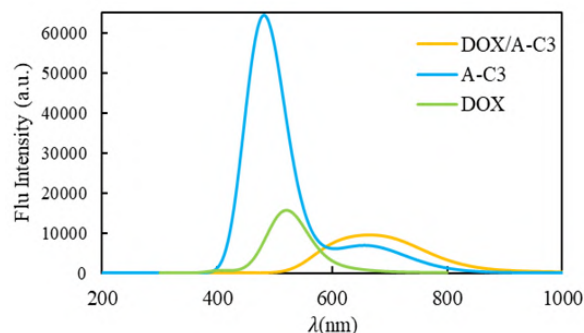

Fig.2: Fluorescence emission spectra of DOX, carrier, and their DOX/CC complex.

22nd Iranian Chemistry Congress (ICC22)
Iranian Research Organization for Science and Technology (IROST)
13-15 May 2024

03231-97589

The fluorescence spectra of DOX exhibits one main band centered at 521 nm that can be associated with the π→π* and n→π* transitions according to the hole and electron distributions. The coronene-based carriers are fluorophore compounds and show entirely distinct emission properties in water. The CC system is a bright blue-emitting fluorophore with a maximum emission wavelength of 484 nm. As evident from Fig. 2, after the adsorption of DOX, the intensity of the fluorescence peak of carriers decreases, however, the complexes still have fluorescence signals in the visible region. The quencher role of the DOX allows us to track the DDS from the complex formation to the drug release via color-changing.

hydrogen bond formation between DOX and carrier stabilizes the excited state and reduces the transition energy, which in turn leads to the red-shifted fluorescence emission as compared to the isolated carriers. This observation evidences the good photostability of the designed DDS in the fluorescence imaging process. Our results are also consistent with earlier studies where simultaneous quenching and red-shift in the fluorescence spectrum of GQDs have also been reported for hydrogen-bonded complexes [9].

Conclusions

The adsorption of DOX drug on coronene-based carrier has been theoretically investigated using the DFT methods. The results indicate that the DOX/CC complex is stable and the adsorption is exothermic in both vacuum and aqueous media. The results of the fluorescence spectra of the systems showed that CC exhibits chromophore behavior which is suitable for bioimaging and real-time monitoring of DDS. Thus, the coronene nanoparticles could be expected to serve as a useful platform for drug delivery and bioimaging as well as for tracking of anticancer drug DOX release.

References

[1] Zhao, N. A., Woodle, M. C., & Mixson, A. J. (2018). Advances in delivery systems for doxorubicin. Journal of nanomedicine & nanotechnology, 9(5).

[2] Jana, A., Nguyen, K. T., Li, X., Zhu, P., Tan, N. S., Ågren, H., & Zhao, Y. (2014). Perylene-derived single-component organic nanoparticles with tunable emission: efficient anticancer drug carriers with real-time monitoring of drug release. ACS nano, 8(6), 5939-5952.

[3] Markopoulou, P., Panagiotou, N., Li, A., Bueno-Perez, R., Madden, D., Buchanan, S., ... & Forgan, R. S. (2020). Identifying differing intracellular cargo release mechanisms by monitoring in vitro drug delivery from MOFs in real time. Cell Reports Physical Science, 1(11).

[4] CHIN, H. L. (2007). Development of a fluorescence correlation spectroscopy method for the study of biomolecular interactions.

[5] Xue, H., Yan, Y., Hou, Y., Li, G., & Hao, C. (2018). Novel carbon quantum dots for fluorescent detection of phenol and insights into the mechanism. New Journal of Chemistry, 42(14), 11485-11492.

[6] Nair, A., Haponiuk, J. T., Thomas, S., & Gopi, S. (2020). Natural carbon-based quantum dots and their applications in drug delivery: A review. Biomedicine & Pharmacotherapy, 132, 110834.

[7] Neese, F. (2012). Wiley interdiscip. Rev.: Comput. Mol. Sci, 2(1), 73-78.

[8] Tomasi, J., Mennucci, B., & Cammi, R. (2005). Quantum mechanical continuum solvation models. Chemical reviews, 105(8), 2999-3094.

[9] Berezin, M. Y., & Achilefu, S. (2010). Fluorescence lifetime measurements and biological imaging. Chemical reviews, 110(5), 2641-2684.

22nd Iranian Chemistry Congress (ICC22)
Iranian Research Organization for Science and Technology (IROST)
13-15 May 2024

03231-97589

IROST

Synthsis of 2-Arylamido4-metylthiazol-5ylacetate andcomparison of its experimental and theoretical NMR spectra

Nadia Tafazzoli*, Ashraf Sadat Shahvelayatia, Leila Hajiaghababaeia, Jamshid Najafpoura, Roya Ahmadi

Department of Chemistry, Yadegar-e-Imam Khomeini (RAH) Shahre Rey Branch, Islamic Azad University, Tehran, Iran.

Abstract: In this study, to preparation of 2-Arylamido4-metylthiazol-5ylacetate, phenyl isothiocyanate was added toAlanine amino acid in the presence of of Acetitril solvent. The reaction was carried out at temperature 40-50℃ for 12 hours with good yield [1]. Thin layer chromatography was used to product confirmation. The structure was verified via Nuclear Magnetic Resonance (NMR). Theoretical studies were done on synthesized compound. The geometry of the conformers has been optimized (Fig. 1). Calculations were done by Density Functional Theory with B3LYP method and 6-31G (d, p) basis set in the vacuum and in the chloroform. 1H chemical isotropic shielding of compounds was calculated by Gauge Including Atomic Orbitals method at B3LYP/6-31G (d, p) levels of theory. Calculated theoretical 1H chemical shift values in terms of ppm for C6-H10-H11-H12, C19-H25-H26-H27, NH-H9, C17-H22, C18-H24,C21-H29,C23-H30 were 1.96, 2.18, 6.61, 7.80, 7.80,8.35 respectively, and also the experimental values in terms of ppm for C6-H10-H11-H12, C19-H25-H26-H27, NH-H9, C17-H22, C18-H24,C21-H29,C23-H30were 2.15, 2.37, 7.26, 8.30, 8.30,8.38,8.38 respectively. The obtained results showed that the experimental NMR results are is good agreement with the theoretical 1H chemical shifts.
Keywords: 2-Arylamido4-metylthiazol-5ylacetate, 'Density Functional Theory'

Introduction

Nuclear Magnetic Resonance (NMR) spectroscopy has become a powerful tool in chemistry and molecular biology [1-4]. There is no straightforward relationship between the structural properties of a molecule and the measured NMR signals, therefore, a reliable method to predict NMR chemical shifts is needed. *Ab initio* and DFT calculations could be used to calculate the NMR spectra [2].

Chemical shift is the most important parameters available in NMR. Both proton and 13C chemical shifts provide chemists with a wealth of structural information. Many *ab initio* methods have been developed to predict the chemical shifts in terms of the chemical properties of atoms, by shielding tensor [3-8].
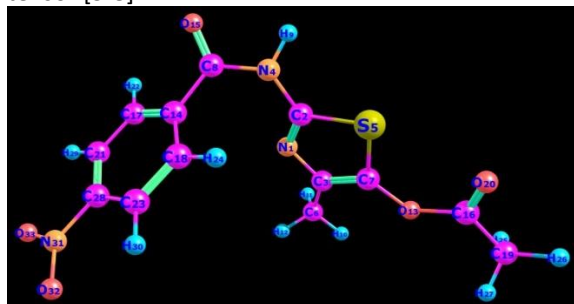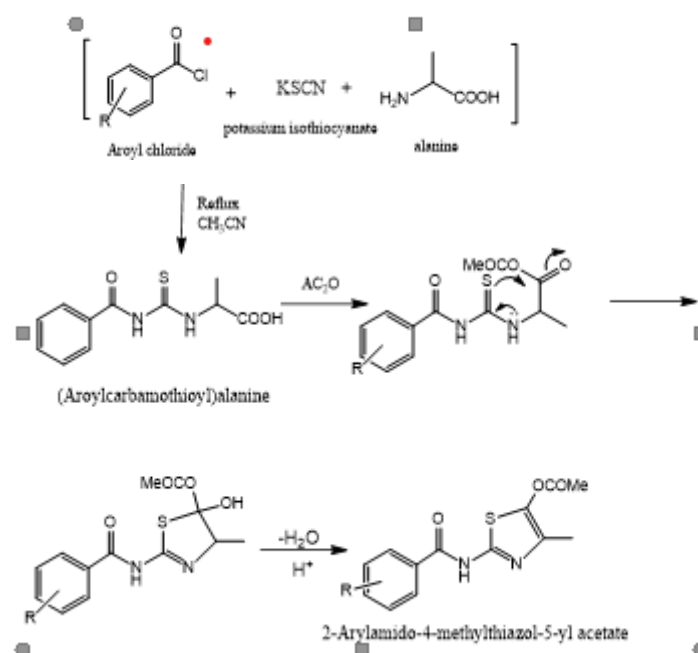

Fig.1: 2-Arylamido4-metylthiazol-5ylacetate

Experimental Section

Results and Discussion

The obtained results showed that the experimental NMR results are is good agreement with the theoretical 1H chemical shifts.

22nd Iranian Chemistry Congress (ICC22)
Iranian Research Organization for Science and Technology (IROST)
13-15 May 2024

03231-97589

IROST

References

[1]Wenjing Bai,Jianxin Ji, Qiang Huang,Wei Wei Synthesis and evaluationof new thiourea derivativeas antitumor and antiangiogenic agents,ELSEVIER, 2020.

[2] Bifulco G., Dambruoso P., Gomez-Paloma L., Riccio R., Determination of Relative Configuration in Organic Compounds by NMR Spectroscopy and Computational Methods, *Chem. Rev.*, **107**(9): 3744-3779 (2007).

[3] Ditchfield R., Molecular Orbital Theory of Magnetic Shielding and Magnetic Susceptibility, *J. Chem. Phys.*, **56**(11): 5688-5691 (1972).

[4] Ditchfield, R., Self-Consistent Perturbation Theory of Diamagnetism, *Mol. Phys.*, **27**(4): 789-807 (1974).

[5] Wolinski K., Hinton J. F., Pulay P., Efficient Implementation of the Gauge-Independent Atomic Orbital Method for NMR Chemical Shift Calculations, *J. Am. Chem. Soc.*, **112**(23): 8251-8260 (1990).

[6] Cheeseman J. R., Trucks G. W., Keith T.A., Frisch M. J., A Comparison of Models for Calculating Nuclear Magnetic resonance Shielding Tensors, *J. Chem. Phys.*, **104**(14): 5497-5509 (1996).

[7] Adamo C., Barone V., Exchange Functionals with Improved Long-Range Behavior and Adiabatic Connection Methods Without Adjustable Parameters: The mPW and mPW1PW Models, *J. Chem. Phys.*, **108**(2): 664-675 (1998).

[8] Adamo C., Barone V., Toward Reliable Density Functional Methods Without Adjustable Parameters: The PBE0 Model, *J. Chem. Phys.*, **110**(13): 6158-6170 (1999).

Analysis of trifluralin pesticide in food samples by MOF/COF hybrid solid-phase microextraction followed by ion mobility spectrometer

Kamal Azadkish[a], Ardeshir Shokrollahi[a]*, Zahra Rafiee[a], Mohammad Reza Rezayat[b], Kowsar Davoodi-Rad[a]

Corresponding Author E-mail: ashokrollahi@yu.ac.ir

[a] Department of Chemistry, Yasouj University, Yasouj, 7591874831, Iran.

[b] Department of Chemistry, University of Isfahan, Isfahan, 81746-73441, Iran.

Abstract: Metal-organic framework (MOF) based on manganese and melamine-rich covalent organic framework (COF) were combined, resulting in an effective nanocomposite sorbent of Mn-terephthalic acid (TA) /COF. Corona discharge ionization-ion mobility spectrometer (CD-IMS) was applied as a detection system for determination of trifluralin molecules. The limit of detection (LOD) 0.08 ng mL^{-1} and linear dynamic range (LDR) 0.25 - 10.00 ng mL^{-1} were obtained.

Keywords: Microextraction; CD-IMS; Ultra-trace analysis; Trifluralin; MOF/COF

Introduction

During the 1940s, organochlorine pesticides (OCPs) were introduced and extremely applied in agriculture. Despite the OCPs are cheap with high efficient, the ecosystems and human health may sustain significant harm as a result of the OCPs persistence and bioaccumulation and accordingly, OCPs have been banned from the mid-1970s [1]. Different sample pretreatment techniques based on liquid- and solid-phase microextraction have been introduced to determine of analytes. The sample pretreatment methodology with the significant features of being rapid, solvent-free, portable, and user-friendly, named SPME, was first offered by Arthur and Pawliszyn in 1990 [2]. In 1970, Karasek and Cohen proposed the gas-phase ion separation method named ion mobility spectrometry (IMS) [3-4].

Experimental Section

Trifluralin standard (96.2 % purity) as the target compound was bought from Kavosh Kimia (Kerman, Iran). Materials such as nicotinamide as a king of standard to calculate reduced mobility, dimethyl sulfoxide (DMSO), terephthalic acid (TA), melamine, manganese (II) nitrate tetrahydrate (Mn(NO3)2·4H2O), terephthaldehyde, ethylenediamine, N,N-dimethylformamide (DMF), and ethanol for the preparation of MOF/COF and phosphoric acid, boric acid, sodium hydroxide, and acetic acid were obtained from Merck Company (Darmstadt, Germany) to prepare a universal buffer as pH regulators.

Results and Discussion

pH of the sample, extraction time, stirring rate, extraction temperature as well as desorption time were optimized for trace analysis of trifluralin from food sample. Under the optimized conditions, the LOD and LOQ and LDR were calculated 0.09, 0.25 and 0.25 - 10.00 ng mL^{-1}, respectively. To examine the proposed method's precision, the relative standard deviation which was related to intra - and inter-day RSDs (n=3) is obtained 2.65 %, 9.9 % for 0.25 ng mL^{-1}, 1.59 %, 6.8 % for 10 ng mL^{-1}, respectively. RSD related to fiber-to-fiber variations (n=3, inter-day) also showed satisfactory reproducibility (9.7 %) for fiber preparation. Enrichment factor of 2000 was also obtained in this study.

Table1: Typical operating conditions related to CD-IMS for determination of trifluralin using SPME-CD-IMS method.

Parameters	Setting
IMS mode	Positive
Target electrode voltage	6.8 kV
Needle voltage	2.6 kV
Drift electric field	450 V cm^{-1}
Injector temperature	220 °C
Shutter grid pulse	240 µs
Drift tube length	11 cm
Shutter grid voltage	200 V

Conclusions

In this research study, Mn-TA/COF as a new and highly efficient nanocomposite sorbent was successfully synthesized by the solvothermal method through hybridization of Mn-TA MOF and imine-linked COF and used as an adsorbent layer for solid-phase micro-extraction as a simple, well-known and cost-effective method. The proposed method is used to extract and analyze ultra-trace amounts of the widely used herbicide trifluralin in target samples such as agricultural waters and food samples including onion, lettuce and grape using

22nd Iranian Chemistry Congress (ICC22)
Iranian Research Organization for Science and Technology (IROST)
13-15 May 2024

03231-97589

IROST

the corona discharge ionization-ion mobility spectrometer.

References

[1] Zang, X., Chang, Q., Pang, Y., Wang, C., Washino, N., & Wang, Z. (2021). Solid-phase microextraction of eleven organochlorine pesticides from fruit and vegetable samples by a coated fiber with boron nitride modified multiwalled carbon nanotubes. Food Chemistry, 359, 129984

[2] Azadkish, K., Shokrollahi, A., Rezayat, M.R., & Rastgar, M. (2023). Development of dispersive liquid–liquid microextraction with solid-phase evaporation as a novel hyphenated method prior to ion mobility spectrometry and its application for trace analysis of fluoxetine. Analytical and Bioanalytical Chemistry, 415, 2665-2676.

[3] Eiceman, G.A., Karpas, Z., Ion mobility Spectrometry, 2nd Edn, CRC Press, Boca Raton, FL, 2005.

[4] Azadkish, K., Jafari, M. T., & Ghaziaskar, H. S. (2017). Performance evaluation of oxygen adsorbents using negative corona discharge–ion mobility spectrometry. Analytica Chimica Acta, 953, 32-39.

Study of essential oil composition of fresh and dry peel of orange fruits peel (Citrus sinensis)

Fatemeh Nazari

Corresponding Author E-mail: ftnazari@gmail.com

Department of chemistry, Research Institute for Applied Sciences, ACECR, Shahid Beheshti University, Evin, Tehran, P.O. Box 19615–1171, Iran.

Abstract: This study investigates the yields, compositions, and identities of EO extracted from peel of Valencia orange cultivated in Iran. The EO yields in dried and fresh orange flavedo were 0.67% & 1.04%. GC results revealed that samples had 90.64 % & 76.61 %, limonene respectively in dried and fresh peel.

Keywords: essential oil; Citrus sinensis; compositions.

Introduction

Citrus is among the major fruits in the worldwide, which has 150 genera and 1600 species. One of the most important citrus fruits globally, is orange that grows in subtropical and tropical regions [1]. The annual global production of orange is more than 47 million tons, of which Iran contributed 3 million tonnes, that sustained increases. A significant portion of oranges, approximately one-third, is processed into various food products like juice, jams, and marmalade, resulting in substantial waste generation. Effective solid waste management is crucial in citrus-processing industries due to this substantial waste accumulation [1].

One of these involves extracting essential oil from orange peels, a by-product of orange processing. Orange essential oil is highly valued for its aromatic properties and finds applications in various products such as beverages, desserts, air fresheners, and perfumes. Additionally, it is prized for its antimicrobial, anti-inflammatory, antitumor, antioxidant, and neuroprotective properties. The chemical structures and classification of citrus essential oils (EOs) can vary depending on factors such as extraction method, species, origin, climate, and harvest time. Typically, orange EOs constitute approximately 0.2–1.7% (F.W.) of citrus peels, with variations across different citrus species. These oils are primarily composed of volatile compounds, accounting for about 93–96% of the total composition, while the remaining 4–7% comprises non-volatile constituents like coumarins, diterpenoids, sterols, and fatty acid. The volatile fraction of citrus EOs mainly consists of monoterpene and sesquiterpene, which are polymers of two or three isoprenes. Monoterpenes, constituting nearly 90% of citrus EOs, include compounds like limonene, α-pinene, β-pinene, α-terpinene, α-terpineol, perillyl alcohol (POH), carvone, and cis- and trans-carveol (CAR), which are predominantly cyclic with unsaturated bonds and may also include oxygen derivatives. Limonene is typically the most abundant monoterpene in citrus EOs, ranging from 60% to 95% in various citrus species. Other minor monoterpenes found in citrus EOs include linalool, nerol, and geraniol [2].

The objective of the present study was to compare the variation in yield and the chemical composition of two essential oils extracted from sun-dried and fresh orange peels using hydro-distillation.

Experimental Section

The oranges were purchased from the local market of Tehran. The samples were washed and manually peeled to separate the flavedo (external part of the orange). The flavedo were washed with distilled water and were divided into two parts; one part was dried and ground before extraction while the other part was extracted immediately.

Hydrodistillation of both fresh and dried orange peels was carried out for 3 hours using a Clevenger-type apparatus according to the method recommended by the European Pharmacopoeia (1997).

The essential oils (EO) were analyzed on the Agilent GC-MS system consisting of a 7693 autosampler and 7890A gas chromatograph connected to a 5975C mass spectrometer (Santa Clara, CA, USA) (inert XL EI/CI MSD with Triple-Axis detector), controlled by 5975-7890GC-MS software (Santa Clara, CA, USA). The GC was equipped with HP-INNOWax (30 m × 0.25 mm i.d., film thickness 0.25 µm) and HP-1 capillary columns (30 m × 0.25 mm i.d., film thickness 0.25 µm). Nitrogen was used as a carrier gas at a flow rate of 0.8 mL/min. The injector and detector temperatures were 250 °C. The oven temperature was programmed from 60 to 180 °C at a rate of 5 °C/min, then from 180 to 240 °C (5 min) at a rate of 10 °C/min. The injection volumes were 0.8 µL. The split injection was conducted with a split ratio of 1:40. The mass spectra were recorded at 70 eV (EI) and were scanned in the range

22nd Iranian Chemistry Congress (ICC22)
Iranian Research Organization for Science and Technology (IROST)
13-15 May 2024

03231-97589

IROST

30–500 m/z. The components were identified by comparing their real retention indices relative to the *n*-alkanes (C_7–C_{30}) and the mass spectra with the NIST.

Results and Discussion

The percentage EO yields in dried and fresh orange flavedo were 0.67% and 1.04%. These compare favorably with the findings of other researchers on EO yields from orange peels. Boukhatem *et al.* (2016) reported 0.42% for Valencia orange peels. Fakayode and Abobi Essential (2018) obtained EO yield between 0.57–3.24% [3,4]. These differences may be attributed to the nature of the fruits and the extraction methods utilized to the processing conditions. The results of the essential oil composition of both fresh and air-dried peel of C. sinensis are presented in Table 1. The identified compounds appertain to hydrocarbon and oxygenated classes such as monoterpenes, sesquiterpenes, monoterpenols, aldehydes, alcohols and esters. Quantitatively, limonene was the major monoterpene identified in the samples. This is not unexpected because previous works had shown limonene to be the dominant terpene in the essential oils of citrus species. Monoterpenes hydrocarbons, oxygenated monoterpenes hydrocarbons and sesquiterpene hydrocarbons were the major classes of terpenes present in the essential oils of the samples. The results of the total percentage of essential oils are showed in Table 1. Monoterpenes are present in the highest percentage in both samples. Sesquiterpenes have the small percentage in dried sample.

Conclusions

After The essential oil yields in dry samples are lower than the fresh and the percentage concentration of the major compounds are higher in the fresh than the dry. The fresh sample had higher percentage of

limonene and myrcene. The dried sample had higher percentage of limonene and valencene. This study highlights the industrial, pharmaceutical and medical potentials of the samples studied.

Table1: Essential oil composition of both fresh and air-dried peel of C. sinensis

N	Compounds	F %	D %
1	(+)-3-Carene	0.43	-
2	Camphene	0.3	-
3	p-Cymene	0.27	-
4	α-Pinene	1	-
5	β-Myrcene	3.77	0.95
6	Limonene	90.97	76.61
7	Citronellol	0.32	0.49

N	Compounds	F %	D %
8	trans-Carveol	-	0.33
9	Linalool	-	0.64
10	Terpin-4-ol	0.19	-
11	α-Terpineol	0.2	-
12	(E)Caryophellene	-	0.58
13	α- Copaene	-	0.33
14	β-Elemene	-	0.37
15	α-Panasinsene	-	0.45
16	β-Panasinsene	-	0.26
17	Valencene	-	9.84
18	β-Selinene	-	1.5
19	α-Sinensal	-	1.5
20	β-Sinensal	-	-
21	Veridiflorol	-	-
22	Germacrene D	-	-
23	α.-Farnesene	-	-
24	Nootkaton	-	-
25	δ-Cadinene	-	-
26	Tridecane	-	-
27	Decanal	1.09	-
28	tridecanal	-	-
29	(-)-trans-Isopiperitenol	-	-
30	Tridecane	0.18	-
31	Limonene oxide, trans-	-	-
32	2-Caren-4-ol	-	-
33	Dodecane	-	-
34	Isobutyl pentyl oxalate	-	-
35	Citronellyl acetate	-	-

References

[1] Dikmetas, D. N., et al. (2024). Sequential Extraction and Characterization of Essential Oil, Flavonoids, and Pectin from Industrial Orange Waste. ACS Omega 9 (12), 14442-14454. https://doi.org/10.1021/acsomega.4c00112.

[2] Karn, A., et al. (2020). In-vivo biotransformation of citrus functional components and their effects on health. Critical Reviews in Food Science and Nutrition. https://doi.org/10.1080/10408398.2020.1746234

[3] Ferhat, M. A., et al. (2016). Cold pressing, hydrodistillation and microwave dry distillation of citrus essential oil from Algeria.,A comparative study. Electronic Journal of Biology S 1, 30-41.

[4] Fakayode, O. A., Abobi, K.E., (2018). Optimization of oil and pectin extraction from orange (Citrus sinensis) peels: a response surface approach, J Anal Sci Technol 9

22nd Iranian Chemistry Congress (ICC22)
Iranian Research Organization for Science and Technology (IROST)
13-15 May 2024

03231-97589

IROST

Effect of Ultrasound on Chemical Composition of *Thymus vulgaris* L. Essential Oil

Hossein Dehghan *[a], Asma Amoozegaran [b]

Corresponding Author E-mail: h.dehghan@shahed.ac.ir

[a] Medicinal Plants Research Center, Shahed University, Tehran, Iran.

[a] Department of Applied Chemistry, Faculty of Science, Islamic Azad University, South Tehran Branch, Tehran, Iran.

Abstract: A few researchers have studied the role of ultrasound waves in stimulating chemical reactions on the essential compounds of plants. This research was conducted with the aim of investigating the effect of ultrasound on the components of essential oil of Thymus vulgaris L., after extracting the essential oil and without the presence of plant tissue.

Keywords: Thyme; Essential oil; Sonication

Introduction

Many researches have been conducted to introduce ultrasound as an auxiliary factor to increase the efficiency of extraction of essential oils from medicinal plants [1]. But few researchers have studied the role of ultrasound waves in stimulating chemical reactions on the essential compounds of plants. This research was conducted with the aim of investigating the effect of ultrasound on the components of essential oil of *Thymus vulgaris* L., after extracting the essential oil and without the presence of plant tissue.

Experimental Section

The aerial parts of the plant were harvested in June 2021 from the south of Tehran at the flowering stage. The essential oil of the plant was extracted using a distillation apparatus (Clevenger) and its compounds were determined by GC and GC-MS [2]. Subsequently, ultrasonic waves were applied to the extracted essential oil by a titanium probe (400 w) and with three variable factors: temperature, time and ratio of essential oil/ water at three levels. Finally, 27 treated essential oils were prepared and their chemical compounds were quantified by GC.

Results and Discussion

The primary essential oil contained 44.37% thymol, 29.80% p-cymene and 21.24% γ-terpinene. The results showed that the application of ultrasound to the essential oil increased the amount of thymol and decreased the amount of γ-terpinene and p-cymene. By optimizing the conditions (1:0 ratio of thyme essential oil and water, 20°C and 10 min), we succeeded in reducing the active ingredient thymol from 44.37% to 70.18% (Table 1).

Table1: Chemical composition of the 27 prepared essential oils

	Thymol	γ-Terpinene	p-Cymene
Control	44.37	21.24	29.8
1	55.46	14.02	26.59
2	70.18	8.46	17.33
3	60.47	12.87	21.68
4	53.36	16.5	26.36
5	51.18	17.93	27.27
6	44.63	21.33	29.66
7	52.18	16.46	24.39
8	52.94	17.7	24.65
9	47.32	20.18	28.33
10	46.95	1962	28.85
11	46.67	20.23	29.04
12	45.8	20.28	28.41
13	47.33	19.47	27.59
14	48.29	19.26	28.15
15	48.44	19.06	28.06
16	46.33	20.17	29.47
17	47.94	1937	28.6
18	4637	20.21	28.94
19	46.67	19.85	28.84
20	46.85	20.14	28.95
21	45.59	20.4	28.8
22	45.92	20.03	29.5
23	45.81	19.89	27.55
24	46.46	20.38	28.9
25	44.91	20.89	29.8
26	49.56	18.09	24.97
27	46.09	20.28	29.1

Ultrasonic waves in the presence of water and oxygen cause the production of hydroproxyl radical (HOO·) and then carry out oxidation reactions to produce thymol from γ-terpinene and p-cymene (Fig. 1).
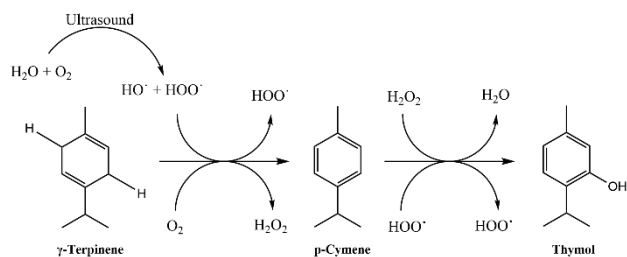
22nd Iranian Chemistry Congress (ICC22)
Iranian Research Organization for Science and
Technology (IROST)
13-15 May 2024

03231-97589

IROST

Fig.1: Proposed mechanism of conversion of γ-terpinene and *p*-cymene to thymol due to application of ultrasound

Conclusions

The results show that, in addition to helping to increase the efficiency of extraction, ultrasound can cause a change in the chemistry and ratio of phytochemical compounds in the essential oil by stimulating radical reactions.

References

[1] Darabad, A. H., Rahimi, M., & Rafati, H. (2022). Continuous hydrodistillation-ultrasonication flow batch-mode operation system to enhance essential oil extraction from Satureja khuzistanica and evaluation of in vitro anti-inflammatory activity. Industrial Crops and Products, 188, 115540.

[2] Dehghan, H., & Habibi, M. (2024). Phytochemistry and antimicrobial activity of the essential oil of Ferula latisecta Rech. f. & Aellen. oleo-gum resin. Journal of Essential Oil Bearing Plants, 1-7.

Combination of Thin Film Microextraction and Dispersive Liquid-Liquid Microextraction Method Followed by Ion Mobility Spectrometry for Analyzing of Chlorpyrifos Pesticide from Food and Water Samples

Mohammad R. Rezayat, Mohammad T. Jafari*, Leila Mohammadipour

Corresponding Author E-mail: jafari@iut.ac.ir

Department of Chemistry, Isfahan University of Technology, Isfahan 84156-83111, Iran.

Abstract: A novel configuration for the combination of the dispersive liquid-liquid microextraction method based on the total vaporization procedure and thin film microextraction was used to extract of chlorpyrifos compound (as the model compound). Corona discharge ionization-ion mobility spectrometer (CD-IMS) was utilized as an identification system. The limit of quantification and limit of detection were obtained at 0.1 and 0.03 $\mu g\ L^{-1}$, respectively.

Keywords: Hyphenated technique; CD-IMS; Ultra-trace determination; Chlorpyrifos; TFME-DLLME

Introduction

The influence of the sample matrix, known as matrix effects, can hinder the direct analysis of complex matrices. These matrix effects can be due to various factors, such as the presence of other chemical compounds, the nature of the sample, and the interactions between the analyte and the matrix. As a result, when we try to analyze a complex matrix directly, without any prior separation steps, these matrix effects can make it difficult to measure the analyte accurately. Different sample preparation methods such as dispersive liquid-liquid microextraction (DLLME) and thin film microextraction (TFME), as two well-known methods, were introduced to minimize the effect of the matrix components [1-2]. In 2003, TFME was introduced by Bruheim et al. [3]. The analyte distribution between an aqueous solution and a thin film is the basis of this method. In 2006, Rezaee et al. introduced the DLLME method as a solvent-based microextraction method [4]. The goal of this studied method was combining of the DLLME with the TFME method for improvement of the extraction efficiency of chlorpyrifos pesticide (as a model compound).

Experimental Section

Chlorpyrifos pesticide (98% purity) was purchased from Kavosh Kimia Kerman Co. (Kerman, Iran). Methanol, ethanol, and acetonitrile (all HPLC grade) were provided from Sigma-Aldrich Co. (St. Louis, USA). Dichloromethane (CH_2Cl_2), toluene, and tetrachloromethane (CCl_4) were prepared from Merck Co. (Darmstadt, Germany).

Results and Discussion

In order to achieve a high extraction efficiency by the proposed approach, different effective parameters, including extraction and disperser solvent types and its volumes, sample pH, organic solvent type, ionic strength, extraction temperature, centrifugation time, and extraction time were investigated and optimized. Under the optimized conditions, the linear dynamic range (LDR), limit of detection (LOD), and limit of quantification (LOQ) were calculated 0.1-7.0 $\mu g\ L^{-1}$, 0.03 $\mu g\ L^{-1}$ and 0.1 $\mu g\ L^{-1}$, respectively. At the three analyte concentrations, the relative standard deviations (RSDs) as a repeatability index were determined 6%, 5%, and 4% for intra-day and 9%, 6%, and 5% for inter-day, respectively. The enrichment factor (EF) was calculated to be 3630 (analyte concentration; 1.0 $\mu g\ L^{-1}$).

Table1: Applied parameters of the CD-IMS instrument

Parameters	Setting
IMS mode	Positive
Detector	Faraday cup
Target electrode voltage	7.5 kV
Needle voltage	4 kV
Drift electric field	420 V cm^{-1}
Injector temperature	220 ℃
Shutter grid pulse	300 μs
Drift tube length	11 cm
Shutter grid voltage	170 V

Conclusions

The TFME-DLLME method was introduced as a novel sample preparation technique for the extraction of chlorpyrifos pesticide and ion mobility spectrometry apparatus was also used for the determination of the studied compound. The proposed approach showed a better preconcentration factor and cleaning-up due to using of two steps of analyte extraction, decreasing the matrix interference.

22nd Iranian Chemistry Congress (ICC22)
Iranian Research Organization for Science and Technology (IROST)
13-15 May 2024

03231-97589

References

[1] Risticevic, S., Niri, V. H., Vuckovic, D., & Pawliszyn, J. (2009). Recent developments in solid-phase microextraction. Analytical and bioanalytical chemistry, 393, 781-795.

[2] Zgoła-Grześkowiak, A., & Grześkowiak, T. (2011). Dispersive liquid-liquid microextraction. TrAC Trends in Analytical Chemistry, 30(9), 1382-1399.

[3] Bruheim, I., Liu, X., & Pawliszyn, J. (2003). Thin-film microextraction. Analytical chemistry, 75(4), 1002-1010.

[4] Rezaee, M., Assadi, Y., Hosseini, M. R. M., Aghaee, E., Ahmadi, F., & Berijani, S. (2006). Determination of organic compounds in water using dispersive liquid–liquid microextraction. Journal of Chromatography a, 1116(1-2), 1-9.

Developing Visual and Instant Copper Metal Sensors in Aqueous Environments Using Polymeric Nanocomposite for Detection of Trace Amounts

Hamed Javadi, Roya Sedghi*

Corresponding Author E-mail: r_sedghi@sbu.ac.ir

Department of Polymer& Materials Chemistry, Faculty of Chemistry & Petroleum Sciences, Shahid Beheshti University, G.C, 1983969411 Tehran, Iran.

Abstract: A portable and sensitive polymeric nanocomposite sensor was developed for detecting Cu^{2+} ions in water. It displayed exceptional selectivity and sensitivity, with a reported detection limit (LOD) of 1 ppm. The sensor induced a significant color change to green in solutions containing copper ions.

Keywords: Copper ion determination; Polymeric nanocomposite; Colorimetric sensor

Introduction

Copper ions (Cu^{2+}) play vital biological roles, but imbalances can lead to neurological disorders. Drinking water should adhere to recommended metal ion levels set by organizations like WHO and EPA. The maximum permissible limits for Cu^{2+} in drinking water are 1.3 mg/L (EPA) and 2 mg/L (WHO) [1]. Various instrumental methods exist for Cu^{2+} detection, but colorimetry provides a cost-effective and rapid approach, allowing visual detection through color changes. Researchers have enhanced titanium dioxide nanoparticles (NPs) with polymers due to their economic benefits and resistance to corrosion[2]. Coating TiO_2 nanoparticles with polymers improves durability, sensitivity, and selectivity, while also enhancing supramolecular interactions and multivalency[3]. This study utilized a new polymeric nanocomposite as a colorimetric sensor with exceptional selectivity and sensitivity for detecting extremely low concentrations of copper ions. Solutions in which the solvent is water. To create the polymeric shell on the surface of the TiO_2 NPs, we utilized N-(4-(3-(4-nitrophenyl)thioureido)N-4-aniline)methacrylamide (NPhTAM) as a monomer, methylenbisacrylamide as a comonomer probe, and MBA as a cross-linker. MBA was specifically chosen as a cross-linker to give the polymeric shell a three-dimensional structure, allowing for optimal interaction with fluoride ions. The sensor caused a chromatic shift to green in solutions containing Cu^{2+}. The low levels of detection achieved can be attributed to the repetitive structure of the polymer and the large surface area of the resulting polymer-nanocomposite material.

Experimental Section
Synthesis of TiO_2 and TiO_2-MAPTMS

In the synthesis of TiO_2 nanoparticles (NPs), a solution containing 0.75 mol L-1 aqueous Titanium (IV) chloride and 1.5 mol L-1 aqueous ammonium sulfate was stirred at 75 °C for 90 min. Ammonium hydroxide was added drop by drop until reaching a pH of 7. The resulting white precipitate was washed with distilled water/ethanol, centrifuged, and dried at 65 °C. It was further heated at 350 °C for 4 h to crystallize the TiO_2 NPs. For the formation of nanostructured TiO_2-MAPTMS, 0.5g of TiO_2 NPs was dissolved in 20ml of toluene and subjected to sonication for 15 min. Subsequently, 1.5 mL of MAPTMS was added to the TiO_2 and toluene mixture. The solution was stirred under atmospheric nitrogen gas at room temperature for 24 h. The final product was washed with a centrifuge and twice with toluene, followed by drying under vacuum at 60 °C for 24 h.

Synthesis of NPhTAM Monomer

In a 50-ml flask, 0.162 g of 1-isothiocyanato-4-nitrobenzene was dissolved in 8 mL of DCM solution. To this stirring solution, 0.1 g of Para-Phenylene-Diamine (PPD) was added dropwise, and the resulting complex was kept at 25°C for 3 h. After the completion of the reaction, any unreacted PPD and the solvent were separated using rotary evaporation. The product obtained was a faded yellow solid with a yield of 96%. Furthermore, 0.25 g of the above product was dissolved in 6 mL of DMF. This solution was added to a stirring mixture consisting of 376 of dry TEA. At 0°C, 87 μL of methacryloyl chloride, which had been dehydrated in 4 mL of DMF, was added dropwise to the reaction solution over 15 min.

Polymerization

AM (0.15 g), MBA (0.36 g), NPhTAM (0.15 g), vinyl-adjusted TiO_2 (0.28 g). The mixture was stirred in a 1:5 solution of 10 ml DMSO/2-propanol at atmospheric temperature for 1 h. Then, AIBN (0.045 g) was added, and the mixture was exposed to nitrogen gas for 15 min. It was then heated at 80 °C for 5 h.

22ⁿᵈ Iranian Chemistry Congress (ICC22)
Iranian Research Organization for Science and Technology (IROST)
13-15 May 2024

03231-97589

IROST

Results and Discussion

Colorimetric sensor responses

The visual response of the chemosensor to various cations such as Fe^{2+}, Ca^{2+}, Mg^{2+}, Mn^{2+}, Hg^{2+}, Pb^{2+}, Ni^{2+}, Co^{2+}, Cd^{2+}, Zn^{2+} and Cu^{2+}, was investigated using colorimetric analysis. By adding aforementioned anions to receptor solutions of chemosensor with a 2:1 ratio, a significant color change to green was immediately observed exclusively in the presence of fluoride ions at pH =5.5. (Figure 1).

Fig.1: Colorimetric response of chemosensor in the presence of Cu^{2+}; color changes in aqueous solution (100 ppm) at pH = 5.5.

Colorimetric sensor responses

SEM images of TiO_2 nanoparticles (a) and a sensor (b) were provided in Figure 2. The SEM results revealed that both the nanoparticles and polymeric nanocomposites have a spherical shape and smooth surface morphology, with a very narrow size distribution. The particle sizes were approximately 35 nm and 90 nm, respectively.
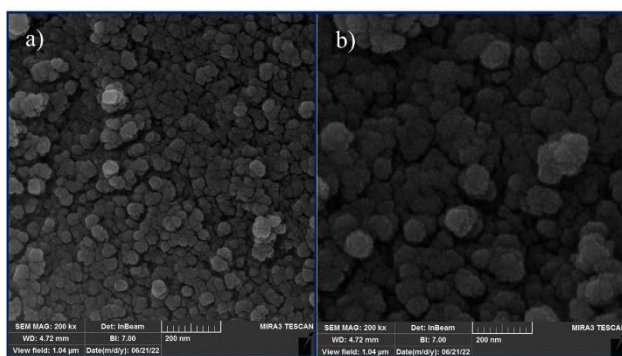
Fig.1: SEM images of TiO_2 NPs (a) and sensor(b)

X-ray diffraction analysis

The TiO_2 nanoparticles exhibit distinct X-ray diffraction (XRD) patterns that correspond to reflections in the anatase phase. These reflections are characterized by peaks at certain angles, namely 25.35°, 37.77°, 47.83°, 54.22°, 62.92°, 75.40°.44 Although organic moieties were added to the surface of TiO_2 NPs, the characteristic Bragg

diffraction peaks remained, indicating that the TiO_2 NPs remained stable during the polymerization procedure. In addition, a wide diffraction peak ranging from $2\theta = 10°$ to 30° was detected, which indicates the scattering of an amorphous polymeric shell (Figure 3).
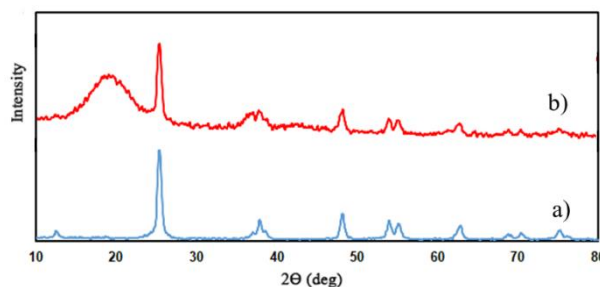
Fig.3: XRD patterns of TiO_2 NPs (a) and sensor(b)

Conclusions

To summarize the present study, the x sensor was designed to detect Cu^{2+} ions in an aqueous solution based on a calorimetric method containing a thioureido section. By applying this noble sensor, the color of the queous solution would convert to green in the presence of Cu^{2+} ions. The present sensor could be defined as a low-cost, non-polluting, environment-friendly, simple-to-use and fast-response invention. Due to the high selectivity of this sensor, the LOD was determined to be 1 ppm.

References

[1] Ramdzan, N. S. M., Fen, Y. W., Anas, N. A. A., Omar, N. A. S., & Saleviter, S. (2020). Development of biopolymer and conducting polymer-based optical sensors for heavy metal ion detection. Molecules, 25(11), 2548; https://doi.org/10.3390/molecules25112548

[2] Razak, N. H. A., Tan, L. L., Hasbullah, S. A., & Heng, L. Y. (2020). Reflectance chemosensor based on bis-thiourea derivative as ionophore for copper (II) ion detection. Microchemical Journal, 153, 104460. https://doi.org/10.1016/j.microc.2019.104460

[3] Sedghi, R., Heidari, B., Javadi, H., & Sayyari, N. (2022). Design and synthesis of colorimetric sensor based on dithizone@ TiO2/poly (tert-butyl acrylate-acrylic acid) nanocomposite for fast visual detection of mercury, lead and cadmium ions in aqueous media. Environmental Nanotechnology, Monitoring & Management, 18, 100670. https://doi.org/10.1016/j.enmm.2022.100670.

Removal of heavy metal zinc from wastewater by microbial fuel cell

Somaye Sobhani [a], Morteza Esfandyari*[b], Hossein Delavari Amrei[b]

Corresponding Author E-mail: m.esfandyari@ub.ac.ir

[a] Master's student in Chemical Engineering, Faculty of Engineering, University of Bojnord.

[b] Associate Professor, Department of Chemical Engineering, Faculty of Engineering, University of Bojnord.

Abstract: By using a microbial fuel cell, it is possible to produce energy while treating wastewater and removing heavy metals. According to the results, the use of microbial fuel cell is very effective in removing zinc metal from wastewater. Using the microbial fuel cell used in this experiment, the removal rate was 75.32% and also the results showed that the MFC used in higher concentrations of zinc metal, has a higher removal.

Keywords: microbial fuel cell; Removal; Wastewater; Zinc.

Introduction

Environmental pollution caused by heavy metals is considered as one of the important issues in its durability, toxicity and bioaccumulation[1]. Heavy metals are extremely harmful environmental pollutants due to their chronic toxicity, non-biodegradability and environmental accumulation, which are dangerous even at low concentrations because they are not biodegradable[2]. There are various methods to treat industrial wastewater containing heavy metals, such as solvent extraction, filtration, ion exchange, coagulation, sedimentation, oxidation and absorption [3]. These methods not only increase the operation cost but also increase the complexity of wastewater treatment [4]. The use of microbial fuel cells to remove or recover heavy metals from wastewater streams and soil has been studied in recent years. Microbial fuel cells can be used to generate energy during the treatment of wastewater containing heavy metals to reduce their concentration before discharge into the environment[3]. This system is based on electrochemically active microbes in the anode (called bioanode) to It not only provides a reduction potential to support the cathode in the reduction of metals, but also for wastewater treatment by oxidizing organic matter[4]. In this research, we intend to remove zinc metal from the wastewater and reduce its amount in the outgoing wastewater by using a two-chamber microbial fuel cell, which we will explain below.

Experimental Section

A two-chamber microbial fuel cell was designed and built. The material of the chambers is 5 mm thick transparent plexiglass and the volume of each of them was 700 cc. Holes were created under the chambers for aeration of the microbial fuel cell, which were controlled by small valves. To transfer protons from the anode to the cathode, the cathode chamber and the anode were separated by a low pressure reverse osmosis membrane made of Composite Polyamide. The electrode used in the anode and cathode chambers was made of magnesium metal and copper metal, respectively, with a cross-sectional area of 32 square centimeters and a thickness of 3 mm. The cathode chamber was filled with phosphate buffer solution in different concentrations of 25, 50 and 75 mM with a pH of 7.01 to keep the pH of the catholyte solution constant. The anode chamber was filled with 200 ml of raw sewage as a substrate and 400 ml of aerobic activated sludge as a biocatalyst from the treatment plant of Bojnord city as anolyte solution. The activated sludge used in this research contains microorganisms such as Rotifers, Flagellates, Ciliates and Amoebae. Due to the low and close to zero concentration of zinc metal in the wastewater entering Bojnord treatment plant, we increased the concentration of anolyte solution to 100 and 200 mg/liter of zinc chloride to increase the amount of zinc metal in the anolyte solution. In order to perform the required analyzes on the sample, samples were taken from the device at time intervals of 0, 24 and 48 hours, and the concentration of zinc metal was immediately measured using a Hach DR5000 spectrophotometer.

The percentage of zinc metal removal was calculated using the following formula:

$$\%Removal = 100 - \left(\frac{C_t}{C_{t0}}\right) * 100$$

where C_t is the concentration of zinc metal at time T and C_{t0} is the concentration of zinc metal at the start of the test, which are measured

Results and Discussion

According to the analysis of zinc metal concentration in the samples, the amount of zinc metal removal was investigated in different states and the effect of time parameters, initial concentration and buffer concentration was investigated. As you can see in Figures 1 and 2, the amount of removal increases significantly with increasing time, and you can also see the effect of buffer concentration on the amount of metal removal. Also, according to Table 1, by increasing the initial

22nd Iranian Chemistry Congress (ICC22)
Iranian Research Organization for Science and
Technology (IROST)
13-15 May 2024

03231-97589

IROST

concentration of zinc chloride from 100 to 200, the removal rate of zinc metal increased. The highest removal rate of 75.32% was obtained in the condition of initial concentration of 200 ppm of zinc chloride, phosphate buffer concentration of 75 mM and in 48 hours after the start of the test.
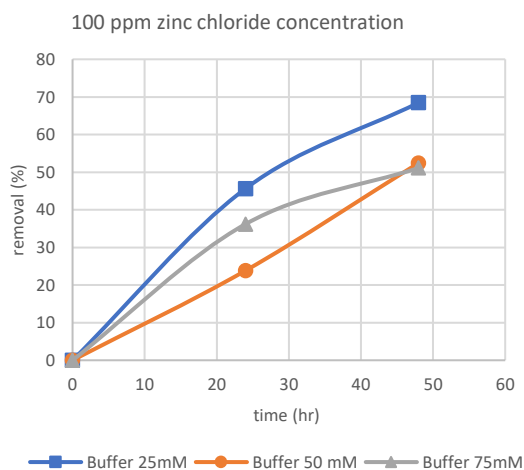

Fig.1: The removal rate of zinc metal over time in different buffer concentrations at 100 ppm zinc chloride
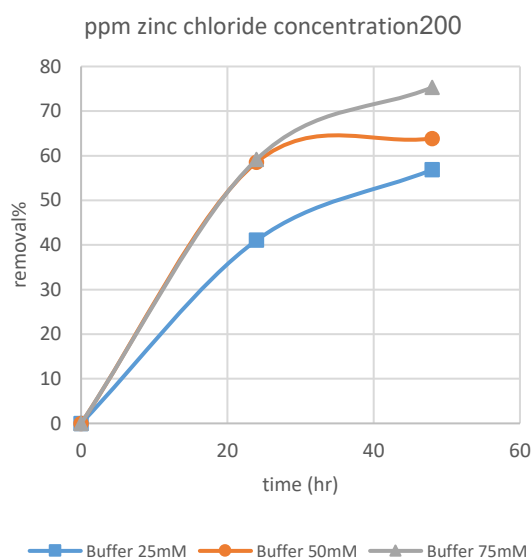
Fig.2: The removal rate of zinc metal over time in different buffer concentrations at 200 ppm zinc chloride

Table1: Percentage of removal in concentrations of 100 and 200 ppm on chloride under the same conditions

Zinc chloride concentration (ppm)	Time(hr)	Phosphate buffer concentration(mM)	%Removal
100	48	75	51.12
200	48	75	75.32

Conclusions

According to the results obtained from this experiment, it was observed that the microbial fuel cell has a significant effect in removing zinc metal from the wastewater and reduces its amount in the outgoing wastewater.

Also, according to the results, it was observed that the parameters of time and initial metal concentration have a direct effect on the removal of zinc metal

References

[1] Do, M. H., Ngo, H. H., Guo, W., Chang, S. W., Nguyen, D. D., Pandey, A., ... & Hoang, N. B. (2022). A dual chamber microbial fuel cell based biosensor for monitoring copper and arsenic in municipal wastewater. Science of The Total Environment, 811, 152261.

[2] Zaynab, M., Al-Yahyai, R., Ameen, A., Sharif, Y., Ali, L., Fatima, M., ... & Li, S. (2022). Health and environmental effects of heavy metals. Journal of King Saud University-Science, 34(1), 101653.

[3] Al-Asheh, S., Bagheri, M., & Aidan, A. (2022). Removal of heavy metals from industrial wastewater using microbial fuel cell. Engineering in Life Sciences, 22(8), 535-549.

[4] Lim, S. S., Fontmorin, J. M., Pham, H. T., Milner, E., Abdul, P. M., Scott, K., ... & Yu, E. H. (2021). Zinc removal and recovery from industrial wastewater with a microbial fuel cell: Experimental investigation and theoretical prediction. *Science of the Total Environment*, *776*, 145934.

22nd Iranian Chemistry Congress (ICC22)
Iranian Research Organization for Science and Technology (IROST)
13-15 May 2024

03231-97589

IROST

3, 4-dihydropyrimidin-2(1H)-ones: Synthesis, anticancer activity evaluation, and Molecular modeling studies

Seyyede Faeze Mortazavi[a,b], Ahmad Ebadi[c], Mahsa Toolabi[a,b], Mohammad Navid Mohammadian[a,b], Ayyub Mojaddami [a,b ,*]
Corresponding Author E-mail: mojaddami.a@gmail.com

[a] Toxicology Research Center, Medical Basic Sciences Research Institute, Ahvaz Jundishapur University of Medical Sciences, Ahvaz, Iran.
[b] Department of Medicinal Chemistry, School of Pharmacy, Ahvaz Jundishapur University of Medical Sciences, Ahvaz, Iran.
[c] Department of Medicinal Chemistry, School of Pharmacy, Medicinal Plants and Natural Products Research Center, Hamadan University of Medical Sciences, Hamadan, Iran.

Abstract: A series derivatives of 3, 4-dihydropyrimidin-2(1H)-ones were synthesized through the Biginelli multi-component reaction and tested for effectiveness against cancer cells. The results showed that the Compound 5l were more effective against A549 cancer cells. Additionally, Molecular docking and dynamics studies were performed on this derivative in the active site of Eg5 and AKT1 enzymes.

Keywords: Cancer; 3,4-dihydropyrimidinones; Cytotoxicity; Molecular Modeling; EG5, AKT1

Introduction

The development of new drugs to treat cancer is crucial, as it is the second leading cause of death worldwide [1]. Dysregulation of the Eg5 receptor pathway plays an important role in cancer progression and making this receptor an attractive molecular target for anticancer drug discovery [2,3]. Several studies have unraveled the potential of dihydropyrimidinone (DHPM) scaffold toward generating cancer agents [4,5].

Experimental Section

In this study, a series of 3, 4-dihydropyrimidin-2(1H)-one C5 amide (**5a-l**) were synthesized through the Biginelli reaction (Fig.1). The efficacy of these compounds against MCF-7, A549, and HeLa cells was evaluated using the MTT method. A pharmacology network analysis was conducted to identify a potential target protein for the dihydropyrimidine derivatives, besides the Eg5 enzyme, and AKT1 protein was chosen as another target protein at the end of molecular docking and dynamics simulations were performed on both enzymes using compound **5l** (The most potent compound obtained from MTT) a racemic mixture of R and S enantiomers.

Results and Discussion

The synthesized compounds were tested for their cytotoxic activity on 3 different cell lines. The results showed that compounds 5a-l were more effective against A549 cancer cells, with compound 5l being the most potent (IC50=23.65±1.87μM). Further analysis revealed that compound 5l induced apoptosis in A549 cancer cells in a dose-dependent manner. Additionally, molecular docking and dynamics simulations were carried out on both enzymes using compound 5l as the ligand. The results showed that the R enantiomer had a more stable complex and a higher binding affinity to the Eg5 enzyme

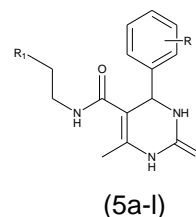active site compared to the S enantiomer and the R-S enantiomer in AKT1.

(5a-l)

Fig.1: These compounds synthesized through the Biginelli reaction

Conclusions

According to the results obtained from MTT and docking and molecular dynamics, DHPM derivative with 4-(4-chlorobenzaldehyde) substituent **5l** shows the greatest inhibitory effect on the Eg5 receptor, so the cytotoxicity of compounds that have an electron-withdrawing group (-Cl) Generally, it is about 4 times more than the compound that shows an electron-donating group (-CH3).

References

[1] Bray F, Laversanne M, Weiderpass E, Soerjomataram I. (2021). The ever-increasing importance of cancer as a leading cause of premature death worldwide. Cancer. 127(16):3029-30. https://doi.org/10.1002/cncr.33587.

[2] Sarli V, Giannis A. (2006). Inhibitors of mitotic kinesins: next-generation antimitotics. ChemMedChem: Chemistry Enabling Drug Discovery. 1(3):293-8. DOI:10.1002/cmdc.200500045.

[3] El-Nassan HB. (2013). Advances in the discovery of kinesin spindle protein (Eg5) inhibitors as antitumor agents. European journal of medicinal chemistry. 62:614-31. https://doi.org/10.1016/j.ejmech.2013.01.031.

[4] de Fátima Â, Braga TC, Neto LdS, Terra BS, Oliveira BG, da Silva DL, et al. (2015). A mini-review on Biginelli adducts with notable pharmacological properties. Journal of advanced research. 6(3):363-73. https://doi.org/10.1016/j.jare.2014.10.006.

[5] Nagarajaiah H, Mukhopadhyay A, Moorthy JN. (2016). Biginelli reaction: an overview. Tetrahedron Letters. 57(47):5135-49. https://doi.org/10.1016/j.tetlet.2016.09.047.

Investigating the treatability of latex glove wastewater using chemical coagulation

M.Khanipour [a], A. Pendashteh [a, b], S. Niazi [b]

Corresponding Author E-mail: Morteza.khanipour76@gmail.com

[a] Department of Chemical Engineering, Faculty of Engineering, University of Guilan, Rasht, Iran.

[b] The Caspian Sea Research Center, University of Guilan, Rasht, Iran.

Abstract: Latex used in glove production generates non-biodegradable wastewater with a high organic load. This study investigated the treatability of wastewater from a latex glove manufacturing plant using chemical coagulation to identify the optimal coagulant type and operational conditions (concentration and pH). The results indicated that ferric chloride has the best performance and at a pH of 4 and a concentration of 1000 mg/L, achieved a COD removal efficiency of approximately 48% under optimal conditions.

Keywords: Latex ;Non-biodegradable; Chemical Oxygen Demand, Wastewater Treatment

Introduction

Natural rubber latex (NRL), a biocompatible and biologically active polymer, is exctracted from the Hevea brasiliensis tree, which is known as the rubber tree[1]. Treatment of wastewater containing natural rubber latex is crucial due to the high content of chemical oxygen demand (COD) of the remaining latex and nitrogenous compounds, which can pollute the environment. Treatment methods for this wastewater are selected based on the pollution load and desired discharge standards. These methods can include advanced oxidation processes, biological treatment, chemical coagulation, or combinations of these techniques[2]. The main purpose of this study is to investigate the efficiency of the coagulation-flocculation process for treating latex-containing wastewater . In this regard, the effect of the influencing parameters on the process efficiency, including pH, coagulant type, and coagulant concentration, were examined. Finally, the optimal condition to achieve the highest level of COD removal was determined.

Experimental Section

A raw wastewater sample was collected from the a latex glove manufacturing plant located in Guilan province, Iran. The sample was then transferred to the water and wastewater laboratory of Guilan University for physical and chemical analyses, as summarized in Table 1. Coagulation-flocculation experiments were conducted using a Jar test apparatus (Zag Chemie) with different coagulant types (polyaluminum chloride (PAC), aluminum sulfate (alum), and ferric chloride) at varying doses and pH conditions. Coagulation process was conducted using the chosen coagulant at the desired dosage. The sample pH was then adjusted using 5 M sodium hydroxide (Merck). Rapid mixing (5 minutes at 120 rpm) followed by slow mixing (20 minutes at 30 rpm) was applied at each stage. Poly acrylamide (5 mg/L) was used as a coagulant aid. After a one-hour settling period, the supernatant was analysed for COD using a COD photometer device.

Table 1: Characteristics of the raw wastewater

Row	parameter	unit	value
1	pH	-	1.5
2	COD	ppm	645
3	TSS	ppm	142
4	NH_4^+	ppm	60

Results and Discussion

The following presents the analytical results comparing the performance of coagulants at optimal pH and various concentrations for COD reduction.
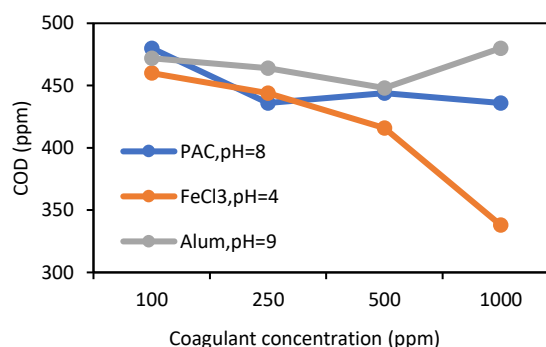

Fig.1: Effects of pH and coagulants dosage on COD reduction

The optimal COD reduction for PAC (32%) was achieved at 250 ppm and a pH of 8. At elevated pH values, increased positive charge on aluminum species enhances destabilization and coagulation of dissolved and colloidal materials through charge neutralization[3] Highest COD removal for alum (26%) was observed at 500 ppm and a

22nd Iranian Chemistry Congress (ICC22)
Iranian Research Organization for Science and
Technology (IROST)
13-15 May 2024

03231-97589

pH of 9. As pH increases, aluminum hydroxide with a high positive charge can effectively settle organic materials with a negative charge, colloids, and particles present in the wastewater through charge neutralization and flocculation mechanisms[4]. The best performance for $FeCl_3$ in COD reduction (48%) was achieved at a pH of 4 and a concentration of 1000 ppm. When $FeCl_3$ is added to wastewater, it dissociates into ferric ions (Fe^{3+}) and chloride ions (Cl^-) in the solution. The positively charged ferric ions (Fe^{3+}) balance the negative charges on colloidal particles and suspended particles in the wastewater. This action causes the particles to destabilize, allowing them to come closer together and reduce the repulsive electrostatic field[5].

Conclusions

This study investigated the treatability of latex glove manufacturing wastewater using coagulation-flocculation to identify the optimal coagulant type and operational conditions (concentration and pH) with the assistance of a polyelectrolyte coagulant aid. The effective parameters including coagulant type, concentration, and pH were examined, and the results were analyzed. It was found that the ferric chloride coagulant at a pH of 4 and a concentration of 1000 ppm yielded the best result, reducing the final COD to 338 mg/L, indicating a removal efficiency of approximately 48%. The results showed that the COD of the wastewater from the latex glove components unit was mostly soluble, and the chemical coagulation process is suitable as a pretreatment and for aiding subsequent treatment units.

References

[1] Guerra, N.B., et al., *Biomedical applications of natural rubber latex from the rubber tree Hevea brasiliensis.* Materials Science and Engineering: C, 2021. **126**: p. 112126.

[2] Nguyen, H.N. and T.T. Luong, *Situation of wastewater treatment of natural rubber latex processing in the Southeastern region, Vietnam.* Journal of Vietnamese Environment, 2012. **2**(2): p. 58-64.

[3] Duan, J. and J. Gregory, *Coagulation by hydrolysing metal salts.* Advances in colloid and interface science, 2003. **100**: p. 475-502.

[4] Amirtharajah, A. and K.M. Mills, *Rapid-mix design for mechanisms of alum coagulation.* Journal-American Water Works Association, 1982. **74**(4): p. 210-216.

[5] Mobasher Moghadam, E. and E. Fataei, *Efficiency of Ferric Chloride (FeCl3) and Poly-Ferric Sulfate (PFS) as coagulants to remove turbidity and organic materials in Ardabil Water Treatment Plant.* Journal of health, 2017. **8**(1): p. 65-73.

Phase Diagrams of the ATPSs composed of PVP$_{10000}$ + Li$_2$SO$_4$ + Water, and the and Partitioning of Ciprofloxacin Drug: The Effect of Temperature and pH

Reza Azizi Adeh [a], Ebrahim Nemati-Kande [a], Vahid Hosseinpour Hashemi [c]

Corresponding Author E-mail: e.nemati@urmia.ac.ir

[a] Department of Physical Chemistry, Chemistry Faculty, Urmia University, Urmia, Iran.

[b] Department of Chemistry, University of New Hampshire, Durham, New Hampshire 03824, USA.

Abstract: The study explored phase diagrams of aqueous two-phase systems with polyvinyl pyrrolidone (PVP) polymer and lithium sulfate salt, investigating temperature and pH effects. Empirical and thermodynamic equations effectively modeled the experimental results. Partitioning of ciprofloxacin was studied, revealing optimal conditions at 308.15 K and neutral pH.

Keywords: Aqueous Two-Phase Systems; Polyvinyl Pyrrolidone; Lithium Sulfate; Ciprofloxacin; Drug

Introduction

Ciprofloxacin, an FDA-approved antibiotic, treats various bacterial infections. Two-phase systems, including aqueous systems, are crucial for separation processes. Polymer-salt ATPSs offer cost-effective and biocompatible solutions for biological applications [1-3]. Research on ATPSs explores factors like temperature and pH affecting phase formation, with implications for drug delivery advancements in pharmaceutical sciences [4]. This study examines the behavior of an ATPS with PVP$_{10000}$/lithium sulfate/water at various temperatures and pH levels, using models to analyze data. The research aims to enhance drug delivery and formulation methods in pharmaceutical sciences through a deeper comprehension of Ciprofloxacin's behavior in complex systems.

Methodology

The cloud-point titration method was used to determine the binodal data point and make the binodal curves that separate monophasic and biphasic areas. In this method, about 2 grams of concentrated PVP solution were titrated with drops of a concentrated solution (~35% w/w) of lithium to observe the turbidity in the cell. Water drops were then added by a micro syringe into the cell till the disappearance of turbidity and emerge of a clear solution. To collect tie-line data, solutions with a mass fraction of approximately 18% w/w of PVP10000 and Li$_2$SO$_4$ solutions with mass fractions ranging from ~8-13% w/w were combined in 15 ml screw cap vials. Also, ~0.001 grams of ciprofloxacin were added to the prepared tie-line compositions, and the samples were placed in the same condition to achieve thermodynamic equilibria. The concentration of ciprofloxacin in two-separetd phases was measured by a UV-Vis spectrometer at λ = 274 nm.

Results and Discussions

Fig. 1 illustrates the graphical representation of binodal curves at various temperatures, demonstrating the impact of the temperature on the formation of phases in the investigated ATPSs. Fig. 1 shows an expansion in the two-phase area at higher temperatures which represents the higher salting-out effect by increasing temperature. In other words, Li$_2$SO$_4$ can defeat PVP$_{10000}$ in the ongoing competition to interact with water molecules which decreases the number of available water molecules for PVP$_{10000}$ that results in fewer polymer-water interactions. To compensate for being beaten, polymer monomers start to interact with the other polymer monomers which causes the separation of polymer as a separate phase from the rest of the system. This self-interaction increases at higher temperatures which shows the higher tendency of phase separation. The phase separation was more efficiently affected by the temperature, while, in salt-rich areas there is a small change in the binodal curves, as the temperature changed.

The designed ATPSs were also used to study the partitioning of ciprofloxacin drug, and the impact of the temperature and pH were employed, as these two parameters can alter the partitioning coefficients. Finally, the concentration of the drug in both Li$_2$SO$_4$-rich and PVP-rich phases was calculated and consequently, the partitioning coefficient of the drug was determined using

$$D = C_{top} / C_{bot} \tag{1}$$

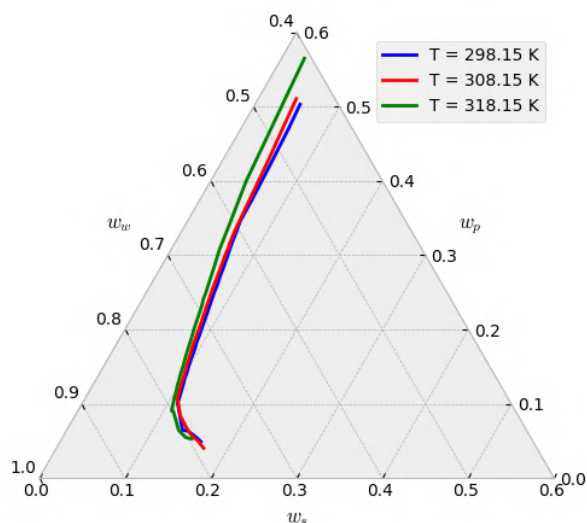here, C represents the concentration of ciprofloxacin (ppm).

22nd Iranian Chemistry Congress (ICC22)
Iranian Research Organization for Science and
Technology (IROST)
13-15 May 2024

03231-97589

IROST

Fig. 1: Comparison of the binodal curves at T = 298.15, 308.15, and 318.15 K for ATPSs containing PVP$_{10000}$ (*p*) + Li$_2$SO$_4$ (*s*) + water (*w*).
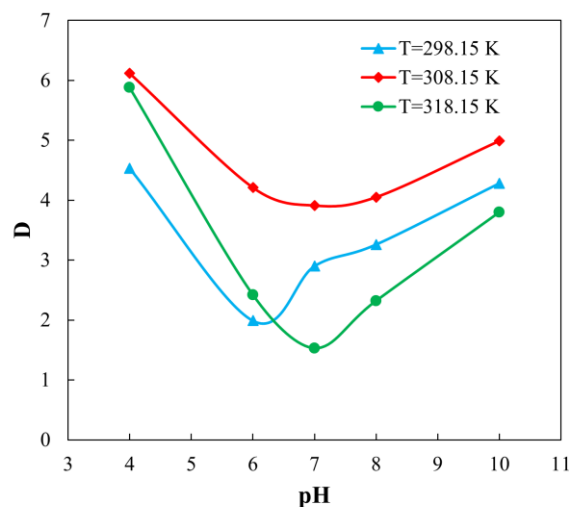

Fig. 2: Distribution coefficient (*D*) of Ciprofloxacin on tie-lines of Li$_2$SO$_4$ (s) for PVP$_{10000}$ (*p*) + Li$_2$SO$_4$ (*s*) + water (*w*) ATPSs at different temperature and pH.

The obtained D values as a function of temperature and pH are shown in Fig. 2. This figure displays that the lowest *D* value was obtained at pH = 7.0 and the D values increase by any change in the pH at all temperatures. The graphs are almost symmetrical around pH = 7.0. It should be noted that D values are larger in acidic pHs than the basic ones. In addition, pH = 6.0 shows the lowest D value at T = 298.15 K. The uppermost D value was measured at T = 308.15 K, while, at the other temperatures the lower values were measured. Figure 8 illustrates that the separation of the drug in polymer- and salt-rich phases can be adjusted by having a proper environment and changing the temperature and pH. It can be concluded that the highest D values can be obtained at neutral and slightly acidic pHs and T = 308.15 K.

Conclusions

The study analyzed an ATPS with PVP$_{10000}$/Li$_2$SO$_4$/H$_2$O at temperatures from 298.15 to 318.15 K and pH levels from 4.0 to 10.0, constructing binodal curves and tie-line compositions. Results showed increased phase formation at higher temperatures, impacting the system's behavior. Ciprofloxacin partitioning was studied, with optimal separation coefficients observed at T = 308.15 K and pH ≤7.

References

[1] Hosseinpour Hashemi, V.; Nemati-Kande, E.; Azizi, Z. Journal of Chemical & Engineering Data 2022, Article ASAP. DOI: DOI: 10.1021/acs.jced.2c00284.

[2] Mokarizadeh, M.; Nemati-Kande, E. *Journal of Chemical and Engineering Data* **2022**, *67* (5), 1237-1249. DOI: 10.1021/acs.jced.2c00091.

[3] Nemati-Kande, E.; Azizi, Z.; Hashemi, V. H. *Journal of Chemical and Engineering Data* **2023**, *68* (4), 945-956. DOI: 10.1021/acs.jced.3c00004.

[4] Zafarani-Moattar, M. T.; Nemati-Kande, E. Calphad-Computer Coupling of Phase Diagrams and Thermochemistry 2011, 35 (2), 165-172. DOI: 10.1016/j.calphad.2011.02.004.

Liquid-Liquid Equilibria of PEG$_{6000}$ + Na$_2$WO$_4$ + water ATPS at Different Temperatures

Reza Azizi Adeh [a], Ebrahim Nemati-Kande [a], Vahid Hosseinpour Hashemi [c]

Corresponding Author E-mail: e.nemati@urmia.ac.ir

[a] Department of Physical Chemistry, Chemistry Faculty, Urmia University, Urmia, Iran.

[b] Department of Chemistry, University of New Hampshire, Durham, New Hampshire 03824, USA.

Abstract: Herein, the liquid-liquid equilibrium of PEG$_{6000}$ + Na$_2$WO$_4$ + water ATPS at T = 288.15, 298.15, 308.15, and 318.15 K was measured and modelled using the e-Wilson, Othmer-Tobias and Bancroft models. Results showed that, by increasing the temperature, the biphasic region of the phase diagram was also expanded.

Keywords: Aqueous Two-Phase Systems; e-Wilson; Thermodynamics; Liquid-Liquid Equilibria

Introduction

Polymer + salt+ water two-phase systems, known as aqueous two-phase systems (ATPS), are ideal alternatives for aqueous-organic two-phase systems, because, water is the majour component of these systems, and therefore they will have the least amount of toxicity and damage to the environment [1-4]. Different kinds of ATPSs are widely used in laboratory and industrial scales to separate different types of materials. In this work the liquid-liquid equilibria of an ATPS composed of PEG$_{6000}$ + Na$_2$WO$_4$ + water components were studied experimentally at T = 288.15, 298.15, 308.15, and 318.15 K, and modelled using the e-Wilson, Othmer-Tobias and Bancroft models.

Methodology

The cloud-point titration method was used to determine the binodal curves that separate monophasic and biphasic areas. In this method, about 2 grams of concentrated PEG solution were titrated with drops of a concentrated solution (~35% w/w) of Na$_2$WO$_4$ to observe the turbidity in the cell. Water drops were then added by a micro syringe into the cell till the disappearance of turbidity and emerge of a clear solution. To collect tie-line data, solutions with a mass fraction of approximately 18% w/w of PEG and Na$_2$WO$_4$ solutions with mass fractions ranging from ~8-13% w/w were combined in 15 ml screw cap vials. Also, ~0.001 grams of ciprofloxacin were added to the prepared tie-line compositions, and the samples were placed in the same condition to achieve thermodynamic equilibria. The concentration of ciprofloxacin in two-separetd phases was measured by a UV-Vis spectrometer at λ = 274 nm.

Results and Discussions

Fig. 1 illustrates the graphical representation of binodal curves at various temperatures, demonstrating the impact of the temperature on the formation of the phases in the investigated ATPSs. Fig. 1 shows an expansion in the two-phase area at higher temperatures which represents the higher salting-out effect by increasing temperature. In other words, Na$_2$WO$_4$ can defeat PEG in the ongoing competition to interact with water molecules which decreases the number of available water molecules for PEG that results in fewer polymer-water interactions. To compensate for being beaten, polymer monomers start to interact with the other polymer monomers which causes the separation of the polymer as a separate phase from the rest of the system. This self-interaction increases at higher temperatures which shows the higher tendency of phase separation. The tie-line cmpositions of the proposed ATPS at T = 298.15 K also was shown in Fig. 2, as an instance.

The designed ATPSs were also used to study the partitioning of ciprofloxacin drug, and the impact of the temperature was also employed. Finally, the concentration of the drug in both slat-rich and polymer-rich phases was calculated and consequently, the partitioning coefficient of the drug was determined using

$$D = C_{top} / C_{bot} \qquad (1)$$

here, C represents the concentration of ciprofloxacin (ppm).

Obtained results confirmed that, the tendency of the drug to extract to the polymer-rich phase is about 6 times greater than the slat-rich phase, which may be used in the purification of the drug.
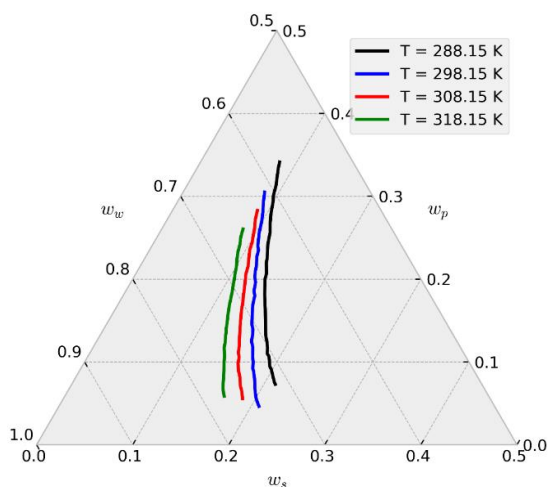
Fig. 1: Comparison of the binodal curves at T = 288.15, 298.15, 308.15, and 318.15 K for ATPSs containing PEG$_{6000}$ (p)+ Na$_2$WO$_4$ (s) + water (w).
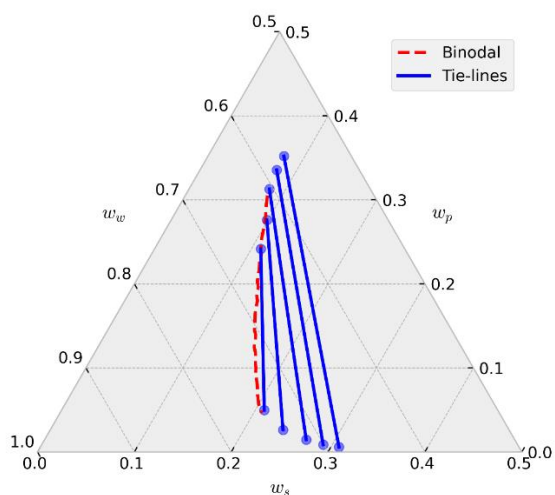

Fig. 2: binodal curve (red) and tie-line compositions (blue) of PEG$_{6000}$ (p)+ Na$_2$WO$_4$ (s) + water (w)ATPS at T = 298.15 K.

Conclusions

The study analyzed an ATPS with PEG$_{6000}$ + Na$_2$WO$_4$ + water components at temperatures from 288.15 to 318.15 K, constructing binodal curves and tie-line compositions. Results showed increased two-phase formation at higher temperatures. Ciprofloxacin partitioning was also studied, with optimal separation coefficients observed at T = 308.15 K.

References

[1] Hosseinpour Hashemi, V.; Nemati-Kande, E.; Azizi, Z. Journal of Chemical & Engineering Data 2022, Article ASAP. DOI: DOI: 10.1021/acs.jced.2c00284.

[2] Mokarizadeh, M.; Nemati-Kande, E. *Journal of Chemical and Engineering Data* **2022**, *67* (5), 1237-1249. DOI: 10.1021/acs.jced.2c00091.

[3] Nemati-Kande, E.; Azizi, Z.; Hashemi, V. H. *Journal of Chemical and Engineering Data* **2023**, *68* (4), 945-956. DOI: 10.1021/acs.jced.3c00004.

[4] Zafarani-Moattar, M. T.; Nemati-Kande, E. Calphad-Computer Coupling of Phase Diagrams and Thermochemistry 2011, 35 (2), 165-172. DOI: 10.1016/j.calphad.2011.02.004.

PES and Transport Properties for He…ZnH2 van der Waals Complex Using Quantum and Classical Kinetic Theory Methods

Ebrahim Nemati-Kande*, Atefeh Akbarpoor

Corresponding Author E-mail: e.nemati@urmia.ac.ir

Department of Physical Chemistry, Faculty of Chemistry, Urmia University, Urmia, Iran.

Abstract: In this study, the transport and relaxation properties of van der Waals complex between Zn atom and H_2 molecule have been investigated. This is done using a new potential energy surface. The results of the kinetic theory of quantum mechanics have been compared with the results of classical molecular dynamics simulations.
Keywords: PES; van der Waals; MD Simulations; Quantum mechanics; Relaxation properties

Introduction

In recent years, attention has been paid to calculate the intermolecular potential energy of small structures, and atom…two-atom van der Waals (vdW) complexes are of great interest. In general, a complex or a vdW compound refers to compounds in which atoms are placed together with weak intermolecular vdW forces. One of the main categories studied is the investigation of the potential energy between an element and small gas molecules [1]. Currently, quantum computing methods have attracted more attention, the main reason for these attentions is the appropriate time and very high calculation accuracy of these methods[2]. In this work, the intermolecular potential of the Zn…H_2 system was calculated by the CCSD(T) method and using Dunning's basis functions of the cc-pvXz-BF type (X = D, T and Q).

Computational details

The ab-inition calculatios were carried out using Gaussian 16 software under the Linux operating system.
The coordinate system used to describe the intermolecular potential of the Zn…H_2 complex is as follows:
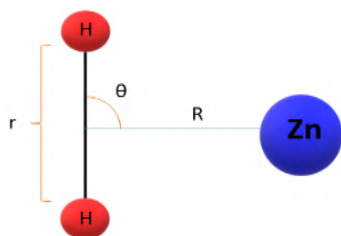
Fig.1: Molecular configuration of the Zn…H_2 complex.

The resulting potential is a function of the bond length of H_2 molecule (r), the distance between the center of the bond vector with the Zn atom (R), and the angle between these two vectors (θ), i.e., U=U(r,R,θ). Here, we assumed that the H2 molecule is a rigid-rotor with the fixed bond length and therfore, U=U(R,θ).

In this work, the angle θ=0° is used for H-H...Zn linear configuration and θ=90° is for T-shape configuration. Potential calculations were performed using the supramolecular method. Also, in calculating the intermolecular potential, BSSE correction was applied by Boyd and Bernardi method. The BSSE corrrected intermolecular energies (U) were calculated as:

$$U (Zn…H_2) = E_{Zn..H2} - (E_{Zn} + E_{H2}) + E_{BSSE} \qquad (1)$$

Where, E_{Zn} and E_{H2} represent the energy of separate Zn and H2 components, respectively. $E_{Zn..H2}$ is the energy of the complex, and E_{BSSE} the BSSE correction energy.

The obtained PES was expanded using the orthonormal Legendre functions, and further fitted using the LJ(12,6), Morse, and Vashishta intermolecular force-filed models. The last three models were used in calculation of the viscosity and diffusion coefficients using the classical time-correlation function formalism of Einstein as implemented in LAMMPS simulation package.

Results and Discussion

The calculated ab-initio potentials was fitted with LJ(12,6) and Morse potentials models, which are generally two-body interaction potentials, i.e., the PES was depicted to be the summation of only two-body interactions of Zn…H type:

$$U(r,\theta) = \sum_{\substack{i,j \\ i \neq j}} V(r_{i,j}) + \varepsilon \qquad (2)$$

Here, $V(r_{i,j})$ is the model potential model (LJ(12,6) or Morse), and ε represents the error arising from the inconsistency of the fitted and ab-initio potentials.
Results of the fitting using the LJ(12,6) and Morse models are shown in Figs. 2 and 3, respectively. The poor fitting of both models and especially the LJ(12,6) is obvious from these figures, which can be related to the low number of

22nd Iranian Chemistry Congress (ICC22)
Iranian Research Organization for Science and
Technology (IROST)
13-15 May 2024

03231-97589

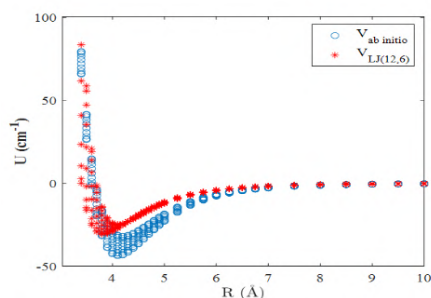the fitting parameters and also the elimination of the three-body interactions.

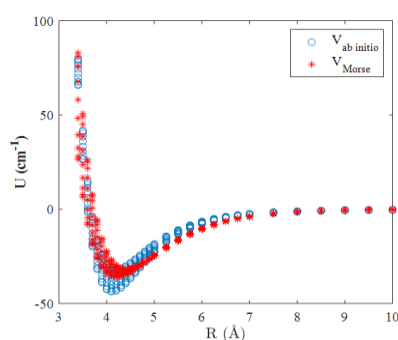**Fig.2:** Fitting results of LJ(12,6) model potential.

Fig.3: Fitting results of Morse model potential.

To solve the defect of the LJ (12,6) and Morse two-body potential models, an effort was also made to consider the contribution of three-particle interactions by choosing a suitable potential model. The potential model presented by Vashita and his colleagues is one of the successful classical models in which the contributions of two-particle and three-particle interactions are considered.

Because the length of the H_2 bond was constant in the extraction of the initio-ab potential data, only the interactions of two ZnH particles are involved. For the interactions of three particles, all three potentials U_{ZnHH}, U_{HZnH} and U_{HHZn} were considered.

$$U_{ZnHH} = (U_{ZnH} + U_{UZnH}) + (U_{ZnHH} + U_{HZnH} + U_{HZnH}) \qquad (3)$$

The configurations used in the extraction of the angles and distances of the Vashishta model was shown in Fig. 4.
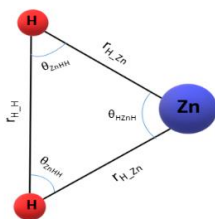
Fig.4: molecular configuration in the Vashishta potential.

The fitting results of Vashishta potential model were compared with the ab-initio potentials in Fig. 5. It is obvious that this model is excellent in presentation of the ab-initio results.
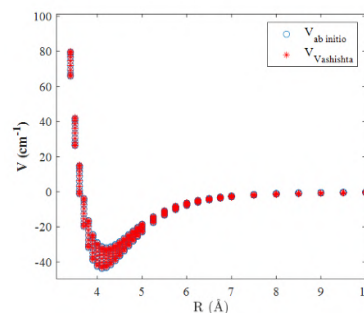
Fig.5: Fitting results of Vashishta potential model.

Also, according to the form obtained for the potential L.J, it can be understood that the calculations are less accurate in the short-range section.

Conclusion

An ab-initio potential model was calculated for Zn…H2 vdW complex and then ab-initio data were used to find LJ(12,6), Morse, and Vashishta potentials. The results obtained from both two-body models are poor due to the elimination of the three-body interactions. However, Vashishta model is excellent in fitting of the ab-initio data. All three models can be used for calculation of different thermophysical properties using classical molecular dynamics simulations.

Reference

[1] Sadeghi, S. E. Nemati-Kande, The Journal of Physical Chemistry A, 2023.**127**(4):p.1053-1067. https://doi.org/10.1021/acs.jpca.2c05901

[2] Nemati-Kande, E., F. Aghababaei, S. Sadeghi, Physical Chemistry Chemical Physics, 2023. **25**(19): p. 13521-13532. https://doi.org/10.1039/D2CP05924J

Evaluation of PVA composite nanofibers for drug delivery

Ali Ghasemi, Masoumeh Taherimehr*

Corresponding Author E-mail: m.taherimehr@nit.ac.ir

Department of Analytical Chemistry, Faculty of Basic Sciences, Babol University of Technology, Babol, Iran.

Abstract: In this study, we employed the electrospinning technique to fabricate metformin hydrochloride-loaded nanofibers using a PVA polymer materials. To mitigate the rapid dissolution of these nanofibers in a PBS medium, a cross-linking process was utilized. The drug release profile was monitored for a duration of 48 hours using a UV-VIS device. The morphology of the nanofibers was examined using FESEM imaging, while EDX analysis and mapping were conducted to identify and quantify the elemental composition of the sample and its spatial distribution. Our findings indicate that electrospinning is an economical and effective method for the production of the desired nanofibers. Successful drug distribution within the fibers was achieved, and the application of cross-linking effectively reduced the high solubility of the nanofibers in aqueous environments, facilitating a sustained and stable drug release over a 48-hour period.

Keywords: drug delivery; drug release; nanofibers; electrospinning; polyvinyl alcohol; metformin hydrochloride

Introduction

Polyvinyl alcohol (PVA) has recently received attention due to its biocompatibility, biodegradability, non-toxicity, and its properties as an ideal place in drug delivery systems. This polymer has a semi-crystalline structure and shows biocompatibility, biodegradability and hydrophilicity, which makes it suitable for various applications such as drug delivery through the skin, tissue engineering and wound protection[1], [2].Extensive research on drug delivery systems through the skin has shown that various factors such as drug molecular weight, concentration and surface area of the carrier affect drug release in PVA-based systems[3].

Electrospinning is a cost-effective and simple tool that is used for the preparation of drug delivery systems using natural, synthetic, and blended polymers. Electrospinning has excessively been used for the development of different drug delivery systems and the process parameters mentioned above significantly affect the fiber morphology[4], [5]. Metformin is a water-soluble drug that was cleared rapidly in the body, but wound healing is a slow process, resulting in the poor bioavailability of metformin. Thus, the controlled release of metformin was probably the good choice to its application in tissue regeneration. The various biomaterials scaffolds with the release of metformin have been developed to promote the cell differentiation for tissue regeneration through the anti-inflammatory pathway[6], [7].

Unfortunately, most of the fibers prepared in the field of release of this drug do not have good biocompatibility and biodegradability and do not have good compatibility with the skin. In this research, cross-linked polyvinyl alcohol fibers have been used in a non-toxic, non-harmful and cost-effective way, which recommends its use in biomedical science.

Experimental Section

Polyvinyl alcohol nanofibers were prepared at an optimal concentration of 10% w/v in distilled water solvent. To prepare the precursor for electrospinning, a 10% w/v solution was placed on a hot plate at 80 °C for 2 h and stirred at 300 rpm. Then the solution was cooled at room temperature (for 24 hours) and its bubbles disappeared. And to create crosslinking, 3% anhydrous citric acid and 1.5% sodium hypophosphite were added to the solution in proportion to the weight of the polymer and stirred for 30 hours. Metformin hydrochloride was then added to the polymer solution at a ratio of 1% by weight of the polymer. When the drug was added to the solution, the solution was kept in a container of ice and away from sunlight (to prevent drug degradation). Then the solution was taken for electrospinning and the nanofibers were successfully prepared according to the controlled and stable conditions, and then placed in a 150°C oven for 30 minutes to create cross-linking and esterification reaction, and drug release was checked in pH 7 solution. It should be noted that non-cross-linked polyvinyl alcohol fibres were not investigated for release because they were rapidly dissolved in aqueous environments.

Results and Discussion

According to the results of FESEM analysis, the nanofibers were successfully prepared without knots and uniform drug loading was confirmed by elemental analysis. The drug was released for 48 hours and 70% of the drug was continuously and stably released. In Figure 1, you can see

22nd Iranian Chemistry Congress (ICC22)
Iranian Research Organization for Science and Technology (IROST)
13-15 May 2024

03231-97589

the image of nano fibers, which are of good quality. And in Figure 2, we can see the result of age analysis.
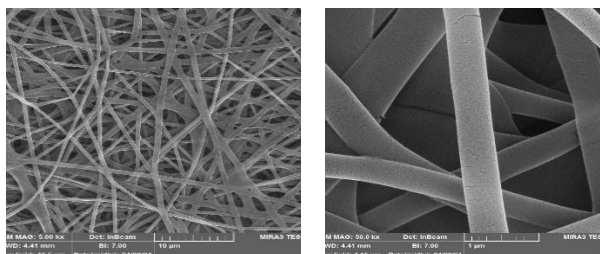
Fig.1: FESEM of PVA Nanofibers loaded with Metformin hydrochloride after crosslinking
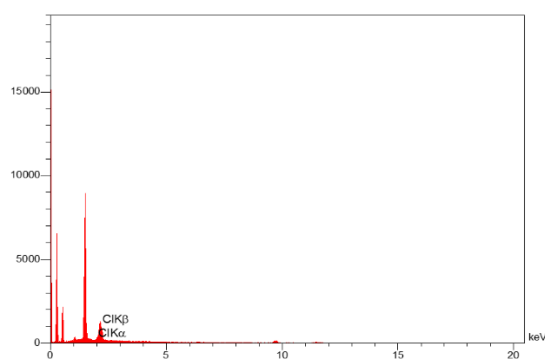
Elt	Line	Int	Error	K	Kr	W%
C	Ka	324.9	205.1685	0.9138	0.4254	84.73
N	Ka	4.7	205.1685	0.0134	0.0062	11.30
Cl	Ka	22.4	72.3265	0.0728	0.0339	3.97
				1.0000	0.4655	100.00

Fig.2: Diagram related to elemental analysis of drug-containing electrospun nanofibers

Table1: Electrospinning parameters

Distance from collector	Voltage	Polymer concentration
15-16 cm	25-26 Kv	PVA 10%(W/V)

Conclusions

According to the results of FESEM analyze, nano fibers were successfully prepared. The process of drug loading and cross-linking prevented drug degradation and rapid drug release. In addition, sustained and sustained drug release was observed over a 48-hour period. These findings show that such nanofibers have promising potential for application in wound dressings, especially for patients with diabetes. This could pave the way for innovative treatments in diabetic wound management.

References

[1] R. Augustine, S. R. ur Rehman, J. K. S., and A. Hasan, "Stromal cell-derived factor loaded co-electrospun hydrophilic/hydrophobic bicomponent membranes for wound protection and healing," *RSC Adv.*, vol. 11, no. 1, pp. 572–583, 2020, doi: 10.1039/d0ra04997b.

[2] F. T. Zahra, Q. Quick, and R. Mu, "Electrospun PVA Fibers for Drug Delivery: A Review," *Polymers*, vol. 15, no. 18. 2023. doi: 10.3390/polym15183837.

[3] S. Sa'adon, S. I. Abd Razak, A. E. Ismail, and K. Fakhruddin, "Drug-Loaded Poly-Vinyl Alcohol Electrospun Nanofibers for Transdermal Drug Delivery: Review on Factors Affecting the Drug Release," in *Procedia Computer Science*, 2019, pp. 436–442. doi: 10.1016/j.procs.2019.09.073.

[4] A. Luraghi, F. Peri, and L. Moroni, "Electrospinning for drug delivery applications: A review," *Journal of Controlled Release*. 2021. doi: 10.1016/j.jconrel.2021.03.033.

[5] M. M. Abdul Hameed, S. A. P. Mohamed Khan, B. M. Thamer, N. Rajkumar, H. El-Hamshary, and M. El-Newehy, "Electrospun nanofibers for drug delivery applications: Methods and mechanism," *Polymers for Advanced Technologies*. 2023. doi: 10.1002/pat.5884.

[6] S. T. Torunoglu, A. Zajda, J. Tampio, M. Markowicz-Piasecka, and K. M. Huttunen, "Metformin derivatives – Researchers' friends or foes?," *Biochemical Pharmacology*, vol. 215. 2023. doi: 10.1016/j.bcp.2023.115743.

[7] L. Xu *et al.*, "Metformin Hydrochloride Encapsulation by Alginate Strontium Hydrogel for Cartilage Regeneration by Reliving Cellular Senescence," *Biomacromolecules*, vol. 22, no. 2, pp. 671–680, 2021, doi: 10.1021/acs.biomac.0c01488.

Synthesis of COF-POSS-PCL nanocomposite scaffold and investigation of its characteristics

Fatemeh Rahmani, Leyla Bagheri*, Hasan Valizadeh

Corresponding Author E-mail: Leyla.baghery@yahoo.com

Department of Chemistry, Faculty of Sciences, Azerbaijan Shahid Madani University, 53714-161 Tabriz, Iran.

Abstract: In the present study, the aim is to attach the covalent organic framework (COF) to polyhedral oligomeric silsesquioxane- Polycaprolactone (POSS-PCL) nanocomposite. With the synthesis of nanocomposite, the next path is the synthesis of nanofibers of the mentioned nanocomposite, and finally the characterization has been done by FTIR spectroscopy. We hope that in the continuation of the current study, these nanofibers will open a field for investigations in the direction of bone tissue engineering.
Keywords: Composite. COF, POSS, PCL

Introduction

COF are newly progressed macromolecules, the knowledge of these combinations has not yet advanced much, and due to their structure and features, they have been able to make waves of eagerness among investigators for novel studies (Li et al., 2020; Pachfule et al., 2018). Côté et.al. in 2005 stated the synthesis of the first COFs that were based on the boron ring. The COFs chemistry is related to the chemistry of macromolecules. The synthesis of macromolecules such as COFs by attracting more attention has opened the field to provide new designs for molecular engineers (Haase & Lotsch, 2020; Liu et al., 2024). Unlike most silicones, POSS molecules contain organic substituents on their outer surfaces, making them compatible or miscible with most polymers. POSS derivatives can be prepared with one or more covalently bonded reactive functionalities suitable for polymerization, grafting, blending, or other transformations. Unlike traditional organic compounds, POSS derivatives are nonvolatile, odorless, and environmentally friendly (Ibrahim et al., 2024; Wang, Chen, Han, Zhou, & Li, 2024). PCL is a synthetic biodegradable polyester. It has good resistance to water, oil, solvent, and chlorine. Polycaprolactone (PCL) is a hydrophobic, semi-crystalline polymer; having a glass transition temperature (T_g) of −60 °C and melting point ranging between 59 and 64 °C, dictated by the crystalline nature of PCL which enables easy formability at relatively low temperatures (Jiang et al., 2024; Roberts et al., 2024). The present study focuses on a combination of POSS, COF, and PCL. Here POSS is expected to act as a nano-scale filler to modify the COF and PCL matrix and potentially result in nanocomposites with new or improved properties.

Experimental Section

Synthesis of COF-POSS-PCL Nanofibers

The electrospinning system was used for the production of COF-POSS-PCL nanofibers. So, a 5 ml syringe containing COF-POSS-PCL (15 wt.%) solution was located on the syringe pump, and a 20cm×15cm aluminum foil was placed in the system as a gatherer, and the essential parameters comprising distance, injection, and voltage were regulated, and then the electrospinning machine turned on. To attain a layer-by-layer COF-POSS-PCL membrane, the parameters were replicated at all steps, constantly. In this process, distance=12cm, injection=2.5 ml/h, voltage=15kV were chosen.

Results and Discussion

Structural characterization of COF‑POSS-PCl

The COF FTIR spectroscopy is showed in Fig. 1a, the recognized peaks in FTIR spectrum (KBr window, cm^{-1}) are: ν(NH) 3400; ν(CH) 2893-2980; ν(C=C) 1650; ν (Triazine ring) 1470-1557. The POSS FTIR spectroscopy is showed in Fig. 1b: ν(OH) 3490; ν(CH) 2883-2970; ν(SiOSi) 1110. The COF-POSS FTIR spectroscopy is showed in Fig. 1c: ν(OH) 3490; ν(CH) 2883-3000; ν(C=C) 1650; ν (Triazine ring) 1470-1557; ν(SiOSi) 1130, and the COF-POSS-PCL FTIR spectroscopy is showed in Fig. 1d: ν(OH) 3480; ν(CH) 2883-3000; ν(C=C) 1715; ν(C=C) 1650; ν (Triazine ring) 1470-1557; ν(SiOSi) 1160.

EDX investigations approved the attendance of C, O, N, and Si, elements in the COF-POSS-PCL (Fig. 2).

X-ray diffraction curves display POSS-PCL-Zeolite crystallinity (Fig. 3). Three distinctive peaks are viewed in 2θ=21˚ and 24.8˚.

The thermograms obtained from DSC clearly showed that the temperature ranges of 30 to 230 ˚C do not show any degradation for these nanoparticles and nanocomposites, but they will likely be degraded at 238–242 ˚C (Fig. 4).

The COF-POSS-PCL scaffold, which consists of biocompatible, porous components with a strong covalent bond of POSS and COF, these components increase the mentioned characteristics by being placed next to each other and connecting to each other. Since they have organic and mineral components, it can be a good simulation for bone.
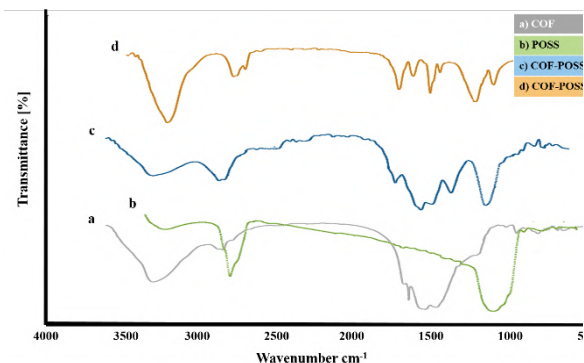
22nd Iranian Chemistry Congress (ICC22)
Iranian Research Organization for Science and Technology (IROST)
13-15 May 2024

03231-97589

Fig.1: The COF-POSS-PCL FTIR spectroscopy

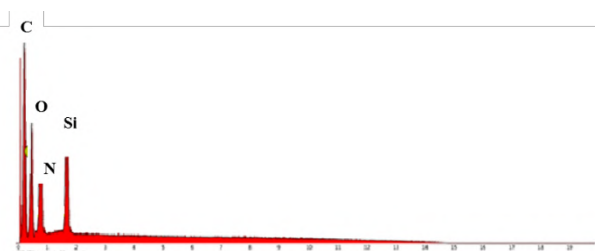**Fig.2:** EDX image of COF-POSS-PCL. The EDX spectrums display the constituent elements of the compound.
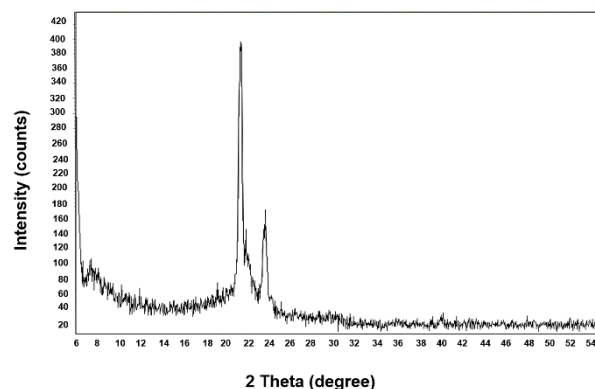

Fig.3: XRD spectra of POSS-PCL-Zeolite nanoparticles.

Conclusions

In this study, each of the components of POSS and COF were synthesized and then they were connected to each other, and by connecting to polycaprolactone, they synthesized a COF-POSS-PCL nanocomposite scaffold, the resulting bonds were examined by the spectrum FTIR. It is hoped that this scaffold can play a role in more ways in the future.
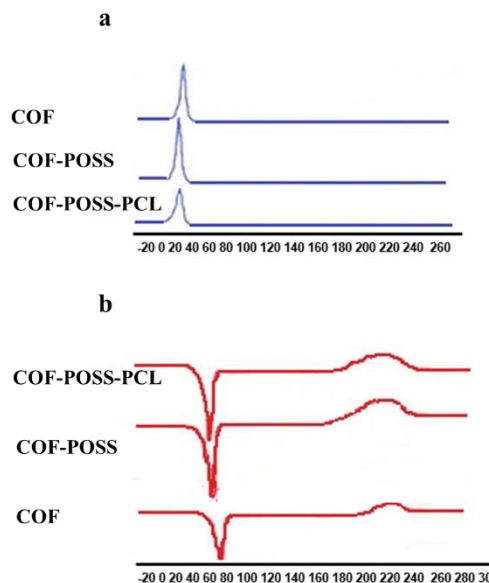
Fig.4: Differential scanning calorimetry analysis (DSC) of COF, COF-POSS, and COF-POSS-PCL

References

[1] Haase, F., & Lotsch, B. V. J. C. S. R. (2020). Solving the COF trilemma: towards crystalline, stable and functional covalent organic frameworks. *49*(23), 8469-8500.

[2] Ibrahim, A., Gardner, O. F., Rodriguez-Florez, N., Hutchinson, J. C., Seifalian, A., Thomas-Vazque, D., . . . Ferretti, P. J. B. M. (2024). Mimicking 3D bone microenvironment using a hybrid hydrogel-nanocomposite scaffold and human adipose-derived stem cells for bone differentiation and vascularization. *2*(1).

[3] Jiang, X., Li, X., Wang, Q., Song, Q., Liu, J., & Zhu, Z. J. I. F. (2024). Multi-sensor data fusion-enabled semi-supervised optimal temperature-guided PCL framework for machinery fault diagnosis. *101*, 102005.

[4] Li, J., Jing, X., Li, Q., Li, S., Gao, X., Feng, X., & Wang, B. J. C. S. R. (2020). Bulk COFs and COF nanosheets for electrochemical energy storage and conversion. *49*(11), 3565-3604.

[5] Liu, Y., Wang, Y., Shang, J., Peng, J., Zhu, T. J. A. C. B. E., & Energy. (2024). Construction of a novel metal-free heterostructure photocatalyst PRGO/TP-COF for enhanced photocatalytic CO2 reduction. *350*, 123937.

[6] Pachfule, P., Acharjya, A., Roeser, J., Langenhahn, T., Schwarze, M., Schomäcker, R., . . . Schmidt, J. J. J. o. t. A. C. S. (2018). Diacetylene functionalized covalent organic framework (COF) for photocatalytic hydrogen generation. *140*(4), 1423-1427.

[7] Roberts, C. T., Beck, S. K., Prejean, C. M., Graul, L. M., Maitland, D. J., & Grunlan, M. A. J. J. o. M. C. B. (2024). Star-PCL shape memory polymer (SMP) scaffolds with tunable transition temperatures for enhanced utility.

[8] Wang, X., Chen, G.-X., Han, R., Zhou, Z., & Li, Q. J. P. i. O. C. (2024). Controlled synthesis of non-functionalized POSS nanoparticles with hydrophobic to hydrophilic wettability transition. *191*, 108398.

A high-performance hybrid supercapacitor based on CuNiTe nanoarrays

Akbar Mohammadi Zardkhoshoui[a*], Saied Saeed Hosseiny Davaran[b*]

Corresponding Author E-mail: mohammadi.bahadoran@gmail.com; ss-hosseiny@sbu.ac.ir

[a] Iranian Research Organization for Science & Technology, Tehran, Iran.
[b] Department of Chemistry, Shahid Beheshti University, G. C., 1983963113, Evin, Tehran, Iran.

Abstract: Herein, CuNiTe nanoarrays are prepared for supercapacitors. Benefiting from the unique structure, the designed CuNiTe nanoarrays possess sufficient electroactive sites. Therefore, the CuNiTe based electrode shows a good capacity of 1100.2 C g^{-1}.

Keywords: Supercapacitors; Nanoarrays; CuNiTe.

Introduction

The performance of hybrid supercapacitors is largely contingent upon the quality of the electrode materials utilized [1]. Among the diverse range of potential materials, battery-type electrode materials have emerged as a prominent focus of research, chiefly due to their potential to facilitate a myriad of redox reactions, enabling them to achieve a high specific capacity [2]. These materials predominantly encompass transition metal compounds such as oxides, hydroxides, sulfides, and selenides [3]. As a result, there is a mounting necessity to explore electrode materials that exhibit high conductivity, positioning this criterion as a pivotal focus in the ongoing advancement of supercapacitor technology. In this context, Tellurium (Te), a rare-earth mineral, demonstrates substantial potential, attributable to its inherent metallic attributes. Its superior conductivity (10×10^3 S m^{-1}), in comparison to Se (1×10^{-3} S m^{-1}) and S (5×10^{-28} S m^{-1}), augmented by its expansive atomic size and lower electronegativity, amplifies its capacity to retain carriers, thereby catalyzing the diffusion kinetics [4]. Consequently, Te-based materials are poised to offer accelerated reaction kinetics, remarkable electrochemical activity, and an increased population of active species throughout the Faraday process.

Herein, we introduce an innovative and powerful approach utilizing hydrothermal and tellurization techniques to create CuNiTe nanoarrays on nickel foam for supercapacitors.

Experimental Section

An aqueous solution (50 mL) mixed with Ni(NO$_3$)$_2$.6H$_2$O (0.80 mmol), Cu(NO$_3$)$_2$.6H$_2$O (2 mmol), CO(NH$_2$)$_2$ (4 mmol), and NH$_4$F (2 mmol) was prepared and stirred for 30 min. Then, the solution was heated for 8 h at 100 °C in an auto-clave comprising the nickel foam. Then, the nickel foam with the deposited precursor was rinsed with H$_2$O and dried. The construction of the CuNiTe nanoarrays was achieved by a tellurization procedure. This entailed situating the obtained precursor and 50 mg of Te powder

at separate locations on a porcelain boat within a tube furnace, arranging the Te powder upstream. The furnace's temperature was gradually elevated to 350 °C at an increment of 1 °C per minute, sustained for 3 hours under a nitrogen (N$_2$) atmosphere.

Results and Discussion

Characterization

Fig.1 reveals the XRD pattern of the CuNiTe sample. For the sample, characteristic peaks of NiTe (JCPDS no. 89-2019) and CuTe (JCPDS no. 22-0252) are evident, demonstrating successful construction. The CuTe peaks appear at 12.9° (001), 26.25° (002), 39.2° (003), 46.4° (112), and 48.85° (103), while NiTe shows pronounced peaks at 30.8° (101), 42.6° (102), 45.7° (110), 56.2° (201), 58.1° (103), 64.5° (202), and 75.3° (211) [4,5].
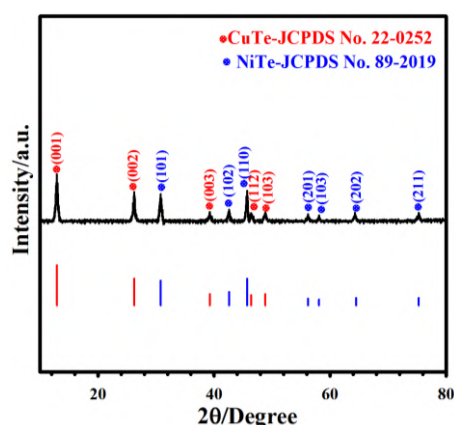

Fig. 1: XRD pattern of the CuNiTe sample.

To study the morphological properties of the CuNiTe sample, we have conducted FE-SEM test. Fig.2 shows the FE-SEM images of the CuNiTe sample. As depicted in Fig.2a, a wide array of wire-like structures are regularly grown on nickel foam. The magnified FE-SEM image (Fig. 2b) reveals that the nanowires demonstrate a rough surface decorated with ultra-small nanosheets.
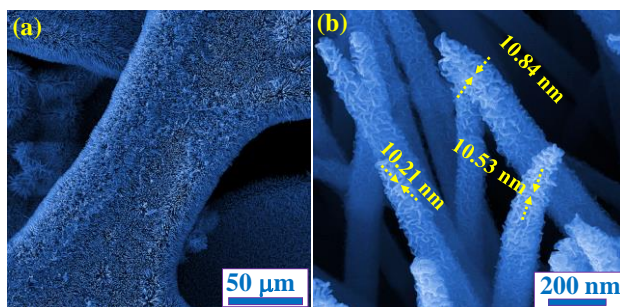
22nd Iranian Chemistry Congress (ICC22)
Iranian Research Organization for Science and
Technology (IROST)
13-15 May 2024

03231-97589

Fig. 2: (a, b) FE-SEM images of the CuNiTe sample.

Electrochemical studies

To evaluate the supercapacitive characteristics, the samples were examined using a three-electrode setup with 6.0 M KOH as the electrolyte. Fig. 3a displays the CV profiles for the nickel foam, CuNiLDH, and CuNiTe electrodes within a 0-0.60 V potential range at a scan rate of 20 mV s^{-1}. The CuNiTe electrode exhibited the largest CV curve area, indicating a remarkable increase in specific capacity. Fig. 3b illustrates the GCD cycles of the CuNiLDH and CuNiTe electrodes at 1 A g^{-1}. Notably, the CuNiTe electrode displayed the longest discharge duration, a feature attributed to its wide active surface area arising from its porous structure. Also, the capacity values of the CuNiLDH and CuNiTe at 1 A g^{-1} are 545.5 and 1100.2 C g^{-1}, respectively (Fig. 3c).

References

[1] Li, Y., Zhang, J., Chen, Q., Xia, X., & Chen, M. (2021). Emerging of Heterostructure Materials in Energy Storage: A Review. *Advanced Materials*, *33*, 210085.

[2] Mohammadi Zardkhoshoui, A., Ameri, B., & Hosseiny Davarani, S. S. (2021). α-MnS@Co$_3$S$_4$ hollow nanospheres assembled from nanosheets for hybrid supercapacitors. *Chemical Engineering Journal*, *422*, 129953.

[3] Zhou, Y., Qi, H., Yang, J., Bo, Z., Huang, F., Islam, M. S., Lu, X., Dai, L., & Amal, R. (2021). Two-birds-one-stone: multifunctional supercapacitors beyond traditional energy storage. *Energy & Environmental Science*, *14*, 1854-1896.

[4] Dehghanpour Farashah, D., Beigloo, F., Mohammadi Zardkhoshoui, A., & Hosseiny Davarani, S. S. (2023). Boosting energy storage performance: An exploration of tellurium-based hollow FeNiCoTe nanocubes in hybrid supercapacitors. *Chemical Engineering Journal*, *474*, 145584.

[5] Salmón-Gamboa, J. U., Barajas-Aguilar, A. H., Ruiz-Ortega, L. I., Garay-Tapia, A. M., & Jiménez-Sandoval, S. J. (2018). Vibrational and electrical properties of Cu$_{2-x}$Te films: experimental data and first principal calculations. *Scientific Reports*, *8*, 8093.

Fig. 3: (a) CV plots of the nickel foam, CuNiLDH, and CuNiTe electrodes. (b) GCD graphs of the CuNiLDH and CuNiTe electrodes at 1 A g^{-1}. (c) Specific capacities of the CuNiLDH and CuNiTe electrodes at 1 A g^{-1}.

Conclusions

In conclusion, this work successfully synthesized wire-like structures of CuNiTe on nickel foam by a combination of hydrothermal and tellurization methods, offering a novel electrode material for hybrid supercapacitors. These structures not only enhance ion and electrolyte transport due to their morphology but also ensure a high number of redox active sites and improved electrical conductivity.

22nd Iranian Chemistry Congress (ICC22)
Iranian Research Organization for Science and Technology (IROST)
13-15 May 2024

03231-97589

IROST

A Hyper Cross-Linked Imidazolium-Based Magnetic Ionic Nanomaterial: As an Efficient Support for Acid-Catalyzed Esterification

Maryam Faraji [a], Fariborz Mansouri* [b], Babak Karimi*[a,c]

Corresponding Author E-mail : karimi@iasbs.ac.ir, f.mansouri@irost.ir

[a] Department of Chemistry, Institute for Advanced Studies in Basic Sciences (IASBS), Zanjan 45137-66731, Iran.

[b] Department of Chemical Technologies, Iranian Research Organization for Science and Technology (IROST), P.O. Box: 15815–3538, Tehran, Iran.

[c] Research Center for Basic Science & Modern Technologies (RBST), Institute for Advanced Studies in Basic Sciences (IASBS). Zanjan 45137-66731, Iran.

Abstract: A new magnetic ionic nanomaterial (MIN) comprising core-shell magnetic nanoparticles as a support and immobilized imidazolium ionic liquid linkers was prepared via a two-step micro emulsion and radical polymerization method. The material demonstrated a combination of interesting features such as three-dimensional network structure, high thermal decomposition temperature, good surface area, high ionic density, high organic content and flexibility, excellent dispersibility and easy separation from the reaction medium using external magnet. Subsequently, by the anion exchange method, the sulfonic acid anion stabilized on the support to prepare a solid acid catalyst. Solid acid catalyst was used in the direct esterification reaction alcohols and acetic acid. The catalyst demonstrated excellent catalytic activity, stability, dispersibility, reusability and easily separation of reaction medium in esterification reaction.

Keywords: Ionic liquids; Magnetic nanoparticles; Acid catalyst; Esterification reaction

Introduction

Esters are of great importance in organic chemistry because they are intermediates in the synthesis of pharmaceuticals, plastics and coating, paint and varnishes, perfumes, flavoring chemicals, preservatives in food products, soap and cosmetics, solvents, and chiral auxiliaries [1]. There are different methods for producing esters, such as Fischer, Schotten-Baumann, Finkelstein, transesterification, etc. However, the simpler and most widely employed method is the reaction of an alcohol with a carboxylic acid, with a Bronsted acid as catalyst, the commonest being concentrated H_2SO_4 [2]. But these acids are very corrosive and their separation and neutralization in the reaction environment is very difficult and time-consuming. The use of heterogeneous catalysts is a very suitable solution for esterification reactions. Among the heterogeneous catalysts, magnetic catalysts are of great interest due to their easy separation using an external magnet and good dispersion in the reaction medium [3].

According to previous work done in the group[4], in this work we prepared a Brønsted acidic magnetic catalyst based on polymeric ionic liquids with a network structure for the direct esterification reaction of various alcohols with acetic acid. For the synthesis of magnetic nanoparticle via silica shell we used microemulsion method. The final catalyst is synthesis via supporting a task-specific ionic liquid on the modified magnetic nanoparticles by free radical polymerization. Then we used ion exchange of bromide ion with HSO_4^- to achieved Brønsted acidic catalyst.

Experimental Section

All chemicals including sodium dodecylbenzenesulfonate (SDBS), $FeCl_2.4H_2O$, $Fe(NO_3)_3.9H_2O$, hydrazine 34%, tetraethylorthosilicate (TEOS) and also solvents were purchased from Merck, Sigma-Aldrich and Across company. Philips CM-200 and Titan Krios transmission electron microscopy (TEM) were utilized for studying the structure of synthesized material. Thermogravimetric analysis was performed from room temperature to 800 °C in nitrogen and oxygen flow using a NETZSCH STA 409 PC/PG instrument. The nitrogen sorption analysis obtained by BELSORP-BELMAX, Japan instrument. FT-IR spectra were recorded using a Bruker Vector 22. The magnetic properties were recorded using a homemade vibrating sample magnetometer (Meghnatis Daghigh Kavir Company, Iran) at room temperature from −10000 to +10000 Oe. Gas chromatography analyses were obtained on a Varian CP-3800 using a flame ionization detector (FID).1HNMR and13CNMR spectra were measured on a DMX-250 and DMX-400 MHz Bruker Advance spectrometer.

The magnetic nanoparticles $Fe_3O_4@SiO_2$ core-shell were synthesized via microemulsion method in reverse water in oil micelles of sodium dodecylbenzensulfunate (SDBS) as a surfactant. In this way, first, SDBS (5 mmol, 1.75 gr) was dissolved in Xylene (15 ml) and sonicated for 30 min.

22nd Iranian Chemistry Congress (ICC22)
Iranian Research Organization for Science and Technology (IROST)
13-15 May 2024

03231-97589

IROST

An aqueous solution of iron salts containing $FeCl_2.4H_2O$ (0.75 mmol) and $Fe(NO_3)_3.9H_2O$ (1.5 mmol) in deionized water (0.75 ml) was prepared. The prepared aqueous was added to the oil solution under vigorous stirring. The microemulsion was stirred for 12 hours at room temperature. In next step, the microemulsion temperature was slowly raised to $90°C$ over an hour and placed under reflux and argon gas. When the temperature stabilizes at $90 °C$, aqueous hydrazine solution (1 ml, 34% wt) was injected dropwise into the reaction mixture to form a black precipitate Fe_3O_4. After 3 hours contiguous stirring under the flow of argon gas, the mixture cooled down to $40 °C$ in an hour. In order to form a silicate shell around the magnetic core of Fe_3O_4, tetraethyl orthosilicate (TEOS) (9mmol, 2 ml) was added dropwise to the mixture and stirred at $40 °C$ for 15 hours under the flow of argon gas. At the end, the prepared superparamagnetic nanoparticles were collected by a magnet and were washed with deionized water and ethanol until the surfactant is completely removed. The obtained material was dried at $80 °C$ in oven and finally a reddish-brown powder was obtained.

In the next part, magnetic nanoparticles functionalized with a hyper cross-linked poly ionic liquid material and then treated with $KHSO_4$ to prepare final catalyst.

Results and Discussion

The prepared materials in each step were accordingly characterized by various techniques, including TGA, FTIR, N_2 adsorption–desorption, elemental CHNS, TEM and VSM analysis. The FT-IR spectrum (figure 1) of $Fe_3O_4@SiO_2$ showed peaks related to stretching vibrations of Fe-O bond (500 cm^{-1}), symmetric and asymmetric stretching of Si-O-Si bond and stretching vibration of Si-OH (800 and 1300 cm^{-1}) which indicate the present of Fe_3O_4 and SiO_2 in the compound.
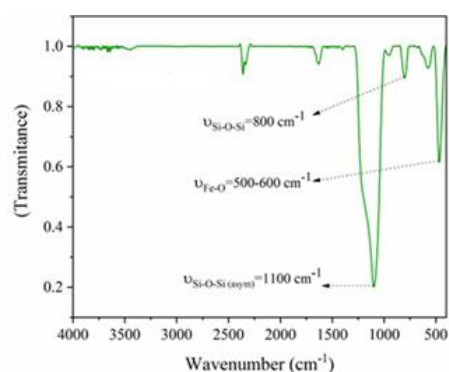

Fig.1: FT-IR spectra for $Fe_3O_4@SiO_2$ core-shell nanoparticle

The catalytic performance of developed catalyst was investigated in solvent free esterification reaction of 3-phenyl-1-propanol and acetic acid. In the first step, the

reaction conditions, including reaction temperature and time, amount of alcohol and acetic acid, and mol% of the catalyst were optimized. Finally, using 0.1 mol% of the catalyst and 5 equivalents of acetic acid, the coresponding ester was prepared with 98% yield at 85 °C at solvent-free condition.

Conclusions

A new magnetic ionic network (MIN) comprising core-shell magnetic nanoparticles as a support and immobilized imidazolium ionic liquid linkers was prepared via a two-step micro emulsion and radical polymerization method. The material demonstrated a combination of interesting features such as three-dimensional network structure, high thermal decomposition temperature, good surface area, high ionic density, high organic content and flexibility, excellent dispersibility and easy separation from the reaction medium using external magnet. Subsequently, by the anion exchange method, the sulfonic acid anion stabilized on the support to prepare a solid acid catalyst. Solid acid catalyst was used in the direct esterification reaction of 3-phenyl-1-propanol and acetic acid. The catalyst demonstrated excellent catalytic activity, stability, dispersibility, reusability and easily separation of reaction medium in esterification reaction.

References

[1] Khan, Z., Javed, F., Shamair, Z., Hafeez, A., Fazal, T., Aslam, A., ... & Rehman, F. (2021). Current developments in esterification reaction: A review on process and parameters. *Journal of Industrial and Engineering Chemistry*, *103*, 80-101.

[2] Barbosa, S. L., Dabdoub, M. J., Hurtado, G. R., Klein, S. I., Baroni, A. C., & Cunha, C. (2006). Solvent free esterification reactions using Lewis acids in solid phase catalysis. *Applied Catalysis A: General*, *313*(2), 146-150.

[3] Karimi, B., Mansouri, F., & Mirzaei, H. M. (2015). Recent Applications of Magnetically Recoverable Nanocatalysts in C⎯C and C⎯X Coupling Reactions. *ChemCatChem*, *7*(12), 1736-1789.

[4] Karimi, B., Tavakolian, M., Mansouri, F., & Vali, H. (2018). Nanopalladium on magnetic ionic nanoparticle network (MINN) as an efficient and recyclable catalyst with high ionic density and dispersibility. *ACS sustainable chemistry & engineering*, *7*(4), 3811-3823.

22nd Iranian Chemistry Congress (ICC22)
Iranian Research Organization for Science and Technology (IROST)
13-15 May 2024

03231-97589

IROST

New Approaches to Direct Electroanalysis Ascorbic Acid in Bio-samples Using a Combined Ultra-microelectrode

Samira Fathi[a], Amir Hatami(e) [a,b*]

Corresponding Author E-mail: amir.hatami@iasbs.ac.ir, amir.hatami@gu.se

[a] Department of Chemistry, Institute for Advanced Studies in Basic Sciences, Zanjan, Iran.
[b] Department of Chemistry and Molecular Biology, University of Gothenburg, Gothenburg, Sweden.

Abstract: We have developed novel combined microelectrodes by modifying carbon fiber (33 µm) coated with an Au nano-film to serve as a working electrode and tiny silver wire as reference electrode. This microscale tool allows for the direct microelectroanalysis and monitoring of ascorbic acid in lemon and cactus bodies, serving as biological matrices and stored fresh juice in different conditions.

Keywords: Ultra-microelectrode; Ascorbic Acid; Electroanalysis.

Introduction

While direct analysis of real biosamples is a complex process compared to other systems, it also yields a set of novel and valuable results. Vitamin C plays a pivotal role in our immune functions; however, in contrast to other vitamins, human body cannot generate it. Therefore, there is a high demand for the development of new tools capable of onsite monitoring and analysis of natural sources without any treatment, even in the field and during the transfer and storage of food products. By leveraging the unique features of microelectrodes, we have developed novel combined microelectrodes by modifying carbon fiber (33 µm) coated with an Au nano-film to serve as a working electrode and tiny silver wire as reference electrode. This microscale tool allows for the direct microelectroanalysis of ascorbic acid in lemon and cactus bodies, serving as biological matrices. Beyond the potential for direct electroanalysis in these bio-matrices, our primary objectives include the examination of the distribution of ascorbic acid content across different sections of lemon fruit and parts of the cactus plant. Both lemon and cactus are recognized sources of vitamin C. Notably, the micro-size of the combined sensor provides sufficient resolution for microscale analysis in fruit and plant samples without sample treatment. Our electrochemical measurements revealed that the center of the lemon contains notably higher levels of Vitamin C compared to its sides. Also, the levels of Vitamin C are higher in the fresh arms of the cactus in comparison to the older arms and the cactus trunk. Furthermore, our observations indicated that improper storage of lemon products in the presence of day light in on week significantly reduces the vitamin's levels. Finally, we believe that these findings hold a significance and practical applicability in the agricultural, medicinal, and food industrial sectors.
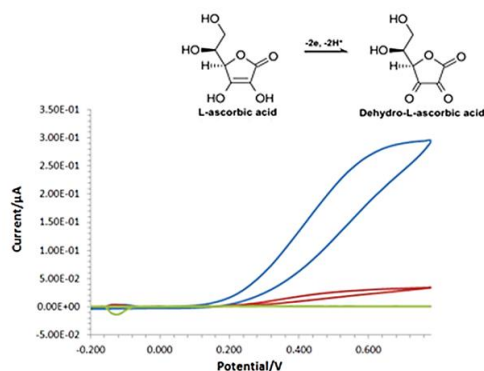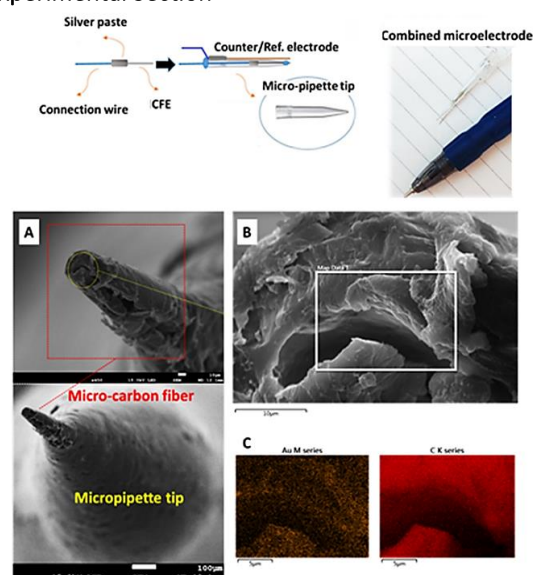
Experimental Section

Fig. 1: (Top) Schematic of fabrication of combined microelectrode (D=33 µm) and its image. (Middle) SEM images of modified carbon microelectrode with Au film (CME@Au). (Bottom) CVs of CME@Au microelectrode in 1.0 mM PBS i the absence (green) and presence (blue) of 0.5 mM AC, CVs o MCFE in 1.0 mM PBS and 0.5 mM AC. (Scan rate:100 mV/s.)

22nd Iranian Chemistry Congress (ICC22)
Iranian Research Organization for Science and Technology (IROST)
13-15 May 2024

03231-97589
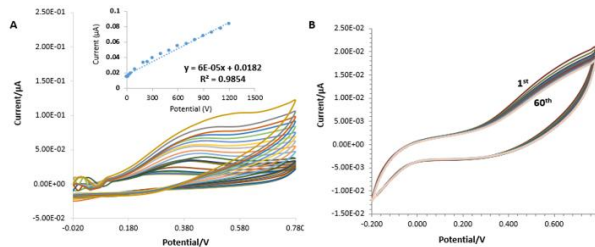
IROST

Results and Discussion

FiG.2: A) CVs of AC in 0.1 M PBS (pH 6.0) containing various concentrations of AC, listed from inner to outer: 5, 10, 20, 50, 35, 100.0, 150, 200, 300, 110, 500.0, 150.0 + 700.0, and 1200.0, respectively. Inset: Plots of i vs. AC concentrations.
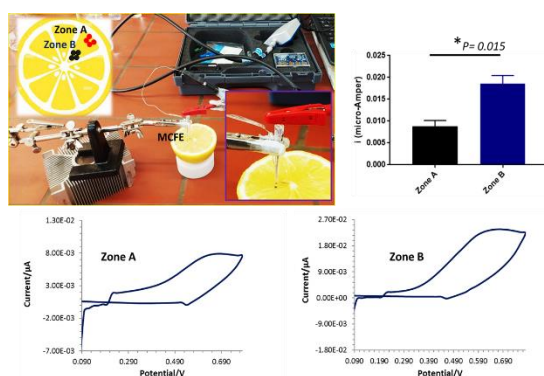
►On site Microanalysis in Lemons

Fig.3: (A) Photograph of in-situ voltammetric analysis and (B) the recorded CVs in a lemon using a combined UME@Au in two zones (Zone A and B). (C) Comparison of average recorded current intensities of AC oxidation at Zone A and B and P value equals 0.05 (The pairs of data sets were compared using the Wilcoxon–Mann–Whitney test).

►Monitoring AC level ins different types of lemon and storage conditions
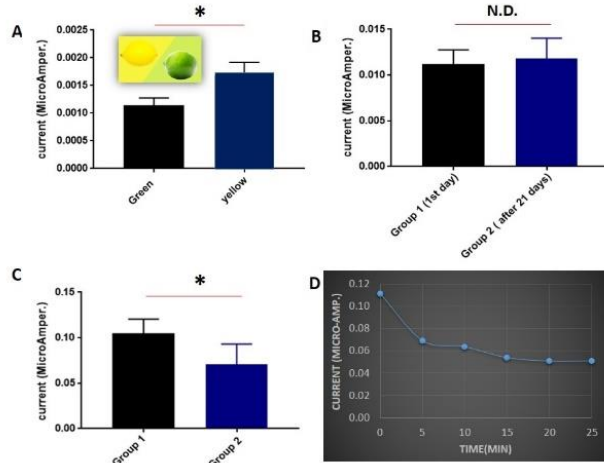
Fig.4: (A) Comparisons of recorded current intensity from voltammetric measurements of AC content by UME@Au in (A) lemons with different colors, (B) fresh lemon samples, and stored lemons in the fridge for three weeks. (C) Lemon samples were stored in front of the daylight and in the shadow in an

airtight container. (For all measurements, the pairs of datasets were compared using the Wilcoxon–Mann–Whitney test). (D) Monitoring AC levels in a fresh single droplet of freshly extracted lemon juice over time.

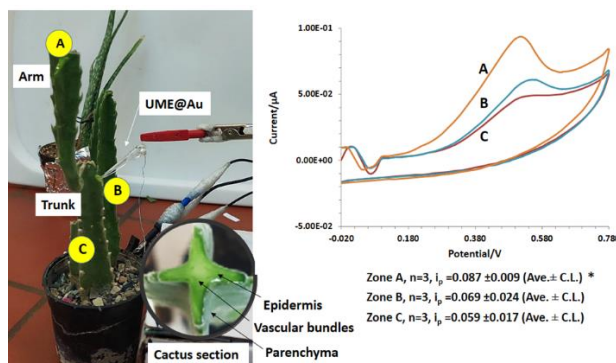### ►In Vivo Electrosensing of AC within Cactus Plant

Fig.5: (a) Electroanalysis of AC within cactus body by implantable combined UME@Au, (b) Recorded cyclic voltammograms (scan rate 0.1 V/sec) of AC oxidation recorded at different points of plants (* Average of signals ± confidence limit).

Conclusions

We used this UME to analyze different sections of a cut lemon, a small volume of lemon juice, evaluate the storage of lemon fruit juice, and to perform in vivo analysis within the body of a cactus plant, obtaining and statistically analyzing interesting results. Our findings are pertinent for farmers and gardeners, providing a new perspective on growing, harvesting (finding suitable times), and suitable storing conditions (air and daylight effects) to produce and store natural products with higher quality.

Additionally, the combined UME demonstrated the potential and capability of electrochemistry in modern agriculture, addressing complex questions about the distribution of chemicals within plants or fruit samples, which can be challenging or expensive with other analytical techniques. We also believe that with some modifications, this UME can be used for monitoring other important molecules in plants, such as glucose, salicylic acid, and growing hormones within plant sections, as well as for some disease and plant stress diagnosis within plants, supporting and improving modern agriculture and smart farming in the near future.

References

[1] Malik, Meghna, Vinay Narwal, and C. S. Pundir. Process Biochemistry 118 (2022): 11-23.

[2] Öri, Zsuzsanna, Lívia Nagy, László Kiss, Barna Kovács, and Géza Nagy. Electroanalysis 27, no. 3 (2015): 808-816.

[3] Paixão, Thiago RLC, Denise Lowinsohn, and Mauro Bertotti. Journal of agricultural and food chemistry 54, no. 8 (2006): 3072-3077.

ZnFe₂O₄@SiO₂@n-pr@PYD-Ni: A novel, green, recyclable, and highly versatile catalyst for the synthesis of polyhydroquinoline derivatives

Sahar Safari, Arash Ghorbani-Choghamarani[*], Hamid Aghavandi

Corresponding Author E-mail: arashghch58@yahoo.com

Department of Organic Chemistry, Faculty of Chemistry, Bu-Ali Sina University, Hamedan, 6517838695, Iran.

Abstract: In this paper, we report the synthesis of ZnFe₂O₄@SiO₂@n-pr@PYD-Ni as a novel magnetic nanocatalyst, in a mild and green environment. The structure of the described magnetic compound was characterized by different physicochemical techniques including XRD, EDS, SEM, FT-IR, X-ray elemental mapping, TGA, and VSM analyses. The prepared magnetic nanoparticles exhibit excellent catalytic activity in synthesizing polyhydroquinoline derivatives under green conditions

Keywords: nano-magnetic catalyst; Polyhydroquinoline; Heterogeneous catalyst

Introduction

In catalytic studies, the recovery and reusability of the catalyst due to its adaptability to the environment are important features of the catalytic process that has received much attention in recent years. The recovery and reusability of catalysts is an important challenge in modern research because the employed catalysts are often very costly or the obtained products are often very valuable from the economical and medicinal points of view. The development of green and environmentally friendly catalytic procedures, along with the design of unique, relies on the improvement of catalyst achievement. Transition metal-based catalysts have been established to be competent for organic transformations. In the past decade, heterogeneous catalysts, which consist of a hybrid organic-inorganic material, have received much attention due to both the advantages of homogeneous and heterogeneous catalysts. Recently, the use of magnetic nanoparticles as catalytic support in the preparation of nanocatalysts in the green method has been considered by scientific researchers. Magnetic materials such as zinc ferrite due to their unique and non-toxic magnetic properties, good biological compatibility, and adjustable magnetic properties, have been used in various fields including cancer therapy, drug delivery, and targeting. Ferrites ZnFe₂O₄ have the same properties as homogeneous catalysts and are also facilely extracted from the reaction by an external magnet and do not require more rigorous methods such as filtration or centrifugation. The use of magnetically separable catalysts is a well-favored and fascinating strategy to bridge the split between heterogeneous and homogenous catalysis processes. As a main member of the ferrite family, ZnFe₂O₄ has promising potential for use as novel catalytic support. Additionally, the surface hydroxyl groups over them facilitate their surface modifications with a wide variety of organic compounds.

Herein, we report ZnFe₂O₄@SiO₂@n-pr@PYD-Ni MNPs as a green, novel, reusable, and eco-friendly nanocatalyst for the synthesis of synthesizing polyhydroquinoline derivatives. ZnFe₂O₄@SiO₂@n-pr@PYD-Ni has a super magnetic property and thus can be simply separated from the reaction mixture using an external magnet [1-2].

Experimental Section

Synthesis of ZnFe₂O₄

At first, for the synthesis of ZnFe₂O₄ magnetic nanoparticles, 2.95 g of iron (II) chloride tetrahydrate (FeCl₂.4H₂O), and 2.36 g of Zn(NO₃)₃·4H₂O were mixed and vigorously stirred in 150 mL of deionized water. In the next step, 5 g NaOH in 50 mL deionized water was solved and added to the reaction mixture dropwise. Subsequently, the mixture reaction was stirred for one hour under a nitrogen gas (N₂) atmosphere. The final product was separated by a magnet, and washed three times, with hot ethanol (30 ml) and deionized water (30 ml). Finally, polycrystalline spinel magnetite nanoparticles (ZnFe₂O₄) were dried at 65°C.

Preparation of nano-ZnFe₂O₄@SiO₂ core shells

In the second step, 1.0 g of the obtained ZnFe₂O₄ was dispersed in a mixture of EtOH (100 mL), 5.0 mL of ammonia solution, 15 mL of H₂O, followed by the addition of 2.64 g of Polyethylene glycol (PEG-400) and 3 mL of tetraethyl orthosilicate (TEOS). After that, the reaction mixture was stirred at 25 c° for 24 h. Eventually, the product was separated by a magnet and washed with EtOH (20 ml) and deionized water (20 ml) five times, and dried at 25°C.

Preparation of ZnFe₂O₄@SiO₂@n-pr@PYD-Ni

The novel ZnFe₂O₄@SiO₂@n-pr@PYD-Ni MNPs were readily synthesized according to the route depicted in Scheme 1. In the next step, ZnFe₂O₄@SiO₂@n-pr@PYD-Ni magnetic nanoparticles were synthesized using the following steps. First for functionalization of

22nd Iranian Chemistry Congress (ICC22)
Iranian Research Organization for Science and Technology (IROST)
13-15 May 2024

03231-97589

ZnFe$_2$O$_4$@SiO$_2$ by 3-(Chloropropyl)-trimethoxysilane, 1 g obtained ZnFe$_2$O$_4$@SiO$_2$ nanoparticles were added to 30 mL of a toluene solution and then 2 mL of 3-(Triethoxysilyl)propylamine was added dropwise to this mixture. The reaction mixture was stirred at reflux condition for 23 h. Then, the resulting solid was filtered, washed with ethanol (30 ml) and water (30 ml) several times, and dried at room temperature. An appropriate amount of ZnFe$_2$O$_4$@SiO$_2$@n-pr (1 g) was dispersed in deionized water (100 mL) by sonication for 20 min. Subsequently, 2.5 mmol of PYD was added and the reaction mixture was stirred at 85 °C for 23 h. The reaction was performed under a nitrogen gas (N$_2$) atmosphere. Finally, to prepare ZnFe$_2$O$_4$@SiO$_2$@n-pr@PYD-Ni, the obtained ZnFe$_2$O$_4$@SiO$_2$@n-pr@PYD (1g) was dispersed in 30 mL by EtOH sonication for 20 min. Subsequently, 2.5 mmol of Nickel nitrate was added to the reaction mixture which was stirred under the nitrogen gas (N$_2$) atmosphere at reflux conditions (90 °C) for 24 hours a day. Afterward, the reaction mixture was cooled at 25°C and, then the final ZnFe$_2$O$_4$@SiO$_2$@n-pr@PYD-Ni (MNPs) were isolated, using a magnet, from the reaction mixture, washed by EtOH (30 ml) and distilled water (30 ml) (several times), to remove the residual impurities and, eventually, and then dried at 75 °C for 20 hours.
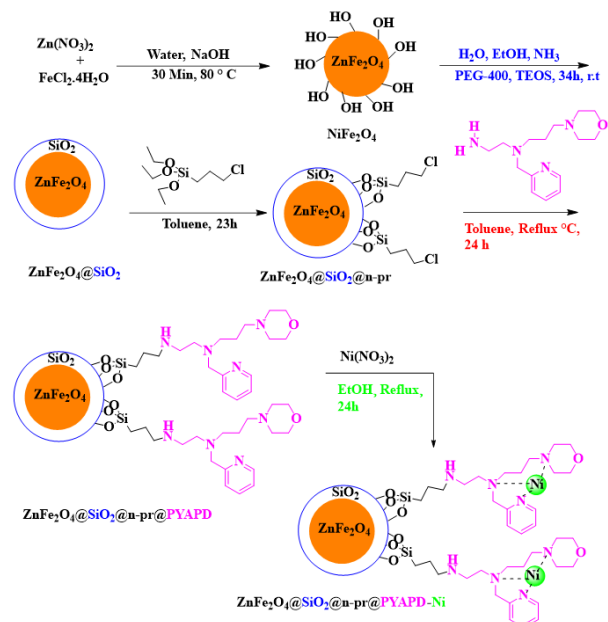
Scheme 1 Synthesis of ZnFe$_2$O$_4$@SiO$_2$@n-pr@PYD-Ni.

Results and Discussion
The XRD spectra was used to check the structure of the ZnFe$_2$O$_4$@SiO$_2$@n-pr@PYD-Ni samples. The compounds (a) have shown severe peaks in the range of 2θ = 8-80 due to their highly crystalline character (Figure 3). According to the sources reported by our research team, in the XRD pattern of ZnFe$_2$O$_4$ nanoparticles, the diffraction peak at (1 1 1), (2 2 0), (3 1 1), (2 2 2), (4 0 0), (4 2 2), (5 1 1), (4 4 0), and (5 3 3), which are indexed to the cubic spinel phase. As shown in Figure 3, the positions of all peaks in the XRD pattern of ZnFe$_2$O$_4$@SiO$_2$@n-pr@PYD-Ni are according to the standard XRD pattern of ZnFe$_2$O$_4$. The compound ZnFe$_2$O$_4$@SiO$_2$@n-pr@PYD-Ni have shown intense peaks in the range of 11–31 due to their crystalline character.
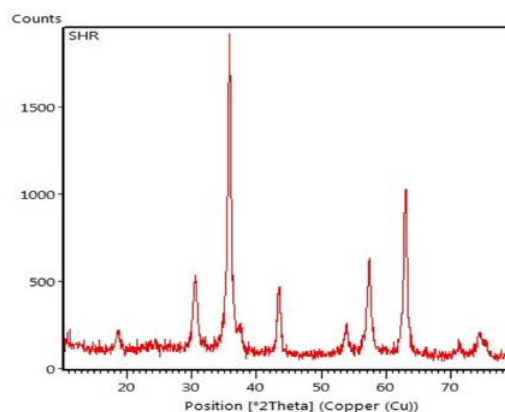

Fig.1: XRD spectrum of ZnFe$_2$O$_4$@SiO$_2$@n-pr@PYD-Ni

Conclusions
In summary, we successfully synthesized ZnFe$_2$O$_4$@SiO$_2$@n-pr@PYD-Ni as an effective and facile novel and green recoverable catalyst. Various techniques, including ICP, EDS, XRD, SEM, Map, FTIR, VSM, and TGA were used to investigate the physicochemical properties of the ZnFe$_2$O$_4$@SiO$_2$@n-pr@PYD-Ni (nanocatalyst). In this project, this nanocatalyst showed good activity for the synthesis of polyhydroquinoline derivatives in green conditions. The ease of recovery and simplicity of operation of this catalyst in the conditions of organic reactions is one of the advantages of this method. Also, this nanocatalyst has high novelty, can be extracted from the reaction by an Neodymium Magnet, and can be reused several times without considerable loss of its activity.

References
[1] A. Anders, A. Vakula, S. Tarapov, and A. Belous, Telecommun. Radio Eng. (English Transl. Elektrosvyaz Radiotekhnika) 75, 1849 (2016).

[2] S. M. Pormazar and A. Dalvand, Int. J. Environ. Anal. Chem. 00, 1 (2020).

Hydrogenation of CO₂ catalyzed by ZIF-67 framework assisted by DBD-plasma

Sayede Manizheh Hosseini, Majid Moghadam*, Shahram Tangestaninejad, Valiollah Mirkhani, Iraj Mohammadpoor, Amir Landarani-Isfahani

Corresponding Author E-mail: moghadamm@sci.ui.ac.ir

Department of Chemistry, Catalysis Division, University of Isfahan, Isfahan 81746-73441, Iran.

Abstract: Direct hydrogenation of CO_2 to methanol is a highly economical carbon reduction strategy. In this work, we applied the novel non-thermal plasma to activate CO_2 at ambient conditions and a ZIF-67 catalyst to selectively synthesize methanol for the selective transformation of CO_2 into methanol.

Keywords: CO_2 hydrogenation; Non-thermal plasma; ZIF-67

Introduction

The conversion of CO_2 into energy sources or valuable products can be seen as an emerging alternative to the CO_2 absorption– desorption process and a promising concept for reducing CO_2 emissions. Converting CO_2 into usable products can be a way to recycle carbon, thus initiating processes that are close to carbon neutrality. In addition, the conversion of CO_2 to energy sources and valuable products generates revenues that can offset the cost of capturing CO2. Hydrogenation of CO2 is one of the main processes for reducing CO_2 to mitigate the greenhouse gas effects. The hydrogenation of CO_2 into oxygenates (methanol, ethanol, and formic acid) has been extensively explored, because of its added value.[1]

Hydrogenation is a versatile option for CO_2 valorization, provided that renewable hydrogen is used. One can alter the reaction parameters (CO_2/H_2 ratio, temperature, and pressure) and the catalyst composition to control the product distribution.[2]

Plasma can be used for converting CO_2 to useful chemicals at near-ambient temperatures and pressures. In non-thermal plasmas, high-energy electrons collide with stable molecules and activate them, while the bulk gas temperature remains low. Catalysts can be introduced into these systems to increase the conversion and control the selectivity. The most common option in plasma catalysis is the dielectric barrier discharge (DBD), among the different types of plasma discharges. This is because DBD reactors usually run at low temperatures and atmospheric pressure, reducing operating costs and complexity, and allow facile combination with catalyst. Despite the growing research activity in plasma-enhanced catalysis, we still do not fully understand the relationship between the catalyst properties and overall reaction performance. This is because of the variety of the reactions and plasma configurations, which lead to different plasma species and different plasma–catalyst interactions. Here, we study the effect of basic catalysts (ZIF-67 catalyst) on conversion and product selectivity during CO_2 hydrogenation. We ran the reaction in a water-cooled DBD plasma catalysis setup, at 35 °C and ambient pressure.[3]

In this work، the influence of Co ZIF-67 on the plasma enhanced catalytic hydrogenation of CO_2 to MeOH was explored using a DBD reactor. The coupled catalytic system of NTP and ZIF 67 was investigated in a water-cooled DBD plasma reactor and showed excellent catalytic results, as 55.2% of CO_2 was directly hydrogenated to MeOH with excellent selectivity (82.5%) at 35 °C and ambient pressure.

Experimental Section

Synthesis of ZIF-67:

In a typical synthesis, 4 mmol of Co(NO3)₂_6H₂O was first dissolved in 100 mL of methanol, while 16 mmol of 2-MIM was added to another glass vial containing 100 mL of methanol. The methanol solution of Co(NO3)₂ was slowly added to the methanol solution of 2-MIM. The resulting mixture was stirred at the ambient temperature for 2 h. Next, the precipitate was collected by centrifugation and washed repeatedly with ethanol. The as-synthesized crystals were dried at 60 C in the ventilation oven for 6 h and then in the vacuum oven 100 _C for 12 h to obtain the final product, ZIF-67.[4]

Plasma Setup and Plasma-Catalytic Tests.

The plasma catalytic tests were performed in a coaxial DBD reactor with a 50 mm discharge length and a 1 mm discharge gap (Scheme 1). An DC high-voltage power supply (with a peak-to-peak voltage of up to 10 kV) was used to ignite the plasma with a fixed frequency of 50 Hz. CO_2 and H_2 (H_2/CO_2 = 3:1) were used as reactants with a total flow rate of 60 mL·min⁻¹. The catalysts (500 mg) were fully packed in the discharge area, the plasma reaction was run for 1.5 h and the products were then analyzed.

Results and Discussion

Characterization

Different techniques have been applied for the characterization of the composite and the determination of their structures. FESEM has been applied to study the

22nd Iranian Chemistry Congress (ICC22)
Iranian Research Organization for Science and Technology (IROST)
13-15 May 2024

03231-97589

IROST

morphology and estimate the particle size of the synthesized nanoparticles. The XRD patterns of ZIF-67, and the composite are shown in Fig. 2. Fig. 3 displays the FESEM image of ZIF67 and in the table 1 it has been shown Conversion and selectivity results related to the system with and without catalyst for hydrogenation of CO_2 the assisted by DBD- plasma.
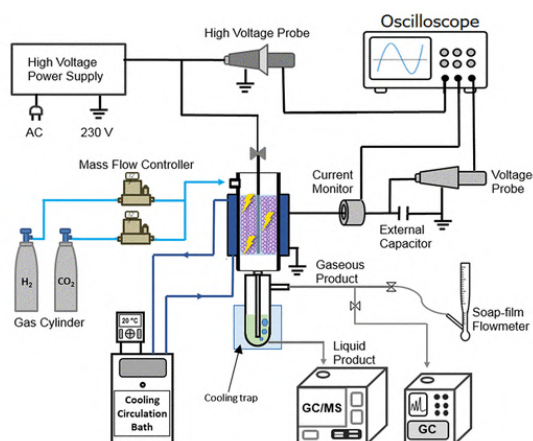
Scheme 1: Diagram of the Plasma-Catalysis DBD Reactor, Showing the Analysis, Feed, and Cooling Units
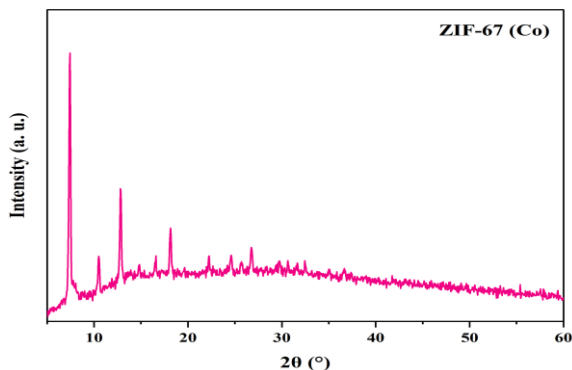
Fig.1: XRD patterns ZIF-67
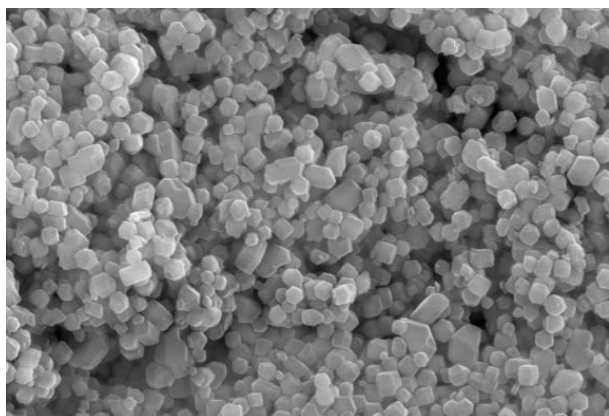
Fig.2. FE-SEM image of ZIF-67

Table 1: Conversion and selectivity results related to the system with and without catalyst for hydrogenation of CO_2 the assisted by DBD- plasma.

		Conversion CH$_3$OH	Conversion CO	Selectivity CH$_3$OH	Total Conversion(%)
Plasma only	40	22.8	45.1	39	67.9
	60	33.8	53.1	33.1	86.9
	80	20.9	36.1	33.3	57
ZIF-67	40	44.0	29.1	66.1	73.1
	60	50.0	24.0	59.4	74
	80	26	30.3	35.2	56.3

Conclusions

In the research CO_2 hydrogenation was successfully realized by relying solely on the plasma discharge (without catalyst), confirming the potential of NTP to efficiently dissociate CO_2 and H_2 at ambient temperature and pressure. When a catalyst (including ZIF-67) was introduced into the plasma discharge zone, the yield of MeOH and the CO_2 conversion increased dramatically.

References

[1] Iliuta, I., & Larachi, F. (2019). Enhanced MeOH synthesis process via an integrated process involving CO_2 hydrogenation under plasma conditions. *Industrial & Engineering Chemistry Research*, *59*(15), 6815-6827. https://doi.org/10.1021/acs.iecr.9b04278

[2] Ronda-Lloret, M., Wang, Y., Oulego, P., Rothenberg, G., Tu, X., & Shiju, N. R. (2020). CO_2 hydrogenation at atmospheric pressure and low temperature using plasma-enhanced catalysis over supported cobalt oxide catalysts. *ACS sustainable chemistry & engineering*, *8*(47), 1739717407.https://doi.org/10.1021/acssuschemeng.0c0-5565

[3] Zou, N., Chen, J., Qiu, T., & Zheng, Y. (2023). Direct hydrogenation of CO 2 to ethanol at ambient conditions using Cu (i)-MOF in a dielectric barrier discharge plasma reactor. *Journal of Materials Chemistry A*, *11*(20), 10766-10775.https://doi.org/10.1039/D3TA00314K

[4] Lin, K. Y. A., & Chang, H. A. (2015). Ultra-high adsorption capacity of zeolitic imidazole framework-67 (ZIF-67) for removal of malachite green from water. *Chemosphere*, *139*,624-631. https://doi.org/10.1016/j.chemosphere.2015.01.041

Engineering Core-Shell Heterostructure Arrays for Enhanced Bi-Functional Electrocatalysis in Alkaline Water/Seawater Electrolysis

Mohsen Abedi [a], Sharifeh Rezaee [a], Saeed Shahrokhian[*b]

Corresponding Author E-mail: shahrokhian@sharif.edu

[a] Department of Chemistry, Sharif University of Technology, Tehran 11155–9516, Iran.

[b] Institute for Nanoscience and Technology, Sharif University of Technology, Tehran, Iran.

Abstract: This study presents a novel NiCoFe-LTH/W$_2$N-WC/CF heterostructure as a high-performance electrocatalyst for alkaline water and seawater electrolysis. The design, featuring core-shell architectures and synergistic effects, achieves impressive catalytic activity with low overpotential values. The bifunctional electrocatalyst demonstrates promise for efficient and sustainable green hydrogen production through electrochemical water splitting.

Keywords: LTH Nanosheet; Core-Shell; Tungsten Carbide; Tungsten Nitride; Water Splitting.

Introduction

Amidst rising concerns over energy consumption, fossil fuel depletion, and environmental issues, the quest for sustainable, clean energy sources intensifies. Hydrogen, particularly through electrochemical water splitting, emerges as a key player. Noble metals like ruthenium and platinum, though efficient, face limitations due to scarcity and cost. Recent studies focus on transition metal compounds, especially NiCoFe-LTH, showcasing superior catalytic activity in both oxygen and hydrogen evolution reactions [1]. To enhance catalyst performance, three-dimensional hierarchical core-shell nanostructures gain prominence. Tungsten derivatives, known for stability, form heterostructures, such as W$_2$N-WC, offering a dual enhancement in OER and HER [2]. Inspired by these advances, we engineered a self-supported NiCoFe-LTH/W$_2$N-WC/CF electrode, demonstrating efficient bi-functional electrocatalytic activities with low overpotentials for HER and OER. This work presents a promising strategy for developing economical and efficient self-supported electrocatalysts for alkaline water splitting, addressing the pressing need for sustainable energy sources.

Experimental Section

WO$_3$ nanowire arrays were hydrothermally synthesized from 0.1 M Na$_2$WO$_4$ solution, adjusted to pH 1.2, with appropriate additives. Sealed in a Teflon-lined autoclave, the solution was kept at 180°C for 16 hours. The WO$_3$/CF electrode underwent further treatment by placing it in a quartz tube with additional amount of C$_2$H$_4$N$_4$. Under Ar flow, the temperature rise to 800°C, held for 2 hours, and cooled to room temperature and W$_2$N-WC/CF was obtained. For the growth of NiCoFe-LTH nanosheets on W$_2$N-WC/CF, immersion in a solution of Co^{2+}, Ni^{2+}, Fe^{3+} and KNO$_3$, followed by electrodeposition at -1.0 mA cm^{-2} for 45 minutes, yielded NiCoFe-LTH/W$_2$N-WC/CF.

Results and Discussion
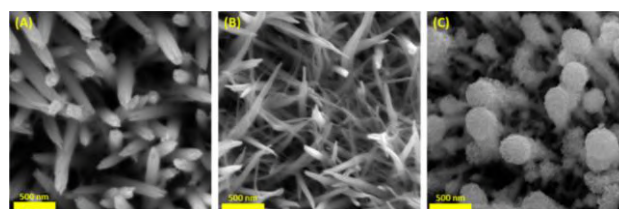
Fig. 1: FE-SEM images of **(A)** WO$_3$/CF, **(B)** W$_2$N-WC/CF, **(C)** NiCoFe-LTH/W$_2$N-WC/CF

FE-SEM images in Fig. 1 revealed that conversion of WO$_3$ nanoneedles to W$_2$N-WC nanowires results in splitting of so-called nanoneedles (Fig. 1A-B). Finally, Fig. 1C shows the snowflake NiCoFe-LTH/W$_2$N-WC/CF core-shell heterostructure, wherein NiCoFe-LTH nanosheets coat the entire surface of W$_2$N-WC/CF nanowires. The excess amount of these nanosheets gathers at the tip of the nanowire, forming dense and porous nanospheres. These hierarchical array structures provide a substantial surface area, featuring numerous electrochemically active sites. This design ensures an efficient flow and short diffusion path for electrolyte ions throughout the entire electrode structure [3]. Moreover, the close integration of NiCoFe-LTH nanosheets with W$_2$N-WC/CF nanowires can induce robust synergistic effects between the core and shell materials and ultimately leading to an augmentation of electrocatalytic activity. In Fig. 2A, the HER LSV polarization curves of the prepared catalysts are presented. According to these curves, NiCoFe-LTH/W$_2$N-WC/CF exhibits a higher HER activity and affords current density of 10 and 100 mA cm^{-2} at a small overpotential of 101 and 177 mV, respectively. In next step, Tafel slopes considered as an important index for evaluating the reaction mechanism and rate determining step during HER process [4]. As shown in Fig. 2B the NiCoFe-LTH/W$_2$N-WC/CF exhibits a Tafel slope of 72 mV dec^{-1} which is much

22nd Iranian Chemistry Congress (ICC22)
Iranian Research Organization for Science and Technology (IROST)
13-15 May 2024

03231-97589

ISC
Islamic World Science Citation Center

IROST

lower than other as-prepared catalysts. Obtained Tafel slope suggests that HER is performed via a Volmer–Heyrovsky mechanism and Heyrovsky reaction is the rate-determining step. Also, similar regularity between Tafel slopes and overpotentials prove that NiCoFe-LTH/W$_2$N-WC/CF owns fast kinetics and verify its desirable HER performance.
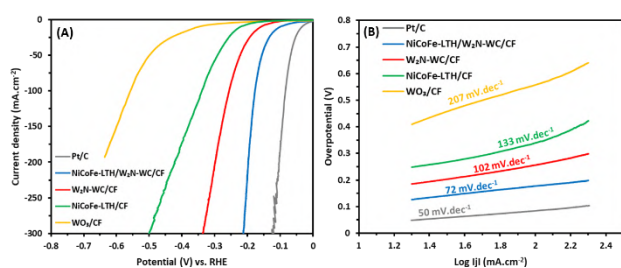
Fig. 2: (A) LSV curves of prepared catalysts for HER in 1.0 M KOH solution at a scan rate of 2 mV s^{-1}. **(B)** The Tafel plots related to the LSV curves in Fig. 2A.

Fig. 3A show the OER LSV curves of the catalysts.
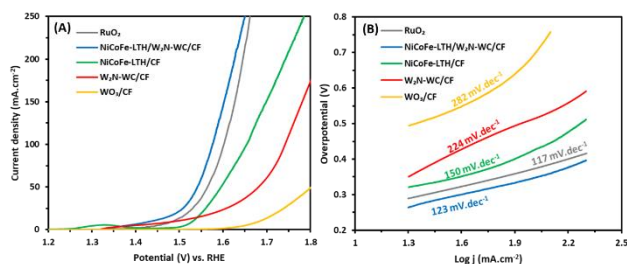
Fig. 3: (A) LSV curves of prepared catalysts for OER in 1.0 M KOH solution at a scan rate of 2 mV s^{-1}. **(B)** The Tafel plots related to the LSV curves in Fig. 3A.

NiCoFe-LTH/W$_2$N-WC/CF displayed the lowest overpotential of 206 and 345 mV to reach 10 and 100 mA cm^{-2}, respectively. As shown in Fig. 3B, a comparison between the Tafel slopes of various catalysts also indicates favourable OER kinetics of NiCoFe-LTH/W$_2$N-WC/CF which possesses the smallest Tafel slope between synthesized catalysts and close to that of commercial RuO$_2$. Based on the good HER and OER catalytic activities, NiCoFe-LTH/W$_2$N-WC/CF was employed as a bi-functional catalyst in construction of a two-electrode electrolyzer system to evaluate the overall water splitting performance in alkaline medium. As displayed in Fig. 4A, the NiCoFe-LTH/W$_2$N-WC/CF electrolyzer needs a low cell voltage of 1.543, 1.668 and 1.752 V to achieve current densities of 10, 50 and 100 mA cm^{-2}, which is compatible with the conventional Pt/C/CF-RuO$_2$/CF electrodes with the same loading. Furthermore, the long-term durability was assessed. The continuous CV test show that LSV curves almost overlap before and after 500 cycles (Fig. 4B). Furthermore, CA test results demonstrated a steady current density over 15 h test period, underscoring the
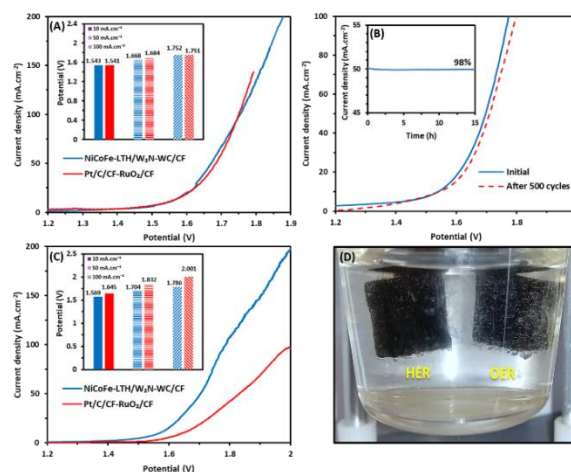

Fig. 4: (A) Polarization curves in 1.0 M KOH at a scan rate of 2 mV s^{-1}. **(B)** LSV curves before and after 500 sequential CV sweeps, Inset: CA curve of NiCoFe-LTH/W$_2$N-WC/CF at potential of 1.67 V. **(C)** Polarization curves in alkaline seawater at a scan rate of 2 mV s^{-1}. **(D)** Photograph of NiCoFe-LTH/W$_2$N-WC/CF during electrolysis.

catalyst's desirable durability. Besides, for exploring the electrocatalyst capability in harsh environments, the water-splitting performances was assessed in a 1.0 M KOH solution prepared using Persia Gulf seawater. It is found that to afford same current densities, the NiCoFe-LTH/W$_2$N-WC/CF couple exhibited significantly lower voltages than that of the commercial Pt/C/CF-RuO$_2$/CF pair. Meanwhile, the photograph in Fig. 4D clearly show that, continuously abundant H$_2$ and O$_2$ bubbles are released from the surface of electrodes at high current densities, indicating the desirable capability of NiCoFe-LTH/W$_2$N-WC/CF as a competent and persistent candidate for use in practical water splitting devices.

Conclusion

In this study, we designed a highly efficient NiCoFe-LTH/W$_2$N-WC/CF electrode for water splitting through a three-step method. The electrode, featuring a hierarchical structure on carbon felt, exhibited excellent catalytic activities for both HER and OER in an alkaline medium. Notably, it demonstrated minimal overpotential in overall water splitting, surpassing literature benchmarks and also performed well in alkaline seawater. Its stability, attributed to the hierarchical morphology and optimized electronic structure, underscores its potential for efficient water splitting.

References

[1] A. Wang, G. Li, *ACS Energy Lett.*, 2016, 1, 445-453.

[2] J. Diao, X. Guo, *Adv. Mater.* , 2020, 32, 1905679.

[3] X. Yin, Q. Gao, *Nanoscale,* 2020, 12, 15944-15969.

[4] Y. Gogotsi, P S. Weiss, *ACS Nano* 2018, 12, 9635–9638.

22nd Iranian Chemistry Congress (ICC22)
Iranian Research Organization for Science and Technology (IROST)
13-15 May 2024

03231-97589

IROST

Simple synthesis of novel Pd-EDTA-MOF: a green, reusable, and versatile catalyst for the production of biodiesel fuel from oleic acid and palmitic acid

Ahmad Jafari, Arash Ghorbani-Choghamarani*, Hamid Aghavandi, Amir Ghanbarpour

Corresponding Author E-mail: arashghch58@yahoo.com

Department of Organic Chemistry, Faculty of Chemistry, Bu-Ali Sina University, Hamedan, 6517838683, Iran.

Abstract: Herein, we reported a novel MOF that was designed and fabricated via hydrothermal reaction of Palladium (II) acetate salt with EDTA as an organic ligand. The prepared MOF was investigated by BET and TGA techniques. The prepared Pd-EDTA-MOF exhibits efficient performance for the esterification of oleic acid under gentle reaction conditions.

Keywords: EDTA, MOF, Pd-EDTA-MOF, Biodiesel, Esterification, Oleic acid.

Introduction

MOFs (Metal-organic frameworks) are a new class of porous materials comprised of ordered networks consisting of metal ions linked together by organic ligands. According to research conducted in recent years, it has been revealed that MOFs have vast applications in biological and catalysis activity. The degree of porosity of MOFs depends on various factors such as temperature, pH, condensation stirring speed, metal, and ligand type, the molar ratio of reactants, and the concentration of substrates. Metal-organic frameworks are of scientific and technological interest because of their special properties such as high specific surface area, pore volume, and uniform pore size, and modifiable surface chemistry. These porous materials have shown great potential in several industrial applications including molecular separations, gas storage, sensors, heterogeneous catalysis,[11] and drug delivery. Furthermore, it is still of extraordinary problem to explore facile techniques for the synthesis of novel metal-organic framework materials bearing unique structures and properties, as well as to widen and deepen the utility of MOF-based totally hybrid materials in the chemical industry. The capability of designing and modification after preparation has led these solids to be suitable as heterogeneous catalysts for organic transformations.[14,15] Notwithstanding the wide-spreading use of these catalysts, the leaching of costly or toxic metals into favorable products is one of the negative aspects of the employing of heterogeneous metal-based catalysts in sustainable nanocatalysis phenomena. To overcome this problem, Metal-organic frameworks (MOFs) as a catalyst for organic reactions seem to be a suitable solution. [1-3]

Experimental Section

A solution of ethylenediaminetetraacetic acid (EDTA) (0.5 mmol) in H_2O (1 mL) was prepared, afterward, a solution of Palladium (II) acetate (1 mmol) in dimethylformamide (7.5 mL) added to the mixture. The reaction mixture was stirred at 70 Celsius degree at PH = 9 for 25 min. Next, the reaction mixture was transferred to an autoclave machine and kept at 160 Celsius degree for 24 h. Then, the obtained powder from the autoclave machine was washed with ethyl acetate. Finally, the obtained Pd-EDTA-MOF was dried under reduce pressure.
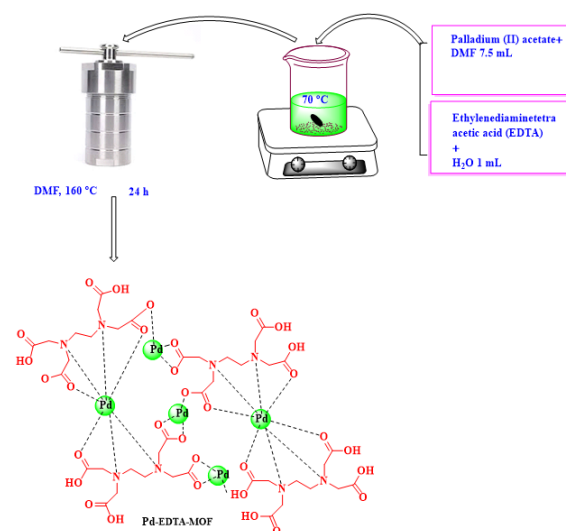

Fig.1: Synthesis of Pd-EDTA-MOF.

Results and Discussion

Figure 2 shows the TGA analysis of Pd-EDTA-MOF. The TGA curve showed a 10% weight loss from 25–250 Celsius degree for the Pd-EDTA-MOF (Figure 2), which is due to

22nd Iranian Chemistry Congress (ICC22)
Iranian Research Organization for Science and
Technology (IROST)
13-15 May 2024

03231-97589

IROST

the desorption of water and organic solvents. The total mass loss for Pd-EDTA-MOF in the temperature range of 250-500 $^{\circ}$C was approximately 40%, which indicates the thermal stability of the synthesized Pd-EDTA-MOF.

The N2 adsorption/desorption of Pd-EDTA-MOF was used to investigate the porosity of synthesized metal organic framework (Figure 3). The results proved that Pd-EDTA-MOF has mesoporous structure. Regarding the N2 adsorption-desorption isotherms, based on BET method, the obtained surface area of Pd-EDTA-MOF is 30.6 (m^2/g). Also, the total pore volumes and mean pore diameter of Pd-EDTA-MOF are obtained by the BJH technique and the values are 0.2 cm3 g-1, and 26 nm, respectively. It can be concluded that the obtained Pd-EDTA-MOF is a porous material.

Conclusions

In this work, a novel crystalline mesostructure of the Pd-EDTA-MOF was successfully fabricated using the reaction of Palladium (II) acetateand EDTA as commercially available starting materials. Pd-EDTA-MOF nanocomposite catalyzed esterification of oleic acid with high yields and purity. The wondrous features of this protocol are novelty, simple synthesis procedure, no use of harmful solvents, suitable stability, and reusability. This reported method had significant advantages in terms of using low amount of the catalyst, easy separation of catalyst, recyclability, and reusability of the catalyst without a notable decrease in catalytic activity.

References

[1] A. Anders, A. Vakula, S. Tarapov, and A. Belous, Telecommun. Radio Eng. (English Transl. Elektrosvyaz Radiotekhnika) **75**, 1849 (2016).

[2] S. M. Pormazar and A. Dalvand, Int. J. Environ. Anal. Chem. **00**, 1 (2020).

[3] E. Leal, J. Dantas, P. T. A. dos Santos, S. M. de C. M. Bicalho, R. H. G. A. Kiminami, M. R. da Silva, and A. C. F. de M. Costa, Appl. Surf. Sci. **455**, 635 (2018).

Fig.2: TGA diagram of Pd-EDTA-MOF.
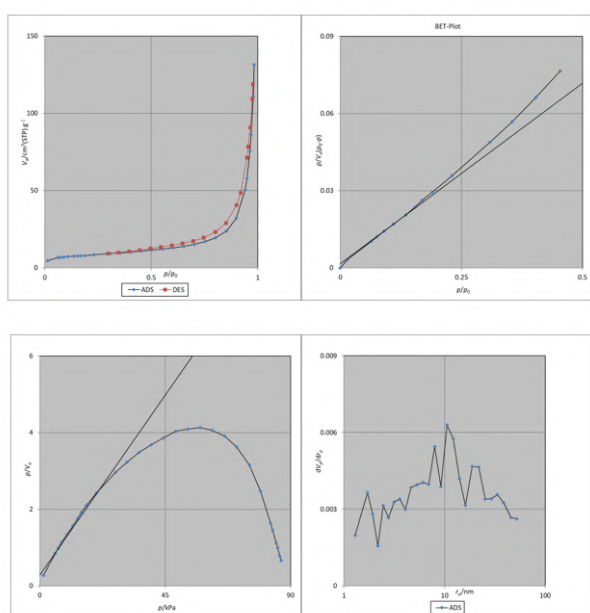
Fig. 3: N$_2$-adsorption isotherms of Pd-EDTA-MOF.

22nd Iranian Chemistry Congress (ICC22)
Iranian Research Organization for Science and Technology (IROST)
13-15 May 2024

03231-97589

IROST

The Preparation of Nanocomposites Based on CMC/Graphene Quantum Dot in Drug Delivery

Nasim Abdi, Abdolreza Abri*

Corresponding Author E-mail: ar.abri@yahoo.com

Chemistry Department, Faculty of Science, Azarbaijan Shahid Madani University, Tabriz, Iran.

Abstract: This research investigates carboxymethyl cellulose (CMC) and graphene quantum dots (GQDs) based nanocomposites as hydrogels for drug delivery. The goal is to develop materials that can control drug release, increase drug stability and transport. The study shows promising results for using these nanocomposites in targeted drug delivery and for improving treatment methods for wounds, skin diseases and inflammatory diseases.

Keywords: Carboxymethyl Cellulose; Graphene Quantum Dot; Nanocomposite; Graphene; Controlled Drug Release

Introduction

In recent years, the development of advanced drug delivery systems has garnered significant attention in the field of biomedical research. Among various drug delivery vehicles, hydrogels have emerged as promising candidates due to their unique properties, such as high water content, biocompatibility, and tunable physicochemical characteristics. Hydrogels are three-dimensional polymeric networks capable of absorbing and retaining large amounts of water or biological fluids. These features make hydrogels ideal for drug delivery applications, as they can provide a controlled and sustained release of therapeutic agents[1].

Carboxymethyl cellulose (CMC) is a widely used natural polymer in the preparation of hydrogels. CMC is a water-soluble derivative of cellulose, obtained by the partial substitution of cellulose hydroxyl groups with carboxymethyl groups. CMC-based hydrogels have been extensively studied for drug delivery applications due to their excellent biocompatibility, biodegradability, and mucoadhesive properties. However, the mechanical strength and drug loading capacity of CMC hydrogels are often limited, which can hinder their practical applications[2]. To overcome these limitations, the incorporation of nanomaterials into CMC hydrogels has been proposed as a promising strategy. Nanocomposites, which combine the advantages of polymeric hydrogels and nanomaterials, have attracted considerable interest in drug delivery. Among various nanomaterials, graphene quantum dots (GQDs) have gained increasing attention due to their unique properties, such as small size, excellent biocompatibility, and high surface area. GQDs are zero-dimensional carbon nanomaterials with lateral dimensions below 100 nm. They exhibit excellent optical and electronic properties, making them suitable for various biomedical applications, including bioimaging, biosensing, and drug delivery.

The incorporation of GQDs into CMC hydrogels can potentially enhance the mechanical strength, drug loading capacity, and controlled release properties of the resulting nanocomposites. The presence of GQDs in the hydrogel matrix can provide additional binding sites for drug molecules through π-π stacking and hydrophobic interactions. Moreover, the unique optical properties of GQDs can be exploited for real-time monitoring of drug release and tracking of the nanocomposites in biological systems[3].

Several studies have reported the preparation and characterization of CMC/GQDs hydrogel nanocomposites for drug delivery applications. For instance, Li et al. (2018) developed a CMC/GQDs hydrogel for the delivery of doxorubicin, an anticancer drug. The nanocomposite hydrogel exhibited enhanced mechanical properties, high drug loading capacity, and pH-responsive drug release behavior. Similarly, Zhang et al. (2019) prepared a CMC/GQDs hydrogel for the delivery of curcumin, a natural polyphenol with anti-inflammatory and anticancer properties. The nanocomposite hydrogel showed improved bioavailability and sustained release of curcumin compared to the free drug. Despite these promising results, there is still a need for further investigation of CMC/GQDs hydrogel nanocomposites in drug delivery applications. The optimization of the synthesis process, comprehensive characterization of the nanocomposites, and evaluation of their performance in various drug delivery scenarios are essential for their successful translation into clinical practice[4].

In this study, we report the preparation and characterization of CMC/GQDs hydrogel nanocomposites for drug delivery applications. The nanocomposites were synthesized by incorporating GQDs into a CMC hydrogel matrix using a facile and green approach. The physicochemical properties, mechanical strength, drug loading capacity, and release behavior of the nanocomposites were systematically investigated.

22nd Iranian Chemistry Congress (ICC22)
Iranian Research Organization for Science and
Technology (IROST)
13-15 May 2024

03231-97589

IROST

Furthermore, the cytotoxicity and cellular uptake of the nanocomposites were evaluated to assess their biocompatibility and potential for targeted drug delivery. The results of this study provide valuable insights into the design and development of advanced hydrogel-based drug delivery systems using graphene quantum dots.
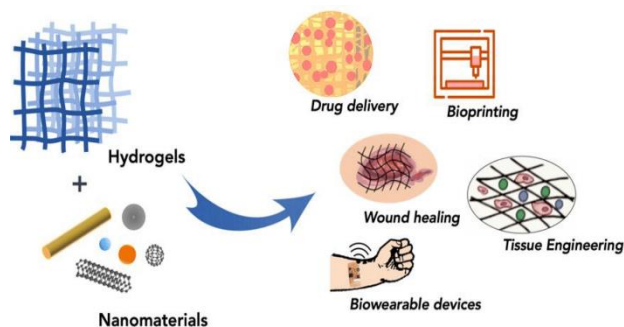

Fig.1: Application of hydrogels in different industries

Experimental Section

The CMC/GQDs nanocomposite is typically prepared using a straightforward chemical process. First, GQDs are synthesized from a carbon source such as graphite via chemical oxidation and exfoliation. Subsequently, these GQDs are combined with CMC in an aqueous solution. The mixture is then subjected to ultrasonication to ensure homogeneity, followed by freeze-drying to obtain the final product.

Results and Discussion

The successful preparation of CMC/GQDs hydrogel nanocomposites and their characterization indicate great potential in the field of drug delivery. The integration of GQDs not only enhanced the thermal stability of the hydrogels but also improved their mechanical properties and drug loading capacity. The pH-responsive swelling and drug release behaviors are particularly advantageous for targeted drug delivery, where the unique environment of the target site (e.g., tumors or inflamed tissues) can trigger the release of the loaded drug.

The observed initial burst release could be advantageous for delivering a quick therapeutic dose, followed by a sustained release that maintains the drug concentration within the therapeutic window over an extended period. This release profile can potentially reduce the frequency of dosing and improve patient compliance. However, the real-world application of these hydrogel nanocomposites in drug delivery would require further in vivo studies to assess their biocompatibility, toxicity, and therapeutic efficacy. Future studies might also explore the loading and release of various drugs, the influence of different crosslinking densities on the hydrogel properties, and the potential for targeting specific diseases or sites within the body. In conclusion, the novel CMC/GQDs hydrogel nanocomposites demonstrate promising features for drug delivery applications, offering a tunable and targeted approach to therapy. Further research in this direction could lead to significant advancements in the development of smart drug delivery systems.

Conclusions

In conclusion, the research provided promising insights into the preparation and application of CMC/GQDs hydrogel nanocomposites in drug delivery. The combination of CMC and GQDs resulted in a novel material with potential advantages such as high drug loading capacity, controlled release, biocompatibility, and the possibility for targeted delivery. These findings underscore the potential of hydrogel nanocomposites in advancing the field of drug delivery, with implications for improving treatment outcomes in various medical conditions.

References

[1] Rakhshaei, R., Namazi, H., Hamishehkar, H., & Rahimi, M. (2020). Graphene quantum dot cross-linked carboxymethyl cellulose nanocomposite hydrogel for pH-sensitive oral anticancer drug delivery with potential bioimaging properties. International journal of biological macromolecules, 150, 1121-1129.

[2] Zhang, W., Liu, Y., Xuan, Y., & Zhang, S. (2022). Synthesis and applications of carboxymethyl cellulose hydrogels. Gels, 8(9), 529.

[3] Zhao, C., Song, X., Liu, Y., Fu, Y., Ye, L., Wang, N., ... & Liu, J. (2020). Synthesis of graphene quantum dots and their applications in drug delivery. Journal of Nanobiotechnology, 18, 1-32.

[4] Javanbakht, S., & Namazi, H. (2018). Doxorubicin loaded carboxymethyl cellulose/graphene quantum dot nanocomposite hydrogel films as a potential anticancer drug delivery system. Materials Science and Engineering: C, 87, 50-59.

Amperometric determination of glucose in human serum using cobalt manganese sulfide nanostructure

Zahra Hajesfandyari, Leila Naderi, Saeed Shahrokhian*

Corresponding Author E-mail: shahrokhian@sharif.edu

Department of Chemistry, Sharif University of Technology, Tehran 11155 9516, Iran.

Abstract: The electrocatalytic response of cobalt manganese hydroxide and sulfide toward glucose detection was investigated. The experimental findings exhibited that CoMn-S nanostructure had better catalytic activity than CoMn-LDH. Under optimal experimental conditions, the sensor showed wide linear ranges of 1- 630 µM and 630 – 2530 µM with high sensitivities of 5148 and 1928 µA mM^{-1} cm^{-2} and low detection limit of 0.88 µM.

Keywords: Glucose determination; Enzyme-free sensor; Electrocatalyst; CoMnS nanostructure

Introduction

According to the announcement of the World Health Organization, in the last four years, with the change in people's lifestyle and the emergence of the deadly corona virus disease, the increase in diabetes has accelerated. It is predicted that by 2045, nearly 700 million people will suffer from diabetes. Diabetes is a chronic disease for which no cure has been found yet. Therefore, controlling the blood sugar level is the only method that can help prevent this disease, hence the demand for commercial glucose sensors has increased. Glucose sensors available in the market are enzyme type that have limitations such as temperature conditions, humidity, pH and single use. Non-enzymatic glucose sensors have been extensively investigated as a suitable alternative to enzymatic sensors due to their low cost, chemical stability, biocompatibility, controllable synthesis and improvement of electron transfer processes.

The electrode active material is a very important to assess the electrocatalyst activity. So far, transition metal oxides/hydroxides have been recognized as the most promising catalytic materials owing to their well- defined redox behavior, low cost, natural abundance, and environmental friendliness. Specially, 2D layered double hydroxides (LDH) materials have attracted many researchers' interests in energy and sensor-related fields because they possessed unique layered structure, high redox activity, high stability and versatility. However, their poor electrical conductivity and easy agglomeration limit the practical application of the LDH materials. Transition-metal sulfides, compared with transition-metal oxides/hydroxides, are also potential catalyst candidates for sensors due to their metalloid properties, layer architecture, and excellent electroconductivity. Thus, sulfurization of the LDH material is considered as an effective rout to increase the electronic conductivity. Moreover, bimetallic sulfides have better electrocatalytic properties relative to mono-metal sulfides. This enhancement can be due to their capability to render high electrical conductivities and plenty valance states for more electrochemical reactions. Besides, the engineering of the nanostructures with large surface area and highly electroactive centers has a considerable impression on improving electrocatalytic activity. In this work, CoMn hydroxide and sulfide were synthesized by a solvothermal procedure. The electrocatalytic performance of the as-synthesized electrodes was evaluated toward glucose sensing by electrochemical techniques.

Experimental Section

To synthesis of CoMn-LDH nanostructure, cobalt and manganese nitrate salts were dissolved in ethanol solution, where total concentration was 0.4 g. The mixed solution was added to autoclave and kept at 180 °C for 6 h. Then, CoMn-LDH was placed into solution containing thioacetamide, and transferred into an autoclave and maintained at 180 °C for 6 h. The suspension was prepared from the synthesized powders and drop-casted on the GCE surface.

Results and Discussion

The morphologies of CoMn-LDH and CoMn-S were studied by FE-SEM. As seen in Figs. 1A and B, the microsphere structure was obtained for CoMn-LDH. The shape and size of prepared spheres are homogenous and the free space between the spheres is obvious. After the sulfidation, the surface of spheres is covered by nanoparticles and become more porous. The presence of Co, Mn, and S elements was confirmed by using EDX and elemental mapping analysis (Fig. 1 C and D).

Using the cyclic voltammetry technique, the electrocatalytic activity of the CoMn-LDH/GCE and CoMn-S/GCE was evaluated toward glucose sensing. The voltammogram of modified electrodes was recorded in 0.1 M NaOH electrolyte with and without of 0.5 mM glucose (Fig. 2a).
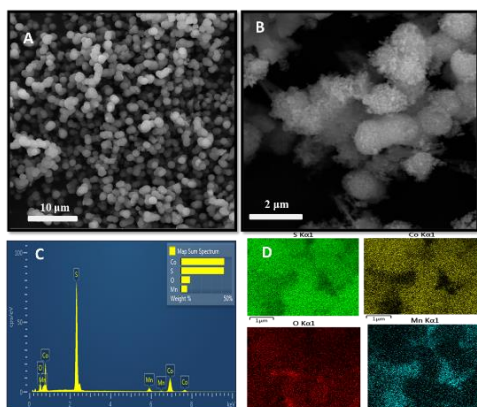
22nd Iranian Chemistry Congress (ICC22)
Iranian Research Organization for Science and
Technology (IROST)
13-15 May 2024

03231-97589

IROST

Fig.1: FE-SEM images of CoMn-LDH (A), CoMn-S (B), and EDX spectra (C), and elemental mapping of CoMn-S (D)

The higher anodic current was observed for the CoMn-S/GCE. The CV curves were recorded for CoMn-S/GCE at various glucose concentrations (Fig. 2C). As can be observed, the catalytic current response of the electrode enhances linearly with the addition of the glucose into alkaline media. To evaluate the electrochemical kinetic process, CV plots were carried out at various sweeping rates in 0.1 M NaOH containing 0.5 mM glucose. As seen in Fig. 2D, anodic peak current increased with the sweeping rate.
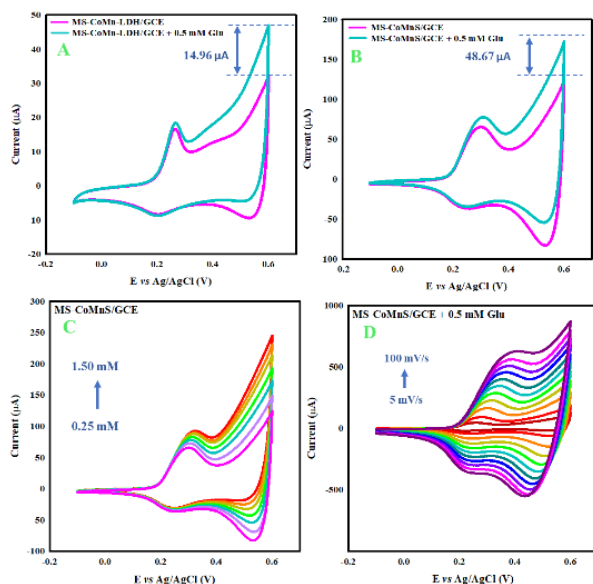
Fig.2: The CV curves of CoMn-LDH/GCE (A) and CoMn-S/GCE (B) in the absence and presence of 0.5 mM Glucose. CV curves of CoMn-S/GCE at different concentrations of glucose (C), and CV curves of CoMn-S/GCE at different scan rates (D)

After choosing the optimal potential for the CoMn-S/GC electrode, amperometric tests were conducted to obtain analytical parameters. After every injection of glucose, the steady state current achieved in a short time of 2 s, demonstrating presence of many active centers that

accelerate oxidation process of glucose. According to Fig. 3, two linear ranges of 1- 630 μM and 630 – 2530 μM with high sensitivities of 5148 and 1928 μA mM^{-1} cm^{-2} and low detection limit of 0.88 μM was achieved for the CoMnS/GC electrode. The reproducibility of CoMnS/GCE was assessed by testing 3 prepared CoMnS/GC electrodes with 100 μM glucose. The relative standard deviation (RSD) of 4.4% was obtained. The capability of CoMnS/GCE sensor were assessed by measuring glucose concentrations in human blood serum. Acceptable recovery values were obtained in serum sample, indicating the high accuracy and reliability of the sensor for glucose measuring.
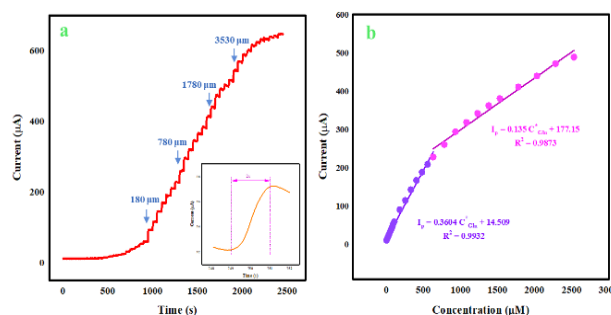

Fig.3: The Amperometric current responses of the CoMnS/GC electrode with successive injection of glucose (a) and the linear calibration curve (b)

Conclusions

CoMn-S/GC enzyme-free glucose sensor was successfully fabricated by a solvothermal procedure. The as-prepared CoMn-S/GCE exhibited high sensitivity (5148 and 1928 μA mM^{-1} cm^{-2}), a low detection limit (0.88 μM), good reproducibility, and quick response time. Moreover, as-prepared sensor platform exhibited excellent ability for measuring glucose in blood serum.

References

[1] Sehit, E., & Altintas, Z. (2020). Significance of nanomaterials in electrochemical glucose sensors: An updated review (2016-2020). Biosensors and Bioelectronics, 159, 112165.

[2] Naderi, L., & Shahrokhian, S. (2023). Metal-organic framework-assisted Co3O4/CuO@ CoMnP with core-shell nanostructured architecture on Cu fibers for fabrication of flexible wire-typed enzyme-free micro-sensors. Chemical Engineering Journal, 456, 141088.

[3] Hekmat, F., Kachouei, M. A., Foshtomi, S. T., Shahrokhian, S., & Zhu, Z. (2023). Direct decoration of commercial cotton fabrics by binary nickel-cobalt metal-organic frameworks for flexible glucose sensing in next-generation wearable sensors. Talanta, 257, 124375.

22nd Iranian Chemistry Congress (ICC22)
Iranian Research Organization for Science and Technology (IROST)
13-15 May 2024

03231-97589

IROST

Preparation and performance evaluation of Chitosan-Thiourea cathode on the titanium mesh substrate in the Electro-Fenton process for removal of ofloxacin from water

Hannaneh Mortaghi Ghasemi, Mahmoud Zarei*

Corresponding Author E-mail: mzarei@tabrizu.ac.ir

Research Laboratory of Environmental Remediation, Department of Applied Chemistry, University of Tabriz, 51666-16471 Tabriz, Iran.

Abstract: The synthesis of Chitosan-Thiourea electrode on titanium mesh in gas diffusion electrode for removal of the ofloxacin from contaminated water in the Electro-Fenton process was investigated. The required carbon of the substrate is obtained by chitosan. Thiourea is contributed as an agent containing nitrogen and sulfur in this process.

Keywords: ofloxacin; Chitosan; Thiourea; Electro-Fenton

Introduction

Favourable reaction time, high performance, cost-effectiveness, low toxicity and environmental compatibility have made the electro-fenton process as one of the most widely used methods in EAOPs for wastewater and pharmaceuticals treatment[1]. In this process, the hydrogen peroxide(H_2O_2) is supplied through the two-electron reduction reaction of dissolved oxygen on the surface of the cathode. Ultimately, the produced hydroxyl radical causes the destruction of the organic pollutant and turns it into carbon dioxide and water[2]. Chitosan biopolymer with nitrogenous functional groups is fascinated in terms of active sites of reaction, degree of carbonization to inhance the conductivity and its porous and mesoporous structure[3]. Thiourea with more active sites, high conductivity and operating the properties of both nitrogen and sulfur heteroatoms simultaneously compared to materials with one heteroatom and other common materials has received more attraction[4].

Experimental Section

For synthesis of electrode's material, the preparation of chitosan-thiourea hydrogel, the solvent was evaporated and then carbonized in the oven to obtain a uniform powder. In the next step, the powder is coated on the titanium substrate. The effect of time, initial pollutant concentration, current intensity and pH in the removal of ofloxacin antibiotic has been investigated.

Results and Discussion

The SEM image(Fig.1) indicates the texture after hydrothermal carbonization of the hydrogel on the titanium substrate. The irregular morphology of the particles on the rough surface of the substrate is due to etching with sodium hydroxide on the main structure of the hydrogel during the carbonization process at high temperature. Through the carbonization, dense structure of chitosan is destroyed and smaller molecules are dehydrated; as a result, the penetration of thiourea molecules into the holes of the accumulated molecules causes an expanded porous carbon structure with smaller holes and more density[5].

In the electro-Fenton process, mainly acidic pH, especially 3, is considered as the best pH. Since at higher pHs, due to the formation of Fe^{3+} complexes and the destruction of hydrogen peroxide, the removal efficiency decreases[6].
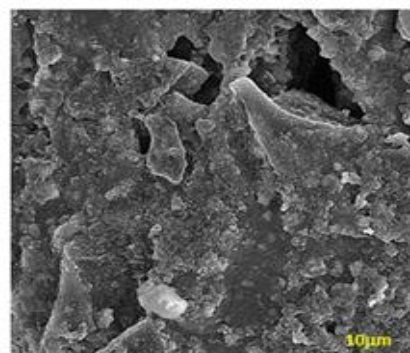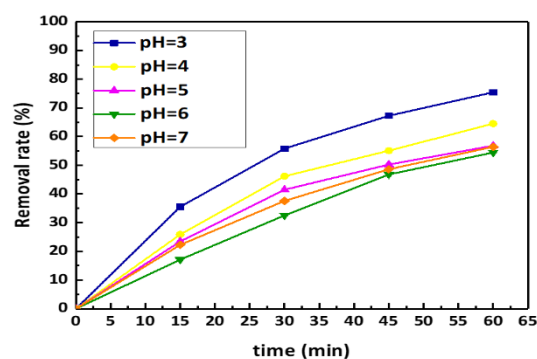

Fig.1: SEM image of Chitosan-Thiourea powder

Fig.2: pH effect on ofloxacin remediation

22nd Iranian Chemistry Congress (ICC22)
Iranian Research Organization for Science and Technology (IROST)
13-15 May 2024

03231-97589

IROST

According to the graph(Fig.2), considering to the highest removal efficiency at pH=3(75.45%) and mentioned reasons, it is known as the optimal pH of this process.

Conclusions

In this research , the synthesis of a novel chitosan-thiourea electrode on a titanium mesh substrate with high electrochemical efficiency during the progress has been successfully carried out. The effect of the mentioned four parameters have been examined by optimizing them in the removal of ofloxacin antibiotic with synthetic cathode during electrofenton process.

References

[1] E. Brillas, I. Sirés, M.A. Oturan,(2009). Electro-Fenton process and related electrochemical technologies based on Fenton's reaction chemistry, Chemical reviews, 109 6570-6631%@00092665. https://doi.org/10.1021/cr900136g

[2] G. Song, M. Zhou, X. Du, P. Su, J. Guo,(2021). Mechanistic insight into the heterogeneous electro-Fenton/sulfite process for ultraefficient degradation of pollutants over a wide pH range, Acs Es&T Water, 1, 1637-1647%@2690-0637. https://doi.org/10.1021/acsestwater.1c00123?rel=cite-as&ref=PDF&jav=VoR

[3] G. Daniel, Y. Zhang, S. Lanzalaco, F. Brombin, T. Kosmala, G. Granozzi, A. Wang, E. Brillas, I. Sirés, C. Durante,(2020). Chitosan-derived nitrogen-doped carbon electrocatalyst for a sustainable upgrade of oxygen reduction to hydrogen peroxide in UV-assisted electro-Fenton water treatment, ACS Sustainable Chemistry & Engineering,8,14425-14440%@1216810485. https://dx.doi.org/10.1021/acssuschemeng.0c04294?ref=pdf

[4] H. Tan, J. Liu, G. Huang, Y. Qian, Y. Deng, G. Chen, (2018).Understanding the roles of sulfur doping for enhancing of hydrophilicity and electrochemical performance of N, S-codoped hierarchically porous carbon, ACS Applied Energy Materials, 1 , 5599-5608 %@ 2574-0962.https://doi.org/10.1021/acsaem.8b01131

[5] D. Meng, Y. Hu, Y. Jing, X. Zhang, S. Mahmud, S. Su, J. Zhu,(2022). One-step carbonization strategy of freeze-dried chitosan to prepare nitrogen-oxygen co-doped porous carbon supercapacitors with ultra-large specific surface area, Fuel, 320 , 124002 %@ 120016-122361.https://doi.org/10.1016/j.fuel.2022.124002

[6] V.D. Thao, N.T. Hoa, N.T. Thuy, N.T. Vinh, N.T.C. Tien, N.T. Dung, K.-Y.A. Lin, D.T.M. Thanh, N.T. Phuong, T.T. Trang,(2023). Synthesis of Fe, Mn-Cporous/CF and its application as cathode for electro-Fenton decomposition of organics in water: A comprehensive study, Journal of Environmental Chemical Engineering, 11 , 109698 %@ 102213-103437. https://doi.org/10.1016/j.jece.2023.109698

Synthesis of 2-aryl -3*H*-indol-3-ones via oxygenation of 2-aryl indoles with molecular oxygen

Ali Akbari

Corresponding Author E-mail: a.akbari@ujiroft.ac.ir

Faculty of Chemistry, University of Jiroft, Jiroft, P.O. Box 8767161167, Iran.

Abstract: We describe the synthesis of 2-aryl-3*H*-indol-3-ones via oxygenation of 2-aryl indoles with molecular oxygen as the oxidant and oxygen source. Under an atmosphere of O_2 (1 atm) or air (1 atm), successfully incorporated one O atom from O_2 into 2-aryl indoles by copper/2,2,6,6-tetramethylpiperidine (TEMP)-catalyzed. The high efficiency, low cost, high oxygen atom economy, and practical operation make the developed oxygenation system very attractive and practical. The advantages of this method include mild reaction conditions, simple procedures, and easy workup.
Keywords: 2-Aryl indoles; 2-Aryl -3*H*-indol-3-ones; Environmental reaction; Oxygenation.

Introduction

Among these oxidative processes, the use of molecular oxygen as an ideal oxidant due to its natural, inexpensive, and environmentally friendly characteristics, and therefore offers attractive academic and industrial prospects. The development of new protocols using molecular oxygen as an ideal oxidant is highly desirable in oxidation chemistry [1]. More importantly, the oxygenation reaction of simple molecules using molecular oxygen as the oxygen source provides one of the most perfect processes for the construction of O-containing compounds [2].

2-Aryl-3*H*-indol-3-ones was found as one of the most important five-membered ring nitrogen heterocyclic compounds which had a wide range of biological activities such as antimalarial [3], antiplasmodial [4], antibacterial [5, 6], and antifungal [7, 8]. Because of these important applications, several methods have been described for the preparation of indol-3-ones derivatives including oxidation of indoles with TEMPO+BF₄ [9]. Although these methods have been used in the literature, they suffer from several disadvantages, such as exclusive substrates and catalysts, relatively low performance, hazardous reagents, limited substrate scope, and inconvenient reaction conditions. Therefore, it is desirable to access indol-3-one compounds *via* oxygenation of 2-aryl indoles with copper(I) bromide and TEMP catalyst (Scheme 1).
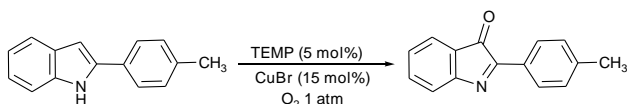
Scheme 1: synthesis of 2-(4-Methy-phenyl)-3*H*-indol-3-one

Experimental Section

2-(4-Methy-phenyl)-1*H*-indole (2.0 mmol), copper(I) bromide (15 mmol%) and TEMP (5 mmol%) were mixed with 50 mL methanol in a 200-mL glass round-bottom flask and the mixture was stirred at room temperature under oxygen bubbling for 12 h (monitoring with TLC). After completing the reaction, 50 mL of cooled water was added and the product was extracted with CH_2Cl_2 (3 × 10 mL). The eluting organic solvent was evaporated with a vacuum evaporator. the residue was chromatographed over a silica gel column, and elution with petroleum ether -ethyl acetate (60%) gave the 2-(4-Methy-phenyl)-3*H*-indol-3-one.
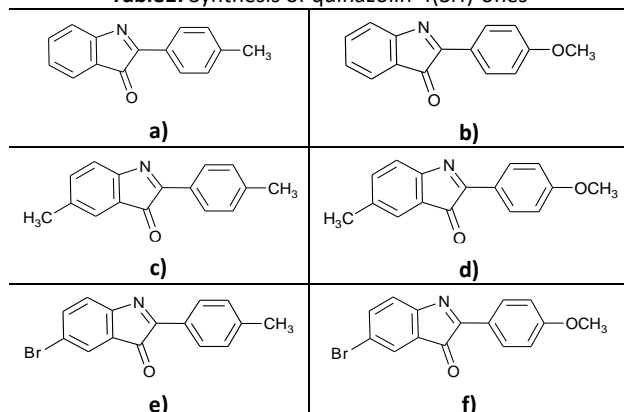
Results and Discussion

The influences of various reaction parameters such as catalyst loading, reaction time, solvent, and temperature on the reaction system were investigated.

The reactions were also tested in the presence of protic solvents such as water, ethanol, and methanol. The reaction results in a moderate yield of product in the presence of water. It was found that the yield of the product was very low when the use of the equal molar ratio of substrates in the absence of the copper(I) bromide. It was found that the yield of the product was very low when the use of the equal molar ratio of substrates in the absence of the TEMP.

Under the optimized reaction conditions, oxygenation of various 2-aryl indoles with molecular oxygen gives 2-aryl -3*H*-indol-3-ones high yields, and the results are shown in Table 1.

22nd Iranian Chemistry Congress (ICC22)
Iranian Research Organization for Science and
Technology (IROST)
13-15 May 2024

03231-97589

Table 1: Synthesis of quinazolin-4(3H)-ones

a)	b)
c)	d)
e)	f)

2-(4-Methy-phenyl)-3H-indol-3-one (**a**); FT-IR ν(cm^{-1}): 1759, 1722, 1535, 1273, 874, 755; ^{1}H NMR (400 MHz, CDCl$_3$): δ 2.38 (s, 3H), 7.19 (d, J=8.08Hz,2H), 7.22-7.32 (m, 2H), 7.39 (d, J=8.04, 2H), 7.47 (t, J=7.48Hz,1H), 7.56 (d, J=6.96Hz, 1H); ^{13}C NMR (100 MHz, CDCl$_3$): δ 21.16, 123.66, 124.55, 125.40, 126.65, 127.51, 129.23, 130.7, 138.10, 140.85, 154.20, 167.88, 193.28.

2-(4-Methoxy-phenyl)-3H-indol-3-one (**b**) FT-IR ν(cm^{-1}): 1763, 1725, 1539, 1257, 1045, 833, 758; ^{1}H NMR (400 MHz, CDCl$_3$): δ 3.84(s,3H), 6.91(d, J=8.92Hz,2H), 7.23-7.29(m, 2H), 7.38-7.61(m, 4H); ^{13}C NMR (100 MHz, CDCl$_3$): δ 55.36, 113.92, 122.89, 124.55, 125.39, 127.42, 128.01, 131.18, 133.43, 154.20, 159.69, 167.94, 193.99.

2,5-Dimethyl -3H-indol-3-one (**c**) FT-IR ν(cm^{-1}): 1757, 1724, 1539, 835, 760; ^{1}H NMR (400 MHz, CDCl$_3$): δ 2.34 (s, 3H), 3.11 (s. 3H), 7.24 (dd, J=7.88, 1 Hz, 1H), 7.37 (d, J=7.88Hz, 1H), 7.69 (s, 1H); ^{13}C NMR (100 MHz, CDCl$_3$): δ 13.77, 21.10, 98.05, 116.40, 124.67, 133.39, 134.51, 138.66, 149.93, 195.92.

2-(4-Methoxy-phenyl)-5-methyl-3H-indol-3-one (**d**) FT-IR ν(cm^{-1}): 1761, 1723, 1537, 1255, 1043, 830, 759; ^{1}H NMR (400 MHz, CDCl$_3$): δ 2.38 (s, 3H), 3.84 (s, 3H), 6.91 (d, J=8.29Hz, 2H), 7.13 (d, J=8.16, 2H), 7.24-7.29 (m, 1H), 7.37 (s, 1H) 7.42 (d, J=8.68, 2H); ^{13}C NMR (100 MHz, CDCl$_3$): δ 20.77, 55.35, 113.91, 123.03, 124.51, 127.88, 128.02, 129.81, 131.80, 133.50, 138.30, 159.69, 167.98, 193.27.

5-Bromo-2-(4-Methy-phenyl)-3H-indol-3-one (**e**); FT-IR ν(cm^{-1}): 1760, 1722, 1536, 1514, 1383, 1250, 831, 757, 650; ^{1}H NMR (400 MHz, CDCl$_3$): δ 2.39(s, 3H), 7.12 (d, J=8.56Hz,2H), 7.20 (d, J=8.04Hz, 2H), 7.38 (d, J=8.04Hz,2H), 7.57 (d, J= 8.32 Hz, 1H), 7.68 (s, 1H); ^{13}C NMR (100 MHz, CDCl$_3$): δ 21.20, 118.49, 123.51, 126.11, 126.62, 129.30, 130.34, 131.65, 138.28, 139.89, 153.84, 166.52, 193.38.

5-Bromo-2-(4-methoxy-phenyl)-3H-indol-3-one (**f**) FT-IR ν(cm^{-1}): 1762, 1724, 1538, 1515, 1384,1253, 1043, 831, 756, 652; ^{1}H NMR (400 MHz, CDCl$_3$): δ 3.84 (S, 3H), 6.91 (d, J=8.8 Hz, 2H) 7.12 (d, J=8.56Hz, 1H), 7.42 (d, J=8.68 Hz, 2H), 7.57 (d, J=7.84 Hz ,1H), 7.67 (s,1H); ^{13}C NMR (100 MHz, CDCl$_3$): δ, 55.35, 114.00, 122.77, 126.13, 127.96, 130.32, 131.70, 133.20, 134.06, 153.85, 159.82, 166.48, 193.33.

Conclusions

In conclusion, we have developed the synthesis of quinazolin-4(3H)-ones *via* oxygenation of 2-aryl indoles with molecular oxygen as the oxidant. Finally, the successful preparation of quinazolin-4(3H)-ones in good to excellent yields and purity is also disclosed. The advantages of this method include mild reaction conditions, simple procedures, easy workup, and low cost.

References

[1] Shi, Z., Zhang, C., Tang, C. & Jiao, N., (2012). Recent advances in transition-metal catalyzed reactions using molecular oxygen as the oxidant, Chemical Society Reviews, 41 3381-3430.

[2] Liang, Y.-F. & Jiao, N., (2017). Oxygenation via C–H/C–C bond activation with molecular oxygen, Accounts of chemical research, 50 1640-1653.

[3] Rakotoarivelo, N.V., Perio, P., Najahi, E. & Nepveu, F., (2014). Interaction between Antimalarial 2-Aryl-3H-indol-3-one Derivatives and Human Serum Albumin, The Journal of Physical Chemistry B, 118 13477-13485.

[4] Najahi, E., Valentin, A., Fabre, P.-L., Reybier, K. & Nepveu, F., (2014). 2-Aryl-3H-indol-3-ones: Synthesis, electrochemical behaviour and antiplasmodial activities, European journal of medicinal chemistry, 78 269-274.

[5] Sridhar, S.K., Saravanan, M. & Ramesh, A., (2001). Synthesis and antibacterial screening of hydrazones, Schiff and Mannich bases of isatin derivatives, European Journal of Medicinal Chemistry, 36 615-625.

[6] Yousif, E.I., Ahmed, R.M., Hasan, H.A., Al-Fahdawi, A.S. & Al-Jeboori, M.J., (2017). Metal complexes of heterocyclic hydrazone schiff-bases: Preparation, spectral characterisation and biological study, Iranian Journal of Science and Technology, Transaction A: Science, 41 103-109.

[7] Wollein, U. & Bracher, F., (2011). The gramine route to pyrido[4,3-b]indol-3-ones - identification of a new cytotoxic lead, Scientia Pharmaceutica, 79 59-68.

[8] Kutschy, P., Suchý, M., Dzurilla, M., Takasugi, M. & Kováčik, V., (2000). A new approach to imidazo[1,5-a]indole derivatives, Collection of Czechoslovak Chemical Communications, 65 1163-1172.

[9] Yan, X., Tang, Y.-D., Jiang, C.-S., Liu, X. & Zhang, H., (2020). Oxidative dearomative cross-dehydrogenative coupling of indoles with diverse CH nucleophiles: Efficient approach to 2, 2-disubstituted indolin-3-ones, Molecules, 25 419.

22ⁿᵈ Iranian Chemistry Congress (ICC22)
Iranian Research Organization for Science and Technology (IROST)
13-15 May 2024

03231-97589

IROST

Pocl₃ is an efficient catalyst for the synthesis of quinazoline-4(3*H*)-ones by 2-aminobenzoic acid, organic acid, and ammonium phosphate

Ali Akbari

Corresponding Author E-mail: a.akbari@ujiroft.ac.ir

Faculty of Chemistry, University of Jiroft, Jiroft, P.O. Box 8767161167, Iran.

Abstract: The preparation of quinazolin-4(3*H*)-ones by various organic acids, 2-aminobenzoic acid, and ammonium phosphate in one-pot reactions using phosphorus oxychloride as a catalyst. We disclose a highly efficient phosphorus oxychloride catalyzed for the synthesis of quinazolinones in good to excellent yields. The advantages of this method include simple procedures, easy workup, and readily available and inexpensive starting materials.

Keywords: Organic acid; Phosphorus oxychloride; Quinazolin-4(3*H*)-one; Synthesis.

Introduction

Quinazolin-4(3*H*)-ones are one of the most important classes of the chemistry of nitrogen-containing heterocyclic compounds. Several compounds of this class have shown a broad area of biological activity, such as anticancer, antimalarial, antiplasmodial activity, antibacterial, antiviral activity, antimycobacterial activity, antifungal, insecticide, and candidates for clinical Anti-HIV activity[1-3]. There are several methods for the synthesis of quinazolin-4(3*H*)-ones including condensing 2-amino benzamides with alcohols /aldehydes using hazardous and expensive oxidants, diaryliodonium, and metal-complex catalysts [2]. Rhodium(III) [4], Fe(II) [5], Mn(I) [6], phosphomolybdic acid [7], and magnesium perchlorate [8] were frequently used as metal complex catalysts to synthesize quinazoline-4 (3*H*)-one derivative. Different approaches reported have been shown to have various limitations such as hazardous reagents and solvents, higher temperatures, longer reaction times, limited substrate scope, and exclusive substrates. In the present work, the quinazolin-4(3*H*)-one's derivative was synthesized in a novel method by reacting anthranilic acid with various organic acids and ammonium phosphate as the starting materials in the presence of phosphorus oxychloride as the catalyst (Scheme 1).
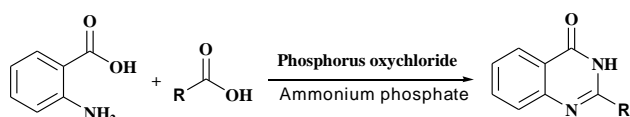
Scheme 1: Synthetic routes of quinazolin-4(3*H*)-ones

Experimental Section

Phosphorus oxychloride (20 mol%), **anthranilic acid** (5.0 mmol), benzoic acid (6.0 mmol), and **ammonium phosphate** (2.0 mmol) were mixed in a 50-mL glass round-bottom flask and the mixture was stirred at room temperature for 90 min during which the reaction was completed. The mixture was dissolved in 30 -mL 2-propanol. The white powder solid was precipitated in the solution. The product was separated with filter paper and the product was purified by recrystallization from 2-propanol.

Results and Discussion

The influences of various reaction parameters such as catalyst loading, reaction time, solvent, and temperature on the reaction system were investigated. The products were isolated with the best yields when 20 mol % phosphorus oxychloride was used as the catalyst and 5 mmol anthranilic acid, 6 mmol benzoic acid, and 2 mmol ammonium phosphate were selected as model substrates. It was found that the yield of the product was very low when the use of the equal molar ratio of substrates in the absence of the phosphorus oxychloride. We found that with the loading of the phosphorus oxychloride, the yield of the product slightly increased and the best condition with a slight excess of equal molar ratio of phosphorus oxychloride.

We also tested various ammoniums such as ammonium nitrate, ammonium chloride, ammonium sulfate, and ammonium phosphate to obtain this reaction, and the yields were achieved at 87%, 85%, 80%, and 93% respectively. This reaction gave a good yield in an aprotic solvent such as carbon tetrachloride, toluene, and pyridine. The reactions were also tested in the presence of protic solvents such as water, and ethanol. The reaction results in a moderate yield of product in the presence of protic solvents. After the complication of the reaction, the solvent was removed with low pressure. The reaction with

22nd Iranian Chemistry Congress (ICC22)
Iranian Research Organization for Science and Technology (IROST)
13-15 May 2024

03231-97589

solvent-free was the best condition in which no applied solvent and didn't have time to remove the solvent. The best results for optimization reaction conditions were achieved at room temperature in solvent-free at 90 mines.

In order to study the potential and general applicability of the developed methodology, various aliphatic and aromatic organic acids and anthranilic acids containing different functional groups were investigated (Table1).

Table1: Synthesis of quinazolin-4(3H)-ones
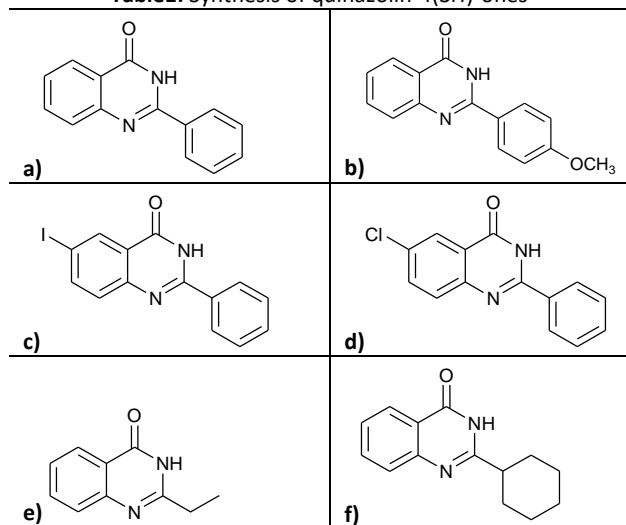
2-Phenylquinazolin-4(3H)-one (**a**), white powder ^{1}H NMR (500 MHz, CDCl$_3$) δ 10.94 (s, 1H), 8.33 (d, J = 7.5 Hz, 1H), 8.19 (dd, J = 7.0, 4.0 Hz, 2H), 7.84 (d, J = 8.0 Hz, 1H), 7.80 (t, J = 8.0 Hz, 1H), 7.65–7.55 (m, 3H), 7.51(t, J = 8.0 Hz, 1H). ^{13}C NMR (125 MHz, CDCl$_3$) δ 163.6, 151.7, 149.5, 134.9, 132.9, 131.7, 129.1, 128.0, 127.3, 126.8, 126.4,120.9.

6-Iodo-2-phenylquinazolin-4(3H)-one (**c**). white powder
^{1}H NMR (500 MHz, DMSO-d$_6$) δ 12.52 (s, 1H), 8.18 (t, J = 8.0 Hz, 3H), 7.84 (t, J = 7.5 Hz, 1H), 7.75 (d, J = 8.0 Hz, 1H), 7.55 (m, 3H). ^{13}C NMR (125 MHz, DMSO-d$_6$) δ 162.7, 152.8, 149.2, 135.1, 133.2, 131.9, 129.1, 128.3, 128.2, 127.1, 126.3, 121.4.

2-Ethylquinazolin-4(3H)-one (**e**). white powder ^{1}H NMR (500 MHz, CDCl$_3$):11.60 (br s, 1H), 8.31 (dd, J = 7.0, 1.5 Hz, 1H), 7.80 (td, J = 7.0, 1.5 Hz, 1H), 7.76 (d, J = 7.0 Hz, 1H), 7.50 (td, J = 6.0, 1.0 Hz, 1H), 2.84 (q, J = 7.0 Hz, 2H), 1.31 (t, J = 7.0 Hz, 3H). ^{13}C NMR (125 MHz, CDCl$_3$): 164.3, 157.0, 149.5, 134.8, 127.2, 126.3, 126.2, 120.5, 29.2, 11.6.

Conclusions

In conclusion, we have developed a phosphorus oxychloride as an efficient catalyst for the synthesis of various quinazolin-4(3H)-ones via a coupling of various organic acids, 2-aminobenzoic acid, and ammonium ions. Finally, the successful preparation of quinazolin-4(3H)-ones in good to excellent yields and purity is also disclosed. This strategy features mild reaction conditions, and broad substrate scope, avoiding the extra ligands, and high reaction temperatures.

Acknowledgments

References

[1] Akbari, A. & Zahedifar, M. (2023). Synthesis of Quinazolin-4 (3H)-ones via a novel approach. Journal of Saudi Chemical Society, 27, 101597.

[2] Laleu, B., Akao, Y., Ochida, A., Duffy, S., Lucantoni, L., Shackleford, D.M., Chen, G., Katneni, K., Chiu, F.C. & White, K.L. (2021). Discovery and Structure–Activity Relationships of Quinazolinone-2-carboxamide Derivatives as Novel Orally Efficacious Antimalarials. Journal of medicinal chemistry, 64, 12582-12602.

[3] Akester, J.N., Njaria, P., Nchinda, A., Le Manach, C., Myrick, A., Singh, V., Lawrence, N., Njoroge, M., Taylor, D. & Moosa, A. (2020). Synthesis, structure–activity relationship, and mechanistic studies of aminoquinazolinones displaying antimycobacterial activity. ACS Infectious Diseases, 6, 1951-1964.

[4] Zhou, G., Huang, Z., Xu, X., Fang, Z., Huang, P., Deng, Z., Li, B. & Zhao, Y. (2022). Rhodium(III)-Catalyzed Synthesis of Quinazolin-4(3H)-ones with N-Methoxyamides as Synthesis Reagents. Synthesis, 54, 3298-3306.

[5] Mondal, R., Chakraborty, G., Guin, A.K., Pal, S. & Paul, N.D. (2021). Iron catalyzed metal-ligand cooperative approaches towards sustainable synthesis of quinolines and quinazolin-4-ones. Tetrahedron, 100, 132479.

[6] Pal, D., Mondal, A. & Srimani, D. (2022). Well-defined manganese complex catalyzed dehydrogenative synthesis of quinazolin-4(3H)-ones and 3,4-dihydro-2H-1,2,4-benzothiadiazine 1,1-dioxides. Catalysis Science & Technology, 12, 3202-3208.

[7] Chi, M., Xiong, W.-L., Yang, D.-Z., Fan, C.-B., Shi, R.-W., Gong, S.-S. & Sun, Q. (2022). A peroxo-Mo(VI)/Mo(VI)-mediated redox synthesis of quinazolin-4(3H)-ones and their aggregation-induced emission property and mechanism. Journal of Physical Organic Chemistry, 35, e4329.

[8] Mishra, S., Das, D., Sahu, A., Patil, S., Agarwal, R.K. & Gajbhiye, A. (2020). Transition Metal-free Approach for the Synthesis of 2-substituted Quinazolin-4 (3H)-one via Anhydrous Magnesium Perchlorate. Current Organocatalysis, 7, 118-123.

22nd Iranian Chemistry Congress (ICC22)
Iranian Research Organization for Science and Technology (IROST)
13-15 May 2024

03231-97589

IROST

Perlite-Supported SbCl5: A Promising Approach for Sustainable CO_2 Fixation Under Solvent Free and Atmospheric Pressure Conditions

Farshid Eskandari[*], Zahra Rafiee Atani

Corresponding Author E-mail: Eskandari2013@yahoo.com

Department of Research and Development, Alvand Metal Chemistry Company, Qazvin, Iran.

Abstract: The use of fossil fuels all over the world has increased the emission of carbon dioxide in the atmosphere, which leads to global warming. One of the solutions is to use carbon dioxide. In this regard, the chemical fixation of carbon dioxide and its conversion into fine chemicals is one of the best options. In this research, the catalytic properties of Perlite-Supported SbCl5 in the CO_2 fixation reaction were investigated. The catalyst and products were identified through FTIR, XRD, SEM, XRF, NMR, and TGA analysis.

**Keywords:** Perlite-Supported SbCl5; CO_2 fixation; Solvent Free; Atmospheric Pressure.

Introduction

The use of fossil fuels all over the world has increased the emission of carbon dioxide in the atmosphere, which is one of the greenhouse gases. which leads to global warming. One of the solutions is the use of carbon dioxide. Therefore, the best way is to capture and use carbon dioxide. There are two methods for the chemical conversion of carbon dioxide: reduction and non-reduction. In carbon dioxide reduction, it is converted into methanol, ethanol, etc. through a catalyst and suitable conditions. In non- reduction conditions, carbon dioxide ,catalyst and other substances form esters, urea, etc. In this regard, the chemical fixation of carbon dioxide and its conversion to cyclic carbonate through cycloaddition reaction is one of the best options. cyclic carbonate is a very valuable and widely used substance that is used in pharmaceutical and polymer precursors, lithium batteries, solvents, active intermediates, electrolytes, etc. At first, researchers focused on the feasibility of changing carbon dioxide, but recently, more attention has been paid to the economy of doing the reaction. In this research, the catalytic properties of Perlite-Supported SbCl5 in the CO_2 fixation reaction were investigated. Perlite-Supported SbCl5 demonstrates efficient catalytic activity in CO_2 fixation, leading to a rapid and high-yielding conversion of the main product. [1-4].

Experimental Section

Initially, the air inside the flask was removed by blowing carbon dioxide. The amount of 0.005 grams of catalysts and 0.03mmol tetrabutylammonium bromide and 2 mmol of epoxide were mixed together. The reaction container was closed.The flask was poured inside the bath oil. At the same time, carbon dioxide entered the reaction container. The progress of the reaction was followed by thin layer chromatography(TLC). The crude product was analyzed by NMR and in the most cases pure products were obtained. In some cases the crude product was purified via chromatograghy to give the corresponding compounds.
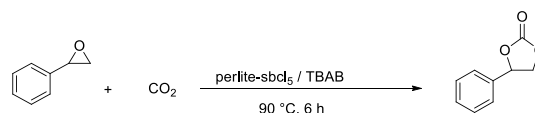
Scheme 1. Model reaction

Results and Discussion

This paper reports results obtained by working on using Perlite-supported SbCl5 as a catalyst to convert CO2 into useful products. The test results are promising the catalyst showed high activity in this conversion process under air pressure and without using a solvent. Efficacy of the reaction was attained at relatively mild conditions; just needing 0-90°C temperature was required (Scheme 1). Additionally, the Perlite-supported catalyst could be reused for up to five cycles, which reflects its cost-effectiveness and environmental. The catalyst and products were identified through FTIR, XRD, SEM, XRF, NMR, and TGA analysis.Optimizing reaction parameters, such as CO2 pressure and reaction time, might lead to even higher conversion rates and product selectivity. Exploring the conversion of CO2 into a wider range of valuable chemicals could broaden the applicability of this method.

Conclusions

This study focuses on the potential of Perlite-Supported SbCl5 as a catalyst for CO_2 fixation under solvent-free and atmospheric pressure conditions. The results reveal that the catalyst is active at temperatures above 25°C, demonstrating a promising behavior that leads to the transformation of CO_2 into valuable products. Besides, the Perlite-supported catalyst reused for as much as five cycles increases its economic and environmental viability

22nd Iranian Chemistry Congress (ICC22)
Iranian Research Organization for Science and Technology (IROST)
13-15 May 2024

03231-97589

as compared to conventional ways. Moreover, expanding the range of valuable chemicals generated by means of this technique would possibly play a big position in increasing the applicability of this method.

References

[1] Wang, Q., Chen, P., Li, X., Liang, Y., & Pan, Y. (2023). Chemical fixation of carbon dioxide into cyclic carbonates catalyzed by porous materials. Asian Journal of Organic Chemistry, 12(8), e202300308.

[2] Yan, T., Liu, H., Zeng, Z. X., & Pan, W. G. (2023). Recent progress of catalysts for synthesis of cyclic carbonates from CO2 and epoxides. Journal of CO2 Utilization, 68, 102355.

[3] Liu, X., Zhang, S., Song, Q. W., Liu, X. F., Ma, R., & He, L. N. (2016). Cooperative calcium-based catalysis with 1, 8-diazabicyclo [5.4. 0]-undec-7-ene for the cycloaddition of epoxides with CO2 at atmospheric pressure. Green Chemistry, 18(9), 2871-2876.

[4] Kulal, N., Vasista, V., & Shanbhag, G. V. (2019). Identification and tuning of active sites in selected mixed metal oxide catalysts for cyclic carbonate synthesis from epoxides and CO2. Journal of CO2 Utilization, 33, 434-444.

22nd Iranian Chemistry Congress (ICC22)
Iranian Research Organization for Science and Technology (IROST)
13-15 May 2024

03231-97589

IROST

Optimized Perlite Filter Aid: A Key to Minimizing Oil Retention and Enhancing Efficiency in Edible Oil Industry Filtration

Farshid Eskandari*, Zahra Rafiee Atani, Habibollah Jamshidi

Corresponding Author E-mail: Eskandari2013@yahoo.com

Department of Research and Development, Alvand Metal Chemistry Company, Qazvin, Iran.

Abstract: In the edible oil industry, perlite is used as a filtering aid in the filtration process. However, If the perlite filter aid is unoptimized. It absorbs a significant amount of oil during the filtration process, leading to substantial waste. In this research, the effect of perlite structure and particle size distribution on oil retention and filtration performance in the edible oil industry is investigated. The results show that optimized perlite with porous structure and optimal particle size distribution can significantly reduce oil retention compared to conventional perlite. Therefore, this leads to increased efficiency of the filtration process, reduced oil waste and improved environmental sustainability. The optimal perlite was identified through FTIR, XRD, SEM, XRF, LPA, and TGA analysis.

Keywords: Edible Oil Industry; Optimized Perlite Filter Aid; Filtration; Oil Retention.

Introduction

The heart of an edible oil factory is its filtration. The production of high quality edible oils relies heavily on efficient filtration processes. Perlite, an aluminum silicate volcanic rock with unique properties, is widely used as an filter aid in this industry. However, unoptimized perlite can have disadvantages and problems. A major concern is its tendency to absorb a significant amount of oil during filtration, leading to significant waste and reduced process efficiency [1-3].

Experimental Section

At first, raw perlite from mines in the west, east and central of the Iran were considered. These samples were analyzed using classical laboratory methods based on perlite institute(worldwide association of perlite) standards ,ASTM and techniques such as FT-IR, XRF, XRD, TGA, and SEM focusing on factors like structure, chemical composition, molecular water content, main phases, and impurities. Among all the perlites, according to the acceptable characteristics of Ardabil mines, it was selected as a pilot plant sample. The selected perlite sample was then carefully granulated, and its particle size distribution was thoroughly analyzed using both sieves and a laser particle size analyzer. Then entered the expansion furnace and carefully the expansion process was controlled under specified temperatures, and finally the expanded perlite size distribution was evaluated sieves and laser particle size analyzer. Then the prepared sample was sent to the oil factory and subjected to edible oil filtration conditions.
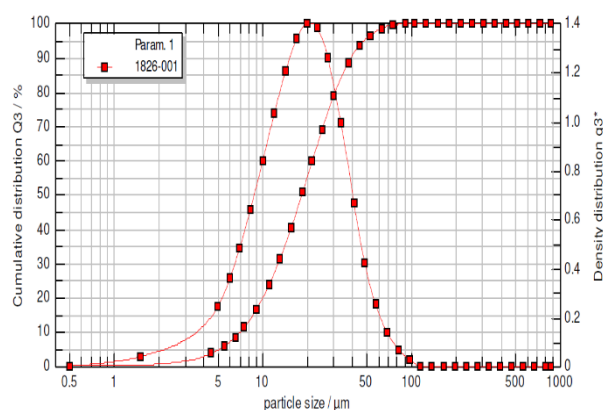

Fig.1: Optimized perlite particle size distribution

Results and Discussion

Figure 2 shows the particle size distribution (x_{10} = 7.06, x_{99} = 71.27, x_{50} = 18.34 μm) of the optimized perlite filter aid sample that has performed the best performance in edible oil filtration. Also structural studies of this sample indicate layer structure. The XRD also shows that the main phase of these samples is amorphous. The results of the XRF and TGA confirm that the sample has molecular water to 4-5 %.analysis.

Conclusions

In summary, in this research, the effect of optimal particle size distribution and structure of perlite filter aid on oil retention in the edible oil filtration process was investigated. The results show that optimized perlite can play an important role in reducing oil retention compared to the conventional and traditional perlite filter aid. The optimal perlite was identified through FTIR, XRD, SEM, XRF, LPA, and TGA analysis.

22ⁿᵈ Iranian Chemistry Congress (ICC22)
Iranian Research Organization for Science and Technology (IROST)
13-15 May 2024

03231-97589

References

[1] Gironás, J., Adriasola, J. M., & Fernández, B. (2008). Experimental analysis and modeling of a stormwater perlite filter. Water environment research, 80(6), 524-539.

[2] Onur, A., Shanmugam, K., Ng, A., Garnier, G., & Batchelor, W. (2019). Cellulose fibre-perlite depth filters with cellulose nanofibre top coating for improved filtration performance. Colloids and Surfaces A: Physicochemical and Engineering Aspects, 583, 123997.

[3] Zafisah, N. S., Ang, W. L., Johnson, D. J., Mohammad, A. W., & Hilal, N. (2018). Effect of different filter aids used in cake filtration process on the removal of suspended solids in anaerobically digested palm oil mill effluent (POME). Desalination and Water Treatment, 110, 362.

22nd Iranian Chemistry Congress (ICC22)
Iranian Research Organization for Science and
Technology (IROST)
13-15 May 2024

03231-97589

IROST

Effects of the Nanowire Length and Metal-Doping on Nonlinear Optical Responses of Drum-Shaped Boron Cluster Assemblies

Maryam Sotudeh, Afshan Mohajeri*

Corresponding Author E-mail: amohajeri@shirazu.ac.ir

Department of Chemistry, College of Sciences, Shiraz University, Shiraz 7194684795, Iran.

Abstract: In the present work, systematic theoretical calculations are performed to study the possible formation of finite-size nanowire assemblies by stacking B_{14} or $B_{14}M$ (M= Fe, Co) building blocks. Our results highlight that the modulation of the first hyperpolarizability by varying the number of stacked units. Among all the examined systems, the highest hyperpolarizability (β_{tot} = 1.35 × 10^5 a.u.) is observed for $(B_{14}Fe)_6$.

Keywords: Static and dynamic NLO.; Boron Cluster; Doping

Introduction

Cluster-assembled materials offer a promising approach toward creating new materials with tailored properties through the careful combining of clusters with precise size and composition [1]. The combination of extraordinary properties of atomic clusters makes cluster-assembled materials a fascinating platform for the development of non-linear optical (NLO) materials.

Over the past decades, NLO materials have gained much interest for their widespread utility in advanced technologies such as all-optical data processing. To meet the need for applications in various fields, designing stable multifunctional NLO materials is urgent. Different strategies have been used so far to obtain high-performance NLO materials, such as donor-π-bridge-acceptor frameworks, octupolar-based compounds and species with excess electrons [2]. Among these, introducing excess electrons into a system through metal doping is considered to be the most rational method for augmenting the NLO response of the host.

Among numerous materials, boron compounds with high thermodynamic stabilities serve as promising hosts for metal doping. Doping boron materials with transition metals provides innovative changes and modifies fundamental characteristics such as stability, and electronic properties.

Several types of doped boron compounds have already been reported such as metallo-borophenes, teetotums, double ring (DR), [3]. Among these, DR and teetotum forms are the most interesting because their special geometrical and electronic characteristics make them potential building blocks for the construction of nanotubes or nanowires. Saha etal. [4] studied the electronic structures of $M@B_{16}$ and $M@B_{14}$ with M= 3d, 4d, and 5d transition metals. They found that in the cases of M = Cr, Mn, Fe, Co, and Ni, the DR drum-shaped $M@B_{14}$

clusters are favored. Accordingly, this work presents a systematic study for the development of new NLO materials based on boron self-assemblies. To this end, we have employed quantum chemistry calculations to study the possible formation of boron tubular assemblies based on B_{14}, $B_{14}M$ (M= Fe, Co) building blocks. The evolution of structure, electronic and NLO properties of $(B_{14})_n$, $(B_{14}Fe)_n$, and $(B_{14}Co)_n$ with the nanowire length has been explored by varying n from 1 to 6.

Computational Methods:

Electronic structure calculations were performed in the framework of density functional theory (DFT) using the Gaussian 09 [5], suite of program packages Geometrical optimizations and subsequent computations of electronic and NLO properties were carried out using the hybrid PBE0 functional with 6-311+G* basis set.

The mean static isotropic (α_{iso}) and anisotropic polarizabilities (α_{aniso}), and the first hyperpolarizability (β_0) are obtained through

$$\beta_0 = \left(\beta_x^2 + \beta_y^2 + \beta_z^2\right)^{1/2} \qquad (1)$$

where the general equation for the calculation of hyperpolarizability along one Cartesian axis is

$$\beta_i = \left(\tfrac{1}{3}\right)\sum_j\left(\beta_{ijj} + \beta_{jji} + \beta_{iij}\right) \qquad i , j = \{x, y, z\} \qquad (2)$$

To explore the NLO response of investigated materials when subjected to an electric field, the frequency-dependent NLO properties in terms of the second harmonic generation (SHG, β (-2ω, ω, ω)), hyper-Rayleigh scattering (HRS, β (-2ω, ω, ω)), and the electro-optical Pockels effect (EOPE, β (-ω, ω, 0)) were calculated at the standard Nd:YAG laser wavelength (1064 nm) through the coupled-perturbed DFT method.

$$\beta(\omega) = \left(\beta_x(\omega)^2 + \beta_y(\omega)^2 + \beta_z(\omega)^2\right)^{1/2} \qquad (3)$$

22nd Iranian Chemistry Congress (ICC22)
Iranian Research Organization for Science and Technology (IROST)
13-15 May 2024

03231-97589

IROST

Results and Discussion

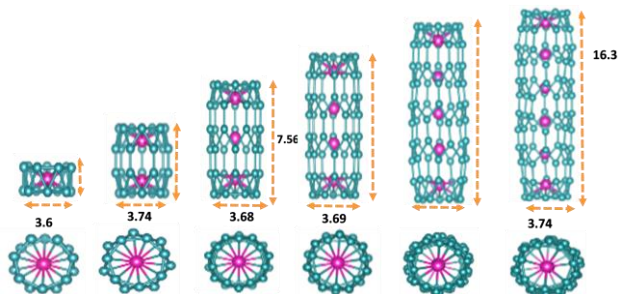The optimized structures of the assembled systems are shown in Figure 1.

Fig.1: Optimized structures of $(B_{14}M)_n$ (M= Fe, Co) with $n = 1–6$. Colore code: blue: boron and pink: Fe, Co.

To the best of our knowledge, this is the first report of the thinnest boron nanowires constructed theoretically by stacking pristine and metal-doped B_{14} blocks. Interestingly the atomic structures of $(B_{14}Fe)_n$ and $(B_{14}Co)_n$ are similar to the carbon nanotubes with all hexagons of boron stabilized by Fe and Co atoms.

To understand the effect of nanowire length and metal doping on the NLO activity of $(B_{14})_n$ assemblies, the mean polarizability, and the static and dynamic first hyperpolarizabilities of the pristine and doped assemblies were presented in Table 1. In both pristine and doped assemblies, the evolution of isotropic and anisotropic polarizability values exhibits a monotonic increasing trend as the nanowire grows.

Table 1 also shows that as the nanowire grows, an enhancement in the NLO responses is observed. In the case of $(B_{14})_n$ systems, a gradually increasing trend occurs with maximum $\beta_0 = 3340.85$ a.u for $(B_{14})_6$. In the cases of $(B_{14}Fe)_n$ and $(B_{14}Co)_n$ systems, the effect of metal doping on the NLO enhancement becomes more pronounced for larger-size nanowires. This can be ascribed to the lowering of the molecular symmetry and enlarging the dipole moment as the nanowire grows.

In addition, The frequency-dependent hyperpolarizability was investigated for the assemblies with n=1-3 units.The results were shown between the static and dynamic hyperpolarizabilities (EOPE, SHG, and HRS) is presented in Figure 2. The following outcomes can be derived from Figure 2; i) For a given assembly, the dynamic hyperpolarizabilities are larger than the corresponding β_0 value. ii) The enhancement of NLO responses with the increase in nanowire length is more pronounced for the dynamic hyperpolarizabilities than the static β_0. iii) $(B_{14})_n$ and $(B_{14}Fe)_n$ exhibited higher dynamic responses as compared to $(B_{14}Co)_n$. Altogether, the results are quite supportive of the application of these nanowires in the NLO field. In particular, the dynamic responses ensure the potential use of these systems in the SHG phenomena.

Table1: Total Dipole Moment (μ_0/D), Isotropic (α_{iso}/a.u) and Anisotropic Polarizabilities (α_{aniso}/a.u), Static First Hyperpolarizability (β_0/ a.u).

| System	μ_0	α_{iso}	α_{aniso}	β_0
B_{14}	0.00	186	59	0
$(B_{14})_2$	0.01	361	54	48
$(B_{14})_3$	0.52	555	283	252
$(B_{14})_4$	0.07	803	671	1395
$(B_{14})_5$	0.16	1092	1203	2211
$(B_{14})_6$	0.40	1430	1878	3341
$B_{14}Fe$	0.00	183	63	1
$(B_{14}Fe)_2$	0.01	356	88	77
$(B_{14}Fe)_3$	0.11	539	293	38
$(B_{14}Fe)_4$	0.33	786	696	1930
$(B_{14}Fe)_5$	0.67	1070	1189	7519
$(B_{14}Fe)_6$	3.30	1310	1592	135067
$B_{14}Co$	0.01	183	52	1
$(B_{14}Co)_2$	0.01	340	35	3
$(B_{14}Co)_3$	1.09	523	278	3109
$(B_{14}Co)_4$	0.08	742	610	415
$(B_{14}Co)_5$	1.94	993	988	5731
$(B_{14}Co)_6$	0.46	1310	1568	2782
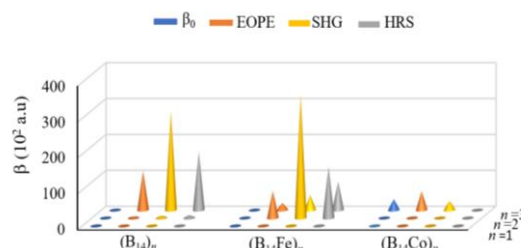
Fig.2: Comparison of static and dynamic hyperpolarizability values for $(B_{14})_n$, $(B_{14}Fe)_n$, and $(B_{14}Co)_n$ assemblies with n=1-3.

Conclusions

Our calculations revealed that the greatest first hyperpolarizability value was recorded for $(B_{14}Fe)_6$ owing to a significant increase in electronic spatial extent and easy excitation of the loosely held electrons. Moreover, it is found that the dynamic NLO responses are more sensitive to the nanowire length. In the case of second-order NLO properties, the SHG process has a stronger response than EOPE and HRS.

References

[1] Claridge, S. A., Castleman Jr, A. W., Khanna, S. N., Murray, C. B., Sen, A., & Weiss, P. S. (2009). Cluster-assembled materials. *ACS nano*, *3*(2), 244-255.

[2] Erickson, M. A., Beels, M. T., & Biaggio, I. (2016). Optimum conjugation length in donor–acceptor molecules for third-order nonlinear optics. *JOSA B*, *33*(12), E130-E142.

[3] Pham, H. T., Duong, L. V., & Nguyen, M. T. (2014). Electronic structure and chemical bonding in the double ring tubular boron clusters. *The Journal of Physical Chemistry C*, *118*(41), 24181-24187

[4] Saha, P., Rahane, A. B., Kumar, V., & Sukumar, N. (2017). Electronic origin of the stability of transition-metal-doped B14 drum-shaped boron clusters and their assembly into a nanotube. *The Journal of Physical Chemistry C*, *121*(20), 10728-10742.

[5] Frisch, M. J. E. A. (2009). gaussian 09, Revision d. 01, Gaussian. *Inc, Wallingford CT*, *201*.

Molecular Dynamics Simulation of Isophthalate Tetracarboxylic Acids on Graphite Surface

Mohammad Reza Azadeh, Afsaneh maleki*

Corresponding Author E-mail: maaleki.chem@gmail.com

Department of Chemistry, Omidiyeh Branch, Islamic Azad University, Omidiyeh, Iran.

Abstract: Model systems are essential for expanding our understanding of how self-assembly work. Two adsorbent was investigated on graphite: biphenyl tetracarboxylic acid (BPTC) and Quarterphenyl Tetracarboxylic acid (QPTC). This study is done with molecular dynamics (MD) simulations. These results help to elucidate molecular behaviour on the graphite surface, and suggests significant similarities between adsorption BPTC and QPTC on the graphite surface.

Keywords: Simulations molecular dynamics.; Isophthalate Tetracarboxylic Acids; Graphite surface

Introduction

Self-assembly of molecules on surfaces shows great potential for creating nanoscale materials through a promising pathway [1]. As in processes that occur in the natural world, molecules can rearrange themselves on a surface without external intervention, forming non-covalent bonds with each other and forming organized structures known as self-assembled molecular networks (SAMNs), which have a wide range of potential uses [2]. Extensive research has been conducted on the self-assembly of molecules containing two to four carboxyl groups on surfaces [3, 4]. the –COOH groups facilitate the formation of ordered hydrogen-bonded arrays on relatively non-reactive surfaces. Adsorbtion of two adsorbent (BPTC) and (QPTC) on graphite surface is performed with molecular dynamic simulation.

Experimental Section

Molecular dynamics simulation was performed using the GROMACS 4.5.5 program package [5]. We simulated a system, containing 2 molecules of QPTC and BPTC adsorbent on graphite surface. A total of 3200 graphite atoms is in two layers, each layer containing 1600 atoms. Opls force field was applied for simulation in the all-atom. After energy minimization, 30 ns production runs were carried out with a 2 fs time-step and 300 k using V-rescale thermostat. Interactions were accounted for using the Particle Mesh Ewald (PME) method.

Results and Discussion

A snapshot of the simulated system is shown in Fig. 1. In the energy diagram is presented in Fig 2. Show that the fluctuations are almost fixed and finally the system become stable.

The Mean Square Displacement, MSD, can be determined from simulation using the following relation:

$$MSD = \langle |r(t) - r(0)|^2 \rangle$$

Mean Square Displacement calculated for QPTC & BPTC bases then the diffusion coefficient is obtained from it about 0.0148 and 6.7268 and $cm^2.s^{-1}$ for BPTC and QPTC, respectively.

Number of hydrogen bonds between molecules, and distance between Isophthalate Tetracarboxylic Acids molecules on graphite surface during the simulation is represented in Fig 3 and 4.
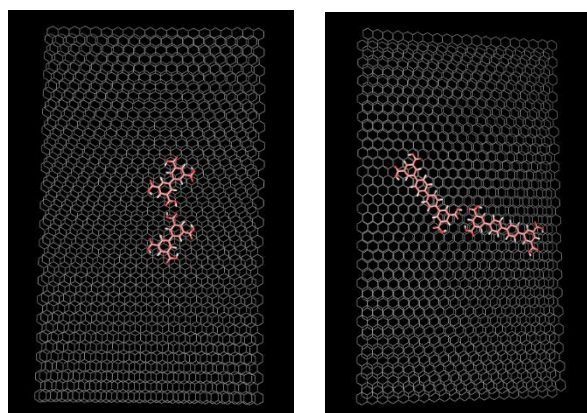

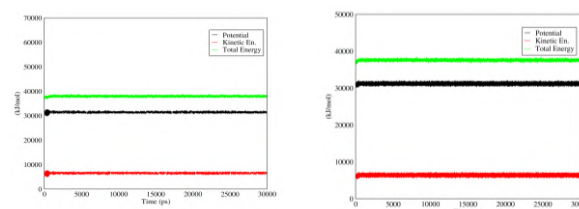**Fig.1:** Top views of surface coverage of dimer BPTC and QPTC molecules on the graphite surface.

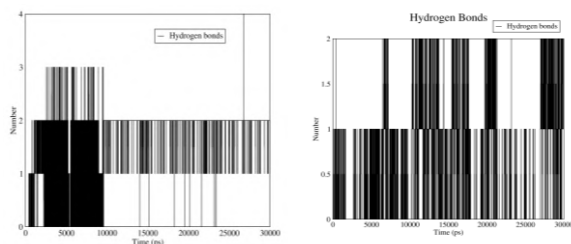**Fig.2:** The Mean Square Displacement for BPTC (left Fig) and QPTC (right Fig).

Fig.3: Number of hydrogen bonds between two molecule BPTC (left) and two molecule QPTC (right).

Number of hydrogen bonds between two molecule BPTC on graphite surface is 2, but for QPTC is between 1 and 2 as shown in fig 3 that which corresponds to information in fig 1.
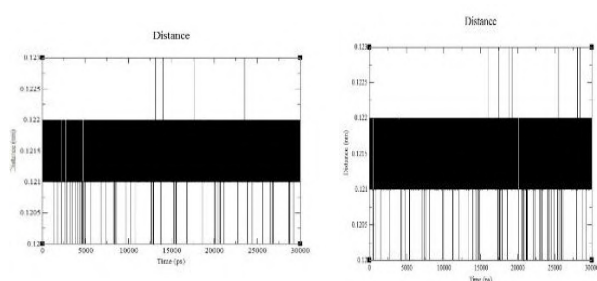

Fig.4: Distance between dimer BPTC (left) and dimer QPTC on the graphite surface (right).

The distance between two molecules to form a dimer on the graphite surface during the simulation is similar for BPTC and QPTC and approximately equal to 0.121 to 0.212 nm.

Conclusions

This type of work is an important step towards developing a systematic understanding of molecular behavior on graphene, where molecular self-assembly plays an emerging role. Molecular dynamics simulation with an all-atom Opls force filed was performed to investigate interactions of Isophthalate Tetracarboxylic Acids with graphite surface. In this work we found this important result that, because of the strong stacking interactions between Isophthalate Tetracarboxylic Acids and graphite surface that is compared with hydrogen bonds between dimers. BPTC and QPTC were adsorbed parallel with graphite surface. And also it seems The number of hydrogen bonds between two BPTC molecules on a graphite surface is 2, while for QPTC it ranges between 1 and 2. These surfaces are usually chosen to promote intermolecular interactions rather than interactions between molecules and the substrate, and are crucial in forming the molecular film.

References

[1] Rosei, F., Schunack M., Naitoh, Y., Jiang,P., Gourdon, Laegsgaard A. E., Stensgaard, I. Joachim, C. & Besenbacher, F. (2003) .Properties of large organic molecules on metal surfaces. Prog. Surf. Sci. 71, 95-146.

[2] Otero, R., Gallego , J. M., de Parga , A. L. V., Martín,N. and Miranda, R. (2011) Molecular self-assembly at solid surfaces, Adv. Mater. 23, 5148-5176

[3] MacLeod, J. M., Ben Chaouch, Z., Perepichka, D. F. and Rosei, F., Two dimensional self-assembly of a symmetry-reduced tricarboxylic acid, Langmuir 29, 7318-7324 (2013). 15, 4353-4360.

[4] Zhang S, Li, J., Gan, J., Zeng, Q., (2023) The self-assembly of a pair of low symmetric tetracarboxylic acid molecules and their co-assembly with bridging molecule at the liquid–solid interface. Nanoscale 15(9)

[5] Hess, B., Kutzner, C., van der Spoel, D., & Lindahl, E. (2008) GROMACS 4: Algorithms for Highly Efficient, Load-Balanced, and Scalable Molecular Simulation. Journal of Chemical Theory and Computation, 4(3), 435-447.

Water production enhancement from the air moisture using thermoelectric cooler

Emad Nazari, Mohammad Hassan Vakili*, Mehdi Reiszadeh

Corresponding Author E-mail: mhvakili@iaush.ac.ir

Department of Chemical Engineering, Shahreza Branch, Islamic Azad University, Shahreza, Iran.

Abstract: In this study, a thermoelectric cooler system was utilized to condense and extract water from humid air. The findings indicated that raising the humidity and temperature of the air entering the system resulted in higher water extraction and improved performance coefficient of the system.
Keywords: thermoelectric cooler; water production; air humidity

Introduction

The thermoelectric cooler is one of the air cooling tools that condenses water without using refrigerant. It is an electronic component that operates based on the Peltier phenomenon [1]. Peter et al. designed a device that included a thermoelectric module utilizing the Peltier effect to condense ambient air humidity for controlled watering of houseplants. [2].

Experimental
Thermodynamic relationships

The thermoelectric system consists of a series of positive and negative semiconductor elements that are thermally connected in parallel and electrically connected in series between ceramic plates. When a voltage is applied to the two ends of the thermoelectric cooler, the flow of electrons and holes in the negative and positive semiconductors causes one side of the thermoelectric to become cold while the other side becomes heated. [3].

the incoming humid air is guided by the suction fan towards the channel, whose two sides are cooled by the cold section of the thermoelectric components. As the air passes through the cold channel, its temperature drops and eventually reaches saturation with additional cooling, causing the moisture in the humid air to condense.

Effect of fin arrangement

the way and location of the fins attached to the sides of each module in the set, as well as the air flow pattern on the fins, can affect the performance of the set. In order to investigate the effect of different arrangements and functional conditions of the modules, three different arrangements have been considered for the set of fins. Parallel fins, co-current flow in series fins and counter-current flow in series fins as shown in figure 1.
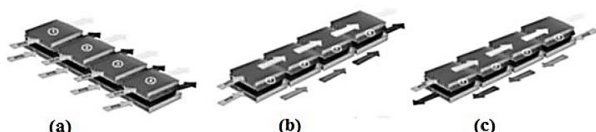

Fig.1: Schematic of fins and air flow layout over them (a) parallel fins (b) co-current flow in series fins (c) counter-current flow in series fins

Experimental

Experimental device consist of a cold finned channel for condensing water from humid air and a cooling water flow channel used to capture heat from the hot side of the thermoelectric as shown in figure 2. This device is also equipped with a fan, pump and a number of tools for measuring temperature, humidity and air velocity.
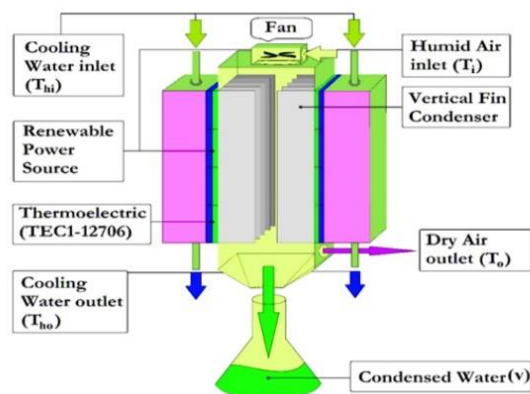

Fig.2: a schematic of experimental device

8 thermoelectric modules of TEC1-12706 have been used to cool the humid air. Thermoelectric are electrically connected in series and thermally connected in parallel.

Results and Discussion
the effect of humidity of inlet air

the number of 8 thermoelectric module were used and the electric current in thermoelectric is 5.366 A, the inlet air temperature is 35 ℃ and the inlet air velocity is 1 m/s and the inlet cooling water temperature is 5 ℃. figure 3 shows the comparison of numerical results and experimental data of the effect of inlet air humidity on the amount of obtained water, the outlet air temperature and the outlet temperature of the cooling water.
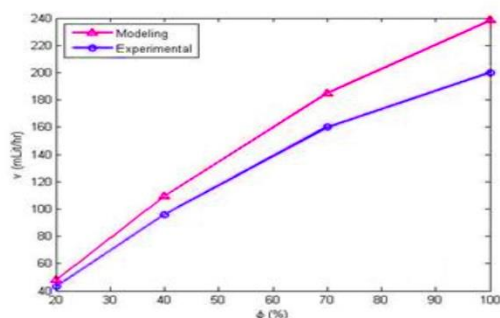
22nd Iranian Chemistry Congress (ICC22)
Iranian Research Organization for Science and
Technology (IROST)
13-15 May 2024

03231-97589

IROST

Fig.3: variation of amount of obtained with inlet air humidity.

It can be seen from figure. 3, increasing relative humidity of inlet air from 20%, to 100%, lead to increase the amount of harvested water in 1 hour from 43 ml to 200 ml.

The effect of inlet air temperature
In this case, the number of 8 thermoelectric module were used and the electric current in thermoelectric is 5.366 A, the relative humidity of the inlet air is 20 % and the inlet air velocity is 1 m/s and the inlet cooling water temperature is 5.℃ figure 4 shows the comparison of numerical results and experimental data of the effect of inlet air temperature on the abovementioned parameter. It is observed that with increasing the inlet air temperature, the obtained water increase, because enhancement of air temperature at a constant relative humidity lead to increase absolute humidity.
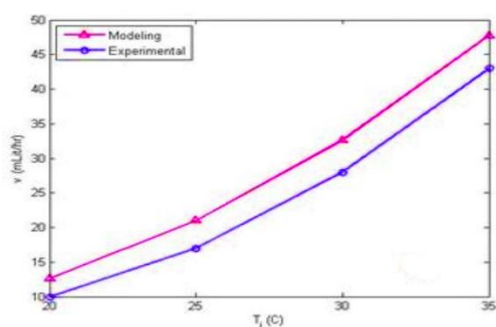

Fig.4: variation of amount of obtained water with the inlet air temperature.

The effect of inlet air velocity
figure 5 shows the comparison of numerical results and experimental data of the effect of inlet air velocity on the abovementioned parameter. It can be seen that with the increase of the incoming air speed, the obtained water increases and after reaching a maximum value, it starts to decrease. In fact, the increase in the velocity of the inlet air is accompanied by an increase in the flow rate, which brings a greater amount of moisture content into the channel, which increases the amount of water harvested.

On the other hand, increasing the velocity reduces the residence time of the air in the channel, so after reaching a velocity of 1 m/s, the effect of the residence time overcomes the input moisture content and the amount of water obtained decreases.
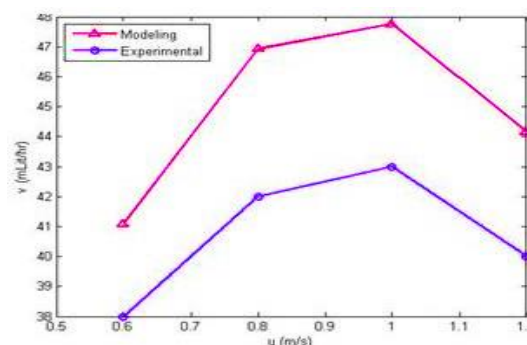

Fig.5: variation of amount of obtained water with the inlet air velocity.

Conclusions
The impact of parameters such as temperature, humidity, and velocity of incoming humid air was examined both experimentally and numerically. The model employed in this research exhibited good agreement with the experimental results. An increase in relative humidity and inlet air temperature positively influenced the quantity of collected water and the performance coefficient of the process. Conversely, raising the inlet air temperature had a detrimental effect on the process. The velocity of the incoming humid air also played a crucial role, with the maximum water collection occurring at the optimal velocity of 1 m/s; at higher velocities, the amount of collected water decreased.

References
[1] Afshari, F., Ceviz, M. A., Mandev, E., & Yıldız, F. (2022). Effect of heat exchanger base thickness and cooling fan on cooling performance of Air-To-Air thermoelectric refrigerator; experimental and numerical study. Sustainable Energy Technologies and Assessments, 52, 102178.

[2] Peeters, J. P., & Berkbigler, L. W. (1997). U.S. Patent No. 5,634,342. Washington, DC: U.S. Patent and Trademark Office.

[3] de Garayo, S. D., Martínez, A., & Astrain, D. (2022). Optimal combination of an air-to-air thermoelectric heat pump with a heat recovery system to HVAC a passive house dwelling. Applied Energy, 309, 118443.

22nd Iranian Chemistry Congress (ICC22)
Iranian Research Organization for Science and Technology (IROST)
13-15 May 2024

03231-97589

IROST

The morphological effect in power conversion efficiency of quantum dot solar cells: carbon-based materials

Tahere Kheshti, Afshan Mohajeri*

Corresponding Author E-mail: amohajeri@shirazu.ac.ir

Department of Chemistry, College of Sciences, Shiraz University, Shiraz 7194684795, Iran.

Abstract: Among the third-generation photovoltaic industry, quantum dot solar cell (QDSC) is a promising candidate because of the unique characteristics of QDs. Herein, to investigate the influence of morphological engineering of carbon-based materials on the performance of QDSCs, the electronic and optical properties, and the photovoltaic performance were calculated using theoretical approaches.

Keywords: Carbon quantum dot; Solar cell; Power conversion efficiency

Introduction

In further search for low-cost solar cells, quantum dot solar cells (QDSCs) have become one of the promising innovative solar devices, owing to their tunable bandgaps, air-stable operation, and high absorption coefficient. In QDSCs, the QD plays the foremost role in light absorption, exciton formation, and charge injection [1]. Recently, graphene quantum dots (GQDs) have gained special attention due to their great potential to improve solar cell efficiency. One of the favorable properties of GQDs is their various morphologies, highly tunable electronic structures, and reactivities [2]. The morphology is controlled by cutting graphene into small pieces resulting in quantum dots having various shapes and edges. Depending on the size, shape, and edge termination, the energy gap of the GQDs and their reactivity change [3]. Inspired by these remarkable properties of carbon-based materials, in this study, we investigated a variety of flake-like GQDs including sunflower, snow-like, elliptical, and kekulene structures to examine their performance for the QCSCs. The electronic structures, absorption properties, short-circuit current density (J_{SC}), open-circuit voltage (V_{OC}), power conversion efficiency (PCE), and voltage-current curves are systematically investigated to explore the impact of morphological engineering on solar cell efficiency. It is worth noting that, the adsorption of QD on the surface of the electron acceptor (TiO₂) is done by using an anchoring group such as COOH.

Methodological Details

Density functional theory (DFT) calculations were performed to investigate the electronic structure properties of the carbon materials. Furthermore, the computations of optical properties have been carried out in the framework of the time-dependent DFT (TDDFT). All the calculations were accomplished by using the b3lyp/6-31g(d,p) level of theory as implemented in the Gaussian 09 code [4]. The solvent effect is considered using a conductor-like polarizable continuum model (CPCM) and the toluene solvent. To estimate the photocurrent performance, J_{SC} theoretically determined by

$$J_{SC} = \int e\, LHE\, (\lambda) I_{sun}(\lambda) d\lambda \qquad (1)$$

where e is the unit charge, LHE denotes the light-harvesting efficiency and I_{sun} represents the solar-radiation intensity. V_{OC} is estimated by the following equation:

$$V_{OC} = \frac{1}{e}\left(E_{LUMO}^{Donor} - E_{CB}^{TiO_2}\right) - 0.3 \qquad (2)$$

E_{LUMO}^{Donor} and $E_{CB}^{TiO_2}$ refer to the energies of the lowest unoccupied molecular orbital (LUMO) of QD and the energy of the conduction band minimum (CBM) of the TiO₂, respectively. 0.3 is V_{OC} loss (from the experiment). The fill factor (FF) obtained as

$$FF = \frac{\upsilon_{OC} - \ln(\upsilon_{OC} + 0.72)}{\upsilon_{OC} + 1} \qquad (3)$$

where υ_{OC} is the normalized V_{OC}. Finally, the power conversion efficiency of solar cells is estimated by [5]

$$PCE = \frac{J_{SC} \cdot V_{OC} \cdot FF}{P_{inc}} \times 100 \qquad (4)$$

Results and Discussion

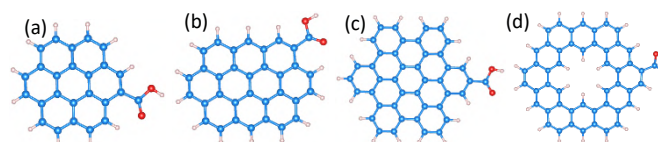Fig. 1 depicts the optimized structures of carboxyl edge-functionalized GQDs in toluene solvent.

Fig.1: Optimized geometries of COOH edge-functionalized of a) coronene, b) G-32, c) HBC, d) Kekulene in toluene solvent.

Based on the obtained dihedral angles, we found that all GQDs possess the planar and quasi-planar geometry, implying enhanced intramolecular charge transfer.

22nd Iranian Chemistry Congress (ICC22)
Iranian Research Organization for Science and
Technology (IROST)
13-15 May 2024

03231-97589

IROST

To guarantee an efficient electron injection from the excited QDs to the photoanode, the LUMO of the QD must be above the CBM edge of the TiO₂ (-4.05 eV), and to ensure efficient QDs regeneration the HOMO (highest occupied molecular orbital) should be lower than the redox energy of I⁻/I₃⁻ (-4.85 eV) [5]. Table 1 presents that the position of the HOMO and LUMO levels satisfies the condition to match the reference energies.

Table 1: the fundamental energies and chemical hardness (η)

GQD	E_{HOMO} (eV)	E_{LUMO} (eV)	E_g (eV)	η (eV)
Coronene	-5.66	-2.00	3.67	1.83
G-32	-5.14	-2.28	2.86	1.43
HBC	-5.44	-1.99	3.44	1.72
Kekulene	-5.45	-2.15	3.30	1.65

η describes the resistance of the dye toward charge transfer and is obtained by $\eta = \frac{E_{LUMO} - E_{HOMO}}{2}$ [5]. The data in Table 1 indicate that G-32 has minimum chemical hardness and can be considered a more efficient QD because a lower value of η generates higher J_{SC} and improves the PCE. The light-harvesting capability of the electron transport layer (ETL) is the key factor that determines the performance of solar cells. The light capture efficiency was plotted in Fig. 2. All considered systems show excellent LHE in the range of 0.78-0.87 values.
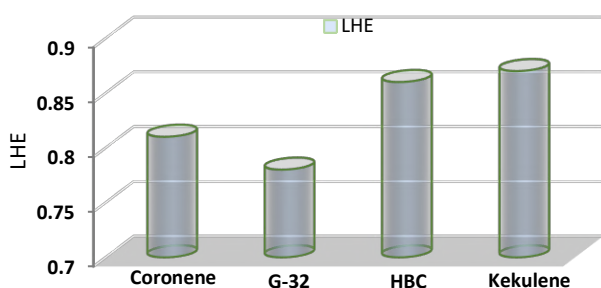

Fig.2. LHE curve of considered GQDs.

The preceding analysis reveals that the investigated GQDs meet the mandatory considerations to be used as ETL in QDSC applications. Therefore, the photovoltaic parameters of all systems were calculated by equations (1)-(4), and the results are plotted in Fig. 3.
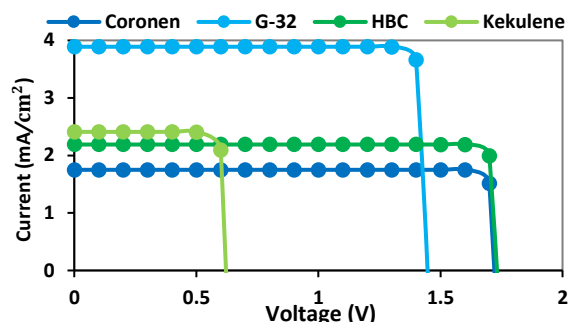

Fig.3. I-V curve of all investigated GQDs.

Based on our findings, among all studied GQDs, G-32 shows the best performance (η =5%) which can be ascribed to the larger V_{OC} and suitable J_{SC}.

Conclusions

In this study, quantum chemical computations were performed to systematically investigate the morphological effect on the power conversion energy of quantum dot solar cells. In this regard, we examined the electronic, optical, and photovoltaic properties of several flake-like carbon quantum dots with different shapes. Taking all parameters together, the G-32 GQD presents better photovoltaic performance, which might be attributed to the minimum chemical hardness.

References

[1] Sharma, V., & Jha, P. K. (2019). Enhancement in power conversion efficiency of edge-functionalized graphene quantum dot through adatoms for solar cell applications. *Solar Energy Materials and Solar Cells, 200*, 109908.

[2] Cuadra, J., Ponce. H., & Rudamas, C. (2018). Optical Properties of Graphene Carbon Quantum Dots for Solar Cells Applications. *2018 IEEE 38th Central America and Panama Convention (CONCAPAN XXXVIII)*, San Salvador, El Salvador, 1-5.

[3] Lari Dashti, N., & Mohajeri, A. (2021). Morphological engineering of carbon-based materials: in the quest of efficient catalysts for overall water splitting. *International Journal Of Hydrogen Energy. 46*, 7284e7296.

[4] Frisch, M. J., Trucks, G.W., Schlegel, H. B., Scuseria, G. E., Robb, M. A., Cheeseman, J. R., Scalmani, G., Barone, V., Mennucci, B., & Petersson, G. A. et al., Gaussian 09 Revision D.01 Program Suite, *Gaussian Inc: Wallingford, CT*, (2013).

[5] Mohajeri. A., & Kheshti, T. (2023). Improving the efficiency of dye-sensitized solar cells based on BODIPY dye and its analogous: the synergistic effect of benzo fusion and phenyl substitution. *Journal of Photochemistry and Photobiology A: Chemistry. 442*, 114781.

22nd Iranian Chemistry Congress (ICC22)
Iranian Research Organization for Science and Technology (IROST)
13-15 May 2024

03231-97589

IROST

Preparation of nanocatalyst base on Fe$_3$O$_4$ NPs modifed with ionic liquid and its applications in some of organic reactions

Zahra Attar [a], Morteza Ziyaadini [a*], Vajihe Nejadshafiee [b]

Corresponding Author E-mail: morteza_ziaadini@yahoo.com

[a] Department of Chemistry, Faculty of Science, Vali-e-Asr University, Rafsanjan, Iran.

[b] Central Lab, Vali-e-Asr University, 77176, Rafsanjan, Iran.

Abstract: A novel ionic liquid functionalized Fe$_3$O$_4$ nanoparticles (Fe$_3$O$_4$ NPs-IL) was prepared by anchoring caffeine ionic liquid on the surface of Fe$_3$O$_4$ NPs. The one-pot reaction proceeds smoothly with Fe$_3$O$_4$ NPs-IL catalyst and affords the products in high to excellent product yields, operational simplicity, environmental friendliness, wide applicability and reusability and easy recovery of the catalyst using an external magnet are the key features of this methodology.

Keywords: Fe$_3$O$_4$ NPs; Ionic liquids; catalyst.

Introduction

Ionic liquids are salts that are liquid at a temperature of one hundred degrees Celsius. Ionic liquids consist of two parts, cationic and anionic, which determine its physical and chemical properties. Among the characteristics of ionic liquids, we can mention their low viscosity, negligible vapor pressure, non-volatility, non-flammability, and high electrical conductivity, which have attracted the attention of researchers, and as a result, they are used in a wide range of organic, mineral, and polymer industries. They are used Ionic liquids are used as electrolytes in the fields of fuel cells, electricity and supercapacitors. Ionic liquids are part of the category of green solvents and replace many common solvents in the pharmaceutical and chemical industries. Among the different types of ionic liquids, we can mention room temperature ionic liquids, hydrophobic ionic liquids, chiral ionic liquids, etc [1,2]. Nanomaterials, including nanoparticles, nanoplates, and nanotubes, have different physical properties compared to their bulk state due to their high surface-to-volume ratio. Among the nanoparticles, the preparation of intermediate element oxide nanoparticles has been well developed. Magnetic iron oxide nanoparticles are an example of these materials, and various preparation methods have been reported for these compounds. The structural characteristics of magnetic iron oxide nanoparticles have made it to be used as a catalyst in chemical reactions, in addition to its use in industry [3,4]. The seven-ring compounds of the ring are widely used in organic chemistry and are used for the preparation of large molecules and the synthesis and discovery of new drugs. In this project, the ring compounds that are used in medicine will be synthesized by green chemistry method. The Fe$_3$O$_4$ NPs-IL as heterogeneous nanocatalyst that has magnetic properties will be used to prepare these compounds.

Experimental Section

FeCl$_3$.6H$_2$O (50 mL, 0.3 M) was added to HCl (0.5 mL, 0.2 M) and the reaction mixture was sonicated under 33 W at room temperature for 5 min. Then a solution of Na$_2$SO$_3$ (20 mL, 0.3 M) was added into 40 mL of the reaction mixture and the color of solution changed from yellow to red. After that, the yellow color of the solution, the suspension was poured into 400 mL of water containing 60 mL of ammonium (25%) and followed by ultrasonic waves for 30 min. After this time, the product was removed by an external magnet and was washed three times with DI water, and dried under vacuum at 60 ºC for 12 h. To prepare the ionic liquid, to a solution of caffine (3.4 g, 50 mmol) in dry toluene (50 mL), 3-chloropropyltrimethoxysilane (12.0 mL, 50 mmol) was added and the mixture was refluxed overnight to produce the zwitterionic caffine salt. The concentrated H$_2$SO$_4$ (0.54 mL, 10 mmol) was added drop wise into the solution of the above residue in ethanol (30 mL) over 30 min and the final mixture was stirred at 50 °C for another 8 h. The final mixture was evaporated under reduced pressure to give the ionic liquid as a viscous white liquid. For immobilization of IL onto Fe$_3$O$_4$ NPs-IL, the solution of IL (containing 0.3 g IL) was diluted with dry CHCl$_3$ and was then added slowly to a suspension of 1 g Fe$_3$O$_4$ NPs-IL in dry CHCl$_3$ (180 mL). The resulting mixture was refluxed for 24 h. After cooling, the solid materials were filtered off and the residue was washed with hot CHCl$_3$ and then dried in oven at 50 °C overnight to give IL matrix immobilized on Fe$_3$O$_4$ NPs.

General procedure for the synthesis of diazepines using Fe₃O₄ NPs-IL as a catalyst.

An mixture of benzaldehyde (1 mmol), ortho phenylenediamine (1mmol), malononitrile (1 mmol) and 20 mg Fe₃O₄ NPs-IL in EtOH (5 mL) was stirred at room temperature for 50 min. The progress of the reaction was monitored by TLC. After completion of reaction, the reaction mixture was filtered. Then, the product was dissolved in mixture of water/ethanol and the catalyst easily separated from the product by attaching an external magnet onto the reaction vessel, followed by decantation of the product solution. This solution was concentrated to generate the pure crude product. The solid crude product was recrystallized from hot ethanol to afford the diazepines as a pure product.

Results and Discussion

The Fe₃O₄ NPs-IL as Nano-Bio catalyst was applied for synthesis of diazepin derivatives (Scheme 1).
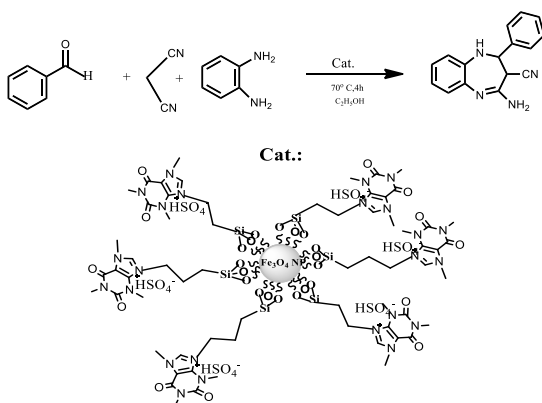
Scheme 1: Synthesis of diazepines.

Fourier transform-infrared (FT-IR) spectra of Fe₃O₄ NPs and Fe₃O₄ NPs-IL are shown in Figure 1.

The band at 567 cm^{-1} was characteristic of Fe-O-Fe in the Fe₃O₄ NPs structure (Figure 1a). The vibration bands at 2853 and 2923 cm^{-1} were assigned to the C–H stretching vibrations of propyl and methyl groups, respectively. The bonds of C=O, C=N and C=C were observed at 1651, 1467 and 1384 cm^{-1}, respectively. The band in the range 1046–1129 cm^{-1} was assigned to Si–O–Si groups and the band at 976 cm^{-1} was attributed to Si–OH groups. A broad band in the region, 3375 cm^{-1} was assigned to the O–H stretching vibrations of surface Fe₃O₄ NPs on Fe₃O₄ NPs-IL (Figure 1b).
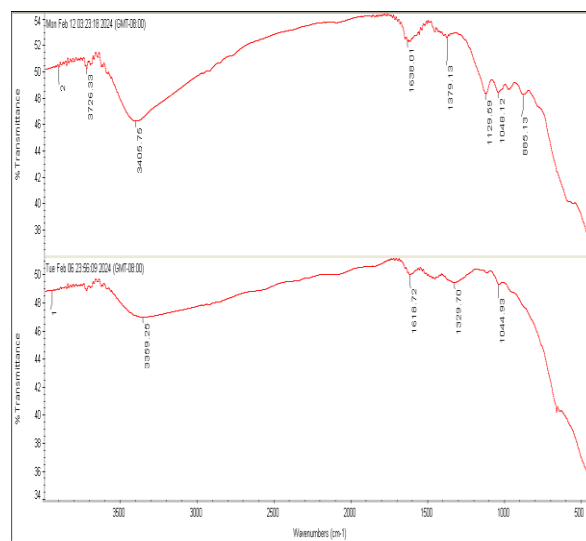

Fig 1. FT-IR spectra of a) Fe₃O₄ NPs and b) Fe₃O₄ NPs-IL.

Conclusion

We successfully developed a novel Fe₃O₄ NPs supported acidic IL and used in a facile, one-pot three-component condensation reaction of benzaldehyde, ortho phenylenediamine, malononitrile to prepare diazepin compounds in excellent yields (up to 95%). Moreover, the catalyst recovery test was performed using an external magnet device, and showed that the catalyst can be reused several times without a significant decrease in its performance and catalytic activity.

References

[1] Clark, J. H., & Tavener, S. J. (2007). Alternative solvents: shades of green. Organic process research & development, 11(1), 149-155.

[2] Plechkova, N. V., & Seddon, K. R. (2008). Applications of ionic liquids in the chemical industry. Chemical Society Reviews, 37(1), 123-150.

[3] Faraji, M., Mehrizi, E. A., Sadani, M., Karimaei, M., Ghahramani, E., Ghadiri, K., & Taghizadeh, M. S. (2012). Isotherms and kinetics of lead and cadmium uptake from the waste leachate by natural and modified clinoptilolite. International Journal of Environmental Health Engineering, 1(1), 26.

[4] Liu, G., Wang, Z., Lu, J., Xia, C., Gao, F., Gong, Q., ... & Gu, Z. (2011). Low molecular weight alkyl-polycation wrapped magnetite nanoparticle clusters as MRI probes for stem cell labeling and in vivo imaging. *Biomaterials*, *32*(2), 528-537.

Design, preparation and identification of SnCl₄ catalyst stabilized on nano-kaolin for the synthesis of spirooxindoles under different conditions

Maryam Hariri, Abdolhamid Bamoniri

Corresponding Author E-mail: bamoniri@kashanu.ac.ir

Department of Organic Chemistry, Faculty of Chemistry, University of Kashan, Kashan, Iran.

Abstract: spirooxindole is a unique compound with medicinal and biological properties that has attracted the attention of many researchers in recent years. So the current research, using SnCl₄ catalyst stabilized on kaolin nanoparticles as a compatible catalyst environmentally friendly and recyclable. It was investigated for the preparation of spirooxindole derivatives in different conditions by green synthesis method.

Keywords: Spirooxindol; SnCl₄ nano kaolin; green synthesis; isatin.

Introduction

Spirooxindole compounds have a complex and unique structure, as a result of the fusion of the spiro ring to the 3-C position of the oxindole ring, it leads to the formation of a tridimensional chiral structure with a quaternary asymmetric center [1]. Synthesis in industry and academia to develop new spirooxindole derivatives with interesting biological activities. In the past, these compounds were isolated in natural alkaloids and used as native medicine [2]. For example: Horsfiline, which is isolated from the root of the Horsfieldia superba shrub, has analgesic properties [3]. Spirooxindole compounds have a wide range of biological and medicinal properties, including: antimicrobial [4], antiviral [5], anti-inflammatory [6], anti-malarial [7], anticancer [8], anti-diabetic [9] and anti-HIV [10]. Recently, the development of the green synthesis process of the derivatives of this compound has become very important to reduce environmental pollution. The nature and role of the catalyst is of vital importance in organic syntheses and chemical industries, the SnCl4 catalyst stabilized on kaolin nanoparticles is used as a solid, heterogeneous, cheap, biodegradable and accessible catalyst for multicomponent one-pot synthesis [11]. In this research, a simple and environmentally friendly route to prepare spirooxindole derivatives using SnCl₄ catalyst stabilized on kaolin nanoparticles, which it can recyclable and compatible with environment, and it is also available from ethanol as a green solvent.

Experimental Section

Spirooxindole by one-pot multicomponent method, with (1 mmol) isatin, (1 mmol) malononitrile, (1 mmol) 1,3 dicarbonyl derivatives, along with snCl4 catalyst fixed on kaolin nanoparticles(1mg) and ethanol(5 ml) as solvent in reflux conditions were synthesized. The progress of the reaction was checked by thin layer chromatography (TLC) with ethyl acetate and normal hexane solvents with ratios (7:3). To separate the catalyst from the product, it was filtered with ethanol and the formed precipitate was purified by recrystallization in method.

Results and Discussion

In the initial study, different conditions and methods for the synthesis of spirooxindole clusters were investigated. After several initial syntheses in the presence of isatin(1) malononitrile(2) dimedone(3) using SnCl₄ stabilized on kaolin nanoparticles in ethanol at a temperature of 60-70 under reflux conditions. The product was formed (Figure 1). This method works with a wide range of reagents and 1 and 3 dicarbonyl and acetonitrile derivatives can be used for the synthesis of spirooxindole derivatives. (Table 1). The synthesized products of spirooxindole were identified by ^{1}H NMR and FT-IR spectral data.
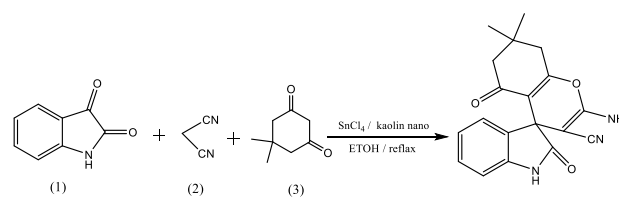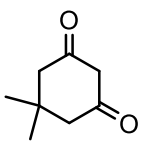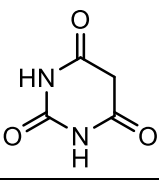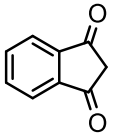

Fig.1: Synthesis of spirooxindole derivatives in the presence of supported SnCl₄ on kaolin nanoparticles .

22nd Iranian Chemistry Congress (ICC22)
Iranian Research Organization for Science and Technology (IROST)
13-15 May 2024

03231-97589

ISC

Table1: Reaction time and yield of compounds 1a-1c, Synthesis of spirooxindole derivatives by 1, 3 dicarbonyl compounds (1a: dimedone) (1b: barbituric acid) (1C: 1, 3 indanedione)

Products	Compound (3)	Time (h)	Yield (%)
1a		2	92
1b		6	89
1c		8	90

Conclusions

As a result, in this research, a practical protocol for the synthesis of spirooxindole derivatives by $SnCl_4$ stabilized on kaolin nanoparticles in different conditions, with commercially available raw materials, was presented. The great importance of these compounds can be seen as a result of their biological characteristics and therapeutic effects, which have become one of the most important intermediates in the pharmaceutical and biological industries and have attracted the attention of chemical researchers. It also has advantages such as: high reaction yield, short reaction time, simple work method, ease of purification, compatibility with the environment due to following the green synthesis method and the use of recyclable catalyst.

References

[1] Sansinenea, E., Martínez, E. F., & Ortiz, A. (**2020**). Organocatalytic synthesis of chiral spirooxindoles with quaternary stereogenic centers. European Journal of Organic Chemistry, 2020(32), 51015118. https://doi.org/10.1002/ejoc.202000470.

[2] Zhang, M., Yang, W., Qian, M., Zhao, T., Yang, L., & Zhu, C. (**2018**). Iodine-promoted three-component reaction for the synthesis of spirooxindoles. Tetrahedron, 74(9), 955-961. https://doi.org/10.1016/j.tet.2018.01.001.

[3] Kulkarni, M. G., Dhondge, A. P., Chavhan, S. W., Borhade, A. S., Shaikh, Y. B., Birhade, D. R., ... and Dhatrak, N. R. (**2010**). Total synthesis of (±)-coerulescine and (±)-horsfiline. Beilstein Journal of Organic Chemistry, 6(1), 876-879. https://doi.org/10.3762/bjoc.6.103

[4] Oktavia, S. H., Cahyana, A. H., Hapsari, M., Yunarti, R. T., & Liandi, A. R. (**2021**). Synthesis and antimicrobial activity of spiro-oxindole-chromene derivative compounds based curcuminoid and chalcone. *Rasayan J. Chem*, *14*, 1990-1997. http://doi.org/10.31788/RJC.2021.1435546.

[5] Xu, J., Xie, X., Ye, N., Zou, J., Chen, H., White, M. A., ... & Zhou, J. (**2019**). Design, synthesis, and biological evaluation of substituted 4, 6-dihydrospiro [[1, 2, 3] triazolo [4, 5-b] pyridine-7, 3'-indoline]-2', 5 (3 H)-dione analogues as potent NS4B inhibitors for the treatment of dengue virus infection. *Journal of medicinal chemistry*, *62*(17), 7941-7960. https://doi.org/10.1021/acs.jmedchem.9b00698

[6] Kumar, R. S., Antonisamy, P., Almansour, A. I., Arumugam, N., Periyasami, G., Altaf, M & Kwon, K. B. (**2018**). Functionalized spirooxindole-indolizine hybrids: Stereoselective green synthesis and evaluation of anti-inflammatory effect involving TNF-α and nitrite inhibition. *European Journal of Medicinal Chemistry*, *152*, 417-423. https://doi.org/10.1016/j.ejmech.2018.04.060.

[7] Lopes, E. A., Mestre, R., Fontinha, D., Legac, J., Pei, J. V., Sanches-Vaz, M., ... & Santos, M. M. (**2022)**. Discovery of spirooxadiazoline oxindoles with dual-stage antimalarial activity. *European Journal of Medicinal Chemistry*, *236*, 114324. https://doi.org/10.1016/j.ejmech.2022.114324.

[8] Arumugam, N., Almansour, A. I., Kumar, R. S., Periasamy, V. S., Athinarayanan, J., Alshatwi, A. A., ... & Menéndez, J. C. (**2018**). Regio-and diastereoselective synthesis of anticancer spirooxindoles derived from tryptophan and histidine via three-component 1, 3-dipolar cycloadditions in an ionic liquid. *Tetrahedron*, *74*(38), 5358-5366. https://doi.org/10.1016/j.tet.2018.04.032.

[9] Murugan, R., Anbazhagan, S., & Narayanan, S. S. (**2009**). Synthesis and in vivo antidiabetic activity of novel dispiropyrrolidines through [3+ 2] cycloaddition reactions with thiazolidinedione and rhodanine derivatives. *European journal of medicinal chemistry*, *44*(8), 3272-3279. https://doi.org/10.1016/j.ejmech.2009.03.035.

[10] Kumari, G., Modi, M., Gupta, S. K., & Singh, R. K. (**2011**). Rhodium (II) acetate-catalyzed stereoselective synthesis, SAR and anti-HIV activity of novel oxindoles bearing cyclopropane ring. *European journal of medicinal chemistry*, *46*(4), 1181-1188. http://dio.org/ 10.1016/j.ejmech.2011.01.037.

[11] Mirjalili, B. B. F., Bamoniri, A., Nazemian, S., & Zare Reshquiyea, R. (**2019**). SnCl$_4$/nano-sawdust as an Efficient Bio-based Catalyst for the Synthesis of 2-Substituted Benzothiazoles and Benzimidazoles. *Journal of Nanostructures*, *9*(1), 183-189. https://dio.org/10.22052/JNS.2019.01.020.

22nd Iranian Chemistry Congress (ICC22)
Iranian Research Organization for Science and Technology (IROST)
13-15 May 2024

03231-97589

IROST

Synergistic Action of Hierarchical Porosity and Multifunctionality for Efficient Catalysis of Asymmetric Reactions

Zahra Sharifzadeh, Ali Morsali*

Corresponding Author E-mail: morsali_a@modares.ac.ir

Department of Chemistry, Faculty of Sciences, Tarbiat Modares University, P.O. Box 14115-175, Tehran, Iran.

Abstract: Here, Q-HKUST-1 possessing a Lewis acid site transformed into an excellent multifunctional chiral MOF (Q-HKUST-Cys), via post-synthetic modification by L-Cysteine. The Q-HKUST-Cys is an efficient catalyst for promoting asymmetric ring-opening of epoxide, nitroaldol, and cycloaddition of CO_2 reactions under mild conditions.

Keywords: Defective-MOFs; heterogeneous catalysis; Pore functionalization.

Introduction

Quasi-MOFs (Q-MOFs) as a subcategory of defective MOFs prepared by limited deligandation in diverse atmospheres under controlled thermal treatment [1]. In Q-MOFs that are intermediate between the primary crystalline MOF and the corresponding final metal compounds, a high concentration of unsaturated metal centers as well as hierarchical pores, provided the suitable platform for the anchoring functional monocarboxylic acid molecules [2]. Herein, the low cost and affinity to copper of L-Cystein was used for fast, one-pot functionalization of Q-HKUST through establishing the Cu-S bond (Figure 1). The Q-HKUST-Cys set up an example for the induction of chirality on other defective MOFs through post-synthesis functionalization. Therefore, we expect it to open a new perspective in the design of functionalized MOF with multi-residual functional groups with different natures for promoting various catalysis reactions requiring Lewis acid and base as well as Bronsted acid.

Experimental Section

Synthesis of Q-HKUST: For the preparation of Q-HKUST, we followed the same procedure as previously reported [3]. For the calcination test, after placing the as-obtained HKUST-1 MOF powder in a glass container, it was heated with a heating rate of 5 °C/min and maintained at 240°C for 30 min. For post-synthesis modification of Q-HKUST-1, 84 mg of the as-prepared Q-HKUST-1 was placed in a 15 mL polypropylene centrifuge tube. Synthesis of Q-HKUST-Cys: A 1 mL portion of the relevant L-Cysteine solution dissolved in Dimethyl sulfoxide (DMSO) (1.5 M) was then added to the tube. The tubes were then covered and their fillings were carefully mixed by shaking and ultrasonication. Lastly, the reaction mixtures were heated at 80ºC for 12 hours.
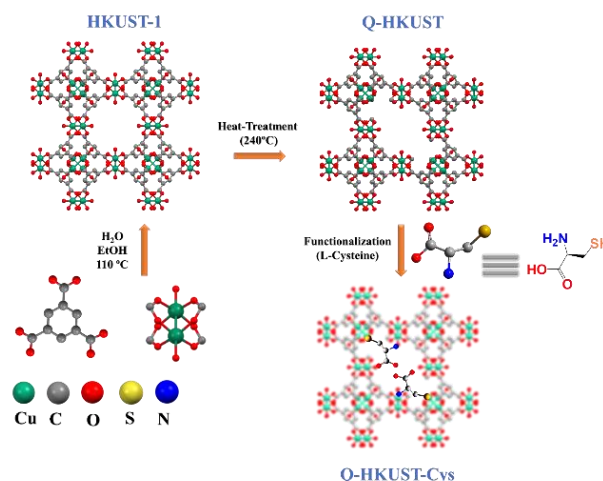

Fig.1: Hypothetical structural model in which L-Cysteine ligands coordinated to the defect sites in Q-HKUST.

Results and Discussion

The chemical stability of the framework after its L-Cysteine decoration was confirmed by comparison of the PXRD pattern of HKUST-1, Q-HKUST, and functional Q-HKUST (Q-HKUST-Cys). Comparing the FT-IR spectra obtained on the samples before and after functionalization, evidently confirmed the successful grafting of the L-cysteine from its thiol groups (Figure 2). By taking into account the FTIR, EDS, NMR, and XRD results, we suggested that the Q-HKUST-Cys can be classified as defective MOFs containing Lewis-Brønsted acid sites as well as Lewis-basic sites. Also, in contrast to pristine HKUST-1 with a narrow pore size that limited the diffusion of the substrate, Q-HKUST and Q-HKUST-Cys benefit from large mesopores, facilitating the entrance and egression of the reactants.
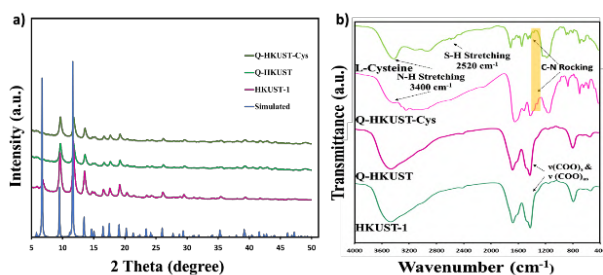
22nd Iranian Chemistry Congress (ICC22)
Iranian Research Organization for Science and Technology (IROST)
13-15 May 2024

03231-97589

Fig.2: (a) PXRD patterns, (b) FT-IR spectra of HKUST-1, Q-HKUST, and Q-HKUST-Cys.

For the ring-opening reaction, under the mild reaction conditions (25mg of catalyst, 12h, 55ºC), Q-HKUST-Cys showed complete conversion.

Under the optimum reaction situations, utilizing Q-HKUST-Cys in the Henry reaction of benzaldehyde demonstrated 99% ee and 90% conversion in 15 h, unveiling the capability of the chiral site as well as the Bronsted acidity of functional groups.

Also, characteristic features of Q-HKUST-Cys along with its optical activity led to achieving high conversion (90%) and enantioselectivity (89%) in the formation of chiral carbonate from epoxy-styrene and CO_2.

Table1: Catalytic performance of Q-HKUST-Cys in three reactions

Reaction	Conversion(%)	Ee(%)
Ring opening	100	99
Nitroaldol	90	99
CO_2-Fixation	90	89

Conclusions

Through precise and controllable thermal treatment, it has been possible to construct a sub-category of defective-MOFs known as quasi-MOF superstructures. Here, we introduce the first attempt at the functionalization of Quasi-MOFs through one-pot implantation of monocarboxylic acid molecules to the unsaturated metal sites. Taking into account the generation of new characteristic features, and especially the simultaneous presence of Bronsted acid and Lewis pair, the as-obtained Q-HKUST-Cys exhibited excellent catalytic performance in various asymmetric reactions under mild conditions. This is due to the Lewis acid sites (Cu^{2+}), Lewis base sites (NH_2 group), and Bronsted acid sites (COOH group) present in the catalyst, which contribute to its high conversion rate. This approach proposes a hopeful playground for fabricating chemically complex environments by the implantation of multiple components for extraordinary opportunities in synergistic phenomena. Investigations are currently proceeding in our lab.

References

[1] B. Liu, W. Han, X. Li, L. Li, H. Tang, C. Lu, Y. Li, X. Li. (2019). Quasi metal organic framework with highly concentrated Cr2O3 molecular clusters as the efficient catalyst for dehydrofluorination of 1, 1, 1, 3, 3-pentafluoropropane, Appl. Catal. B Environ. 257, 117939.

[2] M. Bagheri, M.Y. Masoomi. (2022). Quasi-metal organic frameworks: Preparation, applications and future perspectives, Coord. Chem. Rev. 468, 214643.

[3] M. Bagheri, A. Melillo, B. Ferrer, M.Y. Masoomi, H. Garcia. (2021). Improved catalytic hydrogen release of quasi HKUST-1 compared to HKUST-1, Chem. Commun. 57, 11964–11967.

Water Decontamination over Functionalized Defective Zr-MOFs: Investigation the Competitive Roles of -NH₂ and -SH Sites in Removal of As(III) Species

Sayed Ali Akbar Razavi ‡, Zahra Sharifzadeh ‡, Ali Morsali *

Corresponding Author E-mail: morsali_a@modares.ac.ir

Department of Chemistry, Faculty of Sciences, Tarbiat Modares University, P.O. Box 14117-13116, Tehran, Islamic Republic of Iran.

‡ These two authors contributed equally in this work.

Abstract: Three novel functional Zr-MOFs, were fabricated to investigate the competitive or cooperative roles of free amine/thiol site in the removal of As(III). XPS and ATR revealed that amine sites in Gly@UiO-66 have higher affinity to As(III) (301.4 mg.g^{-1}) than thiol sites in Mer@UiO-66 (239.8 mg.g^{-1}) and Cys@UiO-66.

Keywords Metal-organic frameworks (MOFs) ; Arsenic (III) Removal; Cysteine

Introduction

Arsenic (As) is an abundant carcinogen and toxic chemical element in nature.[1] MOF-based adsorbents based on the chemical properties can be applied as efficient materials for the removal of arsenic contaminants. In this work, the UiO-66 framework was selected as platform to develop amine and/or thiol functionalized defective Zr-MOFs. The functionalized frameworks were developed based on synthesis of defective structure of the UiO-66 material and then installation of functional monocarboxylate linkers including cysteine (–NH₂, –SH), mercaptopropionic acid (–SH) and glycine (-NH₂) on the defective Zr-sites by post-synthesis linker incorporation (PSLI) method[2,3] (Figure 1). The results show that both thiol and especially amine functions can be considered as effective guest-interactive sites with high cooperativity in the removal of As(III) species.

Experimental Section

Synthesis of "Form-UiO-66".

A recent procedure was applied for the synthesis of Form-UiO-66 material.[14,15] 1.2 g of as-synthesized 50Benz-UiO-66, 370 mL DMF, and 15.3 mL 8M HCl were successively added to a 500L Erlenmeyer flask during vigorous stirring. Then, the flask was put in a preheated oven at 100 °C for 24 hours and the top of the flask was loosely covered with a watch glass.

Post Synthetic Functionalization of Form-UiO-66

1 mL portion of the aqueous solution of monocarboxylic acids linkers (0.5M) was added to a tube containing as-synthesized 84 mg of Form-UiO-66 so that the tubes were covered thoroughly with the linker's mixture. Lastly, the reaction mixtures were heated at 85 °C for 16 hours in a preheated oven.
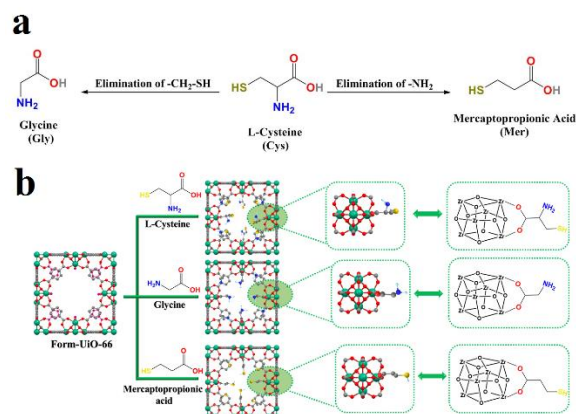

Fig.1: Structural representation of functional Gly@UiO-66, Mer@UiO-66, and Cys@UiO-66 frameworks. **(a)** Functional linkers. **(b)** Functional frameworks and nodes

Results and Discussion

The PXRD patterns of functional frameworks are completely consistent with the simulated and as-synthesized patterns of UiO-66-Ideal. The ¹H-NMR results clearly show that the functional linkers are inserted inside the structure, and the majority parts of the benzoate and formate species were removed (**Figure 2**).

The results of removal of As(III) in different pHs, reveal that the adsorption capacities of all frameworks were increased upon increasing the pH of the solution from 2 to 8. All frameworks show the highest adsorption capacities at pH = 8.

Among functionalized frameworks with one function, Gly@UiO-66 has higher gravimetric and volumetric adsorption capacities than Mer@UiO-66 which shows that there is a higher affinity between –NH₂ sites of Gly@UiO-66 than –SH sites of Mer@UiO-66. Cys@UiO-66 framework which is functionalized with both amine and thiol groups shows the lowest gravimetric adsorption capacity in mg.g^{-1} unit among functional Zr-MOFs. The results display that Cys@UiO-66 has the highest

22nd Iranian Chemistry Congress (ICC22)
Iranian Research Organization for Science and Technology (IROST)
13-15 May 2024

03231-97589

IROST

volumetric adsorption capacity. The simultaneous presence of free –NH$_2$ and –SH functional groups in Cys@UiO-66 leads to the higher density of adsorbed As(III) leading to higher volumetric capacity. This fact shows that amine and thiol sites in Cys@UiO-66 cooperate together in the removal of As(III) species but the low surface area of the adsorbent is adsorption capacity limiting factor (**Figure 3**).

Combination of full-range XPS spectrums of Gly@UiO-66, Mer@UiO-66 and Cys@UiO-66 before and after As(III) removal show that the characteristic of As(III) in binding energies above 46.0 eV has appeared which is indicative of successful elimination of As(III) species in the presence of amine and thiol functional groups. The ATR spectrum of as-synthesized Gly@UiO-66 presents characteristic peaks of amines functions, which are 3230 cm^{-1} for v_{str}(–NH$_2$), 2104 cm^{-1} for v(–NH$_3^+$), and 1261 cm^{-1} for v_{bend}(C–N). These peaks are disappeared after As(III) removal. These changes in the ATR spectrum may relate to –NH$_2$···As(III) coordination interactions. So, The results of XPS and ATR analyses prove the high affinity and possible coordination interaction between As(III) species and amine functions.

Due to the higher capacity of Gly@UiO-66 framework to As(III) species, the selectivity and reusability of this framework were investigated. The selectivity tests in the presence of other ions (K(I), Cu(II), Fe(III), NO$_3^-$, SO$_4^{2-}$, and Cl$^-$) show that no one of these ions has significant effects on the removal capacity of Gly@UiO-66. This implies on the high affinity between As(III) species and free –NH$_2$ sites of the Gly@UiO-66 framework. Also, reusability tests were conducted and the results show that Gly@UiO-66 can be applied for removal of As(III) species at least up to five successful cycles without any significant decrease in the removal process.

Conclusions

In this work, three amine and/or thiol functionalized frameworks were synthesized and applied for direct adsorptive removal of As(III) species from aquatic media. In the comparison of functional frameworks with one functional group, amine decorated Gly@UiO-66 and thiol decorated Mer@UiO-66, Gly@UiO-66 has higher adsorption capacity in both mg.g^{-1} and m^2.g^{-1} which is indicative of higher affinity of Gly@UiO-66 frameworks to As(III) species. In the comparison of Gly@UiO-66 and dual amine/thiol functionalized Cys@UiO-66, the former has higher gravimetric adsorption capacity while the latter has higher volumetric adsorption capacity. The lower gravimetric capacity of Cys@UiO-66 than Gly@UiO-66 is the reason for its significantly lower surface area and pore volume, while its higher volumetric capacity is due to the cooperative roles of –NH$_2$ and –SH sites. In the case of amine and thiol sites, both coordination or deprotonation

(–NH$_3^+$ → –NH$_2$, and –SH → –S$^-$)/coordination mechanisms can be engaged in the removal process. Deprotonation increases the affinity between functional groups and target analytes.
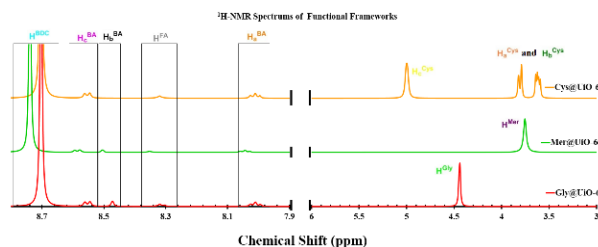

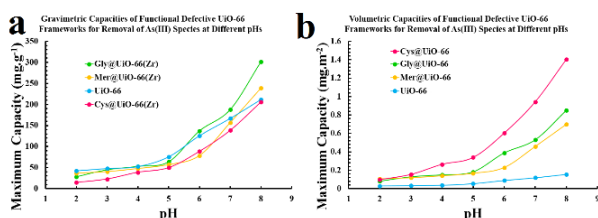**Fig.2:** Comparison of ^{1}H-NMR spectrums of the digested functional frameworks

Fig.3: Adsorption capacity of parent UiO-66-Ideal and using three Gly@UiO-66, Mer@UiO-66, and Cys@UiO-66 functionalized frameworks. **(a)** Gravimetric adsorption capacity. **(b)** Volumetric adsorption capacity.

References

[1] C. Wang, J. Luan, C. Wu, Metal-organic frameworks for aquatic arsenic removal, Water Res. 158 (2019) 370–382.

[2] G.C. Shearer, S. Chavan, S. Bordiga, S. Svelle, U. Olsbye, K.P. Lillerud, Defect Engineering: Tuning the Porosity and Composition of the Metal–Organic Framework UiO-66 via Modulated Synthesis, Chem. Mater. 28 (2016) 3749–3761. https://doi.org/10.1021/acs.chemmater.6b00602.

[3] G.C. Shearer, J.G. Vitillo, S. Bordiga, S. Svelle, U. Olsbye, K.P. Lillerud, Functionalizing the Defects: Postsynthetic Ligand Exchange in the Metal Organic Framework UiO-66, Chem. Mater. 28 (2016) 7190–7193. https://doi.org/10.1021/acs.chemmater.6b02749.

Water Decontamination over Functionalized Defective Zr-MOFs: Investigation the Competitive Roles of -NH₂ and -SH Sites in Removal of of Hg(II) Ions

Zahra Sharifzadeh ‡, Sayed Ali Akbar Razavi ‡, Ali Morsali *

Corresponding Author E-mail: morsali_a@modares.ac.ir

Department of Chemistry, Faculty of Sciences, Tarbiat Modares University, P.O. Box 14117-13116, Tehran, Islamic Republic of Iran.

‡ These two authors contributed equally in this work.

Abstract: Three novel functional Zr-MOFs, were fabricated to investigate the competitive or cooperative roles of free amine/thiol site in the removal of Hg(II). The effect of proton transfer and redox mechanisms on the possible interactions was investigated. Cys@UiO-66, Mer@UiO-66 and Gly@UiO-66 frameworks can adsorb 1288, 593, and 313 mg.g^{-1} Hg(II) respectively.

Keywords: Metal-organic frameworks (MOFs) ; Hg(II) Ions Removal; Cysteine

Introduction

MOFs are applied for the removal of poisonous and harmful species from water or air, particularly heavy Hg(II) ions from wastewater [1–3]. The base of our strategy in this work is founded on the creation of cluster defects in the structure of UiO-66, and then the installation of functional monocarboxylate linkers including cysteine mercaptopropionic acid, and glycine on the defective Zr-sites[4]. The results of this work show how affinity between –NH₂ and –SH functional groups and metal ions, their synergic cooperation, and secondary oxidation/reduction and protonation/deprotonation mechanisms can affect the efficiency of MOF-based adsorbent in the Hg(II) removal process.

Experimental Section

Synthesis of "Form-UiO-66".

A recent procedure was applied for the synthesis of Form-UiO-66 material.[4] 1.2 g of as-synthesized 50Benz-UiO-66, 370 mL DMF, and 15.3 mL 8M HCl were successively added to a 500L Erlenmeyer flask during vigorous stirring. Then, the flask was put in a preheated oven at 100 °C for 24 hours and the top of the flask was loosely covered with a watch glass.

Post Synthetic Functionalization of Form-UiO-66, 1 mL portion of the aqueous solution of monocarboxylic acids linkers (0.5M) was added to a tube containing as-synthesized 84 mg of Form-UiO-66 so that the tubes were covered thoroughly with the linker's mixture. Lastly, the reaction mixtures were heated at 85 °C for 16 hours in a preheated oven.
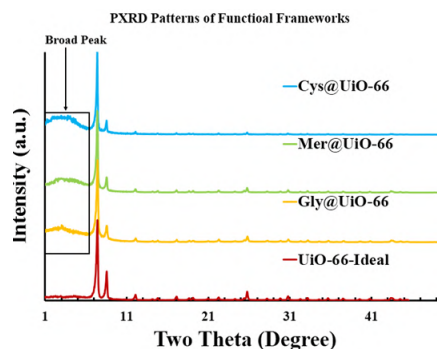

Fig.1: PXRD patterns of as-synthesized functional Zr-MOFs and comparison with an experimental sample of UiO-66-Idael.

Results and Discussion

The PXRD patterns of functional frameworks are completely consistent with the simulated and as-synthesized patterns of UiO-66-Ideal (Figure 1). The ^{1}H-NMR results clearly show that the functional linkers are inserted inside the structure, and the majority parts of the benzoate and formate species were removed. Full-range XPS survey of functional frameworks showed the characteristic peaks of nitrogen and sulfur atoms indicating the fact that the functional linkers are installed on the Zr-sites. For the adsorption studies at pH = 5, the aqueous solution of Hg(II) ions at different concentrations (100 ppm-500 ppm) were prepared with 5 mg of the adsorbent to examine the adsorption behavior of Gly@UiO-66, Mer@UiO-66 and Cys@UiO-66 frameworks. The results show that the upon increasing the initial concertation of Hg(II) ions, the adsorption capacities of the functional MOFs are increased (Figures 2a-2e). Maximum adsorption capacity of functional MOFs at pH = 5 reaches 224 mg.g^{-1} for Gly@UiO-55, 503 mg.g^{-1} for Mer@UiO-66 and 977 mg.g^{-1} for Cys@UiO-66. An ideal

Hg(II) adsorbent must show high selectivity in the presence of interferer
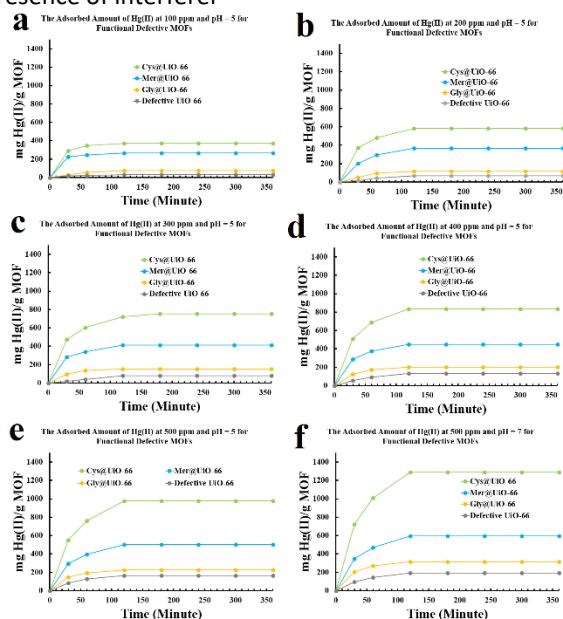

Fig.2: The adsorption capacity of functional MOFs during the adsorption process at specific time intervals. **(a)** 100 ppm Hg(II), pH =5. **(b)** 200 ppm Hg(II), pH =5. **(c)** 300 ppm Hg(II), pH =5. **(d)** 400 ppm Hg(II), pH =5. **(e)** 500 ppm Hg(II), pH =5. **(f)** 500 ppm Hg(II), pH =7.

metal ions.Selectivity tests were conducted in the presence of other ions such as Pb(II), Cd(II), Zn(II), Cu(II), Ni(II), Fe(III), Ca(II) and Na(I) ions at concentration of 500 ppm and the results show that all three functional MOFs, especially Cys@UiO-66, can save their high adsorption capacities in the presence of other ions. It was observed that the adsorption capacities for functional MOFs at pH = 7 is higher than pH = 5 due to the more negative surface charge of the adsorbent and consequent electrostatic attraction between MOF surface and metal ions, lower degree of protonation of functional groups, and diminished competitive adsorption of Hg(II)/H$^+$ ions. The Zeta potential of frameworks were measured at pH = 7 and it was realized that the Gly@UiO-66 (-63.1 mV) and Mer@UiO-66 (-46.0 mV) have more negative surface charge than Cys@UiO-66 (-0.7 mV). If the adsorbent surface charge plays the most important role in the removal process of Hg(II) ions, two Gly@UiO-66 and Mer@UiO-66 frameworks must show higher adsorption capacity than Cys@UiO-66. However, it was observed that the removal capacity of Cys@UiO-66 is much higher. This is due to the fact that the free –NH$_2$ and –SH sites inside the framework of this MOF are more efficient in Hg(II) removal.

Conclusions

In this work, the defective UiO-66 framework was synthesized in the first step, then, it was functionalized with three different monocarboxylate functional linkers, including cysteine (Cys), glycine (Gly), and mercaptopropionic acid (Mer). These amine and thiol functionalized frameworks were applied for the removal of Hg(II) ion to identify the competitive or cooperative roles of free –SH and –NH$_2$ sites and realize how secondary mechanisms can affect the adsorption capacity of functional MOFs through altering the chemical form of the functions and their affinity with Hg(II) ions. After Hg(II) removal, all protonated amine sites of Cys@UiO-66 were deprotonated while a portion remained protonated in the case of Gly@UiO-66 which to a consequent reduction in Hg(II) removal capacity of amine sites. So, in the case of free-SH sites, deprotonation can increase the affinity and capacity of the adsorbent while the redox mechanism can decrease them. In the case of free –NH$_2$ sites, protonation is a serious challenge to reach the maximum capacity of amine sites.

References

[1] M. Gao, G. Liu, Y. Gao, G. Chen, X. Huang, X. Xu, J. Wang, X. Yang, D. Xu. (2021). Recent advances in metal-organic frameworks/membranes for adsorption and removal of metal ions, TrAC Trends Anal. Chem. 137, 116226.

[2] J. Wen, Y. Fang, G. Zeng. (2018). Progress and prospect of adsorptive removal of heavy metal ions from aqueous solution using metal–organic frameworks: a review of studies from the last decade, Chemosphere. 201, 627–643.

[3] P.A. Kobielska, A.J. Howarth, O.K. Farha, S. Nayak. (2018). Metal–organic frameworks for heavy metal removal from water, Coord. Chem. Rev. 358, 92–107.

[4] G.C. Shearer, J.G. Vitillo, S. Bordiga, S. Svelle, U. Olsbye, K.P. Lillerud. (2016). Functionalizing the Defects: Postsynthetic Ligand Exchange in the Metal Organic Framework UiO-66, Chem. Mater. 28, 7190–7193.

Experimental investigation of different concentrations influences of Polyuronate on the reaction rate between carbonate rock and hydrochloric acid in matrix acidizing

Ehsan Kouchaki, Rohallah Hashemi[*]

Corresponding Author E-mail: rhashemi@iut.ac.ir

Department of Chemical Engineering, Isfahan University of Technology, Isfahan, 84156-83111, Iran.

Abstract: Controlling the acid-rock reaction rate is key to effective acidizing that adding a gelling agent can retard the reaction by reducing the diffusion rate. This study investigates Sodium Alginate (SA) efficacy to control acid-rock reaction rate. Increasing SA concentrations retard reaction rates significantly. This eco-friendly approach offers promising prospects for improved oil and gas recovery.

Keywords: Acidizing; Reaction Rate; Gelled Acid

Introduction

A significant portion of the world's oil and gas reserves reside in carbonate reservoirs. Matrix acidizing involves injecting acidic solutions, typically hydrochloric acid (HCl), into oil and gas wells, which leads to permeability alteration via chemical reactions. Matrix acidizing is a crucial process to enhance well productivity by removing formation damage , decreaseing skin factor, increasing near-wellbore permeability and productivity index.[1]

Controlling the acid-rock reaction rate is key to effective acidizing. Rapid acid-rock reaction rate shortens the effective acid penetration distance, hindering production increase. The three main processes involved in acid-rock interaction are H^+ transfer to the rock surface, the reaction between adsorbed H^+ and the rock surface, and mass transfer of reaction products from the rock surface. Diffusion of active acid is the rate-determining step in the acid-rock reaction. Adding a gelling agent can retard the reaction by reducing the diffusion rate. Gelled acid is a critical component in acidizing, including xanthan polymers (XP), guar gum (GG), hydroxyethyl cellulose (HEC), carboxymethyl hydroxyethyl cellulose (CMHEC), polyacrylamide (PAM), polyvinyl alcohol (PVA), and polyvinylpyrrolidone (PVP), among others.[2-3]

Polyuronates or polyuronides are a group of natural polysaccharide biopolymers containing one or more uronic acid moieties in their molecular structure. Alginates are the most widely used polyuronates due to their favorable thickening properties, ease of production, low cost, etc. Alginates have been extensively developed for various applications. They are widely used in different industries as thickeners and gelling agents, viscosifiers, stabilizers, and so on. Sodium alginate (SA) is the most famous polyuronates, which is a polysaccharide obtained from brown seaweed and some bacteria. Polymer chains of SA consist of β-D-mannuronic acid (ManA) and α-L-guluronic acid (GulA) linked by (1→4) glycosidic bonds (**Fig.1**). These G and M units are arranged in polyguluronate (GG), polymannuronate (MM), and mixed GM domains distributed along the polyuronate chains. [4]
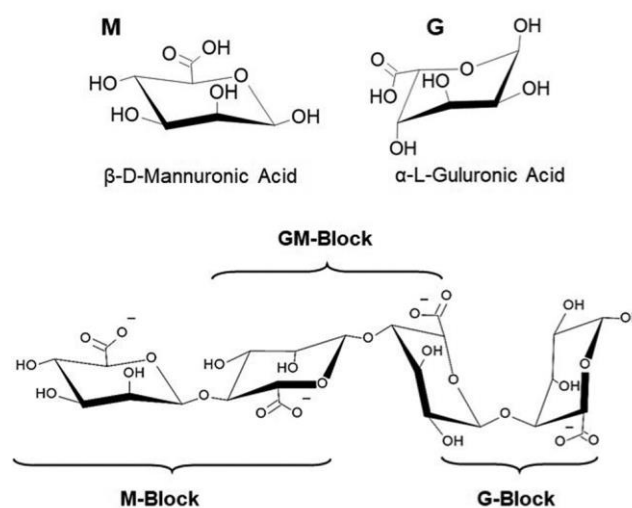

Fig.1 Chemical structures of G and M polyuronides subunits and their arrangement in the biopolymer chain of SA [4]

This paper investigates the application of SA as a gelling agent for producing gelled acid. The gelled acid can be utilized as a natural, economical, accessible, and environmentally friendly additive in oil and gas well acidizing.

Experimental Section

Materials:

- Core sample: The rock used was obtained from the carbonate rock mine in Fars province of Iran and according to XRD and XRF tests, it has 99.4% calcium carbonate. The porosity and permeability of the rock are 9.28% and 1.11 millidarcy, respectively. The diameter of the core used is 3.677 cm, and samples with a height of 1.5 cm were prepared.

- Acid and additive: The acid used is hydrochloric acid 37% w/w from Dr Mojallali company, which is diluted with deionized water to a concentration of 15%. In order to increase the viscosity of the acid and prepare the gelled acid, sodium alginate from Merk company was used.

22nd Iranian Chemistry Congress (ICC22)
Iranian Research Organization for Science and
Technology (IROST)
13-15 May 2024

03231-97589

IROST

Acidizing technique system:

The carbonate rocks are composed mostly of limestone ($CaCO_3$), and when they react with hydrochloric acid (HCl), form carbon dioxide, water and calcium chlorides, according to the **Eq.1** . [2]

$$CaCO_3 + 2HCl \rightarrow CaCl_2 + H_2O + CO_2 \qquad (1)$$
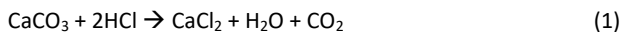
In this experiment, which was conducted as a bottle test at atmospheric pressure and at a temperature of 50 °C, the effect of different concentrations of SA as additives including 0, 2500, 5000, 7500, 10000 and 15000 ppm on the reaction between sample rock and gelled acid was investigated. The volume of acid used is stoichiometric and proportional to the weight of the rock and the reaction time for all samples is 45 minutes. The difference in the weight of dry the rock sample before and after the test was used to investigate the amount acid-rock reaction.

Results and Discussion

Acid and additive compatibility:

Observations reveal that SA powder thoroughly blends with the acid, forming a hydrogel. The viscosity of the resultant gelled acid increases in proportion to the concentration of the additive. **Fig.2** illustrates that even after the rock samples undergo a 45-minute reaction with the acid at 50 °C, there is no evidence of sediment particles or deposits, indicating continued compatibility between the acid and additive. Additionally, the presence of carbon dioxide gas bubbles, a byproduct of the reaction, at concentrations of 10000 and 15000 ppm signifies a high concentration of the additive, further highlighting the strong compatibility between the acid and additive.
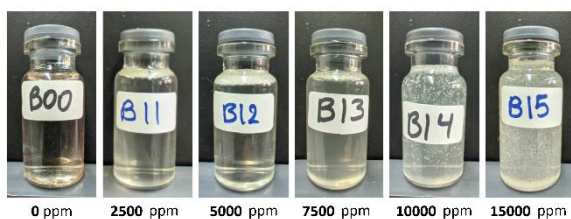

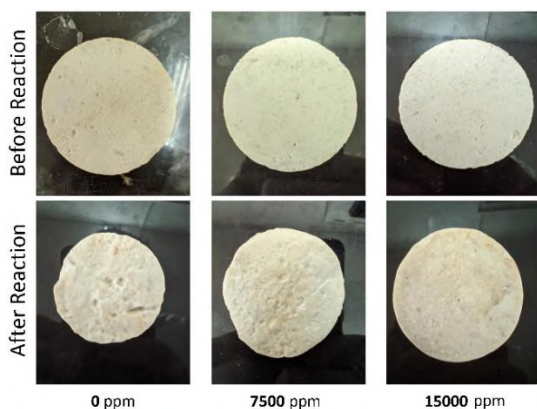**Fig.2** Photographs of samples of spent acid after reaction

Fig.3 Photographs of core surfaces before and after experiments and investigation of the effects of 0, 7500, and 15000 ppm of gelling agent

Effect of increasing concentration on the reaction:

Increasing the concentration affects the reaction rate. For heterogeneous chemical reactions like acid-rock interaction, control can occur through surface reaction or mass transfer rate. When mass transfer rate controls the reaction, the transfer of reactants to the rock surface and product exit slows. As acid viscosity rises, reducing H^+ ion penetration to the rock surface, overall reaction rate decreases [2,3]. **Fig.3** illustrates reduced rock reactivity with gelled acid compared to conventional acid (without additive). **Fig.4** depicts numerical values on a graph, which is indicating significantly decreased reaction completion with increased concentration.
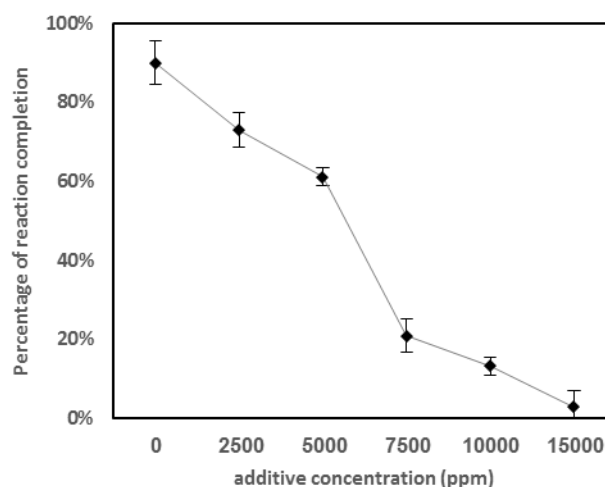

Fig.4 Effect of gelling agent concentration on the acid-rock reaction.

Conclusions

Sodium alginate, which is a polyuronates family, was used to produce gelled acid with different concentrations, and the following results were obtained.

1- The acid and additive used are completely mixed and homogeneous and compatible

2- Gelled acid can reduce the reaction rate and the amount reaction completion by controlling the penetration of H^+ ions, which shows that it can be used in optimal concentrations in matrix acidizing.

References

[1] Crowe, C., Martin, R., and Michaelis, A., *Evaluation of acid-gelling agents for use in well stimulation.* Society of Petroleum Engineers Journal, 1981. 21(04): p. 415-424.

[2] Economides, M.J. and Nolte, K.G., *Reservoir stimulation*. 2000: Prentice Hall Englewood Cliffs, NJ.

[3] Fan, Y., et al., *Experimental study of the influences of different factors on the acid-rock reaction rate of carbonate rocks.* Journal of Energy Storage, 2023. 63: p. 107064.

[4] Augustine, R., et al., *Polyuronates and Their Application in Drug Delivery and Cosmetics*. 2015. p. 239-269.